C55.612:978

PENNSYLVANIA STATE UNIVERSITY
MAY 21 1980
DOCUMENTS COLLECTION

Collected Reprints 1978

Atlantic Oceanographic and Meteorological Laboratories

December 1979

U.S. DEPARTMENT OF COMMERCE
National Oceanic and Atmospheric Administration

Collected Reprints 1978

Atlantic Oceanographic and Meteorological Laboratories
Miami, Florida

December 1979

Boulder, Colorado

U.S. DEPARTMENT OF COMMERCE
Philip M. Klutznick, Secretary

National Oceanic and Atmospheric Administration
Richard A. Frank, Administrator

Environmental Research Laboratories
Wilmot Hess, Director

S. Depository Copy

NOTICE

The Environmental Research Laboratories do not approve, recommend, or endorse any proprietary product or proprietary material mentioned in this publication. No reference shall be made to the Environmental Research Laboratories or to this publication furnished by the Environmental Research Laboratories in any advertising or sales promotion which would indicate or imply that the Environmental Research Laboratories approve, recommend, or endorse any proprietary product or proprietary material mentioned herein, or which has as its purpose an intent to cause directly or indirectly the advertised product to be used or purchased because of this Environmental Research Laboratories publication.

FOREWORD

The Atlantic Oceanographic and Meteorological Laboratories conduct research programs in the areas of physical, chemical, and geological oceanography, and sea-air interaction. Collected Reprints from these laboratories have been published for distribution to the libraries of scientific institutions here and abroad annually since the laboratories were established in 1965. The series provides a single reference source for articles published by AOML personnel in a broad spectrum of scientific and technical publications. Some back issues may be obtained upon request.

The volume, like the laboratories, is organized along functional, disciplinary, lines. Cross-disciplinary contributions resulting from collaboration among staff of the several parts of the organization appear according to the organizational affiliations of the senior author.

It is desired that those recipients with whom we do not already have an exchange arrangement will add the AOML Library to the distribution list for any relevant publications from their institution.

Donald V Hansen

Donald V. Hansen
Acting Director
Atlantic Oceanographic
and Meteorological
Laboratories
15 Rickenbacker Causeway
Miami, Florida 33149

Digitized by the Internet Archive
in 2012 with funding from
LYRASIS Members and Sloan Foundation

http://archive.org/details/collectedreprint1978atla

CONTENTS

Page

Foreword iii

OFFICE OF THE DIRECTOR

1. Rutowski, Dick.

Diving Accident Manual. Florida Underwater Council in Cooperation with the U.S. Department of Commerce NOAA, 16 pages. 1

2. Stewart, H.B., Jr.

How Can the Meteorologists and Oceanographers be of Use to the Mariner? Oceanology International '78, Technical Session E, Meteorology and Hydrography, 15-20. 18

3. Stewart, H.B., Jr.

The Rand McNally Atlas of the Oceans, Bulletin of the American Meteorological Society 59, No. 4, p. 417. 24

PHYSICAL OCEANOGRAPHY LABORATORY

4. deWitt, P.W. and A. Leetmaa.

A Simple Ekman-Type Model for Predicting Thermocline Displacement in the Tropical Pacific. Journal of Physical Oceanography 8, No. 5, 811-817. 25

5. Festa, J.F. and D.V. Hansen.

Trubidity Maxima in Partially Mixed Estuaries: A Two-Dimensional Numerical Model. Estuarine and Coastal Marine Science 7, 347-359. 32

6. Leetmaa, A. and A.D. Voorhis.

Scales of Motion in the Subtropical Convergence Zone. Journal of Geophysical Research 83, No. C9, 4589-4592. 45

7. Leetmaa, A. and A.F. Bunker.

Updated Charts of the Mean Annual Wind Stress, Convergences in the Ekman Layers, and Sverdrup Transports in the North Atlantic. Journal of Marine Research 36, No. 3, 311-322. 49

Page

8. Leetmaa, A.

Fluctuating Winds: An Energy Source for Mesoscale Motions. Journal of Geophysical Research 83, No. C1, 427-430. 61

9. Maul, G.A., P.W. deWitt, A. Yanaway, and S.R. Baig.

Geostationery Satellite Observations of Gulf Stream Meanders: Infrared Measurements and Time Series Analysis. Journal of Geophysical Research 83, No. C12, 6123-6135. 65

10. Maul, G.A., and A. Yanaway.

Deep Sea Tides Determination From GEOS-3. NASA Contractor Report 141435, 23 pages. 78

11. Molinari, R.L.

The Relationship of the Curl of the Local Wind Stress to the Circulation of the Cayman Sea and the Gulf of Mexico. Journal of Physical Oceanography 8, No. 5, 779-784. 104

12. Molinari, R.L., J.F. Festa, and D.W. Behringer.

The Circulation in the Gulf of Mexico Derived From Estimated Dynamic Height Fields. Journal of Physical Oceanography 8, No. 6, 987-996. 110

13. Molinari, R.L. and J.F. Festa

Ocean Thermal and Velocity Characteristics of the Eastern Gulf of Mexico Relative to the Placement of an OTEC Plant: A Progress Report. Proceedings Fifth Ocean Thermal Conference, February 20-22, 1978. Vol. 1 (of 4 volumes), Sections I-III Conf-780236, Dist. Category UC-64, III-64 - III-82. 120

14. Molinari, R.L. and J.F. Festa.

Ocean Thermal Properties in Relation to the Biofouling and Corrosion Experiment in the Gulf of Mexico. Proceedings Ocean Thermal Energy Conversion (OTEC) Biofouling and Corrosion Symposium, October 10-12, 1977, Seattle, WA., PNL-SA-7115, 413-422. 140

Page

15. Molinari, R.L. and L. Lewis.

Current Measurements for the Ocean Thermal Energy Conversion Program. Proceedings of a Working Conference on Current Measurement, Technical Report DEL-SG-3-78, College of Marine Studies, University of Delaware, Newark, DE, 237-254. 150

16. Peterson, D.H., J.F. Festa, and T.J. Conomos.

Numerical Simulation of Dissolved Silica in the San Francisco Bay. Estuarine and Coastal Marine Scinece 7, 99-116. 168

OCEAN CHEMISTRY LABORATORY

17. Cummings, S.R., Jr., D.K. Atwood, and J.M. Parker.

Synthesis and Description of the Existing Historical Inorganic Nutrient Data Sets From Three Potential OTEC Sites: Northern Gulf of Mexico, Puerto Rico, and St. Croix. Proceedings Ocean Thermal Energy Conversion (OTEC), Biofouling and Corrosion Symposium, October 10-12, 1977, Seattle, WA., PNL-SA-7115, 423-445. 186

18. Hatcher, P.G.

The Organic Geochemistry of Mangrove Lake, Bermuda. NOAA Professional Paper 10, 92 pages (Abstract only). 209

MARINE GEOLOGY AND GEOPHYSICS LABORATORY

19. Bennett, R.H., D.N. Lambert, B.A. McGregor, E.B. Forde, and G.F. Merrill.

SLOPE MAP, A Major Submarine Slide on the U.S. Atlantic Continental Slope East of Cape May. U.S. Department of Commerce Map Number A5787. 211

20. Bennett, R.H.

NOAA-Marine Geotechnical-Rational Use of the Seafloor (RUSEF) Program. Present and Recommended U.S. Government Research in Seafloor Engineering. U.S. Department of Commerce, NOAA, Office of Ocean Engineering, 7-13. 218

Page

21. Clarke, T.L.

An Oblique Factor Analysis Solution for the Analysis of Mixtures. Mathematical Geology 10, No. 2, 225-241. 225

22. Drake, D.E., P.G. Hatcher, and G.H. Keller.

Suspended Particulate Matter and Mud Deposition in Upper Hudson Submarine Canyon. Ch. 3 in Sedimentation in Submarine Canyons, Fans, and Trenches, ed. D.J. Stanley and G. Kelling (Dowden, Hutchinson and Ross, Stroudsburg, PA), 33-41. 242

23. Dunlap, W.A., W.R. Bryant, R. Bennett, and A.F. Richards.

Pore Pressure Measurements in Underconsolidated Sediments, Offshore Technology Conference, 10th Annual OTC, Houston, TX, May 8-11, 1978. OTC Proceedings 3168, 1049-1057. 251

24. Gadd, P.E., J.W. Lavelle, and D.J.P. Swift.

Estimates of Sand Transport on the New York Shelf Using Near-Bottom Current Meter Observations. Journal of Sedimentary Petrology 48, No. 1, 239-252. 261

25. Lavelle,, J.W., D.J.P. Swift, P.E. Gadd, W.L. Stubblefield, F.N. Case, H.R. Brashear, and K.W. Haff.

Fair Weather and Storm Sand Transport on the Long Island, New York, Inner Shelf. Sedimentology 25, 823-842. 275

26. Lavelle, J.W. and W.C. Thacker.

Effects of Hindered Settling on Sediment Concentration Profiles. Journal of Hydraulic Research 16, No. 4, 347-355. 295

27. Lavelle, J.W., R.A. Young, D.J.P. Swift, and T.L. Clarke.

Near-Bottom Sediment Concentration and Fluid Velocity Measurements on the Inner Continental Shelf, New York. Journal of Geophysical Research 83, No. C12, 6052-6062. 304

Page

28. McGregor, B.A.

Morphology of the Middle Atlantic U.S. Continental Slope and Rise. Southeastern Geology 19, No. 3, 191-205. (Publ. at Duke University, Durham, NC.) 315

29. McGregor, B.A.

Seismic Reflection Profiles of the United States East Coast Continental Margin. NOAA Technical Report ERL 398-AOML 28, 19 pages (Abstract only). 330

30. Nelsen, T.A.

A Simple and Rapid Normalization Method for Instrumental Drift During Energy-Dispersive X-Ray Analysis. Marine Chemistry 6, 343-349. 332

31. Nelsen, T.A., P.E. Gadd, and T.L. Clarke.

Wind-Induced Current Flow in the Upper Hudson Shelf Valley. Journal of Geophysical Research 83, No. C12, 6073-6082. 339

32. Rona, P.A.

Magnetic Signatures of Hydrothermal Alteration and Volcanogenic Mineral Deposits in Oceanic Crust. Journal of Volcanology and Geothermal Research 3, 219-225. 349

33. Rona, P.A.

Criteria for Recognition of Hydrothermal Mineral Deposits in Oceanic Crust. Economic Geology 73, No. 2, 135-160. 356

34. Rona, P.A.

Near Bottom Water Temperature Anomalies: Mid-Atlantic Ridge Crest at Latitude 26°N. Geophysical Research Letters 5, No. 12, 993-996. 382

35. Rona, P.A.

Book Review: Sedimentary Basins of Continental Margins and Cratons. Developments in Geotectonics, ed. M.H.P. Bott. (Elsevier, Amsterdam, 314 pp). Journal Paleogeography, Paleoclimatology, and Paleoecology 24, 389-390. 386

Page

36. Rona, P.A.

Plate Tectonics, Energy and Mineral Resources: Implications for Marine Engineering. Society of Naval Architects and Marine Engineers, STAR Symposium 2, 2-1 - 2-11. (New London, CT, April 26-29, 1978.) 388

37. Rona, P.A. and R.P. Lowell.

Hydrothermal Systems at Oceanic Spreading Centers. Symposium Report. Geology 6, 299-300. 399

38. Rona, P.A. and G.F. Merrill.

A Benthic Invertebrate from the Mid-Atlantic Ridge. Bulletin of Marine Science 28, No. 2, 371-375. 401

39. Rona, P.A. and E.S. Richardson.

Early Cenozoic Global Plate Reorganization. Earth and Planetary Science Letters 40, 1-11. 406

40. Scott, M.R., R.B. Scott, J.W. Morse, P.R. Betzer, L.W. Butler, and P.A. Rona.

Metal-Enriched Sediments from the TAG Hydrothermal Field. Nature 276, No. 21/28, 811-813. 417

41. Stanley, D.J. and G.L. Freeland.

The Erosion-Deposition Boundary in the Head of Hudson Submarine Canon Defined on the Basis of Submarine Observations. Marine Geology 26, M37-46. 420

42. Swift, D.J.P.

Book Review: Holocene Tidal Sedimentation (Benchmark Papers in Geology, 30), ed. G. Klein, (Wiley, London). Sedimentary Geology 21, 311-312. 430

43. Swift, D.J.P.

Continental-Shelf Sedimentation. The Encyclopedia of Sedimentology, The Encyclopedia of Earth Sciences Series VI, ed. R.W. Fairbridge and J. Bourgeois, 190-199. 432

Page

44. Swift, D.J.P., and G.L. Freeland.

Current Lineations and Sand Waves on the Inner Shelf, Middle Atlantic Bight of North America. Journal of Sedimentary Petrology 48, No. 4, 1257-1266. 442

45. Swift, D.J.P., B.F. Molnia, and R.G. Jackson, II.

Intermittent Structure in the Atmospheric Boundary Layer Made Visible by Entrained Sediment - Example from the Copper River Delta, Alaska. Journal of Sedimentary Petrology 48, No. 3, 897-900. 452

46. Swift, D.J.P., P.C. Sears, B. Bohlke, and R. Hunt.

Evolution of a Shoal Retreat Massif, North Carolina Shelf: Inferences from Areal Geology. Marine Geology 27, 19-42. 456

47. Swift, D.J.P., G. Parker, N.W. Lanfredi, G. Perillo, and K. Figge.

Shoreface-Connected Sand Ridges on American and European Shelves: A Comparison. Estuarine and Coastal Marine Science 7, 257-273. 480

48. Udintsev, G.B., V.M. Litvin, N.A. Marova, M.V. Rudenko, L.Y. Budanova, and P.A. Rona.

Marine Geology: New Data on the Morphostructure of the Central Part of the Mid-Atlantic Ridge. Oceanology 17, No. 5, 544-551 (Academy of Sciences of the USSR). 497

49. Young, R.A.

Suspended-Matter Distribution in the New York Bight Apex Related to Hurricane Belle. Geology 6, 301-304. 505

50. Young, R.A. and J.B. Southard.

Erosion of Fine-Grained Marine Sediments: Sea-Floor and Laboratory Experiments. Geological Society of America Bulletin 89, 663-672. 509

Page

SEA-AIR INTERACTION LABORATORY

51. Cardone, V.J., D.B. Ross, and M.R. Ahrens.

An Experiment in Forecasting Hurricane Generated Sea States. Proceedings 11th Technical Conference on Hurricanes and Tropical Meteorology, Dec. 13-16, 1977, Miami, FL. Volume of Conference Papers (AMS, Boston, Mass.) 688-695. 519

52. Proni, J.R. and H.B. Stewart, Jr.

Acoustic Techniques for Ocean Pollution Studies and Their Easy Transferability to Developing Nations. Interciencia 3, No. 1, ENE, 24-27. 527

53. Proni, J.R., F. Ostapoff, and R.L. Sellers.

Acoustic Observations of High-Frequency, Near-Surface Internal Wave Groups in the Deep Ocean During GATE. Deep-Sea Research 25, 299-307. 531

54. Proni, J.R., F.C. Newman, F. Ostapoff, and D.J. Walter.

Vertical Particulate Spires or Walls Within the Florida Current and Near the Antilles Current. Nature 276, No. 5686, 360-362. 546

55. Ross, D. and V. Cardone.

A Comparison of Parametric and Spectral Hurricane Wave Prediction Products. Turbulent Fluxes Through The Sea Surface, Wave Dynamics, and Prediction, NATO Conference on Turbulent Fluxes Through The Sea Surface, Wave Dynamics and Predicition, France 1977, Series V: Air-Sea Interactions, ed. A. Favre and K. Hasselmann 1, 647-665. 549

56. Ross, D. and W.L. Jones.

On the Relationship of Radar Backscatter to Wind Speed and Fetch. Boundary-Layer Meteorology 13, 151-163. 568

57. Shemdin, O.H., W.E. Brown, Jr., F.G. Staudhammer, R. Shuchman, R. Rawson, J. Zelenka, D.B. Ross, W. McLeish, and R.A. Berles.

Comparison of In Situ and Remotely Sensed Ocean Waves off Marineland, Florida. Boundary-Layer Meteorology 13, 193-202. 581

Page

58. Snyder, R.L., R.B. Long, F.W. Dobson, and J.A. Elliott.

The Bight of Abaco Pressure Experiment. NATO Conference on Turbulent Fluxes Through The Sea Surface, Wave Dynamics and Prediction, France 1977 Series V: Air-Sea Interactions, ed. A. Favre and K. Hasselmann 1, 433-443. 591

59. Teleki, P.G., R.A. Shuchman, W.E. Brown, Jr, W. McLeish, D. Ross and M. Mattie.

Ocean Wave Detection and Direction Measurements With Microwave Radars. MTS/IEEE - Oceans '78 Conference, Washington, D.C, September 6-8, 1978, 639-648. 603

60. Thacker, W.C.

Comparison of Finite-Element and Finite-Difference Schemes. Part I: One-Dimensional Gravity Wave Motion. Journal of Physical Oceanography 8, No. 4, 676-679. 613

61. Thacker, W.C.

Comparison of Finite-Element and Finite-Difference Schemes. Part II: Two-Dimensional Gravity Wave Motion. Journal of Physical Oceanography 8, No. 4, 680-689. 617

62. Thacker, W.C. and J.W. Lavelle.

Stability of Settling of Suspended Sediments. Physics of Fluids 21, No. 2, 291-292. 627

DIVING ACCIDENT MANUAL

by
Dick Rutkowski
National Oceanic and Atmospheric Administration
April 1978

REVISED JANUARY 1979

Edited by Chuck Gibson

CONTENTS

General 1
Who Could Be a Diving Accident Victim 2
On Site Management 3
Mild Symptoms 3
Severe Symptoms 3
Emergency Evacuation Procedures 4
Communications 4
Medical Evacuation Procedures 5
Danger Using in-water Recompression 6
C.P.R. (Figure 1) 6
Treatment Flow Chart (Figure 2) 7
Accident Information 8
Oxygen 9
The Trendelenberg Position 9
Gas Embolism 10
Decompression Sickness 11
Mediastinal Emphysema 12
Subcutaneous Emphysema 12
Pneumothorax 13
Recompression Chamber Requirements 14
Helicopter Evacuation Procedures 14
Bubble Trouble 15

This manual is published to further safety in diving. Articles may be excerpted or reprinted for use in other publications as long as the Florida Underwater Council and the author, Dick Rutkowski, are given credit. All correspondence and orders for additional copies should be addressed to:

Dick Rutkowski
Florida Underwater Council
75 Virginia Beach Drive
Miami, Florida 33149

The information contained in this manual is a simplified version of how to stablize a diving accident victim and get him into the hyperbaric trauma system (diving physician and recompression chamber). It is meant for lay persons, paramedics, physicians and evacuation personnel who have little understanding of hyperbaric medicine (diving medicine), and is not intended to indicate any form of treatment.

The information contained herein comes from many sources and was compiled to provide guidance in the handling of diving accident victims. It is being published to help save time and lives.

The author would like to acknowledge the following organizations for their assistance in the development of this manual:

NOAA'S Atlantic Oceanographic and Meteorological Laboratories

NOAA'S Manned Undersea Science and Technology Office

The United States Coast Guard

The Florida Underwater Council

Dade County Fire Rescue (Florida)

University of Miami School of Medicine, Aquatic Medical Team

REPORTING OF DIVING ACCIDENTS

A complete accident report should be forwarded within one week, fatal or non-fatal, To:

National Underwater Accident Data Center
P. O. Box 68
Kingston, R. I. 02881

Throughout the country, recompression chambers are now appearing, complete with hyperbaric trauma teams. Many divers believe that all their diving problems are solved if a chamber is nearby. Divers should be aware that diving medical problems can be very complex.

A hospital in the community is not going to assist the unconscious victim of a heart attack lying in the street. Someone must begin lifesaving CPR (Cardio-Pulmonary Resuscitation), and call for help. In the case of divers, the situation is the same. A diving accident procedure must be followed to insure that immediate and proper attention is given to the victim at the dive accident site. This initial treatment and procedure may affect the condition of the patient upon arrival at the recompression chamber, as well as influencing the residual problems that the patient may have after treatment.

HOW TO RECOGNIZE A DIVING ACCIDENT VICTIM

A diving accident victim could be any person who has been breathing air underwater regardless of depth. Gas embolism can occur in as little as 2-4 feet of water (70 mmhg) if one ascends holding his breath. Even a well-trained diver may encounter problems because of respiratory medical problems. Asthma, broncholithiasis, congenital or acquired cysts, emphysema, fibrosis, tuberculosis and infection, especially fungal, obstructive lung diseases may result in air trapping during ascent, this expansion of trapped air may be sufficient to rupture air spaces. The escaping air may cause emphysema of the lungs, mediastinum, or neck. Alternatively, it may cause pneumothorax. Finally, arterial air embolism may result.

Decompression sickness (usually the least serious of the barotrauma illnesses) can occur in any individual who violates the decompression tables either willingly or unintentionally when surfacing from depths greater than 30 feet.

Bubble trouble can happen to anyone, anywhere, at anytime, far out at sea, in home swimming pools - lakes - harbors - canals and from submerged cars.

To insure a successful treatment, instructors, divemasters, EMT's, rescue personnel, physicians, and emergency room personnel must be able to recognize the problem, begin diving accident treatment procedures and move the victim into the hyperbaric trauma system as soon as possible.

In the presence of a medical emergency exhibiting any signs resembling those of a diving accident, there is one primary question. "Did the subject breath air underwater?" If the answer is "Yes", you must regard the subject as a diving accident victim, especially in the case of unconsciousness. The diving accident treatment procedure must be initiated immediately. This includes restoration of vital signs, administering oxygen, Trendelenberg Position, and immediate evacuation to the recompression chamber complex.(Follow flow chart, Fig. 2)

ON SITE MANAGEMENT

A major problem with divers is that they tend to ignore the mild symptoms of bubble trouble in the early stages. By doing so, they eventually have more serious symptoms. Immediate diving accident identification can be broken down and handled in two categories - mild and severe symptoms. (See flow chart, Fig. 2) To simplify identification all symptoms of gas embolism and decompression sickness will be considered together. To simplify the procedure, formal medical terms will not be used.

Mild Symptoms

Mild symptoms are those that can be treated at the dive site by the diver using surface oxygen (Flow chart, Fig. 2). Indifference, fatigue, skin rash, and weakness are considered mild symptoms. Although joint pain is also considered a mild symptom, it will be treated as a severe symptom according to the Flow chart because recompression is required.

If a diver comes up from a dive and acts indifferent, appears not to know what is going on, or ignores people trying to communicate with him, this may be an early warning of bubble trouble. The same applies to extreme fatigue, weakness, or skin rash.

Do not hesitate, place this person on surface oxygen, head downward (Trendelenberg Position). Also refer to Flow Chart Fig. 2 and follow the Flow Chart through to the final stage. Doing this often relieves the symptoms or prevents them from getting worse. Surface oxygen, and assuming the Trendelenberg Position has been successful in being the complete treatment. The biggest problem in the early stages is the diver's ego. Divers do not want to admit there is anything wrong with them and refuse to be put on oxygen because they feel others will think less of their diving ability. *Do not let your ego or the patient's ego overule common sense.* Use surface oxygen and place the patient in the Trendelenberg Position immediately. If the symptoms appear to be relieved after the patient has been on oxygen for a short period of time do not remove the oxygen immediately, as bubbles will reload from gases in the surrounding tissue, and the symptoms will reoccur. If symptoms are relieved in 10 minutes, keep the patient on oxygen for 30 minutes total. If symptoms get worse, find new symptom on Flow chart and follow chart recommendations.

SEVERE SYMPTOMS

Severe symptoms are those that require immediate treatment and evacuation into the hyperbaric trauma system (See Flow Chart Fig. 2). If the victims vital signs cease to function, CPR will be required This is first and foremost (CPR Fig. 1) in diving accident treatment. If a patient comes up from a dive, or anytime within 24 hours after a dive, and shows any of the severe symptoms indicated on the Flow Chart, immediately place the patient on surface oxygen and in the Trendelenberg Position after insuring vital signs are functioning properly, and follow the Flow Chart to eventual evacuation to a recompression chamber.

It is important to remember that because these signs/symptoms can develop hours after diving, the patient may show up in a hospital emergency room or other medical facilities in the community. For this reason, it is important for para-medics and physicans to recognize the symptoms and to understand this hyperbaric problem so that the diving accident procedure can be initiated. It is also extremely important that any person delivering a diving accident patient to professional medical personnel explain this procedure to them, so that the patient will receive proper recompression if needed.

EMERGENCY EVACUATION

Once it has been established that the patient is a diving accident victim, and someone is caring for his immediate medical needs (vital signs, surface oxygen, and Trendelenberg Position), someone must also be initiating the evacuation protocol into the hyperbaric trauma system.

Because many divers and/or boaters fail to plan emergency evacuation procedures in advance, a great amount of critical time is often lost, causing needless suffering and possible loss of life. The most important part of any dive and/or boat trip is to know your procedure for emergency evacuation.

Many medical problems, including those resulting from diving accidents, could occur at anytime at sea. Because some symptoms are delayed in their onset, it is not only necessary to know how to contact a hyperbaric trauma team at sea, but also on land. Many divers have been diving in one country and returned to another before symptoms occured.

COMMUNICATIONS

If you have a radio on board, contact the Coast Guard Directly, 2182 HF or channel 16 VHF marine band. Declare an emergency and state type of emergency. E. G."This is a diving accident victim needing treatment in a recompression chamber". Give your exact location by direction and distance from prominent land marks. Give all symptoms of the victim and dive history if applicable. State the condition of victim, ie., can he walk, sit up, or is he unconscious. Describe any unusual circumstances, and the number of victims. Give detailed description of your boat, including any outstanding features for identification. Give weather, sea condition, wind direction and speed.

If you should change your location, keep all concerned advised of your new location and your intentions.

The Coast Guard does monitor CB, CH 9. This is a very unreliable means of communications for many reasons. If you are unable to raise the Coast Guard via CB, contact someone else to relay your messages.

If you have no radio on your boat, if practical, hail a boat with a marine band radio and give them the information to relay to the Coast Guard. Keep them with you for further contacts. The International Convention for safety of life at sea requires the providing of assistance to vessels in distress.

If no other boats are immediately available, proceed immediately to the nearest inhabited dockage and telephone local para-medical or USCG services. Advise them of a diving accident, state your need for transportation and your EXACT location. Have someone remain at the telephone for further assistance. Insure that they are aware at this time that a recompression chamber will be needed.

If symptoms occur on land after diving, contact local para-medics or USCG. They should be able to assist or advise location of nearest recompression chamber.

When the rescue aircraft arrives in your area, wave, fire flares or smokes. LET THEM KNOW YOU ARE THE ONES WHO WANT ASSISTANCE. Do not assume the pilot will recognize you. He may waste valuable time searching for you unnecessarily.

MEDICAL EVACUATION PROCEDURES

The following medical evacuation information should be forwarded with the patient. If possible, take time to explain the following steps to the physician or para-medic. Don't assume they understand the reasons why oxygen should be administered to a diving accident victim. If a person is breathing normally, the physician may take him off oxygen not realizing the patient must be kept on to continue to offload the bubbles. When this has been explained the following steps should be followed:

1. Maintain breathing and heart functions, insure airway is open and remains open.
2. Keep patient on oxygen and incline head downward, left side down, during transportation.
3. Insure para-medic/physicans understand why head downward, left side, on oxygen is required until patient arrives at chamber.
4. Insure para-medics/physicans understand why patient needs to be taken to a recompression chamber instead of a hospital.
5. Do not remove oxygen from diving accident patient unless you need to reopen airway, or he shows signs of oxygen convulsions, even if patient is breathing normally. Without oxygen, bubbles will reload with nitrogen and cause increasing symptoms.
6. Keep patient out of hot sun, watch for possibility of shock.
7. Do not give any pain killing drugs, 1. I.V.'s can be given to prevent vascular collapse or dehydration, (D5LR, Plain LR or D1/2N. S.). 2. Two aspirins orally.
8. Instruct flight crews to fly or pressurize aircraft below 1000 ft. This should only be attempted without hazard to aircraft.
9. Provided the aircraft can handle extra weight, diving buddy should be transported with patient, as he may also need recompression and can be useful with information, comfort and contact with patient's parents/relatives.
10. A complete history of all events leading up to the accident and until evacuation must be forwarded with the patient.
11. Depth gauges, tanks, regulators, and other diving equipment should be forwarded with patient if weight limitations allow, especially if the accident is fatal.

FLORIDA UNDERWATER COUNCIL

DIVING ACCIDENT MANAGEMENT

CARDIOPULMONARY RESUSCITATION (CPR)

IF UNCONSCIOUS

A

AIRWAY OPENED

- LIFT NECK
- EXTEND HEAD

Airway Obstructed

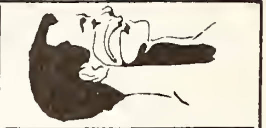

Airway Opened

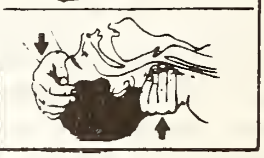

IF APNEIC

B

BREATHING RESTORED

- PINCH NOSE
- OPEN MOUTH
- SEAL AROUND LIPS
- INFLATE LUNGS–WATCH CHEST RISE
- REMOVE MOUTH
- REPEAT 12 TIMES/MIN
  - 20-30 TIMES/MIN FOR CHILDREN

Mouth-to-Mouth
ALSO
Mouth to Nose
Mouth to Adjunct
Mouth to Mask
Bag Valve Mask

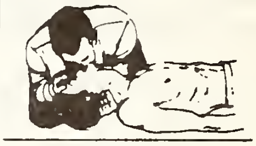

Check Pulse

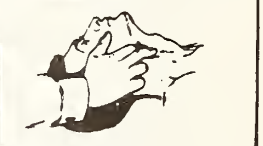

IF PULSELESS

C

CIRCULATION RESTORED

- COMPRESS LOWER 1/2 OF STERNUM
- 60-80 COMPRESSIONS/MIN
- DO NOT COMPRESS OVER XIPHOID
- TWO RESCUERS
  - 5 CHEST COMPRESSIONS
  - 1 INTERPOSED LUNG INFLATION
- ONE RESCUER
  - 15 CHEST COMPRESSIONS
  - 2 QUICK LUNG INFLATIONS

Depress Lower Sternum 1 1/2 to 2 inches

Keep Arms Straight

Check Pupil

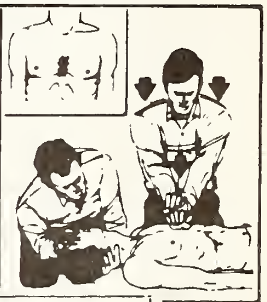

DO NOT INTERRUPT CPR –

DANGER

DO NOT ATTEMPT IN—WATER RECOMPRESSION

In-water recompression should never be attempted in a diving accident. At best it is very dangerous. If a person shows mild signs/symptoms of decompression sickness and is placed in the water for recompression, usually the only thing that happens is that the bubbles are further loaded with nitrogen causing the signs/symptoms to get worse. The prolonged exposure of the diver to the water, regardless of temperature, may eventually force him to the surface with incomplete decompression, not to mention there is usually not enough air at a dive site to accomplish a complete in-water recompression treatment.

The victim should be evacuated as soon as possible, especially in severe symptoms cases according to Flow Chart (Fig. 2). (on oxygen and in the Trendelenberg Position)

Note: Unconscious diver must go immediately and directly to recompression chamber regardless of diving depth.

FLORIDA UNDERWATER COUNCIL

DIVING ACCIDENT MANAGEMENT FLOW CHART

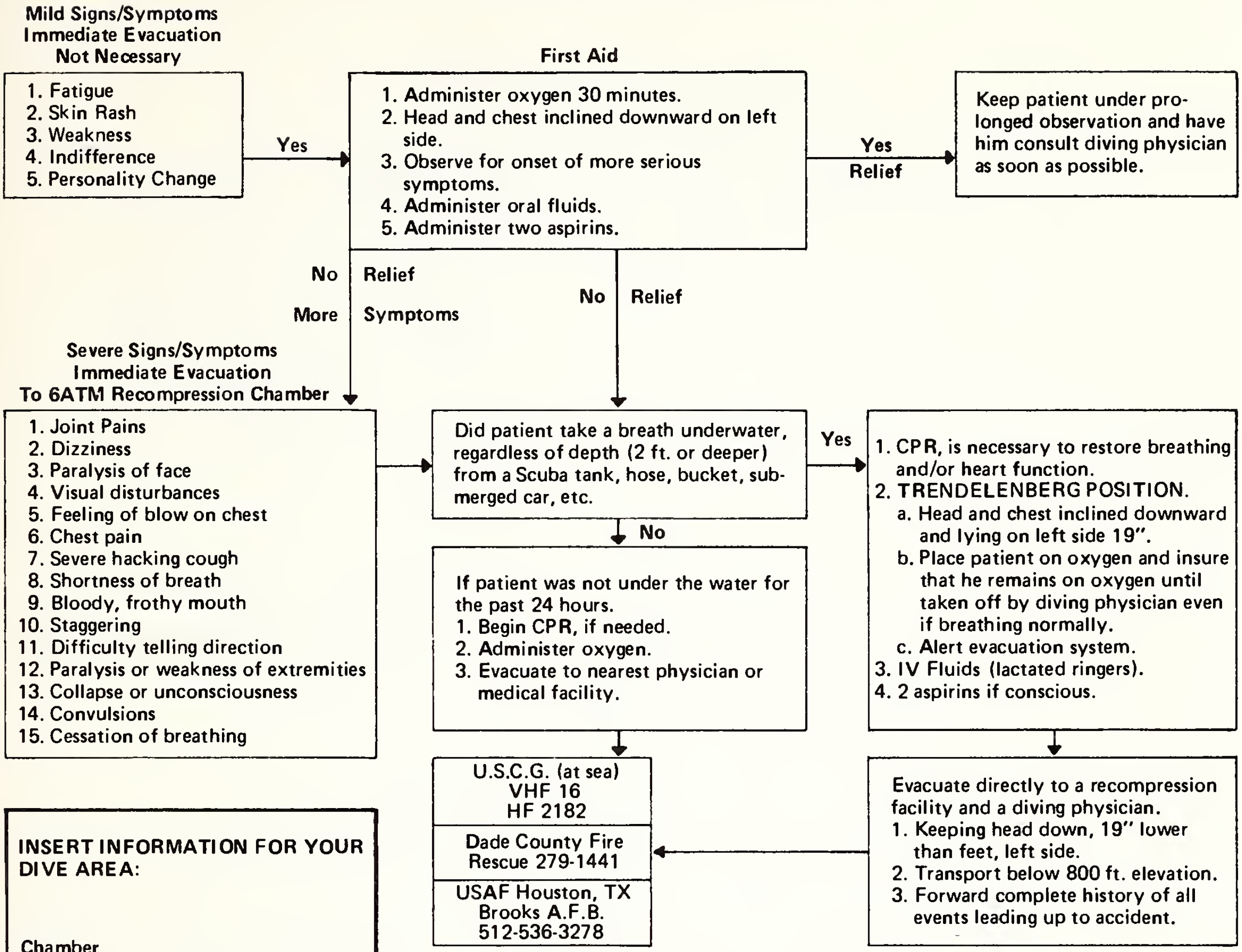

Mild Signs/Symptoms
Immediate Evacuation
Not Necessary

1. Fatigue
2. Skin Rash
3. Weakness
4. Indifference
5. Personality Change

Yes →

First Aid

1. Administer oxygen 30 minutes.
2. Head and chest inclined downward on left side.
3. Observe for onset of more serious symptoms.
4. Administer oral fluids.
5. Administer two aspirins.

Yes Relief →

Keep patient under prolonged observation and have him consult diving physician as soon as possible.

No Relief / More Symptoms ↓

No Relief ↓

Severe Signs/Symptoms
Immediate Evacuation
To 6ATM Recompression Chamber

1. Joint Pains
2. Dizziness
3. Paralysis of face
4. Visual disturbances
5. Feeling of blow on chest
6. Chest pain
7. Severe hacking cough
8. Shortness of breath
9. Bloody, frothy mouth
10. Staggering
11. Difficulty telling direction
12. Paralysis or weakness of extremities
13. Collapse or unconsciousness
14. Convulsions
15. Cessation of breathing

Did patient take a breath underwater, regardless of depth (2 ft. or deeper) from a Scuba tank, hose, bucket, submerged car, etc.

Yes →

1. CPR, is necessary to restore breathing and/or heart function.
2. TRENDELENBERG POSITION.
   a. Head and chest inclined downward and lying on left side 19".
   b. Place patient on oxygen and insure that he remains on oxygen until taken off by diving physician even if breathing normally.
   c. Alert evacuation system.
3. IV Fluids (lactated ringers).
4. 2 aspirins if conscious.

No ↓

If patient was not under the water for the past 24 hours.
1. Begin CPR, if needed.
2. Administer oxygen.
3. Evacuate to nearest physician or medical facility.

U.S.C.G. (at sea)
VHF 16
HF 2182

Dade County Fire
Rescue 279-1441

USAF Houston, TX
Brooks A.F.B.
512-536-3278

Evacuate directly to a recompression facility and a diving physician.
1. Keeping head down, 19" lower than feet, left side.
2. Transport below 800 ft. elevation.
3. Forward complete history of all events leading up to accident.

INSERT INFORMATION FOR YOUR DIVE AREA:

Chamber ____________________

Rescue ____________________

Coast Guard ____________________

Diving Doctor ____________________

DIVING ACCIDENT POSITION (TRENDELENBERG

USE FOR: EMBOLISM, BENDS OR NEAR DROWNING

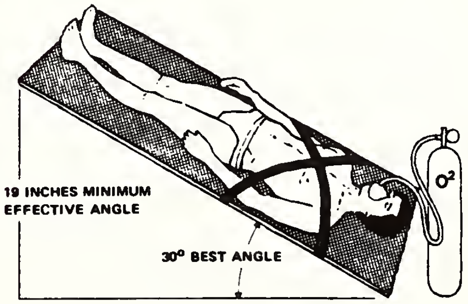

- HEAD LOWERED
- LEFT SIDE LOWER (IF POSSIBLE)
- ADMINISTER 100% OXYGEN (IF AVAILABLE)
- STRAP VICTIM IN PLACE BUT DO NOT INTERFERE WITH RESPIRATION

NOTE: Head down increases pressure and oxygen to upper part of body.

Oxygen begins to off load bubbles and delivers a greater supply to areas cut from oxygen.

Aspirin prevents platelet clumping. Fluids help balance blood electrolytes.

Note: Unconscious diver must go immediately and directly to recompression chamber regardless of diving depth.

by: Dick Rutkowski, NOAA, AOML

UNDERWATER ACCIDENT REPORT

FORWARD REPORT WITH PATIENT

VICTIM INFORMATION

Name of Victim: ....
Last First Middle

Address: ....

.... State ....

Victim's Sex .... Age ...... Hgt. ...... Wgt. ......

Marital Status: M .... S .... D .... W .... UNK .....

Occupation ....

....

DESCRIPTION OF DIVES AND ACTIVITIES

Description of all dives within previous 12 hours including accident dive

Depth	Time Down	Surface Interval
....	....	....
....	....	....
....	....	....
....	....	....
....	....	....
....	....	....

Type of Diving: (Explain if Necessary)

Scuba .... Skin .... Other ...... Unknown ......

Others in accident .... (Yes or No)

Separate report filed .... (Yes or No)

At time of incident, activities engaged in: ......

Recreational ......

Commercial ......

Under instruction ......

Instructing ......

Cave diving ......

Spear fishing ......

Photography ......

Night diving ......

At time of incident, buddy record: ......

Diving alone ......

Diving with buddy ......

Buddy distance ......

Diving with more than one ......

Distance to next nearest diver ......

Vessels involved .... (Yes or No)

U.S. Coast Guard aid sought .... (Yes or No)

(Give Details in "Description of Accident," Name, Captain, Address, Phone, etc.)

WITNESSES

Next of Kin	Address	Phone	Function/Role
....	....	....	....
....	....	....	....
....	....	....	....

WITNESS

Name ....

Address ....

City .... Phone ....

ON SITE PHYSICAN/PARA-MEDIC:

Name ....

Address ....

City .... Phone ....

DETAILED DESCRIPTION OF ACCIDENT

Describe in detail how the accident happened, including what the person was doing, any specific marine life or objects and the action or movement which led to the event. Include details of first aid or resuscitation efforts. Describe any "Decompression" and/or "Recompression-Treatment" in description of accident. List previous known medical problems and/or allergies.

....

....

....

....

....

....

....

....

....

....

....

....

WHY OXYGEN IS ADMINISTERED

When oxygen is breathed, the oxygen partial pressure (PO^2) of the blood is increased. This establishes a steeper gradient across the bubble-tissue interface and aids in the elimination of inert gases (from the bubble), reducing the bubble size to some extent. Additionally, the elevated (PO^2) allows better oxygenation of tissues where the blood supply is marginal, because the initial bubble has impaired that flow. Although this discussion relates to the use of oxygen at sea level as a first aid measure, the same principles apply to the use of oxygen under hyperbaric conditions.

Tissue integrity depends essentially upon two factors: (1) adequate PO^2 and (2) adequate flow to deliver the oxygen. Even though there is some vasoconstriction, the flow should be adequate with the improved PO^2 to help reduce bubble size and to supply oxygen-poor tissues.

THE TRENDELENBERG POSITION

The Trendelenberg Position means head down, but with legs bent at the knees. The Scoltetus Position means head down with the legs straight. Either position would be satisfactory to accomplish the goals mentioned.

A patient is put into the head-down position for several reasons. In the case of embolism, it prevents further intravascular bubbles from reaching the cerebral circulation. This is explainable simply as counteracting gravity, for as the lighter bubbles rise, they will, hopefully, pass to the lower extremities, rather than to the head.

In the case of decompression sickness, the position should be used particularly if the patient is in shock, because it will allow a better flow of blood back to the "core organs" (heart, lungs, brain, and kidneys). If there are bubbles in the systemic circulation (left side of the heart), the position also prevents their migration to the circulation in the same manner as described for embolism cases.

SIGNS AND SYMPTOMS

Knowing the causes, signs and symptoms is necessary to insure the proper treatment of a diving accident victim. You should be able to recognize the following:

GAS EMBOLISM

As a diver surfaces, the gas trapped in the lungs expands, rupturing the alveoli. Bubbles of gas are forced into the circulatory system, to the heart, and distributed to the body tissues. As the ascending diver is normally in a vertical position, these bubbles tend to travel upward toward the brain. As the bubbles enlarge and pass into smaller arteries,they reach a point where they can move no further, and cut off circulation. The effects of halting circulation, especially to the brain, are serious and require immediate treatment. Symptoms of embolism occur within 3-5 minutes of surfacing. One, a few, or all of the symptoms may be present.

Symptoms:

Fatigue
Weakness
Dizziness
Paralysis of extremities or face
Visual disturbances such as blurring
Feeling of blow on chest, progressively worsening
Cough or shortness of breath

Signs:

Sudden unconsciousness (usually immediately after surfacing, possibly before surfacing)
Bloody, frothy sputum
Staggering
Confusion or difficulty in seeing (i.e., moving in a wrong direction, bumping into objects)
Paralysis or weakness in extremities or face
Collapse or unconsciousness
Convulsions
Cessation of breathing

Treatment:

Immediate first aid is to place the victim with head and chest inclined downward and lying on his left side. This position lessens the chances of bubbles being carried to the brain. Also, breathing 100 percent pure oxygen, if available, is indicated. Begin oxygen treatment for air embolism in route to a recompression chamber. Treatment for air embolism is immediate recompression in a recompression chamber. This may reduce the size of the bubbles to the point where the circulation of blood may resume. The victim should be recompressed to 165 feet as soon as possible, and treated on the appropriate treatment table. Under no circumstances should the victim be taken back into the water to depth for treatment.

DECOMPRESSION SICKNESS

Decompression sickness (bends, caisson disease, compressed air illness) is the result of inadequate decompression following exposure to increased pressures. While immediate recompression is not a matter of life and death as with air embolism, the quicker recompression is initiated the better the rate of recovery. While under pressure, the inert portion of the breathing gas (nitrogen, helium, etc.) is passed, into solution in the blood and absorbed by the body tissues. As long as the diver remains under pressure this gas presents no problems. Should the pressure be quickly removed (as in rapid surfacing) the inert gas can come out of solution and form bubbles in the tissues and blood stream. The controlled ascent permits the body to rid itself of excess inert gas at a rate which will enable it to remain in solution.

Symptoms

Symptoms of decompression sickness are extremely varied, and are in many cases similar to air embolism. The effects of air embolism will be noticeable prior to or immediately after the diver surfaces. Any occurrence of symptoms more than ¼ hour after the diver reaches the surface can generally be assumed not to be air embolism. The most frequent symptoms of decompression sickness and frequency with which they occur are listed below.

Symptoms	Frequency of occurence (percent)
Local pain:	
(described as deep-boring	89
Leg	30
Arm	70
Dizziness (staggering)	5.3
Paralysis	2.3
Shortness of breath	1.6
Extreme fatigue and pain	1.3
Collapse and unconsciousness	.5

Signs

Evidence of local pain (rubbing arm, limp, favoring one side)
Staggering, clumsiness, lack of response as if drunk
Paralysis or partial paralysis
Blotchy or noted rash on skin
Shortness of breath
Collapse and unconsciousness

Treatment

The treatment for decompression sickness is recompression as quickly as possible according to the symptoms. Any symptom except a rash and local pain is considered a serious symptom and should be treated as such. Administer 100 percent pure oxygen in route to a recompression chamber.

While decompression sickness may, in some rare cases, occur up to 24 hours after the exposure to pressure, the vast majority of cases (95 percent) will be evident within 3 hours. Fifty percent will occur within 30 minutes and 85 percent within an hour. Only 1 percent will be delayed over 6 hours.

MEDIASTINAL EMPHYSEMA

Mediastinal emphysema may result from a ruptured pleural bubble or injury to the lung, esophagus, trachea, or main stem bronchus. While not serious in itself, it may be an indication of an embolism.

Symptoms

Pain under the breastbone (sternum) which may radiate to the neck, neck bone or shoulder
Shortness of breath
Faintness

Signs

Blueness (cyanosis) of skin, lips, or fingernails
Difficulty breathing
Shock

Treatment

Unless air embolism is also present recompression is not necessary. Medical assistance should be obtained, and oxygen administered if necessary.

SUBCUTANEOUS EMPHYSEMA

Subcutaneous emphysema has the same initiating mechanism as gas embolism but is not as serious as gas embolism. This condition results when air escapes into the tissues just under the skin (subcutaneous) and normally occurs in the area of the neck and/or collarbone.

Symptoms

Feeling of fullness in neck area
Change in sound of voice

Signs

Swelling or inflation around the neck
Crackling sensation when skin is moved
Change in sound of voice
Difficulty in breathing or swallowing

Treatment

Unless complicated by air embolism, recompression is not necessary. Seek the services of a physician and administer oxygen if breathing is impaired.

PNEUMOTHORAX

Pneumothorax is the result of the presence of air between the lung and the inner wall of the chest cavity. As the air continues to expand, partial or total collapse of the lung may result. In serious cases, displacement of the heart could result.

Symptoms

Sudden onset of cough
Shortness of breath
Sharp pain in the chest, usually made worse by breathing

Signs

Blueness (cyanosis) of skin, lips, and fingernails
Pain in chest, evidenced by grimacing or clutching chest
A tendency to bend the chest toward the side involved
Rapid, shallow breathing

Treatment

First aid: administer oxygen. If air embolism is not present, recompression may not be necessary. If breathing is difficult, recompress the victim to a point of relief. Extreme caution must be exercised during subsequent decompression as dissipation of the trapped air may not have taken place. Seek the services of a doctor as in serious cases direct removal of trapped air may be necessary.

HELICOPTER EVACUATION PROCEDURES

Each helicopter evacuation is different, each one presents its own problems, but knowing what to expect and the procedures to follow can save time, effort, and perhaps a life.

1. Try to establish communications with the helicopter. If your boat is unable to furnish the necessary frequency, try to work through another boat.
2. Maintain speed of 10 to 15 knots, do not slow down or stop.
3. Maintain course into wind about 20 degree's on port bow.
4. Put all antennas down if possible, without losing communications.
5. Secure all loose objects on/or around decks.
6. Always let the lifting device (stretcher) touch the boat before handling it to prevent electric shock.
7. Place life jacket on patient.
8. Tie patient in basket, face up.
9. If patient cannot communicate, place in the stretcher as much information as you can about him, such as, name, age, address, what happened, and what medication he has been given.
10. If the patient is a diving accident victim insure flight crew has copy of, or is instructed on, medical procedures for diving accidents.
11. If diving accident victim, insure flight crew delivers victim to hyperbaric trauma system. (recompression chamber complex)
12. If patient dies, inform flight crew so that they take no unnecessary risks.

RECOMPRESSION CHAMBER REQUIREMENTS

Diving accident management protocol suggests a recompression chamber that is muli-lock and 6 atmospheres. Do not take critical diving accident victims to a chamber which is one-man, single lock, 3 atmospheres. There are two major reasons why:

1. Pressure must be sufficient to reduce bubble size (gas embolism requires 6 atmospheres).
2. Physicians have no way getting hands on victim to:
   - (a) Maintain vital signs
   - (b) Keep airway clear
   - ,(c) Perform neurological examinations, necessary to determine proper treatment, or reoccurance of symptoms.
   - (d) Monitor vital signs during treatment.
   - (e) Operations may have to be performed, such as intubation
   - (f) Pulmonary overdistention cases may have air leakage causing a tension pneumothorax which must be relieved, and monitored during decompression periods.
   - (g) Oxygen convulsions may close off victim's glottis, and victim could develop an embolism while dropping pressure to relieve convulsions.

Be very cautious about transporting patients in small onelock chambers for the above reasons. It is often better to transport without chamber and maintain vital signs using surface oxygen and the Trendelenberg Position.

GOING DIVING ?

DO YOU KNOW THE SYMPTOMS OF BUBBLE TROUBLE? LEARN THEM

Any unusual or unexplained sensation occurring after a scuba dive, including:

Pain
Any unusual joint sensation
Extreme fatigue
Itching, possibly with rash
Swelling
Chokes
Blood from the mouth
Shock (collapse)
Indifference or personality change
Visual Disorder
Convulsions
Staggering gait
Weakness or paralysis
Numbness (limbs feel "asleep")
Loss of consciousness
Hearing defect
Dizziness
Facial paralysis

ANY of the above may indicate Bubble Trouble. Seek aid immediately. For Bubble Trouble (decompression sickness or air embolism), recompression is the treatment of choice.

Delay in recompression may cause permanent injury. Don't Avoid Recompression! Better late than never!

TEN COMMANDMENTS OF BUBBLE TROUBLE

1. Administer CPR, if necessary.
2. Place victim on his back with his head lowered and feet elevated.
3. Administer oxygen.
4. If no oxygen is available and victim is breathing, position victim with his left side down, head lowered and feet elevated.
5. Advise nearest chamber of estimated time of arrival.
6. Secure immediate transport to nearest recompression chamber.
7. Maintain victim on oxygen during transport.
8. En route (or as soon as possible):
   - A. Reconstruct dive profiles for last few dives (days).
   - B. Obtain victim's medical history.
   - C. Determine victim's current medications. (Don't give any pain medication.)
9. Dive buddies come to chamber with victim – or as quickly as able – or phone information to chamber.
10. Bring victim's equipment to chamber for examination.

The MIAMI RECOMPRESSION CHAMBER is alerted by calling any of the following:

Dade County Fire Rescue	(305) 279-1441
U.S. Coast Guard	(305) 350-5611
Radio HF	2182
Radio VHF	Channel 16

The emergency number is listed under "Emergency Numbers," on the inside cover of the Greater Miami Alphabetical phone book, under "Recompression Chamber."

KNOW WHERE YOUR NEAREST RECOMPRESSION CHAMBER IS! – KNOW HOW TO ALERT THE CHAMBER! – KNOW HOW TO GET THERE!

This information has been prepared from studying local diving accidents, by the Diving Accident Research Team (DART) of the Florida Underwater Council, and the Aquatic Medicine Team (AMT) of the University of Miami/Jackson Memorial Medical Center.

For Council and Chamber information:

Broward County	Dade County
987-9511 (evenings)	361-5764 (ext. 378) 361-5006 666-4727 (evenings)

Florida Underwater Council, Inc.

Conservation, Education and Safety – supported by your tax deductible donations

2

Technical Session E, Meteorology and Hydrography, Programme Arranged by Underwater Technology, Oceanology International 78, 15-20.

HOW CAN THE METEOROLOGISTS AND OCEANOGRAPHERS BE OF USE TO THE MARINER?

Harris B. Stewart, Jr.
Atlantic Oceanographic & Meteorological Laboratories
NOAA, Virginia Key
Miami, Florida U.S.A.

Most scientists have as the goal of their research the development of some bit of new knowledge, the solution of some previously unresolved problem, the determination of some hitherto unknown cause and effect relationship, or the formulation of a new hypothesis to explain a curious phenomenon. For many scientists, especially those concerned with what has come to be known as "basic research", the discovery and presentation of a "new truth" is their end product and also the end of their interest in that particular research effort.

Personally I heartily dislike the arbitrary split of research into "basic" and "applied" categories, for one man's basic is another's applied. But let me give an example of what I mean, an example that I believe was first put forward by Dr. Harrison Brown of the National Academy of Sciences. Assume that in the mid-19th Century, it was decided that the street lighting in London was totally inadequate and that something needed to be done to improve it. The Royal Society would have been asked to address the problem. They probably would have appointed a parent committee which then would in turn have appointed a group of panels to address specific aspects. One panel on lenses, one on wicks, probably one on fuels and each would have been allotted a certain sum of money to do research to improve the lenses, wicks, and fuels then in use, but there would have been no financial support for, or recognition of the relevance of, the work of Maxwell, Faraday, and the others whose research eventually led to a considerable improvement in the lighting of London's streets.

So at the beginning I will dispense with the basic-applied categorization and will merely refer to research *per se.* Most meteorologists and oceanographers are interested more in understanding the mysteries of the atmosphere and the ocean than they are in how their results can be applied—even as Maxwell and Faraday were more interested in a fascinating phenomenon than they were in improving street-lighting in London. Thus it often devolves onto the shoulders of others to attempt to translate the results of dedicated meteorological and oceanographic researchers into useful tools for those who must deal with the atmosphere and the ocean on a somewhat less research-orientated basis.

With this as my present task, I will attempt to review briefly some of the more recent results of research carried out in meteorology and oceanography at the research laboratories of the National Oceanic and Atmospheric Administration (NOAA) in the U.S.A. I will try especially to show how these results can be used by the mariner and others who work at sea to make their tasks more efficient, less dangerous, or perhaps just easier to accomplish.

Probably surface waves constitute the major problem not only for the mariner but also for those involved in the design of ships and offshore structures. Waves at sea present an incredibly complex problem. Individual wind-induced wave trains are a function of wind speed, the length of time the wind has been blowing, and the fetch—the over-water distance that the wind has been blowing. But the wave trains generated by widely separated storms can travel many hundreds of miles and intersect. When a wave trough from one storm meets a wave crest from another, they tend to cancel each other out, but when the crest of a wave from one storm meets the crest from another, they are added to each other to make a random wave larger than others in the series. Occasionally the wave crests from three or more storms may meet to make a rare monster wave that can cause real problems. How can waves be predicted? What is the scientific community doing about this problem?

Available wave data are sparse. One approach to overcome this is being undertaken on the international level by the World Meteorological Organization of the United Nations, which has established a program to collect and file sea state data on a global basis. In the United States the responsible organization is the NOAA National Climatic Center in Ashville, North Carolina. In the U.K. it is the Meteorological Office in Bracknell, Berkshire, and additional responsibilities for the rest of the sea have been assumed by Germany, Hong Kong, India, Japan, the Netherlands, South Africa, and the USSR. Collecting, filing, and analizing wave data from ships, wave staffs, waverider buoys, and visual observations will be a long and expensive task, but the development of a time-series of wave observations certainly is a valid approach to the problem.

However, several research activities are under way that can speed up our ability to understand wave phenomena and eventually to predict their occurrence. Least-time ship routing has been in operation for a number of years. Using the meteorological prognosis charts, the wind-wave interactions are utilized to prepare wave-distribution charts, and ships are then routed to avoid the more severe wave areas. At NOAA's Atlantic Oceanographic and Meteorological Laboratories (AOML) in Miami, Florida, Duncan Ross of the Sea-Air Interaction Laboratory working with Professor Vincent Cardone of the City University of New York has developed a computer model which predicts the wave pattern under moving severe tropical storms—especially hurricanes. The standard wind-strength, duration, and fetch formula becomes a bit confused when you have a rotating wind in a moving storm such as a hurricane. Using basic relationships between wind, sea, and fetch developed by Ross in the USA and Hasselmann in Germany (Hasselmann *et al.*, 1976), the computer model is able to simulate the wave field generated by a hurricane. Ships quite understandibly tend to avoid hurricanes, so development of the model was not possible from ship data. However, Ross, using a laser wave profiling device and flying into hurricanes with the NOAA research aircraft, has been able to obtain data to develop and refine his model. Wave data obtained from offshore oil platforms and anchored environmental buoys in the Gulf of Mexico during six separate hurricanes, have shown that Ross' storm-wave model can provide a highly accurate prediction of the wave field generated by severe storms—especially hurricanes of the slow-moving (14-20 mph) type typical of the Gulf of Mexico. During hurricane Anita in late August and early September of 1977, Ross put his wave forecast model to its first real test. Just prior to take off of the NOAA research aircraft to penetrate the hurricane, Ross' computer model was run and a wave distribution plot was generated using the predicted storm location and the meteorological parameters available from the NOAA National Weather Service (Figure 1). Once into the storm, Ross discovered his model was so accurate that, using the laser wave profilometer, and his plot of the predicted wave field, he was actually able to navigate the

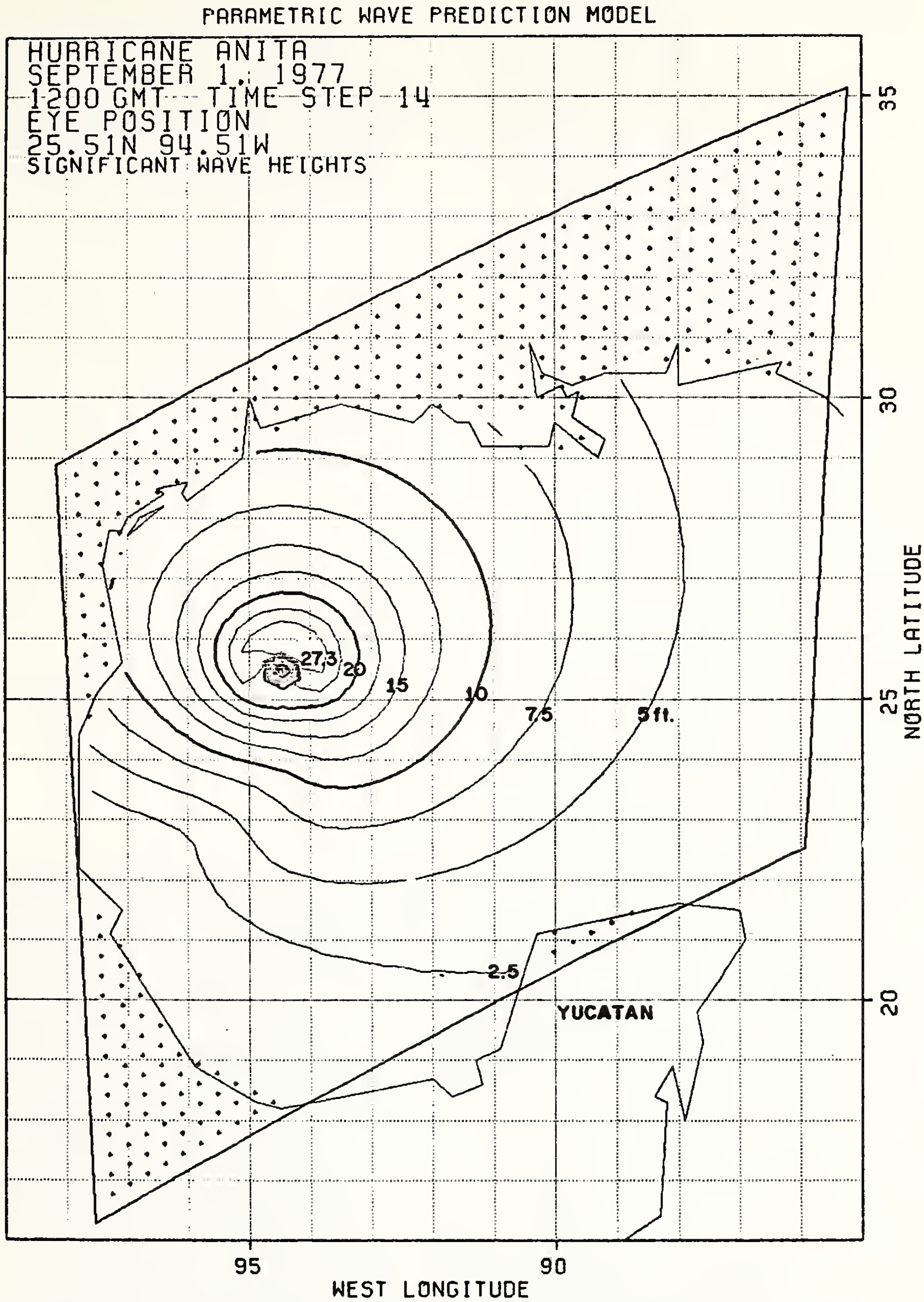
PARAMETRIC WAVE PREDICTION MODEL
HURRICANE ANITA
SEPTEMBER 1, 1977
1200 GMT TIME STEP 14
EYE POSITION
25.51N 94.51W
SIGNIFICANT WAVE HEIGHTS
27.3
20
15
10
7.5
5ft.
2.5
YUCATAN
35
30
25
20
NORTH LATITUDE
95
90
WEST LONGITUDE

Fig. 1 – Forecast of significant wave heights for Hurricane ANITA valid 1200 GMT, 1 September 1977, generated by Ross' computer model

aircraft in relation to the storm's eye as a function of the wave pattern he was measuring beneath the plane.

Now that we know his model is accurate, how can it be used by the mariner and others to whom waves are important? First, we are now in the process of transferring the technique to the NOAA National Weather Service; and for future storms in the Gulf of Mexico, they will include a wave forecast in their hurricane bulletins, information of obvious utility to the mariners. For those concerned with the design of offshore platforms and the laying of seafloor pipelines, knowledge of what has been called the "wave climatology" is extremely important. They must know what waves can be expected where their structures are to be implanted. Although we have yet to be funded for the effort, we want to take the data from the historical storms over the last 30 years for which good meteorological data are available and use Ross' model to hindcast the waves under each one. This would, for the first time, allow the compilation of the historical wave data that designers need if offshore structures are to be built without the expensive over designing to insure safety that is now the usual practice in the absence of valid wave data.

As a sidelight, wave data are an important aspect of the classification process of the American Bureau of Shipping. When supertankers began being used in 1967, ABS initiated a three-year effort to verify the accuracy of the calculated stresses on ships by comparing them with actual stresses measured on numerous ships under at-sea conditions. ABS instrumented four tankers and one bulk carrier in sizes ranging from 66,500 to 326,585 deadweight tons. On these ships, ABS mounted strain gauges and other equipment to record longitudinal bending stresses at critical points in their structures. Sea state conditions were measured at the same time, and "Long term distribution of stresses for all ships in all-weather service were found to agree closely with predicted values" (Reason, 1977). Improved wave climate data along specific sea routes will assist in the more effective design of ships which will use these routes.

A quantum jump in our ability to "now-cast" and, from this, forecast wave conditions on a global basis is expected to be realized with the launching of the SEASAT-A satellite in 1978. This satellite will measure significant wave height with its short-pulse altimeter, with the return pulse broadening as a function of the wave amplitude. Measurements will be good to about ½ meter. A reasonable SEASAT-A schedule will provide accurate measurements of wave height every 50 kilometers to result in some 7,000 observations per day (Apel and Siry, 1974). Wave directional spectra will be available from SEASAT-A's coherent imaging radar, and this combined with the wave height data and the surface wind field obtained by means of a scatterometer and microwave radiometer will provide the basic data needed for ocean wave forecasting (Stewart, 1974).

I would like to be able to provide a meaningful explanation of the so-called "freak" waves that are known to occur off the coast of southeast Africa (Dawson, 1977), but it is not yet possible. It was probably one of these monster waves that caused the loss of the WARATAH which disappeared with a loss of 119 crew and 92 passengers off southeast Africa in 1909 and which has caused considerable damage to numerous ships since. Data, however, are sketchy, as ship owners are reluctant to report minor wave damage for fear insurance rates will be increased. In all probability, these large waves result from an unique combination of storm-generated waves, the strong Agulhas Current, bottom topography, plus local passing storms. These "freak" waves present a real challenge to the oceanographer, and the National Research Institute for Oceanology in South Africa is even now attempting to compile the available data on the occurrence of these waves (F. Anderson, personal communication).

Next to waves, surface currents are probably the most important oceanic characteristic to the mariner. I am pleased to be able to report that significant advances are being made in our understanding of the oceanic circulation.

In the last Century, prior to the advent of steam, the study of oceanic currents received a good deal of attention. Once the sailing vessel with its dependence on wind and current was replaced by ships that could go anywhere regardless of the current and wind, the support for current studies declined drastically. However, in the last decade or so, the realization that a boost of a knot or two in a ship's speed of advance could mean the difference of several hours in a passage and converts relatively easily into dollars or pounds, guilders or rubles, caused a resurgence of interest in ocean currents.

At NOAA's Atlantic Oceanographic and Meteorological Laboratories (AOML), we have concentrated much of our physical oceanographic work on studying the time and space variations of the so-called Loop Current in the Gulf of Mexico.

Traditionally it was thought that the proto-Gulf Stream ran north through the Yucatan Channel between Cuba and the Yucatan Peninsula, turned east along the north coast of Cuba, and then north through the Florida Strait as the Florida Current to join with the Antilles Current to form the Gulf Stream off Cape Hatteras. Early work by oceanographers at Texas A & M University and more recently by scientists at NOAA's Atlantic Oceanographic and Meteorological Laboratories has shown that on an annual basis the current moves way up into the Gulf of Mexico as a current that has been named the Gulf Loop Current. Figure 2 shows successive positions of this current. Although Dr. George Maul of AOML and the other scientists who have been investigating this current have done so primarily out of curiosity to see how this phenomenon works, their results are of considerable relevance to the mariner and others. For example, if a tanker is headed through the Florida Straits for a New Orleans or a Texas port, she could unknowingly buck a two-to-three knot south-flowing current off the west coast of Florida. If, on the other hand, the ship's navigator had knowledge of the location of the Loop Current, he could move a bit further west and take advantage of the north-flowing limb of the current for a saving of several hours.

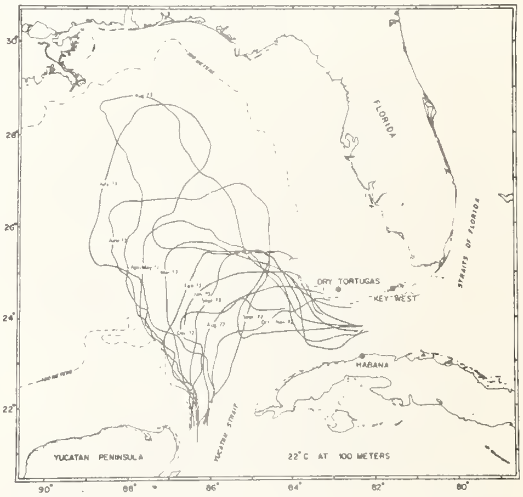

Fig. 2 – Time series of the Loop Current in the Gulf of Mexico, August 1972-September 1973. The pathlines are the location of the 22°C isotherm at 100 meters depth. Each cruise was synchronized with ERTS passes over the area every 36 days. The indicator isotherm was located by expendable bathythermographs from a surface vessel; this isotherm is approximately 20 kilometers to the right of the cyclonic edge facing downstream (after Maul, 1977)

During the winter months when the Gulf of Mexico is relatively cool, the contrasting warm Caribbean water in the Loop Current can be seen on the high-resolution infrared satellite images, and the position of the current can be monitored from space. Once this fact had been established, the NOAA National Weather Service began to include in its regular marine weather broadcasts the location of significant points in this current so the mariner could plot its location and use it to his advantage. The shipping community's response to this service, initiated in 1977, has been very positive, and NOAA will continue it.

However, in summer, the surface temperature difference between the Gulf water and the Loop Current water is too small to show up in the satellite images. Dr. Robert Molinari of AOML has developed a computer model of the Gulf of Mexico using real oceanographic and meteorological data as inputs and has been able to simulate successfully not only the generation of the Loop Current but also the pinching off of the loop to form a large anticyclonic eddy which drifts slowly to the west. Although this model was developed primarily for use in predicting the trajectory of oil spills that might occur in the Gulf, the technique has the possibility of being able to substitute for the satellite data in predicting the Loop Current's location for mariners during the summer.

Donald Barrick and his associates at NOAA's Wave Propagation Laboratory have developed an interesting HF radar system for the remote mapping of surface currents out to 70km from shore (Barrick *et al.,* 1977).The equipment is a two-unit radar system operated with a portable 2.2-kw gasoline generator and controlled by a minicomputer which also does the signal and data processing in the field. Tested at Miami, Florida, with the two radars tens of kilometers apart, the equipment mapped the surface currents over an area of more than 2000 km^2. The radar measurements were compared with measurements made with current drifters, and it was determined that the directional aspects were extremely accurate, and the precision of the velocity measurements (better than 30 cm/sec) was within the expected range considering the difference in the methods, the high degree of lateral variation in the current field, and the inherent inaccuracies in the drifter technique. The technique holds great promise for monitoring nearshore currents in near-real time and will be an extremely useful research tool as oceanographers continue their investigations into the driving forces which cause the observed coastal current patterns. Recent developments in over-the-horizon radar indicate that a somewhat comparable technique can be used to obtain measurements of the surface wave field over large segments of the ocean at distances of hundreds of kilometers (Barrick, 1973).

For those involved in offshore and gravel recovery, the dumping of sewage sludge, harbor maintenance, and channel dredging, the underwater acoustics work of Dr. John Proni of AOML has a high degree of relevance. Using ship-mounted acoustic transducers at frequencies of 20kHz and 200 kHz, he has been able to track the movement of clouds of suspended material within the water column. Until the advent of this technique, dredgers and dumpers had no notion as to the movement or rate of dispersion of their material once it sank beneath the surface. Off the entrance to Miami harbor during a channel-deepening dredge operation, clouds of suspended sediment were monitored acoustically as they moved out along sub-surface density surfaces (Figure 3), and sewage sludge dumped from barges seaward of New York City was tracked for some

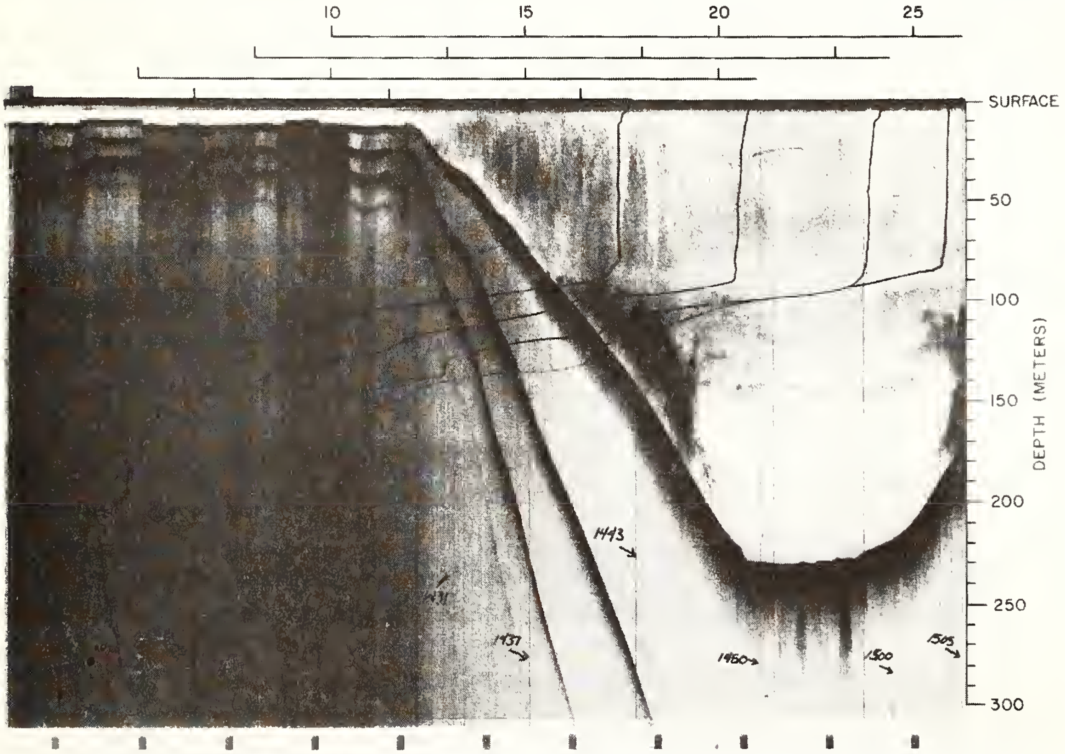

Fig. 3 – Acoustic record (20kHz) seaward of Miami, Florida, showing suspended dredge material at depth with "flows" moving out along density discontinuities between 90 and 140M. The scales at the top are in °C and refer to the superimposed temperature profiles (after Proni et al., *1976)*

15 hours (Proni, *et. al,* in press). From this experiment it was learned that some of the heavier material went directly to the bottom, while less dense material tended to move out in apparent slow flows along density discontinuities (Figure 4). Not only is this information useful to those concerned with the eventual fate of dumped or dredged material, but it allows those who sample such material to know where their samples are obtained relative to the major concentration of suspended material. Additionally, this acoustic technique has enabled oceanographers at AOML to monitor the landward movement of packets of internal waves and has allowed us to see internal waves breaking as they intersect the sloping sea floor—even as surface waves form breakers as they approach the beach. This heretofor unobserved breaking of internal waves puts sea-floor sediments back into suspension and can be an important mechanism for resuspending pollutants which are then moved about by currents.

Another recent development at AOML is the construction and use by Dr. Richard Bennett of a probe (piezometer) that is able to measure the internal pore pressure of marine sediments as much as 20 meters below the mudline (Bennett, in press). His probe was in the bottom off the Mississippi River delta when hurricane Eloise went by, and it measured large incursions in excess sediment pore pressure as the large waves went overhead. One hypothesis is that it is these variations in sediment pore pressure, especially the pumping action induced by large waves, which may cause a rearrangement of clay particles which results in a sediment instability which may account for some of the failures of the legs of offshore rigs. This work is continuing and has already attracted the attention of the offshore engineering community.

Other oceanographic and meteorological work at NOAA's research laboratories includes complex global circulation modeling that couples the sea and the air and is able to reproduce global patterns of motion in both the ocean and the atmosphere, other studies of long-term climate variation and short-term weather forecasting, studies of the downward transport of heat in the sea through mixing, studies of the causes of the serious oxygen depletion that resulted in catastrophic losses in the surf clam fishery off New Jersey in 1976, the generation and movement of sand waves on the continental shelf, the role of submarine canyons as waste conduits, the role of eddies and other scales of motion in the ocean dynamics, ocean-atmosphere interactions during hurricanes, and numerous other research activities directed towards a better understanding of the complex interactions within and among the sediments of the seafloor, the water itself, and the overlying atmosphere.

Although NOAA's studies of waves and currents are of the most direct relevance to the mariner, I believe that the more we can learn of all aspects of that magnificently complex phenomenon known as the ocean, the better will be the lot of the mariner and all others who must daily deal with the global sea. Let us continue to be concerned with better wave and current forecasts, oceanic pollution, and offshore energy development—today's wicks, lenses, and fuels—but it would be tragic if we ignored today's Maxwells and Faradays—those meteorologists and oceanographers who are studying the sea and the atmosphere just because they are fascinated by them and want to understand their complexities. It is on these researchers that we must ultimately depend for the knowledge pool from which future generations must draw for more efficient use of the sea.

REFERENCES

Apel, John R. and J.W. Siry, 1974, "A synopsis of SEASAT-A scientific contributions", in *SEASAT-A Scientific Contributions,* NASA, 1974

Barrick, Donald E., M.W. Evans, and B.L. Weber, 1977, "Ocean surface currents mapped by radar", *Science,* Vol. 198, No. 4313, 14 October 1977

Barrick, Donald, 1973, "The use of skywave radar for remote sensing of sea states", *Journal, Marine Technology Society,* Vol. 7, No. 1, pp. 29-33

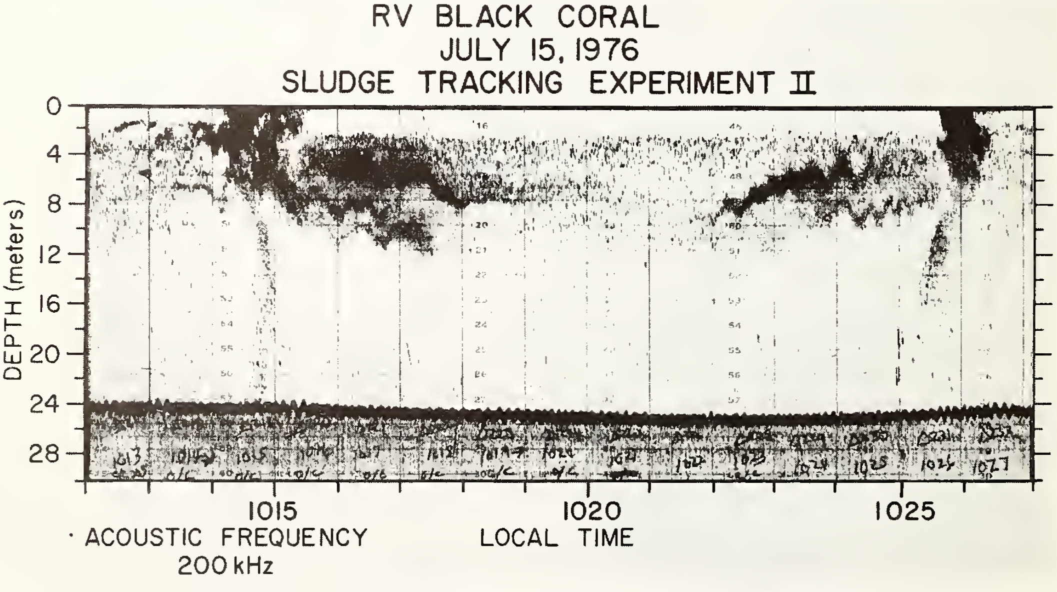

Fig. 4 – Acoustic record (200kHz) of two passes through a sewage sludge dump event seaward of New York Harbor. The ship reversed course at 1021 h. Note especially the "flows" moving out from the center of the dump and the internal waves possibly generated by the impact of the dump itself. Note also the current shear shown by the shape of the column of material extending to the bottom (after Proni et al., *in press)*

Bennett, Richard H. (in press), "Pore water pressure measurements: Mississippi Delta submarine sediments", submitted to *Marine Geotechnology,* presented at the Slope Stability Conference, Baton Rouge, Louisiana, 1976

Dawson, James, 1977, "Freak ocean waves are episodic", *New Scientist,* Vol. 73, No. 1033, January 1977

Hasselmann, K., D.B. Ross, P. Muller, and W. Sell, 1976, "A parametric wave prediction model", *Journal of Physical Oceanography,* Vol. 6, pp. 200-228

Maul, George A., 1977, "The annual cycle of the Gulf Loop Current, Part I: observations during a one-year time series", *Journal of Marine Research,* Vol. 35, No. 1, February 1977, pp. 29-47

Proni, John R., F.C. Newman, D.C. Rona, D.E. Drake, G.A. Berberian, C.A. Lauter, Jr., and R.L. Sellers, 1976, "On the use of acoustics for studying suspended oceanic sediment and for determining the onset of the shallow thermocline", *Deep-sea Research,* Vol. 23, pp. 831-837, 1976

Proni, John R., F.C. Newman, R.A. Young, D. Walter, R. Sellers, and P. McGillivary (in press), "Observations of the intrusion into a stratified ocean of an artificial tracer and the concomitant generation of internal oscillations", submitted to *Journal of Geophysical Research,* 1977

Reason, John, 1977, "The international effort to measure the forces of the sea", *Surveyor,* American Bureau of Shipping, Vol. 11, No. 3, August 1977

Ross, Duncan and Vincent Cardone, (in press), "A comparison of parametric and spectral hurricane wave prediction products", 1977

Stewart, Robert H., 1974, "Satellite measurements of ocean waves", in *SEASAT-A Scientific Contributions,* NASA, 1974

3

Bulletin of the American Meteorological Society 59, No. 4, p. 417.
(Book Review: ed. M. Bramwell, 208 pages. Rand McNally, Co., Chicago.)

The Rand McNally Atlas of the Oceans. Edited by Martyn Bramwell. Rand McNally and Co., Chicago, 1977. 208 pages. $29.95. Hardbound.

Rand McNally's reputation as an atlas maker *par excellence* is in no danger of being eroded as the result of their publication of **The Rand McNally Atlas of the Oceans.** It is difficult to avoid using superlatives in describing the 208-page volume of new photographs, maps, visuals of all sorts, and good text. At $29.95, the 14 cents per page must be one of the best marine bargains of the century. The contributing authors and their institutions read like a Who's Who in marine science. They come from the Scripps Institution of Oceanography, Woods Hole Oceanographic Institution, and NOAA in the United States; from the Institute of Oceanographic Sciences, Institute of Geological Sciences, Lowestoft, Aberdeen, Edinburgh, Plymouth, the British Museum, and Cambridge in the United Kingdom; and from government agencies, universities, and industry. The coverage of contributing authors is as broad as it is talented. They called on the best, and they got the best.

When many people think of the oceans today, they think only of Cousteau and scuba diving, of the potential horrors of marine pollution, and the tuna-porpoise problem. Too often they do not realize that the oceans have in the last 20 years revealed new and exciting truths about the history of our planet, have become an international legal battleground, have become recognized as the source of large quantities of living and mineral resources as yet untapped, and—above all—are an absolutely fascinating 71% of our planet about which a tremendous amount of knowledge has become available, primarily in the scientific literature. **The Rand McNally Atlas of the Oceans** has filtered and sorted all the available material, called on the experts in each field, and distilled a heady brew of *res oceanographica* that will appeal to all who have any interest whatsoever in the oceans.

The volume has absolutely magnificent photographs and other visuals, and the text is uncomplicated and readable for the layman. It is well organized into six sections plus tables, a glossary, and a very complete index that will make the volume a must for college and high school students faced with term papers on the oceans. For the postcollege lovers of the sea, including all oceanographers, it will be a ready reference volume to bring them up to date on the present state of our knowledge of the sea. For the oceanographer and marine meteorologist, it is a ready source of information to inform them surreptitiously on the present state of the art in those fields of marine science other than their own particular one. As an oceanographer, this reviewer learned more than he is willing to admit from a complete reading of the **Atlas**. It is well done.

Sections cover the origin of the seas, continental drift, coastal erosion, sea level, the chemistry of sea water, the ocean's role in climate, tides, currents, waves, the explorers of the seas, man in the sea, ocean politics, the food web, creatures of the sea including sea birds and shore life, fish, oil, minerals, and energy from the sea, and a sea-by-sea description of each of the arms of the global sea. The final section, entitled Encyclopedia of Marine Life, is a catalog of the main families of marine life, their form, anatomy, and special adaptations.

For the meteorologist, the section on air-sea interaction includes the 1974 GATE experiment and a discussion of global ocean-atmosphere interaction with good photographs, satellite images, and drawings of hurricanes, the problems of long range weather forecasting, and energy transfer from the sea to the atmosphere.

The encyclopedia of marine plants and animals is, of necessity, abbreviated, but with text and good line drawings, the major forms are included, and it provides an educational summary of the classification of life in the sea.

Three aspects make this an outstanding volume: the magnificent visuals—and they are the best this reviewer has ever seen related to the ocean, the accurate and comprehensive text, and the very complete coverage of things oceanic. One thing that comes through to the reader is the obvious respect and love the authors have for the sea. The volume should be on the reference shelf of every high school and college. It should also be on the coffee table of every coastal dweller, yachtsman, fisherman, oceanographer, and meteorologist that can spare 14 cents a page for 208 pages of ocean knowledge.—*Harris B. Stewart, Jr.*

Journal of Physical Oceanography 8, No. 5, 811-817.

A Simple Ekman-Type Model for Predicting Thermocline Displacement in the Tropical Pacific

P. WEBB DEWITT AND ANTS LEETMAA

Atlantic Oceanographic and Meteorological Laboratories, NOAA, Miami, FL 33149

(Manuscript received 25 July 1977, in final form 14 April 1978)

ABSTRACT

A linear model is developed for the near-equatorial zone to estimate wind-driven convergences in the near-surface viscous boundary layer. Using the winds observed during EASTROPAC, an attempt is made to relate these convergences to the measured displacements of the tropical thermocline. Between 4° and 15°N, the sign of the displacements is predicted; however, the amplitude is generally underestimated. At the equator, extremely large values of the vertical eddy coefficients are necessary in order to obtain agreement between predicted and observed changes. This probably indicates that some essential physics has been neglected.

---

1. Introduction

In a recent paper, Meyers (1975) examines the relationship between the seasonal variations in the Pacific North Equatorial Current and the wind field. He finds that between 10° and 25°N, most of the temporal variations in the meridional slope of the thermocline could be accounted for by meridional variations in the Ekman pumping. The latter is the vertical velocity that results from the divergence of the horizontal Ekman transport after the mean annual divergence is subtracted out. It is somewhat surprising that such a model should work so well. After all, fluctuating winds of these frequencies should generate baroclinic and barotropic Rossby waves.

Some insight as to why the model possibly works can be obtained from the paper of Anderson and Gill (1975). They consider an initial value problem in which a midlatitude ocean is spun up from rest. The initial mid-ocean response in their model is the Ekman pumping response. This continues until Rossby waves from the eastern boundary arrive, and then a steady Sverdrup balance is obtained. Near the equator a similar situation occurs, except that it is the Kelvin wave that propagates in from the west that stops the initial Ekman pumping response (Moore and Philander, 1977). However, if these waves are eliminated or strongly modified by dissipation, nonlinearities, bottom topography or vertical shear in the horizontal currents, then the local response might dominate.

As evidence against this, White (1977) presented a model for the response of the tropical North Pacific Ocean to wind forcing at the annual period. He found that the response consisted of a locally forced component (as did Meyers) and the baroclinic long waves that propagate in from the eastern boundary. The overall amplitude of the response was determined by the amplitude of the local response. White analyzed the bathythermograph (BT) data files for the entire North Pacific Ocean and appeared to find evidence for the baroclinic long waves, which he calculated to propagate zonally at a phase speed of 40 cm s^{-1} at 11°N and 15 cm s^{-1} at 18°N. In this model, the applied stress was assumed to be independent of longitude.

An examination of the wind stress curl computations of Wyrtki and Meyers (1975) for the tropical Pacific shows a zonal structure to the curl which appears to propagate to the west. The propagation speeds are those that White deduced from the BT data. Thus, in our opinion, there is some question as to whether the presence of the Rossby waves has been demonstrated. With this in mind, an attempt is made to extend the Ekman pumping analysis to the equator. Within a couple of degrees of the equator, the time response of the ocean is extremely rapid (Moore and Philander, 1977). In addition to Rossby waves, Kelvin and Yanai waves are also present. Furthermore, the simple Ekman dynamics that applies in higher latitudes must break down (Robinson, 1966). Most likely nonlinear effects become important. However, these are not tractable in a simple model. Thus the model considered is linear and viscous with the understanding that in the proximity of the equator the physic is probably incorrectly modeled, and that the vertical eddy coefficient might have to be varied as a reflection of this inadequacy.

2. Model formulation

The near-surface layer of the tropical oceans is characterized by a relatively thick [O(100 m)], quasi-homogeneous upper layer, beneath which the temperature very rapidly falls to its deep-water value. We are concerned with predicting changes in thickness of this upper layer. A two-layer ocean is considered with an upper homogeneous layer of depth D[O(100 m)]. Viscous effects are assumed to be confined to this layer. Away from the equator, the Ekman depth might be less than D; close to the equator, viscous effects are important throughout D. At the sea surface a wind stress is applied, and at the bottom of this layer it is assumed that the horizontal frictional velocities go to zero. There can, however, be a vertical velocity at this level which results from frictional convergences throughout the whole layer. This causes the lower interface to move up or down. In the model considered, the mean annual Ekman convergence is subtracted out. Away from the equator, this is balanced in the mean by geostrophic convergence, i.e., the Sverdrup balance holds. The model is concerned not with the mean state, but with fluctuations about this state.

We consider an ocean with an upper homogeneous layer of depth D that is unbounded in the horizontal direction. The coordinate x is positive eastward, y positive northward and z positive upward. The origin is at the sea surface. The respective velocity components are u, v and w. Horizontal pressure gradients are ignored. This is not to say that they are unimportant. Studies have shown that in the *mean* state, the east-west wind stress balances the vertically integrated zonal pressure gradient (Katz, 1977). It is assumed that in this model the pressure gradients are not important in the dynamics of the frictional boundary layer (this is the usual assumption in Ekman-layer theory). However, the frictional convergences do redistribute the mass in the upper ocean and thereby create pressure gradients. These in turn are balanced away from the equator by geostrophic velocities. In this paper there is no discussion about these geostrophic velocities. The motion is also assumed to occur on a time scale longer than that required to set up the frictional boundary layer. Under these assumptions the equations of motion are

$$fu = \gamma v_{zz}, \quad -fv = \gamma u_{zz}, \quad u_x = \frac{\partial u}{\partial x}, \quad \text{etc.,} \tag{1}$$

where $f = 2\Omega \sin\phi$ is the Coriolis parameter and γ is the vertical eddy viscosity.

The boundary conditions are

$$\left.\begin{array}{lll} u_z = \tau^x/\gamma; & v_z = \tau^y/\gamma & (\text{at } z = 0) \\ u = v = 0 & & (\text{at } z = -D) \end{array}\right\}, \tag{2}$$

where τ^x and τ^y are the horizontal components of wind stress at the sea surface. Vanishing of the horizontal velocities at the base of the mixed layer applies only to the frictional velocities. The geostrophic velocities probably do not vanish.

As in classical theory (Ekman, 1905), the solutions to (1) are assumed to be of the form

$$\left.\begin{array}{l} u = Ae^{kz}[\cos(kz + C_1)] + Be^{-kz}[\cos(kz + C_2)] \\ v = Ae^{kz}[\sin(kz + C_1)] - Be^{-kz}[\sin(kz + C_2)] \end{array}\right\}, \tag{3}$$

where A, B, C_1 and C_2 are constants; and

$$k = (f/2\gamma)^{1/2}.$$

After solving for A, B, C_1 and C_2, the solutions for u and v are

$$\left.\begin{array}{l} u = (2k\gamma)^{-1}\left[\begin{array}{l}(\tau^x + \tau^y)(\sinh kz)(\cos kz) + (\tau^x - \tau^y)(\cosh kz)(\sin kz) \\ \quad + (M\tau^x + N\tau^y)(\cosh kz)(\cos kz) + (N\tau^x - M\tau^y)(\sinh kz)(\sin kz)\end{array}\right] \\ v = (2k\gamma)^{-1}\left[\begin{array}{l}(\tau^x + \tau^y)(\cosh kz)(\sin kz) - (\tau^x - \tau^y)(\sinh kz)(\cos kz) \\ \quad + (M\tau^x + N\tau^y)(\sinh kz)(\sin kz) - (N\tau^x - M\tau^y)(\cosh kz)(\cos kz)\end{array}\right] \end{array}\right\}, \tag{4}$$

where

$$M = \frac{\sinh 2kD + \sin 2kD}{\cosh 2kD + \cos 2kD}, \qquad N = \frac{\sinh 2kD - \sin 2kD}{\cosh 2kD + \cos 2kD}.$$

With the boundary condition $(w)_{z=0} = 0$, the continuity equation

$$u_x + v_y + w_z = 0 \tag{5}$$

can be vertically integrated from $z = 0$ to $z = -D$, i.e.,

$$w_{-D} = \int_{-D}^{0} (u_x + v_y)dz. \tag{6}$$

Inserting (4) into (6), performing the indicated differentiation and integration with the further assumption that $f \approx \beta y$, the following solution for Ekman pumping is obtained:

$$
\begin{aligned}
w_{-D} = {} & \left(\frac{2}{\beta y}\right)\left[(\tau^x_x+\tau^y_y)\left(\frac{\sinh kD\sin kD}{\cosh 2kD+\cos 2kD}\right) + (\tau^y_x-\tau^x_y)\left(\frac{1}{2}-\frac{\cosh kD\cos kD}{\cosh 2kD+\cos 2kD}\right)\right] \\
& + \left(\frac{2}{\beta y^2}\right)\left[\tau^x\left(\frac{1}{2}-\frac{\cosh kD\cos kD}{\cosh 2kD+\cos 2kD}\right) - \tau^y\left(\frac{\sinh kD\sin kD}{\cosh 2kD+\cos 2kD}\right)\right] \\
& + \left(\frac{\tau^x D}{\gamma k y}\right)\left[\begin{aligned} & \sin kD\cos^2 kD\cosh kD \\ & - \cos kD\sinh kD\cosh^2 kD \\ & - \sin^2 kD\cos kD\sinh kD \\ & - \sin kD\sinh^2 kD\cosh kD \end{aligned}\right](\cosh 2kD+\cos 2kD)^{-2} \\
& + \left(\frac{\tau^y D}{\gamma k Y}\right)\left[\begin{aligned} & \sin kD\cos^2 kD\cosh kD \\ & + \cos kD\sinh kD\cosh^2 kD \\ & + \sin^2 kD\cos kD\sinh kD \\ & - \sin kD\sinh^2 kD\cosh kD \end{aligned}\right](\cosh 2kD+\cos 2kD)^{-2}, \qquad (7)
\end{aligned}
$$

where

$$k = \left(\frac{\beta y}{2\gamma}\right)^{1/2}$$

and terms containing D_x and D_y are neglected as they can be shown to be small. Asymptotic forms of Eq. (7) turn out to be useful. Near the equator (limit $kD \to 0$), (7) reduces to

$$w_{-D} = \frac{D^2}{2\gamma}(\tau^x_x+\tau^y_y) - \frac{5}{24}\frac{D^4\beta}{\gamma^2}\tau^x. \qquad (8)$$

The product kD may be written as $kD = \pi(D/D_E)$, where D_E is the classical ideal Ekman depth as given by

$$D_E = \pi(2\gamma/f)^{1/2}. \qquad (9)$$

When the Ekman depth is small compared to the depth of the mixed-layer ($kD \gg \pi$), Eq. (7) reduces to

$$w_{-D} \approx \left(\frac{1}{\beta y}\right)(\tau^y_x-\tau^x_y) + \left(\frac{1}{\beta y^2}\right)\tau^x. \qquad (10)$$

Computations of (4) and (7) were made on a Hewlett-Packard 9815-A programable calculator.

In classical Ekman theory for a finite-depth ocean (Ekman, 1905), the nature of the flow is governed by the ratio of the ocean depth H to the ideal Ekman depth D_E [Eq. (9)]. When the ratio $H/D_E \leq 0.1$, the resultant flow is couette-like and the velocity profile is approximately linear in z. As the ratio increases, the classical Ekman spiral emerges.

The u and v fields as given by (4) adhere to the classical Ekman flow for a finite depth (Fig. 1). For discussion purposes, the Ekman pumping model will be divided into three regimes: the regime near the equator where the resultant flow is couette-like, the regime far away from the equator where the classical Ekman spiral is found, and the transition zone between these two regimes.

3. Model results

a. *East-west wind stress*

Before using observed wind stress data, several examples are shown using ideal stresses to demon-

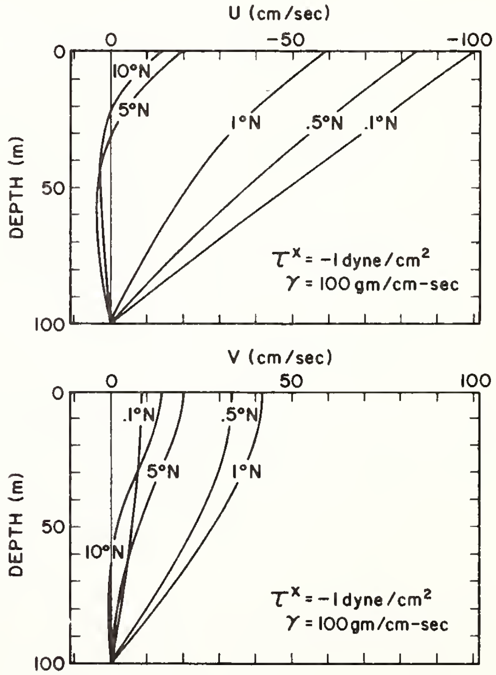

FIG. 1. The horizontal velocity field as computed by Eq. (4) for various latitudes with D = 100 m, $\tau^x = -1$ dyn cm^{-2} and $\tau^y = 0$.

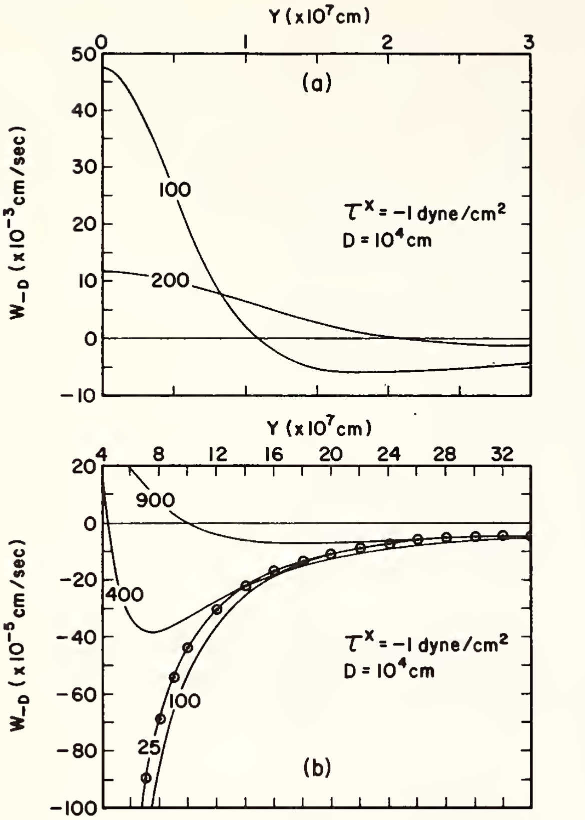

FIG. 2. Vertical velocity (w_{-D}) within 300 km of the equator (a) as computed by (7) for various eddy viscosities (g cm^{-1} s^{-1}) as a function of y, with $\tau^x = -1$ dyn cm^{-2}, and vertical velocity beyond 400 km of the equator (b). The circled points were computed using Eq. (10).

strate the properties of (7). For a constant wind stress from the east ($\tau^x = -1$ dyn cm^{-2}), Eq. (7) indicates a strong divergence (positive w_{-D}) in the couette regime (Fig. 2a). Proceeding northward, the w_{-D} field becomes convergent (negative w_{-D}) as the Ekman spiral regime is encountered. The divergence at the equator is proportional to the inverse square of the eddy viscosity [Eq. (8)], whereas the width of the divergence region is directly proportional to the eddy viscosity.

Fig. 2b indicates the w_{-D} fields for various eddy viscosities. As y increases, the w_{-D} fields approach the ideal Ekman solution as given by Eq. (10). For a particular eddy viscosity and with $y \geqslant (\gamma/5) \times 10^7$ cm, the values of w_{-D} as computed by (7) and (10) are within 5% of each other.

b. North-south wind stress

A constant wind stress from the south ($\tau^y = 1$ dyn cm^{-2}) produces the w_{-D} field shown in Fig. 3a. At the equator, w_{-D} is zero [Eq. (8)]. Proceeding northward, a very strong convergence is predicted in the transition zone between the couette and Ekman regimes. The maximum vertical velocity of the convergence is proportional to the inverse square of the eddy viscosity. The northward location of the maximum convergence is directly proportional to the eddy viscosity. The vertical velocity field south of the equator is the negative of that shown, i.e., there is a strong divergence. A qualitative description of the preceeding is to be found in Cromwell (1953).

The w_{-D} field for various eddy viscosities is shown in Fig. 3b. When D_E for a particular γ becomes less than D, a divergence occurs as shown by the $\gamma = 25$ curve for $y > 3 \times 10^7$ cm.

c. The wind stress curl and gradient

Fig. 4 is presented to illustrate the relative importance of each term in Eq. (7). The stress derivative terms are assumed to have a magnitude of 10^{-8} dyn cm^{-3}, while the stress terms are assigned a value of 0.1 dyn cm^{-2}. These are typical values for the tropics. At the equator, the contribution from the wind stress curl terms is zero, whereas the wind stress gradient terms produce a vertical velocity as given by Eq. (8). Proceeding northward, the wind stress gradient terms become increasingly less important, while the wind stress curl terms go through a maximum, then slowly decrease in importance. In the Ekman spiral regime, the wind stress curl terms dominate, and the contribution

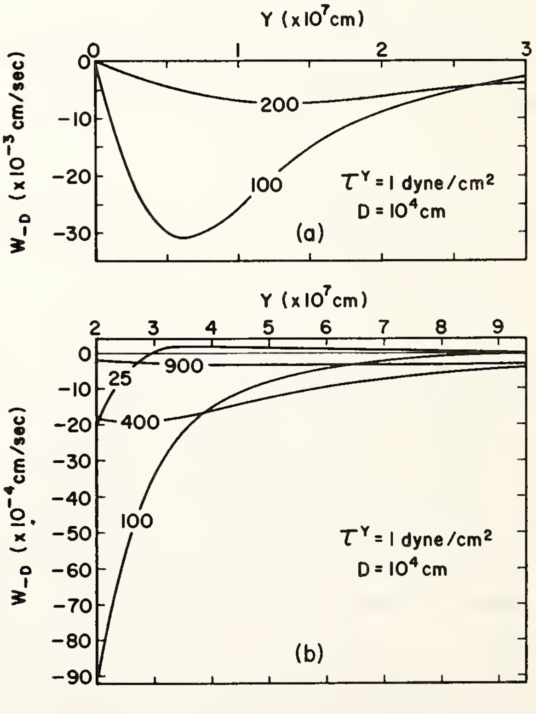

FIG. 3. Vertical velocity (w_{-D}) within 300 km of the equator (a) as computed by (7) for various eddy viscosities as a function of y, with $\tau^y = 1$ dyn cm^{-2}, and vertical velocity beyond 200 km of the equator (b).

from the wind stress gradient terms becomes insignificant.

4. Comparison with observed data

The ability of this model to reproduce fluctuations in the depth of the thermocline was examined along meridian 119°W, between 1° and 15°N. The effects of Ekman pumping at the equator were examined separately at 119° and 98°W.

During the EASTROPAC Experiment, a hydrographic section was taken approximately every two months along 119°W. The depth of the 20°C isotherm, as given in the EASTROPAC Atlases (Love, 1971, 1972a,b, 1973, 1975), was chosen to represent the top of the thermocline. Ekman pumping was used in an attempt to predict the depth fluctuations of this isotherm between consecutive surveys.

The necessary wind stresses for the model were obtained from the bimonthly average wind field charts presented in the EASTROPAC Atlases. From the bimonthly wind velocities, the annual mean wind velocities [as computed over 2° latitude × 10° longitude quadrangles for the experimental area by Wyrtki and Meyers (1975)] were subtracted out to eliminate the mean annual divergence of Ekman transport. The wind stresses were then determined using

$$\left.\begin{aligned}\tau^x &= \rho_a C W W_x\\ \tau^y &= \rho_a C W W_y\end{aligned}\right\}, \qquad (11)$$

where $\rho_a = 1.2$ kg m^{-3} is the density of the atmosphere, $C = 1.5 \times 10^{-2}$, and W is the wind speed in meters per second (Malkus, 1962; Wyrtki and Meyers, 1975).

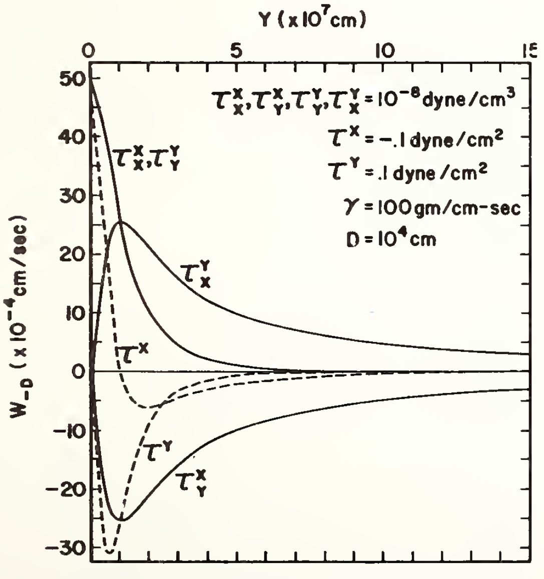

FIG. 4. The relative effects of the various wind stresses on the w_{-D} field (7) as a function of y.

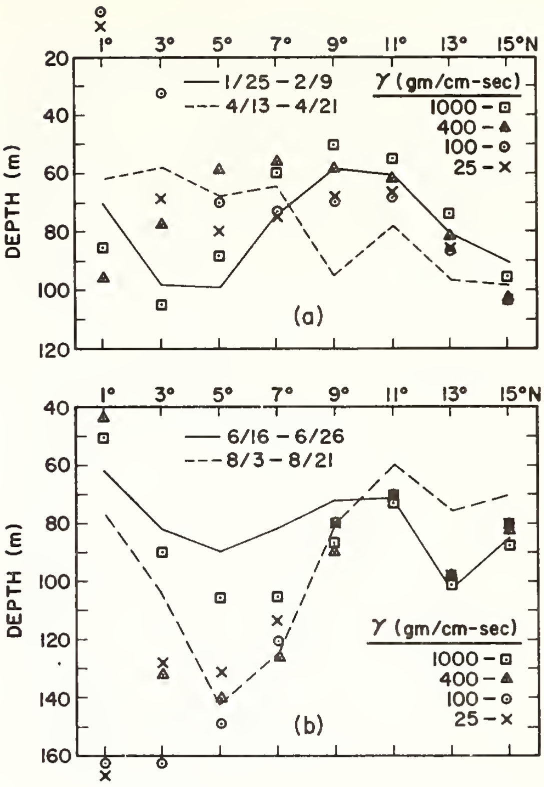

FIG. 5. Comparison between the actual depth fluctuations during the EASTROPAC Experiment of the 20°C isotherm along meridian 119°W, and the predicted depth fluctuations as computed for various eddy viscosities by Eq. (12). The model depth D was chosen to be 100 m. See text for further explanation.

Assuming that the calculated wind stresses were constant over the bi-monthly wind periods, the predicted depth of the 20°C isotherm was determined using

$$z = \int_{t_0}^{t} w_{-D} dt + z_0, \qquad (12)$$

where z_0 is the depth of the isotherm at the initial time t_0. The model depth D was chosen to be 10^4 cm. This is approximately the mean depth of the 20°C isotherm.

a. Ekman pumping along 119° W

Fig. 5 presents the comparison between the predicted thermocline topography for various eddy coefficients and the actual depth fluctuations of the 20°C isotherm. The initial topography of the 20°C isotherm is shown by the solid line; the one several months later is shown by the dashed line; i.e., it is the dashed line that we are attempting to predict.

At 1°N the smaller eddy coefficients (25, 100) greatly overestimate the thermocline displacements in both cases, whereas the larger coefficients (400, 1000) predict movement of more reasonable amplitude in the wrong direction.

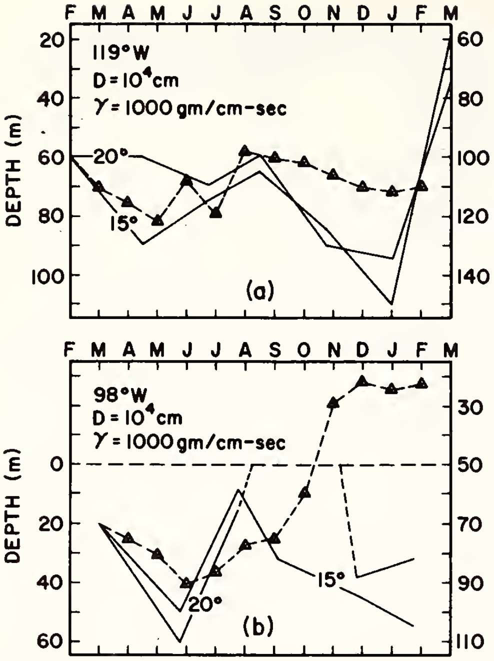

Fig. 6. Comparison between the actual depth fluctuations at the equator (February 1967–March 1968) of the 20°C and 15°C isotherms, and the predicted depth fluctuations as given by Eq. (12). The depth of the 20°C isotherm is given on the left-hand side of the graph, while the depth of the 15°C isotherm is given on the right-hand side. See text for further explanation.

In Fig. 5a, the eddy coefficients of 25 and 100 produce better predictions north of 9°N. However, the magnitudes of the downward predictions are approximately one-half of the actual deepening of the 20°C isotherm. At 5°N, good predictions occurred with $\gamma = 25, 100, 400$. In general the smaller eddy coefficients predict the correct sign for the displacements and reasonable magnitudes.

In Fig. 5b, the very strong deepening of the isotherm between 4° and 9°N is again well predicted. North of 9°N, the direction of movement is correctly ascertained. However, the calculated magnitude of movement is at best a third of the actual movement.

It seems that the model provides reasonable results from about 4° to 15°N. In this region, the midlatitude Ekman solution is still a close approximation to the total solution given by (7). In both Figs. 5a and 5b there appears to be a general underestimation in the calculated magnitude of movement north of 9°N. This discrepancy may be the result of underestimating the wind stress and its curl. Evidence for this comes from Meyers (1975). He predicts extremely well the seasonal depth cycle of the thermocline at 10°N and 155°W using essentially Eq. (10). In that area the winds are steadier and there is more ship traffic providing wind data. Thus, better estimates can be made of the curl.

From 1° to 4°N none of the solutions seem to do a very good job. This is the transition region from the Ekman spiral solution to the couette solution.

It should be noted that the functional dependence of Eq. (7) on the magnitude of the eddy coefficient γ is somewhat complicated (Figs. 5a and 5b). This dependence is better visualized in Figs. 2a and 2b, 3a and 3b with regards to the shifting of the relative positions of the ideal curves for various eddy viscosities.

b. Ekman pumping along the equator

To test (7) [or its asynoptotic limit (8)] at the equator, the depth fluctuations of the 20 and 15°C isotherms, as reported during the EASTROPAC Experiment at 119° and 98°W, were utilized. The necessary wind stresses were computed as in the previous section except that monthly mean wind velocities [as computed during the experiment for 2° latitude × 10° longitude quadrangles (Wyrtki and Meyers, 1975)] were employed instead of the bimonthly winds as reported in the EASTROPAC Atlases. The eddy viscosity used was 1000 g cm^{-1} s^{-1} and the depth D was 10^4 cm. The higher eddy viscosity was necessary in order to obtain reasonable values for the Ekman pumping. As before, the prediction of the thermocline depth was made using (12).

At 119°W (Fig. 6a), the model predicts fairly well the direction of movement of the 15°C isotherm until about August. From that time on, the predicted magnitude of movement is not large enough to match the observed depth changes. At 98°W, the depth changes as predicted coincide well, again until August, with the observed depth changes of the 20 and 15°C isotherms. During September, the observed 20°C isotherm breaks the surface while the 15°C isotherm deepens appreciably with respect to the preceeding observation period. The model during this time does predict a strong divergence—strong enough to cause the isotherms to break the surface.

5. Discussion

It should be emphasized that the main drawback in doing this comparison was the difficulty in estimating the spatial distribution of the wind stress. In our opinion the quantity and quality of the available data were marginal. Nevertheless, between 4° and 15°N, reasonable agreement was obtained between the predicted thermocline displacements and the observed displacements, both in terms of the magnitude of the displacement and the direction. North of 4°N the results of our more complicated solution were quite well reproduced by the simpler midlatitude Ekman solution [Eq. (10)].

This indicated that the more complicated formalism in this region is unnecessary and that the solution is more nearly independent of the eddy coefficients.

At the equator there was limited agreement between the model and the observations. These results perhaps should not be taken too seriously because the flow in this region is probably nonlinear. The thermal structure indicated that the Equatorial Undercurrent was present during most of the time period over which the comparison was made. The agreement does indicate, however, that the displacements are, perhaps, in some complicated way, related to the wind stress. Between the couette and Ekman spiral regimes, the agreement between the model and the observations was poor, and a more complicated dynamics must apply.

Horizontal pressure gradients are ignored in the present model. To reiterate, this is not to say that they are unimportant in the dynamics of the tropical oceans. The present model is intended not to be dynamically complete, but an attempt to model one aspect of a very complicated system, i.e., to see how well the redistribution of mass by Ekman pumping could account for thermocline displacements.

Acknowledgments. The authors are especially grateful to Drs. David Behringer and Robert Molinari for their comments and suggestions during the course of this study. Thanks are also due to Mr. Gary Meyers for making available the annual mean wind data for the study area.

REFERENCES

Anderson, D. L. T., and A. E. Gill, 1975: Spin-up of a stratified ocean, with applications to upwelling. *Deep-Sea Res.*, **22**, 583–596.

Cromwell, T., 1953: Circulation in a meridional plane in the central equatorial Pacific. *J. Mar. Res.*, **12**, 196–213.

Ekman, V. W., 1905: Om jordrotationens inverkan på vindstrommar i hafvet. *Nyt. Mag. Naturvid.*, **20**, Kristiania.

Katz, E. J., and collaborators, 1977: Zonal pressure gradient along the equatorial Atlantic. *J. Mar. Res.*, **35**, 293–307.

Love, C. M., Ed., 1971: *EASTROPAC Atlas*, Vol. 3. Circ. 330, Nat. Mar. Fish. Serv., Washington, DC.

———, 1972a: *EASTROPAC Atlas*, Vol. 1. Circ. 330, Nat. Mar. Fish. Serv., Washington, DC.

———, 1972b: *EASTROPAC Atlas*, Vol. 5. Circ. 330, Nat. Mar. Fish. Serv., Washington, DC.

———, 1973: *EASTROPAC Atlas*, Vol. 7. Circ. 330, Nat. Mar. Fish. Serv., Washington, DC.

———, 1975: *EASTROPAC Atlas*, Vol. 9. Circ. 330, Nat. Mar. Fish. Serv., Washington, DC.

Malkus, J. S., 1962: Large scale interactions. *The Sea*, Vol. 1, M. N. Hill, Ed., Interscience, 88–294.

Meyers, G., 1975: Seasonal variation in transport of the Pacific North Equatorial Current relative to the wind field. *J. Phys. Oceanogr.*, **5**, 442–449.

Moore, D. W. and S. G. H. Philander, 1977: Modeling of the tropical oceanic circulation. *The Sea*, Vol. 6, E. D. Goldberg, I. N. McCave, J. J. O'Brien and J. H. Steele, Eds., Interscience, 319–362.

Robinson, A. R., 1966: An investigation into the wind as the cause of Equatorial Undercurrent. *J. Mar. Res.*, **24**, 179–204.

White, W. B., 1977: Annual forcing of baroclinic long waves in the tropical North Pacific Ocean. *J. Phys. Oceanogr.*, **7**, 50–61.

Wyrtki, K., and G. Meyers, 1975: The trade wind field over the Pacific Ocean: Part I. The mean field and the mean annual variation. Hawaii Inst. Geophys., HIG-75-1, 67 pp.

Estuarine and Coastal Marine Science 7, 347-359.

Turbidity Maxima in Partially Mixed Estuaries: A Two-Dimensional Numerical Model

John F. Festa and Donald V. Hansen

National Oceanic and Atmospheric Administration, Atlantic Oceanographic and Meteorological Laboratories, 15 Rickenbacker Causeway, Virginia Key, Miami, Florida 33149, U.S.A.

Received 17 June 1977

Keywords: numerical model; suspended sediments; estuarine circulation; partially mixed estuary; gravitational circulation; sediment transport; turbidity; settling rates

A steady-state numerical model has been developed to help explain the presence of the turbidity maximum in partially mixed estuaries. The model supports the hypothesis that estuarine dynamics are primarily responsible for its occurrence.

The magnitude and location of the turbidity maximum is shown to depend upon the settling velocity (particle size) of the sediment, the amount of sediment introduced at both the ocean and river source, and the strength of the estuarine circulation. This phenomenon is not simply related to the river input of sediments, since results show the existence of a turbidity maximum for a sediment source which is predominately oceanic. Sediment flux stream functions show the presence of a closed cell when a turbidity maximum exists.

Introduction

Turbidity maxima, regions in which the concentration of suspended sediments is greater than in either the landward or seaward source waters, have been observed in many estuaries. They are observed typically near the landward limit of salt intrusion into the estuary. The most popular, and intuitively appealing, mechanism proposed for the occurrence of the maxima is that they are produced by the estuarine circulation pattern which is convergent in the lower portion of the water column. Postma (1967) gives a particularly lucid account of this hypothesized mechanism. He indicates that the magnitude of the maxima depends upon the amount of suspended material at both the river and ocean source, the settling velocity of the sediment, and the strength of the estuarine circulation. Three other processes, flocculation (Lüneburg, 1939; Ippen, 1966; and others) and deflocculation (Nelson, 1959) regulated by salinity variation, and local resuspension by tidal currents or waves (Schubel, 1968*a*; and others) have been offered as alternative or contributing mechanisms.

The logical connection between estuarine circulation and formation of the turbidity maximum has not been rigorously demonstrated. The purpose of this paper is to investigate this relationship by means of a dynamically consistent model of circulation and suspended sediment transport. The description by Postma (1967) is found to be correct in all of its major features, and further comments are made on some consequences of the process.

Circulation model

A detailed and accurate description of the circulation field is critical to any model simulating the transport of a substance within an estuary. Velocity distributions obtained from a circulation model for partially mixed estuaries (Festa & Hansen, 1976) satisfy such requirements. The circulation model is briefly described below.

The problem considered is that of a steady-state, two-dimensional, laterally homogeneous estuary. The coordinate system is Cartesian in x and z, where x increases toward the river, and z is positive upward. A linear equation of state, $\rho = \rho_0(1+\beta S)$, is assumed, and the Boussinesq approximation (Spiegel & Veronis, 1960) is employed.

The horizontal and vertical momentum balances, continuity of flow, and conservation of salinity are:

$$u_t+uu_x+wu_z = -\rho_0{}^{-1}P_x+(A_h u_x)_x+(A_v u_z)_z, \tag{1a}$$

$$w_t+uw_x+ww_z = -\rho_0{}^{-1}P_z+(A_h w_x)_x+(A_v w_z)_z-\beta g S, \tag{1b}$$

$$u_x+w_z = 0, \tag{1c}$$

$$S_t+uS_x+wS_z = (K_h S_x)_x+(K_v S_z)_z, \tag{1d}$$

where u and w are the horizontal and vertical components of velocity respectively, P is the hydrostatically reduced pressure, S is the salinity field, β is the coefficient of 'salt contraction', ρ_0 is the density of fresh water, A_h, A_v, and K_h, K_v are the horizontal and vertical exchange coefficients of momentum and salt, respectively, and g is the gravitational acceleration.

Although tidal fluctuations have been averaged out the tides are considered to be the primary source of energy for turbulent mixing. For simplicity, the exchange coefficients, a measure of the tidal strength, are chosen to be constant, as are the depth and width of the estuary.

The equations (1a), (1b), and (1c) are used to write a vorticity equation in terms of a stream function. The vorticity and salt equation, (1d), are non-dimensionalized and solved numerically for various river flow conditions, assuming reasonable values for the exchange (diffusion) coefficients. The model describes the transition from river to estuarine dynamics and its variations with river inflow. A detailed description of the model assumptions, boundary conditions, and finite difference techniques have been presented by Festa & Hansen (1976).

Suspended sediment model

The suspended sediment model is consistent with the circulation model, in that the same exchange coefficients are used for sediments as for salinity, and the advection is by currents derived from the circulation model. Consideration is limited to conditions in which sediment concentration has a negligible effect on water density.

Governing equation

The equation governing the distribution of suspended sediment in the estuary is:

$$C'_t+uC'_x+(w+W)C'_z = K_h C'_{xx}+K_v C'_{zz}, \tag{2}$$

where C' is the concentration of suspended sediment, u and w are the circulation velocities, K_h and K_v are the exchange coefficients as previously described, and W represents the settling velocity of the sediment. W is considered to be constant; therefore, specifying W is roughly equivalent to specifying the grain size of the sediment to be modeled.

The concentration, C', is normalized by $C' = C_r C$, where C_r represents the bottom concentration at the river boundary. Equation (2) is then written in terms of a stream function, ψ:

$$C_t = -\mathcal{J}(\psi, C) + K_h C_{xx} + K_v C_{zz} - W C_z, \tag{3}$$

where

$$u = -\psi_z \text{ and } w = \psi_x; \tag{4}$$

$\mathcal{J}$ is the Jacobian.

Boundary conditions

The computational length and depth of the estuary are given by L and H respectively. Zero total vertical flux of sediment is required at both the bottom and top boundaries (the vertical flow, w, is zero at these boundaries):

$$WC - K_v C_z = 0 \text{ at } z = 0,\ H. \tag{5}$$

These conditions require zero net deposition or erosion of bottom sediments and sediment conservation at the upper surface.

Sediment sources are maintained at the bottom at the seaward and river ends:

$$\begin{aligned} C &= R_c^{-1} = C_0/C_r \text{ at } (x, z) = (0, 0), \\ C &= 1 \qquad\qquad\quad \text{ at } (x, z) = (L, 0), \end{aligned} \tag{6}$$

where C_0 and C_r are the sediment concentrations at the ocean and river respectively; R_c is the river-to-ocean source concentration ratio.

An exponential profile is maintained at the river end:

$$C(z) = e^{\lambda Z/H} \text{ at } x = L, \tag{7}$$

where $\lambda = WH/K_v$. This is the appropriate analytical solution at the river end, where the horizontal advective and diffusive sediment flux divergence is zero.

The horizontal diffusive flux of sediment, $K_h C_x$, is required to be unspecified but horizontally non-divergent at the open seaward boundary. This is in agreement with the boundary condition used for modeling the estuarine dynamics (Festa & Hansen, 1976).

Numerical formulation and procedures

The spacing of the finite difference grid is chosen to be uniform in x, z and t such that

$$\begin{aligned} x_i &= i\Delta x,\ i = 0, 1, \ldots\ldots I \\ z_j &= j\Delta z,\ j = 0, 1, \ldots\ldots \mathcal{J} \\ t^n &= n\Delta t,\ n = 0, 1, \ldots\ldots, \end{aligned} \tag{8}$$

where $\Delta x = L/I$, $\Delta z = H/\mathcal{J}$ and Δt is the time step. Diffusion is approximated by the time-centered scheme of DuFort-Frankel (1953) and advection by the conservative form of the Jacobian (Arakawa, 1966) for which both C and C^2 are conserved. The resulting finite difference analog to (3) is:

$$\begin{aligned} (C^{n+1}_{ij} - C^{n-1}_{ij})/2\Delta t = {} & -\mathcal{J}^n(\psi, C)/4\Delta x\Delta z + K_h/\Delta x^2(C^n_{i+1j} + C^n_{i-1j} - C^{n+1}_{ij} - C^{n-1}_{ij}) \\ & + K_v/\Delta z^2(C^n_{ij+1} + C^n_{ij-1} - C^{n+1}_{ij} - C^{n-1}_{ij}) \\ & - W/2\Delta z(C^n_{ij+1} - C^n_{ij-1}). \end{aligned} \tag{9}$$

The numerical formulation of the bottom and top boundary conditions presented a major difficulty in the analysis. Conservative forms (Fix, 1975) of these boundary conditions, (6), are given by:

$$\begin{aligned} W(C_{i0}^{n+1}+C_{i1}^{n+1})/2 &= K_v/\Delta z(C_{i1}^{n+1}-C_{i0}^{n+1}) \text{ at } z = 0, \\ W(C_{iJ}^{n+1}+C^{n+1}_{iJ+1})/2 &= K_v/\Delta z(C_{iJ}^{n+1}-C^{n+1}_{iJ-1}) \text{ at } z = H. \end{aligned} \tag{10}$$

New boundary values, C_{i0}^{n+1} and C_{iJ}^{n+1}, are, therefore, calculated based on the computed interior points next to the boundary. While this is the conservative formulation of the flux condition, the accuracy of the solutions, nevertheless, depends critically upon the grid spacing and the magnitude of λ (see Fix, 1975, for a complete analysis). A 33×33 finite difference grid is used for all calculations.

The procedure followed to obtain the steady-state suspended sediment distribution is:

(1) Compute the steady-state circulation field for the desired mixing coefficients and river flow.

(2) Place this information, via the stream function, into the sediment model.

(3) Specify the settling velocity, W, and initialize the sediment distribution as:

$$C(x, z) = e^{\lambda Z/H}\{R_c^{-1}+(1-R_c^{-1})x/L\}. \tag{11}$$

(4) Start the calculation and continue until the sediment field has converged to a steady state.

(5) Check the suspended sediment distribution for mass conservation.

Model calculations

This model has been developed to help understand the basic processes which influence the distribution of suspended sediments in partially mixed estuaries. As no attempt has been made to model any particular estuary, the reader is cautioned about applying these results quantitatively: qualitatively, the results presented in the following sections will behave similarly for a range of estuarine dynamics; quantitatively they will of course depend critically on the choice of mixing coefficients and river discharge.

Estuarine circulation

The circulation model was run for a depth-averaged river flow, U_f, of 2 cm s^{-1}, depth, H, of 10 m, and length, L, of 120 km. A horizontal salinity difference, ΔS_h, of 30‰ is maintained between the seaward and river boundaries, and the mixing coefficients (in cm^2 s^{-1}) are: $K_v = 1$, $A_v = 10$, $K_h = 10^6$, and $A_h = 10^7$. These parameters are characteristic values typical of coastal plain estuaries (Dyer, 1973; Officer, 1976). As used in the model, they result in an estuary in which the circulation has a seaward transport of 2·4 river discharge volumes per unit width and a landward transport of 1·4.

Salinity and stream function contours [Figures 1(a) and (b)] show a stratified intrusion of salt into the estuary, and the typical estuarine pattern of seaward flow of near surface water and landward flow of deeper water. Contours of the velocity distributions are also presented [Figures 1(c) and (d)]. Maximum horizontal surface velocities exceed 16 cm s^{-1}, while the maximum landward velocities exceed 8 cm s^{-1} at the seaward boundary. Both seaward and landward velocities attenuate landward. The stagnation point (null zone), the location of zero horizontal velocity near the bottom, is at 60 km. The vertical component of flow, w, [Figure 1(d)] is of considerable interest, since sediment-particle settling behavior will depend critically on its magnitude and distribution. The maximum vertical velocity,

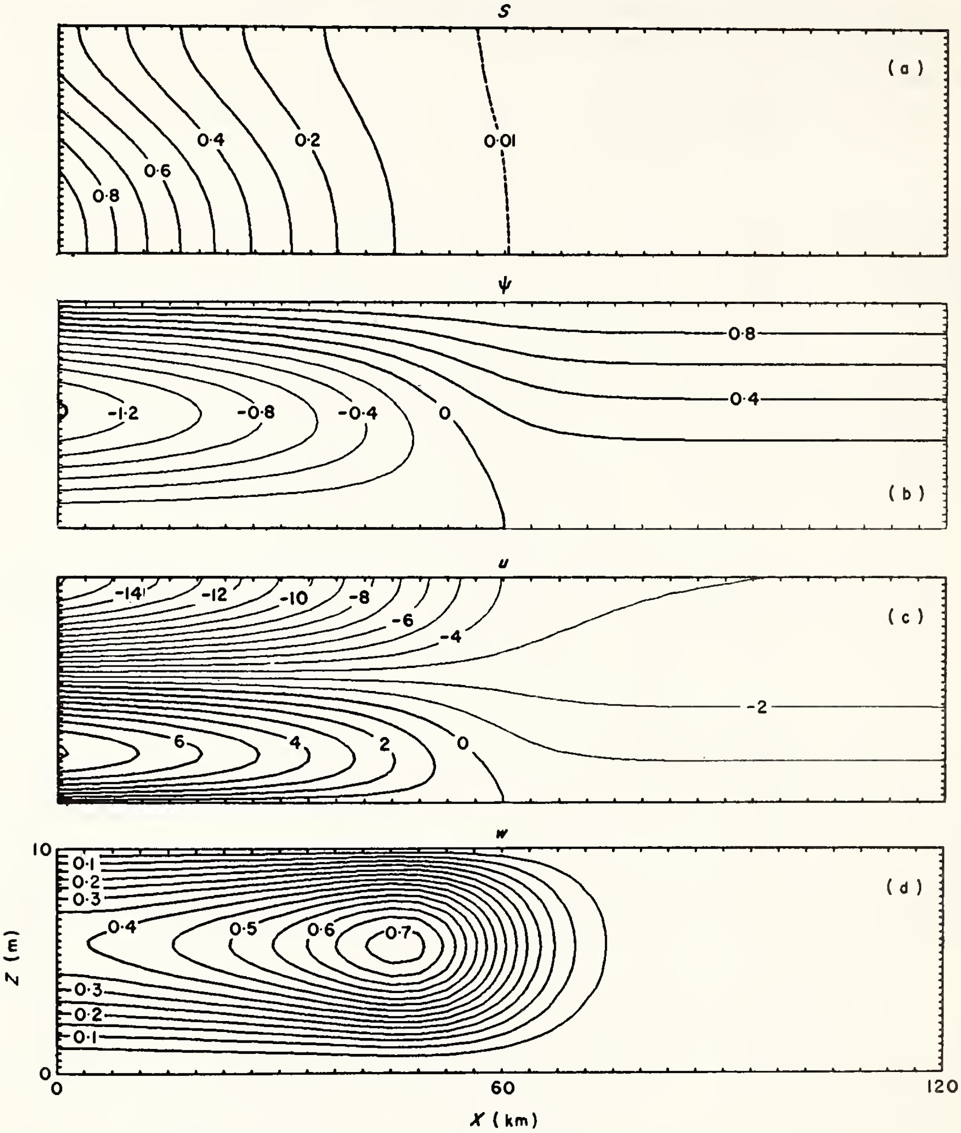

Figure 1. Salinity (a), stream function (b), horizontal velocity (c), and vertical velocity (d) fields for the case of $U_f = 2$ cm s^{-1}, $H = 10$ m and $L = 120$ km. Salinity is scaled by $\Delta S_h = 30‰$, stream function by 2×10^3 cm^2 s^{-1} and w by 10^{-3}. Velocity fields are contoured in cm s^{-1}.

approximately 7×10^{-4} cm s^{-1}, is located some 10 km seaward of the stagnation point. Attenuation of vertical velocity is greatest just landward of the maximum. At any given x, w reaches a maximum near mid-depth.

The effect of varying river flow is discussed in detail in the circulation paper (Festa & Hansen, 1976); a summary of these results is presented here.

As freshwater discharge is increased, there is an increase in both stratification and strength of the estuarine circulation. Increasing river discharge results in an increase in the magnitude of the vertical velocity as well as a seaward displacement of its spatial maximum (Figure 2).

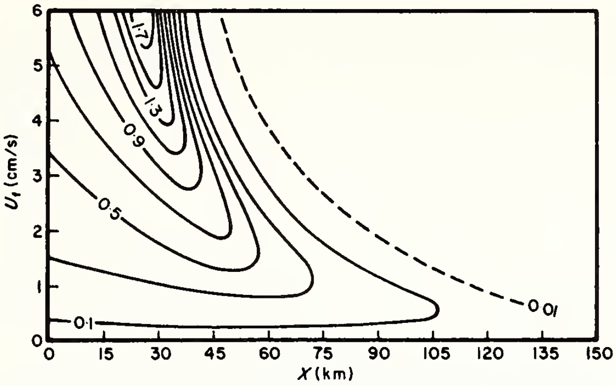

Figure 2. Vertical velocity contours at mid-depth as function of river discharge, U_f. Vertical velocity contours are scaled by 10^{-3} cm s^{-1} with a contour interval of 0·2.

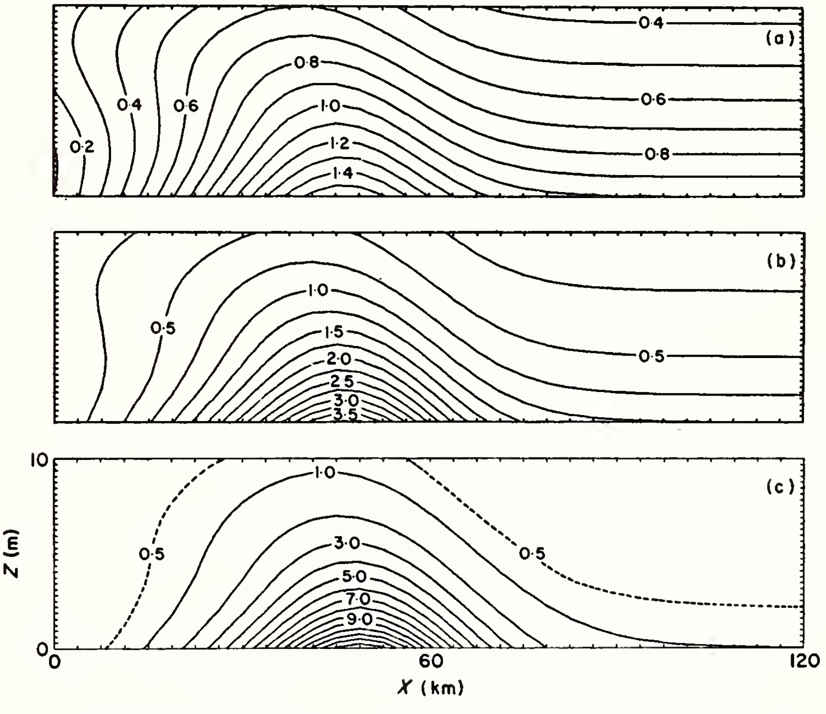

Figure 3. Suspended sediment distributions for particle settling velocities, W, of -1×10^{-3} cm s^{-1} (a), -2×10^{-3} cm s^{-1} (b), and -3×10^{-3} cm s^{-1} (c). The river-to-ocean source ratio, $R_c = 10$ for each case.

Decreasing river discharge allows salt to intrude farther up the estuary and also results in greater landward migration of the stagnation point. The effects of river discharge on the distribution of suspended sediments will be briefly discussed in a later section.

Suspended sediment distribution

Influence of settling velocity. Steady-state suspended sediment distributions are obtained for settling velocities, W, ranging from 0 to -3×10^{-3} cm s^{-1}, for the estuarine circulation associated with $U_f = 2$ cm s^{-1}. These settling velocities correspond to Stokes velocities associated with sediment particle diameters of 1 to 6 μm (clay to very fine silt) for particle densities of 2·65 gm cm^{-3}. This size distribution is commonly observed in partially mixed estuaries (Schubel, 1969; Meade, 1972; Nichols, 1974; Conomos & Peterson, 1977). The concentration of sediment at the river source, for this simulation, is considered to be 10 times the ocean source ($R_c = 10$), a condition similar to estuaries studied by Postma (1967) and Allen *et al.* (1974).

Contours of the suspended sediment distribution (Figure 3) show the presence of a concentration, or turbidity, maximum which is located approximately 45 km from the seaward boundary. This corresponds closely to the location of the maximum vertical velocity associated with the estuarine circulation [Figure 1(d)]. At settling velocities less than -5×10^{-4} cm s^{-1}, but non-zero, the concentration maximum decreases substantially, and its location approaches the stagnation point. Zero settling velocity produces pure advection and gradient diffusion so no concentration maximum occurs; the solutions are nearly the inverse of salinity, with small differences associated with the non-zero ocean source.

Dependence of the magnitude of the maximum on settling velocity (and implicitly on particle size) is better exemplified in Figure 4. A small concentration maximum is present for $W < -5\times10^{-4}$ cm s^{-1}; however, for $W > -5\times10^{-4}$ cm s^{-1} there is a substantial increase in its magnitude. Results are not presented for settling velocities beyond -3×10^{-3} cm s^{-1}, because the choice of mixing coefficients and the vertical resolution used gives erroneous solutions when W exceeds this value. Furthermore, the bottom boundary condition which requires total resuspension is not appropriate for particles having large settling velocities relative to the mixing conditions within an estuary.

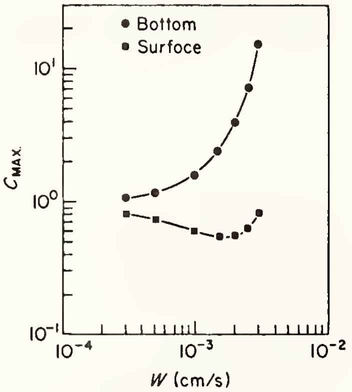

Figure 4. Magnitude of the concentration maximum as a function of particle settling velocity, W, at the surface and bottom boundary.

Influence of sediment sources

The effect of the relative strengths of river and ocean sources of sediment was examined by varying the river-to-ocean source concentration ratio, R_c, from 0·01 to 100. Contours of the suspended sediment for two settling velocities, $W = -1$ and -2 ($\times10^{-3}$ cm s^{-1}), and different values of R_c (Figures 5 and 6) clearly show the dependence of both magnitude and location of turbidity maxima on R_c. Increasing the ocean source concentration

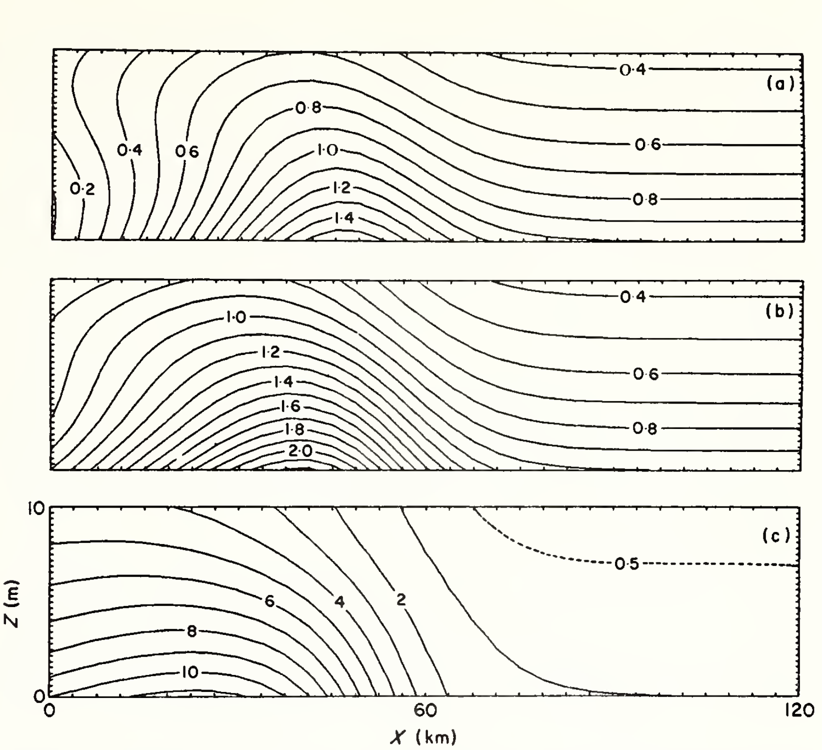

Figure 5. Suspended sediment distributions for a river-to-ocean source concentration ratio, R_c, of 10 (a), 1 (b), and 0·1 (c). Particle settling velocity, W, is -1×10^{-3} cm s^{-1}.

results in an increase in concentration values throughout the estuary. The turbidity maximum shifts seaward as R_c decreases; however, this shift is slight when $W = -2\times10^{-3}$ cm s^{-1}.

The magnitude of the concentration maximum at the bottom boundary, is presented as a function of settling velocity for $R_c = 10$ and 1 (Figure 7). Concentrations become higher as the ocean source becomes equivalent to the river; however, the general behavior is similar for each source ratio. This is also seen (Figure 8) where the source ratio for two settling velocities has been varied over a wider range. When the ocean contributes substantially to the estuarine suspended sediment budget, $R_c < 1$, the water column storage of sediments is not simply related to the river input. For $R_c < 1$, normalizing concentrations by the ocean boundary source is more logical than scaling by the river source. The result of this alternative normalization is also shown (Figure 8). The combination of these normalized curves has a maximum at $R_c = 1$ because the mass sediment flux into the estuary is a maximum at $R_c = 1$. Results of using still a third kind of normalization, the sum of the bottom river and ocean source concentrations as a measure of the total sediment source strength, is also presented (Figure 8). For the estuarine circulation parameters used, and a sediment characterized by a settling velocity of -2×10^{-3} cm s^{-1}, the turbidity maximum is approximately four times the total source concentration, and it is independent of how the source is distributed between the river and the ocean. For a smaller settling velocity (-1×10^{-3} cm s^{-1}) however, the situation is somewhat different. The turbidity maximum then varies from 1·5 times the total source concentration when the source is in the river to less than 1·1 times the source concentration when the source is in the ocean.

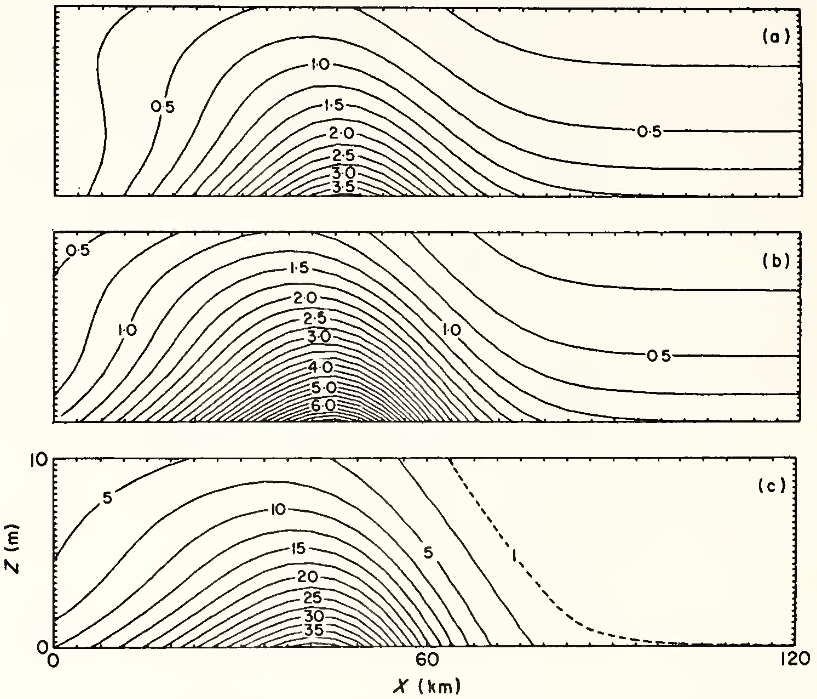

Figure 6. Suspended sediment distributions for river-to-ocean source concentration ratio, R_c, of 10 (a), 1 (b), and 0·1 (c). Particle settling velocity, W, is -2×10^{-3} cm s^{-1}.

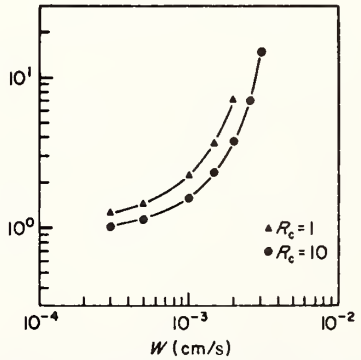

Figure 7. Magnitude of the concentration maximum as a function of particle settling velocity, W, for two river-to-ocean source concentration ratios, R_c.

Sediment flux stream functions

The calculated advective and diffusive fluxes of suspended sediment are used to evaluate[a] a suspended sediment stream function, φ, defined by:

$$uC - K_h C_x = -\varphi_z; \quad (w+W)C - K_v C_z = \varphi_x. \tag{12}$$

[a] This evaluation is readily made by solution of the Poisson equation $\nabla^2\varphi = -\mathbf{k} \cdot \nabla \times \mathbf{F}_s$, where $\mathbf{F}_s$ is the local sediment flux vector, and φ is prescribed around the boundaries.

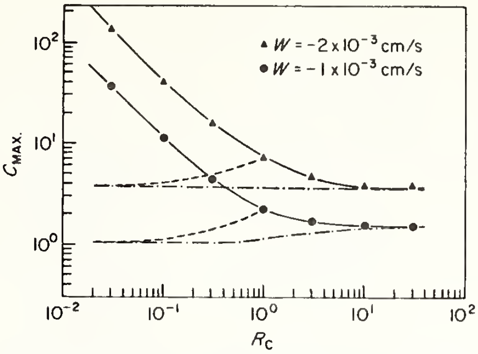

Figure 8. Magnitude of the concentration maximum as a function river-to-ocean source concentration ratio, R_c, for two particle settling velocities, W. Concentrations have been normalized by the river source ————, ocean source – – – – –, and the sum of the river and ocean sources – · – · –.

The function φ is analogous to the stream function [Figure 1(b)], but applies to the mass flux distribution of suspended sediment. Typical flux stream function patterns are presented (Figure 9). Contours for concentrations calculated for zero settling velocities and sources located either solely at the ocean or at the river have also been included. These are applicable to the flux of salt or to a dissolved constituent of the river water respectively as well as the limiting case of sediment of negligible settling velocity from the respective sources. It may be noticed that when river and ocean concentrations of such a substance are equal, there are no gradients, and the flux stream function [Figure 9(b)] is equivalent to the flow stream function [Figure 1(b)].

Perhaps the most interesting feature is the existence of closed sediment circulation cells, even for a constituent introduced at the river and having zero settling velocity, and even for a constituent introduced at the ocean if its settling velocity is as large as -2×10^{-3} cm s^{-1}. The patterns of the sediment flux stream function provides further insight on the mechanism of the turbidity maximum. In particular, the existence of closed flux contours which indicate downward flux of sediment in the seaward portion of the cell and upward flux in the landward portion, seems to be a necessary, but not a sufficient, condition for the occurrence of a turbidity maximum.

Consider the concentration of a substance introduced at the ocean and having zero particle settling velocity (the tracer property of salinity distributions are representative of this limiting case). It is readily understood from Figure 1(a), where gradient diffusion of salinity is everywhere upward and Figure 1(d), where the vertical flow rate, of order 5×10^{-4} cm s^{-1}, is also upward, why a turbidity maximum and closed sediment flux stream function do not develop. Now consider the distribution of a zero settling velocity substance introduced at the river; this differs from the distribution of salinity only in having the concentration increase toward the river and surface. Here, we find that gradient diffusion will be downward everywhere; this downward diffusion alone, while providing closed flux stream function contorus [Figure 9(a)], is nevertheless insufficient to produce a turbidity maximum.

The sufficient condition for the development of the turbidity maximum is that the downward flux by particle settling in the seaward portion of the estuary must be sufficient to overcome the upward flux by advection and diffusion. This condition is met for the examples of a dominant river sediment source (Figure 3, note the region of downward diffusive flux near the ocean boundary), as well as for the examples of equal source strengths [Figures 5(b)

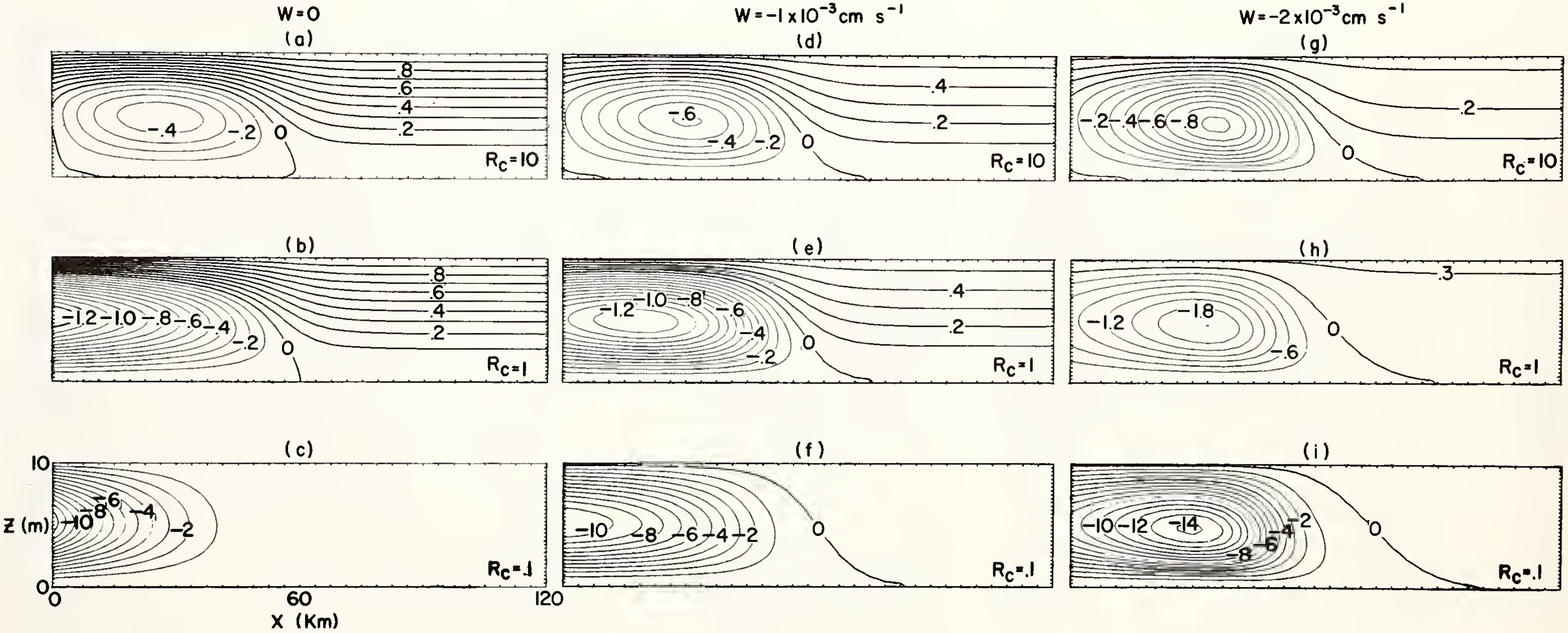

Figure 9. Sediment flux stream function, φ, fields as a function of W and R_c. Contours are scaled by 2×10^{-3}. Panels a, b, and c ($W = 0$), d, e, and f ($W = -1 \times 10^{-3}$ cm s^{-1}) and g, h, and i ($W = -2 \times 10^{-3}$ cm s^{-1}) are for $R_c = 10$, 1, and 0·1, respectively.

and 6(b)]. However a settling velocity as large as -1×10^{-3} cm s^{-1}, or approximately twice the vertical flow rate, does not produce a significant turbidity maximum from an ocean source [Figure 5(c)], because in that circumstance the diffusive flux in the critical region is too strongly upward to allow recirculation [Figure 9(f)] of sediment. If the settling velocity is doubled in the same situation, upward diffusion [Figure 6(c)] is no longer sufficient to prevent recirculation [Figure 9(i)] and the development of a strong turbidity maximum. It may be noted that due to the rearrangement of the concentration field, the upward diffusive flux is also increased.

Conclusion

The magnitude of the turbidity maximum (relative to the river source concentration) has been shown (Figure 8) to depend upon both the particle settling velocity and the contribution of suspended sediment from an oceanic source. This result agrees with statements by Postma (1967). However, relative to the total source concentration, the magnitude of the maximum depends upon the settling velocity and circulation patterns alone, except at the smallest settling velocities for which the phenomenon is poorly developed.

The lower layer of estuarine flow is one of advective convergence of landward flowing, more oceanic, water and seaward flowing river water toward a stagnation point or null zone on the bottom. Model results indicate that maximum concentration occurs slightly seaward of the stagnation point, where the upward vertical circulation is maximum. Vertical flux of sediment into the seaward flowing upper layer provides for advection of sediment out of the estuary to maintain the equilibrium. Horizontal diffusion is important locally to prevent mass accumulation and to help maintain the sediment distribution. Perhaps the most interesting effect of horizontal diffusion is to displace the near-bottom null zone in suspended sediment transport from that in water transport. This displacement is in the direction of the local flux by gradient diffusion; slightly seaward or landward for a zero settling velocity substance introduced at the river or ocean respectively, and strongly landward for material having a significant settling velocity, the more so as the fraction of materials originating in the ocean increases. This behavior depends in detail upon the specific formulation of the diffusive process in the model, but must apply in principle so long as any form of the gradient diffusion concept is valid.

Effects of varying river flow have also been studied, but the results are not presented in any detail in this paper. Basically, it is found that at higher river flows, the estuarine circulation is stronger, the vertical velocities are larger and, thus, larger settling velocities are required to develop a turbidity maximum. The implication of this finding is that individual estuaries will select from the full range of particles supplied to them, a relatively small range of particles for storage in the water column. This effect was inferred by Postma (1967) and Schubel (1968*a*, *b*). The distribution of particle sizes observed in an estuary cannot be expected to be representative of that supplied to it; however, it must be expected to change in response to dynamic adjustment of the estuary to changes in external variables such as river flow or tidal mixing. The location of the turbidity maximum moves seaward with increasing river discharge as do the stagnation point and salt intrusion. The opposite effect occurs at lower river flows, where smaller settling velocities can produce concentration maxima. Thus, the range in size distribution of suspended sediments varies as the estuarine dynamics change.

Simulation of a range of sediment sizes can be effected by superposition of results for appropriate size distributions. Emphasis is again made that the numerical results relating to particule size or settling velocity are functionally related to the parameters defining the circulation model, and are to be considered as exemplary rather than definitive.

Real estuaries tend to be strongly depositional environments in which sediments from the ocean and some fraction of sediments from rivers accumulate. In order to focus on the mechanism of the turbidity maximum by setting aside questions of sediment mass flux and retention rates, a somewhat artificial model with equilibrium 'flow thru' has been postulated. Extrapolation of the concepts presented here in the direction of small (down to zero) settling velocity is expected to be valid. Extension of results to higher settling velocities (Figure 4 or 7) becomes progressively less meaningful because complete resuspension of the larger particle sizes especially is unrealistic. The more complete model would be of interest. The principal problem to be solved for its development is a suitable formulation of the bottom boundary condition on sediment deposition and resuspension rates.

Acknowledgements

The progress of this research has benefitted from numerous discussions and criticisms by Drs D. Behringer, W. Lavelle, A. Leetmaa, C. Thacker and R. Young. The authors give special thanks to Drs J. Conomos and D. Peterson for their helpful suggestions, guidance and encouragement during the conception of this work.

References

Allen, G. P., Castaing, P. & Klingebiel, A. 1974 Suspended sediment transport and deposition in the Gironde Estuary and adjacent shelf. *Memoires de l'Intsitute de Geologie du Bassin d'Aquitaine* **7,** 27–36.

Arakawa, A. 1966 Computational design for long-term numerical integration of the equations of fluid motion. Two-dimensional incompressible flow. Part I. *Journal of Computational Physics* **I,** 119–143.

Conomos, T. J. & Peterson, D. H. 1977 Suspended Particle Transport and Circulation in San Francisco Bay: An Overview. In *Estuarine Processes,* Vol. II, Academic Press, New York. pp. 82–97.

Dufort, E. C. & Frankel, S. P. 1953 Stability conditions in the numerical treatment of parabolic differential equations. *Mathematical Tables and Other Aids to Computation* **7,** 135.

Dyer, K. R. 1973 *Estuaries: A Physical Introduction.* Interscience, New York. 140 pp.

Festa, J. F. & Hansen, D. V. 1976 A two dimensional numerical model of estuarine circulation: the effects of altering depth and river discharge. *Estuarine and Coastal Marine Science* **4,** 309–323.

Fix, G. J. 1975 Finite elements and fluid dynamics. Report number 75–1. *Institute for Computer Applications in Science and Engineering.*

Ippen, A. T. 1966 Sedimentation in estuaries. In *Estuary and Coastline Hydrodynamics.* McGraw-Hill, New York. pp. 648–672.

Lüneburg, H. 1939 Hodrochemische untersuchungen in der Elbmundung mittels elektrokolorimeter. *Archiv der Deutschen Seewarte* **59,** pp. 1–27.

Meade, R. H. 1972 Transport and deposition in estuaries. In *Environmental Framework of Coastal Plain Estuaries.* Geological Society of America. Memoir 133, pp. 91–120.

Nelson, B. W. 1959 Transportation of colloidal sediment in the freshwater-marine transition zone. *1st International Oceanographic Congress preprints,* AAAS, (abstract) pp. 640–641.

Nichols, M. M., 1974 Development of the turbidity maximum in the Rappahannock estuary. *Memoires de l'Institut de Geologie du Bassin d'Aquitaine* **7,** 19–25.

Officer, C. B. 1976 *Physical Oceanography of Estuaries (and Associated Coastal Waters).* Interscience, New York. 465 pp.

Postma, H. 1967 Sediment transport and sedimentation in the estuarine environment, In *Estuaries.* AAAS Publication No. 83, pp. 158–179.

Schubel, J. R. 1968*a* The turbidity maximum of the Chesapeake Bay. *Science* **161,** 1013–1015.

Schubel, J. R. 1968*b* Suspended sediment on the Northern Chesapeake Bay. *C.B.I. Technical Report* No. 35. The Johns Hopkins University, 264 pp.

Schubel, J. R. 1969 Size distributions of the suspended particles of the Chesapeake Bay turbidity maxima. *Netherlands Journal of Sea Research* **4,** 283–309.

Spiegel, E. A. & Veronis, G. 1960 On the Boussinesq approximation for a compressible fluid. *Astrophysics Journal* **131,** 442–447.

Printed in Great Britain by Henry Ling Ltd., at the Dorset Press, Dorchester, Dorset

Journal of Geophysical Research 83, No. C9, 4589-4592.

Scales of Motion in the Subtropical Convergence Zone

A. Leetmaa

National Oceanic and Atmospheric Administration, Atlantic Oceanographic and Meteorological Laboratories
Miami, Florida 33149

Arthur D. Voorhis

Woods Hole Oceanographic Institution, Woods Hole, Massachusetts 02543

Satellite infrared data show that the sea surface temperature pattern in the subtropical convergence consists of meridionally oriented alternating warm and cold plumes with a wavelength of about 200 km. In 1973, shipboard measurements during the Mid-Ocean Dynamics Experiment (Mode) revealed that the cold plumes resulted from southward advection of the surface water on the eastern flank of the Mode eddy and that the warm plumes were a result of northward advection on the western side. Along the edges of the plumes, small-scale frontogenesis was observed but was not resolved by the sampling scheme. Detailed measurements were made in March 1977 of the frontal structure at the southern end of a cold plume. These revealed the presence of smaller-scale motions with wavelengths of the order of 50 km. Temporal evolution of surface features in the vicinity and along the front occurred extremely rapidly and was barely resolved by surveys spaced 3–5 days apart.

Introduction

During the winter, surface temperatures over large areas in the northwestern Sargasso Sea are around 19°C. This cool water is separated from warmer water to the south by a transition zone between 32°N and 25°N. This is known as the subtropical convergence or front. In late winter the mean north-south surface temperature gradient in this region is 0.5°–1°C per degree of latitude [*Schroeder*, 1965]. The strong horizontal gradients are not confined to the surface. They extend to 200 m and perhaps deeper throughout the year. Schroeder's data are too limited in depth to describe the depth of penetration.

Satellite infrared imagery shows that disturbances in the subtropical convergence have a well-defined horizontal structure. During late winter and early spring the zone appears as a series of plumes of cold and warm water that are oriented primarily north-south. The plumes alternate in temperature between warm and cold (Figure 1). Their east-west wavelength, as determined by the distance between two warm (or cold) plumes, is about 200 km. The north-south extent of each plume is also about 200 km.

During the Mid-Ocean Dynamics Experiment (Mode) in 1973, one wavelength of this type of temperature distribution was observed [*Voorhis et al.*, 1976]. At that time the core of the anticyclonic Mode eddy lay under the eastern side of a warm plume. The cold plume to the east of the eddy resulted from southward advection of surface water by the eddy. Similarly, the eddy carried warm water to the north on its western flank. Thus the gross structure of the plume is determined by the mesoscale motion field. No other measurements exist to show this relationship.

During Mode, surface temperature measurements indicated the presence of small-scale fronts along the edges of these plumes. Temperature changes of the order of 1°–2°C over distances of the order of 10 km were observed. Probably, these were intimately tied to the mesoscale deformation fields. However, the Mode sampling scheme was too coarse to resolve the spatial and temporal evolution of the fronts and their detailed relationship to the mesoscale deformation fields.

Recent Observations

During March 1977 we surveyed in detail the southern tip of a cold plume. Satellite imagery was used to guide us to the area shown by the box in Figure 1. The evolution of the sea surface temperature field for most of the study is shown in Figure 2. The temperature contrast between the cold tongue and the warmer water to the south is concentrated in a narrow zone, i.e., a front. The temperature difference across the front is about 1.5°C, which is typical for fronts in this area. However, the density difference is about one half of that implied by this temperature change because the warmer water is also more saline.

The surface temperature field was continually changing (Figure 2). This was contoured subjectively from continuous measurements from the ship's bow thermistor (at a depth of about 4 m) along the indicated track lines. The evolution of the patterns is not resolved by these surveys, which are about 4 days apart. The front that runs in a (generally) easterly direction along 28°45′N changes rapidly. It breaks down in some areas and then intensifies. A breakdown occurs between surveys 2 and 3 at about 69°15′W. By survey 4 it has again intensified in this area and appears to be associated with a subsurface cold core eddy at 68°45′W whose surface expression is shown by the 20°C isotherm during survey 4. This rapid evolution frustrated attempts to observe inflow into the front by using drogues. The drogue measurements will be reported elsewhere by Voorhis. Interestingly enough, even though the smaller-scale patterns evolved rapidly, the larger-scale pattern of the cold pool in the middle of the survey area and warmer water to the south and east changed little. During Mode the time scale for the large plumes to change was observed to be of the order of a month or so.

Expendable bathythermographs (XBT) were launched at intervals of about 11 km along the track lines during surveys 2–4. The thermal field during survey 4 at several levels is shown in Figure 3. The levels were chosen to depict the difference in structure between the surface, the near-surface layers, and the main thermocline. In fact, the patterns are similar at each level. Of special interest is the strongly uplifted area in the depth of the 10° isotherm near 28°35′N, 68°45′W. In this region the 19° isotherm rose about 80 m between surveys 2 and

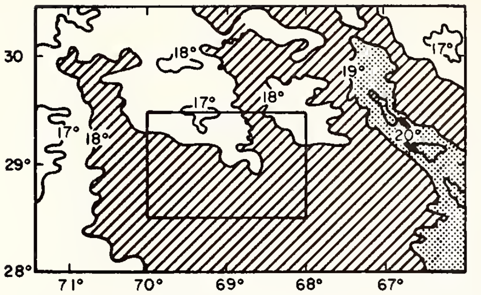

Fig. 1. Uncalibrated digital infrared data at 1°C resolution from Goes satellite showing subtropical convergence on February 28, 1977. The outlined area shows region in which shipboard surveys were conducted during March 1977. Hatched area shows temperatures between 18° and 19°C. Dotted area indicates temperatures greater than this.

3 and 60 m between surveys 3 and 4. This uplifting or 'cyclogenesis' corresponds to an average vertical velocity of about 2×10^{-2} cm/s. No evidence exists to show that this feature was advected into this region. Since there was no water as cold as 20°C at the surface during the previous survey, the presence of it over the uplifted area suggests that upwelling lowered the surface temperature.

The largest changes in the depth of the 14°C isotherm occur in the vicinity of the surface front. This indicates that the frontal structure penetrates the main thermocline. The topography of the 14°C surface exhibits a series of troughs and ridges that have a zonal wavelength of about 50 km. As many as five or six waves can be seen in the lower panel of Figure 3. The other surveys indicate that these are fairly stationary in time and space. The cyclone at the level of 19°C surface lies in the ridge of one of these waves with no apparent phase shift between these two levels (and the surface also). Although these waves do not appear to change over our period of observations, the mean depth of the thermocline over the whole survey area decreased by about 40 m. It is not clear how this decrease is linked to the near-surface cyclogenesis and surface frontogenesis.

Discussion

One is tempted to draw analogies between the long waves (mesoscale motions) and short waves (submesoscale motions) in the subtropical convergence and the long and short waves along the polar front in the atmosphere. In the latter case, baroclinic instability is an important mechanism by which the short waves gain energy from the potential energy field of the long waves [*Palmén and Newton*, 1969]. In the subtropical convergence the mean flow in the upper part of the water column is to the east [*McWilliams*, 1974]. Theoretical studies indicate that such flows are baroclinically stable [*Gill et al.*, 1974]. Thus this instability is an unlikely energy source for the Mode eddy and hence the warm and cold plumes. Furthermore, the time scale of 3–5 days for the observed cyclogenesis along the cold plume is extraordinarily fast for baroclinic instability.

The small-scale frontogenesis along the edges of these plumes is undoubtedly related to the deformation field of the mesoscale eddies. One factor that is necessary for the existence of fronts is the presence of horizontal temperature (density) gradients. The mesoscale deformation fields bring together water masses with differing temperatures. Thus the fronts are observed at the boundaries of the warm and cold tongues. In practice it is extremely difficult to observe the deformation fields themselves. The fronts appear to penetrate the thermocline and consequently modify the thermocline topography from which the deformation fields might be deduced. Furthermore, submesoscale features can be present near the fronts and can evolve rapidly. What is the origin of these features?

One mechanism that could supply energy to smaller-scale motions is the collapse of the cold tongue. A quantitative documentation of such a collapse is impossible from the present data set. A measure of it would be to examine if, in the

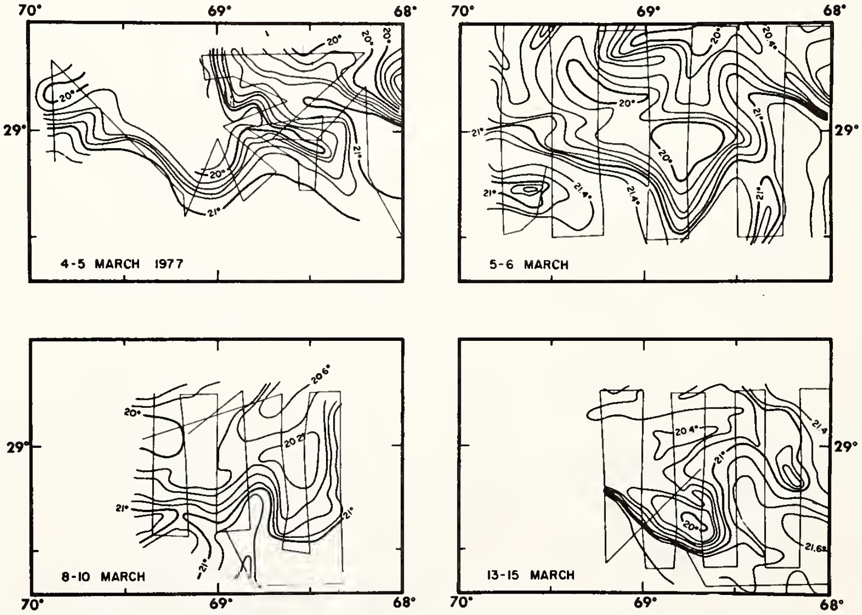

Fig. 2. Evolution of sea surface temperature patterns in area outlined in Figure 1.

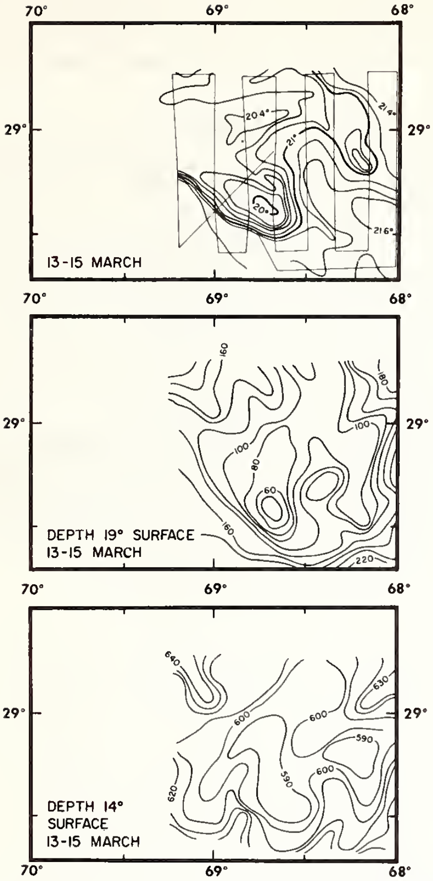

Fig. 3. Vertical structure of thermal field at several levels during survey 4. The top panel is the surface temperature.

mean, there is a reduction of the horizontal temperature gradients. The potential energy that is available for conversion to kinetic energy, i.e., the available potential energy, is proportional to the volume integral of the temperature fluctuations at constant pressure levels [*Lorenz*, 1955]. This quantity is proportional to the volume integral of the fluctuations in the depths of all the isotherms. Table 1 illustrates that there was a decrease in the amplitude of the depth fluctuations in each of the listed temperatures from survey 2 to survey 3. To test further the hypothesis that a sinking of the surface cold pool took place, the vertical velocity was computed from the observed change in the depths of the isotherms (i.e., $w = \partial h/\partial t$). This approach cannot be rigorously defended except if an extremum develops. The vertical velocity field as deduced in this manner from changes in the depth of the 20°C isotherm between surveys 2 and 3 is shown in the upper panel of Figure 4. This isotherm was picked because it lies close to the surface. Its mean depth at this time was about 50 m. The temperature at this level is shown in the lower panel of Figure 4. Comparison of these two figures indicates that a general correlation exists between sinking motion in the colder areas and rising motion in the warmer areas. Thus despite the somewhat questionable nature of the w calculation, the conclusion that one draws is consistent with that drawn from Table 1. Over small parts of the survey area the 20°C isotherm intersected the surface during this time. Close to the surface, nonadiabatic effects might be important. Local heating in this area during this time of the year might raise the average temperature over the top 10 m by about 0.3°C during the survey period [*Stommel et al.*, 1969]. Such a small temperature rise would, of course, affect the whole survey area and would not modify the previous conclusions.

TABLE 1. Mean Depth/Standard Deviation in Depth

Isotherm, °C	Survey 2	Survey 3	Survey 4
20	62/44	43/20	46/27
19	173/39	138/26	124/39
18	333/18	311/17	300/32
17	444/15	427/11	420/20
15	581/11	568/9	556/13
12	728/13	711/12	701/13

The standard deviation in the depths of the isotherm increases again between survey 3 and survey 4. The increase is most pronounced in the temperature range 19°–17°C. This results mostly from the strong uplifting of these isotherms near 28°40'N and 68°40'W (Figure 3). Associated with this uplifting is the occurrence at the surface of a patch of water colder than 20°C and an intensification of the front. Evidently, the vertical motion field was quite important in this frontogenesis.

From this data set it is impossible to follow in any detail the energy conversions. These probably are cyclical, and energy is converted from potential to kinetic and back again. It is interesting to speculate about the mechanisms that might be responsible for the breakdown and reformation of the frontal zone and the associated cyclogenesis. The time scale on which this occurs, i.e., 3–5 days, is extraordinarily fast for baroclinic instability. This suggests that either a mixed baroclinic-barotropic or barotropic instability might be taking place. A necessary condition for the latter is that the anticyclonic shear in the

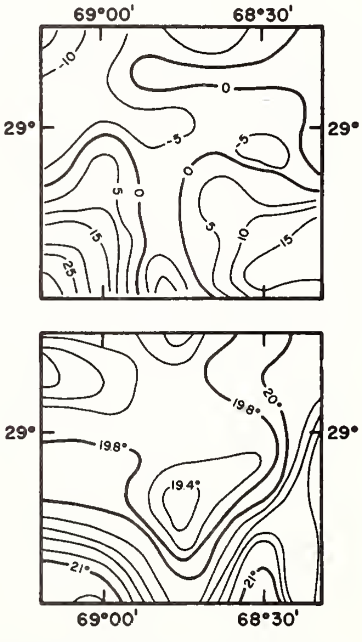

Fig. 4. Upper panel shows vertical velocity pattern between surveys 2 and 3 computed from changes in the depth of the 20°C isotherm. The units are cm/s × 10³. The lower panel shows the temperature at 50 m during survey 2.

front be comparable to f, the Coriolis parameter [*Kuo*, 1949]. A crude scale analysis indicates that cross-frontal shears of this magnitude can occur. The along-frontal velocities were of the order of 70 cm/s, and the cross-frontal scale is about 10 km. This gives a shear of $7 \times 10^{-5}\ s^{-1}$, which is comparable to f. There are several places where unstable disturbances might have been present. These are near 69°30'W during survey 2, near 69°15'W and 68°45'W during survey 3, and near 68°45'W during survey 4. Each of these disturbances occurs on the anticyclonic side of the front.

These observations suggest that small-scale frontogenesis is associated with the spatial and temporal evolution of the surface temperature field that is caused by mesoscale eddies. During their lifetimes the fronts change rapidly. Submesoscale features along the front appear to be partly responsible for this change. These possibly owe their origin to instability of the front itself. The fronts and the submesoscale features appear to penetrate the main thermocline. One can only speculate on the role that these play in the evolution of the mesoscale eddies.

Acknowledgments. This work was supported for one of us (A.D.V.) by the Office of Naval Research under contract N00014-74-C-0262, NR 083-004. Woods Hole Oceanographic Institution contribution 4132.

REFERENCES

Gill, A. E., J. S. A. Green, and A. J. Simmons, Energy partition in the large-scale ocean circulation and the production of mid-ocean eddies, *Deep Sea Res.*, *21*, 499–528, 1974.

Kuo, H. L., Dynamic instability of two-dimensional nondivergent flow in a barotropic atmosphere, *J. Meteorol.*, *6*, 105–122, 1949.

Lorenz, E. N., Available potential energy and the maintenance of the general circulation, *Tellus*, *7*, 157–167, 1955.

McWilliams, J. C., Mode mean currents and eddy surface intensification, *Mode Hot Line News*, *57*, 1974.

Palmén, E., and C. W. Newton, *Atmospheric Circulation Systems*, 603 pp., Academic, New York, 1969.

Schroeder, E. H., Average monthly temperatures in the North Atlantic Ocean, *Deep Sea Res.*, *12*, 323–343, 1965.

Stommel, H., K. Saunders, W. Simmons, and J. Cooper, Observations of the diurnal thermocline, *Deep Sea Res. Suppl.*, *16*, 269–284, 1969.

Voorhis, A., A. Leetmaa, and E. Schroeder, The influence of the deep mesoscale eddies on the surface temperature in the North Atlantic subtropical convergence, *J. Phys. Oceanogr.*, *6*, 953–961, 1976.

(Received November 17, 1977;
revised April 3, 1978;
accepted April 7, 1978.)

Journal of Marine Research 36, No. 3, 311-322.

Updated charts of the mean annual wind stress, convergences in the Ekman Layers, and Sverdrup transports in the North Atlantic

by Ants Leetmaa[1] and Andrew F. Bunker[2]

ABSTRACT

From the wind stress computation of Bunker (1976) for the North Atlantic, the annual mean and seasonal vertical velocities which result from convergences in the Ekman Layers are computed. Charts of the geostrophic and total transport (geostrophic plus Ekman) are constructed using the Sverdrup relationship. Of particular interest are an intense current leaving the coast at the point where the Gulf Stream separates and a cyclonic gyre north of the Stream in this area. Good agreement exists between the computed features of the large scale circulation patterns and the observed ones. Close correspondence exists between the predicted and observed paths of the Gulf Stream; separation from the coast occurs at the maxima in the wind stress.

1. Introduction

As part of a larger investigation to estimate the total energy flux between the ocean and the atmosphere, wind stress distributions were computed by one of us for the North Atlantic Ocean (Bunker, 1976). In recent years a number of authors have constructed charts of the curl of the wind stress in order to estimate large scale ocean transports (Hantel, 1971, Evenson and Veronis, 1975, and Bye, Noye, and Sag, 1975). Since this computation has been done several times recently, the question arises as to why it should be repeated yet again.

Saunders (1976) estimated the annual wind stress in 1° squares over a 10° square in the North Atlantic. Using these values in estimating the curl of the stress, he found that the value of the curl can be greatly underestimated if it is based on 5° square wind stress data. Thus in the previous studies which used that spatial resolution, the curl of the stress, and consequently the ocean transports, were probably underestimated. For the present study, in most areas the stress was computed over areas 2° of latitude × 5° of longitude. This spacing still is larger than the one employed by Saunders. However, most of the spatial variation in the stress occurs in the meridional direction; consequently the lack of resolution in the zonal direction

---

[1] National Oceanic and Atmospheric Administration, Atlantic Oceanographic and Meteorological Laboratories, Miami, Florida, 33149, U.S.A.

[2] Woods Hole Oceanographic Institution, Woods Hole, Massachusetts, 02543, U.S.A.

is not a major drawback in computing the net meridional transports across the whole ocean basin along a latitude circle, and based on Saunders study 2° resolution in latitude should be sufficient.

Comparison of the geostrophic transport at several latitudes in the North Atlantic, as estimated from hydrographic data, with the transport estimated using the curl of the stress from Bunker's (1976) calculation in the Sverdrup relation, shows quite good agreement (Leetmaa, Niiler and Stommel, 1977). This comparison provides some evidence that the present estimates are probably reasonably accurate. They may perhaps be still a bit low because of the limited resolution. It would require a much more ambitious effort to redo these calculations on a finer grid. Even then there are regions such as large areas of the Southeastern Atlantic where the data base is insufficient for reliable estimates of the stress on the finer grid.

2. The observations and error estimates

The National Climatic Center (NCC) has collected weather reports and sea surface temperatures from ships, converted them to uniform formats, eliminated gross errors, and recorded them on magnetic tape. This series of data, designated TDF-11, is described in a notebook by NCC. Data from 66 Marsden Squares (10° squares) for the years 1941-72 were obtained from NCC and processed for the present study. Nearly 12 million reports were read from the tapes. Of these about 4 million reports were rejected, primarily because observations of one or more variables were missing. A computer program was written to check the quality of each report, select the reports with all the variables necessary, compute energy fluxes, and form averages of fluxes. The bulk aerodynamic equations were used to compute the stresses. Drag coefficients were used which vary with wind speed and stability. A complete discussion of the choice of drag coefficients and the computational procedures is given in Bunker (1976).

There are three major sources of error in estimating the wind stress (Bunker, 1976). The first is possible errors in the estimation of the wind. Ship reports are the source of most of the wind observations. Previous investigations have shown that median winds are underestimated by marine vessels relative to weather ships by about 5%. The choice of a value for a drag coefficient adds another 10-20% uncertainty into the stress computation. Additional uncertainty results from inadequate spatial resolution of the wind stress field. The data used in the curl computations usually were averaged over regions measuring 2° of latitude by 5° of longitude. Near coasts and over large areas where little data were available the stresses were averaged over irregularly shaped areas. A spatially centered finite difference scheme was employed to estimate the curl operator where Δx was 10° of longitude and Δy was 4° of latitude. The curl computation was not done in the areas next to the coast. Where Bunker's (1976) data were over irregular shaped areas, these were averaged to areas 2° by 5°. In the region in which Saunders (1976) did his computation, our curl estimates differ from his, averaged to our areas, by ± 30% for the 2° × 5° areas. Additional zonal averaging to areas 2° × 10° reduces this difference to a minus 5 to 10%, i.e. our estimates are lower than his. The larger errors for the smaller averaging region reflect the fact that there is structure in the meridional winds on a scale of less than 5°. This, of course, does not affect the net meridional transport which is a sum over the width of the basin and averages over this structure. Thus the smaller error estimate is the appropriate one. Thus, possible underestimation of the wind speed, uncertainty in the choice of a drag coefficient, and inadequate spatial resolution contribute to an overall uncertainty in our curl computation of about 30%.

3. Mean charts

Contours of the mean annual zonal and meridional wind stress are shown in Figure 1. The largest values of the stress tend to be in the zonal direction. Maxima in the east-west stress occur off the east coast of the United States, off Newfoundland, and at about 55N and 25W. These tend to lie over the boundary between warm and cold water that is defined by the Gulf Stream. Another maximum occurs in the region of the Trade Winds centered near 15N, 50W. The magnitude of the meridional wind stress is generally much less than that of the zonal stress. Large maxima in the meridional stress do occur, however, off the west coast of Africa and south of Greenland. These charts show larger values by about 25-50% of the stress for the maxima and more spatial structure for the maxima than Hellerman's (1968) (as depicted in Evenson and Veronis, 1975).

Using these mean values for the wind stress, the quantity $\mathrm{curl}_z\ (\vec{\tau}/f)$ was computed from curl $z(\vec{\tau}/f) = \frac{\partial}{\partial x}(\tau_y/f) - \frac{\partial}{\partial y}(\tau_x/f)$, where $\vec{\tau} = (\tau_x, \tau_y)$ is the wind stress, $f = 2\Omega \sin \Theta$ is the Coriolis parameter, Ω is the angular velocity of the earth's rotation, and Θ is the latitude. This quantity represents the divergence of the Ekman transport, i.e. the vertical velocity times the density at the base of the ocean Ekman layer, i.e. the net divergence in this layer. Under certain assumptions it is equal to β/f times the total meridional geostrophic transport in the ocean (see Stommel (1965), pp. 154-156, for a discussion about the relationship between the curl of the stress, Ekman convergences, Sverdrup transport, and geostrophic transports). The computations were carried out between 5N and 60N. Close to the equator, it is not clear what the dynamical balances in the near surface boundary layer are. Thus it is not appropriate to use the present formalism to compute the convergence. The regions close to the continental boundaries were also omitted because of possible boundary effects on the dynamics. The results for the mean value of the vertical velocity at the base of the Ekman layer are shown in Figure 2.

One thing to note is that the values are larger than have been reported previously

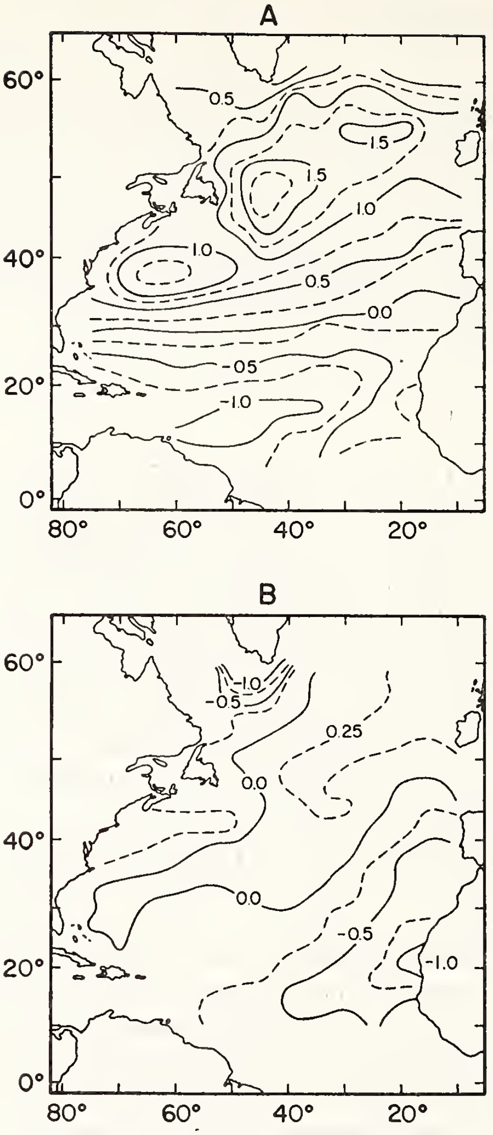
A
60°
40°
20°
0°
80°
60°
40°
20°
0.5
1.5
1.5
1.0
1.0
0.5
0.0
-0.5
-1.0
B
60°
40°
20°
0°
80°
60°
40°
20°
-1.0
-0.5
0.25
0.0
0.0
-0.5
-1.0

Figure 1. A) Contours of annual mean eastward wind stress over the North Atlantic. Units are dynes/cm^2.
B) Contours of annual mean northward wind stress. Units are dynes/cm^2.

(see, for example, Stommel (1964)). The zero line which separates the subpolar (vertical velocity positive) from the subtropical (vertical velocity negative) gyres follows the maxima in the eastward component of the wind stress. The subpolar gyre consists in fact of two gyres—one off the east coast of America and the other

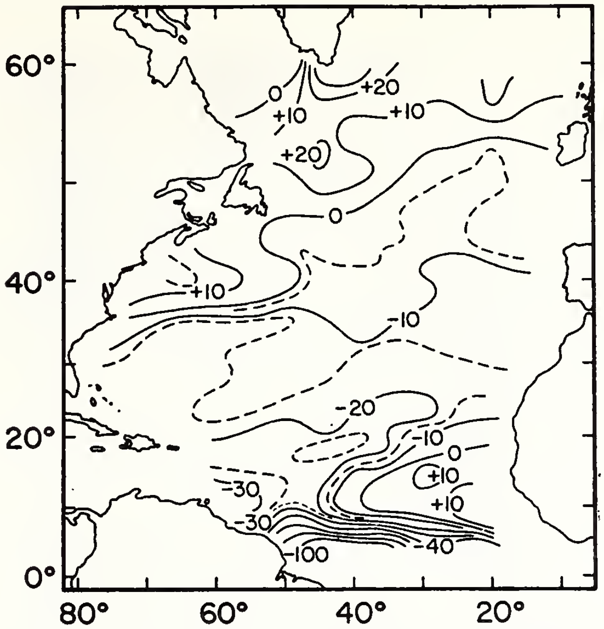

Figure 2. Annual mean vertical velocity at base of Ekman layer. Positive is upward. Units are 10^{-5} cm/sec. Note that off South America the contours between −60 and −100 are left out because of crowding.

north of about 50N. Another region of positive vertical velocities appears off the African coast.

Contours of the Sverdrup mass transport stream function are shown in Figure 3. These were determined by computing first in each 2° × 5° box the meridional Ekman and geostrophic transports. Then starting at the eastern boundary, where the transport function is assumed to be zero, the net meridional transport (Ekman plus geostrophic) at every 5° of longitude is obtained by summing westward. The resulting field is then contoured. The calculated total southward transport at 31N is 32 × 10^{12} g/sec. This is comparable to what is observed to flow northward through the Florida Straits (Leetmaa, et al. 1977). An interesting feature about the distribution of the predicted transport is an intense current that leaves the coast at the latitude that the Gulf Stream is observed to separate from the coast. The maximum in the wind stress that overlies this region is related to the intense winter storms. To the north of this maximum the curl is positive. An oceanic cyclonic gyre whose transport is 10-15 × 10^{12} g/sec, is driven by the positive curl if topographic effects are not important. Perhaps this gyre is related to the observed slope water circulation. Below 12°C slope water is indistinguishable in its *T-S* properties from water in the Gulf Stream. Consequently its transport and the deep recirculation on the Sargasso side of the Stream as postulated by Worthington (1976) com-

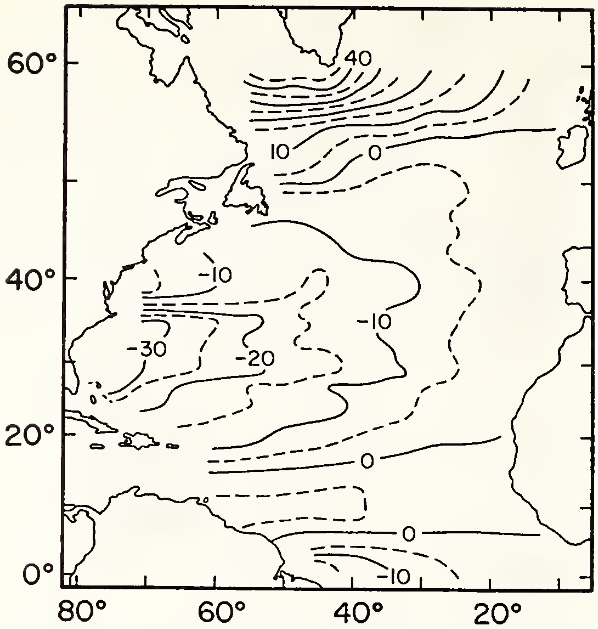

Figure 3. Contours of the annual mean Sverdrup mass transport. Units are 10^{12} g/sec.

plicate the problem of determining the wind-driven contribution to the total measured Gulf Stream transports in this area.

North of about 50N the curl is predominantly positive. This drives a subpolar gyre that has a maximum transport of about 40 Sverdrups. A gyre with comparable transports was derived by Evenson and Veronis (1975). At 59N between 10W and 20W the northward wind-driven flow is about 10×10^{12} g/sec.; this possibly continues into the Norwegian Sea. Worthington (1970) from direct measurements estimated the inflow to be about 8×10^{12} g/sec. However, he postulated that this was driven by thermohaline processes occurring in the Norwegian Sea and not the curl of the stress.

The total transport map (Fig. 3) indicates that by continuity there should be a northward flow (Brazil Current?) along the coast of Brazil to about 5N. However, between 16N and 5N the total transport along the coast in the boundary current should be southward. The Ekman transports in the interior are to the north and greater than the predominantly southward geostrophic transports. Thus the net interior flow is to the north and this results in a southward transport along the coast in the boundary current. This picture of the total transport agrees with the circulation pattern in this area as deduced from the T-O_2 correlations by Metcalf and Stalcup (1967). They concluded that the Brazil Current extends northward only to 5N because between there and 16N water with low oxygen content, associated with

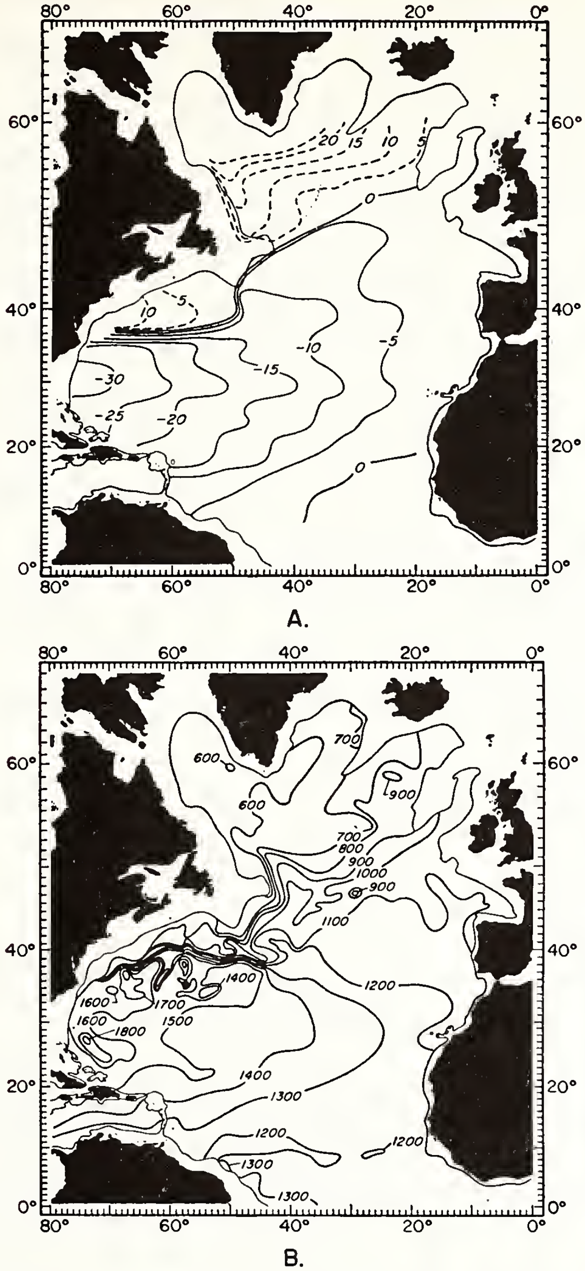
80°
60°
40°
20°
0°
60°
40°
20°
0°
20
15
10
5
0
-5
10
-10
-15
-5
-30
-25
-20
0
A.
80°
60°
40°
20°
0°
60°
40°
20°
0°
700
600
900
600
700
800
900
1000
900
1100
1200
1400
1600
1700
1600
1800
1500
1400
1300
1200
1200
1300
1300
B.

Figure 4. A) Contours of annual mean geostrophic volume transport. Units are 10^{12} g/sec. B) Chart of dynamic topography of 100 db surface relative to 1500 db surface in dynamic meters × 10^3.

temperatures between 13° and 24°C, lies between water with higher oxygen content in this same temperature range to the north and south.

Stream function maps can be drawn for the total transport field since it is horizontally non-divergent. Streamlines cannot formally be drawn for the geostrophic transport field because it is horizontally divergent. However, the divergence is generally small. On the average in any 2° × 5° box the flux into or out of the Ekman layers due to horizontal convergence is only about 5% of the geostrophic transport in that box. This enables "pseudo-geostrophic" streamlines to be constructed. This is done by assuming a zero value of the stream function at the eastern boundary and summing the meridional geostrophic transport westward 5° at a time until the western boundary *or* the point where the curl goes to zero is reached. A rationale for choosing the latter criterion is that the subtropical gyres might be separated from the subpolar gyres by a regime where the isotherms come to the surface. This westward summation is done at every 2° of latitude, and then the resulting field is contoured. This construction can be directly compared to the geostrophic flow field as deduced from a dynamic topography map of the 100 decibar surface relative to the 1500 decibar surface (Leetmaa, et al., 1977). There is great visual similarity between Figures 4A and B. An interesting feature in the predicted flow field is a concentrated flow in about the same location as the observed Stream from 35N to 50N flowing northeastward across the Atlantic. This results because the zero of the curl of $(\vec{\tau}/f)$ lies over the Stream. That it continues to do so all across the Atlantic is rather surprising. Using this construction of the geostrophic transport field the two cyclonic gyres are also quite evident. The one off the east coast of the United States has a transport of 10-15 × 10^{12} g/sec. The total geostrophic transport between this gyre and the subtropical gyre is about 45 × 10^{12} g/sec.

4. Seasonal fluctuations

The seasonal variation of the vertical velocity at the base of the Ekman layer, W_e, is shown in Figure 5. Comparison with Figure 2 shows that the fluctuations in most places are comparable in magnitude to the mean W_e. The largest fluctuations tend to be on the western side of the ocean basin except near 10N. There they extend across the ocean and are probably associated with the annual cycle in the strength and position of the Intertropical Convergence.

The question arises as to whether the seasonal fluctuations in W_e can be related to fluctuations in the transport of the western boundary currents. Theoretically, fluctuating winds at this frequency would produce primarily a barotropic response (see discussion in Evenson and Veronis, 1975). On the other hand, the *mean* Sverdrup transport seems primarily to be concentrated in the upper ocean (Leetmaa, Niiler, Stommel, 1977). Also, most of the evidence about seasonal fluctuations is from hydrographic measurements and only gives information about fluctuations in

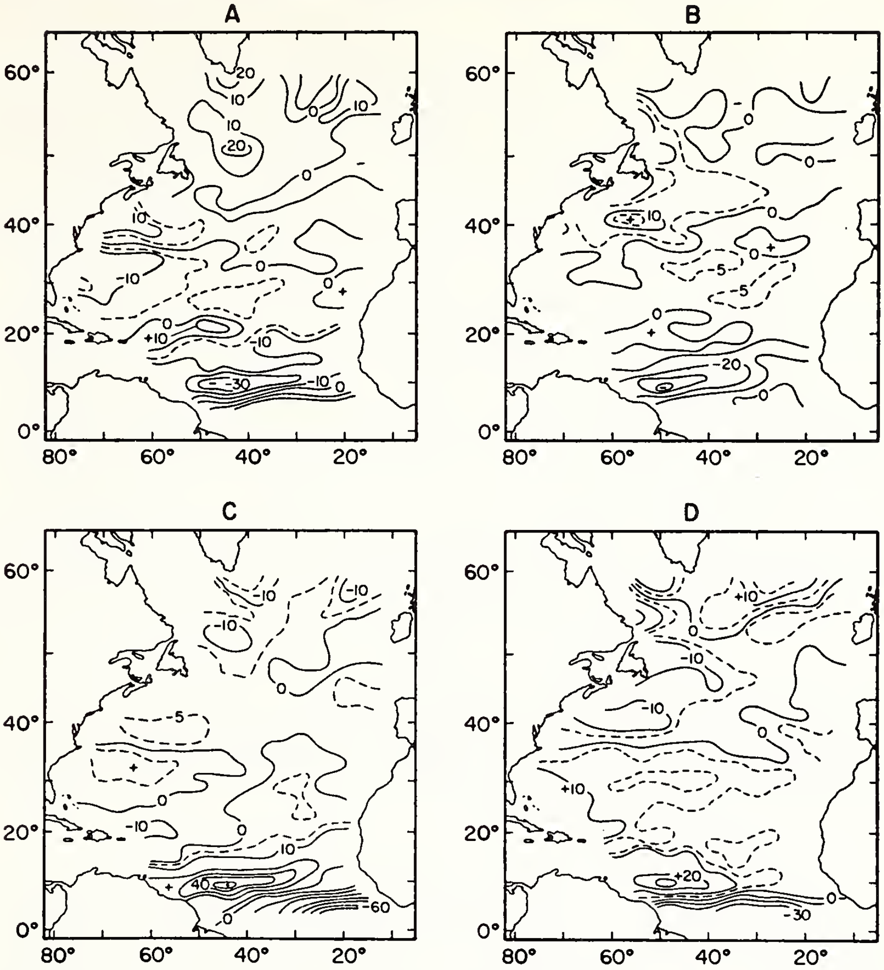

Figure 5. Graphs of the seasonal vertical velocity minus the annual mean vertical velocity at the base of the Ekman layer. Units are 10^{-5} cm/sec.
A) Winter B) Spring C) Summer D) Fall.

the baroclinic transport. So instead of presenting detailed maps of the seasonally varying Sverdrup transport, we presently report only the transports at 31N. These are in units of 10^{12} g/sec: winter, 48; spring, 38; summer, 26; fall, 17. The fluctuations are about 50% of the mean value. Direct measurements are needed to verify the existence of such fluctuations.

5. Discussion

From the recent wind stress computations of Bunker (1976), the mean and seasonally varying vertical velocity at the base of the Ekman layer were computed for

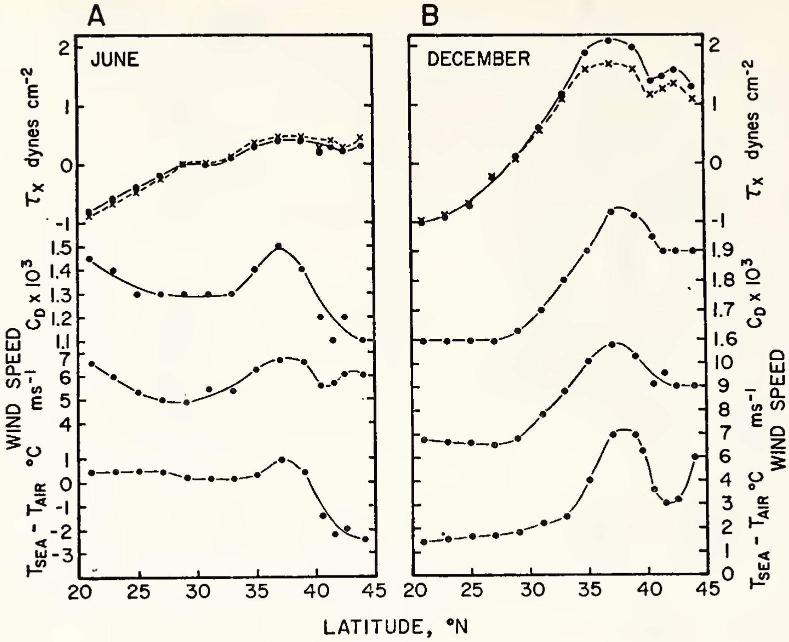

Figure 6. A) Latitudinal variation during June of T_{sea}-T_{air}, wind speed, drag coefficient, and east component of wind stress computed with a variable drag coefficient (•) and with a constant coefficient (*x*), ($C_D = 1.6 \times 10^{-3}$). Averages formed from observations made between 65W and 70W.

B) Same as A) except for December.

the North Atlantic from 5N to 60N. Using these, the Sverdrup relation, and the wind stress, the oceanic total transport, the geostrophic transport, and the Ekman transports were computed. These were compared with dynamic computations of the circulation in the upper ocean. Sverdrup theory does quite well in describing the horizontal distribution of these transports. The computations, however, still fail to account for the large observed transports in the Gulf Stream after it leaves the coast. Observations show this to be an area with intense eddy activity. It is possible that higher order dynamics involving inertial effects, bottom influences, or the eddies can explain the increased transport.

Munk's (1950) estimate of the total southward transport was 36 × 10^{12} g/sec. A value based on Hellerman's more recent stress computations is 24 × 10^{12} g/sec. The present computations give a value of 32 × 10^{12} g/sec. It is remarkable that despite better data, higher spatial resolution, and improved values of the drag coefficient the results have not changed a lot. However, examination of the wind stress distribution Munk used indicates that his estimates of the mean stresses were perhaps too high. Further comparison of such computations to the general circulation is also limited because there are insufficient direct observations of deep transports.

A striking result of these computations is the close correspondence between the observed mean path of the Gulf Stream and the predicted path of the eastward current that underlies the zero in the curl of the $\vec{\tau}/f$. This coincidence of a narrow maximum in the wind stress overlying the Gulf Stream front raises the interesting question of the role this warm water boundary plays in determining the wind stress distribution. The drag coefficients used in this computation are functions of the wind speed and the stability. During the winter the water in the Stream is about 7°C warmer than the overlying air. This destabilizes the air and increases the drag coefficient and hence the stress. In Figure 6 are shown the quantities that enter into the determination of the stress during the winter and summer. During the winter the wind speed and instability of the air work *in* phase to maximize C_D at 37° where the wind speed and the stress are the greatest. To show the effect of the variable C_D, the value of the stress using a constant value of $C_D = 1.6 \times 10^{-3}$ is also plotted. Near 30N use of a variable C_D does not increase the stress; whereas, at 37N and 44N it increases it by 25% and 18% respectively. Thus although the magnitude of the stress is increased slightly by the use of the variable C_D, the main contributor to the shape and magnitude of the stress maximum is the wind speed itself. Whether or not this is influenced by the presence of the Stream remains to be determined. During the summer, use of a variable C_D has little effect.

Acknowledgments. The research of the second author was supported by the Office of Naval Research under contract number N00014-74-C0262.12; NR 083-004. This paper is contribution No. 4023 of the Woods Hole Oceanographic Institution.

REFERENCES

Bunker, A. F. 1976. Computation of surface energy flux and annual air-sea interaction cycles of the North Atlantic Ocean. Mon. Wea. Rev., *104,* 1122–1139.

Bye, J. A., B. J. Noye, and T. W. Sag. 1975. A monthly analysis of global wind stress and the ocean transports predicted from a numerical model. Quart. J. R. Met. Soc., *101,* 749–762.

Evenson, A. J. and G. Veronis. 1975. Continuous representation of wind stress and wind stress curl over the world ocean. J. Mar. Res., *33,* 131–144.

Hantel, M. 1971. Wind stress curl—the forcing function for oceanic motions, *in* Studies in Physical Oceanography, a tribute to Georg Wust on his 80th birthday. A. H. Gordon, ed., New York; Gordon and Breach, 124–136.

Hellerman, S. 1967. An updated view of the wind stress on the world ocean. Mon. Wea. Rev., *95,* 607–626. Corrigenda 1968, Ibid., *96,* 63–74.

Leetmaa, A., P. Niiler, and H. Stommel. 1977. Does the Sverdrup relation account for the Mid-Atlantic circulation? J. Mar. Res., *35,* 1–9.

Metcalf, W. G., and M. C. Stalcup. 1967. Origin of the Atlantic Equatorial Counter Current. J. Geophys. Res., *72,* 4959–75.

Munk, W. H. 1960. On the wind-driven ocean circulation. J. Meteor., *7,* 79–93.

Saunders, P. M. 1976. On the uncertainty of wind stress curl calculations, J. Mar. Res., *34,* 155–160.

Stommel, H. 1964. Summary charts of the mean dynamic topography and current field at the surface of the ocean, and related functions of the mean windstress. Studies in Oceanography, K. Yoshida, ed., Seattle, University of Washington Press, 568 pp.

—— 1965. The Gulf Stream, University of California Press, Berkeley. 248 pp.

Sverdrup, H. V. 1947. Wind-driven currents in a baroclinic ocean; with application to the equatorial currents of the eastern Pacific. Proc. Nat. Acad. Sci. Wash., *33*, 318–326.

Worthington, L. V. 1970. The Norwegian Sea as a Mediterranean Basin. Deep-Sea Res., *17*, 77–84.

Worthington, L. V. 1976. On the North Atlantic circulation. Johns Hopkins Oceanographic Studies, *6*, 110 pp.

Received: *5 October, 1977;* revised: *13 February, 1978.*

Printed in U.S.A. for the Sears Foundation for Marine Research,
Yale University, New Haven, Connecticut, 06520, U.S.A.
Van Dyck Printing Company, North Haven, Connecticut, 06473, U.S.A.

Journal of Geophysical Research 83, No. C1, 427-430.

Fluctuating Winds: An Energy Source for Mesoscale Motions

A. Leetmaa

NOAA Atlantic Oceanographic and Meteorological Laboratories, Miami, Florida 33149

Phillips (1966) considered a linear, barotropic, nondivergent model driven by time-dependent winds in an attempt to explain the *Aries* observations. He found that the model greatly underestimated the response as compared to the observations. The model is reexamined by using newer estimates of the wind stress (Bunker, 1975) and of the eddy kinetic energies (Freeland et al., 1975). With these the model predicts reasonably well the time and space scales and the amplitude of the barotropic mesoscale variability south of Bermuda. It is suggested that the low-frequency temperature fluctuations observed in the *Panulirus* data near Bermuda result from the advection of the mean baroclinic field past Bermuda by the barotropic fluctuations.

Introduction

Since the *Aries* observations in 1959, considerably more has been learned about mesoscale variability in the oceans [*Crease*, 1962; *Schmitz*, 1976]. However, the energy sources for it are still uncertain. A number of different sources have been proposed. One of these is the effect that fluctuating winds have in producing time-dependent baroclinic and barotropic motions. *Phillips* [1966] examined a model in which the forcing was a time-dependent zonal wind. The response at moderately low frequencies and in the western part of the basin was of a broadband nature. The predicted band of frequencies and wavelengths agreed reasonably well with the *Aries* observations; however, the theory seemed to underestimate the amplitude of the response greatly for reasonable values of the wind stress. Phillips suggested that the larger observed amplitudes of the transients resulted because they abstracted energy from the Gulf Stream on reflection from the western boundary.

Gulf Stream meandering and instability have also been suggested as a source for mesoscale variability [*Iselin*, 1961; *Hansen*, 1970; *Holland and Lin*, 1975]. Meandering is observed sometimes to lead to one type of eddy, i.e., Gulf Stream rings. Theoretical studies by *Flierl et al.* [1975] suggest that energy radiation by the rings during their lifetimes might also be a significant source of eddy energy. The numerical experiments of *Holland and Lin* [1975] and further work by W. Holland (private communication, 1976) suggest that Gulf Stream instability is a major eddy-generating process and thus provides energy indirectly for establishing mean circulations in the vicinity of the stream. There is qualitative agreement between the model results and the observations of *Schmitz* [1976].

Another mechanism that has been proposed as a source of eddies is the baroclinic instability of the mean ocean circulation [*Gill et al.*, 1974]. Although the predictions from such theories about the eddy frequencies and spatial scales are consistent with observations, the predicted phase change of the motion with depth has not been observed (at least during the Mid-Ocean Dynamics Experiment (Mode)) (R. Scarlet, unpublished manuscript, 1974). However, more observations need to be made before a definitive statement can be made about the importance of this mechanism.

One of the earliest sources of information about the time scale of the mesoscale variability has been the sea level data at Bermuda and the nearby *Panulirus* hydrographic observations [*Shaw and Donn*, 1964; *Wunsch*, 1972]. These indicate that near Bermuda there is a broad peak in the time scale of the variability which is centered about 4 months. Energetic motions with similar periods are found in the Mode observations [*Richman*, 1976]. Shaw and Donn suggested that the variability with the period of 4–5 months was repeatable from year to year. This point has been overlooked and suggests that direct forcing by the atmosphere should be reexamined as a source for these motions.

In the following sections, wind stress observations from the western Atlantic will be examined to determine the amount of energy in fluctuations of the curl of the stress with periods between 2 and 6 months. This will then be compared with the amount that is required to provide the more recently observed amplitude of the transient north-south currents using Phillips' model. The variability in the curl of the wind stress is shown to account for a substantial portion of the observed currents. A simple model is then put forth to describe the temperature fluctuations in the main thermocline as observed in the *Panulirus* data near Bermuda.

Wind Curl Observations

Using surface marine observations from 1941 through 1972, *Bunker* [1975] computed monthly averages for the wind stress over areas 2° of latitude by 5° of longitude in the North Atlantic. The mean monthly data were obtained from Bunker, and the curl of the stress was computed by using a spatially centered finite difference scheme to estimate the derivatives, where Δx was 10° of longitude and Δy was 4° of latitude. Three such areas were zonally averaged together to give the average curl over a region 2° of latitude by 15° of longitude between 55°W and 70°W. The curl is fairly uniform over this longitude range and decreases to the east of it. This was done for the regions centered at the odd latitudes between 35°N and 23°N.

For several reasons the mean monthly values of the stress were used rather than individual monthly values for each of the 32 years. First, it can be inferred from *Bunker* [1975] that a region 2° × 5° does not contain enough observations in a month to give reliable values for the stress. Second, examination of the 32-year series of monthly averages of the stress for a larger area, an entire Marsden square (10° × 10°), indicates that all the years are very similar. Consequently, the estimates of the spectrum of the curl using mean monthly values should be representative of the actual spectra; however, the energy at periods of 2–4 months is probably still underestimated. Also, the suggestion by *Shaw and Donn* [1964] that there might be a 4- to 5-month periodicity in the sea level fluctuations at Bermuda implies a regularity in the winds that should be present

TABLE 1. Amplitudes of Fourier Components of Curl of Wind Stress

Period, months	Component	Latitude, deg 35	33	31	29	27	25	23
12		1.262	1.116	0.897	0.781	0.644	0.408	0.284
6	a_2	0.287	0.462	0.496	0.517	0.432	0.401	0.358
4	a_3	0.019	0.324	0.323	0.142	0.188	0.117	0.084
3	a_4	0.130	0.149	0.155	0.031	0.054	0.069	0.126
2.4	a_5	0.100	0.153	0.058	0.006	0.019	0.039	0.069.
	$\sum_{i=2}^{i=5} a_i \times 10^{-17}$	1.10	3.64	3.78	2.88	2.25	1.81	1.71

Values are times 10^{-8}.

in the mean monthly data. Finally, there is a practical consideration: the mean data were easily accessible, whereas the individual monthly data were not.

The amplitudes and phases of the 12-, 6-, 4-, 3-, and 2.4-month components were computed by a Fourier decomposition of the 12-month series (Table 1). The annual and mean components account for most of the amplitude of the curl. After these are removed, however, significant variation still occurs at shorter periods (Figure 1).

As can be seen from Table 1, there is a maximum in the amplitude of each period except the annual period between 31° and 33°N. The amplitudes decrease to the north and to the south; the decrease to the north occurs more rapidly. At every latitude there is significant energy at each period. This results from three factors. First, the large amplitude of the curl during the winter occurs too quickly to be accounted for totally in the annual cycle. Second, there is a prominent secondary maximum in the summer that results from the intrusion of the southeast trades into this area. Finally, there is a weakening of the curl in February which occurs at most of the latitudes at which the computation was done. Its cause is unknown.

COMPARISON OF MODEL RESULTS WITH OBSERVATIONS

Phillips [1966] attempted to explain the *Aries* observations by considering the response of a linear, barotropic, nondivergent model with bottom friction to a time-dependent zonal wind stress. He found that at moderate distances from the western boundary there was a peak in the barotropic response at periods between 2 and 6 months. The response for shorter or longer periods died off rapidly from the western boundary except when these were natural frequencies of the basin.

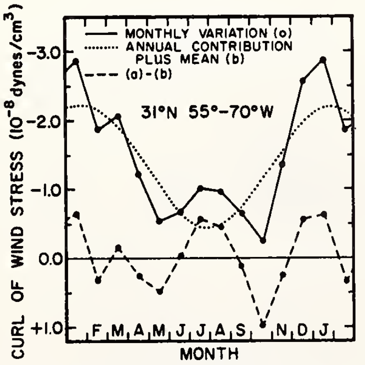

Fig. 1. Monthly variation in the curl of the wind stress in the area bounded by 30°-32°N and 55°-70°W.

His ocean was a square basin with sides of length D. The applied wind stress $\tau = \tau_0(t) \sin (\pi y/D)$ has a curl whose magnitude is $(\tau_0\pi/D)$. It is suggested in this paper that the actual curl of the stress is larger than the basin-wide estimate that Phillips made. This implies that the north-south scale of the wind, D, in the model should be reduced. However, since in his model, x was also nondimensionalized by D, it is not clear from his results what the effect of decreasing just the north-south scale is.

Consequently, the model was reworked with x nondimensionalized by L and y by D. The quantity $\sigma_{\max}$ is now defined as $\sigma_{\max} = \beta L/2\pi$, where L is chosen to be 5000 km, as was done before. With the same assumption and notation an equation similar to Phillips' (3*a*) can be derived for the nondimensional amplitude of the boundary layer form of the meridional response:

$$V = \frac{\pi^2}{\delta}\left(\frac{\mu}{\mu^2 + k^2}\right) \exp\left(-\frac{2\pi k}{\mu^2 + k^2}\right)\frac{x}{L}$$

where δ is the aspect ratio D/L. Dimensionally, the amplitude of the meridional velocity V is

$$V = \frac{2\tau_0}{\rho h \beta L}\,|V| = \frac{2\delta}{\rho h \beta \pi}\left(\frac{\tau_0 \pi}{D}\right)|V| \tag{1}$$

Note that the δ in the amplitude of V cancels that in the response function $|V|$. Consequently, the results of Phillips' calculations for $|V|$ can be used directly.

An expression that can be used to test the model is obtained by squaring both sides of (1):

$$\langle V^2\rangle_{\text{obs}} = \left(\frac{2\delta|V|}{\rho h \beta \pi}\right)^2 \Phi^2 \tag{2}$$

where $\langle V^2\rangle_{\text{obs}}$ is the average value of the square of the meridional velocity and Φ^2 is the power spectrum of the curl. This will be approximated by the sum of the squares of the Fourier components with periods 2.4-6 months (Table 1).

Estimates of $\langle V^2\rangle_{\text{obs}}$ can be obtained from *Schmitz* [1976] and *Freeland et al.* [1975]. They show that $\langle V^2\rangle_{\text{obs}}$ is 8 cm^2/s^2 between 28°N and 30°N and 20 cm^2/s^2 at 33°N. These values are at a depth of approximately 1500 m and are representative of the barotropic mode, since the first baroclinic mode has its zero close to this depth. The curl has its maximum around 31°N. Linear interpolation of $\langle V^2\rangle_{\text{obs}}$ between 33°N and 29°N gives a value of 14 cm^2/s^2 at this latitude. The current observa-

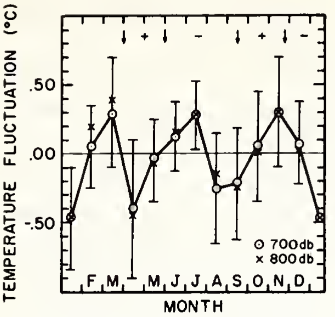

Fig. 2. Mean monthly temperature fluctuations in the main thermocline near Bermuda (32°10′N, 64°30′W) from the *Panulirus* data. Error bars represent 95% confidence limits as determined by two standard deviations of the mean. See text for discussion of arrows and signs.

tions were taken in the vicinity of 70°W. This makes (x/L) close to 0.1, and Figure 2 of Phillips shows that $\delta|V|$ has a value of about 70. When the values $\beta = 2 \times 10^{-13}$, $h = 5 \times 10^5$, and $\Phi^2 = 3.8 \times 10^{-17}$ (Table 1) are used in (2), the predicted $\langle V^2 \rangle$ is about 8 cm²/s². This is about one half of the observed value.

A major part of Φ^2 that was used is the energy at 6 months. The model and the observations indicate that at this distance from the western boundary the response at this period is greatly reduced. If only the energy at 4, 3, and 2.4 months is considered, the predicted value of $\langle V^2 \rangle$ is about 3 cm²/s², or about one sixth of the observed value. This is reasonable agreement considering that energy in the curl at these periods is probably underestimated by the use of the mean monthly wind data. Furthermore, it is not clear what the appropriate value is for (x/L). Since barotropic motions are strongly influenced by the bottom, the true western boundary might be the Blake-Bahama Slope rather than the shelf further to the west. This would decrease (x/L) and correspondingly increase $\delta|V|$, effects which would make the agreement much better.

A MODEL FOR *PANULIRUS* TEMPERATURE FLUCTUATIONS

Shaw and Donn [1964] pointed out that the 4- to 5-month variability observed in the sea level data at Bermuda seemed to be periodic. To see if the *Panulirus* hydrographic data showed a similar phenomenon, the mean monthly temperatures at 700 and 800 m were determined for the years from 1954 to 1969 (Figure 2). These data were obtained from the Naval Oceanographic Data Center. The error bars shown for the temperature represent the 95% confidence limits as given by the t test. Although the error bars are rather large, the periodicity (repeatability from year to year) that was evident in the sea level data appears in the temperature fluctuations in the main thermocline. The reality of the former is further supported by the following calculation. The fluctuation in the depth of the main thermocline implied by the temperature fluctuation in Figure 2 is about 10 m. This implies a variation in the sea level by steric effects of about 1.5 cm. This is of the order of the amount seen by Shaw and Donn in the tide gage data.

What relationship do these fluctuations bear to the variations in the curl of the wind stress? The baroclinic response at these periods is small [*Phillips*, 1966]. It is possible that these temperature fluctuations are related to an advection of the mean temperature field past Bermuda by the barotropic currents. The north-south temperature gradient in the main thermocline is of the order of 1.4°C per 100 km north of Bermuda and 0.5°C (or less) per 100 km south of Bermuda [*Fuglister*, 1960]. For the computation an average value is 1°C per 100 km. The model predicts that the amplitude of the barotropic fluctuations at 33°N is about 3 cm/s. The mean speed over half a period is $(2/\pi) \times 3 = 2$ cm/s. Thus the total amplitude of the fluctuation is 2 cm/s × 2 months = 100 km. The predicted amplitude of the temperature fluctuation is 1°C; i.e., the fluctuation is ±0.5°C. This agrees quite closely with the observations shown in Figure 2.

Can anything be said about the phase of the temperature fluctuations relative to that of the forcing? When the flow is to the south, the temperature should be increasing. This is because the thermocline deepens to the north. In Phillips' model the meridional component of flow at periods of 4–5 months rapidly alternates in sign as it decays away from the western boundary. If the longitude of Bermuda were such that southward flow occurred when the curl was positive, then the signs in Figure 2 indicate when the temperature should be increasing (+) or decreasing (−). The arrows indicate when the meridional flow changes sign as determined by changes in the sign of the curl (Figure 1).

For this choice of phase between the curl and the direction of flow the sign of the temperature fluctuations is predicted reasonably well. It should be emphasized that this choice was arbitrary. The comparison was only done to suggest the type of intercomparison that might be done with a better model and with more complete information about the time and space scales of the curl.

DISCUSSION

In retrospect, *Phillips'* [1966] model is rather successful in predicting the time scales and amplitudes of the barotropic mesoscale variability in the northwestern Atlantic. The early pessimism about its relevance resulted from his overestimation of $\langle V^2 \rangle_{\text{obs}}$ and an underestimation of the curl of the stress. The value of $\langle V^2 \rangle_{\text{obs}}$ of 100 cm²/s² which he used now appears to be too large except in the vicinity of the Gulf Stream. In this region, Gulf Stream meandering and rings are the major sources of eddy energy. Subsequent measurements have shown $\langle V^2 \rangle$ to decay rapidly, southward away from the stream.

The curl of the wind stress is also a complicated function of time and space. It is fairly uniform in the zonal direction between 70°W and 55°W but varies strongly in the meridional direction. In this paper the averaging in the zonal direction was an attempt to approximate the zonally uniform curl which was used in the model. In any case, the actual distribution of the curl is more complicated than the mean, zonally uniform, gyre-wide distribution that Phillips used.

With the present estimates of the curl the model predicts a meridional response whose amplitude is quite close to the observed one but still low. This is not too disconcerting, because the present calculations still probably underestimate the magnitude of the curl at shorter periods because of the use of mean monthly values of the stress. Despite the reasonableness of the prediction the model results should only be considered suggestive that direct atmospheric forcing can be a significant source of energy for mesoscale variability. Such effects as basin geometry, bottom topography, and more complicated spatial and temporal variations in the curl must be important in modifying the details of the response and should be examined.

Acknowledgments. I would like to thank the reviewers for correcting several misconceptions that I had in an earlier version of this manuscript.

REFERENCES

Bunker, A. F., Energy exchange at the surface of the western North Atlantic Ocean, *Rep. WHOI-75-3*, 107 pp., Woods Hole Oceanogr. Inst., Woods Hole, Mass., 1975.

Crease, J., Velocity measurements in the deep water of the western North Atlantic, *J. Geophys. Res.*, *67*, 3173–3176, 1972.

Flierl, G. R., V. Kamenkovich, and A. R. Robinson, Gull Stream meandering and Gulf Stream ring eddy production mechanisms, Dynamics and the Analysis of Mode-I, 250 pp., Mass. Inst. of Technol., Cambridge, 1975.

Freeland, H. J., P. B. Rhines, and T. Rossby, Statistical observations of the trajectories of neutrally buoyant floats in the North Atlantic, *J. Mar. Res.*, *33*, 383–404, 1975.

Fuglister, F. C., *Atlantic Ocean Atlas*, Woods Hole Oceanographic Institution, Woods Hole, Mass., 1960.

Gill, A., J. Green, and A. Simons, Energy partition in the large scale ocean circulation and production of mid-ocean eddies, *Deep Sea Res.*, *21*, 499–528, 1974.

Hansen, D. V., Correlation of movements in the western North Atlantic, *Tech. Rep. ERL 164-AOML 1*, 19 pp., Environ. Sci. Serv. Admin., Boulder, Colo., 1970.

Holland, W., and L. Lin, On the generation of mesoscale eddies and their contribution to the oceanic general circulation, I, II, *J. Phys. Oceanogr.*, *5*(4), 642–669, 1975.

Iselin, C. O., An interpretation of the deep current meters, *Oceanus*, *7*(3), 9, 1961.

Phillips, N. A., Large-scale eddy motion in the western Atlantic, *J. Geophys. Res.*, *71*, 3883–3891, 1966.

Richman, J., Kinematics and energetics of the mesoscale mid-ocean circulation: Mode, Ph.D. dissertation, Mass. Inst. of Technol., Cambridge, 1976.

Schmitz, W. J., Eddy kinetic energy in the deep western North Atlantic, *J. Geophys. Res.*, *81*, 4981–4982, 1976.

Shaw, P. M., and W. L. Donn, Sea-level variations at Iceland and Bermuda, *J. Mar. Res.*, *22*, 111–122, 1964.

Wunsch, C., Bermuda sea level in relation to tides, weather, and baroclinic fluctuations, *Rev. Geophys. Space Phys.*, *10*, 1–49, 1972.

(Received March 3, 1977;
revised July 13, 1977;
accepted July 15, 1977.)

Journal of Geophysical Research 83, No. C12, 6123-6135.

Geostationary Satellite Observations of Gulf Stream Meanders: Infrared Measurements and Time Series Analysis

George A. Maul,[1,2] P. Webb deWitt,[1] Alan Yanaway,[3] and Stephen R. Baig[4]

The infrared capabilities of the Geostationary Operational Environmental Satellite (Goes) are analyzed to obtain multiyear time histories of Gulf Stream meanders. Radiative transfer calculations using monthly mean profiles of atmospheric temperature and moisture are shown to overestimate cloud-free equivalent soundings by 2–5 K. A simple relation is derived between temperature at the satellite, sea surface temperature, and transmissivity of the atmosphere at 11.6 μm, which allows an observer to determine if a known sea surface temperature gradient is observable from Goes knowing only the precipitable water content along the slant path to the spacecraft. More than 2 years of Goes observations of Gulf Stream meanders are analyzed as a randomly spaced time series using least squares spectral analysis; the dominant periods in the spectra, based on 1976–1978 data, are 250, 65, and 10 days in the Gulf of Mexico; 30 and 6 days off Onslow Bay, North Carolina; and 45 and 5 days off New England. A summary of the meanders between the Yucatan Strait and the Grand Banks shows that the largest latitudinal variability is associated with the Gulf Loop Current. Comparison of meander periods with least squares spectra of historical Florida Current transports suggests that meanders in the Gulf of Mexico are related to variability with 4- to 16-day and 40- to 100-day periods in the flow.

Introduction

Shipboard time series studies of temporal variability in the Gulf Stream System show that different regions of the system seem to have different dominant periods. Based on year-long measurements, *Leipper* [1970] suggests that an annual period dominates the system in the eastern Gulf of Mexico, while *Hansen* [1970] reports that the meanders between Cape Hatteras and the Grand Banks have a period of about 1.5 months. Other, shorter, shipboard surveys indicate periods of 4–10 days in the Straits of Florida off Miami [*Düing*, 1975], 4–7 days offshore of Onslow Bay, North Carolina [*Webster*, 1961], and 10–16 days in the Gulf Stream northeast of Cape Hatteras [*Robinson et al.*, 1974]. Little is known about periods less than a fortnight in the Gulf Loop Current; similarly, little is known about longer (monthly or annual) periods in the Straits of Florida or off Onslow Bay.

To study these meanders over the entire current system from the Yucatan Strait to the Grand Banks by conventional shipboard techniques is not practical. Observations every 2 days are necessary to satisfy the Nyquist theorem for the highest frequencies noted above, and several years of continuous data are required for the lowest frequencies. Thus as a practical matter, satellite observation of the sea surface temperature pattern associated with the entire current system is presently the only viable approach.

Correlation studies between the maximum sea surface temperature gradient and the maximum gradient at 200-m depth in the Cape Hatteras–Grand Banks region [*Hansen and Maul*, 1970] indicate that surface temperature is a good indicator of the Gulf Stream in this region. Other such studies [e.g., *Richardson et al.*, 1973; *Voorhis et al.*, 1976; *Bernstein et al.*, 1977] confirm the correlation between satellite-sensed thermal signatures and subsurface indicators of circulation. These latter studies and recent high-resolution infrared images show detail in the thermal field not realized in shipboard measurements and suggest further investigation is warranted. To a very good approximation, however, the maximum surface temperature gradient, separating the water of highest temperature and the juxtaposed water mass on the cyclonic shear side, is the remotely sensed transition to the Gulf Stream [*von Arx et al.*, 1955; *De Rycke and Rao*, 1973].

Before the launch of the Geostationary Operational Environmental Satellite (Goes) many satellite investigations were limited to case studies using a few good cloud-free examples. Goes, however, has an operational 30-min observation schedule which permits image sequence techniques to be applied. Capitalizing on the order of magnitude difference in advection of atmospheric and oceanic thermal features, *Maul and Baig* [1975] located the entire Gulf Stream between the Yucatan Strait and the Grand Banks using sequence techniques. Subsequent studies of the Stream [*Legeckis*, 1975] used Goes data to investigate meanders off Onslow Bay, North Carolina, and found frequencies similar to *Webster*'s [1961] shipboard observations. These results imply that geostationary observations are potentially capable of providing the necessary data to analyze Gulf Stream meanders stochastically over the observed frequency and geographic scales necessary to construct a synoptic view.

This report is partitioned into several sections. First, the application and limitations of Goes data to the problem are quantified by investigating the atmospheric effects on the infrared radiance, by estimating the thermal variability which acts as noise, and by calculating the range over which the imagery should be contrast stretched in order to optimize sea surface temperature gradient detection. Second, the problem of spectral analysis of randomly spaced data is studied to show that a least squares technique can return accurate estimates of known frequencies in the presence of white noise which is within the range of known Goes current boundary location error. Third, least squares spectra of Gulf Stream meanders, using a wave staff perspective, are calculated for the Gulf of Mexico, the Carolina Capes, and south of New England; spectral peaks reported in historical shipboard studies are seen in these data, and new information is reported. And fourth, correspondence is noted between new spectral analysis of his-

---

[1] Atlantic Oceanographic and Meteorological Laboratories, National Oceanic and Atmospheric Administration, Miami, Florida 33149.

[2] Cooperative Institute for Marine and Atmospheric Science, University of Miami/NOAA, Miami, Florida 33149.

[3] Pacific Marine Center, National Oceanic and Atmospheric Administration, Seattle, Washington 98105.

[4] National Environmental Satellite Service, Miami, Florida 33124.

TABLE 1. Location of Upper Air Stations for Which Individual Radiosondes Were Available and the Normalized Atmospheric Slant Path for Goes at 75°W

Station	Latitude	Longitude	Sec ζ
Barbados	13°04'N	59°29'W	1.09
Bermuda	32°22'N	64°41'W	1.28
Boothville, La.	28°58'N	89°18'W	1.28
Brownsville, Tex.	25°54'N	97°26'W	1.29
Cape Hatteras, N. C.	35°15'N	75°33'W	1.32
Key West, Fla.	24°43'N	81°32'W	1.15
Ocean station H	38°00'N	71°00'W	1.39
Sable Island, N. S.	43°56'N	60°01'W	1.59
San Juan, Puerto Rico	18°26'N	66°00'W	1.09
Swan Island	17°24'N	83°56'W	1.08

torical Gulf Stream transports and the spectra of meanders, suggesting that meanders and transports may be correlated but that a concurrent study is necessary in order to make a definitive statement on such correlation.

APPLICABILITY OF GOES DATA

In applying Goes data to the problem of locating the Gulf Stream, the useful range of infrared radiation detection must be established. The atmospheric effects on the cloud-free radiance range are studied by solving the radiative transfer equation:

$$L_0 = \int_{\nu_1}^{\nu_2} \epsilon(\nu)\xi(\nu)L_s(\nu, T)\tau(\nu)d\nu + \int_{\nu_1}^{\nu_2}\int_0^{s} \xi(\nu)L_a(\nu, T, P)\,\frac{\partial\tau}{\partial P}(\nu, w, P)dpd\nu \qquad (1)$$

where L_0 is the radiance at the top of the atmosphere, ξ is the filter response over the applicable wave number interval ν_1–ν_2, ϵ is the emissivity of the ocean surface, L_s is the radiance of the sea surface at temperature T, τ is the transmittance of the atmosphere, L_a is the radiance of the atmosphere as a function of pressure P, and w is the precipitable water of an atmospheric slab dp thick. Solutions are obtained by numerical integration using the formulation of *Maul and Sidran* [1973]. In the range $950 \leq \nu \leq 800$ cm^{-1} (10.5–12.5 μm), $\epsilon(\nu) \approx 1$ for the ocean, and the blackbody approximation is used; $dp = 1$ mbar and $d\nu = 25$ cm^{-1} are the finite differences.

The usual upper air data sources, such as those from *Monthly Climatic Data for the World*, are monthly means of temperature and relative humidity at 10 selected pressure levels. Unfortunately, mean atmospheric profiles include soundings that have passed through clouds as well as clear air. For oceanic remote sensing, only cloud-free soundings are desired. For this study, upper air data from 10 stations (Table 1) located around and in the North Atlantic are used. In Table 1, the column labeled sec ζ (see (3)) is the ratio of the slant atmospheric path for Goes viewing geometry to the vertical atmospheric path.

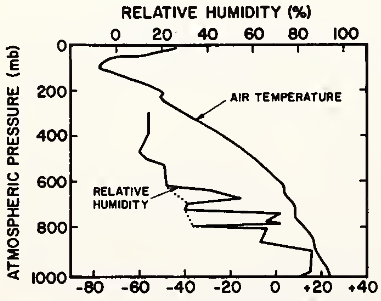

Fig. 1. Vertical profiles of temperature and relative humidity observed at Key West, Florida, on January 8, 1974. Dotted line represents the cloud-free equivalent humidity profile.

Figure 1 is an example of a sounding from Key West, Florida, that has passed through two cloud layers, one at about 744 mbar and another at about 671 mbar. In a sounding, clouds are characterized by a sudden increase in relative humidity and an isothermal lapse rate. An equivalent clear air estimate is made by assuming the clouds are absent (dotted line in the relative humidity profile, Figure 1) and solving (1) for the modified sounding. Assuming a sea surface temperature T_s of 298.15 K, the difference in the equivalent blackbody temperatures at the top of the atmosphere between the observed and the 'cloud-free' sounding in this example is 0.82 K.

To investigate this difference further, cloud-free radiosondes for February 1974 from San Juan, Bermuda, and the Azores were compared with the mean monthly values. Screening for cloud-free soundings was a twofold procedure. First, the Goes image at the time of release was studied, and each location was subjectively catalogued as clear, partly cloudy, mostly cloudy, or cloudy. The soundings that were categorized from the satellite images as clear or partly cloudy were further screened using the surface observer's reports. Soundings with a probability of ≤ 0.25 of being cloudy were made into equivalent cloud-free soundings as in the case shown in Figure 1. Choosing $T_s = 293.15$ K, (1) was then solved for the original 28 soundings and for the equivalent cloud-free soundings at each station, the results being tabulated in Table 2.

The calculations summarized in Table 2 show that the difference between T_s and T_0 is higher at each locale when using the mean of all 28 radiosondes (column labeled 1) compared to using the mean of the selected cloud-free equivalent soundings (column labeled 2). Subtracting column 2 from column 1 shows that the largest error for this experiment is at the Azores and that the smallest error is at San Juan. The average difference is 3.2 K, a value that should be kept in mind when evaluating the effects of Goes viewing geometry on observations of sea surface temperature gradients based on mean or standard atmospheres.

The observation geometry of Goes is shown in Figure 2. For a point P in the northern hemisphere whose latitude, ϕ, and longitude relative to the suborbital point of Goes, $\Delta\lambda$, are known, the angle ψ at the center of the earth is found by solution of the right spherical triangle:

$$\psi = \cos^{-1}[\cos\phi\cos\Delta\lambda] \qquad (2)$$

TABLE 2. Results of Sounding Calculations

Station	Monthly Sounding, $T_s - T_0$, deg (1)	Equivalent Cloud-Free Sounding, $T_s - T_0$, deg (2)	Difference, deg (1 − 2)
San Juan	5.54	3.59	1.95
Bermuda	6.78	4.00	2.78
Azores	13.00	8.22	4.78

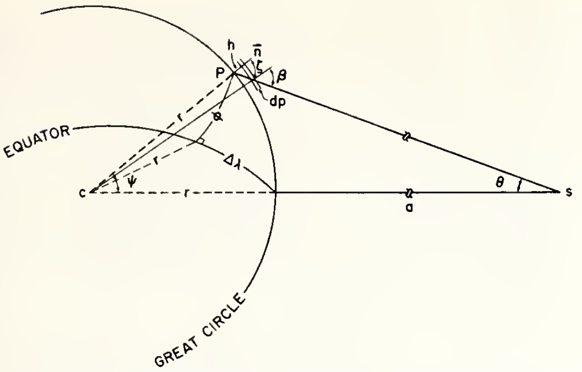

Fig. 2. Geometry for radiative transfer calculations from a geostationary satellite S for a point P on the earth's surface; C is the center of the earth. The spherical trigonometry employs an arbitrary great circle that passes through P and the subsatellite point.

Plane triangle CPS is now solved using the law of tangents with the side CP = r, the earth's radius, and CS = $r + a$, where a is the altitude of Goes. The remaining problem is to find the optical thickness of the atmospheric slab dp at a height h above the surface. As a very close approximation the effective path length (optical thickness) that undeviated photons would take through an atmospheric slab dp is given by $dp \cdot \sec \beta$. From the law of sines and the geometry in Figure 2 the following equation is obtained:

$$\sin \beta = \frac{r}{r + h} \sin \zeta \tag{3}$$

For atmospheric heights of importance to infrared radiative transfer in the range $950 \leq \nu \leq 800$ cm^{-1} (i.e., $h \leq 10$ km, the approximate height of the tropopause) the ratio $r/r + h$ is approximately unity ($r/r + h > 0.998$). Thus sec ζ, which is easily determined, can be assumed to be the normalized effective path length through the troposphere.

Using the geometrical solutions in (2) and (3), the radiative transfer equation is applied to the problem of sea surface temperature gradient determination from Goes. Radiosonde data from the stations listed in Table 1 for February 1977 and August 1976 are screened for cloud-free equivalent soundings by the procedure noted above. Equation (1) is then solved for these two months by using T_s = 293.15 K. Figure 3 shows that a uniform 20°C ocean would appear to have a meridional temperature gradient when viewed from Goes. This north-south gradient is caused by a lower value of L_a in the atmospheric emission term of (1) dominating that due to optical depth, even though the transmittance (including the geometrical effect) decreases from north to south.

Figure 3 is also useful for estimating the effect of spatial variability in atmospheric humidity as a cause of apparent surface temperature gradient. As noted above, the gradients on the scale of Figure 3 are meridional in nature and would not be confused with oceanic fronts because temperature differences of 1 K occur over distances of 500 km or more. However, *Augstein et al.* [1974] note fluctuations in the height of the trade wind inversion which would effectively vary the precipitable water by ±30% over periods of 1 day. This effect is investigated by computing the standard deviation about the mean at Key West, and it amounts to ±0.7 K. This value, coupled with the noise equivalent temperature difference of the Goes radiometer, means that about ±1-K noise which could be misinterpreted as an oceanic front is not known, since Augstein et al. did not make the necessary observation to determine the spatial scales of the fluctuation in the height of the trade wind inversion.

As an aside, the effect of the atmosphere on the absolute sea surface temperature determination from Goes is also studied. Using historical values of T_s, the differences $\Delta T = T_s - T_0$ for the Goes infrared radiometer are plotted (Figure 4) for the same radiosonde stations and months used in Figure 3. The values for ΔT are in good agreement with empirical corrections used by the NOAA Satellite Field Services Station in Miami. The calculated distribution reflects that the variability in ΔT is less in August than in February. More important are the large values of ΔT in the summer over the Gulf of Mexico–Florida Current region. When atmospheric effects are large, the effective sea surface temperature gradient at the top of the atmosphere is reduced. This can be seen by writing (1) in its spectral form,

$$L_0 = L_s \tau + \int_0^s L_a \frac{\partial \tau}{\partial p} \, dp \tag{4}$$

where the blackbody assumption is made, and all variables are tacitly assumed to be wave number dependent. Transforming to τ coordinates,

$$L_0 = L_s \tau + \int_\tau^1 L_a \, d\tau \tag{5}$$

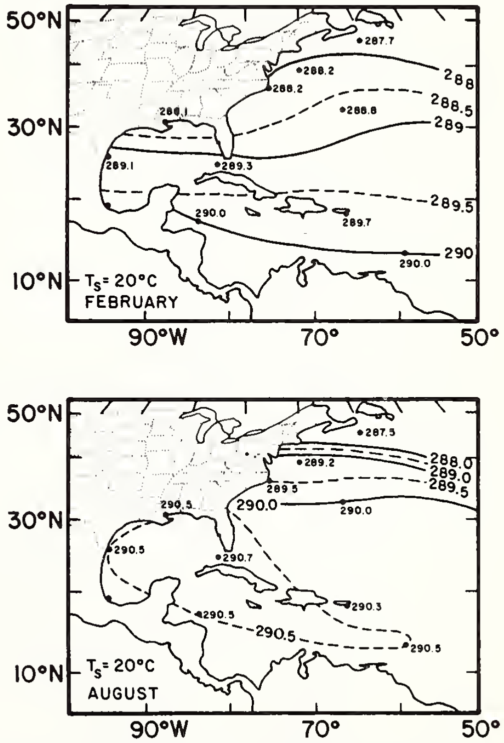

Fig. 3. Contours of calculated temperature as would be observed by Goes (at suborbital point 0° latitude, 75°W longitude) if the sea surface temperature were a uniform 20° (293.15 K), for a cloud-free equivalent atmosphere. The upper panel is based on atmospheric data for February 1977; the lower panel is based on atmospheric data for August 1976.

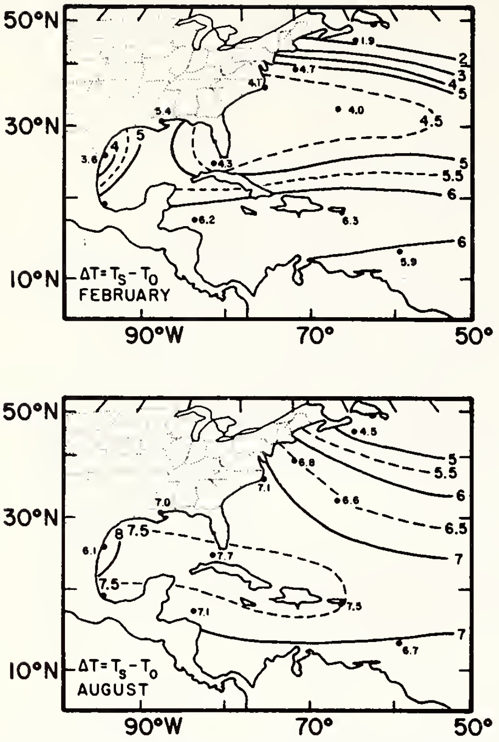

Fig. 4. Contours of temperature difference between historical values of sea surface temperature and calculated (satellite observed) temperature for a cloud-free equivalent atmosphere and a satellite subpoint of 0° latitude, 75°W longitude. The upper panel is based on atmospheric data for February 1977; the lower panel is based on atmospheric data for August 1976.

and applying the mean value theorem,

$$\bar{L}_a = \frac{1}{(1-\tau)}\int_\tau^1 L_a d\tau \tag{6}$$

(5) can be written

$$L_0 = L_s\tau + (1-\tau)\bar{L}_a \tag{7}$$

In the spectral region $950 \leq \nu \leq 800$ cm^{-1}, radiance is nearly linear with temperature. Substituting T_0, T_s, and $\bar{T}_a$ for L_0, L_s, and $\bar{L}_a$ in (7) and assuming that τ and $\bar{T}_a$ are constant over short distances, the horizontal spatial derivative yields

$$\nabla_h T_0 = \tau \cdot \nabla_h T_s \tag{8}$$

The physical interpretation of (8) is that for a given sea surface temperature gradient the temperature gradient observed at the satellite is dependent only on the transmittance of the atmosphere. Since $0 \leq \tau \leq 1$ and $\partial T_0/\partial T_s \leq 1$, sea surface temperature gradients such as those that are used to locate the Gulf Stream are reduced at satellite altitudes.

Goes digitizes the radiance in equivalent temperature steps of 0.5 K. For δT_0 of this value the corresponding δT_s must be greater by a factor of $1/\tau$ as shown in (8). Equation (8) is wavelength dependent, and in the Goes spectral interval ν_1-ν_2 the function of interest is

$$\frac{\int_{\nu_1}^{\nu_2} \xi(\nu)\tau(\nu)d\nu}{\int_{\nu_1}^{\nu_2} \xi(\nu)d\nu} \tag{9}$$

Equation (9) is very closely approximated by τ at $\nu = 862.5$ cm^{-1} (11.6 μm). Transmittances at this wavelength are computed and summarized in Table 3 for cloud-free stations in February and August. The table presents selected values of $\nabla T_0/\nabla T_s$ (columns 1 and 3) with their associated calculated values of δT_s ($\delta T_0 = 0.5$) in columns 2 and 4. In the Cape Hatteras–Grand Banks region, radiative transfer calculations based on ocean weather station H data indicate that $\delta T_s = 0.7$°C in winter and $\delta T_s = 0.9$°C in summer and that they are the minima needed for detection. *Hansen and Maul* [1970] report a minimum $\delta T_s = 2$°C across the Gulf Stream front between Cape Hatteras and the Grand Banks in August, which suggests that Goes is capable of observing in that region all year long. Further south, data from Bermuda suggest that in the Cape Canaveral–Cape Hatteras area the Gulf Stream is marginally detectable in the summer. In the Gulf of Mexico, comparison with *Robinson*'s [1973] atlas and individual ship tracks indicates that Goes infrared detection is not feasible for about 4–6 months.

Columns 1 and 3 of Table 3 show the relative contribution of the two terms on the right-hand side of (1); it is not unusual for more than half of the radiance from the ocean to be absorbed and reemitted by the atmosphere (at a different temperature). Since transmittance is shown to control the useful range of current boundary detection temperatures (equation (8)), it is valuable to be able to determine τ without having to solve (1). The most important variable is the amount of precipitable water w in the air column. Fortunately, a simple relation between $\tau(\nu = 862.5$ cm$^{-1})$ and w(g cm^2) is found as shown in Figure 5, which is a plot of τ versus w for all 160 cloud-free soundings summarized in Table 3. The second-

TABLE 3. Transmittances for Cloud-Free Stations in February and August

	February		August	
Station	$\nabla T_0/\nabla T_s$ ($\tau \pm 1\sigma$)	δT_s($\delta T_0 = 0.5$), deg	$\nabla T_0/\nabla T_s$ ($\tau \pm 1\sigma$)	δT_s ($\delta T_0 = 0.5$), deg
Barbados	0.52 ± 0.02	1.0	0.49 ± 0.02	1.0
Bermuda	0.67 ± 0.04	0.8	0.45 ± 0.09	1.1
Boothville	0.70 ± 0.04	0.7	0.51 ± 0.01	1.0
Brownsville	0.63 ± 0.07	0.8	0.38 ± 0.07	1.3
Cape Hatteras	0.78 ± 0.08	0.6	0.43 ± 0.07	1.2
Key West	0.58 ± 0.10	0.9	0.41 ± 0.07	1.2
Ocean station H	0.73 ± 0.07	0.7	0.54 ± 0.05	0.9
Sable Island	0.81 ± 0.06	0.6	0.44 ± 0.13	1.1
San Juan	0.49 ± 0.02	1.0	0.44 ± 0.03	1.1
Swan Island	0.46 ± 0.02	1.1	0.43 ± 0.04	1.2

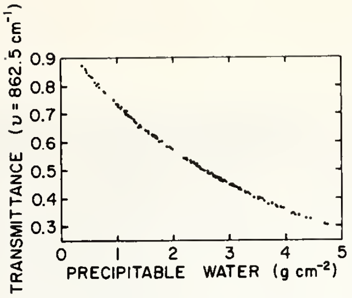

Fig. 5. Atmospheric infrared transmittance (ν = 862.5 cm^{-1}; λ = 11.6 μm) in the center of the Goes spectral window as a function of the precipitable water along the slant path. Calculations cover the range of nadir angles, θ, and atmospheric conditions for Goes sensing of Gulf Stream surface temperature gradients.

order least squares fit is

$$\tau = 0.941 - 0.221w + 0.019w^2 \qquad (10)$$

This relation holds for the central wavelength of the 11.6-μm atmospheric radiation window and for a wide variety of atmospheric and nadir angle situations within the range $0.3 < w < 5.0$. By simply calculating $w \cdot \sec \zeta$ from a sounding, an observer can, through the use of (10), determine whether infrared satellite or aircraft observations are locally useful in observing sea surface temperature gradients.

A final set of calculations using (1) is made to determine the temperature range at the top of the atmosphere for the known sea surface temperature range in the western North Atlantic. Based on monthly atlas averages of T_s ± 2 standard deviations, the expected range is $276 \leq T_0 \leq 300$ K. This spread forms the basis for contrast-stretching the images. An example of an image stretched over this range is given in Figure 6; the inset in the lower right-hand corner graphically depicts the enhancement curve. In this enhancement curve, clouds are almost uniformly white because their temperatures are below 276 K. The discontinuities in the enhancement curve at 276 and 300 K are suggested by P. McClain and R. Legeckis (personal communication, 1977) as they serve to separate film densities at these temperatures for better cloud and land discrimination.

Stochastic Analysis of Randomly Spaced Time Series

Satellite observations of Gulf Stream meanders have several difficulties that must be addressed: the satellite-sensed Gulf Stream front must be consistently defined, image sequence techniques require image registration which accounts for variations in the orbit as well as a constant scale for the projected film loop, the data set is randomly spaced because clouds prohibit seeing the current on a routine schedule, and folding and eddy separations must be accounted for in a wave staff analysis of current meanders. These issues are discussed in this section, and a preliminary stochastic analysis of available Goes data on the Gulf Stream is presented.

Advanced video techniques are being developed to navigate, register, and sequence images from Goes [*Chatters and Soumi*, 1975; *Smith*, 1975]. This technology is not yet incorporated into the operations of the National Oceanic and Atmospheric Administration (NOAA) National Environmental Satellite Service (NESS), and any attempt to construct a 3-year (or longer) time history of Gulf Stream meanders is by necessity tied to the routine operations of the satellite service. Therefore the photographic technique of image sequencing used by NOAA/NESS is employed in this study. Experience shows that skilled photographic technicians can manually register and collate Goes images such that the error in location is ±1–2 picture elements [*Gaby et al.*, 1977]. In the Gulf of Mexico, low-frequency meanders are 10 times larger than the ±10 to 20-km error implied in image location [cf. *Leipper*, 1970; *Maul*, 1977]. In the offing of Onslow Bay and in the region at 70°W the meanders are 4–5 times larger than location error [cf. *Webster*, 1961; *Hansen*, 1970; *Robinson et al.*, 1974]. By comparing the satellite-derived location on a day-to-day basis the error can be kept within acceptable limits, as will be discussed later.

For these analyses the satellite-sensed Gulf Stream front is defined as the demarcation in the enhanced images of the $\nabla_h T_0$ maxima juxtaposed to the warmest water, provided that the warmest water is a continuous elongated filament and not an eddylike feature. For example, in Figure 6 the 70°W meridian can be considered a wave staff, with zero arbitrarily set at 40°N. Using this definition, the Gulf Stream front is located at 38.2°N. Note that other complicated thermal fronts in the New England Slope water are not confused with the Gulf Stream by this definition.

Choosing the front is not always as simple as this example. Figure 7 illustrates a sequence of folded meanders such as *Legeckis* [1975] observed off Onslow Bay, North Carolina. The abscissa in Figure 7 can be imagined to be the coast of North Carolina. Alternatively, the abscissa can be imagined as a scale with arbitrary units of time; the meanders are allowed to advect past the observer from left to right, with $t = 0$ as the wave staff. At time $t = 30$ the Gulf Stream front, as defined in the preceding paragraph, would be at a distance offshore of $d = 30$. At $t = 60$, however, a folded wave exists. Thus $d = 17$ and $d = 35$. Recent work off the Georgia coast by T. N. Lee (personal communication (1977); cf. *Lee* [1975]) suggests that these folded waves are precursors to spinoff eddies. The main flow of the Gulf Stream is most likely at $d = 35$ in this example, and the offshore measurement is used throughout this analysis of meanders from a wave staff perspective.

Time series analysis of the meanders sketched in Figure 7 produces a spectrum as shown at the bottom of the figure. Points used in the analysis were chosen from the offshore edge, as discussed above, causing a sudden increase in d whenever a new folded wave reaches the wave staff (i.e., at t = 5, 45, 93, and 124). The spectrum, calculated by the least squares technique of *Vanicek* [1971], shows its largest peak at period $p = 39$ and a second one at $p = 84$. The spectral peak at $p = 39$ reflects that there are four folded waves or meanders in a record whose length is 160 time units long. The cause of the spectral peak at $p = 84$ is not clear, but it is probably associated with the meander centered at $t = 60$ being stretched larger than the others.

In *Vanicek*'s [1971] method the ordinate is percentage variance, which for a continuous record such as $\Sigma A_i \cos(\omega_i t - \Psi_i)$ would simply be

$$\text{percentage variance} = \frac{A^2 i}{\Sigma A^2 i} \cdot 100 \qquad (11)$$

This technique, programed by *Wells and Vanicek* [1976] in Fortran for use on almost any moderate sized computer, is a least squares calculation and can handle input data randomly spaced in time.

Taylor and Hamilton [1972] tested the *Vanicek* [1971]

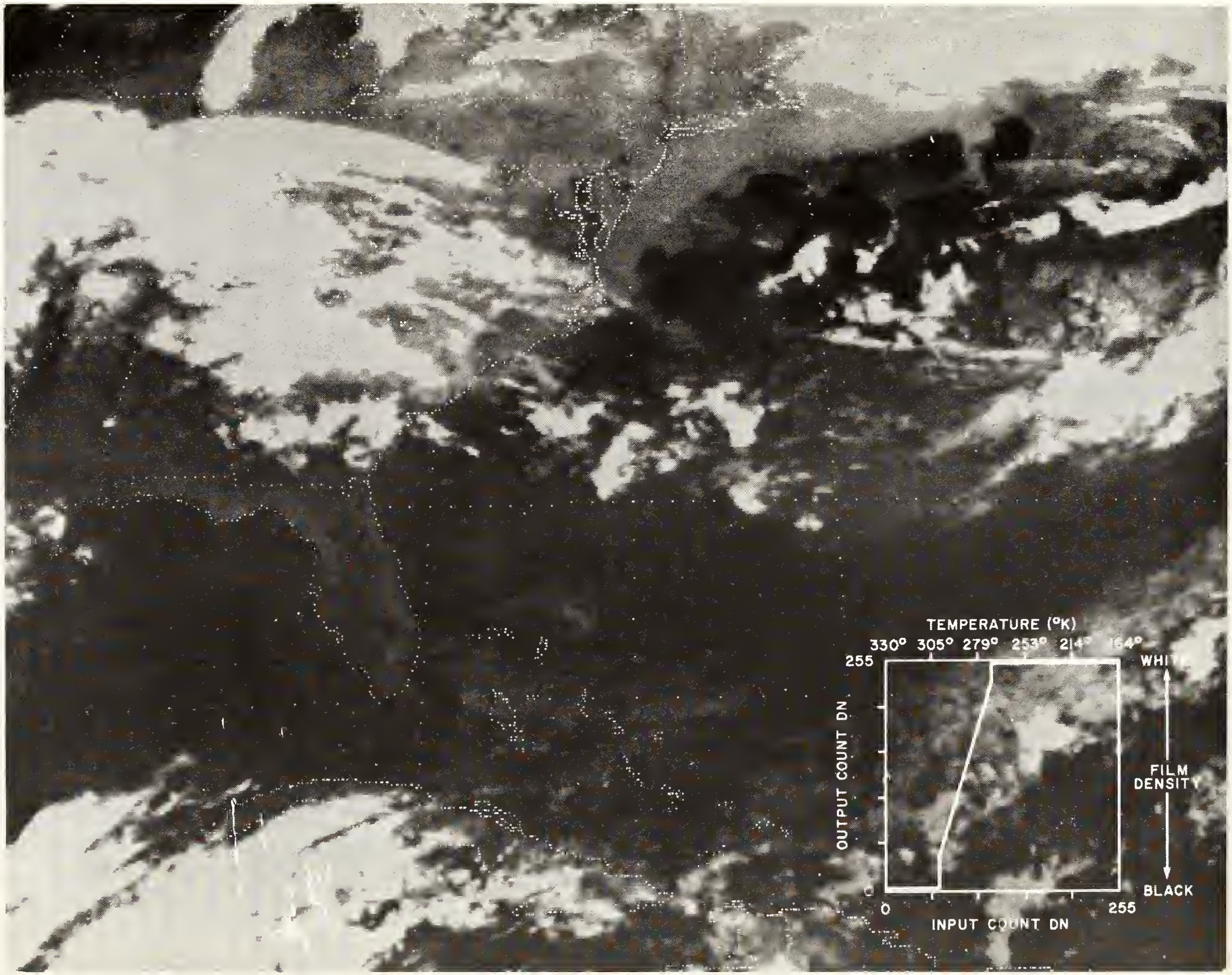
TEMPERATURE (°K)
330° 305° 279° 253° 214° 164°
255
OUTPUT COUNT DN
0
0
255
INPUT COUNT DN
WHITE
FILM DENSITY
BLACK

Fig. 6. Goes infrared image enhanced for ocean radiances using the enhancement curve shown in the lower right-hand corner. Cool features such as clouds are white; warm Gulf Stream is black. Several anticyclonic rings can be easily seen south of Cape Cod. Image acquired at 0100 UT on May 1, 1977.

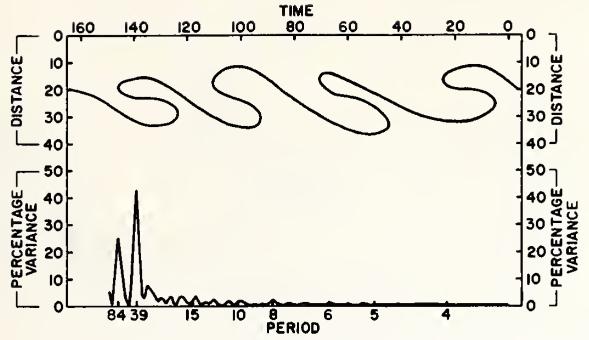

Fig. 7. (Top) Sketch of folded wavelike Gulf Stream meanders such as those observed off Onslow Bay, North Carolina. (Bottom) Spectral analysis of the meanders as they advect past a wave staff located at time $t = 0$ in the upper sketch. Measurements of meander amplitude are from $d = 0$ to the largest value whenever folding gives double-valued distances.

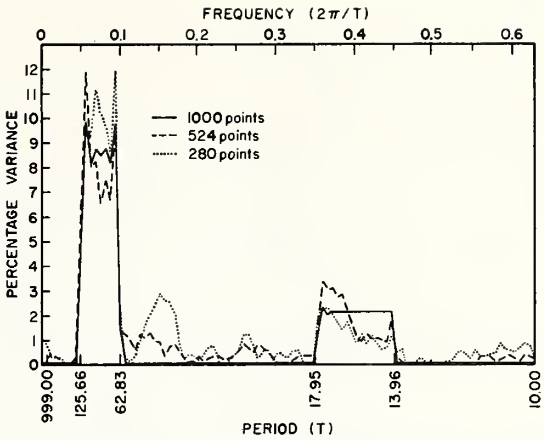

Fig. 8. Least squares spectral analysis of (12). Solid line is for all 1000 data points used to generate time series mathematically. Dashed line is analysis when 50% of the 1000 points were randomly selected out; 524 data points remained. Dotted line is analysis when 70% of the 1000 points were randomly selected out; 280 data points remained.

method on equally spaced data and found that the method does not displace a spectral peak close to known systematic noise (which can be removed by this method), that it distorts the amplitude of the spectral peak less than the conventional method of analysis, and that it intensifies side lobes. Vanicek's method was tested herein with randomly spaced data, using *Thompson*'s [1971] function,

$$f(t + 450) = \frac{\sin(0.10t) - \sin(0.05t)}{t} + \frac{\sin(0.45t) - \sin(0.35t)}{2t} \qquad (12)$$

which was chosen because it has the spectrum

$$\begin{aligned} S(\omega) &= 1.0 \qquad 0.05 < \omega < 0.10 \\ S(\omega) &= 0.5 \qquad 0.35 < \omega < 0.45 \qquad (13) \\ S(\omega) &= 0 \qquad \text{otherwise} \end{aligned}$$

Test data of 1000 points, approximately equivalent to 3 years of daily observations, were chosen. Percentage variance using (12) is a function of the record length because the average values of sine $x/x \to 0$ as the record length approaches $\pm\infty$. Results of using Vanicek's method with (12) are summarized in Figure 8.

Each of the three curves in Figure 8 is based on a record length of 1000 points. A random number generator was used to select out 50% of the data (dashed curve) and to select out 70% of the data (dotted curve); 524 points and 280 points, respectively, remained. The solid line, which uses all 1000 points from (12), reproduces the frequency response predicted in (13) quite accurately; the percentage variance is essentially zero outside the intervals $0.05 < \omega < 0.10$ and $0.35 < \omega < 0.45$. Ordinate height when using all 1000 points is essentially uniform in the high-frequency peak and somewhat less uniform in the low-frequency peak. Randomly decreasing the number of points in the record (but maintaining the record length) maintains the frequency identity of the two peaks, but the percentage variance in each peak is less square shaped, and the continuum between peaks is raised. The peak at frequency $f = 0.15t^{-1}$ in Figure 8, of the calculation using 280 points, is quite large but is an artifact of the particular series of random numbers used in the calculation; when five different sets of random numbers are used with the same 70% removal specification, and the five spectra averaged, the percentage variance at $f = 0.15t^{-1}$ is only 0.8%. This result emphasizes the need for spectral smoothing by variations of a Barlett or Hanning type technique, which will be applied after records of sufficient length are obtained.

The several sources of error in making wave staff type analysis, as discussed earlier, can lead to measurement noise of as much as 25% of the meander amplitude. The effect of white noise of 10 and 25% on (12) was calculated using *Vanicek*'s [1971] techniques and is summarized in Figure 9. A random number generator was used to add noise with a ratio to the maximum value of (12) of 0.10 and 0.25, respectively; all 1000 points are included. The net effect is to lower the percentage variance in each spectral peak, not to affect the continuum to any significant degree, and not to affect the frequency at which the peaks arise. Physically, the effect of noise in these ranges is to mask the smallest meanders. However, meanders with amplitudes of 20 km or larger should be detectable by using Goes satellite imagery.

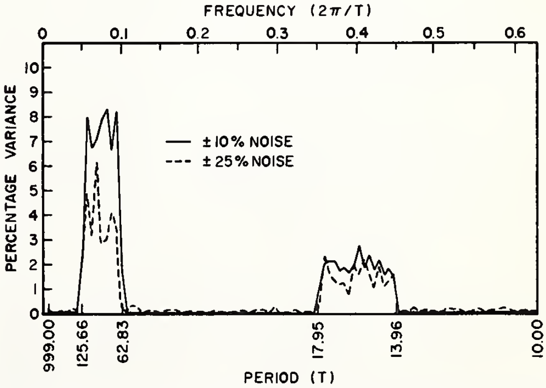

Fig. 9. Least squares spectral analysis of (12), using all 1000 points, but with white noise added to the mathematically generated time series. Solid line is for ±10% of maximum value of (12); dashed line is for ±25% of the maximum value.

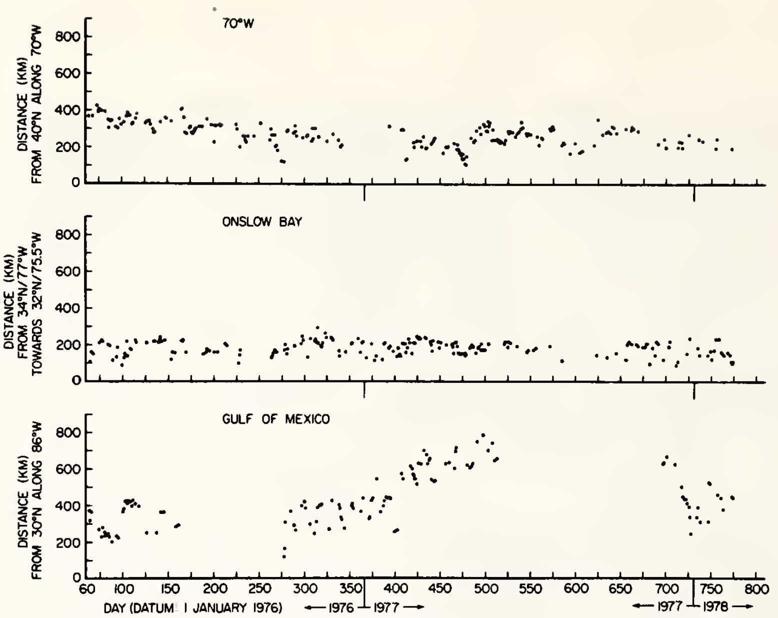

Fig. 10. Goes satellite measurements of Gulf Stream meanders during period March 1976 through February 1978. Abscissa is time in days, referenced to day 1 on January 1, 1976. Spectrum of upper time series is given in Figure 11*a*, spectrum of middle time series is given in Figure 11*b*, and spectrum of lower time series is given in Figure 11*c*.

SPECTRA OF GULF STREAM MEANDERS

Measurements in a wave staff mode were attempted using existing daily data. Ocean-enhanced images were obtained at the NOAA Miami Satellite Field Service Station for 9 hours a day on a priority below that for meteorological services. This data base provided the opportunity to make a stochastic analysis of randomly spaced wave staff type measurements of Gulf Stream meanders. Spectra of the 700 or so days of available data were made using the least squares technique discussed above.

Three test wave staff locations are chosen as a datum for Gulf Stream meanders: (1) along 86°W referenced to 30°N in the eastern Gulf of Mexico, (2) between 34°N/77°W (reference point) and 32°N/75°W off Onslow Bay, and (3) along 70°W referenced to 40°N off New England. The data to be analyzed are shown in Figure 10; the upper time series is from 70°W, the middle time series is from Onslow Bay, and the lower time series is along 86°W. Gaps in the data from 70°W are generally short and are associated more with periods of extensive cloudiness rather than with loss of $\nabla_h T_s$ due to summer insolation. The largest gap occurs around day 375, which is in January 1977, and data are also sparse around day 700, which is in December 1977. The largest gap in the Onslow Bay record occurs around August 1977, with another large one in September 1976. These gaps are due to loss of $\nabla_h T_s$ rather than cloudiness, although clouds associated with the atmospheric Jet Stream often cause gaps of as much as a fortnight. The Onslow Bay data set was the most complete of the three records. In the Gulf of Mexico (bottom, Figure 10) there are two large gaps, each in the summer, which are associated with the loss of $\nabla_h T_s$ due to insolation. Excluding these large gaps, the average sample interval was about 3 days over the 700 days analyzed herein.

The record at 70°W shows a linear northward displacement from day 60 to about day 475; the northern edge of the Gulf Stream is at least 100 km further north in April 1977 than in March 1976. Since this is a linear trend, it is difficult to ascribe the displacement to a seasonal event such as the severe winter of 1976–1977 [*Leetmaa*, 1977]. Using Leetmaa's values for the deepening of the thermocline, it can be shown that two-layer potential vorticity conservation is not an adequate explanation for the northward trend observed by satellite. Amplitude of the least squares annual harmonic is only 20 km. Based on the Goes data, it is not possible to assess further the northward trend; perhaps a longer record will.

The record off Onslow Bay does not show a linear trend, nor is there any obvious seasonal displacement. The least squares annual harmonic off Onslow Bay has an amplitude of only 5 km, which is not statistically significant. In the Gulf of Mexico, however, a southward trend of over 400 km occurs in the winter-spring of 1976–1977. *Molinari et al.* [1977] report that a large anticyclonic eddy had separated in March 1977 (ca. day 460), but this is not evident in Figure 10 because the 86°W meridian is not well oriented with respect to this particular eddy separation area. During the 'spring intrusion' [*Leipper*, 1970] the Loop Current penetrates by growing to the north and shifting to the west. As the eastern boundary shifts to the west, a wave staff along 86°W should show a southward trend. Choice of a reference datum notwithstanding, the amplitude of the annual least squares harmonic is 75 km. When a longer data set has been acquired, the Gulf of Mexico wave staff will be changed to a more northwest-southeast orientation, and the series reanalyzed.

Two spectra are calculated for each locale. The lower spectrum in each part of Figure 11 is calculated from the entire record length. T. N. Lee (personal communication, 1977) notes that the spectrum which used the full 2 years of data would not show detail in the 4- to 16-day band. This is due to many fluctuations with many different periods within this 4- to 16-day band, which would tend to smooth out the variance within the band when analyzed together. In order to investi-

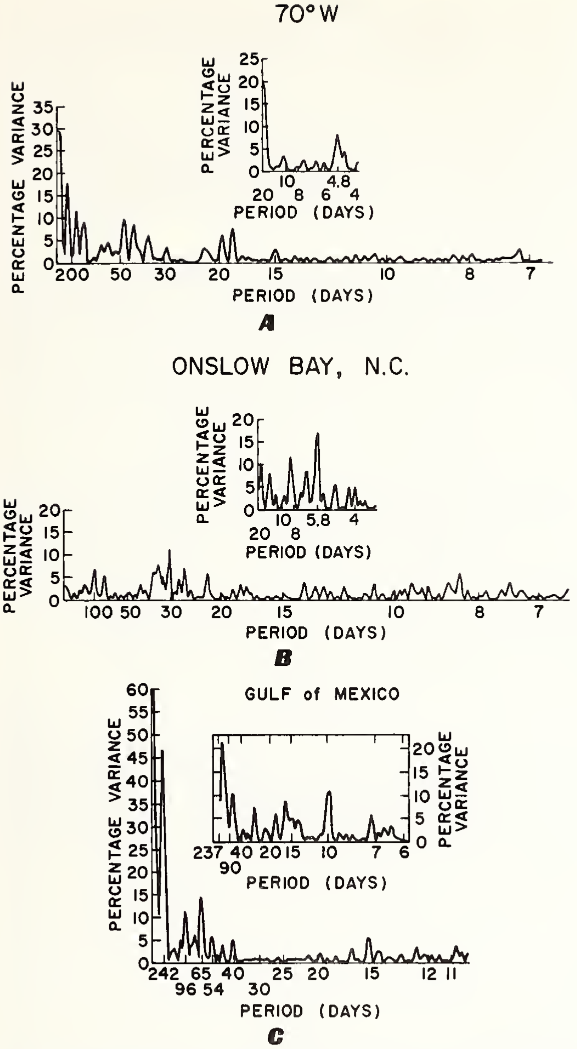

Fig. 11. Least squares analyzed spectra of Gulf Stream meanders at three locations: (*a*) South of Cape Cod along 70°W longitude; inset is 70° spectrum for days 420–522 only; (*b*) along a line orthogonal to the coast in the offing of Onslow Bay; inset is Onslow Bay spectrum for days 402–504 only; (*c*) along 86°W longitude in the eastern Gulf of Mexico; inset is Gulf of Mexico spectrum for days 277–514 only. See Figure 14 for sketch of locations.

gate these 4- to 16-day periods, spectra based on a short record length during the winter of 1976–1977 were calculated for each locale as shown as an inset above the spectrum based on the full record.

Figure 11*a* is the spectrum of Gulf Stream meanders along 70°W, using the full record; the inset is for days 420–522 during which the data base is more complete. This area is in the region where *Hansen* [1970] shows a period of about 1.5 months for the meanders. The present spectrum shows peaks at about 45 days, which is in agreement with the shipboard study. Except for the higher variance at longer periods, the spectrum has a few other peaks at 36, 29, 21–18, and 15 days. *Robinson et al.* [1974] report time scales in their experiments of 13 ± 3 days and 3 ± 1 days; their longer period is reflected in the main spectrum in Figure 11*a*, but the shorter periods are below the Nyquist, which is about 6 days in the main spectrum and about 4 days in the short-period spectrum as shown in the inset. The spectral peak at about 250 days along 70°W is also seen in the Gulf of Mexico (Figure 11*c*). The peak at 4.8 days in the inset could be an aliased period of 3.3 days which would be in agreement with Robinson et al. However, 4.8 days is quite close to the average period of mid-latitude weather events and is probably associated with atmospheric frontal activity.

The full spectrum in Figure 11*b* is of Gulf Stream meanders in the offing of Onslow Bay; the inset is for days 402–504, during which two samples are available for every 3 days. The record lengths are approximately the same as the length used for Figure 11*a*, but the shape of this spectrum is markedly different. The full spectrum shows spectral variance at about 100, 36–30, and 22 days. The energy in the shorter periods (see inset) is probably associated with the features observed by *Webster* [1961] and *Legeckis* [1975], but the longer periods, i.e., those greater than 2 months, seem to be completely different. There is very little spectral variability at periods greater than 40 days off Onslow Bay, whereas along 70°W most of the variability is in the lower frequencies. The short periods shown in the inset have important peaks at 5.8 and 8.5 days. This inset spectrum is calculated for approximately the same time interval as the inset in Figure 11*a*, and there is a small peak at 4.8 days off Onslow Bay, but there are no corresponding peaks at 5.8 and 8.5 days along 70°W.

Figure 11*c*, taken along 86°W, shows a third distinct spectrum. There is a large spectral peak at 242 days, along with smaller peaks at 96-, 65-, 54-, 40-, and 16-day periods. There is a spectral gap between 20 and 40 days in this spectrum which is distinctly different from Onslow Bay (Figure 11*b*) and south of New England (Figure 11*a*). Figure 11*c* is based on a data set with two large gaps in the summer. However, in the winter-spring of 1976–1977 an 8-month datum is available for the short-record analysis. The results are shown inset in Figure 11*c*. The inset spectrum has the linear trend removed (a feature of *Vanicek*'s [1971] analysis technique). The high-frequency energy in the Gulf Loop Current is dominated by a peak at 10 days, a feature not observed off Onslow Bay or along 70°W.

Probably the most striking result of comparing the spectra in Figure 11 is that there is little detailed resemblance from locale to locale, although there are several common bands of increaesd variance. Each locale has quite different bottom topography; the wind regimes are also dissimilar, particularly in the Gulf of Mexico. Atmospheric forcing can be reasonably invoked to explain the variance in the shorter periods [cf. *Düing et al.*, 1977], but the energy in the 30- to 100-day period band is not so easily explained. Periods longer than 100 days probably have little significance with these 2-year records, although there is some indication of annual scale periods in the Gulf of Mexico data (cf. Figure 10). There are several other forcing sources that would cause the spectra to be as observed, one of which is investigated in the next section.

Comparison of Meander Periods With Transport Variations

Von Arx et al. [1955] suggest that cyclonic edge shingle structures, as observed by aircraft infrared surveys of the Gulf Stream, could be caused by Florida Current transport fluctuations. Concurrent measurements of transport variability in the Gulf Stream are not available for the 1976–1978 time frame studied in the present report. However, it is of interest to investigate historical data in this context and to see if any of the meander periods reported on herein are coincident with the periods of transport variation. As will be shown, there are some correlations which suggest avenues for future research.

Niiler and Richardson [1973] report direct measurements of total transport across the Straits of Florida between Miami and Bimini in the years 1964–1970. Their data form a randomly spaced time series which we analyzed by the least squares method of *Vanicek* [1971]. The distribution of time (t) of the volume transports (T_{vol}) and the spectral calculations are summarized in Figure 12. The raw spectrum of the entire *Niiler and Richardson* [1973] data set is shown by a solid line in the drawing which has a range in period from 60 to 1215 days along the abscissa. The dominant period at 365 days is in agreement with their conclusion of an annual cycle. The dotted line in this drawing is the residual spectrum after removal of the annual cycle characterized by

$$T_{vol}(t) = Mn + A\cos(\omega_A t - \psi) \qquad (14)$$

where Mn is the mean volume transport, A is the amplitude, ω_A is the annual frequency, and ψ is the phase. Niiler and Richardson calculated that $Mn = 29.5 \times 10^6$ m^3 s^{-1}, $A = 4.1 \times 10^6$ m^3 s^{-1}, and $\psi = 2.7$ rad relative to January 1. Application of *Vanicek*'s [1971] technique yields $Mn = 29.2 \times 10^6$ m^3 s^{-1}, $A = 4.0 \times 10^6$ m^3 s^{-1}, and $\psi = 2.8$ rad, which is in agreement with Niiler and Richardson's results.

Niiler and Richardson also report several closely spaced observations of transport over time intervals of from 7 to 31 days. Transport variability in five of these short time intervals is presented at the bottom of Figure 12 on an expanded scale. A least squares estimate of the transport spectrum from these five observation periods, adjusted to a common mean transport datum, is calculated and is shown as an inset above the full spectrum in Figure 12. The inset spectrum is in good agreement with other reports on Florida Current fluctuations in the 2- to 20-day period range [cf. *Wunsch and Wimbush*, 1977; *Brooks and Niiler*, 1977]. Based on a discontinuous 2-year current meter station off Miami, *Düing et al.* [1977] report spectral energy maxima for the north component of velocity in three bands: 2–3 days, 4–5 days, and 8–25 days. Inasmuch as velocity and transports are related, it appears that historical transport spectra in these short periods are similar to historical spectra of current meanders [cf. *Webster*, 1961, *Düing*, 1975; *Robinson et al.*, 1974] and with the data observed by satellite (inset, Figure 11).

Owing to lack of observations, low-frequency transport variability is less well known. Düing et al. report that the annual signal in their current meter data accounted for 14% of the variance and had $\phi = 1.9$ rad. Düing et al. also report that in contrast to open ocean spectra, there was no energy increase toward very low frequencies (their spectra of the north component of velocity show as much energy at 100 days as at 8 days, but the energy at greater than 100 days decreases) and that 80% of the variance (excluding tidal bands) was provided by time scales greater than 8 days. The spectrum from Niiler and Richardson's data (Figure 12) also shows less variance at low frequencies after the annual harmonic is removed. This is not the case with the spectrum of Florida Current transport based on electric potential measurements between Key West and Havana.

Electric potential transports (T_{EP}) were calculated from

$$T_{EP} = d\cdot\Delta\phi/H \qquad (15)$$

where d is the depth of the channel, H is the vertical component of the earth's magnetic field, and $\Delta\phi$ is the potential difference across the channel. Transport estimates using (15) between Key West and Havana have been tabulated by *Stommel* [1957, 1959, 1961] and *Broida* [1962, 1963]. Each data point was based on a 24-hour average of $\Delta\phi$, usually for

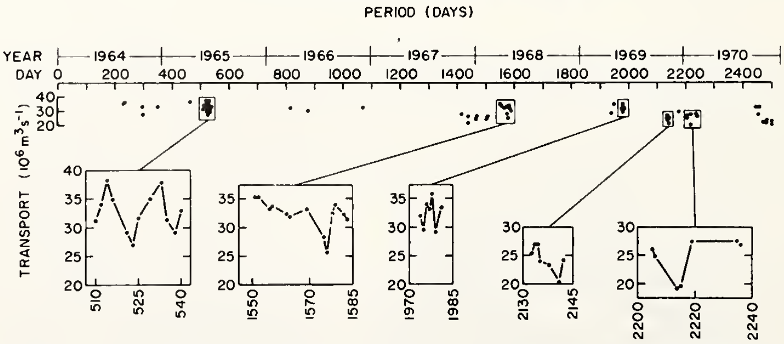

Fig. 12. Least squares spectral analysis of *Niiler and Richardson*'s [1973] direct transport measurements between Miami, Florida, and Bimini, Bahamas. The upper spectrum is based on the five short records of intense sampling shown in expanded detail at the bottom. The lower spectrum is based on all the data (solid line) and on the data after the annual cycle is removed (dotted line).

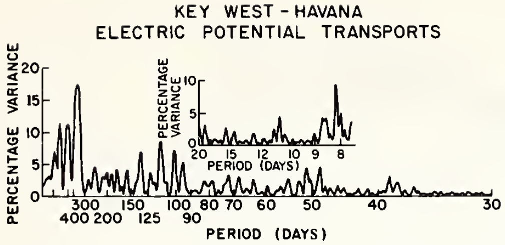

Fig. 13. Least squares spectral analysis of *Stommel*'s [1957, 1959, 1961] and *Broida*'s [1962, 1963] electric potential volume transport measurements between Key West, Florida, and Havana, Cuba, from August 1952 to September 1961. The upper spectrum is based on a 600-day record in 1953–1954 for which the data density was a maximum. The lower spectrum is based on the entire data set; the spectrum from 30 days to the Nyquist at 13.6 days had less than 1% variance at all periods.

Saturday and Sunday, between 1952 and 1961. There were eight intervals where observations were not taken for a month or longer, leaving nine sets of observation periods, each of which was treated in the present study as being on a different datum. The average value of T_{EP} during each of the nine observation periods ranged from 25.1×10^6 m^3 s^{-1} to 41.3×10^6 m^3 s^{-1}. The least squares spectrum (Figure 13) was calculated with the nine observation periods adjusted to a common datum and with the annual harmonic removed; 490 data points were used, and the Nyquist period was 13.6 days. The high frequencies (inset, Figure 13) were calculated from the most complete record, a 600-day period in 1953–1954. The Nyquist period for the inset spectrum was 7.6 days.

Most of the residual variance in Figure 13 is seen to be in the 300- to 400-day period even after removal of the annual cycle (for which $A = 1.6 \times 10^6$ m^3 s^{-1} and $\psi = 2.2$ rad). *Wertheim* [1954] postulates that the variability in T_{EP} could be caused by meandering of the current, and he calculates that a 20-km meander could affect T_{EP} by 20% due to changes in d. It is now known [*Maul*, 1977] that meanders of more than 50 km occur in the Key West–Havana channel, which means that the effective depth can change by a factor of 2 or more (H. Stommel, personal communication, 1977). Considering the annual cycle both in Niiler and Richardson's transports (T_{vol}) and in the Key West–Havana electric potential transports (T_{EP}), neglecting the small difference in ψ, then the ratio $T_{vol}/T_{EP} \approx 2.5$, which is a reasonable estimate of the variability in d. Thus the spectra in Figure 13 are better interpreted as percentage variance in T_{vol}/d. In view of the geophysical assumptions in using (15), the range of average transport in the nine datum levels, and the effect of varying depth being greater than the range of transport variability, it is concluded that the reported values of T_{EP} are not directly applicable to the problem of correlating Gulf Stream meanders and transport variability. Future observations of $\Delta\phi$ may prove more useful if an independent estimate of d can be made through (satellite) monitoring of the current boundary.

Comparison of intermediate period peaks (60–150 days) in the spectrum of Niiler and Richardson transports (dotted line, Figure 12) with intermediate period peaks in the Gulf of Mexico meander spectrum (Figure 11*c*) shows that only the peak at 65 days is seen in both spectra. If it is postulated that some intermediate period peaks in the transport spectrum are caused by shorter periods which are folded about the Nyquist period and aliased, then four of the five peaks between 40 and 100 days as calculated in the Gulf of Mexico meander spectrum are also in the Straits of Florida transport spectrum. In general, all three meander spectra show increased levels of percentage variance in the 30- to 100-day band, which is in agreement with the spectrum of Niiler and Richardson transports and with the spectrum of current meter data reported by Düing et al. That there may be interannual periods is hinted at in Figures 12 and 13, but this cannot be assessed in the meanders until a decade or so of observations are obtained.

In summary, it is not possible to make any definitive statement about the correlation between meander periods and transport (velocity) variability except to note that an annual cycle with $1.9 \leq \psi = 2.8$ is common to both transport (velocity) and meander spectra, except at Onslow Bay. Also, there are two broad bands of increased spectral variance, 4–16 days and 30–100 days, that appear in all transport (velocity) spectra and in all meander spectra, which further suggests that meander variability may be related to transport variability. One working hypothesis is that meanders in the Gulf of Mexico act as a variable blocking mechanism to the Florida Current as they advect downstream. A definitive study of cause, effect, and feedback requires concurrent transport and velocity measurements.

CONCLUDING REMARKS

Approximately 9 months of satellite-derived weekly composite Gulf Stream positions from March to November 1976 are summarized in Figure 14. Also shown are the locations of the three wave staffs used for Figures 11*a*, 11*b*, and 11*c*. From the Straits of Florida northward the overall impression is of a spreading envelope with downstream modulation. The Onslow Bay region has a wider envelope than that at Cape Hatteras or off Jacksonville, Florida, possibly as a potential vorticity-conserving response to the step in the bottom topography of the Blake Plateau [*Pashinsky and Maul*, 1973; *Brooks and Bane*, 1978]. The greatest latitudinal variability is in the eastern Gulf of Mexico, larger even than that reported off the Grand Banks [*Hansen*, 1970]. The minimum variability is in the region off Miami, Florida.

Niiler [1975] summarizes recent studies on variability in western boundary currents and notes how few and how short the continuous records are. Niiler discusses a 6-month acoustic record, which has strong spectral peaks between 4 days and a fortnight, which is in agreement with several other investigators with shorter data sets (cf. Figures 11, 12, and 13). The meander data reported herein extend these shorter records and hold the promise of providing a very long quasi-continuous time history from which new spectral estimates can be made. *Niiler* [1975] also reviews the theories of Gulf Stream fluctuations and notes that these '. . . theories are no further advanced than the observations.' Satellite measurements are not the panacea for all observational needs; however, the results reported herein do show that Goes imagery opens another dimension in Gulf Stream time series acquisition and analysis.

Spectra such as those given in Figures 11*a*, 11*b*, and 11*c* provide information necessary in designing sampling strategy. For example, the variability in the 65-day period in the Gulf of Mexico (Figure 11*c*) could not, with any degree of confidence, be gleaned from *Leipper*'s [1970] or *Maul*'s [1977] cruises. Conversely, studies such as *Düing*'s [1975] or *Webster*'s [1961] contribute to knowledge of higher-frequency perturbations such as the 7- to 10-day periods recorded in Figure 11, but logistically they cannot hope to study the lower-frequency phenomena along the entire current. As the length of the satellite-derived time series increases, and as a means of esti-

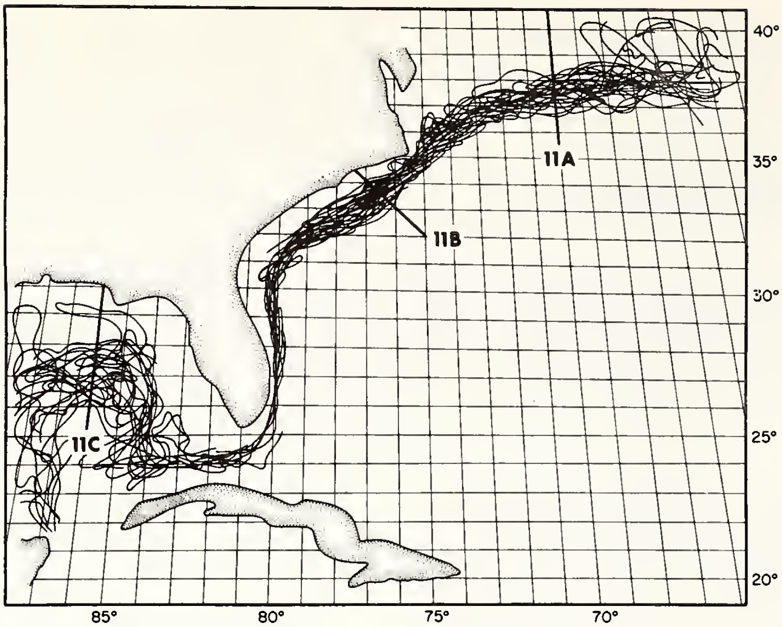

Fig. 14. Nine-month composite of locations of Gulf Stream front from Goes between February and November 1976. based on weekly composites. Heavy lines marked 11A, 11B, and 11C refer to data discussed in Figures 11*a*, 11*b*, and 11*c*. Chart base is an adaptation of exact projection given in Figures 3 and 4.

mating confidence limits in least squares spectra are derived, a more rigorous statement on sampling strategy can be made.

Future efforts using the enhanced 24-hour Goes data will be centered on several activities. Shipboard experiments will be conducted to determine more about the relation between the satellite signature of the stream and more conventional indicators; this will involve cooperative investigations with the many Polymode (and related) shipboard projects over the 1977–1980 time frame. Spectra from many locations will be investigated in order to determine the representativeness of the results given in Figure 11 and to determine the coherence between closely spaced stations. The 3-year data set will also be useful in providing statistics on the frequency of Gulf Stream ring formation, their advection and fate, and for studying other fronts, such as the coastal fronts along the continental shelf break; no attempt will be made at this writing to assess the value of Goes data for this and several other purposes. We will, however, solicit suggestions from the community in this regard.

REFERENCES

Augstein, E., H. Schmidt, and F. Ostapoff, The vertical structure of the atmospheric planetary boundary layer in undisturbed Trade Winds over the Atlantic Ocean, *Boundary Layer Meteorol.*, *6*, 129–150, 1974.

Bernstein, R. L., L. Breaker, and R. Whritner, California current eddy formation: Ship, air, and satellite results, *Science*, *195*, 353–359, 1977.

Broida, S., Florida Straits transports: April 1960–January 1961, *Bull. Mar. Sci. Gulf Carib.*, *12*(1), 168, 1962.

Broida, S., Florida Straits transports: May 1961–September 1961, *Bull. Mar. Sci. Gulf Carib.*, *13*(1), 58, 1963.

Brooks, D. A., and J. M. Bane, Jr., Gulf Stream deflection by a bottom feature off Charleston, South Carolina, *Science*, *201*, 1225–1226, 1978.

Brooks, I., and P. Niiler, Energetics of the Florida Current, *J. Mar. Res.*, *35*(1), 163–191, 1977.

Chatters, G. C., and V. E. Soumi, The applications of McIDAS, *IEEE Trans. Geosci. Electron.*, *GE-13*(3), 137–146, 1975.

De Rycke, R. J., and P. K. Rao, Eddies along a Gulf Stream boundary viewed from a very high resolution radiometer, *J. Phys. Oceanogr.*, *3*(4), 490–493, 1973.

Düing, W. O., Synoptic studies of transients in the Florida Current, *J. Mar. Res.*, *33*, 53–73, 1975.

Düing, W., C. Mooers, and T. Lee, Low frequency variability in the Florida Current and relations to atmospheric forcing from 1972 to 1974, *J. Mar. Res.*, *35*(1), 129–161, 1977.

Gaby, D. C., J. B. Lushine, B. M. Mayfield, S. C. Pierce, K. O. Poteat, and F. E. Torres, Atlantic tropical and subtropical cyclone classifications for 1976, *Rep. TM-NESS-87*, Nat. Oceanic and Atmos. Admin., Washington, D. C., 1977.

Hansen, D. V., Gulf Stream meanders between Cape Hatteras and the Grand Banks, *Deep Sea Res.*, *17*, 495–511, 1970.

Hansen, D. V., and G. A. Maul, A note on the use of sea-surface temperature for observing ocean currents, *Remote Sensing Environ.*, *1*(3), 161–164, 1970.

Lee, T. N., Florida Current spin-off eddies, *Deep Sea Res.*, *22*, 753–765, 1975.

Leetmaa, A., Effects of the winter of 1976–1977 on the northwestern Sargasso Sea, *Science*, *198*, 188–189, 1977.

Legeckis, R., Application of synchronous meteorological satellite data to the study of time dependent sea-surface temperature changes along the boundary of the Gulf Stream, *Geophys. Res. Lett.*, *2*(10), 435–438, 1975.

Leipper, D. F., A sequence of current patterns in the Gulf of Mexico, *J. Geophys. Res.*, *75*(3), 637–657, 1970.

Maul, G. A., The annual cycle of the Gulf Loop Current, I, Observations during a one-year time series, *J. Mar. Res.*, *35*, 29–47, 1977.

Maul, G. A., and S. R. Baig, A new technique for observing mid-latitude ocean currents from space, in *Proceedings, 41st Annual Meeting*, pp. 713–716, American Society of Photogrammetry, Washington, D. C., 1975.

Maul, G. A., and M. Sidran, Atmospheric effects on ocean surface temperature sensing from the NOAA satellite scanning radiometer, *J. Geophys. Res.*, *78*(12), 1909–1916, 1973.

Molinari, R. L., S. Baig, D. W. Behringer, G. A. Maul, and R. Legeckis, Winter intrusions of the Loop Current, *Science*, *198*, 505–507, 1977.

Niiler, P. P., Variability in western boundary currents, in *Numerical*

Models of Ocean Circulation, pp. 216–236, National Academy of Sciences, Washington, D. C., 1975.

Niiler, P. P., and W. S. Richardson, Jr., Seasonal variability of the Florida Current, *J. Mar. Res.*, *31*, 144–167, 1973

Pashinsky, D., and G. A. Maul, Use of ocean temperature while coasting between the Straits of Florida and Cape Hatteras, *Mar. Weather Log.*, *17*(1), 1–3, 1973.

Richardson, P. L., A. E. Strong, and J. A. Knauss, Gulf Stream eddies: Recent observations in the western Sargasso Sea, *J. Phys. Oceanogr.*, *3*(3), 297–301, 1973.

Robinson, A. R., J. R. Luyten, and F. C. Fuglister, Transient Gulf Stream meandering, 1, An observational experiment, *J. Phys. Oceanogr.*, *4*(2), 237–255, 1974.

Robinson, M. K., Atlas of monthly sea-surface and subsurface temperature and depth of the top of the thermocline, Gulf of Mexico and Caribbean Sea, *Scripps Inst. Oceanogr. Ref.*, *73*(8), 106, 1973.

Smith, E. A., The McIDAS system, *IEEE Trans. Geosci. Electron.*, *GE-13*(3), 123–136, 1975.

Stommel, H., Florida Straits transports: 1952–1956, *Bull. Mar. Sci. Gulf Carib.*, *7*, 252–254, 1957.

Stommel, H., Florida Straits transports: June 1956–July 1958, *Bull. Mar. Sci. Gulf Carib.*, *9*, 222–223, 1959.

Stommel, H., Florida Straits transports: July 1958–March 1959, *Bull. Mar. Sci. Gulf Carib.*, *11*, 318, 1961.

Taylor, J., and S. Hamilton, Some tests of the Vanicek method of spectral analysis, *Astrophys. Space Sci.*, *17*, 357–367, 1972.

Thompson, R. O. R. Y., Spectral estimation from irregularly spaced data, *IEEE Trans. Geosci. Electron.*, *GE-9*(2), 107–110, 1971.

Vanicek, P., Further development and properties of spectral analysis by least-squares, *Astrophys. Space Sci.*, *12*, 10–33, 1971.

von Arx, W. S., D. F. Bumpus, and W. S. Richardson, On the finestructure of Gulf Stream front, *Deep Sea Res.*, *3*, 46–65, 1955.

Voorhis, A. D., E. H. Schroeder, and A. Leetmaa, The influence of deep mesoscale eddies on sea-surface temperature in the north Atlantic Subtropical Convergence, *J. Phys. Oceanogr.*, *6*(6), 953–961, 1976.

Webster, F., A description of Gulf Stream meanders off Onslow Bay, *Deep Sea Res.*, *8*, 130–143, 1961.

Wells, D. E., and P. Vanicek, Least-squares spectral analysis, report, Bedford Inst. of Oceanogr., Dartmouth, Nova Scotia, 1976.

Wertheim, G., Studies of the electric potential between Key West, Florida, and Havana, Cuba, *Eos Trans. AGU*, *35*(6), 872–882, 1954.

Wunsch, C., and M. Wimbush, Simultaneous pressure, velocity and temperature measurements in the Florida Straits, *J. Mar. Res.*, *35*(1), 75–104, 1977.

(Received April 3, 1978;
revised June 6, 1978;
accepted June 29, 1978.)

10

NASA Contractor Report #141435, 23 pages.

Deep Sea Tides Determination From GEOS-3

George A. Maul
and
Alan Yanaway

National Oceanic and Atmospheric Administration
Atlantic Oceanographic and Meteorological Laboratories
Miami, Florida 33149

Prepared under Purchase Order No. P-57579 (G)

National Aeronautics and
Space Administration

Wallops Flight Center
Wallops Island, Virginia 23337
AC 804 824-3411

Table of Contents

Page

Introduction 1

Data Management and Processing 6

Data Analysis 9

Results 14

Conclusions 19

References 22

Introduction

One of the outstanding problems of geophysics is the global determination of the oceanic tide. The coastal tide can be markedly different from the oceanic tide due to the influence of bottom topography (Redfield, 1958). Many measurements exist of the coastal tide, but few are known in the deep sea. If a radar altimeter on a satellite could adequately detect deep-sea tides (NASA, 1969), the need for sea-floor pressure gages could be significantly reduced. Zetler and Maul (1971) showed that it was possible to retrieve the most important tidal amplitudes and phases from a simulated satellite altimeter in the presence of noise which was larger than the signal. A practical test of this concept was performed using the GEOS-3 altimeter data and is reported herein.

Geometry of the measurements is shown in Figure 1. Height of the spacecraft above the ellipsoid and the corrected altitude measurement are provided by the NASA Wallops Flight Center; details of the tracking techniques and microwave propagation corrections are given in Leitao, et al. (1975). For the purposes of this report, the oceanic tide will be considered the temporal variability of the sea-surface height at a particular location in certain tidal frequencies (see again Fig. 1). Perturbations in the sea-surface height due to wind waves, swell, quasi-geostrophic currents and eddies, and to steric changes are considered along with tracking and propagation inaccuracies, to be noise.

Test site for this experiment is the GEOS-3 calibration area off the east coast of the United States. Surface truth for the

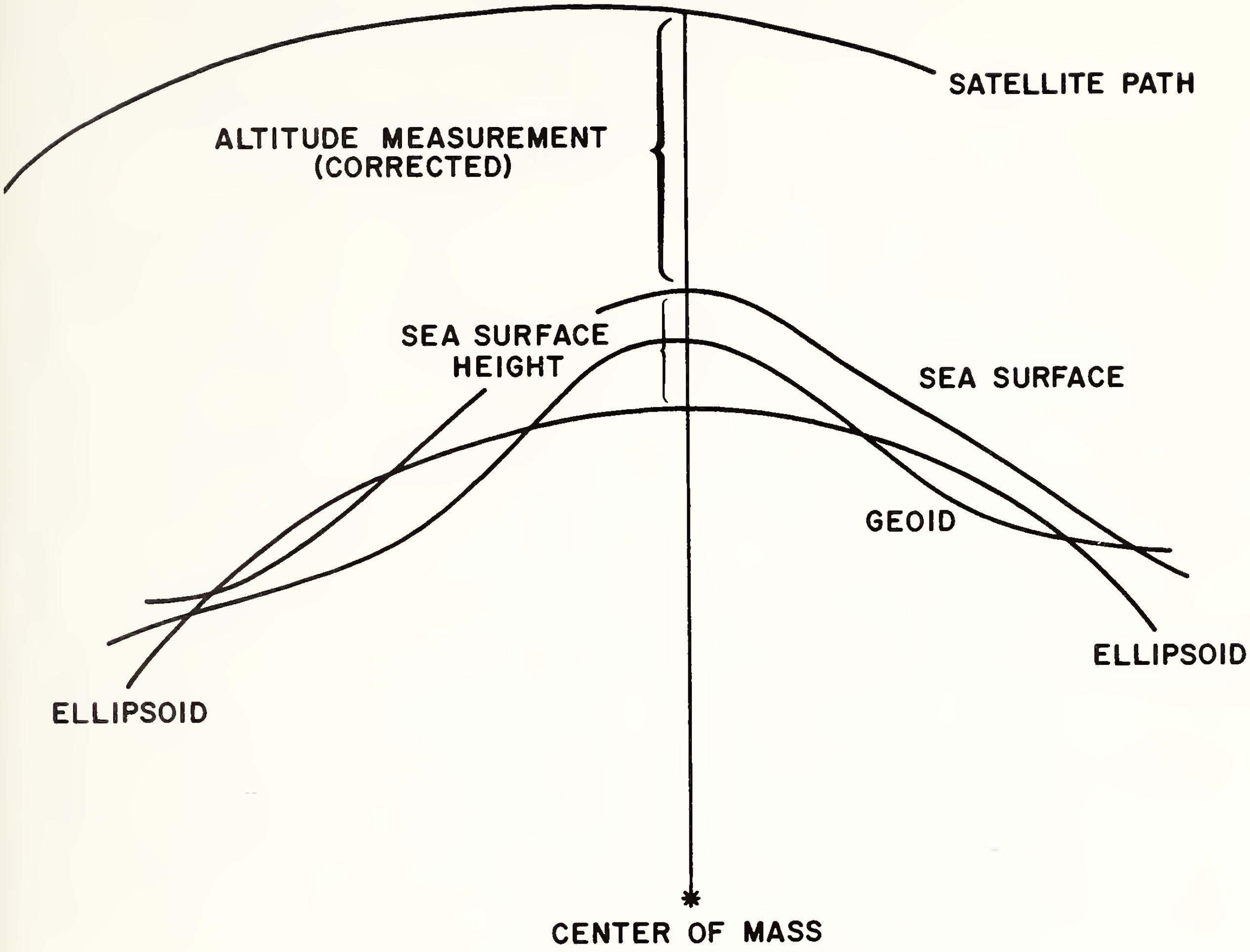
SATELLITE PATH
ALTITUDE MEASUREMENT (CORRECTED)
SEA SURFACE HEIGHT
SEA SURFACE
GEOID
ELLIPSOID
ELLIPSOID
CENTER OF MASS

Figure 1. Skematic of the measurement geometry. Height of the spacecraft above the reference ellipsoid is determined from tracking data; altitude measurement is from the corrected radar altimeter data. Note that the ellipsoid, the geoid, and the sea-surface vary independently of each other.

observation of oceanic tides does not require concurrent measurements if the amplitude and phase of the tidal constituents are well known. For the GEOS-3 calibration area, Mofjeld (1975) developed an empirical tidal prediction model; development of that model was part of this contract. Mofjeld's model, when compared with a deep-sea tide gage within the GEOS-3 calibration area, had a standard deviation of ± 3 cm. The amplitude of the tide in this area is approximately 60 cm. Signal to noise ratio due to inaccuracies in the model is 20:1, which is adequate for this analysis.

To analyze altimeter data for tides, the calibration area was divided into $1^{\circ}x1^{\circ}$ squares of latitude and longitude. Referring again to Figure 1, consider a $1^{\circ}x1^{\circ}$ square centered on the vertical line connecting to the center of mass. An altimeter measurement of the sea surface taken at another point along the curve of the ellipsoid within the $1^{\circ}x1^{\circ}$ square will be subject to a difference due to the combination of the slope of the geoid and the slope of the tidal wave. It is desired to relate each measurement within the $1^{\circ}x1^{\circ}$ square to the center; this can most simply be accomplished by neglecting geoid and tidal effects, if they are small enough.

Mofjeld's (1975) model shows that for an area even as large as $5^{\circ}x5^{\circ}$, the error due to assuming a uniform areal rise and fall is less than ± 5 cm in the GEOS-3 calibration zone. Marsh and Vincent's (1974) gravimetric geoid shows a broad minimum in the vicinity of $30^{\circ}N$, $70^{\circ}W$ (Fig. 2); geoidal variance is about ± 1 m in a $5^{\circ}x5^{\circ}$ square here, and this variance is within the noise range that Zetler and Maul (1971)

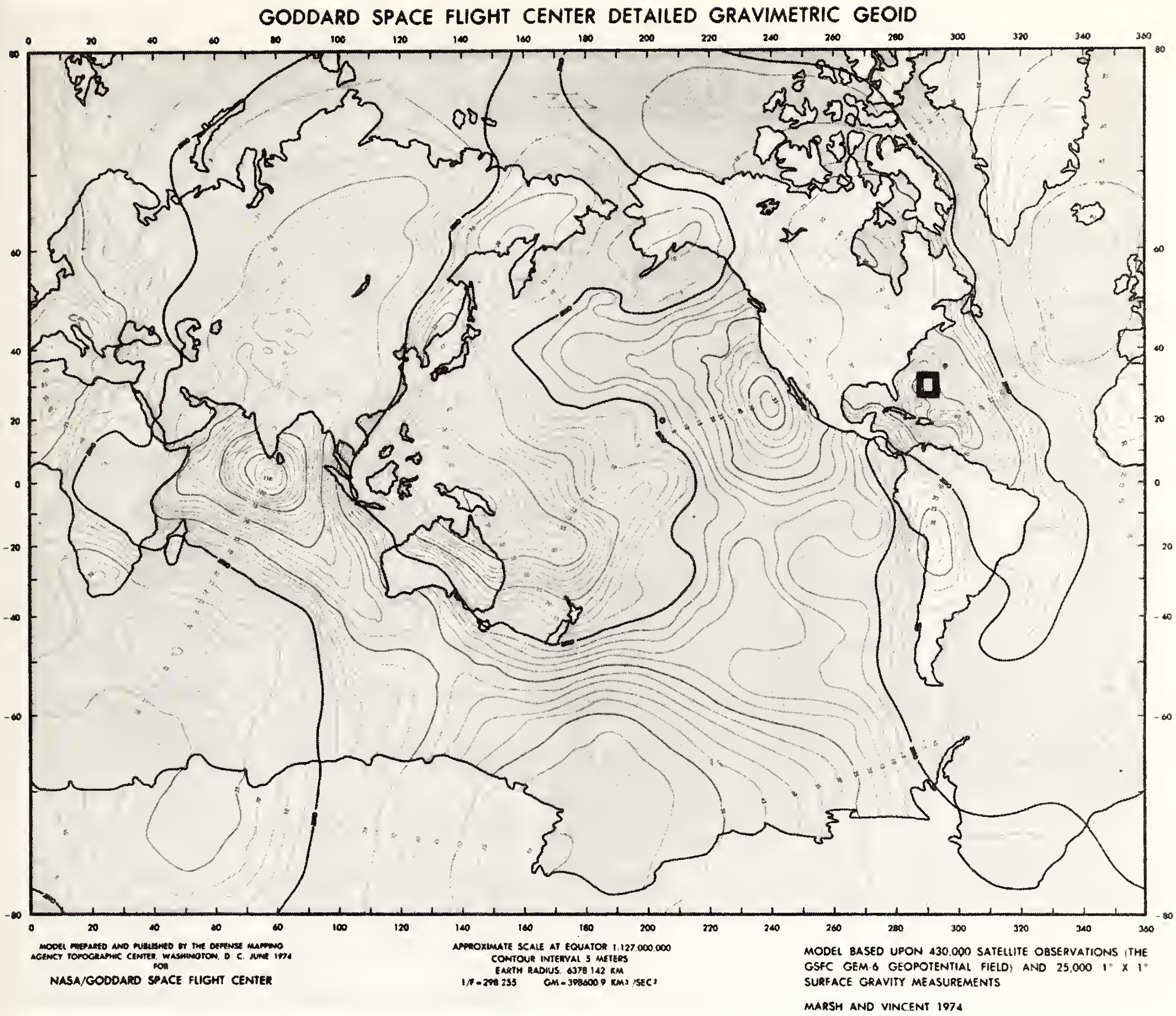
GODDARD SPACE FLIGHT CENTER DETAILED GRAVIMETRIC GEOID
0 20 40 60 80 100 120 140 160 180 200 220 240 260 280 300 320 340 360
80 60 40 20 0 -20 -40 -60 -80
MODEL PREPARED AND PUBLISHED BY THE DEFENSE MAPPING AGENCY TOPOGRAPHIC CENTER, WASHINGTON, D. C. JUNE 1974 FOR
NASA/GODDARD SPACE FLIGHT CENTER
APPROXIMATE SCALE AT EQUATOR 1:127,000,000
CONTOUR INTERVAL 5 METERS
EARTH RADIUS, 6378 142 KM
1/F = 298 255 GM = 398600.9 KM³/SEC²
MODEL BASED UPON 430,000 SATELLITE OBSERVATIONS (THE GSFC GEM-6 GEOPOTENTIAL FIELD) AND 25,000 1° X 1° SURFACE GRAVITY MEASUREMENTS
MARSH AND VINCENT 1974

Figure 2. NASA's Goddard Space Flight Center detailed gravimeter geoid based on the work of Marsh and Vincent (1974). Center of the analysis region used herein is marked by a rectangle near 29.5°N, 70.5°W (289.5°E).

successfully retrieved the tides. Bottom topography (Bush, 1976) is quite uniform in this region (known as the Hatteras Abyssal Plain), which supports Marsh and Vincent's calculations. Finally, a deep-sea tide gage (Zetler, et al., 1975) was located at 28°08'N, 69°45'W, and the amplitudes and phases of the tidal constituents are well known. Based on these facts, the 5°x5° square centered on 29.5°N, 70.5°W was chosen for the analysis, and to first order, it is assumed that the tides and geoid are uniform.

Data Management and Processing

Initially GEOS-C data were received in one of two formats: the 7-track binary packed decimal, and the 7-track card image BCD. These formats existed until January, 1977 when the binary 7-track format was replaced by the binary 9-track format. The 7-track BCD formatted tape was eliminated. Seventy-one (71) 9-track tapes were received. The final mailing of 20 tapes was received in late August, 1977. Nine more tapes were received on 29 September, 1977. These had been sent to an incorrect address and were forwarded by the recipient.

These 71 tapes were difficult to read and necessitated the option that parity and frame count errors be ignored on reading. On reading a record, the format indicator was unpacked to determine the data rate. This determined which number was a valid altimeter status word for that record. All status words were then compared to this standard, and for all data rates each sample had to be valid in order for that record to be acceptable.

The latitude and longitude were then unpacked and, if in the calibration area, were accepted. The various parameters were then unpacked. All these data were arranged chronologically and ready for analysis.

The summary report computer printout distributed by Wallops Flight Center indicates that 357 days of data were acquired and distributed. These data varied from one to ten orbit segments per day; the elapsed time between the first and last data tape is 18 months. There are then no data for one third of the time these tapes cover. The elapsed time in that portion of the calibration area represented by the $5^{o}x5^{o}$ shaded box (Fig. 3), is 498 days. There are 97 days for which data are available in this area and a total of 148 separate data points within the 97 days. These points are scattered throughout the $5^{o}x5^{o}$ area.

Both high and low intensity mode data were used in this study in order to have adequate samples. Whenever a pass crossed any $1^{o}x1^{o}$ box, all altimeter values in that pass were averaged, and that single averaged value was considered a measurement of the sea-surface height (see Fig. 1). Each average includes an error due to variations in the tides and the geoid across each $1^{o}x1^{o}$ box. Maximum range of the geoid in any $1^{o}x1^{o}$ box in the $5^{o}x5^{o}$ area (Fig. 3) is 1 meter, the average value being approximately 0.2 meters. In summary, the error introduced by averaging a pass across a $1^{o}x1^{o}$ box (tidal and geoid), is no more than ±0.5 m, and for the most part is ± 0.15 m.

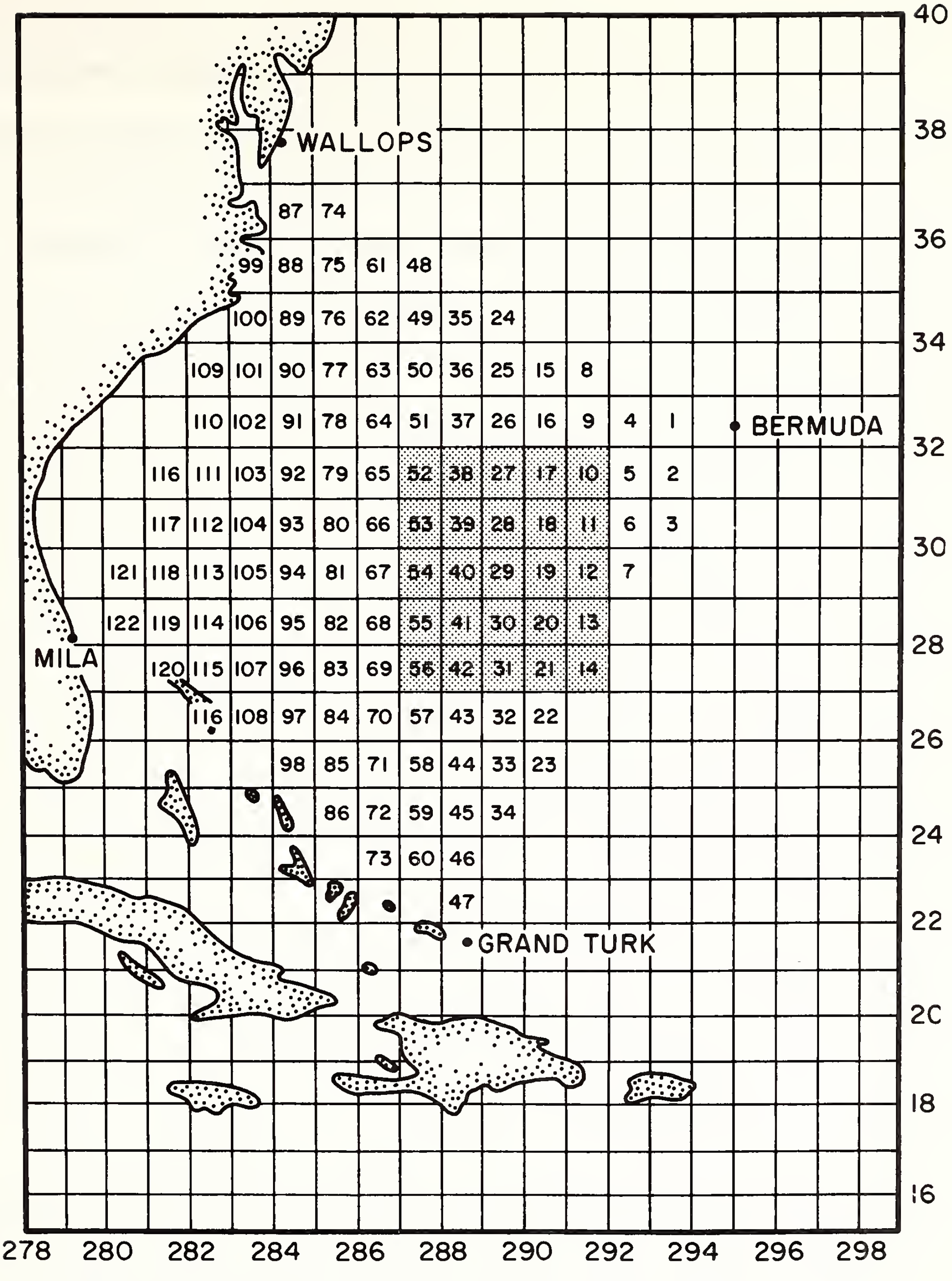

WALLOPS
BERMUDA
MILA
GRAND TURK
87 74
99 88 75 61 48
100 89 76 62 49 35 24
109 101 90 77 63 50 36 25 15 8
110 102 91 78 64 51 37 26 16 9 4 1
116 111 103 92 79 65 52 38 27 17 10 5 2
117 112 104 93 80 66 53 39 28 18 11 6 3
121 118 113 105 94 81 67 54 40 29 19 12 7
122 119 114 106 95 82 68 55 41 30 20 13
120 115 107 96 83 69 56 42 31 21 14
116 108 97 84 70 57 43 32 22
98 85 71 58 44 33 23
86 72 59 45 34
73 60 46
47
40
38
36
34
32
30
28
26
24
22
20
18
16
278
280
282
284
286
288
290
292
294
296
298

Figure. 3. $1^o x 1^o$ squares of latitude and longitude in the GEOS-3 calibration area. Analysis region used herein is lightly shaded. The deep-sea tide gage used as surface truth was located in box number 20.

Data Analysis

Analysis of the GEOS-3 altimeter data for ocean tides was performed using two independent methods, both of which are least squares techniques. The methods of Zetler et al. (1965) have been applied to a simulation of this problem (Zetler and Maul, 1971) and require no further verification. Another technique derived by Vanicek (1971) is also applied, but since it is not well known to the oceanographic community, it was tested with simulated tidal data.

Consider a time series of the form

$$H(t) = H_o + \sum_i A_i \cos (w_i t - \phi_i) \tag{1}$$

where the height (H) of the tide at time (t), is the sum of the mean value (H_o) plus a series (i) of cosine terms with amplitude (A), frequency (w), and phase (ϕ). From well known trignometric identities equation (1) may be written

$$H(t) = H_o + \sum_i C_i \cos (w_i t) + \sum_i S_i \sin (w_i t) \tag{2}$$

where $A^2 = C^2 + S^2$ and $\phi = \tan^{-1} (S/C)$.

A time series using equation (1) was generated for the M_2, S_2, N_2, O_1, and K_1 tides, and C, S, and ϕ given in equation (2), and the variance spectra were calculated by Vanicek's (1971) method using the program of Wells and Vanicek (1977). In order to simulate randomly acquired data, a random number generator (R) on the interval (0,1) was used to degrade the data generated by equation (1) progressively until 100%, 90%, 80%...10% (R = 1, 0.9, 0.8,...,0.1) of the original data remained. Results of those calculations are given in Table 1.

Listed at the top of Table 1 are the original input values for the five constituents and the mean value. Record length is 2160 hours (3 months), and $\phi = 0$ for all inputs. The least squares analysis is within a few tenths of a percent of the input data when 100% of the original data are used (row 1.0). Even when only 10% of the original data are input (row 0.1), the maximum error in amplitude is 0.6% and the maximum error in phase is 3°. Thus, for a geophysical process where the frequency is well known, randomly spaced gappy data sampled without regard to the Nyquist theorem can be successfully analyzed.

If the frequencies are unknown, Vanicek's (1971) technique is still useful. Figure 4 is a variance spectrum for the semi-diurnal species input as before (Table 1). The ordinate in Figure 4 is the percentage variance, defined as

$$\frac{A_i^2}{\sum_i A_i^2} \qquad (3)$$

and the abscissa is the period. It is clear that the spectrum using 100% of the data (dotted line) and the spectrum computed from 10% of the data (solid line) are quite similar. There are no errors in period, and the maximum error in percentage variance is 5% which occurs

Table 1

$H(t) = H_o + \sum_i C_i \cos \omega_i t + \sum_i S_i \sin \omega_i t$

$\Sigma t = 2150$ hrs

		O_1 (25.82^h)		K_1 (23.93^h)		N_2 (12.66^h)		M_2 (12.42^h)		S_2 (12.00^h)	
Ran. No.	H_o	C	S	C	S	C	S	C	S	C	S
Input	100	1	0	3	0	7	0	10	0	5	0
1.0	99.999	0.999	0.051	2.998	-0.113	7.003	0.013	10.000	-0.080	4.996	-0.007
0.9	100.000	0.999	0.051	2.998	-0.113	7.003	0.013	10.001	-0.080	4.996	-0.007
0.8	99.999	0.999	0.050	2.998	-0.113	7.003	0.013	9.999	-0.080	4.998	-0.008
0.7	99.998	0.997	0.050	2.998	-0.113	7.002	0.014	9.999	-0.079	4.993	-0.007
0.6	99.999	1.000	0.049	2.997	-0.113	7.003	0.013	10.001	-0.080	4.994	-0.007
0.5	100.000	0.999	0.053	2.996	-0.112	7.002	0.013	9.999	-0.078	4.996	-0.007
0.4	100.002	1.002	0.048	2.997	-0.112	7.001	0.015	10.003	-0.079	4.997	-0.006
0.3	99.999	0.998	0.048	3.002	-0.115	7.001	0.011	10.003	-0.081	4.995	-0.007
0.2	99.998	0.992	0.051	2.998	-0.117	7.001	0.013	10.004	-0.080	5.003	-0.010
0.1	100.000	0.999	0.054	3.000	-0.120	7.004	0.014	9.996	-0.077	4.994	-0.006

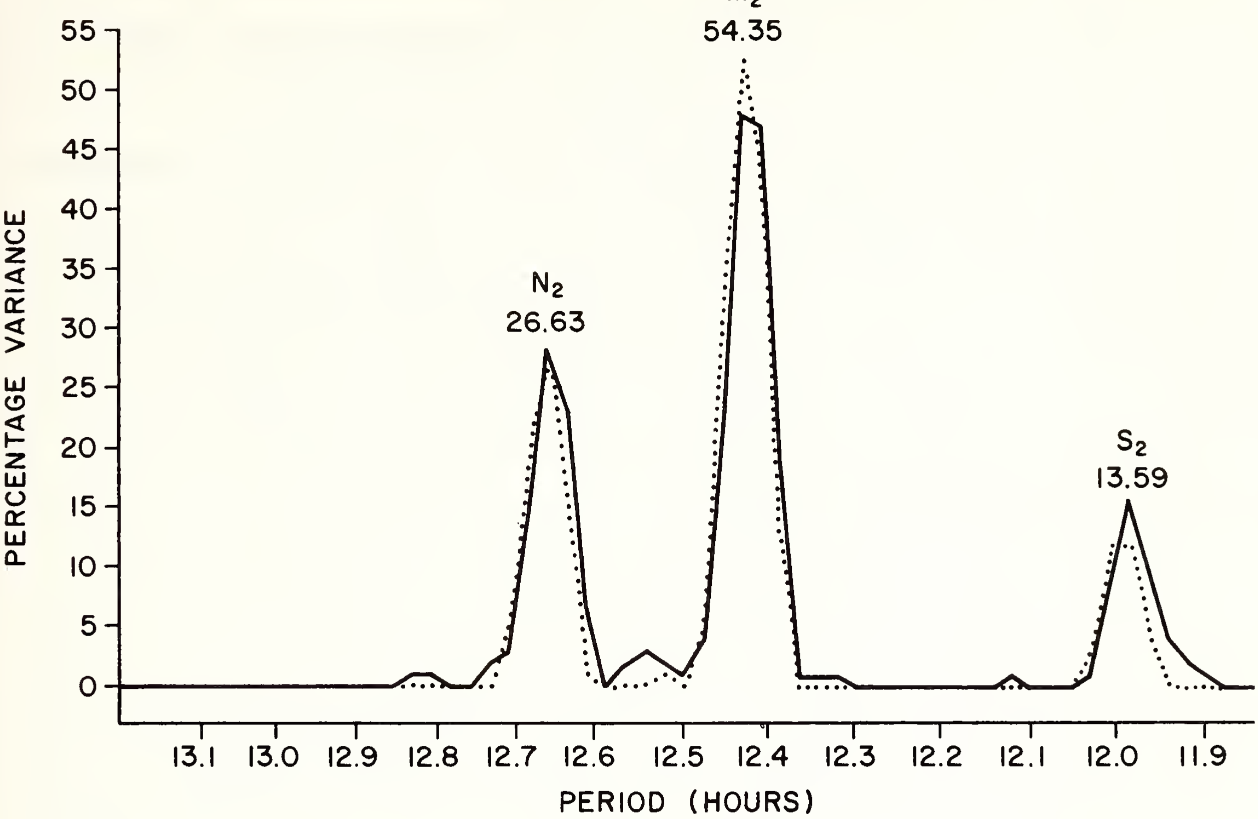

Figure 4. Comparison of the variance spectrum for the semi-diurnal constituents using least squares analysis. Dotted line used 2160 hourly values; solid line used 10% of the 2160 values randomly chosen. Theoretical values of the percentage variance age given below their identifying constituent abbreviation.

in the M_2 constituent. Thus, if the signal to noise is low (there being no noise in this example), it appears that an unknown period can be detected, and then once detected, its amplitude and phase calculated.

The analysis techniques tested above were applied to the GEOS-3 data in the calibration zone. It should be noted that the calibration zone is typical of oceanic regions, and imposes a reasonable test. The number of observations would be increased by using a higher latitude site; the signal to noise would also be impaired by choosing an area with large tidal range. The intent herein is to question the applicability of GEOS-3 data for determining the global tide, rather than a proof of concept.

Results

Table 2 summarizes the calculations using the methods of Vanicek (1971) and Zetler et al. (1965); the known tidal constituents from Zetler et al. (1975) are listed at the bottom of the table. Tabulated are the amplitudes in meters, and the phases in degrees (relative to 0000 GMT, 1 March , 1975). The number of samples in each area size is based on 18 months of data. The average number of samples is 1.5 per month in each $1^{\circ}x1^{\circ}$ square (Zetler and Maul (1971) used more than 9 samples per month in their analysis which was based on different orbital parameters). Sparcity of samples undoubtedly contributes to the poor agreement between predicted values and observed in the GEOS-C data.

In most cases (Table 2) the GEOS-C derived amplitude is an order of magnitude more than the values reported by Zetler, et al. (1975). The phase calculations are equally uncorrelated. Comparisons of the two analysis methods (see $5^{\circ}x5^{\circ}$ rows) show some consistency in the calculation of amplitude (within 93%), but the phases are poorly related.

The correlation is graphically displayed in Figure 5. Observed sea-level heights from GEOS-3 are plotted along the ordinate, and the values predicted due to ocean tides by Mofjeld's (1975) model are along the abscissa. The range of the tide (signal) is at best an order of magnitude less than the measurement variability (signal + noise). Thus, the tidal signal to noise ratio is approximately 0.1, which is seven times smaller than assumed by Zetler and Maul (1971) in their successful theoretical analysis. Table 3 summarizes the

Table 2

	Area Size	No. Samples	S_2	M_2	N_2	K_1	O_1
			Ampl./Phase				
Vaniček (1971)	$1^\circ x 1^\circ$	26	1.92/75.9	1.55/32.2	1.59/27.6	2.02/81.5	1.25/36.9
	$2^\circ x 2^\circ$	58	0.46/12.1	1.52/294.4	0.37/327.6	2.05/75.9	1.0/42.4
	$3^\circ x 3^\circ$	92	0.98/69.3	1.67/347.1	0.739/3.2	2.11/85.8	.96/337.2
	$4^\circ x 4^\circ$	119	1.24/42.5	1.83/1.7	0.577/29.8	2.16/280.0	.476/338.8
	$5^\circ x 5^\circ$	148	.81/20.6	1.35/315.5	0.75/18.8	1.86/303.4	.91/86.4

	Area Size	No. Samples	S_2	M_2	N_2	K_1	O_1
			Ampl./Phase				
Zetler et al. (1965)	$1^\circ x 1^\circ$	26	.49/166.8	1.21/330.2	1.39/133.7	1.98/99.5	1.43/132.4
	$2^\circ x 2^\circ$	58	.48/354.6	1.49/279.1	.39/209.3	2.25/94.7	.96/179.6
	$3^\circ x 3^\circ$	92	1.01/309.6	1.63/228.4	.71/310.0	2.11/89.0	.95/249.0
	$4^\circ x 4^\circ$	119	1.20/335.4	1.85/215.4	.37/277.5	2.13/78.1	.49/251.1
	$5^\circ x 5^\circ$	148	.78/337.8	1.31/231.8	.62/307.8	2.01/70.2	.96/271.6

	S_2	M_2	N_2	K_1	O_1
	Ampl./Phase				
Zetler et al. (1975)	0.071/30.8	0.345/0.6	0.080/339.8	0.077/194.7	0.061/197.

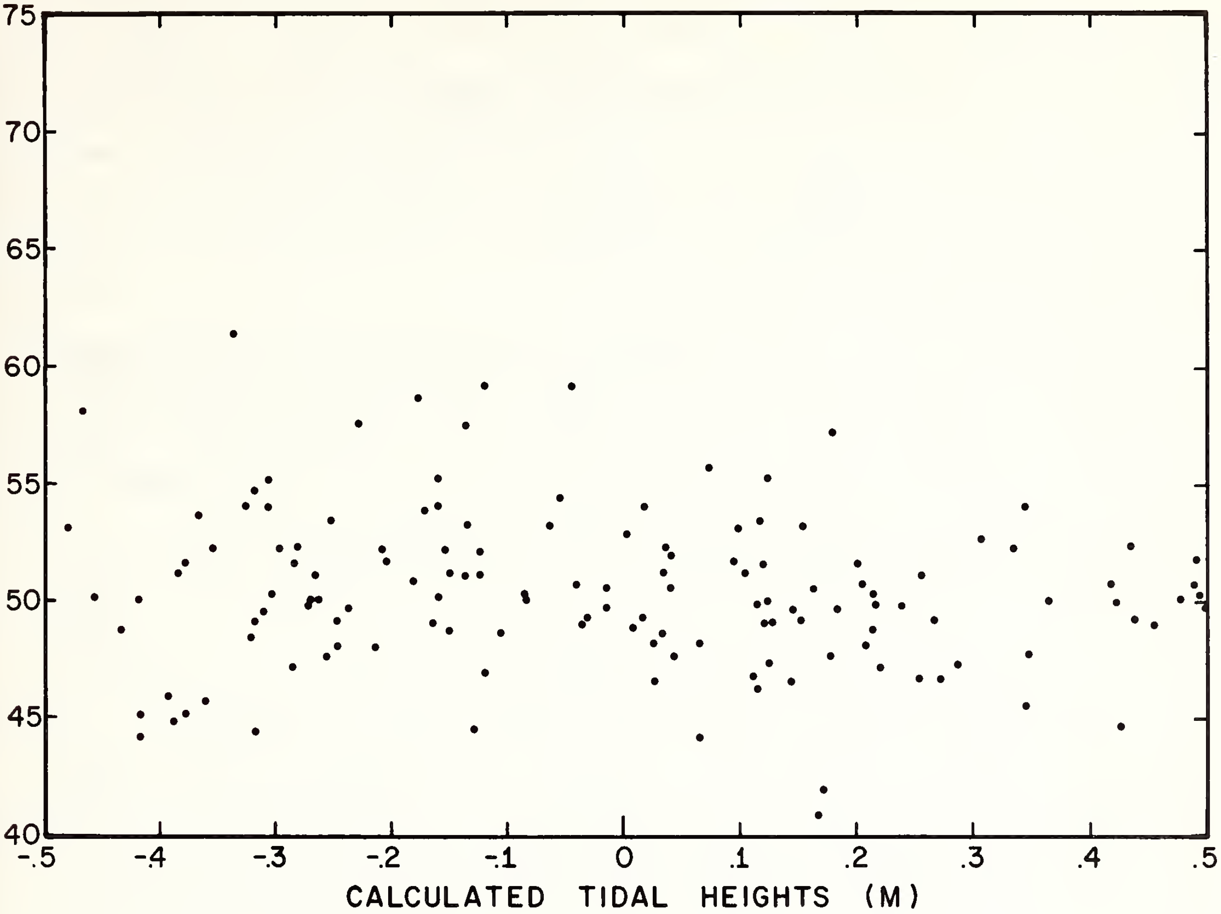

Figure 5. Comparison of tidal height observed by the GEOS-3 altimeter versus computed tides (Mofjeld, 1975) in the $5^o x 5^o$ calibration area. Observed values are corrected for atmospheric effects but not for spatial variation in the geoid.

variance of sea-level height above the ellipsoid from the GEOS-3 altimeter in the $5^\circ x 5^\circ$ square shaded in Figure 3. Mean height of sea-level in this $5^\circ x 5^\circ$ square is 50.7 (±1.3) meters below the ellipsoid. The low standard deviation is in agreement with the Marsh and Vincent (1974) gravimeter geoid (cf. Fig. 2), and confirms that geoid variability does not significantly contribute to the inability of the GEOS-3 data to discriminate the oceanic tide.

However, to further insure that geoid variability is not important, the calculations summarized in Table 2 were repeated after subtracting the Marsh and Vincent (1974) geoid. That is, the Vanicek (1971) and Zetler et al. (1965) techniques were applied to the temporal term

$$H(t) = h_{ss} - h_g \tag{4}$$

where h_{ss} is the GEOS-3 determined height of the sea-surface above the ellipsoid, and h_g is the height of the Marsh and Vincent 5'x5' geoid. The results of those calculations were essentially identical to the results summarized above, leading to the conclusion that the GEOS-3 data, in the form provided, is not useful for observing ocean tides.

As a final test of using GEOS-3 altimeter data to study temporal variability of the sea-surface, the percentage variance spectrum (cf. Equation 3) was computed for the $5^\circ x 5^\circ$ calibration area. Tidal frequencies have been removed in this application of Vanicek's (1971) least squares technique. Because of the signal to noise analysis above, it is difficult to have a great deal of confidence in this spectrum. However, some

Table 3

Mean and standard deviation of the GEOS-3 height of sea-level above the ellipsoid in the 5^ox5^o calibration area (see Fig. 3).

1^ox1^o Box	Number of Points	Mean (Meters)	Std Dev (Meters)
10	24	-48.6	±3.9
11	24	-50.9	±6.8
12	22	-51.1	±7.1
13	28	-49.6	±7.1
14	34	-49.7	±2.8
17	36	-50.6	±5.9
18	33	-51.3	±6.1
19	26	-52.0	±3.3
20	26	-50.9	±3.3
21	31	-51.2	±3.7
27	27	-51.1	±2.7
28	35	-51.3	±3.2
29	33	-51.5	±3.6
30	28	-51.8	±3.8
31	24	-52.4	±3.5
38	30	-51.2	±3.9
39	32	-51.7	±3.1
40	35	-51.5	±3.8
41	32	-51.3	±4.0
42	28	-50.7	±4.7
52	31	-51.4	±4.2
53	31	-51.6	±4.3
54	29	-50.3	±3.5
55	31	-47.6	±7.2
56	34	-47.2	±9.6

features are common to a similar analysis of Gulf Stream meanders made from infrared measurements by Maul, deWitt, Yanaway, and Baig (in preparation). The numerous spectral peaks with a period of a fortnight or so and less are commonly reported in the oceanographic literature. At 38 days, a strong peak (Fig. 6) is evident, which is probably due to the 37 day cycle in the GEOS-3 orbit. The most intriguing peak, however, is at 56 days. Hansen (1970) noted that the average periods of Gulf Stream meanders is about 1½ months, which is close to 56 days, and Maul et al. noted this too in their spectra of meanders. This raises the interesting possibility that sea-level in the Sargasso Sea pumps up-and-down in response to the meanders, as well as to other forcing.

Conclusions

The GEOS-3 altimeter data as processed by the NASA Wallops Flight Center were analyzed for deep-sea tides in the calibration area of the western North Atlantic Ocean. It was found that the signal to-noise ratio of the data was about 0.1, and that only one observation every four days was available in a $5^{\circ}x5^{\circ}$ latitude & longitude area for the 18 months analyzed. Using two independent methods, the tides could not be resolved. Tidal variability will not detract from geoid determination if data averaging is used, however, other error sources such as orbit determination, altimeter correction, or mean (steric) sea level will influence the accuracy of the marine geoid.

The consistency of the calculated tidal amplitudes (Table 2) raises the question of tidal frequency errors in the tracking of GEOS-3. If there are undetectable errors of these frequencies in the data, it may never be possible to do deep-sea tide determinations with

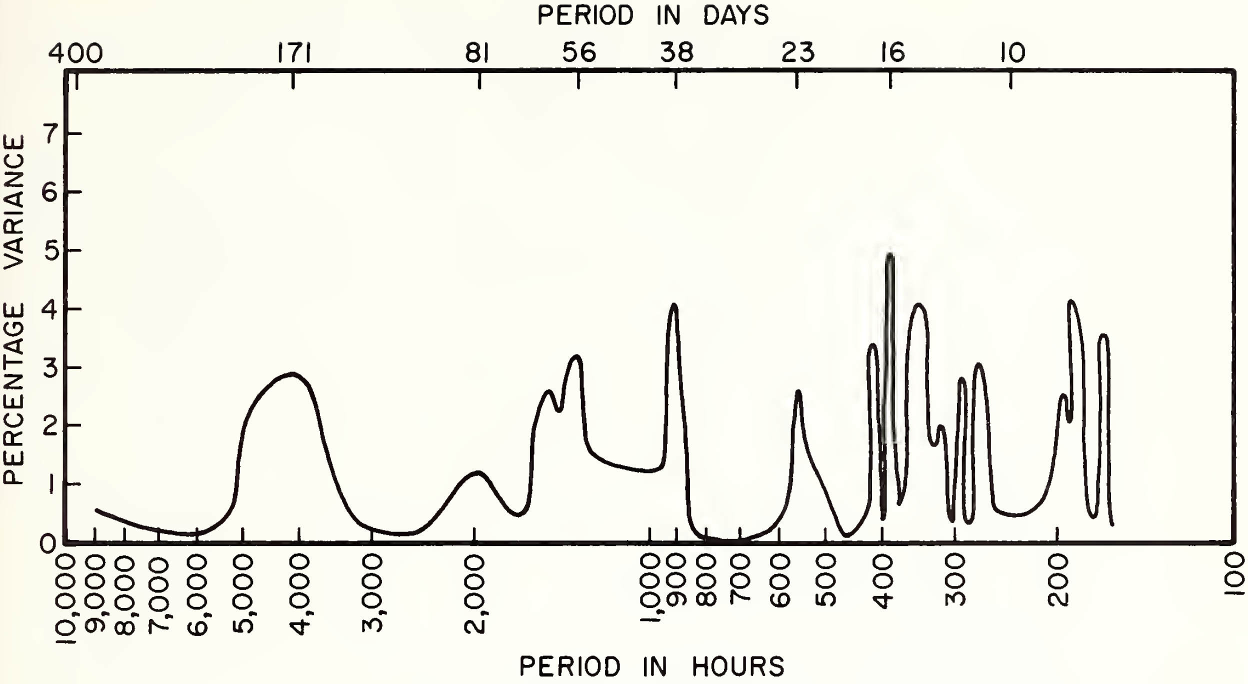

Figure 6. Percentage variance of sea-surface heights in the 5°x5° calibration area as a function of period in hours. Note the variance at 38 days.

future vehicles such as SEASAT-A. The average of the standard deviations given in Table 3 is ±0.5 m of which can be attributed to variations of the geoid and oceans tides. SEASAT-A's radial orbit determination error is specified as ±2 m; unless that can be improved upon by a factor of at least 2, it does not seem possible to extract tides from that data either, unless a refined approach is taken.

Refinement of the approach used herein forms the basis for suggestions for further research. From conversations held at the GEOS-3 Principal Investigator's Meeting (November, 1977) it appears that better orbit determinations would give the most marked improvement in the signal to noise ratio. Thus, a new analysis of the spectrum of variability (cf. Fig. 6) would identify known periods, such as the 37 day cycle, which could be filtered out. If filtering etc. increases the signal to noise by half an order of magnitude, it is reasonable to expect that the ocean tides would be observed. Success does not seem possible with these GEOS-3 data, but with improvements in the orbit determinations, SEASAT-A is still a viable contender.

References

Bush, P. A. (1976). Bathymetry of the MODE-1 region. Deep-Sea Res., 23, pp. 1105-1113.

Hansen, D. V. (1970). Gulf Stream Meanders between Cape Hatteras and the Grand Banks. Deep-Sea Res., 17, pp. 495-511.

Leitao, C. D., C. L. Purdy, and R. L. Brooks (1975). Wallops GEOS-C altimeter preprocessing report. NASA Technical Memorandum, NASA TM X-69357, Wallops Flight Center, Wallops Island, Va. 68 pgs.

Marsh, J. G., and S. Vincent (1974). Global detailed geoid computation and model analysis. Geophys. Surveys, 1, pp. 481-511.

Mofjeld, H. O. (1975). Empirical model for tides in the western North Atlantic Ocean. NOAA Technical Report ERL 340-AOML 19, Boulder, Co. 27 pgs.

National Aeronautics and Space Administration (1969). The terrestrial environment, solid earth and ocean physics; application of space and astronautic techniques. Report of a study at Willimstown, Mass.

Redfield, A. C. (1958). The influence of the continental shelf on the tides of the Atlantic Coast of the United States. J. Mar. Res, 17, pp. 432-448.

Vanicek, P. (1971). Further development and properties of the spectral analysis by least squares. Astrophys. and Space Phys., 12, pp. 10-33.

Wells, D. E., and P. Vanicek (1977). Least squares spectral analysis. Submitted to Computers and Geosciences.

Zetler, B. D., M. D. Schuldt, R. W. Whipple, and S. D. Hicks (1965). Harmonic analysis of tides from data randomly spaced in time. J. Geophys. Res., 70, pp. 2805-2811.

Zetler, B. D., and G. A. Maul (1971). Precision requirements for a spacecraft tide program. J. Geophys. Res., 76(27), pp. 6601-6605.

Zetler, B. D. W. Munk, H. Mofjeld, W. Brown, and F. Dormer (1975). MODE tides. J. Phys. Oceano., 5, pp. 430-441.

1. Report No.
NASA CR-141435

2. Government Accession No.

3. Recipient's Catalog No.

4. Title and Subtitle
DEEP SEA TIDES DETERMINATION FROM GEOS-3

5. Report Date
February 1978

6. Performing Organization Code

7. Author(s)
George A. Maul and Alan Yanaway

8. Performing Organization Report No.

9. Performing Organization Name and Address
National Oceanic and Atmospheric Adminstration
Atlantic Oceanographic and Meteorological Laboratories
Miami, Florida 33149

10. Work Unit No.

11. Contract or Grant No.
P57,579(G)

12. Sponsoring Agency Name and Address
National Aeronautics and Space Administration
Wallops Flight Center
Wallops Island, Virginia 23337

13. Type of Report and Period Covered
Final Report

14. Sponsoring Agency Code

15. Supplementary Notes

16. Abstract

GEOS-3 altimeter data in a 5°x5° square centered at 30°N, 70°W were analyzed to evaluate deep-sea tide determination from a spacecraft. The signal to noise ratio of known tidal variability to altimeter measurement of sea level above the ellipsoid was 0.1. A sample was obtained in a 5°x5° area approximately once every four days. The randomly spaced time-series was analyzed using two independent least squares techniques, but it was not possible to retrieve the amplitude and phase of the M_2, S_2, N_2, O_1, or K_1 constituents.

17. Key Words (Suggested by Author(s))
GEOS-3
ocean tides

18. Distribution Statement
Unclassified - unlimited

STAR Category - 42,47,48

19. Security Classif. (of this report)
Unclassified

20. Security Classif. (of this page)
Unclassified

21. No. of Pages
26

22. Price*

*For sale by the National Technical Information Service, Springfield, Virginia 22151

Journal of Physical Oceanography 8, No. 5, 779-784.

The Relationship of the Curl of the Local Wind Stress to the Circulation of the Cayman Sea and the Gulf of Mexico

ROBERT L. MOLINARI

Environmental Research Laboratories, Atlantic Oceanographic and Meteorological Laboratories, NOAA, Miami, FL 33149

(Manuscript received 3 March 1977, in final form 15 May 1978)

ABSTRACT

The curl of the annual mean wind stress is proposed as the forcing mechanism for the anticyclonic gyre observed in the Cayman Sea. A simple wind-driven model is presented to illustrate how a steady-state gyre in the Cayman Sea and another gyre in the western Gulf of Mexico can be spun-up by the wind. The model results also indicate that the exchange of mass between the two basins can be enhanced by the wind field. Temporal changes in the upper layer temperature structure of the Cayman Sea gyre are consistent, qualitatively, with changes predicted by a simple wind-forcing model. The same model does not appear valid in the western Gulf of Mexico.

1. Background

Three large-scale anticyclonic circulation features are indicated on climatological temperature charts of the Cayman Sea and the Gulf of Mexico. Fig. 1, taken from Robinson (1973), shows a basin-wide gyre in the Cayman Sea, the Loop Current which intrudes into the eastern Gulf of Mexico, and a closed gyre in the western Gulf during January and July. These features vary in size and intensity, as inferred from changes in the observed thermal gradients.

Little is known of the annual cycle of the Cayman Sea gyre. This feature is bounded on the south and west by two intense currents, the Cayman Current and the Yucatan Current (Molinari, 1976). The surface speeds of the Yucatan Current vary with a strong annual signal. Highest speeds have been observed in June and lowest in November (Cochrane, 1963).

The intrusion of the Loop Current north into the eastern Gulf of Mexico has, on the average, an annual signal. The maximum intrusion occurs during the summer and the minimum intrusion during the winter (Leipper, 1970; Maul, 1975; Behringer *et al.*, 1977). However, the variability about this mean cycle is large, with maximum intrusions also observed in the winter (Molinari *et al.*, 1977).

Sturges and Blaha (1976) have proposed a semi-annual period for the intensity of the gyre in the western Gulf. Behringer *et al.* (1977) present temperature data which support this proposal.

Variability in both circulation and thermal patterns can be induced by variability in the distribution of the curl of the wind stress. A two-layer ocean with the lower layer at rest can be used to demonstrate the effect of the wind curl on the upper layers of the ocean. White and McCreary (1974), for instance, derive a linear, quasi-geostrophic vorticity equation for the two-layer system which can be written as

$$\frac{\partial}{\partial t}\left(\nabla^2 h - \frac{f^2}{g'D} h\right) + \beta \frac{\partial h}{\partial x} + \frac{\sigma}{D}\nabla^2 h = \frac{-f}{\rho g'D}\frac{\partial \tau_x}{\partial y}, \qquad (1)$$

where h is the upper layer thickness, f the Coriolis parameter, g' reduced gravity, D the undisturbed upper layer depth, β the change of Coriolis parameter with latitude, σ the interlayer stress, and τ_x the zonal component of the wind stress vector. It is further assumed that the meridional component of the wind stress is negligible. If the upper layer thickness is decomposed into steady-state $\bar{h}$ and time-varying h' components, the equations for each component are

$$\beta \frac{\partial \bar{h}}{\partial x} + \frac{\sigma}{D}\nabla^2 \bar{h} = -\frac{f}{\rho g'D}\frac{\partial \bar{\tau}_x}{\partial y}, \qquad (2)$$

$$\overset{(1)}{\frac{\partial}{\partial t}\left(\nabla^2 h'\right.} - \overset{(2)}{\left.\frac{f^2}{g'D} h'\right)} + \overset{(3)}{\beta \frac{\partial h'}{\partial x}} + \overset{(4)}{\frac{\sigma \nabla^2 h'}{D}} = \overset{(5)}{\frac{-f}{\rho g'D}\frac{\partial \tau'_x}{\partial y}}, \qquad (3)$$

where $h' = h - \bar{h}$, and $\tau' = \tau - \bar{\tau}$.

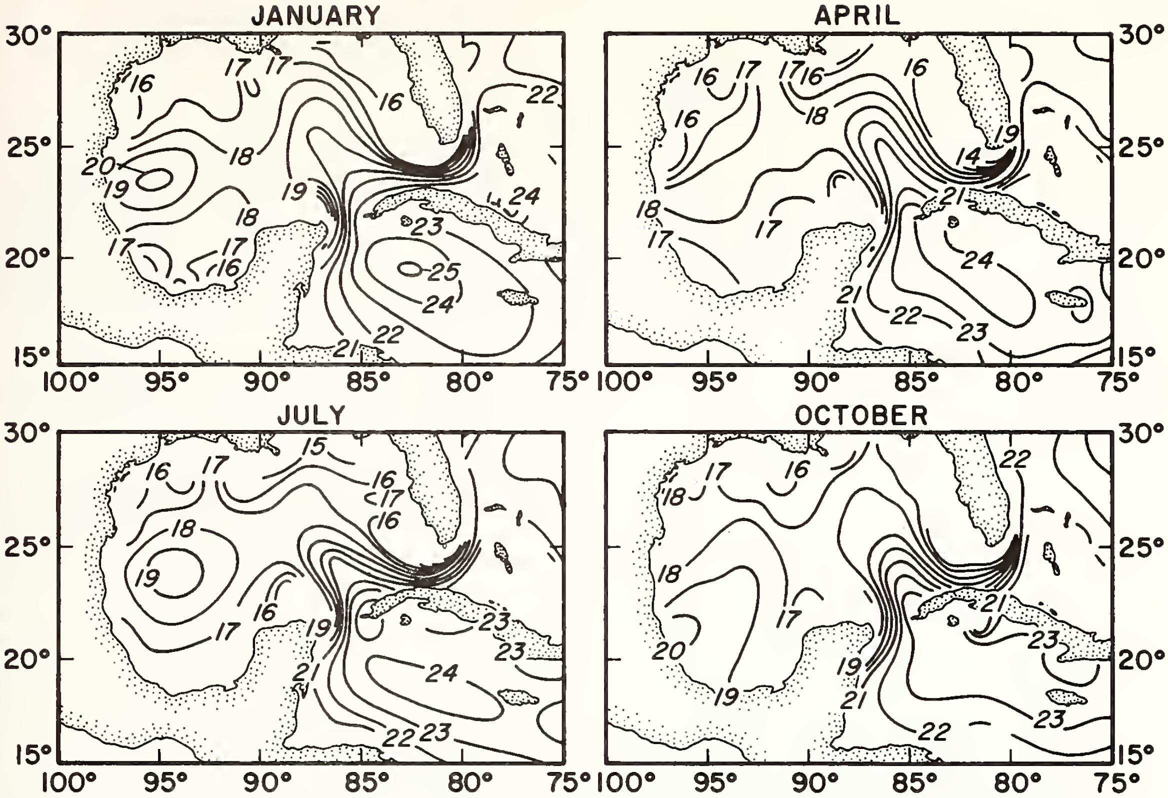

FIG. 1. January, April, July and October mean temperature distributions at 150 m adapted from the charts of Robinson (1973).

Many forms of (3) have been used to study the response of the ocean to time-dependent wind forcing. For instance, Sturges and Blaha (1976), invoking the Sverdrup balance (terms 3 and 5) have proposed that the intensity of the western Gulf gyre should vary with a semiannual period in response to a semiannual forcing by the observed curl field.

Meyers (1975), in an observational study, found that the primary balance affecting the thermal field in the tropical Pacific was between terms 2 and 5. This local effect of the curl of the wind stress on the thermal field has been called Ekman pumping. However, White (1976) found in a theoretical and observational study that term 3 may be important because of the generation of Rossby waves at the eastern boundary of the ocean. The variation of the thermal field in the Pacific is a combination of local Ekman response and Rossby wave response according to White. Finally, Anderson and Gill (1975), in a theoretical study, added term 1 to 2, 3 and 5, and found that in addition to the generation of nondispersive waves at the eastern boundary, there were dispersive short waves generated at the western boundary.

In the present study, the mean annual curl of the wind stress is proposed as the forcing mechanism for the steady-state component of the Cayman Sea and western Gulf of Mexico gyre. Eq. (2) is solved numerically to illustrate how the Cayman Sea and western Gulf gyres may be formed by the wind stress, and how the Cayman gyre may supplement the current which enters the Cayman Sea through the passage separating Jamaica and Honduras and flows into the Gulf of Mexico. Finally, the time-varying component of the thermal field in the two gyres is considered in relation to the temporal variability in the wind stress curl distribution.

2. Data sources

Surface wind stress components over the Gulf of Mexico and Cayman Sea were computed by Mr. A. Bakun of the Pacific Environmental Group of the National Fisheries Service, NOAA, from mean monthly atmospheric pressure data for the period between January 1946 and June 1974. Geostrophic wind speeds were computed from the surface pressure distribution. The wind stress was assumed equal to the wind speed squared times a drag coefficient of 0.0013. Zonal and meridional stress components were determined for each month at 3° square grid spacing.

Monthly and annual wind stress means were computed for each 3° square. The model monthly stresses shown in Fig. 2 were consistent with those of Hellerman (1965), except for the region of the Bay of Campeche. There the 3° squares centered at 18°N include land, and the stresses appear to be high. These values were not included in this study.

3. Steady-state components of the Cayman Sea and western Gulf of Mexico gyres

The simple wind-driven model of Stommel (1948) can be used to show how the permanent gyre in the Cayman Sea and western Gulf of Mexico can be established by the curl of the wind stress. By setting $\psi = (g'/f)\bar{h}$ and assuming a cosine distribution for the wind stress, Eq. (2) becomes Stommel's (1948) vorticity relation

$$\frac{D\beta}{\sigma}\frac{\partial\Psi}{\partial x} + \nabla^2\Psi = \frac{F\pi}{\sigma b}\sin\frac{\pi y}{b}\,, \tag{4}$$

where F is the maximum wind stress and b the north-south basin dimension. The numerical relaxation scheme which is used to solve (4) was tested by reproducing Stommel's solution for a rectangular closed basin.

Sets of model solutions were computed using representative parameters for the Gulf of Mexico and Cayman Sea. Two types of forcing were used, the curl of the wind stress, and the specification of the mass transport inflow at the passage separating Jamaica and Honduras and the outflow at the Straits of Florida. Fig. 2 gives the wind stress curl used in the model and the mean annual curl computed from the observed data. The undisturbed upper layer thickness D is taken as 200 m. The frictional coefficient σ is taken as 0.02. The maximum transport in this portion of the water column is arbitrarily taken as 5×10^6 m^3 s^{-1} at the Jamaica-Honduras passage. This transport is approximately one-sixth of the mean annual transport for the entire column observed at the Straits of Florida (Niiler and Richardson, 1973). The model runs for which steady-state solutions were obtained are listed in Table 1.

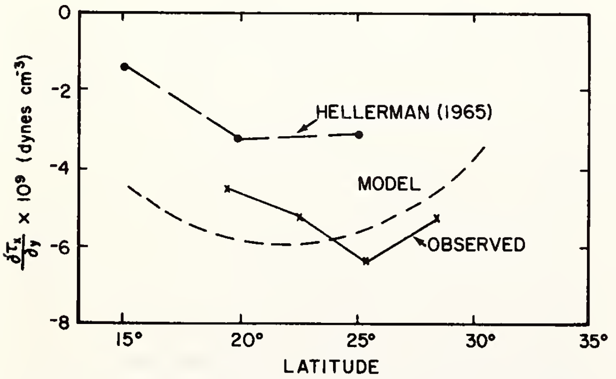

FIG. 2. The curl of the annual mean wind stress, as approximated by $-\partial\bar{\tau}_x/\partial y$, over the Gulf of Mexico and Cayman Sea determined from the 3° wind stress grid discussed in text (solid line) and the 5° wind stress grid given by Hellerman (1965) (dot-dashed line). Also shown is the curl of the wind stress approximation used in the numerical model (dashed line).

TABLE 1. Forcing used in model runs.

Model run	Straits Jamaica-Honduras	 Yucatan	 Florida	Forcing
A	Closed	Closed	Closed	Wind-stress curl
B	Closed	Open	Closed	Wind-stress curl
C	Open	Open	Open	Mass inflow at Jamaica-Honduras Passage
D	Open	Open	OPen	Wind and mass inflow

The solutions are presented in Fig. 3. The contours represent transport streamfunctions, i.e., ψ multiplied by D. It should be stressed that the dynamics of the currents in the western Cayman Sea and eastern Gulf of Mexico are not adequately represented by Eq. (4). The Yucatan and Loop Currents are inertial flows in which the nonlinear advective terms are significant. However, it is assumed that linear dynamics may be sufficient to describe the steady-state conditions in the central Cayman Sea and western Gulf of Mexico.

The curl of the wind stress establishes two gyres, one in the Cayman Sea and the other in the western Gulf of Mexico (Fig. 3a). As in the Stommel case, the interior balance in both basins is between the β term and wind curl term in (4). A western boundary current provides the necessary return flow to the north. The balance in this frictional boundary layer is between the lateral friction term and the wind curl term. In the case of an open Yucatan Straits (Fig. 3b), there is an exchange of mass between the two basins.

Western intensification caused by the β effect also occurs in the Cayman Sea when the driving mechanism is only mass inflow through the Jamaica-Honduras passage and outflow through the Straits of Florida (Fig. 3c). When both wind stress and flow through drive the system, the western boundary current is a linear sum of the two independent boundary currents. Therefore, in Fig. 3d, the flow through the western section of the Yucatan Straits into the Gulf is intensified, but the total transport into the Gulf remains the same. Other cases (not shown) in which the curl induced transport is greater than the flow through transport, show an exchange of mass between the two basins (as in Fig. 3b).

Sturges and Blaha (1976) computed the Sverdrup transport for the western Gulf gyre by assuming that the feature extended across the entire Gulf, as in the model results of Fig. 3a. However, the presence of the Loop Current in the east complicates the circulation pattern in a manner which cannot be accounted for in the Sverdrup theory.

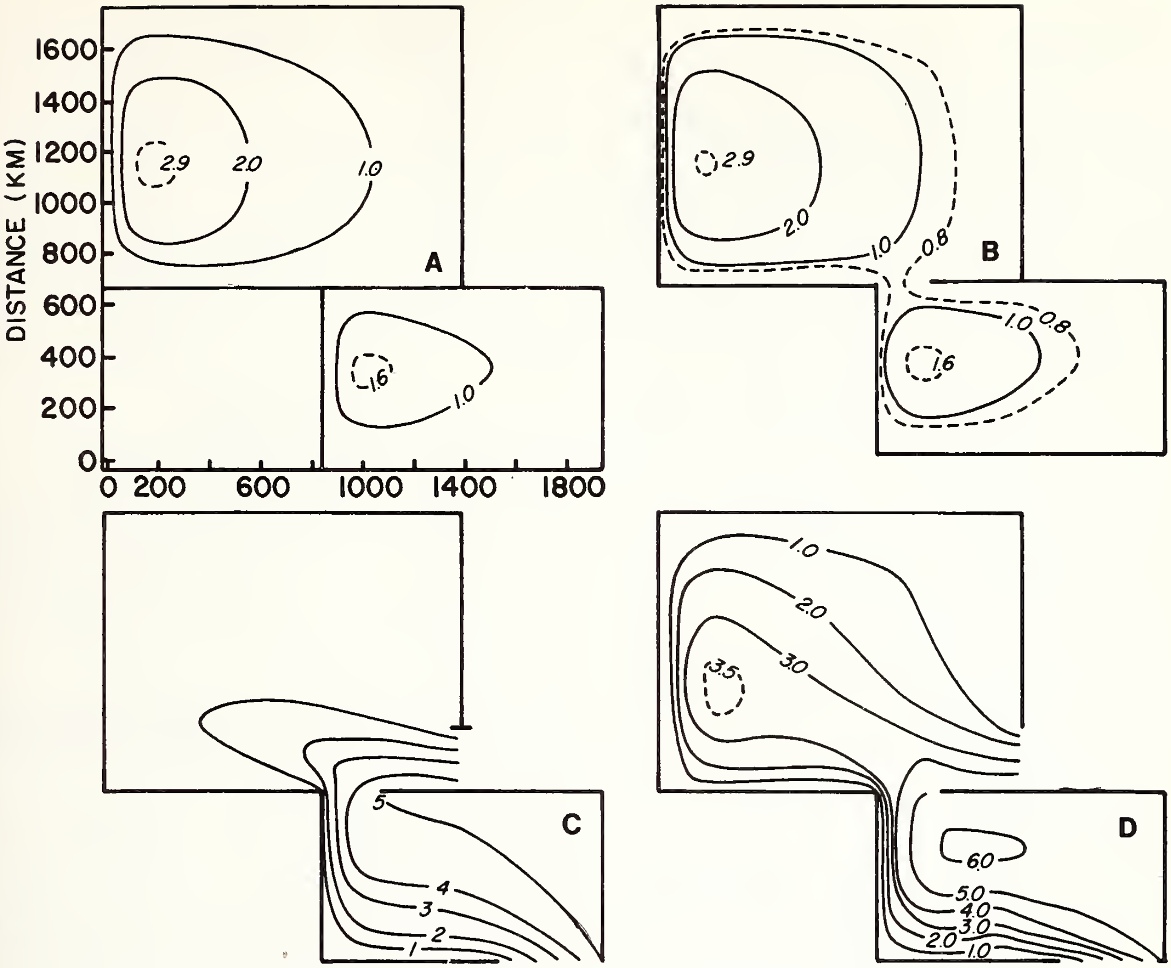

FIG. 3. Transport streamfunction contours (10^6 m^3 s^{-1}) determined from the Stommel model. The insets are lettered to coincide with the model runs listed in Table 1.

Therefore, if the Sverdrup transport is computed from only the wind data in the western Gulf alone, the annual transport for the western Gulf gyre is 3.1×10^6 m^3 s^{-1}. In comparison, Surges and Blaha (1976) computed a summer transport of 3×10^6 m^3 s^{-1} and a winter transport of 6×10^6 m^3 s^{-1}.

4. Time-dependent components of the temperature distributions in the Cayman Sea and western Gulf of Mexico gyres

The seasonal variations of the temperature at 150 m within the Cayman Sea and western Gulf of Mexico gyres (Fig. 4) are taken from the charts of Robinson (1973) as the warmest temperature within the respective gyres at 150 m (except when this isotherm appears to be defined by a single grid point). The time-dependent components of the curl of the wind stress (Fig. 4) are computed from the data of Bakun, described previously. In the Cayman Sea, the curl data represent the average curl along 19.5°N from 87 to 81°W, and in the western Gulf, the average curl along 22.5°N from 96 to 93°W.

The curl of the wind stress has two maxima during the year in both basins. In the Cayman Sea, the maxima (cyclonic curls) are in May and October and the minima (anticyclonic curls) are in January through March and July. These extrema are approximately in phase with periods of greatest temperature change. For instance, the July anticyclonic minima coincides with a temperature increase, while the October cyclonic maxima coincides with a temperature fall, which is consistent with simple Ekman pumping [terms 2 and 5 of relation (3)].

However, the temperature and curl distributions in the western Gulf of Mexico appear 180° out of phase. The maxima in wind stress curl (April–May and September) occur at times of minimum temperature, while minima in wind stress curl (July and December) are coincident with maximum temperatures.

5. Discussion

The results of a simple wind-driven model indicate that the curl of the wind stress could spin-up a gyre in the Cayman Sea. Furthermore, the linear results suggest that the wind-induced gyre would serve to enhance the exchange of mass between the two basins by increasing the transport into the Gulf above that which enters the Cayman Sea from the eastern Caribbean Sea. In this simple model, this additional flow into the Gulf must be returned on the eastern side of the Yucatan Straits. However, in reality, deeper compensating flows are possible.

Although the major currents of the Cayman Sea are nonlinear and time-dependent (Molinari, 1976), a steady-state dynamics might suffice in the interior of the basin to describe the presence of a permanent gyre and its associated transport. Leetmaa *et al.* (1977) have proposed a similar interior dynamics to account for the mean annual transport of the Gulf Stream at Miami.

Sturges and Blaha (1976) argued for a wind-driven gyre in the western Gulf. Other investigators, such as Cochrane (1972), have proposed that the gyre is a remnant of Loop Current eddies which have drifted west after separation from the Loop. A crude energy calculation is presented to show that both mechanisms can provide comparable amounts of energy to the western Gulf.

If Eq. (1) is multiplied by $(g')^2Dh/f^2$ and some algebraic manipulation is performed, an energy equation for the two-layer geostrophic system results. The total energy in this system consists of a kinetic energy component $(u^2 + v^2)D/2$ and an available potential energy component $g'(h - D)^2/2$, where u and v are the geostrophic velocity components and D the undisturbed upper layer depth. The total energy for a circular eddy in this system can be computed by assuming that the distribution of the upper layer thickness h is Gaussian, i.e., $h = D + h_0 \exp(-r^2/2s^2)$, where h_0 is the maximum disturbance of the interface, r radial distance, and s the half-width of the feature. The eddies energy can be computed by multiplying the two energy components by $2\pi r$ and integrating the resulting expression. A detached eddy can be characterized by $D = 200$ m, $h_0 = 100$ m, $s = 100$ km, and $g' = 2.0 \times 10^{-2}$ m s^{-2}. The energy input from one such eddy entering the western Gulf per year is of the order 6×10^{15} J.

The energy input by the wind is given by $(g'h/f)$ curl $\bar{\tau}$, or using the streamfunction defined previously, ψ curl$\bar{\tau}$. From Figs. 3a or 3b, a suitable value for ψD is 2×10^6 m^3 s^{-1}, or for ψ, 10^4 m^2 s^{-1}. A mean curl of 5×10^9 dyn cm^{-3} acting over a 4° × 4° area for one year gives an energy input of about 3×10^{15} J. These crude estimates are sufficiently close so that neither of the mechanisms, wind or detached eddy, can be eliminated as the forcing function for the circulation in the western Gulf.

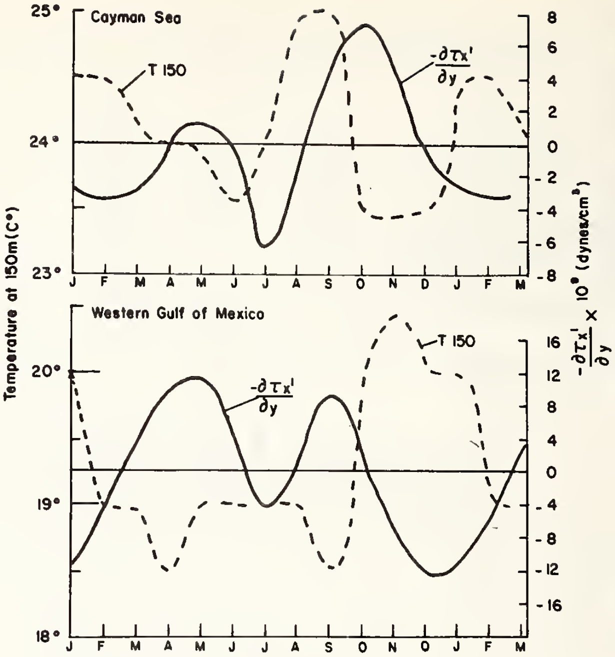

FIG. 4. Mean monthly temperatures at a depth of 150 m in the center of the Cayman Sea and western Gulf of Mexico gyres from the charts of Robinson (1973). Also shown are the mean monthly wind stress curls approximated by $-\partial\tau_x'/\partial y$ (see text for definition of τ_x').

If terms 2 and 5 are dominant in Eq. (3), the upper layers of the ocean will respond locally to the effect of Ekman pumping. In this case, an anticyclonic wind stress curl causes convergence and sinking of the upper isothermal surfaces. Conversely, a cyclonic wind stress causes divergence and rising of these surfaces. This movement of the isotherms is induced by variations in the local curl rather than the mean curl (Meyers, 1975).

Although the thermal response in the Cayman basin appears to be consistent with the dynamics of local Ekman response, the analysis is insufficient to hypothesize a balance between terms 2 and 5 in Eq. (3) to explain this correlation. Meyers (1975) found a similar balance in the Pacific, but White (1976) found that boundary-induced Rossby waves [term 3, Eq. (3)] and local forcing act together to cause the observed thermal response. Since the curl of the wind stress (Fig. 2) has the same structure across the entire length of the Cayman Sea, it is likely that Rossby waves are excited in this basin also. The lack of sufficient ocean data precludes an observational study such as completed by White (1976) in the Pacific.

If the temperature structure in the center of the western Gulf gyre is related to the intensity of the gyre, i.e., the warmer the central temperature, the

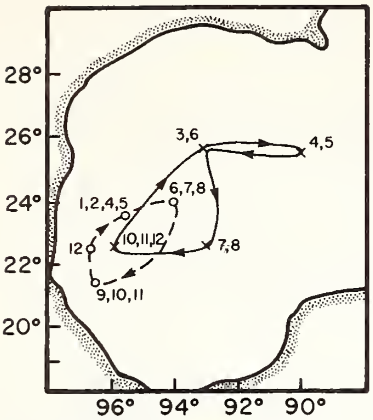

FIG. 5. The migration of the center of the western Gulf gyre (dashed line) determined from Robinson (1973). The month is given by number, i.e., 1 = January, 2 = February, etc. A March position is not plotted because this center position is not consistent with the locations observed in the surrounding months. The positions of the maximum curl of the wind stress are connected by the solid line. September is not plotted because of the small curls throughout the region.

more intense the gyre, then the curl and temperature data presented in Fig. 5 support the contention of Sturges and Blaha (1976). They suggest that the circulation in the western Gulf of Mexico responds almost instantaneously to changes in the intensity of the curl of the wind stress, i.e., terms 3 and 5 are dominant in Eq. (3). Molinari *et al.* (1978) have computed geostrophic transports for the upper 200 m of the southern limb of the western Gulf gyre. In the western Gulf, as in the Pacific, the geostrophic transports are in phase with the wind stress curl. The average geostrophic transport of the upper 200 m layer is 2.2×10^6 m^3 s^{-1}, with maxima in transport in January and August.

As in the case of the Cayman Sea, the exact phase relation between the wind and circulation cannot be determined without further study. A final piece of evidence suggests that such a relation does exist, and warrants further effort. The center of the gyre in the western Gulf of Mexico as determined from the 150 m temperature charts of Robinson (1973) migrates in a clockwise loop (Fig. 5). A position is not given for March because the center is not well-defined during this month. Also shown on this figure are the positions by month of the maximum wind stress curls determined from the 3° × 3° grid of wind data in the region of the gyre. This position migrates in a clockwise loop very similar to the loop made by the gyre center.

Acknowledgments. The wind data supplied by Mr. A. Bakun of the National Marine Fisheries Service and the temperature data supplied by NODC are gratefully acknowledged. The significant contributions toward the clarification of the analysis and presentation of this paper made by Professor R. O. Reid of Texas A&M University and two reviewers are also greatly appreciated.

REFERENCES

Anderson, D. L. T., and A. E. Gill, 1975: Spin-up of a stratified ocean, with applications to upwelling. *Deep-Sea Res.*, **22**, 583–596.

Behringer, D. W., R. L. Molinari and J. F. Festa, 1977: The variability of anticyclonic current patterns in the Gulf of Mexico. *J. Geophys. Res.*, **82**, 5469–5476.

Cochrane, J. D., 1963: Yucatan current. Ref. 63-18A, unpublished report, Dept. Oceanogr. Meteor., the A&M College of Texas, 6–11.

——, 1972: Separation of an anticyclone and subsequent developments in the Loop Current (1969). *Contributions on the Physical Oceanography of the Gulf of Mexico*, L. R. A. Capurro and J. L. Reid, Eds., Gulf Publ. Co., 91–106.

Hellerman, S., 1965: Computations of wind stress fields over the Atlantic Ocean. *Mon. Wea. Rev.*, **93**, 239–244.

Leetmaa, A., P. P. Niiler and H. Stommel, 1977: Does the Sverdrup relation account for the Mid-Atlantic circulation? *J. Mar. Res.*, **35**, 1–10.

Leipper, D. F., 1970: A sequence of current patterns in the Gulf of Mexico. *J. Geophys. Res.*, **75**, 637–657.

Maul, G. A., 1975: An evaluation of the use of the Earth Resources Technology Satellite for observing ocean current boundaries in the Gulf Stream system. NOAA Tech. Rep. ERL 335-AOML 18, 125 pp.

Meyers, G., 1975: Seasonal variation in transport of the Pacific North Equatorial Current relative to the wind field. *J. Phys. Oceanogr.*, **5**, 442–449.

Molinari, R. L., 1976: An overview of the Cayman Sea-Gulf of Mexico circulation based on CICAR Survey Month and other data. Abstract from *Proc. of CICAR II Symp., Progress in Marine Research in the Caribbean and Adjacent Regions*, H. B. Stewart, Ed., Caracas, Venezuela.

——, J. F. Festa and D. W. Behringer, 1978: Circulation in the Gulf of Mexico: Geostrophic computations. *J. Phys. Oceanogr.* (in press).

——, S. Baig, D. Behringer, G. Maul and R. Legeckis, 1977: Winter intrusions of the Loop Current. *Science*, **198**, 505–507.

Niiler, P. P., and W. S. Richardson, Jr., 1973: Seasonal variability of the Florida Current. *J. Mar. Res.*, **31**, 144–167.

Robinson, M. K., 1973. Atlas of monthly mean sea surface and subsurface temperature and depth of the top of the thermocline: Gulf of Mexico and Caribbean Sea. SIO Ref. 73–8, Scripps Inst. of Oceanography, 105 pp.

Stommel, H., 1948: The westward intensification of wind-driven ocean currents. *Trans. Amer. Geophys. Union*, **29**, 202–206.

Sturges, W., and J. P. Blaha, 1976: A western boundary current in the Gulf of Mexico. *Science*, **192**, 367–369.

White, W. B., 1976: Annual forcing of baroclinic long waves in the tropical North Pacific Ocean. *J. Phys. Oceanogr.*, **7**, 50–61.

White, W. B., and J. P. McCreary, 1974: Eastern intensification of ocean spin-down: Application to El Nino. *J. Phys. Oceanogr.*, **4**, 295–303.

Journal of Physical Oceanography 8, No. 6, 987-996.

The Circulation in the Gulf of Mexico Derived from Estimated Dynamic Height Fields

ROBERT L. MOLINARI, JOHN F. FESTA AND DAVID W. BEHRINGER

Atlantic Oceanographic and Meteorological Laboratories, NOAA, Miami, FL 33149

(Manuscript received 5 January 1978, in final form 15 May 1978)

ABSTRACT

Monthly mean dynamic height topographies for the upper 500 m of the Gulf of Mexico, seasonal mean topographies for the upper 1000 m and annual topographies for the deep flow are presented. The dynamic height values on a 1° × 1° grid were determined from observed temperature values and salinities derived from mean *T-S* relations. The seasonal intrusion of the Loop Current is observed and found to vary directly with the geostrophic transport through the Yucatan Straits. At the Straits, the transport in the upper 500 m is a maximum in June. The transports in the upper 500 m of an anticyclone in the western Gulf are a maximum in winter and summer, and a minimum in spring and fall. There is a permanent westerly flow on the Texas Shelf. After turning cyclonically, this flow joins the eastward transport of the northern limb of the anticyclone in the western Gulf of Mexico. Most of this eastward flow recirculates in the anticyclone; however, a portion flows east across the central Gulf to become entrained in the Loop Current. The deep circulation between 1500 and 3000 m is dominated by an anticyclonic gyre which fills the entire deep basin.

1. Introduction

Behringer *et al.* (1977), using synoptic and climatological data, reappraised ideas concerning the circulation in the Gulf of Mexico. They inferred an average annual cycle for the intrusion of the Loop Current, similar to the cycle first hypothesized by Leipper (1970), by analyzing the temperature distribution at 200 m in the eastern Gulf of Mexico. On the average, the Loop intrudes northward into the Gulf during the winter and spring and it becomes a detached eddy in the early summer. The eddy then drifts westward during the summer and fall. Their analysis of the synoptic data suggests that a cycle of intrusion and eddy detachment occurs annually but that the time of occurrence of a particular event in the cycle varies considerably. For example, fall and winter intrusions and eddy separations have been observed (Molinari *et al.*, 1977) and the periods between eddy separations have been as short as eight months and as long as 17 months.

Behringer *et al.* (1977) also presented data which implied the year-round persistence of an anticyclonic gyre in the western Gulf of Mexico. Although the data coverage is sparse, there are indications that the circulation in the gyre may be greatest in summer and winter. Sturges and Blaha (1976) have suggested that these two maxima would be expected if the gyre were driven by the observed curl of the wind stress.

Nowlin (1972) reviewed some of the previous efforts at producing climatological dynamic height charts of the Gulf of Mexico. He noted that the averages of Collier *et al.* (1958) and Duxbury (1962), for instance, produced very complicated circulation patterns, particularly in the western Gulf. He suggested these patterns were an artifact of combining data collected over many months, and did not represent actual current patterns. Circulation features deduced from the mean monthly distribution charts of the temperature at 200 m given by Behringer *et al.* (1977) are, in general, consistent with patterns deduced from synoptic charts. For instance, the spring intrusion and western Gulf gyre appear in both types of data representations. Therefore, average dynamic height charts based on the data set used by Behringer *et al.* (1977) should provide an approximation to the geostrophic flow patterns in the Gulf. In addition, the circulation patterns deduced in the deeper portions of the water column, where the temporal variability should be considerably less, are more likely to represent the mean current field.

The complete data set from which Behringer *et al.* (1977) extracted temperature data is used in this paper to compute the geostrophic circulation in the Gulf of Mexico. Dynamic height topographies computed relative to various depths and averaged over time intervals ranging from monthly to annual are presented. Geostrophic transports are also calculated.

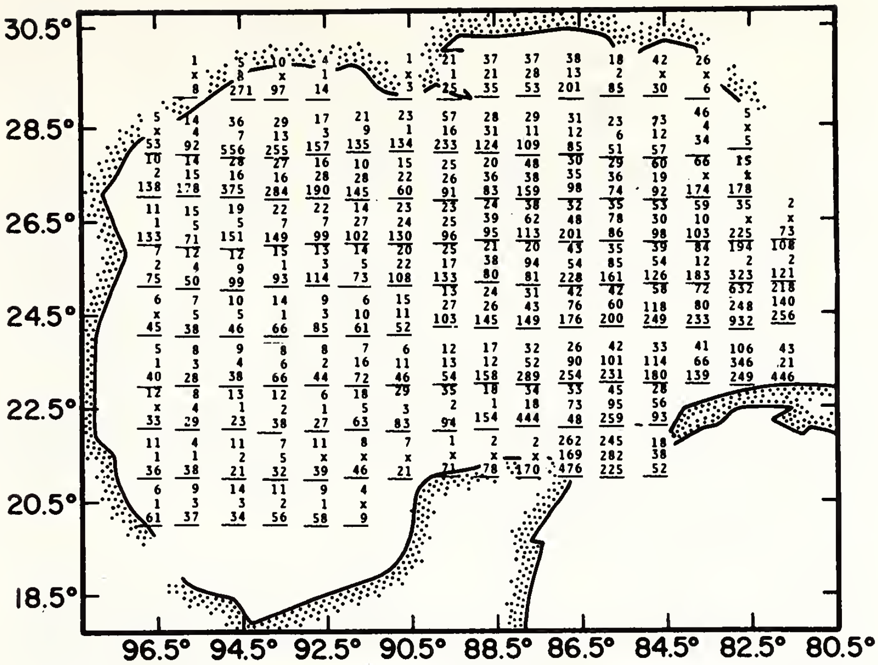

FIG. 1. Distribution of temperature data sources by 1° quadrangles. For each quadrangle, the top line is the number of Nansen stations, the middle line is the number of XBT stations, and the bottom line is the number of MBT stations.

2. Data preparation

The National Oceanographic Data Center (NODC) of the National Oceanic and Atmospheric Administration provided monthly 1° quadrangle averages of temperature and salinity values at NODC standard depths. The total number of observations for all months is shown on Fig. 1. The distribution of Nansen stations on time scales less than semiannual (not shown) is poor. Temperature data from mechanical and expendable bathythermograph (MBT and XBT) stations (Fig. 1) were therefore used to supplement the Nansen station data. Salinity data were derived by means of an average *T-S* relation.

Average *T-S* relations, by season, were constructed by NODC for the nine regions shown on Fig. 2. The regions were selected to represent several broadly defined topographic and circulation regimes. For example, in the deep Gulf, regions 3 and 5 represent, respectively, areas dominated by the Loop Current and western Gulf gyre; while on the shelf, region 8 represents the area directly influenced by Mississippi River discharge. The winter (December–February), spring (March–May), summer (June–August) and fall (September–November) seasons were based on the annual cycle of the Loop penetration given by Leipper (1970) and Behringer *et al.* (1977).

Each *T-S* curve was subjectively edited to remove inconsistent data, and then smoothed by a three-point running average. Caruthers (1972) has shown there is little seasonal variability in the *T-S* relation below 17°C in regions 1–6. Therefore, below 17°C only an annual *T-S* curve was used in each region. Seasonal relations were used for temperatures above 17°C.

Areas 7, 8 and 9 are primarily shelf areas. The waters of these areas show considerable temporal variability in the *T-S* relations at all temperatures. Since the present study is not concerned primarily with the circulation on the shelf, the *T-S* relation of the nearest region with mid-basin characteristics was used for temperatures below 17°C. Seasonal relations were used for temperatures above 17°C. Examples of *T-S* curves for a deep basin and a shelf region are shown in Fig. 3. It should be noted that the high variability in the *T-S* relation of region 8 is due to the influence of Mississippi River outflow, and is not characteristic of the other shelf regions.

Vertical sections along latitude lines were constructed from the 1° quadrangle temperature averages supplied by NODC. Inconsistent temperature values, such as those causing unrealistic inversions in the deeper layers, were removed. No further editing or smoothing of the temperature data were performed. The corresponding salinity data were then obtained from the appropriate *T-S* relations. In each case, the salinity values were smoothed horizontally to reduce the large gradients at the boundaries of the nine regions.

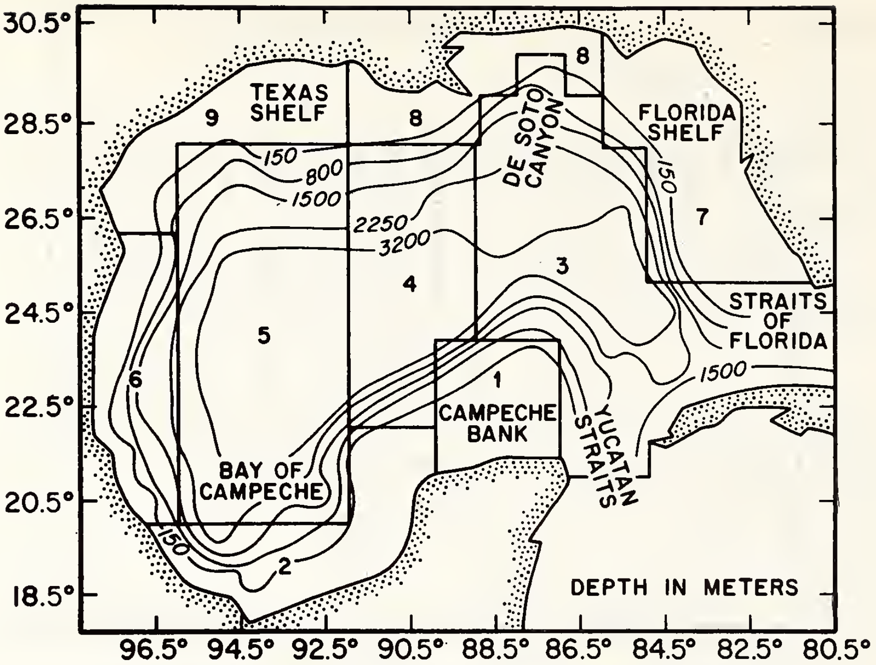
30.5°
28.5°
26.5°
24.5°
22.5°
20.5°
18.5°
96.5° 94.5° 92.5° 90.5° 88.5° 86.5° 84.5° 82.5° 80.5°
TEXAS SHELF
9
8
DE SOTO CANYON
FLORIDA SHELF
7
150
800
1500
2250
3200
3
4
5
6
STRAITS OF FLORIDA
1500
1
CAMPECHE BANK
YUCATAN STRAITS
BAY OF CAMPECHE
150
2
DEPTH IN METERS

FIG. 2. The nine regions for which seasonal *T-S* relations were computed.

Because the MBT and XBT data do not extend below maximum depths of 250 and 750 m, respectively, the amount of data at depths greater than 500 m was insufficient to compute monthly geostrophic properties. Therefore, monthly dynamic height topographies were computed only for the surface relative to 500 m. Seasonal topographies were computed for the surface relative to 1000 m. Finally, for the levels between 1000 and 2500 m relative to 3000 m, it was possible to compute only annual topographies.

3. Geostrophic computations

The annual mean dynamic topographies at 1000, 1500, 2000 and 2500 m computed relative to 3000 m are shown in Fig. 4. The anticyclonic Loop Current is clearly evident on the 1000 m surface as a ridge with dynamic height values greater than found elsewhere in the Gulf. Although this ridge appears at greater depths, its maximum dynamic height values do not exceed values found elsewhere in the Gulf. Therefore, at these deeper levels, its existence as a feature independent of the larger Gulf circulation is not clear.

A cyclonic feature in the vicinity of the DeSoto Canyon 87.5°W (Fig. 2) is apparent at all depths. The cyclone extends south as a trough across the narrowest portion of the deep basin. Finally, in the western Gulf, anticyclonic circulation appears at all levels.

Sea surface dynamic height topographies were computed relative to 1000 m for four 3-month intervals (Fig. 5). Two anticyclonic circulation features, the Loop Current in the eastern Gulf and an anticyclonic gyre in the western Gulf, are present during all seasons. The penetration of the Loop Current varies with season as previously described.

Transports computed for sections through the western Gulf anticyclone and along 90.5°W (see Fig. 5 for section locations) are given in Table 1.

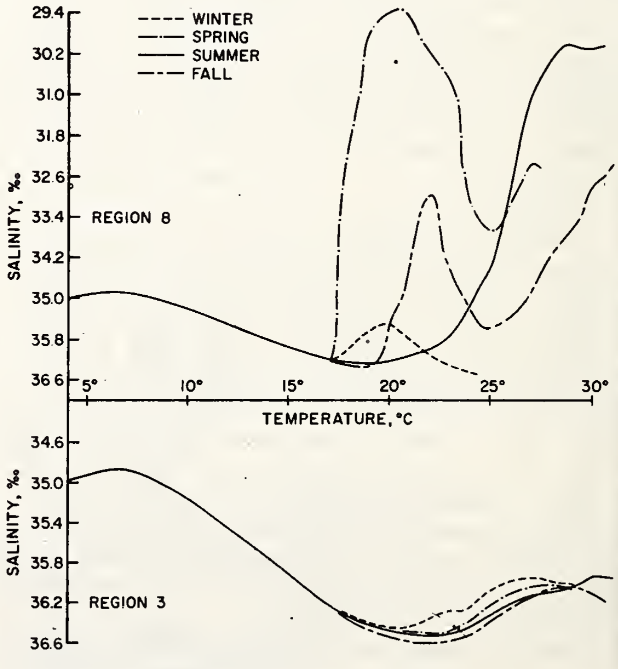

FIG. 3. The seasonal *T-S* relations for regions 3 and 8 of Fig. 2.

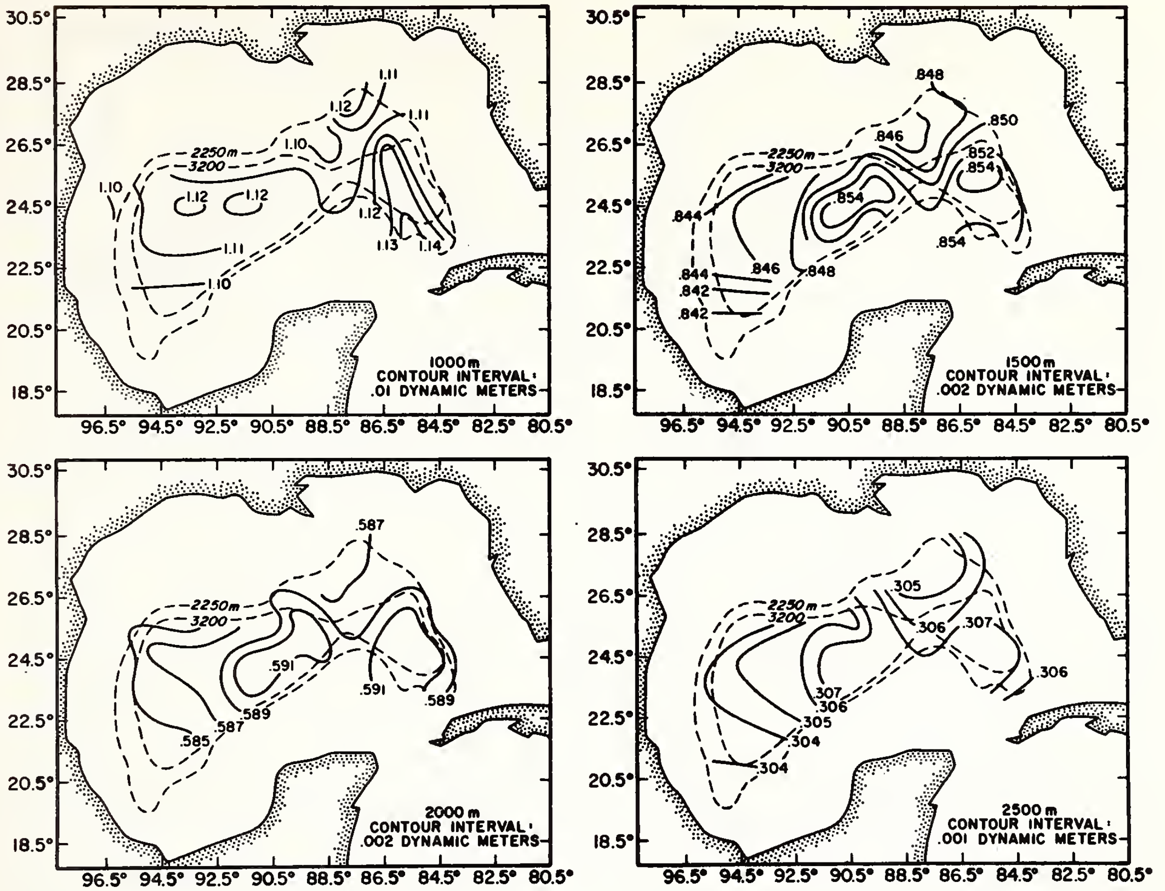
30.5°
28.5°
26.5°
24.5°
22.5°
20.5°
18.5°
96.5° 94.5° 92.5° 90.5° 88.5° 86.5° 84.5° 82.5° 80.5°
2250m
3200
1.11
1.12
1.11
1.10
1.10
1.12
1.12
1.12
1.11
1.10
1.13
1.14
1000m
CONTOUR INTERVAL:
.01 DYNAMIC METERS
.848
.850
.846
.852
.854
.854
.844
.854
.846
.848
.844
.842
.842
1500m
CONTOUR INTERVAL:
.002 DYNAMIC METERS
.587
.591
.591
.589
.589
.587
.585
2000 m
CONTOUR INTERVAL:
.002 DYNAMIC METERS
.305
.306
.307
.306
.307
.306
.305
.304
.304
2500 m
CONTOUR INTERVAL:
.001 DYNAMIC METERS

FIG. 4. Annual mean dynamic height topographies (in dynamic meters) at 1000, 1500, 2000 and 2500 m computed relative to 3000 m. Also shown are several isobaths. The dynamic height contours appear at depths which are shallower than 3000 m because the dynamic height distributions were determined from data averaged onto a 1° × 1° grid.

The sections are not fixed in space, but were chosen as nearly as possible to cross the same circulation feature and conserve transport as closely as possible in each season. Some averaging was done to obtain the summer transports through the western Gulf anticyclone. The averaging reduced excessively high transport values, which appear to be inconsistent with the adjacent seasons.

A large fraction of the transport of the northern limb of the western Gulf anticyclone is apparently supplied by a westerly flow along the Texas Shelf (cf. sections A′A″ for spring and A′A″ for fall). However, the residuals of the anticyclone, defined as the sum of the northern limb, southern limb and Texas Shelf transports, indicate that additional westerly transport is required to obtain a mass balance in the western Gulf. A similar imbalance exists along the 90.5°W section with a net eastward transport during all seasons (Table 1). The spring data show that a recirculation of anticyclonic water and water spun-off from the Yucatan Current combine to flow along the Campeche Bank to supply a portion of the needed westerly flow (Fig. 5).

Monthly sea surface dynamic height topographies computed relative to 500 m were constructed for the entire Gulf of Mexico (Figs. 6 and 7). The Leipper cycle for the intrusion of the Loop is observed with the addition of a secondary intrusion in October, possibly extending through November. This secondary intrusion has been noted by Behringer *et al.* (1977). Insufficient data exist to define the circulation in December. If the start of the intrusion cycle is taken in January, the Loop intrudes at an average rate through June of ~1.5 cm s^{-1}. The July pattern is indicative of a detached eddy. The Loop Current appears less intense in August and September because of the large variability in the position of the Loop during these months (Behringer *et al.*, 1977).

Geostrophic transports computed relative to 500 m were determined for the flow at the Yucatan Straits and Straits of Florida (Fig. 8). The Yucatan transport is computed at 21.5°N. The Straits of Florida transport can be determined at 81.5, 82.5 or 83.5°W, but frequently the transport at one or the other of these sections could not be computed or

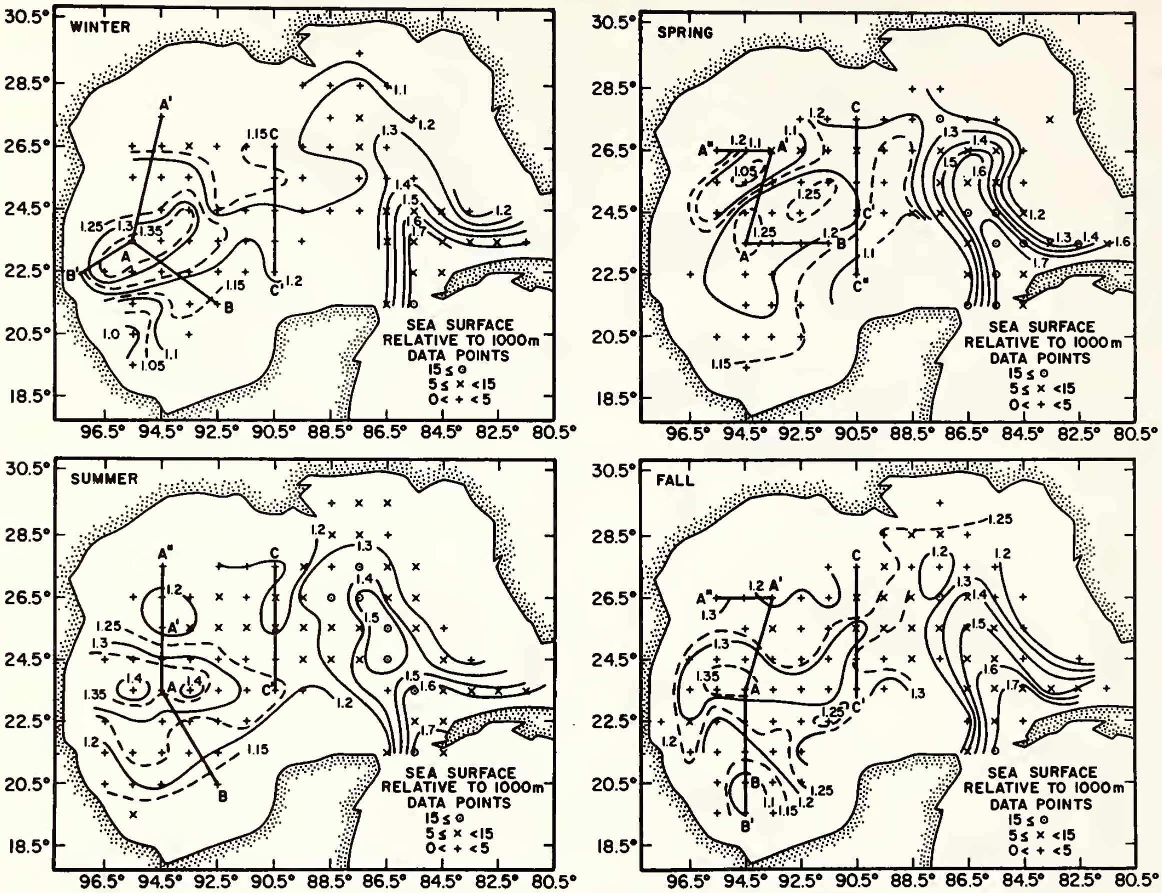

Fig. 5. Seasonal dynamic height topographies (in dynamic meters) computed relative to 1000 m. Also shown are the number of data points available at 1000 m. The sections used to compute the transports in Table 1 are given.

was clearly inconsistent with the others. Therefore, the transport at 81.5, 82.5 or 83.5°W closest to the concurrent month's transport at the Yucatan Straits was used in Fig. 8. The annual cycle, in a least-squares sense, was computed for each strait, and the parameters of each fit are given in Table 2. The mean transport and phases of the maximum transports through the two straits are essentially identical.

In the central and western Gulf only seasonal transports relative to 500 m have been computed from the data since they were inadequate for

Table 1. Geostrophic transports computed relative to 1000 m along the sections (in parentheses) given on Fig. 5. Units of transport are 10^6 m^3 s^{-1}, and flow is positive to the north and east.

	Western Gulf of Mexico				90.5°W		
	Anticyclone						
	Northern limb	Southern limb	Texas shelf	Additional transport necessary to balance columns (1)–(3)	Easterly flow	Westerly flow	Additional transport necessary to balance columns (4) and (5)
	(1)	(2)	(3)		(4)	(5)	
Winter	21 (AA′)	−12 (AB) −9 (AB′)		−9 −12	10 (CC′)		−10
Spring	18 (AA′)	−11 (AB)	−7 (A′A″)	0	13 (CC′)	−8 (C′C″)	−5
Summer	19 (AA′)	−6 (AB)	−3 (A′A″)	−10	10 (CC′)		−10
Fall	18 (AA′)	−11 (AB) +3 (BB′)	−8 (A′A″)	−2	12 (CC′)		−12

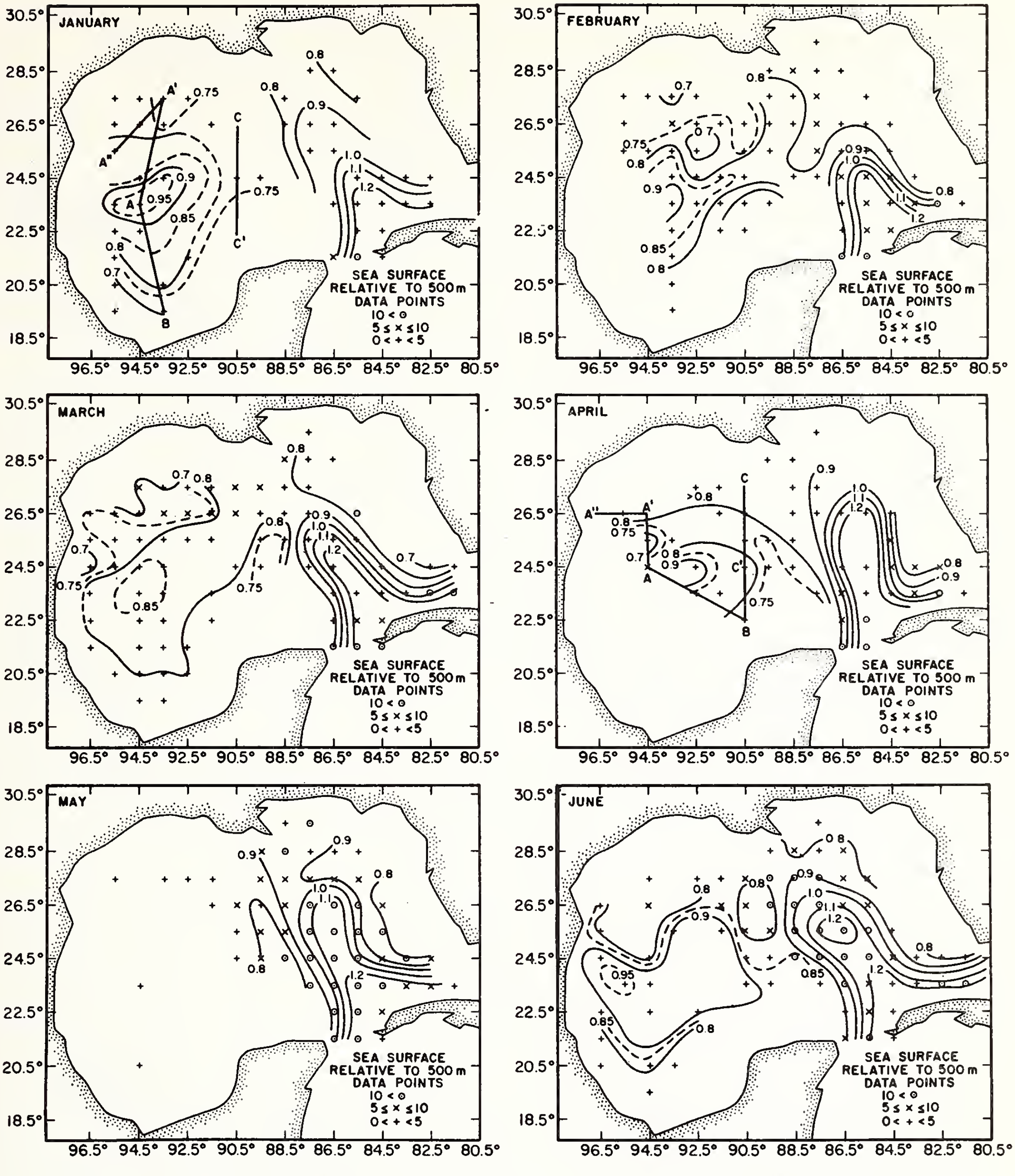
JANUARY
FEBRUARY
MARCH
APRIL
MAY
JUNE
SEA SURFACE
RELATIVE TO 500m
DATA POINTS
10< ○
5≤ × ≤10
0< + <5
30.5°
28.5°
26.5°
24.5°
22.5°
20.5°
18.5°
96.5° 94.5° 92.5° 90.5° 88.5° 86.5° 84.5° 82.5° 80.5°
A
A'
A''
B
C
C'
0.7
0.75
0.8
0.85
0.9
0.95
1.0
1.1
1.2

FIG. 6. Monthly dynamic height topographies (in dynamic meters) computed relative to 500 m for the months January through June. Also shown are the number of data points available at 500 m. The sections for which the transports in Table 3 are computed are shown on the January (winter) and April (spring) charts.

monthly computations. The sections from which these transports are computed are given on the mid-month of the season in Figs. 6 and 7; i.e., winter sections are given on the January chart, spring sections on the April chart, etc. As before, the sections were selected to conserve volume transport. The results are listed in Table 3.

Dynamic height topographies computed relative to 200 m are not shown, because the Loop Current intrusion is similar to that indicated by the 500 m topographies, and the temporal variability of the anticyclone in the western Gulf and mid-Gulf circulation can be derived from consideration of their volume transports. Table 4 lists these transports

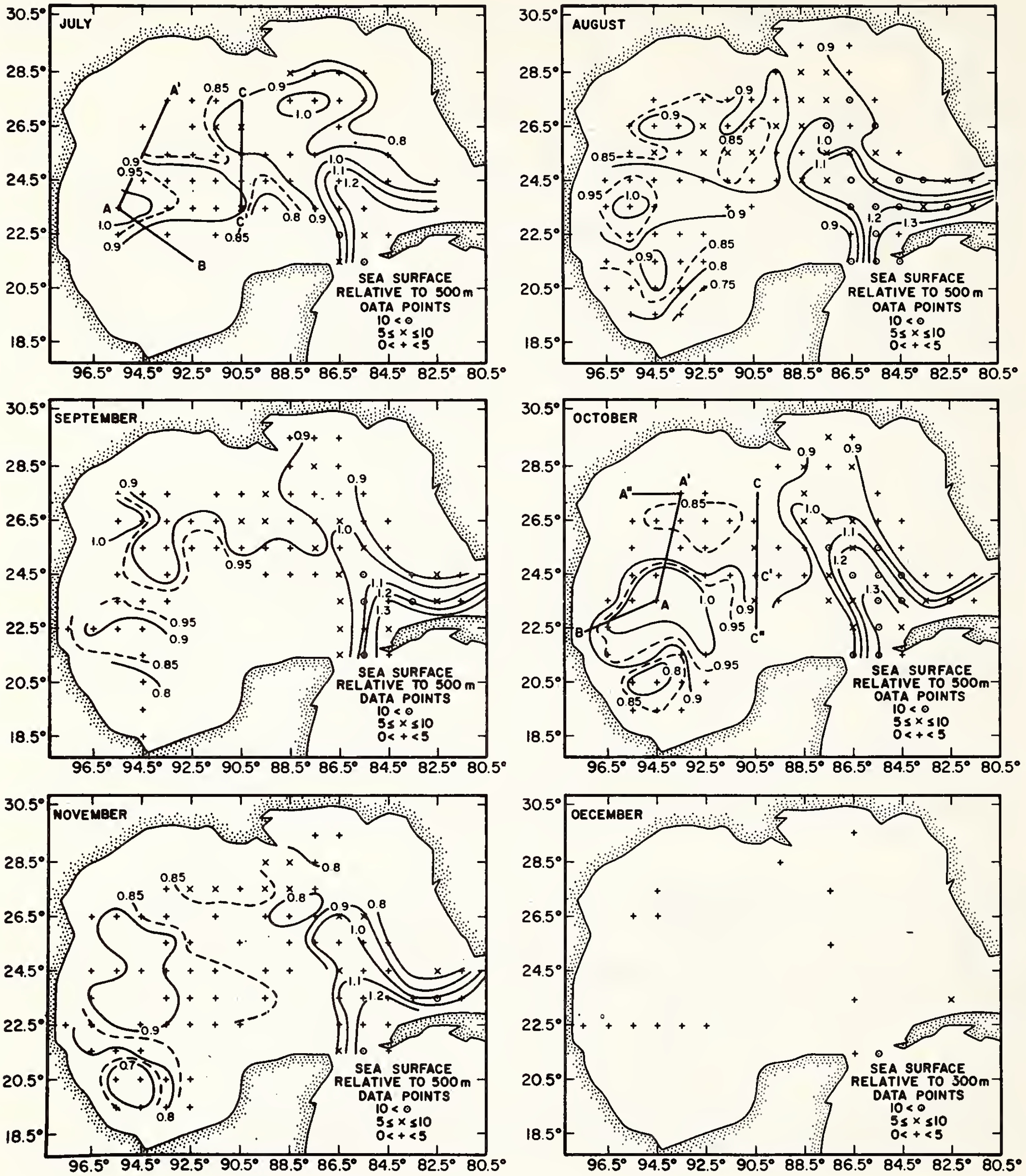
JULY
AUGUST
SEPTEMBER
OCTOBER
NOVEMBER
DECEMBER
30.5°
28.5°
26.5°
24.5°
22.5°
20.5°
18.5°
96.5° 94.5° 92.5° 90.5° 88.5° 86.5° 84.5° 82.5° 80.5°
A
A'
A"
B
C
C'
C"
SEA SURFACE RELATIVE TO 500 m
SEA SURFACE RELATIVE TO 300 m
DATA POINTS
10 < ⊙
5 ≤ × ≤ 10
0 < + < 5
0.7
0.75
0.8
0.85
0.9
0.95
1.0
1.1
1.2
1.3

FIG. 7. As in Fig. 6 except for July–December. The sections for which the transports in Table 3 are computed are shown on the July (summer) and October (fall) charts.

computed relative to 200 m, along sections similar to those used in the 500 and 1000 m computations.

The 500 m transports (Table 3) through the various limbs of the western Gulf anticyclone are more nearly in balance than are the 1000 m transports of this feature. Particularly when sufficient data exist, i.e., in winter, spring and fall, the transports necessary for a balance are small. The contribution from the Texas Shelf to the northern limb of the gyre is on the average one-third of the total of the easterly flow (Tables 3 and 4).

The 200 and 500 m transports through the southern limb of the anticyclone (Tables 3 and 4) indicate an annual signal which is not found in the deeper transports (Table 1). The gyre has largest transports in the summer and winter, and smaller transports

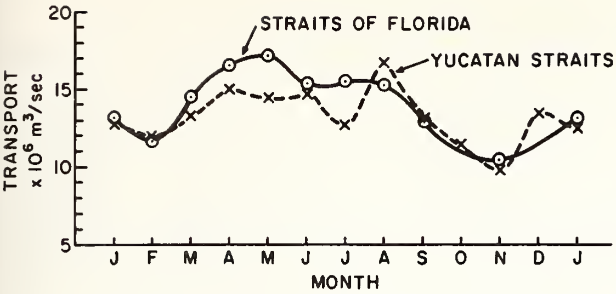

FIG. 8. Monthly volume transports computed relative to 500 m for the transports through the two 1° quadrangles across the Yucatan Straits and Straits of Florida (see text).

in spring and fall. The 200 m (not shown) and 500 m topographies (Figs. 6 and 7) indicate little transport from the Loop Current west along the Campeche Bank. Thus, most of the upper 500 m of the southern limb of the western Gulf anticyclone is comprised of water recirculating around the gyre.

4. Discussion

The authors are aware of only one other discussion of the circulation in the deeper portions (>1500 m) of the Gulf of Mexico. Nowlin and McLellan (1967) find a weak anticyclonic circulation pattern in the western Gulf and no distinct pattern in the eastern and central Gulf between 1500 and 2000 m. The dynamic height topographies suggest that an anticyclonic gyre fills the entire basin between 1500 and 3000 m (Fig. 4). The strong presence of the Loop Current at 1000 m and not 1500 m is consistent with the calculations of Nowlin and McLellan (1967) who show a distinct Loop in the dynamic field at 1000 m relative to 1500 m. Thus, the Loop Current may not penetrate to the sill depth of the Yucatan Channel at 2000 m.

Although the monthly average transports computed relative to 500 m for the Yucatan Straits and Straits of Florida are only approximations which underestimate the flow through these ports, their times of maximum transport are consistent with the results of past studies. In particular, the phases computed for seasonal variation of the flow relative to 500 m (Table 2) agree with the June maximum in Yucatan Current surface speed computed from ship drift reports by Cochrane (1965) and with the phase in directly measured Florida Current transport observed by Niiler and Richardson (1973). The magnitudes in Table 2, however, are about a factor of 2 smaller.

Maul (1977) suggested that the intrusion of the Loop Current is associated with a phase lag between the maximum transports through the Yucatan Straits and Straits of Florida. The transports relative to 500 m (Table 2) indicate no lag. However, the maximum transports appear to be in phase with the maximum intrusion of the Loop. Thus, there may be a connection between the magnitude of the transport through the Yucatan Straits and the phase of the Loop cycle.

A cyclonic circulation is apparent in the Bay of Campeche in the fall 1000 m dynamic height topography (Fig. 5). Its transport is 3×10^6 m^3 s^{-1} (Table 1). This feature also appears in the September, October and November 200 m dynamic height topographies (not shown). Nowlin (1972) and Vazquez (1975) have observed this feature in synoptic studies.

The water of the southern limb of the western Gulf anticyclone appears to be predominantly water recirculating in that gyre. There is some indication of flow separating from the Loop Current in the spring and flowing west along the Campeche Bank (Fig. 5), but the amount of transport is small.

The 200 and 500 m transports through the southern limb of the western Gulf anticyclone (Tables 3 and 4) indicate an annual cycle which is not found in the deeper transports (Table 1). The gyre has largest transports in the summer and winter, and smaller transports in spring and fall. Sturges and Blaha (1976) have hypothesized that the western Gulf anticyclone is wind-driven and should have maximum intensity during times of maximum wind-stress curl over the Gulf of Mexico. This occurs in the summer and winter. The maximum transports given on Tables 3 and 4 are consistent with this hypothesis, but the lack of such a cycle at 1000 m (Table 1) suggests that this response may be limited to the upper layers.

The northern limb of the western Gulf anticyclone is a combination of transport from the southern part of the gyre and the Texas Shelf. The shelf flow can be as much as one-third of the total transport of the easterly flow (Tables 1, 3 and 4). This Texas Shelf flow was observed by Nowlin and McLellan (1967) in their February–March 1962 data set and was attributed to the influence of river discharge on the circulation. They computed an

TABLE 2. Properties of the annual component, $A_0 + A_1 \cos (wt-\phi)$, of the transport relative to 500 m through the Yucatan Straits and Straits of Florida.

	Mean A_0 ($\times 10^6$ m^{3}s^{-1})	Amplitude A_1 ($\times 10^6$ m^{3}s^{-1})	Phase ϕ (weeks from 1 January)
Yucatan Straits	13.2	1.5	22.1
Straits of Florida	13.7	2.8	22.5

Table 3. Geostrophic transports computed relative to 500 m along the sections in parentheses given on Figs. 8 and 9. Units of transport are 10^6 m^{3}s^{-1}, and flow is positive to the north and east.

	Western Gulf of Mexico				90.5°W		
	Anticyclone						
	Northern limb (1)	Southern limb (2)	Texas shelf (3)	Additional transport necessary to balance columns (1)–(3)	Easterly flow (4)	Westerly flow (5)	Additional transport necessary to balance columns (4) and (5)
Winter (Section locations on Fig 8, January)	13 (AA′)	−9 (AB)	−4 (A′A″)	0	4 (CC′)		−4
Spring (Section locations on Fig. 8, April)	8 (AA′)	−6 (AB)	−3(A′A″)	+1	4 (CC′)	−3 (C′B)	−1
Summer (Section locations on Fig. 9, July)	12 (AA′)	−9 (AB)		−3	4 (CC′)		−4
Fall (Section locations on Fig. 9, October)	9 (AA′)	−6 (AB)	−2(A′A″)	−1	6 (CC′)	−3(C′C″)	−3

addition to the transport of the northern limb of approximately 10 × 10^6 m^3 s^{-1}. They suggested that the Texas Shelf flow may be intermittent, but present analysis indicates it is a permanent circulation feature (Table 4).

The 1000 m transports (Table 1) indicate a net transport out of the western and central Gulf to the eastern Gulf. However, at 500 m when sufficient data exist (Table 3), there is essentially a balance in the mass transport into and out of the western Gulf. It appears that the 1° quadrangle averaging can contribute to the inbalance at the greater depths, since the westerly flow is located at shallower depths, i.e., along the Texas Shelf and Campeche Bank.

The transports at 90.5°W suggest a mechanism for exchange of shelf and deep basin between the western and eastern Gulf. A portion of the Texas Shelf water which joins the northern limb of the western Gulf anticyclone could be advected through the western and central Gulf to become entrained in the Loop Current. In addition, a smaller amount of water may spin off from the Yucatan Current, circuit the Campeche Bank and western Gulf anticyclone, and finally rejoin the Loop Current.

Acknowledgments. This effort was partially funded through Bureau of Land Management Interagency Agreement 08550-IA5-26 with the Environmental Research Laboratories of the National Oceanic and Atmospheric Administration.

Table 4. Geostrophic transports computed relative to 200 m through the features indicated. Units are 10^6 m^{3}s^{-1}, and flow is positive to the north and east.

	Western Gulf of Mexico				90.5°W			
	Anticyclone					Westerly flow		
	Northern limb (1)	Southern limb (2)	Texas shelf (3)	Additional transport necessary to balance columns (1)–(3)	Easterly flow (4)	Texas shelf (5)	Campeche bank (6)	Additional transport necessary to balance columns (4)–(6)
January	3.3	−3.1	−0.5	+0.3	2.0	−0.4	0	−1.6
February	3.0	−2.2	−0.3	−0.5	1.9	0	0	−1.9
March	2.8	−2.5	−0.8	+0.5	1.8	−1.1	−1.1	+0.4
April					1.4	−1.3	−0.6	+0.4
May	2.3	−1.2	−0.3	−0.8	1.4	0	0	−1.4
June	3.3	−2.5	−0.9	+0.1	1.9	0	−1.2	−0.7
July	3.5	−2.7	−1.2	+0.2	1.8	0	−1.9	+0.1
August	3.3	−2.8	−1.0	+0.5	1.9	0	−0.5	−1.4
September	3.5	−1.9	−1.1	+0.5	2.6	0	−0.4	−2.2
October	2.2	−1.4	−0.4	+0.6	0.8	−0.4	0	−0.4
November	3.1	−2.3	−1.8	+1.0	+1.2	0	−0.6	−0.6
December	5.1		−2.0					

REFERENCES

Behringer, D. W., R. L. Molinari and J. F. Festa, 1977: The variability of anticyclonic current patterns in the Gulf of Mexico. *J. Geophys. Res.*, **82**, 5469.

Caruthers, J. W., 1972: Water masses at intermediate depths. *Contributions on the Physical Oceanography of the Gulf of Mexico*, L. R. A. Capurro and J. L. Reid Eds., Gulf Publ. Co., 53–64.

Cochrane, J. D., 1965: The Yucatan Current. Annual Report, Project 186, Texas A&M University, Ref. 65-17 T, 20 pp.

Collier, A., K. H. Drummond and G. B. Austin, 1958: Gulf of Mexico physical and chemical data from ALASKA cruises, with a note on some aspects of the physical oceanography of the Gulf of Mexico. *Spec. Sci. Rep. Fish. Wildlife Serv.*, No. 249.

Duxbury, A. C., 1962: Averaged dynamic topographies of the Gulf of Mexico. *Limnol. Oceanogr.*, **1**, 428–431.

Leipper, D. F., 1970: A sequence of current patterns in the Gulf of Mexico. *J. Geophys. Res.*, **75**, 637–657.

Maul, G. A., 1977: The annual cycle of the Gulf Loop Current Part I: Observations during a one-year time series. *J. Mar. Res.*, **35**, 29–47.

Molinari, R. L., S. Baig, D. Behringer, G. Maul and R. Legeckis, 1977: Winter intrusions of the Loop Current. *Science*, **198**, 505–507.

Niiler, P. P., and W. S. Richardson, 1973: Seasonal variability of the Florida Current. *J. Mar. Res.*, **31**, 144–167.

Nowlin, W. D., 1972: Winter circulation patterns and property distributions. *Contributions on the Physical Oceanography of the Gulf of Mexico*, L. R. A. Capurro and J. L. Reid, Eds., Gulf Publ. Co., 3–51.

Nowlin, W. D., and H. J. McLellan, 1967: A characterization of the Gulf of Mexico waters. *J. Mar. Res.*, **25**, 29–59.

Sturges, W., and J. P. Blaha, 1976: A western boundary current in the Gulf of Mexico. *Science*, **192**, 367–369.

Vazquez, A. M., 1975: Currents and waters of the upper 1200 meters of the Southwestern Gulf of Mexico. Masters thesis, Texas A&M University, 99 pp.

13

Proceedings Fifth Ocean Thermal Conference 1 (of 4 volumes), Sections I-III Conf-780236, Dist. Category UC-64, III-64 - III-82.

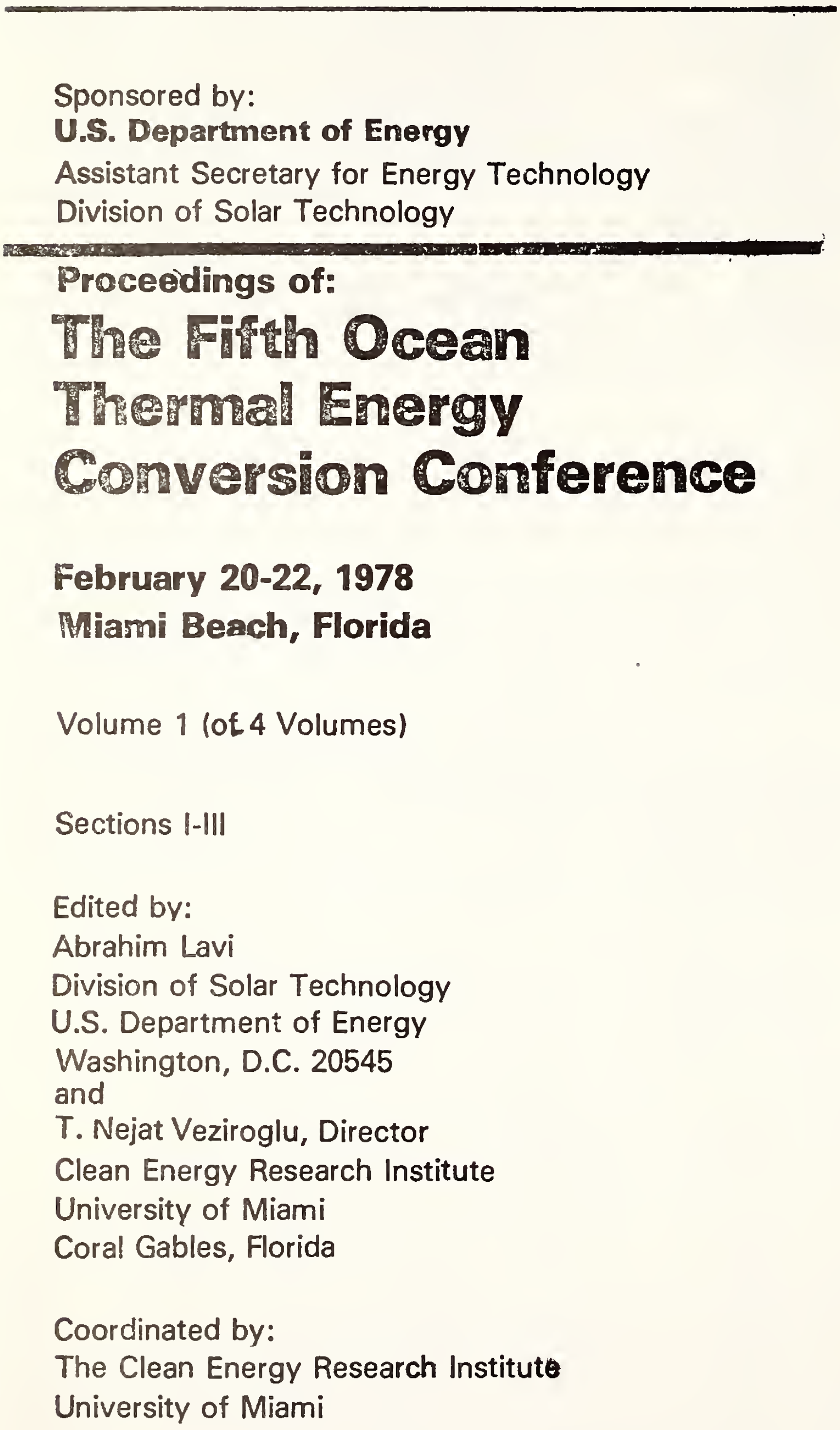

Sponsored by:
U.S. Department of Energy
Assistant Secretary for Energy Technology
Division of Solar Technology

Proceedings of:

The Fifth Ocean Thermal Energy Conversion Conference

February 20-22, 1978
Miami Beach, Florida

Volume 1 (of 4 Volumes)

Sections I-III

Edited by:
Abrahim Lavi
Division of Solar Technology
U.S. Department of Energy
Washington, D.C. 20545
and
T. Nejat Veziroglu, Director
Clean Energy Research Institute
University of Miami
Coral Gables, Florida

Coordinated by:
The Clean Energy Research Institute
University of Miami

OCEAN THERMAL AND VELOCITY CHARACTERISTICS OF THE EASTERN GULF OF MEXICO RELATIVE TO THE PLACEMENT OF AN OTEC PLANT: A PROGRESS REPORT

R. L. Molinari and J. F. Festa
Atlantic Oceanographic and Meteorology Laboratories
Miami, Florida U.S.A.

ABSTRACT

Historical temperature and current data collected in the Gulf of Mexico are reviewed to produce data representations needed in the design and placement of an OTEC plant and the evaluation of the impact of the plant on the environment. Specific products include horizontal plots of mean monthly vertical temperature differences and mixed layer depths. Regions selected by the Department of Energy a s potential OTEC sites are subdivided into smaller regions, for which annual and seasonal exceedence diagrams of these thermal properties are computed. Synoptic cruise data are reviewed to ascertain those regions which warrant further study, and to determine the cause of the variability in the smaller regions. Finally, a method to obtain crude estimates of the distribution of surface speeds is presented.

INTRODUCTION

The Gulf of Mexico is one of several regions under consideration by the Department of Energy for the placement of an OTEC plant. Several preliminary studies (Wolff (1977) [1] and Miller (1977) [2], for instance) have presented the available thermal resource in the Gulf. Based on these studies and other considerations, the Department of Energy has selected several areas in the Gulf for additional characterization studies. Figure 1 shows these areas, which hereafter will be referred to as the OTEC regions.

Mavor et al. (1977) [3] and Molinari and Festa (1978) [4] have listed some of the ocean thermal and velocity data which are necessary for the efficient design and placement of an OTEC plant. For instance, vertical temperature differences, mixed layer and thermocline depths, and vertical profiles of horizontal velocity are among these requirements. Our preliminary efforts in computing these properties from the historical data set are summarized in the following sections. In addition to providing data for design, this study is intended to provide data for impact efforts and to define environmental features which warrant future observational effort. We begin with a review of the results of past studies in the region.

RLM

HISTORICAL BACKGROUND

The OTEC regions are located on the continental slopes of the eastern and north-central Gulf of Mexico (Figure 1). The oceanic properties of these regions are determined by both periodic and aperiodic factors. For instance, the upper layer temperature and velocity fields are influenced by the seasonal changes in atmospheric variables. Although this forcing is seasonal, there is interannual variability caused by the year-to-year variability in the intensity of meteorological systems (cold fronts, for instance). The entire water column, to a depth of at least 1000m, is influenced by the Loop Current and large eddies (order of 100 km's) which separate from the Loop. The Loop and/or eddies intrude north and west into the Gulf during various times of the year replacing ambient Gulf waters with those of a tropical character.

The Loop Current has been defined as that portion of the North Atlantic gyre which extends from the Yucatan Channel to the Straits of Florida. Intense temperature gradients, associated with large speeds, facilitate the identification of the Loop on temperature maps (Figure 2). The thermal and velocity characteristics of the Loop are significantly different from those observed in non-Loop regions. The Loop is an anticyclonic (clockwise) circulation feature which transports and encompasses warm tropical waters. Upper layer isothermal surfaces can dip as much as 150m as one proceeds from outside the Loop towards the center of the gyre (Figure 2). In addition, the axis of the Loop is characterized by speeds rangirg from 1 to 2 m/s .

Leipper (1971) [5] was the first to observe an annual cycle for the northward intrusion of the Loop into the Gulf. During Leipper's survey, the Loop intruded north into the Gulf during the spring, and north and west during the summer. An eddy detached from the Loop during the late summer (Figure 2) and continued to drift west during the fall. Molinari _et al_. (1977) [6] have shown that, although this cycle occurs once a year, the intrusion and eddy break-off can occur during any season.

The maximum intrusion of the Loop also varies from year to year. During 1967, the Loop extended only to 26.5°N before an eddy separated (Figure 3), while, during 1966, the Loop had extended to 28°N. In addition, some detached eddies drift west, during 1966, for instance, while others drift southwest, during 1967. In summary, the Loop and its detached eddies have been observed in both regions shown in Figure 1 during all seasons of the year. The distinct characteristics of these features warrant detailed study since they have an impact on all aspects of the OTEC siting problem.

In the absence of the Loop/and or an eddy, the environmental conditions in the shaded areas of Figure 1 are influenced by the seasonally varying atmospheric forcing. For instance, winter cold fronts cool the surface layers, deepen the mixed layer, and induce larger currents than found in their absence. Summer heating tends to errode the mixed layer and produce a seasonal thermocline. Few data are available in the needed regions to produce an accurate representation of the ocean's response to this seasonal forcing.

HORIZONTAL PLOTS OF MEAN MONTHLY THERMAL PROPERTIES

We prepared horizontal plots of several design requirements to identify areas which might require further study, to provide data representations which might be useful in impact studies, and to provide verification for the results obtained by considering smaller regions. The averages were computed from data collected from 1965 through 1976. Although the data in any one subregion might be sparse and therefore suspect, some verification is possible if these results are consistent with the results obtained from surrounding subregions.

All averages referred to in this paper are obtained in the following way. A mean value is computed for each month and year for the region of interest. These mean values are then averaged for the time period of interest. For example, mean monthly values for April are obtained by averaging the mean values of April (1965), April (1966),...April (1976). This procedure, which we shall refer to as the month/year class method, removes biasing caused by excessive sampling in any particular month/year.

Figure 4 is a plot of the mean annual temperature distribution at 1000m obtained by averaging data in 1° x 1° squares. The largest gradients and variability occur in the region of the Loop Current where synoptic representations indicate that, at 1000m, in the center of the Loop the temperature can be as high as 6°C. However, in the OTEC regions the range of temperatures at 1000M is quite small. Therefore, only a mean annual temperature distribution will be used to compute vertical differences. This assumption will introduce a maximum error in the difference computations of about 0.5°C.

Mean monthly sea surface temperature (SST) maps for four months are given in Figure 5. The effect of the Loop Current is obvious in these charts, causing warmer SST's in regions where the Loop is found. Thus, when the Loop is well developed or an eddy appears in the winter, the surface layers are considerably warmer than they would be in the absence of these features. The thermal resource can increase some 1°C to 2°C in these instances (Figure 6). However, since the Loop seems to intrude during all seasons, with a possible preference in the summer, the occurence of deep intrusions in the winter is not assured.

Mean monthly mixed layer depth distributions are also computed (Figure 7). Outside the Loop Current, the mixed layer deepens in the winter and becomes more shallow in the summer. However, this annual cycle is perturbed by the Loop Current and detached eddies. Along the edge of the Loop or eddy, isothermal surfaces rise dramatically and can reduce the mixed layer depth below that found in the absence of the Loop. Thermocline depth charts are also to be produced for the final report.

SYNOPTIC REPRESENTATIONS OF THE THERMAL PROPERTIES

For considerations in this discussion, synoptic data-sets will be those in which the data were collected over intervals less than one month.

Figure 8 is a plot of the position of the 150m contour of the 20°C isothermal surface obtained from data collected in July and August. Molinari et al. (1977) [6] and others have used this contour to delineate the axis of the Loop Current and detached eddies. These types of synoptic data representations provide information on the representativeness of mean monthly plots, and the cause of variability in 1° x 1° square averages.

The large variability in the position of the Loop Current during July-August and other months (not shown) can cause large variability in the 1° x 1° square data (see Wolff, 1977) [1]. The large spatial temperature gradients associated with the Loop and detached eddies will increase the variability in a 1° square if either feature is present. In addition, since there is large year-to-year variability in the position of the Loop/eddy (Figure 8), a type of temporal variability is also introduced into the 1° averages.

We are currently generating a monthly time history of the Loop Current from 1965 through 1976 to evaluate the cause of variability in the OTEC regions. If the variability in these regions is caused by the spatial variability inherent in the Loop Current/eddy, an appropriate site to take advantage of the Loop could be selected. If the variability is caused by year-to-year differences in winter cooling, for instance, other sites might be more desirable.

The mean monthly charts suggest some features which deserve further consideration when studying the synoptic charts. For instance, the SST charts (Figure 5) suggest that the DeSoto Canyon is a region of northward advection of warmer water during the winter. Preliminary analysis of synoptic SST charts suggests that this feature is real and not merely an artifact of the averaging process. Thus, the water column in the vicinity of the topographic feature could have desirable properties for the siting of an OTEC plant. In addition, an area of upwelling off the coast of Florida appears on both average and synoptic charts. Both features are being studied.

THERMAL PROPERTIES BY SUBREGIONS

The OTEC regions shown in Figure 1 are subdivided into smaller subregions which are given in Figure 9. These subregions were selected on the basis of their bottom topography characteristics and thermal properties, with the objective of minimizing the variability in a subregion, while keeping the subregion large enough to insure sufficient data coverage. If the objective of regionally uniform ocean properties is realized, it will facilitate the mechanics of the observational program, since only a few carefully positioned measurement stations need be occupied to characterize the conditions over a larger area.

Exceedence diagrams, such as given in Figures 10 and 11 for the annual sea surface temperature distribution, are being produced for each region for vertical temperature differential, mixed layer depth, and thermocline depth. These plots will also be generated for seasonal time increments. The data do not warrant a finer time increment.

SURFACE CURRENT SPEEDS

Figure 12 gives several examples of the speed along the Loop Current. The speeds were directly measured using Lagrangian drifters tracked by ship. The speeds range from 1.2 to 1.4 m/s, found along the northern edge of the Loop, up to 2m/s along the eastern flank of the Loop Current. The observations were taken in three different seasons, and the speeds are very similar. An average distribution of the speed along the axis will be developed from these data. Cross-stream geostrophic velocity sections indicate the core of the maximum flow is approximately 100 km wide, with speeds dropping off from the core (Molinari (1977), for instance) [7]. This information can be used to ascertain the region of influence of the Loop and/or eddy, as follows. The time series of monthly Loop Current positions described previously will be used to center the speed axis. Speeds along the axis are assumed constant and are determined from the Lagrangian speeds. An assumed cross-stream speed distribution will be input, and the region of the Loop Current/eddy influence will be computed on a monthly basis. A time series will then be developed to give a crude estimate of surface speeds on a 1° x 1° grid in those areas where the Loop is found.

RLM

REFERENCES

1. Wolff, P. (1977) OTEC Thermal Resource Report for Central Gulf of Mexico, Ocean Data Systems, Inc., Rept. to ERDA, contract # EC-77-C-01-4028.

2. Miller, A. R. (1977) A Preliminary Report on Ranges and Extremes of the Natural Environment. Woods Hole Ocn. Inst. Tech. Rept., WHOI-77-A, 73 pp.

3. Mavor, J. S., H. O. Berteaux, J. R. McCullough, A. R. Miller, S. W. Smith (1977) Interpretation of Oceanographic Data for OTEC Design. Woods Hole Ocn. Inst. Tech. Rept., WHOI-77-65, 51 pp.

4. Molinari, R. L. and J. F. Festa (1978) Ocean Thermal and Current Velocity Data Requirements for Design of an OTEC Demonstration Plant. NOAA Tech. Memo. ERL AOML-30, 18 pp.

5. Leipper, D. F. (1970) A Sequence of Current Patterns in the Gulf of Mexico. J. Geophys. Res., 75; 637-657.

6. Molinari, R. L., S. Baig, D. W. Behringer, G. A. Maul, and R. Legeckis (1977) Winter Intrusions of the Loop Current. Science, 198, 505-506.

7. Molinari, R. L. (1977) Synoptic and Mean Monthly 20°C Topographies in the Eastern Gulf of Mexico. NOAA Tech. Memo. ERL AOML-27, 33 pp.

RLM

FIGURE LEGEND

Figure 1. Regions defined by the Department of Energy for further study, based on their thermal resources.

Figure 2. The topography of the 20°C isothermal surface during May 1973 (left panel) and July 1973 (right panel). The Loop Current and detached eddy are located in the regions of most intense temperature gradients.

Figure 3. The topography of the 20°C isothermal surface during two years of different maximum Loop Current intrusion.

Figure 4. Mean annual temperature distribution at 1000m. The numbers on each grid point indicate the number of months/years (see text) of data within each 1° x 1° square.

Figure 5. Mean monthly sea surface temperature maps for four months. The numbers on each grid point indicate the number of years of data within each 1° x 1° square.

Figure 6. Temperature differences between the sea-surface and 1000m, using the sea-surface temperature on Figure 5 and the constant 1000m temperature distribution given on Figure 4.

Figure 7. Mean monthly mixed layer depth distributions computed only from mechanical bathythermograph (MBT) data. The mixed layer depth criterion is $\Delta T/\Delta Z \leq .1$°C/10m.

Figure 8. The position of the 150m contour of the 20°C isothermal surface obtained from data collected in July and August. This contour is approximately coincident with the axis of Loop Current/detached eddy.

Figure 9. Subregions of the OTEC regions given in Figure 1.

Figure 10. Annual exceedence diagrams for sea surface temperature in subregions 1 through 6.

Figure 11. Same as Figure 10, except for subregions 7 through 12.

Figure 12. Directly measured sea surface speeds along the axis of the Loop Current.

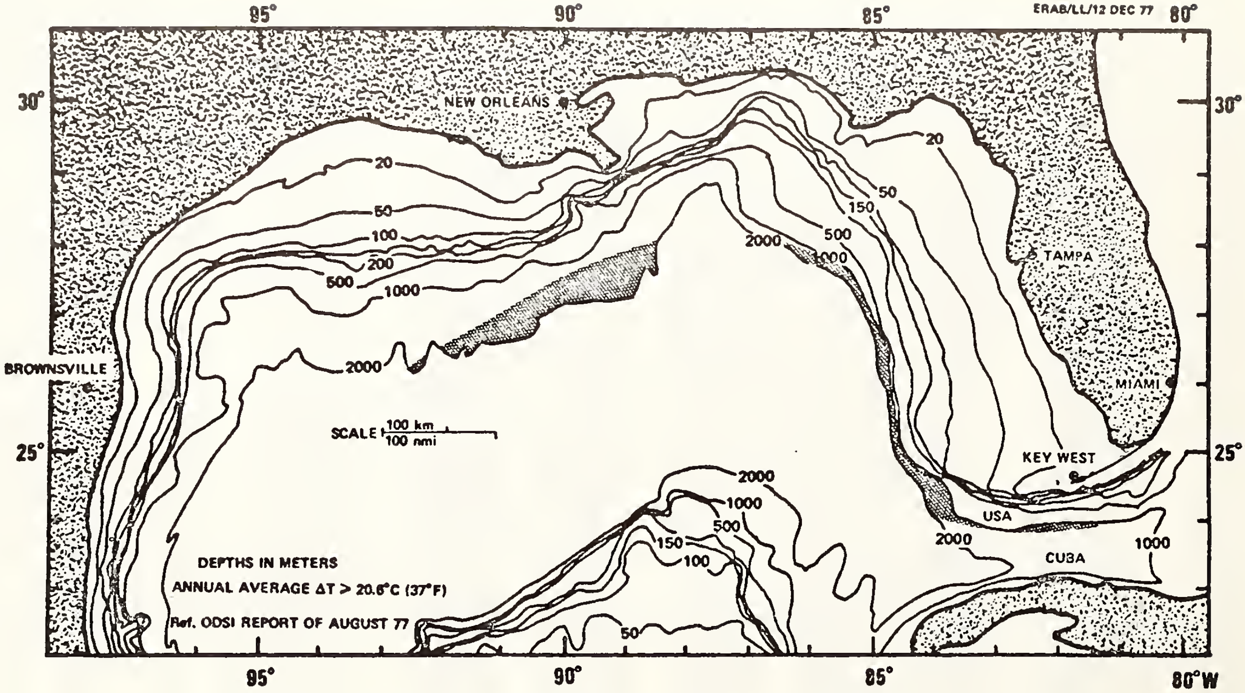
ERAB/LL/12 DEC 77
95°
90°
85°
80°
30°
25°
25°N
80°W
NEW ORLEANS
BROWNSVILLE
TAMPA
MIAMI
KEY WEST
USA
CUBA
20
50
100
150
200
500
1000
2000
SCALE 100 km 100 nmi
DEPTHS IN METERS
ANNUAL AVERAGE ΔT > 20.6°C (37°F)
Ref. ODSI REPORT OF AUGUST 77

OTEC RESOURCE REGION - GULF OF MEXICO

Figure 1. Regions defined by the Department of Energy for further study, based on their thermal resources.

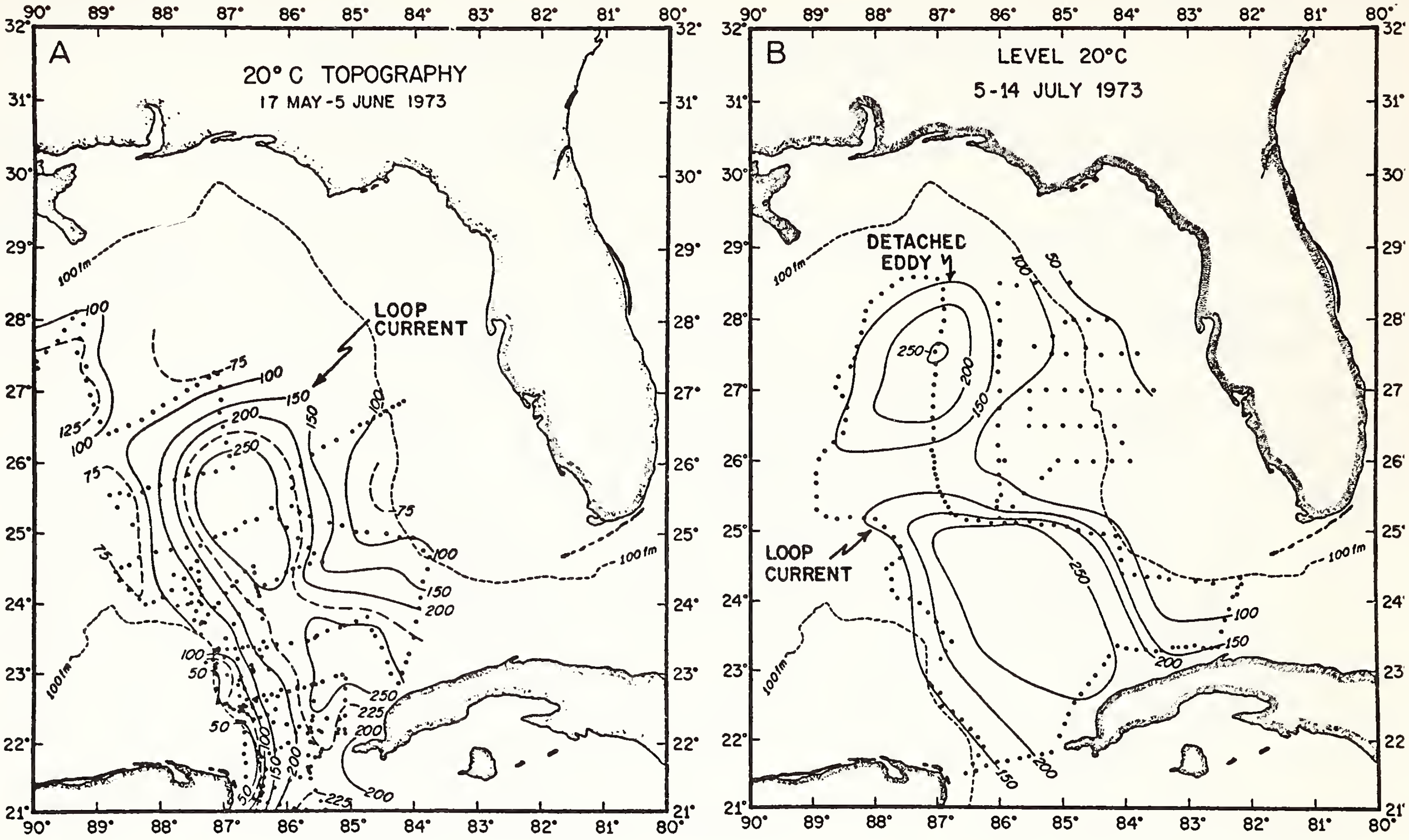
A
20° C TOPOGRAPHY
17 MAY-5 JUNE 1973
LOOP CURRENT
100fm
B
LEVEL 20°C
5-14 JULY 1973
DETACHED EDDY
LOOP CURRENT
100fm
90°
89°
88°
87°
86°
85°
84°
83°
82°
81°
80°
32°
31°
30°
29°
28°
27°
26°
25°
24°
23°
22°
21°

Figure 2. The topography of the 20°C isothermal surface during May 1973 (left panel) and July 1973 (right panel). The Loop current and detached eddy are located in the regions of most intense temperature gradients.

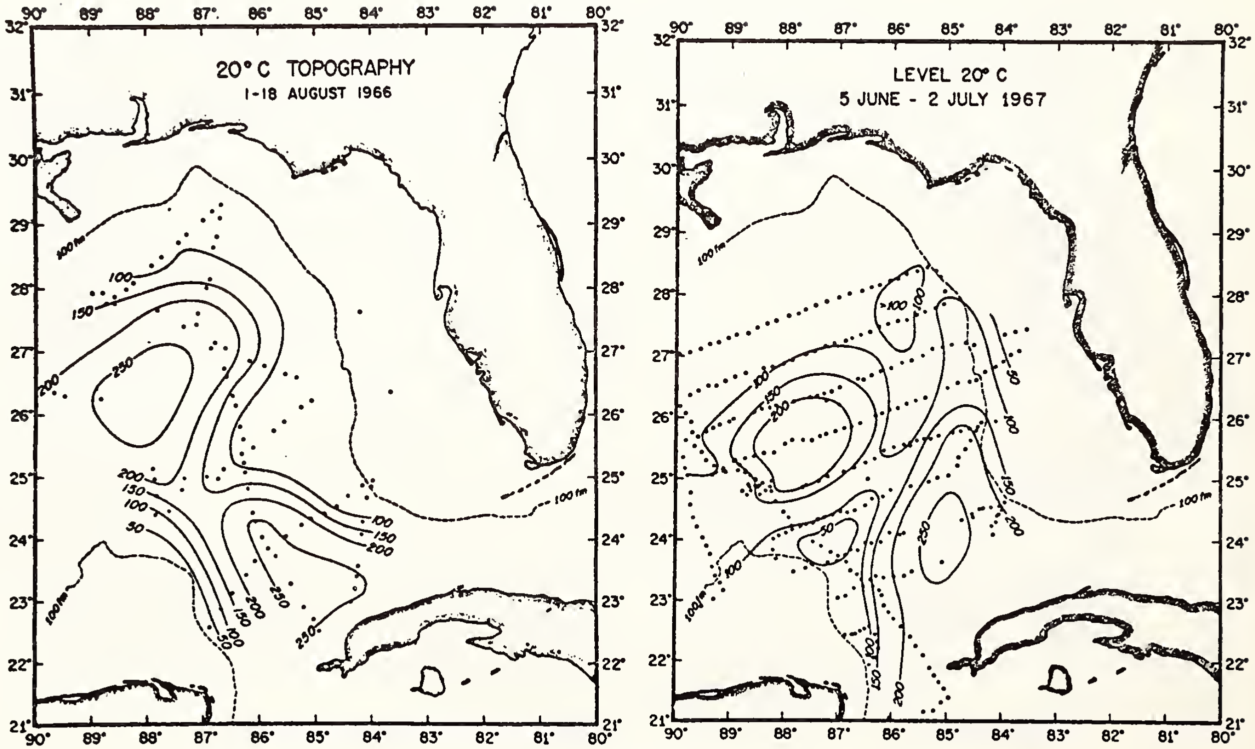
20° C TOPOGRAPHY
1-18 AUGUST 1966
LEVEL 20° C
5 JUNE - 2 JULY 1967
100 fm
50
100
150
200
250
90°
89°
88°
87°
86°
85°
84°
83°
82°
81°
80°
32°
31°
30°
29°
28°
27°
26°
25°
24°
23°
22°
21°

Figure 3. The topography of the 20 C isothermal surface during two years of different maximum Loop Current intrusion.

MEAN ANNUAL TEMPERATURE AT 1000m

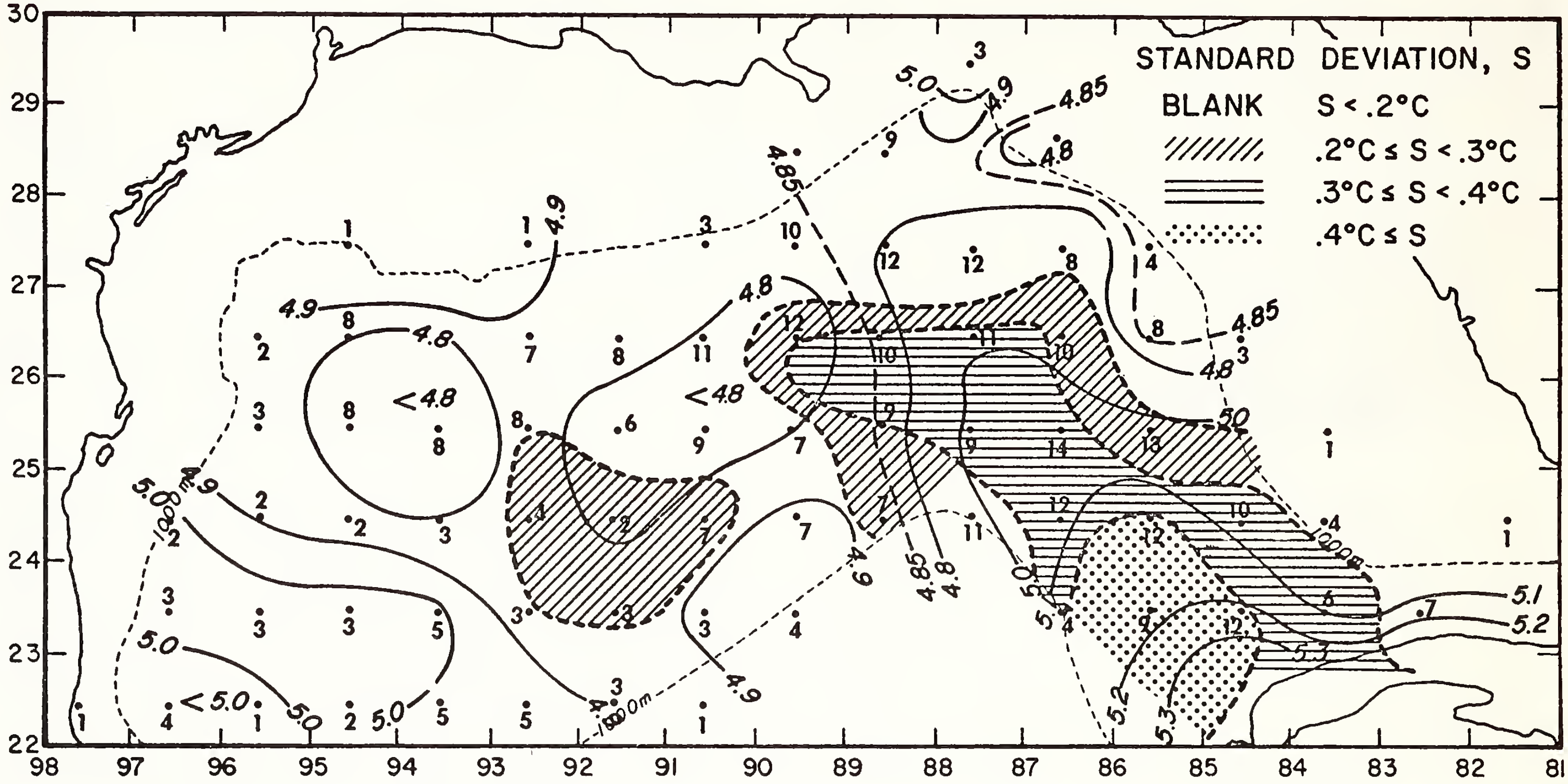
STANDARD DEVIATION, S
BLANK S < .2°C
▨ .2°C ≤ S < .3°C
☰ .3°C ≤ S < .4°C
░ .4°C ≤ S
30
29
28
27
26
25
24
23
22
98
97
96
95
94
93
92
91
90
89
88
87
86
85
84
83
82
81
4.9
4.8
<4.8
4.85
5.0
5.1
5.2
5.3
<5.0
1000m

Figure 4. Mean annual temperature distribution at 1000m. The number on each grid point indicate the number of months/years (see text) of data within each 1° x 1° square.

RLM

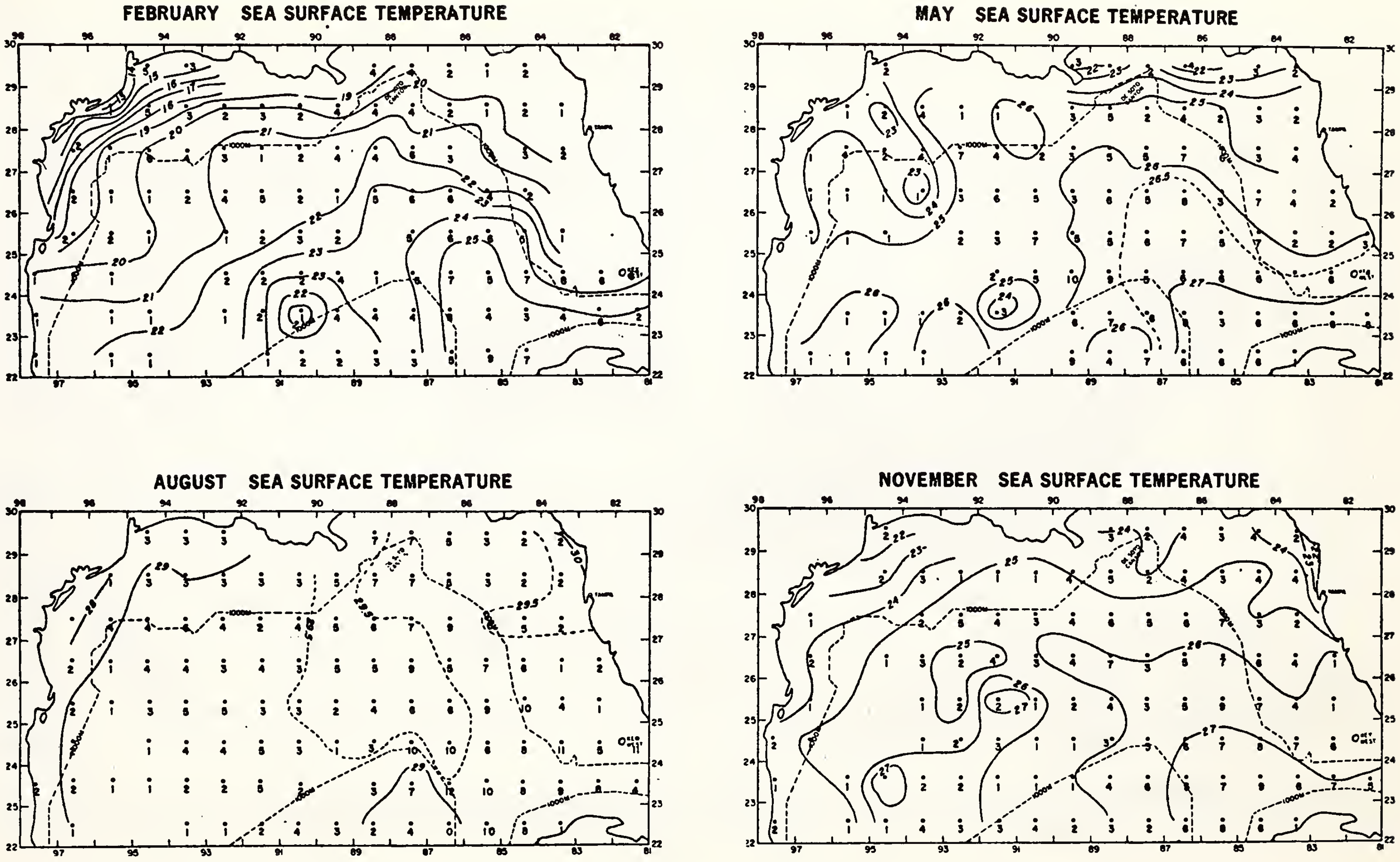

FEBRUARY SEA SURFACE TEMPERATURE

MAY SEA SURFACE TEMPERATURE

AUGUST SEA SURFACE TEMPERATURE

NOVEMBER SEA SURFACE TEMPERATURE

Figure 5. Mean monthly sea surface temperature maps for four months. The numbers on each grid point indicate the number of years of data within each 1° x 1° square.

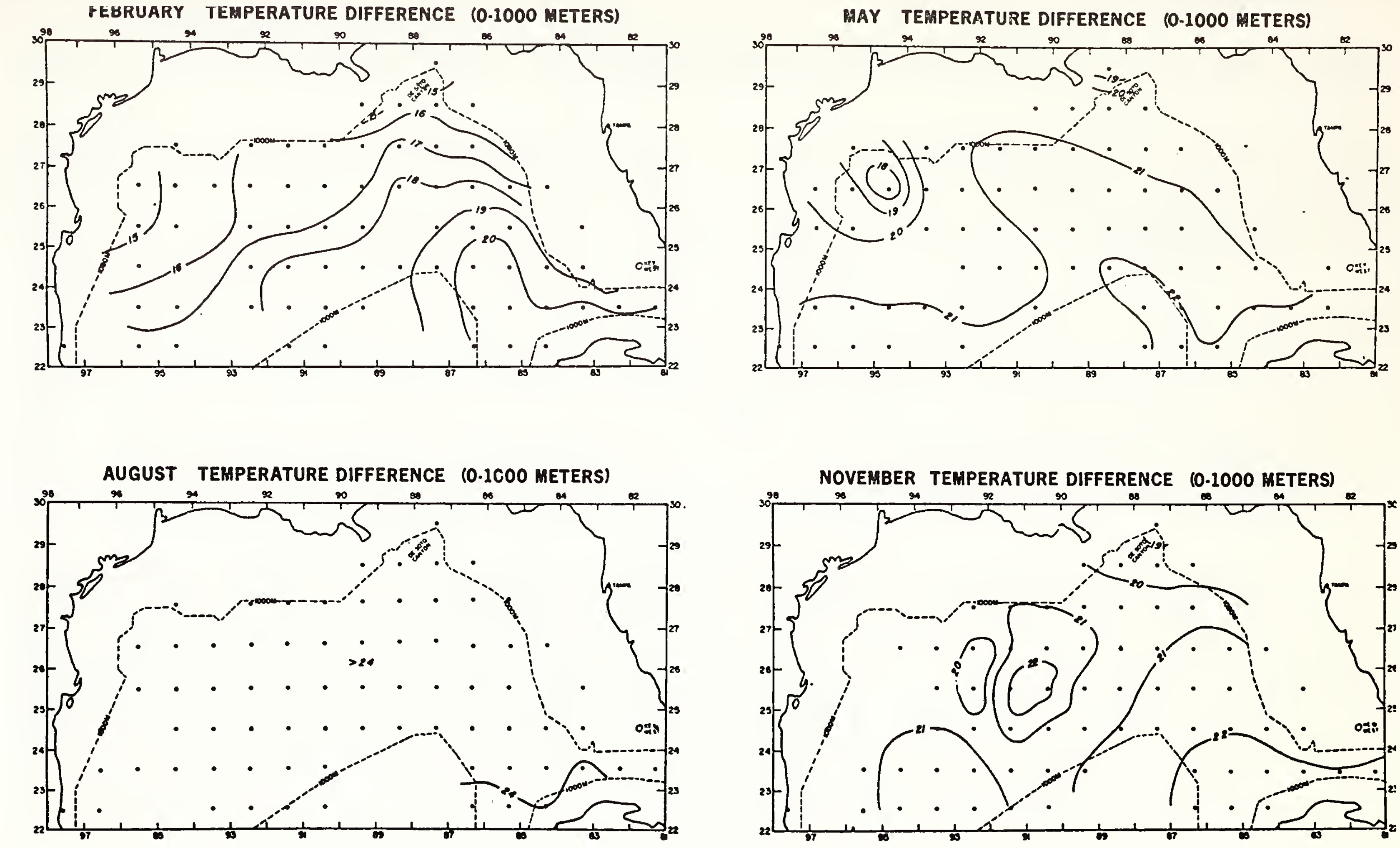

FEBRUARY TEMPERATURE DIFFERENCE (0-1000 METERS)
MAY TEMPERATURE DIFFERENCE (0-1000 METERS)
AUGUST TEMPERATURE DIFFERENCE (0-1000 METERS)
NOVEMBER TEMPERATURE DIFFERENCE (0-1000 METERS)
98
96
94
92
90
88
86
84
82
97
95
93
91
89
87
85
83
81
30
29
28
27
26
25
24
23
22
15
16
17
18
19
20
21
22
24
>24
1000M
DE SOTO CANYON
TAMPA
KEY WEST

Figure 6. Temperature differences between the sea-surface and 1000m, using the sea-surface temperature on Figure 5 and the constant 1000m temperature distribution given on Figure 4.

RLM

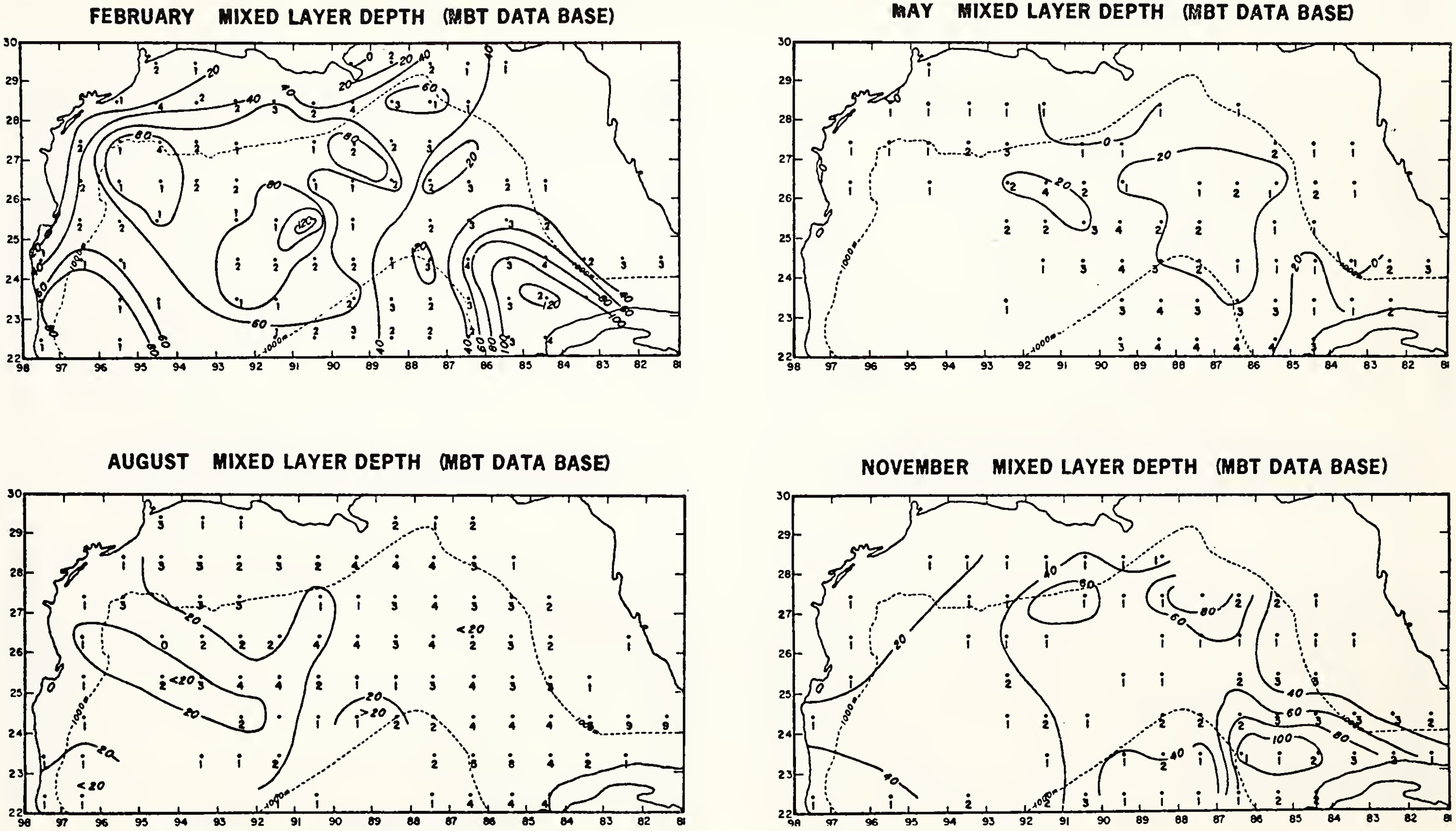

FEBRUARY MIXED LAYER DEPTH (MBT DATA BASE)

MAY MIXED LAYER DEPTH (MBT DATA BASE)

AUGUST MIXED LAYER DEPTH (MBT DATA BASE)

NOVEMBER MIXED LAYER DEPTH (MBT DATA BASE)

30
29
28
27
26
25
24
23
22
98
97
96
95
94
93
92
91
90
89
88
87
86
85
84
83
82
81
1000m
20
40
60
80
100
120
<20
>20

Figure 7. Mean monthly mixed layer depth distributions computed only from mechanical bathythermograph (MBT) data. The mixed layer depth criterion is ΔT/ΔZ ≤ .1°C/10m.

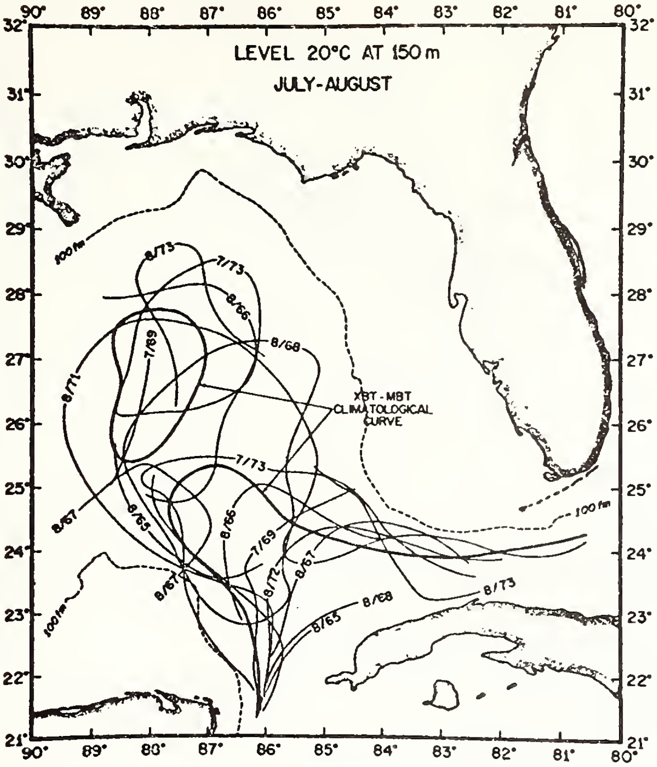
LEVEL 20°C AT 150 m
JULY-AUGUST
90°
89°
88°
87°
86°
85°
84°
83°
82°
81°
80°
32°
31°
30°
29°
28°
27°
26°
25°
24°
23°
22°
21°
100 fm
8/73
7/73
8/66
8/68
7/89
8/71
XBT-MBT CLIMATOLOGICAL CURVE
7/73
8/67
8/65
8/66
7/69
8/67
8/72
8/67
8/73
8/68
8/65
100 fm
100 fm

Figure 8. The position of the 150m contour of the 20°C isothermal surface obtained from data collected in July and August. This contour is approximately coincident with the axis of Loop Current/detached eddy.

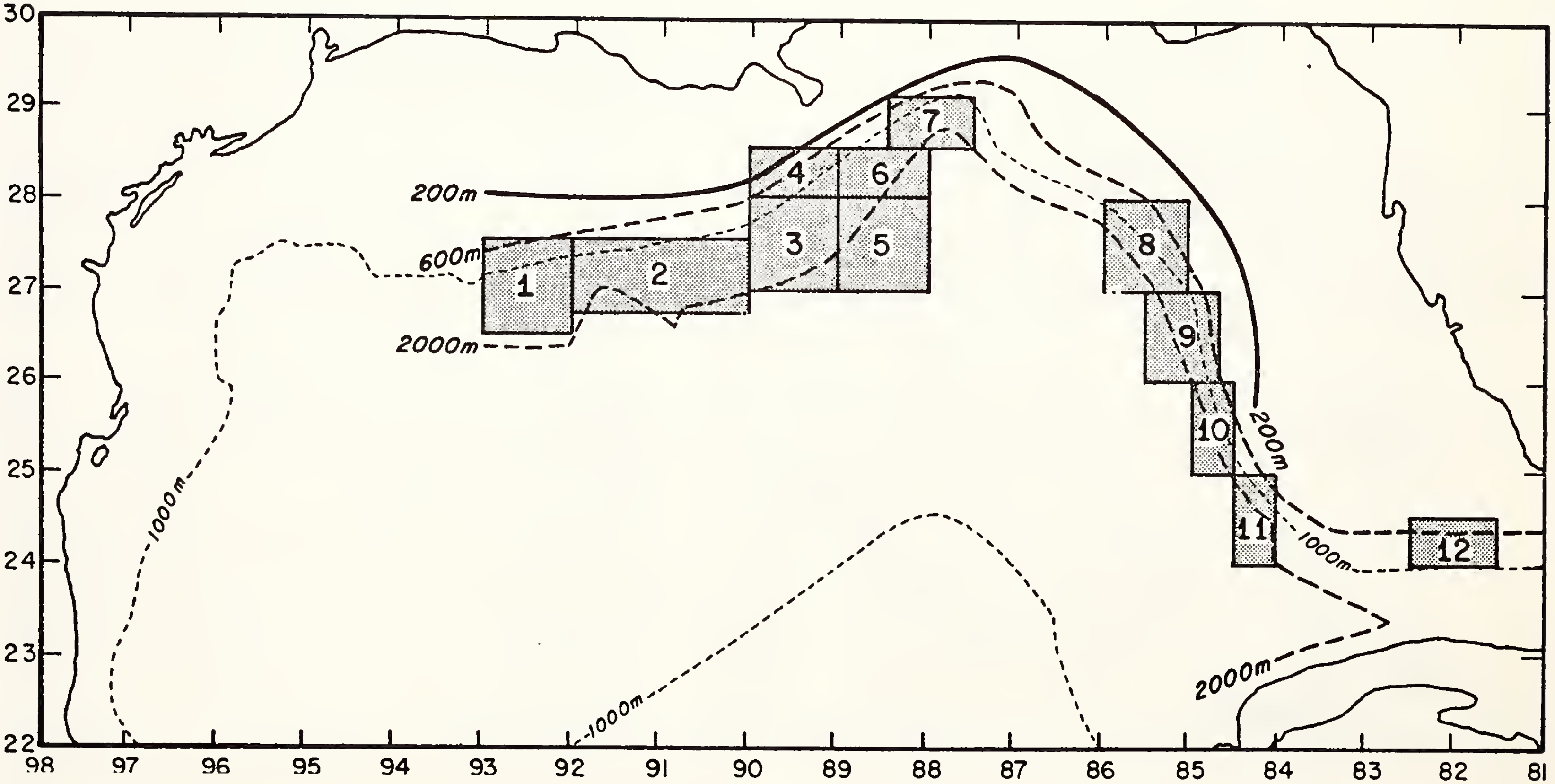
30
29
28
27
26
25
24
23
22
98
97
96
95
94
93
92
91
90
89
88
87
86
85
84
83
82
81
1
2
3
4
5
6
7
8
9
10
11
12
200m
600m
2000m
1000m
200m
1000m
2000m
1000m
1000m

Figure 9. Subregions of the OTEC regions given in Figure 1.

RLM

ANNUAL

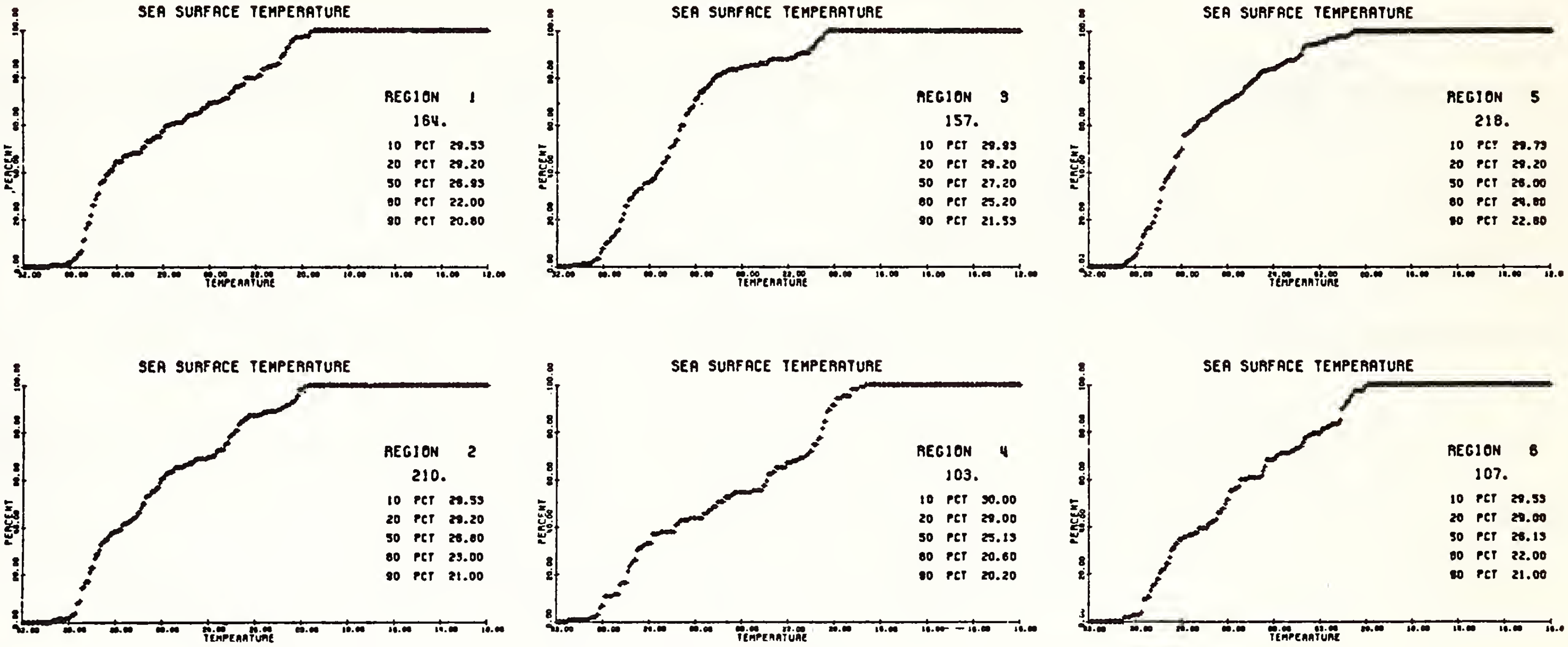

Figure 10. Annual exceedence diagrams for sea surface temperature in subregions 1 through 6.

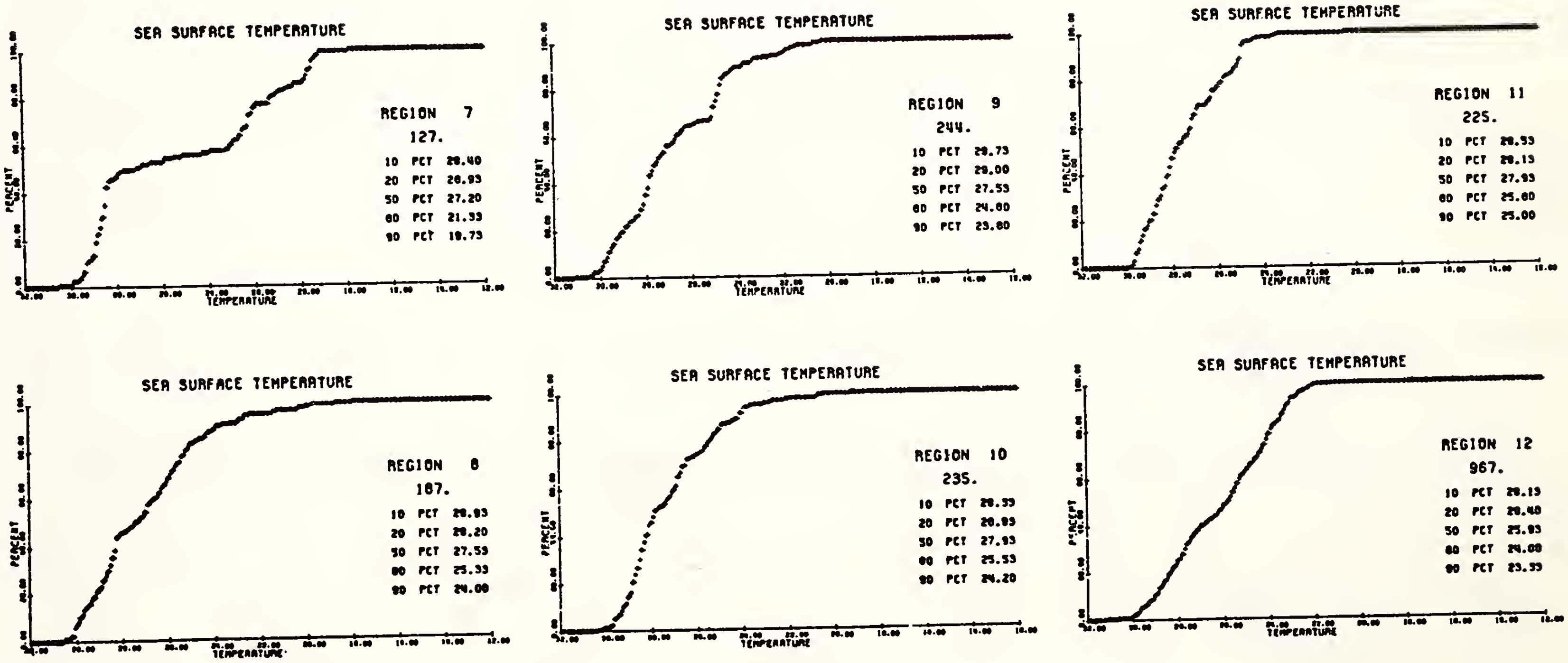

Figure 11. Same as Figure 10, except for subregions 7 through 12.

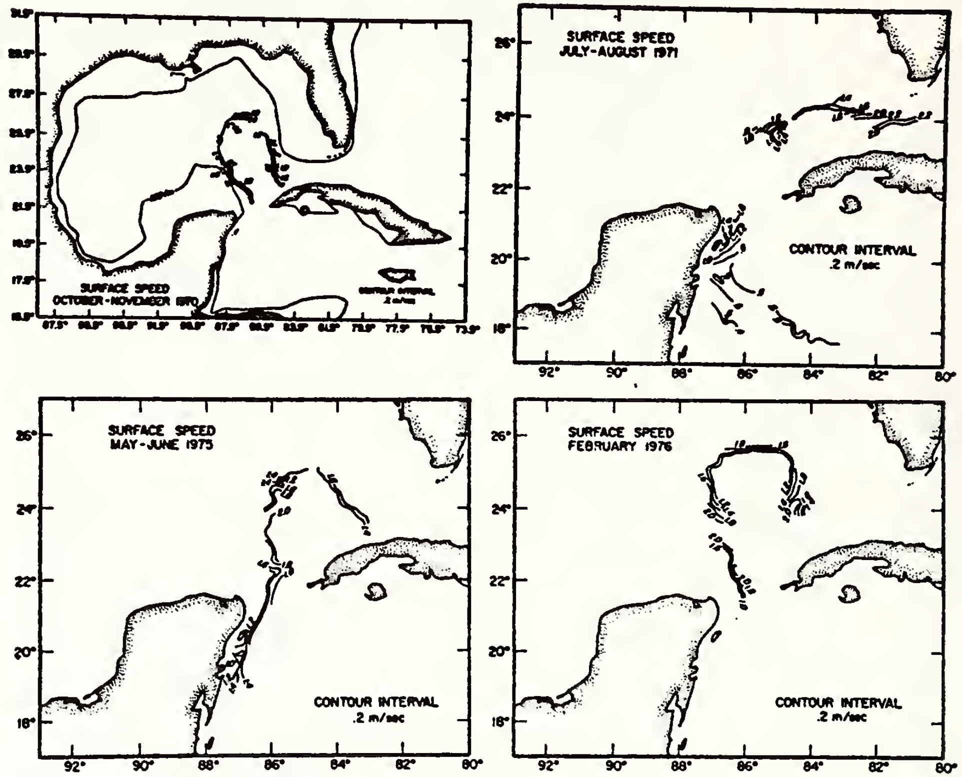
SURFACE SPEED
OCTOBER-NOVEMBER 1970
CONTOUR INTERVAL
.2 m/sec
SURFACE SPEED
JULY-AUGUST 1971
CONTOUR INTERVAL
.2 m/sec
SURFACE SPEED
MAY-JUNE 1975
CONTOUR INTERVAL
.2 m/sec
SURFACE SPEED
FEBRUARY 1976
CONTOUR INTERVAL
.2 m/sec
26°
24°
22°
20°
18°
92°
90°
88°
86°
84°
82°
80°

Figure 12. Directly measured sea surface speeds along the axis of the Loop Current.

RLM

Proceedings Ocean Thermal Energy Conversion (OTEC) Biofouling and Corrosion Symposium, PNL-SA-7115, 413-422.

OCEAN THERMAL PROPERTIES IN RELATION TO THE BIOFOULING AND CORROSION EXPERIMENT IN THE GULF OF MEXICO

R. L. Molinari and J. F. Festa
National Oceanic and Atmospheric Administration
Atlantic Oceanographic and Meteorological Laboratories
15 Rickenbacker Causeway, Virginia Key
Miami, Florida 33149

ABSTRACT

Ocean thermal properties at a Gulf of Mexico biofouling and corrosion test site are reviewed in relation to their potential effects on biofouling rates. Primary biological differences in water masses affecting the site are discussed. Deep basin waters have less productivity, greater species diversity, and different dominant species than shelf and estuarine waters. Thermal characteristics of various water masses are included to aid interpretation of biofouling results. Frequency of occurrence of several events affecting the site are also given. Loop current eddies which transport deep basin chemical and biological species to the site have been observed from 2 to 4 times in 10 different yr. A table is presented showing number of monthly occurrences of tropical storms and hurricanes which can upwell deep chemical and biological species to the surface.

INTRODUCTION

Biofouling and corrosion experiments are underway or being planned at several potential Ocean Thermal Energy Conversion (OTEC) sites. One experiment is located in the Gulf of Mexico, a region where oceanic conditions can change rapidly. Since biofouling and corrosion rates may vary in such a region, they must be defined in relation to environmental conditions. Preliminary characterization of thermal and circulation properties at the site utilized archived data to provide background information for investigators in biofouling, corrosion, and other OTEC programs.

This paper discusses some initial results from the site characterization study. Circulation in the Gulf of Mexico, in general, and the OTEC site in particular, are reviewed. We will emphasize those events having relevance to the biofouling/corrosion effort. Relevance will be demonstrated through presentation of some biological implications of these events.

CIRCULATION AND WATER MASS BACKGROUND

The Gulf of Mexico is a semi-enclosed basin with openings at the Yucatan Straits and the Straits of Florida. The Yucatan Straits provides an entrance for waters from the Caribbean Sea and Atlantic Ocean, while the Straits of Florida provides an exit for Gulf waters and possibly an entrance for Atlantic waters. A proposed Gulf of Mexico OTEC site is at 29°N latitude and 88°W longitude on the western edge of De Soto Canyon (Figure 1, Uchupi, 1971).

Most oceanographic current studies assume that there is a balance on the horizontal plane between Coriolis force and the pressure gradient force. Furthermore, vertical current shear is proportional to the horizontal gradient of mass density. In strong current regions, temperature distribution in the upper layers is a good approximation to the density field. Thus, one can estimate current position from temperature surfaces.

Robert H. Gray, Editor

Sponsored by
United States Department of Energy
Division of Solar Energy
Washington, D.C. and
Pacific Northwest Laboratory
Richland, Washington

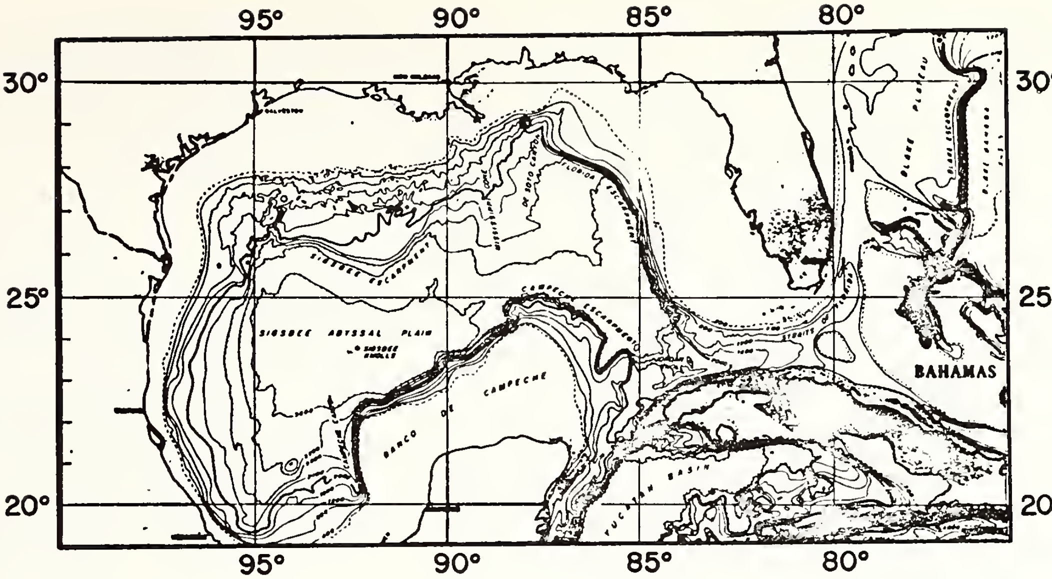
95°
90°
85°
80°
30°
25°
20°
SIGSBEE ESCARPMENT
SIGSBEE ABYSSAL PLAIN
SIGSBEE KNOLLS
CAMPECHE ESCARPMENT
BANCO DE CAMPECHE
FLORIDA ESCARPMENT
DE SOTO CANYON
YUCATAN BASIN
STRAITS
BAHAMAS

FIGURE 1. Bottom Topography of the Gulf of Mexico as Given by Uchupi (1971) Depths are in meters The site proposed for a biofouling and corrosion experiment is at 88°W 29°N

The topography of the 20°C isothermal surface observed in July and August 1971 is shown in Figure 2. The core of the intensest flow, easily discerned by its associated intense gradients, is about coincident with the 150 m contour of the 20°C surface (Molinari, 1977). Names of principal currents in the region are also given in Figure 2.

Water masses, at the Yucatan Strait identified by Wust (1964), are shown in Figure 3 on a Temperature-Salinity (T-S) plot. Subtropical Underwater (SUW), characterized by a salinity maximum at 22.5°C, is found beneath the surface layers. The water mass is formed in the Atlantic where evaporation strongly exceeds precipitation (Worthington,

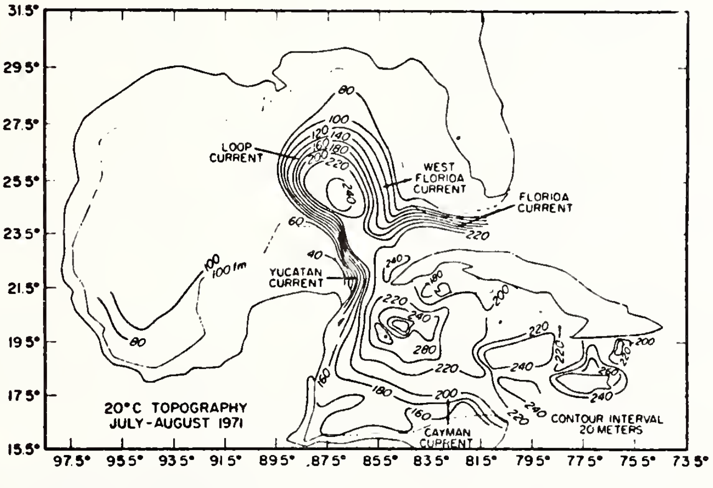
31.5°
29.5°
27.5°
25.5°
23.5°
21.5°
19.5°
17.5°
15.5°
97.5°
95.5°
93.5°
91.5°
89.5°
87.5°
85.5°
83.5°
81.5°
79.5°
77.5°
75.5°
73.5°
LOOP CURRENT
WEST FLORIDA CURRENT
FLORIDA CURRENT
YUCATAN CURRENT
CAYMAN CURRENT
100 fm
20°C TOPOGRAPHY
JULY-AUGUST 1971
CONTOUR INTERVAL 20 METERS
40
60
80
100
120
140
160
180
200
220
240
260

FIGURE 2. The 20°C Topography as Determined from Data Collected in July and August 1971 The 100 fathom isobath is also shown

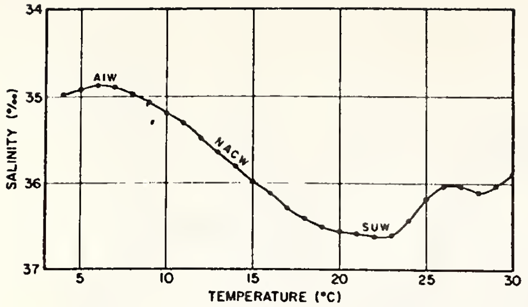

FIGURE 3. The Average Temperature-Salinity Relation Computed from a Historical Data Set Collected at the Yucatan Straits All salinity values within a 1°C temperature range were averaged to obtain a mean salinity for temperature at the center of the interval Water masses noted are Subtropical Underwater (SUW), North Atlantic Central Water (NACW), and Antarctic Intermediate Water (AIW)

1976). The straight line portion of the curve between about 10°C and 17°C (Figure 3) is North Atlantic Central Water (NACW). The salinity minimum at 6°C is a remnant of Antarctic Intermediate Water (AIW) formed at the Antarctic Convergence Zone. Higher salinity waters with temperatures below 5°C could be remnants of Mediterranean or North Atlantic Deep Water (NADW) (Ichiye and Sudo, 1971). In addition to characteristic T-S relations, the water masses also have identifiable oxygen and nutrient properties (Cummings et al., 1978). Figure 4 shows depths where some of the water masses can occur.

Cochrane (1963, 1966, 1967) reported extensively on flow through the Yucatan Straits and suggested an annual cycle with strongest surface currents observed in May and June, and weakest in November. Schlitz (1973) found an average geostrophic transport of 30 x 10^6 m^3/sec, relative to the ocean bottom at three April 1970 transects.

The northern extension of the Yucatan Current is the Loop Current, so named because of its loop-like path over the eastern Gulf basin. An annual cycle, proposed to describe the intrusion of the Loop Current (Leipper, 1970), is characterized by a spring intrusion northward into the Gulf, a fall spreading of the current or an eddy detachment toward the west, and minimum intrusion in winter. Figure 5 shows a portion of the data set considered by Leipper (1970). Recent data suggest there is considerable variability in occurrence of a particular phase of the cycle. For example, during 2 of the past 3 yrs, deep loop intrusions and eddy break-offs were observed in winter (Molinari et al., 1977).

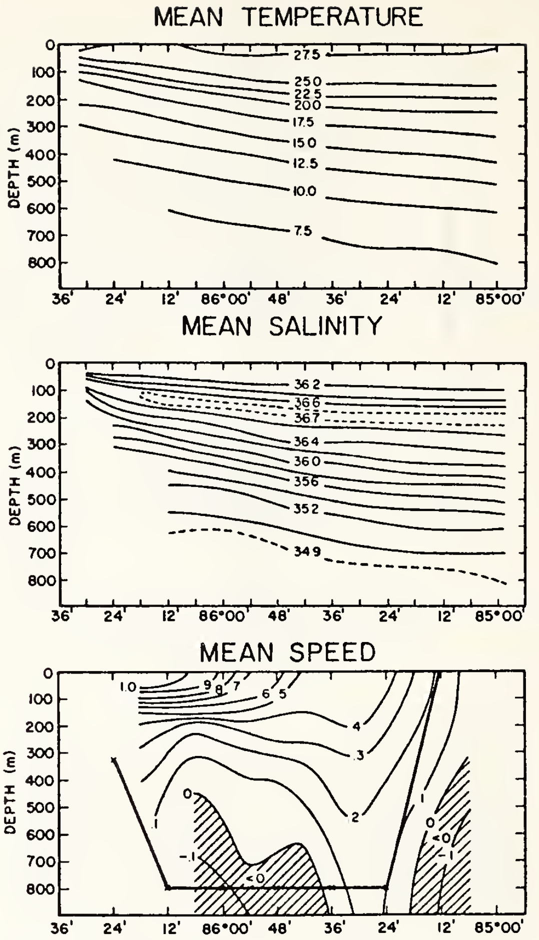

FIGURE 4. Average Temperature, Salinity and Speed Sections Across the Yucatan Straits Observed in May 1972 Mean values were obtained by averaging all data over 12 min bands of longitude Geostrophic speeds were computed relative to absolute surface speeds determined from a surface drifter-type instrument. Data from 15 or more stations were available above the solid line

The distinctive properties of waters entering the Gulf through the Yucatan Straits which are transported by eddies include the SUW salinity maximum (S>36.5°/oo) and the

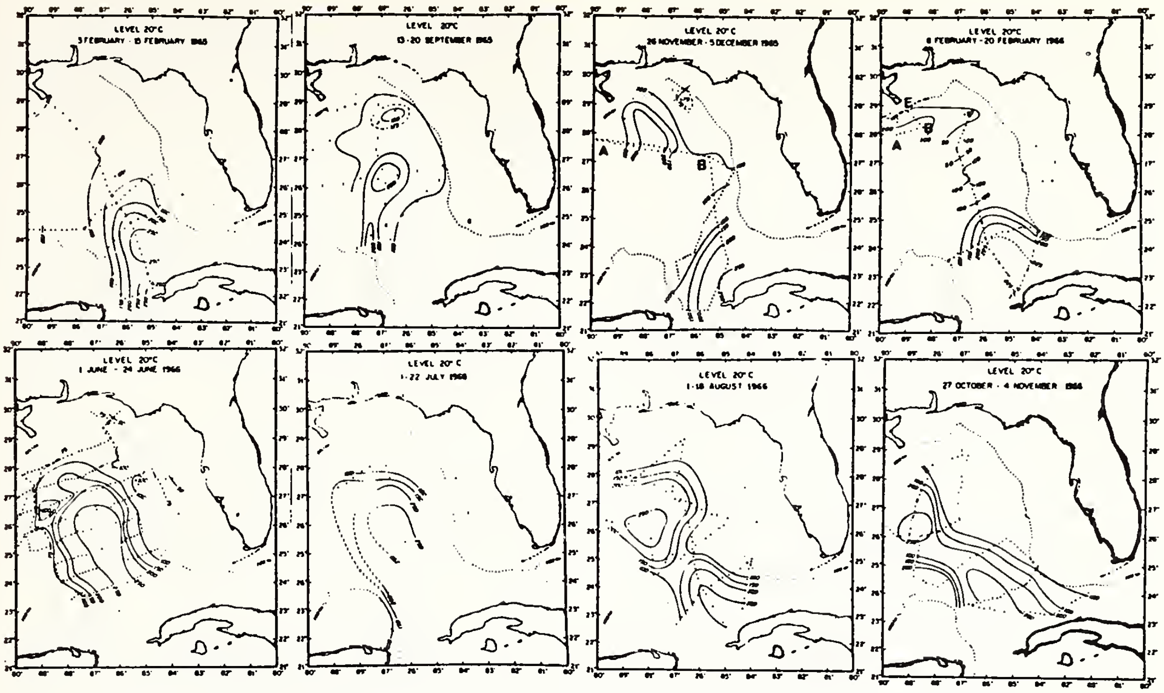
LEVEL 20°C 3 FEBRUARY - 15 FEBRUARY 1965
LEVEL 20°C 13-20 SEPTEMBER 1965
LEVEL 20°C 26 NOVEMBER - 5 DECEMBER 1965
LEVEL 20°C 6 FEBRUARY - 20 FEBRUARY 1966
LEVEL 20°C 1 JUNE - 24 JUNE 1966
LEVEL 20°C 1-22 JULY 1966
LEVEL 20°C 1-18 AUGUST 1966
LEVEL 20°C 27 OCTOBER - 4 NOVEMBER 1966
A
B
E

FIGURE 5. Portion of the Data Set Considered by Leipper (1970) to Demonstrate Instrusion of the Loop Current during 1965-1966

O_2 minimum (O_2<2.75 ml/l) separating NACW and AIW. The properties are evident in the salinity and oxygen section (Figure 6b) across 2 detached eddies. The position of these eddies are shown on the dynamic topography map for September 1965 (Figure 6a).

Circulaton in the northeastern Gulf of Mexico is a complex combination of wind drift, geostrophic flow, tidal currents, and motions induced by shelf waves and eddies. Hydrography is influenced by river outflow, Loop Current eddies, seasonal effects, and

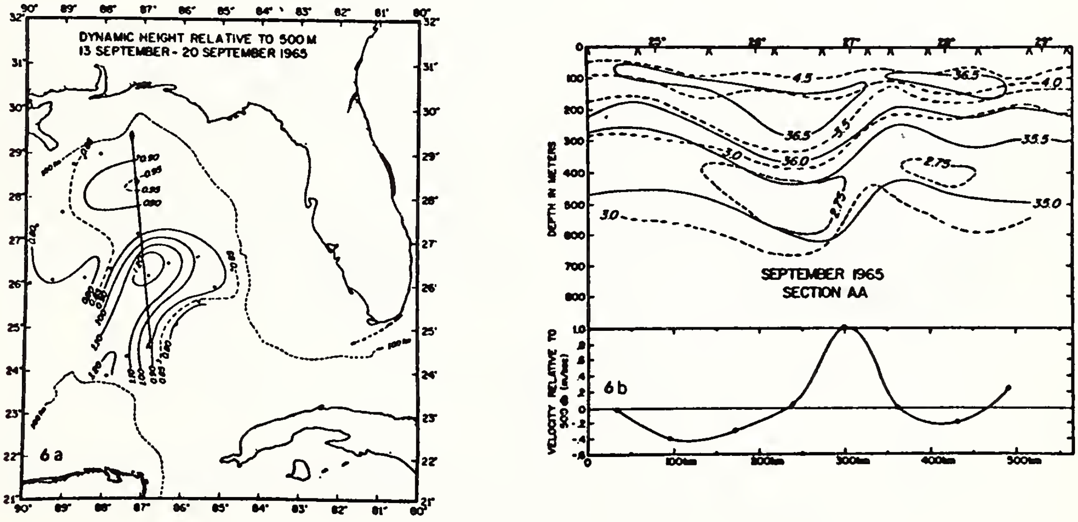

FIGURE 6. (a) The Dynamic Height Topography of the Sea Surface Relative to 500 m Constructed from Data Collected in September 1965

(b) A Salinity, Oxygen, and Geostrophic Speed Section through the Stations along Line AA (6a) meteorological events. However, few direct current measurements have been made in the region. Gaul (1967) found evidence of a quasi-permanent anticyclonic feature at the head of De Soto Canyon, 87.5°W longitude, 28.5°N latitude (Figure 1). The feature had a horizontal scale of 100 km and a vertical scale of at least 500 m.

Climatological winter conditions on the shelf (depth <100 m) are characterized by isothermal water columns. Summer conditions approximate a 2-layer system. Winter extremes occur in February and summer extremes in August (Gaul, 1967), with the transitions a function of cold-front passages (State University System of Florida Institute of Oceanography, 1975). Climatological conditions are altered by intrusions of Loop Current waters.

Surface salinities off the Mississippi Delta are in phase with Mississippi run-off. Lowest salinities are observed in spring during maximum runoff (State University System of Florida Institute of Oceanography, 1975). Figure 7 shows the possible extent of the Mississippi River plume. Upper layer salinities increase offshore of the shelf in the absence of Loop Current eddies. When Loop Current water impinges on the shelf, higher salinities are observed (Figure 6b).

Hurricanes which often traverse the region can considerably influence the upper water column. Theoretical and observational studies show that hurricanes can induce upwelling underneath the eye of the storm. Figure 8 (Molinari and Franceschini, 1972) indicates the degree of upwelling possible.

BIOLOGICAL BACKGROUND

The Gulf of Mexico can be divided into distinct biological provinces. Most classifications divide the Gulf into estuarine, coastal, and open Gulf regions. Each region is characterized by different species concentration and diversity. Steidinger (1973)

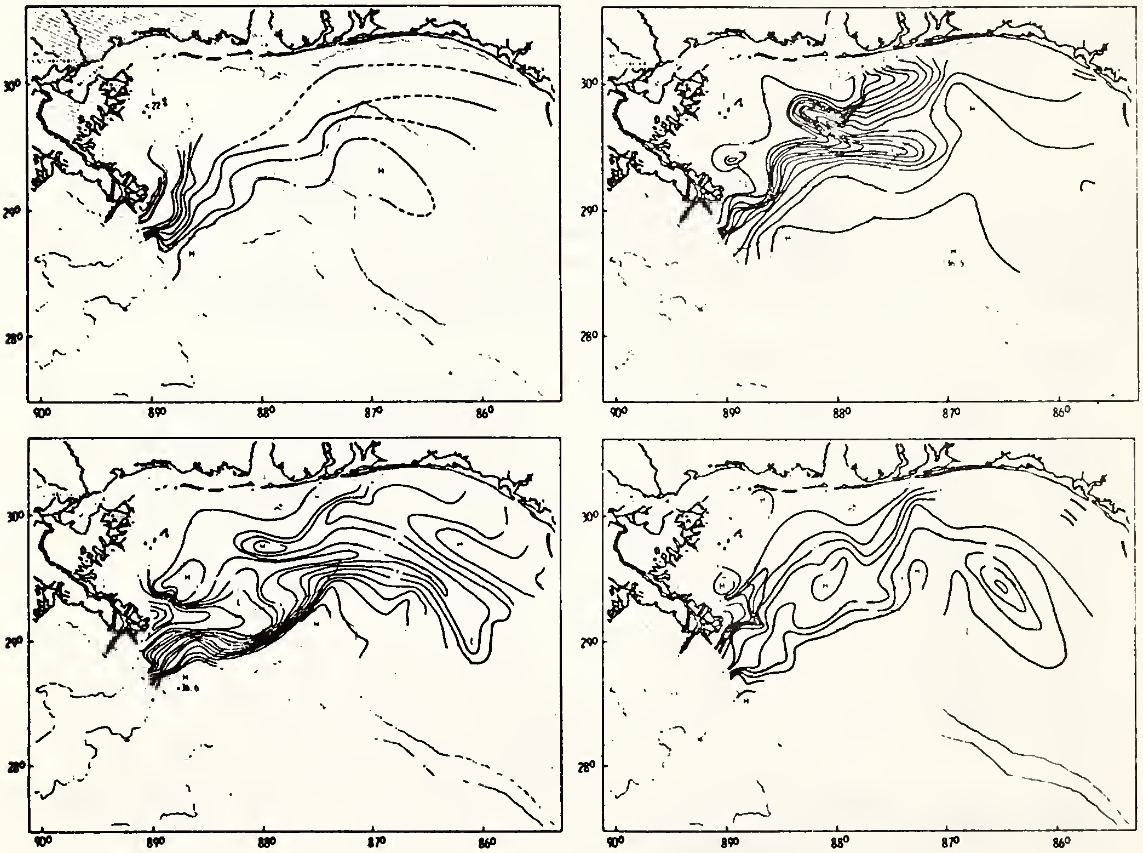

FIGURE 7. Surface Salinity Pattern in the Vicinity of the Mississippi Delta

identified four phytoplankton assemblages: estuarine, estuarine-coastal, coastal-open Gulf, and open Gulf. Proceeding seaward from the coast, Steidinger (1973) observed: a) a reduction in primary production, b) an increase in species diversity, and c) an increase in holoplanktonic (entire life in water column) over meroplanktonic (portion of life in water column) forms. The seaward decrease in plankton concentration was also observed by Bogdanov et al.

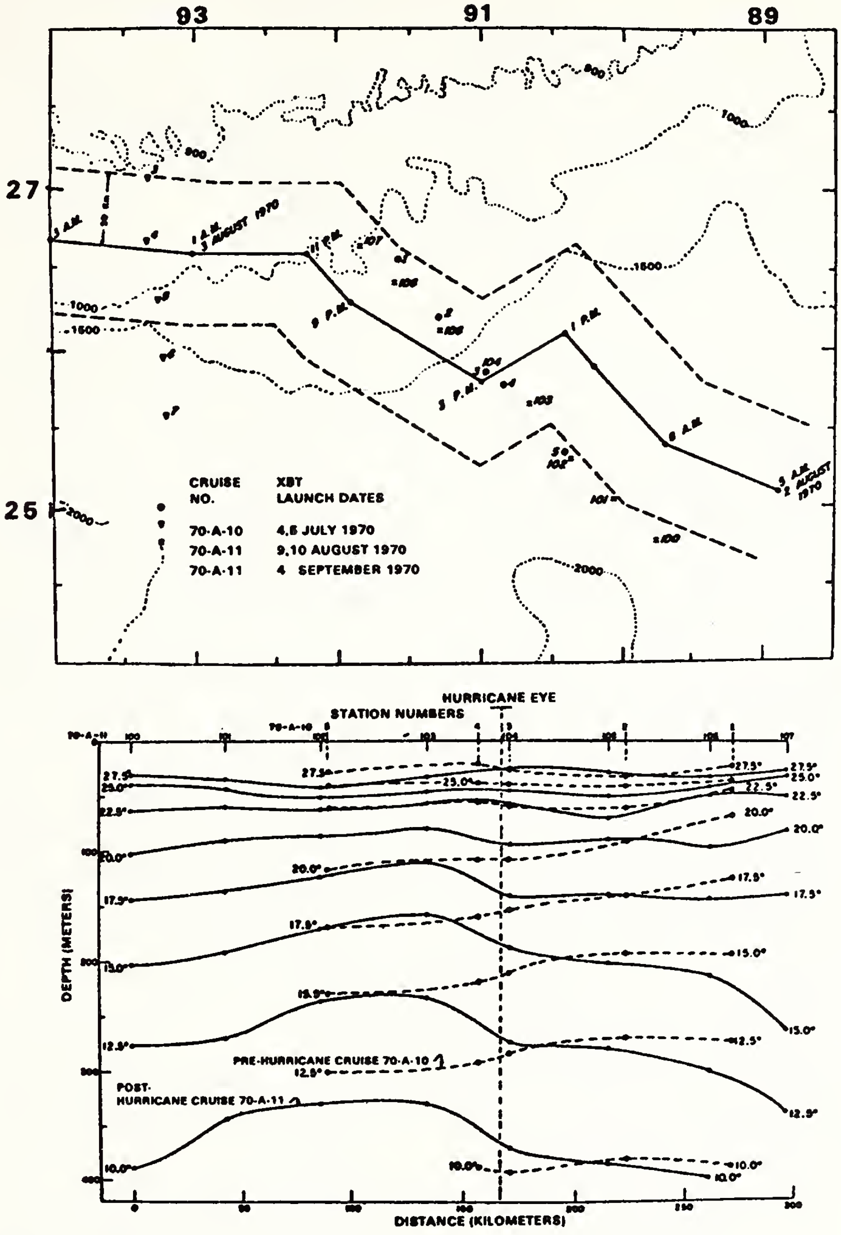

FIGURE 8. Upwelling Observed (Lower Panel) Along the Path of Hurricane CELIA (Upper Panel), 1970

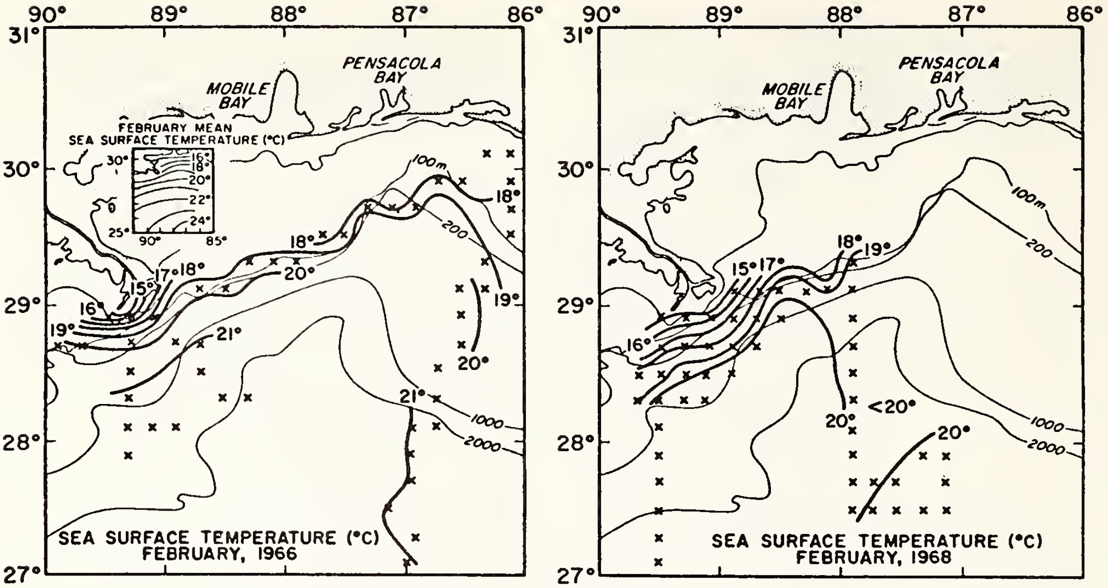

SEA SURFACE TEMPERATURE (°C) FEBRUARY, 1966

SEA SURFACE TEMPERATURE (°C) FEBRUARY, 1968

90°
89°
88°
87°
86°
31°
30°
29°
28°
27°
MOBILE BAY
PENSACOLA BAY
FEBRUARY MEAN SEA SURFACE TEMPERATURE (°C)
30°
16°
18°
20°
22°
24°
25°
90°
85°
100m
200
1000
2000
15°
16°
17°
18°
19°
20°
21°
<20°

FIGURE 9. Sea Surface Temperature Fields Observed During February 1966 and 1968 Near the Mississippi Delta Inset shows mean February sea surface temperature distribution adapted from Robinson (1973)

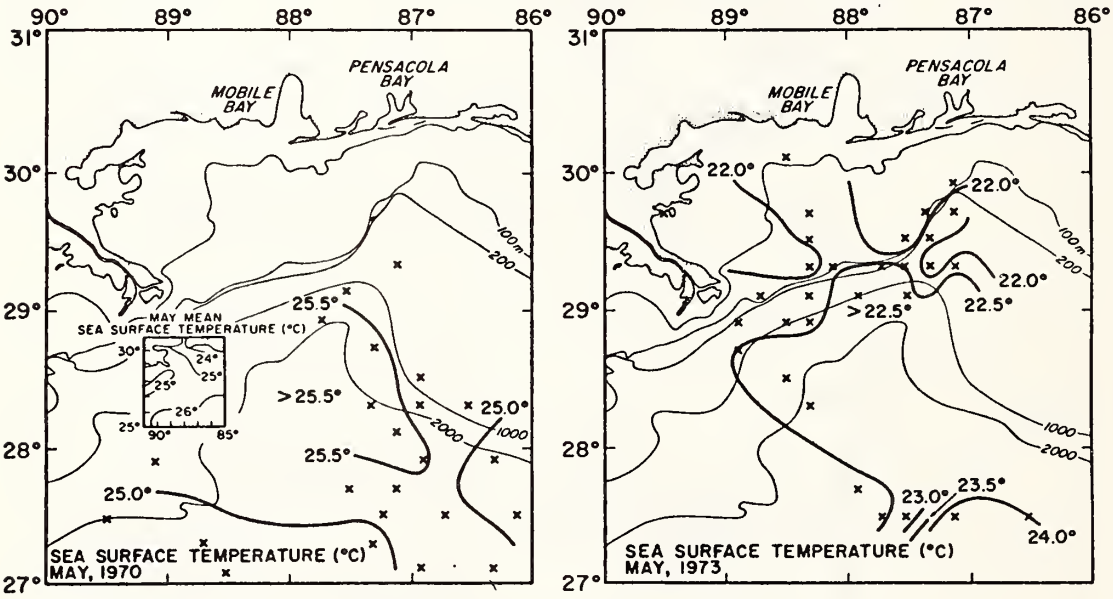

SEA SURFACE TEMPERATURE (°C) MAY, 1970

SEA SURFACE TEMPERATURE (°C) MAY, 1973

90°
89°
88°
87°
86°
31°
30°
29°
28°
27°
MOBILE BAY
PENSACOLA BAY
MAY MEAN SEA SURFACE TEMPERATURE (°C)
30°
24°
25°
26°
90°
85°
100m
200
1000
2000
25.5°
>25.5°
25.0°
22.0°
>22.5°
22.5°
23.0°
23.5°
24.0°

FIGURE 10. Sea Surface Temperature Fields Observed During May 1970 and 1973 Near the Mississippi Delta Inset shows mean May sea surface temperature distribution adapted from Robinson (1973)

(1968). Largest plankton concentrations occur in estuarine and estuarine-coastal zones off the mouth of the Mississippi River and along the Mississippi-Alabama coast. Plankton concentrations in these regions are seasonal and in phase with the discharge of the Mississippi River and winter upwelling (Hopkins, 1973).

Austin (1971) found more Foraminifera and Pteropoda species in deep basin than in coastal waters. This is consistent with historical studies showing that tropical waters typically have greater species diversity than temperate waters. The Loop Current possesses tropical water mass characteristics.

The seaward transition from mero- to holoplanktonic forms occurs in dominant species of various biological provinces. For example, diatoms, blue-green algae, and seagrasses are found in greater concentrations in estuaries, while dinoflagellates dominate open water distributions (Steidinger, 1973).

Current and water mass patterns in the Gulf of Mexico are frequently changing. Seasonal changes in temperature and salinity fields are modulated by passage of meteorological and oceanographic events. Loop Current waters have been frequently found on the northeastern Gulf shelf and Mississippi River discharge has been tracked to the Straits of Florida (State University System of Florida Institute of Oceanography, 1975). The interchange and mixing of water masses introduces new biological species.

Pequegnat and Pequegnat (1968) provided an example of how interchanges can affect results of biofouling and corrosion experiments. Their work was conducted off Panama City at three stations, in 18 m, 30 m, and 46 m of water. They proposed an intrusion of Loop Current waters to explain the tropical species at the bottom of seaward moorings and suggested a relation between fouling rates and upwelling and mixing caused by severe storms.

SITE CHARACTERIZATION

Our approach in characterizing the thermal field at the Gulf of Mexico site is to consider data on an event basis rather than just to consider average or annual thermal distributions. A more realistic estimate of horizontal and vertical gradients should result from the approach.

The "event" component occurs randomly. For example, incursion of Loop Current eddies at the site is apparently a nonseasonal occurrence. "Events" will affect the biological activity at sites. The "annual" component occurs about the same time each year, with possible yearly variation in the magnitude of effect. That is, although there is an annual cycle in the thermal field, winter temperatures may be signficantly colder one year than in other years. Biological activity during a cold year may be different than during a "normal" year.

Some preliminary results of the site characterization are presented below. Annual components of the temperature field will be considered and two event components, Loop Current eddies, and hurricanes will be discussed.

Annual Component

Interannual variability in monthly sea surface temperature (SST) fields is shown in Figures 9 and 10. February SST distributions for 2 yr and the climatological mean (Robinson, 1973) are shown in Figure 9. May SST distributions are given in Figure 10.

The large SST gradients extending east from the Mississippi River, particularly during February (Figure 9), are more pronounced in synoptic charts than in climatological charts. The front marks the leading edge of a Mississippi plume and biologically separates estuarine and shelf zones. The front can extend vertically to at least 45 m (Chew et al., 1961). Additional analyses are planned to define further the horizontal and vertical extent of this feature.

Annual differences in seasonal onset of warmer temperatures are apparent in May SST charts (Figure 10). Temperatures in May 1973 were considerably cooler than in May 1970.

Event Components

The vertical temperature structure associated with the 1965-1966 Loop Current eddy (Figure 5) is shown in Figure 11. The large southern eddy was first observed in September 1965 and remained in the region through February 1966 (Figure 5). Other data (Molinari, 1977) indicate that similar features were observed in the site area at least once (1952) and possibly twice (1971, 1973) in 10 yr.

Smaller-scale eddies, like the northern eddy in Figure 6, have also been observed in the region. Frequency of occurrence of these events is unknown.

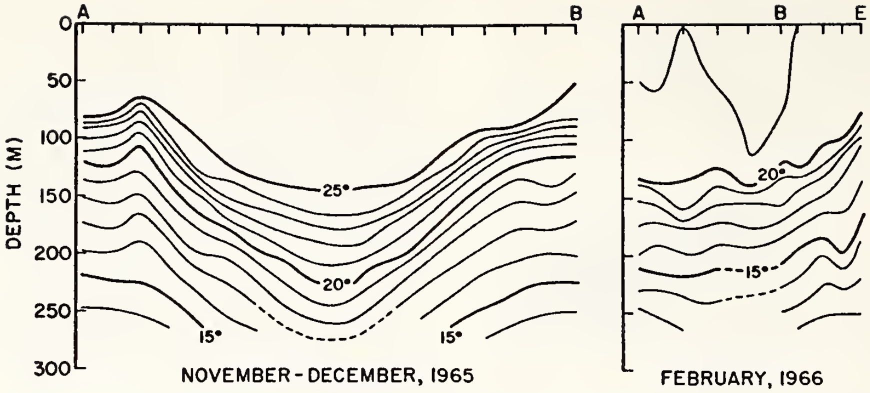

FIGURE 11. Temperature Sections Through the Detached Eddy Observed Near the Mississippi Delta During November-December 1965 and February 1966 Section locations are given in Figure 5

Figure 8 represents an observed response of the upper ocean thermal structure to a hurricane. Since ocean response is a function of storm intensity and forward speed, different responses are possible (Gentry, 1971).

Data from the Monthly Weather Review show the number of hurricanes and tropical storms observed in the 5° x 5° square bounded by 25°N and 30°N latitude and 85°W and 90°W longitude (Table 1). Hurricanes are wind systems with velocities greater than 64 knots. Tropical storms, are systems with speeds from 35 to 64 knots. Although most storms and hurricanes in the region occurred in late summer and early autumn, many occurred in June.

DISCUSSION

At the conclusion of our study a more detailed site characterization will be prepared. Additional information concerning frequency of occurrence of Loop Current eddies should result. The data will be useful in interpreting biofouling and corrosion study results.

ACKNOWLEDGMENTS

We thank Drs. Hansen, Stewart, and Chew for reviewing the manuscript. This work is funded by the Division of Solar Energy, Department of Energy (formerly Energy Research and Development Administration).

TABLE 1. Number of Hurricanes and Tropical Storms Observed by Month in the 5° x 5° Square 85°W to 90°W Longitude; 25°N to 30°N Latitude; 1889-1976

	June	July	August	September	October	November-May
Hurricanes	3	4	9	25	4	0
Tropical Storms	13	7	10	20	15	2

REFERENCES

Austin, H. M. 1971. The Characteristics and Relationships Between the Calculated Geostrophic Current Component and Selected Indicator Organisms in the Gulf of Mexico Loop Current System. Ph. D. Dissertation, Florida State Univ., Dept. of Ocn., 369 pp.

Bogdanov, D. V., V. A. Sokolov, and N. S. Khromov. 1968. Regions of high biological and commercial productivity in the Gulf of Mexico and Caribbean Sea. Oceanolosy 8: 371-381.

Chew, F., K. L. Drennan, and W. J. Demoran. 1961. On the temperature field east of the Mississippi Delta. J. Geophs. Res. 67: 271-279.

Cochrane, J. D. 1963. Yucatan Current. Rept. of Dept. of Ocn., Texas A&M Univ., Ref. 63-18A. pp. 6-11.

Cochrane, J. D. 1966. The Yucatan Current. Texas A&M Univ., Dept. of Ocn., Ref. 66-11T, pp. 14-25.

Cochrane, J. D. 1967. Upwelling off Northeast Yucatan. Texas A&M Univ., Dept. of Ocn., Ref. 67-8T, pp. 16-17.

Cummings, S. R., J. M. Parker, and D. K. Atwood. 1977. Analysis of Existing Nutrient Data from Three Potential OTEC Sites, Northern Gulf of Mexico, Puerto Rico, and St. Croix. In: Proceedings of the Ocean Thermal Energy Conversion (OTEC) Symposium. (R. H. Gray, ed). Pacific Northwest Laboratory, Richland, WA.

Gaul, R. D. 1967. Circulation over the Continental Margin of the Northeastern Gulf of Mexico. Ph.D. Dissertation. Texas A&M Univ., Dept. of Ocn., 172 pp.

Gentry, R. C. 1971. Hurricanes, one of the major features of air-sea interaction in the Caribbean Sea, pp. 79-87. In: Symposium on Investigations and Resources of the Caribbean Sea and Adjacent Regions. UNESCO, Paris.

Hopkins, T. L. 1973. Zooplankton, pp. III F-1-III F-10. In: A Summary of Knowledge of the Eastern Gulf of Mexico. State University System of Florida Institute of Oceanography, St. Petersburg, Florida.

Ichiye, T., and H. Sudo. 1971. Saline Deep Water in the Caribbean Sea and in the Gulf of Mexico. Texas A&M Univ., Dept. of Ocn., Ref. 71-16-T, 29 pp.

Leipper, D. F. 1970. A sequence of current patterns in the Gulf of Mexico. J. Geophys. Res. 75: 637-657.

Molinari, R. L., and G. A. Franceschini. 1972. Bathythermograph sections across the path of Hurricane CELIA, pp. 259-262. In: Contributions on the Physical Oceanography of the Gulf of Mexico, Capurro and Reid, Editors, Gulf Publ. Co., Houston, Texas.

Molinari, R. L. 1977. Synoptic and Mean Monthly 20°C Topographies in the Eastern Gulf of Mexico. NOAA Tech. Memo. ERL-AOML 27.

Molinari, R. L., S. Baig, D. W. Behringer, G. A. Maul, and R. Legeckis. 1977. Winter intrusions of the Loop Current. Science, 198:505-507.

Pequegnat, W. E. and L. H. Pequegnat. 1968. Ecological Aspects of Marine Fouling in the Northeastern Gulf of Mexico. Texas A&M Univ., Dept. of Ocn., Ref. 68-22T, 88 pp.

Robinson, M. K. 1973. Atlas of Monthly Mean Surface and Sub-Surface Temperature and Depth of the Top of the Thermocline Gulf of Mexico and Caribbean Sea. Scripps Institute of Oceanography. Ref. 73-8, 105 pp.

Schlitz, R. J. 1973. Net Total Transport and Net Transport by Water Mass Categories for Yucatan Channel Based on Data for April 1970. Ph.D., Dissertation, Texas A&M Univ., Dept. of Ocn., 107 pp.

State University System of Florida Institute of Oceanography. 1975. Compilation and Summation of Historical and Existing Physical Oceanographic Data from the Eastern Gulf of Mexico. Final Report to BLM under Contract No. 08550-CT4-64.

Steidinger, K. A. 1973. Phytoplankton, pp. III E-1-III E-18. In: A Summary of Knowledge of the Eastern Gulf of Mexico. State University System of Florida Institute of Oceanography, St. Petersburg, Florida.

Uchupi, E. 1971. Bathymetric Atlas of the Atlantic, Caribbean, and Gulf of Mexico. Woods Hole Ocn. Inst. Ref. No. 7-72.

Worthington, L. V. 1976. On the North Atlantic Circulation. Johns Hopkins University Press, Baltimore, Maryland, 110 pp.

Wust, G. 1964. Stratification and Circulation in the Antilles-Caribbean Basins. Columbia University Press, New York, New York, 201 pp.

Proceedings Working Conference on Current Measurements, Technical Report DEL-SG-3-78, College of Marine Studies, University of Delaware, Newark, DE., Woodward, Mooers, and Jensen, Eds., 237-254.

CURRENT MEASUREMENTS FOR THE OCEAN THERMAL ENERGY CONVERSION PROGRAM

Robert L. Molinari
National Oceanic and Atmospheric Administration
Atlantic Oceanographic and Meteorological Laboratories
Miami, Florida 33149

Lloyd Lewis
Department of Energy
Division of Solar Energy
Washington, D.C. 20545

ABSTRACT

The Ocean Thermal Energy Conversion (OTEC) Program of the Department of Energy is directed toward obtaining electrical power from a heat engine driven by the temperature differential between warm surface and colder subsurface waters. Preliminary design concepts envision a large surface plant, moored and/or actively propelled, attached to a long (order of 100 m's) cold water pipe. Water is pumped into the plant at the surface and bottom of the pipe, and discharged at some mid-depth. The designer of an OTEC plant must consider currents in order to minimize the effect of the plant on the environment and the effect of the environment on the plant. For instance, current data are required to evaluate the effect of the plant effluent on the environment. Also, the dynamic loading on the plant caused by ambient currents must be computed to design a suitable mooring or propulsion system. Current data are necessary to design a cold water pipe which will neither collapse nor bend. The observational programs developed for obtaining current velocity data at potential OTEC sites are presented.

INTRODUCTION

The Ocean Thermal Energy Conversion (OTEC) Program is an alternative solar energy program of the Department of Energy. The program's ultimate goal is to extract energy from the sea in order to generate electrical power. The current measurement needs of this program are discussed in the following presentation.

Information on some initial plant design configurations is presented first to provide background for the remainder of the report. The requirements for ocean current data in the design process and the types of data which can satisfy these requirements will be discussed. Possible efficient methods for obtaining these data are identified. Finally, a brief discussion of the limitations in this method is given.

BACKGROUND

The OTEC power plant can be considered simply as a heat engine driven by the temperature differential between the warm surface waters and the colder subsurface waters. The immediate output of the plant is the production of electrical energy, the use of which is frequently discussed in terms of two concepts. One concept calls for the electrical output of a moored or grazing plant to be hard-wired to a land-based power grid (Trimble et al., 1975; Douglas, 1975; and Goss et al., 1975, for example). The other calls for using the electrical output of a grazing plant to power, at sea, an energy-intensive manufacturing process, such as ammonia production (Dugger et al., 1975). However, in both cases, many of the design features of the plants are similar.

Tables 1 and 2 summarize some of the preliminary proposals relating to OTEC platform and power plant design. Some of these design concepts are no longer under consideration, but all are presented for completeness. Also, the data in these tables may not represent the latest thinking of the proponents.

The design concepts, although diverse, have important similarities. All include a large, near-surface vessel to house the power plant, which will be attached to a long cold-water pipe. The warm water intakes are within 150 ft (50 m) of the surface, and the cold-water intakes range from 1100 feet to 4000 feet (370 m to 1300 m). All power plants require large amounts of warm and cold water to operate. The vertical temperature gradients driving the plants also are similar.

Figure 1 presents a portion of a milestone chart for the OTEC program. OTEC-1 and OTEC-5 are test platforms to be used to verify heat exchanger concepts and other OTEC systems. The Demonstration Plant is nominally a 100 megawatt output system for which the design criteria in Tables 1 and 2 have been developed. Several regions, shown on Figures 2 and 4, have been proposed as potential sites for moored OTEC plants.

Table 1: Preliminary Plant Design Specifications

Proponent	Hull Geometry, Dimensions, Material	Cold Water Pipe Design, Material	Mooring or Positioning	Manning	Life Expectancy	Depth Warm/ Cold Water Intake	Depth Warm/ Cold Water Discharge
Carnegie Mellon University	Cylindrical Spar, 2000' long x 50' wide, reinforced concrete	Lower part of spar	Guy wires	Unmanned	40 years	?/2000'	?/?
University of Massachusetts	Submerged twin-hull catamaran, hulls-870' x 100' reinforced concrete	Cylinder, 66' diameter, concrete	Single point mooring	Manned	40 years	45'/1120'	?/465'
Sea-Solar Power Incorporated	Rectangular surface vessel, 380' x 650', steel and aluminum	Stockade cylinder, 38' diameter, steel	Dynamic positioning	Manned	25 years	Surface/ 2000'	290'/150'
Applied Physics Laboratory Johns Hopkins University	Surface vessel, 275' x 225' x 175' deep, aluminum	Cylinder, 45' diameter	Grazing	Manned	?	Surface/ 2000'	Surface/ 175'
TRW	Cylindrical surface vessel, 340' diameter, 170' deep, concrete	Cylinder, 50' diameter, reinforced plastic	Positioning by water exhaust	Manned	25 years	100'/200'	400'/1500'
Lockheed	Submerged spar, 432' diameter 410' deep, concrete	Telescoping cylinder, 129' maximum diameter, concrete	Single point mooring	Manned	25 years	100'/200'	400'/1500'

Table 2: Preliminary Power Plant Specifications

Proponent	Net/Gross Power (MWe)	Heat Exchanger Type/Material	Enhancement	Heat Transfer Coefficient (BTU/hr-°F-ft^2)	Condenser or Evaporator area 10^6 ft^2)	Working Fluid	Vertical ΔT Required °F/°C	Warm/Cold Water Supply 10^6gpm	Warm/Cold Water ΔT °F	Remarks
CMU	100-140	shell & tube aluminum	tubes fluted on NH_3-side	1000	2-6	ammonia	40/22	8.5/ 8.1	3.6/ 3.6	Designed for optimum heat exchange
U Mass	400/500	plate & fin 90-10 copper nickel	fins on NH_3 side	200-400	10-40	propane	32/18	7.6/ 8.1	1.9/ 5.0	Designed to minimize biofouling corrosion
SSPI	100/125	plate & fin aluminum	thin walls	200	3-10	R-12/31	36/20	10.0/ 4.9	3.0/ 6.0	Designed to minimize cost
APL-JHU	?	aluminum				ammonia	36/20		3.6/ 3.6	
TRW	100/122-138	shell & tube titanium		400	4	ammonia	38/21	~10.0/ ~ 7.8	4.1/ 4.1	Designed to use state-of-the-art technology
Lockheed	160/240	shell & tube		500	3	ammonia	33/18	6.3 8.1	2.2/ 1.7	Designed to use state-of-the-art technology
DSS Engineers, Inc.		plate & fin plastic		271		ammonia				

Figure 1. Project milestone chart for several OTEC components (ERDA, 1977).

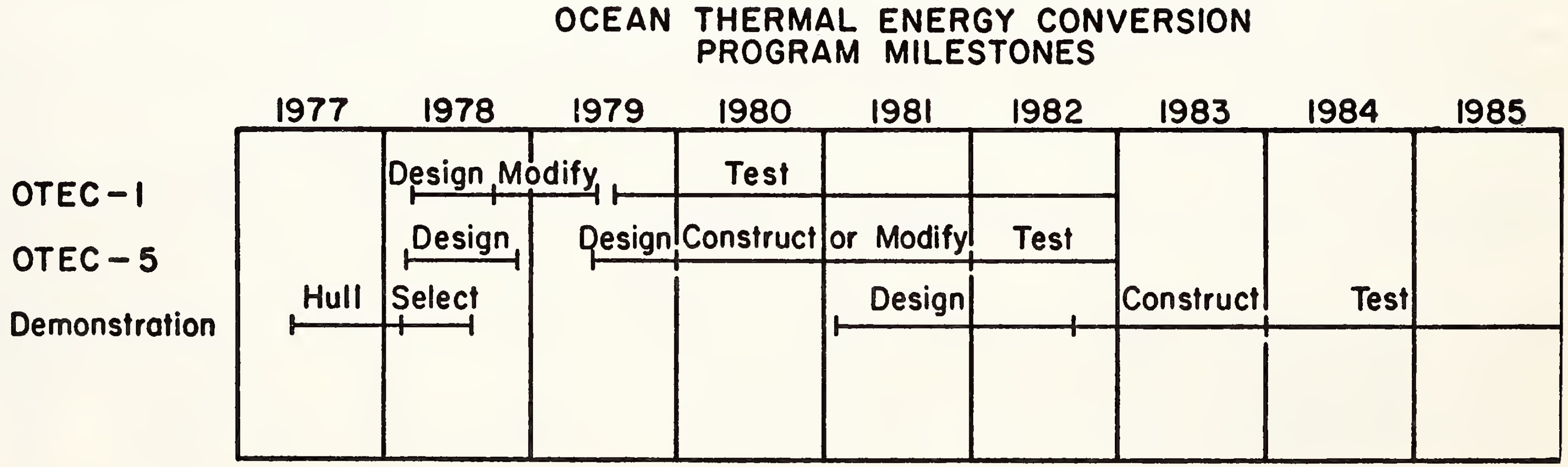

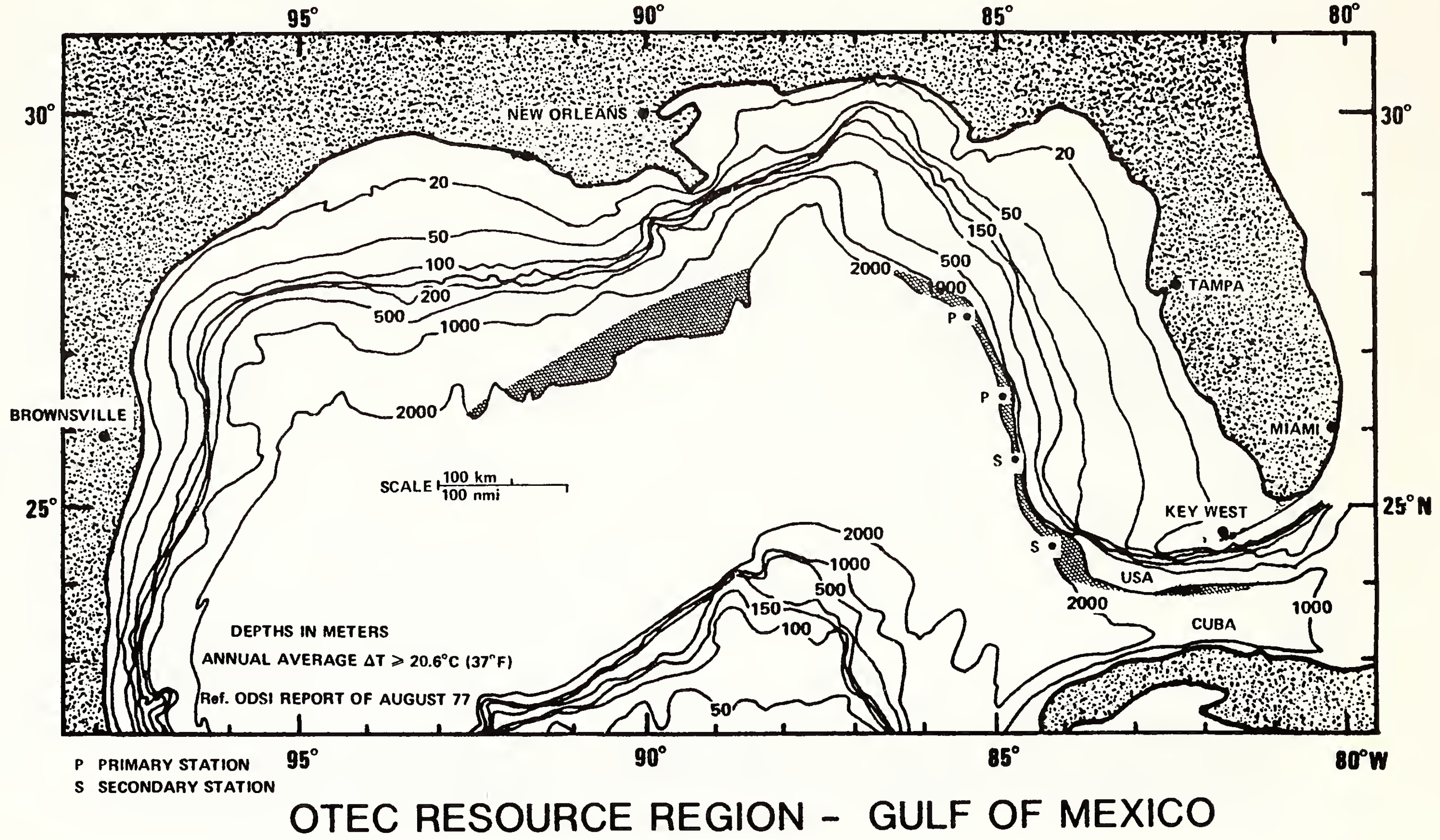
95°
90°
85°
80°
30°
25°
25°N
80°W
NEW ORLEANS
BROWNSVILLE
TAMPA
MIAMI
KEY WEST
USA
CUBA
20
50
100
150
200
500
1000
2000
P
S
SCALE 100 km 100 nmi
DEPTHS IN METERS
ANNUAL AVERAGE ΔT ≥ 20.6°C (37°F)
Ref. ODSI REPORT OF AUGUST 77
P PRIMARY STATION
S SECONDARY STATION
OTEC RESOURCE REGION - GULF OF MEXICO

Figure 2. Potential OTEC sites (shaded areas) in the Gulf of Mexico.

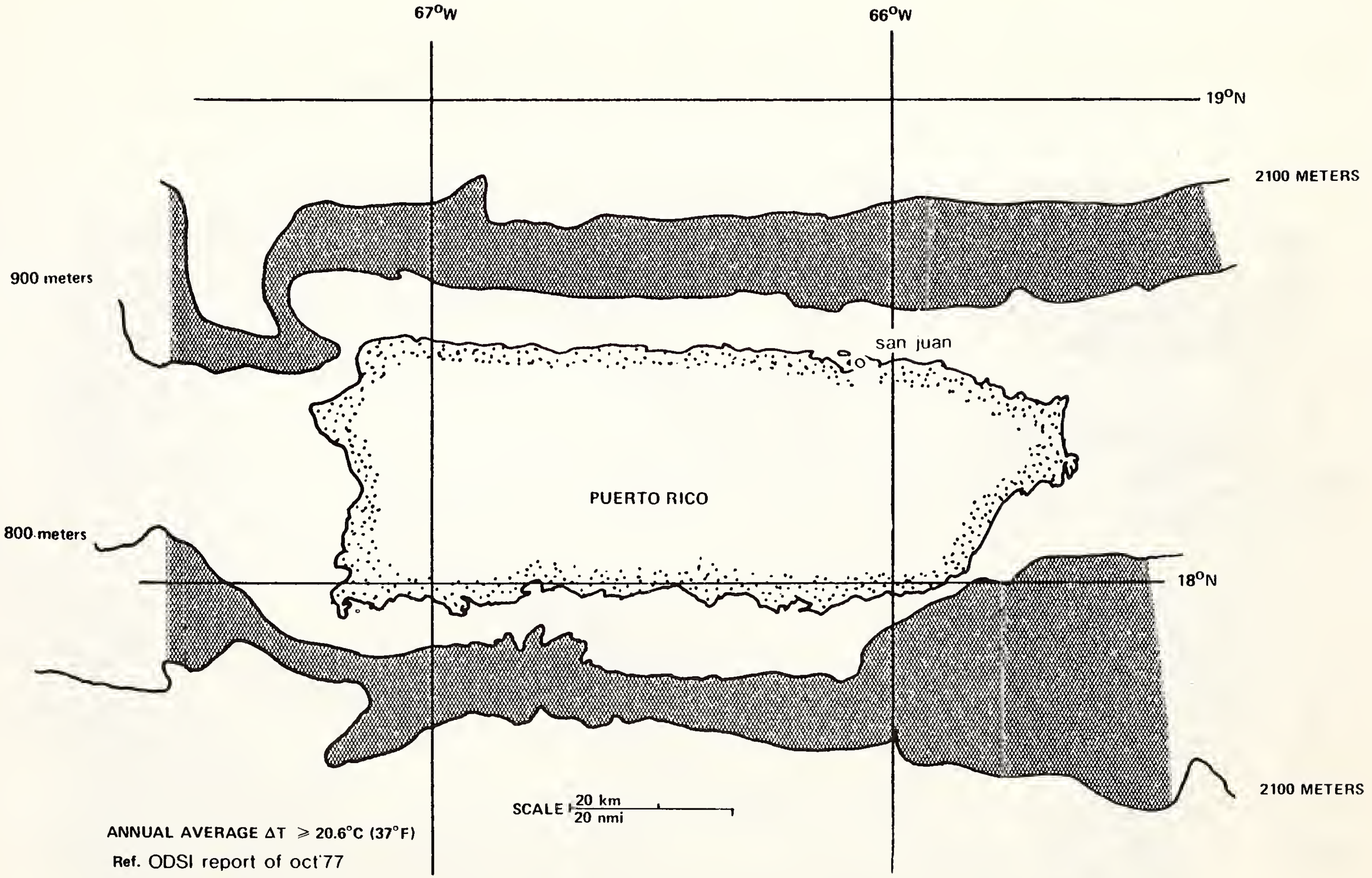
67°W
66°W
19°N
18°N
2100 METERS
900 meters
800 meters
2100 METERS
san juan
PUERTO RICO
SCALE 20 km 20 nmi
ANNUAL AVERAGE ΔT ⩾ 20.6°C (37°F)
Ref. ODSI report of oct'77

OTEC RESOURCE REGION - PUERTO RICO

Figure 3. Potential OTEC sites (shaded areas) in the region of Puerto Rico.

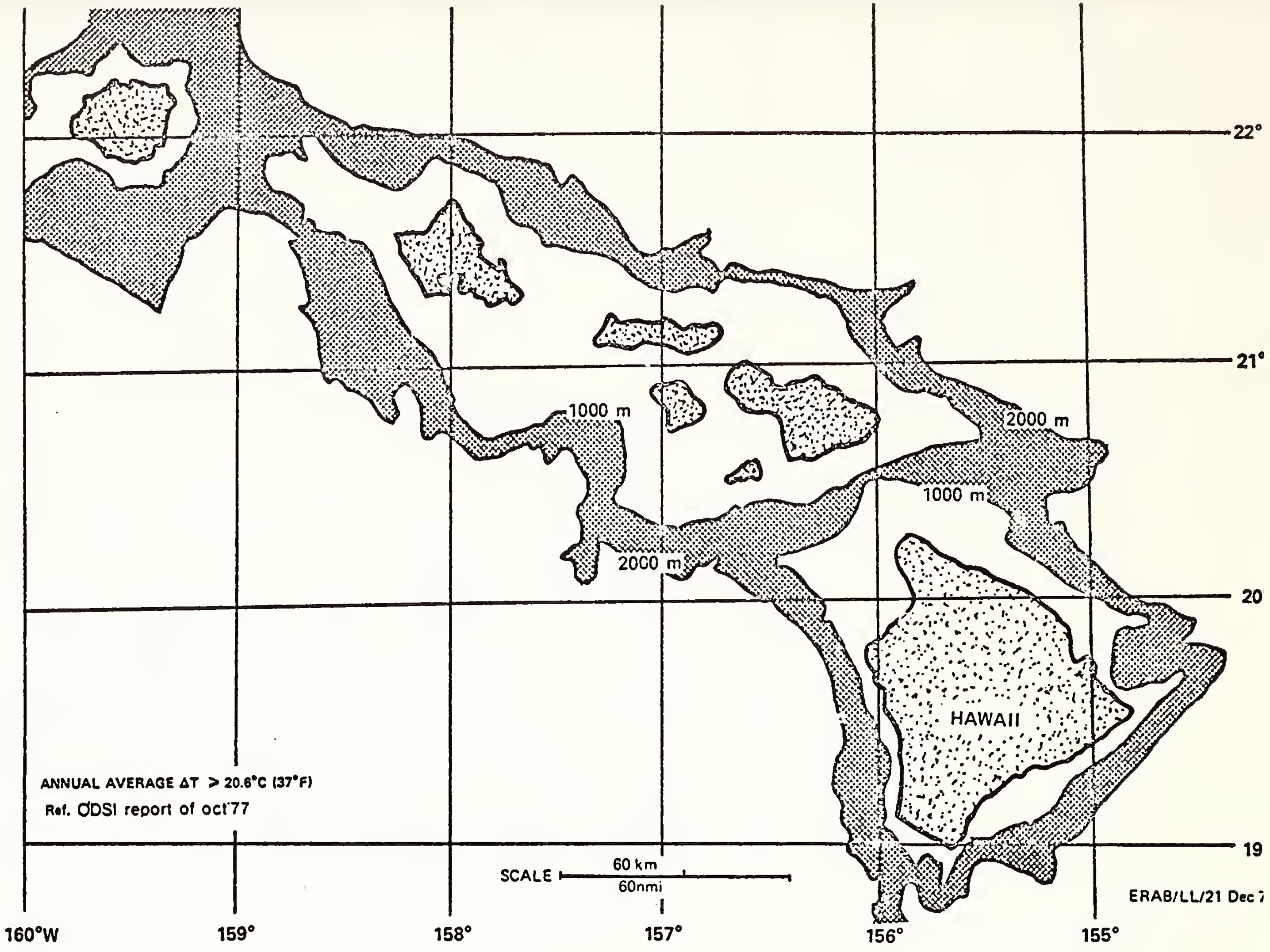
22°
21°
20
19
160°W
159°
158°
157°
156°
155°
1000 m
2000 m
1000 m
2000 m
HAWAII
ANNUAL AVERAGE ΔT > 20.6°C (37°F)
Ref. ODSI report of oct'77
SCALE
60 km
60nmi
ERAB/LL/21 Dec 7

OTEC RESOURCE REGION - THE HAWAIIAN ISLANDS

Figure 4. Potential OTEC sites (shaded areas) in the region of Hawaii.

The South Atlantic off Brazil (Figure 5) has been considered as one potential site for a grazing plant. Current measurements are required at these sites for all stages of the program leading to the eventual commercialization of OTEC.

If it is assumed that the final design of the demonstration plant will be some variation of the concepts given in Tables 1 and 2, rather than a totally different design, then the common properties of these proposals allow for a generic specification for current data requirements. These requirements should be valid for the most important design similarities and are discussed next.

REQUIREMENTS FOR CURRENT DATA IN DESIGN AND IMPACT STUDIES

Current data are required in the design process and for impact studies to minimize:

(1) the detrimental effect of the plant on the environment;
(2) the detrimental effect of the environment on the plant;
(3) the cost of plant construction; and
(4) the cost of daily plant operation.

The final design of an OTEC plant will require accurate site-specific data. However, even at this early stage in plant development, the design requirements for current data should address these four items.

Ocean velocity fields will have an impact on many aspects of the OTEC design process. Examples of these impacts are presented in Table 3. Recirculation refers to the possibility of water discharged from the plant returning to the intake port and thereby degrading the thermal resource. A mixed discharge is one wherein cold and warm water are mixed internally in the plant before discharge, or in the near field of the plant upon discharge.

Before a sufficient data-set can be developed to address the impacts given in Table 3, the mechanisms by which the data are actually input into the design process are required. The American Petroleum Institute (API, 1977), for example, gives a recommended practice for the design of fixed offshore platforms, in which various data-dependent expressions are presented to evaluate the effect of the environment on the platform. A similar format will be followed for the OTEC ocean velocity data. However, in contrast to the API report, the relations presented here are merely examples of where ocean data are needed in the design effort. They are not guidelines for use in design.

Surface Vessel

Velocity Profiles. Vertical profiles of the horizontal velocity are necessary to compute the current loading on the plant. Current

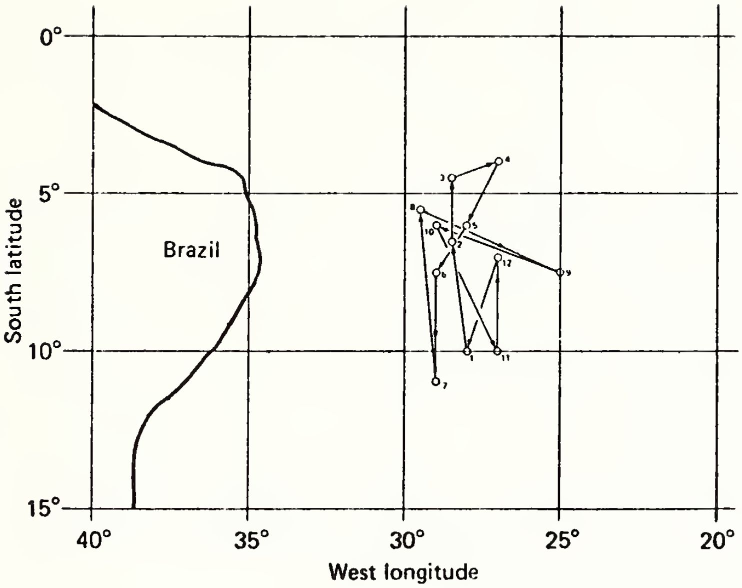
0°
5°
10°
15°
South latitude
Brazil
1
2
3
4
5
6
7
8
9
10
11
12
40°
35°
30°
25°
20°
West longitude

Figure 5. Possible trackline for a grazing OTEC plant in the South Atlantic (Francis and Seelinger, 1977).

Table 3: Impacts of Current Velocity on Design Process

1. Surface Vessel
    - a. Drag computations
    - b. Plant motions
    - c. Streamlining requirements
2. Cold Water Pipe
    - a. Drag computations
    - b. Pipe buckling
    - c. Bending moments
    - d. Vibrations
3. Positioning Method
    - a. Dynamic positioning propulsion requirements
    - b. Static mooring requirements
        - i. Strength of mooring
        - ii. Scouring around anchor
4. Recirculation
    - a. Potential for recirculation
    - b. Type and position of discharge - mixed or separate
5. Environmental Impact
    - a. Advection of harmful plant discharges

loading can be separated into two components, drag and lift (API, 1977). The drag component is caused by the frictional stress on the object, and the lift component is due to the unsteady forces linked to vortex shedding. Both forces are proportional to the current speed squared. Because of this dependence, the total plant loading is very sensitive to the velocity profile used. Streamlining to reduce coupling between the plant and medium may be required if the lift and drag forces are too large.

Near-surface current data also are necessary to determine the potential for motion of a particular plant design. Plant motion is a factor in evaluating worker safety and comfort.

Cold-Water Pipe Design

Velocity Profiles. Ocean current velocity data are required to compute the drag and lift forces, as described above, on the cold-water pipe (CWP). In addition, current velocity data are used to determine the minimum wall thickness of a CWP to avoid pipe collapse due to nonuniform external pressures generated by ocean currents. The minimum wall thickness required to prevent collapse is proportional to the ocean velocity raised to the two-thirds power (Wu, 1976). The minimum wall thickness required for a CWP to be free from local buckling is proportional to the ocean current speed.

Current Accelerations. Acceleration data are required to determine the possibility of CWP fatigue failure. Fatigue failure can occur if significant internal wave energy exists at the shorter periods (order of tens of minutes).

Positioning Requirements

Velocity Profiles. Current data are required to compute the total drag on the plant, CWP, and mooring line system, and thus determine mooring line and anchor requirements. If a drifting plant is used, current data are needed to compute propulsion requirements, since the propulsion power is proportional to the plant velocity cubed (Olsen and Pandolfini, 1975).

Bottom Currents. Data on bottom currents, particularly during extreme events such as hurricanes, are necessary to determine the potential for scour around an anchor.

Recirculation

Velocity Profiles. Sundaram et al. (1977) find that the percent recirculation is a function of several nondimensional parameters, one of which is Q/d^2u, where Q is the discharge flow rate, d is the separation between intake and discharge, and u is the current speed. Jirka et al. (1977) find that recirculation potential is inversely proportional to current speed. Therefore, site-specific current profiles are needed to evaluate recirculation potentials.

Distribution of Horizontal Currents. The identification of eddy structures at an OTEC site is important because of their possible role in increasing recirculation. Eddies (circular current structures) with spatial scales ranging from 10's to 100's of kilometers have been observed in the ocean, and the smaller ones in particular could quickly advect parcels of discharged water back to the plant. Small ambient currents (non-eddying) can be useful in advecting away plant discharges.

Environmental Impact

Small-Scale Current Variability. Local turbulence data are required to evaluate the effect of the momentum discharge of a plant on the local ambient current field (ERDA, 1977a).

Regional Current Fields. The advective field in the vicinity of an OTEC site determines the trajectories of harmful material which may be discharged from the plant.

OCEAN DATA TO MEET DESIGN REQUIREMENTS

Table 4 lists the current velocity data requirements to address the design issues discussed previously. Horizontal current distributions are listed as requirements for several reasons in addition to those described above. They are necessary to determine the validity of extrapolating data from a point to the surrounding region, since even a moored plant will experience some excursion around the mooring. The structure of current features also will determine the most efficient trajectory of a grazing plant.

Two types of data are necessary, those which address operational conditions and those which address extreme conditions. Operational conditions are those which occur regularly, following a seasonal cycle. This cycle could be induced by the seasonal march of atmospheric variables. The seasonal cycle can vary from year-to-year due to yearly differences in seasonal heating or cooling, for instance.

Extreme conditions occur at irregular time intervals and impose severe stresses on the plant. In addition to determining their frequency of occurrence and persistence at a site, it is important to be able to determine precisely when an event will occur. Only then can appropriate action be taken on the plant or ashore to reduce the impact of the event.

An extensive historical data-set is required to compute the variables given in Table 4. The operational current velocity data are available only from long-term, site-specific current meter arrays. Extreme conditions can be extrapolated to the site from data collected in regions with similar ocean conditions. The operational horizontal current distribution can be estimated from geostrophic computations. These data can be used in environmental impact studies and in determining power requirements for

Table 4: Current Data for Design

Current Variable	Vertical Spatial Resolution	Horizontal Spatial Resolution	Temporal Resolution	Additional Requirements
1. Velocity profiles a. Operational	0, 30m, 100m, 200m, 300m, 600m, 1000m	Site-specific	Tidal (i.e. diurnal)	Additional vertical resolution at subsurface maxima, countercurrents, etc. Variability about tidal cycle.
b. Extreme	0, 30m, 100m, 200m, 300m	Site-specific	Event time-scale	Frequency of occurrence, persistence of event, predictability
2. Distribution of horizontal currents a. Operational	Sea surface, discharge depths	25 km	Monthly	Variability about monthly mean
b. Extreme	Event-dependent	10 km	Event time-scale	Frequency of occurrence, persistence of event, predictability

drifting plants. The extremes in horizontal velocity shears, which are probably related to events such as hurricanes, can only be determined from closely spaced current measurements. These measurements can be Eulerian, such as by current meter, or Lagrangian, such as by drifting buoy.

The designer of an OTEC plant must consider the survival environmental state caused by a nonlinear combination of extreme wind and wave, as well as current velocity events at a particular site. One method of specifying an extreme condition is to determine the magnitude of the individual conditions, independent of their direction, and add them linearly. A second approach is to determine statistically the joint probability distribution of these events, considering both magnitude and direction. The second approach is likely to provide a more realistic estimate of the survival state and reduce the initial cost of the plant.

None of the sites proposed to date has sufficient data to meet the requirements stated above (Atwood, 1976; Bathen, 1975; and Molinari and Festa, 1977). Therefore, a data acquisition effort is required to ensure a data-set for input to the design and impact process.

All available data and literature should be reviewed to design an efficient measurement program. The data and literature should be examined for those conditions which could have significant impact on the OTEC operation at a particular site. For instance, hurricanes have been observed at the Puerto Rico and Gulf of Mexico sites (Atwood, 1976; Molinari and Festa, 1977), while Loop Current eddies have been observed at the Gulf of Mexico site (Molinari and Festa, 1977).

However, if no or minimal data exist, a reconnaissance survey is necessary to establish the background for a more detailed survey. Table 5 lists the requirements for such an effort. Requirements for temperature data are also listed, since these data can be obtained concurrently to evaluate the thermal resource. Many of these specifications are transferable to the detailed study.

A number of current meters exist which can meet the specifications in Table 5. Therefore, particular current meter types are not specified. It is important that the mooring be properly designed. The procedure for designing a mooring given by Walden and Silva (1976) is one means of ensuring that a mooring will survive environmental conditions.

Present state-of-the-art current meter design and mooring technology prohibit the inexpensive collection of in situ current data at depths less than 100 m. Therefore, this information must be approximated with current profile data from a ship servicing the deeper current meter moorings, or from Lagrangian techniques.

These data needs will be updated as the plant design becomes more refined. For instance, once the shape and draft of the platform are known, it will be possible to rearrange the vertical placement of the

Table 5: Site-Specific Reconnaissance Survey for Design

Ocean Variable	Instrument	Vertical Resolution	Horizontal Resolution	Temporal Resolution	Accuracy	Duration	Remarks
1. Temperature (vertical structure)	Thermister (thermister string)	0-300 m, every 50 m 300-1500 m every 200 m	on-site	hourly	±0.5°C	1 year	
2. Current (vertical structure)	Current meters on same mooring as above	1 mooring, meter placement 0-300 m, every 100 m, 300-1000 m, every 350 m	on-site	hourly	Direction: ±15° Magnitude; 10% of speed (minimum ±5 cm/sec)	1 year	Present state-of-the-art mooring technology makes surface measurements unreliable. If resources are limited, a minimum of 4 meters would be sufficient.
3. Temperature (horizontal structure)	STD or XBT	Continuous to 1500 m	25 km station spacing in a box around the site	every two months	0.02°C	1 year	Accomplished during servicing of meters. In addition a 3 day serial station on-site taking temperature and current profiles.
4. Current (horizontal structure)	Profiler	Continuous to 500 m	same as 3 above	same as 3 above	Direction: ±10° Magnitude: ±5° cm/sec	1 year	Same as 3.

current meters to sample more efficiently. When the depth and type of discharges are determined, more detailed current data can be obtained to evaluate recirculation potential.

LIMITATIONS IN PRESENT TECHNOLOGY IN REGARD TO OTEC

State-of-the-art current meter and mooring technology limit the usefulness of near-surface measurement techniques for OTEC. Inexpensive methods are required because of the need for measurements at many sites for long periods of time to ensure that severe events are sampled. This requirement for current measurements at depths shallower than 100 m, particularly during extreme events, eliminates most systems presently used.

REFERENCES

American Petroleum Institute (1977). API Recommended Practice for Planning, Designing, and Constructing Fixed Offshore Platforms. API RP 2A, Eighth Edition, April 1977, 46 pp.

Atwood, D. K. (1976). Ocean Thermal Energy Conversion: Resource assessment and environmental impact for proposed Puerto Rico site. Final Report NSF Grant No. AER 75-00145 Univ. of Puerto Rico, Dept. of Marine Sciences, 104 pp.

Bathen, K. H. (1975). Oceanographic aspects of ocean thermal energy conversion pilot plant in subtropical Hawaiian waters. In: Proceedings Third Workshop on Ocean Thermal Energy Conversion, G. L. Dugger, Ed. APL/JHU SR 75-2, 162-173.

Douglas, R. H. (1975). Ocean Thermal Energy Conversion: An engineering evaluation. In: Proceedings Third Workshop on Ocean Thermal Energy Conversion, G. L. Dugger, Ed. APL/JHU SR 75-2, 22-38.

Dugger, G. L., H. L. Olsen, W. B. Shippen, E. J. Francis, and W. H. Avery (1975). Tropical ocean thermal pilot plants producing ammonia or other products. In: Proceedings Third Workshop on Ocean Thermal Energy Conversion, G. L. Dugger, Ed. APL/JHU SR 75-2, 106-115.

ERDA (1977). Environmental Development Plan (EDP). Ocean Thermal Energy Conversion 1977. U.S. Environ. Res. and Dev. Admin., Office of Assistant Administrator for Solar, Geothermal and Advanced Energy Systems, 48 pp.

ERDA (1977a). Proceedings OTEC Resource and Environmental Assessment Workshop. McCluney and Lewis, Eds., Rep. No. RD-77-2, 36 pp.

Francis, E. J. and J. Seelinger (1977). Market definition, commercial development plan and OTEC financing. In: Proceedings Fourth Annual Conference on OTEC, G. E. Ioup, Ed., Univ. of New Orleans.

Goss, W. P., W. E. Heronemus, P. A. Mangarella, and J. C. McGowan (1975). Summary of University of Massachusetts research on Gulf Stream based ocean thermal power plants. In: Proceedings Third Workshop on OTEC, G. L. Dugger, Ed., APL/JHU SR 75-2, 51-63.

Jirka, G. H., D. J. Fry, R. P. Johnson and D. R. S. Harleman (1977). Investigations of mixing and recirculation in the vicinity of an ocean thermal energy conversion plant. In: Proceedings Fourth Annual Conference on OTEC, G. E. Ioup, Ed., Univ. of New Orleans, IV-35 to 41.

Molinari, R. L. and J. F. Festa (1977). Ocean thermal properties in relation to the biofouling and corrosion experiment in the Gulf of Mexico. Presented at: Symposium on Biofouling and Corrosion in OTEC, Seattle, Wash., R. H. Gray, Chairman.

Olsen, H. L. and P. P. Pandolfini (1975). Analytical study of two-phase-flow heat exchangers for OTEC systems. Johns Hopkins Univ. Applied Physics Lab., APL/JHU AEO-75-37, 113 pp.

Sundaram, T. R., E. Sambuco, A. M. Sinnarivalla, and S. K. Kapur (1977). The external flow induced by an OTEC power plant. In: Proceedings Fourth Annual Conference on OTEC, G. E. Ioup, Ed., Univ. of New Orleans.

Trimble, L. C., B. L. Messinger, H. G. Ulbrich, G. Smith, T. Y. Lin (1975). Ocean thermal energy conversion system study report. In: Proceedings Third Workshop on OTEC, G. L. Dugger, Ed., APL/JHU SR 75-2, 3-21.

Walden, R. G. and E. A. Silva (1976). Deep ocean current measurement systems for obtaining construction design data. In: Proceedings 1976 Offshore Technology Conference, Houston, Texas, 495-505.

Wu, C. C. (1976). Design and modeling of solar sea power plants by geometric programming. Tech. Report ERDA/SE/E (11-1), 2895/TR/76/1, 147 pp.

Estuarine and Coastal Marine Science 7, 99-116.

Numerical Simulation of Dissolved Silica in the San Francisco Bay

David H. Peterson,[a] **John F. Festa**[b] **and T. John Conomos**[a]

[a] *U.S. Geological Survey, 345 Middlefield Road, Menlo Park, CA 94025 U.S.A.*

[b] *Atlantic Oceanographic and Meteorological Laboratories, National Oceanographic and Atmospheric Administration, 15 Rickenbacker Causeway, Virginia Key, Miami, FL 33149, U.S.A.*

Received 28 March 1977 and in revised form 26 July 1977

Keywords: partially mixed estuary; silica; river flow; simulation; numerical model; San Francisco Bay

A two-dimensional (vertical) steady-state numerical model that simulates water circulation and dissolved-silica distributions is applied to northern San Francisco Bay. The model (1) describes the strong influence of river inflow on estuarine circulation and, in turn, on the biologically modulated silica concentration, and (2) shows how rates of silica uptake relate to silica supply and mixing rates in modifying a conservative behavior. Longitudinal silica distributions influenced by biological uptake (assuming both vertically uniform and vertically decreasing uptake situations) show that uptake rates of 1 to 10 µg-at. l^{-1} day^{-1} are sufficient to depress silica concentrations at river inflows of 100–400 $m^3 s^{-1}$, respectively, and that the higher rates appear ineffective at inflows above 400 $m^3 s^{-1}$. The simulations further indicate that higher silica utilization in the null zone is not essential to depress silica concentrations strongly there. Advective water-replacement times at river inflows of 400, 200 and 100 $m^3 s^{-1}$ are computed to be less than 25, 45 and 75 days, respectively, for a 120-km estuary-river system.

Introduction

Physical processes control the distributions and behavior of many biologically reactive substances in estuaries. Although there are difficult problems which require increased understanding of the factors controlling currents and salinity distributions (cf. Dyer, 1976), our present knowledge of estuarine dynamics is sufficient for modelling some general features of biologically reactive substances. Seasonal variations in water chemistry and phytoplankton abundance in San Francisco Bay estuary (Peterson *et al.*, 1975*a*) appear to be closely related to the general water circulation patterns in the estuary. In this paper we contribute some understanding of water-circulation effects on nonconservative (biological and chemical) distributions in partially mixed estuaries. We describe a steady-state numerical model of dissolved silica and apply it to the seasonal silica variations in northern San Francisco Bay, estimating silica-utilization rates which produce nonconservative distributions.

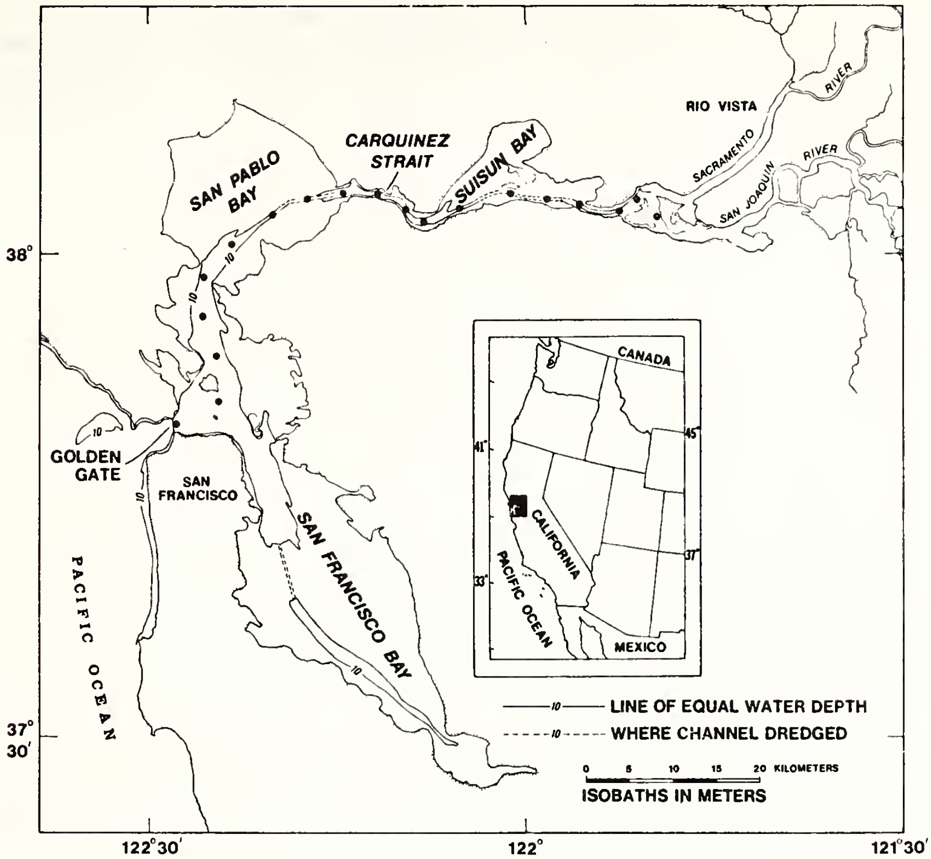
RIO VISTA
SACRAMENTO
RIVER
SAN JOAQUIN
RIVER
CARQUINEZ STRAIT
SUISUN BAY
SAN PABLO BAY
GOLDEN GATE
SAN FRANCISCO
SAN FRANCISCO BAY
PACIFIC OCEAN
CANADA
CALIFORNIA
PACIFIC OCEAN
MEXICO
45°
41°
37°
33°
10
LINE OF EQUAL WATER DEPTH
WHERE CHANNEL DREDGED
0 5 10 15 20 KILOMETERS
ISOBATHS IN METERS
38°
37° 30'
122°30'
122°
121°30'

Figure 1. San Francisco Bay system and environs. The study area is between Rio Vista and Golden Gate, the entrance to the ocean. All field data presented herein were collected at mid-channel stations.

Seasonal differences in water circulation in the northern bay (Figure 1) are created primarily by high (winter) and low (summer) river flow. Although average wind speeds are higher in summer than winter (Conomos & Peterson, 1976) the seasonal effect in this portion of the system is probably secondary to that of river inflow. We have examined this strong influence of river inflow on circulation and in turn on the silica concentrations by assuming simple distributions of silica uptake by phytoplankton production. The silica concentrations are primarily controlled by rates of river supply, biological removal, and dilution with seawater.

The real system: circulation, phytoplankton and silica

During much of the year the northern Bay is a partially mixed estuary with its circulation and salinity responding to variations in river inflow. During winter, salt water intrudes landward to San Pablo Bay and in summer to Rio Vista (Figure 1). The salt field probably never fully achieves steady-state adjustment with the water circulation even after a period of weeks of near-uniform river inflow. The salinity is generally low in relation to river inflow during summer and may be high during winter because of the lag in response of salinity to discharge (Ward & Fischer, 1971).

The few current-meter surveys in the main channel suggest that the null zone (where river and density currents are equal and opposite) is located about 20 km from the seaward end of the estuary (Golden Gate) when river discharge is 2000 $m^3 s^{-1}$ and 80 km when it is 100 $m^3 s^{-1}$ (Peterson *et al.*, 1975*b*). The corresponding distances of salinity penetration are 40 and 90 km from the seaward end.

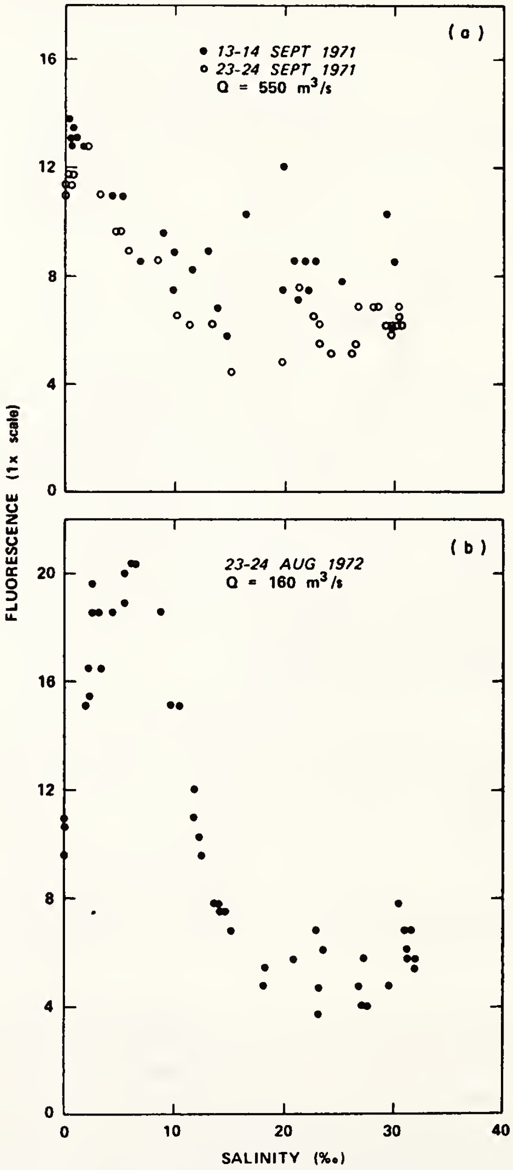

Figure 2. Longitudinal covariance of *in vivo* chlorophyll *a* with salinity (2-m depth) at different river inflows. Chlorophyll *a* measured with Turner fluorometer and expressed as fluorescence units. *Q* is combined mean monthly inflows of the Sacramento and San Joaquin rivers.

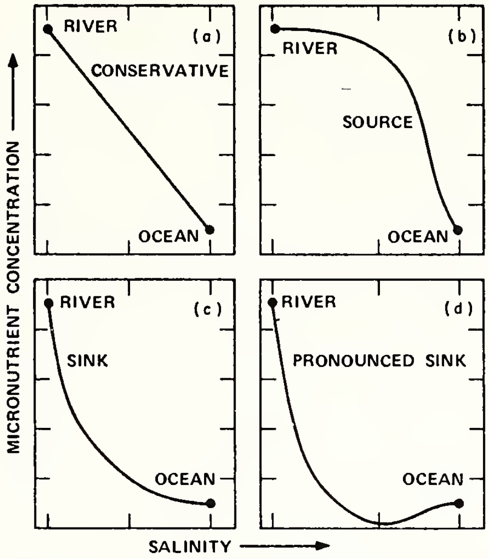

Figure 3. Idealized longitudinal distributions of salinity covarying with a nonconservative substance which has a higher concentration in river water than seawater. (a) Horizontal mixing rates dominate and effects of internal sources or sinks are negligible; (b) secondary source is present; (c) sink is present; (d) sink is pronounced relative to the horizontal mixing rate. After Peterson *et al.* (1975*a*).

Winter river inflows are typically above 400–500 $m^3 s^{-1}$; summer inflows are lower. During winter the phytoplankton distribution (as indicated by chlorophyll *a* measurements) is relatively uniform, whereas during summer the phytoplankton levels may increase in the upper estuary (phytoplankton maximum), particularly during lower-than-normal inflows (Figure 2). Phytoplankton productivity per unit volume is often highest in the phytoplankton maximum (Conomos & Peterson, 1974). Based on a unit area, however, productivity may be lower in the phytoplankton maximum than in a seaward direction where the euphotic zone is deeper (cf., Williams, 1966; Flemer, 1970). Diatoms are usually the most abundant phytoplankton, and increases in chlorophyll parallel increases in silica uptake.

The influence of nonconservative processes on the distribution of reactive substances is probably best demonstrated by relating the substances, such as silica, to salinity. In the Bay, silica-salinity distributions are represented by three [Figure 3(a), (c) and (d)] of four simple examples, with internal silica sources negligible [Figure 3(b)]. This is not always the case; in the Hudson River estuary, for example, internal silica sources (sewage) are excessive (Simpson *et al.*, 1975).

The seasonal silica-salinity variations are not steady-state distributions (Peterson *et al.*, 1975*a*). All data indicate that it takes weeks to depress silica to low concentrations from near-linear values. During summer, silica departs from near-linear values with salinity at river inflows less than 400–500 $m^3 s^{-1}$ (Figure 4) and is depressed the most during the lowest inflows of less than 100 $m^3 s^{-1}$.

Although silica uptake by phytoplankton is a depth-dependent process (unpublished data), differences in silica-salinity distributions have not been observed between surface and bottom waters (Figure 5). Effects of depth-variable silica uptake are apparently reduced or eliminated by vertical mixing.

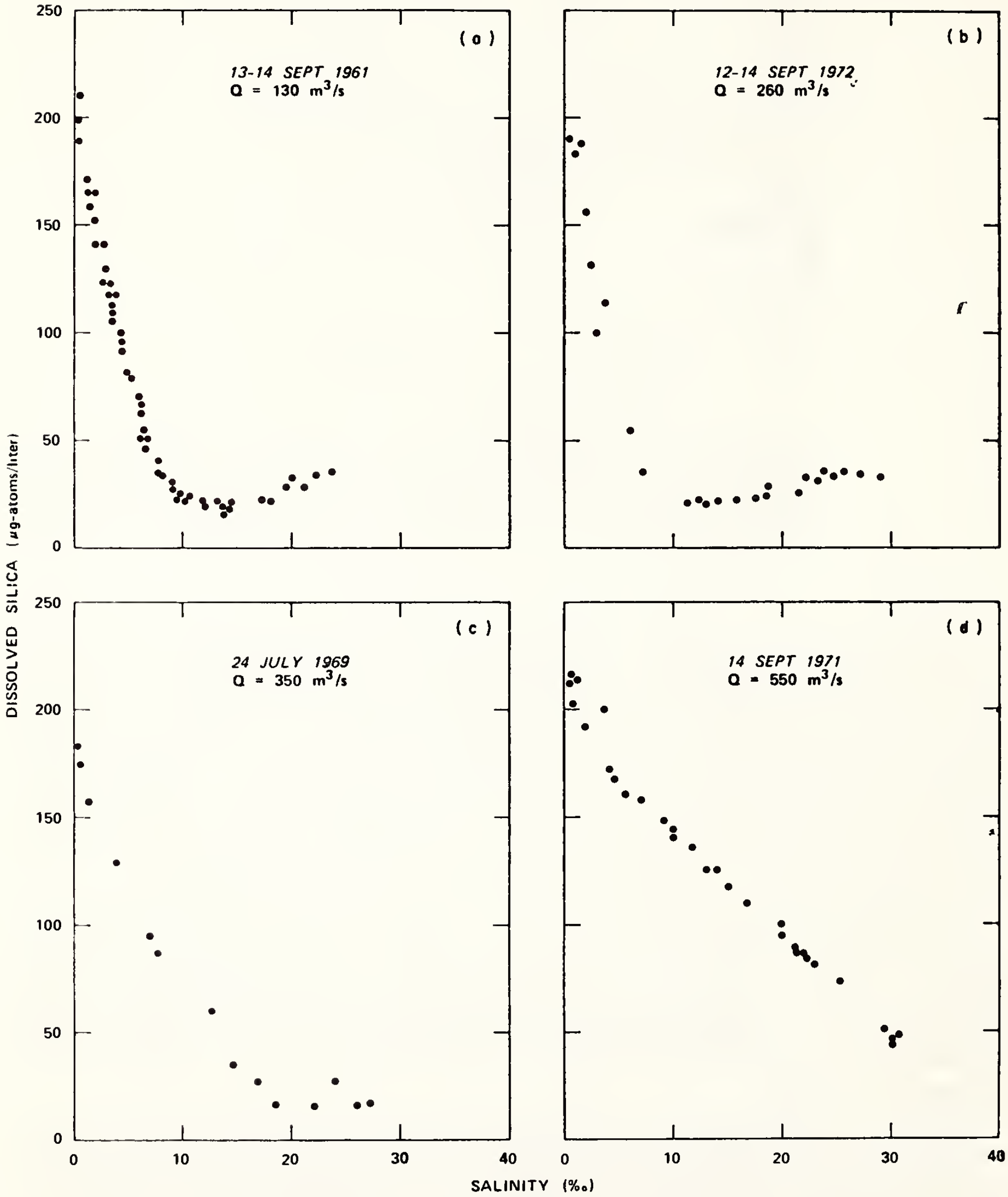

Figure 4. Observed silica-salinity covariance (2-m depth) for different mean monthly river inflows (Q). Data in (a) are from McCarty *et al.* (1962).

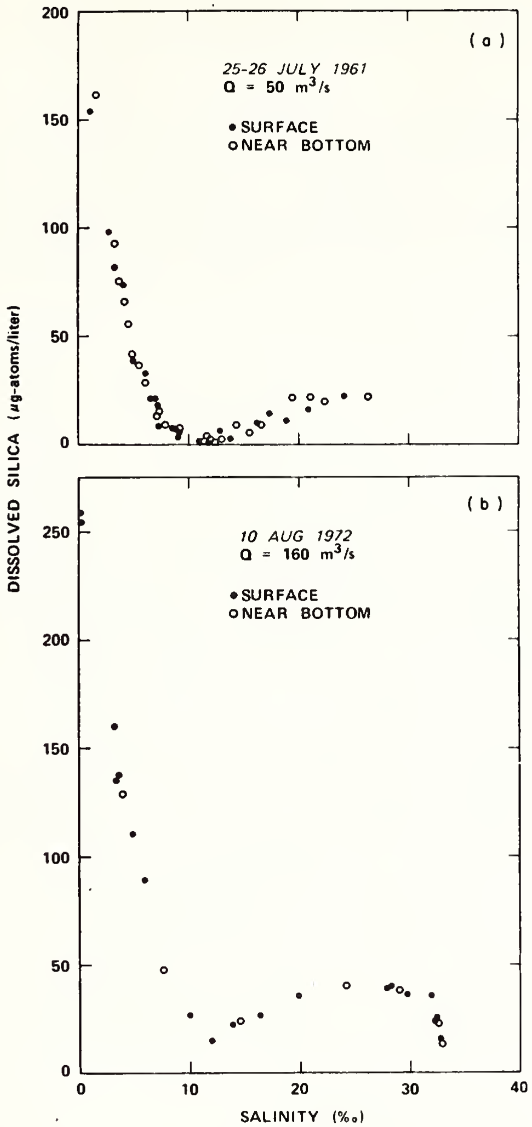

Figure 5. Observed silica-salinity covariance in surface (1-m depth) and bottom waters during periods of maximum biological removal. Data in (a) are from McCarty *et al.* (1962). *Q* is mean monthly river inflow.

The numerical silica model

Because of the lack of field data, the dynamics of San Francisco Bay estuary are defined using the numerical model of Festa & Hansen (1976) which describes a two-dimensional, steady-state, gravitational circulation. The depth and width of the estuary are assumed constant, as are the mixing coefficients of salt and momentum. This circulation model is especially advantageous for our needs because it describes the dynamics of the transition from river to estuary and the variations in dynamics with river inflow.

Development of our silica model is consistent with the Festa-Hansen description of circulation in partially mixed estuaries (Festa & Hansen, 1976). The governing equation for the silica concentration is:

$$\frac{\partial Si}{\partial t} + uSi_x + wSi_z = K_h Si_{xx} + K_v Si_{zz} - \text{uptake}, \qquad (1)$$

where Si is the silica concentration (μg-at. l^{-1}); u and w are the horizontal and vertical components, respectively, of tidally averaged velocity; K_h and K_v are the horizontal and vertical exchange coefficients of silica and represent a measure of the strength of tidal mixing; and 'uptake' is the parametric representation of the silica utilization rate by phytoplankton production (μg-at. l^{-1} day^{-1}).

Representative boundary values for silica are:

$$Si\,(x = \text{ocean},\ z = 10\text{ m}) = 30\ \mu\text{g-at. } l^{-1};$$
$$Si\,(x = \text{river}) = 200\ \mu\text{g-at. } l^{-1}.$$

The depth, H, is specified at 10 m and represents a typical value of the main channel where velocity, salinity, and silica data have been collected (Figure 1). The finite-difference techniques used to model silica are exactly the same as those developed for the circulation field.

Effects of the riverflow, silica-uptake rates, and vertical exchange coefficients on silica distributions were considered. River inflows of 100, 200, 400 and 2000 $m^3\,s^{-1}$ were simulated by approximating river currents of 1, 2, 4 and 20 cm s^{-1} at the river boundary. The first three inflow rates represent typical low, intermediate, and high summer river levels. The last, 2000 $m^3\,s^{-1}$, is a typical high winter rate. Bottom water salinity at the ocean boundary of 30‰ was specified in all cases, except for a value of 25‰ at 2000 $m^3\,s^{-1}$. Silica-uptake rates and vertical exchange coefficients, which were varied, are discussed in the following section.

We first approximated the water-circulation and salinity-diffusion processes using the Festa-Hansen model, and then applied this field to the silica model. The general circulation of Bay waters (Conomos, 1975) and some of its variations with river inflow (Peterson *et al.*, 1975*b*) provided an approximation for evaluating the response of the Festa-Hansen model to river inflow as well as a basis for estimating the mixing coefficients. No attempt was made to adjust closely the Festa-Hansen model to various field conditions because of simplifications in the numerical model and our limited knowledge of the real circulation. Our major concern is to produce a reasonable approximation of gravitational circulation for various river inflows, as this circulation drives the flow in our silica model.

The numerical simulation

Vertical velocity and salinity distributions generated by the Festa-Hansen circulation model are presented for river inflows of 100, 200, 400 and 2000 $m^3\,s^{-1}$ (Figure 6). The seaward movement of the null zone with increasing inflow is similar to results obtained from the few available current-meter observations. The response of water circulation and salinity to variations in vertical exchange of salt (K_v) and momentum (A_v) is also examined (Figure 7). The model indicates that increasing vertical exchange of momentum weakens estuarine circulation, and that increasing vertical exchange of salt strengthens the circulation.

The circulation and salinity fields obtained using the vertical exchange coefficients of $A_v = 20\ cm^2\,s^{-1}$ and $K_v = 4\ cm^2\,s^{-1}$ give a reasonable approximation to field conditions, and were thus used to generate the dynamics for the silica model.

Effects of river inflow on silica distributions were examined using two hypothetical cases for silica uptake: (1) Constant and vertically uniform uptake throughout the estuary (Figure 8),

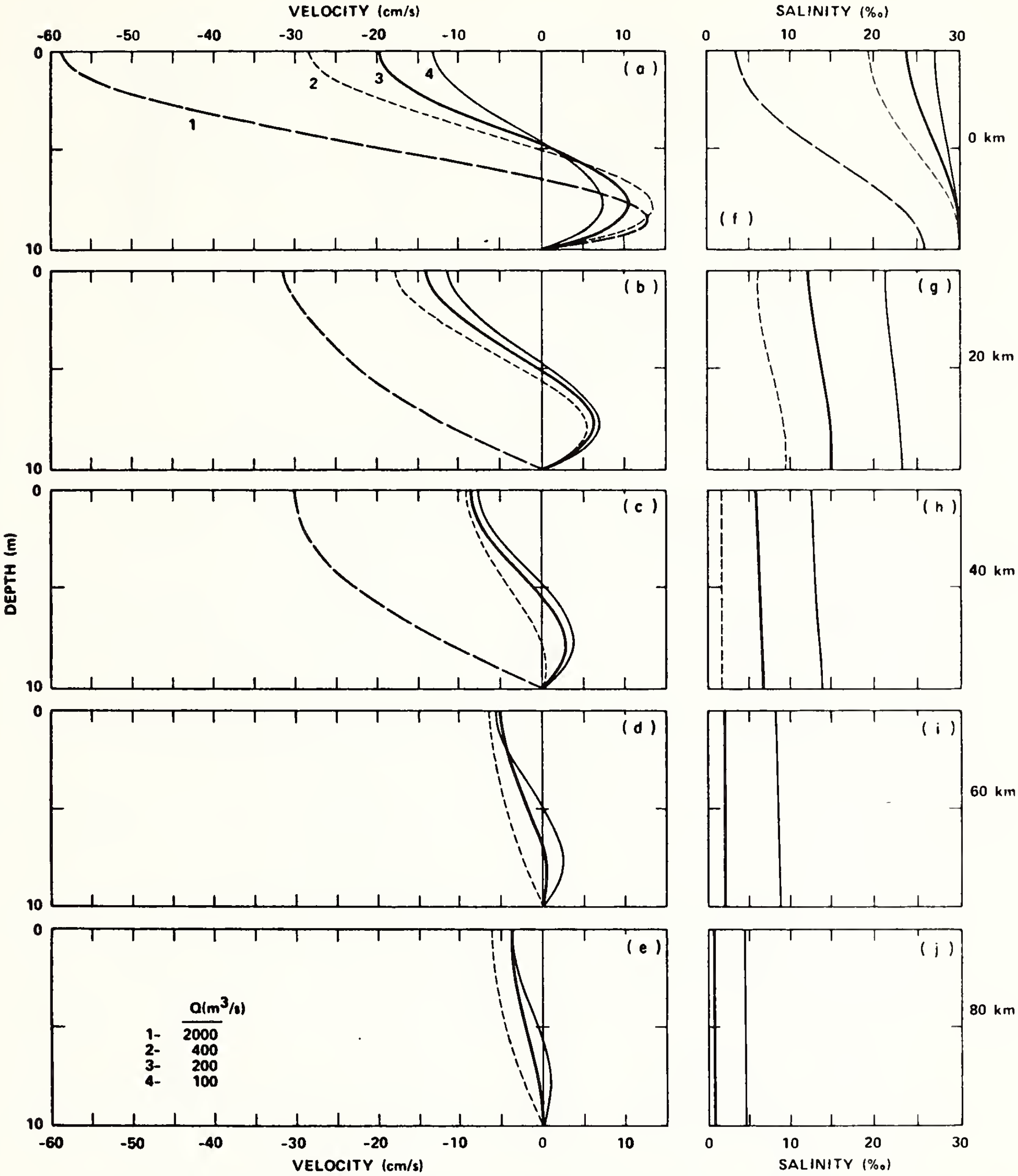

Figure 6. Simulated longitudinal variations of velocity and salinity for various river inflows (Q) at several locations in the estuary. Computational length for river currents of 1, 2, 4, and 30 cm s^{-1} are 160, 120, 64 and 48 km respectively. The horizontal mixing coefficients of salt (K_h) and momentum (A_h) were specified at 4×10^6 and 10^7 cm^2 s^{-1}, respectively; the vertical mixing coefficients are $K_v = 4$ and $A_v = 10$ cm^2 s^{-1}, respectively.

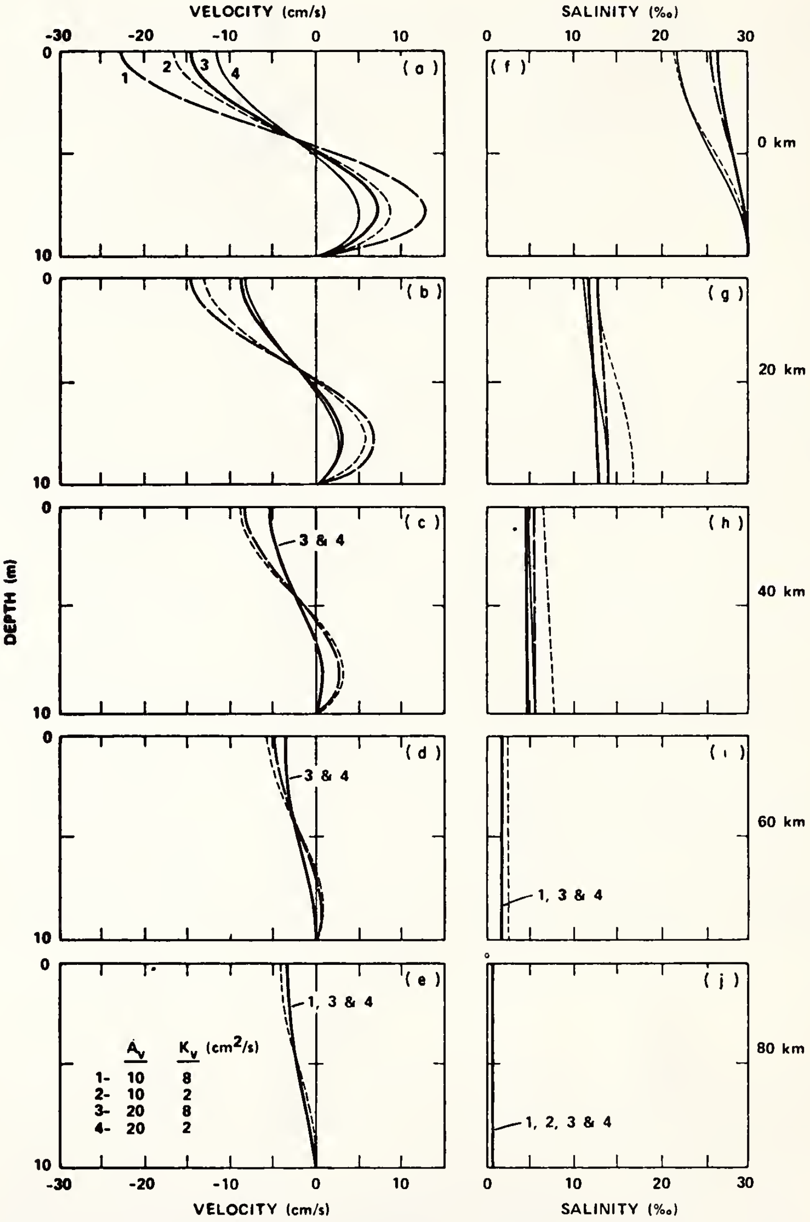

Figure 7. Simulated longitudinal variations of velocity and salinity for various vertical mixing coefficients of salt (K_v) and momentum (A_v) at different locations in the estuary. The river current is constant at 2 cm s^{-1}. $K_h = 4 \times 10^6$ and $A_h = 10^7$ cm^2 s^{-1}.

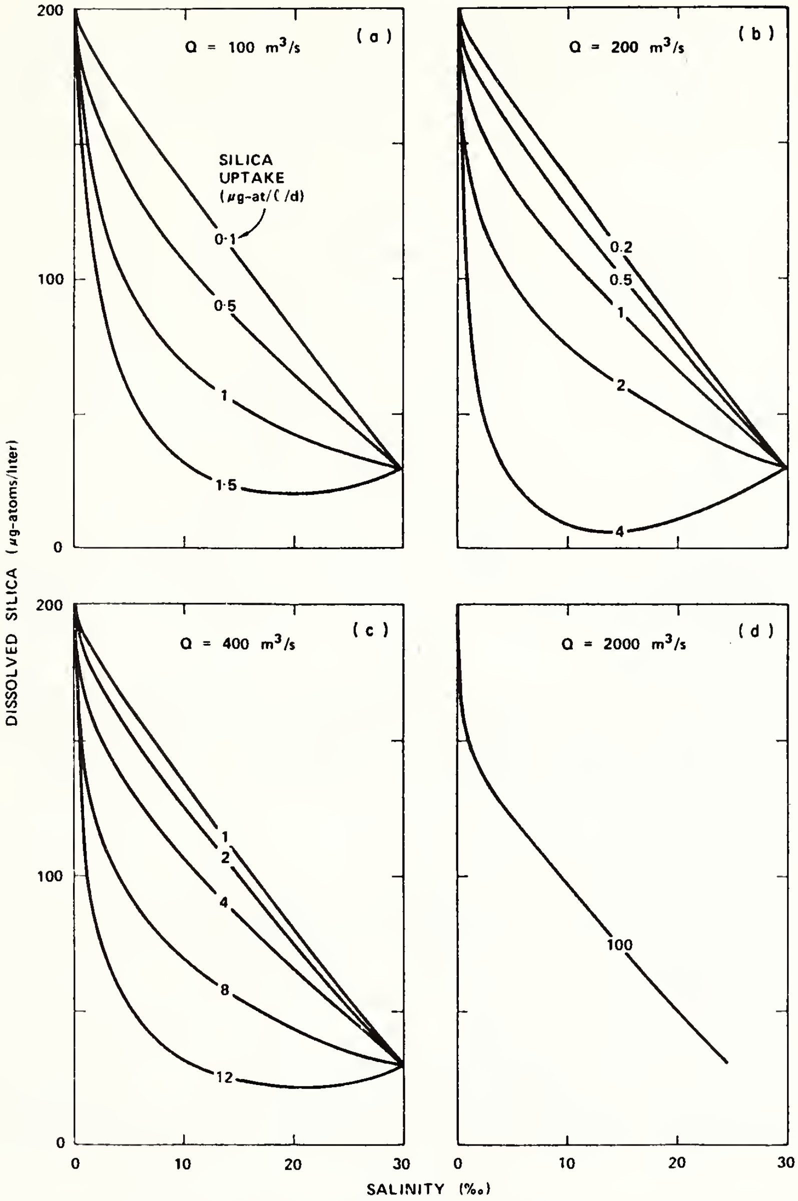

Figure 8. Simulated silica-salinity covariance for different river inflow (Q) and silica uptake rates. $K_v = 4$ and $A_v = 20\ \mathrm{cm}^2\ \mathrm{s}^{-1}$; $K_h = 4 \times 10^6$ and $A_h = 10^7\ \mathrm{cm}^2\ \mathrm{s}^{-1}$. Silica uptake for each simulation is vertically uniform throughout the estuary.

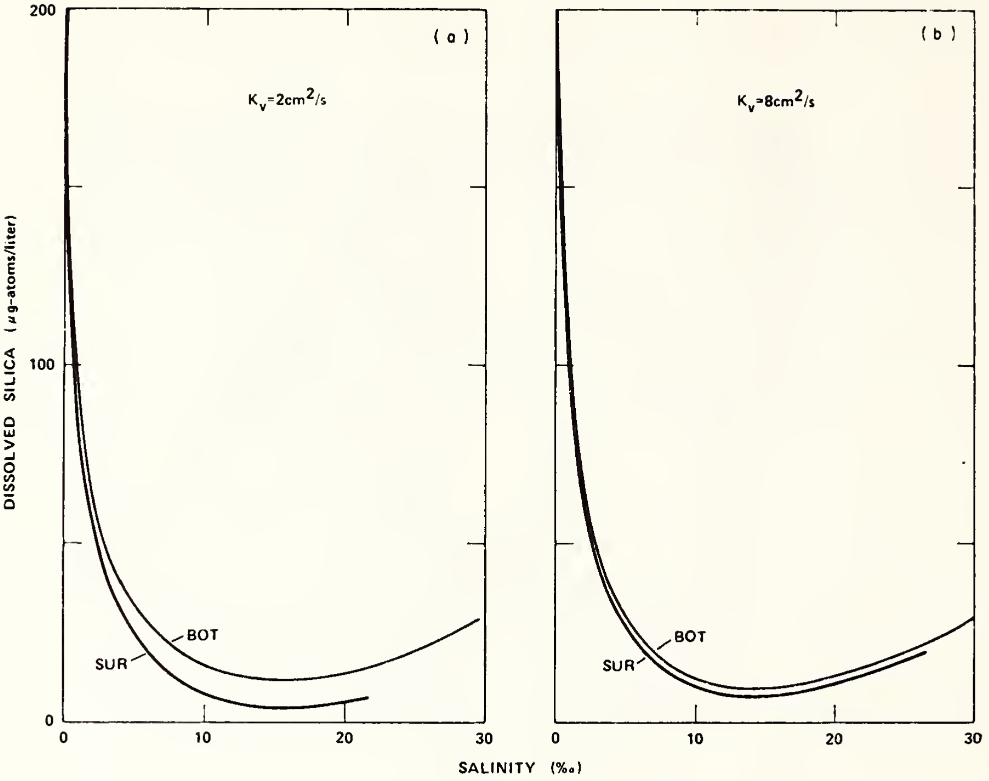

Figure 9. Simulated silica-salinity covariance in surface (SUR) and bottom (BOT) waters as a function of varying vertical salt (and silica) mixing coefficients (K_v). A_v is 20 $cm^2\ s^{-1}$, and the river current is 2 $cm\ s^{-1}$. Silica uptake is 12 μg-at. l^{-1} day^{-1} in upper 2·5 m and zero below that depth.

and (2) constant uptake in the upper few meters and zero uptake below (Figure 9). The latter seems more realistic since uptake rates are near zero below the euphotic zone. In both cases the conservative effects of water advection and diffusion were initially simulated for zero silica uptake throughout the estuary. Solutions were then obtained for relatively small utilization rates, and were gradually increased until the minimum silica concentrations approached the growth-rate limiting concentrations of 4 to 12 μg-at. l^{-1} (Paasche, 1973*a*, *b*; Davis *et al.*, 1973; Harrison, 1974; Goering *et al.*, 1973), and for completeness, an unrealistically large value of 100 μg-at. l^{-1} day^{-1} [Figure 8(d)]. Limiting maximum uptake rates in this fashion eliminated the complication of introducing utilization terms which depend on silica.

Results from constant silica uptake throughout the estuary show that 1·5 μg-at. l^{-1} day^{-1} (15 mg-at. m^{-2} day^{-1}) is sufficient to depress strongly silica concentrations at an inflow of 100 $m^3\ s^{-1}$ [Figure 8(a)]. This rate has only a moderate effect on the silica-salinity distribution at 200 $m^3\ s^{-1}$ [Figure 8(b)] and produces only a minor departure from a linear (conservative) distribution at 400 $m^3\ s^{-1}$ [Figure 8(c)].

Silica-salinity distributions obtained from constant uptake in the upper 2·5 m and zero below (Figure 9) are similar to those assuming constant and vertically uniform uptake throughout the estuary (Figure 8). In this formulation, however, the utilization rates must be 4 times higher since they are applied to only one-fourth the water depth.

Depth variations of observed silica-salinity distributions are on the order of a few μg-at. l^{-1}, the equivalent of the observed variability (Figures 4 and 5). Such variations are approached for simulations in which the vertical exchange coefficient, K_v, is 8 $cm^2 s^{-1}$ [Figure 9(b)]. This coefficient, which also gives reasonable circulation fields, results in a silica diffusive time scale, H^2/K_v, of approximately 1·4 days, and indicates that surface water of the euphotic zone may be mixed over the entire water column in nearly 1 day.

Conservative versus nonconservative processes

Our immediate interest in modelling silica was to estimate rates of biological removal at which silica behaves conservatively and nonconservatively for various river inflows, and thus, to determine under what conditions physical processes maintain near-linear silica-salinity distributions. Water circulation and uniform biological uptake of silica are considered as two independent but competing processes. Estuarine silica-salinity distributions would either remain linear, vary seasonally or remain non-linear and should depend on the relative strengths of these processes. Model results indicate utilization rates necessary to produce three of these possibilities [Figure 8(a), (b) and (c)].

Field observations illustrate a seasonal variation in silica-salinity concentrations (Figure 4). Although depression of silica concentrations is a common occurrence during low summer inflow, such depression has never been observed in over 10 years of near-monthly surveys at inflows greater than 400 $m^3 s^{-1}$.

If the silica uptake rates required to produce a marked non-linear silica-salinity distribution are unrealistic, it would explain why the natural conditions remain near-linear at discharges greater than 400 $m^3 s^{-1}$. If we assume an inflow of 400 $m^3 s^{-1}$, a 10-m water column, and a 1-m euphotic zone (the field conditions of the phytoplankton-turbidity maximum), uptake in the upper meter must approach 120 μg-at. Si l^{-1} day^{-1} to depress strongly the silica concentrations. Phytoplankton productivity would be more than 5000 mg C m^3 day^{-1}, assuming a (moderate) Si : C ratio of 1 : 4. Limited field observations (unpublished) indicate that this production rate is an order of magnitude too high. Thus the model provides an estimate of average silica utilization rates (1–10 μg-at. l^{-1} day^{-1}) which are roughly equivalent to that from other methods (e.g., carbon productivity).

Residence time

Water residence time, the average time required for water to enter and leave the estuary, is influenced by both advective and diffusive processes. River inflow and density currents control advective processes, while wind and tidal mixing control diffusive processes. Wind is omitted in the following discussion.

In general, river currents decrease in the seaward direction with increasing cross-channel area, whereas inward flowing density currents ultimately weaken to equal the opposing river current (null zone); tidal mixing attenuates landward. The net effect of these processes may produce a longitudinal variation in the advective and diffusive replacement time of a substance (Figure 10).

As the river flow increases the null zone shifts seaward and the residence time decreases. Average bottom density currents seldom exceed 15 cm s^{-1} and do not increase dramatically with increasing river inflow (Officer, 1976). It follows that as river currents increase to 10

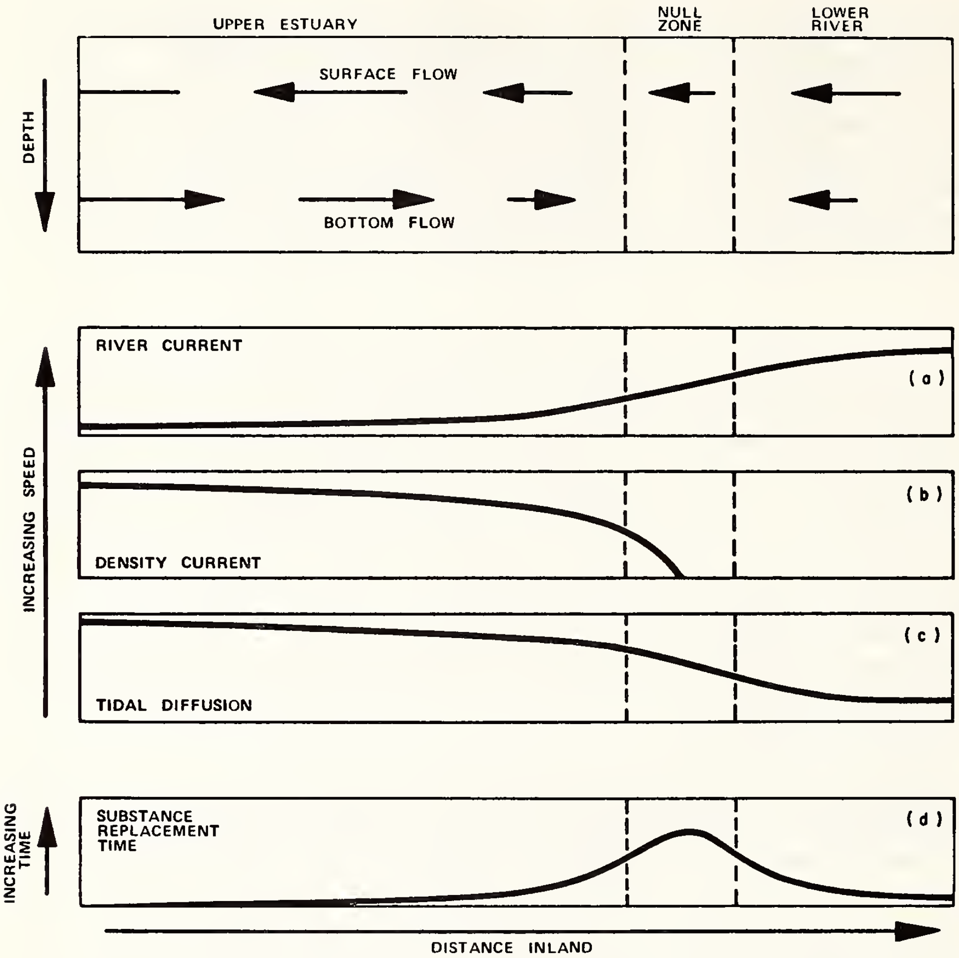
UPPER ESTUARY
NULL ZONE
LOWER RIVER
SURFACE FLOW
BOTTOM FLOW
DEPTH
RIVER CURRENT
(a)
(b)
DENSITY CURRENT
(c)
TIDAL DIFFUSION
INCREASING SPEED
SUBSTANCE REPLACEMENT TIME
(d)
INCREASING TIME
DISTANCE INLAND

Figure 10. Qualitative contributions of river current (a), density current (b), and tidal diffusion (c) to longitudinal variations in substance replacement time (d) in a hypothetical estuary. Modified after Peterson *et al.* (1975*a*).

cm s^{-1}, longitudinal variations in advective water replacement time may be relatively small.

Model results (Figures 8, 9) indicate that higher phytoplankton productivity in the null zone is not essential for development of the observed silica salinity distribution. It is possible that even with lower rates of silica uptake, silica concentrations are still strongly depressed in the null zone. Such effects can be produced by an increased water and particle (phytoplankton) residence time in the inner estuary: a column of water there may not necessarily receive more sunlight per unit time than in the outer estuary, but the water (and phytoplankton) may receive sunlight over a longer time.

Advective water-replacement time per unit width and length are estimated from the 10-m depth model:

$$\bar{V}_{\text{river inflow}(ri)} = \frac{1}{10}\int_{0}^{10} V(z)_{ri}\,\mathrm{d}z \qquad (2)$$

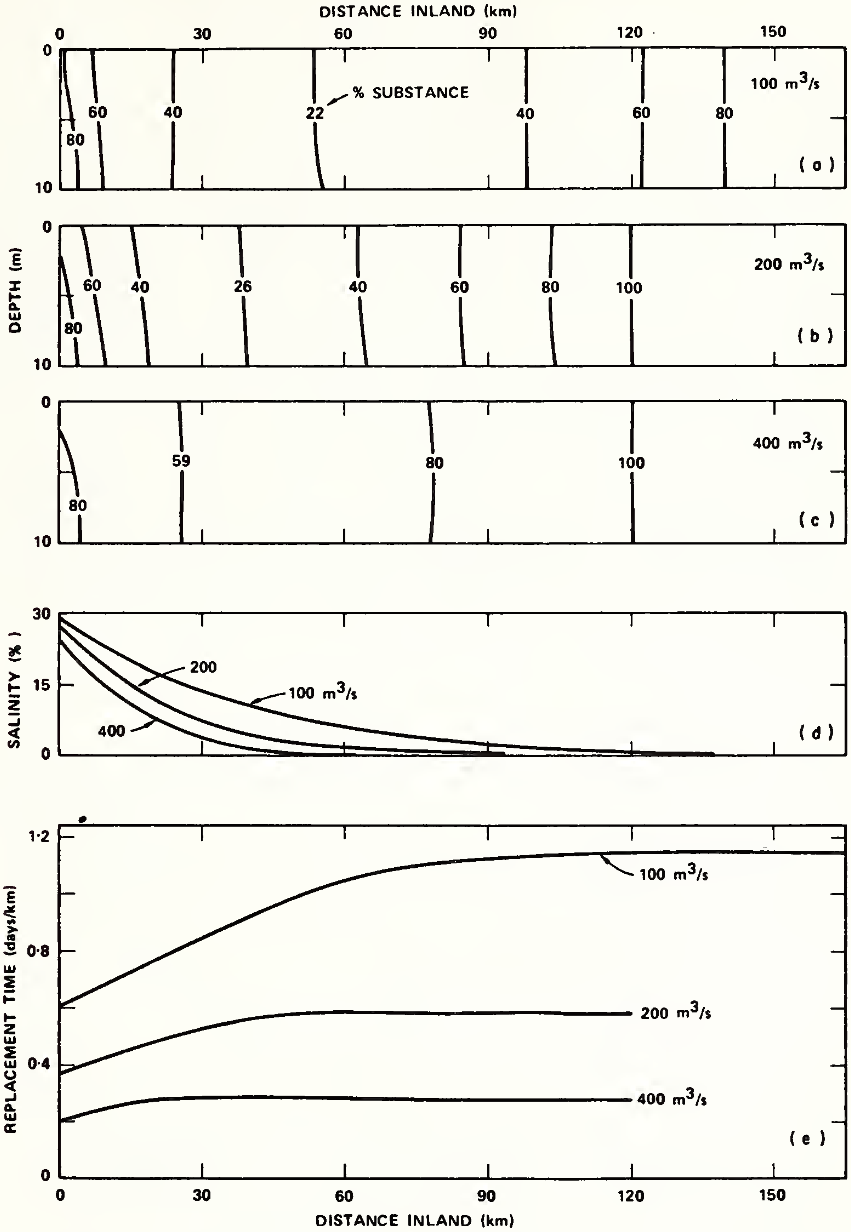

Figure 11. Simulated distribution of a nonconservative substance (per cent present) with distance as functions of various river inflows (a, b, c) assuming 100% input of substance at both river and ocean boundaries and a continuous uptake of 1% day^{-1} for 100 m^3 s^{-1} and 2% day^{-1} for 200 and 400 m^3 s^{-1}. (d) Simulated salinity distribution at 5 m at various river inflows. (e) Simulated nonconservative substance replacement time for averaged water column as a function of distance at various river inflows. $K_v = 4$ and $A_v = 20$ cm^3 s^{-1}.

$$\bar{V}_{\text{ocean inflow}(ot)} = \frac{1}{10} \int_{0}^{z,\ \text{where}\ V_{ot} = 0} V(z)_{ot}\, dz \tag{3}$$

$$\text{and replacement time} = \frac{\text{Length}}{\bar{V}_{rt} + \bar{V}_{ot}} \tag{4}$$

where $\bar{V}$ is the mean current speed. Note that because the model represents constant width, maximum water-replacement time is in the river [Figure 11(e)].

Advective water-replacement times per unit width, for a 120-km river-estuary system, are estimated from the model to be 75, 45 and 25 days for river inflows of 100, 200 and 400 $m^3\,s^{-1}$ respectively ($A_v = 20\ cm^2\,s^{-1}$; $K_v = 4\ cm^2\,s^{-1}$). In these time periods, on the average, a conservative substance introduced continuously at the center of the 120-km system may move by eddy diffusivity ($K_h = 4 \times 10^6\ cm^2\,s^{-1}$) about 70, 55 and 40 km, respectively ($\sqrt{2K_hT}$).

The silica model can be used to illustrate effects of advective and diffusive processes on substance replacement time by maintaining 100 units of silica at both river and ocean boundaries. Note the seaward shift in minimum concentration with increasing river inflow [Figure 11(a), (b) and (c)]. In a typical simulation, the minimum (steady-state) concentration was about 26 units in the null zone for a river discharge of 200 $m^3\,s^{-1}$ and a uniform uptake rate of 2 units per day. We can estimate that it takes (100—26)/2 units per day, or a 37-day maximum silica-replacement time, to produce this distribution (Figure 12). Because diffusive processes are included, this is less than the advective replacement time estimated above.

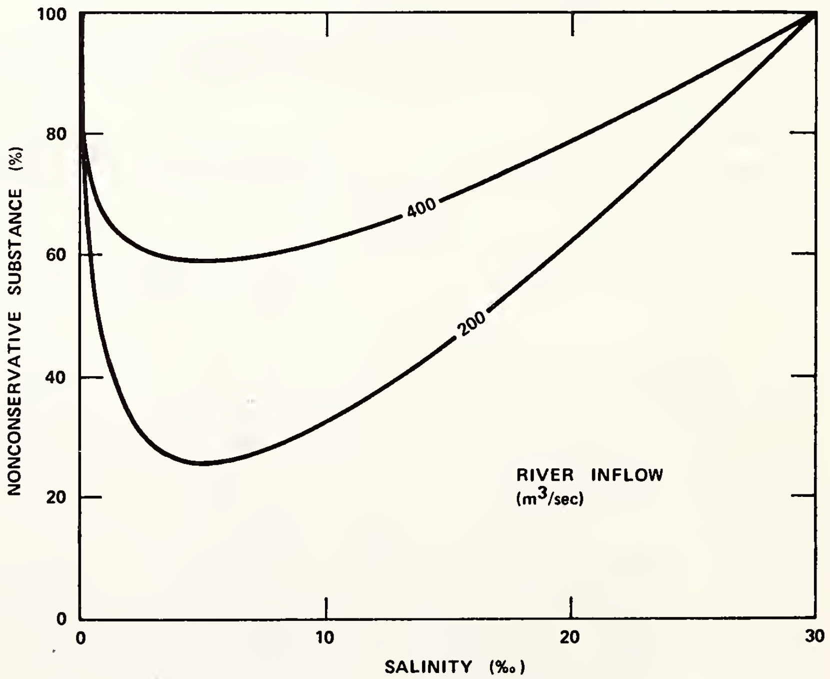

Figure 12. Simulated distribution of a nonconservative substance with salinity as a function of various river inflows assuming 100% input of substance at both river and ocean boundaries and a constant uptake of 2% per day. $K_v = 4$ and $A_v = 20$ $cm^2\,s^{-1}$.

The combination of an uptake of 1 unit per day and a river discharge of 100 $m^3\ s^{-1}$ has a silica distribution similar to the 200 $m^3\ s^{-1}$ example, and indicates an 80-day maximum silica replacement time for a 160-km system.

Average rates of silica utilization can be estimated using the above results. For example, the maximum departure of silica concentrations from a conservative distribution is about 125 μg-at. l^{-1} at 130 $m^3\ s^{-1}$ [Figure 4(a)]. If the water residence time is approximately 60 days at this inflow, estimated silica uptake is 2 μg-at. l^{-1} day^{-1}. The silica-salinity distribution in Figure 4(b) is essentially identical to Figure 4(a) but inflow is twice as high, giving an average uptake of about 4 μg-at. l^{-1} day^{-1}. These are gross estimates because the field data are not true steady state distributions. As such, the silica-salinity distribution measured at 260 $m^3\ s^{-1}$ may be influenced by the lower (160 $m^3\ s^{-1}$) inflow of the preceding month producing a lower estimated utilization rate. It may also be difficult to estimate total inflow, especially during low summer flows when the amount of water consumption by agricultural activities downstream of river gauging sites is appreciable and not clearly determined.

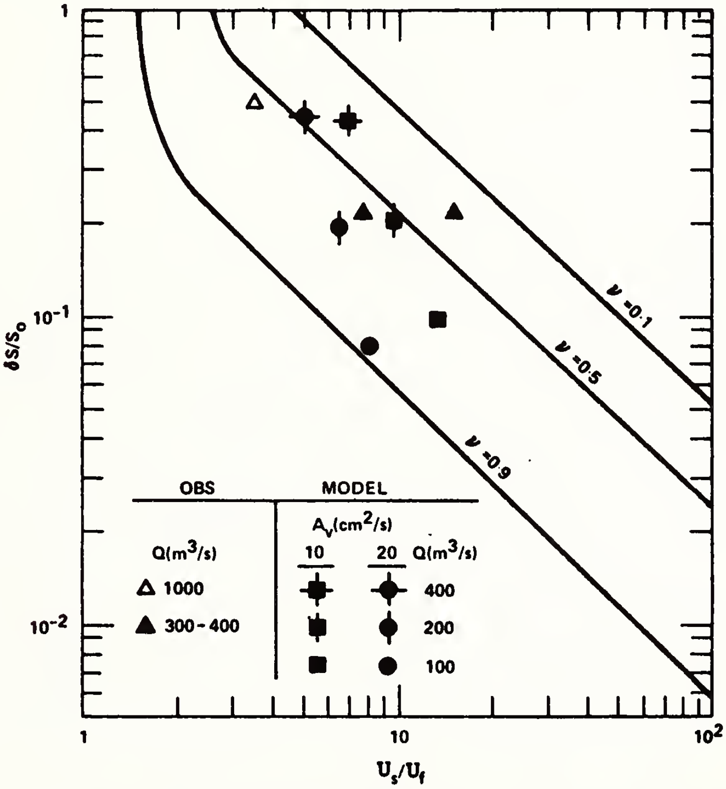

Figure 13. Observed and simulated fractions (v) of horizontal salt balance by diffusion as functions of salinity stratification ($\delta S/S_o$) and estuarine circulation (U_s/U_f). Values from numerical simulation (MODEL) represent circulation at the seaward boundary. Observed data (OBS), from Peterson & Conomos (1975) and were collected at Carquinez Strait (Figure 1). Note variation with increased river inflow (Q) and with increased vertical mixing coefficients of momentum (A_v). Diagram from Hansen & Rattray (1966).

Advective and diffusive processes

Knowledge of the relative strengths of advective and diffusive processes is helpful in understanding the development of non-conservative silica distributions in estuaries. The Hansen-Rattray (1966) estuarine classification diagram provides an estimate of the relative contribution of either process toward landward salt transport and is especially appropriate for describing results from the Festa-Hansen circulation model (Figure 13).

For illustrative purposes, we selected the model circulation-salinity values from its seaward boundary (and the few field observations at Carquinez Strait, Figure 1). Increasing river inflow shifts these values diagonally toward the upper left of the diagram with an associated decrease in water replacement time.

This diagram can characterize the circulation when silica behaves conservatively. Obviously, a field in the diagram of increased river inflow (upper left) is a regime of linear or near-linear silica-salinity distributions as long as the silica utilization rate giving conservative distributions at lower inflow does not increase. Hence, silica may always appear conservative during 'high' inflow. It is interesting that linear silica-salinity distributions may typify most temperate estuaries (Fanning & Pilson, 1973; Boyle *et al.*, 1974); unfortunately, their position on the Hansen-Rattray diagram is usually undefined.

A hypothetical season

We summarize the effects of estuarine dynamics on silica distributions by describing a typical spring to fall sequence of river inflow.

During late spring, inflow decreases to approximately 400–500 $m^3 s^{-1}$ and insolation increases. The longitudinal distribution of phytoplankton is uniform. A larger portion of the estuary is influenced by the density currents, as is shown by increased salt penetration and by landward movement of the null zone. The maximum replacement time is approximately 20 days and silica uptake rates (averaged over the water column) are between 1 and 2 μg-at. l^{-1} day^{-1}. Silica-salinity distributions remain conservative (near-linear) at these utilization rates, since it takes more than 20 days to depress silica strongly.

Inflow continues to decrease during summer, while phytoplankton increases in abundance particularly in the upper estuary. Rates of silica uptake may increase slightly. More significantly, however, the river supply rate of silica decreases and water residence time increases. At an inflow of 200 $m^3 s^{-1}$, the replacement time is about 40 days. Silica concentrations become depressed in approximately one month, producing non-conservative distributions. If inflow decreases to 100 $m^3 s^{-1}$ a conspicuous phytoplankton maximum persists in the upper estuary where the non-tidal currents are weak, and average silica uptake rates may exceed 1 to 2 μg-at. l^{-1} day^{-1}. Replacement time is more than 70 days; silica concentrations are well below 70 μg-at. l^{-1} from their predicted conservative concentrations and may approach growth-rate limiting levels.

Inflow increases during fall, silica input exceeds removal by phytoplankton, and eventually silica-salinity distributions become conservative (linear).

This scenario is illustrated by all years for which there are silica data (1961–64 and 1968–present) with the exception of 1976, an unusually dry year during which silica remained near-linear during low inflow. Such 'anomalous' behavior is currently under investigation.

Acknowledgements

We thank W. W. Broenkow, D. E. Hammond, D. V. Hansen and C. B. Officer for helpful discussions and criticisms.

References

Boyle, E., Collier, R., Dengler, A. T., Edmond, J. M., Ng, A. G. & Stallard, R. F. 1975 On the chemical mass-balance in estuaries. *Geochimica et Cosmochimica Acta* **38**, 1719–1728.

Conomos, T. J. 1975 Movement of spilled oil as predicted by estuarine nontidal drift. *Limnology and Oceanography* **20**, 159–173.

Conomos, T. J. & Peterson, D. H. 1974 Biological and chemical aspects of the San Francisco Bay turbidity maximum. *Memoirs de l'Institut de Géologie du Bassin d'Aquitaine* **7**, 45–52.

Conomos, T. J. & Peterson, D. H. 1976 Suspended-particle transport and circulation in San Francisco Bay: an overview. *Proceedings of the 3rd Meeting of the International Estuarine Research Federation Conference* (in press).

Davis, C. O., Harrison, P. J. & Dugdale, R. C. 1973 Continuous culture of marine diatoms under silicate limitation, I. Synchronized life cycle of *Skeletonema costatum*. *Journal of Phycology* **9**, 175–180.

Dyer, K. R. (in press) Lateral effects in estuaries. *Symposium on Estuaries, Geophysics, and the Environment*. AAAS Meetings, 1976.

Fanning, K. A. & Pilson, M. E. Q. 1973 The lack of inorganic removal of dissolved silica during river-ocean mixing. *Geochimica et Cosmochimica Acta* **37**, 2405–2415.

Festa, J. F. & Hansen, D. V. 1976 A two-dimensional nu~~co~~mmercial model of estuarine circulation: the effects of altering depth and river discharge. *Estuarine and Coastal Marine Science* **4**, 309–323.

Flemer, D. A. 1970 Primary production in the Chesapeake Bay. *Chesapeake Science* **11**, 117–129.

Goering, J. J., Nelson, D. M. & Carter, J. A. 1973 Silicic acid uptake by natural populations of marine phytoplankton. *Deep-Sea Research* **20**, 777–789.

Hansen, D. V. & Rattray, M. Jr. 1966 New dimensions in estuary classification. *Limnology and Oceanography* **11**, 319–326.

Harrison, P. J. 1974 Continuous culture of the marine diatom *Skeletonema costatum* (Grev.) Cleve under silicate limitation, Ph.D. thesis, Univ. Washington, Seattle, 140 pp.

McCarty, J. C., Wagner, R. A., Macomber, M., Harris, H. S., Stephenson, M. & Pearson, E. A. 1962 An investigation of water and sediment quality and pollutional characteristics of three areas in San Francisco Bay 1960–61. Sanitary Engineering Research Laboratory, University of California, Berkeley, California. 571 pp.

Officer, C. B. (in press) Longitudinal circulation and mixing relations in estuaries. *Symposium on Estuaries, Geophysics, and the Environment*. AAAS Meetings, 1976.

Paasche, E. 1973*a* Silicon and the ecology of marine plankton diatoms. I. *Thalassiosira pseudonana* (*Cyclotella nana*) grown in a chemostat with silicate as limiting nutrient. *Marine Biology* **19**, 117–126.

Paasche, E. 1973*b* Silicon and the ecology of marine plankton diatoms. II. Silicate-uptake kinetics in five diatom species. *Marine Biology* **19**, 262–269.

Peterson, D. H., Conomos, T. J., Broenkow, W. W. & Scrivani, E. P. 1975*a* Processes controlling the dissolved silica distribution in San Francisco Bay. In *Estuarine Research—Chemistry and Biology* (Cronin, L. E., ed.). Academic Press, London and New York, Vol. 1, pp. 153–187.

Peterson, D. H., Conomos, T. J., Broenkow, W. W. & Doherty, P. C. 1975*b* Location of the nontidal current null zone in northern San Francisco Bay. *Estuarine and Coastal Marine Science* **3**, 1–11.

Peterson, D. H. & Conomos, T. J. 1975 Implications of seasonal chemical and physical factors on the production of phytoplankton in northern San Francisco Bay. In *Proceedings of the Workshop on Algal-Nutrient Relationships in the San Francisco Bay and Delta*. (Brown, R. L., ed.). The San Francisco Bay and Estuarine Association. pp. 147–165.

Simpson, H. J., Hammond, D. H., Deck, B. L. & Williams, S. C. 1975 Nutrient budgets in the Hudson River Estuary. In *Marine Chemistry in the Coastal Environment*. (Church, T. M., ed.). A.C.S. Symposium Series, No. 18, pp. 618–635. 710 pp.

Ward, R. B. & Fischer, H. B. 1971 Some limitations on use of the one-dimensional dispersion equation, with comments on two papers by R. W. Paulson. *Water Resources Research* **7**, 215–220.

Williams, R. B. 1966 Annual phytoplankton production in a system of shallow temperate estuaries. In *Some Contemporary Studies in Marine Science*. (Barnes, H., ed.). George Allen and Unwin Ltd., London, pp. 689–716.

Printed in Great Britain by Henry Ling Ltd., at the Dorset Press, Dorchester, Dorset

17

Proceedings Ocean Thermal Energy Conversion (OTEC) Biofouling and Corrosion Symposium, PNL-SA-7115, 423-445.

SYNTHESIS AND DESCRIPTION OF THE EXISTING HISTORICAL INORGANIC NUTRIENT DATA SETS FROM THREE POTENTIAL OTEC SITES: NORTHERN GULF OF MEXICO, PUERTO RICO, AND ST. CROIX

S. R. Cummings, Jr., D. K. Atwood and J. M. Parker
Atlantic Oceanographic and Meteorological Laboratories
15 Rickenbacker Causeway, Virginia Key
Miami, Florida 33149

ABSTRACT

A historical data set for inorganic nutrients was assembled from records supplied by NODC and others. Nutrient concentrations were reviewed at three proposed Ocean Thermal Energy Conversion (OTEC) sites: Northern Gulf of Mexico, Puerto Rico, and St. Croix. Nutrient variation in the Caribbean was small as denoted by tightly-packed scatter diagrams. Seasonal variation of nutrient concentrations was not seen in the Caribbean data set. Nutrient curves from the Northern Gulf of Mexico demonstrated the same general shapes as those from the Caribbean. However, the Northern Gulf was considerably more variable and richer. Large nutrient variations at the surface reflected the Mississippi River influence. Two Loop Current Eddy intrusions were reviewed. The effect was to inject higher dissolved oxygen and lower inorganic nutrient Caribbean water into the Gulf of Mexico. Work is continuing to elucidate range of nutrient variation caused by Eddies.

INTRODUCTION

Oceanic nutrient concentrations are important in defining an area's potential productivity. Principal open ocean inorganic nutrients include nitrate (NO_3-N), nitrite (NO_2-N), phosphate (PO_4-P), silicate (SiO_3-Si) and oxygen (O_2). Frequently, one or more of the nutrients occurs in low concentrations and limits biological activity of a particular community component. Energy flow between the lower trophic levels, including bacteria, may directly utilize the primary producers or their excreted by-products (Bell and Mitchell, 1972). For this reason, if the biofouling phenomena is bacteria related, inorganic nutrient concentrations are of concern to Ocean Thermal Energy Conversion (OTEC) design engineers, microbiologists and ecologists.

Our synthesis of existing historical data has afforded a long-term base with which to view inorganic nutrient concentrations at three proposed OTEC sites: northern Gulf of Mexico, Puerto Rico, and St. Croix. Data were collected by many investigators conducting private and public research in several different countries. Most data, after review by its respective investigator, was forwarded to the National Oceanographic Data Center (NODC) for storage and dissemination on request.

Some group efforts encompassed large geographic areas. El Sayed et al. (1972) produced a chemical/biological overview of the Gulf of Mexico. The State University System of Florida Institute of Oceanography (SUSIO) focused on the eastern Gulf of Mexico (Jones et al., 1973; Smith, 1974). The University of Puerto Rico studied the Puerto Rico area (Atwood et al., 1976). In general, for our regions of interest, chemical summaries were few and data were collected sporadically, both geographically and temporarily.

Unfortunately, the summaries did not contain sufficient data to answer questions proposed by OTEC engineers and ecologists.

Robert H. Gray, Editor
Sponsored by:
United States Department of Ener
Division of Solar Energy
Washington, D. C. 20545 and
Pacific Northwest Laboratory
Richland, Washington 99352

Therefore, a survey of historical data at several proposed OTEC sites was initiated. We began an intensive effort to synthesize existing historical data.

METHODS

Station data from the entire Gulf of Mexico and Caribbean were requested from (NODC) and Atlantic Oceanographic and Meteorological Laboratory (AOML) sources. Private investigators and research institutes were also solicited for data; however, little pertinent to proposed OTEC sites was found that had not already been forwarded to NODC or was available at AOML. Special files under the auspices of NODC; i.e., Mississippi, Alabama, Florida (MAFLA), and South Texas, were investigated. However, the data found were already in the NODC Master File or in pending monthly updates. Although no data were known to be in transit, several data sets were being prepared for transmittal to NODC at an unannounced date.

The assembled data set was partitioned into subsets for the Puerto Rico, St. Croix, and northern Gulf of Mexico regions. Sampling distribution with respect to time was tabulated for each area to describe the generally uneven sampling distribution within years; i.e., seasonal, and among years. Scatter plots of nutrients and dissolved oxygen versus depth were made to describe the concentration of envelopes for each variable. Scatter diagrams of nutrients and dissolved oxygen were also plotted against Potential Temperature (θ). θ is the temperature which would result if a water sample was collected at depth and then raised adiabatically to the surface. This procedure "removes" the heating caused by pressure and allows temperatures of different water masses at different depths to be compared. Plots versus temperature (θ in this case) also can be used to demonstrate seasonal temperature fluctuation in the surface waters. Central trends indicated by the denser parts of the scatter diagrams were compared. Vertical contour sections, programs developed by Niedrauer and Herman (1978) and scatter diagrams were used to describe the variation caused by Loop Current Eddies in the Gulf of Mexico.

RESULTS AND DISCUSSION

Shaded areas (Figure 1) indicate: I. northern Gulf of Mexico OTEC Site; II. Puerto Rico OTEC Site; and III. St. Croix OTEC Site. Data temporally collected in the shaded areas were not evenly distributed (Tables 1-3). The number of stations sampled in a 5-yr block were tabulated by months (i.e., 1971 through 1975, would appear under 1975, for each area). Generally, all areas were sampled infrequently until after 1960. Sampling effort at the Puerto Rico and St. Croix sites was most intense between 1971 and 1975, partially in response to the resource assessment at these proposed OTEC sites (Froelich and Atwood, 1974; Atwood et al., 1976; Atwood et al., 1977). Intensive sampling occurred in the Gulf of Mexico during the late 1960's. Monthly sample distribution was skewed toward the winter months at all three sites.

Caribbean OTEC Sites

Temperature versus salinity (T-S) diagrams are diagnostic of water masses. The T-S diagrams of Puerto Rico and St. Croix (Figures 2 and 3) are very similar, suggesting no differences in water masses or mixing zones. The water masses identified by the Puerto Rico and St. Croix T-S diagrams are presented in Table 4. The increased scatter displayed (Figures 2 and 3) by the Tropical Surface Water (TSW) includes seasonal variability.

Interpretation of scatter diagrams will be limited to general trends. We believe a few fluctuating data points may denote rare natural phenomenon or analytical error rather than recurring variations.

The Puerto Rico and St. Croix sites are very similar with respect to dissolved oxygen and nutrient concentrations, so only Puerto Rico data will be presented. The central trend curves for dissolved oxygen and nutrients versus depth (Figure 4) are not averages, but rather curves drawn through areas of most dense data points (Figures 5 through 7). The low dispersion within the concentration envelopes shown in these figures demonstrates the low variability of nutrient concentration in the upper 1000 m at the Puerto Rico and St. Croix sites.

Seasonal variation is biased by the large number of samples during the winter months and the relatively few samples collected during the summer months. The nutrient concentration levels at the surface approach zero, except for dissolved oxygen, causing small changes to be lost as the lower limits of detectability are approached and the margin of error increases. However, the scatter diagrams (Figures 5 through 7) show a similar narrow range of scatter over the whole water column. Thus, seasonal variability appears minimal in this data set, but the set is biased toward the winter.

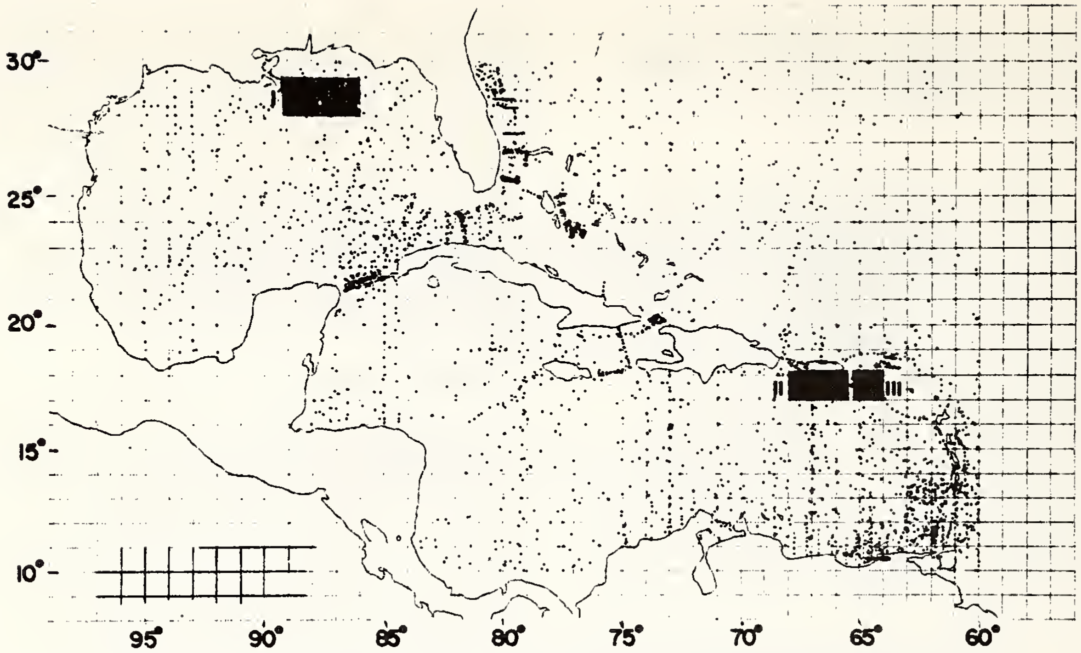

FIGURE 1. Geographical Location of OTEC Study Areas and Nutrient Station Data in the Gulf of Mexico and Caribbean

TABLE 1. Sample Distribution with Respect to Time at the Proposed Northern Gulf of Mexico OTEC Site (28°N, 88°W)

	1940	1945	1950	1955	1960	1965	1970	1975	1980	Total
January	0	0	0	2	0	0	6	0	0	8
February	0	0	0	0	0	1	13	0	0	14
March	7	0	0	0	0	6	6	0	0	19
April	0	0	0	0	0	0	8	0	0	8
May	0	0	0	3	0	0	6	0	0	9
June	0	0	0	5	2	2	8	0	0	17
July	0	0	0	0	0	0	3	0	0	3
August	0	0	0	4	0	0	6	0	0	10
September	0	0	0	0	0	27	4	0	0	31
October	0	0	0	0	0	0	2	0	0	2
November	0	0	0	0	0	0	5	0	0	5
December	0	0	0	0	0	0	28	0	0	28
Total	7	0	0	14	2	36	95	0	0	154

TABLE 2. Sample Distribution with Respect to Time at the Proposed Puerto Rico OTEC Site (18°N, 65°45'W)

	1940	1945	1950	1955	1960	1965	1970	1975	1980	Total
January	1	0	0	0	0	0	0	4	0	5
February	0	0	0	0	0	0	3	15	0	18
March	1	0	0	0	0	0	0	18	0	19
April	0	0	0	5	0	0	0	18	0	23
May	0	0	0	0	0	0	0	5	0	5
June	0	0	0	1	0	0	0	5	0	6
July	0	0	0	0	0	0	0	1	0	1
August	0	0	0	0	0	0	0	1	0	1
September	0	0	0	0	0	6	0	2	0	8
October	0	0	0	0	0	1	0	2	0	3
November	0	0	0	0	1	0	1	2	0	4
December	0	0	0	0	0	0	1	2	0	3
Total	2	0	0	6	1	7	5	75	0	96

TABLE 3. Sample Distribution with Respect to Time at the Proposed St. Croix OTEC Site (17°45'N, 64°45'W)

	1940	1945	1950	1955	1960	1965	1970	1975	1980	Total
January	1	0	0	0	0	0	0	0	0	1
February	0	0	0	0	4	0	0	5	0	9
March	2	0	0	0	0	0	0	8	0	10
April	0	0	0	0	0	0	0	10	0	10
May	0	0	0	0	0	1	5	0	0	6
June	0	0	0	0	0	0	0	1	0	1
July	0	0	0	0	0	0	0	1	0	1
August	0	0	0	0	0	2	0	0	0	2
September	0	0	0	0	0	2	0	0	0	2
October	0	0	0	0	0	0	0	0	0	0
November	0	0	0	0	0	0	0	1	0	1
December	0	0	0	0	0	0	0	0	0	0
Total	3	0	0	0	4	5	5	26	0	43

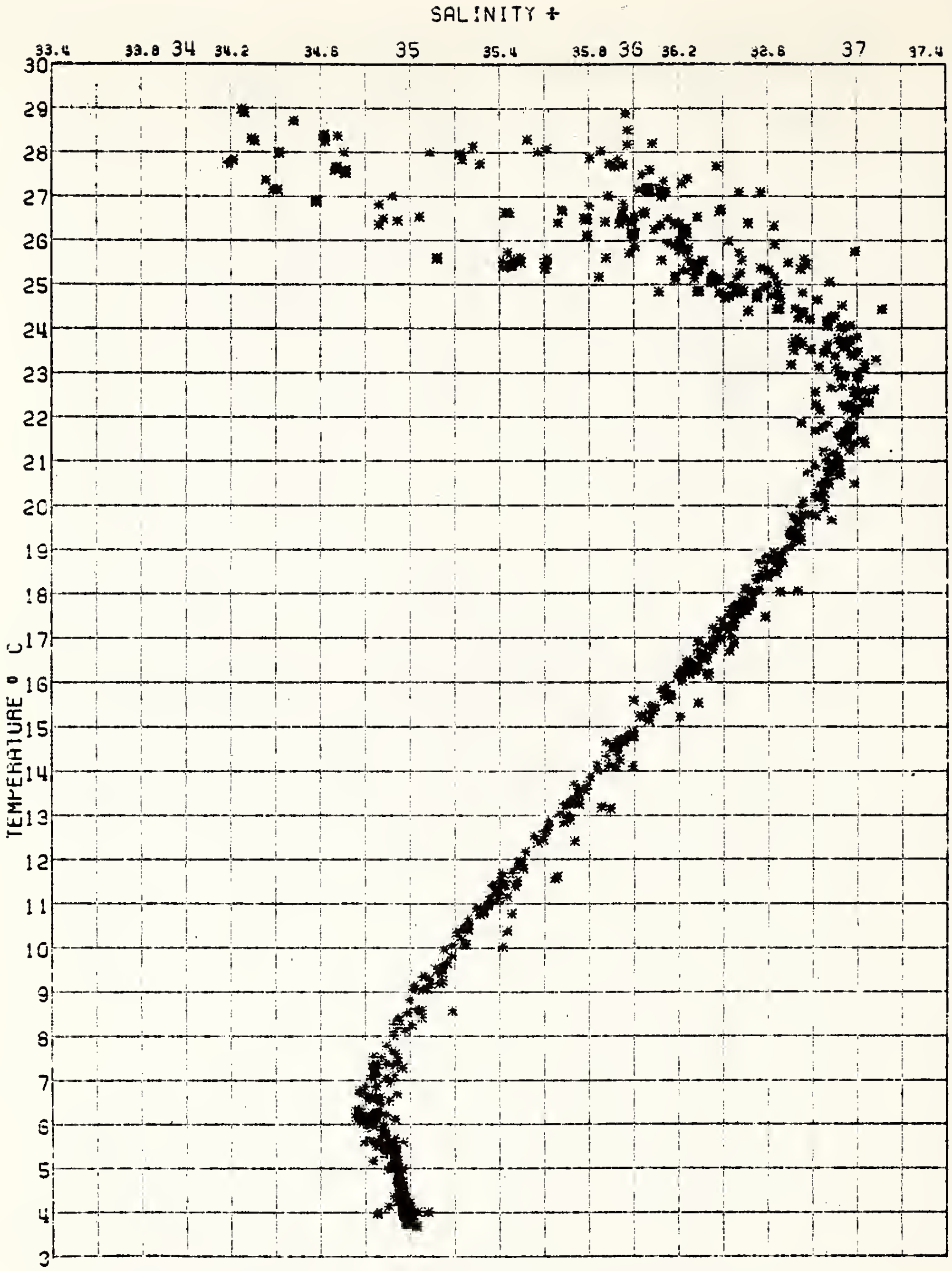

FIGURE 2. Salinity versus Temperature at the Puerto Rico OTEC Area

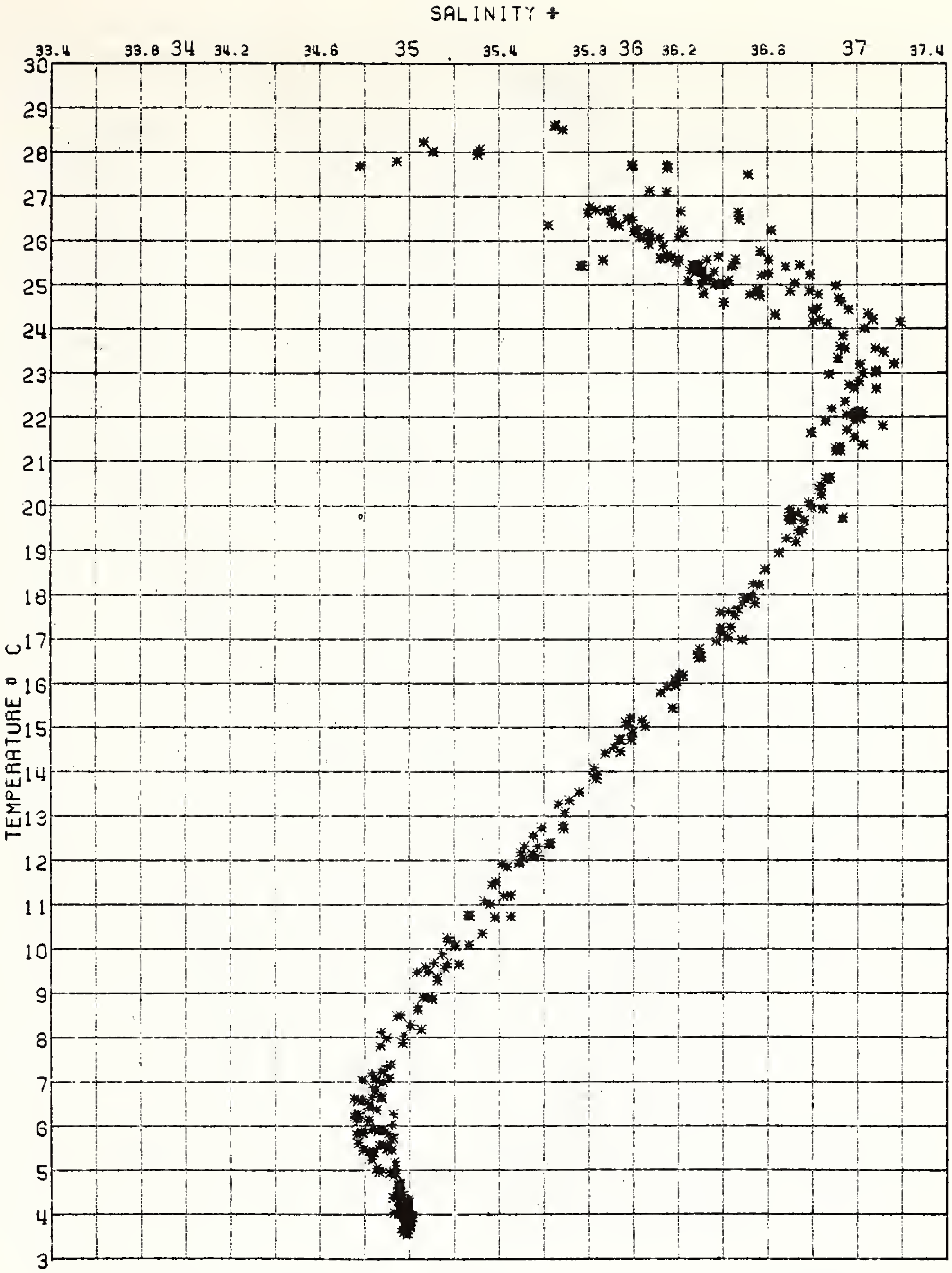

FIGURE 3. Salinity versus Temperature at the St. Croix OTEC Area

TABLE 4. Characteristics of Water Masses Found at Proposed Puerto Rico, St. Croix, and Northern Gulf of Mexico OTEC Sites

Water Mass	Temperature	Salinity
Tropical Surface Water (TSW)	>24°C	<36.8
Subtropical Underwater (SUW)	22-23°C	>37.0
North Atlantic Central Water (NACW)	9-18°C	35.1-36.2
Antartic Intermediate Water (AIW)	6- 7°C	34.8
Venezuela Basin Water (VBW)	< 5°C	35.0

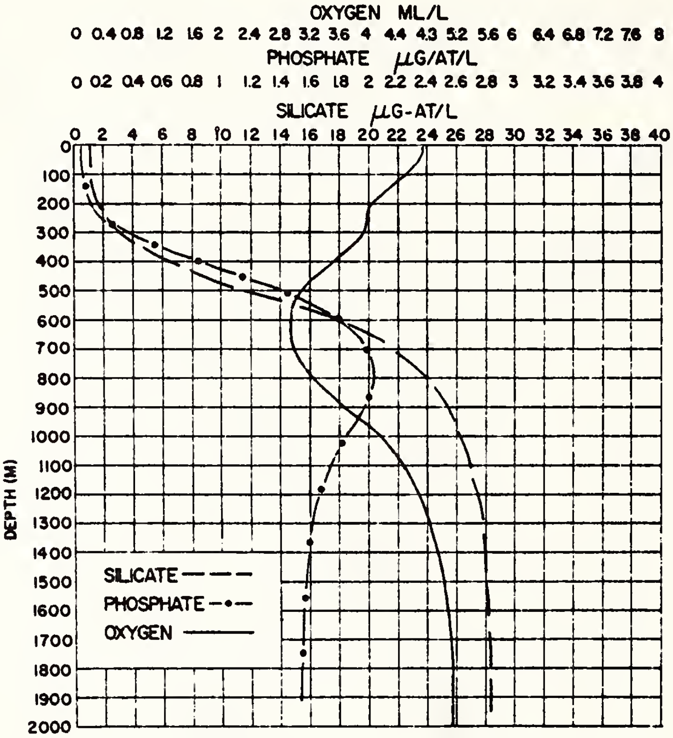

FIGURE 4. Central Trends of Dissolved Oxygen and Nutrient Concentrations versus Depth in the Puerto Rico OTEC Area

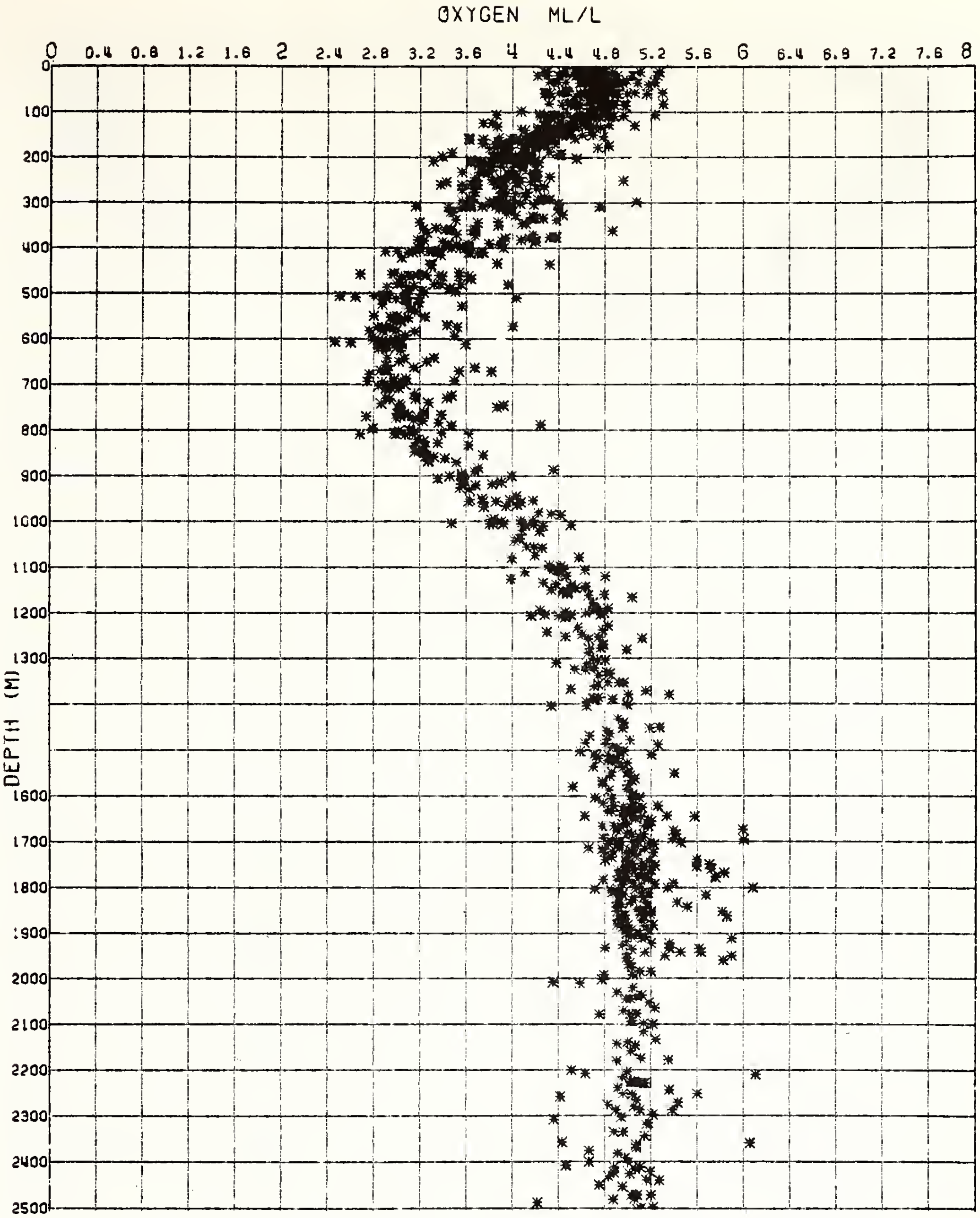

FIGURE 5. Dissolved Oxygen versus Depth at the Puerto Rico OTEC Area

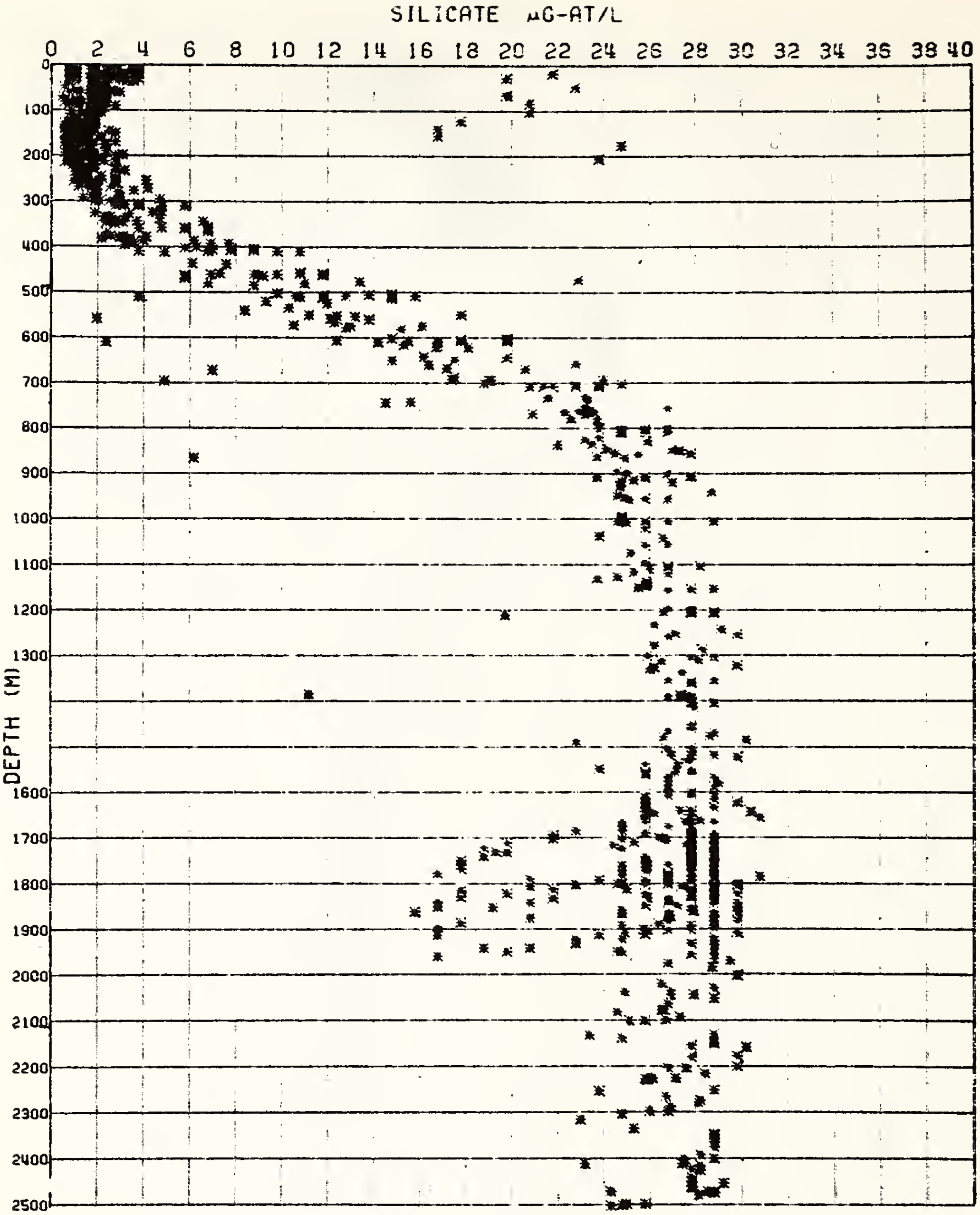

FIGURE 6. Silicate (SiO_3-Si) versus Depth at the Puerto Rico OTEC Area

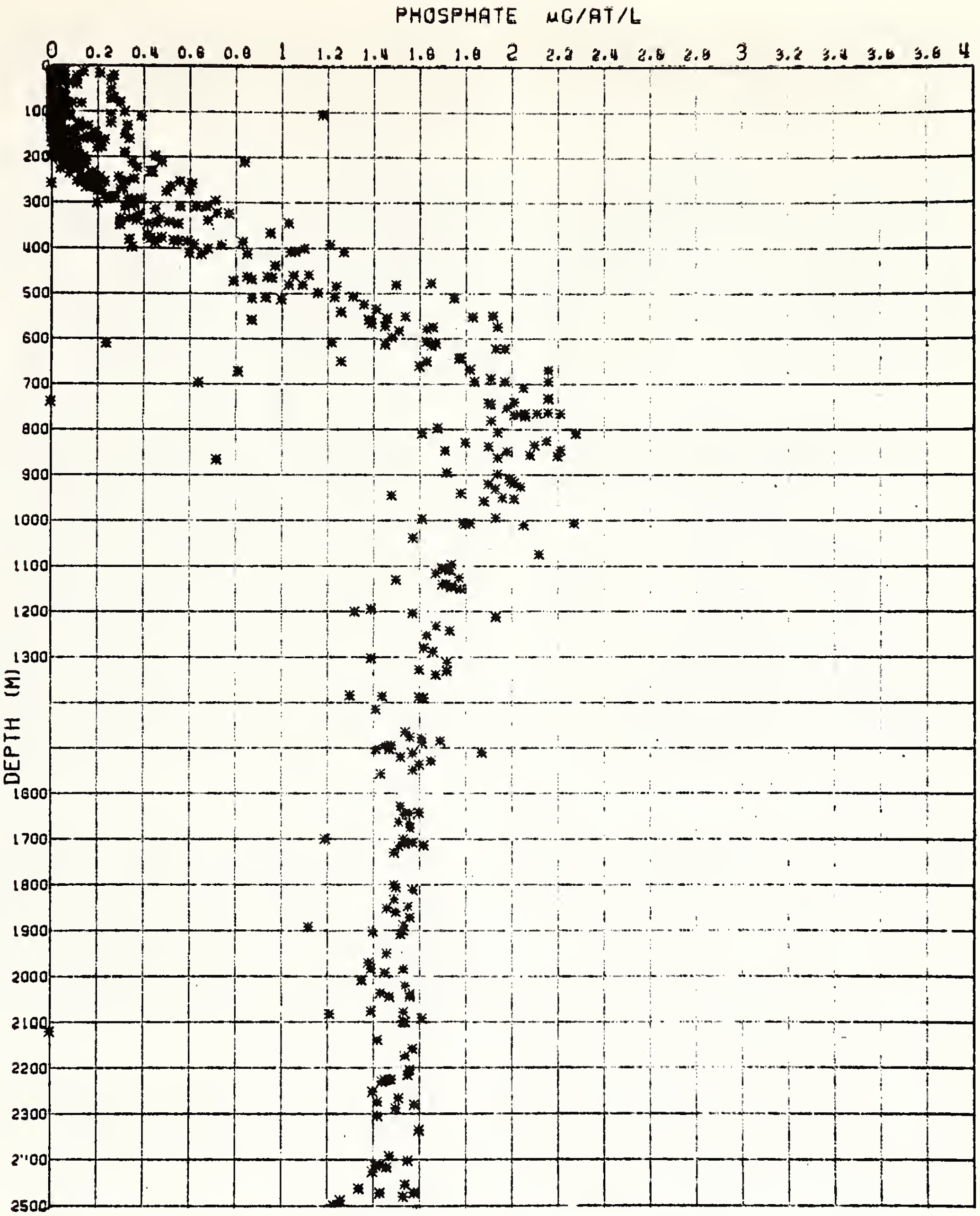

FIGURE 7. Phosphate (PO_4-P) versus Depth at the Puerto Rico OTEC Area

The noticeable decrease in silicate (SiO_3-Si, Figure 6) at 1800 m is suggestive of deep water renewal (Froelich et al., 1974) and is being investigated further.

Northern Gulf of Mexico Site

The northern Gulf of Mexico (northern Gulf) OTEC area shows greater variability of dissolved oxygen and nutrients than the Caribbean OTEC areas. This is immediately obvious when comparing the northern Gulf T-S diagram (Figure 8) to those of Puerto Rico and St. Croix (Figures 2 and 3). Below approximately 600 m is a very dynamic area which will be the focus of our attention.

The central trends of nutrient and dissolved oxygen concentration are shown in Figure 9. These trends are based on the scatter diagrams of observations in the northern Gulf of Mexico OTEC areas (Figures 10 through 13). Table 5 summarizes the comparison between the northern Gulf of Mexico OTEC site and the Caribbean areas. Generally, nutrients are higher in the surface 600 m in the northern Gulf of Mexico than near Puerto Rico or St. Croix. The reverse is true for dissolved oxygen; lower oxygen values are found in the surface waters of the northern Gulf of Mexico than the Caribbean area. Below 600 m, the differences are relatively small when compared to the variation above this depth.

The large surface variation seen in silicate, phosphate, and nitrate can be explained as follows. Silicate concentrations in the upper 50 m range from 0.0 to 30.8 μg-at/l SiO_3-Si; however, the variation is only 0.0 to 4.0 μg-at/l SiO_3-Si (Figure 11) if stations within 20 miles of the Mississippi River Delta are not used indicating the heavy influence of the river plume. A single offshore station 40 miles south of the Delta in December 1969, gave concentrations of 15-17 μg-at/l SiO_3-Si in the upper 2 m of water. However, the surface salinity increased from 27.74 °/oo to 32.40 °/oo at 3 m, with a corresponding drop in the silicate to 4.0 μg-at/l SiO_3-Si indicating that the high silicate values resulted from plume water floating on the surface.

Phosphate variation in the upper 100 m is also influenced by the Mississippi River (Figure 12). Stations having phosphate concentrations greater than 0.9 μg-at/l PO_4-P are close to the Mississippi River Delta. The December 1969 station previously mentioned had 1.58 μg-at/l PO_4-P in the surface plume water and .38 μg-at/l PO_4-P at 10 m.

Nitrate variation (Figure 13) can be explained for the same reasons as silicate and phosphate. Stations within the Mississippi River plume near the River Delta typically have higher than expected values.

Seasonal variation can best be seen on the scatter plots of θ versus concentration. In general, it can be seen that nutrient concentration levels above 18°C rapidly approach zero. Silicate (Figure 14) shows a conspicuous spike near 18°C which can be attributed to spring runoff. Nitrate (Figure 15) was not influenced by spring runoff. Phosphate varies near the surface irrespective of temperature (Figure 16).

The amount of nutrient variation below 100 m in the northern Gulf is considerable in comparison to the Caribbean. In certain cases, when documentation exists, this can be explained in terms of Loop Current Eddy intrusion. These eddies are derived from the Gulf Loop Current (Figure 17) arching high up into the Gulf of Mexico and then "pinching off" when the current core meanders (Nowlin et al., 1968; Molinari, 1977; Molinari et al., 1977). The resulting eddy cell then drifts westward across the Gulf of Mexico. Frequently, these Loop Current Eddies traverse the northcentral Gulf of Mexico water. This assumption would lead us to expect concentration differences close to those summarized in Table 5.

A vertical contour of dissolved oxygen along transect 'AA' (Figure 17) shows a high concentration oxygen "bubble" (Figure 18). The Eddy position is confirmed by the high salinity Subtropical Underwater (SUW) water from the Caribbean (Figure 19). Vertical contours of nutrients along transect 'BB' (Figure 20) show low nutrient concentration similar to Caribbean waters. Silicate, phosphate and nitrate show a similar depression of nutrient values.

The nutrient signature does not have unique values such as the high salinity of SUW water. For this reason, nutrient variability in the Gulf of Mexico can be explained.

CONCLUSIONS

The historical inorganic nutrient data set at three potential OTEC sites is small and, geographically and temporally, unevenly distributed. The Puerto Rico and St. Croix OTEC sites and Caribbean Control Area are similar in the upper 100 m. Seasonal variation appears minimal.

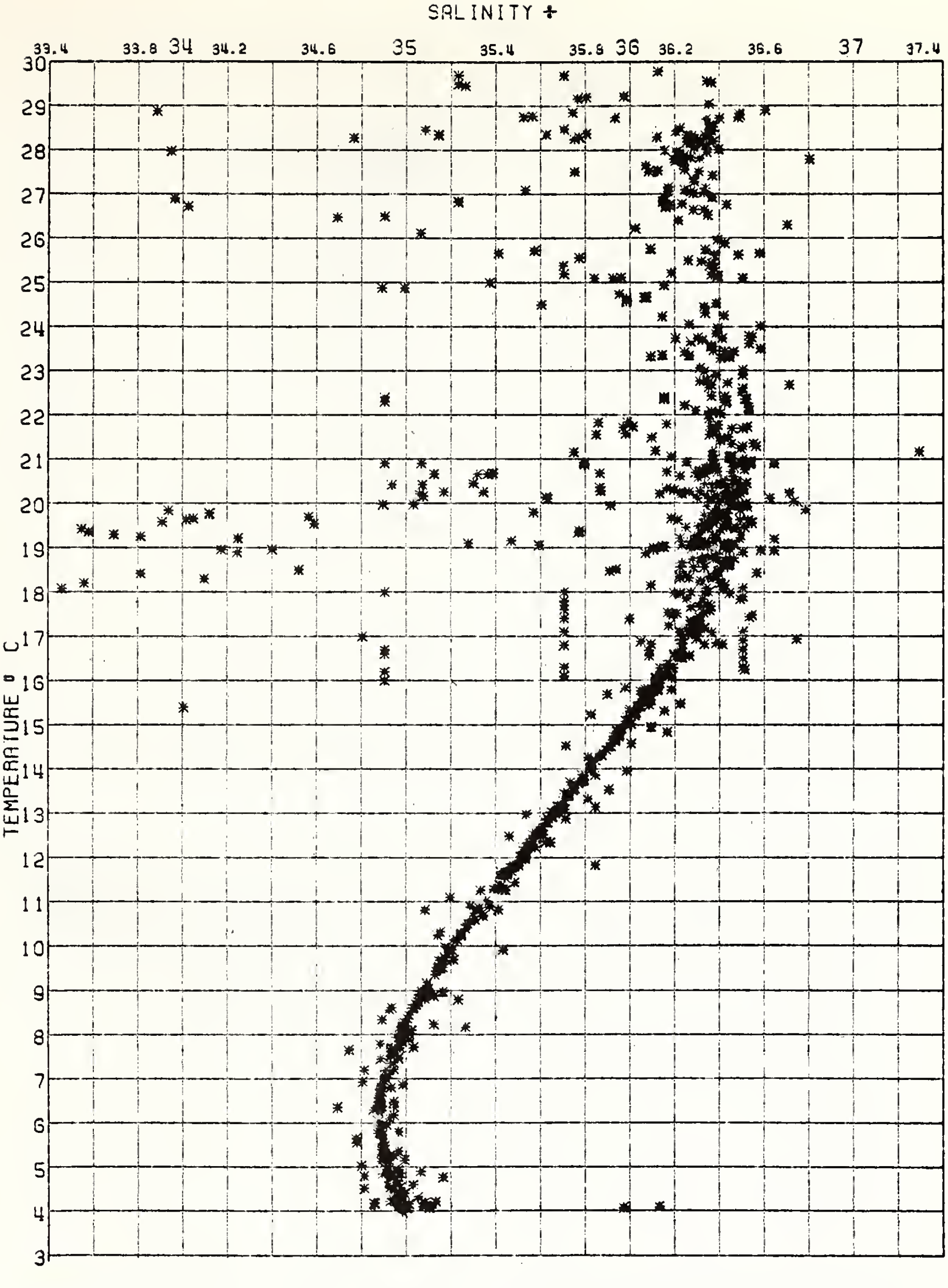

FIGURE 8. Salinity versus Temperature at the Northern Gulf of Mexico OTEC Area

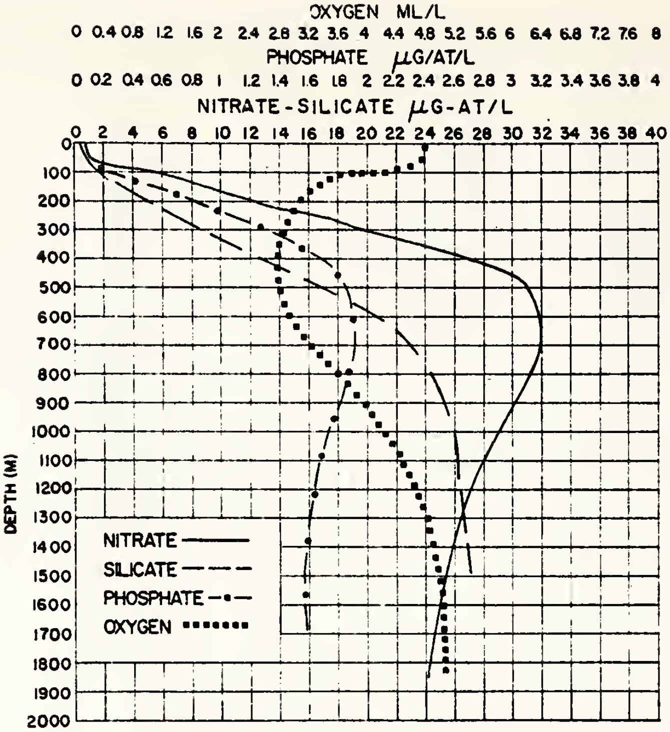

FIGURE 9. Central Trends of Dissolved Oxygen and Nutrient Concentrations versus Depth in the Northern Gulf of Mexico OTEC Area

---

TABLE 5. Central Trend Differences Between the Proposed OTEC Sites in the Northern Gulf of Mexico and the Puerto Rico and St. Croix Areas Negative numbers indicate the Gulf of Mexico value was lower than the Caribbean value Nitrate (NO_3-N) was not compared for lack of data in the Caribbean

Depth (M)	Concentration of Differences in µg-at/l		
	ΔO_2	ΔSiO_3-Si	ΔPO_4-P
0	.1	0.0	.0
50	.1	0.0	.0
100	-.2	1.0	.1
200	-.9	3.0	.7
300	-1.1	5.0	1.0
400	-.7	6.0	.8
500	-.3	5.0	.4
600	.0	2.0	.1
700	.2	1.0	-.1
800	.4	0.0	-.2
900	.3	0.0	-.2
1000	.1	0.0	-.1
1100	.0	-1.0	-.1
1200	.0	-1.0	.0
1500	.0	-1.0	.0
2000	.0	-1.0	.0

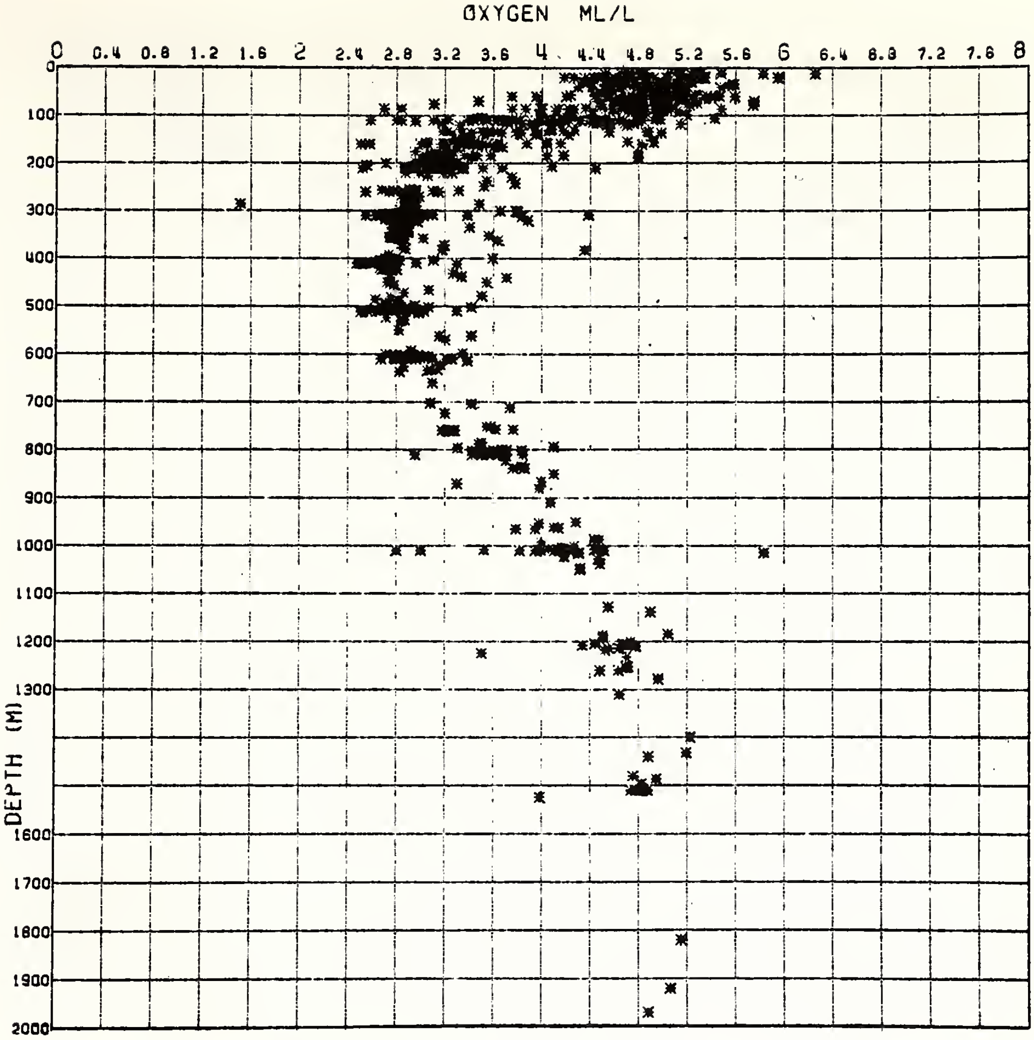

FIGURE 10. Dissolved Oxygen versus Depth in the Northern Gulf of Mexico OTEC Area

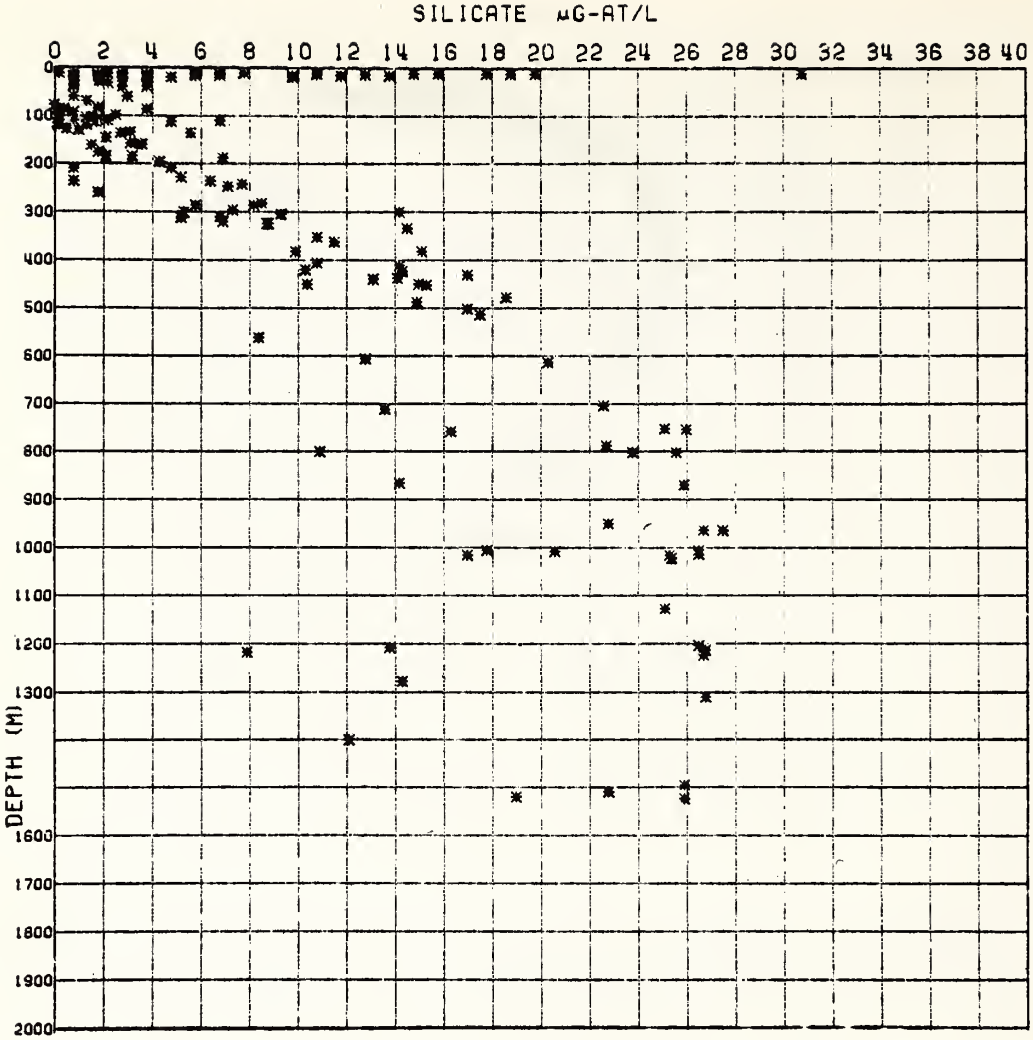

FIGURE 11. Silicate (SiO_3-Si) versus Depth in the Northern Gulf of Mexico OTEC Area

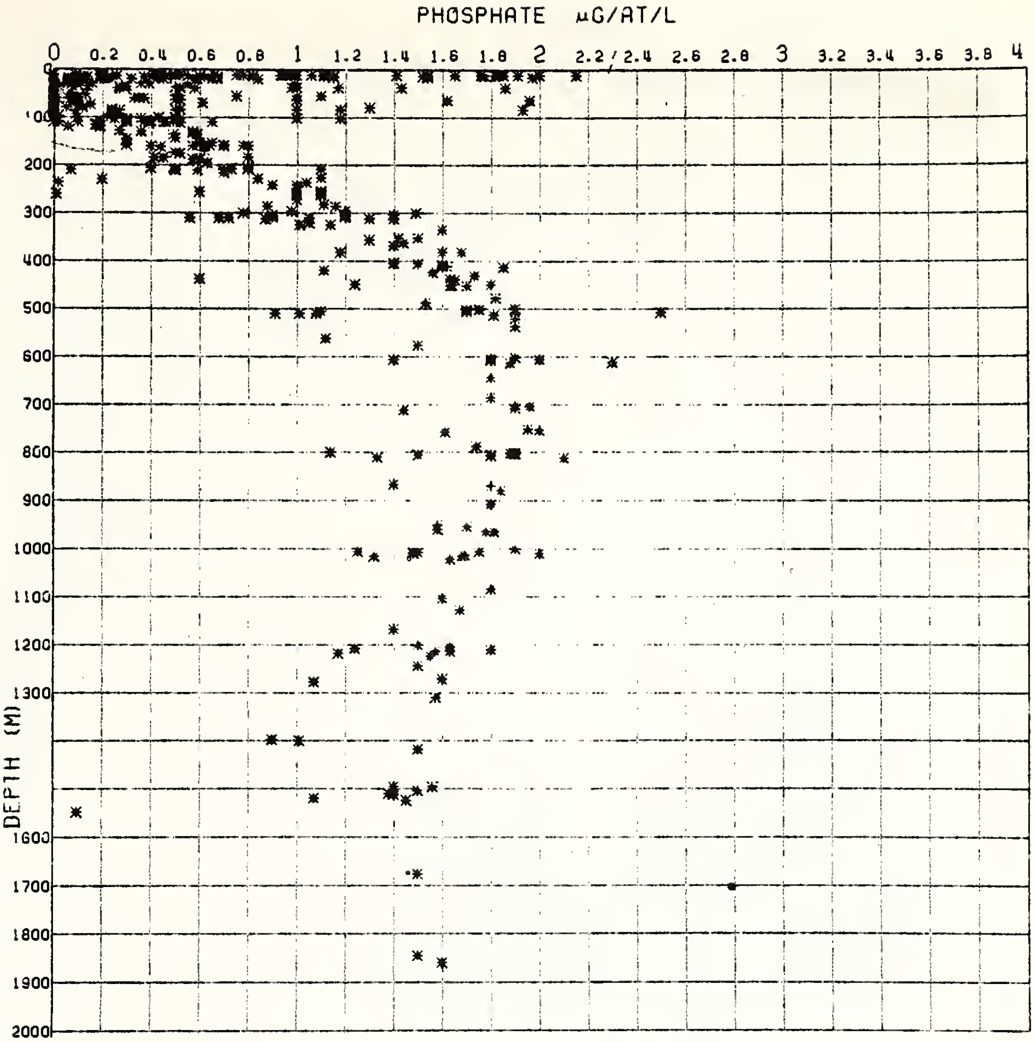

FIGURE 12. Phosphate (PO4-P) versus Depth in the Northern Gulf of Mexico OTEC Area

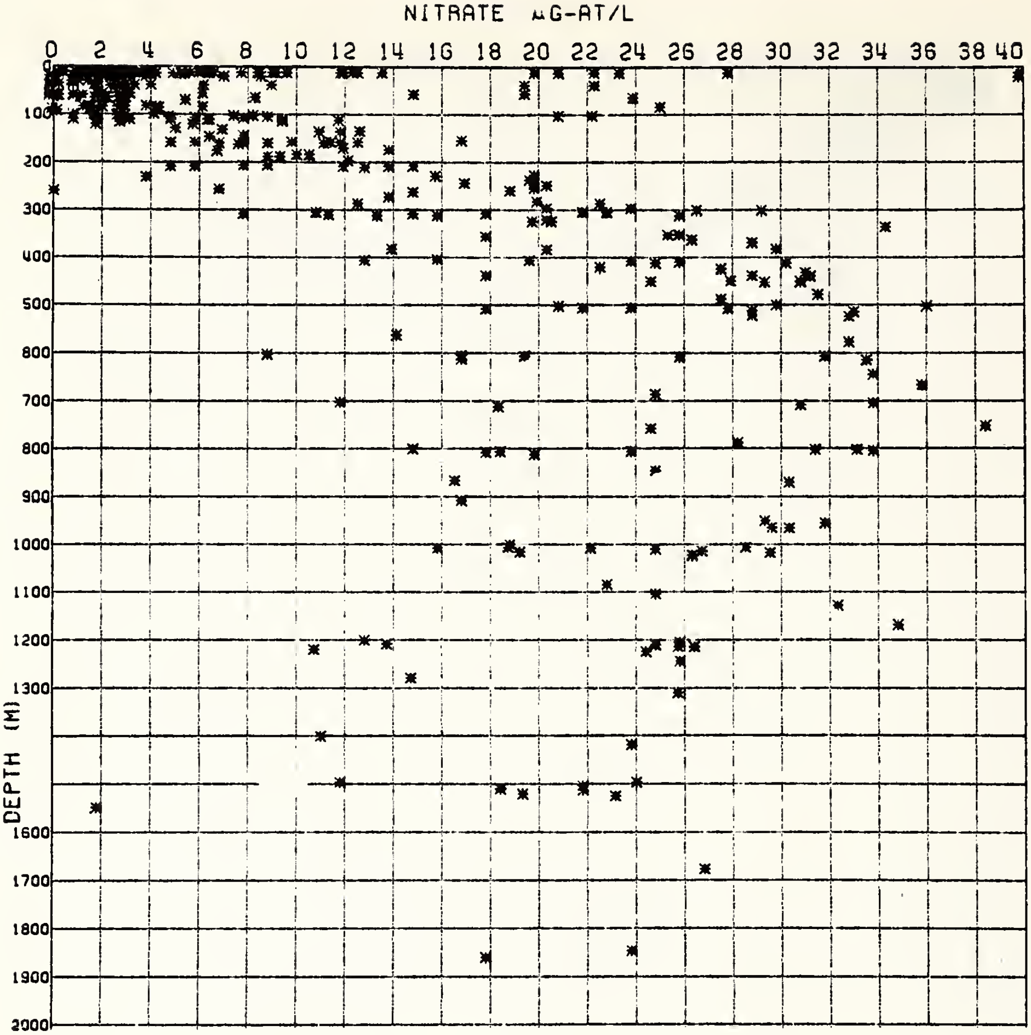

FIGURE 13. Nitrate (NO_3-N) versus Depth in the Northern Gulf of Mexico OTEC Area

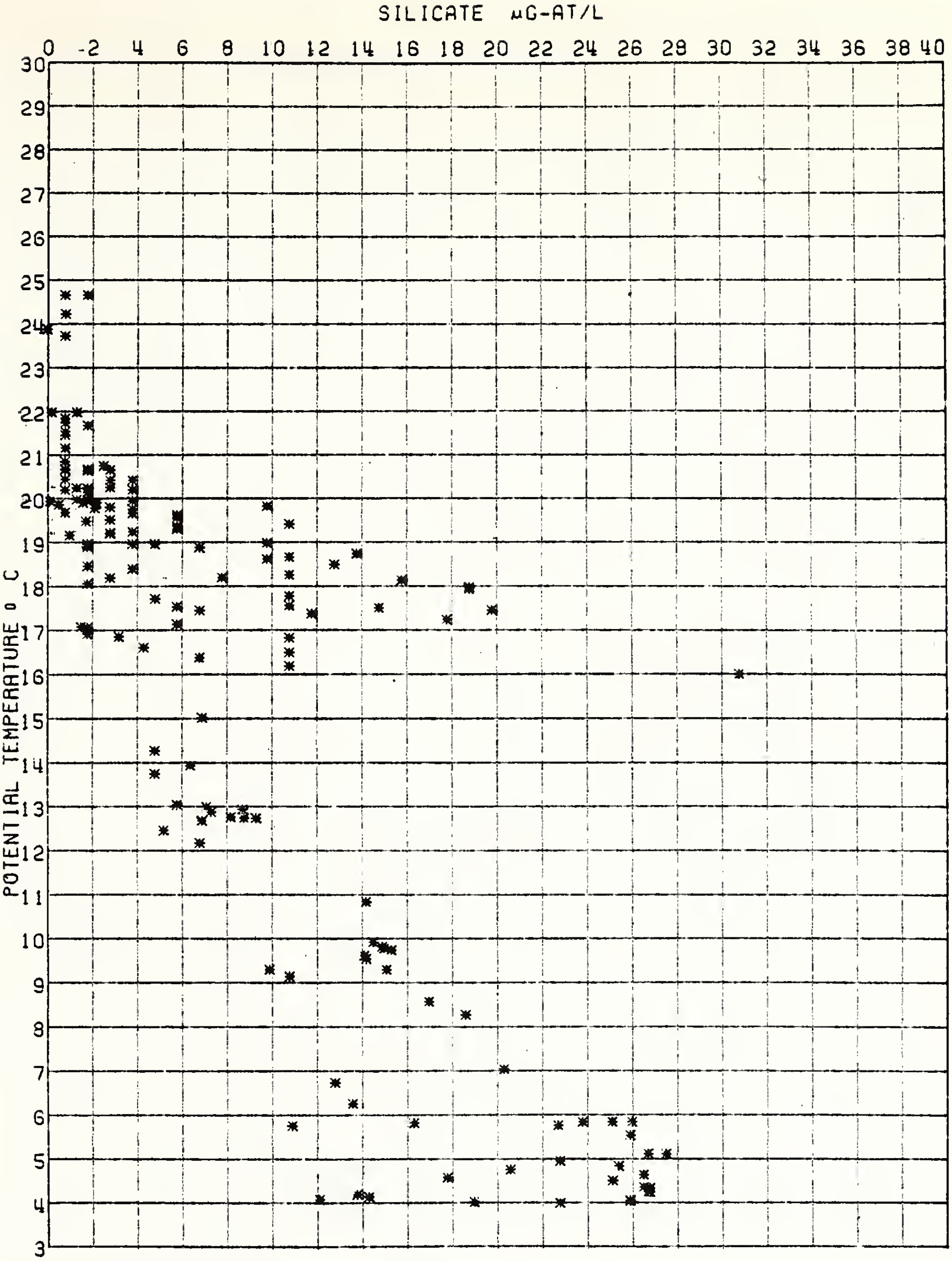

FIGURE 14. Silicate (SiO_3-Si) versus Potential Temperature in the Northern Gulf of Mexico OTEC Area

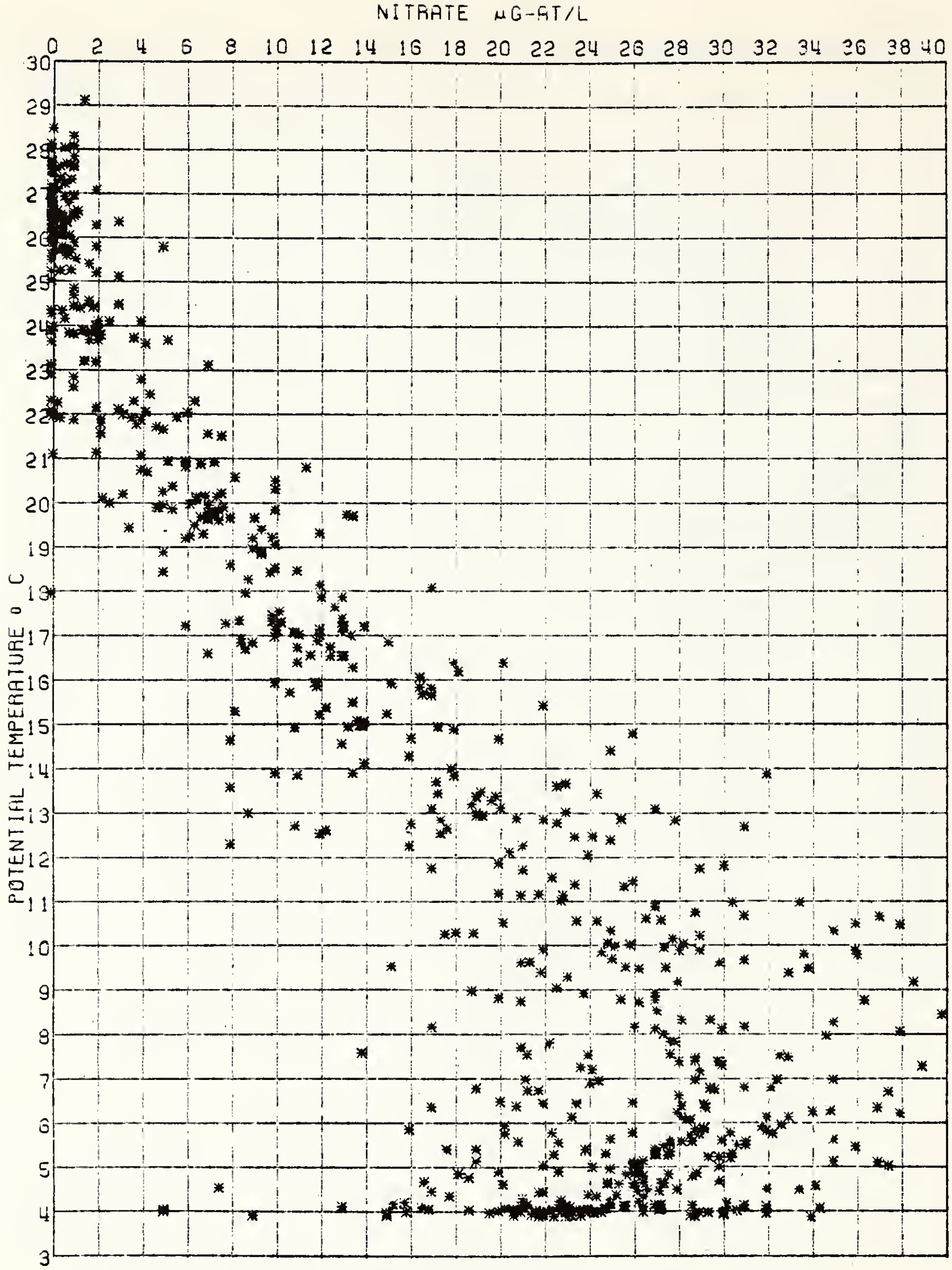

FIGURE 15. Nitrate (NO_3-N) versus Potential Temperature in the Northern Gulf of Mexico OTEC Area

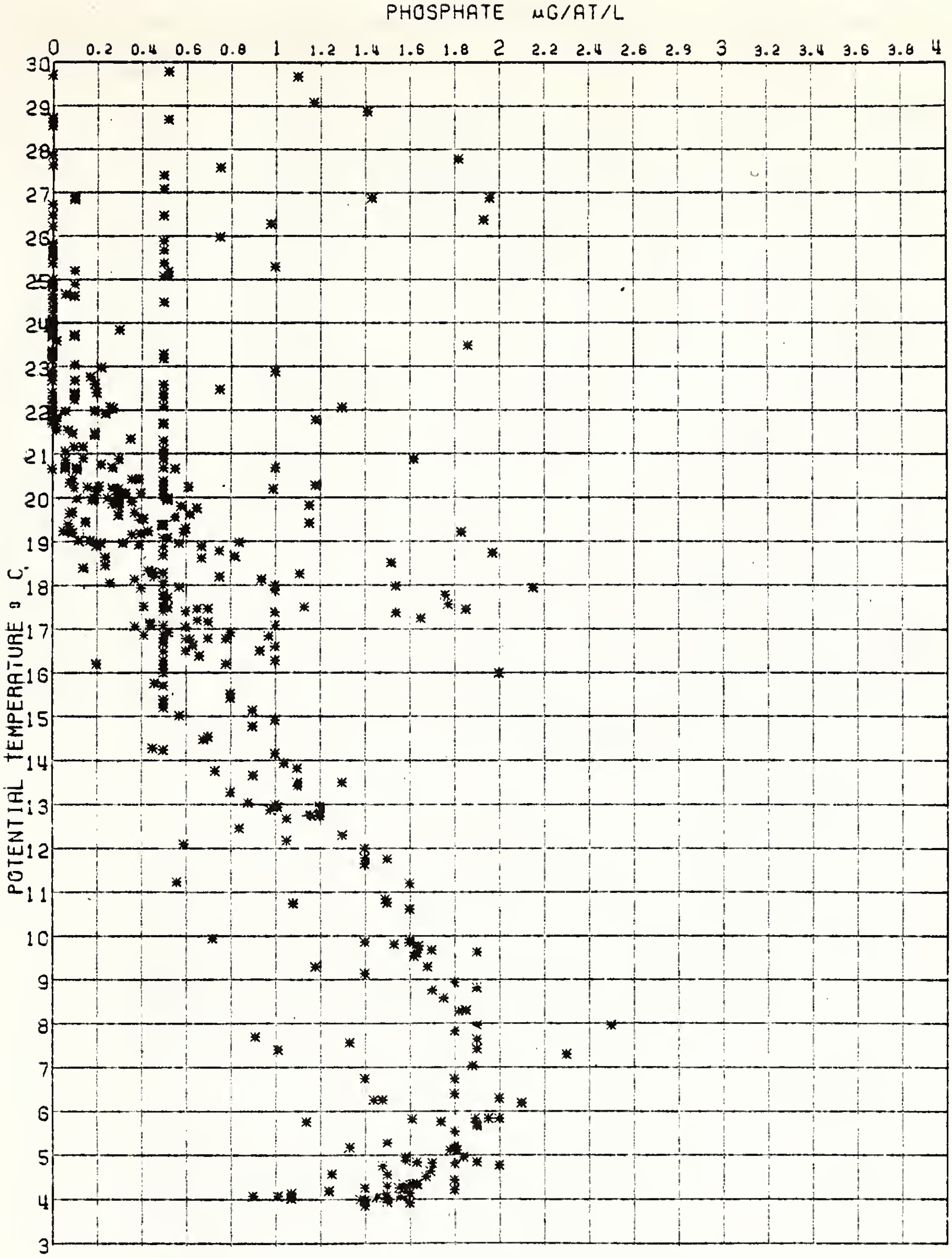

FIGURE 16. Phosphate (PO_4-P) versus Potential Temperature in the Northern Gulf of Mexico OTEC Area

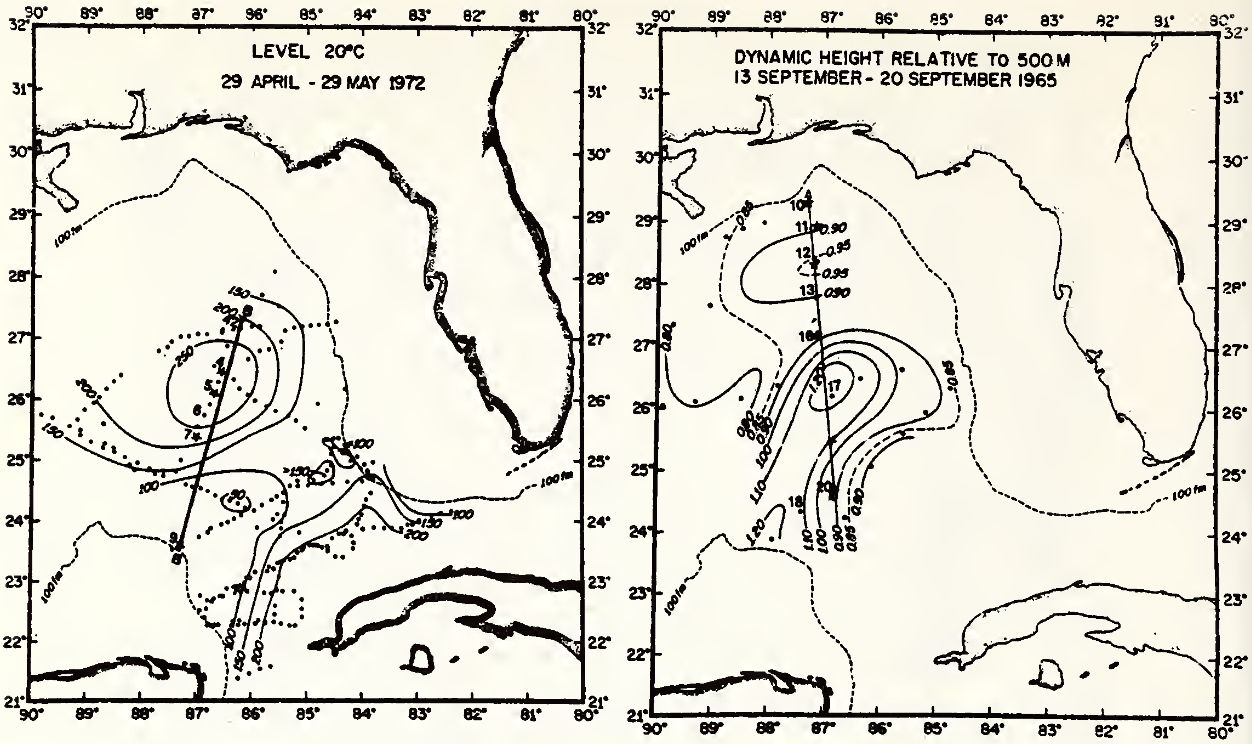
LEVEL 20°C
29 APRIL - 29 MAY 1972
DYNAMIC HEIGHT RELATIVE TO 500 M
13 SEPTEMBER - 20 SEPTEMBER 1965
90°
89°
88°
87°
86°
85°
84°
83°
82°
81°
80°
32°
31°
30°
29°
28°
27°
26°
25°
24°
23°
22°
21°
100 fm
150
200
250
100
0.90
0.95
0.85
0.80
1.00
1.10
1.20
10
11
12
13
16
17
18
20

FIGURE 17. Loop Current Eddies in the Gulf of Mexico during September 1965 and May 1972

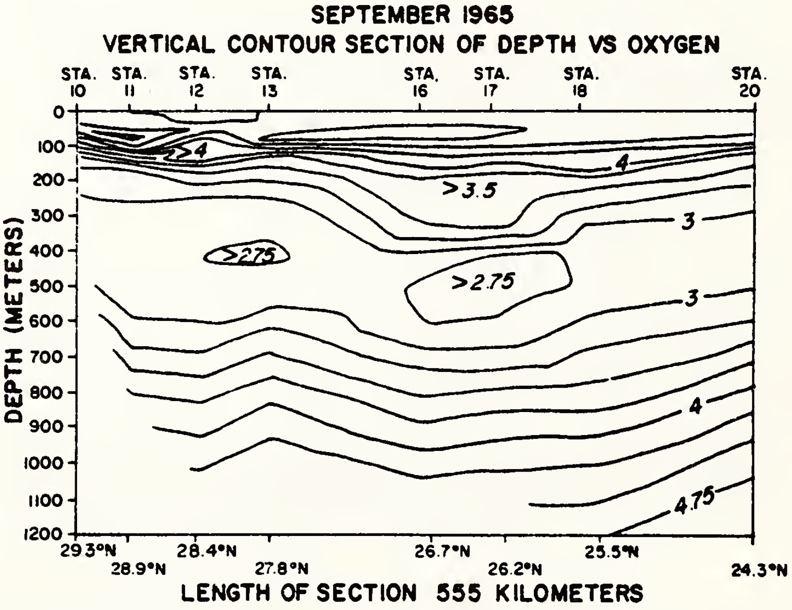

FIGURE 18. Vertical Contour Section of Dissolved Oxygen Along Transect 'AA' (Figure 18) September 1965

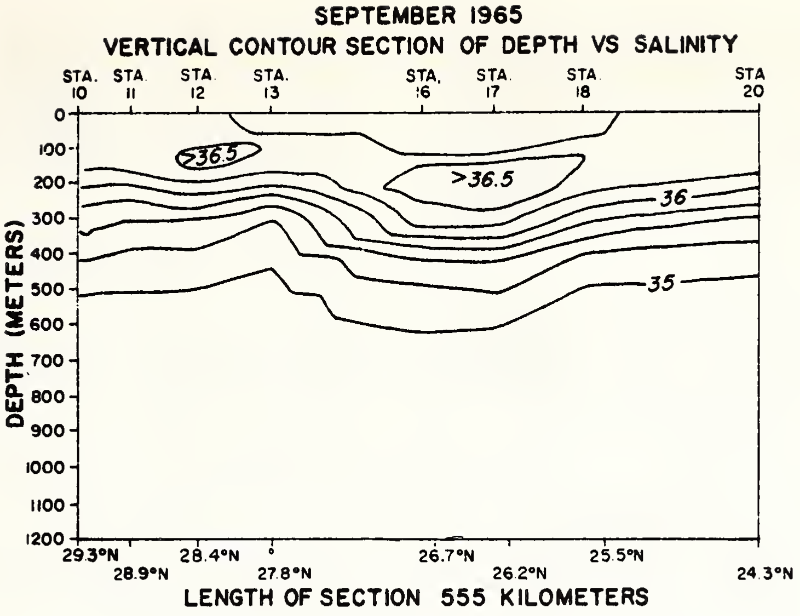

FIGURE 19. Vertical Contour Section of Salinity Along Transect 'AA' (Figure 18) September 1965

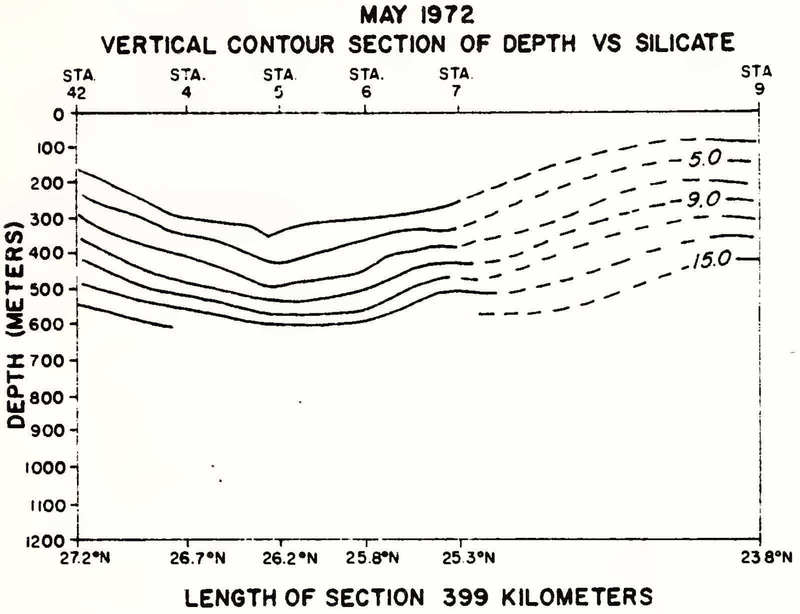

FIGURE 20. Vertical Contour Section of Silicate (SiO_3-Si) Along Transect 'BB' (Figure 18) May 1972)

The northern Gulf of Mexico site shows greater variability than Caribbean sites. A major source of surface variability is the Mississippi River in an area near the delta region. The Loop Current Eddies account for much of the midwater, 50-800 m variation of nutrient concentrations. Below 1000 m, all three areas are similar showing minimal concentration variability and minor differences.

ACKNOWLEDGMENTS

We thank NODC, Dr. Robert L. Molinari, and Mr. George Berberian for supplying data and Dr. George Harvey, Dr. Peter Ortner, and Mr. George Berberian for their helpful suggestions and review of the manuscript.

REFERENCES

Atwood, D. K., P. Duncan, M. C. Stalcup, and M. J. Barcelona. 1976. Ocean Thermal Energy Conversion: Resource Assessment and Environmental Impact for Proposed Puerto Rico Site. NSF Report submitted to NSF Grant No. AER 75-00145. 104 pp.

Atwood, D. K., P. N. Froelich, M. E. O. Pilson, M. J. Barcelona, and J. L. Vilen. 1977. Deep silicate content as evidence of renewal processes in the Venezuela basin. Submitted to Deep-Sea Research.

Bell, W. and R. Mitchell. 1972. Chemotactic and growth responses of marine bacteria to algal extracellular products. The Biological Bulletin 143(2):265-277.

El-Sayed, S. Z., W. M. Sackett, L. M. Jeffrey, A. D. Fredericks, R. P. Saunders, P. S. Conger, G. A. Fryxell, K. A. Steidinger, and S. A. Earle. 1972. Chemistry, primary productivity, and benthic algae of the Gulf of Mexico. In: Serial Atlas of the Marine Environment. American Geographical Society. New York, New York.

Froelich, P. N., Jr., and D. K. Atwood. 1974. New evidence for sporadic renewal of Venezuela basin water. Deep-Sea Research 21:969-975.

Jonew, J. I., R. E. Ring, M. O. Rinkel, and R. E. Smith, Eds. 1973. A Summary of Knowledge of the Eastern Gulf of Mexico. State University System of Florida Institute of Oceanography (SUSIO) St. Petersburg, Florida.

Molinari, R. L., D. W. Beringer, G. A. Maul, and R. Legreckis. 1977. Winter intrusions of the LOOP Current. Science 198:505-507.

Molinari, R. L. 1977. Synoptic and Mean Monthly 20°C Topographies in the Eastern Gulf of Mexico. NOAA Technical Memorandum ERL-AOML-27, 33 pp.

Niederauer, T. and A. Herman. 1978. Computer Programs for the Automated Contouring of Vertical Sections. NOAA Technical Memorandum ERL-AOML-31.

Nowlin, W. D., Jr., J. M. Herberty, and R. O. Reid. 1968. A detached eddy in the Gulf of Mexico. J. Mar. Res. 26:185-186.

Smith, R. E., Ed. 1974. Proc. of Marine Environmental Implications of Offshore Drilling Eastern Gulf of Mexico. State University System of Florida Institute of Oceanography (SUSIO) St. Petersburg, Florida.

18

NOAA
Professional Paper 10

The Organic Geochemistry of Mangrove Lake, Bermuda

Patrick G. Hatcher
Environmental Research Laboratories
Atlantic Oceanographic and Meteorological Laboratories
Ocean Chemistry Laboratory
Miami, Florida 33149

January 1978

U.S. DEPARTMENT OF COMMERCE
Juanita M. Kreps, Secretary

National Oceanic and Atmospheric Administration
Richard A. Frank, Administrator

The Organic Geochemistry of Mangrove Lake, Bermuda

Patrick G. Hatcher

ABSTRACT.—The sedimentary deposits of Mangrove Lake, Bermuda, were examined to delineate their organic geochemical nature as it relates to early diagenesis of organic matter in a reducing marine environment. The recent environment and older sedimentary sequences were examined, primarily for total organic carbon, hydrogen, nitrogen, carbohydrates, and proteins. The various amino acids, *n*-alkanes, and *n*-fatty acids also were examined as part of a more comprehensive program to define the geology and chemistry of the lake.

Since its formation over 9,000 years ago, the lake had accumulated roughly 18 m of sediments, which indicate three different depositional environments—a peat, a fresh-water gel, and a brackish-water gel. Physical boundaries between these sedimentary sequences are substantiated by ostracod distributions, by changes in organic geochemical parameters, and by other measured parameters.

Observed parameters indicate that early diagenetic transformations are occurring. Major changes are reflected in the carbohydrates and proteins. These may be undergoing condensation to form humic substances.

The *n*-alkanes and *n*-fatty acids also were examined, as a function of time in the sedimentary column, but no identifiable relationships were found in support of the hypothesis that *n*-alkanes in petroleum are derived from *n*-fatty acids. However, the profile of *n*-fatty acids did indicate that some maturation was occurring, similar to that expected for petroleum formation.

This study of Mangrove Lake was exploratory in nature. It was designed to identify certain diagenetic processes that might be thoroughly examined later.

U.S. Department of Commerce Map Number A5787.

SLOPE MAP

A MAJOR SUBMARINE SLIDE ON THE U.S. ATLANTIC CONTINENTAL SLOPE EAST OF CAPE MAY

Richard H. Bennett, Douglas N. Lambert, Bonnie A. McGregor,
Evan B. Forde and George F. Merrill
Marine Geotechnical Program, Marine Geology and Geophysics Laboratory
Atlantic Oceanographic and Meteorological Laboratories, NOAA
15 Rickenbacker Cswy Miami, Fla 33149

1978

(Slope Map with text available from the authors.)

INTRODUCTION

The first modern bathymetric contour maps of the sea floor on the U.S. Atlantic Continental Margin were constructed by Veatch and Smith (1939) for selected areas of the shelf and slope. With the advent of echo sounding techniques, data for these bathymetric maps were collected by the U.S. Coast and Geodetic Survey, (now National Ocean Survey, NOAA) during the period of 1930 to 1938. These maps were constructed at a scale of 1:120,000 and depicted the broad scale features of the continental shelf, slope, and major submarine canyons. Later, Sterns and Garrison (1967) produced a detailed bathymetric map of the shelf between Great South Channel to approximately the entrance of the Chesapeake Bay using the U.S. Coast and Geodetic Survey soundings and covering intra-coastal areas. These maps were produced at a scale of 1:125,000. The entire U.S. Atlantic east coast continental shelf and slope were contoured at a scale of 1:1,000,000 by Uchupi (1968a). Later the shelf and slope were contoured at a scale of 1:750,000 covering the area just south of Wilmington Canyon to Veatch Canyon (Uchupi, 1970). The soundings for these maps were, for the most part, provided by marine surveys of the U.S. Coast and Geodetic Survey. All of these various scale bathymetric maps have contributed substantially to the understanding of the general geomorphological characteristics of the sea floor of the U.S. Atlantic continental margin. Only a limited number of large scale bathymetric maps depicting the details of selected areas of the continental margin are available.

The nation's increasing demands for energy have stimulated considerable activity in offshore areas of the continental shelf and slope where potential petroleum reserves are being explored and tapped and where various areas are being considered for additional construction sites and exploitation purposes. The increasing engineering activities in the hostile offshore marine environments dictate the urgent requirements for detailed oceanographic data including geotechnical information particularly with regard to sea floor characteristics and environmental conditions. The various national needs and requirements in offshore engineering, including detailed bathymetric maps and marine geotechnical studies, generally have been well documented in reports by the National Advisory Committee on Oceans and Atmosphere (1974, 1976) and the Committee on Sea Floor Engineering, National Research Council (1976).

In an effort to help meet these national needs, the Marine Geotechnical Program of NOAA'S Atlantic Oceanographic and Meteorological Laboratories is carrying out numerous geotechnical studies of which this detailed bathymetric and slope map is a small part.

This slope map of a selected continental slope area seaward of the Baltimore Trough serves three principal purposes. It provides:

1. Bathymetric contours depicting detailed sea floor morphology for an area of engineering and geological significance.
2. Bathymetric data in the form of a slope map which displays the relative extent of specified slope zones that clearly portray characteristic sea floor morphological features and declivities of engineering and geological significance.
3. A basic map of sea-floor slopes for engineering analyses and sea floor stability studies in terms of the sediment geotechnical properties.

This slope map is intented to serve as a model analysis for further marine geotechnical studies of offshore areas presently being carried out at NOAA-AOML in Miami, Florida.

STUDY AREA

The study area chosen for the development of the slope map is located slightly northeast of Wilmington Canyon on the continental slope east of Cape May, New Jersey (Fig. 1). This site was selected after examination and study of small scale bathymetric maps of the continental margin. These maps revealed that the area was characterized by morphological features indicative of sea floor instability and slumping. Stanley (personal communication, 1974) suggested that the slope northeast of Wilmington Canyon was a likely area to investigate submarine slides. Several geological/geophysical studies have been made by Uchupi (1968b), Stanley and Kelling (1968), Kelling and Stanley (1970), and Lyall, et al., (1971), but geotechnical studies and detailed bathymetry of submarine slides had not been made in this area. The slope map described here is part of a detailed marine geotechnical study of the slide and has been initially discussed by McGregor and Bennett (1977), Bennett, et al.,(1977), and McGregor, (1977).

Bathymetric contours commonly reveal features of submarine slides and slump blocks. Slide scars are often characterized by tightly spaced upslope trending contours which "open" (become more widely spaced) at the head of a slump block and sometimes completely reverse direction downslope over the slump block proper (see Fig. 2 for an example of these types of features). These characteristics were observed on small scale maps and were the criteria used in delineating the initial slide area. Observation and study of this bathymetric map, which was originally contoured at a scale of 1:10,000, also revealed the diagnostic morphology of slumping.

A seismic reflection survey of the area has shown that the slump block proper has an estimated sediment volume of approximately 11 km^3 (McGregor and Bennett, 1977.) This is a larger volume of sediment than could be estimated based strictly on interpretations made from the bathymetric map. Obviously, geophysical techniques are necessary for delimiting the full extent of the submarine slide (three dimensionally) not possible through the limited use of bathymetric mapping. Details of the geophysical nature, stratigraphy, and geologic history of the submarine slide are discussed by McGregor and Bennett (1977) and McGregor, (1977).

CONSTRUCTION OF SLOPE MAP

This slope map was constructed from the detailed bathymetric map which was developed from a marine survey aboard the NOAA Ship RESEARCHER during two cruises in 1974 and 1975. Narrow beam echo sounding (NBES) with a half angle beam width of about seven degrees (12.2×10^{-2} rad) was carried out over the selected area (7.5 by 13.0 km) with approximately 0.5 km track line spacings (Fig. 3). Loran C supplemented with satellite fixes provided a navigational precision of about 250 m. This precision was later improved by adjusting the tracklines based on approximately 350 crossings. Bathymetric contours are in 10-meter intervals (water depths used are in corrected meters using the tables of Matthews, 1939) and are considered to be representative of the survey precision. Water depths range from 460 to 1680 meters in the study area and cover the upper to the lower part of the continental slope.

Slope maps, also referred to as clinometric maps, provide slope information depicted by map contours whereby local areas having similar gradients (slopes) are grouped into a single map unit. This slope map was constructed from the bathymetric map by measuring the spacing between the contour lines. Distances or spacings between contours are measured perpendicular to the lines. Slope is the gradient of the inclined surface or declivity of the sea floor, and the degree of slope is a function of magnitude of the angle between the inclined sea floor surface (or segment thereof) and the horizontal plane. In slope map construction, the degree of slope is determined by the amount of sea floor relief per unit of horizontal distance (here map distance in meters versus number of contour lines). Effectively, this is the ratio of the vertical distance (relief) to the horizontal distance which defines the slope angle for a given segment of the sea floor. Commonly, slope is expressed in degrees, percent, or as a ratio. The relationships among these three means of expressing slope are described and shown in Figs. 4 and 5. These relationships and Figs. 4 and 5 have been modified from Schmoll and Dobrovolony (1972) to conform to bathymetric slope map construction.

The four slope categories used in this map were chosen because they best portray the major morphological features of the sea floor in this study area of the continental slope. These categories were considered adequate also for use in slope stability analyses (presently under study) for this area of the sea floor. Three major morphological features are apparent and include 1) the slide scar of moderately steep slopes, 2) the slump block proper characterized by nearly flat to gentle slopes "superimposed" on some moderately steep slopes, and 3) an incised valley and valley and ridge complex characterized by steep to very steep slopes. Each of the four slope categories is shown as a map unit which represents the corresponding range of slope (see Fig. 5 and the description of each map unit). The four slope map units were combined from the units of a map originally constructed with eight slope categories. Use of these four map units simplifies the map considerably as compared to the original map. During the final smoothing of the slope map, isolated slope zones having a width of only two contours were eliminated. In some cases, however, isolated slope zones only two contours wide were included into the area of a nearby major category when the isolated slope zone fell within that major slope category. This was done in order to eliminate any possible bias of contour spacing between track lines and any implied precision of slope based on only a separation of two contours. Slopes where checked and verified were possible along track lines using NBES profiles.

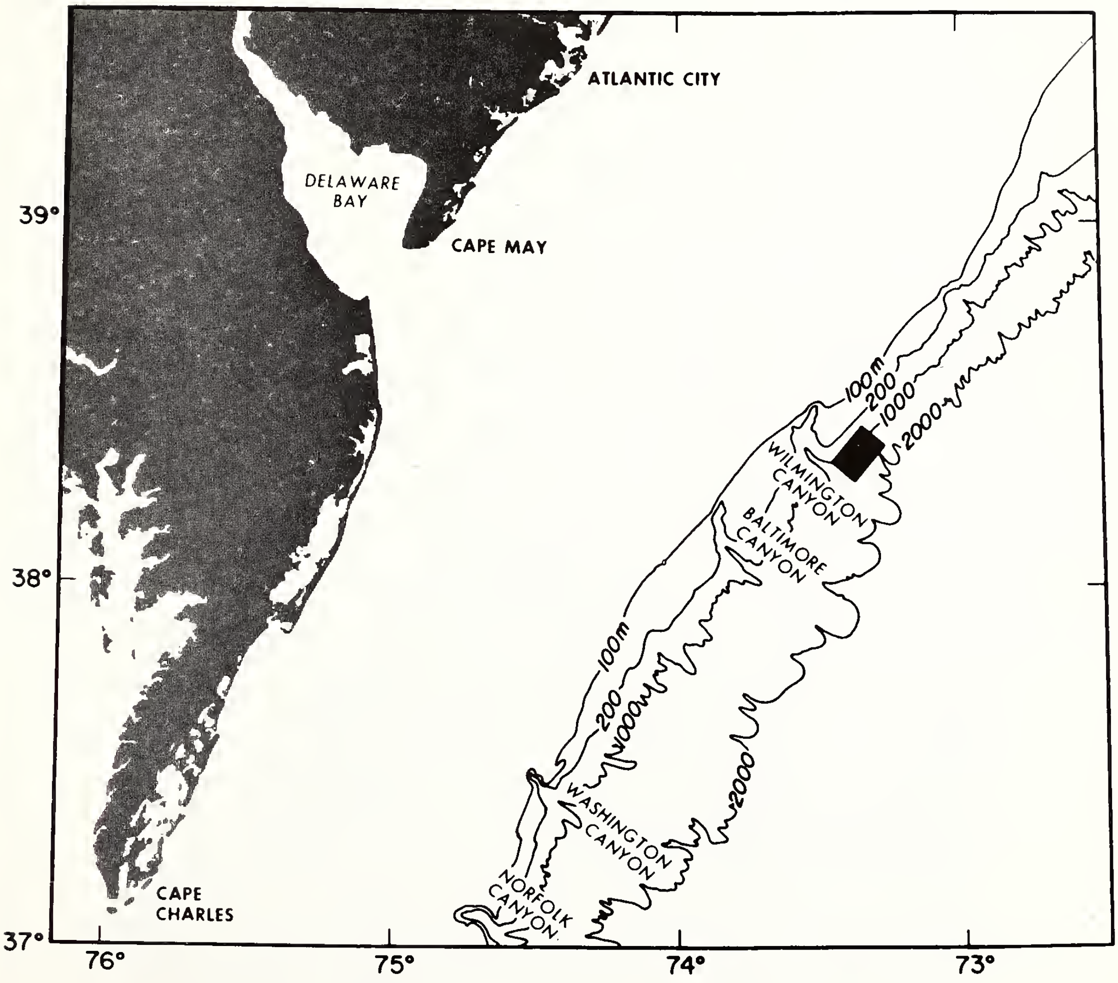

FIG. 1 LOCATION MAP

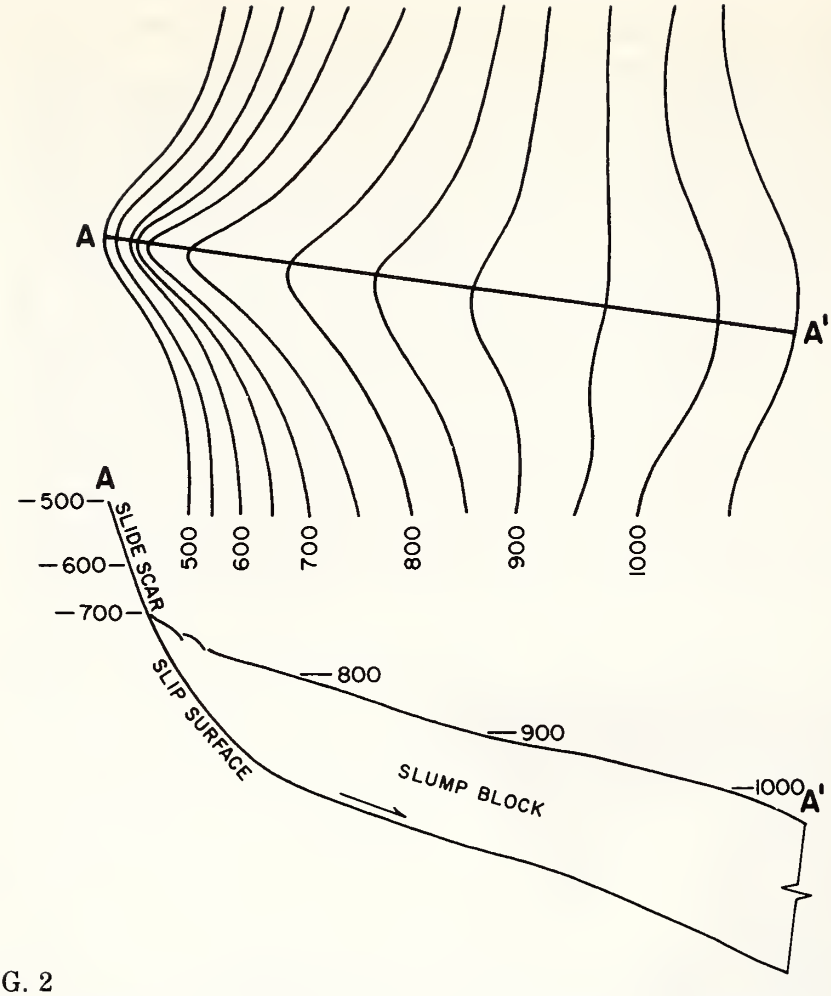

FIG. 2
PLAN VIEW AND PROFILE OF AN IDEALIZED SUBMARINE SLIDE

SEDIMENTS

Piston, box, boomerang, and hydroplastic cores were collected to assess the sedimentological and geotechnical properties of the surficial sea floor deposits associated with the submarine slide. Initial results and details of the sediments and their mass physical properties were discussed by McGregor and Bennett (1977), and Bennett et al., (1977). The sediments of the slide area are predominantly silty clays and clayey silts with an abundance of illite with lesser quantities of feldspar, chlorite, kaolinite, quartz and smectite minerals. Some heavy minerals occur in the sand and silt fractions of the upper slope sediments. Sediments on the upper slope above the slump block proper are characterized consistently by several centimeters of topmost sand and coarse sandy silt overlying the muds. These topmost sandy sediments are absent downslope on the slump block proper. Generally, the amount of sand throughout the silty clays and clayey silts is considerably less than 10% for these continental slope sediments. Authigenic pyrite is common as globular masses and as burrow replacements. Calcium carbonate is present in the form of calcareous tests scattered throughout the muds (Bennett et al., 1977).

Atterberg limits were determined on the sediment cores collected in the slide area. Based on the Plasticity Chart (Casagrande, 1948), these continental slope sediments are inorganic clays which range from relatively low plasticity to high plasticity increasing in the downslope direction. Plasticity index-liquid limit values generally fall slightly above the "A" line on the Plasticity Chart, and, although a few exceptions occur, these sediments are identified as CL and CH material in the Unified Soil Classification (ASTM, 1977). Further details of the geotechnical properties and sedimentology are discussed by Bennett et al., (1977).

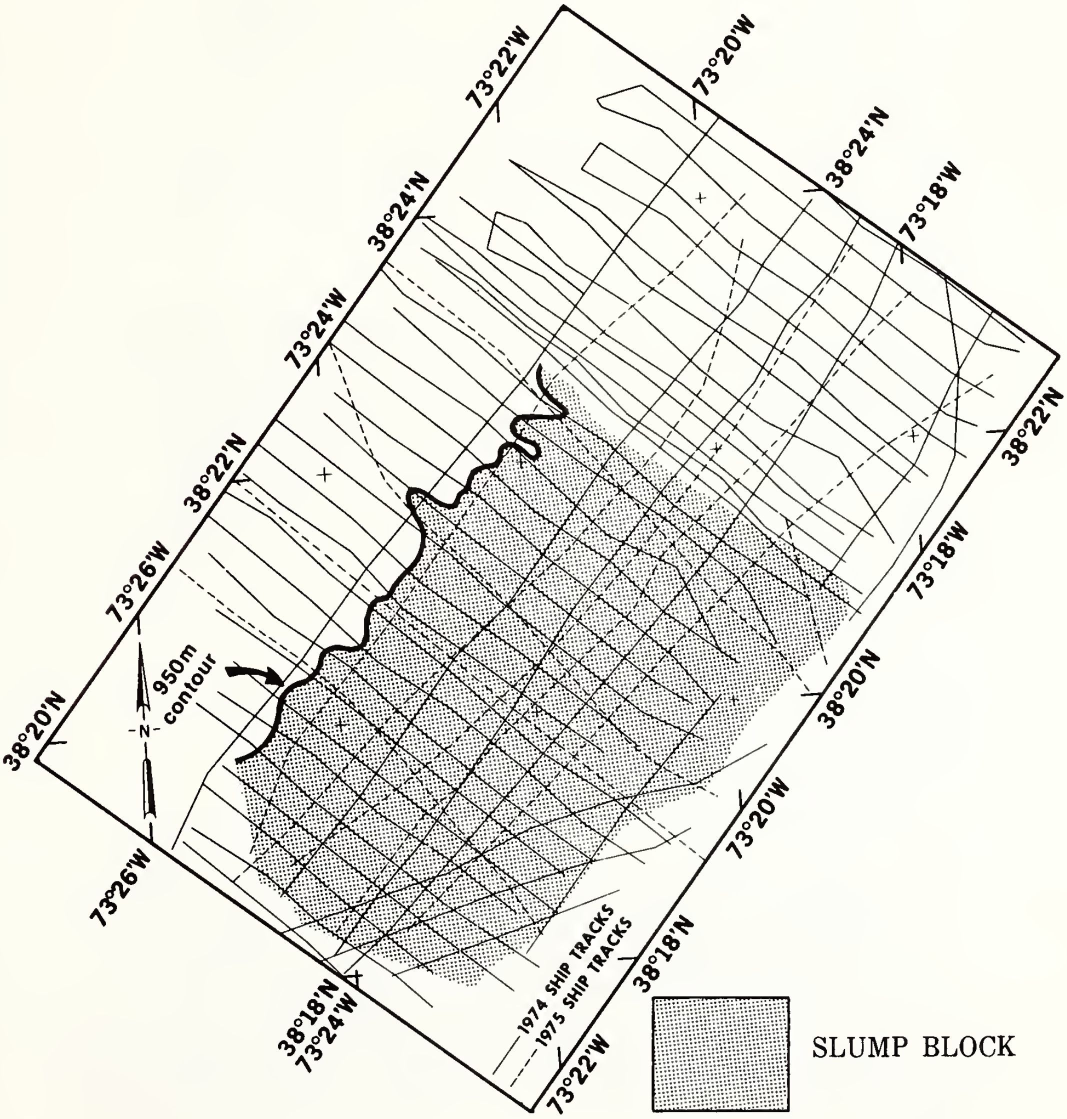
73°22'W
73°20'W
38°24'N
38°24'N
73°18'W
73°24'W
38°22'N
38°22'N
73°26'W
73°18'W
950m contour
N
38°20'N
38°20'N
73°20'W
73°26'W
1974 SHIP TRACKS
1975 SHIP TRACKS
38°18'N
38°18'N
73°24'W
73°22'W
SLUMP BLOCK

FIG. 3
NBES TRACKLINE AND
SLUMP BLOCK LOCATION MAP

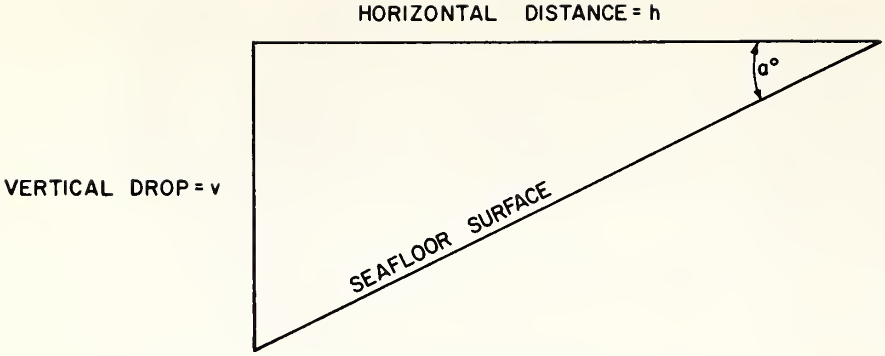
HORIZONTAL DISTANCE = h
a°
VERTICAL DROP = v
SEAFLOOR SURFACE

EXPLANATION OF SLOPE TERMS

TERMS		EXAMPLES
SLOPE ANGLE IN DEGREES	= a°	45°
SLOPE IN PERCENT	= v/h x 100	100%
SLOPE RATIO	= h:v	1:1

FIG. 4 DIAGRAM OF SLOPE MEASURING TERMS

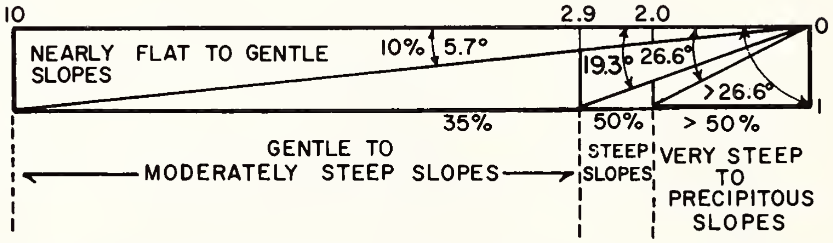
10
2.9
2.0
0
1
NEARLY FLAT TO GENTLE SLOPES
10%
5.7°
19.3°
26.6°
>26.6°
35%
50%
> 50%
GENTLE TO MODERATELY STEEP SLOPES
STEEP SLOPES
VERY STEEP TO PRECIPITOUS SLOPES

FIG. 5 ILLUSTRATION OF SLOPE CATEGORIES USED ON THIS MAP

ACKNOWLEDGEMENTS

This research was supported by the National Oceanic and Atmospheric Administration (NOAA), Atlantic Oceanographic and Meteorological Laboratories (AOML). The support given by the officers and crew of the NOAA Ocean Survey Ship RESEARCHER in carrying out the surveys is appreciated. The authors appreciate the assistance given by Ms. Frances L. Nastav, Dr. Matthew Hulbert, Mr. George Lapiene, Mr. William Sawyer, Ms. Pamela Bates, and Mr. David Grove during various phases of this study. We appreciate the encouragement and support given by Dr. Harris B. Stewart, Jr., Mr. John W. Kofoed, and Dr. George H. Keller during this investigation. The authors are grateful to Mr. Henry R. Schmoll, U.S.G.S., for critically reviewing this manuscript and slope map.

REFERENCES

A Report for: The Secretary of Commerce, 1974, Engineering in the Oceans, by the National Advisory Committee on Oceans and Atmospheres, 54 p.

A Report to: The President and the Congress, 1976, by the National Advisory Committee on Oceans and Atmosphere, 64 p.

American Society for Testing Materials (ASTM), 1977, Standard test method for classification of soils for engineering purposes. ANSI/ASTM, D-2487-69 (Reapproved 1975), p. 310-314.

Bennett, R.H., D.N. Lambert, and M.H. Hulbert, 1977, Geotechnical properties of a submarine slide area on the U.S. continental slope northeast of Wilmington Canyon. Marine Geotechnology, V.2, p. 245-261.

Casagrande, A., 1948, Classification and identification of soils. Amer. Soc. Civ. Eng., Trans., v. 113, p. 901-931.

Committee on Sea Floor Engineering, National Research Council, 1976, Seafloor engineering: national needs and research requirements. National Academy of Sciences, 81 p.

Kelling, G., and D.J. Stanley, 1970, Morphology and structure of Wilmington and Baltimore submarine canyons eastern United States. Jour. Geol., v. 78, p. 637-660.

Lyall, A.K., D.J. Stanley, H.N. Giles, and A. Fisher, Jr., 1971, Suspended sediment and transport at the shelf-break and on the slope, Wilmington Canyon area, eastern U.S.A. Marine Geotech, Jour., v. 5, p. 15-27.

McGregor, B.A., 1977, Geophysical assessment of a submarine slide northeast of Wilmington Canyon. Marine Geotechnology, V.2, p. 229-244.

McGregor, B.A., and R.H. Bennett, 1977, Continental slope sediment instability northeast of Wilmington Canyon. AAPG, v. 61, no. 6, p. 918-928.

Matthews, D.J., 1939, Tables of the velocity of sound in pure water and sea water for use in echo sounding and sound ranging. Admiralty Hydrographic Dept., London, Publ. H.D. 282, 52 p.

Schmoll, H.R., and E. Dobrovolony, 1972, Slope map of Anchorage and vicinity, Alaska. USGS Map I-787-B Folio of Anchorage and vicinity, Alaska, scale 1:24,000.

Stanley, D.J., and G. Kelling, 1968, Sedimentation patterns in the Wilmington Submarine Canyon area: in, Nat. Symp. Oceanogr. Sci. Eng. Atlantic Shelf, Trans., Marine Technol. Soc., Philadelphia, Pa., p. 127-142.

Sterns, F., and L.E. Garrison, 1967, Bathymetric map, C&GS Series, publ. by U.S. Department of Commerce, ESSA, Coast and Geodetic Survey and U.S. Department of the Interior, Fish and Wildlife Service, scale 1:125,000.

Uchupi, E., 1968a, Atlantic continental shelf and slope of the United States - physiography. U.S. Geological Survey Prof. Paper 529-C, U.S. Govt. Printing Office, p. 30. Map scale 1:1,000,000.

Uchupi, E., 1968b, Sedimentary framework of the continental terrace off the east coast of the United States. Southeastern Geol., v. 9, no. 4, p. 269-271.

Uchupi, E., 1970, Atlantic continental shelf and slope of the United States - shallow structure. U.S. Geological Survey Prof. Paper 529-I, U.S. Govt. Printing Office, p. 44. Map scale 1:750,000.

Veatch, A.C., and P.A. Smith, 1939, Atlantic submarine valleys of the United States and Congo submarine valley. Geol. Soc. Amer. Spec. Paper 7, 101 p.

Present and Recommended U.S. Government Research in Seafloor Engineering, A.F. Richards and H.Matlock, Consultants. U.S. DOC, NOAA, Office of Ocean Engineering Publ., 7-13.

NATIONAL OCEANIC AND ATMOSPHERIC ADMINISTRATION

Atlantic Oceanographic and Meteorological Laboratories by Richard H. Bennett

Introduction.--NOAA's Marine Geotechnical-Rational Use of the Seafloor (RUSEF) Program of the Atlantic Oceanographic and Meteorological Laboratories (AOML) Marine Geology and Geophysics Laboratory is an ongoing research effort having its inception in 1966 with investigations that were focused on deep ocean basin research. These early studies were concerned with the geotechnical or mass physical properties of deep sea submarine sediments. Early research was concerned not only with regional aspects of the North Atlantic and Pacific Basin sediments but also with the geotechnical properties of selected marginal sea deposits and site-specific areas. During the early 1970's a major effort was given to a comprehensive evaluation of the geotechnical program carried out aboard the Glomar Challenger, Deep-Sea Drilling Project, and as part of this project, research was carried out on the geotechnical properties of deep cores recovered from the Panama Basin and eastern equatorial Pacific. The first shear strength measurements performed on carefully selected DSDP cored sediment were carried out during these investigations on Leg 16.

During the early and middle 1970's emphasis in marine geotechnical research at AOML changed from deep ocean basin studies to a major research effort devoted to the investigation of the U. S. Atlantic Continental Margin and site-specific areas of the Mississippi Delta. In response to the nation's increasing interest in offshore petroleum reserves and the intimately-related engineering activities associated with the recovery of these resources, AOML's Marine Geotechnical-Rational Use of the Seafloor Program responded to basic and fundamental research needs, required in this hostile environment.

AOML's Marine Geotechnical-RUSEF investigations are directed towards an understanding of the important geological processes active on the continental margin, of seafloor geotechnical properties, and of stability-instability factors and conditions that are extremely relevant to man's activity, ultimate safety, and impact on the marine environment.

Clearly, the nation's increasing demands for offshore natural resources have stimulated considerable activity in numerous areas of the continental shelf, slope, and rise. Present and future plans for the emplacement of structures on and within the seafloor deposits (drilling platforms, pipelines, storage tanks, and atomic reactors) and the removal of seafloor deposits and the dumping of waste materials, dictate the urgent requirement for an understanding of the geotechnical properties, geological processes, and potential geological hazards associated with continental margin deposits. These aspects must be assessed and elucidated to predict with confidence (1) the potential natural environmental hazards to man-placed structures on the seafloor, and (2) the potential environmental stresses placed on an offshore area due to the emplacement of structures, the removal of natural resources, and the dumping of waste materials.

General Areas of Investigation and Goals.--The Marine Geotechnical-RUSEF Program combines research efforts with major emphasis placed on a multi-interdisciplinary approach to problem solving and investigations, drawing from such disciplines as geology, geophysics, chemistry, physical oceanography, soil mechanics, and mapping. Research efforts are focused on the western Atlantic Continental Margin from New England to the Bahama Platform and the Gulf of Mexico. Bywords of this program are processes, mechanisms, and soil properties related to the sedimentary framework and seafloor stability-instability on the continental shelf, slope, rise, and abyssal plain. The overall purpose of these studies is to provide geotechnical information for rational decision-making regarding intelligent use of the seafloor.

More specifically, the program studies are concerned with those processes taking place today that influence the erosion, transport, and deposition of sediment along the continental margin. Studies are made of the older sedimentary sequences, through geophysical techniques and correlation with existing deep bore-hole data, to understand the depositional history of this geomorphic province. Study is also made of submarine canyons and their role in the transport of sediment from coastal areas to the deep sea. The program also deals with slope stability and gravitational processes, such as slides, slumping, creep, and turbidity flows. These studies are directed towards gaining an insight into processes associated with sediment mass movement and the delineation of "key" mechanisms and soil properties associated with and/or responsible for submarine sediment stability-instability.

Geotechnical studies are designed to provide an understanding of regional and site-specific patterns, variability laterally and with depth below the mudline, and to characterize seafloor deposits both on a local and a broad scale in terms of the mass physical properties. Of paramount importance also is an understanding of certain seafloor deposits in terms of their behavior under not only static but also dynamic conditions; specifically, the response of the soils and pore pressure during active storm periods. These studies provide a better understanding of sediment stability-instability and potential mass movement for a diversity of environments and soil types particularly in the regions of national interest. Ultimate goals are the capability of assessing cause and effect relationships of seafloor stability-instability factors, the development of reliable predictive models of sediment movement, and the assessment of potentially unstable areas on the continental margins relating to currents, waves, and gravity-induced forces.

Specific Areas of Investigation and Accomplishments, East Coast.--Studies presently focus on the U. S. east coast continental margin between Cape Cod and Cape Canaveral (Fig. 1). These studies were initiated in 1974 and to date over 300 bottom sediment samples have been collected including piston cores, hydroplastic cores, and grabs recovered from canyons and transects perpendicular to the margin. Core transects normal to the margin were taken at approximately 80 km intervals to determine sediment characteristics and geotechnical properties. Sediment cores were also collected on the upper rise to assess the sediment and geotechnical properties and regional patterns of these seafloor deposits. Selected cores are being studied in cooperation with researchers of the University of South Florida, Duke University, Oregon State University, Florida International University, Florida State University, and Texas A & M University. Approximately 9,000 nautical miles of seismic reflection and 3.5 kHz profiles were run parallel to the margin on the outer shelf, upper and lower slope, upper rise, and in selected canyons and intercanyon areas (site-specific areas) to determine sediment distribution and processes that are presently active and those processes that were active in the geologic past. Detailed geophysical studies, bottom sampling in selected canyons, submersible observations, and current meter data, are being integrated to determine processes active in the canyons and the role of the canyons in the transport of material to the deep sea.

The suite of data collected on the continental margin, both regionally and in site-specific areas on the slope, rise, and in specific canyons, includes: narrow-beam echo soundings (NBES), 3.5 kHz and seismic profiles, bottom samples (cores and grabs), bottom photographs, and current meter data.

In addition to the regional studies and submarine canyon investigations, detailed site-specific areas are being studied on the slope,

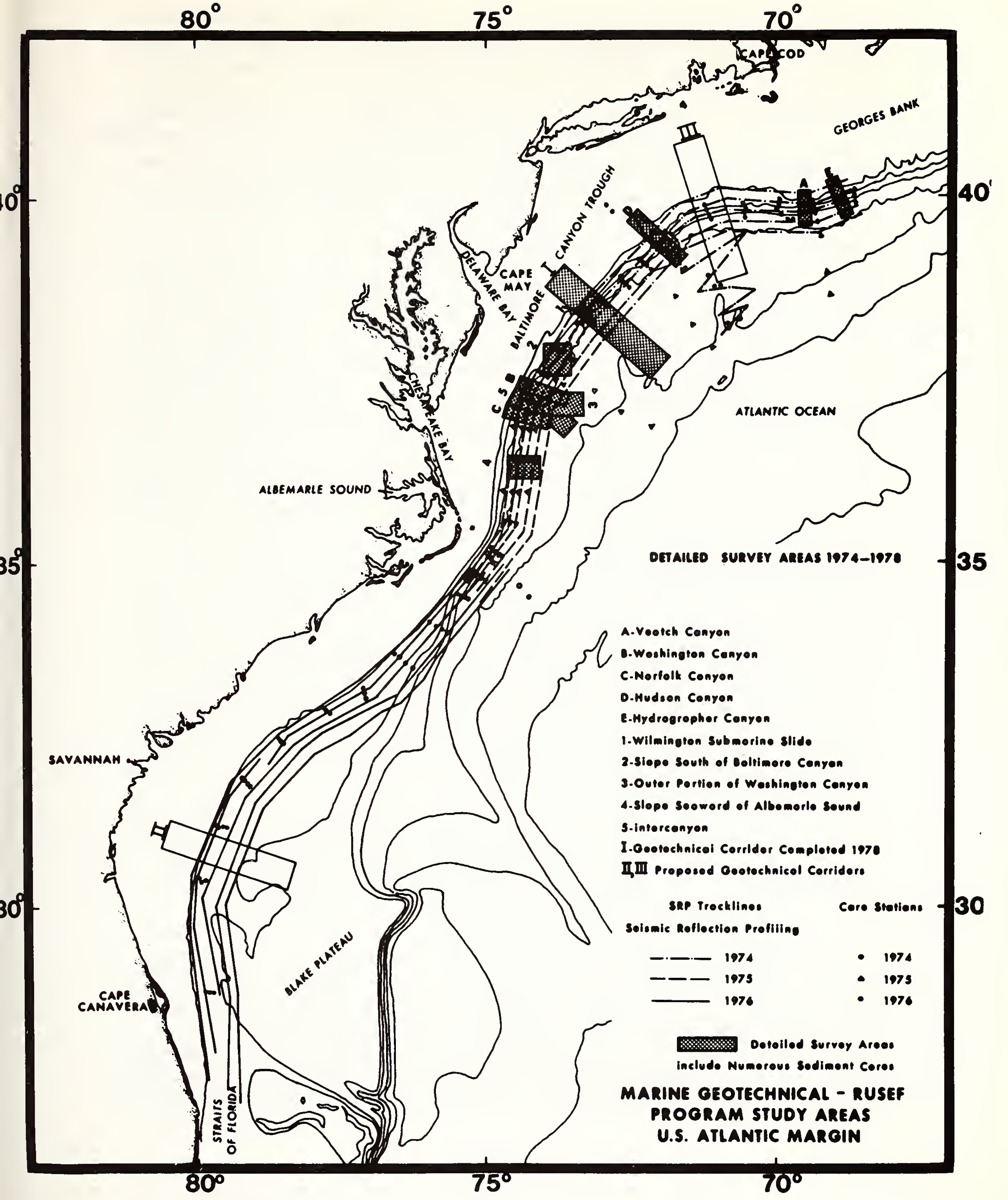
80°
75°
70°
40°
35°
30°
CAPE COD
GEORGES BANK
III
II
A
E
D
CANYON TROUGH
I
CAPE MAY
DELAWARE BAY
BALTIMORE
2
C
5
B
3
4
1
CHESAPEAKE BAY
ALBEMARLE SOUND
ATLANTIC OCEAN
DETAILED SURVEY AREAS 1974–1978
A-Veatch Canyon
B-Washington Canyon
C-Norfolk Canyon
D-Hudson Canyon
E-Hydrographer Canyon
1-Wilmington Submarine Slide
2-Slope South of Baltimore Canyon
3-Outer Portion of Washington Canyon
4-Slope Seaward of Albemarle Sound
5-Intercanyon
I-Geotechnical Corridor Completed 1978
II,III Proposed Geotechnical Corridors
SRP Tracklines
Seismic Reflection Profiling
Core Stations
1974
1975
1976
1974
1975
1976
Detailed Survey Areas include Numerous Sediment Cores
MARINE GEOTECHNICAL - RUSEF PROGRAM STUDY AREAS U.S. ATLANTIC MARGIN
SAVANNAH
CAPE CANAVERAL
BLAKE PLATEAU
STRAITS OF FLORIDA

FIG. 1

northeast of Wilmington Canyon, south of Baltimore Canyon and seaward of Albermarle Sounds, and on the upper rise between Washington and Norfolk Canyons. These areas are being studied in terms of their geological, geophysical, sedimentological, and geotechnical characteristics. Among some of the more important questions being addressed are: seafloor stability, geological history and stratigraphy, geological and sedimentological processes, oceanographic processes, geotechnical properties variability, and sediment characteristics of the surficial submarine sediments and sedimentation patterns.

In response to offshore engineering needs defined in the 1976 report of the Committee on Seafloor Engineering, National Research Council, there has been initiated in the Marine Geotechnical-RUSEF program detailed investigations in a geotechnical corridor seaward of Cape May off the coast of New Jersey and northeast of Wilmington Canyon (Fig. 1). This 30 x 70 nautical mile corridor crosses the Baltimore Canyon Trough where oil exploration is presently underway. Field work was initiated in 1977 during which seismic reflection, 3.5 kHz, NBES profiles, and core samples were collected. The remainder of the geophysics and coring was completed during a cruise in May 1978. This corridor is considered to be representative of the continental margin between Hudson Canyon and seaward of Cape Hatteras. Two additional geotechnical corridors are planned for future years: one seaward from Rhode Island will provide data on a previously glaciated portion of the continental margin; the other corridor seaward of Savannah off the Georgia coast will cover part of the Blake Plateau and the Georgia embayment where substantial cycles of erosion and deposition have occurred. Each selected corridor is considered to be representative of the respective offshore regions, and the studies are expected to provide representative parameters of the geophysics, stratigraphy, sediments, geology, bathymetry, and geotechnical properties characteristic of the selected areas.

To date approximately 95% of the cores and bottom samples held at AOML have been described and analyzed and the majority of the geophysical data have been reduced and preliminary interpretations completed. Several reports have been published and others are in press or in preparation.

Gulf of Mexico.--AOML's geotechnical studies in the Gulf of Mexico have been site-specific in selected areas of the Mississippi Delta and problem oriented. Clay fabric and geotechnical properties investigations were initiated in 1972 in cooperation with Texas A & M University, Department of Oceanography, personnel. Studies are directed towards an understanding of the fabric characteristics of various Mississippi pro-delta muds and the relationships of the clay fabric to the geotechnical properties. Of fundamental significance is that clay fabric, or particle-to-particle relationships, plays an important role in determining the ultimate response of a sediment to static and dynamic loads and is important as well in determining the ultimate nature of the mass physical properties of the electrolyte-gas-solid system of seafloor deposits.

More recent developments initiated in 1975 at AOML have demonstrated the criticality of pore-water pressure measurements in the determination of excess pore pressures as applied to the engineering properties of seafloor sediments. In response to this need, AOML has developed shallow-water piezometer probes and is conducting in situ experiments with these instruments in the Mississippi Delta. The purpose of these experiments is to measure and monitor sediment pore pressures under static and dynamic (during storm periods) conditions to assess the magnitude and importance of these pressures and pressure perturbations to sediment stability-instability in high porosity, low shear-strength soils. Initial results at three sites have revealed significant excess pore pressures in these sediments. A long-term experiment showed a definite response of the pore waters to the influence of Hurricane Eloise.

AOML's Mississippi Delta studies have been carried out in cooperation with Texas A & M University and during specific studies with Louisiana State University, U. S. Geological Survey, Lehigh University, and Sandia Corporation.

Current and Future Plans.--AOML researchers actively involved in the Marine Geotechnical-RUSEF Program and cooperating scientists and engineers from various institutions plan to continue investigations on the U. S. Atlantic Continental Margin in the geotechnical corridors and in site-specific areas of particular interest. In-depth studies are underway into the problems of seafloor stability, geologic processes, and the characterization of seafloor deposits in terms of their geotechnical properties, morphology, and geologic setting.

A continuation of site-specific studies is planned for 1978 and ensuing years in the Mississippi Delta region and the Gulf of Mexico. Investigations will focus on specific geotechnical problems of clay fabric, pore pressures, sediment stability, and the in situ state of stress. Plans are for better piezometer data acquisition systems suitable for collection of data under severe storm and related environmental conditions which are considered acute periods in the ultimate stability of submarine sediments. Detailed studies of clay fabrics from samples obtained using a newly developed pressurized core barrel designed and fabricated by Texas A & M are planned for 1978-79.

Program review booklets giving details of the Marine Geotechnical-Rational Use of the Seafloor Program are available through the NOAA-AOML. Personal communications with AOML staff are encouraged.

Mathematical Geology 10, No. 2, 225-241.

An Oblique Factor Analysis Solution for the Analysis of Mixtures[1]

Thomas L. Clarke[2]

The problems involved in the factor analysis of data consisting of measurements of material quantity or proportion are discussed, and the inability of existing factor analysis solutions to properly model such data is pointed out. A new factor analysis solution using the linear programming technique is presented which properly analyzes mixture data. A numerical example is presented in which a body of suspended sediment grain-size distribution data is analyzed using the new factor analysis solution. FORTRAN-IV subroutines for computing this solution are included in an Appendix. KEY WORDS: factor analysis, linear programming, sedimentology.

INTRODUCTION

Factor analysis, more specifically, Q-mode analysis, is a method for extracting the essential information contained in a large set of data. Commonly the data are not completely random, and factor analysis enables the data to be explained in terms of a relatively small number of hypothetical variables or factors. In geology factor analysis has found application in the analysis of grain-size distribution data (Imbrie and Purdy, 1962; Klovan, 1966) and in the analysis of suspended sediment characteristics (Yamamoto, 1976). Spencer (1966) has applied factor analysis to elemental distributions in shale bands, and Rozett and Peterson (1976) have applied it to the classification of mass spectra of chemical compounds. Factor analysis and its variants have many other uses, but the above applications have in common data comprised of measurements of material quantity or proportion. In these situations the data can be modeled as samples mixed from a small set of component fractions. Alternately, the data may be the result of a process in which individual samples are obtained by subtracting or winnowing the component fractions from a parent mixture. A factor analysis should facilitate the expression of the samples as the result of mixing.

---

[1] Manuscript received 31 March 1977; revised 16 October 1977.

[2] Atlantic Oceanographic and Meteorological Labs, 15 Rickenbacker Causeway, Miami, Florida, USA, 33149.

Most existing factor analysis solutions fail to satisfactorily decompose a set of mixture data. If each data point consists of n numbers, the result of a factor analysis is a set of orthogonal vectors or factors in Euclidean n-space. A subset of m of these factors is chosen which accounts for most of the variance in the data. In general, m is less than n, and the dimensionality of the data is reduced. If the measurements are of material quantity or proportion, they must all be positive, and data vectors must lie in the positive quadrant of n-space. The orthogonality of the factors makes it extremely unlikely that they will all lie in the positive quadrant of this n-space; and unless they do so, they cannot be interpreted as component fractions. The data are closely reproduced by linear combinations of the factors, but unless the individual factors can be identified with hypothetical component fractions, these linear combinations cannot be easily interpreted as mixtures. Thus, orthogonality must be abandoned and an oblique factor solution used.

The simplest method for oblique solution is to manually choose, on the basis of high communality and high factor loading, samples which are representative of the components derived from factor analysis. There are also a number of objective methods of calculating an oblique solution (Harman, 1967; Spencer, 1967), but these fail to guarantee that the solution vectors will lie in the positive quadrant of n-space. Thus, these solutions are not directly interpretable in terms of mixing.

Miesch (1976a; Klovan and Miesch, 1976) has presented a method of applying factor analysis to mixture data which ensures that the components of the linear combinations which reproduce the data have a constant sum. Assuming the factors can be interpreted as component fractions, these linear combinations can be interpreted as mixtures. The choice of factors is not specified by this solution and, as in the above oblique solutions, must be based on substantive criteria.

In what follows, a new oblique solution is given which uses linear programming to find a set of oblique factors. These oblique factors are extremal, in the sense that they lie on the edge of the positive quadrant of n-space, and are those extremal factors which are closest to a given set of vectors in n-space. This set of vectors may be the factors given by an initial factor solution, or they may be chosen by some other criteria. A set of FORTRAN-IV subroutines for calculating this solution is presented in an appendix.

NEW OBLIQUE SOLUTION

If N is the number of data points, n is the number of measurements comprising each data point, X is the $N \times n$ data matrix, and W is the row normalized version of X, the object of Q-mode factor analysis is to find matrices ($Q_0(N \times n)$ and $F_0(n \times n)$ so that

$$W = Q_0 F_0$$

and such that successive rows of F_0 account for successively smaller amounts of the variance of the data. F_0 and Q_0 are then truncated to $F\ (m \times n)$, the factor score matrix, and $Q\ (N \times m)$, the factor loading matrix, so the m rows of F account for a satisfactory amount of the variance of the data (e.g., 95%); the product QF is then a good approximation to W in the least-square sense. The matrices of Q_0 and F_0 can be calculated by a number of techniques, but that given by Klovan (1971) is perhaps the most convenient.

Q-mode analysis may be regarded as finding a closest-fit hyperplane to the set of data vectors in n-space (Pearson, 1901). The data vectors are projected onto this hyperplane and reexpressed in a coordinate system in the hyperplane. The rows of F, $\{C_1, \ldots C_m\}$, are the coordinate vectors (factors) of the hyperplane, and the rows of Q are the coordinates of the projections of the data vectors on the hyperplane (factor loadings). The coordinate system may be rotated to simplify the structure of the factor analysis as in a varimax rotation. An oblique coordinate system may also be used to locate the projections of the data vectors on the closest fit hyperplane (Harman, 1967).

Formally the problem of finding a mixture solution is to construct a set of vectors (oblique factors),

$$\{B_1, \ldots, B_m\}$$

which span the subspace generated by the initial factors,

$$\{C_1, \ldots, C_m\}$$

and which are close to a given set of reference vectors (directions)

$$\{D_1, \ldots, D_m\}$$

that is, B_i is close to D_i, and which satisfy

$$b_{ij} \geqslant 0, \qquad j = 1, \ldots, n$$

where b_{ij} is the jth coordinate of B_i.

Figure 1 shows the situation for $n = 3$ for unnormalized data which sum to 3. The sample vectors (.) must lie on the plane P_1 which passes through (1,0,0), (0,1,0), and (0,0,1). The factor analysis indicates that the data vectors all lie near the plane P_2 which intersects P_1 in the line L. The analysis also gives C_1 and C_2 as basis vectors for P_2. A mixture solution could be based on vectors B_1 and B_2 which are both possible data vectors and which permit a close approximation of each data vector as a mixture of B_1 and B_2. C_1 and C_2 are unsatisfactory; data vectors to the left of C_1 along L require a negative admixture of C_2, and, because C_2 is outside of the positive quadrant, it cannot be interpreted as a component fraction.

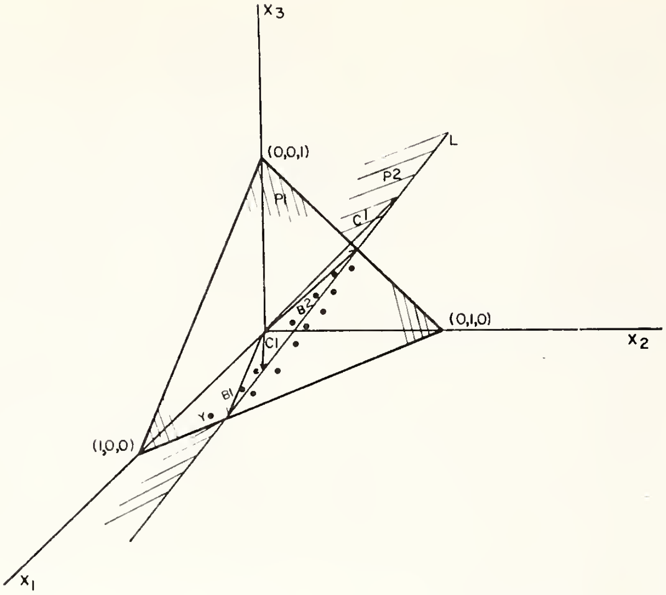

Figure 1. Spatial situation in a factor analysis of three variables giving two factors.

The problem of finding a set of basis vectors which admit interpretation as a mixture can be put into the form of a linear programming problem if the measure of closeness of B_i and D_i is linear. In order to guarantee that the B_i span the solution space, it is convenient to express the B_i as linear combinations of the C_i:

$$B_i = \sum_{k=1}^{m} a_{ik} C_k, \qquad i = 1, \ldots, m$$

where the a_{ik} are numbers giving the composition of the oblique factors in terms of the initial factors. If the measure of closeness, $\rho(B_i, D_i)$, is linear, it can be expressed in the form

$$\rho(B_i, D_i) = \sum_{k=1}^{m} u_{ik} a_{ik}, \qquad i = 1, \ldots, m$$

where the u_{ik} are a set of weights.

A modification of the simplex method (Hillier, 1967) can then be used to maximize the objective function,

$$\sum_{k=1}^{m} u_{ik} a_{ik} \tag{1}$$

subject to the constraints

$$b_{ij} = \sum_{k=1}^{m} a_{ik}c_{kj} \geqslant 0, \qquad j = 1,\ldots,n \tag{2}$$

where c_{ij} is the jth coordinate of C_i.

It is convenient to add the constraint

$$\sum_{j=1}^{m} b_{ij} = \sum_{k=1}^{m} a_{ik} \sum_{j=1}^{n} c_{kj} = 1 \tag{3}$$

to ensure the existence of a solution. Without this constraint either the origin will be the solution or there will be no bounded solution. What is important is the direction of the solution vectors; they can be scaled as desired later. These m linear programming problems can easily be solved via the simplex method on a digital computer; a set of FORTRAN-IV subroutines which solves these problems is presented in the Appendix. Note that only the objective function changes from problem to problem, the constraints remain the same. The set of a_{ik} so obtained will then give a set of basis vectors which admits interpretation as a mixture.

The obvious distance function to use is the dot product of D_i and B_i

$$\rho(D_i,B_i) = \sum_{j=1}^{n} d_{ij}b_{ij} = \sum_{k=1}^{m} a_{ik} \sum_{j=1}^{n} c_{kj}d_{ij}$$

where d_{ij} is the jth coordinate of D_i. Thus, in this case,

$$u_{ik} = \sum_{j=1}^{n} c_{kj}d_{ij}$$

which is just the dot product of C_k and D_i.

If no natural set of directions presents itself, it is convenient to use $C_i = D_i$. For this case,

$$u_{ik} = \begin{cases} 1, & i=k \\ 0, & i\neq k \end{cases}$$

if the initial factors C_i are orthogonal as is commonly the case. The idea here is to form B_i from C_i, admixing only as much of the other initial factors as is necessary to ensure that B_i lies in the positive quadrant, and at the same time subtracting as much of the other initial factors to maximize the contribution of C_i to B_i.

Geometrically the set of possible sample vectors consists of the polygon formed by bounding the hyperplane

$$\sum_{j=1}^{n} x_j = 1$$

by the coordinate hyperplanes. The desired solution vectors are the extremal intersections of the sample space with this polygon. The B_i can be found via a search over the perimeter of the polygon, but this is what the linear programming algorithm accomplishes. In fact, linear programming can be viewed as a search for extremal points on a convex polygon.

In practice it is necessary to change the sign of the C_i as necessary to ensure that

$$\sum_{j=1}^{n} c_{ij}$$

is positive. If this is not done, the same solutions will be obtained, but not in the desired order. When solving for B_i, if

$$\sum_{j=1}^{n} c_{ij} < 0,$$

then a_{ij} will be forced low, and the resulting B_i will be close to some other C_k rather than C_i.

If the data are the result of additive and subtractive processes, then a different set of direction D_i and objective function weights u_{ij} are appropriate. In this case some directions will be identified with the additive processes, say

$$D_i, \qquad i = 1, \ldots, m_1$$

where m_1 is the number of additive directions, and the remainder with the subtractive processes

$$D_i, \qquad i = m_1 + 1, \ldots, m$$

In addition, if the additive oblique factors lie in the positive quadrant of n-space and the subtractive oblique factors lie in the negative quadrant of n-space, mathematically, the additive and subtractive processes can be treated as a single additive process. The additive oblique factors should be as far as possible from the subtractive directions, and the subtractive oblique factors as far as possible from the additive directions.

A natural way to find a set of B_i which satisfies these requirements is to require

$$\sum_{j=1} d_{ij} \begin{cases} \geqslant 0 & \text{for additive directions} \\ \leqslant 0 & \text{for subtractive directions} \end{cases} \tag{4}$$

The C_i are required to have positive sum as before.

In addition, constraints (2) and (3) become

$$\sum_{k=1}^{m} a_{ik} c_{kj} \begin{cases} \geqslant 0 & \text{for additive directions} \\ \leqslant 0 & \text{for subtractive directions} \end{cases} \tag{2a}$$

and

$$\sum_{k=1}^{m} a_{ik} \sum_{j=1}^{n} c_{kj} \begin{cases} = 1 & \text{for additive directions} \\ = -1 & \text{for subtractive directions} \end{cases} \tag{3a}$$

Then the problem is to maximize

$$\sum_{k=1}^{m} u_{ik} a_{ik} \tag{1a}$$

The constraints (2a) will force additive oblique factors into the positive quadrant, and subtractive oblique factors into the negative quadrant. The sign changes specified by (4) together ensure that the signs in objective function (1a) are such that the oblique factors are close to the appropriate directions. The B_i which lie in the positive quadrant can be interpreted as additive component fractions of a parent population, whereas the B_i in the negative quadrant represent fractions winnowed from the parent population.

Once a set of oblique factors has been found, the factor scores of the data points must be found. The product QF closely reproduces the row normalized version of the matrix W. Similarly, the factors $\{C_i\}$ are row normalized so that

$$\sum_{j=1}^{n} c_{ij}^2 = 1$$

What is needed is T, the $m \times m$ transformation matrix between the basis $\{C_i\}$ and the row normalized version of the basis $\{B_i\}$. Let

$$q_i = 1/\left(\sum_{j=1}^{n} b_{ij}^2\right), \qquad i = 1,\dots,m$$

be the multipliers necessary to change basis $\{B_i\}$ into normalized basis

$$\{B_i'\} = \{q_i B_i\}.$$

Some of the factors C_i had their signs changed in the construction of $\{B_i\}$. If

$$s_i = \begin{cases} 1 \text{ if sign of } C_i \text{ was unchanged} \\ -1 \text{ if sign of } C_i \text{ was changed} \end{cases}$$

then the matrix A whose entry at the ith row and jth column is $s_j q_i a_{ij}$, that is,

$$A = [s_j q_i a_{ij}]$$

is the transformation matrix from the basis $\{B_i'\}$ to the basis $\{C_i\}$. Therefore, $T = A^{-1}$, and the new factor loading matrix is

$$Q' = QT$$

It would be preferable to construct the row normalized oblique factors $\{B_i'\}$ directly from the factors $\{C_i\}$. However, this would require the constraint (3) to have the form

$$\sum_{j=l}^{n}\left(\sum_{k=l}^{m} a_{ik} c_{kj}\right)^2 \leqslant 1 \tag{5}$$

which is nonlinear in the numbers a_{ik}. With this normalization constraint, the dot product of D_i and B_i equals the usual cosine θ distance measure of factor analysis, provided D_i is normalized. Unfortunately, it is not possible to introduce a constraint of the form (4) into a linear programming problem. There is a mismatch between the factor analysis technique and this linear programming technique. Possibly the transformation techniques of Miesch (1976b) can be applied to this problem. However, if the computation of the a_{ik} and the B_i are carried out as outlined above, good results are obtained as shown in the following example.

Table 1. Partial Varimax Factor Loadings Matrix

Sample number	Communality	Factor loadings		
		1	2	3
6020	0.9841	0.2700	−0.8047	−0.5135
6030	0.8769	0.2423	−0.8887	−0.1684
6040	0.9664	0.2184	−0.5868	−0.7592
6050	0.9469	0.4020	−0.7151	−0.5234
6060	0.9900	0.3118	−0.6508	−0.6850
6070	0.9796	0.5360	−0.4814	−0.6787
6075	0.9597	0.2759	−0.6718	−0.6575
6080	0.9393	0.2484	−0.8337	−0.4273
6090	0.9340	0.2579	−0.8240	−0.4342
6100	0.9568	0.2411	−0.6329	−0.7072
6110	0.9806	0.3191	−0.7298	−0.5884
6120	0.9547	0.2489	−0.6859	−0.6498
6130	0.9747	0.2683	−0.6873	−0.6560
6140	0.8945	0.2504	−0.8188	−0.4016
6150	0.9492	0.1729	−0.5098	−0.8120
6160	0.9543	0.2310	−0.6513	−0.6904
6170	0.9539	0.3910	−0.6061	−0.7116
6180	0.9753	0.3698	−0.8118	−0.4237
6190	0.9090	0.2738	−0.9019	−0.1458
6200	0.8150	0.8970	0.0154	0.1005
6210	0.9098	0.3005	−0.7338	−0.5301
6220	0.9596	0.3078	−0.8334	−0.4126
6230	0.7996	0.2863	−0.7469	−0.3998
6240	0.9509	0.2418	−0.9421	−0.0697
6250	0.9571	0.1952	−0.7061	−0.6484
8225	0.9868	0.9558	−0.1794	−0.2028
10232	0.9340	0.2299	−0.9300	−0.1271
10080	0.9409	0.4063	−0.1091	−0.8740

Table 2. Varimax Solution Vectors, Normalized to Variance of 21

Phi interval	Factor		
	1	2	3
4.00	0.556	−2.137	1.058
4.25	0.534	−1.939	0.687
4.50	0.249	−2.155	0.215
4.75	−0.076	−2.352	−0.432
5.00	−0.087	−1.109	−1 159
5.25	−0.154	−0.790	−1.694
5.50	−0.059	−0.499	−1.748
5.75	0.088	−0.181	−1.930
6.00	0.442	0.174	−2.053
6.25	0.817	0.294	−1.647
6.50	1.048	0.213	−0.896
6.75	1.196	0.082	−0.317
7.00	1.416	0.061	−0.015
7.25	1.482	0.101	0.137
7.50	1.464	0.128	0.230
7.75	1.423	0.137	0.252
8.00	1.506	0.168	0.257
8.25	1.510	0.216	0.249
8.50	1.378	0.200	0.230
8.75	1.067	0.133	0.139
9.00	0.974	0.102	0.127

NUMERICAL EXAMPLE

A data set consisting of 660 suspended sediment grain-size analyses taken from NOAA's Marine Ecosystems Analysis Program on the New York continental shelf (Drake, 1973; Nelsen, 1977) was subjected to a factor analysis using the CABFAC (Klovan, 1971) factor analysis program. The data were obtained from a Coulter Counter Model T and consisted of percentages in 21, 1/4-phi intervals from 4.0 phi to 9.0 phi. Three factors explained 91 percent of the variance. The three solution vectors were subjected to a varimax rotation.

A partial listing of factor loadings is presented in Table 1. Table 2 gives the coordinates (factor scores) of the rotated solution factors. With the exception of the first, none can be interpreted as a sample vector. End members exhibiting high communality and high loading on one of the factors were chosen by hand. Histograms of these are presented in Figure 2.

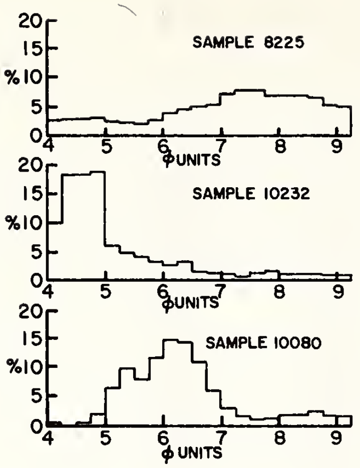

Figure 2. Histograms of manually selected extreme samples.

Table 3. Mixture Solution Vectors, Normalized to Sum to 100

Phi interval	Factor		
	1	2	3
4.00	2.86	16.62	0.00
4.25	2.89	15.34	1.73
4.50	1.52	17.03	4.83
4.75	0.00	18.66	8.90
5.00	0.16	9.48	10.04
5.25	0.00	7.31	12.39
5.50	0.54	5.21	12.08
5.75	1.43	3.05	12.56
6.00	3.46	0.83	12.87
6.25	5.38	0.05	10.57
6.50	6.35	0.40	6.47
6.75	6.93	1.16	3.45
7.00	8.04	1.38	1.95
7.25	8.34	1.03	0.99
7.50	8.19	0.72	0.32
7.75	7.94	0.57	0.10
8.00	8.41	0.44	0.10
8.25	8.43	0.08	0.03
8.50	7.69	0.04	0.00
8.75	5.98	0.24	0.30
9.00	5.46	0.37	0.33

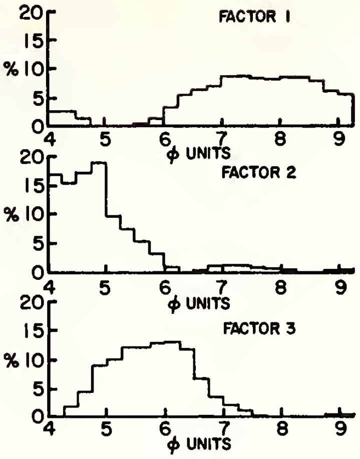

Figure 3. Histograms of mixture solution basis vectors.

The rotated solution vectors were then used to find oblique factors for a mixture solution via the method presented here. All factors were considered to be additive and the original factors were used as directions. Table 3 gives the coordinates of these oblique factors, and Figure 3 shows their histograms. The oblique factors closely resemble the hand-picked end members. They are, however, extreme members in a more formal sense and can be considered to more truly represent the components of the observed suspended sediment. In particular, sample 8225, while composed primarily of Factor 1, seems to be contaminated by Factor 2. Similarly, sample 10080 is composed of Factor 3 contaminated by Factor 2.

Table 4 gives the results of transforming the factor loadings in Table 1 into the mixture solution coordinate system.

Factors 2 and 3, separately and together, were reinterpreted as subtractive factors, still using the original rotated factors as direction. The resulting factor loadings did not make much sense as a subtractive process. The loadings on the subtractive factors were mostly negative, indicating that these factors are best interpreted as being additive. A negative factor subtracted is the same as a positive factor added.

Thus, for this data set the best interpretation seems to be that it is the result of an additive process whose component fractions closely resemble the oblique factors shown in Table 3 and Figure 3.

CONCLUSION

The new oblique factor analysis solution presented here should prove useful whenever a body of data consists of measurements of physical quantity or proportion and invites interpretation as a mixture. Not only can the number

Table 4. Partial Oblique Mixture Solution Factor Loadings Matrix

Sample number	Communality	Factor loadings		
		1	2	3
6020	0.9841	0.3055	0.9472	0.3202
6030	0.8769	0.2430	1.0203	−0.2059
6040	0.9684	0.2804	0.7046	0.6037
6050	0.9469	0.4424	0.8976	0.2941
6060	0.9900	0.3671	0.8022	0.4984
6070	0.9796	0.5978	0.6994	0.5889
6075	0.9597	0.3276	0.8117	0.4546
6080	0.9393	0.2749	0.9690	0.1177
6090	0.9340	0.2854	0.9621	0.1308
6100	0.9588	0.2977	0.7599	0.5257
6110	0.9806	0.3639	0.8862	0.3535
6120	0.9547	0.2992	0.8173	0.4371
6130	0.9747	0.3194	0.8255	0.4451
6140	0.8945	0.2749	0.9535	0.0958
6150	0.9492	0.2407	0.6090	0.6950
6160	0.9543	0.2855	0.7756	0.4974
6170	0.9589	0.4510	0.7824	0.5559
6180	0.9753	0.3984	0.9868	0.1342
6190	0.9090	0.2731	1.0445	−0.2292
6200	0.8150	0.9024	0.2849	−0.0293
6210	0.9098	0.3395	0.8831	0.2843
6220	0.9596	0.3339	0.9885	0.1064
6230	0.7996	0.3127	0.8899	0.1301
6240	0.9509	0.2327	1.0747	−0.3364
6250	0.9571	0.2440	0.8205	0.4216
8225	0.9868	0.9864	0.5151	0.2277
10232	0.9340	0.2262	1.0590	−0.2671
10080	0.9409	0.4919	0.2670	0.9703

of constituents and their relative importance in each sample be determined, but an optimal composition can be determined for each. In addition, the factor loadings obtained can be interpreted as the composition of each sample in terms of the constituents.

ACKNOWLEDGMENTS

I would like to thank both Terry A. Nelsen for prodding me with the question, "What is a factor?", and Dr. J. William Lavelle for discussing the nature of the answer.

APPENDIX

These two FORTRAN-IV subroutines calculate the oblique factors $\{B_i\}$, the coordinate transformation matrix T, and the new factor loadings matrix F' for an additive mixture model as outlined in this paper. Subroutine CLOSE sets up the linear programming problems and calculates T and F'. Subroutine SIMPLE solves the linear programming problems via a modified simplex method. Subroutine CLOSE is designed to be called from the factor analysis program CABFAC (Klovan and Imbrie, 1971). The calling statements below should be inserted after line 345 of their program (p. 71, 2nd line from bottom, of above reference).

```
C     ----------------------------------------------------------------------
C     INSERT THESE STATEMENTS AFTER STATEMENT 345 OF PROGRAM CABFAC
C     NUMBER OF FACTORS IS LIMITED TO 8 BECAUSE TAIL END OF ARRAY F IS
C     USED FOR TEMPORARY STORAGE BY SUBROUTINE CLOSE
C
C     INDICATE ALL FACTORS ARE ADDITIVE
        DO 2000 I=1,NF
 2000 F(1100+I,9)=1.0
C     SOME OF F(1100+I,9) MIGHT BE SET TO -1.0 TO INDICATE SUBTRACTIVE
C     FACTORS
C
    USE EIGENVECTORS (A) AS REFERENCE VECTORS ALSO
        DO 3000 J=1,NF
        IND=(J-1)*50
        DO 3000 I=1,NV
 3000 F(I+IND,9)=A(I,J)
C     HERE VARIOUS COMBINATIONS OF THE EIGENVECTORS IN A
C     OR ENTIRELY DIFFERENT VECTORS (E.G. SELECTED DATA VECTORS)
C     MIGHT BE USED AS REFERENCE VECTORS
C
C     THIS STATEMENT CALLS SUBROUTINE CLOSE TO CALCULATE OBLIQUE MIXTURE
C     SOLUTION FACTORS SCORES AND FACTOR LOADINGS
        CALL CLOSE(NS,NV,NF,F(601,9),F(1111,9),A,F(1,9),F(1101,9),
       1 F(501,9),ID,COM,TITLE,F)
        SUBROUTINE CLOSE(NS,NV,NF,S,T,E,D,P,A,ID,COM,TITLE,F)
        DIMENSION F(1500,10)
        DIMENSION A(NF,NF),ID(1),COM(1),T(1)
        DIMENSION E(50,50),S(50,10),D(50,10),P(10)
        DIMENSION SGN(10),SUM(10),DSGN(10)
        COMMON KT1,KT2,KT3,KT4,KT5,NFILE
C     FINDS OBLIQUE MIXTURE SOLUTION
C     NF IS NO. OF FACTORS, NV NO. OF VARIABLES, AND NS NO. OF SAMPLES
C     F IS FACTOR LOADINGS MATRIX
C     E IS MATRIX (ROWWISE) OF EIGENVECTORS (FACTOR SCORES)
C     D IS MATRIX (ROWWISE) OF REFERENCE VECTORS
C     P IS VECTOR  INDICATING TYPES OF OBLIQUE FACTORS
C     +1.0 IF ADDITIVE, -1.0 IF SUBTRACTIVE
C     S IS MATRIX (ROWWISE) OF NEW OBLIQUE FACTOR SCORES
C     ID IS MATRIX OF SAMPLE IDENTIFIERS
C     T IS TEMPORARY WORKING MATRIX
C     COM IS MATRIX OF SAMPLE COMMUNALITIES
C     A IS COORDINATE TRANSFORMATION MATRIX
C          T.L. CLARKE
C          MARINE GEOLOGY AND GEOPHYSICS
C          ATLANTIC OCEANOGRAPHIC AND METEOROLOGICAL LABORATORY - NOAA
C          REVISED SEPTEMBER 1977
        DATA IBLK/6H FCT 0/
        DATA FACT,BLNK/6HFACT  ,6H
        NFF=NF-1
        NFM=NF
        NFP=NF+1
C     PARTITION TEMPORARY ARRAY FOR USE OF LINEAR PROGRAMMING ROUTINE
```

```
      IA=NF+NV+3
      IB=IA+(NF+1)*(NV+3)
      IROW=IB+NV+3
      IVAR=IROW+NV+NF+3
      IRES=NF**2+1
      IVAL=IRES+NF**2+1
C   NORMALIZE EIGENVECTORS (FACTOR SCORES) SO ALL HAVE POSITIVE SUM
      DO 120 J=1,NF
      SGN(J)=1.0
      SUM(J)=0.0
      DSGN(J)=1.0
      DSUM=0.0
      DO 100 I=1,NV
      DSUM=DSUM+D(I,J)
  100 SUM(J)=SUM(J)+E(I,J)
      IF(SUM(J).LT.0.0) SGN(J)=-1.0
      IF(DSUM.LT.0.0) DSGN(J)=-1.0
  120 CONTINUE
      DO 1000 J=1,NF
C   SET UP OBJ FUNCTION
C   MAXIMIZE DOT PRODUCT OF JTH REFERENCE VECTOR WITH NEW OBLIQUE FACTOR,
C   SCORE
      TSUM=0.0
      DO 160 I=1,NF
      DOT=0.0
      DO 165 K=1,NV
  165 DOT=DOT+E(K,I)*D(K,J)
      DOT=DOT*SGN(I)*DSGN(J)*P(J)
      T(IA+I-1)=DOT
      TSUM=TSUM+DOT
  160 CONTINUE
      T(IA+NF)=-TSUM
C   SET UP CONSTRAINTS
C   NV POSITIVITY CONSTRAINTS
      DO 140 I=1,NV
      JND=I*NFP+NF+IA
      T(JND)=0.0
      DO 140 K=1,NF
      IND=I*NFP+K+IA-1
      T(JND)=T(JND)+E(I,K)*SGN(K)*P(J)
  140 T(IND)=-E(I,K)*SGN(K)*P(J)
C   USE SMALL NON-ZERO CONSTRAINT TO AVOID DEGENERATE SOLUTIONS
      DO 130 I=1,NV
  130 T(IB+I)=1.0E-4
      T(IB)=0.0
C   TWO SUMMATION CONSTRAINTS - TWO .LE. CONSTRAINTS MAKE ONE .EQ.
      JND=(NV+1)*NFP+NF+IA
      T(JND)=0
      DO 145 K=1,NF
      IND=(NV+1)*NFP+K+IA-1
      T(JND)=T(JND)-SUM(K) *SGN(K)
      T(IND+NF+1)=-SUM(K)*SGN(K)
  145 T(IND)=SUM(K)*SGN(K)
      T(JND+NF+1)=-T(JND)
      T(IB+NV+1)=P(J)
      T(IB+NV+2)=-P(J)
C   SOLVE FOR EIGENVECTOR COMPONENTS
C   USE NF+1 VARIABLES TO ALLOW FOR NEGATIVE COMPONENTS
      CALL SIMPLE(T(IA),T(IB),T,T(IROW),T(IVAR),NV+3,NF+1)
C   SUBTRACT NF+1ST VARIABLE TO ALLOW NEGATIVITY
      DO 150 I=1,NF
  150 T(I)=(T(I)-T(NF+1))
      PRINT 101,(T(I),I=1,NF)
  101 FORMAT(1H ,13F10.2)
C   CALCULATE OBLIQUE FACTOR SCORES
      SUMSQ=0.0
      DO 650 I=1,NV
      S(I,J)=0.0
      DO 600 JJ=1,NF
      S(I,J)=S(I,J)+E(I,JJ)*T(JJ)*SGN(JJ)
  600 CONTINUE
  650 SUMSQ=SUMSQ+S(I,J)**2
      SUMSG=SQRT(SUMSQ/NV)
C   SAVE WEIGHTS TO CALCULATE COORDINATE TRANSFORMATION
C   DIVIDE BY SUMSQ TO NORMALIZE
      DO 700 JJ=1,NF
  700 A(JJ,J)=T(JJ)*SGN(JJ)/SUMSQ
      PRINT 101,(S(I,J),I=1,NV)
 1000 CONTINUE
      PRINT 101,(SGN(J),J=1,NF)
      PRINT 101,(DSGN(J),J=1,NF)
      PRINT 101,((A(I,J),I=1,NF),J=1,NF)
C   CALCULATE COORDINATE TRANSFORM
C   MINV IS STANDARD  IBM MATRIX INVERSION ROUTINE
      CALL MINV(A,NF,DET,T(1),T(NV))
      PRINT 101,DET
      PRINT 101,((A(I,J),I=1,NF),J=1,NF)
C   DISPLAY OBLIQUE FACTOR SCORES
      PRINT 2003,TITLE
      PRINT 2007,(J,J=1,NF)
 2007 FORMAT(1H0,'OBLIQUE FACTOR SCORE MATRIX',//,11X,'VAR',5X,10I8//)
      DO 2010 I=1,NV
C   NORMALIZE TO PERCENTAGES
      DO 2015 J=1,NF
 2015 T(J)=S(I,J)*100.0
 2010 PRINT 2009,I,(T(J),J=1,NF)
 2009 FORMAT(1X,I10,5X,10F10.2)
C   CALCULATE AND DISPLAY OBLIQUE FACTOR LOADINGS
      PRINT 2003,TITLE
 2003 FORMAT(1H1,20A4///)
      PRINT 2005,(J,J=1,NF)
 2005 FORMAT(1H0,'OBLIQUE FACTOR LOADINGS',//,13X,'COMM.',4X,10(I5,4X))
      DO 2000 L=1,NS
      TSUM=0.0
 2020 DO 2100 J=1,NF
      T(J)=0.0
      DO 2050 I=1,NF
 2050 T(J)=T(J)+F(L,I)*A(I,J)
 2100 TSUM=TSUM+T(J)
      TSUM=1.0
      DO 2200 J=1,NF
 2200 T(J)=T(J)/TSUM
      PRINT 2001,L,ID(L),COM(L),(T(J),J=1,NF)
 2001 FORMAT(1H ,I5,2X,A6,11F9.4)
 2000 CONTINUE
      END
      SUBROUTINE SIMPLE(A,B,X,IROW,IVAR,N,M)
      DIMENSION A(M,N),B(1),IVAR(1),IROW(1),X(M)
C   SOLVES LINEAR PROGRAMMING PROBLEM
C   MAXIMIZE SUMMATION X(I)*A(I,1),I=1,M
C   SUBJECT TO  SUMMATION A(I,J)*X(I), I=1,M .LE. B(J) FOR J=2,N
C   AND X(I) .GE. 0.0
C   THERE ARE N-1 CONSTRAINTS, M VARIABLES
C   METHOD:  MODIFIED SIMPLEX METHOD
C   IROW(I), IF POSITIVE, POINTS TO ROW(EQUATION) FOR WHICH VARIABLE
C   I IS BASIC , I.E.  X(I)=B(IROW(I))
C   IF IROW(I) IS NEGATIVE, -IROW(I) POINTS TO THE COLUMN OF MATRIX A
C   WHICH CONTAINS THE COEFFICIENTS OF VARIABLE I, HERE X(I)=0
C   IVAR(J) POINTS TO THE VARIABLE  WHICH IS BASIC IN ROW J
C       T.L. CLARKE
C       MARINE GEOLOGY AND GEOPHYSICS
C       ATLANTIC OCEANOGRAPHIC AND METEOROLOGICAL LABORATORY - NOAA
C       REVISED SEPTEMBER 1977
C
C  SET UP INDEX ARRAYS, INITIALLY SLACK VARIABLES ARE BASIC
      NIT=0
      IROW(1)=1
      IVAR(1)=1
      DO 40 I=2,N
      K=M+I
```

I

```
      IROW(K)=I
      IVAR(I)=K
   40 CONTINUE
      DO 50 I=1,M
   50 IROW(I+1)=-I
      NN=N+M
      LAST=0
      GO TO 800
   10 CONTINUE
C   FIND ENTERING VARIABLE WHICH INCREASES OBJECTIVE FUNCTION MOST
      AMAX=0.0
      IF(NIT.EQ.0) AMAX=-1.0E6
      NIT=NIT+1
      IENT=0
      DO 200 I=2,NN
      IF(I.EQ.LAST) GO TO 200
      IF(IROW(I).GT.0) GO TO 200
      J=-IROW(I)
C   FIND BASIC VARIABLE WHICH MOST CONSTRAINS ENTERING VARIABLE
      KMAX=0
      TMIN=1.0E6
      DO 100 K=2,N
      IF(A(J,K).LE.1.0E-5) GO TO 100
      TEST=B(K)/A(J,K)
      IF(TEST.GE.TMIN) GO TO 100
      TMIN=TEST
      KMAX=K
  100 CONTINUE
C   ENTERING VARIABLE IS UNCONSTRAINED
      IF(KMAX.EQ.0) GO TO 200
C   ENTERING VARIABLE IS NEGATIVE
      IF(TMIN.LE.0.0) GO TO 200
C   TEST FOR MAXIMALITY
      TEST=TMIN*A(J,1)
      IF(TEST.LE.AMAX) GO TO 200
      AMAX=TEST
      IENT=I
      JENT=J
      LEAV=KMAX
  200 CONTINUE
C   NO VARIABLE INCREASES OBJECTIVE FUNCTION, FINISHED
      IF(IENT.EQ.0) GO TO 1000
C   EXCHANGE ENTERING AND LEAVING VARIABLES
C   NORMALIZE ROW SO A(JENT,LEAV)=1.0
      SAV=1.0/A(JENT,LEAV)
      B(LEAV)=B(LEAV)*SAV
      DO 300 I=1,M
  300 A(I,LEAV)=A(I,LEAV)*SAV
C   SUBTRACT ROW MULTIPLES SO COLUMN JENT IS VIRTUALLY ZERO
      DO 400 I=1,N
      IF(I.EQ.LEAV) GO TO 400
      B(I)=B(I)-B(LEAV)*A(JENT,I)
      FACT=A(JENT,I)
      DO 450 J=1,M
      IF(J.EQ.JENT ) GO TO 450
      A(J,I)=A(J,I)-A(J,LEAV)*FACT
  450 CONTINUE
  400 CONTINUE
C   CALCULATE NEW ENTRIES FOR COLUMN JENT
      DO 500 I=1,N
  500 A(JENT,I)=-A(JENT,I)*SAV
      A(JENT,LEAV)=SAV
C   UPDATE INDEX ARRAYS
      IROW(IENT)=LEAV
      IND=IVAR(LEAV)
      IROW(IND)=-JENT
      IVAR(LEAV)=IENT
      LAST=IND
  800 CONTINUE
C    OPTIONALLY PRINT OUT UPDATED A,B,IROW,IVAR ARRAYS HERE
       GO TO 10
```

```
 1000 CONTINUE
C   CALCULATE VALUES OF VARIABLES
      DO 1100 I=1,M
      X(I)=0.0
      IF(IROW(I+1) .LT.0) GO TO 1100
      J=IROW(I+1)
      X(I)=B(J)
 1100 CONTINUE
      RETURN
      END
```

REFERENCES

Drake, D. E., 1974, Suspended particulate matter in the New York Bight Apex, September–November 1973: NOAA Tech. Rept. ERL 318-MESA 1.

Harman, H. H., 1967, Modern factor analysis (2nd ed.): Univ. Chicago Press, Chicago, 474 p.

Hillier, F. S., and Lieberman, G. J., 1967, Introduction to operations research: Holden-Day, Inc., San Francisco, 639 p.

Imbrie, J., and Purdy, E. G., 1962, Classification of modern Behemian carbonate sediments: Am. Assoc. Petroleum Geologists Mem. 1, p. 252–272.

Klovan, J. E., 1966, The use of factor analysis in determining depositional environments from grain-size distributions: Jour. Sed. Pet., v. 36, no. 1, p. 115–125.

Klovan, J. E., and Imbrie, J., 1971, An algorithm and FORTRAN-IV program for large-scale Q-mode factor analysis and calculation of factor scores: Jour. Math. Geol., v. 3, no. 1, p. 61–76.

Klovan, J. E., and Miesch, A. T., 1976, Extended CABFAC and QMODEL computer programs for Q-mode factor analysis of compositional data: Computers and Geosciences, v. 1, no. 3, p. 161–178.

Miesch, A. T., 1976a, Q-mode factor analysis of compositional data: Computers and Geosciences, v. 1, no. 3, p. 147–159.

Miesch, A. T., 1976b, Q-mode factor analysis of geochemical and petrologic data matrices with constant row-sums: U.S. Geol. Survey Prof. Paper 574G.

Nelsen, T. A., 1977, WCC 6-13, NOAA Tech. Report, in press.

Pearson, K., 1901, On lines and planes of closest fit to systems of points in space: Phil. Mag., Ser. 6, v. 2, p. 559–572.

Rozett, R. W., and Peterson, E. M., Classification of compounds by the factor analysis of their mass spectra: Anal. Chem., v. 48, no. 6, p. 817–825.

Spencer, D. W., 1967, Factor analysis II: A description of the application of oblique solutions: Woods Hole Oceanographic Inst., Ref. No. 67–59, 37 p.

Yamamoto, S., 1976, Multivariate correlation analysis of suspended sediment characteristics: Jour. Math. Geol., v. 8, no. 1, p. 57–74.

Sedimentation in Submarine Canyons, Fans, and Trenches, ed. D.J. Stanley and G. Kelling, 33-41 (Dowden, Hutchinson and Ross, Stroudsburg, PA).

Chapter 3

Suspended Particulate Matter and Mud Deposition in Upper Hudson Submarine Canyon

DAVID E. DRAKE

U.S. Geological Survey
Menlo Park, California

PATRICK G. HATCHER

Atlantic Oceanographic and Meteorologic Laboratories
Miami, Florida

GEORGE H. KELLER

School of Oceanography
Oregon State University, Corvallis

ABSTRACT

Concentrations of suspended matter of 2,210 to 3,440 μg/liter were present near the bottom at depths of 200 m to 450 m in Hudson Canyon during March 1974. The suspended matter was mostly inorganic mineral grains and two samples contained significant amounts of coarse silt (10-20 percent) and very fine sand (5-10 percent). Suspended matter concentrations near the sea floor declined both shoreward and seaward from the head of the canyon; concentrations of about 600 μg/l were measured at 893 m in the canyon and values of 400-600 μg/l were present over the surrounding shelf.

Current measurements at 3 m above bottom in the canyon head (223 m) revealed reversing flows of tidal period with peak speeds of 25-35 cm/sec and a strong net downcanyon component which averaged about 8 cm/sec over a six-day period. The combined suspended matter and current velocity data indicate important resuspension of the fine-grained components of the canyon head sediments followed by transport to deeper water along the axis of the canyon.

A 5 m piston core recovered in the canyon axis at 430 m contained an apparently continuous record of silt and clay accumulation. Radiocarbon dates at three levels in the core suggest a mean sedimentation rate of about 80 cm/10^3 years over the past 6,300 years. If this single core is representative of the sedimentation regime in this part of Hudson Canyon, the implication is that much of the sediment resuspended in the head of the canyon (<300 m depths) is deposited before moving far downcanyon. Furthermore, the textural character of the core sediments implies that vigorous bottom scour has been infrequent over the past several thousand years except in the shallowest portions of the canyon. Sediment transport by turbidity currents of high velocity appears to be unimportant in this canyon at the present time.

INTRODUCTION

Recent observations in Hudson Canyon have indicated a large variability in suspended matter concentrations near the bottom (Keller et al. 1973). In order to investigate the suspended matter and bottom currents in the canyon, current meters were deployed and water samples were obtained during March 1974 aboard the NOAA ship *Researcher* (Figures 3-1 and 3-2). The following year a piston core was recovered from the axis of the canyon at a depth of 430 m. The results of this work provide an initial assessment of the recent sedimentary history and ongoing sedimentary processes in a large canyon that is at present relatively distant from major sources of terrigenous sediment. In addition, previous investigations of suspended matter concentrations in the vicinity of Hudson Canyon (Manheim et al. 1970; Meade et al. 1975; Biscaye and Olsen 1975) were performed during summer and fall seasons. As will be shown, the results of our late winter survey differ substantially from the previous findings.

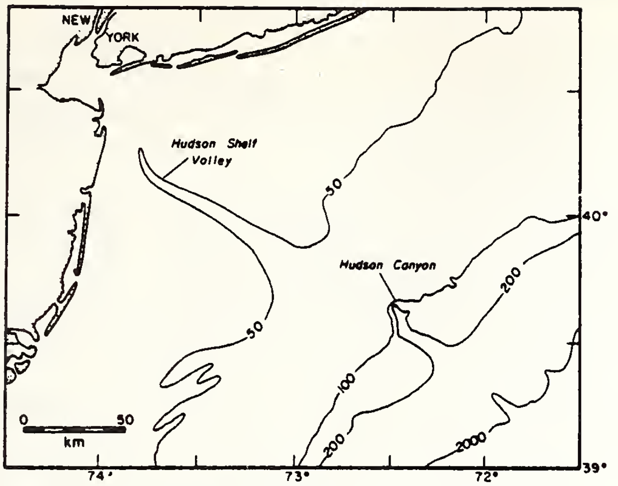
NEW
YORK
Hudson Shelf Valley
Hudson Canyon
50
200
50
100
200
2000
0
50
km
74°
73°
72°
40°
39°

Figure 3-1. Location map showing Hudson Shelf Valley and Hudson Canyon. Note: Generalized depth contours are given in meters.

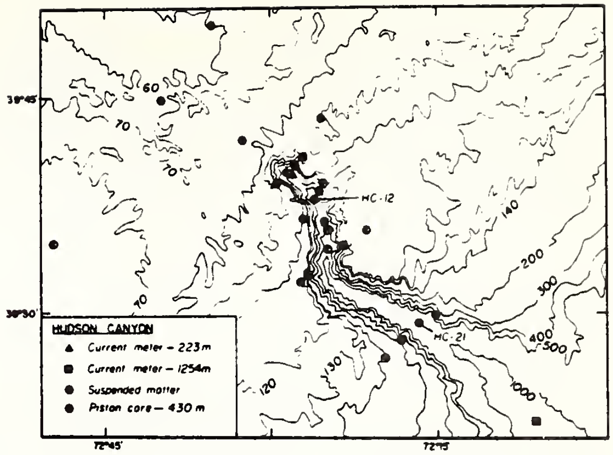
HUDSON CANYON
▲ Current meter – 223m
■ Current meter – 1254m
● Suspended matter
● Piston core – 430 m
HC-12
HC-21
60
70
70
70
120
130
140
200
300
400
500
1000
39°45'
39°30'
72°45'
72°15'

Figure 3-2. Bathymetric map of upper Hudson Canyon showing station locations and current meter sites.

INSTRUMENTS AND METHODS

F. P. Shepard and G. H. Keller deployed self-contained Savonius rotor current meters near the bottom (3 m and 30 m above bottom) at depths of 223 m, 514 m and 1,254 m in the axis of Hudson Canyon. Useful data were obtained from the sensors at 223 m and 1,254 m (see Figure 3-2). In the course of the present discussion important aspects of these current measurements as they relate to the suspended matter problem will be presented. The reader is directed to Chapter 2 for detailed discussion and interpretation of current meter data in this and other canyons.

Samples for suspended matter analysis were obtained at twenty three stations with a *General Oceanics*[a] Niskin rosette system mounted on a *Plessey* 9060 salinity-temperature-depth sensor. Samples within 5 m of the sea floor were collected with the aid of a pinger attached to the cable a known distance above the sampling package. Measured volumes of the water samples were vacuum filtered immediately aboard ship using preweighted 47 mm *Nuclepore* (0.4 μm pore size) polycarbonate membranes mounted in *Millipore* in-line filter holders. A minimum of 50 ml of filtered distilled water was used to free the entire surface of each filter of sea salts. The filters were then dried at 50° C for six hours and stored in self-sealing plastic petri dishes. At our shore laboratory the sample filters plus a series of control filters were placed in dessicators for several days and reweighed to a precision of ± 10 μg. None of our samples contained less than 300 μg of suspended matter and, consequently, analytical errors are considered negligible (<10 percent).

All surface water and near-bottom samples and a selected number of samples from intermediate depths were examined with a polarizing microscope and scanning electron microscope (SEM). Small sections of each filter were cut for the SEM study and the remaining filter was reweighed and set aside for combustion analysis. Point counts for two hundred particles were made at magnifications of 50x and 500x (using SEM photo-micrographs) to estimate the percentages of detrital and biogenic minerals and amorphous organic matter. Several counts on the same filter indicate a reproducibility of about ± 10 percent.

The remaining large portion of each filter was combusted for six hours at 550° C in tared platinum foil crucibles according to the method of Manheim et al. (1970). Fresh *Nuclepore* filters were combusted along with each batch

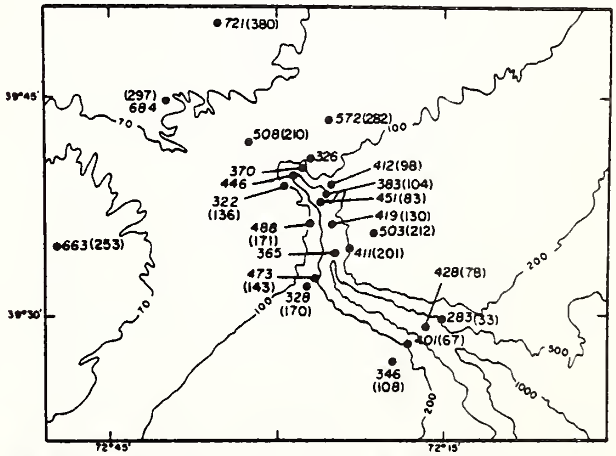
721(380)
(297)
684
572(282)
508(210)
326
370
446
322
(136)
412(98)
383(104)
451(83)
419(130)
503(212)
488
(171)
365
411(201)
663(253)
473
(143)
328
(170)
428(78)
283(33)
401(67)
346
(108)
70
70
100
100
200
200
500
1000
39°45'
39°30'
72°45'
72°15'

Figure 3-3. Concentrations of total suspended matter in the surface water, March 1974. Note: The noncombustible fractions are shown in parentheses. All values are in μg/1. The maximum and mean values are significantly above those measured by Manheim et al. (1970) and Meade et al. (1975).

---

[a] The use of brand names in this chapter is for identification purposes only and does not imply endorsement by the U.S. Geological Survey.

of sample filters and our results show that these filters have an average ash residue of 0.12 percent or about 1 μg/cm^2. This correction was applied to our samples. As should be noted, the ash residue of suspended matter is composed of both biological and inorganic particles. Estimates of the relative amounts of these components were obtained using microscope analyses.

RESULTS

Suspended Matter

Concentrations of total suspended matter (TSM) in the surface waters ranged from 295 to 721 μg/l (Figure 3-3). Values above 500 μg/l were confined to our shallowest shelf stations (<80 m depth). In general, the concentrations of combustible organic matter did not change significantly over our survey area, but the ash residue values show a general seaward decrease that accounts for the southeastward decline in TSM (see Figure 3-3).

Fine to coarse silt-sized aggregates of amorphous organic matter, biogenic hard parts, and terrigenous minerals were present in all surface water samples. Estimates of the concentrations (by number) of aggregates using SEM and standard microscope point counts suggest a slight decrease from about 1,500/liter to 1,100/liter between our shallowest and deepest water stations. However, this trend may not be significant in view of the limited accuracy of this analytical technique.

At all stations TSM decreased at intermediate levels in the water column and the percentages of combustible matter declined to values in the range of 22 to 46 (for the minimum TSM sample at each station). Minimum TSM values ranged from a high of 328 μg/l at our shallowest shelf station to a low of 84 μg/l at our deepest canyon station (Figure 3-4). Thus, the regional TSM concentration pattern tended to mirror that present at the surface.

Concentrations of suspended matter and percentages of the terrigenous mineral fraction increased significantly near the sea floor (see Figure 3-4 and Figure 3-5). TSM values in excess of 3,000 μg/l were present 5 m above bottom at three stations in the head of the canyon (see Figure 3-5), and significant, although less dramatic, increases occurred over the adjoining shelf. Ash percentages ranged between 66 and 82 at shelf stations shoaler than 200 m, and SEM examination shows that ~50-80 percent of this material was inorganic silt and

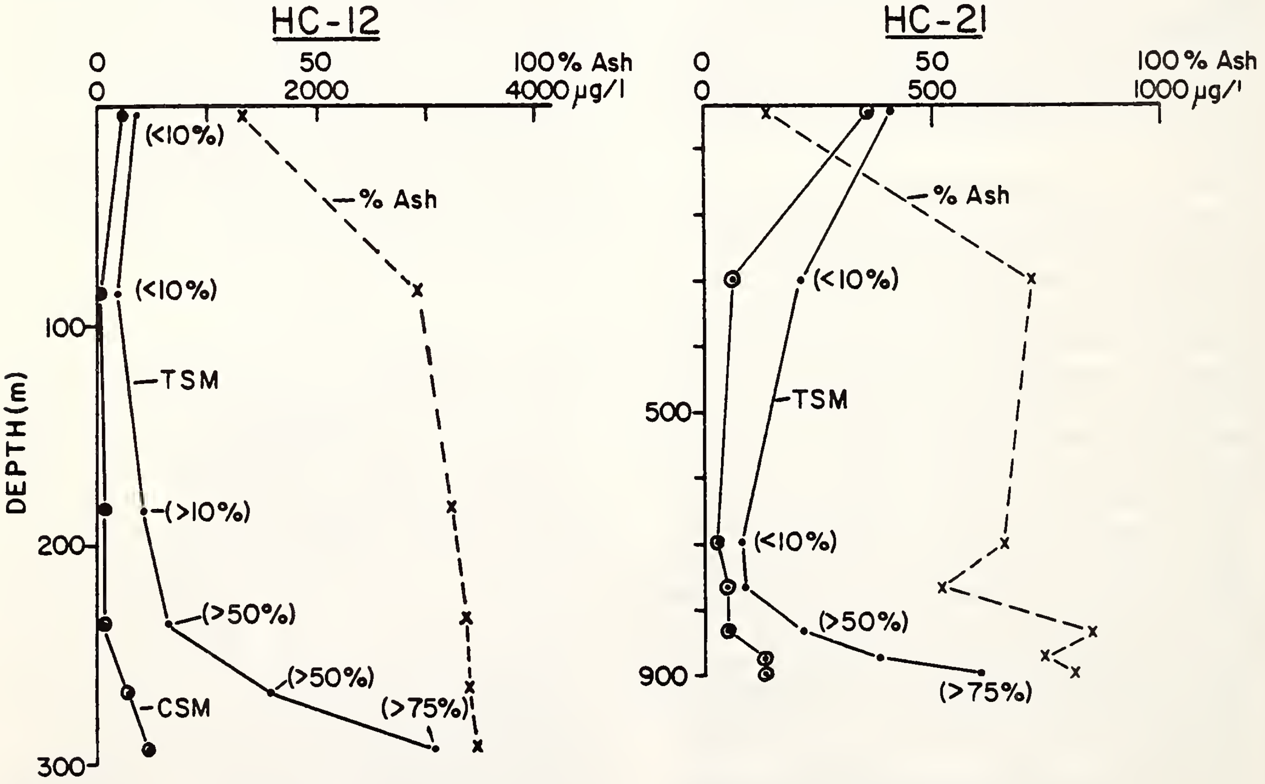

Figure 3-4. Suspended matter concentrations and compositions at 300 m and 900 m in the axis of Hudson Canyon (see Figure 3-2). Note: Percent ash and combustible suspended matter (CSM) were determined by combustion at 550° C. Estimates of amounts of inorganic detritus in TSM are shown in parentheses. Also note scale changes.

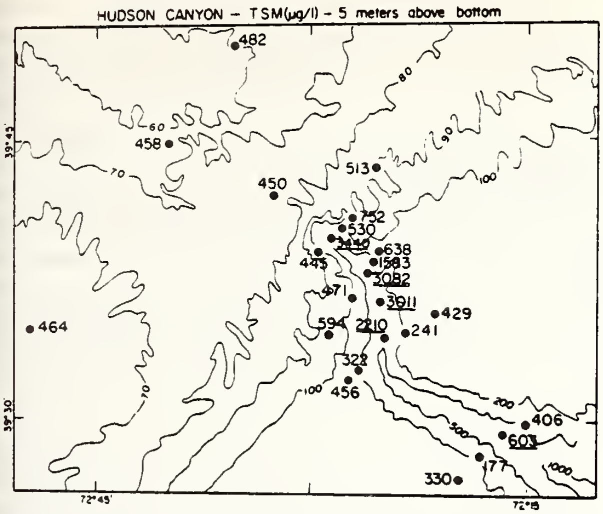

Figure 3-5. Total suspended matter in µg/l at 5 m above the sea floor. Note: Underlined values denote canyon axis samples. Depths are in meters.

clay. In contrast to the spatial gradients in TSM concentrations at the sea surface and intermediate levels in the water column (see Figure 3-3), the near-bottom values show little meaningful correlation with depth except within the canyon.

We occupied five stations in the axis of the canyon: four between the depths of 200 m and 450 m and one at 893 m. Extremely high TSM concentrations were present in the bottom 50 m of the water column in the head of the canyon (see Figure 3-4). The highest concentration of 3,400 µg/1 was present at our shallowest canyon station and TSM decreased gradually to 2,210 µg/1 at 450 m. We have no data between this station and our deepest station (893 m) where the near-bottom concentration had declined to 603 µg/1.

Examination of our samples using scanning electron microscopy reveals significant changes in the quantities of coarse-grained mineral particles in suspension along the axis of the canyon. Our two shallowest near-bottom samples (TSM>3,000 µg/1) contain from 7 to 14 percent (by number) very fine sand (62 to 125 µm), and 12 to 24 percent coarse silt particles (31 to 62 µm). In contrast, the near-bottom suspended matter at 400 m, 450 m, and 893 m lacked the very fine sand components (<1 percent) and the coarse silt fraction (>31 µm) had decreased to 18, 16, and, 7 percent, respectively. The presence of the rapidly settling sand grains several meters above the floor of the canyon at depths of 200 m and 300 m indicates a significant intensification of bottom currents capable of resuspending and transporting the canyon sediments. The fact that the TSM concentrations near the bottom over the canyon walls and the shelf were substantially lower than those present above the canyon floor provides additional evidence for localized resuspension.

Although the bottom current meter at 223 m in the canyon axis was ideally located to examine the resuspension process, the sensor failed seven days after deployment and two days prior to our water sampling. The recovered data show that several days before we sampled the suspended matter, the head of the canyon was swept by reversing flows of tidal period with peak speeds of 25-35 cm/sec (Figure 3-6). To our knowledge there are no comparable data on bottom currents in the canyon head for other time periods. Consequently, we do not know whether the current speeds that we measured are normal or unusually high. Bottom grab samples taken during our survey recovered silty, noncohesive fine to medium sands near the current meter site. Available information on bed scour suggests that currents of at least 25-35 cm/sec (at 3 m above bottom) would be required to initiate bed movement and fine sediment resuspension (Sternberg 1972; White 1970). Our data suggest that currents of the proper velocity range occurred in March, and in light of the presence of very fine sand several meters above bottom, the possibility exists that the actual currents were substantially greater when we collected our water samples.

A progressive vector diagram of the flow at 223 m demonstrates a high degree of asymmetry in the oscillating canyon floor currents (Figure 3-7). The net flow was decidedly down the canyon, and if taken at face value, an advection averaging 7 cm/sec occurred over a period of six days. If we assume that this characteristic of the currents had not changed when we sampled the canyon water, the net downcanyon transport of suspended matter would be approximately 20 kg/m² /day. Attempting a more accurate calculation is meaningless because we cannot determine the spatial gradients in the bottom currents or suspended matter concentration. Nevertheless, substantial amounts of sediment were clearly resuspended and

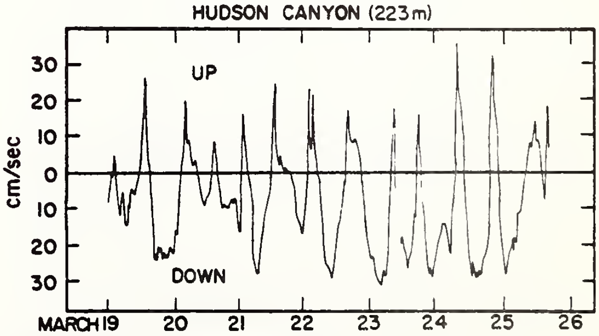

Figure 3-6. Current velocity 3 m above bottom at 223 m in upper Hudson Canyon. Note: Strong down- and upcanyon flows occurred for four days prior to sensor failure on March 26.

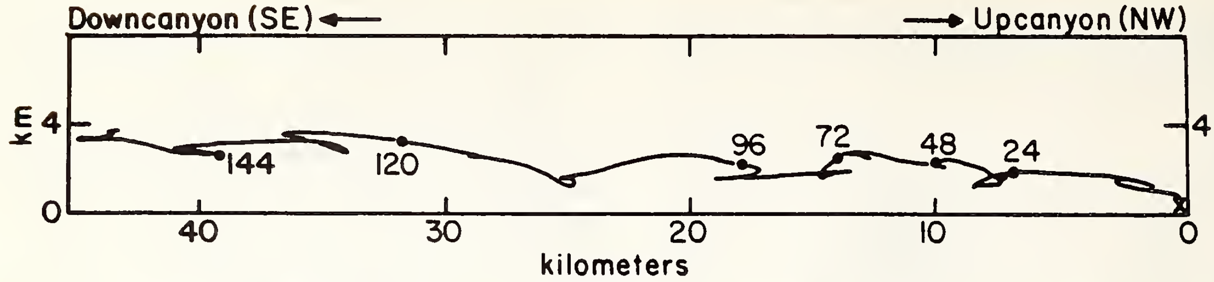

Figure 3-7. Progressive vector diagram based on data from 223 m, 3 m above bottom (see Figure 3-6). Note: Net flow averaged nearly 7 cm/sec downcanyon for almost seven days.

moved to deeper water by the canyon-controlled currents.

The gradual downcanyon decrease in TSM concentrations from 3,400 μg/l at 200 m to 603 μg/l at 893 m combined with the textural fining of the suspended terrigenous particles suggests that on the order of 80 percent of the sediment dropped from suspension within the upper Hudson Canyon.[b] Furthermore, these data demonstrate a significant reduction in the ability of the canyon currents below about 400 m to resuspend material or maintain particles in suspension.

We did not collect current meter data at deeper locations in Hudson Canyon during March 1974, but F. P. Shepard successfully measured the bottom currents at 1,254 m for twenty one days in April 1974 (see Chapter 2). Shepard's results show that peak velocities rarely exceeded 20 cm/sec, and net flow (Figure 3-8) was downcanyon (Shepard and Marshall 1976). As is noteworthy, the reversing currents at 1,254 m exhibit relatively long intervals during which speeds fall below 5 cm/sec in contrast to the abrupt current reversals typical of the canyon head. This aspect of the deeper currents would allow deposition of the more rapidly settling particles in the near-bottom water. Once deposited, subsequent current pulses of 20 cm/sec (3 m above bottom) probably would not achieve complete resuspension, and only the slowly settling components of the suspension would continue downcanyon.

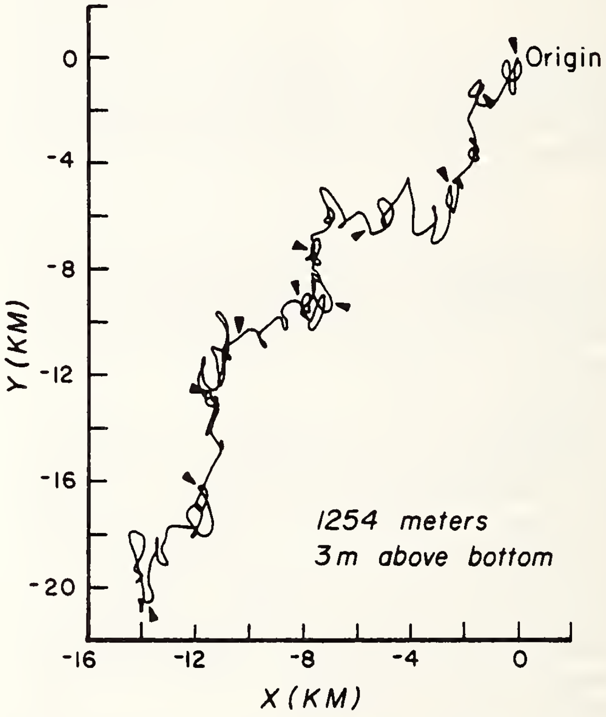

Figure 3-8. Progressive vector diagram for the current 3 m above bottom at 1,254 m in upper Hudson Canyon. Note: Arrows show twenty four-hour time marks beginning on April 11, 1974. The net drift was downcanyon (SE) at about 1-2 cm/sec. (Source: Data were kindly furnished by F.P. Shepard, Scripps Institution of Oceanography, and D.A. Cacchione, U.S. Geological Survey.)

Sedimentation Rates of Hudson Canyon Muds

The foregoing results along with earlier work reported by Keller et al. (1973) strongly suggest that sediments resuspended in the head of the canyon (<300 m) were transported seaward, but a significant portion of the material was deposited, beginning at canyon axis depths of 400-450 m. Keller and his associates made a unique set of direct observations and measurements in upper Hudson Canyon by using the submersible *Alvin*. Dives in the canyon axis at depths less than ~300 m revealed extensive exposures of bare rock along the canyon walls, evidence of headward erosion and rock sliding, and canyon floor sediments composed of fine to coarse terrigenous sands containing minor amounts of silt and clay. Below a canyon axis depth of about 400 m the character of the surficial bottom sediments changes dramatically to silty clays and clayey silts rich in organic

[b] The term *upper* Hudson Canyon is used herein to denote that portion of the canyon which is <1,000 m deep, and *canyon head* is arbitrarily defined to mean that part of the canyon floor less than 300 m deep.

matter. The shear strength of these muds proved to be exceptionally low, and visual appearances indicated that they would be especially susceptible to bottom current erosion. Surprisingly, during one dive, the bottom current reached 27 cm/sec with no discernible effect on the mud sediment. The sediments may have developed an *in situ* cohesiveness that was not accurately depicted by shear strength measurements. Alternatively, the difference in effective boundary shear stress produced by equivalent currents over the roughened canyon head sands and the relatively smooth muds may explain the lack of erosion.

In order to examine the time-dependent aspects of sedimentation in this zone of mud deposition, we collected a 5 m piston core at 430 m. Care was taken to insure that the ship was above the axis of the canyon and that this position was maintained during the cǒring operation. On the basis of our observations during the field sampling, we suspected that some portion of the surface sediment, which Keller et al. (1973) had described as "fluffy," had been lost. However, subsequent inspection of the core showed loose, highly organic, watery sediments from the surface to about 30 cm and a radiocarbon age of 665 ± 105 at 50 cm indicated a minimal loss of surface sediment (probably <20 cm).

Figure 3-9 presents a visual description of the core along with the results of radiocarbon dating of 5 cm sections centered at 50 cm, 250 cm, and 505 cm (the bottom of the core). Because the core underwent several other analyses that required relatively large amounts of sediment, using total carbon for the age dating was necessary.

We have not detected any lithologic changes in the core that might reflect major variations in sediment accumulation, slump-in, or loss of section. The core is predominantly composed of intensely bioturbated, olive gray and dark gray clayey silt with scattered 1 to 2 cm mollusc shells. Thin layers of silt and very fine sand are present at 186 cm, 423 cm, and 431 cm. Poorly developed laminations of silt and clay are present at 324 cm to 330 cm, and these are the only sedimentary structures in the core, as confirmed by radiographs. Although the activities of benthic burrowers undoubtedly destroyed some other laminated sections and thin sand beds, the overall textural uniformity and fineness of the sediment are indicative of persistent low-energy depositional conditions. However, silt and clay deposition was interrupted on at least three occasions by events of higher energy that resulted in deposition of thin (<1 cm) fine sand layers. The fact that medium- and coarse-grained terrigenous sands are not important components of the core strongly indicates that transport by high-velocity turbidity currents has been negligible in the Hudson Canyon over the time period represented by our core (~6,300 years). Nevertheless, our suspended matter samples at 400 m and 450 m contained substantial amounts of medium and coarse silt particles that were probably being advected down-canyon. We suspect that silt laminations (with a minor amount of very fine sand) would be common in our piston core if it were not for the intense mixing activities of burrowing organisms.

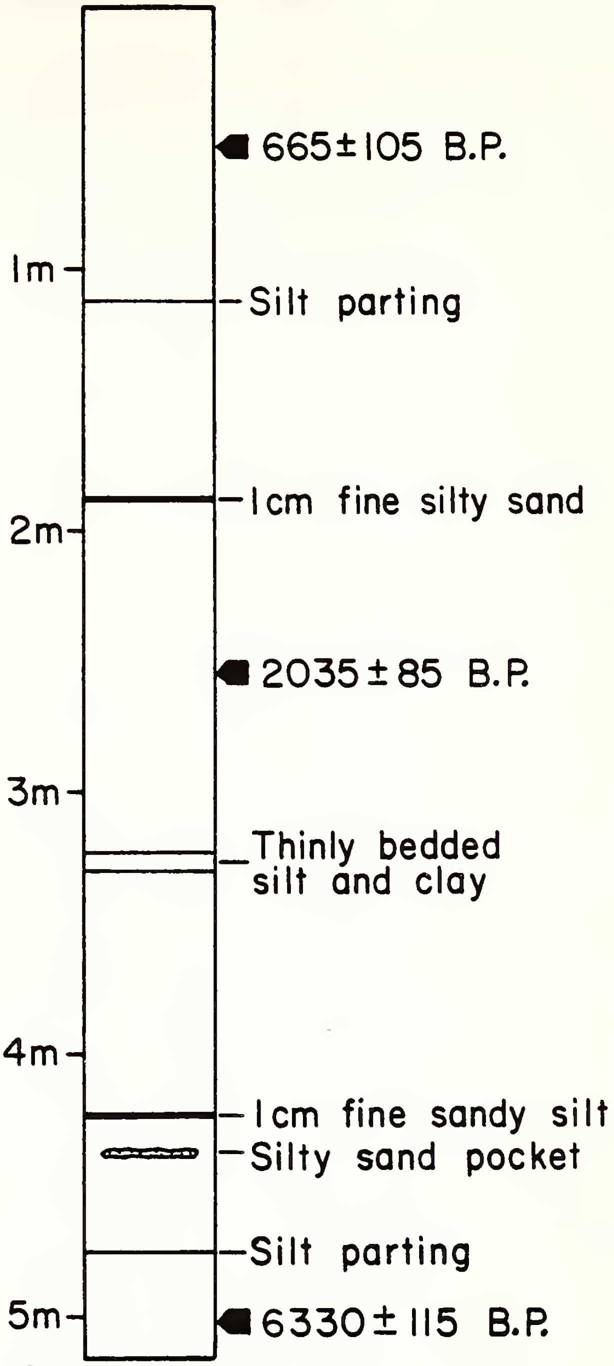

Figure 3-9. Lithology of piston core HM-3 recovered at 430 m in the axis of Hudson Canyon. Note: Intervals at 50 cm, 250 cm, and 505 cm were dated by using radiocarbon analysis of total organic carbon.

The radiocarbon dates show that an environment of silt and clay deposition has persisted just seaward of the canyon head for at least 6,300 years. The radiocarbon ages also suggest an approximately twofold increase in the sedimentation rate from 2,000 B.P. to the present (see Figure 3-9). Analyses are underway to determine whether this apparent change is real or simply a function of compaction. In any case, the average rate of sedimentation over the past 6,300 years has been on the order of 70-80 cm/10^3 years or five to ten times faster than rates measured on the nearby continental slope and rise (Turekian 1968; Doyle et al. 1976). The distribution of canyon axis sediments observed by Keller et al. (1973) suggests that our core is probably representative of the shallow end of a lens of mud extending from depths of about 400 m to at least 1,000 m.

DISCUSSION

A comparison of the basic characteristics of the suspended matter during our March survey with data presented by Manheim et al. (1970), Meade et al. (1975), and Biscaye and Olsen (1975) for the outer shelf and upper Hudson Canyon reveals substantial differences in both the surface and near bottom waters (Table 3-1). The sets of data of Manheim et al. (1970) and Meade et al. (1975) are based on samples collected during fair weather conditions in early and late summer. Manheim and his colleagues restricted their sampling to the surface waters where they found <125 μg/1 of TSM; combustion analyses showed that this material contained 80-90 percent amorphous organic matter. Meade et al. (1975) occupied four stations in Hudson Canyon and three stations within 100 km along the shelf break and upper slope. Their data for surface water TSM and an additional set of data collected in July 1975 by Biscaye and Olsen (1975) are in agreement with the results of Manheim et al. (1970).

In contrast, TSM concentrations in the surface waters during our survey ranged from 285 to 721 μg/1. The ash weight data (see Table 3-1) suggest the TSM difference was caused by a significant increase in noncombustible components in March 1974. We believe that this additional material, largely composed of grain aggregates, was resuspended from the bottom over the shelf by a storm that moved through the area on March 21 and produced moderately heavy seas (2-3 m) from March 21 to March 28 when conditions calmed sufficiently to allow water sampling. Relatively calm seas prevailed for about thirty six hours (March 28-30) before a second storm front forced curtailment of deck operations. The near-bottom currents that are associated with such winter storms in the Middle Atlantic Bight can exceed 50 cm/sec at depths of 50-100 m (Beardsley and Butman 1974), and Butman (personal communication, 1976) has obtained bottom photographs that provide direct evidence of shelf sediment resuspension by winter storm currents. The frequent storms that are a well-known characteristic of the North Atlantic from November through March must account for a significant proportion of the sediment transport on the outer shelf.

As expected, TSM and ash residue concentrations within 5 m of the shelf bottom exceeded previous measurements substantially (see Table 3-1). The most comparable sets of data (in terms of station density) were reported by Biscaye and Olsen (1975). These workers found 100-400 μg/1 within 10 m of the bottom over the shelf adjacent to Hudson Canyon during October 1974 and July 1975. Our "storm-influenced" TSM concentrations exceed this range by 50 to 100 percent.

Suspended matter samples have been collected in Hudson Canyon by Meade et al. (1975), Biscaye and Olsen (1975), and indirectly by Amos et al. (in press) by using a moored nephelometer and current meter at 803 m. Meade et al. (1975) reported TSM concentrations of 190 and 260 μg/1 at 320 m and 345 m in the canyon (within 5 m of bottom), and Biscaye and Olsen (1975) have shown that a lens of turbid water typically occupies the upper Hudson Canyon. However, the values observed by the latter researchers (see Table 3-1) are well below those present from the head of the canyon (>3,000 μg/1) to a depth of 900 m (603 μg/1) in March 1974. In fact, to our knowledge concentrations >2,000 μg/1 have not been measured previously seaward of the inner shelf (<40 km from shore) in the Middle Atlantic Bight. The results of the present study demonstrate that this situation is mainly a product of how and when we sample the shelf water column. Sediment entrainment and transport are highly nonlinear functions of the flow regime, and as is important to realize, fairweather data are likely to give a distorted picture of these processes.

Clearly, large variations occur in the amounts of material in suspension near the floor of upper Hudson Canyon. These changes probably reflect equally important variations in the velocity of the canyon currents and their ability to redistribute sediments. Unfortunately, while we believe that the storms that influenced the surrounding shelf also to some degree intensified the reversing currents in the head of the canyon, we have no current meter data from other time periods to form a basis for comparison. The present lack of long-term (one month or more) bottom current and suspended matter measurements at various positions in submarine canyons precludes an adequate understanding of the timing and intensities of sediment transport events.

On the other hand, the longer-term aspects of the sedimentary regime in upper Hudson Canyon are indicated by the distribution and accumulation rates of the postglacial sediments. The apparently abrupt change in sediment

Table 3-1. *Suspended Matter: Hudson Canyon Area*

	Survey		*Surface*	*Near Bottom*	
Component	*Time*	*Source*	*Water*	*Shelf*	*Canyon*
TSM[a] (μg/l)	6/65	1	<125		
	9/69	2	50-100	200-920[c]	190-260
	10/74	3		200-400	400-600
	7/75	3	<100	100-200	200-400
	3/74	4	285-721	241-752	603-3440
ASH (μg/l)	6/65	1	<20		
	9/69	2	<10	50-200	130-250
	3/74	4	33-380	210-680	520-3110
CSM[b] (%)	6/65	1	80-90		
	6/69	2	80-95	30-40	4-30
	3/74	4	50-90	18-34	12-23

[a] TSM = total suspended matter.

[b] CSM = combustible suspended matter.

[c] The value of 920 μg/l was present 100 km NW of Hudson Canyon near the location of relict clayey silt bottom sediments. The bulk of the data (Meade et al. 1975) indicated a mean concentration of 300-400 μg/l near Hudson Canyon.

Sources: 1, Manheim et al. (1970); 2, Meade et al. (1975); 3, Biscaye and Olsen (1975); and 4, This Study.

texture from relatively clean coarse sands in the head of the canyon to clayey silts at 350 m to 450 m coupled with the evidence from our piston core that suggests the minor role of high-energy turbidity currents at 430 m, leads to two conclusions. First, high-velocity turbidity currents have not been a significant transport agent for the past several thousand years; and secondly, the energy associated with canyon currents that oscillate in response to tides and internal waves (Shepard et al. 1974) seems to be stratified with respect to depth. The accumulation of mud in Hudson Canyon begins at approximately the same depth as the base of the permanent pycnocline: 400 m to 500 m (Drake, unpublished data; Gordon et al. 1976). Although our interpretation must be regarded as speculative without longer current meter records at many depths in the canyon, a possibility is that the flow intensification caused by winter storms may extend to the pycnocline but diminish rather rapidly below that level (400 m to 500 m). Simultaneous current measurements at 200-300 m and 500-600 m during the winter period would resolve this question.

The current meter record at 223 m reveals a strong net flow downcanyon. This type of current, superimposed on the up- and downcanyon oscillations, has been observed in many canyons (Shepard et al. 1974; Shepard and Marshall 1973) and remains one of the most important unexplained aspects of the flow regime. Recently, Inman et al. (1976) summarized many years of observations in the head of the La Jolla-Scripps Canyon systems. Their analysis suggests that periods of canyon current intensification are correlated to periods of intensified shelf water circulation during storms. They conclude that resuspension of sediment occurs in and around the head of the canyon as the velocities of the oscillating currents increase. If this process of flow intensification continues, enough sediment is placed in suspension to generate a turbidity current that can overcome the density stratification of the water column and produce strong downcanyon flow of up to several meters per second.

Important components in this model are wave and wind setup and topographically controlled circulations caused by edge waves. All of these factors diminish in importance as depth and distance from shore increase. Consequently, in the case of Hudson Canyon, the storm-related currents may be sufficient to stir the sediments in the head of the canyon, but incapable of producing the suspended sediment concentrations required for high-velocity, through-going turbidity flows.

Although this model appears to be compatible with the data we have presented, there are complications. For example, Cacchione et al. (Chapter 4) report a three-day observation of bottom currents in lower Hudson Canyon (~3,400 m) that shows essentially unidirectional downcanyon advection; visual observation from *Alvin* showed no unusual concentrations of suspended matter in the water column. As is quite apparent, the canyon current system is too complex to be properly understood on the basis of bits of data from different depths and different times.

While the exact cause of downcanyon near-bottom flow is not understood, there can be no doubt that this feature of the current system produces an important flux of sediment along the canyon axis. In particular, the distribution of organic carbon in surface sediments on the continental slope near Hudson Canyon (Figure 3-10) demonstrates the importance of the canyon as a supplier of organic matter to the deep sea (see Chapter 4).

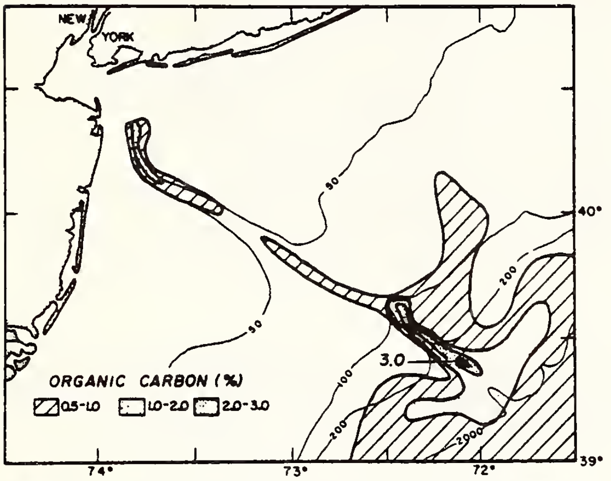

Figure 3-10. Organic carbon content of surface sediments in upper Hudson Canyon and on adjacent shelf and slope. Note: Depth contours are given in meters.

In summary, our results indicate that Hudson Canyon is both a sink and a transport conduit for sediment introduced to the head of the canyon. The fate of the suspended matter in the canyon appears to be a function of particle settling rates and depth stratification of current energy; rapidly settling particles (sand, silt and aggregates of clay and organic matter) are largely retained in the upper canyon (<1,000 m), whereas the more slowly settling particulate matter remains in suspension and is carried further through the system. Storm intensification of the normal reversing canyon currents may be an especially important factor in the transport regime. Finally, we believe that substantial progress in the study of present-day mechanisms of sediment transport in canyons will only be achieved when the proper long-term observations of currents and suspended matter concentrations become available.

ACKNOWLEDGMENTS

The authors express appreciation to F. P. Shepard, Scripps Institution of Oceanography, for making copies of his current meter results available; to Gary G. Sullivan, Scripps Institution of Oceanography, for help in the field; and to Otis Finley and Helen Gibbons for laboratory work and preparation of illustrations. The authors also thank Pierre Biscaye and Curtis Olsen, Lamont-Doherty Geological Observatory, for helpful discussions of their research in the Middle Atlantic Bight.

This research was supported by the NOAA COMSED project. The senior author participated in this investigation while he was supported by a NRC postdoctoral grant at the Atlantic Oceanographic and Meteorological Laboratories, NOAA, Miami, Florida.

REFERENCES

Amos, A.F., Baker, T., and Daubin, S., Jr. Near bottom currents and sediment transport in Hudson Canyon. *J. Geophys. Res.* (in press)

Beardsley, R.C., and Butman, B.,1974. Circulation on the New England continental shelf: Response to strong winter storms. *Geophys. Res. Lett.*, 1: 181-84.

Biscaye, P.E., and Olsen, C.R., 1975. Suspended particulate concentrations and compositions in the New York Bight. *Proc. Special Symposium on New York Bight.* Amer. Museum Nat. History, New York, Nov. 1975.

Doyle, L.J., Woo, C.C., and Pilkey, O.H., 1976. Sediment flux through intercanyon slope areas: U.S. Atlantic continental margin (Abst.) *Geol. Soc. Am. Prog.*, 8:843.

Gordon, A.L., Amos, A.F., and Gerard, R.D., 1976. New York Bight water stratification–October 1974, In: M.G. Gross (ed.), *Middle Atlantic Continental Shelf and the New York Bight.* Amer. Soc. Limn. Oceanogr., Lawrence, Kans., pp. 58-68.

Inman, D.L., Nordstrom, C.E., and Flick, R.E., 1976. Currents in submarine canyons: An air-sea-land interaction. *Ann. Rev. Fluid Mechanics*, 8: 275-310.

Keller, G.H., Lambert, D., Rowe, G. and Staresinic, N., 1973. Bottom currents in the Hudson Canyon. *Science*, 180:181-83.

Manheim, F.T., Meade, R.H. and Bond, G.C., 1970. Suspended matter in surface waters of the Atlantic Continental Margin from Cape Cod to the Florida Keys. *Science*, 167: 371-76.

Meade, R.H., Sachs, P.L., Manheim, F.T., Hathaway, J.C., and Spencer, D.W., 1975. Sources of suspended matter in waters of the Middle Atlantic Bight. *J. Sed. Petrol.*, 45: 171-88.

Shepard, F.P., and Marshall, N.F., 1973. Currents along floors of submarine canyons. *Amer. Assoc. Pet. Geol. Bull.*, 57: 244-64.

_____, and Marshall, N.F., 1976. Currents in submarine canyons and their relation to deep-sea fans (Abst.). *Amer. Assoc. Pet. Geol. Bull.*, 60: 721-22.

_____, Marshall, N.F., and McLaughlin, P.A., 1974. Currents in submarine canyons. *Deep-Sea Res.*, 21: 691-706.

Sternberg, R.W., 1972. Predicting initial motion and bedload transport of sediment particles in the shallow marine environment, In: D.J.P. Swift, D.B. Duane, and O.H. Pilkey (eds.), *Shelf Sediment Transport: Process and Pattern.* Dowden, Hutchinson & Ross, Stroudsburg, Pa., pp. 61-82.

Turekian, K.K., 1968. *Oceans.* Prentice-Hall, Englewood Cliffs, N.J., 120 pp.

White, S.J., 1970. Plane bed thresholds of fine grained sediments, *Nature*, 228: 152-53.

Offshore Technology Conference, 10th Annual OTC, Houston, TX. OTC Proceedings 3168, 1049-1057.

PORE PRESSURE MEASUREMENTS IN UNDERCONSOLIDATED SEDIMENTS

by Wayne A. Dunlap and William R. Bryant, Texas A & M University,
Richard Bennett, NOAA-AOML, and Adrian F. Richards, Lehigh University

1978, Offshore Technology Conference

This paper was presented at the 10th Annual OTC in Houston, Tex., May 8-11, 1978.

ABSTRACT

Pore pressures in the sediment were measured at two locations in the East Bay area of the Mississippi delta. These measurements showed the sediment to be highly under-consolidated with the effective stress approaching zero even at significant depths below the mudline. During storms the pore pressures exhibited cyclic response to the wave-induced bottom pressures. In at least two instances the pore pressures increased significantly during storms, which is probably indicative of major sub-bottom movements.

Several different piezometers systems were utilized to make the pore pressure measurements. Each system is described in detail and the advantages and shortcomings of the systems with respect to measurements of pore pressures in the marine environment are presented.

Analysis of the data leads to the conclusion that pore gas, rather than pore water, pressure was measured in most instances even though in one set of experiments high air entry stones were utilized to exclude gas from the measuring system.

Introduction

The two projects known as SEASWAB I and SEASWAB II were aimed at studying sediment behavior in the Mississippi delta under the action of storm waves. Details of the projects have been discussed elsewhere[1,2] and will not be repeated here. During both SEASWAB projects, pore pressures in the sediment were measured. These measurements were made to help determine the degree of consolidation in the sediments, and to detect gross subsurface movements. The rationale for the latter was that any significant subsurface slides or sediment collapse would be accompanied by a marked change in pore pressures. Further, it was anticipated that the pore pressures would exhibit a cyclic response to the wave-induced bottom pressures which have been hypothesized as a cause for sub-bottom movements in soft sediments[3,4].

The primary purpose of this paper is to describe the pore pressure measuring systems that have been used to accomplish these functions, to discuss the suitability of the various systems, and to present a preliminary analysis of the pore pressure results. Detailed analysis of the pore pressure data is still underway.

Seaswab I

SEASWAB I was initiated in September 1975 when several sensors were implanted in South Pass Block 28 in East Bay. Among the sensors installed were an accelerometer to measure mudline motions, a wave staff, and a bottom pressure transducer. However, the two systems of primary interest to this paper were probes for measuring pore pressures which were developed at Lehigh University and at the Atlantic Oceanographic and Marine Laboratory of NOAA in Miami, Florida.

Devices used to measure pore pressures in soils are termed piezometers. They may range from a simple open stand pipe with a well point at the tip to the more sophisticated closed system utilizing an electronic pressure transducer. Closed system piezometers can be remotely read and if a "hard" system is utilized the response times to changes in pore pressures are very rapid. All of the piezometers described in this paper were of the closed system type and they utilized small displacement electronic pressure transducers to obtain a hard or small volume change system. Pressure transducers can be obtained with extremely high sensitivities or with high pressure ranges, but not with both capabilities. Thus, if it is necessary to measure small variations in pore pressure when the ambient pressure is high, it is best to utilize a differential type of piezometer device such as described by Richards et al.[5]. Such a device for pore pressure measurements might have the hydrostatic pressure acting on one side of the pressure sensing membrane and the pore water pressure acting on the other side. The pressure transducer would thus be directly measuring the

---

References and illustrations at end of paper excess (over hydrostatic) pore pressure with great accuracy regardless of the magnitude of the total pore water pressure. The only disadvantage of this approach is that it is not possible to distinguish a change in pore pressure from a change in hydrostatic pressure. In fact if the bottom pressures from waves produce simultaneous and equal changes in pore pressures, the two pressure changes will cancel each other and the differential piezometer will indicate no change from the ambient excess pore pressure.

The alternative approach, i.e., the use of an absolute pressure transducer which measures total pore water pressure, can result in reduced accuracy for the reason alluded to earlier, i.e., the pressure sensing element must be so rigid to resist the total pressure that it will not adequately respond to small pore pressure fluctuations. Amplification of the transducer signal will not alleviate the problem because this also increases the electronic "noise" of the system which can mask small variations in pore pressure. If absolute measurements are made, it is helpful to have simultaneous measurements of the hydrostatic pressure at the same depth to provide a reference for calculation of excess pore pressures.

Lehigh Piezometer

The Lehigh piezometer installed during SEASWAB I was a differential type piezometer[6]. The sensing elements were interconnected fluid-filled bourdon tubes connected to vibrating wire strain gages. Pore pressure was transferred to the sensing element through a cylindrical coarse porous stone located at a depth of 21 feet below the mudline (Fig. 1). The signal was transmitted through a 7-conductor armored cable along the sea floor to a two-channel strip chart recorder located on a production platform approximately 500 ft from the piezometer. The piezometer was constructed from standard drill rod, it was rugged, and it was easily deployed owing to its relatively light weight. Differential pore pressures up to psi could be measured. A distinct advantage of the vibrating wire strain gages used in this piezometer is that they have a large output signal which allows the signal to be transmitted significant distances through a conductor wire with little signal attenuation.

NOAA Piezometer

The NOAA device (Fig. 2) was an absolute type piezometer which measured total pore pressures at two depths below the mudline, 28 and 50 feet[7]. Hydrostatic pressures were also measured at two depths (5 and 50 feet) to serve as a reference for the calculation of excess pore pressures, and as an indication of bottom pressures resulting from storm waves. Variable reluctance type pressure transducers were utilized as the pressure sensors; the pore pressures were transferred to the transducers through coarse porous stones which were inset into the piezometer pipe and ground to the pipe radius. The transducers were mounted inside oil-filled capsules spaced in the probe and connected to the pressure ports with short pieces of metal tubing. The signals from the transducers were transmitted through armored cable to signal conditioners and filtering systems before being recorded on a strip chart recorder. The output signal generated by variable reluctance transducers is subject to degeneration by electronic noise when transmitted over long lengths of cable. This can be largely overcome by use of commercially available downhole amplifiers. However, amplifiers were not required for this application. The pressure transducers used in this piezometer had a range of 100 psi with a reproducibility of ± 0.5 psi.

The piezometer was constructed of 4 inch O.D. thin wall pipe.

Installation and Recovery

The piezometers were implanted from the Texas A&M University research vessel GYRE on September 18 (Lehigh) and September 19 (NOAA), 1975. They were spaced about 20 feet apart in a water depth of 62 feet. The procedure for installing both piezometers was quite simple. A weight stand was constructed near the top of each piezometer (Figs. 1 and 2) and the amount of weight calculated to force each piezometer to the desired penetration below the mudline was added to the weight stand. (The calculation of the correct weight was greatly facilitated by a test at the site prior to installation using a weighted piece of pipe.) Each piezometer with attached weights was lowered by crane to the desired penetration below the mudline. A diver then removed a pin which separated the weight stand from the piezometer and the weight stand was returned to the surface. A short time after implantation, the transducers were disconnected while the cables were spooled along the bottom and connected to the recording equipment on the platform.

After six months of continuous service, the piezometers were removed using the crane aboard a Bo-Truc work boat. The 4-inch diameter NOAA piezometer exhibited "set-up" and nearly one-half hour of continuous tension with the crane was required to break it loose from the sediment. Diver observations indicated both piezometers had not moved from their original implanted depths.

Transducers on both piezometers were recalibrated after recovery. One of the two circuitry channels in the vibrating wire piezometer malfunctioned shortly after installation, but the calibration of the other circuit was essentially the same after recovery as before installation, indicating a stable system throughout the installation.

Both piezometers, constructed of mild steel with some stainless steel components, were in excellent shape upon removal, showing no signs of corrosion or deterioration of piezometer components or cables. The NOAA Piezometer also contained some painted aluminum parts, and these showed no signs of corrosion.

Results

The measurements from the two piezometers have been discussed elsewhere in detail[6,7,8,9] and are summarized herein.

After inserting a piezometer a "stress adjustment time lag" is observed[10] while the pore pressures around the piezometer readjust to the ambient following sediment disturbance. Both piezometers clearly displayed this phenomenon (Figs. 3 and 4), which was manifested as a dissipation of pore pressures. Shortly after the piezometers were installed, the effects of Hurricane Eloise were felt at the site. This event affected the pore pressure dissipation and hampered the determination of the initial excess pore pressures. Nevertheless, it does appear that the Lehigh piezometer essentially reached an equilibrium excess pore pressure of 4.6 psi. This is not quite as clear for the larger diameter NOAA piezometer, but it does appear that pore pressures at the 27 foot depth were essentially equilibrated at 4.5 psi. At the 50 foot depth, the pore pressures may have still been dissipating when Eloise struck; for purposes of discussion, the initial pore pressure is taken as 9.5 psi.

These initial pore pressures are plotted in Fig. 5. Also plotted in the figure is a line representing the effective overburden pressure, $\bar{p}$, which is based on unit weights obtained from samples in an adjacent geotechnical boring. The calculated effective overburden pressure is an artificial pressure in this case which assumes zero excess pore pressure. The difference between the calculated overburden pressure and the measured pore pressures represents the actual effective overburden pressure. For the SEASWAB I site, Fig. 5 shows the actual effective pressure to be zero or even negative.

It is known that sediments in this area of the Mississippi delta contain methane gas[11] and many of the cores removed during the geotechnical boring were observed to expand when the in situ pressure was released. To determine what effect this might have on the measured unit weights and the subsequent calculation of effective overburden pressures, a simple test was performed in which samples were sealed in their sample liners with caps of thin latex rubber and subjected to pressure. The change in sample volume was measured as the pressure was increased, and from this the change in unit weight with pressure was calculated. Using these corrected unit weights, a new effective overburden pressure was calculated which is shown as a dashed line in Fig. 5. Even with this correction, the effective stress is still essentially zero before Hurricane Eloise affected the site.

Eloise produced significant wave heights estimated at 5 feet in the vicinity of the piezometers. Deformations at the mudline of inches were measured. During the storm, the Lehigh piezometer measured maximum cyclic variations in pore pressure of ± 0.75 psi about the pre-storm values. After the storm effects had subsided, the pore pressures remained at approximately 4.6 psi, the pre-storm value.

The NOAA piezometer showed a total variation in pore pressures of 2.0 psi during Eloise at both the 27 and 50 foot levels. The mean pore pressure at the 50 foot level continued to decline during the hurricane. For a period of about six days after the hurricane, the excess pore pressures at both levels increased. This was followed by a gradual decline of the pore pressures at the 50 foot level while those at the 27 foot level remained essentially constant for several days and then started increasing slightly. This resulted in a crossover of the excess pore pressures approximately 15 days after installation which is still unexplained.

To summarize these measurements, both piezometers showed pore pressure variations during the period of intense storm activity. At the level of 21 feet below the mudline, the post-storm pore pressures returned to the original values and remained relatively static, whereas at the 27 and 50 foot depths the pore pressures continued to change in a rather erratic fashion for some time after the storm. The initial pore pressures seemed much too high for the East Bay area which, as an interdistributary bay, has much lower sedimentation rates than the delta front.

Since the sediments in the area are gassy, the question arose as to whether the pore gas rather than the pore water pressure was actually being measured. Theoretically, the pressure in the gas, if it exists as occluded bubbles, should be higher than the surrounding water pressure. The porous stones used in both piezometers were too coarse to exclude gas from the measurement system, and it is very likely that pore gas pressures were being measured. If this were the case then a revised effective stress law should be used. Furthermore, gas in the measuring system could have an effect on dynamic pore pressure changes measured during storms.

One other aspect of SEASWAB I which has not been measured previously was the difficulty in maintaining the strip chart recorders used in conjunction with the piezometers. Much data were lost or rendered unuseable when recorders broke, or when pens clogged, or when recorders were running at too slow a chart speed at a time when dynamic data were desired.

SEASWAB II

This experiment was a general repeat of SEASWAB I but in shallower water (approximately 42 feet) where the bottom pressures from waves would be greater and thereby induce larger sediment motions. The site was again in East Bay approximately 6,000 feet northeast of the SEASWAB I location.

The problems encountered during SEASWAB I with loss of data during crucial periods, and the occasional poor resolution of data, were all but eliminated by use of a sophisticated data acquisition system furnished by Sandia Laboratories[13]. This system included a long-playing analog tape recorder located on a production platform near the site, and a telemetry system which allowed constant remote monitoring at Texas A&M University of all instrumentation at the site.

The majority of the instrumentation was located in a bottom "deformational feature" as determined from side scan sonar records. It is currently believed that these deformational features will continue their movement, although there is no guarantee of this. The major interest in pore pressures was basically the same as in SEASWAB I, but there was an intense effort to increase the number of sensors, particularly at depth, and also to separately measure pore water and pore gas pressures. Piezometers were supplied by Lehigh University, NOAA, and Texas A&M University (in conjunction with the U.S. Geological Survey). Two piezometers (Lehigh and TAMU-USGS) were installed within 20 feet of each other in the approximate center of the deformational feature, and the NOAA piezometer was installed in undisturbed (?) sediment outside of the deformational feature approximately 200 feet from the Lehigh and TAMU-USGS piezometers. All three piezometers contained high air entry (bubbling pressure) ceramic stones to measure the pore water pressure. The NOAA and TAMU-USGS piezometers also contained coarse porous stones to measure, presumably, the pore gas pressure. Crudely speaking, a fine-pore high air entry stone acts as a screen or filter to exclude gas bubbles from the measuring system. As long as continuity of the water is maintained, only the pore water pressure is transferred through the stone and to the measuring system. The concept is commonly used in soil physics and soil mechanics laboratories, and high air entry piezometers have been implanted in dams, for example. As far as is known, this is the first time this approach has been used in the marine environment.

Lehigh Piezometer

The Lehigh piezometer had basically the same configuration as previously. However, the coarse porous stone at the tip (21 feet below the mudline) was replaced with a cylindrically-shaped high air entry stone. The bubbling pressure of this stone was 75 psi. A transducer to measure hydrostatic pressure at the sea floor was installed on the flat plate immediately beneath the weight stand. Both transducers were of the semiconductor variety with a pressure range of 0-50 psi. All of the required electronics are built into these transducers and it is only necessary to supply the appropriate DC voltage to the transducers. The simplicity of these transducers and the fact that they are relatively inexpensive owing to the absence of associated electronics means that these devices could be deployed in large numbers for SEASWAB type projects. The present project represented an excellent opportunity to examine their long term behavior in the marine environment.

NOAA Piezometer

The NOAA piezometer (Fig. 6) again utilized variable reluctance pressure transducers; the distance of approximately 2000 feet over which the signal had to be transmitted was thought to be the limit of hard-lined transmission without benefit of "downhole" amplifiers. However, the only detrimental effect seemed to be occasional noise in the data resulting from radio transmission on the platform housing the data acquisition equipment. Pore pressures were measured at the following depths below the mudline: 21 feet (coarse stone for pore gas pressure), 41 feet (coarse stone), and 51 feet (high air entry stone for pore water pressure as well as a coarse stone). Hydrostatic pressures were measured at 21 and 51 feet below the mudline. The configuration of this piezometer differed from that utilized in SEASWAB I. A long slender aluminum tip was utilized to provide information for a separate study involving pore pressure dissipation. The capsules containing the pressure transducers at the various levels in the piezometer were constructed of aluminum. The high air entry stone was a 75-psi stone which was cemented into a stainless steel housing using a two-part epoxy cement. The cavity between the porous stones and pressure transducers was filled with a light silicone oil. An armored 14-conductor cable was used to transmit the signal to the data acquisition equipment which consisted of strip chart recorders as well as the Sandia Laboratories package.

TAMU-USGS Piezometer

This piezometer (Fig. 7) used thin film strain gage transducers with 100 psia capacity to measure pore gas pressure at two levels (10 feet and 41 feet below the mudline), pore water pressure at one level (41 feet) and hydrostatic pressure at one level (10 feet). The strain gage amplifiers necessary for this type of transducer were installed downhole adjacent to each transducer. The total electronics circuitry consisted of a deck control package placed adjacent to the tape recorder on the platform, and a downhole package. The deck package regulated the supply voltage which was transmitted through the connecting cable to the downhole package. Here, the voltage was further regulated and applied to the transducer strain gages. The output from the strain gages went to an instrument grade operational amplifier where it was then transmitted back to the deck package at a level ranging from 0-5 vdc depending on the pore pressure (20 psi ~ 1 v). With this method, the output signal from the downhole amplifier could be transmitted over a significant length of cable without loss of signal strength or generation of electronic noise.

Calibration circuitry was also incorporated into the piezometer. Once each hour, the master clock on the platform activated sequencing circuitry which first placed a resistance equivalent to approximately 10 psi across one arm of the strain gage bridge and then grounded the excitation voltage to the strain gage bridge. The first operation provided a continuous check on the transducer calibration while the second operation provided a means of detecting long-term drift in the transducer output. Over nearly one year of piezometer operation, the maximum drift observed on any transducer did not exceed an amount equivalent to 0.3 psi, thereby indicating extremely stable circuitry.

Externally, the TAMU-USGS piezometer resembled the NOAA SEASWAB I piezometer. It used 4-inch O.D. pipe and accepted the same weight stand used by the NOAA piezometer. Two cylindrical stainless steel sections (4-inch diameter) were constructed to hold transducers, downhole amplifiers and porous stones. After the electronic packages were placed in the steel sections, they were encased in a waterproof potting compound. As further protection against leakage, the steel sections were welded shut.

The path from porous stone to pressure transducer contained a vent port to aid in deairing the pressure measuring system. The efficiency of the deairing was checked by attaching a mercury filled capillary U-tube of known diameter to the system and measuring the mercury movement upon application of 100 psi pressure. All four systems had total displacements of approximately 3×10^{-4} cubic inches which can be attributed to the volume change of the transducers.

Porous stones were epoxied into stainless steel retaining discs which were sealed into the 4-inch diameter stainless steel cylinders in the field. The disc containing the high air entry stone was attached to a special fixture in a triaxial compression chamber, and the stone was saturated by forcing deaired water through the stone at a pressure of 100 psi. The air entry value of the stone/epoxy seal was checked and found to be slightly greater than the rated 75 psi after saturation. The saturated stone was stored in deaired water until it was mounted on the piezometer prior to installation. The coarse porous stones were placed in water and saturated in a vacuum atmosphere.

The response time of closed system piezometers using pressure transducers is generally considered to be quite rapid. However, in this application where it was possible that pore pressure changes might result from the action of short period waves, the response time - particularly for the high air entry stone - was important. This was checked by sealing a domed cap over the high air entry stone and attaching a water-filled tube to the cap. By quickly opening a valve located at the top of the cap, the water column pressure was instantaneously applied to the stone and the time for full equilibration of this pressure could be measured. As shown in Fig. 8, approximately 50 percent of the pressure from a wave of 10 second period will be measured by the piezometer. The delay time is primarily the result of the impedance to flow of the porous stone. Gas in the measuring system will greatly increase the response time; however, no experiments were performed to measure this effect.

The TAMU-USGS piezometer utilized a 14-conductor neoprene coated unarmored cable to transmit the signal from piezometer to data acquisition equipment.

Installation and Recovery

The installation procedure was essentially the same as for SEASWAB I. However, the shallow water depth allowed the use of a small jack-up barge which greatly simplified the installation.

The assumption that the shear strength of the sediment in the SEASWAB II deformational feature would approximately equal that at the SEASWAB I site proved to be erroneous, and not enough weights were available to force either piezometer to their desired depth. For the TAMU-USGS piezometer, hooks were welded to the uppermost weight (train wheel) and a crane raised and dropped the wheel similar to a pile-driving hammer, to drive the piezometer approximately 5 feet to the desired depth. The Lehigh piezometer required only light driving and the added weight of a diver to force it to grade. This driving operation hampered the determination of initial pore pressures, and it may have contributed to later problems with both the Lehigh and TAMU piezometers. During the process of spooling the cables from the piezometers to the production platform, considerable problems occurred with kinks forming in the small diameter armored cables used for the Lehigh piezometer. This may have weakened the cable and eventually allowed water to leak in and cause a short in the cable.

The Lehigh and TAMU-USGS piezometer were installed on December 3, 1976. The NOAA piezometer, located outside the deformational feature, was installed without difficulty on March 10, 1977. At the same time the Lehigh piezometer, which had been malfunctioning since January 13, 1977, was removed. A continuity check showed that the cable was the cause of the trouble. The piezometer was reinstalled, since the hydrostatic transducer was still operative.

The plans for pullout included calibration of the transducers immediately after the piezometers were removed from the sediment while they were still connected to the data acquisition system on the platform. This was to be accomplished for the NOAA and TAMU-USGS piezometers by sealing a domed cap over the porous stones and applying pressure to the fluid-filled dome with a dead weight gauge tester. Several operational problems were encountered which prevented all transducers from being calibrated in this manner. One difficulty was the surprisingly slow response time of the transducers with high air entry stones. When the porous stones were subsequently removed from the piezometer, hardly any fluid was left in the cavity behind the stones (whether high air entry or coarse stones) confirming earlier thoughts that gas had diffused through all stones during the time they were implanted.

During pullout, several of the bottom resting instruments in the deformation zone were found below their original installed position[2]. The TAMU-USGS piezometer had sunk approximately 5½ feet into the sediment, and the Lehigh piezometer, which had been removed and replaced once, was 6 feet below its original position. The NOAA piezometer had settled less than a foot below its original position, even though it was installed at the same time the Lehigh piezometer was removed and reinstalled. None of the piezometers were designed to be neutrally bouyant in the sediment and some sinkage might be expected. However, the severe sinkage of the Lehigh and TAMU-USGS piezometers was not consistent with the difficulty obtained in getting these devices to depth during installation. The Lehigh piezometer also had a bearing plate near the top (Fig. 1). Using a conservative undrained shear strength of 50 psf, this plate should have supported a load of approximately 500 pounds.

After pullout, it was also observed that the high air entry stone on the Lehigh piezometer was cracked, and that the interior cavity leading to the transducer was filled with sediment. Almost certainly, this was the result of driving the piezometer during the initial installation, and it was a problem which was not anticipated after the trouble free installation during SEASWAB I. The general condition of the piezometers after recovery was excellent except for various aluminum components of the NOAA piezometer which were not painted as in the SEASWAB I Piezometer. These parts showed extreme effects from corrosion.

Results

SEASWAB II was intended to be operative during the 1976-77 winter storm period, i.e., for 5-6 months. However, as a result of the unusual winter weather, it was decided to maintain the instrumentation and gain data from summer tropical storms or hurricanes if they came into the area. Hurricanes Anita and Babe both passed close enough to produce effects at the site. Also, a few of the winter storms produced significant bottom movements. Before the data are presented, several points should be mentioned which have influenced the data analysis.

The analog tape recorder in the Sandia data acquisition system at the SEASWAB site could record the signal from only 14 out of the 18 transducers that were utilized. Although it was seldom that all 18 transducers were simultaneously working, it was not convenient to continually switch connections to the operative transducers. Since the signals from all transducers were transmitted to the monitoring station at Texas A&M University, it was envisioned that data from the transducers not being recorded on the analog tape recorder would be periodically recorded, particularly during storms, at Texas A&M.

It was planned that all four TAMU-USGS transducers and the Lehigh pore pressure transducer would be recorded on the analog tape recorder. Due to operational difficulties, the Lehigh pore pressure was not initially recorded and thus, initial pore pressures are not available for this device. The TAMU-USGS pore gas transducer at the 41 foot level malfunctioned approximately 3 hours after installation. It is suspected that this was caused by the shock due to driving the piezometer at installation. At a later date, the Lehigh pore pressure transducer replaced the tape recorder channel occupied by the malfunctioning TAMU-USGS transducer, but the net result was that pore pressures for the Lehigh piezometer are available for a period of a little over one month before the cable shorted out. During this period, the excess pore pressures ranged from 0 to 1.5 psi with a average of 1 psi. The periodic data recorded at the Texas A&M monitor have yet to be analyzed, and the Lehigh piezometer results are still subject to change.

Fig. 9 shows excess pore pressures for the TAMU-USGS piezometer for a period of approximately 60 days after installation. Zero time was arbitrarily taken as the time at which the piezometer was driven to grade. At the 41 foot level, the excess pore water pressure decreased from a high of 12.5 psi to approximately 11 psi at 7 hours after installation. At the 10 foot level, the pore gas pressures varied somewhat erratically and then appeared to level off at 3 psi about 24 hours after installation. Then, both pressures rapidly decreased and leveled off at 8.3 psi (41 foot level) and 2 psi (10 foot level). Approximately 20 days after installation the pressures started increasing slightly.

Fig. 10 shows excess pore gas pressures for the NOAA piezometer at the 21, 41, and 51 foot levels. The excess pore water pressures from the high air entry stone at the 51 foot level are also shown in Fig. 10. These pore pressures appeared to have followed a conventional pattern, with dissipation occurring gradually over a several day period. The equilibrium or initial excess pore gas pressures are considered to be 1.6 psi, 3.4 psi and 6.3 psi at the 21, 41 and 51 foot levels, respectively. The equilibrium excess pore water pressure at the 51 foot leves is approximately 3.6 psi.

The initial excess pore pressures from all piezometers are plotted versus depth in Fig. 11. To compare the pore pressures with the overburden pressures, sediment unit weights obtained at the nearby SEASWAB I location were utilized. It is seen that the pore pressures within the deformational feature are again nearly equal to the total stress, i.e., the effective stress is essentially zero. In the undisturbed area the effective stresses, although low, are positive. It has been suggested that deformational features such as the one at the SEASWAB II site are the result of degassing or dewatering of the sediment. However, the results in Fig. 11 indicate that this is not the case.

The difference between pore water and pore gas pressures shown by the NOAA piezometer at the 51 foot level is a matter of interest. Initially, the pore gas pressure was 4 to 5 psi higher than the pore water pressure. Approximately 7½ days after installation, the pore water pressure started increasing and it rose steadily over a period of 2 days until it essentially equalled the pore gas pressure. It is suspected that this is due to gas slowly diffusing through the high air entry stone until finally the transducer was measuring gas rather than water pressure. The diffusion of gas through semi-permeable membranes associated with the pressure-membrane method of determining soil suction is well known[14]. The TAMU-USGS pore water pressures at the 41 foot level did not show this dramatic increase in pressure; in fact, the pressure decreased somewhat after approximately one day and remained at this level for nearly two months. Yet, based on observations at pullout of the piezometer, gas did diffuse through the stone. It is possible that the pounding received during installation caused gas to immediately intrude through the stone and that all measurements at the 41 foot level were pore gas rather than pore water pressures. At present it is not possible to make a definite conclusion and it will be assumed that pore water pressure was initially measured at the 41 foot in the deformational feature.

The first significant winter storm after installation occurred on December 25, 1976. This was followed by several other winter storms during January and early February, 1977. These storms caused some minor pore pressure fluctuations, but after the passage of the storms, no residual pore pressures were observed. Starting on February 22, two major storms occurred in rapid succession. On February 23, the TAMU-USGS piezometer showed an abrupt increase in excess pore pressures of 2.4 psi at the 10 foot level and 5.0 psi at 41 foot level. These pore pressures started dissipating, but before they reached their pre-storm level additional winter storms struck the area. Even after the winter storms ceased, excess pore pressures remained at levels higher than the ambient after installation.

The NOAA piezometer was installed after the February storms. Although several more winter storms occurred after the NOAA installation, they appeared to have caused only minor variations in pore pressures both within and outside the deformational feature.

The pore pressures suggest that a major sediment movement occurred in the deformational feature during the late February storm, and that this resulted in a significant pore pressure increase. At this time the piezometer either settled into the sediment or else the sediment subsided. This is indicated by a 1.5 psi increase in the hydrostatic pressure, and is also consistant with the vertical displacement of the piezometers noted during the recovery operations. The data and observations seem to indicate that the movement was more akin to liquefaction (as observed in sands) rather than a gross downslope movement. Regardless of the mechanics of movement, it seems fairly certain that the process which initially produces the deformational feature does not serve to stabilize the area by causing degassing or dewatering of the sediment.

Although the data are still being analyzed, it should be mentioned that major movements again occurred within the deformational feature during the passage of Hurricanes Anita and Babe. It is certain at this time that major pore pressure increases occurred as a result of these movements.

CONCLUSIONS

Equipment

Four types of pressure transducers were used to measure pore pressures. One of the two vibrating wire strain gages installed did malfunction during SEASWAB I. Also, it appears that the downhole electronics associated with the thin-film strain gage transducers (TAMU-USGS piezometer) might be vulnerable to shock. Otherwise, the pressure transducers utilized appear satisfactory for long-term use in the marine environment. The use of small diameter armored cable is to be discouraged owing to the possibility of kinking during placement and subsequent water leakage into the cable. The use of high air entry porous stones to measure pore water pressures in gassy sediments will apparently be successful for only a very short period of time as gas will quickly diffuse through the stones.

Pore Pressures

Significant excess pore pressures were measured both within and outside a deformational feature. These pore pressures approached the overburden pressures, thus the effective stresses approached zero. Owing to the limitations of the high air entry stones mentioned above, it is not clear whether pore water or pore gas pressures were measured in the deformational feature; it is suspected that pore gas pressures were measured. Significant pore pressure changes occurred during at least two separate instances within the deformational feature. These are probably indicative of major movements within the deformational feature.

ACKNOWLEDGEMENTS

This study is part of the U.S. Geological Survey's Delta project, supervised by Dr. Louis Garrison.

We wish to thank the following people for their assistance: Dick Zimmer, Eddie Denk and Ron Boggess for work on the TAMU-USGS Piezometer, Richard Faris and John Burns for their help on the NOAA Piezometer and Dennis Schafer of Shell Oil Company for his continued interest and time. In addition we would like to express our appreciation for the help received from the field personnel of the Shell Oil Company in East Bay, Louisiana.

REFERENCES

1. Garrison, L. E., "The SEASWAB Experiment," Marine Geotechnique, Vol. II, 1977.
2. Hottman, W.E., Suhayda, J.N., and Garrison, L.E., "SEASWAB II (Shallow Experiment to Assess Storm Wave Affects on the Bottom)," Proceedings, Offshore Technology Conference, 1978.
3. Henkel, D., "The Role of Waves in Causing Submarine Landslides," Geotechnique, Vol. 20, No. 1, 1970.
4. Bea, R.G., "How Sea-floor Slides Affect Offshore Structures," The Oil and Gas Journal, November, 1971.
5. Richards, A.F., Oieu, K., Keller, G.H., and Lai, J., "Differential Piezometer Probe for an In Situ Measurement of Sea-floor Pore-pressure," Geotechnique, Vol. 25, 1975.
6. Hirst, T.J, and Richards, A.F., "Excess Pore Pressure in Mississippi Delta Front Sediments: Initial Report," Marine Geotechnology, Vol. 1, 1976.
7. Bennett, R.H., Bryant, W.R., Dunlap, W.A., and Keller, G.H., "Initial Results and Progress of the Mississippi Delta Sediment Pore Water Pressure Experiment," Marine Geotechnology, Vol. 1, 1976.
8. Hirst, T.J. and Richards, A.F., "In Situ Pore Pressure Measurements in Mississippi Delta Front Sediments," Marine Geotechnology, Vol. 2, 1977.

9. Bennett, R.H., "Pore Water Pressure Measurements: Mississippi Delta Submarine Sediments," Marine Geotechnology, Vol. 2, 1977.

10. Hvorslev, J., "Time Lag and Soil Permeability in Ground-water Observations," Bulletin No. 36, U.S. Army Engineers Waterways Experiment Station, 1951.

11. Whelan, T., Coleman, J.M., and Suhayda, J.N., "The Geochemistry of Recent Mississippi River Delta Sediment: Gas Concentration and Sediment Stability," Proceedings, Offshore Technology Conference, 1975.

12. Suhayda, J.N., Whelan, T., Coleman, J.M., Booth, J.S., and Garrison, L.E., "Marine Instability: Interaction of Hydrodynamic Forces and Bottom Sediments," Proceedings, Offshore Technology Conference, 1976.

13. Niper, E.D. and Williams, G.N., "Project SEASWAB: Real-time Acquisition/Reduction of Submarine Sediment Data," Proceedings, Offshore Technology Conference, 1977.

14. Williams, P.J., "Movement of Air Through Water in Partly Saturated Soils," Nature, December 24, 1966.

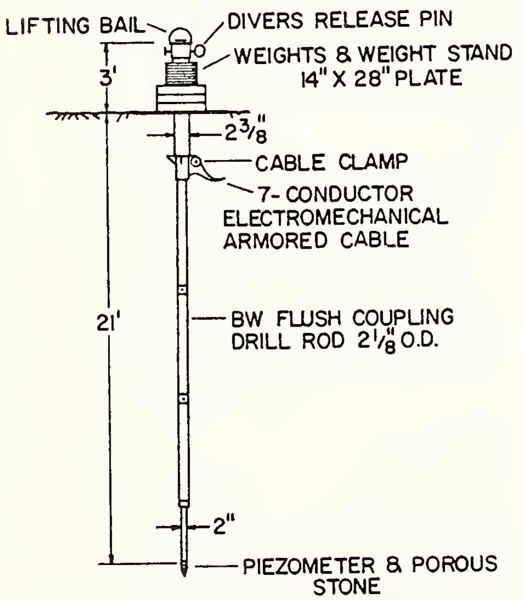
LIFTING BAIL
DIVERS RELEASE PIN
WEIGHTS & WEIGHT STAND 14" X 28" PLATE
3'
2 3/8"
CABLE CLAMP
7-CONDUCTOR ELECTROMECHANICAL ARMORED CABLE
21'
BW FLUSH COUPLING DRILL ROD 2 1/8" O.D.
2"
PIEZOMETER & POROUS STONE

Fig. 1 - The Lehigh differential piezometer stand used in SEASWAB I and II.

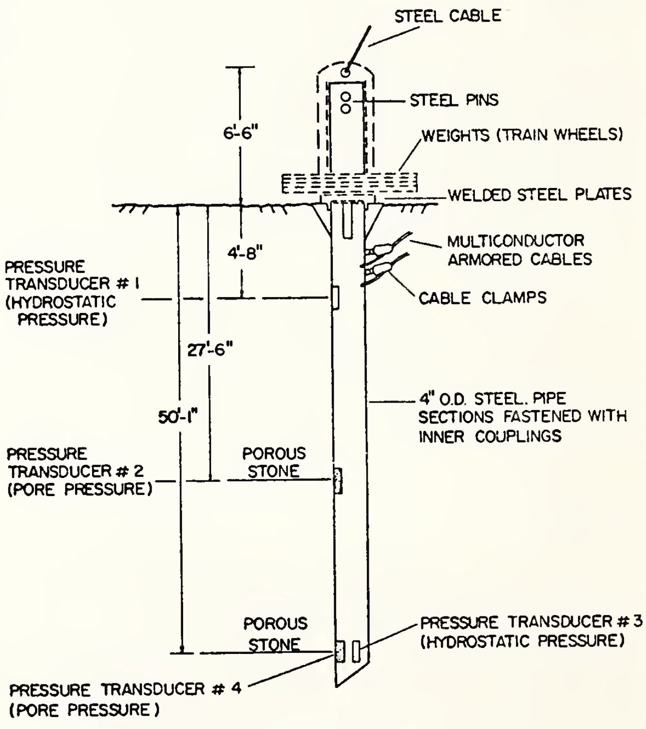
STEEL CABLE
STEEL PINS
6'-6"
WEIGHTS (TRAIN WHEELS)
WELDED STEEL PLATES
MULTICONDUCTOR ARMORED CABLES
4'-8"
CABLE CLAMPS
PRESSURE TRANSDUCER # 1 (HYDROSTATIC PRESSURE)
27'-6"
4" O.D. STEEL PIPE SECTIONS FASTENED WITH INNER COUPLINGS
50'-1"
PRESSURE TRANSDUCER # 2 (PORE PRESSURE)
POROUS STONE
POROUS STONE
PRESSURE TRANSDUCER # 3 (HYDROSTATIC PRESSURE)
PRESSURE TRANSDUCER # 4 (PORE PRESSURE)

DWG. NOT TO SCALE

Fig. 2 - NOAA piezometer and weight stand used in SEASWAB I.

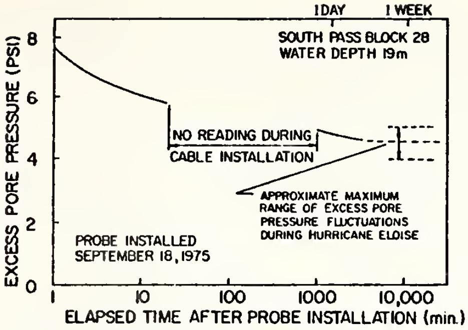

Fig. 3 - Sediment excess pore pressures measured by Lehigh piezometer in SEASWAB I.

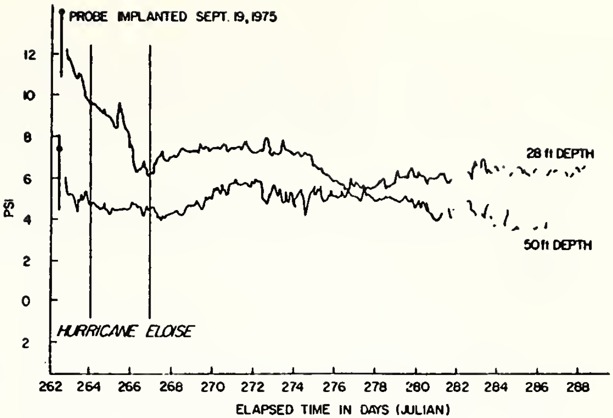

Fig. 4 - Sediment excess pore pressure measured by NOAA piezometer in SEASWAB I.

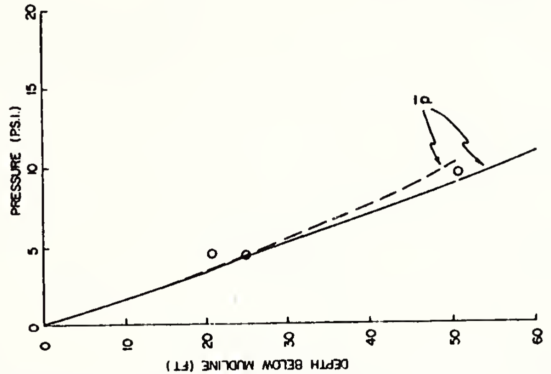

Fig. 5 - Initial excess pore pressure and calculated overburden pressures with respect to depth; SEASWAB I.

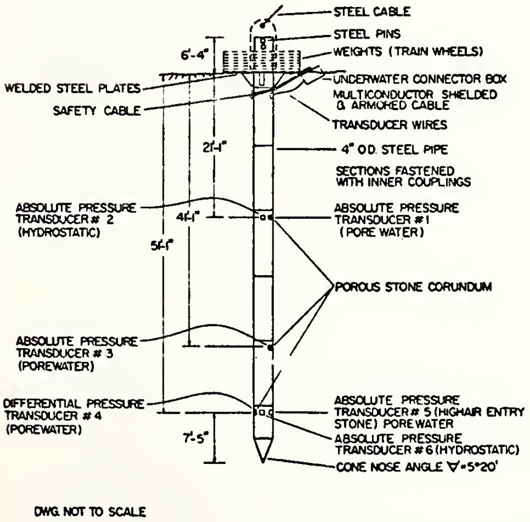
STEEL CABLE
STEEL PINS
WEIGHTS (TRAIN WHEELS)
6'-4"
WELDED STEEL PLATES
UNDERWATER CONNECTOR BOX
MULTICONDUCTOR SHIELDED & ARMORED CABLE
SAFETY CABLE
TRANSDUCER WIRES
21'-1"
4" O.D. STEEL PIPE
SECTIONS FASTENED WITH INNER COUPLINGS
ABSOLUTE PRESSURE TRANSDUCER # 2 (HYDROSTATIC)
41'-1"
ABSOLUTE PRESSURE TRANSDUCER # 1 (PORE WATER)
54'-1"
POROUS STONE CORUNDUM
ABSOLUTE PRESSURE TRANSDUCER # 3 (POREWATER)
DIFFERENTIAL PRESSURE TRANSDUCER # 4 (POREWATER)
ABSOLUTE PRESSURE TRANSDUCER # 5 (HIGHAIR ENTRY STONE) POREWATER
7'-5"
ABSOLUTE PRESSURE TRANSDUCER # 6 (HYDROSTATIC)
CONE NOSE ANGLE ∀=5°20'
DWG. NOT TO SCALE

Fig. 6 - NOAA piezometer and weight stand used in SEASWAB II.

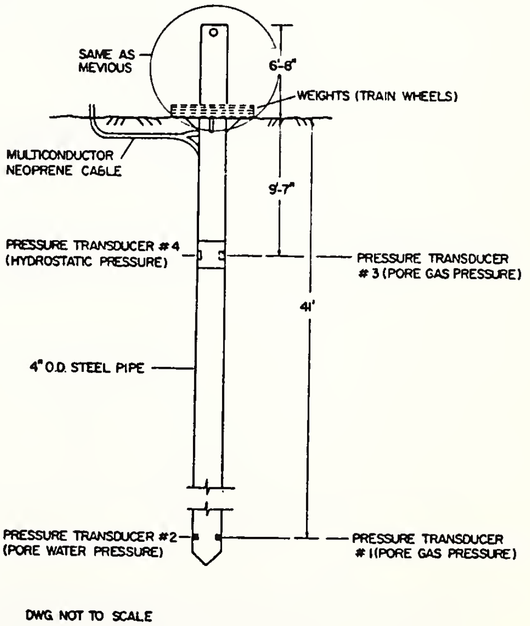
SAME AS PREVIOUS
6'-8"
WEIGHTS (TRAIN WHEELS)
MULTICONDUCTOR NEOPRENE CABLE
9'-7"
PRESSURE TRANSDUCER # 4 (HYDROSTATIC PRESSURE)
PRESSURE TRANSDUCER # 3 (PORE GAS PRESSURE)
41'
4" O.D. STEEL PIPE
PRESSURE TRANSDUCER # 2 (PORE WATER PRESSURE)
PRESSURE TRANSDUCER # 1 (PORE GAS PRESSURE)
DWG. NOT TO SCALE

Fig. 7 - TAMU-USGS piezometer and weight stand used in SEASWAB II.

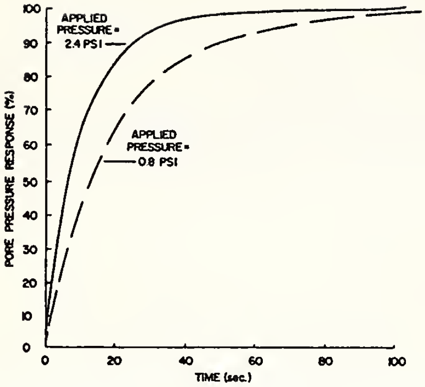

FIG. 8 - PRESSURE RESPONSE CHARACTERISTICS OF HIGH AIR ENTRY SYSTEM ON TAMU-USGS PIEZOMETER.

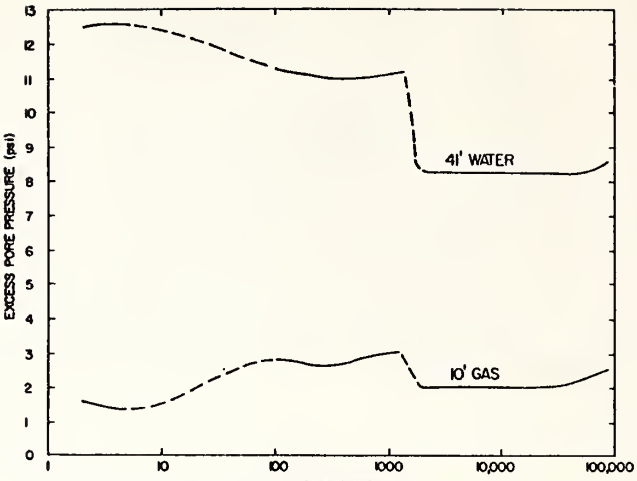

FIG. 9 - SEDIMENT EXCESS PORE PRESSURES MEASURED BY TAMU-USGS PIEZOMETER IN DEFORMATIONAL FEATURE; SEASWAB II.

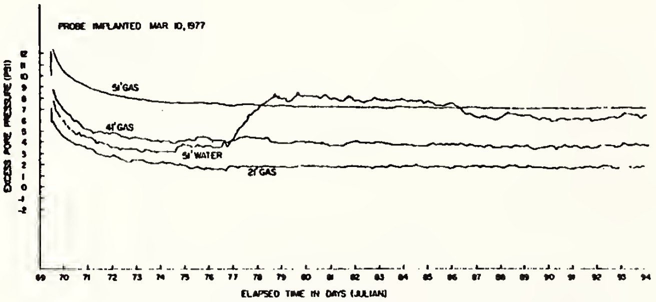

FIG. 10 - SEDIMENT EXCESS PORE PRESSURES MEASURED BY NOAA PIEZOMETER OUTSIDE DEFORMATIONAL FEATURE; SEASWAB II.

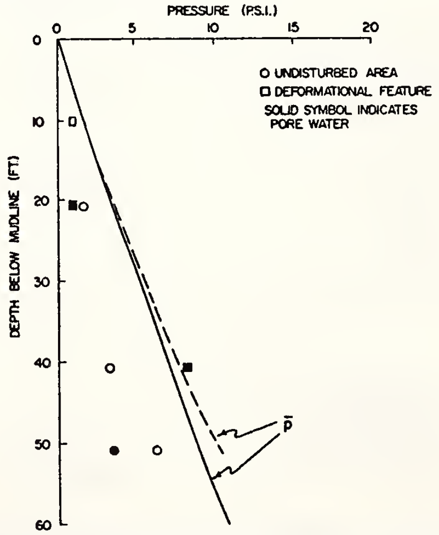

FIG. 11 - INITIAL EXCESS PORE PRESSURES AND CALCULATED OVERBURDEN PRESSURES WITH RESPECT TO DEPTH; SEASWAB II.

Journal of Sedimentary Petrology 48, No. 1, 239-252.

ESTIMATES OF SAND TRANSPORT ON THE NEW YORK SHELF USING NEAR-BOTTOM CURRENT METER OBSERVATIONS[1]

P. E. GADD, J. W. LAVELLE, D. J. P. SWIFT
National Oceanic and Atmospheric Administration, Atlantic Oceanographic and Meteorological Laboratories,
15 Rickenbacker Causeway, Miami, Florida 33149, U.S.A.

ABSTRACT: Calculations of cohesionless bottom-sediment movement within the New York Bight have been made by applying the transport formulae of Bagnold (1941, 1956, 1963), Einstein (1950), and Yalin (1963) to near-bottom current meter and surficial sand size observations. Current data were drawn from the records of eighteen long-term Savonius rotor current meter deployments at various locations within the Bight during Fall of 1973 and Spring of 1974.

The assumptions underlying the calculations are that wave activity was minimal at recording sites, that a drag coefficient of 3×10^{-3} reflecting small scale roughness and large boundary layer Reynolds number is suitable to convert measured currents to friction velocities, and that laboratory threshold velocities apply in the marine environment.

The calculations suggest that oceanic bottom sediment movement reaches maximum intensity during the fall and winter due to the added energy input from strong meterological events. Calculated transport quantities on the inner shelf tend to decrease as depth and distance from shore increase. However, during the Fall of 1973, the deep waters near the head of the Hudson Shelf Valley exhibited current flows directed to the north in excess of 40 cm/sec. These up-channel flow events appear to be in response to strong, sustained westerly winds. The maximum sediment transport rate caused by these current velocities is two orders of magnitude greater than that occurring at much shallower depths along the New Jersey coast during the same measurement period. The Spring 1974 current velocity field yields transport rates of lesser magnitudes relative to the previous fall, with a net down-channel sediment flux at the head of the Hudson Shelf Valley. The New York Harbor entrance appears to be the site of near-continual sediment transport generated by swift tidal currents.

INTRODUCTION

Assessment of marine sediment transport is of particular importance as man seeks to expand his utilization of the oceanic environment. It is well recognized that potentially harmful contaminants released into the oceans are mobile; the particulate material of the seabed being one vehicle of transportation. Similarly, sediment mobility is a major concern of those who propose to undertake ocean engineering projects. Numerous observations of the past have illustrated the sensitivity of shoreline stability to offshore construction. An understanding of sediment response to fluid flow is essential if seaside areas are to be protected from the damaging effects of coastal erosion. In addition, sediment stability must be investigated prior to the construction of offshore facilities, the integrity of which depends on the load supporting ability of the seabed.

Sediment transport measurements may be made by means of tracers (*e.g.* Lavelle *et al.*, 1976), sediment traps, and bottom stake fields (*e.g.* DeAlteris *et al.*, in press). The most serious limitation of these tools is that a synoptic regional description of sediment movement is impossible to achieve. Quite difficult, but within reach of present oceanographic measurement techniques and analysis, is the regional description of the near-bottom current velocity field. Such measurements coupled with empirical transport formulae allow regional descriptions of sediment movement to be made.

The study reported here is the exploration of the consequences of coupling near-bottom flow measurements taken from the New York Bight with the transport formulae of Bagnold (1941, 1956, 1963), Einstein (1950), and Yalin (1963). The assumptions underlying the calculations are that wave activity is minimal compared to mean flow at the recording sites, that a drag coefficient of 3×10^{-3} reflecting small scale roughness lengths and a large boundary layer Reynolds number is suitable

---

[1] Manuscript received October 21, 1976: revised June 23, 1977.

to convert measured currents to friction velocities, and that laboratory threshold velocities apply in the marine environment. These assumptions will be discussed in the course of the work.

The results of the calculations are total and net transport rates, and transport directional roses at each current meter site. The eighteen current records used in the study begin to suggest the seasonal, spatial structure of transport in the Bight apex. Computed fluxes are thought to approximate the directions and relative intensities of transport, while each absolute transport rate may represent no better than an order of magnitude estimate. Comparison of computed and tracer measured transport suggest this to be the case. Input information and transport formulae will be discussed prior to the presentation of the computational results.

METHODS

Current Measurements

Eighteen near-bottom current meters were deployed in the New York Bight apex during the Fall of 1973 and the Spring of 1974. Interval-averaged speed and instantaneous current direction were recorded at a 10 minute sampling interval using an Aanderaa RCM-4 internally recording Savonius rotor current meter. The stations were of the taut wire, subsurface float design with the meters located approximately one meter above the seabed (Charnell and Mayer, 1975). Height for the purposes of these calculations was set at 1 m. Starting dates and durations of deployments were variable. Fall meters spanned the interval from late August to mid-December; Spring meters spanned the interval from early April to late June. The effects of variable record length has been reduced by the calculation of time-averaged transport rates.

Substrate Sampling

Surficial sediments were sampled at each current meter site using a Shipek grab sampler. Mean particle size was determined in order to estimate the threshold velocity of initial sediment motion. All locations sampled exhibited fine to medium sand with mean diameters ranging from 0.11 to 0.56 mm. Three locations contained percentages of fine-grained material ($<62\ \mu m$) in excess of 1.5 percent by weight. The sample with the greatest percentage of fine particles (19% $<62\ \mu m$) was found at the head of the Hudson Shelf Valley. Due to the small quantities of silt and clay-sized particles found at our study locations, it is assumed that theories of cohesionless particle transport may be applied to the observations. A sediment density of 2.65 gm/cm^3 is used throughout.

Threshold Velocity

Research regarding the force needed to erode an unconsolidated bed of sand grains has yielded a number of competency curves which form a basis for predicting sediment motion. While the results reported by Shields and others (Graf, 1971) were derived from flume studies using relatively uniform sized particulate matter, Sternberg (1972) notes that measurements of initial sediment movement in Puget Sound tidal channels agree favorably with those laboratory results. Threshold velocities for sediment movement in this study were therefore taken to lie in the range 15.5 cm/s to 20.0 cm/s. Because of the small range of mean grain sizes measured at the current meter sites, the variation of threshold velocity over the experimental range of grain diameter was nearly linear.

Bedload Transport Calculations

Bagnold Technique.—In order to perform transport calculations using only current velocities and sediment size characteristics, the volume of bedload transport may be taken proportional to the frictional energy expended upon the seabed by the motion of the fluid flowing above it (Bagnold, 1956, 1963). This concept has undergone testing in the coastal sand dunes of Baja California (Inman *et al.*, 1966) and in a tidal channel of Puget Sound, Washington (Kachel and Sternberg, 1971). The Bagnold concept is expressed by the following relationship:

$$q = \frac{\rho_s}{(\rho_s - \rho)g} \kappa\omega \qquad (1)$$

where q is mass discharge of sediment per unit width ($gm\ cm^{-1}\ s^{-1}$), ρ_s and ρ are sediment and fluid densities respectively, g is acceleration due to gravity, and κ is the experimentally determined coefficient that expresses the efficiency with which a given flow transports sediment. The power per unit area expended on the seabed by the flowing fluid, ω, can be written as the product of the boundary shear stress, τ_0, and the friction velocity, U_*, (Inman, 1966):

$$\omega = \tau_0 U_* . \qquad (2)$$

When the boundary shear stress is expressed in terms of the friction velocity, ($\tau_0 = \rho U_*^2$), Eq. 2 becomes:

$$\omega = \rho U_*^3 . \qquad (3)$$

The efficiency coefficient, κ, in Eq. 1 was originally thought to depend only on sediment characteristics, primarily grain size (Bagnold, 1963). Investigations by Kachel and Sternberg (1971) showed a dependence of the κ value on both sediment size and excess shear stress, $(\tau_0 - \tau_T)/\tau_T$, where τ_T is the threshold shear stress for initial sediment motion. Later, a comparison of transport equations with the data of Guy, Simons, and Richardson (1966), will show that some of the dependence of the efficiency factor can be removed by restructuring the velocity dependence of Eq. 1.

Recent oceanographic convention has dictated that the boundary layer flow velocity be characterized by the velocity measured at the standard height of 100 centimeters above the seabed. The drag coefficient, C_{100}, relates that velocity to the shear velocity through the expression

$$C_{100} U^2_{100} = U_*^2 . \qquad (4)$$

The Bagnold sediment transport equation then becomes

$$q = \frac{\rho_s \rho}{(\rho_s - \rho) g} \kappa C_{100}^{3/2} U_{100}^3 \qquad (5)$$

Two flows with identical values of U_{100} can therefore produce unequal transport rates when the momentum transfer to the bed, characterized by C_{100}, is not identical. Ludwick (1975) has shown that C_{100} values can vary over several orders of magnitude. Sternberg (1972), while reporting a wide range of determined C_{100} values, found that for large Reynolds numbers and small bedforms, C_{100} seems to approach a value near 3.1×10^{-3}. For fixed C_{100}, Eq. 5 shows that mass transport is proportional to the third power of the reference velocity, U_{100}. In support of this parameterization, Colby (1964) and Nordin (1975) independently found that sediment flux varied as the cube of stream discharge, which is proportional to mean stream velocity.

The flume transport data of Guy et al. (1966) has been used to fix the efficiency coefficient in Eq. 5. Thirty experimental runs providing mass sediment flux measurements over a range of mean flow velocities were used in the calibration (Fig. 1). It was assumed that for large Reynolds numbers, the drag coefficient is constant over all runs and is equal in flume and marine situations. The mean velocity in the flume, $\bar{U}$, is taken to be equal to that expected near 100 cm from

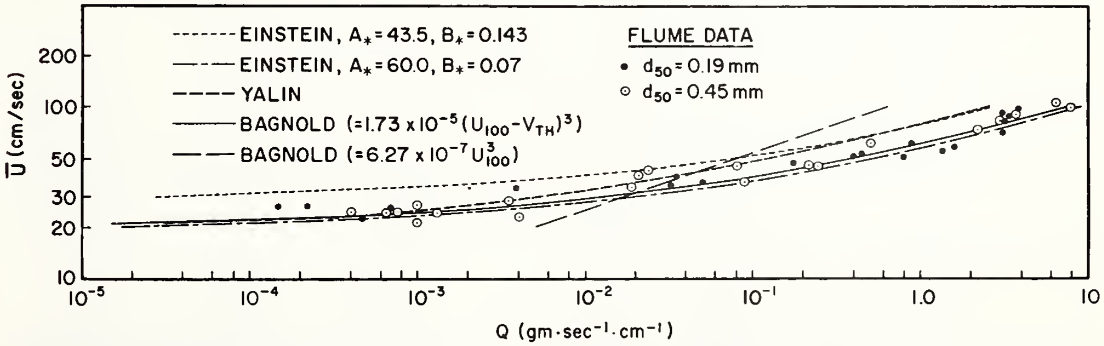

FIGURE 1.—Sediment flux data of Guy, Simons, and Richardson (1966) for mean grain sizes 0.19 mm and 0.45 mm. Superimposed are the sediment flux predictions based on the Bagnold, Einstein, and Yalin formulae described herein. Calibration of the formulae was against the 0.45 mm data and using threshold velocity of 19.0 cm/s.

the bed. The justification is based on Figure 1 where the sediment transport rate is seen to approach zero at a threshold velocity near 20 cm/s. If the assumption was grossly unfair, such agreement could not be expected.

Equation 5 was rewritten to isolate the overall transformation coefficient, α:

$$\alpha = q\bar{U}^{-3} \qquad (6)$$

In Table 1, values of sediment transport rates and mean velocities are given along with values of α derived from them. For each grain size, a mean α value was also computed. For a grain size of 0.45 mm, the mean value of α (6.27×10^{-7} gm cm^{-4} s^{2}) was used to construct the Bagnold transport curve of Figure 1. The discrepancies between the experimental data and the curve (Fig. 1) suggests that another parameterization of flux should be sought.

To this point, a basic assumption of our approach has been that a critical tractive force, measurable as a particular threshold velocity existant at some height above the seabed, is a requirement for particle motion. This belief, in conjunction with the behavior of Eq. 5, implies a discontinuity in the sediment discharge rate at the point where the tractive force equals the critical value.

In light of these arguments, the proportionality of the sediment discharge rate and the cube of the excess velocity has also been examined. This formulation was first introduced by Bagnold (1941) in his investigations

TABLE 1.—*Proportionality coefficients needed to quantify the sediment transport rate for Bagnold formulae (Eqs. 6 and 7) using data of Guy, Simons, and Richardson (1963).*

TRIAL #	MEAN FLOW VELOCITY, $\bar{U}$ (cm/s)	SEDIMENT TRANSPORT INDEX $(\bar{U} - U_{TH})^3$	SEDIMENT TRANSPORT RATE, Q (gm cm^{-1} s^{-1})	β $[=Q/(\bar{U} - U_{TH})^3]$	$\bar{U}^3$	α $[=Q/\bar{U}^3]$
SEDIMENT GRAIN SIZE, D_{50} = 0.18 mm, THRESHOLD VELOCITY, U_{TH} = 16.0 cm/s						
1	23.0	343	8.7×10^{-3}	2.54×10^{-5}	12,167	7.15×10^{-7}
2	25.0	729	2.3×10^{-2}	3.16×10^{-5}	15,625	1.47×10^{-6}
3	22.5	274	2.4×10^{-2}	8.74×10^{-5}	11,391	2.11×10^{-6}
4	22.0	216	1.0×10^{-1}	4.63×10^{-4}	10,648	9.39×10^{-6}
5	28.0	512	1.0×10^{-1}	1.95×10^{-4}	21,952	4.56×10^{-6}
6	35.0	6,859	1.7×10^{-1}	2.48×10^{-5}	42,875	3.97×10^{-6}
7	35.0	6,859	2.7×10^{-1}	3.94×10^{-5}	42,875	6.30×10^{-6}
8	40.0	13,824	3.5×10^{-1}	2.53×10^{-5}	64,000	5.47×10^{-6}
9	38.0	10,648	4.5×10^{-1}	4.23×10^{-5}	54,872	8.20×10^{-6}
10	42.0	17,576	4.5×10^{-1}	2.56×10^{-5}	74,088	6.07×10^{-6}
11	40.0	13,824	5.5×10^{-1}	3.98×10^{-5}	64,000	8.59×10^{-6}
12	48.0	32,768	7.0×10^{-1}	2.14×10^{-5}	110,592	6.33×10^{-6}
13	46.0	27,000	7.7×10^{-1}	2.85×10^{-5}	97,336	7.91×10^{-6}
14	51.0	42,875	7.8×10^{-1}	1.82×10^{-5}	132,651	5.88×10^{-6}
15	55.0	59,319	9.8×10^{-1}	1.65×10^{-5}	166,375	5.88×10^{-6}
				$\bar{\beta}_{.18} = 7.22 \times 10^{-5}$		$\bar{\alpha}_{.18} = 5.52 \times 10^{-6}$
SEDIMENT GRAIN SIZE, D_{50} = 0.45 mm, THRESHOLD VELOCITY, U_{TH} = 19.0 cm/s						
16	24.4	157	4.0×10^{-4}	2.54×10^{-6}	14,527	2.8×10^{-8}
17	24.4	157	6.5×10^{-4}	4.13×10^{-6}	14,527	4.5×10^{-8}
18	24.4	157	7.6×10^{-4}	4.76×10^{-6}	14,527	5.2×10^{-8}
19	21.3	12	1.0×10^{-3}	8.22×10^{-5}	9,664	1.03×10^{-7}
20	27.0	512	1.0×10^{-3}	1.95×10^{-6}	19,683	5.1×10^{-8}
21	24.4	157	1.3×10^{-3}	8.25×10^{-6}	14,527	8.9×10^{-8}
22	28.5	857	3.5×10^{-3}	4.08×10^{-6}	23,149	1.51×10^{-7}
23	23.0	64	4.0×10^{-3}	6.25×10^{-5}	12,167	3.29×10^{-7}
24	34.0	3,375	1.9×10^{-2}	5.48×10^{-6}	39,304	4.89×10^{-7}
25	40.0	9,261	2.1×10^{-2}	2.27×10^{-6}	64,000	3.28×10^{-7}
26	43.0	13,824	2.4×10^{-2}	1.74×10^{-6}	79,507	3.02×10^{-7}
27	46.0	19,683	8.1×10^{-2}	4.12×10^{-5}	97,336	8.32×10^{-7}
28	37.0	5,832	9.0×10^{-2}	1.54×10^{-5}	50,653	1.78×10^{-6}
29	46.0	19,683	2.2×10^{-1}	1.12×10^{-5}	97,336	2.26×10^{-6}
30	46.0	19,683	2.5×10^{-1}	1.24×10^{-5}	97,336	2.57×10^{-6}
				$\bar{\beta}_{.45} = 1.73 \times 10^{-5}$		$\bar{\alpha}_{.45} = 6.27 \times 10^{-7}$
				$\bar{\beta}_{TOTAL} = 4.48 \times 10^{-5}$		$\bar{\alpha}_{TOTAL} = 3.07 \times 10^{-6}$

of wind-driven sand transport.

If β represents the proportionality coefficient, then

$$q = \beta(u_{100} - U_{TH})^3. \qquad (7)$$

Table 1 gives the values of β associated with the experimental runs of Guy *et al.* (1966). The mean value of β for a grain size of 0.45 mm has been used to construct a graphical representation of Eq. 7 shown on Figure 1, reproducing well the trend of the data. The mean value of β for both experimental grain sizes and that considered to be most suitable for application to the entire spectrum of sand sizes observed at the current meter locations discussed herein (0.11 mm to 0.56 mm) is 4.48×10^{-5} gm cm^{-4} s^2. Equation 7 has the property of falling to zero at the threshold value; when U_{100} is less than threshold, q is set to zero.

Einstein Technique.—Empirical sediment transport research undertaken by Einstein (1950) has yielded an empirical approach which differs from Bagnold's approach in two ways. The definition of a critical value of shear stress for the initiation of sediment motion is such a difficult proposition that Einstein entirely avoided the concept. In addition, he suggested that the bedload transport is related to the fluctuations of the fluid motion rather than to the average value of the velocity. Initiation and termination of particle motion are expressed in terms of probability, relating instantaneous hydrodynamic lift forces to the particle weight.

Einstein's results show that the probability of particle motion, P, follows the normal-error law, such that

$$P = 1 - \frac{1}{\sqrt{\pi}} \int_{-B_*\psi_* - 1/\eta_0}^{B_*\psi_* - 1/\eta_0} e^{-t^2} dt. \qquad (8)$$

where $\eta_0 = 0.5$ and B_* is a constant determined from experimental data.

Einstein's "flow intensity," ψ_*, expressed in terms of shear velocity is:

$$\psi_* = g\left(\frac{\rho_s - \rho}{\rho}\right)\frac{d}{U_*^2} \qquad (9)$$

where definitions of elements in the expression have been given previously. The flow intensity, ψ_*, is the reciprocal of the dimensionless shear parameter used in the discussions of threshold of motion (Graf, 1971). Utilizing the assumed proportionality between the shear velocity, U_*, and our velocity measure, U_{100}, yields

$$\psi_* = g\left(\frac{\rho_s - \rho}{\rho_s}\right)\frac{d}{C_{100}U_{100}^2}. \qquad (10)$$

Einstein derives a dimensionless measure of the bedload transport which he refers to as the "intensity" of transport:

$$\phi = \frac{q}{\rho_s}\left(\frac{\rho}{(\rho_s - \rho)gd^3}\right)^{1/2} \qquad (11)$$

where q is the bedload mass discharge rate per unit of width. Further considerations of Einstein yield a relationship between this "intensity" of sediment transport, ϕ, and the probability of erosion, P:

$$\frac{P}{1 - P} = A_*\phi. \qquad (12)$$

Solving Eqs. 11 and 12 for the bedload transport rate, q, yields the following:

$$q = \frac{P}{1 - P}\,\frac{\rho_s}{A_*}\left(\frac{(\rho_s - \rho)}{\rho}\,gd^3\right)^{1/2} \qquad (13)$$

The coefficient, A_*, as in the case of B_*, was experimentally determined by Einstein using flume data in which large grained particle transport was studied (d_{50} − 0.785 mm and 28.65 mm). The values classically prescribed ($A_* = 43.5$, $B_* = 0.143$) were found to yield transport predictions which deviated substantially from the flume data compiled by Guy *et al.* (1966), as seen in Figure 1. Note, for example, that use of these A_* and B_* values yields the prediction that medium size sand particles remain immobile until a bottom current speed of 30 cm/sec is reached. A least-squares analysis of the more recent flume data was performed in order to re-evaluate the coefficients to describe the transport of granular particles of sizes comparable to those found at our study locations. The values which yield a best fit of the Einstein transport expression to the experimental data involving medium to fine sands were determined to be $A_* = 60.0$ and $B_* = 0.07$. Graphical representation of the Einstein method using the two A_*-B_* pairs is shown in Figure 1.

Yalin Technique.—The average lift acting on a sediment particle is considered in the transport formula of Yalin (1963). The particle motion is presumed to be by saltation, and Yalin believes that an increase in bedload discharge is due to increased particle path length and not necessarily due to the number of particles participating in the motion. The existence of a critical tractive force is assumed. Yalin found that the bedload mass transport rate, q, is related to the near bottom fluid flow as follows:

$$q = 0.635\rho_s d U_* S(1 - (aS)^{-1}\ln(1 + aS)) \tag{14}$$

where the excess stress, S, is equal to $(U_*^2/(U_{*TH})^2 - 1)$, where U_{*TH} is the threshold friction velocity, and where

$$a = 2.45(\rho/\rho_s)^{0.4}\left(\frac{\rho U_{*TH}^2}{(\rho_s - \rho)gd}\right)^{1/2} \tag{15}$$

Without calibration, the Yalin technique for a grain size of 0.45 mm yields predictions for transport rates which show agreement with the flume data at velocities near threshold (Figure 1). At higher flow velocities, predicted transport rates using this technique are substantially less than the measured rates described by the flume data of Table 1.

APPLICABILITY OF EQUATIONS TO MARINE FLOW

In the study of near-bottom flow regimes, two distinct modes of fluid motion are possible; a slowly varying current generated by the action of surface winds and tide, and the high frequency wave generated motion which promotes large-scale advective sediment movement only when flowing in conjunction with a superimposed unidirectional current (Komar, 1974). Wave activity was, of necessity, assumed to be minimal at the recording sites for the purposes of these calculations. Currents were measured with Savonius rotor-vane current meters which are unable to resolve swiftly oscillating wave generated bottom flow. Where wave activity is a significant component of near bottom flow, the effect on transport is not to be ignored. A model of sediment transport which incorporates both wave activity and longer period flows has been given by Madsen and Grant (1976).

While the assumption of no wave activity was forced by the current recording system, the neglect of wave activity does not, we think, invalidate the order of magnitude calculations reported in this paper. Aside from measurements made at the mouth of New York Harbor, most measurements were made in water on the order of 20 m or deeper. At those depths wave activity likely takes a subordinate role to storm induced events. At the Harbor mouth, tidal currents likely dominate wave motion.

A measure of the validity of the transport estimates made herein may be found in a comparison of predicted fluxes with transport estimates taken from a radioisotope sand tracer experiment performed in the New York Bight during the fall and winter of 1974–1975 (Lavelle *et al.*, 1977). That experiment consisted of near bottom current measurements at 10 minute intervals and triweekly surveys of tagged sand dispersal. Sediment threshold velocities were intermittently exceeded with a single storm event dominating transport. The tracer surveys bracketed identifiable transport events. Sediment flux calculations for two periods of transport were made using a plume model. Although the experimental configuration allowed only minimum values of the flux to be computed, they can serve as a rough check on the validity of the calculations discussed in this report. The tracer experiments and assumptions underlying tracer flux estimates are fully described in Lavelle *et al.* (1977).

Near bottom currents for intervals represented by the observed tracer dispersal patterns were used with the algorithms previously described. Measured near-bottom current data in periods November 12–25, 1974, and November 25–December 4, 1974, were introduced into each transport algorithm and the total sediment mass transport, |Q|, was computed. Scalar summation of each 10-minute flux prediction was deemed adequate in light of the similarity of transport directions during each interval. The drag coefficient was set to 3.0×10^{-3} (Sternberg, 1976) and a threshold velocity of 18 cm/s was selected.

Table 2 provides the results of those computations alongside tracer estimates. Tracer estimates in all cases are found to be within an order of magnitude of the

TABLE 2.—*Comparison of predicted sediment flux to those derived from tracer measurements.*

TRANSPORT INTERVAL	TRANSPORT DURATION	|Q| TRACER	|Q| BAGNOLD	|Q| EINSTEIN	|Q| YALIN
November 12–25, 1974	6.0×10^4s	3.2×10^{-3}	2.2×10^{-2}	8.8×10^{-3}	2.8×10^{-3}
November 25–December 4, 1974	1.7×10^5s	1.7×10^{-1}	2.2×10^{-1}	8.9×10^{-2}	2.3×10^{-2}

formulae predictions; the formulae predictions vary amongst themselves by as much as an order of magnitude. The scatter represented by the flux estimates in Table 2 should be seen in the light of flume measurements of sediment flux which can vary by an order of magnitude for similar flows (Guy, Simons, and Richardson, 1963).

The remaining assumption requiring discussion is that of the assignment of a value to the drag coefficient. Sternberg (1976) reports a mean drag coefficient value of 3.0×10^{-3} for small scale roughness elements (<20 cm) and for hydrodynamically rough flow ($U_{100} > 15$ cm/sec). Because threshold velocities in these calculations exceed 15 cm/sec and because bedforms in the Bight are 20 cm or less in height in most cases, a C_{100} value of 3.0×10^{-3} was used in all computations.

The assumption of that value is likely to be unfair only at the harbor mouth. Ludwick (1975) found a considerable range of values for C_{100} at the tidally controlled entrance to the Chesapeake Bay. Values of the drag coefficient were generally larger than the value adopted in this report, reflecting large scale roughness elements. Equation 5, which approximates the transport rate, shows that a larger value for C_{100} would lead to greater transport than predicted at the harbor mouth; transport direction would remain unchanged. The result is that true values of transport for the harbor entrance are at least as large as those calculated and reported here.

Formulae Application

For each 10-minute sampling interval of the current meter series, each velocity reading was transformed into a sediment transport rate, q, using the empirical formulae of Bagnold (Eq. 7), Einstein, and Yalin, as previously described. A unit vector in the direction of the near-bed fluid velocity was assigned the transport. These instantaneous transport vectors were vectorally averaged over an entire current meter record for each of the three approaches. In addition, sediment transport roses representing the number of occurrences and intensities along compass directions were also calculated.

Table 3 lists the sediment transport rates (gm cm^{-1} s^{-1}) at each current meter site derived from the three empirical approaches. The absolute transport rate, |Q|, was calculated by summing the scalar magnitude of the individual sediment transport events of each record with no regard to the direction of particle motion. Dividing this sum by the sampling length, T, yields an average rate of discharge that provides an indication of the total transport activity at each current meter location.

$$|Q| = \frac{1}{T} \int_0^T |\vec{q}|\, dt \tag{16}$$

The *net* transport rate, $\vec{Q}$, is a time-averaged vector sum calculated as follows:

$$\vec{Q} = \frac{1}{T} \int_0^T \vec{q}\, dt \tag{17}$$

where $\vec{q}$ is the sediment transport vector for each sampling interval. The net transport vector is reported in terms of magnitude and direction in Table 3. The threshold exceedance value, the percentage expression of the ratio of the number of sampling intervals in which threshold velocity was exceeded to the total number of samples, is also to be found in Table 3. The exceedance value is a measure of the transport activity at each location. It can be noted at this time that the directions of net transport (Table 3) calculated using the three methods shows good agreement; in 14 of the 18 locations, directional variance of the three net transport vectors is less than 10°.

TABLE 3.—*Sediment transport rates based on Bagnold, Einstein, and Yalin formulae for designated current meter locations.*

CURRENT METER	DURATION (DAYS)	MEAN GRAIN DIAMETER (mm)	THRESH-OLD VELOCITY (cm/s)	% OF TIME $U_{100} > V_{TH}$	BAGNOLD TRANSPORT RATES		EINSTEIN TRANSPORT RATES		YALIN TRANSPORT RATES	
					ABSOLUTE (gm/cm/s)	NET (gm/cm/s)	ABSOLUTE (gm/cm/s)	NET (gm/cm/s)	ABSOLUTE (gm/cm/s)	NET (gm/cm/s)
OCTOBER-DECEMBER 1973										
A	48.1	0.178	16.0	31.6	3.46×10^{-2}	3.18×10^{-2},347°	2.63×10^{-2}	2.19×10^{-2},347°	8.76×10^{-3}	7.85×10^{-3},348°
D	73.1	0.355	17.2	66.5	2.67	2.06 167°	2.19×10^{-1}	1.57×10^{-1},130°	8.33×10^{-1}	6.36×10^{-1},164°
I	5.5	0.395	17.8	81.8	7.83×10^{-1}	3.85×10^{-1},151°	4.46×10^{-2}	1.99×10^{-2},152°	2.88×10^{-1}	1.39×10^{-1},153°
J	8.0	0.505	19.0	90.5	8.02×10^{-1}	3.44×10^{-1},298°	7.34×10^{-2}	3.04×10^{-2},295°	3.21×10^{-1}	1.38×10^{-1},297°
K	48.3	0.418	18.0	9.5	2.44×10^{-3}	1.89×10^{-3},187°	1.09×10^{-3}	8.71×10^{-4},185°	1.09×10^{-3}	8.21×10^{-4},187°
R	26.1	0.378	17.8	43.0	8.46×10^{-3}	7.46×10^{-3},359°	4.55×10^{-3}	4.02×10^{-3},359°	3.69×10^{-3}	3.22×10^{-3},359°
F	29.5	0.430	18.5	0.4	1.65×10^{-6}	1.51×10^{-6},086°	4.72×10^{-7}	4.33×10^{-7},086°	1.73×10^{-6}	1.70×10^{-6},090°
L	17.0	0.220	17.0	17.1	4.98×10^{-4}	3.09×10^{-4},007°	1.29×10^{-3}	7.80×10^{-4},007°	2.29×10^{-4}	1.41×10^{-4},004°
APRIL-JUNE 1974										
CM1	60.2	0.290	17.5	24.8	4.55×10^{-3}	9.28×10^{-4},315°	3.94×10^{-3}	8.37×10^{-4},319°	1.70×10^{-3}	3.58×10^{-4},312°
CM2	60.8	0.502	19.0	3.0	6.59×10^{-5}	1.61×10^{-5},256°	1.29×10^{-5}	2.70×10^{-4},267°	4.78×10^{-5}	1.26×10^{-5},254°
CM3	61.6	0.560	20.0	3.2	6.31×10^{-5}	1.60×10^{-5},086°	1.01×10^{-5}	3.83×10^{-6},089°	4.97×10^{-5}	9.46×10^{-6},082°
CM5	60.9	0.420	18.5	1.3	2.09×10^{-5}	3.65×10^{-6},257°	9.11×10^{-6}	1.62×10^{-6},251°	1.44×10^{-5}	2.74×10^{-6},277°
CM6	33.0	0.149	15.8	7.3	1.40×10^{-4}	6.74×10^{-5},268°	6.71×10^{-4}	2.87×10^{-4},255°	5.69×10^{-5}	2.62×10^{-5},262°
CM7	43.0	0.345	17.3	32.2	1.49×10^{-2}	9.65×10^{-3},188°	6.52×10^{-3}	4.23×10^{-3},188°	6.19×10^{-3}	3.72×10^{-3},188°
CM10	50.1	0.490	19.0	1.5	8.58×10^{-5}	6.78×10^{-5},175°	2.62×10^{-5}	2.16×10^{-5},175°	5.02×10^{-5}	3.79×10^{-5},175°
CM11	21.9	0.210	16.5	1.7	5.17×10^{-5}	5.09×10^{-5},158°	3.99×10^{-4}	3.73×10^{-4},157°	2.19×10^{-5}	2.15×10^{-5},160°
CM12	78.7	0.116	15.5	6.0	1.71×10^{-3}	1.00×10^{-3},187°	2.71×10^{-3}	9.04×10^{-4},181°	3.82×10^{-4}	2.23×10^{-4},187°

RESULTS

Maps of Sediment Transport

The results of bedload sediment transport calculations within the New York Bight for the two periods, Fall, 1973, and Spring, 1974, are to be found in Figures 2 and 3, superimposed on a surficial grain size distribution plot (waste disposal sites are also designated). The arrow emanating from each circled current meter site is the net sediment transport vector computed via the Bagnold method (Eq. 7). The magnitude of each vector (gm $cm^{-1} s^{-1}$) is noted at the head of each vector to facilitate comparison.

Current roses adjacent to each location represent the directional distribution of all sediment transport vectors calculated at that site. The length of each radial bar is a measure of the average magnitude of transport within that direction class. Bar widths represent duration of events within each class. Exceedance values, not shown, range from less than 1% in offshore areas during fair weather flow regimes to 90% in the shoal regions adjacent to the New York Harbor entrance which are regularly subjected to intense tidal currents.

Sediment Transport in the New York Harbor Entrance

In the Fall of 1973 (Fig. 2), the high speed ebb and flood tidal currents at the entrance to New York Harbor resulted in the most intense sediment transport found in our study. Peak bottom current speeds of 80 cm/s are not uncommon here. The characteristic estuarine two-layer flow has been detected here (Duedall *et al.*, 1977); the less saline upper water flows seaward as the denser bottom water experiences residual landward flow. The interface of the two oppositely directed water masses appears to be tilted by the Coriolis effect so that the northern side of the entrance is flood-dominated while the southern side exhibits a seaward flow residual. Bathymetric surveys reveal the pattern of banks and channels that is characteristic of wide estuary mouths and which occurs as a consequence of the interfingering zones of ebb- and flood-dominated flow (Swift and Ludwick, 1976). In such areas, sand from littoral drift finds its way to the shoals that grow in the zones of nearly closed sand circulation between channels. Our data are not adequate to spatially resolve a transport pattern of this complex character. However, the apparent convergence of bottom sediment transport in the vicinity of Sandy Hook may be a reflection of such a transport pattern.

Sediment Transport at the Head of the Hudson Shelf Valley

Another interesting feature of sediment movement in the Bight is the relatively strong and frequent northward transport in the head of the Hudson Shelf Valley and again near the Christiaensen Basin during the Fall, 1973, period of current measurement. In Figure 4, data gathered during this study period show local wind conditions and current speed at the two locations, "K" and "A." Current velocity vectors are plotted for flow periods during which the threshold velocity is exceeded. Wind and current vectors represent direction towards which the wind and current are moving. The similar response of bottom water flow at the two sites is evident. During this eight-day autumn period, a southerly, or down-channel flow of bottom water and sediment occurs at times of sediment-entraining current speeds.

A subsequent eight-day record is presented in Figure 5. Up-channel flow occurs at this time with recorded bottom speeds in the Shelf Valley in excess of 40 cm/s. The shallow water meter located at site "K" records modest flow speeds with maximum values of only 22 cm/s. These up-channel transport events at site "A" correspond entirely to periods of winds exhibiting a strong westerly component. During such flow periods, bottom currents serve to transport sediments to the north at a comparatively high rate; indeed, for the entire fall study period, the sand transport occurring at a depth of 44 meters at site "A" has been computed to be 10 times greater than that at site "K," lying at a depth of 19 meters. In addition, during this period, sediment-entraining speeds existed 32% of the time at site "A," a frequency three times greater than at site "K."

In the Spring of 1974 (Fig. 5), sediment movement is directed to the south at the head of the Hudson Shelf Valley at an

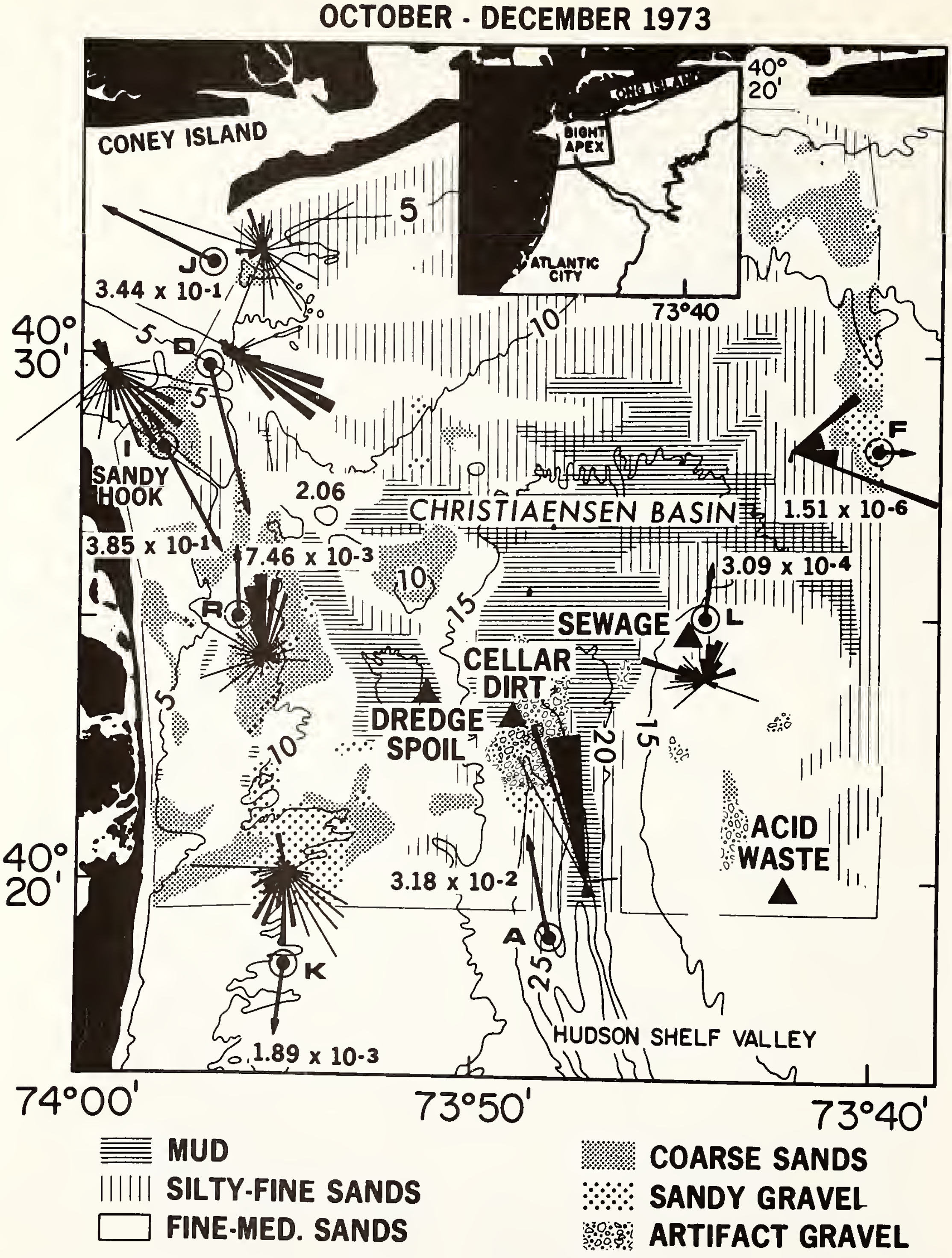
OCTOBER - DECEMBER 1973
CONEY ISLAND
LONG ISLAND
BIGHT APEX
ATLANTIC CITY
40° 20'
73°40
5
10
15
20
25
J
3.44 x 10-1
40° 30'
D
I
SANDY HOOK
2.06
3.85 x 10-1
7.46 x 10-3
R
CHRISTIAENSEN BASIN
1.51 x 10-6
F
3.09 x 10-4
L
SEWAGE
CELLAR DIRT
DREDGE SPOIL
ACID WASTE
40° 20'
3.18 x 10-2
A
K
1.89 x 10-3
HUDSON SHELF VALLEY
74°00'
73°50'
73°40'
MUD
SILTY-FINE SANDS
FINE-MED. SANDS
COARSE SANDS
SANDY GRAVEL
ARTIFACT GRAVEL

FIGURE 2.—Surficial sediment map of the New York Bight apex showing sand transport activity at various current meter locations for the Fall, 1973. Current roses represent directional distribution of the sediment transport events computed for each location using the Bagnold formula (Eq. 7). Radial bar length and width represent mean sediment transport rate and frequency, respectively, for each direction class. Arrow emanating from each current meter location reflects the resultant or vector sum, of all sediment transport events. Magnitude of net sediment transport rate (gm cm^{-1} s^{-1}) is noted at the head of each vector.

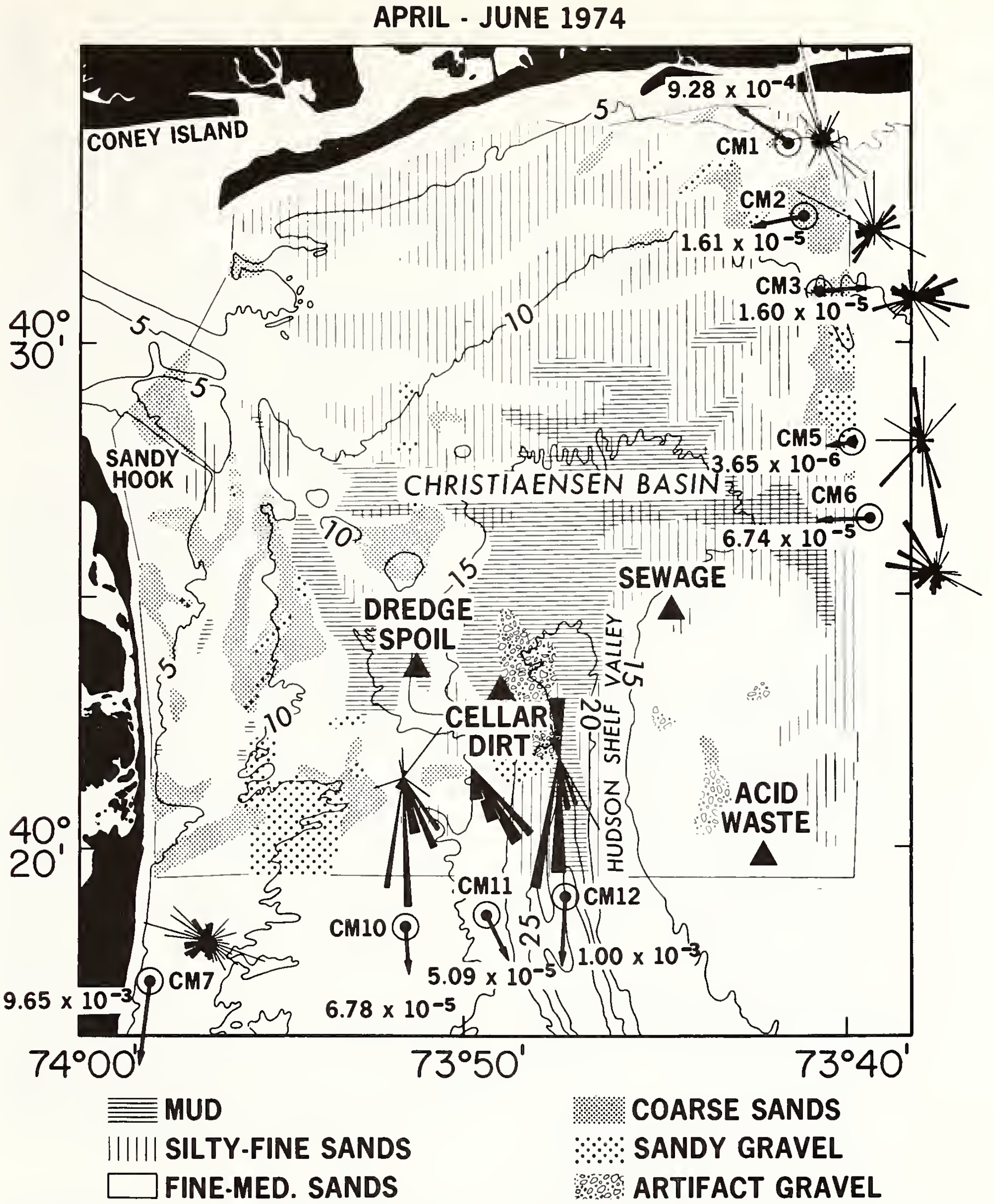
APRIL - JUNE 1974
CONEY ISLAND
SANDY HOOK
CHRISTIAENSEN BASIN
DREDGE SPOIL
CELLAR DIRT
SEWAGE
ACID WASTE
HUDSON SHELF VALLEY
CM1
9.28 x 10⁻⁴
CM2
1.61 x 10⁻⁵
CM3
1.60 x 10⁻⁵
CM5
3.65 x 10⁻⁶
CM6
6.74 x 10⁻⁵
CM7
9.65 x 10⁻³
CM10
6.78 x 10⁻⁵
CM11
5.09 x 10⁻⁵
CM12
1.00 x 10⁻³
5
10
15
20
25
40° 30'
40° 20'
74°00'
73°50'
73°40'
MUD
SILTY-FINE SANDS
FINE-MED. SANDS
COARSE SANDS
SANDY GRAVEL
ARTIFACT GRAVEL

FIGURE 3.—Sand transport activity at locations in New York Bight during Spring, 1974. See caption to Figure 2.

average rate that is approximately 97% less than that of the northward transport of the previous fall season. Sediment-entraining speeds were achieved with 20% the frequency of that observed in the Fall, however, the transport rate calculated in the *axis* of the Shelf Valley (CM12) exceeded those observed at sites CM10 and CM11 in the shallower waters to the west. This southerly flow of bottom water during the spring may be related to the high incidence of southerly surface winds which increase in the sea

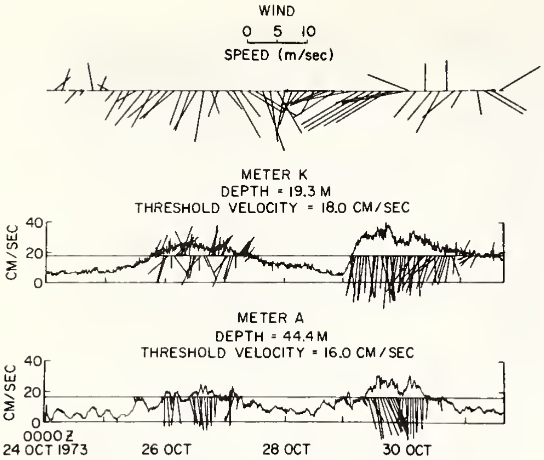

FIGURE 4.—Wind and bottom currents at Station K and A (Figure 2) for down-channel flow at the head of Hudson Shelf Valley. Wind velocity vectors point in the direction (degrees-true) towards which the wind was blowing. The jagged line represents current speed and associated vectors portray magnitude and direction of current when measured flow velocity exceeds threshold velocity for initiation of sediment motion.

surface elevation along the Long Island shore, promoting a downwelling flow.

It is clear that the Hudson Shelf Valley serves as an important avenue for the discharge of sediment both into and out of the Bight apex. An attempt is being made to predict the existence of up-channel flow along the axis of the Shelf Valley by noting the frequency of sustained westerly winds as measured at nearby Kennedy International Airport (Nelsen *et al.*, 1976). Analysis of wind data of the past three years suggests that major up-channel flow events occur approximately 25% of the time during the period from October through April. In the summer months (May-September) the frequency of such occurrences falls to 6% of the time. The question of which direction of sediment motion predominates in the Shelf Valley over extended periods of time is unresolvable, however, due to our inability to accurately transform wind stress at the sea surface to sediment transport activity at the seabed.

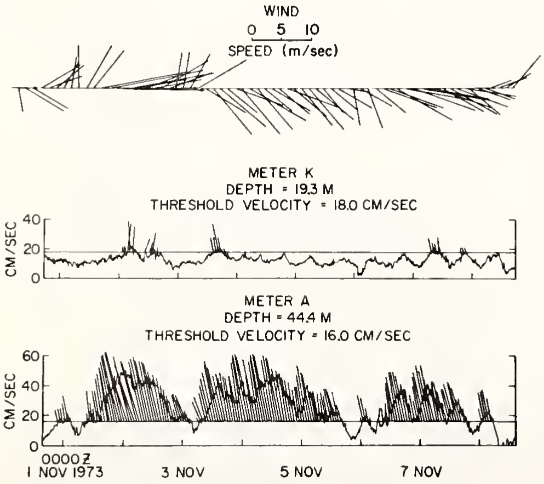

FIGURE 5.—Wind and bottom currents at Station K and A (Figure 2) showing up-channel flow at the head of the Hudson Shelf Valley.

Long Island Transect

A current meter transect extending to the south from Long Island during the spring of 1974 (Fig. 3) generally shows net westward sediment flux at modest rates which decrease with depth. The reversal of transport direction of meter CM3 from the general counterclockwise sediment flow is enigmatic.

A seabed drifter study of the Middle Atlantic Bight (Bumpus, 1965) indicates the tendency of the net near-bottom flow in this region to be directed to the west and south with an on-shore velocity component, although high variability in time and space effectively mask this residual flow. Analysis of flow conditions of the Spring, 1974 (Fig. 3), show agreement with this observation. Charnell and Mayer (1975) note a general clockwise gyral circulation pattern in the Bight, in agreement with our findings during the Fall of 1973 (Fig. 2). This apparent contradiction to conclusions reached by Bumpus (1965) serves to substantiate the high variability of near-bottom circulation that exists in the Bight apex due, in part, to the influence of the Hudson Shelf Valley.

Nearshore Sediment Transport

During the springtime survey, the current meter closest to the Long Island coastline revealed a strong onshore component of sand transport due possibly to wind-induced upwelling. The landward-directed asymmetry of bottom wave surge may be present as well; however, this mode of transportation cannot be recognized by our measurement technique. The meter located closest to the

New Jersey coastline during this period of time provides evidence of southerly-flowing alongshore sediment flux. Examination of the current roses of these nearshore meters shows wide directional scatter which may be due to inadequate directional response of the sensor to high frequency wave activity. As a result, we place limited credence in our net transport determinations at these locations.

Representativeness of the Estimates

General statements concerning bottom water circulation patterns and resulting sediment movement must be made with caution. The effect that an extraordinary flow event has over general sediment circulation was seen during the course of the radioisotope sand tracer experiment previously described (Lavelle *et al.*, 1977). Based on current meter information gathered in the Fall of 1973, a prediction of residual eastward transport prediction for that time of year would result. While eastward transport was inferred through the course of the tracer experiment, a "northeaster" of two days duration dominated sand transport activity. Bottom material at a water depth of 20 m was transported a distance of 1500 m westward during the storm event. In terms of beach erosion, this particular storm was considered the worst to impinge upon the south shore of Long Island since the devastating "Ash Wednesday" storm of 1962 (C. Galvin, Coastal Engineering Research Center, personal communication).

Because prediction based on 1973 current data differed from true transport during winter 1974, the results presented here must be considered typical of these seasons and areas only to the extent that the measured flow regimes were typical.

CONCLUSIONS

Rates of bottom sediment transport have been calculated based on substrate grain size and near-bottom current meter observations. Because the calculated transport rate for a particular location can be biased by the choice of threshold speed as well as the functional dependence on velocity, and because subtle spatial and temporal structure was not resolved by the current recording system, fine detail within our results should be taken lightly. However, four broad conclusions resulting from the calculations appear to be independent of the model parameterization.

1) Intense and near continual bedload transport exists at the New York Harbor entrance.

2) Ebb-directed transport occurs in the central channel of the Harbor entrance.

3) Sediment was transported to the north (up-channel) at the head of the Hudson Shelf Valley during the Fall of 1973, coincident with periods of high speed, sustained westerly winds.

4) Net down-channel sand transport of moderate intensity, with substantially less frequency relative to the previous autumn, likely occurred at the head of the Shelf Valley during the spring of 1974.

ACKNOWLEDGEMENTS

The current meter data utilized in our calculations are part of an extensive program of current measurements initiated in the New York Bight in 1973 by NOAA's Miami-based Physical Oceanography Laboratory.

Support for this project has come from the New York Bight Marine Ecosystems Analysis Program of NOAA.

REFERENCES

Bagnold, R. A., 1941, The physics of blown sand and desert dunes: Methuen and Company, London, 265 p.

———, 1956, The flow of cohesionless grains in fluids: Phil. Trans. Roy. Soc. London, v. 249, p. 234–297.

———, 1963, Mechanics of marine sedimentation: *In* Hill, M. N. (*ed.*), The sea, Interscience Publ., p. 507–582.

Bumpus, D. F., 1965, Residual drift along the bottom on the continental shelf in the Middle Atlantic Bight area: Limnol. and Oceanogr., v. 10, Suppl., p. R50–R53.

Charnell, R. L., and D. A. Mayer, 1975, Water movement within the apex of the New York Bight during the summer and fall of 1973: NOAA Tech. Memo. ERL-MESA-3, 29 p.

Colby, B. R., 1964, Discharge of sands and mean-velocity relationships in sand-bed streams: Geol. Surv. Prof. Paper 462-A, 47 p.

Dealteris, J. T., J. R. Roney, L. E. Stahl, and C. Carr, in press, A sediment transport study, offshore New Jersey: Proc. Ocean Eng. III Conf., ASCE.

Duedall, I., H. B. O'Connors, J. B. Parker, R. Wilson, W. Miloski, and G. Hules, 1977, The abundances, distribution, and flux of nutrients and chlorophyll α in the New York Bight apex: Estuanine and Coastal Mar. Sci., v. 5, p. 81–105.

Einstein, H. A., 1950, The bedload function for sediment transportation in open channel flows: Tech. Bull. 1026, U.S. Dept. Agriculture, 71 p.

Graf, W. H., 1971, Hydraulics of sediment transport: McGraw-Hill, New York, 513 p.

Guy, H. P., D. B. Simons, and E. V. Richardson, 1966, Summary of alluvial channel data from flume experiments 1955–1961: Geol. Surv. Prof. Paper 462-I, U.S. Govt. Printing Office, 96 p.

Inman, D. L., G. C. Ewing, and J. B. Corliss, 1966, Coastal sand dunes of Guerrero Negro, Baja California, Mexico: Geol. Soc. Amer. Bull., v. 77, p. 787–802.

Kachel, N. B., and R. W. Sternberg, 1971, Transport of bedload as ripples during an ebb current: Mar. Geol., v. 10, p. 229–244.

Komar, P. D., 1974, Transport of cohesionless sediment on continental shelves: *In* Stanley, D. J., and D. J. P. Swift (*eds.*), The new concepts of continental margin sedimentation, II, sediment transport and its application to environmental management, Amer. Geophys. Inst., p. 215–267.

Lavelle, J. W., P. E. Gadd, G. C. Han, D. A. Mayer, W. L. Stubblefield, D. J. P. Swift, R. L. Charnell, H. R. Brashear, F. N. Case, K. W. Haff, and C. W. Kunselman, 1976, Preliminary results of coincident current meter and sediment transport observations for wintertime conditions on the Long Island inner shelf: Geophys. Res. Letters, v. 3, p. 97–100.

———, D. J. P. Swift, P. E. Gadd, W. L. Stubblefield, F. N. Case, H. R. Brashear, and K. W. Haff, 1977, Fair weather and storm sand transport on the Long Island inner shelf: unpublished report.

Ludwick, J. C., 1974, Tidal currents and zig zag sand shoals in a wide estuary entrance: Geol. Soc. Amer. Bull., v. 85, p. 717–726.

———, 1975, Variations in the boundary-drag coefficient in the tidal entrance to Chesapeake Bay, Virginia: Mar. Geol., v. 19, p. 19–28.

Madsen, O. S., and W. D. Grant, 1976, Sediment transport in the coastal environment: Report No. 209, Dept. Civ. Eng., Mass. Inst. Tech., 105 p.

Nelsen, T. A., P. E. Gadd, and T. Clarke, 1976, Wind induced current flow in the New York Bight apex: a possible predictor of contaminant dispersal: unpublished report.

Nordin, C. F., Jr., 1975, Field data to calibrate mathematical models for sediment transport in unsteady flow: EOS, Trans. AGU, v. 56, p. 981.

Sternberg, R. W., 1972, Predicting initial motion and bedload transport of sediment particles in the shallow marine environment: *In* Swift, D. J. P., D. B. Duane, and O. H. Pilkey (*eds*), Shelf sediment transport: process and pattern, Dowden, Hutchinson and Ross, Stroudsburg, Pa., p. 61–82.

———, 1976, Measurements of boundary-layer flow and boundary roughness over Campeche Bank, Yucatan: Mar. Geol., v. 20, p. M25–M31.

Swift, D. J. P., and J. C. Ludwick, 1976, Substrate response to hydraulic process: grain size frequency distributions and bed forms: Ch. 10, *In* Stanley, D. J., and D. J. P. Swift (*eds*), Marine sediment transport and environmental management, John Wiley and Sons, New York, p. 159–196.

Yalin, M. S., 1963, An expression for bed-load transportation: Jour. Hydraulics Div., Proc. Amer. Soc. Civ. Eng., p. 221–250.

Sedimentology 25, 823-842.

Fair weather and storm sand transport on the Long Island, New York, inner shelf

J. W. LAVELLE,* D. J. P. SWIFT, P. E. GADD,
W. L. STUBBLEFIELD, F. N. CASE,†, H. R. BRASHEAR†
and K. W. HAFF†

NOAA/Atlantic Oceanographic and Meteorological Laboratories,
15 *Rickenbacker Causeway, Miami, Florida* 33149, *U.S.A.* and
†*Oak Ridge National Laboratory, P.O. Box X, Oak Ridge,*
Tennessee 37830, *U.S.A.*

ABSTRACT

Both spring–summer and fall–winter sand transport have been observed on the Long Island, New York, inner shelf at water depths of 20–22 m using a radioisotope sand tracer system. The extent of dispersal of the tagged, fine sand was measured at 3 week intervals in two 70 day experiments. In the late spring and early summer, movement was primarily diffusive in nature, extending 100 m around the line of tracer injection, while late fall–winter patterns had strong advective features, including an ellipsoidal outline extending approximately 1500 m westward of the injection points after the passage of several storms with strong northeasterly winds. Near-bottom current observations made with Savonius rotor sensors identify the event responsible for the bulk of the transport over the 135 day observation period as a storm flow of 2 days duration. Tracer and current observations together suggest that westward winter storm flow along the Long Island shelf is the major mechanism of sand transport at these depths on a yearly time scale. A least-squares fit of several of the observed winter patterns with a plume model yields average sediment mass flux lower bounds of $3{\cdot}2\times 10^{-3}$ gm/cm/sec and $1{\cdot}7\times 10^{-1}$ gm/cm/sec for 'typical' and extreme winter storm activity.

INTRODUCTION

Two experiments were conducted on the Long Island, New York, inner shelf during 1974–1975 which were designed to examine the movement of bottom sediment at a depth of 20–22 m. Each experiment had the same operational form: indigenous fine sand was tagged with a radioisotope and released on the bottom, and its dispersion was traced at 3 week intervals with a bottom-towed detection system. Additionally, near-bottom currents were measured in the vicinity of the tracer work several times each hour over the duration of each experiment. The sediment dispersion data were gathered to examine the spatial extent of the sand transport, and the current data were gathered to infer the temporal structure of the observed movement. The purpose of the experiment was threefold: to qualitatively characterize the strength, direction, and frequency of sand transport; to estimate the sediment mass flux during times of transport; and to examine the influence of local bathymetric features on transport patterns. Because appreciable seasonal dependence of sediment movement had been anticipated, the experiments were timed so that one would take place during a relatively fairweather period, while the other was designed to investigate the sediment and near-bottom fluid movement associated with the more severe late fall and early winter storm activity. A preliminary report describing some of the results of the fall–winter experiment has already been made (Lavelle *et al.,* 1976).

---

*Present address: NOAA/Pacific Marine Environmental Laboratory, 3711 15th Ave. N.E., Seattle, Washington 98105.

Shelf sediment tracer studies have generally been confined to areas where surface wave activity has played an important role. Examples are the studies of Inman & Chamberlain (1959), Komar & Inman (1970), and Duane (1970a). In the latter two, observations of longshore transport were made with transects of tagged material extending from the beach through the surf zone. In the immediate nearshore, the magnitude and direction of wave activity were shown to control the strength and direction of transport. In deeper water where surface wave activity may be expected to play a decreasing role in near-bottom fluid movement, the time scales of movement may lengthen to roughly those of strong meteorological events which could cause bottom currents of sufficient strength to move sediment. Depth of water alone does not determine the hydraulic environment, however; fluorescent tracer work of Vernon (1966) off the California coast showed short term sediment movement at 30 m depth was decidedly wave-influenced. A good review of tracer work in the nearshore environment has been provided by Ingle & Gorsline (1973).

The study presented here differs from previous tracer studies in that sediment movement was not expected to be wave dominated. The long term observations of these experiments show that advective sediment transport along this coast and at these depths occurs only intermittently and in response to storm flows. The data also show that the dominant sediment transport event occurred during the same time interval as the most significant mean flow event in the current record. Because current velocities were 50% larger during that flow event than recorded at any other time during the fall–winter experiment, and because sediment flux increases non-linearly with increases in flow (e.g. Guy, Simons & Richardson, 1966), most of the observed transport has been associated with a single storm event. The storm was characterized by strong northeasterly winds.

Tagged sediment transport rates for several storm events have been quantified using a plume model description of the data. This analysis approach is similar to that used in flume measurements of sediment discharge (Russell, Newman & Tomlinson, 1963), and for calculation of littoral drift rates (Rance, 1963), although the circumstances of transport in the experiments reported here are considerably different from those two investigations. Such a model requires fixed locations for tracer sources which, within experimental accuracy, is suggested by the data of these experiments. Although the transport during an actual event is time varying, event-averaged quantities are used in this analysis to describe the sediment movement. During a sand transport event, material was therefore hypothesized to be emitted from source points in a constant and continuous manner and advected downstream, much in the manner of smoke from a stack in a wind. Constant emission rate and advection velocity estimates, and consequently tagged material flux estimates, were calculated from the data. Because total sediment flux must be equal to or greater than tagged material flux, the tracer data have been used to estimate lower bounds to the average mass flux of sediment for the events represented by the tracer observations.

As regards the last experimental goal, the influence of local bathymetric features on the transport of sediment was found in a single tracer survey; a minor limb of a tracer plume was found to be oriented along the axis of coastline–oblique ridge and trough topography.

METHODS

To provide a tagged sample representative of the composition and form of material in the experimental area, sand used in the study was extracted from grab samples taken in the New York Bight. The sand was sieved to produce a sample with a size distribution that was roughly Gaussian, with a mean diameter of 0·15 mm, a standard deviation of 0·03 mm, and no material larger than 0·25 mm or smaller than 0·06 mm. The narrowness of the size distribution reflects the attempt to reduce as much as possible the effects of differential sorting of the tagged sample by the currents. The variation between the critical entrainment stresses at the mean grain size and at one standard deviation from the mean grain size is less than 10% (Bagnold, 1963), resulting in at most a 5% variation (approximately ±1 cm/s) about the threshold velocity mean (approximately 18 cm/s) for the bulk of the sample. After sieving, the material was washed with 2N HCl to remove carbonates and other acid soluble components; the residual material was composed primarily of quartz and feldspar.

Isotope preparation and sediment tagging was performed at Oak Ridge National Laboratory. Ten Curies of the isotope Ruthenium (^{103}Ru) were used to surface coat approximately 590 g of indigenous sand; the isotope has a half life of 39·8 days. The tagged sand was washed after tagging and the wash checked for soluble ^{103}Ru activity. Laboratory leach tests conducted for periods of up to 90 days in both quiescent and agitated solutions showed total loss of activity to be less than 0·1%.

After tagging, the sand was divided into thirty-six parts for convenience in handling and was packaged in small water soluble bags, each of which had a volume of roughly 11 cm^3. Under laboratory tests at water temperatures known to exist in the Bight, the bags dissolved in 15 min. The bags were released over the side from a shielded container at the experimental site.

Once the tagged material had been reintroduced onto the bottom, surveys of the induced radioactivity were made with the Radioisotope Sand Tracing (RIST) system (Case, Acree & Brashear, 1971; Duane, 1970b). This system uses a bottom-towed detector consisting of a sturdy meshed cylindrical housing for scintillation crystals and photomultiplier tubes, the signals from which are brought on board through an electromechanical towing cable. Since the detector itself has a mass of nearly 250 kg, at slow survey speeds (~1·5 m/sec) the detector rests on or rolls across the bottom. The distance of the detector from the bottom is thereby fixed, eliminating the effect of a variable radiation path length through the water column. The swath width of the detector is approximately 1 m. In these experiments, the radiation count rate and the position of the ship were recorded at two-second intervals on magnetic tape. The position of the survey vessel was determined by a Raydist navigation system which has ±10 m resolution (Jeffers, 1960). Survey dates and survey durations are listed in Table 1.

Laboratory processing of the radiation data consisted of: calculating each radiation sample position based on the ship's position at the time of measurement; subtracting low level background radiation from each count-rate; and amplifying the resultant count-rates by an exponential radioactive decay correction factor. Contour patterns herein represent strengths of radioactivity corresponding to injection-day levels.

Table 1. Survey date, duration, and assigned positional calibration error

Survey	Date	Duration (h)	East–west calibration error (m)	North–south calibration error (m)
EXP I–1 (Fig. 2a)	24 April 1974	2·5	20	0
EXP I–2 (Fig. 2b)	26 April 1974	4·5	0	0
EXP I–3 (Fig. 2c)	16 May 1974	12·2	20	0
EXP I–4 (Fig. 2d)	11 June 1974	11·6	0	−10
EXP I–5 (Fig. 2e)	2 July 1974	11·8	−30	50
EXP II–1 (Fig. 5a)	25 November 1974	6·7	0	0
EXP II–2 (Fig. 5b)	17–19 December 1974	6·9	−10	−10
EXP II–3 (Fig. 5c)	10 January 1975	4·7	−60	−60
EXP II–4 (Fig. 5d)	27 January 1975	6·1	0	0

The position of a radiation measurement was calculated from the recorded ship's position, ship's heading, the distance of towing tie point to the ship's Raydist antenna, the average depth of water, and the cable length. The sample location was the locus of a circle, the radius of which was the effective cable length (depth corrected) centred at the tie point, and the line joining the previous sample location and tie point. Cable length varied, but was typically 107 m. Attention to this detail was found to be important; for example, in the spring–summer experiment the width of the dispersal pattern was on the same order as the cable length.

Although the relative horizontal position of the detector during each survey could be determined with a precision of ±10 m, absolute locations could be determined only within the accuracy of the initial calibration of the Raydist system, accomplished with sextant fixes on landmarks, Ambrose Light Tower, or in several cases (as required by sea or weather conditions), buoys at known locations. The assignment of absolute locations to the radiation sample points is uncertain to the extent of error incurred in such calibration. One possible measure of calibration error is the translation distance which would bring the apparent maxima of each dispersion pattern in each experiment into coincidence. The average distance to do so is approximately 20 m (Table 1).

We believe that the offsets of Table 1 do in fact reflect navigational calibration error, and consequently that the points of highest tracer concentrations in each experiment are stationary. That conclusion is based on the lack of recognizable advective features in the spring–summer experiment, the coincidence of highest concentration points during the fall–winter first and last surveys, and the lack of a systematic explanation to the offsets in the current data. The absolute locations for each survey were therefore adjusted by the distances in Table 1.

Low level background radiation was subtracted from the sampled radiation values before decay corrections were applied. In the spring–summer experiment, background radiation levels in the source area were computed by interpolation from data taken on the periphery of the drop points the day of isotope release. The first survey of the area began within 2 h of the tracer release and encompassed an area of 400 m (N–S) by 1 km (E–W) around the drop points. Background in an area of 140 m (N–S) by 350 m (E–W) in the vicinity of the source line was constructed by interpolation. Background levels varied smoothly from 120 counts/sec at the western edge of the survey to 30 counts/sec on the eastern edge. Radiation levels at the source points were of the order of 10^6 counts/sec. In the fall–winter experiment, a pre-injection survey was used to determine background levels. Background levels showed less spatial variation than during the spring–summer experiment; the mean background value of the second experiment was approximately 100 counts/sec.

Each datum was compared to the background activity mean plus two background standard deviations (approximately 50 counts/sec). If the datum was larger, the mean background value was subtracted. Otherwise, the measurement was given a value of zero. Values were corrected for decay with the factor $e^{\alpha T}$, where T was the elapsed time in days from the day of isotope release and where α had the value 0·0174/day.

The resulting radiation values from each survey were smoothed by reducing the entire measurement set to values on a square grid. Each grid value represented the arithmetic mean of all radiation falling within a grid unit area about the grid point. Data points were gridded to 10×10 m and 20×20 m for the two experiments respectively. Grid units where no survey data had been taken were filled by evaluating a weighted average of neighbouring grid points. The weighting function was an exponential with an e-folding distance of one grid unit. This procedure was checked against the results of manually estimating grid points based on neighbouring data, and no significant difference in the contoured patterns could be observed. The contour plots were made using standard machine contouring techniques.

Count rate values as represented in the contour plots can be converted to mass units (g/m^2) through the equivalence

$$3{\cdot}6 \times 10^6 \text{ counts/sec} = 1 \text{ g/m}^2.$$

This equivalence is based on the observations: (1) at the time of injection, the tagged sample was composed of approximately 590 g of sand on which 10 Ci of ^{103}Ru had been affixed; (2) the efficiency of the detector for ^{103}Ru is essentially unchanged from that measured with ^{198}Au based on theoretical considerations; and (3) the detector calibration with ^{198}Au showed that $2{\cdot}5 \times 10^4$ counts/sec represent 1 μCi/m^2 (Case *et al.*, 1971). The effect of tracer burial on the equivalence above and on the transport rates is to be discussed later.

Aanderaa RCM-4 Savonius rotor current meters recording instantaneous direction and integrated average speed at 10 min or 20 min intervals were taut-wire moored in the vicinity of each tracer experiment. Near-bottom currents were measured approximately 150 cm from the bed. Although both experiments were conducted in approximately 20 m of water where wave activity was expected to be small, some directional scatter was observed in instantaneous direction measurements at isolated periods in the current records. Although directional variance was generally not large at those times, the absolute accuracy of the speed measurements is held suspect. Current speeds reported herein are therefore thought to represent only a reasonably fair measure of the near-bottom fluid motions during the experiment. Directional scatter has been eliminated in the data presented by data windowing (Bath, 1974).

TRACER AND CURRENT OBSERVATIONS

Spring–Summer experiment

Both experiments reported here were conducted near the apex of the New York Bight. The location and bathymetry of the spring–summer experimental area is given in Fig. 1. The experimental site was located toward the upper eastward edge of the Christiaensen Basin, at the head of the Hudson Shelf Valley. Positions of near-bottom

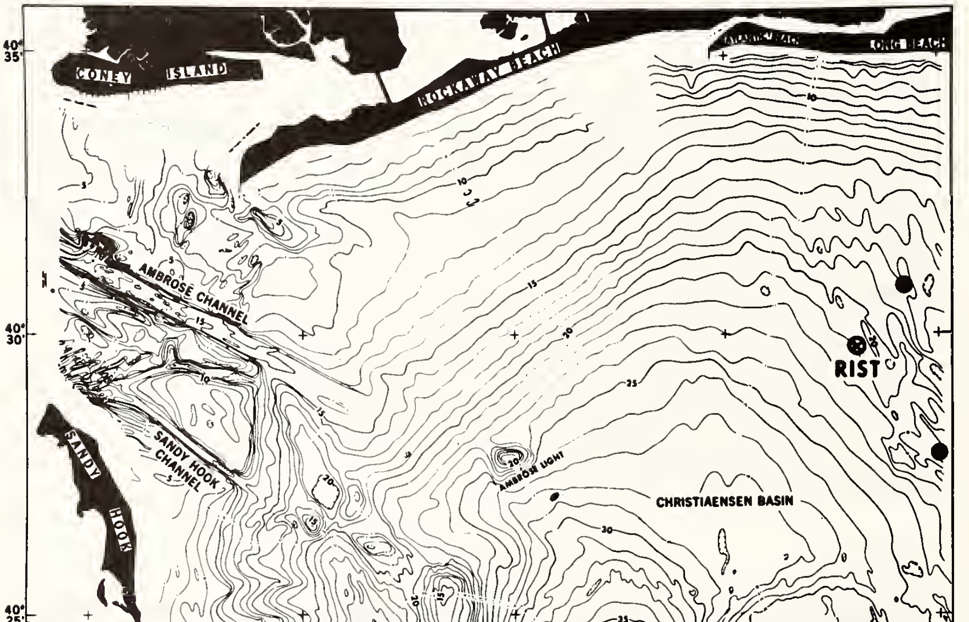
40° 35'
40° 30'
40° 25'
40° 20'
CONEY ISLAND
ROCKAWAY BEACH
ATLANTIC BEACH
LONG BEACH
AMBROSE CHANNEL
SANDY HOOK CHANNEL
SANDY HOOK
AMBROSE LIGHT
RIST
CHRISTIAENSEN BASIN
CHOLERA BANK
HUDSON SHELF VALLEY
LONG I.
NEW YORK BIGHT
CONTOURED IN METERS
74° .0'
73° 55'
73° 50'
73° 45'
73° 40'

Fig. 1. Location of the spring–summer sand tracer experiment (RIST) and current meter locations (●).

current meters are marked by solid dots. Prior current observations indicated that the area is sometimes subject to a relatively strong current moving up the Hudson Shelf Valley and then eastward (Charnell & Mayer, 1975). The area has considerable surficial grain size variability, being very coarse to the east and fining to the west into the muddy fine sands of the Basin.

Contours of the radiation levels representing the dispersion of the tagged sand during the spring–summer experiment are shown in Fig. 2. Isolines are drawn at logarithmic intervals. The 3·0 isoline represents 1000 counts above background measured over a 2 sec period, the integration interval of the detector.

To verify the initial tracer configuration, the initial survey of the experiment began within 2 h after the tracer injection. The tagged material was released overboard during a 4 min interval with the ship adrift before a moderate northwest wind, resulting in a line source of material of about 100 m length. The nature of the source causes the northwest–southeast lineation visible in each pattern. The source was spread to enhance the detection probability on the day of the injection. The time sequence shows diffusive growth of the pattern but little advection is apparent.

The lowest contour in these patterns (2·5 isoline) represents decay corrected radiation of roughly 160 counts/sec. Because of the enhancement by the decay correction factor, the lowest contours in the last panels represent data which were much

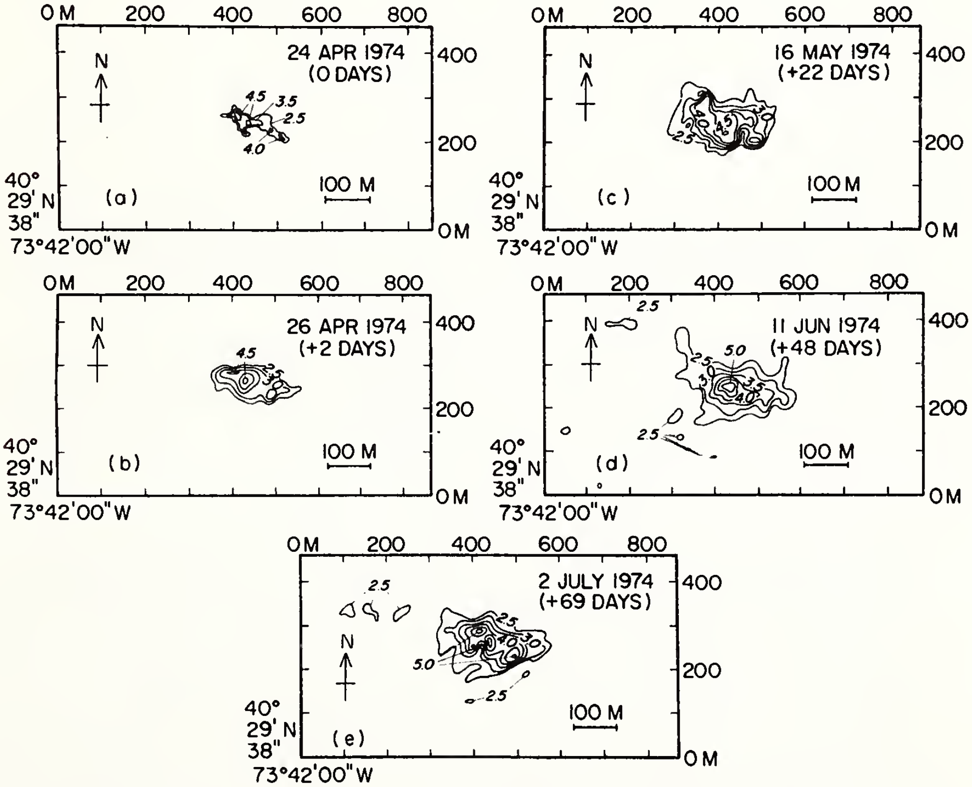

Fig. 2. Sequence of tracer dispersal patterns measured in the spring–summer experiment. Contoured values represent the measured count rate over a two second accumulation interval on a common logarithmic scale. Initial source configuration was a line.

closer to the background radiation mean plus two standard deviations than the lowest contours of the first several panels. The isolated islands of data, therefore, may not be real. No contours greater than five are shown in the diagram because the use of a grid to smooth the data has reduced larger peaks. Finer grid resolution was not possible with the available number of data points. Source points were too localized to be identified satisfactorily with the detector. The relative stability of the size of the dispersal patterns with time may reflect a decrease of near bottom turbulence activity during the summer months.

Figure 3 represents a plot of current speeds measured at 40°31·0′ N, 70°40·7′ W, about 0·6 km from the drop site. The meter was positioned 1·5 m from the bottom and recorded over the first 61 days of the experiment at a 10 min interval. The mean for the current record was 10·7 cm/sec; currents did not exceed 29 cm/sec. The diffusive nature of the patterns and the strength of the observed currents are consistent with an entrainment threshold for 0·15 mm sands near 20 cm/sec.

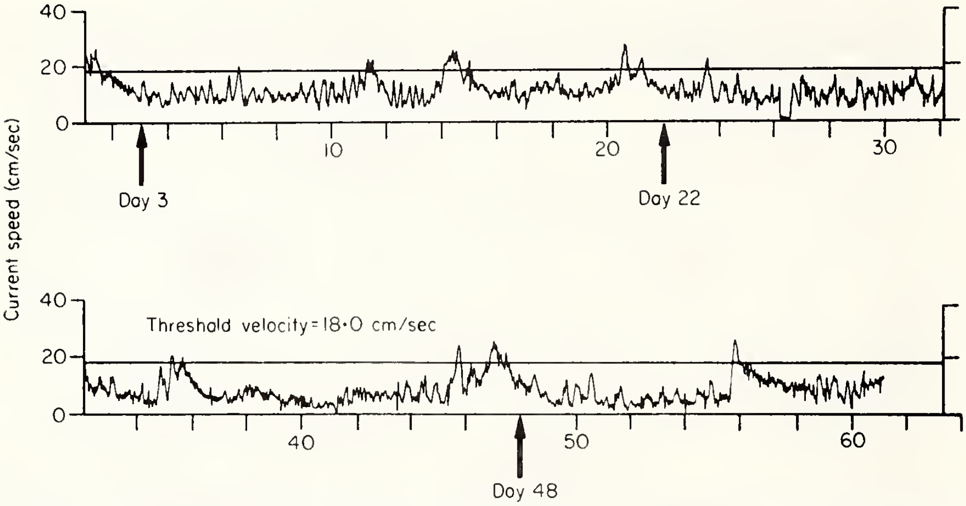

Fig. 3. Near-bottom current speeds recorded at 40°31·0′ N and 73°40·7′ W during the spring–summer experiment, with an estimated threshold velocity of 18 cm/sec superimposed. Survey days are marked with arrows.

Fall–Winter experiment

The fall–winter study (Fig. 4) was centred at 40°33′ N and 73°25′ W, halfway between Jones and Fire Island Inlets, Long Island, New York, some 9 km offshore. The study area, an 8 × 10 km rectangle, was located in an area of undulating morphological features described in Duane *et al.* (1972) as ridge and swale topography. Such topography is widespread on the North American Atlantic continental shelf (Swift, Duane & McKinney, 1973). Bedforms have wave-lengths of approximately 1 km with wave heights of 4–7 m, trend obliquely toward the shoreline, and are composed of relatively clean, medium to fine sands. Figure 4 shows also that the shoreline trends 75° true as measured by the shoreface isobaths between Jones and Fire Island Inlets, and that the trough axis trends slightly to the west-northwest. The ridges are asymmetrical with steeper southwest-facing flanks.

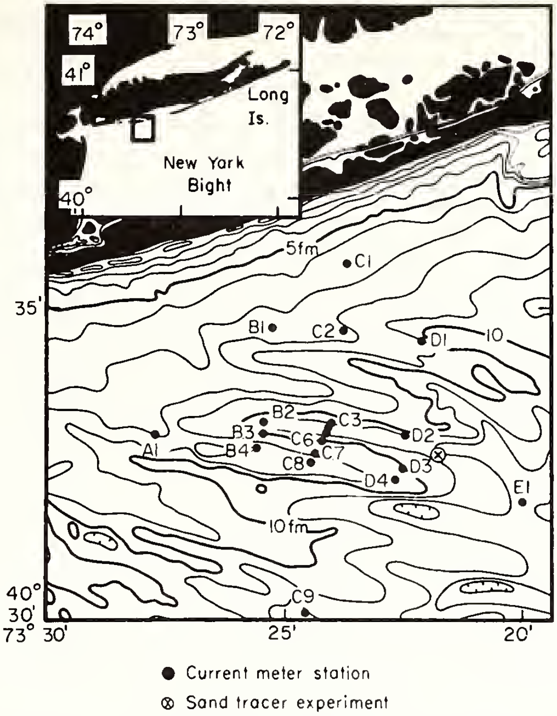

Fig. 4. Bathymetry and current meter station locations for the fall–winter sand tracer and flow field experiments. Data from C5, 1·5 m from the bottom, is used in this report.

The sequence of measured dispersion patterns from the fall–winter experiment is found in Fig. 5. On 12 November 1974, equal portions of tagged sand were released in a triangular array of points at the east end of the main trough of the ridge and swale systems. The equilateral array had sides whose length measured approximately 100 m. As a result of this initial configuration, more shore-normal transport is suggested by the patterns than actually occurred. Weather prevented a survey of the source immediately following injection.

The first pattern, measured 13 days after the drop, shows advective ellipsoidal contours trending east of the source points by nearly 200 m. That panel is enlarged in Fig. 6a. By the time a second survey had been made, there had been an increase in the transport volume and a reversal of transport direction (Fig. 5b). As measured by the 3·0 contour isolines, the material was found as far westward as 1500 m. The 2·5 isoline is not plotted in the diagram because of insufficient sampling in the downstream direction in Fig. 5b to adequately reconstruct the full pattern.

Detail within the central portion of Fig. 5b is probably not real. Note that the general pattern of the source configuration is maintained in Fig. 5b, c and d. With all three panels overlaid, the breakup in the central portion of Fig. 5b seems more likely attributable to insufficient sampling density than to actual central pattern detail. Figures 5c and d also suggest through their orientation and intensities that they represent the vestige of sediment movement first detected in the previous survey (Fig. 5b). No appreciable lateral sediment movement subsequent to the December

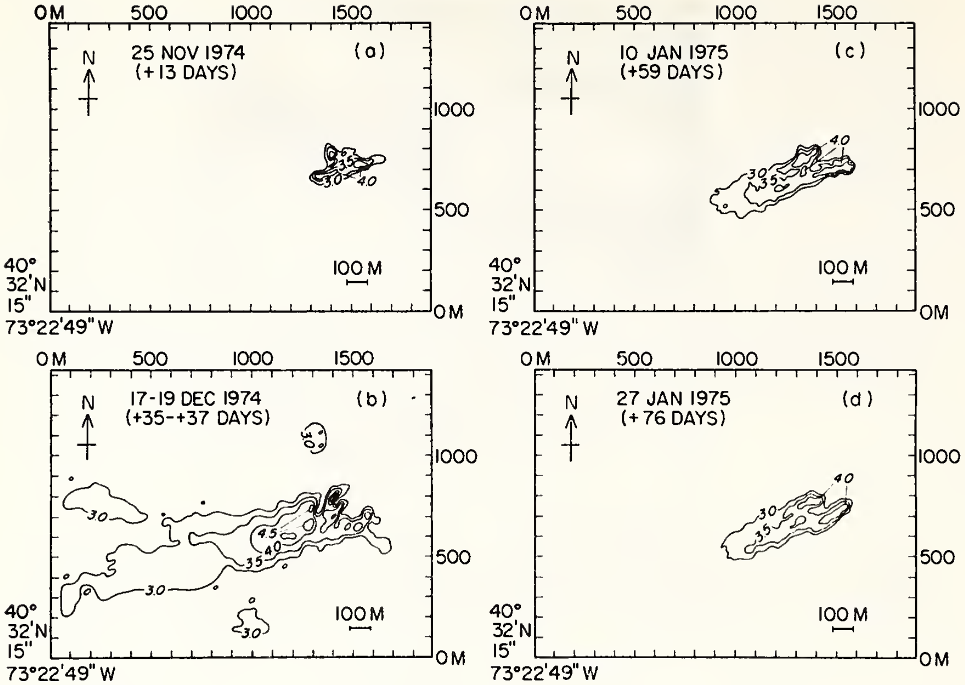

OM 500 1000 1500
N
25 NOV 1974
(+13 DAYS)
(a)
17-19 DEC 1974
(+35-+37 DAYS)
(b)
10 JAN 1975
(+59 DAYS)
(c)
27 JAN 1975
(+76 DAYS)
(d)
1000
500
OM
100 M
3.0
3.5
4.0
4.5
40° 32'N 15"
73°22'49" W

Fig. 5. Dispersion patterns of tracer during the fall–winter experiment. Intensity is scaled as in Fig. 2. The initial configuration was that of a triangular array of point sources separated by roughly 100 m.

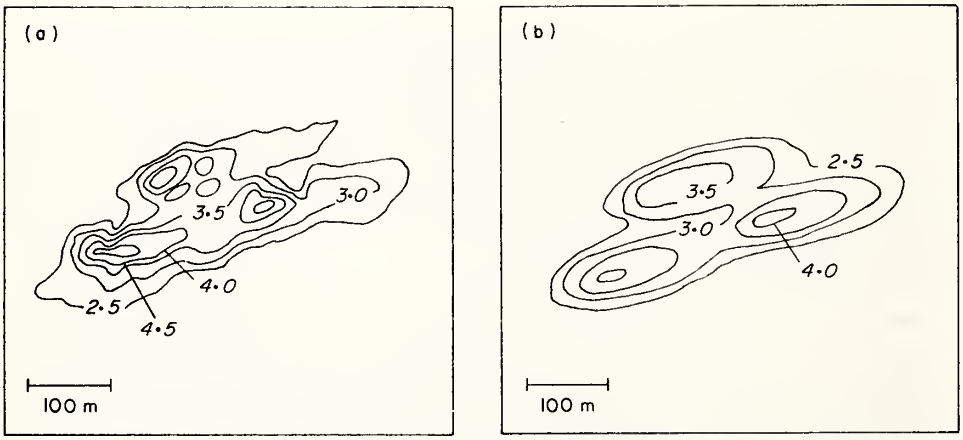

(a)
3·0
3·5
4·0
2·5
4·5
100 m
(b)
2·5
3·5
3·0
4·0
100 m

Fig. 6. (a) Detail of the dispersion of Fig. 5a; (b) contours of activity generated by the plume model using the least squares fit parameters.

17–19 survey seems to have occurred. If it had, one would expect to see an expansion from the pattern of Fig. 5b. No such expansion is apparent. In fact, an enigmatic shrinkage of the pattern is evident. Changes in detector sensitivity, checked by holding a constant source to the detector face prior to each of the surveys, are known not to have occurred. Bioturbation may account for some shrinkage, but it is unlikely to be responsible for the bulk of signal reduction in patterns Fig. 5c and d. The magnitude of signal attenuation resulting from tracer burial will be discussed later.

As evidenced by the patterns of Fig. 5, sediment transport is principally in the longshore direction. One should also note that in Fig. 5b a limb of the sediment plume extends to the west-northwest in the general direction of the trough axis, suggestive either of movement along the axis of the trough, or subsequent winnowing of this material off the crest of the ridge. In either case, local topography has some influence on the movement of fine sediment through the area.

Figure 7 provides a record of near-bottom current speed versus time over the length of the experiment; currents to 6 December, 1974, were recorded at 40°33·05′ N, 73°24·25′ W (Station 5c, Fig. 4) at a 10 min interval; a meter redeployed at 40°33·1′ N, 73°24·45′ W on 7 December 1974, which recorded at a 20 min interval, provided 53 additional days of current data. Superimposed on the entire record is an estimate of sediment threshold velocity of 18 cm/sec.

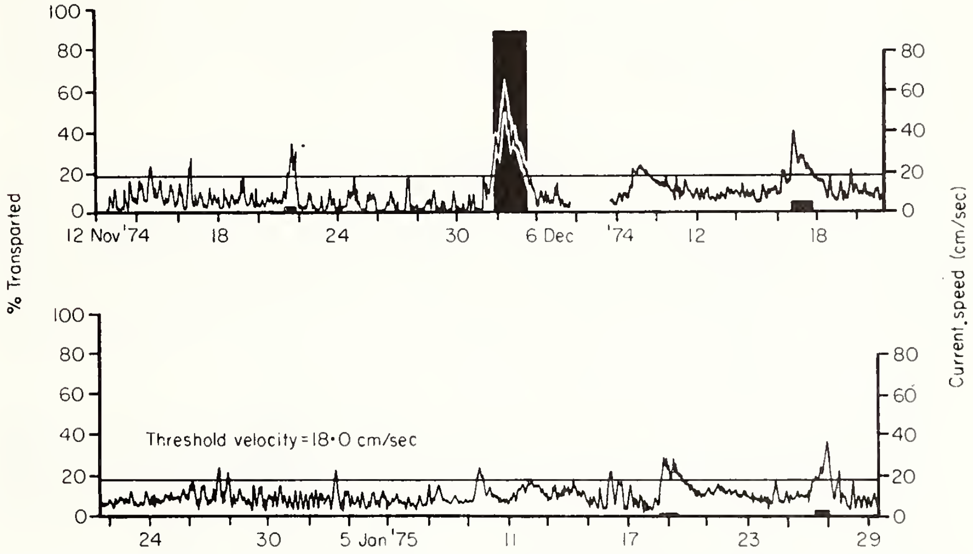

Fig. 7. Current speeds over the length of the tracer experiment from meters located 150 cm from the bottom. Solid bars represent relative rates of transport based on a threshold value of 18 cm/sec and the representation of sediment flux as the third power of the difference between instantaneous and threshold velocities (Lavelle *et al.*, 1976).

The strongest westward flow during the experimental period occurred during the storm of 1–4 December 1974. Currents during this period exceeded the threshold velocity for sediment movement several times over. The second most important sustained flow during the observation period began 16 December and was also to the west. Because no intermediate surveys were made, however, separation of the 1–4 December event from the weaker 16–17 December storm event in the sand dispersal data is not possible. In view of the similarity of transport direction, however, the occurrence of a second storm prior to the survey of 17–19 December does not substantially change any conclusion concerning the effect of the early December storm. If the much weaker event of the 16th had occurred on 5 December, the current records indicate it would have appeared as a minor limb of the major storm, and observations of 17–19 December would be no different from those observed.

Estimates of the relative role each transport event played in the overall transport record are represented as solid bars in Fig. 7. The rate of transport was taken to be proportional to the third power of the difference between instantaneous and threshold velocities (Lavelle *et al.,* 1976), based on similar power law behaviour for aeolian (Bagnold, 1941) and flume (Kennedy, 1969) sediment transport. Figure 7 shows that most of the transport of the entire observation period occurred during the early December storm event. While the calculated transport index may be biased by the choice of threshold speed as well as the functional dependence on velocity, any other reasonable parameterization of transport is likely to lead to the same general conclusion. Figure 5b is, therefore, primarily a reflection of transport which occurred during a single storm event.

Current and wind data during the initial 22 days of the fall–winter experiment are represented as vertical time series of vectors in Fig. 8. Current data have been 40 h low-pass Lanczos windowed (Bath, 1974) and resampled at hourly intervals. The wind data are taken from the 3 h logs kept at John F. Kennedy International Airport, New York City. The wind data is plotted so as to represent the direction toward which the wind is blowing.

Figure 8 shows that from 12 November, the day of tracer release, to 25 November, the first tracer survey, flow was predominantly eastward in response to the westerly winds. Because fall and winter storms generally provide nothwesterly and westerly winds to the area, Fig. 5a is taken to represent sediment movement associated with 'typical' winter storm activity. In contrast, Fig. 5b reflects the work of the northeasterly storm event shown at the bottom of both columns of Fig. 8. Winds during much of the time were in the longshore direction and rose to a maximum of 16 m/sec during the initial 36 h of the period.

Although westerly winds of strength comparable to that which occurred during 1–4 December are seen in the data at other times (Fig. 8), near-bottom easterly currents are considerably smaller than those recorded during the westerly storm flow beginning on 1 December. Observations of fluid responding asymmetrically to westward and eastward wind stress in this general area have been previously reported (Beardsley & Butman, 1974; Scott & Csanady, 1976).

FLUX ESTIMATES

The stationariness of the points of highest tracer concentration and the ellipsoidal nature of the tracer dispersal patterns (Fig. 5a and b) away from the source points bring to mind an atmospheric analogue: plumes of smoke from stacks advecting and diffusing in winds of unknown strength. In contrast to the smoke plume, however, the vertical structure of the sediment plume is not observed; the sand tracer detector integrates the signal of all tagged material beneath it. The description of the sediment plumes is therefore written in two dimensions.

Tracer mass is conserved when material leaving the source points is described by a conventional advection-diffusion equation:

$$\frac{\partial C}{\partial t} + V_x \frac{\partial C}{\partial x} - D_x \frac{\partial^2 C}{\partial x^2} - D_y \frac{\partial^2 C}{\partial y^2} = 0. \quad (1)$$

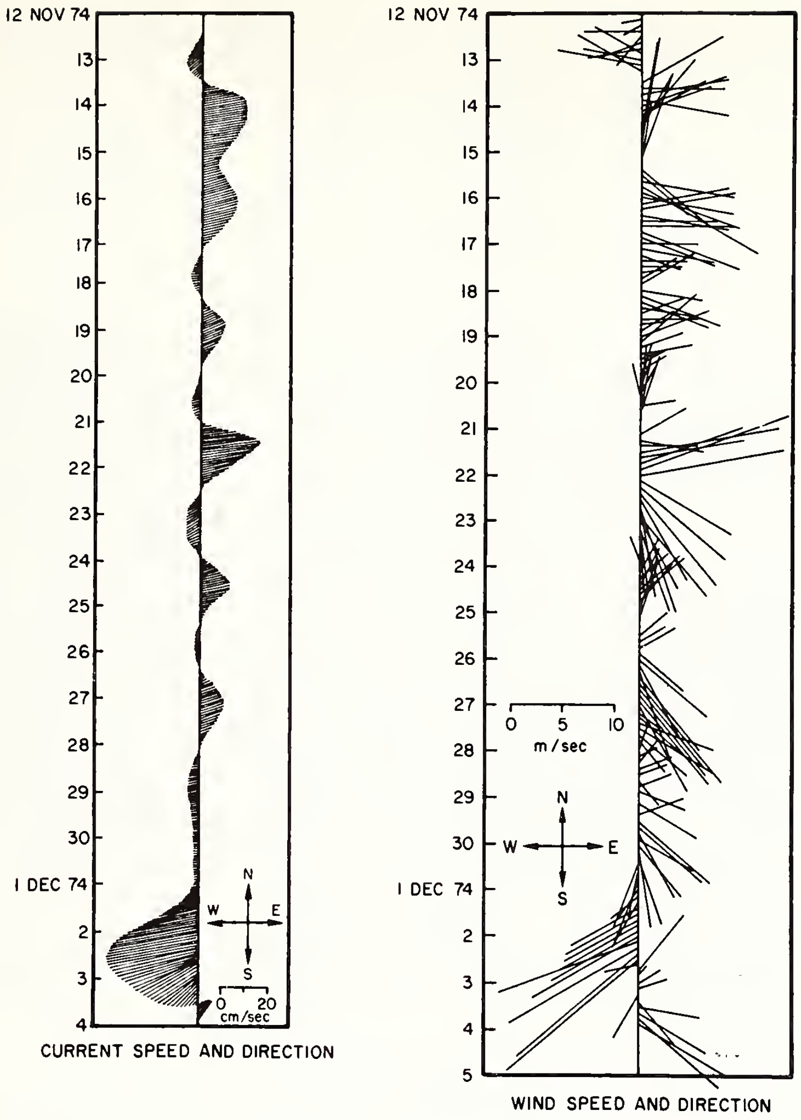

Fig. 8. (a) Partial record of near bottom currents showing the directionality of currents in the area. Currents have been windowed to eliminate high frequencies, and resampled at hourly intervals; (b) wind measurements from John F. Kennedy International Airport during the same period. Wind directions are those toward which wind was blowing.

$C(x, y, t)$ represents a concentration of tagged material at points x and y and time t which has been advected from the source. The principal direction of transport (x direction) is taken to be longshore (75°), based on current meter directional means. The sediment advection velocity, V_x, and the sediment diffusion coefficients, D_x and D_y, in this analysis are taken to be constant as will be discussed later. Each represents the average of the corresponding quantity over the time material was in movement. The advection velocity, V_x, is that of the sediment, and need not be equal to the velocity of the overlying fluid. No decay factors are required in the model inasmuch as the data have been decay corrected prior to this plume analysis.

Conditions imposed on the solution of Equation 1 are:

$$C(x, y, 0)=0 \qquad \forall\, x, y \tag{2}$$

$$\frac{\partial C}{\partial t}(x, y, t)=R \qquad \begin{array}{c} 0<t<T \\ -h<x<h \\ -h<y<h \end{array}$$

R is a constant rate of emission of tagged material over time T from a square source area, a side of which is $2h$ in length. T is the length of time between tracer surveys during which transport was occurring. The source area, $4h^2$, is assumed constant. Each tracer pattern is considered to be a separate realization of this process.

In this analysis, the emission rate, the advection velocity, and the diffusion coefficients are taken to be time independent quantities. Certainly during a shelf sediment transport event, varying mean currents exceeding threshold lead to time dependent advection velocities and emission rates. The above description of transport, therefore, does not model the detail of the event. A single post-event measurement of tracer dispersion provides insufficient information to resolve such detail. The single dispersal measurement is sufficient, however, to estimate event-averaged quantities, and it is those quantities which are used in the calculation of transport rates. This assumption is not unlike those made in previous tracer studies in which flux calculations are made by taking the properly normalized product of the tracer centre-of-mass and the traction layer thickness (Courtois & Monaco, 1969; Komar & Inman, 1970). In fact, using the integral representation of the model which is to be described below, one can show that the advection velocity, V_x, is equal to one-half the centre-of-mass of the advected tracer divided by the duration of transport.

The utility of a plume model description resides in the possibility of evaluating a tagged sediment transport rate, $|\vec{Q}|$, once the plume model has been fitted to the data:

$$|\vec{Q}|=R|\vec{V}_x|T. \tag{3}$$

Contrary to more conventional evaluations of sediment transport rates, the depth of burial of tagged material (traction layer thickness) is not an explicit factor in this flux rate estimation. Without a measurement of the depth of burial, however, one must accept the fact that an estimate of only the minimum value for tagged material flux can be made.

Burial of tagged material affects the estimate of tagged material flux in the following way. As tagged material is transported downstream, it may be worked into the bed, coming to rest below the bed surface. Attenuation of the radiation by the overlying sediment weakens the signal measured by the detector. Therefore, the surficial expression of tagged material partially buried is less than it would be if all tagged sediment were lying at the bed surface; the measured count-rates represented in the patterns of Fig. 2 and Fig. 5 are lower bound estimates of the tagged material at any sampled point. Because the sediment dispersal patterns are lower bound expressions of the actual sediment movement, the estimated tagged sediment flux is also a lower bound estimate.

The following argument suggests how an upper bound to the tagged material flux can be set. If tagged material were uniformly buried to depth l, and if μ were the attentuation coefficient for ^{103}Ru in fine sand, the ratio of observed signal intensity, I to true signal intensity, I_{total}, would be:

$$I/I_{\text{total}} = \frac{1}{\mu l}\,[1-e^{-\mu l}]. \tag{4}$$

Using a bulk density of 1·8 cm^{-3} to estimate a value of μ of 0·18 cm^{-1} and setting $l = 10$ cm as a worst case limit based on the burial observation in wave dominated environments (Komar & Inman, 1970; Courtois & Monaco, 1969) the ratio in Equation 4 is $I/I_{\text{total}} = 0{\cdot}46$. If burial had occurred to these depths during these experiments, flux estimates would be low by a factor of approximately 2·2.

A direct measure of the depth of burial was not possible in these experiments. Plugs or cores are useful only when sufficient quantity of tagged material can be found in such a sample. With radioisotope tracers, however, one generally works with small volumes of tagged material. The tracer is detectable when integrated over a substantial area by an *in situ* detector, but is not detectable in a grab sample or core of workable size.

An integral representation of the plume model and a description of its application to the data can now be given. In the limit of $h \ll d$, where d is the distance of a source point to any measured concentration value, the solution of Equation 1 with the given conditions is (Crank, 1956; Csanady, 1973):

$$C(x, y) = \int_0^T \frac{Rh^2}{\pi\sqrt{D_x D_y t^2}}\, e^{-\left(\frac{(x-V_x t)}{\sqrt{4D_x t}}\right)^2} e^{-(y/\sqrt{4D_y t})^2}\, dt. \tag{5}$$

Because the model was applied to the data represented in Fig. 5a and b and because the source configuration was three points, Equation 5 is generalized to

$$C(x, y) = \sum_{i=1,3} \int_0^T \frac{Rh^2}{\pi\sqrt{D_x D_y t^2}}\, e^{-\left(\frac{(x-x_i-V_x t)}{\sqrt{4D_x t}}\right)^2} e^{-[(y-y_i)/\sqrt{4D_y t}]^2}\, dt \tag{6}$$

where x_i and y_i represent the source point coordinates.

The four parameters, R, V_x, D_x, and D_y, of Equation 6 were determined by a least squares fit for the data of Fig. 5a and b. The measure of error for the least squares was the difference between the logarithm of the measured concentration and the predicted concentration. Concentration values used in the fits of Fig. 5a and b represented arithmetic means within grid units of 10 m × 10 m and 20 m × 20 m respectively.

The data represented by Fig. 5c and d were not fitted because they represent vestiges of the December storm quantified using Fig. 5b data, nor were those of Fig. 2 because they lack advective features. Grid averages were used in the interest of computational economy. Values of measured concentration within two grid units of any source point were not used in determining best fit values. The numerical search for the least-squares parameter values was based on the Marquandt algorithm (Marquandt, 1963), a weighted steepest descent and Gaussian expansion approach. The results of the fit are listed in Table 2. Contours of activity generated with the plume model and the best fit parameters for the 25 November 1974 survey are to be found in Fig. 6b alongside the measured tracer data (Fig. 6a).

In the evaluation of Equation 6, source point coordinates, x_i and y_i, the duration of transport, T, and the area of each source, $4h^2$, all were presumed known. Effective durations of transport, T, were estimates based on near bottom current speeds and a threshold velocity of 18 cm/sec. Source point area was determined in a laboratory test which showed that the surface area of a 10 cm^3 parcel of sand in mildly agitated water was approximately 30 cm^2 after its release from a water soluble bag. Therefore, each of the three sources in the fall–winter experiment was assigned an area of 360 cm^2. The relative positions of the three drop points were inferred from the four contour patterns of Fig. 5.

Having determined best estimates for the parameters, the average flux rate, $|\vec{Q}|$ associated with each event was evaluated using Equation 3 (Table 2). The mass flux for the event associated with the pattern in Fig. 5b is roughly fifty times that associated with the weaker eastward movement represented by Fig. 5a (see also Fig. 6a). The total amount of material leaving the area of the source points during each transport event, P, is three times the area of an individual source ($4h^2$) times the emission rate (R) times the duration of the transport event (T). Table 2 shows that the total measured mass of tagged material which has left the drop area after both events represented about 40% of the mass of tagged material originally injected (243 g/590 g).

Calculations to this point have involved only tagged sediment flux, not total sediment flux. Tagged sediment flux represents total sediment flux only if all sand particles leaving the source area were tagged. More generally, total sediment flux is equal to tagged sediment multiplied by the factor $(1+r)$, where r is the ratio of untagged to tagged particles at the source point.

It can be argued that the stationariness of source points during each of these experiments is a manifestation of tagged material having been worked into the bed. Both tagged and untagged material would then be emitted during a transport event, and r would be clearly non-zero. Even if that were not the case, r would still be non-zero during a transport event, as some untagged material would come to rest, even if only temporarily, at the source point and be subsequently emitted along with tagged material. Measurements in these experiments do not provide sufficient information to determine the untagged/tagged particle ratio at the source points.

It is clear, however, that the total sediment flux must be equal to or greater than tagged material flux. The lower bound estimate to tagged flux previously calculated is, therefore, also the lower bound estimate to total sediment flux. This estimate of the minimum flux is represented by an inequality sign in Table 2. Comparison of these minimum fluxes with predictions based on measured currents and empirical transport formulae may be found in Gadd, Lavelle & Swift (1978).

Table 2. Plume parameter and sediment mass flux estimates for designated fall–winter intervals

Survey	Date	Transport duration, T (h)	Plume emission rate, R g/cm²/sec	Plume advection velocity, V_x (cm/sec)	Plume diffusion coefficients (cm²/sec)		Total material emission, P (g)	Tracer sediment flux, $\lvert\vec{Q}\rvert$ (gm/cm/sec)
					x direction	y direction		
EXP II-1	25 November 1974	16·7	$3{\cdot}5\times10^{-7}$	$1{\cdot}5\times10^{-1}$	$3{\cdot}3\times10^{2}$	$4{\cdot}1\times10^{1}$	$2{\cdot}3\times10^{1}$	$>3{\cdot}2\times10^{-3}$
EXP II-2	17–19 December 1974	47·2	$1{\cdot}2\times10^{-6}$	$-8{\cdot}5\times10^{-1}$	$7{\cdot}8\times10^{2}$	$1{\cdot}8\times10^{3}$	$2{\cdot}2\times10^{2}$	$>1{\cdot}7\times10^{-1}$

SUMMARY

Along the Long Island coast at depths of 20–22 m, non-diffusive sand transport is seasonal in character. Patterns of tagged sediment transport reflected only modest diffusive growth during a 69 day observation interval in the spring and summer of 1974. In contrast, during a 76 day observation period in the fall and winter of 1974–1975, tracer patterns document the occurrence of substantial advective sand transport. Transport is more frequent and intense in the fall and winter than in the spring and summer.

Observations of near-bottom fluid velocities and the apparent validity of laboratory threshold conditions in the marine environment (Sternberg, 1971) allow inferences to be drawn about the temporal nature of the observed sediment transport. Superposition of the estimated threshold velocity on the near-bottom speed record organizes the current data into isolated periods when sediment was in movement. The result is that at these depths on this coast, transport events appear to have durations on the order of hours to several days.

The intermittency of sediment transport suggested by the current data is also supported by the fall–winter tracer observations. The argument is based on the relative strength of eastward and westward transport represented by Fig. 5a and b. A threshold velocity much below 12 cm/sec would cause sediment to be in motion in the predominant current direction (eastward) during most of the experiment. The result would be more eastward transport than was observed. If the threshold velocity was greater than 12 cm/sec, then there were periods during the experiment when no sediment movement occurred (Fig. 7). Sediment movement was, therefore, intermittent. We believe that the relative extent of the dispersion patterns of Fig. 5a and b supports the threshold velocity adopted in this report (18 cm/sec).

Near-bottom currents significantly exceeding threshold velocity, and consequently sediment transport events, occur contemporaneously with strong winds. The predominantly westerly and northwesterly winds of fall–winter storms in the New York Bight can cause near-bottom flow of sufficient intensity to move sediments eastward. Less frequent northeasterly and easterly winds can cause westward fluid and sediment movement.

The data demonstrate the importance of exceptional storm flow in determining patterns of sediment transport. If simple excess velocity parameterizations of sediment flux which are consistent with laboratory observations hold true in the marine environment, nearly all of the sediment movement over the 135 days represented in this report took place during a 2 day interval in early December, 1974. That single event was the response to usually strong storm forced near-bottom flow.

Based on the relative strengths of the eastward and westward tagged sand transport as well as previous New York Bight current observations (Beardsley & Butman, 1974; Scott & Csanady, 1976) showing a stronger response of fluid to westward then eastward wind stress, we conclude that over time scales of a year, the more frequently occurring but less intense eastward bottom movement of sediment is overwhelmed by the bottom sediment response to storm events associated with northeasterly winds. The net bedload sediment transport direction in this area is different from the direction of net fluid movement.

The principal direction of bedload sediment transport, in response to the overlying fluid, was found to be parallel to the shore and oblique to the axis of the ridge and swale system. The tagged sediment observed lying in the trough of the ridge and swale system (Fig. 5b) may be an indication of sediment movement along the trough, but it may also reflect winnowing of tagged material off the crest of the ridge. In either case bottom sediment movement is affected by the local topography. Because the ridges are asymmetrical with steeper southwestward facing flanks, it appears that the accumulated effect of westward sediment flows control the morphology of these features.

The following modifications in equipment and procedures should be made to improve the accuracy of tracer flux and fluid correlation measurements of the kind reported here. First, absolute position of source points and each tracer survey should be established to higher accuracy than achievable in these studies. Secondly, improved resolution of the concentration field by increasing the spatial density of samples near the source point and improved detector dynamical range are essential if better accuracy is sought in the case of weak transport; for widely dispersed patterns, present equipment is adequate. Thirdly, if improvements in positioning resolution are attained, a single source point is desirable; the areal extent of the source would be better controlled by diver-assisted implantation from a specially designed isotope carrier. Finally, more attention should be given to resolving near-bottom current conditions at these experimental depths in order to sort high frequency from longer period flows.

ACKNOWLEDGMENTS

We would like to thank the captains and crews of the NOAA Ship Ferrel, R/V Annadale, R/V Venture, R/V Advance II, and the R/V Black Coral, who participated in the operational aspects of these experiments. We also gratefully acknowledge the assistance of Carl Kunselman, Robert Charnell, Tom Clarke, Richard Permenter, Dennis Pepe and Ned Austin in the course of this work.

Support for this work has come from NOAA New York Bight Marine Ecosystems Analysis (MESA) Project, NOAA Environmental Research Laboratories, and DOE/ Division of Biomedical and Environmental Research. Oak Ridge National Laboratory, Oak Ridge, Tennessee, is operated by Union Carbide Corporation for the U.S. Department of Energy.

REFERENCES

Bagnold, R.A. (1941) *The Physics of Blown Sands and Desert Dunes.* Methuen and Co., London.

Bagnold, R.A. (1963) Beach and near-shore processes, I: mechanics of marine sedimentation. In: *The Sea*, Vol. **3** (Ed. by M. N. Hill), pp. 507–528. Interscience Publishers, New York.

Bath, M. (1974) *Spectral Analysis in Geophysics.* Elsevier Scientific Publishing Co., New York.

Beardsley, R. & Butman, B. (1974) Conditions on the New England continental shelf: response to strong winter storms. *Geophys. Res. Lett.* **1**, 181–184.

Case, F.N., Acree, E.H. & Brashear, H.R. (1971) Detection system for tracing radionuclide labeled sediment in the marine environment. *Isotopes and Radiation Technology,* **8,** 412–414.

Charnell, R.L. & Mayer, D.A. (1975) Water movement within the apex of the New York Bight during summer and fall of 1973. *Technical Memo ERL-MESA*-3, National Oceanic and Atmospheric Administration, Boulder, Colorado.

Courtois, C. & Monaco, A. (1969) Radioactive methods for the quantitative determination of coastal drift rate. *Mar. Geol.* 7, 183–206.

Crank, J. (1956) *The Mathematics of Diffusion*. Clarendon Press, Oxford.

Csanady, G.T. (1973) *Turbulent Diffusion in the Environment*. D. Reidel Publishing Co., Boston.

Duane, D.B. (1970a) Synoptic observations of sand transport. In: *Proc. 12th Coastal Eng. Conf., Am. Soc. Civ. Engrs, New York*, **2**, 799–813.

Duane, D.B. (1970b) Tracing sand movement in the littoral zone: progress in the radio isotopic sand tracers (RIST) study, July 1968–February 1969. *Coastal Eng. Res. Center Misc. Paper, Washington D.C.*

Duane, D.B., Field, M.E., Meisburger, E.P., Swift, D.J.P. & Williams, S.J. (1972) Linear shoals on the Atlantic inner continental shelf, Florida to Long Island. In: *Shelf Sediment Transport: Process and Pattern* (Ed. by D. J. P. Swift, D. B. Duane, O. H. Pilkey), pp. 477–498. Dowden, Hutchinson and Ross, Stroudsburg, Pa.

Gadd, P.E., Lavelle, J.W. & Swift, D.J.P. (1978) Estimates of sand transport on the New York Shelf using near-bottom current meter observations. *J. sedim. Petrol.* **48**, 239–252.

Guy, H.P., Simons, D.B. & Richardson, E.V. (1966) Summary of alluvial channel data from flume experiments, 1956–61. *Prof. Pap. U.S. geol. Surv.* **462-I.**

Ingle, J.C. & Gorsline, D.S. (1973) Use of fluorescent tracers in the near-shore environment. In: *Tracer Techniques in Sediment Transport*, Technical Report Series No. 145, pp. 125–148. International Atomic Energy Agency, Vienna.

Inman, D.L. & Chamberlain, T.K. (1959) Tracing beach sand movement with irradiated quartz. *J. Geophys. Res.* **64**, 41–47.

Jeffers, K.B. (1960) *Hydrographic Manual*. Publ. 20–2, U.S. Govt. Printing Office, Washington, D.C.

Kennedy, J.F. (1969) The formation of sediment ripples, dunes, and antidunes. In: *Annual Review of Fluid Mechanics* **1** (Ed. by W. R. Sears), pp. 147–168. Annual Reviews, Inc., Palo Alto, Claifornia.

Komar, P.D. & Inman, D.L. (1970) Longshore sand transport on beaches. *J. Geophys. Res.* **30**, 5914–5927.

Lavelle, J.W., Gadd, P.E., Han, G.A., Mayer, D.A., Stubblefield, W.L., Swift, D.J.P., Charnell, R.L., Brashear, H.R., Case, F.N., Haff, K.W. & Kunselman, C.A. (1976) Preliminary results of coincident current meter and sediment transport observations for wintertime conditions on the Long Island inner shelf. *Geophys. Res. Lett.* **3**, 97–100.

Marquandt, D.L. (1963) An algorithm for least-squares estimation of non-linear parameters. *J. Soc. Indust. Appl. Math.* **2**, 431–441.

Rance, P.J. (1963) The dispersion of quantities of sediment transport in oscillatory motion by consideration of the dispersion of tracer-sediment. *Proc. 10th Cong., Int. Ass. Hydraul. Res., London*, **1**, 181–188.

Russell, R.C.H., Newman, D.E. & Tomlinson, K.W. (1963) Sediment discharges measured by continuous injection of tracers from a point. *Proc. 10th Cong., Int. Ass. Hydraul, Res., London*, **1**, 69–76.

Scott, J.T. & Csanady, G.T. (1976) Nearshore currents off Long Island. *J. Geophys. Res.* **81**, 5401–5409.

Sternberg, R.W. (1971) Measurements of incipient motion of sediment particles in the marine environment. *Mar. Geol.* **10**, 113–119.

Swift, D.J.P., Duane, D.B. & McKinney, T.F. (1973) Ridge and swale topography of the Middle Atlantic Bight, North America: secular response to the Holocene hydraulic regime. *Mar. Geol.* **15**, 227–247.

Vernon, J.W. (1966) *Shelf Sediment Transport System*. Unpublished Ph.D. thesis, University of Southern California, Los Angeles.

(*Manuscript received* 9 *November* 1977; *revision received* 18 *April* 1978)

Journal of Hydraulic Research 16, No. 4, 347-355.

EFFECTS OF HINDERED SETTLING ON SEDIMENT CONCENTRATION PROFILES

L'INFLUENCE DE LA SEDIMENTATION FREINEE SUR LES PROFILS DE CONCENTRATION DES SEDIMENTS

by

J. W. Lavelle

NOAA/Pacific Marine Environmental Laboratory 3711 - 15th Ave. N.E. Seattle, Washington 98105 USA

and

W. C. Thacker

NOAA/Atlantic Oceanographic and Meteorological Laboratories, 15 Rickenbacker Causeway
Miami, Florida 33149 USA

Summary Suspended sediment distributions which take into account concentration-dependent settling velocities have been derived. The distributions have been compared to and have been found to be in good agreement with the high concentration data of Einstein and Chien [1]. The analysis shows that concentrations at the sediment bed in the Einstein-Chien data are close to those of saturated sediments, which leads to the suggestion that the reference level in the distributions always be taken at the bed where the reference concentration is flow independent. A suspended sediment distribution constructed in this way guarantees a reasonable value for concentration near the bed and depends on two diffusivity parameters which the Einstein-Chien concentration data indicate are related.

Résumé Nous avons déduit les répartitions des matériaux en suspension qui tiennent compte des vitesses de chute dépendant de la concentration de ces matériaux. La comparaison de ces distributions avec les valeurs de concentration élevée déterminées par Einstein et Chien [1] a révélé une bonne concordance entre ces deux ensembles de résultats. L'analyse montre que les valeurs des concentrations à la couche de matériaux déposés sur le fond selon Einstein et Chien sont voisines de celles correspondant aux sédiments saturés, ce qui conduit à la proposition que l'on devrait toujours situer le niveau de référence au voisinage du fond, zone dans laquelle la concentration de référence est indépendante de l'écoulement. La détermination, par cette voie, d'une répartition des matériaux en suspension garantit l'obtention d'une valeur raisonnable de la concentration au voisinage du fond; cette répartition dépend de deux paramètres de diffusivité, lesquels, d'après les concentrations déterminées par Einstein et Chien, seraient liées par une relation.

Introduction

Since the pioneering work of Hurst [2] and O'Brien [3], it has been recognized that the steady state distribution of suspended sediment in open-channel as well as other flows reflects the balance of an upward diffusive and a downward gravitational settling flux of particles. Using the O'Brien [3] expression of flux equilibrium and an eddy diffusivity varying quadratically with the distance from the bottom, Rouse [4] derived a distribution of suspended sediments for open-channel flow

---

Received June 29, 1977 and revised May 29, 1978

which generally agrees with suspended sediment measurements except for those taken near the bed where the sediment concentration is high [e.g. 5]. HUNT [6] pointed out that if attention were paid to the two-phase nature of the flow, the settling term in the flux equilibrium statement of O'Brien [3] would be modified by a factor of $1-C$, where C is the volume fraction of sediment is suspension. The resulting suspended sediment distribution better fits high concentration near-bed data, and, unlike the distribution of Rouse, remain finite at the sediment bed. EINSTEIN and CHIEN [1] pointed out that the flux equilibrium expression and the resulting suspended sediment distribution might be changed even further when other factors which reduce single particle settling velocities are considered.

Hindered settling is the term which describes the reduction of settling velocity due to increased sediment concentrations. In a recent investigation of the consequences of a two-phase description of a fluid-sediment system in which both mass and momentum balance were considered, THACKER and LAVELLE [7] showed that the hindered settling could be accounted for by a factor of $(1-C)^{\alpha}$ multiplying the single particle fall velocity. This dependence of the fall velocity on concentration is consistent with the compilation of hindered settling data of MAUDE and WHITMORE [8] when α ranges between 4 and 9 and with the kinematics of the two phase system. The kinematical factor of $(1-C)$ which HUNT [6] introduced into the gravitational flux expression to account for the upward flow of water through the downward settling of particles, and an additional factor of $(1-C)$ due to the increase in apparent pressure due to the sediment in suspension are both accounted for with the exponent α.

In this paper, the effects of hindered settling on sediment concentration profiles for open-channel flow are examined. The distributions have been compared to the high-concentration near-bed data of EINSTEIN-CHIEN, in which volume fractions concentrations as high as 0.23 make the hindered settling effect apparent. Although concentration measurements are generally made in regions and flows where the hindered settling factor, $(1-C)^{\alpha}$, is nearly unity, the effect is not without practical consequences. As an example, the use of a distribution which incorporates hindered settling is unavoidable if a realistic extrapolation of measured concentration to the bed is to be made. That realistic extrapolation would be necessary in an estimation of horizontal sediment flux where the bulk of the transport is in the near-bed region.

Formulae for sediment concentration profiles

The form of the concentration profile in the case of horizontally homogeneous flow is governed by the requirement that in steady state the vertical flux of material is zero:

$$wC+A\frac{\partial C}{\partial z}=0 \tag{1}$$

where w is the sediment fall velocity, usually assumed to be a constant. THACKER and LAVELLE [7] showed that this same equation arose out of a two-phase flow analysis of a system which included balances of both mass and of momentum for water and for sediment phases. Equation (1) above is the expression of mass conservation for sediment and accounts for hindered settling when the sediment velocity is given the form suggested by MAUDE and WHITMORE [8]:

$$w=w_0(1-C)^{\alpha} \tag{2}$$

where w_0 is the fall velocity for low concentrations. In this analysis, α will be set equal to five, based on the MAUDE and WHITMORE [8] evaluation of data, which shows a preponderance of the hindered settling measurements close to that value.

Two forms will be considered for the eddy diffusivity. The first,

$$A = a + bz \tag{3}$$

where z is the distance above the bottom, has widespread applicability in marine boundary layer studies. (If a similar form is used for eddy viscosity, a constant stress boundary layer corresponds to a logarithmic velocity profile.) With this expression for eddy diffusivity, equation (1) can be integrated to obtain an implicit expression for the sediment concentration profile C,

$$\ln\left(\frac{1-C}{C}\right) - \sum_{j=2}^{\alpha} \frac{1}{(j-1)} \frac{1}{(1-C)^{j-1}} = + \frac{w_0}{b} \ln\left(\frac{a+bz}{a+bz_R}\right) + \ln\left(\frac{1-C_R}{C_R}\right) - \sum_{j=2}^{\alpha} \frac{1}{(j-1)} \frac{1}{(1-C_R)^{j-1}} \tag{4}$$

where C_R is a reference concentration corresponding to reference height z_R and α is an integer greater than or equal to two.

The second form for the eddy diffusivity,

$$A = (a+bz)(d-z)/d \tag{5}$$

where d is the flow depth, is more customary for flow in a channel since it reflects the eddy scale at the surface of the water. (A form similar to this for eddy viscosity leads to a logarithmic velocity profile for stress varying linearly with z.) If hindered settling is neglected by setting $\alpha = 0$ and if a is taken to be zero in this expression for diffusivity, then equation (1) yields Rouse's sediment concentration profile [4]:

$$C = C_R \left[\frac{z_R(d-z)}{z(d-z_R)}\right]^{w_0/b} \tag{6}$$

When hindered settling is not neglected and $a \neq 0$, equation (1) with this expression for diffusivity yields

$$\ln\left(\frac{1-C}{C}\right) - \sum_{j=2}^{\alpha} \frac{1}{(j-1)} \frac{1}{(1-C)^{j-1}} = + \frac{w_0}{(b+a/d)} \ln\left(\frac{z+a/b}{z-d} \cdot \frac{z_R-d}{z_R+a/b}\right) + \ln\left(\frac{1-C_R}{C_R}\right) - \sum_{j=2}^{\alpha} \frac{1}{(j-1)} \frac{1}{(1-C_R)^{j-1}} \tag{7}$$

For $z \ll d$, equation (7) reduces to equation (4).

If A represented momentum diffusivity in equations (3) and (5), then the coefficient b might be expressed as κU_*, where κ is the von Karman coefficient and U_* is the friction velocity, a measure of stress on the bed. Likewise, a might be expressed as $\kappa U_* z_0$, where z_0 is a roughness length. For sediment diffusivity, analogous definitions will apply.

Figure 1 represents the dissimilarity of concentrations predicted in the region of small z for various values of α using equation (4). The profiles were made by assigning a reference concentration volume fraction of .015 at 2.0 cm above the bed, by assuming a sediment density of 2.65 gm/cm^3 and a fall velocity of 1 cm/s, and by choosing arbitrary values for the sediment diffusivity coefficients ($a = .010$ cm^2/s, $b = .5$ cm/s). Assignments of those constants is consistent with concentration values of 1.6 g/l at 10 cm and 16.0 mg/l at 100 cm. Concentrations above 2 cm are effectively independent of the value of α. Concentrations near the bed, on the other hand, are quite strongly dependent on the value of α. For unhindered settling, $\alpha = 0$, the predicted bed concentration exceeds 1.0 ($C_0 = 59.9$), a value not achievable for a volume fraction concentration.

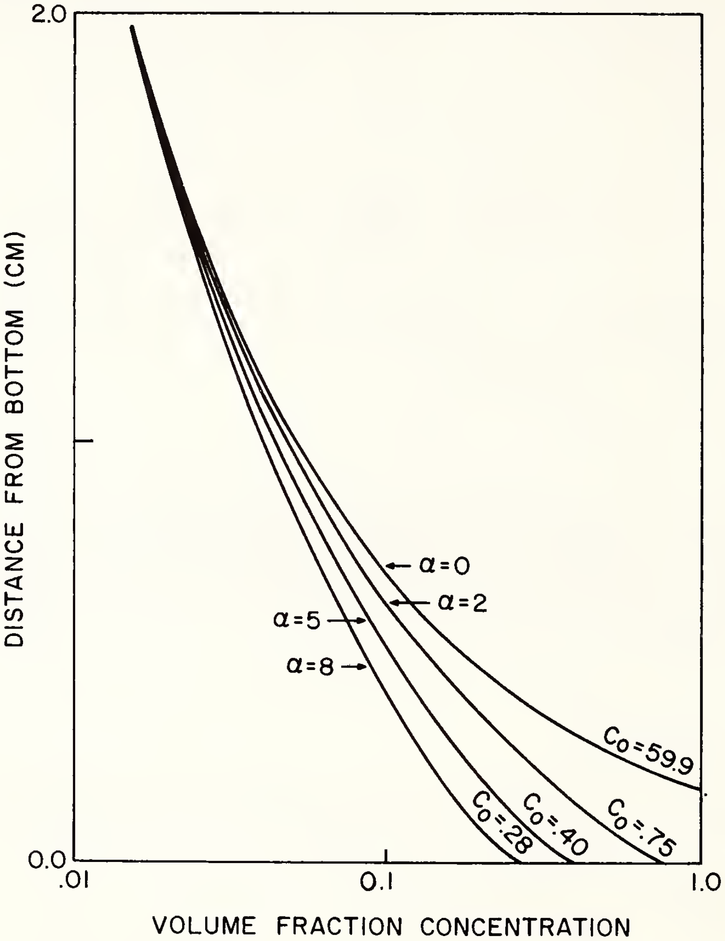

Dependence of near-bed volume fraction concentrations on the exponent of the hindering factor, α. Concentrations at the bed are C_0.

Fig. 1.

Dépendance des concentrations de la fraction située au voisinage du fond de l'exposant du coefficient de ralentissement, α. C_0 désigne les concentrations au fond.

Comparison with experiment

Because very high sediment concentrations are required to resolve hindered settling effects, the theory has been compared to the fine sediment flumes series (S-11 to S-16) of Einstein and Chien [1] in which volume fraction concentrations as high as 0.23 were achieved. Data taken by Einstein and Chien [1] with coarser sediment and lower mean concentrations are not considered.

Measurements were made in a 12 m metal flume having a width of 31 cm and a flow depth ranging from 11 to 14 cm. Particles of the same size as were in suspension ($d_0 = .274$ mm) were glued to the flume bed to create the appropriate bed roughness, and the average flow velocity (1.8 to 2.2 m/s) was set high to prevent sedimentation from occurring during the measurements. Suspended sediment was sampled using a siphoning tube which removed 1 liter of the fluid-sediment mixture for gravimetric analysis at a rate such that the flow at the entrance of the sampler was minimally disturbed. Sediment concentrations from this planar bed configuration were sampled at approximately 10 depths in the lower half of the flow.

Fig. 2 is a plot of the ratio, $-C(1-C)^{\alpha}/(\partial C/\partial z)$ evaluated using runs S-15 and S-16, with estimates of concentration gradient based on averages of forward and backward differences. In each set, a datum at small z, thought spurious because it reflected a concentration inversion, was not included. This ratio isolates the hindered settling effect in the data and displays the near-bed behavior of eddy diffusivity (see equations (1) and (2)). Three points should be noted. The first is that there is a distinct difference in the cases where hindered settling is considered (crosses) and when it is neglected (triangles). The second is that a straight line provides a good fit, which indicates that the diffusivity does vary linearly near the bottom. The third is that, if the slopes of the lines representing the best fit to the lowest seven points are converted to von Karman coefficients, using the experimental friction and settling velocity, the values of 0.12 and 0.14 for these two cases

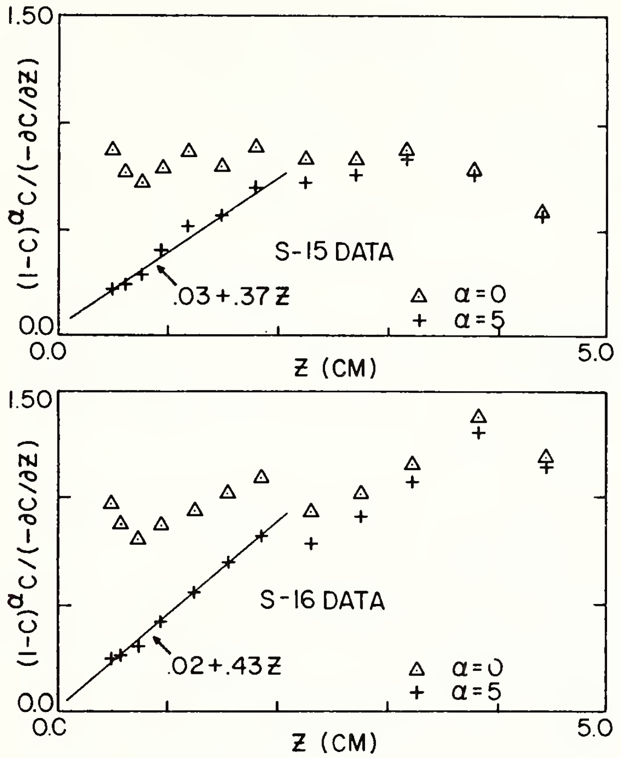

Fig. 2. Eddy diffusivity versus z (see equations (1) and (2)) for the S-15 and S-16 experimental series of Einstein and Chien with and without the effects of hindering.

Variation de la diffusivité tourbillonnaire en fonction de z (voir les équations (1) et (2)) pour les séries d'essais S-15 et S-16 d'Einstein et Chien, avec et sans phénomènes de freinage.

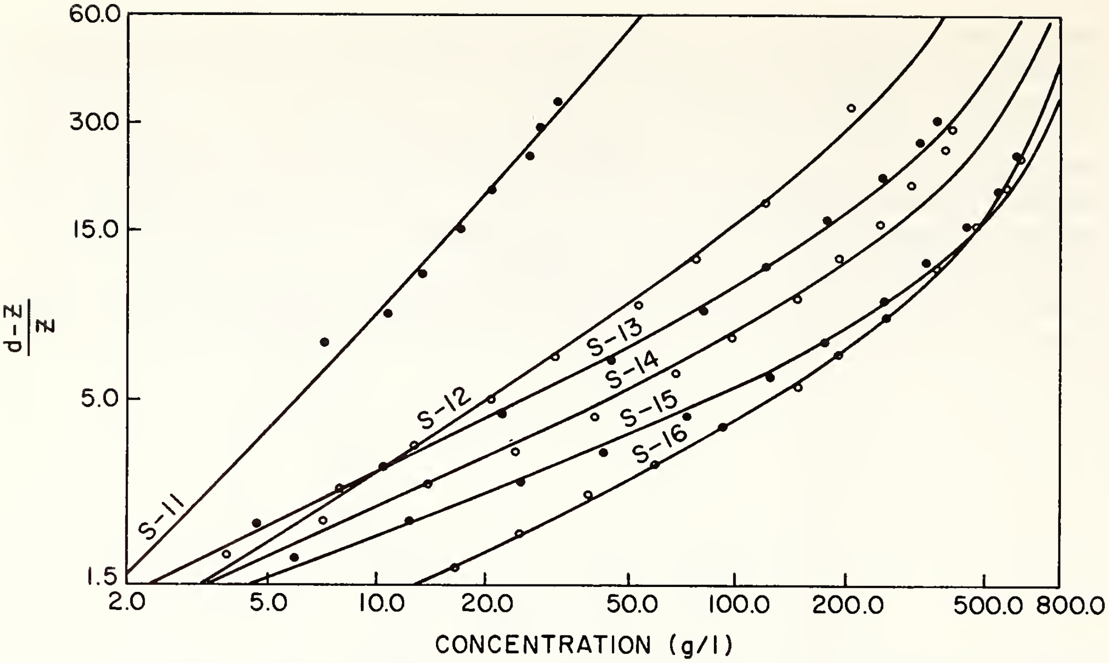

Fig. 3.

Solid lines representing the three parameter best fit curves of the present theory superimposed on the concentration profile data of Einstein and Chien. Flume flow depth is d, and z is the distance from the bed.

Lignes continnes représentant la superposition des courbes de la meilleure approximation de trois paramètres de la présente théorie, sur les profils de concentration déterminés par Einstein et Chien. d désigne la profondeur du canal, et z la distance du fond.

compare well with the corresponding values of 0.17 and 0.18, respectively, which are based on corresponding velocity profiles. Slopes of lines through the triangles (neglecting hindering) would lead to considerably smaller von Karman coefficients.

Because all data points should be included in the determination of the eddy diffusivity, we have taken the integral form of the concentration profile, equation (7), and have least-squares fit the six experimental series of EINSTEIN and CHIEN [1] for the parameters C_0, a and b. The measure of error for the least squares was the square of the difference between the logarithms of the measured concentration and the logarthim of the predicted concentration. The least-squares parameter search was based on the Marquandt algorithm [9], a weighted steepest-descent and Gaussian expansion approach. The reference level in equation (7) was taken to be the bed ($z_R = 0$), α was set at five,

Table 1. Einstein-Chien flume data and estimates of bottom concentrations and eddy diffusivity parameters.

run no.	d (cm)	U^* (cm/s)	a (cm²/s)	b (cm/s)	C_o	κ_s	κ_w	κ_w/κ_s	z_{os} (cm)	z_{ow} (cm)	z_{ow}/z_{os}
S-16	11.9	12.45	4.0×10^{-2}	1.80	.47	.144	.182	1.25	2.2×10^{-2}	1.4×10^{-1}	6.4
S-15	12.4	12.04	3.1×10^{-2}	1.46	.50	.121	.168	1.39	2.1×10^{-2}	1.5×10^{-1}	7.1
S-14	12.3	12.1	1.6×10^{-2}	1.74	.49	.143	.218	1.52	9.2×10^{-3}	6.0×10^{-2}	6.6
S-13	13.4	10.49	1.5×10^{-2}	1.85	.47	.176	.237	1.35	8.1×10^{-3}	4.0×10^{-2}	4.9
S-12	13.2	10.09	2.7×10^{-3}	2.40	.48	.238	.274	1.15	1.1×10^{-3}	3.3×10^{-2}	30.0
S-11	13.2	10.58	1.1×10^{-3}	4.00	.34	.378	.398	1.05	2.7×10^{-4}	4.0×10^{-3}	14.8
S-11a	13.2	10.58	5.8×10^{-6}	4.01	.48	.379	.398	1.05	1.4×10^{-6}	4.0×10^{-3}	2.9×10^{3}

and the velocity, w_0, was taken to be 3.74 cm/sec, based on the mean sediment grain size used in the experiments ($d_0 = .274$ mm). Fig 3 is a plot of the best fit curves against the Einstein-Chien data; least-squares parameter values are to be found in Table 1.

Other entries in Table 1 were either taken from the original experimental report or derived as follows. The friction velocity, U_*, was found by equivalencing the bottom stress, ϱU_*^2, with the flume down channel body force, $\varrho g R S$, where S is the flume slope and R is the hydraulic radius. By analogy to the eddy viscosity parameterization, a von Karman coefficient associated with sediment concentration, κ_s, is defined through the expression $\kappa_s U_* = b$ and the roughness length associated with concentration, z_{0s}, is defined to be the ratio of a/b.

Values of κ_s in Table 1 are seen to be, on the average, 30% smaller than the von Karman coefficients based on the fluid velocity profiles, κ_w. Values of κ_s close to but not identical with κ_w have been found in other studies [e.g. 10, 11]. Roughness lengths associated with concentration are, on the average, an order of magnitude smaller than the fluid roughness elements, z_{0w}. Table 1 also shows a clustering of bed concentration values around 0.48 in the first five of the six cases, which leads us to suggest that the reference concentration is flow independent when the reference level is taken at the bed.

A volume fraction concentration of 0.48 for fine quartz sediment indicates a bulk density of

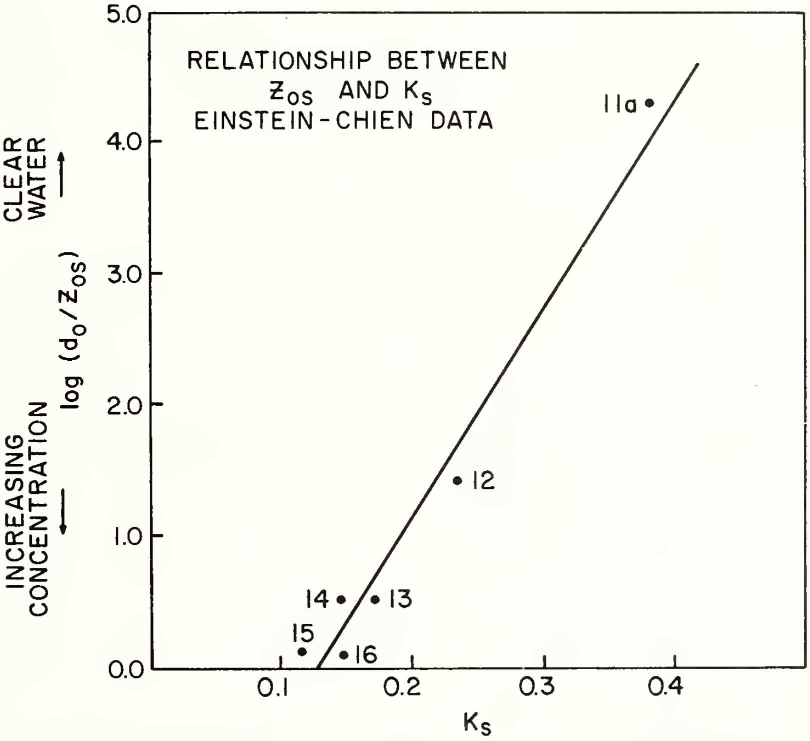

Relationship between the roughness length associated with concentration, z_{os}, and the von Karman coefficient associated with the concentration, κ_s. The straight line is a hand-drawn best fit. The mean grain size of sediment in the experiments is d_0.

Fig. 4.

Variation de la longueur de rugosité liée à la concentration, (z_{os}), en fonction du coefficient de von Karman correspondant à la concentration (κ_s). La droite, tracée à la main, correspond à la ligne de meilleure approximation. d_0 désigne la granulométrie moyenne des matériaux expérimentaux.

approximately 1.79 g/cm^3, which may be compared to a saturated volume fraction of 0.56 and a saturated bulk density of 1.93 g/cm^3 [12]. This comparison suggests that the sediment bed in the Einstein-Chien experiments was close to being maximally packed. It also suggests that in other applications of the hindered settling distribution, the reference concentration might be assigned a value based on a measurement of the bed bulk density.

Because of low maximum concentration in the data set S-11, resolution of the parameters C_0 and a by the data is poor. Because other C_0 values are nearly constant, we have refitted the S-11 data with the two parameters a and b, having fixed C_0 at 0.48. The result of that fit is listed as S-11a in Table 1. As could be expected, a is several orders of magnitude smaller than in the S-11 fit to compensate for increased C_0.

When the reference concentration is fixed at the bed as the Einstein-Chien data suggests, the amount of material in suspension is dependent primarily on the sediment diffusivity parameter a (equation (3)). If a determines the amount of sediment in suspension and the sediment in suspension reduces the turbulence away from the bed [e.g. 1, 10, 11, 13], one might expect to see a relationship between a and b in the data. That relationship has been examined by plotting the von Karman coefficient for sediment, which is equal to b/U_*, versus the logarithm of the roughness length for sediment, which is equal to a/b, where the roughness length has been non-dimensionalized by the mean sediment grain diameter, d_0. In the case of velocity profiles, a linear relationship between those arguments was found by Einstein and Chien [1].

A similar relationship appears to exist for the sediment diffusivity parameters in the data sets examined when the S-11a rather than the S-11 parameter values are used (Fig. 4). The implication of the relationship is, of course, that a single independent parameter determines the magnitude of eddy diffusivity.

Conclusions

If turbulent flux is accounted for with a conventional expression of eddy diffusivity, the inclusion of the factor $(1-C)^{\alpha}$ in the settling velocity results in a formula which successfully accounts for the high-concentration measurements of Einstein and Chien [1]. When realistic concentration estimates are required near the bed, as is the case in sediment transport, the suspended sediment distribution which incorporates hindered settling must be used to extrapolate from measured values taken at some distance from the bed. This analysis also suggests that the integration constants in the hindered settling distribution can be made flow independent; when the reference level is set at the bed, the reference concentration is determined from a measurement of bed bulk density. The amount and distribution of sediment in suspension with a fixed reference concentration is then determined by the eddy diffusivity parameters, which can be expressed as von Karman and roughness length type coefficients. Hindered settling permits the parallelism of turbulent mixing of sediment and momentum to be demonstrated, even to the extent that the von Karman and roughness length coefficients associated with the sediment distribution vary with increasing concentrations in a manner similar to the corresponding parameters associated with the momentum distribution. The parallel question of the effect of hindered settling on the momentum distribution has not been addressed.

Acknowledgements

We wish to thank R. A. Young, D. J. P. Swift, and J. W. Kofoed for their helpful comments.

References — Bibliographie

1. Einstein, H. A., and N. Chien, 1955, Effects of heavy sediment concentration near the bed on the velocity and sediment distribution. Univ. California Inst. Eng. Res. and U.S. Army Corps of Engineers, Missouri River Division, MRD Sediment Series, No. 8, 76 pp.
2. Hurst, H. E., The suspension of sand in water, Proceedings, Royal Soc. of London, Series A, **124**, pp. 196–201.
3. O'Brien, M. P., 1933, Review of the theory of turbulent flow and its relation to sediment transport, Trans. Am. Geophys. Union, **14**, pp. 487–491.
4. Rouse, H., 1938, Fluid mechanics for hydraulic engineers. Dover Publications, New York, N.Y., 422 pp.
5. Vanoni, V. A., 1946, Transportation of suspended sediment by water, Trans. A.S.C.E., **111**, pp. 67–133.
6. Hunt, J. N., 1954, Turbulent transport of suspended sediment in open channels, Proceedings, Royal Soc. of London, Series A, **224**, pp. 322–335.
7. Thacker, W. C. and J. W. Lavelle, 1977, Two-phase flow analysis of hindered settling. Phys. of Fluids, **20**, pp. 1577–1579.
8. Maude, A. D., and R. L. Whitmore, 1958, A generalized theory of sedimentation. Brit. J. Appl. Phys., **9**, pp. 477–482.
9. Marquardt, D. L., 1963, An algorithm for least-squares estimation on non-linear parameters. J. Soc. Indust. Apl. Math., **2**, pp. 431–441.
10. Vanoni, V. A., 1954, Some effects of suspended sediment on flow characteristics. In: Proceedings of the Fifth Hydraulics Conference, State Univ. Iowa Studies in Eng. Bull., 34, pp. 137–158.
11. Vanoni, V. A., and G. N. Nomicos, 1959, Resistance properties of sediment-laden streams. Proc. Am. Soc. Civil Engrs., J. Hydraulics Div., **85**, HY5, pp. 77–107.
12. Daly, R. A., G. D. Manger, and S. P. Clark, Jr., 1966, Density of Rocks. In: Handbook of Physical Constants, S. P. Clark, Editor, Geological Society of America, New York, N.Y., pp. 19–26.
13. Yalin, M. S., 1972, Mechanics of Sediment Transport. Pergamon Press, Oxford, 290 pp.

Notations

A	Eddy diffusivity
a	Eddy diffusivity at the bed
b	Eddy diffusivity slope
C	Volume fraction concentration
C_0	Volume fraction concentration at the bed
C_R	Reference volume fraction concentration
d	Flow depth in flume
d_0	Sediment grain diameter
g	Gravitation acceleration
R	Hydraulic radius
S	Flume slope
U_*	Friction velocity
w	Settling velocity
w_0	Unhindered settling velocity
z	Distance from the bed
z_R	Reference level distance from bed
z_0	Roughness length
z_{0s}	Roughness length obtained from sediment concentration data
z_{0w}	Roughness length obtained from velocity data
α	Exponent of hindering factor
κ	Von Karman coefficient
κ_s	Von Karman coefficient obtained from sediment concentration data
κ_w	Von Karman coefficient obtained from velocity data
ϱ	Fluid density

27

Journal of Geophysical Research 83, No. C12, 6052-6062.

Near-Bottom Sediment Concentration and Fluid Velocity Measurements on the Inner Continental Shelf, New York

J. W. LAVELLE,[1] R. A. YOUNG, D. J. P. SWIFT, AND T. L. CLARKE

NOAA/Atlantic Oceanographic and Meteorological Laboratories, Miami, Florida 33149

Prototype instrumentation designed to measure light scattering and transmission and the horizontal components of fluid velocity at a point 100 cm off the sea floor was deployed on the Long Island inner shelf for a 27-day period in October and November of 1976. Depth at the point of deployment was 10.5 m. Data were taken from sensors in hourly bursts consisting of 468 consecutive 1-s samples. Measurements taken with the electromagnetic current sensor were converted to absolute units by using a laboratory calibration, while absolute calibration of the turbidimeter in terms of suspended matter concentration was accomplished by using a combination of laboratory and field measurements. The results from the deployment show the effects of water motions at both wave and subtidal frequencies on sediment concentrations. Although burst mean fluid motions during the observation interval were primarily of tidal frequency, a single wind-forced event caused burst mean currents in excess of 38 cm/s. During that same event, suspended particulate concentrations rose to a burst mean of 79 mg/l from a prestorm level of 5 mg/l, an order of magnitude increase occurring over a period of approximately 12 hours. During the storm event, individual burst records show that fluid motions at surface wave frequencies and with amplitudes of over 100 cm/s occurred at the experimental site. The near-bottom suspended matter field at that time was found to have appreciable energy at surface wave frequencies as well. Changes in suspended matter concentration of the order of 130 mg/l were observed to occur in a period of 3–5 s. Increased burst mean concentration was seen to accompany increased wave activity, although increased mean flow with declining wave activity also led to increased suspended particulate concentration. When storm conditions (wave activity and mean flow much above deployment interval ambients) abated, concentrations returned to ambient levels in approximately 12 hours. Coherence between suspended matter concentration and horizontal fluid velocity was found to be statistically significant during four intervals of the deployment. In most cases the significance was centered around a broad frequency band near 0.1 Hz. Vertical near-bottom wave velocities were inferred from the current measurements. The analysis of coherence and phase between the vertical velocity and concentration supports the hypothesis that part of the measured concentration signal was due to the vertical oscillatory advection of the mean concentration field past the turbidimeter during the passage of surface waves.

INTRODUCTION

This paper reports the first of a series of experiments designed to investigate the relationship between near-bottom fluid velocity and suspended matter on the inner continental shelf south of Long Island, New York. In the experiment reported here the temporal structure of both fields was examined at a single site over a 27-day interval by using prototype instrumentation developed expressly for this purpose. For these measurements, fluid motions and particulate concentrations were assumed to have appreciable energy content at surface wave frequencies and also at tidal and subtidal frequencies with little energy content in the intermediate range. Based on this assumption, data taken in bursts were considered suitable for the initial measurements of both fluid motion and particulate concentration. High-frequency motion was observed by burst sampling velocity and suspended matter sensors at 1-s intervals during 8-min bursts, while lower frequencies were observed by separating the bursts by 1 hour. Measurements were made 1 m from the bottom in 10.5 m of water.

Simultaneous observations of near-bottom fluid and sediment motions of this kind in the marine environment have only recently begun to appear in the literature, although such studies in rivers and estuaries are more common (summarized by *Graf* [1971]). Starting in the mid-1960's, Sternberg (summarized by *Sternberg* [1972]) and co-workers have made extensive boundary layer measurements of velocity profiles coupled with simultaneous photographic and closed circuit television observations of ripple and bedload transport. Such transport observations are difficult to quantify. In some instances, bottle samples of suspension concentration were obtained, but these measurements could not resolve the rapidly varying fluctuations in concentration nor elucidate their relationship to rapidly fluctuating near-bottom velocities. In addition, these measurements were made in tidal channels and therefore did not include the effects of surface waves, an important aspect of sediment transport on the open continental shelf. *McCave* [1973] was able to shed some light on transport in a tidal channel over beds of varying roughness, but his measurements of suspended sediment concentration were also of the bottle type. *Butman and Noble* [1977] have recently described measurements of the transport in the boundary layer on the mid-shelf and have reported evidence of bottom wave surge during fair weather at a depth of about 70 m.

Low-frequency bottom water motions associated with tides in the area of study are generally weak (<10 cm/s) and are thought to be of little importance in resuspending sediments. At lower frequencies, major storm events cause near-bottom currents to exceed thresholds for sediment movement and may account for the bulk of sediment eroded and transported on the continental shelf [e.g. *Rodolfo et al.*, 1971; *Lavelle et al.*, 1976]. Superimposed on both of the above scales of motion are the higher-frequency motions associated with surface gravity waves which are present during all times of the year. It is our hypothesis, shared with many previous workers, that during fair weather, bottom wave surge is the mechanism that resuspends bottom sediments and causes them to be transported by weaker mean currents which on their own would be incapable of causing resuspension and transport. Obviously, during storm events, when wave surge is greatly intensified and vertical diffusion of resuspended sediments is large, resuspension and transport is also greatly enhanced, but it is precisely during those times that the requisite measurements are more difficult to obtain.

---

[1] Present address: NOAA/Pacific Marine Environmental Laboratory, Seattle, Washington 98105.

In view of the above the scarcity of simultaneous measurements of high-frequency changes in flow and sediment concentration in the bottom boundary layer is not surprising, and to date we know of only one set of experiments designed to resolve motions with periods of 2–200 s outside the breaker zone [*Lesht,* 1977]. In an open shelf deployment, Lesht used three small bidirectional propeller-type current meters to obtain velocity profiles within the first 100 cm above the sea floor and a transmissometer to record changes in light absorbtion at 15 cm above the bed [*Lesht,* 1978]. Those measurements consisted of several continuous series of 12-hour length with each sensor sampled at a 1.6-s interval. Thus, although surface wave and tidal frequencies were resolved, the event-scale frequencies (storms) were not observed. Instrumentation used in the present experiment was designed to record both surface wave and event-scale features of both fields.

INSTRUMENTATION

The concentration-velocity (CV) probe used in the present study consists of a sensor platform and a separate housing for data storage and power systems connected by an electromechanical umbilicus 65 m in length (Figure 1). The sensor platform is hexagonal with a width of 84 cm and a height of 6.5 cm, having a relatively smooth top surface and an expanded metal bottom bearing surface for traction. The weight of the platform is approximately 170 kg. A horizontal crossarm approximately 80 cm in length supports the sensors, a Marsh-McBirney electromagnetic current velocity sensor, and a Monitek turbidimeter. The sensors are mounted at opposite ends of the crossarm to reduce the shadowing of the current sensor by the turbidimeter. The crossarm is attached to a vertical post by a locking ball joint arrangement. When the platform is in place on the bottom, the sensors are positioned 1 m from the bed.

Deployment of the system is diver assisted. The sensor platform, enclosed by a removable protective shroud, is supported near the bottom by a surface float while the umbilicus is payed out and the data acquisition and power housing are placed on the bottom. The sensor platform is then lowered to the bottom up to 65 m from the data acquisition and power package. The protective shroud is removed by the divers, who level and set the crossarm to the proper azimuth with the aid of a compass mounted on it. In order to check the constancy of that azimuthal direction during the deployment, a General Oceanics film recording inclinometer has been mounted on the sensor platform.

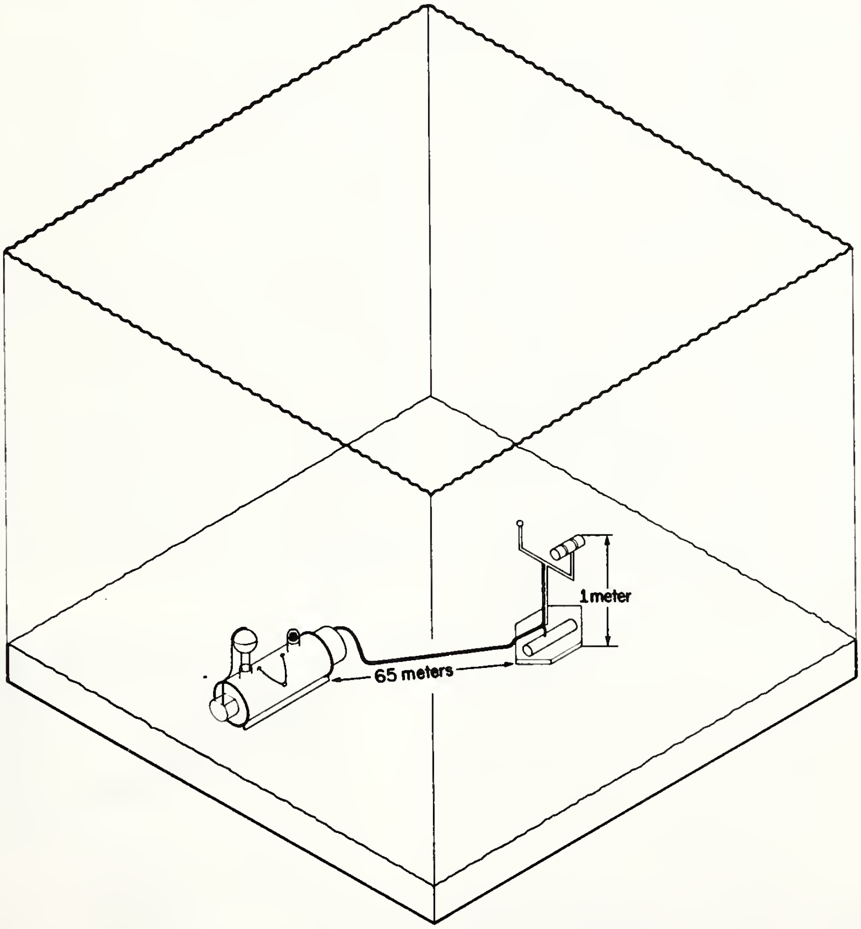

Fig. 1. Disposition of sensor platform and data acquisition and power supply system on the sea floor.

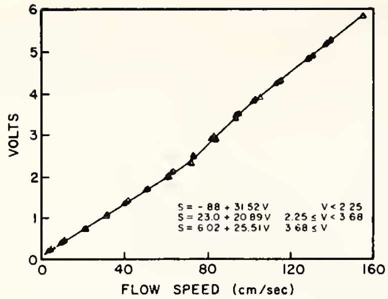

Fig. 2. Data and calibration equations for electromagnetic current sensor used in the measurements. See text for discussion.

The data acquisition and power package consists of a recorder, sensor electronics, and a 12-V gel cell power supply. An acoustically triggered mechanism on the same housing releases, on command, a small marker buoy used to locate the device for recovery.

The current sensor is a two-axis Marsh-McBirney model 511 electromagnetic current meter with a diameter of 3.8 cm. The pole faces are orthogonal and horizontally mounted, allowing two horizontal flow components to be measured. The cutoff frequency of the sensor is 5 Hz. Filters were used to limit the response to 1 Hz to avoid aliasing at the sample rates used. Maximum velocity measureable with this instrument configuration is approximately 150 cm/s. Calibration experiments for the current sensor will be described in the following section.

The turbidimeter is a modified Monitek model 350/136 which measures light attenuation and low forward angle scattering. The Monitek housing contains a pair of incandescent light sources separated from a pair of photodiode light sensors by a water path distance of 10 cm. A 3-cm baffle separating the two photodiode sensors extends from the half of the housing containing the two sensors and insures that the scattered light received has been scattered through an angle of approximately 5°–35°. The light sources are driven alternately while the sensors record the direct and scattered signals simultaneously. The measure of suspended material is the square root of the product of successive ratios of scattered to directly transmitted light. By alternating sources the effects of instrumental drift and window occlusion are eliminated [*Monitek,* 1977]. This is possible because the factor which modifies the direct channel signal, when one source is occluded for example, also modifies the succeeding scattered channel signal. Because the factor shows up in both the numerator and denominator of the product of the ratios of scattered to direct light, the occlusion does not change the resulting concentration value. The modified probe may be driven at a frequency of 1 Hz. The spectral peak of the incandescent light sources is filtered through a yellow (5700 A) filter before transmission. Calibration of the sensor is discussed below.

No pressure recordings have been made in conjunction with this instrument deployment, but in future deployments, bottom pressure will be recorded at the same frequency as the horizontal velocity components. The CV probe was built and calibrated by Engineering Development Laboratories, NOAA, Washington, D. C.

CALIBRATION

The velocity sensor response was calibrated using a closed, recirculating flow tunnel. Azimuthal orientation of the probes was controlled so that both x and y velocity components could be independently calibrated. Asymmetry of the response of the sensor to reverse flow was examined by sensor rotation of 180°. No significant differences among any of the orientations or axes were apparent over the range 0–155 cm/s, and no distinction of axes or orientation was made in the calibration analysis.

Figure 2 shows the speed calibration and best fit to the points, corresponding to at least four measurements at each of 14 flow speeds. Because a break in slope occurs in the vicinity of 80 cm/s, the data have been fit with three connected straight line segments. The break is probably a result of flow separation around the sensor. The residual error about the best fit is given in Figure 3, which shows a relatively uniform error distribution over the whole range of flow speeds. Maximum error is less than 2.5 cm/s. Calibration of the sensor in oscillatory flow was not attempted.

A system calibration was also performed following the initial deployment of the probe. The platform with both the velocity and concentration sensors attached was inverted and towed through still water at a known speed. Again the azimuthal orientation of the sensor platform was varied. Results at two different flow speeds (L. Huff, personal communication, 1977) show that the instrumental response is slightly anisotropic, likely resulting from the shadowing of the current meter by the turbidimeter. The maximum velocity defects at 13.5 and 50 cm/s amount to 22% and 12%, respectively. In view of the small number of towing speeds, however, we were not able to define a better calibration curve for the velocity sensor than that presented in Figure 2. It will be reasonable, nonetheless, to expect some consequences of the observed anisotropy in the current data to be presented.

Figure 4 presents calibration data for the turbidimeter. Points presented on the plot are both field and laboratory in origin. Concentration data at 8 mg/l and below were taken in the field on October 20 and again on November 15 and 16, 1976, within 100 m of the probe deployment site during 8-hour sampling periods. Hourly samples with some replicate sampling were taken with Niskin 2-l plastic bottles which were suspended approximately 1 m above the bottom from a weighted wire line. The bottle was lowered over the side until the weight reached the bottom as determined by release of tension on the line, then slightly raised to approximately 1 m. Time was allowed for material that may have been resuspended by the weight to be advected away from the bottle site, and the bottle was then tripped by messenger. Samples were filtered through preweighed filters with nominal 0.4-μm pore sizes, washed, dried, and reweighed. Detailed description of the sampling procedure, analysis, and results is to be found in R. A. Young et al. (manuscript in preparation, 1978). Sample

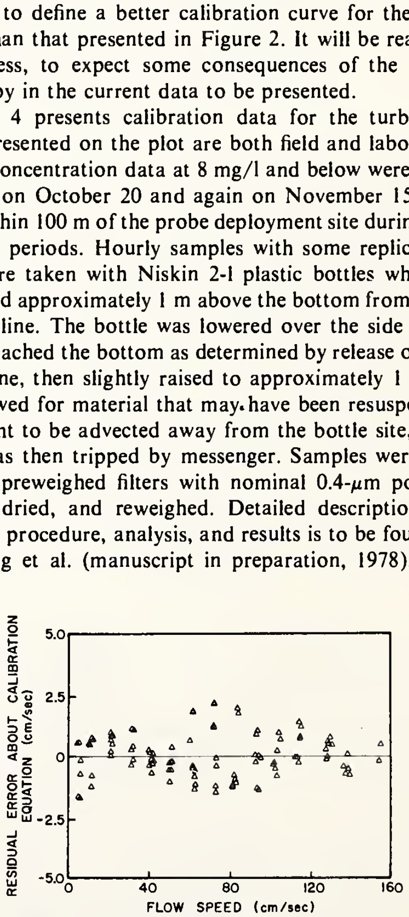

Fig. 3. Residual error about the calibration equation for the current sensor.

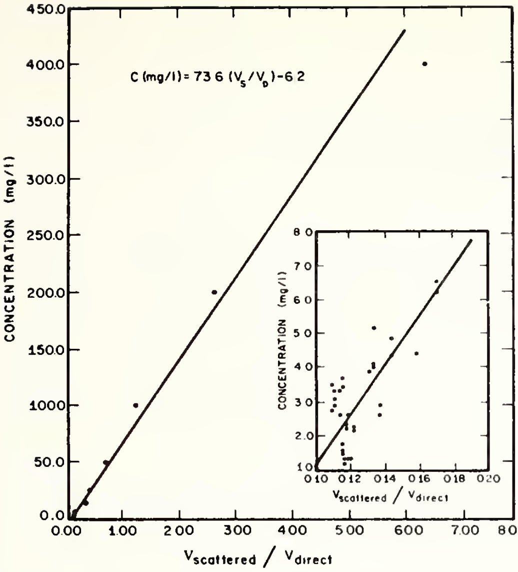

Fig. 4. Data and calibration equation for the Monitek turbidimeter based on laboratory and field observations. Inset shows data from field observations. V_s and V_D are the voltages associated with the scattered and direct light transmissions, respectively.

acquisition was so timed that a bottle sample was taken while the deployed instrument was acquiring data.

Laboratory points (Figure 4) are those at 15 mg/l and above and were taken with standard solutions of the polymer Formazin [*Franson,* 1977], which are only roughly equivalent to the corresponding mass concentration of suspended matter in milligrams per liter. Justification for plotting laboratory points as mass concentration rather than in nephelometric turbidity units (NTU) comes from the approximate colinearity of field and laboratory points when the latter are assigned mass concentrations. This method of extending the calibration into the high-concentration region, where field measurements were unavailable, precludes the assignment of confidence limits to the high concentration values reported herein.

The nephelometer voltages associated with each water sample in Figure 4 represent burst-averaged scattered and direct voltage signals. Direct channel voltages recorded during the first half of the deployment period were corrected for linear voltage drift. In the second half of the deployment after the instrument was serviced at sea, both an offset and a drift were observed in the direct voltage channel. Although corrected points from the second half of the deployment have been included in the calibration analysis and fall about the line which would be approximately the result of a calibration without them (Figure 4), further discussion of the data from the second half of the deployment will not be made in this report.

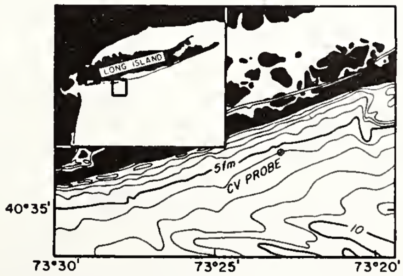

Fig. 5. Location of study area off the Long Island coast. The deployment location is marked by a crosed circle.

The equation in Figure 4 is a best fit to the data using an ordinate weighting of the data points. Error in the instrument-measured concentration within the context of this calibration ranges from about 75% at low concentrations to about 20% at high concentrations. Effects due to changes in composition, shape, or size distributions of particulates which may have occurred during the deployment could not be explicitly considered. Cumulative size distributions taken at the beginning and end of the deployment are reasonably similar (R. A. Young et al., manuscript in preparation, 1978), suggesting that long-term changes in the optical properties of the particulates at the deployment site likely did not occur. However, suspended particulate samples from storm intervals were unavailable. The intensity of wave activity at those times may have resuspended particulate material from the bottom which would not usually be found in the water column. That might have led to a change in the overall index of refraction, which would have temporarily changed the turbidimeter calibration in an unknown way. Absolute values for concentration reported herein must be judged in that light.

Field Measurements

The instrument described above was deployed on October 19, 1976, at a site 2 km west of Fire Island Inlet, Long Island, New York (40°35.8'N, 73°23.5'W) approximately 2 km offshore at a water depth of 10.5 m (Figure 5). The location chosen was along a straight coastline where longshore variations in flow and concentrations would be minimal. The area is one in which the hydraulic climate had previously undergone study [*Lavelle et al.,* 1976] and has also been the site of extensive substrate studies [*Freeland et al.,* 1977]. Bed material at the site was a medium sand, which was reported to be rippled by the deployment divers. Three grab samples taken during the deployment showed that mean sediment size was 0.16 mm.

The experiment was conducted during late October and November, months in which increasingly energetic fluid motions result from the onset of late fall storms sweeping through the area. The probe began taking usable data on October 19 at 1600 hours EST in a burst acquisition mode. Bursts consisted of 468 samples of the two horizontal velocity components and a like number of samples of direct and scattered light intensities each at a 1-s interval; the bursts were spaced at hourly intervals. Data storage and battery capacity were such that 15 days of data could be taken before servicing was required. The meter was serviced on November 4 and 5, 1976, and the instrument continued recording until November 16, 1976. Problems with one light source of the nephelometer system resulted in the actual acquisition of concentration data at a 2-s interval.

The burst-mean time series of both fluid velocity and suspended matter concentration are shown in Figure 6. The burst mean velocity data shows a strong semidiurnal tidal signal, the amplitude of which is nearly 6.5 cm/s, and the direction of which is primarily longshore. (The longshore direction indicated on the figure was taken as the trend of the 5-m isobath in the area (Figure 5); in all figures, 'easterly' represents the 75° direction true.) Significant subtidal energy, also in the longshore direction, was recorded at the experimental site during the storm of October 20–23. A rapid flow reversal was also recorded during that storm. Longshore currents changed

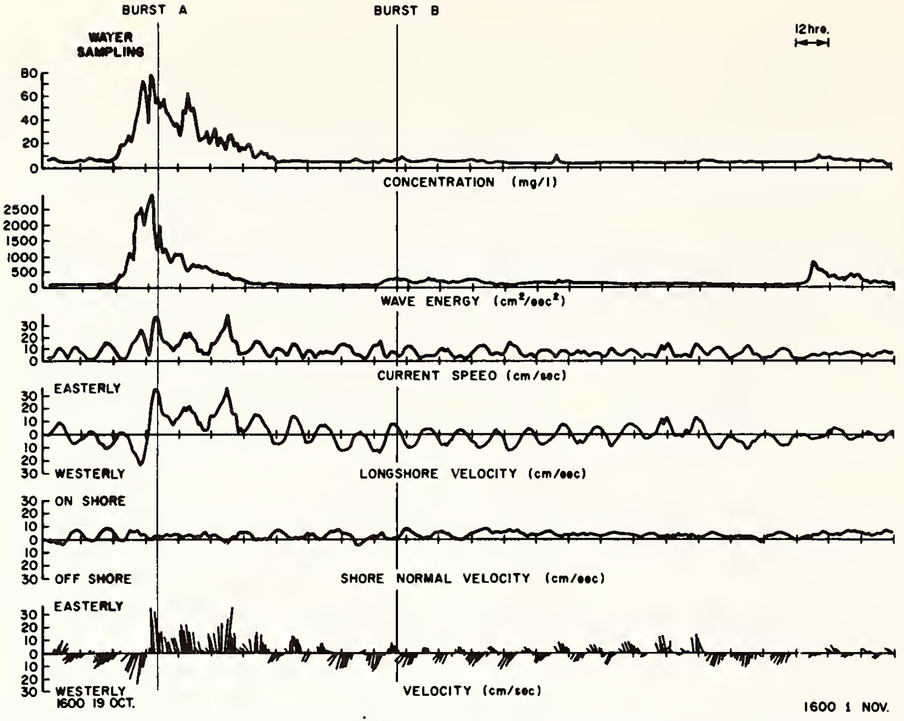

Fig. 6. Record of burst means for the period 1600 October 19 to 1600 November 1, 1976. Bursts A and B are shown in Figures 8 and 9. Suspended particulate samples used in the turbidimeter calibration were taken on an hourly basis during the interval marked by stippling.

from 27 cm/s in the westerly direction at 0200 October 21 to 39 cm/s in the easterly direction by 0700 October 21. Winds at Fire Island Coast Guard Station some 2 km from the site measured at maximum 13 m/s in the westerly direction and 15 m/s in the easterly direction during the same time interval. The prevalent net onshore direction of the burst mean currents over the entire deployment period may reflect the shadowing of the current probe by the turbidimeter as previously discussed.

The term 'wave energy' in Figure 6 denotes the variance of the speed about the burst mean. Wave energy grew rapidly at the onset of the storm of October 20–23, increasing 40 fold within a 16-hour period (1500 October 20 to 0600 October 21). In apparent response to significant oscillatory activity during that interval, the sensor platform (weighing approximately 170 kg) rotated 12° in the clockwise direction at approximately 0300 October 21, as was indicated by records from the base-mounted inclinometer. The resultant orientation of the instrument put the sensor arm within 5° of the onshore-offshore direction.

Wave energy increase during this interval was associated with an increase in the suspended particulate concentration of the near-bottom water (Figure 6). Concentration values increased from about 5 mg/l (the mean over the first 24 hours of deloyment) to 73 mg/l within 12 hours. Concentrations also return to ambient levels in approximately 12 hours, when the mean flow conditions and wave activity return to deployment interval ambient values. The maximum concentrations of 79 mg/l recorded during the storm follows a shift in winds to the west and is an order of magnitude larger than prestorm concentrations. Implications concerning the synopticity of concentration measurements taken during a storm interval and the temporal representativeness of measurements, though synoptic, during a nonstorm interval may be drawn from these observations.

Details of the changes in concentration, mean flow, wave, and wind activity during the October 20–23 interval are found in Figure 7. The vertical line passing through all data at 0500 October 21 marks a local minimum in both fluid speed (4 cm/s) and suspended particulate concentration (36 mg/l). It also denotes the time of flow reversal. Flow at 13 cm/s in a westerly direction and a particulate concentration level of 71 mg/l occurred an hour before. An hour later, flow was 25 cm/s in an easterly direction, and suspended particulate concentration was 79 mg/l. The decrease in mean particulate concentration by as much as 35 mg/l between 0400 and 0500 October 21 suggests that material with substantial settling velocity which was held in suspension by the combined action of waves and mean flow had settled in response to the decrease in mean flow; wave energy shows relatively little variation about the time marked by the vertical line in the figure.

As previously noted, the flow reversal was in response to a directional change in the wind. That change was also followed closely by the initiation of wave energy decrease, probably resulting from the limitation of fetch available to wave generation. Diminution of wave energy is seen to be a factor in decreasing suspended particulate concentration levels following the wind directional shift, although it is also clear that wave energy is not the sole factor in determining concentration levels. Note the increase in suspended particulate concentration at 2000 October 21, during a period of declining wave energy and increasing mean flow. That particulate concentration peak may represent advection of material from outside the local area as well as the local effect of increased mean fluid velocity. The concentration variance has been plotted (Figure 7) based on the suggestion of *Chriss and Pak* [1977] that high

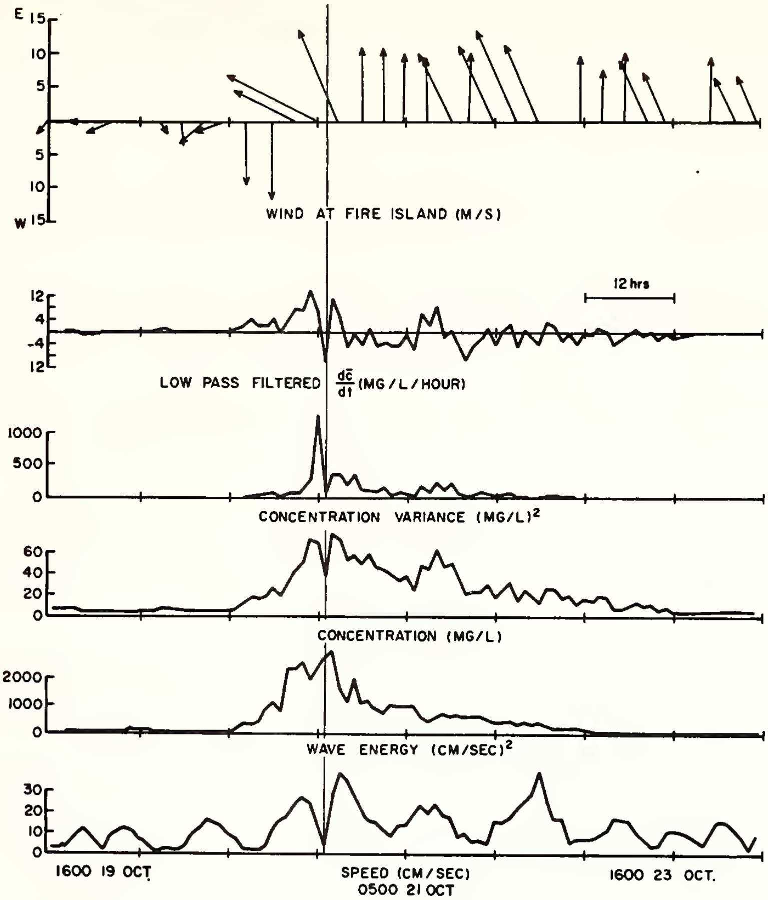

Fig. 7. Mean current speed, wave energy, sediment concentration and variance, the rate of change of concentration and winds recorded at Fire Island Coast Guard Station, New York, during the storm of October 20–23.

concentration variance is an indicator of local erosion activity. The values of concentration variance during the interval in question do show some slight increase above those of neighboring intervals. Note also the substantial variance increase during declining mean flow at 0400 October 21.

Individual burst records corresponding to a storm interval and a more quiescent interval are shown in Figures 8 and 9. The position of each burst in the deployment has been marked on Figure 6. The first, taken during the storm, shows a mean flow of 39 cm/s. Oscillatory flow had a primary frequency near 0.1 Hz, had a maximum speed greater than 100 cm/s, and was primarily in the shore normal direction as is expected of shoreward propagating surface waves. The suspended particulate concentration is highly variable in magnitude with an occasional excursion past 100 mg/l. The instantaneous sediment flux (Figure 8) is a product of current speed and sediment concentration.

The second burst (Figure 9), taken during a more quiescent interval, shows a mean current speed of 5.2 cm/s. Although oscillatory flow was primarily in the shore-normal direction and was due to surface waves, the frequency was considerably higher than that of the former burst, while the flow amplitude (approximately 20 cm/s) was considerably reduced. The concentration values are again seen to have some temporal variability about a mean of 6 mg/l, but the fluctuations are no more than ±2 mg/l.

Concentration measurements in six consecutive bursts (Figure 10) show both the extent of burst-to-burst and within-burst variations in suspended particulate concentration. Note the concentration scale changes in each of the panels in the figure. The data taken at 0400 October 21 correspond to the burst with the highest concentration variance recorded during the measurement period. It was previously seen to be associated with a rapidly falling burst mean current magnitude. Instantaneous concentration values of nearly 190 mg/l occur at several points in the record. The same panel shows a 3 to 5-s interval during which a change of concentration of approximately 130 mg/l occurred, reflecting the rapid settling of material locally eroded or the advection of a strong concentration front past the sensor. The data show more generally rapid concentration changes of substantial size during the storm interval. A very long period (approximately 180 s) variation, seen both in the 0400 October 21 data and to a lesser extent in the 0600 October 21 data, may be associated with wave trains. Resolution of the low-frequency spectral content of the concentration signal for a storm interval may require burst lengths of duration longer than those used in the present experiment.

DISCUSSION

A representative horizontal velocity spectrum averaging information from six consecutive storm bursts (1000–1500 Octo-

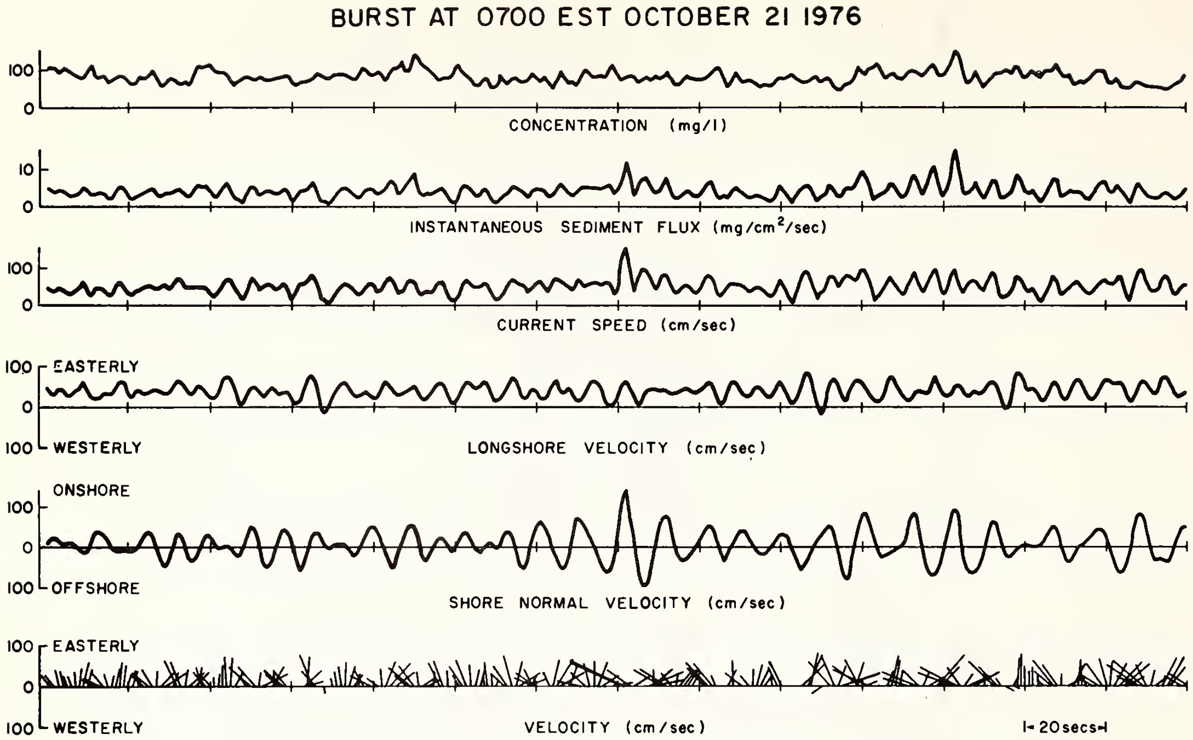

Fig. 8. Time series from burst A, acquired during the storm of October 20–23. Time of burst is noted in Figure 6.

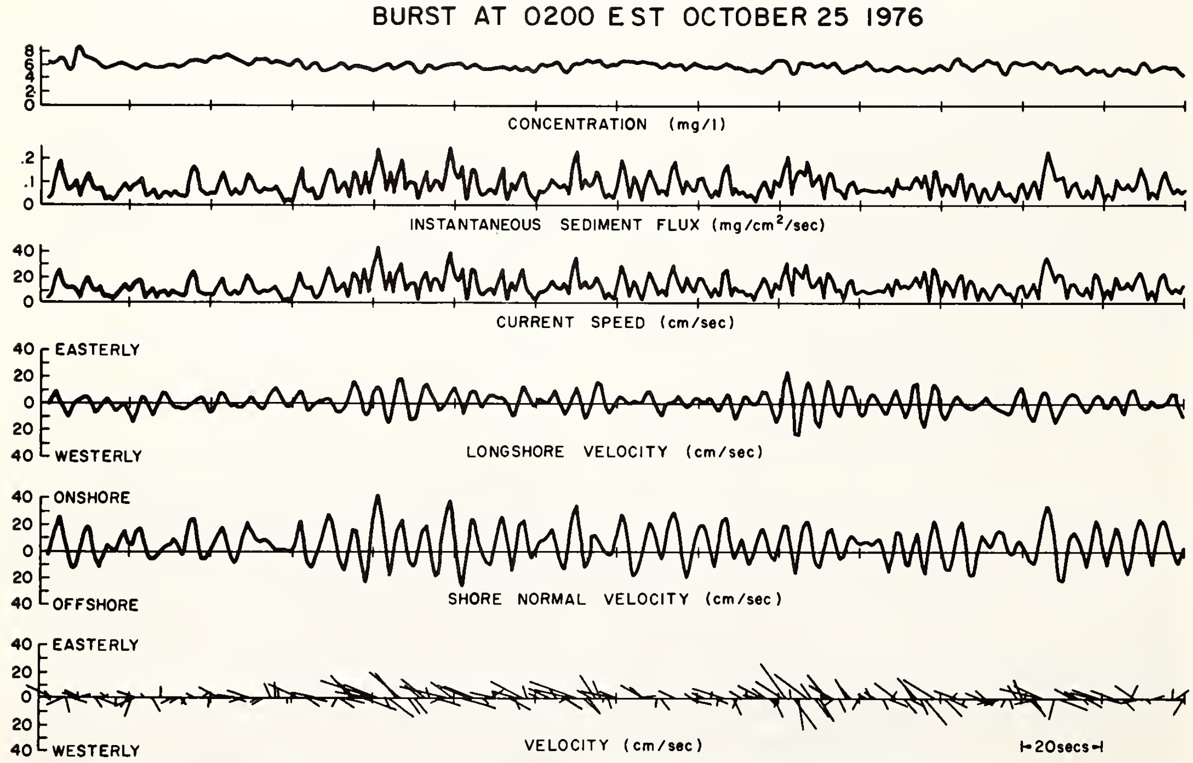

Fig. 9. Time series from burst B, acquired during a fair weather period on October 25. Time of burst is noted in Figure 6.

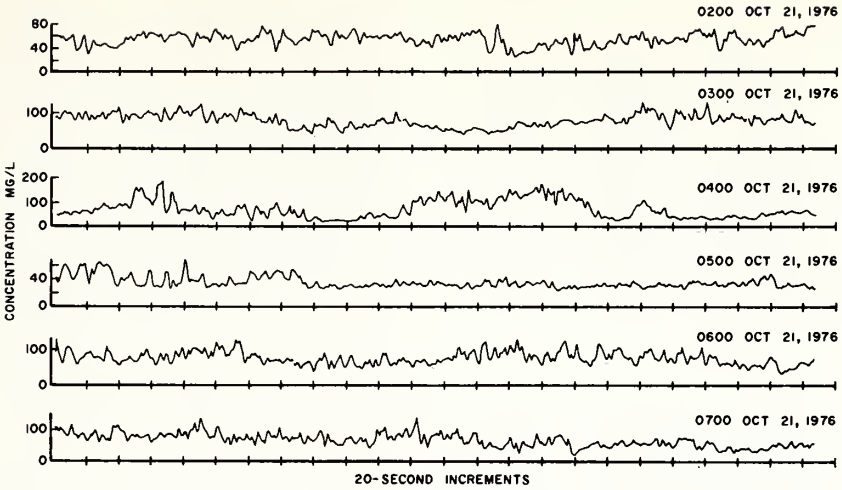

Fig. 10. Variation in sediment concentration in successive bursts during the storm of October 20–23. The 0500 October 21 burst was a local minimum in current speed and suspended particulate concentration (Figure 7).

ber 21) is given in Figure 11. A rotary spectral representation [*Gonella,* 1972; *Mooers,* 1973] was chosen for the presentation because in addition to energy content, it provides a measure of the linearity of oscillation at each constitutive frequency: equivalence of right- and left-hand spectral components at a single frequency indicates a linear oscillation, while a dominance of either the right- or the left-hand component indicates a rotary oscillation. Linearity in an oscillation is expected from a propagating wave, while turbulence should show no preference as either a linear or rotary oscillation. This spectrum indicates principal energy in near linear oscillations with a period near 10 s, with a secondary peak in linear oscillations near 6–7 s.

The energy spectrum of the suspended particulate concentration (Figure 12) for the same bursts as those used above has two salient features: dominance by low-frequency oscillations and a relatively narrow but significant peak near 0.1 Hz. The cause of the low-frequency dominance of the spectrum is suggested by the traces of Figure 10, even though the two figures represent data spanning close but different time intervals. Low-frequency spectral dominance over this data set is peculiar to the storm period. The spectral peak near 0.1 Hz occurs at the same frequency as the dominant peak in the velocity spectrum. A secondary broad peak about 0.16 Hz likewise falls at a frequency at which a significant peak in the velocity spectra was observed.

To examine the relationship between the particulate concentration and fluid velocity more fully, the coherence and phase between the two measurements (Figure 13) were calculated from data spanning 10 consecutive storm bursts (1000–1900 October 21). Coherence is plotted on an arctangent ordinate scale [*Jenkins and Watts,* 1968]. For the available degrees of freedom the 95% level of significance is 0.31. That analysis confirms that the relationship between particulate concentration and horizontal velocity, previously suggested by the spectra, is statistically significant. In addition, Figure 13 suggests that low-frequency components of velocity at the experiment site during the storm occurred along with associated concentration fluctuations. Increased burst length during storm intervals is required to resolve such components.

The spectra and coherence figures of the previous paragraphs represent a sample of fluid and particulate behavior

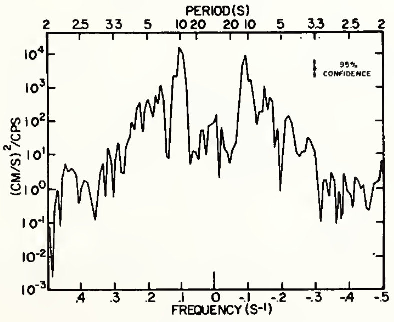

Fig. 11. Rotary horizontal velocity spectrum for the interval 1000 October 21 to 1500 October 21. Right-handed rotations are denoted by positive frequencies. Normalization of spectrum is uncorrected for energy reduction resulting from the use of a cosine data window [*Bath,* 1974] in the analysis.

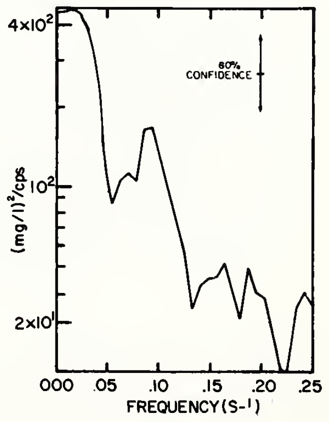

Fig. 12. Suspended particulate concentration spectrum for the interval 1000 October 21 to 1500 October 21. Because of instrumental difficulties, data acquisition interval was 2 s. Left and right sides of the spectrum have been summed; normalization of the spectrum was not corrected for cosine data windowing [*Bath,* 1974] in the analysis.

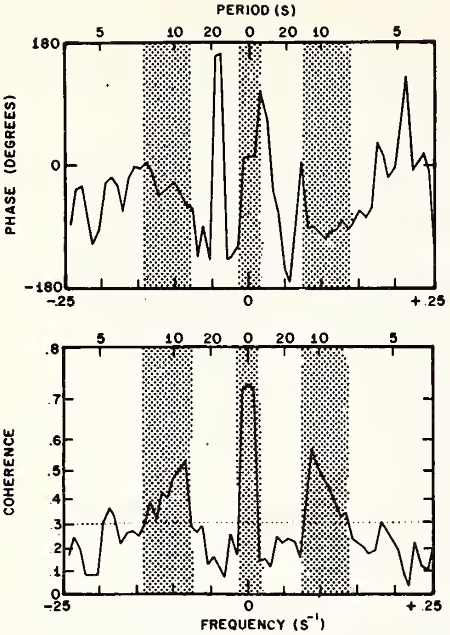

Fig. 13. Inner coherence and inner phase [*Mooers*, 1973] between horizontal velocity components and concentration data for the interval 1000 October 21 to 1900 October 21. The 95% level of significance is denoted by a dotted line. The region of significant coherence has been stippled.

and their interrelationship over a 10-hour period or less. The behavior of wave spectra and particulate concentration-fluid velocity coherence over the first 15 days of the deployment is found in the time series of Figure 14. Wave energy contours have been given in logarithmic units with arbitrary normalization. Right- and left-hand sides of the spectra have been averaged. Wave energy has a maximum during the second day of the deployment as previously noted. The trend of shaded contours (high energy) from higher to lower frequency over three separate time intervals is indicative of local wave generation. The subsequent cascade of energy from lower to higher frequency during the storm of October 20–23 occurred after the shift of wind to the westerly direction had occurred.

The coherence time series (Figure 14) makes evident the occurrence of four periods where coherence passed the 95% level of significance. The single occurrence of coherence at low frequencies occurs at a time when burst mean currents show that flow is to the west, overriding the tidal reversal (Figure 6). Coherence at higher frequencies is seen to be generally coincident with relatively high wave energy periods, but it also makes clear that high wave energy is apparently not a sufficient condition for high coherence.

One mechanism which might lead to periodicity in suspended particulate concentrations at high frequencies is that of the vertical oscillatory movement of suspended sediment by surface waves. In laboratory experiments studying sediment in suspensions over rippled beds, periodicity in suspended sediments is observed in two forms. In closely controlled experiments, *Nakato et al.* [1977] determined that concentration

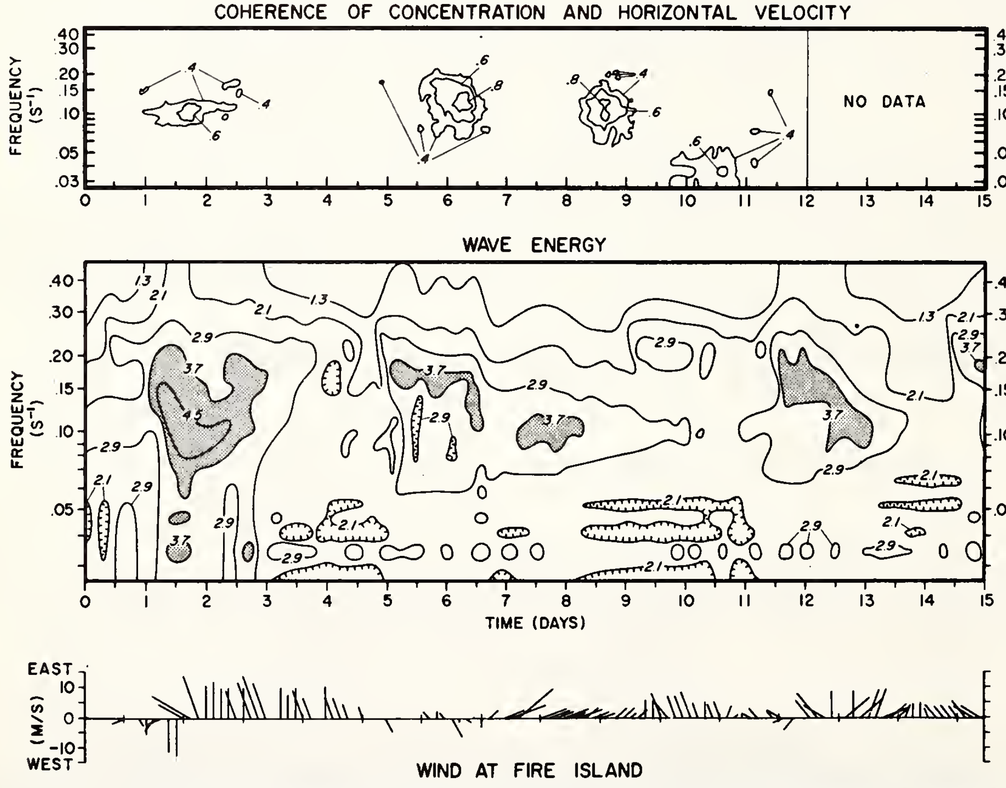

Fig. 14. (*a*) Time series of coherence of suspended particulate concentration and horizontal velocity. The coherence is an average over both velocity components. (*b*) Time series of horizontal velocity power spectra. Spectra of individual components have been averaged. (*c*) Vector time series of wind measured at Fire Island Coast Guard Station, New York. Starting time in all series is 1600 October 19, 1976.

fluctuations of fine sand at twice the frequency of the driving wave was caused in part by eddies, developing in the lee of ripples, which suspended material transported over the ripple crest by mean oscillatory flow. The strength of this type of signal drops off rapidly from the bed, and it seems unlikely, even for very fine sediments, that this component of the suspension field could be observed at 1 m from the bed where our measurements were made.

The second type of oscillatory signal was noted by *Homma et al.* [1965], who observed an oscillation at the same frequency of the driving wave at the top of an apparently well delineated suspended particulate layer. Such an oscillatory component in the concentration signal would appear to reflect the vertical oscillatory advection of material, the settling velocity of which is much smaller than the quotient of the layer thickness and wave period. It is clear that particulate concentrations with any vertical concentration gradient, not necessarily a well delineated particulate layer, may lead to similar observations.

Based on the observation of *Homma et al.* [1965], a possible explanation for the significant coherence between concentration and fluid was sought through the hypothesis that part of the concentration signal reflects the vertical oscillation of a mean suspended matter field past the light sensor. The requirement on settling velocity as outlined above is satisfied by both the fine particulate material taken in water samples at the experimental site and by bed material. A mean particulate size of 20 μm for the sampled suspended particulates (R. A. Young et al., manuscript in preparation, 1978) yields a Stokes settling velocity of 0.06 cm/s [*Graf,* 1971]. Even for bed material with a mean diameter of 0.16 mm and therefore a settling velocity of 1.5 cm/s, the settling velocity is considerably smaller than the quotient of the measurement height (1 m) and a characteristic wave period (10 s).

To examine the hypothesis, the vertical velocity time series was constructed from the measured horizontal velocity time series by using linear wave theory. Because no pressure data were available to sort high-frequency surface waves from high-frequency turbulent fluctuations, an assumption was made that all recorded motion above the burst mean was due to waves. Although only that part of the horizontal velocity correlated with pressure should be used, the assumption is not as severe as it would first appear. At those frequencies where it is not fair, the random phase relationship between concentration and velocity of different data segments in the analysis should lead to both coherence below the level of significance and an arbitrary phase.

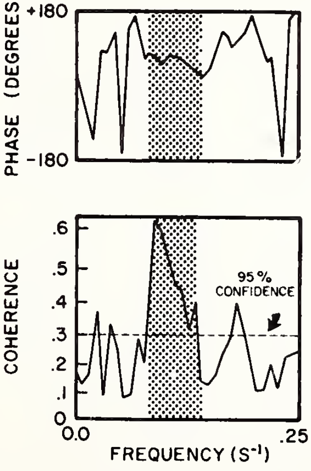

Fig. 15. Coherence and phase between inferred vertical wave velocity with suspended particulate concentration for the interval 1000 October 21 to 1900 October 21. The 95% level of significance is marked by a dashed line. The region of significant coherence has been stippled.

The horizontal velocity time series was Fourier analyzed into its fundamental frequencies, resulting in a wave amplitude and oscillation orientation at each frequency. The Fourier coefficient of vertical velocity, W, at each frequency was determined from the relationship

$$W(\omega) = \pm i\theta(\omega)\frac{\sinh k\tilde{h}}{\cosh k\tilde{h}}\left\{\frac{[U(\omega)]^2 + [V(\omega)]^2}{[U(\omega)]^2}\right\}^{1/2} U(\omega)$$

$$-\omega_{NQ} < \omega < \omega_{NQ} \qquad (1)$$

where U and V are the complex Fourier coefficients at the frequency, ω, θ is the antisymmetric step function with unit value at positive frequencies, ω_{NQ} is the Nyquist frequency, and $\tilde{h}$ is the distance between the sensor and the bottom. The wave number, k, is determined from the dispersion condition [*Lamb,* 1879]

$$\omega^2 = kg \tanh (kh) \qquad (2)$$

where h is the depth of the water. The sign ambiguity in (1) represents the difference in propagation directions for the wave. The ambiguity was removed by presuming that waves at all constituent frequencies are propagating in a shoreward direction. Because much of the recorded wave energy (e.g., Figure 11) seems to be associated with linear oscillations at typical surface wave frequencies and because they are likely moving shoreward, the assumption is not expected to lead to serious errors. Fourier coefficients for the vertical velocity time series were constructed in this way and were inverse transformed. The resultant vertical velocity time series was resampled at a 2-s interval to match the concentration sampling interval.

Figure 15 represents the coherence and phase between concentration and the constructed vertical velocity for a single ten hour period (1000–1900 October 21). The coherence is found to be significant in a broad band near 0.1 Hz but not significant at low frequencies, in contrast to the concentration-horizontal velocity coherence (Figure 13). The phase relationship between the concentration and the vertical velocity near 90° is to be found over the range of frequencies characterized by significant coherence (stippled region in Figure 15). The spectra represented by Figures 11 and 12 and this analysis suggest to us that the hypothesis that at some frequencies surface waves are driving the mean concentration field past a stationary measuring point is a reasonable one. With a better indication of the settling velocity of particulates in suspension during intervals of coherence, this observation might be exploited to provide an estimate of the vertical eddy diffusivity coefficient in this type of flow regime.

Conclusions

The following set of conclusions is site specific, and generalizations to other areas must be based on similarities of depth, bed composition, wave climatology, and mean flow structure. If conditions are reasonably similar one might expect that sampling near-bottom suspended matter concentrations with conventional survey techniques in coastal areas which are wave and wind controlled is unlikely to yield representative samples in any but the most quiescent of conditions. Rapid changes in concentrations within a 12-hour period and the inconstancy of the concentration levels during storm conditions lead to this conclusion. If spatial distributions of near-bottom suspended matter are sought at times of unusual wave or current conditions, the results from this study pose the question as to whether a synoptic view can be gathered without an array of in situ instrumentation.

Large-amplitude, high-frequency oscillations in both currents and suspended particulate concentrations suggest, in addition, that near-bottom water samples taken during storm conditions must integrate over several wave cycles for a sample to be representative. The alternative is to know the location and time of sample to a greater accuracy than is now economically achievable. This conclusion follows from the observed high-frequency concentration fluctuations, including changes by as much as 130 mg/l with a period of 3–5 s.

The near-bottom suspended matter field may have low-frequency components (as was observed in this study) which are poorly resolved by a burst length of even 10 min. A continuous (nonbursted) record may be required to resolve suspended matter activity at low frequency during storm intervals.

Significant coherence of suspended matter concentration and inferred vertical fluid velocity in some frequency bursts with an approximate 90° phase difference between the two variables may indicate that part of the oscillation in concentration signal is due to the vertical advection of a quasi-stationary concentration field past a fixed viewing level. With additional measurements of sediment characteristics during those intervals, that fact might be used to provide information on the turbulence maintaining the sediment in suspension.

Acknowledgments. The work presented here could not have been accomplished without the engineering and logistical efforts of Lloyd Huff, Doug Frlske, and their associates at the Engineering Development Laboratories, NOAA, Washington, D. C., and we thank them for their help. The work was supported by the NOAA/Marine Ecosystems Analysis Program, DOE/Division of Biomedical and Environmental Research, and NOAA/Environmental Research Laboratories.

REFERENCES

Bath, M., *Spectral Analysis in Geophysics*, 563 pp., Elvesier, London, 1974.

Butman, B., and M. Noble, Observations of bottom current and bottom sediment movement on the Mid-Atlantic continental shelf (abstract). *Eos Trans. AGU, 58*, 408, 1977.

Chriss, T. M., and H. J. Pak, Optical evidence of sediment resuspension—Oregon continental shelf (abstract), *Eos Trans. AGU, 58*, 410, 1977.

Franson, M. A. (Ed.), Nephelometric method—nephelometric turbidity units, in *Standard Methods for Examination of Water and Wastewater*, American Public Health Association, Washington, D. C., pp. 132–134, 1977.

Freeland, G. L., J. W. Lavelle, D. J. P. Swift, and R. A. Young, NOAA's waste disposal studies in the New York Bight (abstract), *Amer. Ass. Petrol. Geol. Bull., 61*, 786, 1977.

Gonella, J., A rotary-component method for analyzing meteorological and oceanographic vector time series, *Deep Sea Res., 19*, 833–846, 1972.

Graf, W. H., *Hydraulics of Sediment Transport*, 513 pp., McGraw Hill, New York, 1971.

Homma, M., K. Horikawa, and R. Kajima, A study of suspended sediment due to wave action, *Coastal Eng. Jap. 8*, 85–103, 1965.

Jenkins, G. M., and D. G. Watts, *Spectral Analysis and Its Applications*, 525 pp., Holden-Day, San Francisco, 1968.

Lamb, H., *Hydrodynamics*, 738 pp., Dover, New York, 1879 (1945 facsimile of 6th (1932) edition)

Lavelle, J. W., H. R. Brashear, F. N. Case, R. L. Charnell, P. E. Gadd, K. W. Haff, G. A. Han, C. A. Kunselman, D. A. Mayer, W. L. Stubblefield, and D. J. P. Swift, Preliminary results of coincident current meter and sediment transport observations for wintertime conditions, Long Island inner shelf, *Geophys. Res. Lett., 3*, 97–100, 1976.

Lesht, B. M., Frequency distribution of bottom shear stresses within a tidal cycle on the inner continental shelf (abstract), *Eos Trans. AGU, 58*, 408, 1977.

Lesht, B. M., Field measurements of the bottom frictional boundary layer in the New York Bight, *NOAA Tech. Rep.*, in press, 1978.

McCave, I. N., Some boundary-layer characteristics of tidal currents bearing sand in suspension, *Mem. Soc. Roy. Sci. de Liege, 6*, 187–206, 1973.

Monitek, Monitek model 350/136 submersible turbidimeter, Monitek Technol., Inc., Redwood City, Calif., 1977.

Mooers, C., A technique for the cross spectrum analysis of pairs of complex-valued time series, with emphasis on properties of polarized components and rotational invariants, *Deep Sea Res., 20*, 1129–1141, 1973.

Nakato, T., F. A. Locher, J. R. Glover, and J. F. Kennedy, Wave entrainment of sediment from rippled beds, *ASCE J. Waterways Port Coastal Ocean Div.*, 83–99, 1977.

Rodolfo, K. S., B. A. Bus, and O. R. Pilkey, Suspended sediment increase due to Hurricane Gerda in continental shelf waters off Cape Lookout, North Carolina, *J. Sed. Petrol., 41*(4), 1121–1125, 1971.

Sternberg, R. W., Predicting initial motion and bedload transport of sediment particles in the shallow marine environment, in *Shelf Sediment Transport: Process and Pattern*, edited by D. J. P. Swift, D. B. Duane, and O. H. Pilkey, pp. 61–82, Dowden, Hutchinson and Ross, Stroudsburg, Pa., 1972.

(Received March 3, 1978;
revised May 24, 1978;
accepted June 12, 1978.)

Southeastern Geology 19, No. 3, 191-205.

MORPHOLOGY OF THE MIDDLE ATLANTIC U. S. CONTINENTAL SLOPE AND RISE

By

Bonnie A. McGregor
Atlantic Oceanographic and Meteorological Laboratories*
National Oceanic and Atmospheric Administration
Miami, Florida 33149

ABSTRACT

The continental margin off the Delaware and Maryland coast between Baltimore and Washington Canyons has a different morphology from that of adjacent regions of the U. S. east coast continental margin. A series of ridges extends down the continental slope to the rise, perpendicular to the margin. Seismic reflection profiles parallel to the margin were obtained to determine the internal structure of the ridges, and the processes that may have been active in their formation. A 600-800 m thick sequence of stratified sediment is present on the slope with many unconformities. Numerous periods of deposition and erosion are believed to have been responsible for forming the morphology of this area. Levee or large submarine slide origin, though implied by the morphology, are not supported by the seismic reflection profiles.

INTRODUCTION

The U. S. east coast continental margin off the Delaware-Maryland coast and seaward of the Baltimore Canyon Trough between Washington and Baltimore Canyons displays a different morphology and a varied depositional environment when compared with other slope regions from Georges Bank to Cape Hatteras. A series of broad ridges extends down the continental slope to the upper rise (Figure 1). The continuation of profile 3 (Figure 1) along the slope from south of Hudson Canyon to south of Norfolk Canyon shows the change in morphology between Washington and Baltimore Canyons (Figure 2). Adjacent portions of the slope, north of Baltimore Canyon and south of Washington Canyon, have a dissected morphology with many small, closely spaced valleys. Between Washington and Baltimore Canyons large, broad ridges are present on the slope.

Using the NOAA ship RESEARCHER, five seismic reflection

---

*Present address: Department of Oceanography
Texas A&M University, College Station, TX 77843

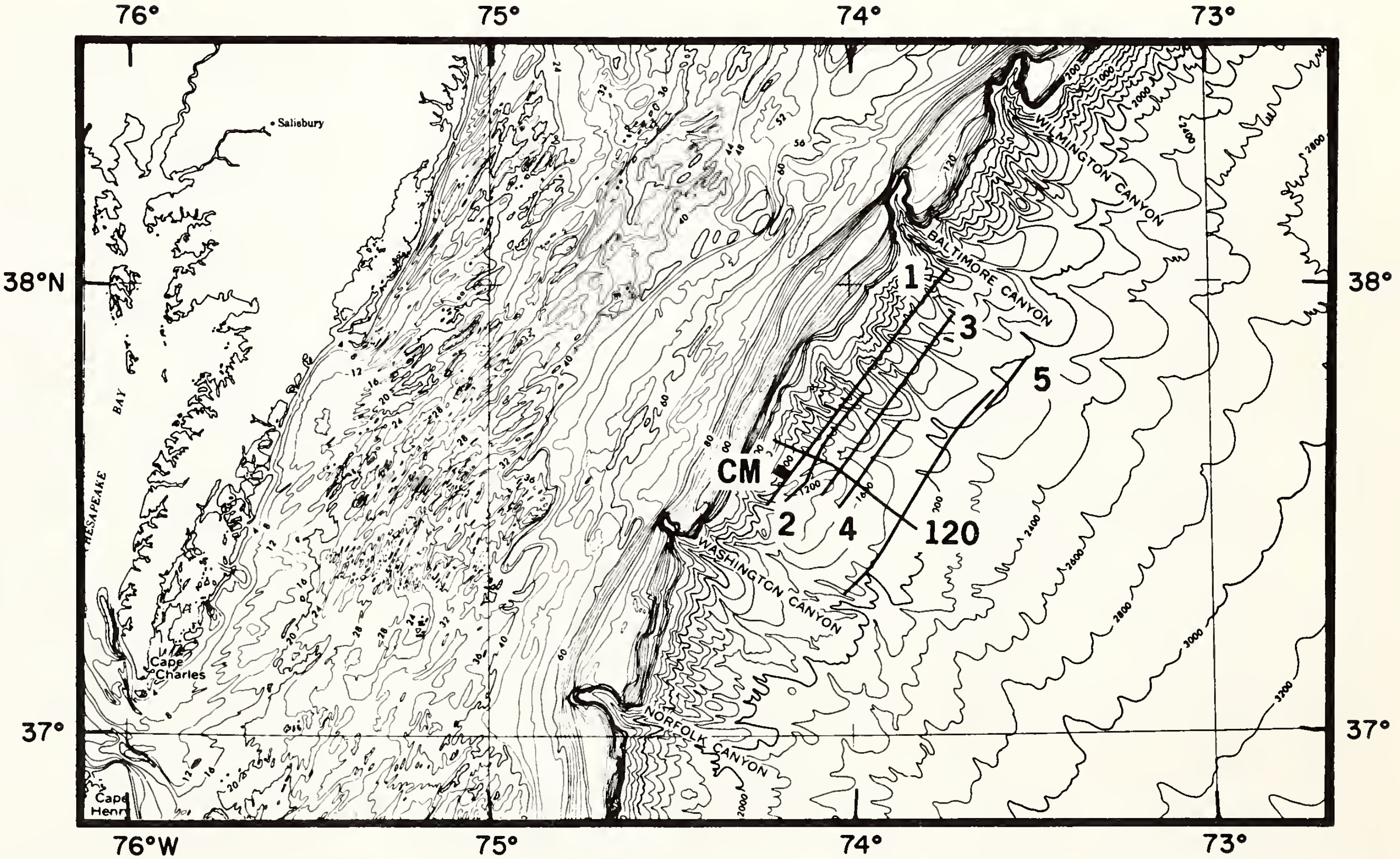
76°
75°
74°
73°
76°W
38°N
37°
38°
Salisbury
CHESAPEAKE
BAY
Cape Charles
Cape Henry
WILMINGTON CANYON
BALTIMORE CANYON
WASHINGTON CANYON
NORFOLK CANYON
CM
1
2
3
4
5
120
200
1000
2000
2400
2600
2800
3000
3200

Figure 1. Bathymetric map after Uchupi (1970) with location of seismic reflection profiles. Numbers are profile designations for Figures 2 through 8. CM is current meter location.

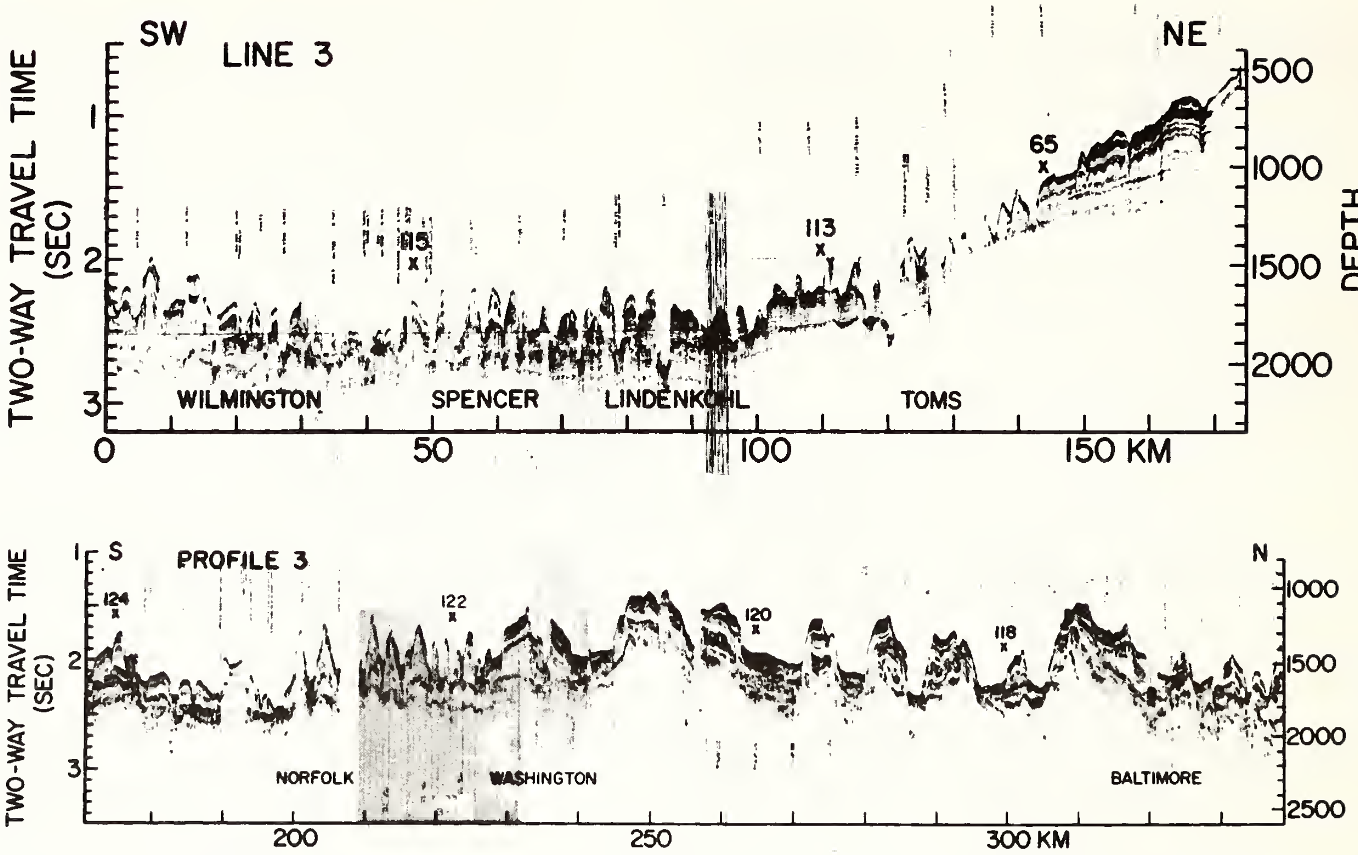

Figure 2. Seismic reflection profile parallel to the continental margin from just south of Hudson Canyon to south of Norfolk Canyon. The track is an extension of line 3, Figure 1. X's and numbers refer to crossing profiles of Uchupi and Emery (1967).

profiles were run parallel to the margin along the slope and rise (Figure 1) to determine the internal structure of the ridges that trend perpendicular to the margin and to characterize their origin and the processes that have been active during their formation. The seismic system used as sound sources 160 cc (10 in^3), 640 cc (40 in^3), and/or 1920 cc (120 in^3) air guns depending on water depth. The firing rate was approximately seven seconds with 1800-2000 psi air pressure in the guns. A 50-element hydrophone was used as a receiving unit, and a recorder displayed the data. The return signal was filtered at 140-430 Hz except for profiles 2 and 4 which were filtered at 63-160 Hz. Photographs of the original records are shown in Figure 3 through 7.

A Savonius rotor current meter was planted on the slope 3 m above the bottom in 910 m of water (Figures 1 and 3) and obtained records for a 14 day period, September 3-17, 1975.

Acknowledgments

I wish to thank George H. Keller and Richard H. Bennett for assisting in the data collection and for reviewing the manuscript. I am grateful to John W. Kofoed for also reviewing the manuscript. Thanks also to the officers and crew of the NOAA ship RESEARCHER for their assistance in gathering the data during March, April, and September, 1975. This work was supported by the National Oceanic and Atmospheric Administration.

SEISMIC REFLECTION PROFILES

The morphology and sedimentary framework of the continental slope changes with water depth. The ridges are well developed between the depths of 1200 and 1500 m (Figures 3-4). Maximum subbottom penetration is approximately 800 m assuming the same sound velocity as in water. The sedimentary section is well stratified with many unconformities throughout. Few reflecting horizons are shown within the upper 400 m of the sea floor on profile 1 (Figure 3), because multiples and width and character of the outgoing signal mask the return from any horizons present. At depth the reflecting horizons on the upper slope (profile 1) appear to be rather continuous. Crossing profiles 120 and 118 of Uchupi and Emery (1967) can be used to approximately line up the profiles.

Profile 2 (Figure 4), located about 3. 5 km seaward of profile 1, shows a thick sequence (700 m) of stratified sediment with many unconformities. The width of the ridges and intervening valleys has increased. The slope is smoother in surface expression south of profile 120 with a decrease in relief from 150 m to 50 m. In general the slope is not dissected by as many valleys as on profile 1. Small scale slumping has occurred on the north side of the ridges. The stratified sequence

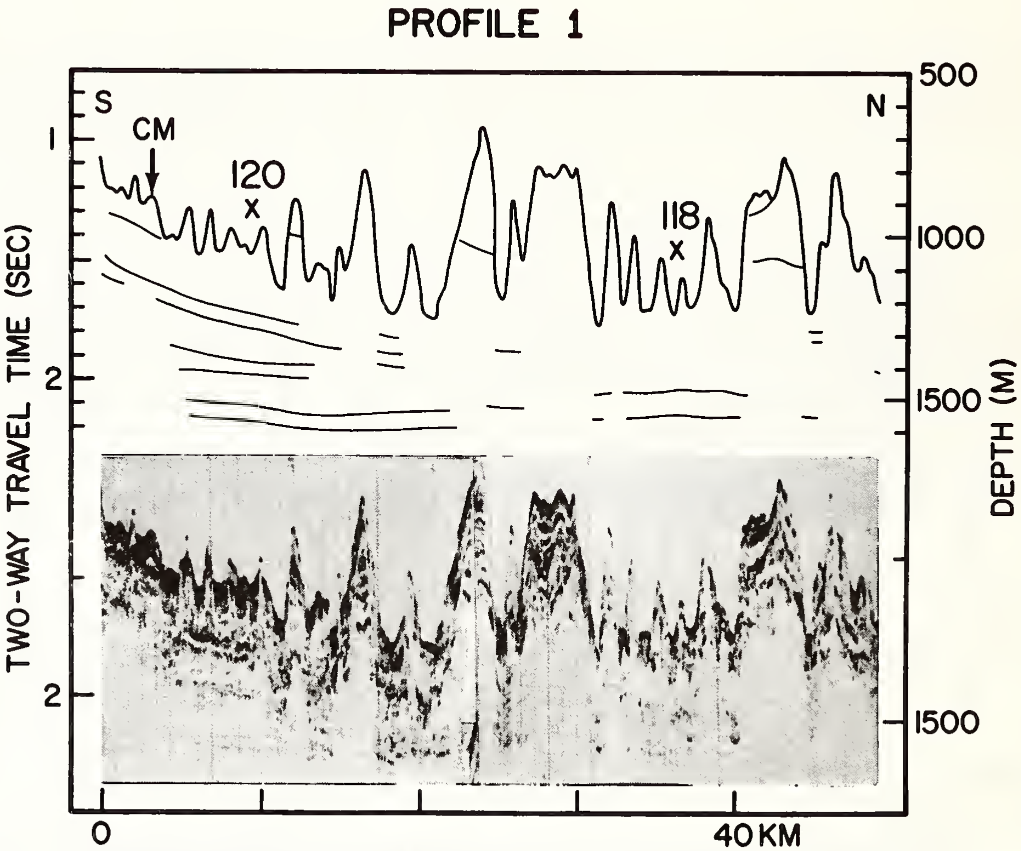

Figure 3. Line drawings and photographs of original seismic reflection records for profile 1. Both 10 and 120 in^3 air guns were used as the sound source. See Figure 1 for location. CM indicates current meter location. "X"s and numbers refer to location of crossing profiles of Uchupi and Emery (1967).

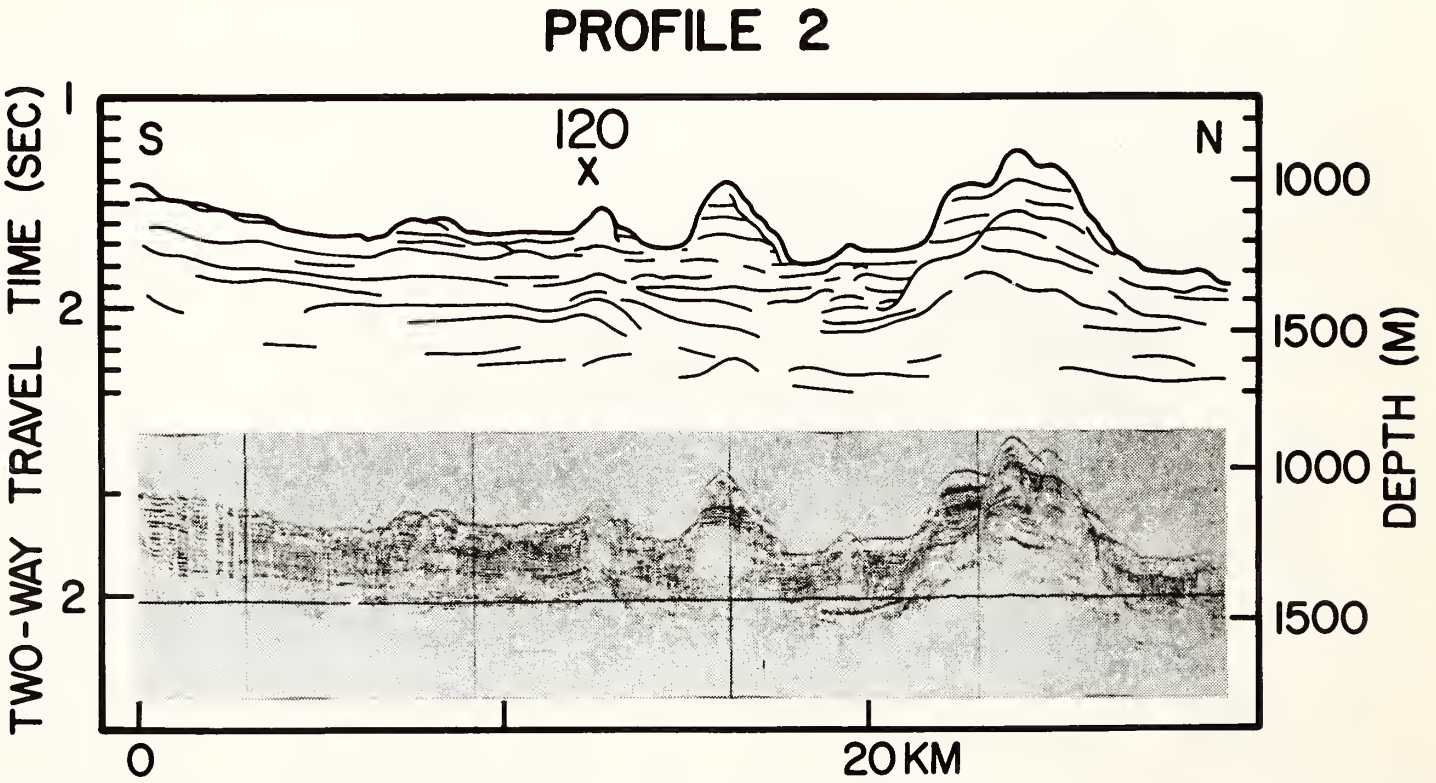

Figure 4. Line drawings and photographs of original seismic reflection records for profile 2. A 40 in^3 air gun was used as a sound source. See Figure 1 for location. "X"s and numbers refer to location of crossing profiles of Uchupi and Emery (1967).

of reflectors 100 m below the surface in the ridge at kilometer 16 appears to correlate with the sequence 100 m below the surface in the ridge at kilometer 23 based on the nature of the reflecting horizon and its subsurface level. Except for this example, the reflecting horizons within the ridges are not correlatable between the ridges. At approximately 500 m beneath the ridges reflecting horizons are much more continuous.

Uchupi and Emery's profile 120 (Figure 8), transverse to the slope, crosses the topography obliquely (Figure 1) (along a ridge on the upper slope, across a valley on the mid-slope, and across the end of a ridge on the lower slope). The reflecting horizons are continuous normal to the margin.

Farther down slope the ridges are more clearly developed on profile 3 (Figures 2 and 5). A thick sequence of stratified sediment with unconformities is present in the ridges. The ridges appear asymmetric in shape with a smoother side on the south and slumping on the north side making the slope more irregular. Reflecting horizons cannot be correlated between the ridges, however, depositional and erosional events must be coincident over such a small area.

On the lower slope and upper rise the ridges have subdued relief (profiles 4 and 5, Figures 6 and 7), however, stratified sediments are still present. The morphology of the continental margin changes as one goes seaward down the continental slope to the rise from a dissected upper slope with many small valleys, to a pronounced ridge and valley sequence, to an irregular but subdued rise. Little hint of this morphology change is shown on profile 120 (Figure 8), however, erosion is indicated by truncation of horizons at the sea floor.

Records of the shallow sediment pattern were also made using a 3. 5 kHz sound source along profiles 2 and 4. Stratification shown in profile 4 (Figure 6) can be extended to the upper 70 m of sediment along much of the profile with some thinning of layers on the north side of the feature near crossing profile 120. On profile 2, buried irregular surfaces are present in the upper 70 m of sediment in the topographic lows. Truncation of internal reflectors at the sea floor on the south side of the ridges at km 16 and 21 (Figure 4) is confirmed on the 3. 5 kHz record, indicating erosion or lack of sediment accumulation on the south facing slopes. The north slope of both ridges has an irregular surface and is suggestive of small scale slumping.

The age of the sediments shown in the profiles can only be inferred from correlation with drill hole data. Data from DSDP site 108 (Hollister _et al._, 1972) on the continental slope 170 km to the north, 4 km southeast of crossing profile 113 (Figure 2) dated the strong reflector at 2. 5 s as Eocene and the continuous horizon at 2. 8 s is believed to be late Cretaceous. Kelling and Stanley (1970) and Uchupi and Emery (1967) believe the continental margin in this area is composed of Tertiary sediments, with canyon erosion in the vicinity of Baltimore Canyon occurring during the Tertiary. A major unconformity shown

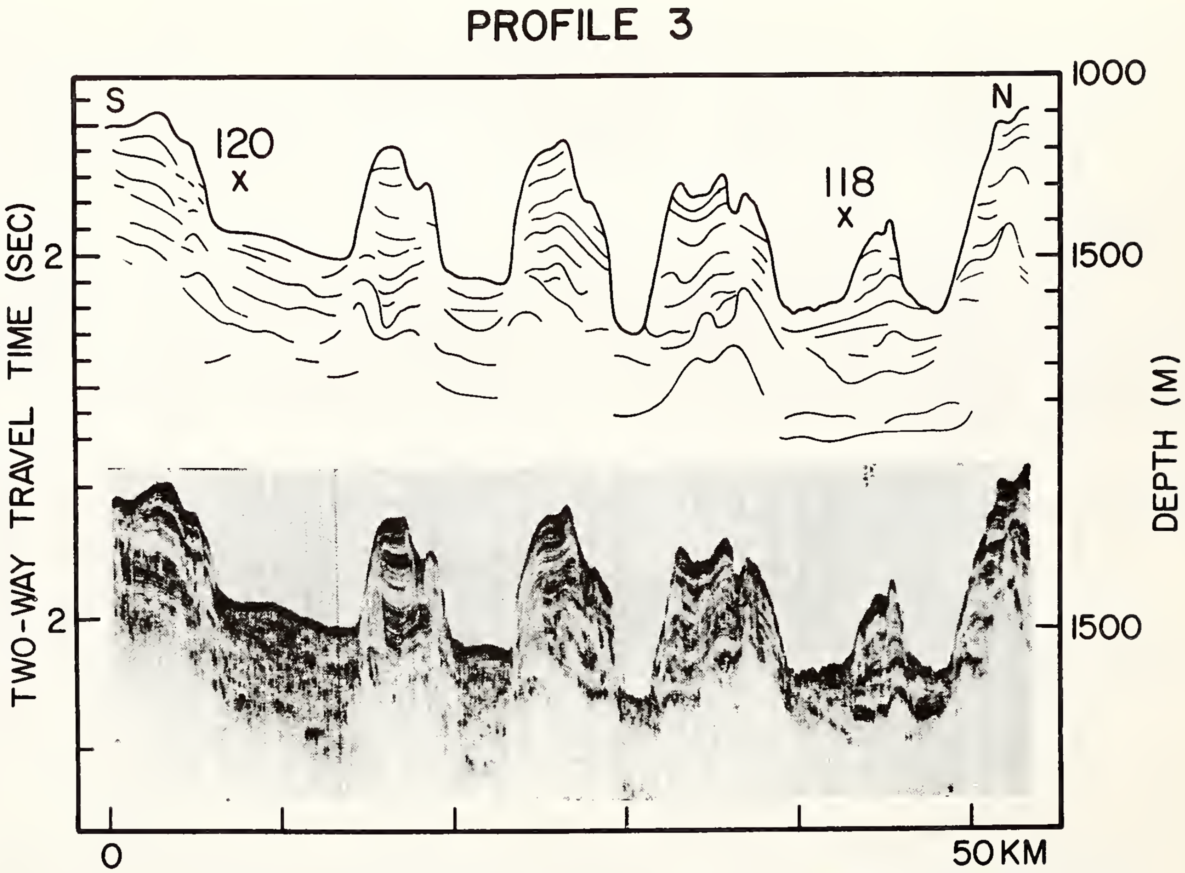

Figure 5. Line drawings and photographs of original seismic reflection records for profile 3. Both 10 and 120 in^3 air guns were used as the sound source. See Figure 1 for location. "X"s and numbers refer to location of crossing profiles of Uchupi and Emery (1967).

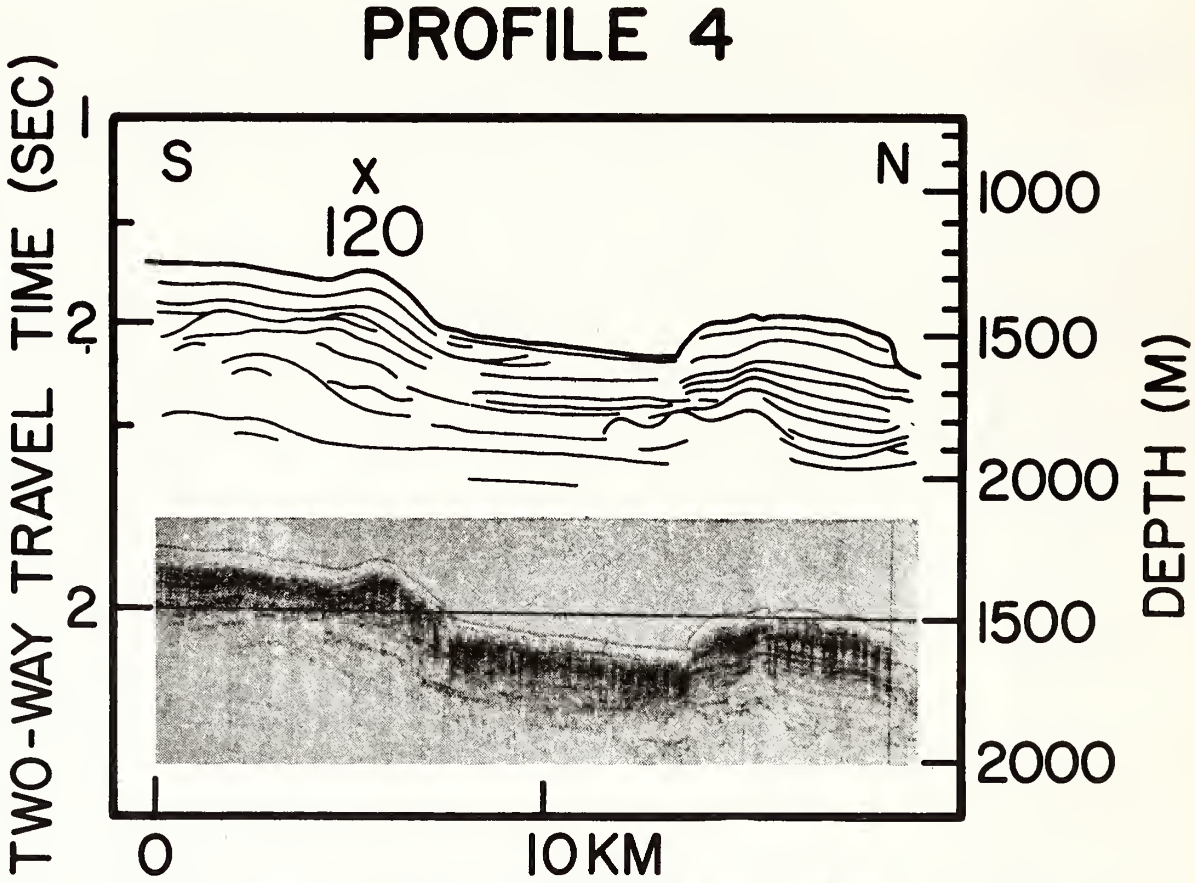

Figure 6. Line drawings and photographs of original seismic reflection records for profile 4. A 40 in^3 air gun was used as a sound source. See Figure 1 for location. "X"s and numbers refer to location of crossing profiles of Uchupi and Emery (1967).

on profile 120 is reported by Uchupi and Emery (1967) to be within the Tertiary followed by renewed deposition and subsequent erosion (Figure 8). To the north on the slope near Wilmington Canyon a 200 m thick sediment accumulation is believed to be Pleistocene in age (McGregor and Bennett, 1977). Because the ridges are composed of sediment over 500 m thick, it is inferred that some of this sediment must be Tertiary in age. However, if the sediments are younger than Tertiary, then this region has had a significantly different sediment accumulation pattern from the Pleistocene to recent than adjacent portions of the continental slope.

DISCUSSION

Because the morphology of the Delmarva portion of the middle and lower continental slope is different from adjacent slope areas (Figure 2) the processes that have been and are active in shaping it are of interest. On profile 1 along the upper slope, the morphology is similar to that found in other areas along the Atlantic continental margin with dissection of the slope by small valleys. In most areas this morphology continues down the slope onto the upper rise. Some stratification may be present in the ridges, but it cannot be resolved. The frequency of the valleys and ridges on profile 1 is greater than on profile 3 (Figures 3 and 5) indicating the upper slope is more dissected than the mid-slope. Uchupi and Emery's profile 120 (Figure 8) also shows that erosion is more extensive on the upper slope. Profiles 2 and 3 show broad ridges composed of stratified sediment. The ridges have remained in approximately the same location with only slight migration and just built upward with time. Farther offshore (profiles 4 and 5) the morphology and internal structure are again similar to that found on the rise off other areas; subdued topography and continuity of horizons parallel to the margin.

Comparing the slope off the Delmarva coast with other areas shows similar and dissimilar characteristics. The Nova Scotian slope seaward of Sable Island Bank has a scalloped topography (Stanley and Silverberg, (1969) which is similar in appearance on contour maps to the continental slope between Baltimore and Washington Canyons. The valleys which trend down slope are rounded rather than V-shaped (Stanley and Silverberg, 1969), which is the same characteristic of the Delmarva slope except for profile 1 (Figure 3) where the valleys are V-shaped. The topography of the Nova Scotia slope is attributed to mass gravity processes (Stanley and Silverberg, 1969) because sub-bottom profiles reveal large slide blocks on the lower slope and rise. In the Delmarva area the sub-bottom profiles (Figures 3-7) show unconformities within and beneath the ridges. No strong continuous reflector is present to indicate the slip surface, as was the case of a submarine slide on the slope northeast of Wilmington Canyon (McGregor and

Bennett, 1977). Massive gravity sliding does not seem to be a major process which has been active in this area. Small scale slumping, however, is present on the ridges as shown on the seismic records.

The seaward extensions on the rise of most of the U. S. east coast canyons have large levees (Pratt, 1967). Figure 2 shows the levees associated with some of the major submarine canyons, such as those of Washington and Baltimore Canyons. Both canyons are flanked by stratified sediment masses containing many unconformities. The levees are asymmetric in cross section with the steeper side facing the canyon which is V-shaped, and the larger, higher levee is on the right as one looks down slope. The right side looking down slope of the U. S. east coast canyons usually has the larger levee and the valleys tend to migrate and hook to the left, because of the Coriolis effect (Menard, 1955; Komar, 1969; Stanley et al., 1971). The ridges on the Delmarva slope have some characteristics in common with levees. The trend normal to the slope and are composed of stratified sediments with many unconformities. Their cross-section is asymmetric. The valleys between the ridges tend to bend slightly to the left looking down slope, implying down slope flow (Figure 1 and Veatch and Smith, 1939). The major leveed canyons have shelf valleys and are or were part of major drainage systems (Swift and Sears, 1974). No evidence of a major drainage system is present on the shelf adjacent to the slope between Baltimore and Washington Canyons, however, the Delaware valley and associated mid-shelf delta are present near the northern part of this portion of slope (Swift and Sears, 1974), and Twichell et al. (1977) have traced the Delaware River valley across the shelf to Wilmington Canyon. Arkosic sediments present on the slope are believed to have been deposited by the Delaware River during the last Pleistocene low stand of sea level (Milliman et al., 1972). A large levee-like ridge is present on the south side of Baltimore Canyon between kilometer 310-320 (Figure 2), and although larger is similar to the ridges on the slope further south between kilometer 250-300. The unconformities in the ridges (Figures 3-7) show they have migrated slightly while building upward similar to what one would expect in a levee. The ridges die out on the rise (profiles 4 and 5; Figures 6 and 7) sooner than the levees of adjacent submarine canyons (Stanley et al., 1971). Although the morphology has some similarity to canyons and levees, it also is dissimilar. The canyon valleys of Baltimore and Washington between the levees are narrow and V-shaped (Figure 2), whereas the valleys between the ridges on the slope between these two canyons are broad and U-shaped. From the number of ridges, five valleys are inferred, yet none of the ridges looks like a levee pair except possibly the ridges at kilometer 285 and 290 (Figure 2). A levee-like ridge adjacent to Wilmington Canyon called the Nyckel Ridge (Stanley and Kelling, 1970) is similar in morphology and internal structure to the ridges discussed here. Stanley and Kelling (1970) believe the Nyckel Ridge is not a levee, although similar in morphology, but rather is structural in origin

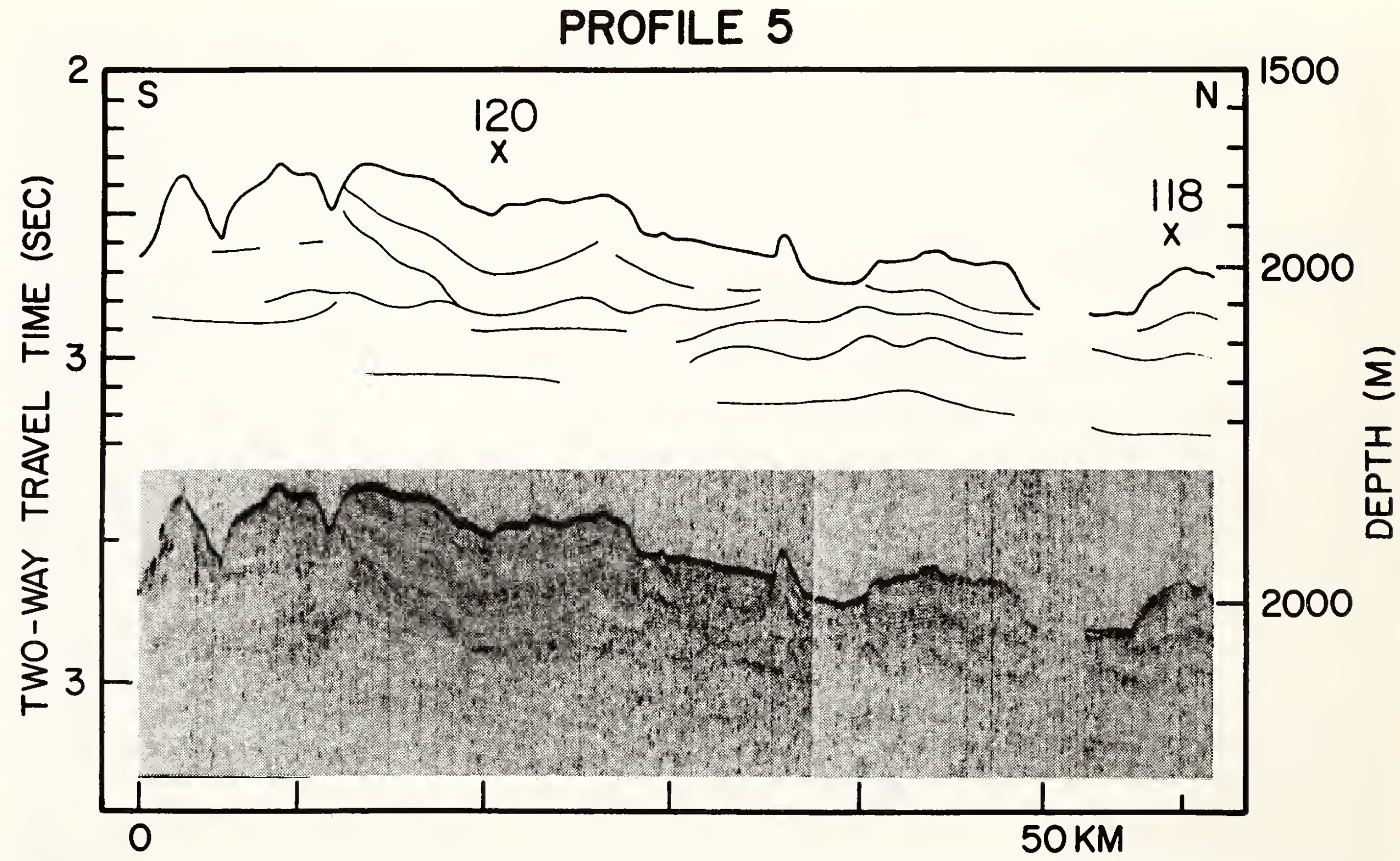

Figure 7. Line drawings and photographs of original seismic reflection records for profile 5. Both 10 and 120 in^3 air guns were used as sound source. See Figure 1 for location. "X"s and numbers refer to location of crossing profiles of Uchupi and Emery (1967).

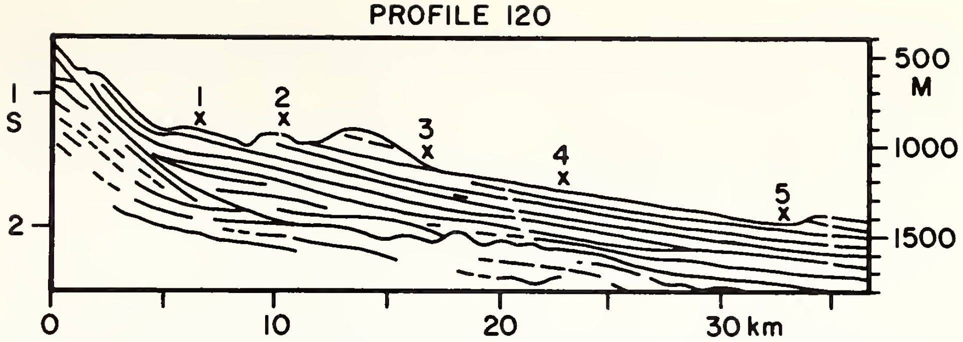

Figure 8. Portion of profile 120 from Uchupi and Emery (1967). X's show crossing locations of profiles in Figures 3 through 7.

composed of faulted pre-Quaternary consolidated rock. Their seismic reflection profiles over the Nyckel Ridge are similar in appearance to the ridges in profile 1 (Figure 3).

Bottom current activity is a process responsible for many bedforms such as the morphology of the rise (Zimmerman, 1971; Heezen et al., 1966; Schneider et al., 1967). Currents have been found just south of this area off Cape Hatteras having both a northward and southward flow along the margin at the intersection of the slope and upper rise (Richardson and Knauss, 1971; Barrett, 1965). These currents have been found by Betzer et al. (1974) to also be transporting relatively large quantities of suspended matter. The current meter data for September 3-17, 1975 (see Figures 1 and 3 for meter location), showed very low velocities with a maximum of 10 cm/sec. Flow was primarily tidal with up and down slope motion. Such a short duration record does not adequately predict the velocity or flow direction one might expect on the slope in this area.

SUMMARY

From seismic reflection data, a varied sedimentation history has characterized the continental margin seaward of the Delmarva area which is different in morphology than adjacent portions of the middle and lower continental slope. Neither large submarine slides nor levees are able to account for the morphology and stratigraphic framework of this area. A large volume of sediment from the Delaware and possibly Chesapeake Bay drainage systems has been deposited on the continental margin in this area under the influence of varied bottom processes since reflecting horizons are not flat nor can they be traced laterally over any distance. Alternating periods of erosion and deposition have occurred with the buildup of the ridges in approximately the same location through time. Erosional processes including slumping, bottom currents, and possibly turbidity currents must have been active in shaping the morphology of the slope. More extensive study and measurements are necessary to determine if and at what rate these processes are occurring on the margin today and if not active today what environment in the past was conducive to the formation of this morphology.

REFERENCES CITED

Barrett, J. R., Jr., 1965, Subsurface currents off Cape Hatteras: Deep-Sea Res., v. 12, p. 173-184.

Betzer, P. R., Richardson, P. L., and Zimmerman, H. B., 1974, Bottom currents, nepheloid layers and sedimentary features under the Gulf Stream near Cape Hatteras: Mar. Geol., v. 16, p. 21-29.

Heezan, B. C., Hollister, C. D., and Ruddiman, W. F., 1966, Shaping of the continental rise by deep geostrophic contour currents: Science, v. 152, p. 502-508.

Hollister, C. D., Ewing, J. I., Habib, D., Hathaway, J. C., Lancelot, Y., Luterbacher, H., Paulus, F. J., Poag, C. W., Wilcoxon, J. A., and Worstell, P., 1972, Initial reports of the Deep Sea Drilling Project. Vol. XI, Washington (U. S. Govt. Printing Office): p. 357-363.

Komar, P. D., 1969, The channelized flow of turbidity currents with application to Monterey Deep-Sea Fan Channel: J. Geophys. Res., v. 74, p. 4544-4558.

McGregor, B. A., Keller, G. H., and Bennett, R. H., 1975, Seismic profiles along the U. S. northeast coast continental margin: EOS, v. 56, p. 382.

McGregor, B. A. and Bennett, R. H., 1977, Continental slope sediment instability northeast of Wilmington Canyon: Amer. Assoc. Petroleum Geologists Bull., v. 61, p. 918-928.

Menard, H. W., 1955, Deep-sea channels, topography, and sedimentation: Amer. Assoc. Petroleum Geologists Bull., v. 39, p. 236-255.

Milliman, J. D., Pilkey, O. H., and Ross, D. A., 1972, Sediments of the continental margin off the eastern United States: Geol. Soc. Amer. Bull., v. 83, p. 1315-1334.

Pratt, R. M., 1967, The seaward extension of submarine canyons off the northeast coast of the United States: Deep-Sea Res., v. 14, p. 409-420.

Richardson, P. L., and Knauss, J. A., 1971, Gulf Stream and western boundary undercurrent observations at Cape Hatteras: Deep-Sea Res., v. 18, p. 1089-1109.

Schneider, E. D., Fox, P. J., Hollister, C. D., Needham, H. D., and Heezen, B. C., 1967, Further evidence of contour currents in the western North Alantic: Earth and Planet. Sci. Letters,

v. 2, p. 351-359.

Stanley, D. J. and Silverberg, N., 1969, Recent slumping on the continental slope off Sable Island Bank, southeast Canada: Earth and Planet. Sci. Letters, v. 6, p. 123-133.

Stanley, D. J. and Kelling, G., 1970, Interpretation of a levee-like ridge and associated features, Wilmington submarine canyon, eastern United States: Geol. Soc. Amer. Bull., v. 81, p. 3747-3752.

Stanley, D. J., Sheng, H., and Pedraza, C. P., 1971, Lower continental rise east of the Middle Atlantic States. Predominant sediment dispersal perpendicular to isobaths: Geol. Soc. Amer. Bull., v. 82, p. 1831-1840.

Swift, D. J. P., and Sears, P., 1974, Estuarine and littoral deposition patterns in the surficial sand sheet, central and southern Atlantic shelf of North America: In: G. P. Allen (ed.), Shelf and Estuarine Sedimentation, a Symposium. Univ. Bordeaux, Institut de Geologie du Bassin d'Aquitaine, Talence, France, Memoir 7, p. 171-189.

Twichell, D. C., H. J. Knebel, and D. W. Folger, 1977, Delaware River: evidence for its former extension to Wilmington Submarine Canyon: Science, v. 195, p. 483-485.

Uchupi, E. and Emery, K. O., 1967, Structure of the continental margin off Atlantic coast of United States: Amer. Assoc. Petroleum Geologists Bull., v. 51, p. 223-234.

Uchupi, E., 1970, Atlantic continental shelf and slope of the United States - shallow structure: Geol. Survey Prof. Paper 529I, p. 1-44.

Veatch, A. C. and Smith, P. A., 1939, Atlantic submarine valleys off the United States and the Congo submarine valley: Geol. Soc. Amer. Spec. Paper 7, 101 p.

Zimmerman, H. B., 1971, Bottom currents on the New England continental rise: J. Geophys. Res., v. 76, p. 5865-5876.

29 NOAA Technical Report ERL 398-AOML 28, 19 pages.

Seismic Reflection Profiles of the United States East Coast Continental Margin

Bonnie A. McGregor

Atlantic Oceanographic and Meteorological Laboratories
Miami, Florida

April 1978

U. S. Department of Commerce
Juanita M. Kreps, Secretary

National Oceanic and Atmospheric Administration
Richard A. Frank, Administrator

Environmental Research Laboratories
Boulder, Colorado
Wilmot Hess, Director

SEISMIC REFLECTION PROFILES OF THE U.S. EAST COAST CONTINENTAL MARGIN

Bonnie A. McGregor

Abstract. Five profiles of seismic reflection data from the United States east coast are described. From these profiles, two localized areas of extensive slope deposition are identified, one seaward of Albemarle Sound and the other seaward of the Delaware-Maryland-Virginia coast. The profiles show levees along the lower slope and rise portions of some of the major submarine canyons. A regional unconformity on the rise extends from Georges Bank to Wilmington Canyon and is believed to be Pliocene in age. The upper slope between Cape Hatteras and Hudson Canyon is dissected by many small valleys which are believed to have been cut during the late Pleistocene, whereas northeast of Hudson Canyon the upper slope is cut only by major submarine canyons. The Florida-Hatteras slope and Blake Plateau have many unconformities with one in late Tertiary truncating an extensive sequence of foreset beds on the north end of the Blake Plateau. The shelf width and the deposition and erosion pattern of the Florida-Hatteras slope and the adjacent Blake Plateau appear to be controlled by the Gulf Stream.

Marine Chemistry 6, 343-349.

A SIMPLE AND RAPID NORMALIZATION METHOD FOR INSTRUMENTAL DRIFT DURING ENERGY-DISPERSIVE X-RAY ANALYSIS

TERRY A. NELSEN

NOAA-AOML, Miami, Fla. 33149 (U.S.A.)

(Revision accepted March 27, 1978)

ABSTRACT

Nelsen, T. A., 1978. A simple and rapid normalization method for instrumental drift during energy-dispersive X-ray analysis. Mar. Chem., 6: 343—349.

Fluctuations in scanning electron microscope (SEM) beam current necessitate normalization of energy-dispersive analysis (EDA) data collected in conjunction with the SEM. A normalization method based on monitoring the total integrated count of a stainless-steel reference before and after sample counting was developed and yielded high precision (correlation coefficient = 0.996) data from a 48-sample testing set. The technique is independent of sample composition, counting time, time between sample analyses, magnification during analysis, and requires no modification to the basic SEM—EDA system.

INTRODUCTION

Elemental analysis of materials by SEM—EDA has become a popular tool for scientific research over the last few years. However, its utility for comparison of relative elemental abundance from sample to sample is influenced by time-dependent SEM beam current fluctuations, SEM stage geometry, and sample geometry. To alleviate this problem, a dependable time-independent normalization technique is required.

One normalization technique specifies a preset number of total counts for a chosen element with all other elements being ratioed to it. The utility of this method is limited to sample suites which contain at least one common element. Another method (Mulligan and Lapi, 1976) utilizes the specimen's initial count rate and the electron-gun beam current monitored at the SEM stage. This technique requires the addition of a current meter on the microscope stage and therefore limits its application to SEM units so equipped.

To overcome the limitations of the normalization procedures cited above, a method was developed which is independent of the sample's composition and does not require modifications to the SEM.

THE TECHNIQUE

For a given SEM stage and sample geometry, total X-ray intensity is proportional to SEM beam current. Therefore, this parameter was chosen to monitor the beam current variation.

The SEM system used in this work was an Advanced Metals Research (AMR) Model 900 equipped with an EDAX brand Model 707A energy-dispersive analysis unit. Corrections for energy-dispersive background radiation were performed by a Nova 4K mini-computer which is an integral part of the EDAX system. SEM operating conditions were standardized to a 30-KV accelerating voltage with a constant detector take-off angle and specimen-to-detector distance. The optimum stage tilt angle was determined by 100-sec integrated counts from 2° tilt to 50° tilt in 2° increments. The maximum count rate was recorded at 24° tilt for an effective detector take-off angle of about 50°.

The normalization reference specimen used in this procedure was a polished stainless steel square one quarter inch on a side, with a scribed central reference mark.

The analysis procedure was as follows. After placing four study samples and the stainless reference into the SEM vacuum chamber, the standard operating conditions were established, and the stainless reference was placed under the electron beam. The beam intensity was regulated to produce a counts-per-second (cps) rate of approximately 2000 cps through adjustment of the second condenser lens and filament saturation controls. Counts were accumulated for 100 sec on the stainless standard at the scribed reference point, and a background-corrected total count was recorded. Next, each of the four study samples was analyzed and after all samples were run, a final 100-sec analysis was made on the stainless reference. Each stainless corrected total count was then divided by the counting time to yield total counts per second. This value was then divided by the initial setting of 2000 cps, and the reciprocal of this quotient was then taken. This resulted in a number generally near unity. This final number will hereafter be referred to as the stainless factor (SF). This can be expressed as:

$$\Sigma\ \text{Counts}_{\text{stainless}}/\Sigma\ \text{Count Time} = \text{cps}_{\text{stainless}}$$

$$1/(\text{cps}_{\text{stainless}}/2000\ \text{cps}) = \text{SF}$$

The elemental intensities from EDA of each study sample were then multiplied by the appropriate SF value interpolated from pre- and post-analysis SF values for each sample suite.

Within any suite of samples all analyses were done at a uniform magnification. In the examples to follow, all SEM magnifications were 50x. This allowed the returning EDA signal to be integrated over the largest possible sample area thus minimizing the effects of any sample inhomogeneity.

TESTING OF NORMALIZATION PROCEDURES

Suspended particulate matter

Since the author's primary study samples were membrane-filtered suspended particulate matter (SPM), a testing set of 25 different SPM samples was used for the initial evaluation of the normalization procedure. The samples chosen for evaluation were obtained from the surface waters of the New York Bight Apex. The samples were analyzed several times so that a comparison of uncorrected and corrected data could be made. For the first set of duplicate runs the SEM was set up for EDA, and uncorrected data were collected. A plot of those data, for Fe, is seen in Fig.1A. The data are expressed as total counts per 100 sec and normalized to the total mass of SPM in 1l of sample water. It is obvious from the scatter of data in Fig.1A that uncorrected EDA data have a low precision for duplicate runs. The SEM was then adjusted to standard conditions, as described above, and a set of drift-corrected data for 25 samples was obtained, of which three samples were duplicate runs for checking precision. To increase the number of data points for the precision check, the values for Al, Si, K, Ca, Ti, as well as Fe are plotted in Fig.1B. Comparison of Figs.1A and 1B indicates a substantial improvement in count precision for drift-corrected data over uncorrected data. It should be noted here that the total counts for drift-corrected data are higher than for the uncorrected data. This results from the adjustment of the filament saturation and second condenser lens to optimum standard condition of 2000 cps on the stainless standard as opposed to random count rates under uncontrolled conditions.

The practical application of this drift correction manifests itself in the ability to compare samples with reasonable assurance that the variation in total elemental counts, and hence relative abundance, is real and not an artifact of instrument instability. An example of the practical application of this normalization technique is drawn from the 25-samples suite mentioned above. Figure 1C is a plot of corrected relative Fe abundances for SPM in the surface waters of the New York Bight Apex. As seen in this figure, the Fe abundances form a NE—SW trending central high. In an attempt to verify this Fe distribution, subsequent analyses of particulate size distributions (Coulter Counter analysis) and visual observation (SEM) were made on separate aliquots of the samples used to produce the EDA data of Fig.1C. Results of this size and visual analysis revealed that several central stations contained a suite of particles that were essentially indistinguishable from known dump material (T. A. Nelsen, unpubl. data) which is estimated (Mueller et al., 1976) to supply 17 metric tons of Fe per day to the New York Bight Apex. The geographical distribution of these particles, as seen in Fig.1D, suggests a positive spatial relationship between the data of Figs.1C and 1D, and implies that the drift-corrected EDA data for Fe in Fig.1C are a meaningful estimate of relative Fe abundance and distribution.

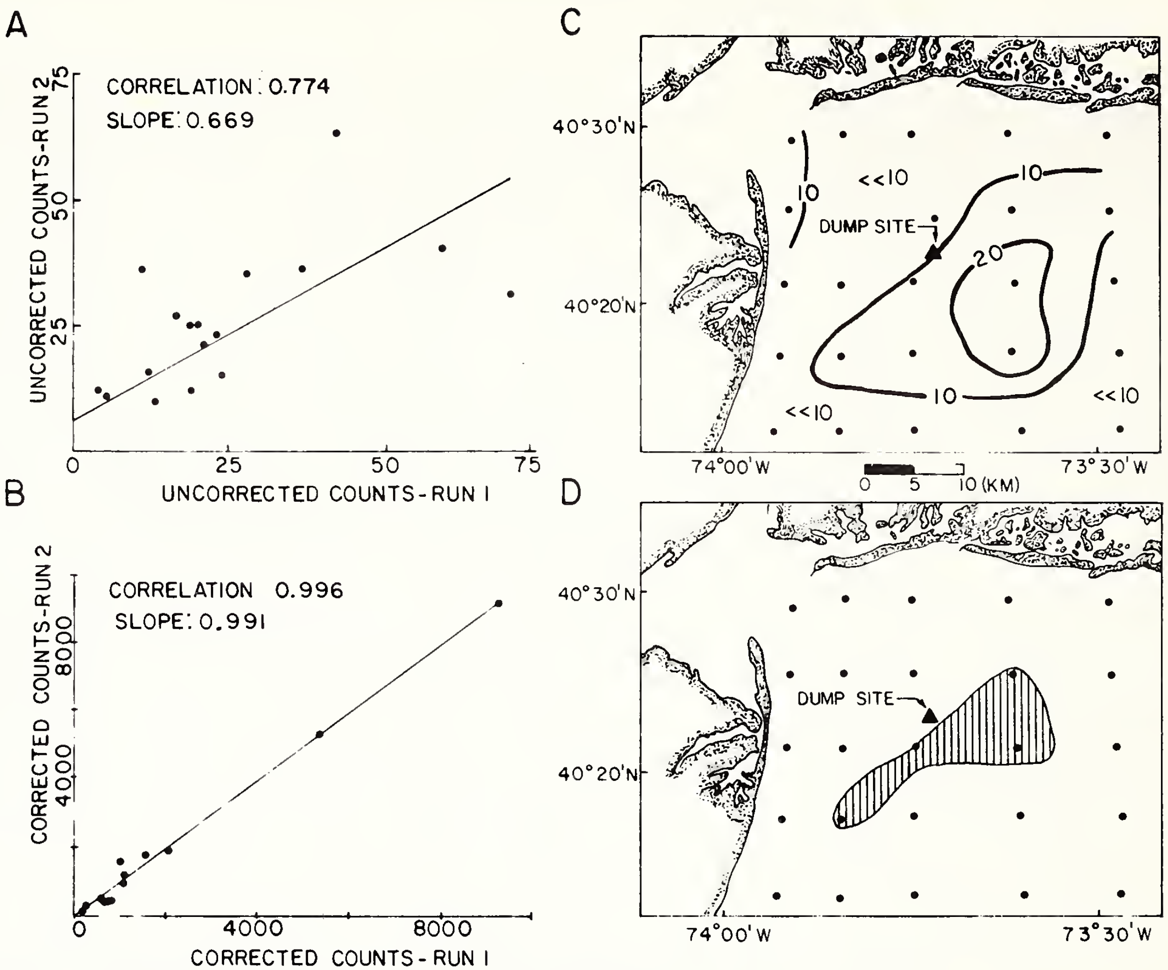

Fig.1. Energy dispersive analysis data expressed as total counts per 100 sec. A, scatter plot of uncorrected data for Fe; B, scatter plot of drift-corrected data for Al, Si, K, Ca, Ti, and Fe; C, distribution of drift-corrected data of relative Fe abundance in the surface water of the New York Bight Apex during a water sampling cruise; D, qualitative distribution of Fe-rich dump material as determined from size and SEM observations of aliquots of samples used in C above.

Bottom sediments

In an attempt to broaden the scope of utility for this drift-correction technique, a suite of eight mud samples were obtained from a bottom sediment core. After drying to hardness, the mud samples underwent duplicate EDA runs and a plot of the data for Al, Si, K, Ca, Ti, and Fe is presented in Fig.2A. The duplicate runs reported in this figure represent, as with the previously reported SPM data, a time span of several hours to several weeks between runs one and two. The high correlation (0.974) between the two drift-corrected runs is particularly encouraging since a different sample area was analyzed during each run. Since these mud samples displayed a randomly oriented surface topography with a relief of up to 2 mm, the question was asked, "Does varying sample topography influence the precision of EDA data?" To answer this question, three samples were analyzed such that runs one and two were sequential and covered the exact same area and hence the

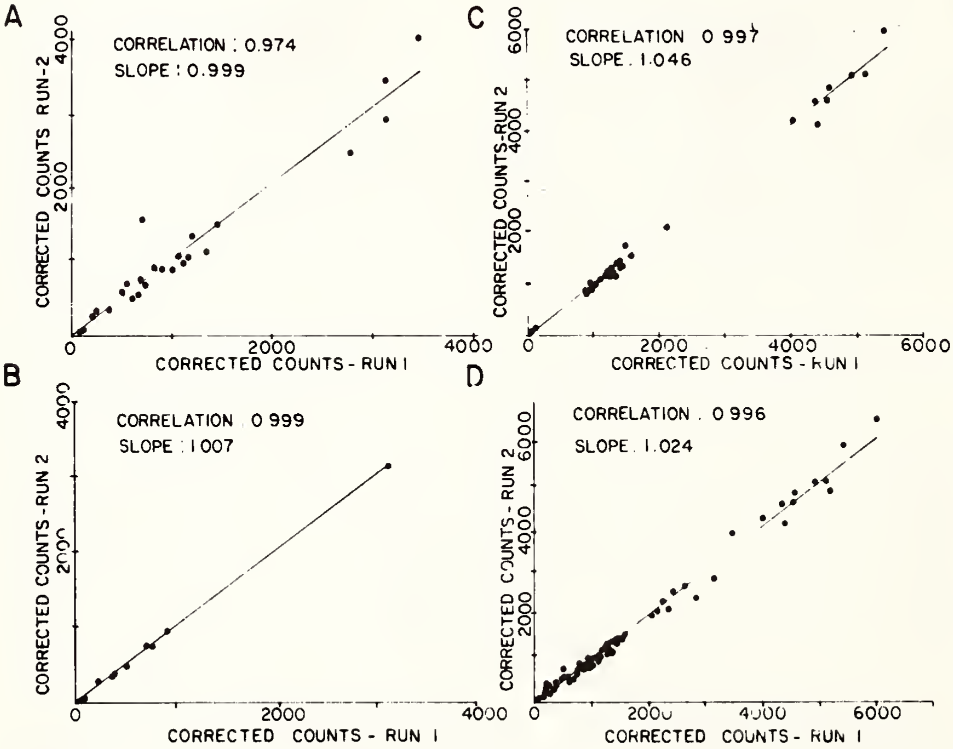

Fig.2. Energy dispersive analysis data for Al, Si, K, Ca, Ti, and Fe expressed as total counts per 100 sec. A, scatter plot of drift-corrected data for samples with surface relief of up to 2 mm. Analyses one and two occupied different positions on the sample surface; B, as in A above, except analysis positions one and two are identical; C, as in A above except analysis surface of each sample is flat; D, an overall scatter plot of drift-corrected EDA data for 48 bottom sediment and SPM samples.

exact same surface topography. The plot of these data, for the above-mentioned elements, is shown in Fig.2B. It is clear from a comparison of Figs.1A and 1B that the variation about the least-squares line is improved as reflected in the improved correlation value. This implies that the varying sample topography influences the EDA data. To address this problem, the eight mud samples were shaved until the analysis surface of each was flat with a remaining surface relief slightly in excess of component grain diameters ($<62\mu$). The samples were then rerun in duplicate and the drift-corrected elemental intensities of each plotted in Fig.2C. A comparison of statistical parameters for "blocky" samples (Fig.2A) and "shave" samples (Fig.2C) shows a slight improvement in correlation for the latter. However, a subtle yet significant variation can be seen for the overall mean total counts of "blocky" and "shaved" samples. A comparison of the mean of all data presented in Fig.2A vs. the mean of all data presented in Fig.2C showed that the "shaved" data had a mean total count that was 68% higher than the "blocky" data. This indicates a significant effect on comparative EDA arising from the shadowing and scattering effects of varying sample topography.

DISCUSSION AND CONCLUSIONS

From the data presented above, it is reasonable to conclude that the previously described normalization technique can effectively compensate for variation in relative elemental abundances arising from instrument drift during EDA. The only limitation noted during development of this technique was a requirement for a planar sample analysis surface. This should prove no problem for typical geological samples such as membrane-filtered SPM or bottom sediments which can be filtered onto a membrane filter. In the case of dried core muds an analysis surface may be prepared by shaving a surface to flatness as in the examples presented above. To date the author has run a total of 48 samples in duplicate with anywhere from a few hours to several months elapsed time between runs one and two. Drift-corrected data for Al, Si, K, Ca, Ti, and Fe constitute the 123 data points used to produce Fig.2D. The overall correlation of 0.996 indicates a high precision for drift-corrected relative elemental abundances. This implies that drift-corrected EDA data can now be used for spatial and temporal variation among samples with reasonable assurance that observed relative variation is a function of sample variation and not an instrument artifact.

Although not investigated in this study, the normalization method presented here should be equally applicable to any sample with a planar analysis surface. Some additional examples from geology might be marine basalts, ferromanganese nodules, and carbonates which can easily be ground to flatness by standard thin-section techniques. Guided by the principles outlined above, the biologists and chemists may find applications for the normalizing technique in their work.

ACKNOWLEDGEMENT

The useful suggestions of Donald Marszalek on SEM technique are acknowledged and appreciated.

REFERENCES

Mueller, J. A., Jervis, J. S., Anderson, A. R. and Hughes, C. F., 1976. Contaminant inputs to the New York Bight. NOAA Tech. Memo. ERL MESA-6, 347 pp.

Mulligan, T. J. and Lapi, L. H., 1976. Normalization procedure for x-ray microanalysis which accounts for fluctuations in beam current. Proc. 9th Annu. SEM Symp., IIT Res. Inst., Chicago, Ill., 1976.

Journal of Geophysical Research 83, No. C12, 6073-6082.

Wind-Induced Current Flow in the Upper Hudson Shelf Valley

Terry A. Nelsen, Peter E. Gadd,[1] and Thomas L. Clarke

NOAA/Atlantic Oceanographic and Meteorological Laboratories, Miami, Florida 33149

Drawing from wind and current meter data, an empirical, semiquantitative model has been developed for wind-induced current flow in the New York Bight apex portion of the Hudson Shelf Valley. Data have shown that winds from 270°T (±50°), blowing for at least 9 hours at speeds of greater than 5 m/s, can cause northward (upchannel) bottom flow in the shelf valley at velocities in excess of 40 cm/s. Southern (downchannel) flow is initiated by winds from 75°T (±35°) blowing for at least 6 hours at speeds of 4 m/s or more. Seasonal variation in the wind field results in predominant upchannel flow during October–April with downchannel flow throughout the rest of the year.

INTRODUCTION

The New York Bight is defined as that part of the Atlantic continental shelf bounded on the north by Long Island and on the west by New Jersey (Figure 1, inset). From this figure it can be seen that the Hudson Shelf Valley, the drowned remnant of the ancestral Hudson River Channel, is a prominent physiographic feature of the Bight apex which extends across the continental shelf in a general southeast direction until it loses its bathymetric expression on the outer shelf.

Although the Hudson Shelf Valley is a dominant physiographic feature, its role in regional circulation is not clearly understood. Inferences from trace metal [*Carmody et al.*, 1973] and organic chemistry investigations [*Hatcher and Keister*, 1975] suggest transport both up and down valley and to the northeast. Analysis of suspended particulate matter (SPM) data (T. A. Nelsen, manuscript in preparation, 1978*a*) suggests periodic northward intrusions of relatively particle deficient water up the valley and into the Bight apex. Prior reporting of this phenomenon by *Drake* [1974] and current meter observations by *Charnell and Mayer* [1975] tend to substantiate this interpretation. In another recent study just south of the Bight apex, *Lavelle et al.* [1975] made an 11-day observation of bottom currents in the axis of the valley. Although their summertime study was of limited duration, they concluded that the observed net downchannel transport contained both upchannel and downchannel flow components which were apparently controlled by surface winds.

The purpose of this paper will not be to provide an exhaustive theoretical treatment of current motion in the Bight apex but rather to produce an empirical, semiquantitative model of wind-driven circulation from existing data. Drawing from synoptic wind and current meter data as well as synoptic wind and SPM data, the proposed model will attempt to correlate the apparent relationship between the wind field and water motion suggested by prior workers in this submarine shelf valley.

METHODS

Current measurements. Current velocity measurements for this study were obtained by using Aanderaa model RCM-4 (Savonius rotor) internally recording current meters which gave interval-averaged speed and instantaneous direction during each 10-min sampling interval. The moorings were of the taut wire, subsurface float design with the instrument positioned approximately 1 m above the seabed [*Charnell and Mayer*, 1975]. Current meter A (Figure 1) was located in the axis of the shelf valley (40°19.0′N, 73°48.0′W) where the water depth is 44.4 m. Current meter K was located in 19 m of water, 5 km east of the New Jersey shore (40°18.0′N, 73°55.0′E). The bottom topography at this point slopes gently eastward toward the shelf valley. Both current meters operated continuously for 48 days beginning on October 23, 1973. All references to current direction will have the oceanographic convention of the direction to which the current is flowing.

Wind observations. Wind vector time series for John F. Kennedy International Airport (Long Island, New York), Newark Airport (Newark, New Jersey) and the Aviation Facilities Experimental Center (Atlantic City, New Jersey) (Figure 1, inset) were analyzed for spectral coherence and temporal variation by the method of inner-cross correlation as described by *Mooers* [1973]. In 11 of 12 inner-cross correlation computations the maximum correlation occurred at the zero time lag position, indicating that the wind response lag time between these stations was less than the sampling interval (3 hours). The spatial coherence assessment produced an average in-phase inner-cross correlation coefficient of 0.75 with an angle of divergence between the mean wind vectors of 5.7°. For lag times greater than about 18 hours the correlation dropped below the confidence level of 0.065 [*Jenkins and Watts*, 1968], indicating statistical independence of the wind beyond this lag.

Based on these computations, wind data from Kennedy Airport were adopted as valid estimates of the surface winds active over the New York Bight apex, and these data alone will be used in this study for correlations with current meter observations. All references to wind direction will have the meteorological convention of referring to the direction from which the wind blows.

Suspended particulate matter. Suspended particulate matter was collected and analyzed for concentration and size distributions. Concentration data were obtained by vacuum filtration of known volumes of seawater through preweighed Nuclepore membrane filters. All concentration values were expressed in milligrams of SPM per liter of water.

Size distribution analysis of the SPM was accomplished by the use of a Coulter counter (model T). All size distribution data are expressed as volume-frequency percent per class interval. The size domain covered in this study represents boundaries imposed by equipment rather than by natural size limits.

Normalized volume-frequency size distribution data were used in conjunction with Q mode factor analysis as a means of

---

[1] Now at Pacific Marine Center, National Ocean Survey, Seattle, Washington 98102.

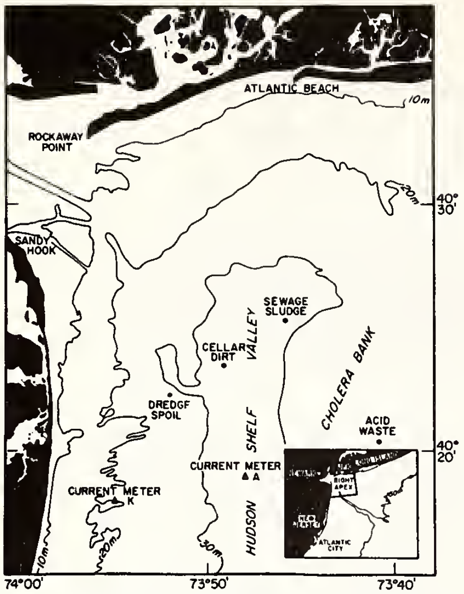

Fig. 1. General regional map of the New York Bight (inset) with a detailed map of the Bight apex showing current meter stations (A, K), dump sites, and general bathymetry.

conveniently and effectively analyzing hundreds of size distributions for significant trends and component end members (factors). The Q mode factor analysis program [*Clarke*, 1978] was patterned after concepts presented in the geological literature by *Imbrie and van Andel* [1964] and *Klovan and Imbrie* [1971] but first applied to SPM data by T. A. Nelsen (manuscript in preparation, 1978*b*). It is worth noting that factors are defined solely by the character of the particle size distribution and are totally independent of sample concentrations. It is for this reason that factor percentage isopleths, to be shown later, can and do at times fail to parallel SPM concentration isopleths in the same water body. The *Imbrie and van Andel* [1964] article is suggested for the reader seeking a detailed explanation of factor analysis. In this paper, SPM, with the aid of factor analysis, will be used to identify water masses and thereby will help to infer circulation patterns in the New York Bight apex.

Observations

Upchannel flow in the Hudson Shelf Valley. Figure 2 shows local wind conditions and near-bottom current speed at current meter sites K and A during late October 1973. Vectors (stick diagrams) representing hourly current velocity averages are superimposed on the current speed record in order to emphasize flow direction. Upchannel flow within the Hudson Shelf Valley (site A) occurs throughout the record with recorded bottom speeds in excess of 40 cm/s(0.8 kn). The current meter operating at the shallower site (K) recorded maximum current values of only 22 cm/s(0.4 kn) flowing northward. Synoptic wind data from Kennedy Airport, at the top of Figure 2, indicate that these upchannel flow events are coincident with periods of strong winds having a predominantly western component. While the current velocity tends to remain relatively constant at the shallow water site (K), there exist definite maxima and minima in the current speed recorded at site A in the valley axis. Specifically, there are four periods of relatively low current velocity evident in Figure 2 which are coincident with the occurrence of brief southerly (November 1, 3, and 9) and northerly (November 6) winds.

The stick diagram for meter A in Figure 2 shows that the current flow is essentially unidirectional. At this site the direction of the bottom water flow is oriented 349°T, exactly the direction of the valley axis. This conduitlike channeling is remarkable when one realizes that the depth-to-width ratio of the Hudson Shelf Valley at site A is 1: 100.

Further evidence of upchannel flow activity within the valley exists during two later intervals of the 48-day current observation period. In Figure 3*a* a northerly flow event occurs between November 17 and November 19. The onset of this northerly flow is again characterized by sustained westerly winds. The upchannel flow ceases on November 19 with the onset of northerly winds with a very slight easterly component. Figure

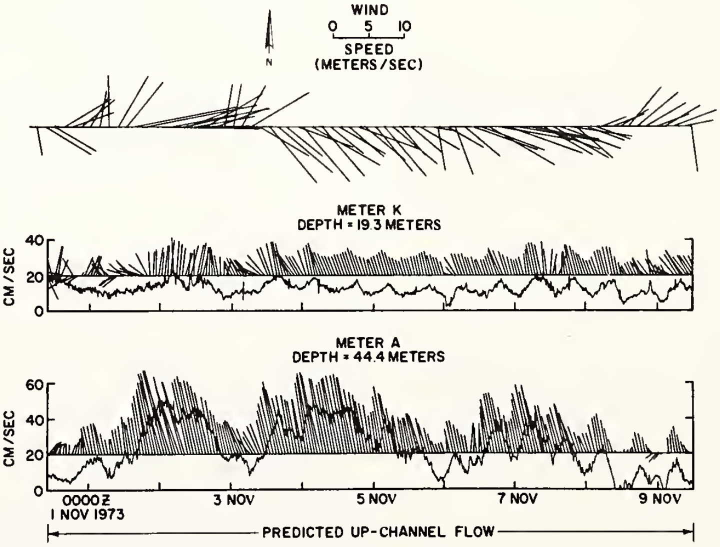

Fig. 2. Coincident vector time series of winds at Kennedy Airport (top) and currents at sites K and A in the Bight apex.

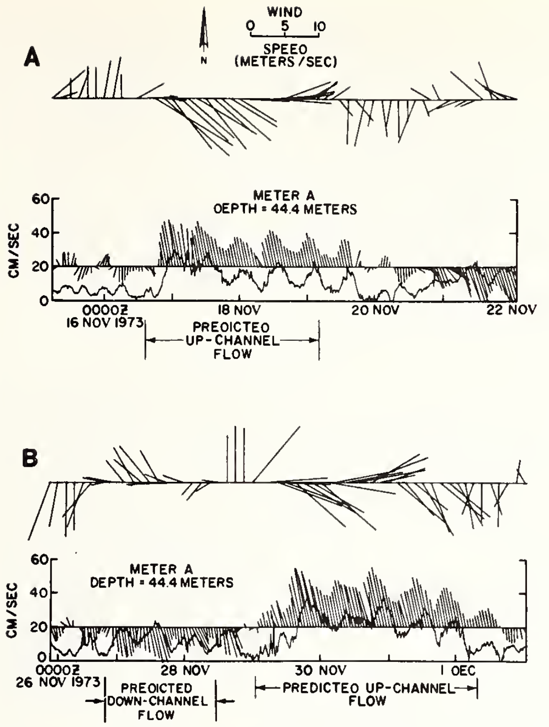

Fig. 3. Coincident vector of winds at Kennedy Airport (top) and currents at site A for (*a*) predicted upchannel flow and (*b*) predicted upchannel and downchannel flow.

3*b* shows the downchannel flow initiated on November 20 continuing until November 29. Then, during periods of easterly winds, as the wind shifts from the east to the west, upchannel flow is initiated (November 29) and is maintained for 3 days. As was observed in Figure 3*a*, northerly current flow is terminated when the wind no longer exhibits a westerly velocity component (December 1).

Downchannel flow in the Hudson Shelf Valley. Figure 4 shows two downchannel (southerly) flow events which occurred during October 1973. Here downchannel flow occurs in the shelf valley during northeasterly winds, while oscillatory flow at tidal frequency is evident during periods of low current velocity. The current speeds achieved at site A (30 cm/s) in the axis of the valley are of lesser magnitude than those measured in the shallower waters (40 cm/s) to the west at site K. The velocity-depth relationship is exactly opposite to the one observed in upchannel flow (Figure 2). An explanation of this apparent contradiction will be considered in a later section.

Historical wind data. The average monthly wind conditions for Kennedy Airport are recorded in Table 1. These values were obtained from the vector mean wind charts of *Lettau et al.* [1976], whose data represent vector averages of at least 5648 observations for each month. From the data in this table it can be seen that the direction of wind predominance shifts in a seasonal counterclockwise progression with winds from the northwest and west predominating from October through April, while lower-velocity southerly winds are most prevalent from May through September. The winds partition into a fall-winter season dominated by northwesterly winds and a late spring-summer dominated by southerly winds. The implications and consequences of this seasonably variable wind field will be discussed in a later section.

CRITERIA FOR WIND-INDUCED FLOW IN THE HUDSON SHELF VALLEY

Upchannel flow. From observations of recorded wind and bottom water flow at site A, an empirical test was devised which requires only wind information from Kennedy Airport to predict periods of northerly flow within the Bight apex portion of the Hudson Shelf Valley.

The test criteria established for initiation of upchannel flow require the winds to blow from an envelope of ±50° about due west (220°T ≤ wind direction ≤ 320°T) at speeds in excess of 5 m/s (10 kn) for a duration of greater than 9 hours. Once this condition is met, the test eases the wind speed and direction restrictions in the belief that once initiated, milder wind activity will maintain the current flow. The conditions for maintenance are found to be a wind of at least 4 m/s (8 kn) with a nonnegative westerly component (180°T ≤ wind direction ≤ 360°T). When these conditions do not exist, experimentation with the data showed that upchannel flow along the axis of the shelf valley rarely occurs. The periods of predicted upchannel flow based strictly on this test are recorded below the current meter records of Figures 2–4. It should be noted that Figures 2–4 represent a nearly continuous record of current activity from October 24 to December 2, 1973, and as such emphasize peak flow events. The ambient currents that exist at meters A and K during intervening periods not shown display a low-velocity flow (<8 cm/s) with repetitive north-south oscillation at tidal frequency. An example of this is seen for both meters, starting on October 24 and continuing through midday of October 25 in Figure 4.

Subsequent to the establishment of the test for upchannel flow, primarily developed from the above data, additional wind data were analyzed for conditions which met the criteria for upchannel flow. Of the several additional predicted events we identified, those that were coincident with our limited current meter data invariably showed upchannel flow as in the figures above, while other predicted events (Figure 9) were sustained by indirect evidence such as SPM and remote sensing which will be discussed in following sections.

As a consequence of the apparent success with which this test predicts observed upchannel flow which occurred during the fall of 1973 (Figures 2–4), the test was subsequently applied to wind data collected at Kennedy Airport from January

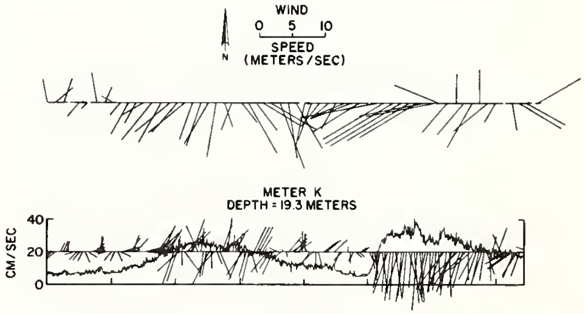

Fig. 4. Coincident vector time series of winds at Kennedy Airport (top) and currents at sites K and A in the Bight apex.

TABLE 1. Average Monthly Wind Conditions at Kennedy Airport, New York*

Month	Mean Speed, m/s	Prevailing Direction
January	2.9	NW
February	2.5	NW
March	1.9	NW
April	0.9	W
May	0.8	SSW
June	1.6	SSW
July	1.8	SSW
August	1.3	SSW
September	0.4	SW
October	0.9	NW
November	1.8	NW
December	2.5	NW

**Lettau et al.* [1976].

1, 1973, to January 1, 1976. Figure 5*a* shows the predicted incidence of upchannel flow time (not volume transport) within the shelf valley based solely on the application of the established test criteria to the wind records. All predicted flow events with durations of less than 24 hours were eliminated from this computation in order to maintain a conservative interpretation of data. Substantial yearly variation in predicted upchannel flow is evident in this figure. The most predicted upchannel flow occurred in 1973, with peaks in January, April, and November. For a clearer understanding of long-term seasonal trends in predicted upchannel flow, the data for each month in Figure 5*a* were averaged, and Figure 5*b* is a plot of those averages. Figure 5*b* shows that the majority of predicted upchannel flow takes place between October and April with an average of 212 hours per month (29% of the month). During the remainder of the year (May–September), relatively minor upchannel flow is predicted for a monthly average of 42 hours (6% of the month).

Downchannel flow. The empirical test for initiation of downchannel flow requires a surface wind to blow from 40°T through 110°T at a speed exceeding 4 m/s (8 kn) for a period of at least 6 hours. When this condition has been met, the directional envelope is increased to include winds from between 340°T and 160°T with a velocity of at least 2.5 m/s (5 kn). This test is based on bottom current observations taken during the fall of 1973 (Figures 3 and 4) as well as data obtained during the early summer of 1974 (P. E. Gadd, unpublished data, 1974). Predicted downchannel flow events are noted in Figures 3 and 4. By applying the criteria for downchannel flow to the same 3-year wind data as those used for Figure 5, an estimate was made of the frequency of wind-induced downchannel flow events (not volume transport) in the shelf valley. Figure 6*a* shows the yearly variation of monthly downchannel flow activity from 1973 through 1975. The mean monthly values for the 3-year period appear in Figure 6*b*. A strong seasonal control of wind-induced downchannel flow is not evident in these data. However, for comparison with previous calculations on the seasonal upchannel flow, these data were similarly divided and averaged. For the months of October through April, predicted wind-induced downchannel flow occurred on an average of 62 hours per month (8.7%), whereas during May through September a nearly identical average of 59 hours per month (8.2%) was predicted.

Net wind-induced flow in the Hudson Shelf Valley. From Figures 5 and 6 it is clear that of the predicted wind-induced currents in the shelf valley, upchannel flow predominates. To quantify this, data from Figures 5*b* and 6*b* were combined to produce a net annual wind-induced flow budget for the shelf valley (Figure 7). Based on the assumptions of the test criteria, the annual net predicted upchannel flow time accounts for nearly an order of magnitude more time (1090 hours) than downchannel flow (125 hours). From Figure 7 it is also apparent that predicted upchannel flow is dominant from October through April, whereas with the exception of July, minor downchannel flow predominates from May to September. It should be reemphasized here that the data of Figure 7 are an estimate of net upchannel and downchannel flow time and not net volume transport.

TESTING THE MODEL

Suspended particulate matter. Although a model has been proposed to predict wind-induced upchannel and downchannel flow in the Hudson Shelf Valley, a broader picture of wind-coupled circulation in the Bight apex is desirable. In the absence of extensive current meter coverage, observations of SPM will serve as corroborating evidence of general circulation patterns in the Bight apex. A series of water column characterization (WCC) cruises have monitored the water of the Bight apex since August 1973 on approximately a monthly basis. Data from two of these cruises will be presented to illustrate distributions of SPM and implied wind-driven water movement. Because of the lack of appropriate winds during the WCC cruise series, no examples of wind-driven, downchannel flow can be presented.

WCC-9. Figure 8 illustrates the SPM data for cruise WCC-9 (July 16–20), while Figure 9*a* illustrates synoptic wind data from Kennedy Airport. By applying the previously described test for upchannel flow in the Hudson Shelf Valley, the test criteria are satisfied for a 15-hour period just prior to the cruise and for a period at the end of the final sampling day (Figure 9*a*). Although the second predicted upchannel flow

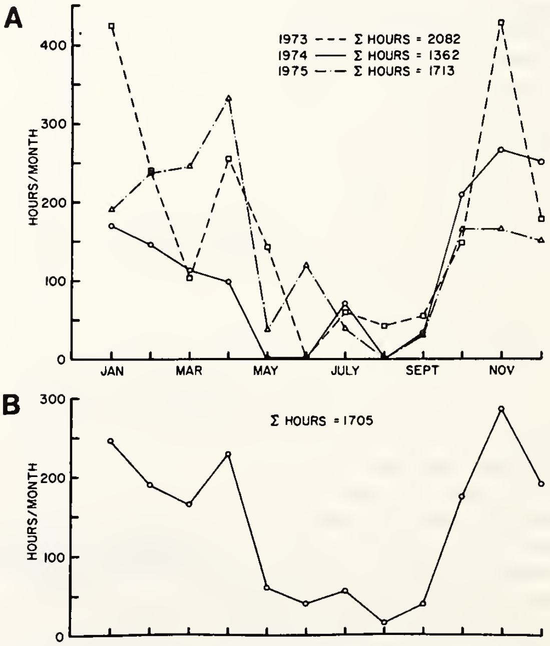

Fig. 5. Total hours per month of predicted wind-induced upchannel flow in the Hudson Shelf Valley for (*a*) 1973–1975 and (*b*) the averaged monthly values for those years.

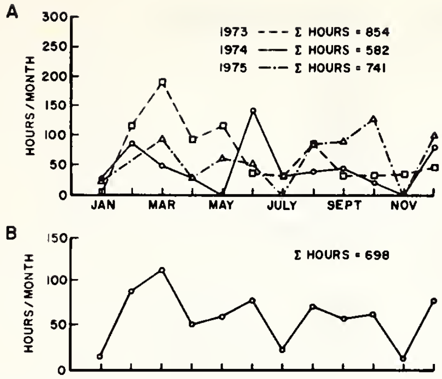

Fig. 6. Total hours per month of predicted wind-induced downchannel flow in the Hudson Shelf Valley for (*a*) 1973–1975 and (*b*) the averaged monthly values for those years.

event occurred after water sampling was completed, evidence for the first predicted event was observed. Suspended particulate matter concentration data for WCC-9 (Figure 8*a*) showed only the relatively turbid nearshore and surface water associated with the Hudson Estuary outflow. However, factor analysis of the SPM size data for WCC-9 identified three significant factors (Figure 10) from a suite of 85 samples. The unique character of the SPM for these three factors was substantiated by visual inspection of each sample with a scanning electron microscope. The inspection revealed the following compositions: factor I, the dinoflagellate *Polykrikos* sp. and amorphous organic material; factor II, the dinoflagellates *Ceratium longipes, C. fusus,* cocospheres, and various other test fragments, and factor III, the diatoms *Chaetoceros* sp. and *Thalassiosira* sp. The station position of these factor samples can be located by referring to the lower right panel of Figure 11*a*. From Figure 8*a* it can be seen that factors I and III are representing nearshore samples of high SPM concentration (3.45 and 2.50 mg/l, respectively), while factor II had the lowest SPM concentration (1.30 mg/l) and was found at the most seaward extent of the sample grid. Figure 8*b* illustrates the distribution of these factors and strongly suggests that for 10- and 20-m depths, water bearing factor II type particles intruded from the south and moved northward in conformity with Bight apex bathymetry (Figure 1). The distribution of factor II is substantiated by sigma *t* data for the same cruise [*Hazelworth et al.,* 1975], which revealed an intrusion of similar extent at both 10 and 20 m. The patchy distribution of factors I and III in the surface water is speculated to result from mixing by subsequent variable winds, which failed to influence deeper waters because of the developing seasonal thermocline located at about 5 m [*Hazelworth et al.,* 1975]. We therefore feel that it is reasonable to conclude that the minor upchannel flow event did take place as predicted, but because of its short duration and insufficient flow, the intruding water mass did not breach the seasonal thermocline.

WCC-13. Starting on December 9 and continuing through December 11, 1974, a sustained westerly wind averaging 6.5 m/s (13 kn), gusting to 12 m/s (24 kn), blew over the Bight apex (Figure 9*b*). Based on the previously established criteria for wind-induced currents, a massive upchannel flow event was predicted for this time. During the final 2 days of this event, water sampling for WCC-13 took place, and Figure 11 illustrates the concentration distributions of SPM observed during this cruise. From Figure 11*a* it is evident that relatively particle-deficient water is present at all depths over the shelf valley with a clockwise gyral advection suggested at 10 m. A cross-sectional view of these data (Figure 11*b*) clearly illustrates the spatial correlation of the relatively particle-deficient water with the shelf valley. Factor analysis data sustained this interpretation. Particularly noteworthy in Figure 11*b* are the nearly vertical SPM concentration isopleths which define a high gradient boundary between the turbid nearshore waters and the inferred intrusive water mass. The significance of this is that if upchannel flow is taking place as predicted, then this northward flow extends to the surface, as suggested by cross sections C-C′, D-D′, and especially E-E′ of Figure 11*b*. It is also evident from this figure that although the position of the intruding water mass seems strongly controlled by the Bight apex bathymetry, the particle-deficient waters are not confined to the shelf valley but extend onto its flanks as well.

To investigate further the nature of the particle-deficient water, the SPM was visually inspected with a scanning electron microscope to characterize the constituent particles of each sample. As was expected, material from the shelf valley showed a definite compositional variation from that found in surrounding waters. The particle-deficient water was composed of planktonic organisms, whereas the surrounding SPM was composed primarily of mineral grains, fibrous and unidentified organic material, and some phytoplankton tests and test fragments. From these data it is reasonable to conclude that upchannel flow in the Bight apex occurred during WCC-13 as predicted.

Remote sensing. Remotely sensed images can supply valuable information by virtue of their inherent ability to gather truly synoptic data over large areas. The application of remote sensing to oceanography became more prevalent with the deployment of the Earth Resources Technology Satellite (Erts). Using Erts multispectral scanner data, workers were able to observe and semiquantify SPM in lakes [*Strong,* 1974], rivers [*Kritikos et al.,* 1974], and the marine environment [*Klemas et al.,* 1974; *Szekielda,* 1974; *Szekielda and Duvall,* 1976] and interpret near-surface circulation patterns from these data [*Charnell et al.,* 1974; *Strong,* 1974; *Klemas et al.,* 1974; *Szekielda,* 1974; *Szekielda and Duvall,* 1976]. From the above studies it is generally recognized that backscattered radiation from SPM is best detected on Erts multispectral scanner bands 4 (500–600 nm) and 5 (600–700 nm). Depth penetration into the water column is a function of SPM concentration, but 10 m (band 4) and 3 m (band 5) are commonly accepted average values [*Kritikos et al.,* 1974]. Based on the data presented in

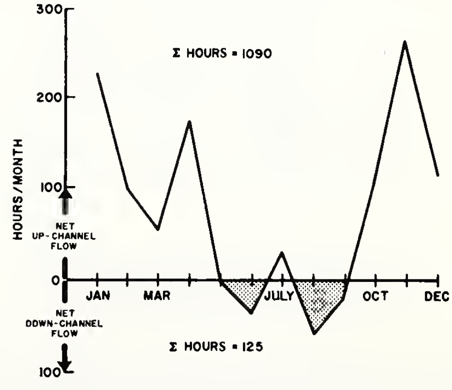

Fig. 7. Net predicted wind-induced flow in the Hudson Shelf Valley based on Figures 6 and 7.

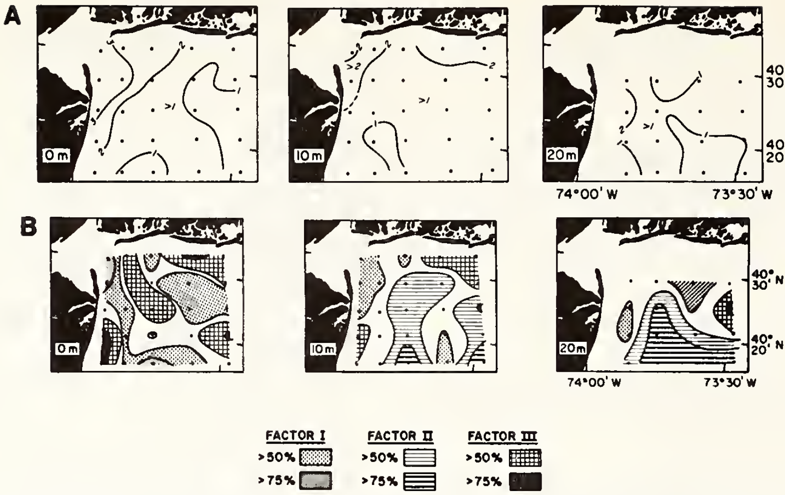

Fig. 8. Suspended particulate matter data for cruise WCC-9 (July 16–20, 1974) showing (*a*) concentration (mg/l) and (*b*) factor analysis data for surface, 10, and 20 m.

Figure 11*b*, which suggested that major upchannel flow events can include surface waters, we feel that the following remotely sensed data will contribute meaningful information to this study.

Figure 12 is a black and white photograph of a multispectral scanner image obtained by NASA's coastal zone color scanner. The spectral bands represented in Figure 12 fall in the blue (470 ± 10 nm), yellow (583 ± 10 nm), and red (662 ± 10 nm) portions of the electromagnetic spectrum and were selected for maximum detection of SPM in water (Warren A. Hovis, unpublished report, 1977). The area covered by Figure 12 is essentially identical to that of Figure 1. In Figure 12, Long Island, New York, and Sandy Hook, New Jersey, land masses are represented by a dot pattern, and the Bight apex waters are represented by the dark areas, while the various intensities of light area represent backscattered radiation arising from SPM in the water. The word 'turbidity' will be used hereafter to designate unquantified concentrations of SPM in the water. The assumption that the turbidity seen in Figure 12 represents SPM is based on synoptic sensing and sea-truth observations in the New York Bight [*Charnell et al.,* 1974] in which observed turbid plumes from waste dumping and the Hudson Estuary outflow were essentially identical in shape and location to those seen in Figure 12. The straight white line in Figure 12 indicates the position of the axis of the Hudson Shelf Valley which terminates approximately at the end of the arrow labeled B. The bottom end of the white line marks the southern boundary of the Bight apex, while the northern end projects toward Rockaway Beach on Long Island.

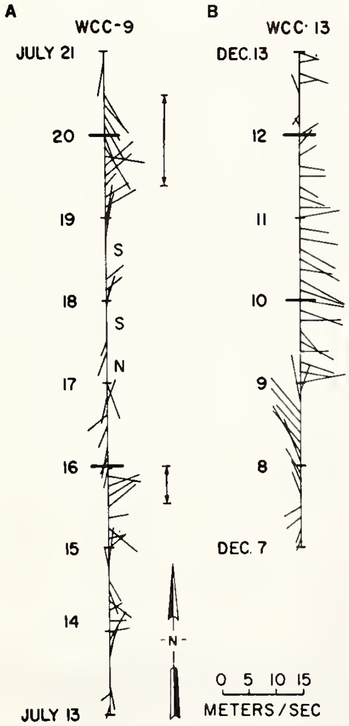

Fig. 9. Wind vector time series at Kennedy Airport for (*a*) cruise WCC-9 (July 16–20, 1974), where the letters S and N indicate southerly and northerly winds, respectively, and (*b*) cruise WCC-13 (December 10–11, 1974). Predicted upchannel flow in the Hudson Shelf Valley is indicated by double-ended arrows adjacent to wind vectors.

Starting approximately 32 hours before and continuing past the time that the Figure 12 image was taken, westerly winds began to blow over the Bight apex. Interestingly enough, the wind criteria presented earlier failed to predict an upchannel flow event because a single wind velocity value fell 0.5 m/s below the proposed velocity criterion. Since the test for upchannel flow is qualitative, we felt justified in ignoring a single data point. In doing so, predicted upchannel flow was initiated 21 hours before the image was taken, and the subsequent winds, which averaged 5.4 m/s from 327°T, maintained the predicted flow for a minimum of 39 hours. Supportive evidence for this upchannel flow, we believe, is suggested in Figure 12 from features observed at points marked by arrows A and B. At A the seaward side of Rockaway Beach is characterized by relatively low turbidity in the nearshore and surf zones, while these zones to the west (left) and east (right) show relative turbidity maxima. Emanating from the Hudson Estuary, a turbidity maximum appears south along the New Jersey shore as well as southeast into the Bight apex as a

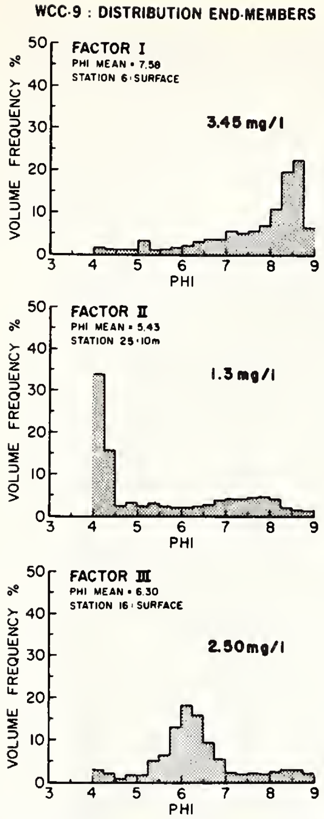

Fig. 10. Particle size distribution histograms for the three significant factors in the New York Bight apex during cruise WCC-9.

turbidity plume. The tip of arrow B indicates the front edge of the turbidity plume which has apparently been displaced northward, a movement contrary to its predominant southeast advection. These features have been interpreted by the authors to indicate a northward displacement of water over the shelf valley entraining part of the plume advecting from the Hudson Estuary during ebb tide, while less turbid waters continuing northward impinged on the south shore of Long Island, creating a nearshore turbidity minimum. We speculate that after impinging on the surf zone, the upchannel flow bifurcates to the west and east where longshore currents and normal surf action once again produce high turbidity nearshore zones.

Quantitative correlation of winds and bottom currents. To quantify the relationship between winds and bottom currents, time series of wind stress and current velocities were used to calculate inner-cross correlation versus lag time (τ) following the methods of *Mooers* [1973]. The wind stress computations followed the methods outlined by *Wu* [1969] for light and strong winds. The value of lag τ, at which the inner-cross correlation is a maximum, represents a best estimate of the lag in the response of the current velocity to a wind stress event. The phase of this lag is an estimate of the angle between the wind and current flow. On the basis of 10% Gaussian noise superimposed on the two time series, the standard deviation of the inner-cross correlation is approximately 0.01 [*Jenkins and Watts,* 1968]. In order to estimate properly the inner-cross correlation, the current time series were averaged in such a way that its sample interval was the same as that available for the wind data (3 hours). The magnitude and the phase of the inner-cross correlation for two time intervals are recorded in Table 2. The first time series in this table (October 31–November 12) coincides with the predicted upchannel flow event illustrated in Figure 2. From Table 2 it is seen that the maximum inner-cross correlation occurs at a lag of 6 hours. The mean current direction was computed to be north at 349°T, while the winds blew from a mean direction of 285°T. It is worth noting here that the mean current direction conforms to the linear trend of the Hudson Shelf Valley at this point, while the mean wind direction falls within the directional envelope prescribed for predicting upchannel flow. The second, somewhat more variable time series (October 24–31) includes downchannel flow as illustrated in Figure 4. Once again the maximum inner-cross correlation (0.75) occurs at a lag greater than zero (τ = 12 hours). As before, the mean current direction is apparently controlled by the topography of the Hudson Shelf Valley with a southward flow toward 172°T, while the mean wind direction of 35°T falls only 5° outside the directional envelope prescribed for predicting downchannel flow but within the directional envelope for flow maintenance.

From these data we believe that the reality of predictable upchannel and downchannel flow is strongly reinforced.

Mechanisms of Wind-Induced Current Flow in the Hudson Shelf Valley

Upchannel flow. As observed from current meters (Figures 2 and 3) and inferred from remotely sensed data (Figure 12), sustained westerly winds can promote upchannel (northerly) flow in the Hudson Shelf Valley. Acting as a forcing mechanism, the westerly winds are interpreted to promote offshore Ekman transport of the surface waters with a subsequent sea

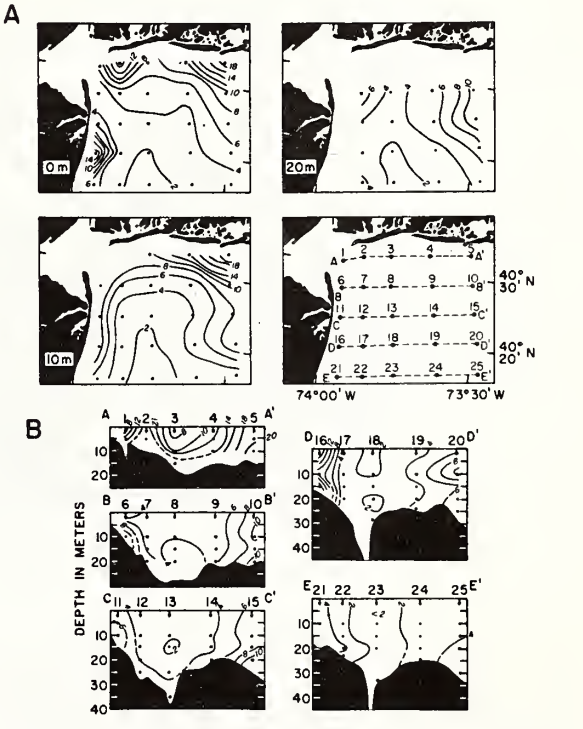

Fig. 11. Suspended particulate matter data for cruise WCC-13 (December 10–11, 1974) showing (*a*) concentration (mg/l) data for surface, 10, and 20 m as well as an index for (*b*) cross-sectional views of the New York Bight apex.

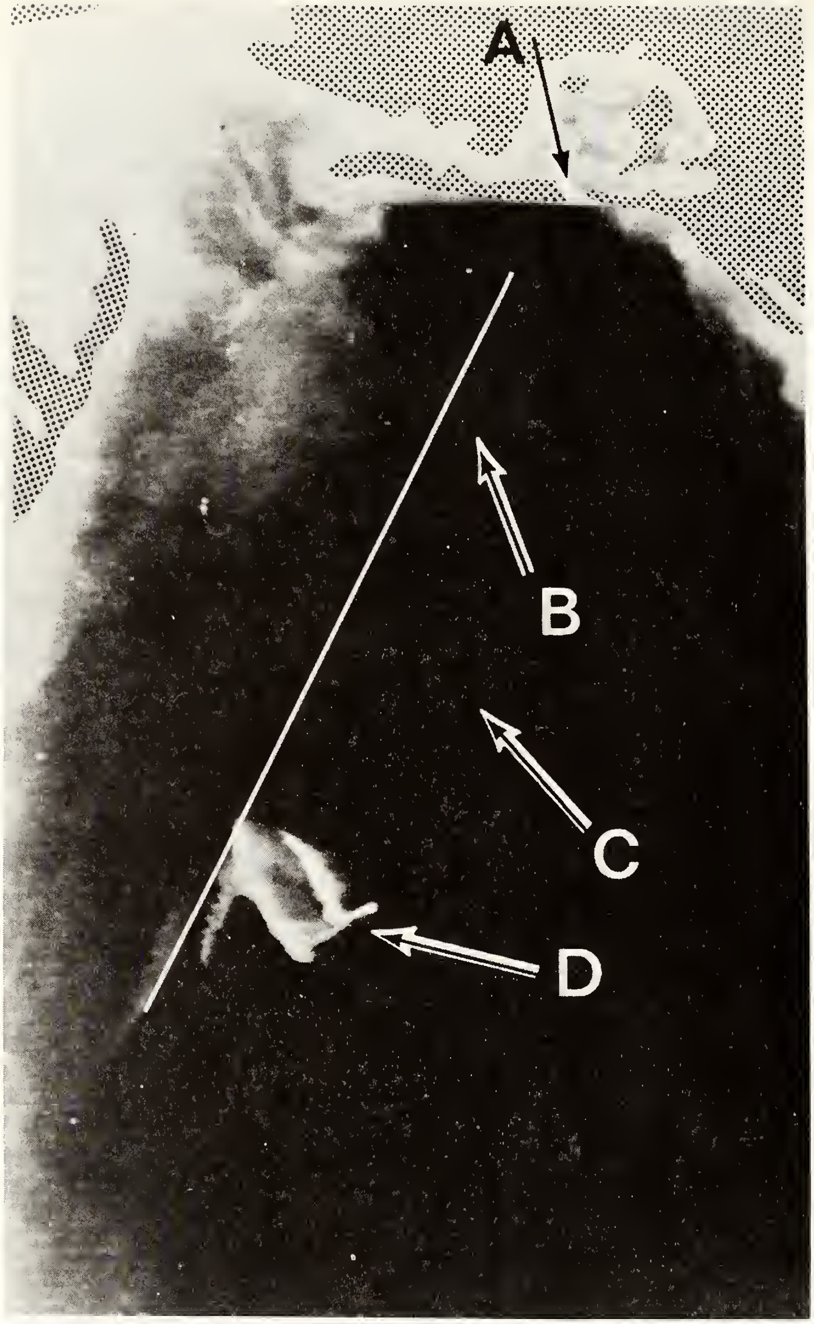

Fig. 12. Multispectral scanner image of the New York Bight apex. Land masses are symbolized by the dot pattern, while turbidity in the water appears as various shades of white. Features are (*a*) an anomalously low turbidity zone at Rockaway Beach, (*b*) a northward displaced portion of the Hudson Estuary plume, (*c*) location of the sewage sludge dump site, and (*d*) an old plume of dumped acid waste material.

surface setdown along the Long Island coast. As a consequence of this setdown, seaward flowing surface water must be balanced by landward flowing bottom water. This bottom return flow would be least retarded by friction where the water is the deepest, as in the Hudson Shelf Valley. Although upchannel flowing bottom waters were monitored at only two sites in the Bight apex (Figure 1), northward flow in the Bight apex most likely has a greater lateral extent as suggested in Figure 11. As a consequence of the proposed wind forcing and nearshore setdown, the compensating northward currents are pressure-driven flows, a phenomenon which normally exhibits increased flow velocity with depth. The current data of Figure 2 substantiate this interpretation.

In relating wind to water velocity, *Caston* [1976] found in the southern North Sea that wind-driven bottom currents attained a velocity from 1.4–2% of the average wind speed.

TABLE 2. Inner–Cross Correlation Coefficients: Wind Stress Versus Bottom Currents at Meter A

	Oct. 31–Nov. 12	Oct. 24–31
Correlation coefficients		
Zero lag value	0.61	0.68
Maximum value	0.66	0.75
Maximum value lag time τ, hours	6	12
Mean wind direction, °T	285	35
Mean current direction, °T	349	172
Phase, deg	67	97
Number of data points	96	64
Significance*	0.10	0.13

*Jenkins and Watts [1968].

Although wind-induced upchannel flow in the Hudson Shelf Valley is interpreted as a pressure-driven phenomenon, similar calculation based on six upchannel flow events indicated that these flows closely match Caston's data and are from 1.7 to 3.4% of the mean wind speed.

From juxtaposed wind and current meter stick diagrams (Figures 2–4) as well as lag τ (6 hours), computed for the maximum inner–cross correlation, it is clear that the current flow has a rapid response to wind forcing. In some cases a flow reversal results in approximately 3 hours (Figure 3, November 16), implying a very rapid transfer of momentum from the wind to the water column. This phenomenon has also been observed in recent work by *Scott and Csanady* [1976].

Downchannel flow. Evidence has been presented (Figures 3 and 4) that intense downchannel flow in the Hudson Shelf Valley is apparently in response to northeast winds. Historical data (Table 1) have shown that winds from the northeast do not occur frequently enough to dominate monthly mean wind patterns. However, when present, storms known as 'northeasters' have the capacity to promote wind-driven currents intense enough to act as mechanisms for significant sand transport on the inner shelf of the Bight [*Lavelle et al.*, 1976]. Other workers [*Beardsley and Butman*, 1974] have studied the relationship of shelf circulation to strong winter storms on the New England continental shelf including the New York Bight. Their results showed that currents, initiated by the wind stress of two northeasters, accounted for two thirds of the westward mass transport, although the storms totaled only 4 days of a 33-day observation.

Characteristically, water movement responding to wind stress has a velocity profile which decreases with depth. As cited earlier, downchannel flow events monitored at sites A and K typically showed lower velocities at the deeper station, suggesting that this flow is in response to direct wind stress and not a result of pressure-driven circulation. This is evident from the October 29–30 event (Figure 4), in which meters A and K recorded peak current velocities of 30 and 40 cm/s, respectively.

Although not observed in this study, data presented earlier suggest another mechanism for downchannel flow in the Hudson Shelf Valley if not the entire Bight apex. Table 1 shows that southerly winds predominate throughout the summer season. The authors speculate that with wind-driven surface water moving northward, sea surface elevation along Long Island would increase, thus promoting coastal downwelling with an associated compensatory southerly bottom flow. However, the seasonal thermocline which develops and exists concurrently with the southerly winds may be an adequate barrier to downwelling, thereby promoting either diverging east-west shore-parallel surface flow or middepth return flow at the thermocline.

In this paper, emphasis has been placed on interpretation of observed flow events which are presumed to be wind induced. It is clear, however, that other mechanisms are at work in the Bight apex which promote southerly advection of water. *Bumpus* [1965], for example, notes a general westerly and southerly drift of bottom waters within the Bight which he calculates to be of the order of 5 cm/s, a value in agreement with more recent work by *Scott and Csanady* [1976] and modeling by *Han et al.* [1978]. This residual flow would continue to be a cause of southerly transport of SPM during periods when more pronounced wind-induced current activity is not present. However, Han's model also suggests that transport within the apex portion of the Bight and the Hudson Shelf Valley is predominantly shoreward with the mass balance maintained by a quasi-estuarine circulation. In addition, current meter records (Figures 3*a* and 4) show oscillation of the bottom waters at semidiurnal tidal frequency. Although this component is not investigated in this study, it could also be a very important constituent of the net flow field during periods of low-velocity currents.

Summary and Conclusions

From wind, current meter, SPM, and remote sensing data, a predictable relationship has been developed between wind data from Kennedy Airport and resultant wind-induced current flow in the Hudson Shelf Valley. Dominant wind direction and, consequently, net flow time in the Hudson Shelf Valley were shown to vary seasonally, with upchannel flow predominating during the winter months (October–April) and downchannel flow predominating during the summer months (May–September). By strict adherence to the test criteria, some apparent upchannel flow events (Figure 12) were not initially predicted, leading to the conclusion that the wind-induced current model developed in this paper is a conservative one and that estimated flow budgets for the Hudson Shelf Valley probably represent minimum values.

The model developed here can have implications for environmental considerations as well. Waste materials from the New York metropolitan area are barged to their respective disposal sites (Figure 1), where they are dumped into the surface waters of the Bight apex [*Gross*, 1972]. Depending on the season, the nature of the dumped material, and the currents and physical nature of the water column, these wastes can settle to the bottom, diffuse in the water column, advect with the ambient currents, or any combination thereof. If the implications of Figure 12 are correct, waste material, especially sewage sludge, has a good chance of being advected directly toward Rockaway Beach, a popular summer bathing beach. The health problems reported at this beach [*Cabelli et al.*, 1975] seemingly support this hypothesis.

Although this study was limited to the New York Bight apex, we believe that the following broader conclusions can be drawn:

1. Currents initiated by a given wind velocity can be maintained by sustained lower-velocity winds.
2. Seasonal wind variation can produce seasonal current variation.
3. Peak wind events can transfer momentum to the water column rapidly (6 hours, Table 2) to produce peak flow events as well as very rapid flow reversals (3 hours, Figure 3).
4. Item 3 should suggest to workers in sediment transport that ephemeral but intense wind events should be considered

as potential contributors to net sediment transport and that long-term current averages may be misleading by filtering out these ephemeral events.

5. Shallow shelf valleys may have highly channelized periodic currents, which are not only controlled by regional wind events but are predictable from local wind data.

Acknowledgments. Part of this study was funded by the Mesa Program of NOAA's Environmental Research Laboratories. The Mesa current meter data were graciously furnished by NOAA's Miami-based Physical Oceanography Laboratory. Personal gratitude is extended to Warren Hovis for providing the remotely sensed image, a product of NASA Goddard's Coastal Zone Color Scanner Program. Critical review of the manuscript by John W. Lavelle, George Maul, Carlisle Thacker, Donald J. P. Swift, and Robert A. Young is acknowledged and appreciated.

REFERENCES

Beardsley, R. C., and B. Butman, Circulation on the New England continental shelf: Response to strong winter storms, *Geophys. Res. Lett., 1,* 181–184, 1974.

Bumpus, D. F., Residual drift along the bottom on the continental shelf in the Middle Atlantic Bight area, *Limnol. Oceanogr., 10,* R50–R53, 1965.

Cabelli, V. J., A. P. Dufour, M. A. Levin, and P. W. Habermann, The impact of pollution on marine bathing beaches: An epidemiological study (abstract), in *Special Symposium, The Middle Atlantic Continental Shelf and New York Bight Nov. 3-5, 1975,* American Society of Limnology and Oceanography, New York, 1975.

Carmody, D. J., J. B. Pearce, and W. E. Yasso, Trace metals in sediments of the New York Bight, *Mar. Pollut. Bull., 4,* 132–135, 1973.

Caston, V. N. D., A wind-driven near-bottom current in the southern North Sea, *Estuarine Coastal Mar. Sci., 4,* 23–32, 1976.

Charnell, R. L., and D. A. Mayer, Water movement within the apex of the New York Bight during summer and fall of 1973, *NOAA-ERL-MESA Tech. Memo. 3,* 29 pp., Nat. Oceanic and Atmos. Admin., Washington, D. C., 1975.

Charnell, R. L., J. R. Apel, W. Manning, and R. H. Qualset, Utility of Erts-1 for coastal ocean observation: The New York Bight example, *J. Mar. Tech. Soc., 8,* 42–47, 1974.

Clarke, T. L., An oblique factor analysis solution for the analysis of mixtures, *Math. Geol., 10*(2), 1978.

Drake, D. E., Suspended particulate matter in the New York Bight apex: September–November, 1973, *NOAA-ERL-MESA Tech. Rep. 318,* 53 pp., Nat. Oceanic and Atmos. Admin., Washington, D. C., 1974.

Gross, G. M., Geologic aspects of waste solids and marine waste deposits, New York metropolitan region, *Bull. Geol. Soc. Amer., 83,* 3163–3176, 1972.

Han, G., D. V. Hansen, and A. Cantillo, Diagnostic model of water and oxygen transport in the New York Bight, *in Oxygen Depletion and Associated Mass Mortalities in the New York Bight, 1976,* National Oceanic and Atmospheric Administration, Washington, D. C., 1975.

Hatcher, P. G., and L. E. Keister, Carbohydrates and organic carbon in New York Bight sediments as possible indicators of sewage contamination (abstract), in *Special Symposium, The Middle Atlantic Continental Shelf and New York Bight,* American Society of Limnology and Oceanography, New York, 1975.

Hazelworth, J. B., B. L. Kolitz, R. B. Starr, R. L. Charnell, G. A. Berberian, and M. A. Weiselberg, New York Bight Project, Water column sampling cruises #9–12 of the NOAA ship *Ferrel,* July–Nov. 1974, NOAA-ERL-MESA data rep., 170 pp., Nat. Oceanic and Atmos. Admin., Washington, D. C., 1975.

Imbrie, J., and T. H. van Andel, Vector analysis of heavy mineral data, *Bull. Geol. Soc. Amer., 75,* 1131–1156, 1964.

Jenkins, G. M., and D. G. Watts, *Spectral Analysis,* Holden-Day, San Francisco, 1968.

Klemas, V., D. Bartlett, W. Philpot, R. Rogers, and L. Reed, Coastal and estuarine studies with Erts-1 and Skylab, *Remote Sensing Environ., 3,* 153–174, 1974.

Klovan, J. E., and J. Imbrie, An algorithm and Fortran-IV program for large-scale Q-mode factor analysis and calculation of factor scores, *Math. Geol., 3,* 61–77, 1971.

Kritikos, M., L. Yorinks, and H. Smith, Suspended solids analysis using Erts-A data, *Remote Sensing Environ., 3,* 69–78, 1974.

Lavelle, J. W., G. H. Keller, and T. L. Clarke, Possible bottom current response to surface winds in the Hudson Shelf Valley, *J. Geophys. Res., 80,* 1953–1955, 1975.

Lavelle, J. W., P. E. Gadd, G. C. Han, D. A. Mayer, W. L. Stubblefield, D. J. P. Swift, R. L. Charnell, H. R. Brashear, F. N. Case, K. W. Haff, and C. W. Kunselman, Preliminary results of coincident current meter and sediment transport observations for wintertime conditions on the Long Island inner shelf, *Geophys. Res. Lett., 3,* 97–100, 1976.

Lettau, B., W. A. Bower, and R. G. Quayle, *Marine Climatology, MESA New York Bight Atlas Monograph 7,* pp. 199–211, New York Sea Grant Institute, Albany, N. Y., 1976.

Moores, C. N. K., A technique for the cross spectrum analysis of pairs of complex-valued time series, with emphasis on the properties of polarized components and notational invariants, *Deep Sea Res., 20,* 1129–1141, 1973.

Scott, J. T., and G. T. Csanady, Nearshore currents off Long Island, *J. Geophys. Res., 81,* 5401–5409, 1976.

Strong, A. E., Remote sensing of algal blooms by aircraft and satellite in Lake Erie and Utah Lake, *Remote Sen. Environ., 3,* 99–107, 1974.

Szekielda, K. H., Observations of suspended material from spacecraft altitudes, *Sonderdruck Deut. Hydrogr. Z., 27*(4), 159–170, 1974.

Szekielda, K. H., and J. T. Duvall, Pattern recognition of suspended material, *J. Cons. Cons. Perma Int. Explor. Mer, 36,* 205–216, 1976.

Wu, J., Wind stress and surface roughness at air-sea interface, *J. Geophys. Res., 74,* 444–455, 1969.

(Received January 24, 1978;
revised May 24, 1978;
accepted June 7, 1978.)

Journal of Volcanology and Geothermal Research 3, 219-225.

MAGNETIC SIGNATURES OF HYDROTHERMAL ALTERATION AND VOLCANOGENIC MINERAL DEPOSITS IN OCEANIC CRUST

PETER A. RONA

National Oceanic and Atmospheric Administration, Atlantic Oceanographic and Meteorological Laboratories, Miami, Fla. (U.S.A.)

(Received May, 9, 1977; revised and accepted August 8, 1977)

The realization that hydrothermal mineral deposits including metallic oxides and sulfides can form at oceanic spreading centers (Boström and Peterson, 1966; Spooner and Fyfe, 1973; Hutchinson, 1973; Sillitoe, 1973; Bonatti, 1975) has stimulated the search for such deposits in oceanic crust. Although inaccessible to present exploitation, hydrothermal mineral deposits at oceanic spreading centers provide natural laboratories to study ore-forming processes, and knowledge of their distribution is necessary to evaluate the metallic mineral potential of oceanic crust. Only a few concentrated hydrothermal mineral deposits have so far been discovered at oceanic spreading centers, including the deposits of the Red Sea (Degens and Ross, 1969; Bäcker and Schoell, 1972), the TAG Hydrothermal Field on the Mid-Atlantic Ridge at latitude 26°N (Rona et al., 1976), and the Mounds Hydrothermal Field at the Galapagos spreading center in the equatorial Pacific (Moore and Vogt, 1976; Corliss et al., 1976; Lonsdale, 1977). These hydrothermal deposits were found largely by trial and error bottom sampling. The need exists for rapid reconnaissance criteria to guide the slow and localized bottom sampling procedure to potential sites of hydrothermal mineral deposits in oceanic crust both at and away from the 52,000 km long oceanic ridge system. A growing body of field evidence supported by laboratory studies indicates that concentrated hydrothermal activity may affect the intensity of magnetization of basalt, producing a characteristic magnetic signature that may be associated with sites of hydrothermal mineral deposits.

Field evidence favoring the existence of a magnetic signature indicative of hydrothermal deposits is as follows:

(1) A distinct low in residual magnetic intensity (approximately 200 gammas) coincides with the TAG Hydrothermal Field at the crest of the Mid-Atlantic Ridge and is absent both to the north and south of the TAG Hydrothermal Field (Figs. 1, 2; McGregor and Rona, 1975). The magnetic low occurs within the positive magnetic anomaly of the Brunhes magnetic polarity epoch, that is normally associated with the axis of oceanic spreading centers.

(2) A distinct low in residual magnetic intensity occurs at the Atlantis II

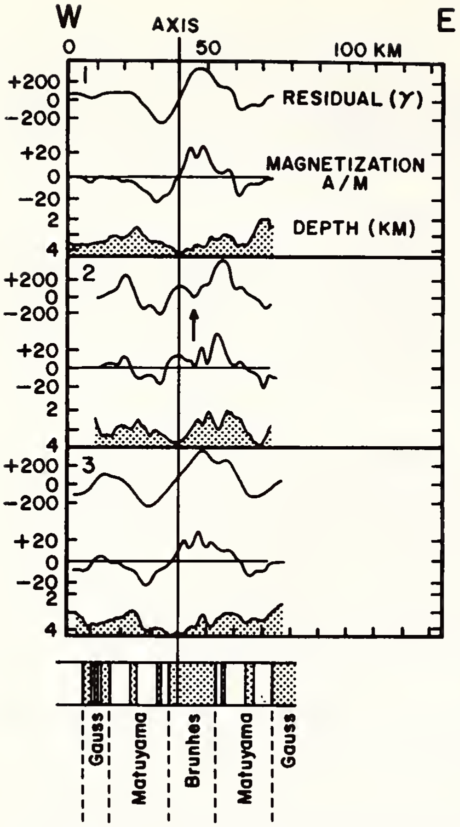

Fig.1. Profiles of residual magnetic intensity (γ; gammas), magnetization of the basalt layer computed by the inverse method (A/m; 1 ampere/meter = 0.001 emu/cm^3), and depth (km), across the axis of the rift valley of the Mid-Atlantic Ridge at latitude 26°N (modified from McGregor et al., 1977). A distinct low in residual magnetic intensity within the positive axial magnetic anomaly (Brunhes magnetic polarity epoch) and in the computed magnetization (arrow in profile 2), coincides with the TAG Hydrothermal Field. The magnetic low is absent in profiles north (profile 1) and south (profile 3) of the field. The location of the profiles is shown in Fig.2.

Deep (approximately 650 gammas) in the axial trough of the Red Sea (Figs. 3, 4; Hunt et al., 1967; Phillips et al., 1969). The magnetic low is absent at the adjacent Chain Deep and Discovery Deep, which are associated with magnetic highs (approximately 350 gammas) typical of the axis of oceanic spreading centers. The thermal brine in these three deeps is inferred to discharge at

Fig.3. Magnetic and bathymetric profiles across the axial trough of the Red Sea (modified from Phillips et al., 1969). An index map shows locations of the profiles and of the hot brine deeps. A distinct low in magnetic intensity occurs over the Atlantis II Deep (profile *A—A'*), the locus of hydrothermal discharge. High magnetic intensity characteristic of the axis of oceanic spreading centers, occurs over the axial trough outside the area of the hot brine deeps (profile *B—B'*).

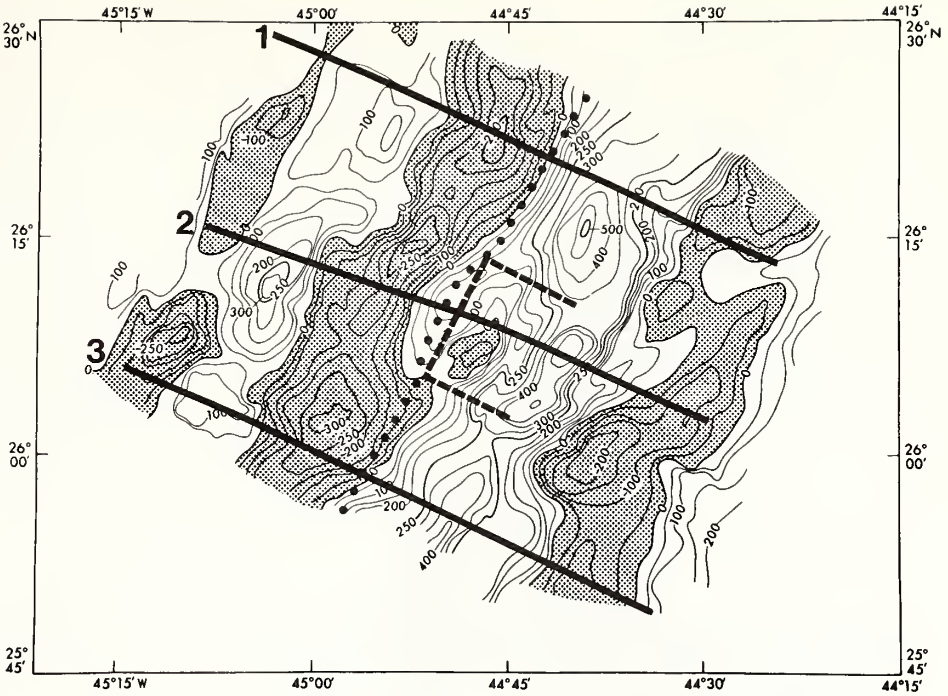
45°15'W
45°00'
44°45'
44°30'
44°15'
26° 30' N
26° 15'
26° 00'
25° 45'
1
2
3
-100
-250
0
100
200
250
300
400
500

Fig.2. Residual magnetic map (50-gamma contour interval) of the Mid-Atlantic Ridge crest at latitude 26°N (modified from McGregor et al., 1977). Shaded areas are negative. The location of profiles 1—3 in Fig.1 (solid lines), the TAG Hydrothermal Field (dashed lines), and the axis of the rift valley (dotted line) are shown. Low to negative values of residual magnetic intensity are present within the positive axial magnetic anomaly at the TAG Hydrothermal Field.

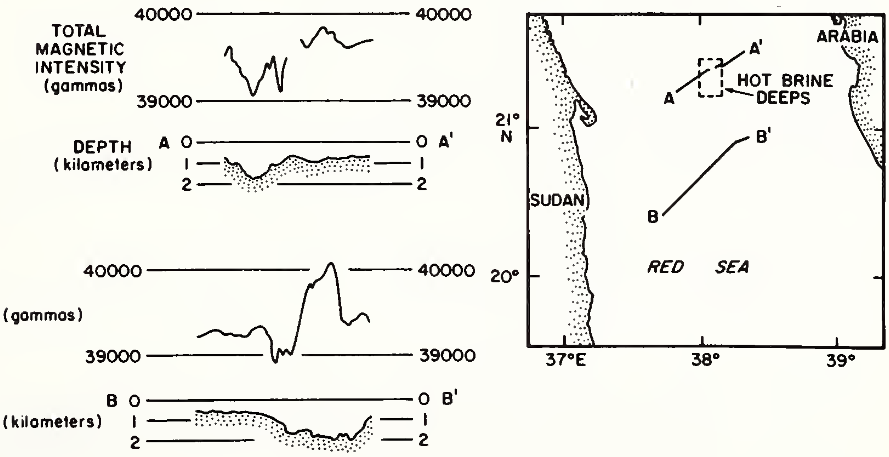

Fig.3.

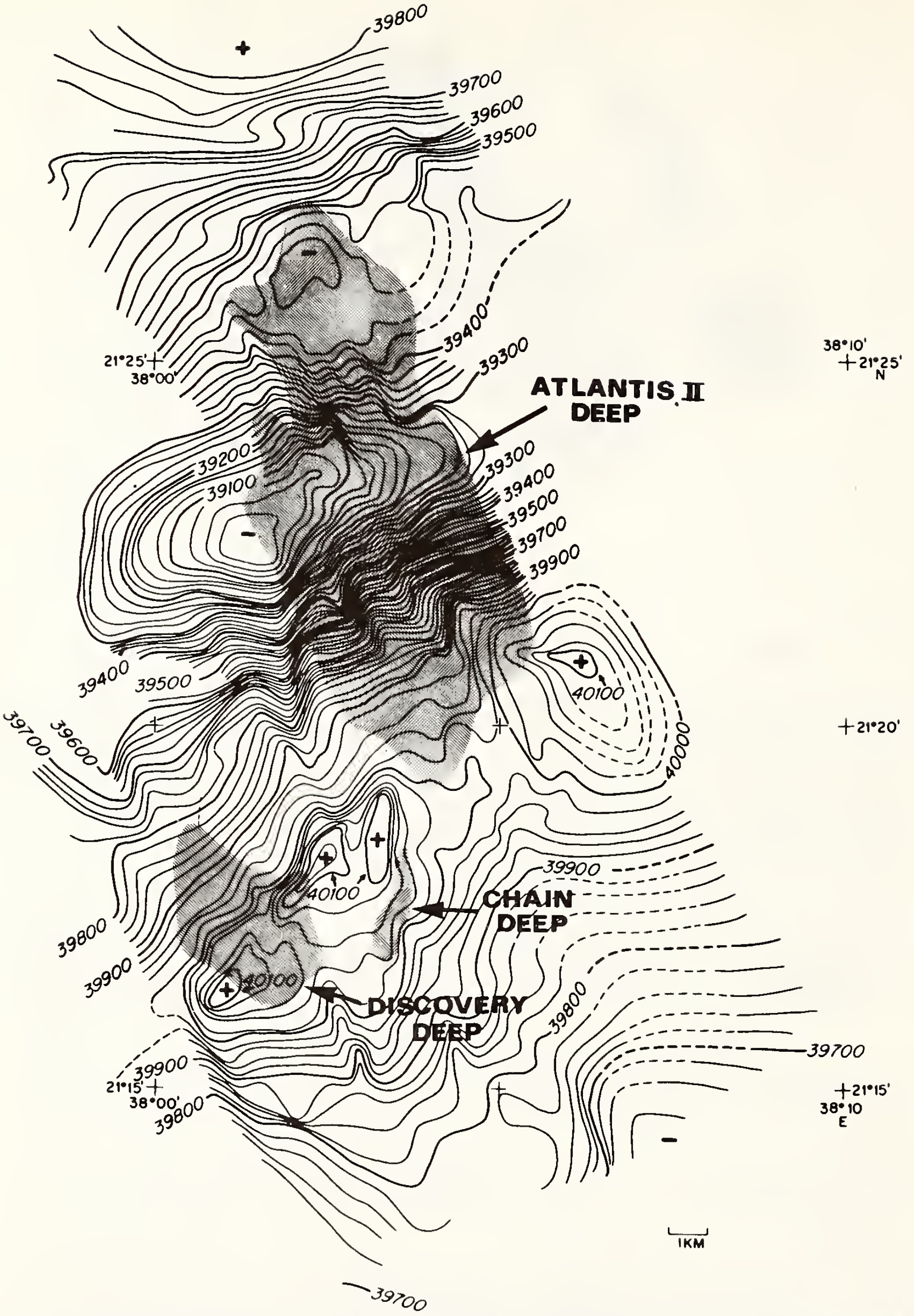
39800
39700
39600
39500
39400
39300
ATLANTIS II DEEP
21°25' 38°00'
38°10' 21°25' N
39200
39100
39300
39400
39500
39700
39900
39400
39500
39700
39600
40100
40000
21°20'
39900
CHAIN DEEP
40100
39800
39900
40100
DISCOVERY DEEP
39800
39700
39900
21°15' 38°00'
39800
21°15' 38°10 E
1KM
39700

Fig.4. Total intensity magnetic map (20-gamma contour interval) of the hot brine deeps of the Red Sea outlined in Fig.3 (modified from Phillips et al., 1969). A magnetic low (-) occurs at the Atlantis II Deep; magnetic highs (+) occur at the Discovery Deep and Chain Deep. A hydrothermal discharge zone in the Atlantis II Deep is the source of the thermal brines and metalliferous sediments in the three deeps.

a minimum temperature of 100°C from a single zone in the Atlantis II Deep, based on distribution of metalliferous sediments, chemistry of the brine and interstitial water, and brine temperature relations (Brewer et al., 1969; Brooks et al., 1969; Ross et al., 1969; Ross, 1972). The association of the magnetic low with a zone of hydrothermal discharge was not noted previously.

(3) A distinct low in residual magnetic anomaly (approximately 200 gammas) coincides with the subaerial Reykjanes hydrothermal field in Iceland at the axis of the Mid-Atlantic Ridge, where the thermal brine attains temperatures of 300°C (Björnsson et al., 1972).

(4) Distinct lows in residual magnetic intensity occur at certain other subaerial hydrothermal fields in volcanic rocks, including Mesa in the Salton Trough of southwestern United States, where measured temperatures attain 216°C (Koenig, 1967; Black, 1975); Wairakei of New Zealand, where measured temperatures attain 250°C (Banwell et al., 1957; Studt, 1959); and Rabaul, New Britain (Studt, 1961).

Laboratory studies of basalt alteration explain the cause of the lows in residual magnetic intensity observed at both submarine and certain subaerial hydrothermal fields, as follows:

(1) Unaltered tholeiitic basalt has high magnetic susceptibility (typical values 6—30 emu/cm^3 X 10^4) and remanent magnetization (typical values 36 to 113 emu/cm^3 X 10^4), because of its content of fresh Fe-Ti oxide, especially titanomagnetite (Luyendyk and Melson, 1967; Irving et al., 1970a; b; Watkins and Paster, 1971; Ade-Hall et al., 1971; Marshall and Cox, 1972; Fox and Opdyke, 1973).

(2) Unaltered basalt is metamorphosed to greenstone by hydrothermal alteration within the range of temperatures and pressures encountered in hydrothermal discharge zones (Spooner and Fyfe, 1973; Helgeson, 1968, 1969; Melson et al., 1968; Miyashiro et al., 1971). The discharge zones of hydrothermal convection systems are the loci of hydrothermal mineral deposition (Spooner and Fyfe, 1973).

(3) Greenstone, in which Fe-Ti oxide has been replaced by sphene and other minerals, has low values of susceptibility (typical values 0.4—0.6 emu/cm^3 X 10^4) and remanent magnetization (typical values 0.02—0.11 emu/cm^3 X 10^4) (Luyendyk and Melson, 1967; Irving et al., 1970a, b; Watkins and Paster, 1971; Ade-Hall et al., 1971; Marshall and Cox, 1972; Fox and Opdyke, 1973).

(4) The presence of altered basalts and greenstones has been confirmed where rocks have been recovered from hydrothermal fields associated with magnetic lows (Rona et al., 1976; Björnsson et al., 1972; Studt, 1959, 1961).

(5) Computer modelling of the magnetic low at the TAG Hydrothermal Field using forward and inverse methods (Fig.1), is consistent with attribution of the low to reduction in remanent magnetization within the basalt of oceanic crustal layer 2 (the basaltic layer of oceanic crust; McGregor et al., 1977).

(6) The hydrothermal alteration involved specifically pertains to basalt, because alteration of other rock types may produce different magnetic effects. For example, fresh peridotites lacking magnetite alter to rocks rich in serpentine and magnetite with increase in magnetic susceptibility (Luyendyk and Melson, 1967; Fox and Opdyke, 1973).

Development of magnetic lows by alteration of the magnetic mineral component of basalts in high-temperature discharge zones of sub-sea floor hydrothermal convection systems may provide a rapid reconnaissance criterion to guide bottom sampling to potential sites of concentrated hydrothermal mineral deposits at oceanic spreading centers. The effectiveness of this criterion remains problematic with regard to detection of hydrothermal deposits in oceanic crust away from oceanic spreading centers, where the magnetic signature may be obscured by magnetic polarity reversals, off-axis volcanism and, in the case of ophiolites, by metamorphism and subaerial alteration.

REFERENCES

Ade-Hall, J.M., Palmer, H.C. and Hubbard, T.P., 1971. The magnetic and opaque petrological response of basalts to regional hydrothermal alteration. R. Astron Soc. Geophys. J., 24: 137—174.

Bäcker, H. and Schoell, M., 1972. New deeps with brines and metalliferous sediments in the Red Sea. Nature Phys. Sci., 240: 153—158.

Banwell, C.J., Cooper, E.R., Thompson, G.E.K. and McCree, K.J., 1957. Physics of the New Zealand thermal area. N.Z. Dep. Sci. Ind. Res. Bull., 123, 109 pp.

Björnsson, S., Arnórsson, S. and Tómasson, J., 1972. Economic evaluation of Reykjanes thermal brine area, Iceland. Am. Assoc. Pet. Geol. Bull., 56: 2380—2391.

Black, H.T., 1975. A subsurface study of the Mesa geothermal anomaly, Imperial Valley, California. National Science Foundation, Washington D.C., Report No. NSF-RA-N-75-126, 58 pp.

Bonatti, E., 1975. Metallogenesis at oceanic spreading centers. In: Annual Reviews Earth Planetary Science, 3. Annual Reviews, Inc., Palo Alto, Calif., pp. 401—431.

Böstrom, K. and Peterson, M.N.A., 1966. Precipitates from hydrothermal exhalations on the East Pacific Rise. Econ. Geol., 61: 1258—1265.

Brewer, P.G., Densmore, C.D., Munns, R. and Stanley, R.J., 1969. Hydrography of Red Sea brines. In: E.T. Degens and D.A. Ross (Editors), Hot Brines and Recent Heavy Metal Deposits in the Red Sea. Springer-Verlag, New York, N.Y., p. 138.

Brooks, R.R., Kaplan, I.R. and Peterson, M.N.A., 1969. Trace element composition of Red Sea geothermal brine and interstitial water. In: E.T. Degens and D.A. Ross (Editors), Hot Brines and Recent Heavy Metal Deposits in the Red Sea. Springer-Verlag, New York, N.Y., p. 180.

Corliss, J.B., Dymond, J., Lyle, M., Doerge, T., Crane, K., Lonsdale, P., Von Herzen, R.P. and Williams, D., 1976. Sediment mound ridges of hydrothermal (?) origin along the Galapagos Rift. EOS, Trans. Am. Geophys. Union, 57: 935—936.

Degens, E.T. and Ross, D.A. (Editors), 1969. Hot Brines and Recent Heavy Metal Deposits in the Red Sea. Springer-Verlag, New York, N.Y., 600 pp.

Fox, P.J. and Opdyke, N.D., 1973. Geology of the oceanic crust: magnetic properties of oceanic rocks. J. Geophys. Res., 78: 5139—5154.

Helgeson, H.C., 1968. Evaluation of irreversible reactions in geochemical processes involving minerals and aqueous solutions, I. Thermodynamic relations. Geochim. Cosmochim. Acta, 32: 853—877.

Helgeson, H.C., 1969. Thermodynamics of hydrothermal systems at elevated temperatures and pressures. Am. J. Sci., 267: 729—804.

Hunt, J.M., Hayes, E.E., Degens, E.T. and Ross, D.A., 1967. Red Sea: detailed survey of hot-brine areas. Science, 156: 514—516.

Hutchinson, R.W., 1973. Volcanogenic sulfide deposits and their metallogenic significance. Econ. Geol. 68: 1223—1246.

Irving, E., Robertson, W.A. and Aumento, F., 1970a. The Mid-Atlantic Ridge near 45°N, 6. Remanent intensity, susceptibility, and iron content of dredged samples. Can. J. Earth Sci., 7: 1—13.

Irving, E., Park, J.K., Haggerty, S.E., Aumento, F. and Loncarevic, B., 1970b. Magnetism and opaque mineralogy of basalts from the Mid-Atlantic Ridge at 45°N. Nature, 228: 974—976.

Koenig, J.B., 1967. The Salton-Mexicali geothermal province. Calif. Div. Mines, Geol. Min. Inf. Serv., 20: 75—81.

Lonsdale, P., 1977. Deep-tow observations at the Mounds Abyssal Hydrothermal Field, Galapagos Rift. Earth-Planet. Sci. Lett. 36: 92—110.

Luyendyk, B.P. and Melson, W.G., 1967. Magnetic properties and petrology of rocks near the crest of the Mid-Atlantic Ridge. Nature, 215: 147—149.

McGregor, B.A. and Rona, P.A., 1975. Crest of Mid-Atlantic Ridge at 26°N. J. Geophys. Res., 80: 3307—3314.

McGregor, B.A., Harrison, C.G.A., Lavelle, J.W. and Rona, P.A., 1977. Magnetic anomaly pattern on Mid-Atlantic Ridge crest at 26°N. J. Geophys. Res., 82: 231—238.

Marshall, M. and Cox, A., 1972. Magnetic changes in pillow basalt due to sea floor weathering. J. Geophys. Res., 77: 6459—6469.

Melson, W.G., Thompson, G. and Van Andel, T.H. 1968. Volcanism and metamorphism in the Mid-Atlantic Ridge, 22°N. J. Geophys. Res., 73: 5925—5941.

Miyashiro, A., Shido, F. and Ewing, M., 1971. Metamorphism in the Mid-Atlantic Ridge near 24° and 30°N. Philos. Trans. R. Soc. Lond., Ser. A, 268: 589—603.

Moore, W.S., and Vogt, P.G., 1976. Hydrothermal manganese crust from two sites near the Galapagos spreading axis. Earth Planet. Sci. Lett., 29: 349—356.

Phillips, J.D., Woodside, J. and Bowin, C.O., 1969. Magnetic and gravity anomalies in the central Red Sea. In: E.T. Degens and D.A. Ross (Editors), Hot Brines and Recent Heavy Metal Deposits in the Red Sea. Springer-Verlag, New York, N.Y., p. 98.

Rona, P.A., Harbison, R.N., Bassinger, B.G., Scott, R.B. and Nalwalk, A.J., 1976. Tectonic fabric and hydrothermal activity of Mid-Atlantic Ridge crest (lat. 26°N). Geol. Soc. Am. Bull., 87: 661—674.

Ross, D.A., 1972. Red Sea hot brine area: revisited. Science, 175: 1455—1457.

Ross, D.A., Hays, E.E. and Allstrom, F.C., 1969. Bathymetry and continuous seismic profiles of the hot brine region of the Red Sea. In: E.T. Degens and D.A. Ross (Editors), Hot Brines and Recent Heavy Metal Deposits in the Red Sea. Springer-Verlag, New York, N.Y., p. 82.

Sillitoe, R.H., 1973. Environments of formation of volcanogenic massive sulfide deposits. Econ. Geol., 68: 1321—1336.

Spooner, E.T.C. and Fyfe, W.S., 1973. Sub-sea-floor metamorphism, heat and mass transfer. Contrib. Mineral. Petrol., 42: 287—304.

Studt, F.E., 1959. Magnetic survey of the Wairakei hydrothermal field. N.Z. J. Geol. Geophys., 2: 746—754.

Studt, F.E., 1961. Preliminary survey of the hydrothermal field at Rabaul, New Britain. N.Z. J. Geol. Geophys., 4: 274—282.

Watkins, N.D. and Paster, T.P., 1971. The magnetic properties of igneous rocks from the ocean floor. Philos. Trans. R. Soc. Lond., Ser. A, 268: 507—550.

33

Economic Geology 73, No. 2, 135-160.

Criteria for Recognition of Hydrothermal Mineral Deposits in Oceanic Crust

Peter A. Rona

Abstract

Hydrothermal mineral deposits in oceanic crust include metalliferous sediments and encrustations and massive sulfides. The occurrence of these deposits is explained by the hypothesis that they are concentrated at the discharge zones of high intensity subsea-floor hydrothermal convection systems involving the circulation of sea water through oceanic crust and upper mantle at oceanic spreading centers.

Criteria that have proven most useful for recognition of hydrothermal deposits in oceanic crust based on known deposits at oceanic spreading centers include petrology of the deposits and surrounding rocks; structural conditions that create exceptionally high permeability and thermal gradients; seismicity in the form of microearthquakes and earthquake swarms; geochemical properties of hydrothermal discharge (^{3}He, ^{222}Rn, ferric hydroxides, silica); contrasts in acoustic impedence between normal sea water and hydrothermal solutions; anomalous gravity as an indicator of geologic structure; electrical properties of the hydrothermal solutions and deposits; an associated low in residual magnetic intensity attributed to hydrothermal alteration of the magnetic mineral component of basalt; patterns of deposition in early rift and advanced oceanic ridge stages of opening of an ocean basin; and distribution of hydrothermal deposits both parallel and perpendicular to an oceanic spreading center.

The seismic, geochemical, acoustic, thermal, and certain electrical criteria are applicable to recognition of active discharge zones of subsea-floor hydrothermal convection systems. The petrologic, structural, gravity, magnetic, and other electrical criteria are applicable to recognition of hydrothermal deposits in all of oceanic crust which underlies ocean basins covering two-thirds of the Earth and is emplaced on land as ophiolites.

Introduction

Oceanic crust is the most widespread crustal type on Earth, underlying the ocean basins that cover two-thirds of the Earth and also tectonically emplaced in certain islands and continents as ophiolites (Fig. 1). The metallic mineral potential of oceanic crust other than in manganese nodules is poorly known, and its evaluation will require more exploration at sea and on land (Rona, 1977). This paper endeavors to develop criteria to guide exploration for hydrothermal mineral deposits in oceanic crust based on recent work by both oceanographers and students of ore deposits (Rona, 1976a). The deposits under consideration comprise metalliferous sediments, metalliferous encrustations, and massive sulfide bodies that share a common origin as precipitates from hydrothermal solutions in regions of volcanism and high heat flux at oceanic spreading centers. The hydrothermal deposits are distinguished from hydrogenous deposits which include metalliferous sediments, encrustations, and nodules that were precipitated from normal sea water over wide areas of ocean basins (Table 1).

The exploration criteria are based on geological, geochemical, and geophysical characteristics of hydrothermal mineral deposits where these are actually forming at oceanic spreading centers. Oceanic spreading centers are the loci of generation of all oceanic crust. The characteristics of oceanic spreading centers are related to their tectonic settings which, in turn, influence the occurrence of associated hydrothermal deposits. One evolutionary sequence of tec-

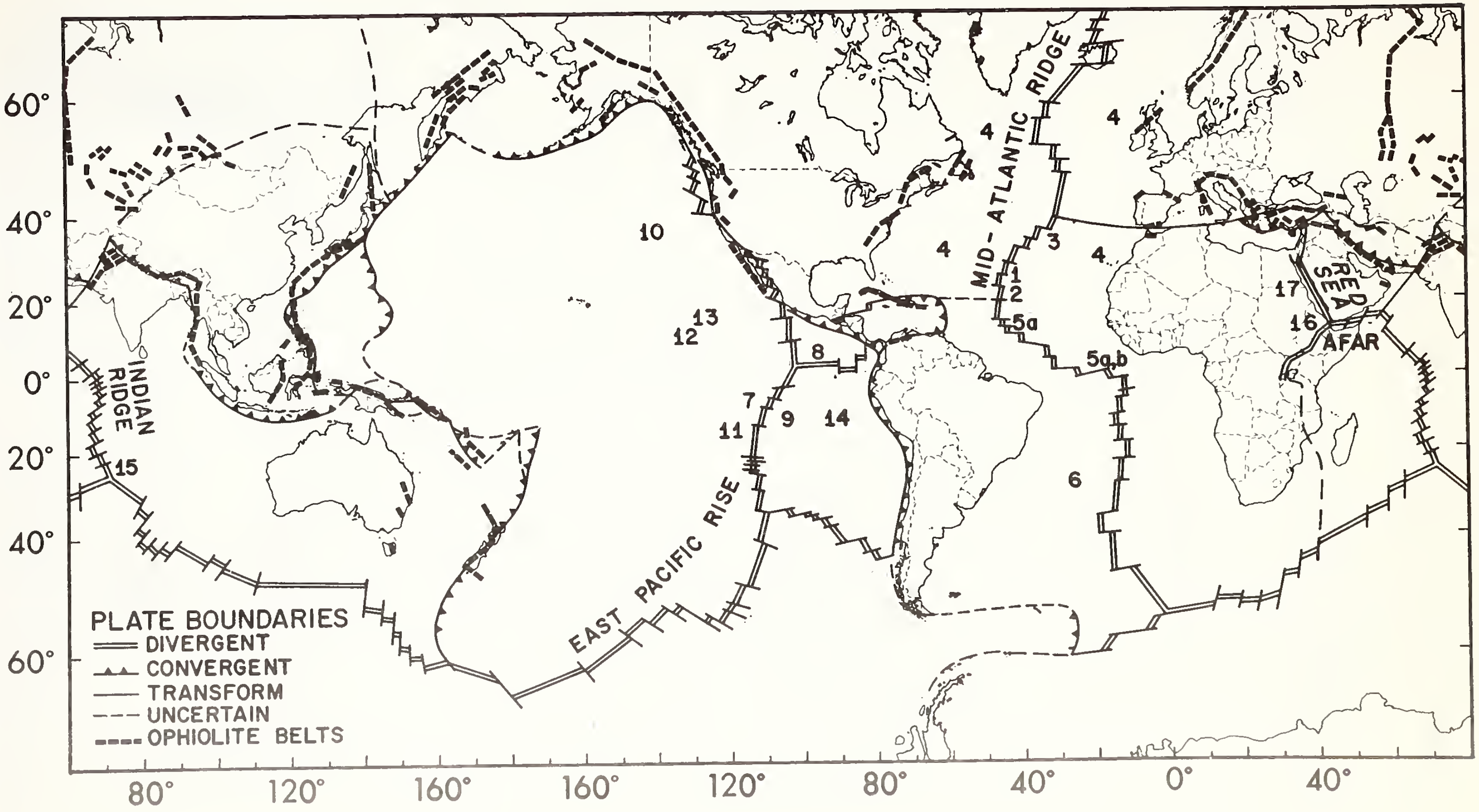
MID-ATLANTIC RIDGE
EAST PACIFIC RISE
INDIAN RIDGE
RED SEA
AFAR
1
2
3
4
5a
5a,b
6
7
8
9
10
11
12
13
14
15
16
17
PLATE BOUNDARIES
DIVERGENT
CONVERGENT
TRANSFORM
UNCERTAIN
OPHIOLITE BELTS
60°
40°
20°
0°
20°
40°
60°
80°
120°
160°
160°
120°
80°
40°
0°
40°

Fig. 1. World map showing lithospheric plate boundaries and location of known hydrothermal deposits in ocean basins. Numbers refer to locations described in Table 2. Ophiolite belts are also shown (after Coleman, 1971, 1977).

Table 1. Comparison of Hydrothermal and Hydrogenous Metalliferous Deposits (Bonatti et al., 1972b; Table 2)

	Hydrothermal		Hydrogenous		
	Sediment	Encrustation	Sediment	Encrustation	Nodule
Stratigraphic position	Overlies basalt	Overlies basalt	Present throughout sedimentary column	Overlies bedrock	Overlies sediment
Fe/Mn ratio	<0.1 and >1	Fe-rich: 12–237 Mn-rich: 0.002–0.14	0.5 to 5	≃1	≃1
Trace metal content	Low (see Fig. 4; Table 2)	Low (see Fig. 4; Table 2)	High (see Fig. 4)	High (see Fig. 4)	High (see Fig. 4)
U/Th content	>1	>1	<1	<1	<1
Accumulation rate	Fast	100 to 1,000 mm per 10^6 yr	Slow	1 to 10 mm per 10^6 yr	1 to 10 mm per 10^6 yr

tonic settings involves stages in the development of an ocean basin about a spreading center from a rift zone, exemplified by the axial trough of the Red Sea, to an oceanic ridge, exemplified by the Mid-Atlantic Ridge. Another evolutionary sequence involves the opening of a basin marginal to a continent about a spreading center associated with a volcanic island-arc system, exemplified by the marginal basins of the western Pacific (Karig, 1971).

Metalliferous sediments and encrustations of hydrothermal origin are known from a number of locations at oceanic spreading centers (Fig. 1, Table 2). The metalliferous sediments occur at the base of the sedimentary layer (layer 1) and the encrustations at the top of the basaltic layer (layer 2) of oceanic crust (Figs. 2, 3). Disseminated sulfides, particularly pyrite and chalcopyrite, are not uncommon in altered basalt of layer 2 (Figs. 2, 3; Table 2, location 5a; Dmitriev et al., 1970; Moore and Calk, 1971; Bonatti et al., 1976a; Czamanske and Moore, 1977). Massive sulfide deposits have not yet been found at active spreading centers, but their occurrence is predicted based on geochemical considerations and their existence in ophiolites (Pereira and Dixon, 1971; Sillitoe, 1972, 1973; Spooner and Fyfe, 1973; Bonatti, 1975). The massive sulfide deposits occur within tholeiitic pillow lava or altered basalt corresponding to oceanic crustal layer 2 of certain ophiolites (Figs. 2, 3); gold and silver may be associated with the sulfides (Keays and Scott, 1976). The basalt of these ophiolites may be overlain by metalliferous encrustations and sediments, like those present at oceanic spreading centers. Examples include the ophiolites of the Troodos Massif, Cyprus (Wilson and Ingham, 1959; Moores and Vine, 1971; Searle, 1972; Constantinou and Govett, 1973; Miyashiro, 1973; Spooner et al., 1974); the Semail region of Oman (Bailey and Coleman, 1975); the northern Apennines (Spooner et al., 1974; Ferrara et al., 1976; Bonatti et al., 1976c); and Newfoundland

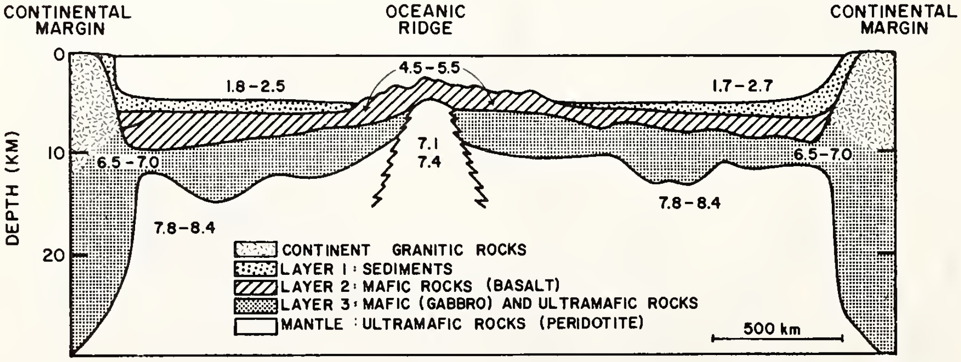

Fig. 2. A schematic section across an opening ocean basin like the Atlantic to show layers 1, 2, 3 of oceanic crust and mantle labeled with characteristic ranges of compressional wave seismic velocities in kilometers per second (Ewing, 1969). The actual structure and lithology of oceanic crust are considerably more complex (Peterson et al., 1974; Deep Sea Drilling Staff, 1977).

TABLE 2. Hydrothermal Deposits

Location number (Fig. 1)	Location	Half-rate of sea-floor spreading (cm per yr)	Structure	Type of deposit	Mineralogy
1	TAG Hydrothermal Field on Mid-Atlantic Ridge crest at latitude 26°N (Scott et al., 1974, tables 1b, 2; Rona et al., 1976)	1.3	Block-faulted topographic high	Encrustation	Birnessite, todorokite
2	Mid-Atlantic Ridge at latitude 23°N (Thompson et al., 1975)	1.4	Block-faulted topographic high	Encrustation	Todorokite
3	Mid-Atlantic Ridge crest at latitude 36°N (ARCYANA, 1975)	1.1	Fracture zone (transform fault)	Encrustation	Birnessite, todorokite, Fe- and Mn-rich smectite
4	North Atlantic Ocean basin between latitudes 20°N and 60°N (Horowitz and Cronan, 1976, table 1; DSDP holes 9A, 10, 112, 114, 117A, 118, 136, 137, 138, 141)	1.1–1.5	Basal sediment (106 m.y. ago to Recent) directly overlying basalt of oceanic crustal layer 2	Sediment[1]	Goethite, iron-rich montmorillonite (smectite), manganese hydroxyoxides
5a	Equatorial Mid-Atlantic Ridge at latitudes 11°N and 0° (Bonatti et al., 1976a; Kirst, 1976)	2.0	Vema and Romanche fracture zones (transform faults)	Disseminated grains and veins in metabasalt (chloritic)	Chalcopyrite, pyrite, pyrrotite
5b	Equatorial Mid-Atlantic Ridge at latitude 0° (Bonatti et al., 1976b, table 1)	2.0	Romanche fracture zone (transform fault)	Concretion	Pyrite, goethite
6	South Atlantic Ocean basin between latitudes 28°S and 31°S (Boström et al., 1972, table IV; DSDP holes 14, 15, 16, 19, 20, 21, 22)	2.0	Basal sediment (Late Cretaceous to Pleistocene age) overlying basalt of oceanic crustal layer 2 on west flank of Mid-Atlantic Ridge	Sediment[1]	Siderite; other mineralogical determinations incomplete
7a	East Pacific Rise at latitude 8°S, Fe-rich fraction (Bonatti and Joensuu, 1966, table 1, fraction a; Veeh and Boström, 1971, table 1)	7.5	Volcanic seamount	Encrustation	Goethite
7b	East Pacific Rise at latitude 8°S, Mn-rich fraction (Bonatti and Joensuu, 1966, table 1, fraction b)	7.5	Volcanic seamount	Encrustation	Not specified
8a	Galapagos spreading center (Moore and Vogt, 1976, table 1)	3.2	Block-faulted topographic high	Encrustation	Birnessite, todorokite
8b	Mounds Hydrothermal Field 20 to 30 km south of axis of Galapagos spreading center (Corliss et al., 1976, 1977; Lonsdale, 1977b)	3.2	Block-faulted topography	Encrustation	Manganese hydroxyoxides
9	Bauer Deep (Sayles and Bischoff, 1973, table 3; Scientific Staff, 1974; Lyle et al., 1977)	—	Oceanic basin	Sediment[1]	Smectite, goethite, todorokite

at Oceanic Spreading Centers

Composition (plotted on Fig. 4)											
Weight percent (range)					ppm (range)						
Si	Al	Fe	Mn	Fe/Mn	Ba	Co	Cu	Ni	Zn	U	Th
—	—	0.01–0.11	38–39	0.0003–0.0027	—	14–25	11–119	50–790	—	9–16	2–5
—	—	Low	High	0.0007	—	—	>1,000	—	—	—	—
—	—	High	High	0.2–237	—	<15	<15	<15	—	—	—
—	4.7–16.1 (Al_2O_3)	2.3–10.5	0.03–0.7	5–130	—	—	25–167	20–370	62–267	—	—
1.8–5.2	—	32–41	<0.1	>80	—	—	5–50%	—	—	—	—
12–38 (SiO_2)	1.6–7.6 (Al_2O_3)	41–73 (Fe_2O_3)	0.07–0.25 (MnO)	166–884	35–220	27–75	35–590	90–270	82–220	—	—
—	1.6–12.1	1.1–16	0.02–7.3	1–50	—	—	—	—	—	—	—
12–18 (SiO_2)	<1–1 (Al_2O_3)	29–33	0.6–2.4	12–52	100–115	32–120	60–120	90–460	—	1.3	<0.002
8.1 (SiO_2)	0.4 (Al_2O_3)	5.5	38.7	0.14	1,700	290	>500	4,500	—	—	—
—	—	Low	47–58	0.0002–0.0230	—	15–86	9–203	58–500	85–4,860	4–6	0.01–0.4
—	—	—	—	—	—	—	—	—	—	—	—
18–28	1–4	9–18	2–7	2–7	8,000–28,000	90–330	710–1,200	410–1,700	110–680	—	—

Table 2—(*Continued*)

Location number (Fig. 1)	Location	Half-rate of sea-floor spreading (cm per yr)	Structure	Type of deposit	Mineralogy
10	Central North Pacific Ocean basin between latitudes 32°N and 41°N (Dymond et al., 1973, tables 2, 6; DSDP sites 37, 38, 39)	—	Basal sediment (32–60 m.y.) overlying basalt of oceanic crustal layer 2	Sediment[1]	Goethite, iron-rich montmorillonite (smectite), manganese hydroxyoxides
11	East Pacific Rise crest between latitudes 12°S and 14°S (Boström and Peterson, 1969, table III; Veeh and Boström, 1971, table 1)	8.0	Oceanic ridge	Sediment[1]	Goethite, iron-rich montmorillonite (smectite), manganese hydroxyoxides
12	East Pacific Rise between latitudes 10°N and 15°N (Cronan, 1973, table 1; DSDP sites 159, 160, 161, 162, 163)	4.5	Basal sediment (Early Campanian to Late Oligocene) overlying basalt of oceanic crustal layer 2 on west flank of oceanic ridge	Sediment[1]	Goethite, iron-rich montmorillonite (smectite), manganese hydroxyoxides
13	Northeast Pacific nodule area (Bischoff and Rosenbauer, 1977, table 2); latitude 15°12.2′N, longitude 126°58.6′W; depth 4,295 m below sea level	—	Abyssal hills between Clarion and Clipperton fracture zones. Metalliferous sediment may be relict	Sediment[1]	Globules averaging 100 μm diameter composed of semiopaque reddish yellow aggregates and detrital clay minerals of low refractive index, along with minor amounts of radiolarian debris, volcanic glass, and micronodules
14	East Pacific Rise between latitudes 9°S and 13°S (Boström et al., 1976, table 5; DSDP holes 319, 320, 321)	7.5	Basal sediment (Late Oligocene to Quaternary) overlying basalt of oceanic crustal layer 2 on east flank of oceanic ridge	Sediment[1]	Goethite, iron-rich montmorillonite (smectite), manganese hydroxyoxides
15	Indian Ocean Ridge between latitudes 16°S and 40°S (Boström et al., 1969, table 2)	4.0	Ocean ridge	Sediment	Not specified
16a	Afar Rift, Fe-rich deposits (Bonatti et al., 1972a, tables 2, 3)	—	Axial trough at rift zone of incipient oceanic spreading center	Encrustation	Goethite, nontronite (smectite)
16b	Afar Rift, Mn-rich deposits (Bonatti et al., 1972a, tables 2, 3)	—	Axial trough at rift zone of incipient oceanic spreading center	Encrustation	Pyrolusite, birnessite, todorokite, strontiobarite, rhodocrosite, opal, gypsum
17	Red Sea (Degens and Ross, 1969; Bischoff, 1969; Hendricks et al., 1969, table 8; Stephens and Wittkopp, 1969; Garson and Krs, 1976)	1.0	Basins at intersections with fracture zones in the axial trough at rift zone of an incipient oceanic spreading center	Sediment	Iron-montmorillonite (smectite), goethite, hematite, lepidocrosite, barite, sulfides (sphalerite, marcosite, chalcopyrite, pyrite, marmatite), manganosiderite, anhydrite, manganite (birnessite), todorokite

---

[1] Bulk chemical analysis of sediment on a $CaCO_3$-free basis.

Composition (plotted on Fig. 4)											
Weight percent (range)					ppm (range)						
Si	Al	Fe	Mn	Fe/Mn	Ba	Co	Cu	Ni	Zn	U	Th
4.3–8.9	1.5–3.4	21.1–27.8	5.7–7.6	3–4	1,500–15,000	55–110	800–1,490	570–800	480–690	2.0–5.8	—
9–38 (SiO_2)	1.5–16 (Al_2O_3)	5.7–22.6	0.6–8.8	3–9	—	75–280	510–1,800	250–1,200	190–530	0.2–12	0.2–3
—	—	2.1–30.6	0.4–9.6	3–16	—	10–183	220–1,814	62–1,680	33–518	—	—
54.92 (SiO_2)	0	23.34 (Fe_2O_3)	12.28 (MnO)	2			2,900 (CuO)				
—	1.3–8.4	4.7–23.3	0.2–9.5	2–80	1,700-14,000	18–290	270–1,700	270–805	220–1,050	—	—
—	0.2–7.4	0.03–7.0	0.1–2.0	3–12	—	—	—	—	—	—	—
14.0–20.8	3.7–5.8	22–29	0.15–0.30	70–200	135–140	17–22	11–60	<5–22	—	0.4–0.5	1.2–1.4
<0.2–4.1	0–1.2	0.03–1.64	31–54	0.0005–0.0700	135–62,500	<5–17	<5–25	<5–20	—	2–4	0.7–1.2
—	0.05–3.0	0.4–47.5	0.03–13.4	1–200	300–20,000	12–198	50–33,400	9–90	400–200,000	—	—

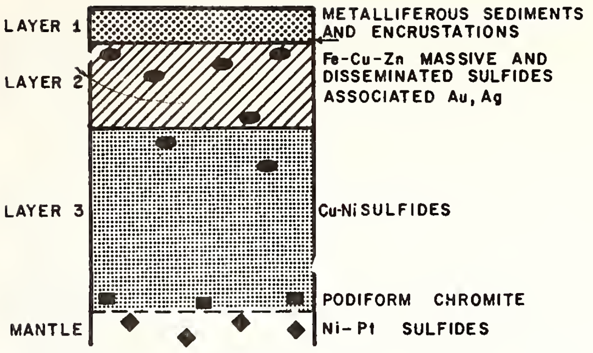
LAYER 1
METALLIFEROUS SEDIMENTS AND ENCRUSTATIONS
LAYER 2
Fe-Cu-Zn MASSIVE AND DISSEMINATED SULFIDES ASSOCIATED Au, Ag
LAYER 3
Cu-Ni SULFIDES
PODIFORM CHROMITE
MANTLE
Ni-Pt SULFIDES

FIG. 3. Schematic section of oceanic crust and upper mantle showing potential distribution of metal deposits.

(Upadhyay and Strong, 1973; Strong, 1974a; Duke and Hutchinson, 1974). Other examples of hydrothermal ore deposits that may have formed at oceanic spreading centers are considered by Sillitoe (1972), Hutchinson (1973), Mitchell and Bell (1973), Mitchell and Garson (1976), and Coleman (1977).

The oceanic crust and incorporated hydrothermal deposits in ophiolites originated at spreading centers located at rift zones, oceanic ridges, and marginal basins associated with island arcs. Systematic compositional (Engel et al., 1965; Miyashiro, 1975) and structural (Dewey and Bird, 1971) differences in the volcanic rock series of the ophiolites may indicate the tectonic setting of their generation. Metallic deposits in addition to those under consideration are known from ophiolites, including podiform chromite (Woodli, 1964; Peters and Kramers, 1974), as well as nickel and platinum sulfide that occur near the base of layer 3 and in the upper mantle (Figs. 2, 3). The deposits of layer 3 and the upper mantle are outside the scope of this paper.

Subsea-Floor Hydrothermal Convection Systems

The effectiveness of criteria employed to search for mineral deposits depends on the validity of the hypothetical basis for the criteria. For example, the anticlinal hypothesis of oil entrapment was the basis for exploration criteria that resulted in discovery of 237 of the 266 known giant oil fields of the world (Halbouty et al., 1970). Analogously, the effectiveness of criteria to locate hydrothermal mineral deposits in oceanic crust depends on the hypothesis employed to account for concentration of the deposits.

Various lines of evidence support the hypothesis that subsea-floor convection systems concentrate hydrothermal minerals in oceanic crust (Spooner and Fyfe, 1973; Hutchinson, 1973; Sillitoe, 1973; Bonatti, 1975). A hydrothermal convection system is composed of a heat source, a recharge system, a circulation system, and a surface discharge system (Elder, 1965). Emplacement of basaltic magma at oceanic spreading centers provides a supply of heat and metals. Cooling of emplaced materials and tectonic processes operating at oceanic spreading centers result in fracture and uplift of rocks in configurations conducive to development of subsea-floor hydrothermal convection (Deffayes, 1970; Lister, 1972, 1974b; Rona et al., 1976).

A hypothetical high-intensity, subsea-floor hydrothermal system involves the following stages (Krauskopf, 1956, 1957; Helgeson, 1964, 1969; Boström and Peterson, 1966; Corliss, 1971; Boström, 1973; Hart, 1973): downward penetration of cold, dense sea water primarily through fractures in oceanic crustal layer 2 and the upper portion of layer 3, as deep as about 5 km beneath the ocean bottom (Fig. 2); progressive warming and reduction as the sea water reacts with a basaltic mineralogy recently cooled from a magmatic state; production of a sequence of metamorphic phases increasing in grade with increasing temperature and depth; high-temperature leaching and mass transfer of transition metals, Si, Ca, K, H, and S, primarily from oceanic crust, and loss of Mg, Na, and O from sea water to oceanic crust; transportation of metals and reduced S species in solution as chloride complexes; possible addition of certain elements transported in volatile phases from the mantle (He^3, F, Hg, S, B, Ba) and injected via the hydrothermal system, either directly or indirectly, by dissolution from basalt; ascent of warm, less dense, enriched solutions through gradients of decreasing temperature and pressure; partial precipitation of disseminated and massive metallic sulfides under reducing conditions in response to decreasing temperature within basalt of layer 2, involving sulfur from crustal (average sulfur content 800 ppm in tholeiitic basalt; Moore and Schilling, 1973), seawater (reduction of SO_4^{2-}), and upper mantle sources; precipitation of metallic oxide encrustations under oxidizing conditions at the basalt-sea water interface; precipitation of amorphous ferric hydroxide particles on cooling, oxidation, and increasing pH of the discharged solution during mixing with oxygenated sea water or, alternatively, precipitation of base metal sulfides on cooling of the discharged solution during mixing with oxygen-deficient sea water; scavenging of heavy metals remaining in solution by colloidal absorption on the ferric hydroxides; and finally, flocculation in the electrolyte and settling as metalliferous sediments.

It is important to distinguish between criteria for low- and high-intensity hydrothermal activity. Low-intensity hydrothermal activity is ubiquitous at oceanic spreading centers. It involves low-intensity hydration which produces prograde metamorphic assemblages within oceanic crustal layer 2; this is controlled by temperature rising at the geothermal gradients that occur at oceanic spreading centers (Spooner and Fyfe, 1973). An example is the prograde zeolitic sequence developed in response to a background geothermal gradient of 65°C/km (Palmason, 1967) in Icelandic basalts (Walker, 1960). Evidence for the ubiquitous nature of low-level hydrothermal activity at oceanic spreading centers includes anomalously low values of conductive heat flow, implying convective removal of heat (Palmason, 1967; Deffayes, 1970; Talwani et al., 1971; Lister, 1972; Anderson, 1972; Williams et al., 1974; Sclater et al., 1974); hydrous metamorphosed oceanic crust requiring a large source of water (Miyashiro et al., 1971; Christensen, 1972); and isotopic compositions of the hydrated rocks requiring a low $\delta^{18}O$ isotopic source, such as sea water (Muehlenbachs and Clayton, 1972; Spooner et al., 1974).

In contrast to the ubiquitous nature of low-intensity hydrothermal activity at oceanic spreading centers, high-intensity hydrothermal activity is extremely localized. The high-intensity hydrothermal activity concentrates mineral deposits associated with metamorphic assemblages produced at geothermal gradients higher than background, involving temperatures and gradients as high as 400°C and 1,300°C/km within the upper 1 km beneath the ocean bottom (Spooner and Fyfe, 1973). This activity may involve thermal powers up to 15 kWm^{-2} (Lister, 1974a). Hydrothermal mineral deposits in oceanic crust are related to the special structural and thermal conditions that increase hydrothermal activity to an intensity sufficient to concentrate the deposits at discrete sites along oceanic spreading centers. Criteria for recognition of these deposits are qualified as preliminary, because subsea-floor hydrothermal convection systems are incompletely understood, and few studies exist of hydrothermal deposits at spreading centers. Emphasis is necessarily placed on those hydrothermal deposits at oceanic spreading centers that have received the most comprehensive interdisciplinary study and on those criteria that have proven most useful in recognizing the deposits. Considerable potential exists for scientific and technological transfer between studies of geothermal energy systems on land and hydrothermal mineral deposits at oceanic spreading centers (Kappelmeyer and Haenel, 1974; United Nations, 1976).

Petrologic Criteria

Metalliferous sediments

Metalliferous sediments of hydrothermal origin are recognized by their distinctive mineralogical, compositional, and isotopic characteristics, as well as their stratigraphic association with volcanic rocks. A sediment layer several meters thick containing varying concentrations of metals directly overlies basalt of oceanic crustal layer 2 both at and away from spreading centers in all major ocean basins (Table 2, locations 4, 6, 9, 10, 11, 12, 13, 14, 15; Fig. 1). Metalliferous sediments of hydrothermal origin may mix with and/or exhibit transitional characteristics with metalliferous sediments of hydrogenous origin. Characteristics of metalliferous sediments considered to be predominantly hydrothermal include (Table 1; Dymond et al., 1973): high contents of transition metals (particularly Fe and Mn), low aluminum contents, high Si/Al ratios, and Fe/Mn ratios between about 1 and 200 (Table 2; Fig. 4); goethite, iron-rich montmorillonite, and manganese hydroxyoxides as the dominant minerals present on oceanic ridges, where oxidizing conditions prevail (Table 2, locations 4, 6, 9, 10, 11, 12, 13, 14, 15; Fig. 1), and in contrast, base metal sulfides which predominate during the rift stage, when near-bottom reducing conditions prevail, as in certain axial troughs of the Red Sea (Table 2, location 17; Fig. 1); sulfur, uranium, and oxygen isotopic compositions usually consistent with formation from sea water at low temperatures, but in several cases anomalous $^{234}U/^{238}U$ ratios were found that suggest leaching from oceanic crust (Veeh and Boström, 1971; Rydell and Bonatti, 1973); strontium isotopic compositions suggestive of equilibrium with modern sea water; lead isotopic compositions that resemble those of oceanic ridge tholeiitic basalts, rather than sea water; rare earth element patterns like sea water; higher U and lower Th contents than in normal pelagic sediments, attributed to more rapid growth of the metalliferous sediments that inhibits incorporation of Th from sea water (Bonatti et al., 1972b); and metal accumulation rates one to two orders of magnitude faster than pelagic sediments

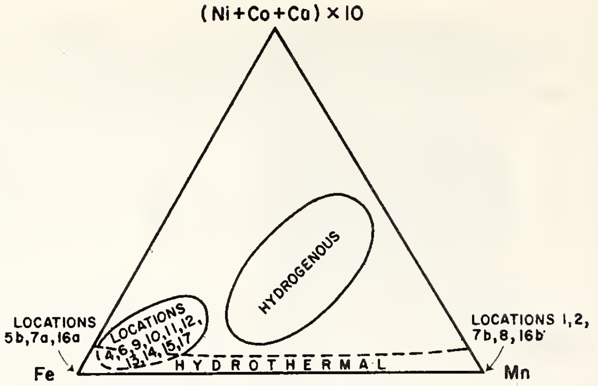

FIG. 4. Ratio Fe, Mn, (Cu + Ni + Co) of hydrothermal mineral deposits from oceanic spreading centers (modified from Bonatti, 1975). Numbers refer to locations shown in Figure 1 and described in Table 2.

(approx 10 to 110 mg/cm^2/10^3 yr; Boström, 1970; Bender et al., 1971; Scott, 1976, 1977).

Metalliferous encrustations

Metalliferous encrustations of hydrothermal origin form on basalt of oceanic crustal layer 2 at discrete sites along oceanic spreading centers (Table 2, locations 1, 2, 3, 7a, 7b, 8a, 8b, 16a, 16b; Fig. 1). The hydrothermal encrustations are recognized by their composition, rate of accumulation, and mineralogy as follows.

Extreme chemical fractionation of Fe from Mn is of two types, an Fe-rich encrustation with Fe/Mn ratios between 12 and 237 (Table 2, locations 3, 7a, 7b, 16a, 16b; Fig. 4), and an Mn-rich encrustation with Fe/Mn ratios between 0.002 and 0.14 (Table 2, locations 1, 2, 7a, 8a, 8b, 16a, 16b; Fig. 4). This extreme fractionation distinguishes encrustations of hydrothermal origin from ferromanganese encrustations and nodules of hydrogenous origin (Table 1). The latter both generally exhibit Fe/Mn ratios of the order of 1 and high trace metal content (Ni, Co. Cu, Zn) relative to Fe and Mn (Fig. 4).

Low trace metal content (Table 2; Fig. 4) occurs as a consequence of extreme chemical fractionation and relatively rapid rate of deposition which limits scavenging from sea water.

Goethite and nontronite (Fe-smectite) are the dominant minerals in the Fe-rich encrustations (Table 1, locations 7a, 16a); birnessite, todorokite, and pyrolusite predominate in the Mn-rich encrustations (Table 2, locations 1, 2, 8a, 8b, 16b).

Minerals incorporating elements derived from hydrothermal sources are present. A prime hydrothermal indicator is barite (Table 2; Arrhenius and Bonatti, 1965; Hanor, 1966; Miller et al., 1966; Craig, 1969; Makharadze and Ikoshvili, 1970; Bonatti et al., 1972b; Bertine and Keene, 1975).

Accumulation rates of hydrothermal encrustations determined radiogenically (approx 100 to 1,000 mm per 10^6 yr; Scott et al., 1974) are one to three orders of magnitude greater than those of hydrogenous ferromanganese encrustations and nodules (approx 1 to 10 mm per 10^6 yr).

Encrustations occur as laminated layers with observed thicknesses up to 2 m (Table 2, location 16) directly overlying basalt and as matrix material in breccia of altered basalt fragments (Fig. 4; Table 2, location 1).

The petrologic characteristics described pertain to hydrothermal mineral deposits. There are two other petrologic characteristics pertaining to hydrothermal alteration and depletion of the volume of rock surrounding the deposits.

Alteration of basaltic rocks under the physical and chemical conditions prevalent at the discharge zone of a subsea-floor hydrothermal convection system produces characteristic low- to intermediate-grade metamorphic mineral assemblages in horizontal and vertical zones, such as at the Reykjanes hydrothermal field of Iceland on the Mid-Atlantic Ridge (Table 3). The mineral assemblages and associated conditions have been determined by the coordination of field observations (Sigvaldason, 1962; Steiner, 1967; Browne and Ellis, 1970; Miyashiro and Shido, 1970; Ade-Hall et al., 1971; Tómasson and Kristmannsdóttir, 1972; Spooner and Fyfe, 1973) and experimental studies (Hawkins and Roy, 1963; Helgeson, 1967, 1968; Helgeson et al., 1969; Mottl et al., 1974; Hajash, 1975; Bischoff and Dickson, 1975).

Manganese-rich hydrothermal solutions may alter sedimentary montmorillonite-group clays to palygorskite (Bonatti and Joensuu, 1968).

A halo of depletion of transition metals may occur in the volume of altered basalt or greenstone that surrounds a hydrothermal mineral deposit. The depletion halo represents the volume of rock fluxed by the hydrothermal system to produce the deposit. Depletion halos have been documented by a number of studies, although the volume of rock fluxed to produce a given deposit is poorly known. For example, holocrystalline basalts from the Mid-Atlantic Ridge at latitude 22°N are depleted in Fe, Mn, Co, Cu, Pb, and rare earth elements relative to associated glassy pillow fragments (Corliss, 1971). Most of the Troodos pillow lava series of Cyprus contains 80 to 200 ppm Ni, corresponding to a Ni content of 70 to 200 ppm in oceanic basalts (Nichols and Islam, 1971); in contrast intensely altered Troodos pillow lavas associated with hydrothermal deposits contain only 20 to 100 ppm Ni, evidencing depletion by hydrothermal processes (Govett and Pantazis, 1971). A decrease in Cu content away from the Troodos Massif may also represent hydrothermal depletion

TABLE 3. Vertical Zonation of Mineral Assemblages at Reykjanes Hydrothermal Field, Iceland (Tómasson and Kristmannsdóttir, 1972; Bjornsson et al., 1972)

Relative depth	Temperature (°C)	Mineral assemblage
Shallow	<200	Montmorillonite, calcite, zeolite, opal ($\leq$300 m), pyrite, hematite ($\leq$150 m), quartz ($\geq$100 m), potassium feldspar, albite, anhydrite
Intermediate	200–280	Mixed-layer montmorillonite, chlorite, prehnite ($\geq$200 m), pyrite, quartz, albite
Deep	>200–300	Chlorite, epidote ($\geq$450 m), albite, pyrite, quartz

(Govett and Pantazis, 1971). A halo zone, characterized by a concentration increase of Mg and Fe and decrease of Ca and of Na/K ratio, occurs within 500 m below and to either side of a hydrothermal massive sulfide deposit ($\geq 82 \times 10^6$ tons containing 9.69 percent Zn, 3.77 percent Pb, 0.29 percent Cu, and 2.46 percent Ag per ton) in felsic volcanic rocks of the Bathhurst region of New Brunswick, Canada (volume of halo approx $125 \times 10^6 m^3$; Goodfellow, 1975).

Geochemical Criteria

Some geochemical criteria for hydrothermal mineral deposits in oceanic crust based on the deposits and surrounding rocks were considered under petrologic criteria. Another category of geochemical criteria pertains to the hydrothermal discharge that may be associated with deposits at oceanic spreading centers, as in the cases of the TAG Hydrothermal Field (Table 2, location 1), and the Galapagos spreading center (Table 2, location 8). The extent of subsurface mixing of normal sea water with hydrothermal solutions influences the chemical properties of the discharge. High dilution favors precipitation of metallic sulfides and oxides, as at the TAG Hydrothermal Field; the hydrothermal solutions are depleted in the elements precipitated. Low dilution favors direct discharge of hot, acid solutions enriched in metals, as at the Galapagos spreading center (Edmond et al., 1977).

^{3}He: Excess of the rare helium stable isotope ^{3}He above oceanic background concentrations is a sensitive indicator of sites where mantle-derived volatiles are being injected by voluminous high-intensity hydrothermal discharge at oceanic spreading centers. Multiple sources contribute to helium in sea water, and include air injection: the ^{3}He/^{4}He ratio in the atmosphere is 1.4×10^{-6} (Clarke et al., 1969); radiogenic ^{3}He: in situ decay of nuclear-era tritium in near-surface water (Jenkins and Clarke, 1976); radiogenic ^{3}He and ^{4}He: decay of U and Th to ^{4}He with ^{3}He production by reactions on Li in crustal rocks with the resulting helium characterized by ^{3}He/^{4}He $\simeq 10^{-7}$, one-tenth of the atmospheric ratio (Lupton et al., 1977a); and flux of primordial helium from the mantle at oceanic spreading centers: the ^{3}He/^{4}He ratio of the mantle component determined in deep water on the East Pacific Rise (Craig et al., 1975) and in helium trapped in submarine basalt glasses from different oceanic spreading centers (Craig and Lupton, 1976) which approximately equals 10^{-5}, about 10 times the atmospheric ratio and 100 times the ratio in crustal helium. Measurements of excess helium in near-bottom water at different spreading centers evidencing a primordial mantle source are presented in Table 4. The measured concentrations of the isotopes and the measurement sensitivity (0.5% for ^{3}He/^{4}He and ^{4}He) indicate that detection limits are dilutions of 1.5×10^6 for ^{3}He and 7×10^4 for ^{4}He (Lupton et al., 1977b).

^{222}Rn: Enrichment of the unstable radon isotope ^{222}Rn (half-life 3.8 days) relative to oceanic background concentration may indicate discharge sites of voluminous hydrothermal convection systems where waters have circulated through the sea floor at oceanic spreading centers (Table 4; Broecker, 1965; Broecker et al., 1967; Chung and Craig, 1972). The ^{222}Rn is produced by radiogenic decay of uranium series isotopes in the thoeliitic basalt through which the hydrothermal convection system flows. Steady-state radon production in tholeiitic basalt that retains uranium series isotopes should be of the order of 7.4×10^{-2} atoms per minute per gram, corresponding to a steady-state activity of 7.4×10^{-2} disintegrations per minute per gram in the rock. The activity in pure hydrothermal discharge should be this value divided by the mass ratio of water to rock in the hydrothermal system.

TABLE 4. Measurements of Excess Helium in Sea Water

Location	δ(^{3}He)[1] (%)	^{3}He/^{4}He ($\times 10^{-6}$)	Concentration per atmospheric solubility[2] (^{3}He)	(^{4}He)	Excess ^{222}Rn[3]	Reference
East Pacific Rise deep water (latitudes 8°N and 6°S)	20–32	—	—	—	—	Clarke et al. (1969); Craig et al. (1975)
Galapagos spreading center hydrothermal plume	36–99	2.8	—	—	80–229	Lupton et al. (1977b)
Western Atlantic Ocean deep water	0–13	—	—	—	—	Jenkins and Clarke (1976)
Red Sea brine from Atlantis II Deep		12.1–12.2	3,260–3,470	370–390	—	Lupton et al. (1977a)

[1] δ(^{3}He)% = 100 [(R/R$_A$) − 1] where R = ^{3}He/^{4}He and R$_A$, the atmospheric ratio = 1.4×10^{-6}.
[2] Supersaturation of ^{3}He and ^{4}He relative to atmospheric solubility equilibrium in sea water.
[3] Disintegrations per minute per 100 kilograms.

Dissolved metals: Anomalous maxima in the concentrations of Zn, Fe, and Cu have been observed together with excess ^{3}He in deep-water masses of the North Atlantic and North Pacific (Brewer et al., 1972). Analysis of hydrothermal effluent including both dissolved and particulate matter from the Galapagos spreading center, where reducing conditions and relatively high flow rates prevail, reveals an increase of Si, Ba, Mg, and Fe and a decrease of Cu, Ni, and Ca with increasing temperature (Edmond et al., 1977).

Ferric hydroxides: Amorphous ferric hydroxides precipitated from hydrothermal solutions discharging into sea water exhibit a halo of suspended weakly acid soluble particulate matter centered at the discharge zone. The ferric hydroxides effectively scavenge metals from hydrothermal solutions. As a consequence of this scavenging action, suspended particulate matter may constitute a more sensitive indicator of hydrothermal discharge than metals in solution. Nephelometer measurements reveal a dense layer of suspended particulate matter interpreted as ferric hydroxides precipitated at the interface between normal Red Sea water (oxidizing, alkaline) and metal-enriched thermal brine (reducing, acidic) in the Atlantis II Deep of the Red Sea (Ryan et al., 1969). Water samples from the central North Atlantic exhibit a decrease in suspended articulate matter below 1,500 m to nearly constant values of 2 μg/l, with marked increases in iron (10×) and manganese (10%) over the Mid-Atlantic Ridge crest, relative to the eastern and western basins (Betzer et al., 1974; Bolger, 1976). Distinguishing between suspended particulate matter directly emanating from hydrothermal discharge and that resuspended from oceanic ridge sediments may be difficult.

Silica: Discharged hydrothermal solutions are saturated with silica when leaving the high-temperature source (Mahon, 1966). The solubility of silica is relatively unaffected by dissolved salts and is ten orders of magnitude greater at 200°C than at 50°C (Holland, 1967). When hydrothermal solutions cool upon discharge from the ocean bottom, they may be 10 to 20 orders of magnitude supersaturated with respect to silica (Spooner and Fyfe, 1973), thereby providing two potential indicators of hydrothermal discharge. Silica saturation itself may indicate hydrothermal discharge, if the concentration clearly exceeds the high background level of silica in sea water. Silica derived from hydrothermal discharge may support proliferation of silica-bearing organisms, especially benthic forms, in the vicinity of the discharge. For example, sponges are observed to proliferate in areas of the rift valley of the Mid-Atlantic Ridge including the TAG Hydrothermal Field (Fig. 5; McGregor and Rona, 1975), although it is unclear whether the control is a concentrated supply of dissolved silica or simply the hard rock substrate. Radiolarian chert beds are characteristically associated with ophiolites, but the relation between planktonic organisms and a supply of hydrothermal silica is even more tenuous. Deep-sea camera and submersible observations of the hydrothermal vents at the Galapagos spreading center (Fig. 1; Table 2, location 8) reveal dense populations of giant clams (20 cm wide), mussels, crabs, sea anemones, limpets, and chitons whose presence is related to proliferation of bacteria in hydrogen sulfide-rich solutions emanating from the vents (Corliss and Ballard, 1977; Corliss et al., 1977; Lonsdale, 1977a, b). Invertebrates and bacteria are absent in the hot brines of the Red Sea deeps (Fig. 11; Watson and Waterbury, 1969).

Structural Criteria

The relation between hydrothermal mineral deposits and structure of oceanic crust is influenced by the rate of sea-floor spreading. Slow spreading at half-rates (rate to one side of a spreading center) up to about 4 cm per year is characterized by the presence of a rift valley and rough topography (Menard, 1967), exemplified by the Mid-Atlantic Ridge and the Galapagos spreading center (Table 2; Figs. 1, 6). Fast spreading at half-rates greater than about 4 cm per year is characterized by the absence of a rift valley and the presence of smooth topography, exemplified by the East Pacific Rise (Table 2). Hydrothermal mineral deposits are present at both slow and fast spreading ridges (Fig. 1, Table 2). However, the occurrence of the deposits may be influenced by differences in crustal structure, in particular permeability and the distribution of heat sources, related to the rate of sea-floor spreading.

Hydrothermal deposits have been found at four types of geologic structures at oceanic spreading centers: block-faulted topographic highs formed adjacent to the rift valley of a slowly spreading oceanic ridge (Table 2, locations 1, 2, 8; Figs. 1, 6); volcanic seamounts on oceanic ridges (Table 2, location 7; Fig. 1); fracture zones that transect oceanic spreading centers (Table 2, locations 3, 5, 17; Fig. 1) where hydrothermal deposits may form in the ridge-ridge offset (transform fault) segment of fracture zones, at the intersection of fracture zones with other ocean basin structures such as those localizing volcanoes, along active oceanic fracture zones in ocean basins (Bischoff and Rosenbauer, 1977), and at their intersections with rejuvenated fault systems at continental margins (Kutina, 1974); and basins along the axial trough present during the rift stage in the

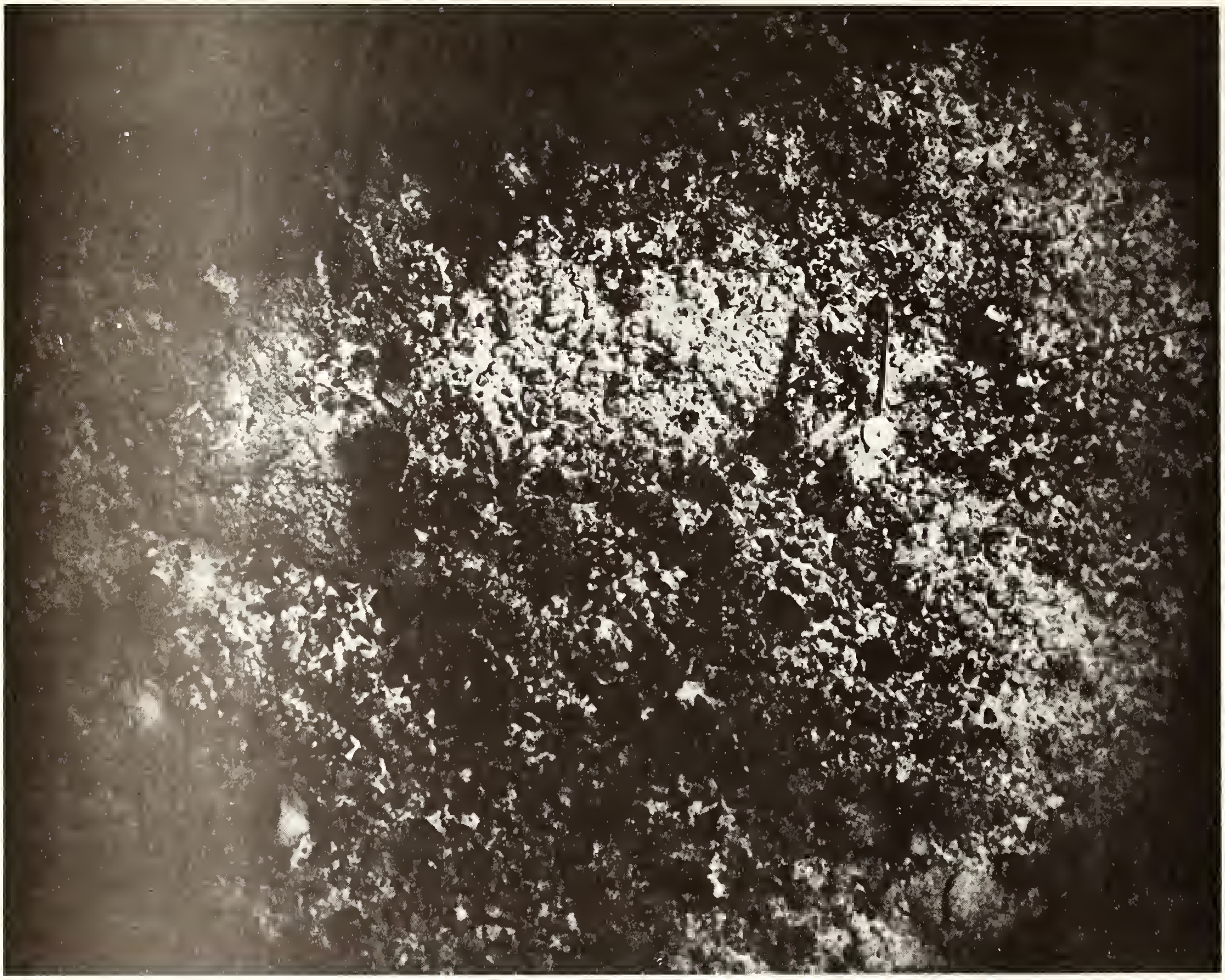

Fig. 5. Bottom photograph (field of view approximately 3 by 4 m) from the TAG Hydrothermal Field showing hydrothermal manganese oxide as a crust on (upper left) and matrix in breccia of basalt fragments (center) at 2,600 m below sea level on the east wall of the rift valley of the Mid-Atlantic Ridge (location 1 in Fig. 1 and Table 2; Rona, 1976b). A sponge is present at the lower left.

opening of an ocean basin (Table 2, location 17; Fig. 1).

The structure of block-faulted topographic highs, which form ridges trending tranverse to the rift valley of slowly spreading oceanic ridges (Fig. 6), acts to focus hydrothermal discharge. The faults and associated fractures provide conduits for hydrothermal flow, and the topographic highs create a geometric effect that forces sea water in a convection cell to flow downward beneath intervening valleys and to flow upward beneath the highs (Fig. 7; Lister, 1972, 1974b). Maximum ease of forcing should occur if the topography has a wavelength twice the cell width, which generally approximately equals the thickness of the permeable layer (Elder, 1965). As a locus of hydrothermal discharge, block-faulted topographic highs are favored localities for the occurrence of hydrothermal deposits.

Hydrothermal deposits have so far been found on only a few block-faulted topographic highs (Table 2, locations 1, 2, 8), although such structures are present adjacent to the rift valley of all slowly spreading oceanic ridges. Additional special structural conditions are required to increase the hydrothermal activity to an intensity sufficient to concentrate hydrothermal deposits. In the case of the TAG Hydrothermal Field, located on a block-faulted topographic high adjacent to the rift valley of the Mid-Atlantic Ridge (Figs. 6, 7), two additional special structural conditions are present (Rona et al., 1976).

An exceptional number of faults and faulted valleys transect the topographic high on which the TAG Hydrothermal Field is located (horizontal spacing tens of meters), compared with similar topographic highs in the region (horizontal spacing hundreds to thousands of meters; Fig. 6). The faults and as-

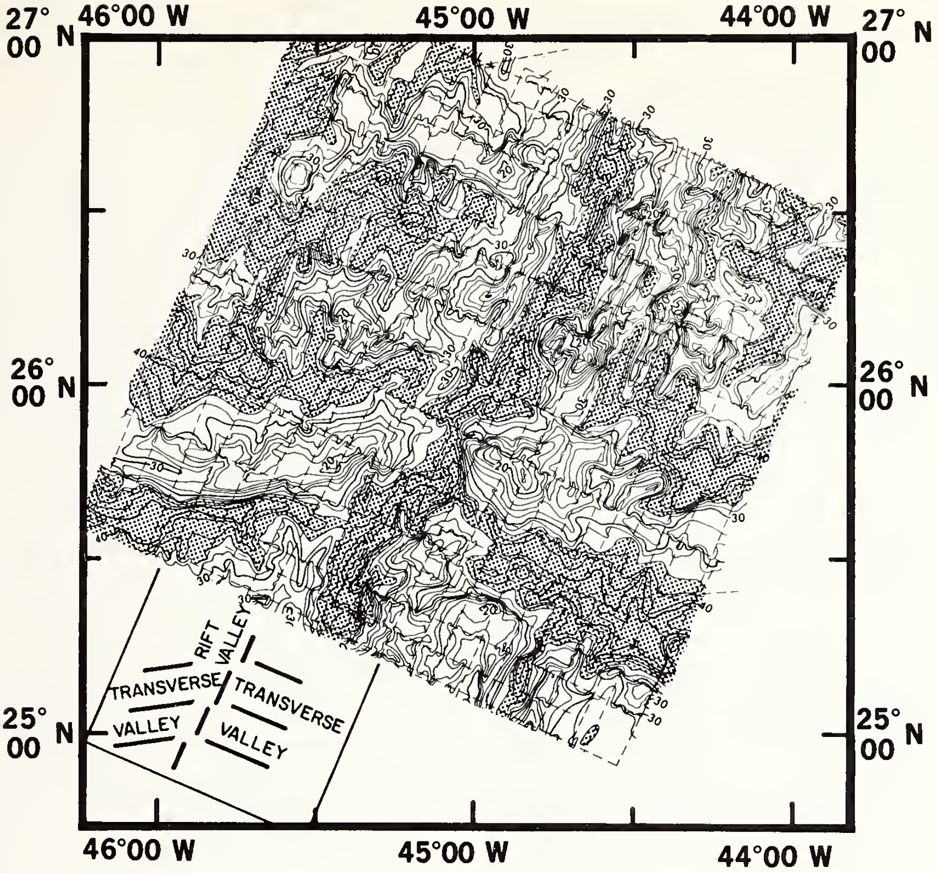

Fig. 6. Bathymetric map (modified from Rona et al., 1976) of an area of the Mid-Atlantic Ridge crest centered on the TAG Hydrothermal Field (Fig. 1, location 1) showing the relation between hydrothermal mineral deposits and topography at a slowly spreading oceanic ridge. The inset, corresponding to the area of the bathymetric map, shows the rift valley and trends of ridges (block-faulted topographic highs) and intervening valleys that strike transverse to the axial valley (shaded on the bathymetric map). The TAG Hydrothermal Field (heavy dashed lines) is located on one of the transverse ridges inferred to be the discharge zone of a subseafloor hydrothermal convection system that recharges with sea water at the intervening valleys (Fig. 7).

sociated fractures (fracture spacing millimeters to meters) increase the permeability of the rocks, thereby facilitating circulation of voluminous hydrothermal fluids.

The segment of the wall of the rift valley formed by the topographic high on which the TAG Hydrothermal Field is located projects as a salient over the floor of the rift valley and is associated with an anomalous narrowing of the valley from about 15 km to 5 km (Fig. 6). The salient is directly over intrusive heat sources beneath the rift valley, causing an exceptionally high thermal gradient that vigorously drives the upwelling limb of the hydrothermal convection system which discharges through faults in the wall of the valley at the TAG Hydrothermal Field.

Exceptionally high permeability and thermal gradients are structurally controlled conditions necessary for the development of high-intensity hydrothermal activity at all the types of structures (block-faulted topographic highs, volcanic seamounts, fracture zones, and axial troughs) in rift zones, ocean basins, and marginal basins. The position of exceptionally permeable structures directly over intrusive heat sources may make the difference between low- and high-intensity hydrothermal activity.

Thermal Criteria

Hydrothermal convection accounts for an estimated 80 percent of the heat loss from lithospheric cooling at oceanic spreading centers and 20 percent of the Earth's total heat loss of 10.2×10^{12} cal/sec (Williams and Von Herzen, 1974). Conductive heat transfer accounts for the remaining 20 percent of heat loss at oceanic spreading centers. Hydrothermal mineral deposits accumulating at oceanic

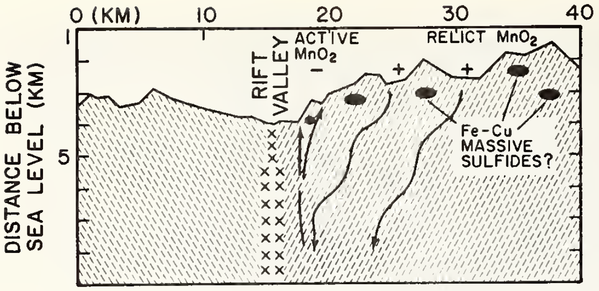

Fig. 7. Diagrammatic cross section of the Mid-Atlantic Ridge at the TAG Hydrothermal Field (vertical exaggeration × 2) showing a subsea-floor hydrothermal convection system like that hypothesized to exist (modified from Rona et al., 1976). Arrows indicate directions of hydrothermal circulation. Slant lines indicate directions of maximum permeability controlled by structural grain including fractures, faults, and dikes. Hydrothermal deposits are actively forming adjacent to the rift valley, and relict deposits are present away from the rift valley, as a consequence of sea-floor spreading. Actually, relict deposits may be covered by off-axis volcanism. Symbols: + = zone of recharge; − = zone of discharge; X = zone of igneous intrusion.

spreading centers are associated with characteristic patterns of convective and conductive heat flow. Highest values of convective heat flow occur at the discharge zones of hydrothermal convection systems, the loci of mineral deposition. The convective heat flow is manifested in the overlying water column in different ways depending on the degree of oceanic circulation. Under conditions of restricted oceanic circulation encountered in the early rift stage, the temperature of the near-bottom water in the vicinity of a hydrothermal discharge zone may increase by the order of 10°C. For example, in certain of the axial troughs of the Red Sea (Atlantis II Deep), hydrothermal solutions with an estimated discharge temperature of 100°C heat the near-bottom water to temperatures of 56°C (normal Red Sea water 22°C), associated with gradients of 1°C per meter warming downward, where stabilized by high salinity and absence of oceanic currents (Ericson and Simmons, 1969; Ross, 1972).

Near-bottom water thermal anomalies attributed to convective hydrothermal discharge under conditions of open oceanic circulation encountered on oceanic ridges are only of the order of 0.1°C due to rapid dissipation of heat by oceanic currents. For example, increases in potential temperature (temperature of a parcel of water raised to surface without any exchange of heat) of about 0.1°C along a horizontal distance between 100 and 300 m at a height of about 10 m above the ocean bottom were measured with thermistor arrays towed across hydrothermal discharge zones at the TAG Hydrothermal Field (Fig. 8; Rona et al., 1975) and at the Galapagos spreading center (Williams et al., 1974; Detrick et al., 1974; Weiss et al., 1977). A near-bottom thermal anomaly caused by hydrothermal discharge may be distinguished from downward mixing of warmer water masses by the presence in the former of a temperature gradient warming downward (0.015°C/m measured at the TAG Hydrothermal Field; Rona et al., 1975) and a potential temperature-salinity relation distinct from that of surrounding water masses (Weiss et al., 1977). Given a measurement precision of 0.004°C, the detection limit of a potential temperature anomaly from a hydrothermal solution discharged at 100°C is a dilution of 2.5×10^4; this detection limit is about two orders of magnitude lower than that cited for ^{3}He (1.5×10^6). Hydrothermal discharge is inferred to be episodic based on consideration of the magnitude of convective heat flux at oceanic ridges, so that convective water temperature anomalies are probably intermittent rather than steady state (Lowell and Rona, 1976).

Values of conductive heat flow, measured by thermoprobes in sediments near the axis of oceanic spreading centers at both the rift and oceanic ridge stages of the opening of an ocean basin, exhibit a large variability between adjacent values (0 to 30 Heat Flow Units) and a high average flux (approx 2.5 HFU; Erickson and Simmons, 1969; Langseth and

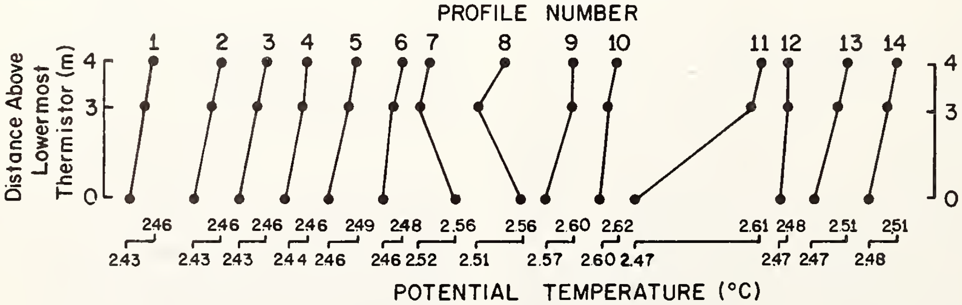

Fig. 8. Successive water temperature profiles, each about 100 m apart, made by a vertical array of three thermistors, with the lowermost thermistor about 10 m above the ocean bottom, across a portion of the TAG Hydrothermal Field (Rona et al., 1975; Lowell and Rona, 1976). An abrupt water-temperature anomaly attributed to hydrothermal discharge is evidenced by the temperature increase and inversion of thermal gradient in profiles 7 to 11.

Von Herzen, 1971; Girdler, 1970; Williams et al., 1974). Theoretical considerations suggest that conductive heat flow may systematically vary as a result of control of hydrothermal circulation by ridge crest topography (Lister, 1972, 1974b), as noted under structural criteria. Low values of conductive heat flow would occur in valleys, where subsea-floor hydrothermal convection systems are inferred to recharge with sea water. Valleys tend to depress the isotherms and therefore are places of preferential separation for the cold columns. High values of conductive heat flow would occur in localized zones on block-faulted topographic highs, where the convection systems are inferred to discharge. Limited conductive heat flow measurements from the Juan de Fuca Ridge (Lister, 1972; Davis and Lister, 1977), the Galapagos spreading center (Williams et al., 1974; Sclater et al., 1974, fig. 9; Von Herzen et al., 1977), and the Mid-Atlantic Ridge at the TAG Hydrothermal Field (Rona et al., 1976) appear consistent with the distribution predicted by theory, although variations in permeability may distort the pattern. If the proposed relation between hydrothermal circulation and topography at slow-spreading oceanic ridges proves to be a general phenomenon, then maps of bathymetry and conductive heat flow can be used to delineate localized zones of hydrothermal discharge that may be associated with mineral deposits.

Acoustic Criteria

A reflecting interface may exist between normal sea water and hydrothermal solutions when a sufficient contrast in acoustic impedence is present due to sound velocity and density differences between the fluids. Conditions of restricted oceanic circulation at the early rift stage in the opening of an ocean basin favor development of a sufficient contrast in acoustic impedance between normal and hydrothermal fluids to produce a reflecting interface. Conditions of open oceanic circulation at the advanced oceanic ridge stage inhibit development of such reflecting interfaces. For example, standard echo sounders (approx 10 kHz frequency) record a reflecting interface between normal Red Sea water (41 per mil salinity, 22°C, sonic velocity 1,550 m/sec, low turbidity) and underlying thermal brine (135 per mil salinity, 44°C, sonic velocity 1,910 m/sec, high turbidity) in the Atlantis II Deep (Dietrich and Krause, 1969; Swallow, 1969; Ostapoff, 1969; Ryan et al., 1969; Pugh, 1969). A reflecting interface is also present between layers within the thermal brine (131 per mil salinity, 44°C temperature, overlying 255 per mil, 56°C). The high content of salt and suspended particulate matter (ferric hydroxides) compensates for the temperature increase of the brine and serves to stabilize interfaces (Turner, 1969) and to establish contrasts in acoustic impedence.

Seismic Criteria

Microearthquake activity may indicate the presence of high-intensity hydrothermal convection systems. An association has been demonstrated between microearthquake activity and hydrothermal systems on continents. For example, 20 to 30 shallow-focus (< 15 km) microearthquakes per day of magnitude less than 2.0 are recorded at hydrothermal areas in the Imperial Valley (Combs and Hadley, 1977; Jarzbeck and Combs, 1976), a landward structural extension of the oceanic spreading center active in the Gulf of California. Hydrothermal areas in the Rio Grande Rift zone of the southwestern United States exhibit 5 to 70 microearthquakes per day, mostly of magnitudes less than 1.5 (Quillan and Combs, 1976; Johnson and Combs, 1976).

Measurements of seismicity in the volcanic zone of southwest Iceland on the Mid-Atlantic Ridge (Ward et al., 1969; Ward and Björnsson, 1971; Klein et al., 1973) indicate that the most active microearthquake zones often coincide with high-temperature hydrothermal systems (> 200°C in upper 1 km). Focal depths of the microearthquakes lie in the upper part of oceanic crustal layer 3 within a subsurface depth range of 2 to 6 km (Ward and Björnsson, 1971).

Earthquake swarms, each consisting of a distinctive sequence of earthquakes closely grouped in time and space with no one outstanding main shock, have been reported from 17 locations along the Mid-Atlantic Ridge crest, both north and south of Iceland. Similar earthquake swarms have been reported from sites along the axes of other slow-spreading centers including the Red Sea rift, the Indian Ridge, the Gorda Ridge, the Galapagos spreading center, and the Gulf of California rift (Francis, 1968; Sykes, 1970). The magnitude of the earthquakes in swarms observed at oceanic spreading centers is generally less than 5.0; focal depths are considered to lie within oceanic crust (< 10 km; Sykes, 1970). It is uncertain whether earthquake swarms at oceanic spreading centers are related to localized sources of high fluid pressures due to magmas or to hydrothermal solutions that may lower the effective strength of rocks and act as concentrated sources of stress (Sykes, 1970).

Gravity Criteria

No direct relation is known between gravity and hydrothermal mineral deposits. Although hydrothermal minerals generally are less dense than primary minerals, the effect on gravity is negligible. Gravity may be indirectly related to hydrothermal mineral deposits through geologic structure. For example, the central trough of the Red Sea exhibits relatively low free-air gravity values caused by terrain effect and high Bouguer values (110 to 135 mgals), consistent with dense underlying material interpreted as intrusive bodies (Phillips et al., 1969). A free-air gravity high caused by terrain effect occurs over the block-faulted topographic high on which the TAG Hydrothermal Field is located (Fig. 6; Rona et al., 1976).

Subaerial hydrothermal systems exhibit both positive (Wairakei and Niland, New Zealand, Beck and Robertson, 1955; Mesa, Imperial Valley, Biehler, 1971) and negative gravity anomalies (Larderello and Mt. Amiata, Italy, Marchesini et al., 1962). The positive and negative gravity anomalies of subaerial hydrothermal systems are controlled by local geologic structure.

Electrical Criteria

Electrical criteria for recognition of hydrothermal deposits in oceanic crust pertain to the electrical properties of metallic deposits and of hydrothermal solutions in rocks. Electromagnetic methods have been extensively applied on land to delineate hydrothermal systems (McNitt, 1965) as well as porphyry and stratabound sulfide deposits (SEG, 1966). Electromagnetic methods are at an early stage of application to the marine environment, where voltage is measured in highly conductive sea water that acts as a short circuit for electric currents.

Self-potentials involving a gradient of redox potential that determines the electromagnetic force of an oxidation-reduction electrochemical cell are associated with metalliferous sediments and massive sulfide bodies of the ocean bottom (Sato and Mooney, 1960). Redox potential gradients as great as 200 mV were measured in the Red Sea metalliferous sediments (Brooks et al., 1969). Calculation of the short-circuit effect in sea water (Brewitt-Taylor, 1975) shows that the voltage is reduced by a factor of the same order as the ratio of conductivities of sea water and the metalliferous sediment, resulting in a signal of tens of millivolts. Self-potentials have been measured in the deep ocean using a towed electrode array (Brewitt-Taylor, 1975) and on the continental shelf at a known sulfide orebody (Corwin et al., 1970).

A towed resistivity array and a towed active source audiomagnetotelluric system have detected conductivity anomalies associated with known vein copper deposits in the Great Lakes (Nebrija et al., 1976). Direct current resistivity measurements of the subaerial Reykjanes hydrothremal field in Iceland reveal values of 1 to 3 ohm meters where basalt is saturated with thermal brines, and 1,000 to 5,000 ohm meters where saturated with fresh water (Björnsson et al., 1972). A start has been made in the application of well logging techniques to the measurement of sea-floor resistivity (Bannister, 1968; Patella and Schiavone, 1974; Whiteley, 1974).

Magnetic Criteria

A growing body of field evidence supported by laboratory studies indicates that hydrothermal activity may affect the intensity of magnetization of basalt, producing a characteristic magnetic signature that may be associated with sites of hydrothermal mineral deposits. The following field evidence favors the existence of a magnetic signature indicative of hydrothermal deposits (Rona, 1978).

A distinct low in residual magnetic intensity (approx 200 gammas) coincides with the TAG Hy-

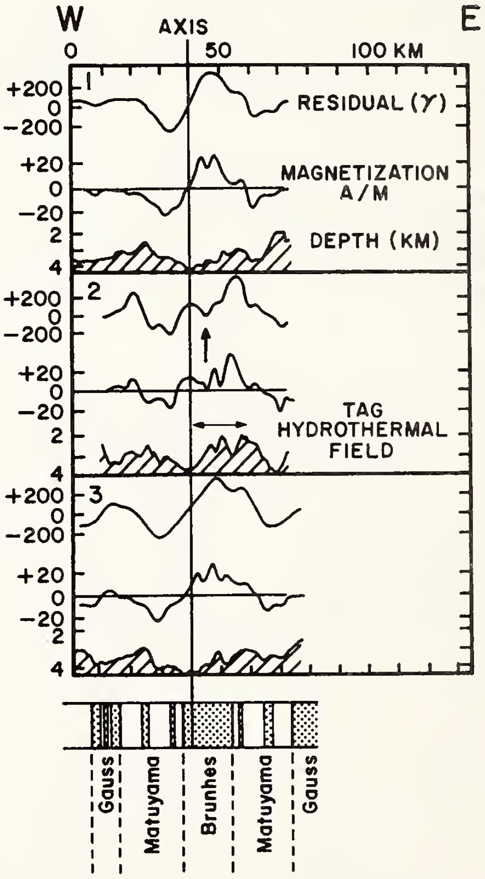

FIG. 9. Profiles of residual magnetic intensity (γ), magnetization of the basalt layer computed by the inverse method (A/M = amperes/meter = 10^{-3} emu/cm^3), and depth (KM), across the rift valley of the Mid-Atlantic Ridge at latitude 26° N (modified from McGregor et al., 1977). A distinct low in residual magnetic intensity within the positive axial magnetic anomaly (Brunhes magnetic polarity epoch) and in computed magnetization (arrow in profile 2) coincides with the TAG Hydrothermal Field. The magnetic low is absent in profiles north (profile 1) and south (profile 3) of the field. The locations of the profiles is shown in Figure 10.

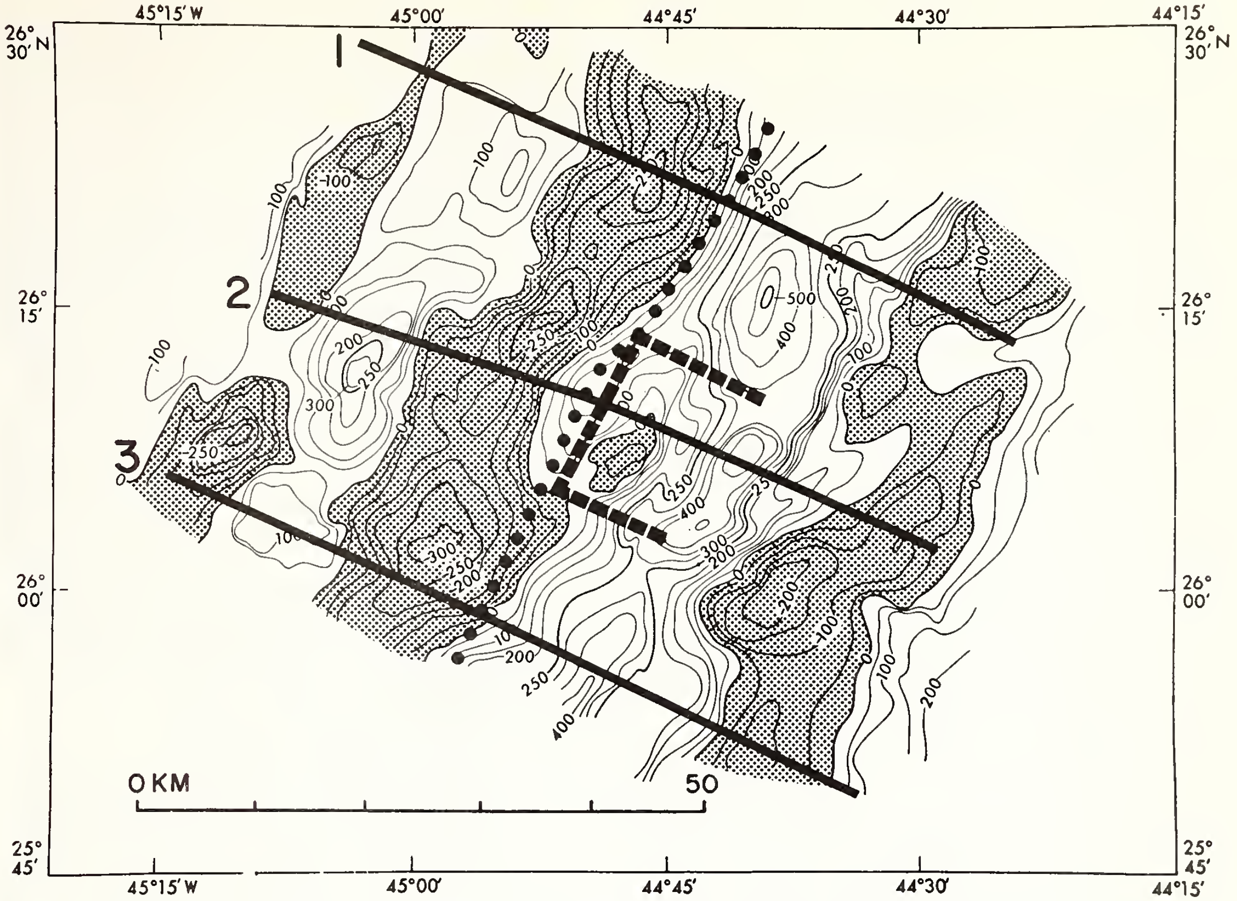

FIG. 10. Residual magnetic map (50 gamma contour interval) of the Mid-Atlantic Ridge crest at latitude 26° N (modified from McGregor et al., 1977). Shaded areas are negative. The location of profiles 1–3 in Figure 9 (solid lines), the TAG Hydrothermal Field (dashed lines), and the axis of the rift valley (dotted line) are shown. Low to negative values of residual magnetic intensity are present within the positive axial magnetic anomaly at the TAG Hydrothermal Field.

drothermal Field at the crest of the Mid-Atlantic Ridge and is absent both to the north and south of the TAG Hydrothermal Field (Figs. 9, 10; McGregor and Rona, 1975). The magnetic low occurs within the positive magnetic anomaly of the Brunhes magnetic polarity epoch that is typically associated with the axis of oceanic spreading centers.

A distinct low in residual magnetic intensity occurs at the Atlantis II Deep (approx 650 gammas) in the axial trough of the Red Sea, although the significance of this low was not noted previously (Fig. 11; Hunt et al., 1967; Phillips et al., 1969). The magnetic low is absent at the adjacent Chain Deep and Discovery Deep, which are associated with magnetic highs (approx 350 gammas) typical of the axis of oceanic spreading centers (Fig. 12). The thermal brine in these three deeps is inferred to discharge at a minimum temperature of 100°C from a single zone in the Atlantis II Deep based on distribution of metalliferous sediments, chemistry of the brine and interstitial water, and brine temperature relations (Brewer et al., 1969; Brooks et al., 1969; Ross et al., 1969; Ross, 1972). These observations indicate that the magnetic low at the Atlantis II Deep is related to the presence of hydrothermal discharge; the magnetic highs at the other two deeps occur where hydrothermal discharge is absent.

A distinct low in residual magnetic anomaly (approx 200 gammas) coincides with the subaerial Reykjanes hydrothermal field in Iceland at the axis of the Mid-Atlantic Ridge, where the thermal brine attains temperatures of 300°C (Björnsson et al., 1972).

Distinct lows in residual magnetic intensity occur in certain other subaerial hydrothermal fields, including Mesa in the Salton Trough of the southwestern United States, where measured temperatures attain 216°C (Koenig, 1967; Black, 1975, table 1); Wairakei of New Zealand, where measured temperatures attain 250°C (Studt, 1959; Banwell et al., 1957); and Rabaul, New Britain (Studt, 1961).

Laboratory studies of basalt alteration explain the cause of the lows in residual magnetic intensity observed at both submarine and certain subaerial hydrothermal fields.

Unaltered tholeiitic basalt has high magnetic susceptibility (typical values 6 to 30 emu/cm^3 × 10^4) and remanent magnetization (typical values 36 to 113 emu/cm^3 × 10^4) because of its content of fresh iron-titanium oxide, especially titanomagnetite (Luyendyk and Melson, 1967; Irving et al., 1970a, b; Watkins and Paster, 1971; Ade-Hall et al., 1971; Marshall and Cox, 1972; Fox and Opdyke, 1973).

Unaltered basalt is metamorphosed to greenstone by hydrothermal alteration within the range of temperatures and pressures encountered in hydrothermal discharge zones (Helgeson, 1968; Helgeson et al., 1969; Melson et al., 1968; Miyashiro et al., 1971; Spooner and Fyfe, 1973).

Greenstone, in which iron-titanium oxide has been replaced by sphene and other minerals, has low values of susceptibility (typical values 0.4 to 0.6 emu/cm^3 × 10^4) and remanent magnetization (typical values 0.02 to 0.11 emu/cm^3 × 10^4) (Luyendyk and Melson, 1967; Irving et al., 1970a, b; Watkins and Paster, 1971; Ade-Hall et al., 1971; Marshall and Cox, 1972; Fox and Opdyke, 1973).

The presence of altered basalts and greenstones has been confirmed where rocks have been recovered from hydrothrmal fields associated with magnetic lows (Studt, 1959, 1961; Björnsson et al., 1972; Rona et al., 1976).

Computer modeling of the magnetic low at the TAG Hydrothermal Field (Fig. 9) is consistent with attribution of the low to reduction in remanent magnetization within the basalt of oceanic crustal layer 2 (McGregor et al., 1977).

Development of magnetic lows by alteration of the magnetic mineral component of basalts in high temperature discharge zones of subsea-floor systems like those described may provide a rapid reconnaissance criterion for recognizing potential sites of hydrothermal mineral deposits in oceanic crust (Rona, 1978). This does not rule out the possibility of a magnetic high controlled by geologic structure at a hydrothermal field, as observed at certain subaerial fields such as Niland (Kelley and Soske, 1936) and Casa Diablo (Henderson et al., 1963) in the southwestern United States. The hydrothermal alteration involved specifically pertains to basalt, because alteration of other rock types may produce different magnetic effects. For example, fresh peridotites lacking magnetite alter to rocks rich in serpentine and magnetite with increase in magnetic susceptibility (Luyendyk and Melson, 1967; Fox and Opdyke. 1973).

Patterns of Deposition

Patterns of deposition are considered insofar as they are useful in locating hydrothermal mineral deposits in oceanic crust. Depositional patterns differ in the rift and oceanic ridge stages of opening of an ocean basin about an oceanic spreading center due primarily to differences in tectonic setting. At the rift stage, oceanic circulation is restricted by the high length/width raito of the opening, by the axial

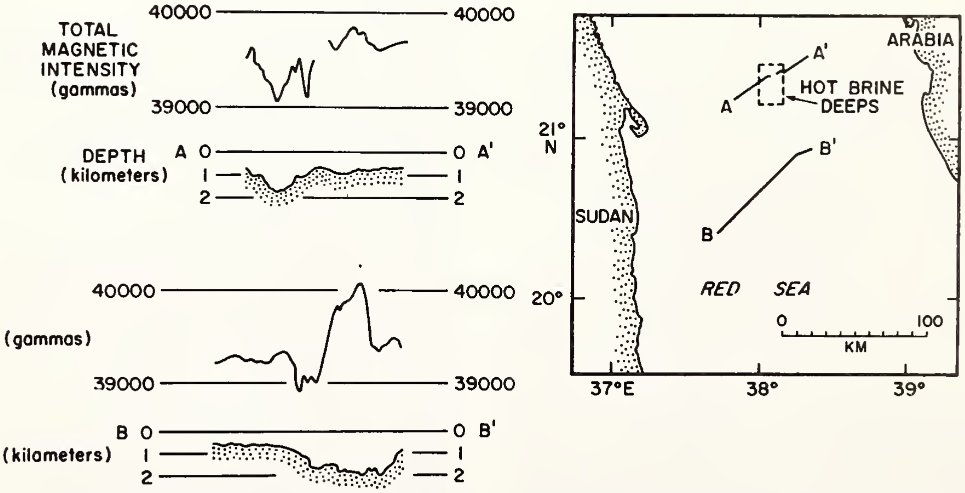

FIG. 11. Magnetic and bathymetric profiles across the axial trough of the Red Sea and an index map showing an area of deeps containing metalliferous sediments and hot brines (modified from Phillips et al., 1969). A distinct low in observed magnetic intensity occurs over the Atlantis II Deep (profile A-A'), the locus of hydrothermal discharge. A high in magnetic intensity, characteristic of the axis of oceanic spreading centers, occurs over the axial trough outside the area of the hot-brine deeps (profile B-B').

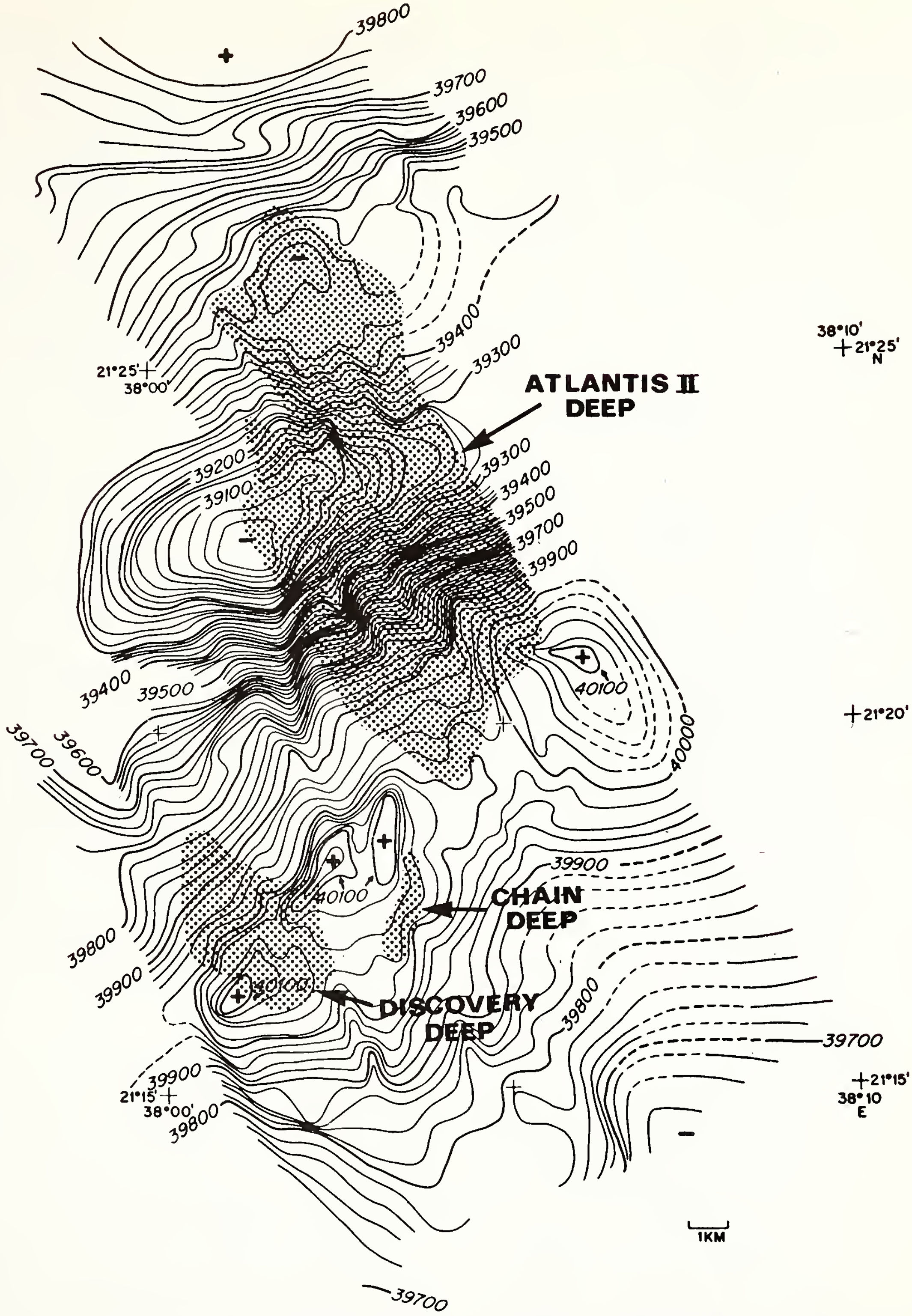
39800
+
39700
39600
39500
−
39400
39300
21°25' 38°00'
38°10' 21°25' N
ATLANTIS II DEEP
39300
39400
39500
39700
39900
39200
39100
−
39400
39500
39700
39600
+
40100
40000
21°20'
+
+
39900
40100
CHAIN DEEP
39800
39900
+
40100
DISCOVERY DEEP
39800
39700
39900
21°15' 38°00'
39800
21°15' 38°10' E
−
1KM
39700

FIG. 12. Total magnetic intensity contour map (20 gamma contour interval) of the hot-brine area of the Red Sea outlined in Figure 11 (modified from Phillips et al., 1969). Each of the three deeps present is shaded. A magnetic low occurs at the Atlantis II Deep; magnetic highs occur at the Discovery Deep and Chain Deep. A hydrothermal discharge zone in the Atlantis II Deep is the source of the thermal brines and metalliferous sediments in the three deeps.

troughs that contain the hydrothermal products, and by the high salinity derived from flow through evaporites that stabilizes the hydrothermal solutions. The presence of evaporites is not simply an artifact of the Red Sea but is a regular feature of the rift stage (Rona, 1969, 1970). As a consequence of these factors, metalliferous sediments, encrustations, and massive sulfides, if present, are deposited at or near the discharge zones of subsea-floor hydrothermal convection systems and exhibit relatively pure hydrothermal compositions. For example, a dispersion halo of manganese-rich sediment about 20 km in diameter is present around the Atlantis II Deep, which is about 5 km wide by 15 km long (Fig. 12; Cronan, 1976; Bignell et al., 1976). Thermal and geochemical anomalies persist in the stably stratified water immediately overlying the deposits.

In contrast, at the oceanic ridge stage, open ocean circulation disperses metalliferous sediments, accounting for their nearly ubiquitous distribution (Fig. 1) and compositional variation (Table 2) related to dilution by biogenic, detrital, and hydrogenous components. Determination of gradients of metal content in metalliferous sediments dispersed on oceanic ridges may lead back to concentrated deposits at hydrothermal discharge zones. For example, contours of transition metal and barium contents of sea-floor sediments exhibit concentration gradients that effectively delineate oceanic spreading centers in the Atlantic, Pacific, and Indian Oceans (Boström et al., 1969, fig. 1; Boström, 1973, figs. 2, 5, 9, 10, 16). Thermal and geochemical anomalies derived from hydrothermal discharge into the near-bottom water are likewise quickly dissipated by oceanic currents and other mixing processes. Metallifeous encrustations and massive sulfides, if present, remain in situ at the hydrothermal discharge zone.

Two principal depositional patterns can be discerned from the limited data available on the distribution of hydrothermal mineral deposits perpendicular to oceanic spreading centers (Rona, 1976b).

The first is controlled by physical and chemical processes within the hydrothermal field. A major process is inferred to be sealing of talus by deposition of hydrothermal minerals from solutions discharged through faults at and adjacent to the wall of the axial valley of an oceanic ridge. In the case of the TAG Hydrothermal Field at the Mid-Atlantic Ridge crest (Table 2, location 1; Figs. 1, 6), the sealing of a given volume of talus (Fig. 5) is inferred to occur during a period of the order of 1×10^5 yr, causing successive migrations of the zone of discharge (Rona, 1976b). The resultant pattern of hydrothermal mineral deposition within the hydrothermal field is a mosaic of patchy deposits, overlapping in time and space, with a predominantly fault-controlled trend subparallel to the axis of the axial valley.

A second pattern is controlled by sea-floor spreading encompassing the entire hydrothermal field. A linear zone of hydrothermal deposits will extend from an active depositional locality at the axial valley of an oceanic ridge along the direction of sea-floor spreading, depending both on the continuity of sea-floor spreading and the persistence in time of the special structural and thermal conditions that concentrate the hydrothermal activity. In the case of the TAG Hydrothermal Field (Figs. 6, 7), the special structural and thermal conditions that have concentrated hydrothermal activity have persisted during sea-floor spreading for at least 1.4×10^6 yr (Rona, 1976b). As a relict hydrothermal deposit is carried away from the axis of an oceanic spreading center by sea-floor spreading, it may become covered by off-axis volcanism (Fig. 7). A criterion to distinguish between axial volcanics that may contain hydrothermal deposits and off-axis volcanics that may cover deposits is the higher K_2O content in the latter (Strong, 1974b).

The distribution of hydrothermal mineral deposits along oceanic spreading centers can presently only be conjectured from the known distribution of 17 active hydrothermal systems over a distance of 250 km in the neovolcanic zone of Iceland on the Mid-Atlantic Ridge (Bödvarsson, 1961) and 17 basins (at least one presently active) containing hydrothermal brine and/or sediment over a distance of 900 km in the Red Sea (Degens and Ross, 1969; Bäcker and Schoell, 1972; Bäcker, 1975). The difficulty of finding hydrothermal mineral deposits in ophiolites is comprehensible in light of their possible covering by volcanics away from oceanic spreading centers and their sporadic occurrence along oceanic spreading centers.

Conclusions

The various criteria presented can be used to guide exploration for hydrothermal mineral deposits in oceanic crust. The seismic, geochemical, acoustic, thermal, and certain electrical criteria apply to recognition of active discharge zones of subsea-floor hydrothermal convection systems, the loci of hydrothermal mineral deposition at oceanic spreading centers including rift zones, oceanic ridges, and marginal basins associated with island arcs. The petrologic, structural, gravity, magnetic, and other electrical criteria also apply to active discharge zones, as well as to recognition of hydrothermal mineral deposits in oceanic crust away from spreading centers at sea and on land (Fig. 1).

Acknowledgments

I would like to thank G. J. S. Govett of the University of New Brunswick for a helpful review and the Office of Marine Minerals of the National Oceanic and Atmospheric Administration (NOAA) for financial support. This work was performed as part of the NOAA Metallogenesis at Dynamic Plate Boundaries Project.

National Oceanic and Atmospheric Administration
Atlantic Oceanographic and Meterological Laboratories
15 Rickenbacker Causeway
Miami, Florida 33149
February 23, August 29, 1977

REFERENCES

Ade-Hall, J. M., Palmer, H. C., and Hubbard, T. P., 1971, The magnetic and opaque petrological response of basalts to regional hydrothermal alteration: Royal Astron. Soc. Geophys. Jour., v. 24, p. 137–174.

Anderson, R. N., 1972, Petrologic significance of low heat flow on the flanks of slow spreading mid-ocean ridges: Geol. Soc. America Bull., v. 83, p. 2947–2956.

ARCYANA, 1975, Transform fault and rift valley from bathyscaph and diving saucer: Science, v. 190, p. 108–116.

Arrhenius, G., and Bonatti, E., 1965, Neptunism and volcanism in the ocean, *in* Sears, M., ed., Progress in oceanography: London, Pergamon Press, v. 3, p. 7–22.

Bäcker, H., 1975, Exploration of the Red Sea and Gulf of Aden during the M.S. VALDIVIA cruises "Erzschlämme A" and "Erzschlämme B": Hannover, Geol. Jahrb., D13, p. 3–78.

Bäcker, H., and Schoell, M., 1972, New deeps with brines and metalliferous sediments in the Red Sea: Nature Phys. Sci., v. 240, p. 153–158.

Bailey, E. H., and Coleman, R. G., 1975, Mineral deposits in the Semail ophiolite of northern Oman [abs.]: Geol. Soc. America, Abstracts with Programs, v. 7, p. 293.

Bannister, P. R., 1968, Determination of the electrical conductivity of the sea bed in shallow waters: Geophysics, v. 30, p. 995–1003.

Banwell, C. J., Cooper, E. R., Thompson, G. E. K., and McCree, K. J., 1957, Physics of the New Zealand thermal area: New Zealand Dept. Sci. Indus. Research Bull. 123, 109 p.

Beck, A. C., and Robertson, E. I., 1955, Geology and geophysics, *in* Grange, L.I., ed., Geothermal steam for power: New Zealand Dept. Sci. Indus. Research Bull. 117, p. 15–19.

Bender, M., Broecker, W., Gornitz, V., Middel, U., Kay, R., and Sun, S., 1971, Geochemistry of three cores from the East Pacific Rise: Earth Planet. Sci. Letters, v. 12, p. 425–433.

Bertine, K. K., and Keene, J. B., 1975, Submarine barite-opal rocks of hydrothermal origin: Science, v. 188, p. 150–152.

Betzer, P. R., Bolger, G. W., McGregor, B. A., and Rona, P. A., 1974, The Mid-Atlantic Ridge and its effect on the composition of particulate matter in the deep ocean: Am. Geophys. Union Trans., v. 55, p. 293.

Biehler, S., 1971, Gravity studies in the Imperial Valley, *in* Cooperative geological-geophysical-geochemical investigations of geothermal resources in the Imperial Valley of California: Univ. California Riverside-IGPP Rept., p. 29–42.

Bignell, R. D., Cronan, D. S., and Tooms, J. S., 1976, Metal dispersion in the Red Sea as an aid to marine geochemical exploration: Inst. Mining Metallurgy Trans., v. 85, sec. B, p. B273–B278.

Bischoff, J. L., 1969, Red Sea geothermal brine deposits, *in* Degens, E. T., and Ross, D. A., eds., Hot brines and recent heavy metal deposits of the Red Sea: New York, Springer-Verlag, p. 348–401.

Bischoff, J. L., and Dickson, F. W., 1975, Seawater-basalt interaction at 200°C and 500 bars: Implications for origin of sea floor heavy mineral deposits and regulation of seawater chemistry: Earth Planet. Sci. Letters, v. 25, p. 385–397.

Bischoff, J. L., and Rosenbauer, R. J., 1977, Recent metalliferous sediment in the North Pacific manganese nodule area: Earth Planet. Sci. Letters, v. 33, p. 379–388.

Björnsson, S., Arnórsson, S., and Tómasson, J., 1972, Economic evaluation of Reykjanes thermal brine area, Iceland: Am. Assoc. Petroleum Geologists Bull., v. 56, p. 2380–2391.

Black, H. T., 1975, A subsurface study of the Mesa geothermal anomaly, Imperial Valley, California: Washington, Natl. Sci. Found. Rept. NSF-RA-N-75-126, 58 p.

Bödvarsson, G., 1961, Physical characteristics of natural heat resources in Iceland: Jökull, v. 11, p. 29–38.

Bolger, G. W., 1976, Chemical evidence that the Mid-Atlantic Ridge is a source of hydrothermally derived suspended particulate material to the deep Atlantic: Unpub. Masters thesis, Univ. of South Florida, St. Petersburg, Office of Naval Research Contract N00014-72-A-0363-0001, 145 p.

Bonatti, E., 1975, Metallogenesis at oceanic spreading centers, *in* Annual Reviews Earth Planet. Sci., v. 3: Palo Alto, Calif., Annual Reviews, Inc., p. 401–431.

Bonatti, E., and Joensuu, O., 1966, Deep-sea iron deposit from the South Pacific: Science, v. 154, p. 643–645.

—— 1968, Palygorskite from Atlantic deep sea sediments: Am. Mineralogist, v. 53, p. 975–983.

Bonatti, E., Fisher, D. E., Joensuu, O., Rydell, H. S., and Beyth, M., 1972a, Iron-managanese-barium deposit from the Northern Afar Rift (Ethiopia): Econ. Geol., v. 67, p. 717–730.

Bonatti, E., Kraemer, T., and Rydell, H., 1972b, Classification and genesis of submarine iron-manganese deposits, *in* Horn, D., ed., Ferromanganese deposits on the ocean floor: Washington, Natl. Sci. Found., p. 149–165.

Bonatti, E., Guerstein-Honnorez, B.-M., and Honnorez, J., 1976a, Copper-iron sulfide mineralizations from the equatorial Mid-Atlantic Ridge: Econ. Geol., v. 71, p. 1515–1525.

Bonatti, E., Guerstein-Honnorez, B.-M., Honnorez, J., and Stern, C., 1976b, Hydrothermal pyrite concretions from the Romanche Trench (equatorial Atlantic): Metallogenesis in oceanic fracture zones: Earth Planet. Sci. Letters, v. 32, p. 1–10.

Bonatti, E., Zerbi, M., Kay, R., and Rydell, H. 1976c, Metalliferous deposits from the Apennine ophiolites: Mesozoic equivalent of modern deposits from oceanic spreading centers: Geol. Soc. America Bull., v. 87, p. 83–94.

Boström, K., 1970, Submarine volcanism as a source of iron: Earth Planet. Sci. Letters, v. 9, p. 348–354.

—— 1973, The origin and fate of ferromanganoan active ridge sediments: Stockholm Contr. Geology, v. 24, p. 149–243.

Boström, K., and Peterson, M. N. A., 1966, Precipitates from hydrothermal exhalations on the East Pacific Rise: Econ. Geol., v. 61, p. 1258–1265.

—— 1969, The origin of aluminum-poor ferromanganoan sediments in areas of high heat flow on the East Pacific Rise: Marine Geology, v. 7, p. 427–447.

Boström, K., Peterson, M. N. A., Joensuu, O., and Fisher, D. E., 1969, Aluminum-poor ferromanganoan sediments on active oceanic ridges: Jour. Geophys. Research, v. 74, p. 3261–3270.

Boström, K., Joensuu, O., Valdés, S., and Riera, M., 1972, Geochemical history of South Atlantic Ocean sediments since late Cretaceous: Marine Geology, v. 12, p. 85–121.

Boström, K., Joensuu, O., Valdés, S., Charm, W., and Glaccum, R., 1976, Geochemistry and origin of East Pacific sediments sampled during DSDP Leg 34: Washington, U. S. Govt. Printing Office, Deep Sea Drilling Proj. Initial Repts., v. 34, p. 559–574.

Brewer, P. G., Densmore, C. D., Munns, R., and Stanley,

R. J., 1969, Hydrography of Red Sea brines, *in* Degens, E. T., and Ross, D. A., eds., Hot brines and recent heavy metal deposits in the Red Sea: New York, Springer-Verlag, p. 138–152.

Brewer, P. G., Spencer, D. W., and Robertson, D. E., 1972, Trace element profiles from the GEOSECS II test station in the Sargasso Sea: Earth Planet. Sci. Letters, v. 16, p. 111–116.

Brewitt-Taylor, C. R., 1975, Self-potential prospecting in the deep oceans: Geology, v. 3, p. 541–542.

Broecker, W. S., 1965, An application of natural radon to problems in ocean circulation: Symposium on Diffusion in Oceans and Fresh Waters, Lamont-Doherty Geol. Observatory, p. 116–145.

Broecker, W. S., Li, Y. H., and Cromwell, J., 1967, Radium 226 and radon 222: Concentration in Atlantic and Pacific oceans: Science, v. 158, p. 1307–1310.

Brooks, R. R., Kaplan, I. R., and Peterson, M. N. A., 1969, Trace element composition of Red Sea geothermal brine and interstitial water, *in* Degens, E. T., and Ross, D. A., eds., Hot brines and recent heavy metal deposits in the Red Sea: New York, Springer-Verlag, p. 180–203.

Browne, P. R. L., and Ellis, A. J., 1970, The Ohaki-Broadlands hydrothermal area, New Zealand: Mineralogy and related chemistry: Am. Jour. Sci., v. 296, p. 97–131.

Christensen, N. I., 1972, The abundance of serpentinites in the oceanic crust: Jour. Geology, v. 80, p. 709–719.

Chung, Y., and Craig, H., 1972, Excess-randon and temperature profiles from the eastern Equatorial Pacific: Earth Planet. Sci. Letters, v. 14, p. 55–64.

Clarke, W. B., Beg, M. A., and Craig, H., 1969, Excess ^{3}He in the sea: Evidence for terrestrial primordial helium: Earth Planet. Sci. Letters, v. 6, p. 213–220.

Coleman, R. G., 1971, Plate tectonic emplacement of upper mantle peridotites along continental edges: Jour. Geophys. Research, v. 76, p. 1212–1222.

—— 1977, Ophiolites: New York, Springer-Verlag, 229 p.

Combs, J., and Hadley, D. M., 1977, Microearthquake investigation of the Mesa geothermal anomaly, Imperial Valley, California: Geophysics, v. 42, p. 17–33.

Constantinou, G., and Govett, G. J. S., 1973, Geology, geochemistry, and genesis of Cyprus sulfide deposits: Econ. Geol., v. 68, p. 843–858.

Corliss, J. B., 1971, The origin of metal-bearing submarine hydrothermal solutions: Jour. Geophys. Research, v. 76, p. 8128–8138.

Corliss, J. B., and Ballard, R. D., 1977, Oases of life in the cold abyss: Natl. Geographic, v. 152, no. 4, p. 441–453.

Corliss, J. B., Dymond, J., Lyle, M., Doerge, T., Crane, K., Lonsdale, P., Von Herzen, R. P., and Williams, D., 1976, Sediment mound ridges of hydrothermal (?) origin along the Galapagos Rift [abs.]: Am. Geophys. Union Trans., v. 57, p. 935.

Corliss, J. B., Dymond, J. Lyle, M., Cobler, R., Williams, D., Von Herzen, R., and van Andel, T., 1977 Observations of the sediment mounds of the Galapagos Rift during the Alvin diving program [abs.]: Geol. Soc. America, Abstracts with Programs, v. 9, p. 937.

Corwin, R. F., Ebersole, W. C., and Wilde, P., 1970, A self potential detection system for the marine environment: Offshore Technology Conf. Houston, Texas 1970, OTC Paper 1258.

Craig, H., 1969, Geochemistry and origin of the Red Sea brines, *in* Degens, E. T., and Ross, D. A., eds., Hot brines and recent heavy metal deposits in the Red Sea: New York, Springer-Verlag, p. 208–242.

Craig, H., and Lupton, J. E., 1976, Primordial neon, helium and hydrogen in oceanic basalts: Earth Planet. Sci. Letters, v. 31, p. 369–385.

Craig, H., Clarke, W. B., and Beg, M. A., 1975, Excess ^{3}He in the deep water on the East Pacific Rise: Earth Planet. Sci. Letters, v. 26, p. 125–132.

Cronan, D. S., 1973, Basal ferruginous sediments cored during Leg 16, Deep Sea Drilling Project: Washington, U. S. Govt. Printing Office, Deep Sea Drilling Proj. Initial Repts., v. 16, p. 601–604.

—— 1976, Implications of metal dispersion from hydrothermal systems for mineral exploration on mid-ocean ridges and in island arcs: Nature, v. 262, p. 567–569.

Czamanske, G. K., and Moore, J. G., 1977, Composition and phase chemistry of sulfide globules in basalt from the Mid-Atlantic Ridge rift valley: Geol. Soc. America Bull., v. 88, p. 587–599.

Davis, E. E., and Lister, C. R. B., 1977, Heat flow measured over the Juan de Fuca Ridge; Evidence for widespread hydrothermal circulation in a highly heat transportive crust: Jour. Geophys. Research, v. 82, p. 4845–4860.

Deep Sea Drilling Staff, 1977, Deep Sea Drilling Proj. Initial Repts., v. 37: Washington, U. S., Govt. Printing Office, 1008 p.

Deffayes, K. S., 1970, The axial valley: A steady-state feature of the terrain, *in* Johnson, H., and Smith, B. L., eds., The megatectonics of continents and oceans: Camden, N. J., Rutgers Univ. Press, p. 194–222.

Degens, E. T., and Ross, D. A., 1969, eds., Hot brines and recent heavy metal deposits in the Red Sea: New York, Springer-Verlag, 600 p.

Detrick, R. S., Williams, D. L., Mudie, J. D., and Sclater, J. G., 1974, The Galapagos spreading center: Bottom water temperatures and the significance of geothermal heating: Royal. Astron. Soc. Geophys. Jour., v. 38, p. 627–637.

Dewey, J. F., and Bird, J. M., 1971, Origin and emplacement of the ophiolite suite: Appalachian ophiolites in Newfoundland: Jour. Geophys. Research, v.. 76, p. 3179–3206.

Dietrich, G., and Krause, G., 1969, The observations of the vertical structure of hot salty water by R. V. Meteor, *in* Degens, E. T., and Ross, D. A., eds., Hot brines and recent heavy metal deposits in the Red Sea: New York, Springer-Verlag, p. 10–17.

Dmitriev, L. V., Barsukov, V. L., and Udıntsev, G. B., 1970, Rift zone in the oceans and the problem of ore formation: Geokhimiya, v. 4, p. 937.

Duke, N. A., and Hutchinson, R. W., 1974, Geological relationships between massive sulfide bodies and ophiolitic volcanic rocks near York Harbour, Newfoundland: Canadian Jour. Earth Sci., v. 11, p. 53–69.

Dymond, J., Corliss, J. B., Heath, J. R., Field, C. W., Dasch, E. J., and Veeh, H. H., 1973, Origin of metalliferous sediments from the Pacific Ocean: Geol. Soc. America Bull. v. 84, p. 3355–3372.

Edmond, J. M., Gordon, L. I., and Corliss, J. B., 1977, Chemistry of the hot springs on the Galapagos ridge axis [abs.]: Am. Geophys. Union Trans., v. 58, p. 1176.

Elder, J. W., 1965, Physical processes in geothermal areas, *in* Lee, W. H. K., ed., Terrestrial heat flow: Am. Geophys. Union, Geophys. Mon. Ser., v. 8, p. 211–239.

Engel, A. E. J., Engel, C. G., and Havens, R. G., 1965, Chemical characteristics of oceanic basalts and the upper mantle: Geol. Soc. America Bull., v. 76, p. 719–734.

Erickson, A. J., and Simmons, G., 1969, Thermal measurements in the Red Sea hot brine pools, *in* Degens, E. T., and Ross, D. A., eds., Hot brines and recent heavy metal deposits in the Red Sea: New York, Springer-Verlag, p. 114–121.

Ewing, J., 1969, Seismic model of the Atlantic Ocean, *in* Hart, P., ed., The Earth's crust and upper mantle: Washington, Am. Geophys. Union, Upper Mantle Proj. Sci. Rept. 21, p. 220–225.

Ferrara, G., Innocenti, F., Ricci, C. A., and Serri, G., 1976, Ocean-floor affinity of basalts from North Apennine ophiolites: Geochemical evidence: Chem. Geology, v. 17, p. 101–111.

Fox, P. J., and Opdyke, N. D., 1973, Geology of the oceanic crust: Magnetic properties of oceanic rocks: Jour. Geophys. Research, v. 78, p. 5139–5154.

Francis, T. J. G., 1968, The detailed seismicity of mid-oceanic ridges: Earth Planet. Sci. Letters, v. 4, p. 39–46.

Garson, M. S., and Krs, M., 1976, Geophysical and geological evidence of the relationship of Red Sea transverse tectonics to ancient fractures: Geol. Soc. America Bull., v. 87, p. 169–181.

Girdler, R. W., 1970, A review of Red Sea heat flow: Royal Soc. [London] Philos. Trans., A, v. 267, p. 191–203.

Goodfellow, W. D., 1975, Major and minor elements halos in volcanic rocks at Brunswick No. 12 sulfide deposit, N.B., Canada, *in* Elliott, I. L., and Fletcher, W. K. eds., Geochemical exploration 1974, 5th Internat. Geochem. Exploration Symposium: Amsterdam, Elsevier Sci. Pub. Co., p. 279–295.

Govett, G. J. S., and Pantazis, Th. M., 1971, Distribution of Cu, Zn, Ni and Co in the Troodos pillow lavas series, Cyprus: Inst. Mining Metallurgy Trans., v. 80, sec. B, p. B27–46.

Hajash, A., 1975, Hydrothermal processes along mid-ocean ridges: An experimental investigation: Contrib. Mineralogy Petrology, v. 53, p. 205–226.

Halbouty, M. T., Meyerhoff, A. A., King, R. E., Dott, R. H., Sr., Klemme, H. D., and Shabad, T., 1970, World's giant oil and gas fields, geologic factors affecting their formation, and basin classification, *in* Halbouty, M.T., ed., Geology of giant petroleum fields: Am. Assoc. Petroleum Geologists Mem. 14, p. 502–555.

Hanor, J. S., 1966, The origin of barite: Unpub. Ph.D. thesis, Harvard Univ.

Hart, R. A., 1973, A model for chemical exchange in the basalt-seawater system of oceanic layer II: Canadian Jour. Earth Sci., v. 10, p. 799–816.

Hawkins, D. B., and Roy, R., 1963, Experimental hydrothermal studies on rock alteration and clay mineral formation: Geochim. et Cosmochim. Acta, v. 27, p. 1047–1054.

Helgeson, H. C., 1964, Complexing and hydrothermal ore deposition: New York, Pergamon Press, 128 p.

—— 1967, Solution chemistry and metamorphism, *in* Abelson, P. H., ed., Researches in geochemistry: New York, John Wiley and Sons, p. 362–404.

—— 1968, Evaluation of irreversible reactions in geochemical processes involving minerals and aqueous solutions—I. Thermodynamic relations: Geochim. et Cosmochim. Acta, v. 32, p. 853–877.

—— 1969, Thermodynamics of hydrothermal systems at elevated temperatures and pressures: Am. Jour. Sci., v. 267, p. 729–804.

Helgeson, H. C., Garrels, R. M., and MacKenzie, R. T., 1969, Evaluation of irreversible reactions in geochemical processes involving minerals and aqueous solutions—II. Applications: Geochim. et Cosmochim. Acta, v. 33, p. 455–482.

Henderson, J. R., White, B. L., and others, 1963, Aeromagnetic map of Long Valley and northern Owens Valley, California: U. S. Geol. Survey Geophys. Inv. Map GP-329.

Hendricks, R. L., Reisbeck, F. B., Mahaffey, E. J., Roberts, D. B., and Peterson, M. N. A., 1969, Chemical composition of sediments and interstitial brines from the Atlantis II, Discovery, and Chain Deeps, *in* Degens, E. T., and Ross, D. A., eds., Hot brines and recent heavy metal deposits of the Red Sea: New York, Springer-Verlag, p. 407–440.

Holland, H. D., 1967, Gangue minerals in hydrothermal systems, *in* Barnes, H. L., ed., Geochemistry of hydrothermal ore deposits: New York, Holt, Rinehart and Winston, p. 382–436.

Horowitz, A., and Cronan, D. S., 1976, The geochemistry of basal sediments from the North Atlantic Ocean: Marine Geology, v. 20, p. 205–228.

Hunt, J. M., Hayes, E. E., Degens, E. T., and Ross, D. A., 1967, Red Sea: Detailed survey of hot-brine areas: Science, v. 156, p. 514–516.

Hutchinson, R. W., 1973, Volcanogenic sulfide deposits and their metallogenic significance: Econ. Geol., v. 68, p. 1223–1246

Irving, E., Park, J. K., Haggerty, S. E., Aumento, F., and Loncarevic, B., 1970a, Magnetism and opaque mineralogy of basalts from the Mid-Atlantic Ridge at 45°N: Nature, v. 228, p. 974–976.

Irving, E., Robertson, W. A., and Aumento, F., 1970b, The Mid-Atlantic Ridge near 45°N, 6, Remanent intensity, susceptibility, and iron content of dredged samples: Canadian Jour. Earth Sci., v. 7, p. 1–13.

Jarzabek, D., and Combs, J., 1976, Microearthquake survey of the Dunes KGRA, Imperial Valley, Southern California [abs.]: Geol. Soc. America, Abstracts with Programs, v. 8, p. 939.

Jenkins, W. J., and Clarke, W B., 1976, The distribution of ^{3}He in the western Atlantic Ocean: Deep-Sea Research, v. 23, p. 481–494.

Jenkins, W. J. Beg, M. A., Clarke, W. B., Wangersky, P. J., and Gray, H., 1972, Excess ^{3}He in the Atlantic Ocean: Earth Planet. Sci. Letters, v. 16, p. 122–126.

Johnson, D. M., and Combs, J., 1976, Microearthquake survey of the Kilbourne Hole KGRA, south central New Mexico [abs.]: Geol. Soc. America, Abstracts with Programs, v. 8, p. 942.

Kappelmeyer, O., and Haenel, R., 1974, Geothermics with special reference to application: Berlin, Gebruder Borntraeger, Geoexploration Monographs, ser. 1, no. 4, 238 p.

Karig, D. E., 1971, Origin and development of marginal basins in the western Pacific: Jour. Geophys. Research, v. 76, p. 2542–2561.

Keays, R. R., and Scott, R. B., 1976, Precious metals in ocean-ridge basalts: Implications for basalt as source rocks for gold mineralization: Econ. Geol., v. 71, p. 705–720.

Kelley, V. C., and Soske, J. L., 1936, Origin of the Salton volcanic domes, Salton Sea, California: Jour. Geology, v. 44, p. 496–509.

Kirst, P. W., 1976, Petrology of metamorphic rocks from the Mid-Atlantic Ridge and fracture zones: Unpub. Ph.D. thesis, Univ. Miami.

Klein, F. W., Einarsson, P., and Wyss, M., 1973, Microearthquakes on the Mid-Atlantic plate boundary on the Reykjanes Peninsula in Iceland: Jour. Geophys. Research, v. 78, p. 5084–5099.

Koenig, J. B., 1967, The Salton-Mexicali geothermal province: California Div. Mines Geology, Mineral Inf. Service, v. 20, p. 75–81.

Krauskopf, K. B., 1956, Factors controlling the concentrations of thirteen rare metals in seawater: Geochim. et Cosmochim. Acta, v. 9, p. 1-32B.

—— 1957, Separation of maganese from iron in sedimentary processes: Geochim. et Cosmochim. Acta, v. 12, p. 61–84.

Kutina, J., 1974, Structural control of volcanic ore deposits in the context of global tectonics: Bull. volcanol., v. 38, p. 1039–1069.

Langseth, M. G., and Von Herzen, R. P., 1971, Heat flow through the floor of the world oceans, *in* Maxwell, A. E., ed., The sea,: New York, Wiley-Interscience, v. 4, part 1, p. 299–352.

Lister, C. R. B., 1972, On the thermal balance of an oceanic ridge: Royal Astron. Soc. Geophys. Jour., v. 26, p. 515–535.

—— 1974a, On the penetration of water into hot rocks: Royal Astron. Soc. Geophys. Jour., v. 39, p. 465–509.

—— 1974b, Water percolation in the oceanic crust: Am. Geophys. Union Trans., v. 55, p. 740–742.

Lonsdale, P., 1977a, Clustering of suspension-feeding macrobenthos near abyssal hydrothermal vents at oceanic spreading centers: Deep-Sea Research, v. 24, p. 857–863.

—— 1977b, Deep-tow observations at the Mounds Abyssal Hydrothermal Field, Galapagos Rift: Earth Planet. Sci. Letters, v. 36, p. 92–110.

Lowell, R. P., and Rona, P. A., 1976, On the interpretation of near-bottom water temperature anomalies: Earth Planet. Sci. Letters, v. 32, p. 18–24.

Lupton, J. E., Weiss, R. F., and Craig, H., 1977a, Mantle helium in the Red Sea brines: Nature, v. 266, p. 244–246.

—— 1977b, Mantle helium in hydrothermal plumes in the Galapagos Rift: Nature, v. 267, p. 603–604.

Luyendyk, B. P., and Melson, W. G., 1967, Magnetic properties and petrology of rocks near the crest of the Mid-Atlantic Ridge: Nature, v. 215, p. 147–149.

Lyle, M., Dymond, J., and Heath, G. R., 1977, Copper-nickel-enriched ferromanganese nodules and associated crusts from the Bauer Basin, northwest Nazcas plate: Earth Planet. Sci. Letters, v. 35, p. 55–64.

McGregor, B. A., and Rona, P. A., 1975, Crest of Mid-Atlantic Ridge at 26°N: Jour. Geophys. Research, v. 80, p. 3307–3314.

McGregor, B. A., Harrison, C. G. A., Lavelle, J. W., and Rona, P. A., 1977, Magnetic anomaly pattern on Mid-Atlantic Ridge crest at 26°N: Jour. Geophys. Research, v. 82, p. 231–238.

McNitt, J. R., 1965, Review of geothermal resources, *in* Lee, H. K., ed., Terrestrial heat flow: Am. Geophys. Union, Geophys. Mon. Ser. 8, p. 240–266.

Mahon, W. A. F., 1966, Silica in hot water discharged from drill holes at Wairakei, New Zealand: New Zealand Jour. Sci., v. 9, p. 135–144.

Makharadze, A. I., and Ikoshvili, D. V., 1970, On barite from the Chiatur manganese deposit: Akad. Nauk SSSR Doklady, v. 190, p. 1204–1206 (in Russian).

Marchesini, E., Pistolesi, A., and Bolognini, M., 1962, Fracture patterns of the natural steam area of Larderello, Italy, from air photographs: Symposium on Photo Interpretation, Delft 1962, p. 524–532.

Marshall, M., and Cox, A., 1972, Magnetic changes in pillow basalt due to sea floor weathering: Jour. Geophys. Research, v. 77, p. 6459–6469.

Melson, W. G., Thompson, G., and van Andel, T. H., 1968, Volcanism and metamorphism in the Mid-Atlantic Ridge, 22° N: Jour. Geophys. Research, v. 73, p. 5925–5941.

Menard, H. W., 1967, Sea floor spreading, topography, and the second layer: Science, v. 157, p. 923–924.

Miller, A. R., Densmore, C. D., Degens, E. T., Hathaway, J. C., Manheim, F. T., McFarlin, P. F., Pocklington, H., and Jokela, A., 1966, Hot brines and recent iron deposits in deep of the Red Sea: Geochim. et Cosmochim. Acta, v. 30, p. 341–359.

Mitchell, A. H., and Bell, J. D., 1973, Island-arc evolution and related mineral deposits: Jour. Geology, v. 81, p. 381–405.

Mitchell, A. H., and Grason, M. S., 1976, Mineralization at plate boundaries: Minerals Sci. Eng., v. 8, no. 2, p. 129–169.

Miyashiro, A., 1973, The Troodos ophiolitic complex was probably formed in an island arc: Earth Planet. Sci. Letters, v. 19, p. 218–224.

—— 1975, Classification, characteristics, and origin of ophiolites: Jour. Geology, v. 83, p. 249–281.

Miyashiro, A., and Shido, F., 1970, Progressive metamorphism in zeolite assemblages: Lithos, v. 3, p. 251–260.

Miyashiro, A., Shido, F., and Ewing, M., 1971, Metamorphism in the Mid-Atlantic Ridge near 24° and 30° N: Royal Soc. [London] Philos. Trans., v. 268, p. 589–603.

Moore, J. G., and Calk, L., 1971, Sulfide spherules in vesicles of dredged pillow basalt: Am. Mineralogist, v. 56, p. 476–488.

Moore, J. G., and Schilling, J. G., 1973, Vesicles water and sulfur in Reykjanes Ridge basalt: Contr. Mineralogy Petrology, v. 41, p. 105–118.

Moore, W. S., and Vogt, P. G., 1976, Hydrothermal manganese crusts from two sites near the Galapagos spreading axis: Earth Planet. Sci. Letters, v. 29, p. 349–356.

Moores, E. M., and Vine, F. J., 1971, The Troodos Massif, Cyprus and other ophiolites as oceanic crust: Evaluation and implications: Royal Soc. [London] Philos. Trans., A, v. 268, p. 443–466.

Mottl, M. J., Corr, R. F., and Holland, H. D., 1974, Chemical exchange between sea water and mid-ocean ridge basalt during hydrothermal alteration: An experimental study [abs.]: Geol. Soc. America, Abstracts with Programs, v. 6, p. 879–880.

Muehlenbachs, K., and Clayton, R. H., 1972, Oxygen isotope geochemistry of submarine greenstones: Canadian Jour. Earth Sci., v. 9, p. 471–478.

Nebrija, E. L., Young, C. T., Meyer, R. P., and Moore, J. R., 1976, Electrical prospecting for copper veins in shallow water: Offshore Technology Conf. Houston 1976, Paper OTC 2454, p. 319–327.

Nicholls, G. D., and Islam, M. R., 1971, Geochemical investigations of basalts and associated rocks from the ocean floor and their implications: Royal Soc. [London] Philos. Trans., A, v. 268, p. 469–486.

Ostapoff, F., 1969, A fourth brine hole in the Red Sea?, *in* Degens, E. T., and Ross, D. A., eds., Hot brines and recent heavy metal deposits in the Red Sea: New York, Springer-Verlag, p. 18–24.

Palmason, G., 1967, On heat flow in Iceland in relation to the Mid-Atlantic Ridge, *in* Björnsson, S., ed., Iceland and mid-ocean ridges: Soc. Sci. Islandica, v. 38, p. 111–127.

Patella, D., and Schiavone, D., 1974, A theoretical study of the kernel function for resistivity prospecting with a Schlumberger apparatus in water: Annali di Geofisica, v. 28, p. 295–313.

Pereira, J., and Dixon, C. J., 1971, Mineralization and plate tectonics: Mineralium Deposita, v. 6, p. 404–405.

Peters, T., and Kramers, J. D., 1974, Chromite deposits in the ophiolite complex of Northern Oman: Mineralium Deposita, v. 9, p. 253–259.

Peterson, J. J., Fox, P. J., and Schreiber, E., 1974, Newfoundland ophiolites and the geology of the oceanic layer: Nature, v. 247, p. 194–196.

Phillips, J. D., Woodside, J., and Bowin, C. O., 1969, Magnetic and gravity anomalies in the central Red Sea, *in* Degens, E. T., and Ross, D. A., eds., Hot brines and recent heavy metal deposits in the Red Sea: New York, Springer-Verlag, p. 98–113.

Pugh, D. T., 1969, Temperature measurements in the bottom layers of the Red Sea brines, *in* Degens, E. T., and Ross, D. A., eds., Hot brines and recent heavy metal deposits in the Red Sea: New York, Springer-Verlag, p. 158–163.

Quillan, R., and Combs, J., 1976, Microearthquake survey of the Radium Springs KGRA, south central New Mexico [abs.]: Geol. Soc. America, Abstracts with Programs, v. 8, p. 1055.

Rona, P. A., 1969, Possible salt domes in the deep Atlantic off northwest Africa: Nature, v. 224, p. 141–143.

—— 1970, Comparison of continental margins of eastern North America at Cape Hatteras and northwestern Africa at Cap Blanc: Am. Assoc. Petroleum Geologists Bull., v. 54, p. 129–157.

—— 1976a, Criteria for recognition of sea floor hydrothermal mineral deposits: Am. Geophys. Union Trans., v. 57, p. 593.

—— 1976b, Pattern of hydrothermal mineral deposition: Mid-Atlantic Ridge crest at latitude 26°N: Marine Geology, v. 21, p. M59–M66.

—— 1977, Plate tectonics, energy and mineral resources: Basic research leading to payoff: Am. Geophys. Union Trans., v. 58, p. 629–639.

—— 1978, Magnetic signatures of hydrothermal alteration and volcanogenic mineral deposits in oceanic crust: Jour. Volcanology Geothermal Research, v. 3 (in press).

Rona, P. A., McGregor, B. A., Betzer, P. R., Bolger, G. W., and Krause, D. C., 1975, Anomalous water temperatures over the Mid-Atlantic Ridge crest at 26°N latitude: Deep-Sea Research, v. 22, p. 611–618.

Rona, P. A., Harbison, R. N., Bassinger, B. G., Scott, R. B., and Nalwalk, A. J., 1976, Tectonic fabric and hydrothermal activity of Mid-Atlantic Ridge crest (lat. 26°N): Geol. Soc. America Bull., v. 87, p. 661–674.

Ross, D. A., 1972, Red Sea hot brine area: Revisited: Science, v. 175, p. 1455–1457.

Ross, D. A., Hays, E. E., and Allstrom, F. C., 1969, Bathymetry and continuous seismic profiles of the hot brine region of the Red Sea, *in* Degens, E. T., and Ross, D. A., eds., Hot brines and recent heavy metal deposits in the Red Sea: New York, Springer-Verlag, p. 82–97.

Ryan, W. B. F., Thorndike, E. M., Ewing, M., and Ross, D. A., 1969, Suspended matter in the Red Sea brines and its detection by light scattering, *in* Degens, E. T., and Ross, D. A., eds., Hot brines and recent heavy mineral deposits of the Red Sea: New York, Springer-Verlag, p. 153–157.

Rydell, H. S., and Bonatti, E., 1973, Uranium in submarine metalliferous deposits: Geochim. et Cosmochim Acta, v. 37, p. 2557–2565.

Sato, M., and Mooney, H. M., 1960, The electrochemical mechanism of sulfide self-potentials: Geophysics, v. 25, p. 226–249.

Sayles, F. L., and Bischoff, J. L., 1973, Ferromanganoan sediments in the equatorial East Pacific: Earth Planet. Sci. Letters, v. 19, p. 330–336.

Scientific Staff, 1974, Leg 34 Oceanic basalt and the Nazca Plate: Geotimes, v. 19, p. 20–24.

Sclater, J. G., Von Herzen, R. P., Williams, D. L., Anderson, R. N., and Klitgord, K., 1974, The Galapagos spreading center: Heat-flow low on the north flank: Royal Astron. Soc. Geophys. Jour., v. 38, p. 609–626.

Scott, M. R., 1976, Accumulation rates of metals along active ocean ridges [abs.]: Joint Oceanographic Assembly, Edinburgh, Scotland 1976, Abstracts, p. 94.

—— 1977, Metal accumulation rates in sediments from the FAMOUS area on the Mid-Atlantic Ridge [abs.]: Am. Geophys. Union Trans., v. 58, p. 420.

Scott, M. R., Scott, R. B., Rona, P. A., Butler, L. W., and Nalwalk, A. J., 1974, Rapidly accumulating manganese deposit from the median valley of the Mid-Atlantic Ridge: Geophys. Research Letters, v. 1, p. 355–358.

Searle, D. L., 1972, Mode of occurrence of the cupiferous pyrite deposits of Cyprus: Inst. Mining Metallurgy Trans., v. 81, sec. B, p. B189–B197.

SEG, 1966, Mining geophysics, v. 1, case histories: Tulsa, Oklahoma, Soc. Exploration Geophysicists, 492 p.

Sigvaldason, G. E., 1962, Epidote and related minerals in two deep geothermal drill holes, Reykjavík and Hveragerdi, Iceland: U. S. Geol. Survey Prof. Paper 450-E, p. 77–79.

Sillitoe, R. H., 1972, Formation of certain massive sulphide deposits at sites of sea-floor spreading: Inst. Mining Metallurgy Trans., sec. B, v. 81, p. B141–148.

—— 1973, Environments of formation of volcanogenic massive sulfide deposits: Econ. Geol., v. 68, p. 1321–1325.

Spooner, E. T. C., and Fyfe, W. S., 1973, Subsea-floor metamorphism, heat and mass transfer: Contr. Mineralogy Petrology, v. 42, p. 287–304.

Spooner, E. T. C., Beckinsale, R.. D., Fyfe, W. S., and Smewing, J. D., 1974, O^{18} enriched ophiolitic metabasic rocks from E. Liguria (Italy), Pindos (Greece), and Troodos (Cyprus): Contr. Mineralogy Petrology, v. 47, p.. 41–62.

Steiner, A., 1967, Clay minerals in hydrothermally altered rocks at Wairakei, New Zealand: Clays Clay Minerals, v.. 16, p. 193–213.

Stephens, J. D., and Wittkopp, R. W., 1969, Microscopic and electron beam microscopic study of sulfide minerals in Red Sea mud samples, *in* Degens, E. T., and Ross, D. A., eds., Hot brines and recent heavy metal deposits of the Red Sea: New York, Springer-Verlag, p. 441–447.

Strong, D. F., 1974a, Plate tectonic setting of Newfoundland mineral occurrences, *in* Strong, D. F., ed., Metallogeny and plate tectonics, a guidebook to Newfoundland mineral deposits: St. John's, Newfoundland, NATO Adv. Studies Inst., p. 3–27.

—— 1974b, An "off-axis" alkali volcanic suite associated with the Bay of Islands ophiolites, Newfoundland: Earth Planet. Sci. Letters, v. 21, p. 301–309.

Studt, F. E., 1959, Magnetic survey of the Wairakei hydrothermal field: New Zealand Jour. Geology Geophysics, v. 2, p. 746–754.

—— 1961, Preliminary survey of the hydrothermal field at Rabaul, New Britain: New Zealand Jour. Geology Geophysics, v. 4, p. 274–282.

Swallow, J. C., 1969, History of the exploration of the hot brine area of the Red Sea—DISCOVERY account, *in* Degens, E. T., and Ross, D. A., eds., Hot brines and recent heavy metal deposits in the Red Sea: New York, Springer-Verlag, p. 3–9.

Sykes, L. R., 1970, Earthquake swarms and sea-floor spreading: Jour. Geophys. Research, v. 75, p. 6598–6611.

Talwani, M., Windish, C. C., and Langseth, M. G., Jr., 1971, Reykjanes Ridge crest: A detailed geophysical study: Jour. Geophys. Research, v. 76, p. 473–517.

Thompson, G., Woo, C. C., and Sung, W., 1975, Metalliferous deposits on the Mid-Atlantic Ridge [abs.]: Geol. Soc. America, Abstracts with Programs, v. 7, p. 1297–1298.

Tómasson, J., and Kristmannsdóttir, H., 1972, High temperature alteration minerals and thermal brines, Reykjanes, Iceland: Contr. Mineralogy Petrology, v. 36, p. 123–134.

Turner, J. S., 1969, A physical interpretation of the observations of hot brine layers in the Red Sea, *in* Degens, E. T., and Ross, D. A., eds., Hot brines and recent heavy metal deposits in the Red Sea: New York, Springer-Verlag, p. 164–173.

United Nations, 1976, United Nations Symposium on the Development and Use of Geothermal Resources, 2nd, San Francisco, May 1975: Washington, U. S. Govt. Printing Office, Proceedings, 3 vols., p. 1–2457.

Upadhyay, H. D., and Strong, D. F., 1973, Geological setting of the Betts Cove copper deposits, Newfoundland: An example of ophiolite sulfide mineralization: Econ. Geol., v. 68, p. 161–167.

Veeh, H. H., and Boström, K., 1971, Anomalous $^{234}U/^{238}U$ on the East Pacific Rise: Earth Planet. Sci. Letters, v. 10, p. 372–374.

Von Herzen, R., Green, K. E., and Williams, D., 1977, Hydrothermal circulation at the Galapagos spreading center [abs.]: Geol. Soc. America, Abstracts with Programs, v. 9, p. 1212–1213.

Walker, G. P. L., 1960, Zeolite zones and dike distribution in relation to the structure of the basalts of eastern Iceland: Jour. Geology, v. 68, p. 515–528.

Ward, P. L., and Björnsson, S., 1971, Microearthquakes, swarms, and the geothermal areas of Iceland: Jour. Geophys. Research, v. 76, p. 3953–3982.

Ward, P. L., Pálmason, G., and Drake, C., 1969, Microearthquake survey and the Mid-Atlantic Ridge in Iceland: Jour. Geophys. Research, v. 74, p. 665–684.

Watkins, N. D., and Paster, T. P., 1971, The magnetic properties of igneous rocks from the ocean floor: Royal Soc. [London] Philos. Trans., A., v. 268, p. 507–550.

Watson, S. W., and Waterbury, J. B., 1969, The sterile hot brines of the Red Sea, *in* Degens, E. T., and Ross, D. A., eds., Hot brines and recent heavy metal deposits in the Red Sea: New York, Springer-Verlag, p. 272–281.

Weiss, R. F., Lonsdale, P., Lupton, J. E., Bainbridge, A. E., and Craig, H., 1977, Hydrothermal plumes in the Galapagos Rift: Nature, v. 267, p. 600–603.

Whiteley, R. G., 1974, Design and preliminary testing of a continuous offshore resistivity method: Australian Soc. Explor. Geophysicists Bull., v. 5, p. 9–13.

Williams, D. L., and Von Herzen, R. P., 1974, Heat loss from the Earth: New estimate: Geology, v. 2, p. 327–328.

Williams, D. L., Von Herzen, R. P., Sclater, J. G., and Anderson, R. N., 1974, The Galapagos spreading center: Lithospheric cooling and hydrothermal circulation: Royal. Astron. Soc. Geophys. Jour., v. 38, p. 587–608.

Wilson, R. A. M., and Ingham, F. T., 1959, The geology of the Xeros-Troodos area, with an account of the mineral resources: Cyprus Geol. Survey Dept. Mem. 1, p. 1–177.

Woodli, R., ed., 1964, Methods of prospecting for chromite: Paris, Organization Econ. Coop. Development, 200 p.

Geophysical Research Letters 5, No. 12, 993-996.

NEAR BOTTOM WATER TEMPERATURE ANOMALIES: MID-ATLANTIC RIDGE CREST AT LATITUDE 26°N

Peter A. Rona

National Oceanic and Atmospheric Administration, Atlantic Oceanographic and
Meteorological Laboratories, 15 Rickenbacker Causeway, Miami, Florida 33149

Abstract. Six water temperature anomalies were measured along two profiles each about 10 km in length at the TAG Hydrothermal Field on the east wall of the rift valley of the Mid-Atlantic Ridge at latitude 26°N. The temperature anomalies were measured using a 3 m-long vertical array of four thermistors towed within 20 m of the ocean bottom. The anomalies exhibit increases in potential temperature up to 0.127°C above ambient and inverse gradients warming downwards as great as 4.2×10^{-2}°C m^{-1}. The temperature anomalies are distributed as point sources in a linear pattern about 7 km in length along known fault zones in the east wall of the rift valley between depths of 2750 and 3200 m below sea level associated with hydrothermal mineral deposits. The characteristics of the temperature anomalies and their geologic setting indicate an origin by discharge of hydrothermal solutions through the faults in the rift valley wall. The magnitudes of the anomalies are consistent with values previously used to estimate a heat output of the order of several megawatts per kilometer of ridge at the TAG Hydrothermal Field.

Introduction

Hydrothermal convection accounts for an estimated 80 per cent of the heat loss from lithospheric cooling at oceanic spreading centers and 20 per cent of the earth's total heat loss of 10.2×10^{12} cal s^{-1} [Williams and Von Herzen, 1974]. In spite of the large convective heat loss, it has proven difficult to directly measure temperatures of the discharge fluid because hydrothermal vents are extremely localized and heat dissipates rapidly in unrestricted oceanic circulation at spreading centers. Only a few temperature anomalies attributed to hydrothermal discharge have been measured in the water column. The measurements have been made either with single temperature sensors incorporated in a CTD (conductivity, temperature, depth) instrument, or with multiple temperature sensors mounted in a vertical array. When single sensor CTD instruments have been used, concurrent temperature and salinity measurements are needed to distinguish between a water temperature increase due to downward mixing of a warmer overlying water mass with a particular T-S (temperature-salinity) relation, and upward discharge of a buoyant hydrothermal fluid with a distinct T-S relation. An example of the application of the single sensor method is a potential temperature anomaly of 0.18°C measured about 10 m above the ocean bottom at the Galapagos Rift [Weiss et al., 1977].

Concurrent salinity measurements are unnecessary with a vertical array of temperature sensors because water temperature gradients are obtained. Normal gradients (temperature anomaly absent) at a depth of several kilometers are nearly neutral over a vertical distance of several meters. Downward mixing of a warmer overlying water mass generally would exhibit a potential temperature gradient cooling downwards; upward discharge of a buoyant hydrothermal fluid would exhibit a strong inverse potential temperature gradient warming downward. An example of the application of the multiple sensor method is a potential temperature anomaly of 0.10°C with an inverse gradient of 1.4×10^{-2}°C m^{-1} measured about 10 m above the ocean bottom at the TAG Hydrothermal Field on the Mid-Atlantic Ridge crest at latitude 26°N [Rona et al., 1975; X in Table 1]. The present paper reports additional near bottom water temperature anomalies attributed to hydrothermal discharge at the TAG Hydrothermal Field. The anomalies form a linear pattern controlled by the underlying geologic structure (Figure 1).

Method

A near bottom water temperature measurement system like that used by Rona et al. [1975] consisted of a thermoprobe recorder (modified Alpine model 323), four thermistor temperature probes (Fenwall part number K2365), and an acoustic pinger (EG&G model 220) mounted on a frame for towing. The thermistors were mounted at heights of 0, 1, 2, and 3 m above the base of the frame and recorded sequentially (Table 1) with an accuracy of ±0.01°C and precision of ±0.004°C. The thermistor array was towed within 20 m of the ocean bottom determined to an accuracy of 2 m by the acoustic pinger. Distance of the array off the bottom was maintained by adjusting the length of towing cable by means of a hydraulic winch; length of cable out and surface angles (vertical and horizontal) of the cable were logged. Ship's speed was 58 m min^{-1} for profile 1 (Figure 2) and 45 m min^{-1} for profile 2 (Figure 3) determined by satellite navigation. A narrow beam bathymetric profile (6° total beam width equivalent to a 400 m diameter area ensonified at 3 km depth) was continuously recorded from the ship. Depth below sea level of the thermistor array was determined to an estimated accuracy within ±100 m (corresponding uncertainty in computation of potential temperature 0.01°C), by determining the position of the array relative to the ship from length, surface angles and calculated catenary of the towing cable, and relating that position both to the narrow beam bathymetric profile along the ship's track and a detailed narrow beam bathymetric map of the area. In addition, the depths were checked by fitting the temperature curves to the bathymetric profile based on the general inverse relation between water temperature and ocean depth, which is apparent in Figures 2 and 3.

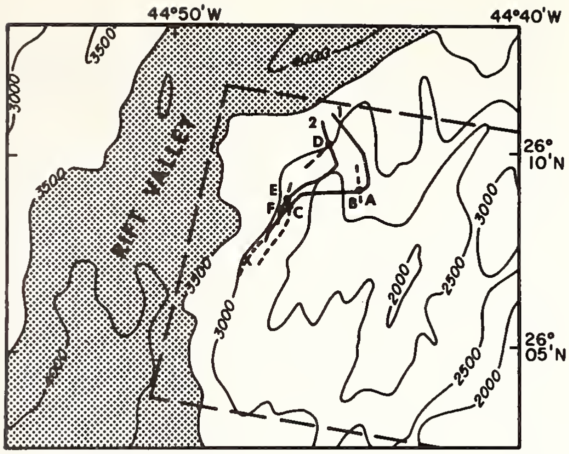

Fig. 1. Narrow beam bathymetry of Mid-Atlantic Ridge crest (500 m isobath interval; Rona et al., 1976) showing the rift valley (shaded), the TAG Hydrothermal Field (dashed rectangle), ship's tracks along temperature profiles 1 and 2 (solid lines), positions of measured potential temperature anomalies A - F (dots), the position of a previously measured temperature anomaly (X; Rona et al., 1975), and linear fault zones (dashed lines) on the east wall of the rift valley.

A water temperature anomaly attributed to hydrothermal discharge is characterized by an increase in potential temperature above ambient and by an inverse gradient of potential temperature warming downwards (Table 1). The increase in water temperature above ambient is defined as the difference between the temperature high at the anomaly and the adjacent ambient temperature recorded on the lowermost thermistor of the vertical array of thermistor temperature probes. The temperature gradient is defined as the difference in temperature between the uppermost and lowermost thermistors, averaged over the length of the array. Where a water temperature anomaly is wide (≥100 m) and persistent relative to distance traversed at a given ship's speed during the recording sequence between uppermost and lowermost thermistors (87 s; Table 1), a complete inverse gradient warming downwards is recorded. Where a water temperature anomaly is narrow (<100 m) or transient relative to distance traversed during the recording sequence between uppermost and lowermost thermistors, an incomplete gradient may be recorded, because the highest temperature may be recorded on other than the lowermost thermistor.

Results

Two water temperature profiles were made on consecutive days in June 1977 at the northern end of the TAG Hydrothermal Field (Figure 1). The TAG Hydrothermal Field occupies a topographic high that forms the east wall of the rift valley (Figure 1; Rona et al., 1976). Profile 1 begins on the northern end of the topographic high, crosses a ridge on the topographic high (5 to 7 km along profile 1; Figure 2), and then runs subparallel to isobaths along the east wall of the rift valley (7 to 10 km along profile 1; Figure 2). Profile 2 also begins on the northern end of the topographic high, obliquely crosses a portion of the ridge on the topographic high (3 to 6 km along profile 2; Figure 3), and then runs subparallel to isobaths along the east wall of the rift valley (6 to 8 km along profile 2; Figure 3).

Temperature profile 1 exhibits three distinct potential temperature anomalies (A, B, C; Figures 1, 2) and a number of other temperature variations. The broad increase in water temperature between 2.5 and 8.5 km along profile 1 results from raising the thermistor array over the topographic high present (Figure 2). The intermediate width variations in water temperature centered at 2.2, 6.0 and 8.0 km along profile 1 are attributed to shorter duration vertical excursions of the thermistor array, evidenced by uniform temperature changes on all four thermistors corresponding to logged variations in length of towing cable out. The narrow temperature fluctuations of the order of 0.01°C, lacking distinctive gradients, such as those at 1.8 and 7.0 km, are considered uninterpretable in light of data limitations.

The three distinct potential temperature anomalies present on profile 1 exhibit increases in water temperature between 0.072 and 0.127°C above ambient and strong inverse temperature gradients between 2.8 and 4.2 x 10^{-2}°C m^{-1} (Figure 2; Table 1). The inverse gradients are complete, indicating that the water temperature anomalies measured were wide (≥100 m) and persistent relative to the duration of the thermistor recording sequence. All these anomalies occur at or near the bases of topographic scarps on the east wall of the rift valley between water depths of 2750 and 2830 m (Figure 2).

Temperature profile 2 exhibits three less distinct potential temperature anomalies (D, E, F; Figures 1, 3) and a number of other temperature variations similar to those observed in profile 1. A broad increase in water temperature between 4 and 7 km along profile 2 corresponds to raising the thermistor array over a portion of the topographic high present (Figure 3). The intermediate width temperature variations centered at 1.5 and 5.0 km along profile 2 are attributed to shorter duration vertical excursions of the array evidenced by uniform temperature changes on all four thermistors corresponding to logged variations in length of cable out. The narrower temperature fluctuations on the order of 0.01°C, lacking distinctive gradients, such as those at 5.5 km, are considered uninterpretable.

The three less distinct potential temperature anomalies on profile 2 exhibit increases in water temperature between 0.031 and 0.051°C above ambient and weak inverse gradients (Figure 3; Table 1). The anomalies are inferred to be narrow (<100 m) or transient relative to the duration of the thermistor recording sequence from the presence of incomplete gradients with highest temperatures recorded on other than the lowermost thermistor in all three cases. The three anomalies of profile 2 occur at or near the bases of scarps on the east wall of the rift valley between depths of 2690 and 3125 m below sea level. Anomaly E of profile 2 occurs within 0.5 km of anomaly C of profile 1 (Figure 1) at a deeper point along what appears to be the same scarp (Figures 2, 3; Table 1).

Table 1. Potential temperature anomalies (Figs. 1-3)

Potential Temperature Anomaly	Time (GMT)	Potential temperature (°C) Thermistor number (Figs. 2, 3) 1 Time sequence (s) 0-30	 2 30-45	 45-60	 3 60-90	 90-105	 4 105-120	Increase in water temperature above ambient (°C)	Temperature gradient (+ normal; - inverse) (°C m^{-1})	Height of lowermost thermistor above bottom (m)	Depth below sea level (m)	Physiographic feature
	1709	Ref	2.762	2.765	Ref	2.764	2.768		-0.002	5 - 15	2765	
	1711	Ref	2.755	2.769	Ref	2.760	2.783		-0.009	5 - 15	2765	
A	1713	Ref	2.766	2.784	Ref	2.854	2.866	0.083	-0.033	5 - 15	2765	scarp
	1715	Ref	2.766	2.776	Ref	2.756	2.764		-0.001	5 - 15	2770	
B	1717	Ref	2.751	2.788	Ref	2.790	2.836	0.072	-0.028	5 - 15	2750	scarp
	1719	Ref	2.778	2.788	Ref	2.791	2.802		-0.008	5 - 15	2650	
	1721	Ref	2.760	2.800	Ref	2.818	2.818		-0.019	5 - 15	2640	
	1814	Ref	2.798	2.801	Ref	2.792	2.796		+0.001	4 - 10	2820	
	1816	Ref	2.756	2.774	Ref	2.717	2.713		+0.014	4 - 10	2825	
C	1819	Ref	2.715	2.725	Ref	2.761	2.840	0.127	-0.042	4 - 10	2830	scarp
	1820	Ref	2.778	2.785	Ref	2.739	2.735		+0.014	4 - 10	2830	
	1822	Ref	2.726	2.740	Ref	2.724	2.732		-0.002	4 - 10	2830	
	1431	Ref	2.425	2.436	Ref	2.435	2.438		-0.004	15 - 20	3120	
	1433	Ref	2.423	2.437	Ref	2.440	2.439		-0.005	15 - 20	3120	
D	1435	Ref	2.424	2.442	Ref	2.481	2.470	0.031	*-0.015	15 - 20	3125	scarp
	1437	Ref	2.471	2.453	Ref	2.437	2.440		+0.010	15 - 20	3140	
	1439	Ref	2.427	2.434	Ref	2.441	2.444		-0.006	15 - 20	3140	
	1600	Ref	2.734	2.740	Ref	2.732	2.706		+0.009	12 - 20	2860	
	1602	Ref	2.684	2.687	Ref	2.597	2.605		+0.026	12 - 20	2870	
E	1604	Ref	2.597	2.604	Ref	2.577	2.606	0.028	*-0.003	12 - 20	2960	scarp
	1606	Ref	2.599	2.613	Ref	2.593	2.578		+0.007	12 - 20	2980	
	1608	Ref	2.564	2.574	Ref	2.573	2.573		-0.003	12 - 20	2995	
	1621	Ref	2.599	2.602	Ref	2.590	2.593		+0.002	5 - 12	3050	
	1623	Ref	2.584	2.591	Ref	2.586	2.593		-0.003	5 - 12	3050	
F	1625	Ref	2.625	2.636	Ref	2.616	2.627	0.051	*-0.001	5 - 12	3045	scarp
	1627	Ref	2.571	2.640	Ref	2.573	2.576		-0.002	5 - 12	3035	
	1629	Ref	2.613	2.631	Ref	2.656	2.656		-0.014	5 - 12	2980	
		0-22	22-44	44-110	110-132	132-154	154-180					
	1638	2.491	2.482	Ref	2.462	Ref	Ref		+0.009	2 - 20	3020	
	1641	2.484	2.470	Ref	2.464	Ref	Ref		+0.007	2 - 20	3005	
†X	1644	2.529	2.518	Ref	2.561	Ref	Ref	0.097	-0.014	2 - 20	2995	scarp
	1647	2.542	2.510	Ref	2.559	Ref	Ref		-0.006	2 - 20	2985	
	1650	2.603	2.599	Ref	2.574	Ref	Ref		+0.010	2 - 20	2970	
	1653	2.617	2.610	Ref	2.598	Ref	Ref		+0.006	2 - 20	2960	
	1656	2.615	2.599	Ref	2.469	Ref	Ref		+0.037	2 - 20	2945	

Ref = reference signal *Incomplete gradient †*Rona et al.*, 1975

Discussion

The oceanographic and geologic setting of the six potential temperature anomalies described within the TAG Hydrothermal Field has been the subject of considerable prior interdisciplinary study. Previous CTD profiles and hydrocasts to within 15 m of the ocean bottom at the TAG Hydro-

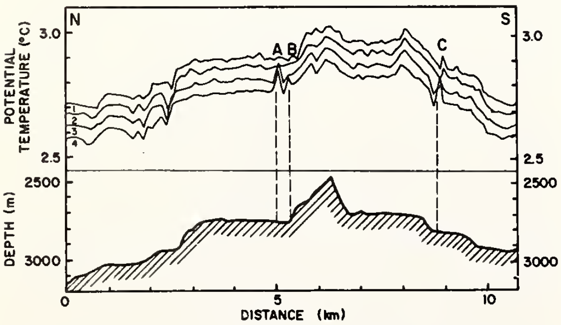

Fig. 2. Potential temperature profile 1 (Fig. 1) showing anomalies A, B, C on four thermistor traces (traces successively displaced 0.05°C above lowermost thermistor 4 to achieve vertical separation) and plot of concurrent narrow beam bathymetric profile.

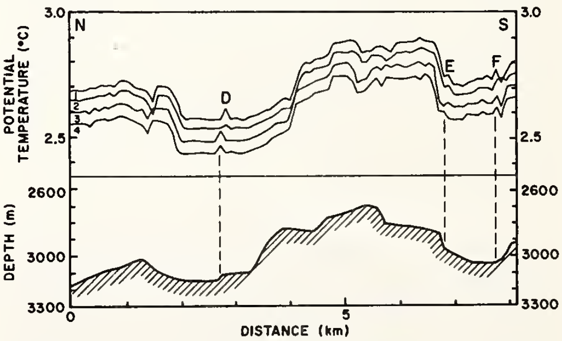

Fig. 3. Potential temperature profile 2 (Fig. 1) showing anomalies D, E, F on four thermistor traces (traces successively displaced 0.05°C above lowermost thermistor 4 to achieve vertical separation) and plot of concurrent narrow beam bathymetric profile.

thermal Field revealed the presence of subadiabatic temperature gradients and normal salinities [Rona et al., 1975]. Systematic narrow beam bathymetric, magnetic, bottom photographic and bottom sampling investigations in this area have revealed that the east wall of the rift valley consists of fault blocks with intervening fault zones topographically expressed as terraces separated by scarps [McGregor and Rona, 1975; Rona et al., 1976; Rona, 1976; Temple et al., 1979]. Three fault zones that trend subparallel to the rift valley between depths of 2750 and 3200 m on the east wall are the sites of most of the hydrothermal deposits (manganese oxide) thus far recovered from the TAG Hydrothermal Field. The hydrothermal manganese oxide occurs primarily as crusts on and matrix in breccias of altered basalt fragments that lie along the bases of the fault scarps. Compositional analysis of sediments sampled from the TAG Hydrothermal Field reveals anomalously high trace metal contents in the rift valley [M. R. Scott et al., 1978] and near the sites of temperature anomalies E, C and F [D. S. Cronan et al., unpublished manuscript, 1978; Figures 1-3]. Analysis of sea water sampled over the fault zones reveals anomalous concentrations of ^{3}He, indicative of hydrothermal discharge [Jenkins and Rona, unpublished manuscript, 1978].

Four of the six potential temperature anomalies measured in the present study (C, D, E, F; Figure 1; Table 1), and the one potential temperature anomaly previously measured (X; Figure 1; Table 1), lie along the known fault zones between depths of 2750 and 3200 m on the east wall of the rift valley. The remaining two anomalies (A, B; Figure 1; Table 1) lie at or near the base of a scarp which appears to express another fault zone within the same depth range. The inferred width ($\geq$100 m) of several of the anomalies (A, B, C; Figure 2) is related to discharge of hydrothermal solutions focused by the faults and diffused by a porous and permeable layer of talus overlying the faults [Rona, 1976].

The water temperature anomalies measured exhibit the same order of magnitude of increase above ambient temperature and inverse gradient as the original anomaly measured by Rona et al. [1975; X in Table 1 and Figure 1]. The new measurements support the estimate of heat output of the order of several megawatts per kilometer of ridge length at the TAG Hydrothermal Field made by Lowell and Rona [1976] based on the original anomaly, which is the same order of magnitude as the heat output of some major continental geothermal systems, like the Wairakei in New Zealand.

Conclusions

The increase in water temperature above ambient, strong inverse gradients, and geologic setting of three distinct temperature anomalies measured on the east wall of the rift valley at the TAG Hydrothermal Field (A, B, C: Figures 1, 2; Table 1) clearly support their interpretation as hydrothermal. Similar but less distinct characteristics of three associated water temperature anomalies (D, E, F; Figures 1, 3) suggest that these other anomalies may also be hydrothermal. The near coincidence in space of two of the temperature anomalies, apparently along the same fault scarps (C, E; Figures 1-3), evidences persistence of hydrothermal discharge for a period of at least one day. The distribution of the temperature anomalies as a series of point sources along a 7 km length of known fault zones on the east wall of the rift valley within the TAG Hydrothermal Field indicates that the fault zones are acting as the principal conduits for hydrothermal discharge. The magnitude of the anomalies measured is consistent with values previously used to estimate a heat output of the order of several megawatts per kilometer of ridge at the TAG Hydrothermal Field.

Acknowledgements. I thank George F. Merrill and Alvyn Meyer for their valuable assistance in collecting the temperature data, and Thomas Clarke for computer processing. Robert P. Lowell made helpful comments. The NOAA Ship RESEARCHER is acknowledged for the exacting coordination of operations required to make the temperature profiles.

This research was supported by the Environmental Research Laboratories of the National Oceanic and Atmospheric Administration.

References

Lowell, R. P., and P. A. Rona, On the interpretation of near-bottom water temperature anomalies, Earth Planet. Sci. Letters, 32, 18-24, 1976.

McGregor, B. A., and P. A. Rona, Crest of Mid-Atlantic Ridge at 26°N, J. Geophys. Res., 80, 3307-3314, 1975.

Rona, P. A., Pattern of hydrothermal mineral deposition: Mid-Atlantic Ridge crest at latitude 26°N, Marine Geology, 21, M59-M66, 1976.

Rona, P. A., R. N. Harbison, B. G. Bassinger, R. B. Scott, and A. J. Nalwalk, Tectonic fabric and hydrothermal activity of Mid-Atlantic Ridge crest (lat. 26°N), Geol. Soc. Amer. Bull., 87, 661-674, 1976.

Rona, P. A., B. A. McGregor, P. R. Betzer, G. W. Bolger, and D. C. Krause, Anomalous water temperatures over the Mid-Atlantic Ridge crest at 26°N latitude, Deep-Sea Res., 22, 611-618, 1975.

Scott, M. R., R. B. Scott, J. W. Morse, P. R. Betzer, L. W. Butler, and P. A. Rona, Metal enriched sediments from the TAG Hydrothermal Field, Nature, in press.

Temple, D. G., R. B. Scott, and P. A. Rona, Geology of a submarine hydrothermal field, Mid-Atlantic Ridge, 26°N lat., J. Geophys. Res., in press.

Weiss, R. F., P. Lonsdale, J. E. Lupton, A. E. Bainbridge, and H. Craig, Hydrothermal plumes in the Galapagos Rift, Nature, 267, 600-603, 1977.

Williams, D. L., and R. P. Von Herzen, Heat loss from the earth: new estimate, Geology, 2. 327-328. 1974.

(Received August 30, 1978;
accepted September 28, 1978.)

35

Journal of Paleogeography, Paleoclimatology, and Paleoecology 24, 389-390.

Sedimentary Basins of Continental Margins and Cratons. Developments in Geotectonics, 12. M.H.P. Bott (Editor). Elsevier, Amsterdam, 1976, 314 pp., Dfl. 90.00, $36.75.

This book treats mechanisms of sedimentary basin formation within plate interiors and observational evidence from stratigraphy and deep structure relevant to the mechanisms. It is based on papers presented at the 1976 Durham Symposium sponsored by the Inter-Union Commission on Geodynamics and was reprinted from a dedicated issue of the journal *Tectonophysics* (1976, Vol. 36, Nos. 1—3).

The book contains twenty-two papers arranged in three sections, as follows:

(1) Rheology and mechanisms: S. A. F. Murrell reviews the rheology of oceanic, continental shield, and "basin and range" types of lithosphere. The gravity loading subsidence mechanism is considered by A. B. Watts and W. B. F. Ryan. The thermal contraction mechanism is developed by N. Sleep. A lower crustal phase transformation is applied by W. F. Haxby and others to subsidence of the Michigan basin. M. H. P. Bott describes a crustal stretching mechanism of local graben formation, as distinguished from mechanisms of regional downwarping.

(2) Continental margin basins: Papers in this section treat the development of Atlantic-type continental margins beginning with the initial rift stage (K. Burke), the later settings of subsidence (R. E. Sheridan, E. H. T. Whitten), a postulated global change from fault controlled to flexural subsidence during the Cretaceous (P. E. Kent), and contrasts in subsidence exemplified by rifted and sheared sections of the continental margins of South Africa (R. A. Scrutton and R. V. Dingle). Carboniferous subsidence in the British, Irish, and Canadian Maritime basins is related to the Hercynian North Atlantic by M. R. Leeder. A single paper treating a Pacific-type continental margin interprets the development of the Peruvian margin during the Mesozoic (E. J. Cobbing).

(3) Craton basins: J. F. Sweeney attributes the subsidence of the Sverdrup basin of the Canadian Arctic to gravity loading. K. E. Burke relates formation of the Chad basin of central Africa to peripheral uplift and draws an analogv with the Michigan basin. The formation of deep Devonian basins of small areal extent in western Norway is related to dip-slip and strike-slip faulting (R. J. Steel). L. N. Kailasam emphasizes geophysical interpretation of deep structure in his description of major sedimentary basins of the Indian craton. The history of both subsidence and uplift within the cratonic areas of the U.S.S.R. is synthesized in papers by V. D. Nalivkin, K. N. Kravchenko and

others, M. Ya. Rudkevich, and E. A. Bazanov and others. Geophysical evidence for the existence of two major basins buried beneath the ice sheet in East Antarctica is presented by D. J. Drewry.

A concise overview by the editor, M. H. P. Bott, categorizes the various mechanisms of basin subsidence considered in the papers, and suggests future tests to distinguish among the mechanisms. The omission of studies of crustal uplift coupled to subsidence is conspicuous but understandable in light of the difficulty of interpreting the record of uplift. The book is a well-conceived representation of the status of studies of the formation of intraplate sedimentary basins that should serve as a useful reference for the generalist as well as the specialist.

PETER A. RONA
Miami, Fla.

Society of Naval Architects and Marine Engineers, STAR Symposium 2, 2-1 - 2-11.

Plate Tectonics, Energy and Mineral Resources: Implications for Marine Engineering

No. 2

Peter A. Rona, Visitor, National Oceanic and Atmospheric Administration, Miami, Florida

ABSTRACT

The conceptual revolution in earth sciences based on the theory of plate tectonics is producing insights into the occurrence of energy and mineral resources with implications for conditions under which future resources may be exploited. The plate tectonic model of the earth's outer shell focuses attention on the interaction of a small number of large plates, the boundaries of which are global seismic belts. Geological processes driven by energy expended at the plate boundaries control to varying degrees the formation of energy and mineral deposits.

Divergent plate boundaries, where crust is generated, form oceanic ridges like the Mid-Atlantic Ridge, and intersect land in certain places. The divergent plate boundaries are associated with hydrothermal metal deposits and geothermal energy sites; the margins of the ocean basins in which these boundaries are situated may be underlain by hydrocarbon accumulations and metal deposits.

Convergent plate boundaries where crust is resorbed into the earth's interior are situated around ocean basins like the Pacific. The convergent plate boundaries are associated with metallic mineral deposits and geothermal energy sites on their landward side, and areas of offshore oil potential on their seaward side.

The outlook for the distribution of energy and mineral resources based on plate tectonics predicts challenging conditions both offshore in increasing water depths and onshore in mountainous regions associated with volcanic and earthquake activity.

INTRODUCTION

The theory of plate tectonics which has been developed by many workers during the past ten years is revolutionizing our understanding of the earth. The earth model prevalent prior to plate tectonics was essentially static in that continents were fixed and ocean basins were permanent. Under this static earth model, only the most accessible energy and mineral occurrences were discovered, largely by trial and error, with limited understanding of why and where the resources might occur. The earth model of plate tectonics is dynamic, allowing continents to drift and ocean basins to open and close. The dynamic plate tectonic model is not only helping to explain the distribution and genesis of known energy and mineral occurrences, but also is revealing new prospects (1,2). This scientific advance has direct implications for engineering with respect to the design and application of methods to explore for and to exploit certain energy and mineral resources both in offshore and onshore environments.

PLATE TECTONICS

The theory of plate tectonics provides a kinematic model of the earth's outer layer, involving the interaction of a small number of large plates the boundaries of which are global seismic belts (3). Plate tectonics views the earth as comprised of a rigid outer layer about 100 kilometers (60 miles) thick, termed the lithosphere, that behaves as if floating on an underlying plastic layer, the asthenosphere (Figure 1). The upper, more brittle part of the lithosphere is the crust of the earth composed of two principal rock types: (1) granitic continental crust, and (2) basaltic oceanic crust. The lithosphere is divided into a number of major plates, each of which may encompass a continent and part of an ocean basin, as well as numerous minor plates (Figure 2). "Tectonics" is a geological term pertaining to earth movements. The movements in question involve the lithospheric plates that are moving with respect to each other over the asthenosphere. Each lithospheric plate consists of an intraplate area surrounded by plate boundaries. As the lithospheric plate moves over the asthenosphere, the intraplate areas remain

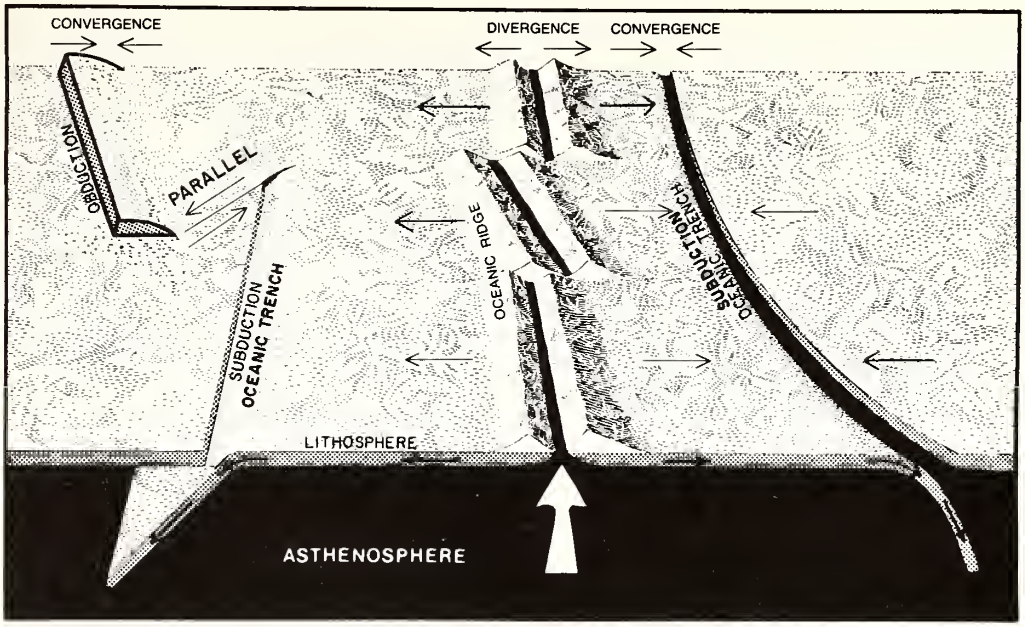
CONVERGENCE
DIVERGENCE
CONVERGENCE
OBDUCTION
PARALLEL
SUBDUCTION OCEANIC TRENCH
OCEANIC RIDGE
SUBDUCTION OCEANIC TRENCH
LITHOSPHERE
ASTHENOSPHERE

Figure 1. Diagram showing plate motions at divergent and convergent plate boundaries. Plates move like two conveyor belts from either side of a divergent plate boundary (oceanic ridge) to convergent plate boundaries where they either descend under the adjacent plate at an oceanic trench (subduction) or override the adjacent plate (obduction) (17).

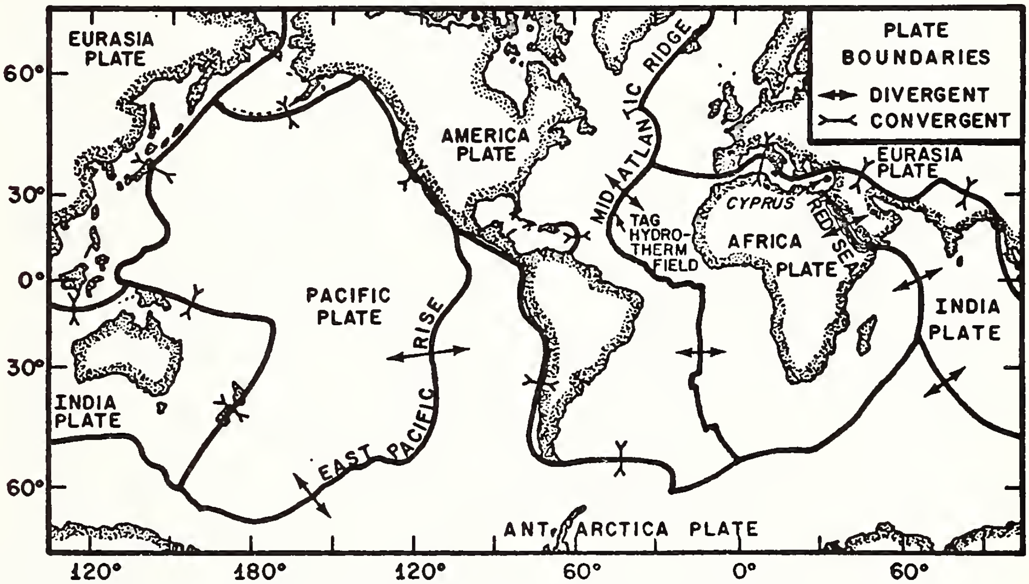
EURASIA PLATE
AMERICA PLATE
MID ATLANTIC RIDGE
PLATE BOUNDARIES
DIVERGENT
CONVERGENT
EURASIA PLATE
CYPRUS
RED SEA
TAG HYDRO-THERM FIELD
AFRICA PLATE
INDIA PLATE
PACIFIC PLATE
EAST PACIFIC RISE
INDIA PLATE
ANTARCTICA PLATE
60°
30°
0°
30°
60°
120°
180°
120°
60°
0°
60°

Figure 2. World map depicting major plates and boundaries between plates which are zones of earthquakes and volcanism (22).

essentially intact while the boundaries between the plates interact and are deformed. The boundaries between the lithospheric plates are delineated by narrow zones of earthquakes generated by the plate movements. Three types of boundaries are recognized. At the first type, a divergent plate boundary, two adjacent plates move apart as new lithosphere is added to each plate by the process of sea floor spreading. The new lithosphere moves more or less symmetrically to each side of the divergent plate boundary like two conveyor belts, carrying the continents apart at a rate of several centimeters (inches) per year in the motion known as continental drift. Divergent plate boundaries extend around the earth through all the major ocean basins as part of a 54,000 km - (30,000 miles) - long undersea oceanic ridge, including the Mid-Atlantic Ridge and the East Pacific Rise (Figure 2).

At the second type of boundary, a convergent plate boundary, two adjacent plates, come together. In the general case termed subduction, one plate descends along an inclined plane under an adjacent plate until the descending plate is resorbed into the interior of the earth (Figure 1). In the special case termed obduction, the edge of one plate is thrust up and overrides the edge of an adjacent plate becoming exposed on an island or a continent (Figure 1). Convergent plate boundaries surround the Pacific Ocean basin and are absent around most of the Atlantic Ocean basin which is bisected by a divergent plate boundary, the Mid-Atlantic Ridge (Figure 2). As a consequence of this distribution of plate boundaries, the Atlantic Ocean basin is opening as lithosphere is created about the Mid-Atlantic Ridge at a rate of several centimeters (inches) per year, while the Pacific Ocean basin is closing as lithosphere is destroyed at surrounding convergent plate boundaries at a rate comparable to the opening of the Atlantic (Figure 3).

The third type of boundary is the parallel (or transform) plate boundary, along which sections of plates move edge to edge accomodating spatial adjustments to the plate motions with neither creation nor destruction of lithosphere. During the course of thousands of millions of years of earth history, the configuration of continents and ocean basins has continuously changed. Ocean basins have opened about divergent plate boundaries and continents have moved closer together as other ocean basins have closed at convergent plate boundaries. Mountain ranges such as the Alps, the Himalayas, the Urals, and the Appalachians have formed where continents have collided. The coexistence of divergent plate boundaries where lithosphere is created, and convergent plate boundaries where lithosphere is destroyed, implies that the diameter of the earth is not radically changing (Figure 3).

The occurrence of energy and mineral resources is related to plate tectonics in three ways:

1. Geological processes driven by energy expended at plate boundaries control to varying degrees the formation of energy and mineral resources.

2. Plate motions create tectonic settings that influence the formation of energy and mineral resources. The two fundamental tectonic settings are opening ocean basins created by divergent plate motions and closing ocean basins created by convergent plate motions.

3. Observed relations between the formation of energy and mineral resources, geological processes at plate boundaries, and tectonic settings can be used to decipher their past relations by interpretive reconstruction of former plate configurations, following the uniformitarian principle of geology, which states that the present is the key to the past.

PLATE TECTONICS AND PETROLEUM

The petroleum industry is the first mineral industry to extensively utilize plate tectonics in their exploration programs because the major oil companies maintain research laboratories that quickly recognized the relevance of plate tectonics to oil finding. They recognized that conditions favorable for the accumulation of petroleum relate to geological processes at present plate boundaries and that reconstruction of former plate boundaries could lead to undiscovered petroleum accumulations.

Prerequisites for the accumulation of petroleum consist of a source of organic matter to generate the petroleum, a natural reservoir to contain it, and a trap to concentrate its fluid and gas constituents. As the progenitor of petroleum, organic matter must accumulate in an environment where it is preserved. The preservation of organic matter is favored by an environment that is toxic to life (so that the organic matter is not consumed as food) and deficient in oxygen (so that the hydrocarbon is not decomposed). How do conditions favorable to the accumulation of petroleum relate to divergent and convergent plate boundaries?

Petroleum and Divergent Plate Boundaries

Divergent plate boundaries may create a habitat favorable for the accumulation of oil, a finding that opens immense possibilities for new petroleum sources in the deep ocean basin. When a divergent plate boundary develops under a continent, the continent is rifted in two and the continental fragments are carried apart on conveyor belts of new lithosphere generated by sea floor spreading about the divergent plate boundary. As the two continental fragments move apart, a sea forms between them. The surrounding continents act as barriers to restrict the circulation of the sea. As a result, organic matter is preserved and, if evaporation of seawater exceeds its replenishment, layers of rock salt are deposited along with the organic matter. As the continental fragments continue to move apart

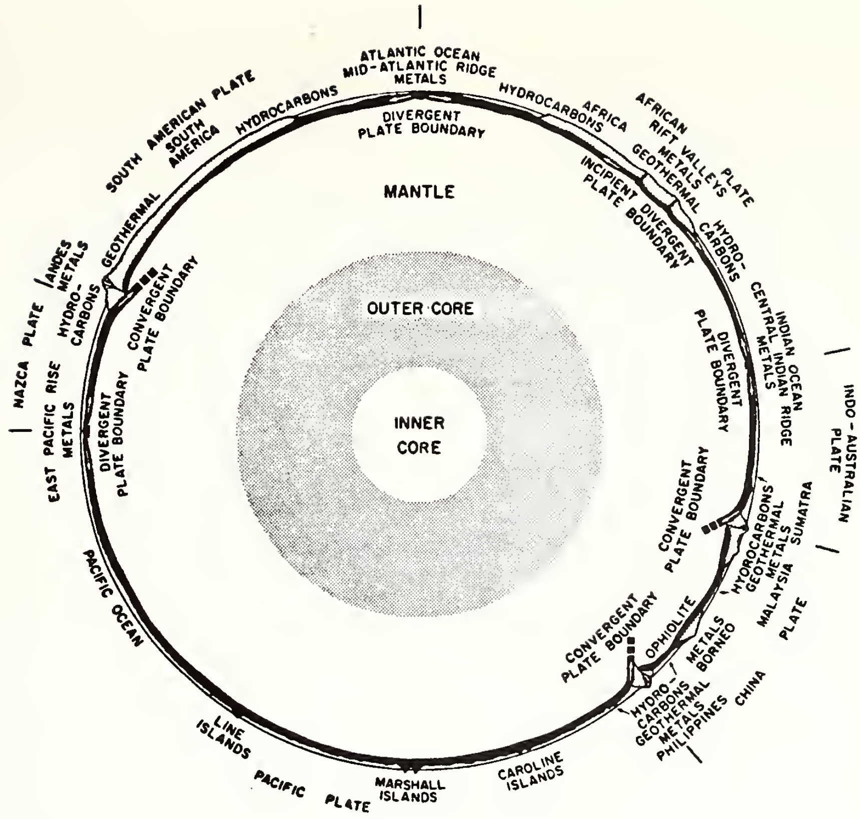
ATLANTIC OCEAN
MID-ATLANTIC RIDGE
METALS
DIVERGENT PLATE BOUNDARY
HYDROCARBONS
AFRICA
AFRICAN PLATE
RIFT VALLEYS
METALS
GEOTHERMAL
INCIPIENT DIVERGENT PLATE BOUNDARY
HYDRO-CARBONS
CENTRAL INDIAN RIDGE
METALS
INDIAN OCEAN
DIVERGENT PLATE BOUNDARY
INDO-AUSTRALIAN PLATE
CONVERGENT PLATE BOUNDARY
HYDROCARBONS
GEOTHERMAL
METALS
SUMATRA
MALAYSIA PLATE
OPHIOLITE
CONVERGENT PLATE BOUNDARY
METALS
BORNEO
HYDRO-CARBONS
GEOTHERMAL
METALS
PHILIPPINES
CHINA
CAROLINE ISLANDS
MARSHALL ISLANDS
PACIFIC PLATE
LINE ISLANDS
PACIFIC OCEAN
EAST PACIFIC RISE
METALS
DIVERGENT PLATE BOUNDARY
NAZCA PLATE
HYDRO-CARBONS
ANDES
METALS
CONVERGENT PLATE BOUNDARY
GEOTHERMAL
SOUTH AMERICAN PLATE
SOUTH AMERICA
HYDROCARBONS
MANTLE
OUTER CORE
INNER CORE

Figure 3. Schematic great circle section through the equator of the earth, showing lithospheric plates, plate boundaries, and occurrences of energy and mineral resources. The thickness of the lithosphere is expanded by a factor of approximately 3 for clarity (2).

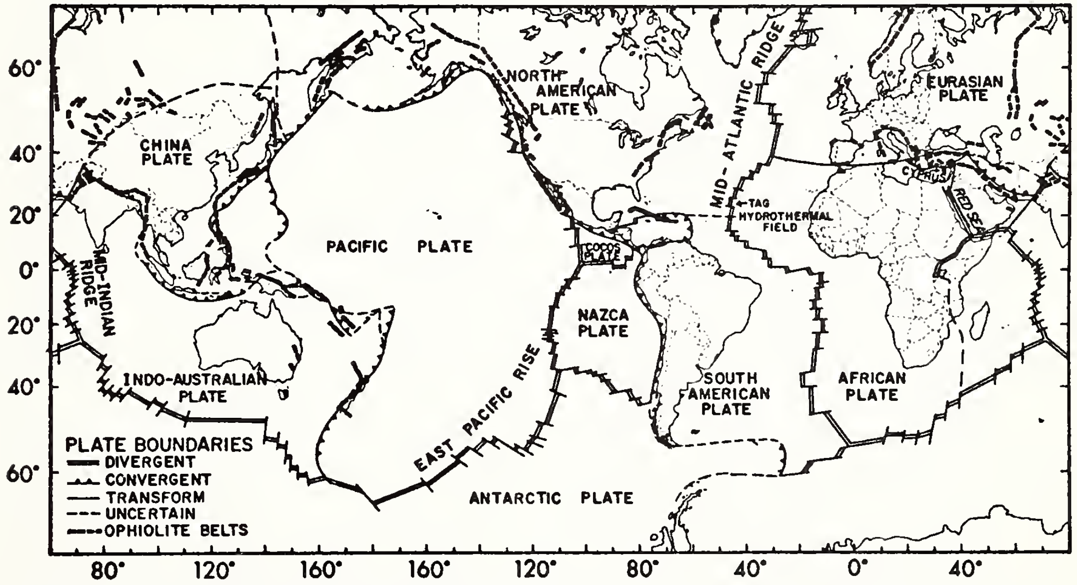
60°
40°
20°
0°
20°
40°
60°
CHINA PLATE
PACIFIC PLATE
NORTH AMERICAN PLATE
MID-ATLANTIC RIDGE
EURASIAN PLATE
CYPRUS
RED SEA
TAG HYDROTHERMAL FIELD
COCOS PLATE
NAZCA PLATE
SOUTH AMERICAN PLATE
AFRICAN PLATE
MID-INDIAN RIDGE
INDO-AUSTRALIAN PLATE
EAST PACIFIC RISE
ANTARCTIC PLATE
PLATE BOUNDARIES
DIVERGENT
CONVERGENT
TRANSFORM
UNCERTAIN
OPHIOLITE BELTS
80°
120°
160°
160°
120°
80°
40°
0°
40°

Figure 4. World map depicting plate boundaries and distribution of oceanic crust exposed on land (ophiolite belts) (2).

and to subside along with the adjacent sea floor, the restricted sea becomes an open ocean. The layers of organic matter and salt are buried under sediments. The organic matter may subsequently develop into petroleum and the salt forms into dome-shaped masses that trap the petroleum. Ocean basins that have opened through the stage of a restricted sea by sea floor spreading about a divergent plate boundary (ocean ridge) are a new potential source of petroleum unrealized before plate tectonics.

The sequence of development of an ocean basin about a divergent plate boundary described, corresponds to the opening of the North Atlantic and South Atlantic Ocean basins about the Mid-Atlantic Ridge during the past 200 million years. Present conditions in the Atlantic Ocean basin are unfavorable for the accumulation of petroleum. However, at an early stage of opening, the Atlantic was a sea with its circulation restricted by the surrounding continents in their positions at that time (4). Conditions in the former Atlantic Sea favored the preservation of organic matter and the decomposition of rock salt. As the Atlantic widened in response to the symmetric creation of new lithosphere by sea floor spreading about the Mid-Atlantic Ridge, the Atlantic Sea became an ocean and the organic matter and salt were buried under sediments, forming the present margins of the Atlantic Ocean. The former existence of an Atlantic Sea is evidenced by salt domes that have recently been discovered extending seaward to water depths of about 5,000 m (16,500 ft.) beneath portions of the continental margins of the North Atlantic and South Atlantic oceans. Petroleum companies are using plate tectonic reconstructions of the opening of the Atlantic to focus their systematic exploration programs on the areas of the Atlantic margins with the greatest potential for petroleum accumulations. Shows of hydrocarbons have been detected by the Deep Sea Drilling Project in sediments of the Atlantic Ocean and Indian Ocean basins, confirming the petroleum potential of deep ocean basins that have developed about divergent plate boundaries (oceanic ridges) (5).

Petroleum and Convergent Plate Boundaries

Convergent plate boundaries where the oceanic portion of a plate is subducted, that is, descends under the margin of a continent, are characteristic of the presence of an oceanic trench running along their length (Figure 1). For example, oceanic trenches run along the entire western margin of North America and South America where the Pacific plate is being subducted under the continents (Figures 2 and 3). Chains of volcanic islands may also be present between the oceanic trench and the continent along certain convergent plate boundaries. Such chains of volcanic islands exist along the western margin of the Pacific, including Indonesia, the Philippines, the Ryukyus, Japan, the Kuriles, and the Aleutians. The islands chains divide the Pacific Ocean basin into smaller marginal basins including the South China Sea, the East China Sea, the Yellow Sea, the Sea of Japan, the Sea of Okhotsk and the Bering Sea.

Both the marginal oceanic trenches and the volcanic island chains create a habitat that is favorable for the accumulation of petroleum in several respects. First, the trenches and island chains act as barriers that catch sediment and organic matter from the continent and the ocean basin. Second, the shape of the trenches and the small ocean basins restricts the circulation of the ocean, so that oxygen is not replenished in the seawater and organic matter is preserved. Third, the accumulation of sediments and the geological structures that develop as a result of the deformation of the sediments by tectonic forces provide reservoirs and traps for the accumulation of petroleum. Fourth, geothermal heat in the oceanic trenches and marginal basins may facilitate the conversion of organic matter to petroleum. The marginal basins of the western Pacific are being systematically explored as some of the most promising areas in the world for petroleum. The oceanic trenches are targets for future exploration because drilling would not be economic at present owing to their great water depth.

PLATE TECTONICS AND GEOTHERMAL ENERGY

Geothermal Energy and Divergent Plate Boundaries

The components necessary for geothermal systems are present at divergent plate boundaries (Figures 2 and 3) including heat supplied by creation of oceanic lithosphere that accounts for 20% of the earth's estimated total rate of heat loss of 10.2×10^{12} cal/s (6), a recharge system involving sea or meteoritic water, a circulation system through fractures in volcanic rocks emplaced at the plate boundary, and a submarine or subaerial discharge system. Geothermal energy was utilized in Iceland long before the island was interpreted as part of the divergent plate boundary that forms the Mid-Atlantic Ridge. Other regions where divergent plate boundaries intersect land offer potential for geothermal development, including the rift valleys of Africa (Figure 3), the Gulf of California, Salton Sea, and Rio Grande Rift of southwestern North America. Geothermal energy is inaccessible as an energy resource along most of the 54,000-km-long (30,000-mile-long) divergent plate boundary system submerged beneath the oceans (Figure 2). Geothermal energy is the driving force of hydrothermal processes that concentrate metallic minerals at divergent plate boundaries.

Geothermal Energy and Convergent Plate Boundaries

Geothermal phenomena including active volcanoes, hot springs, fumaroles, and geysers are distributed along convergent plate boundaries where oceanic lithosphere is being subducted around a closing ocean basin (Figure 1). The geothermal phenomena result from heating due to mechanical factors (friction), chemical reactions (dehydration), and internal heat of the earth associated with descent of the oceanic lithosphere. Despite their spectacular manifestation as the "ring of fire" around the Pacific the estimated rate of heat loss from these surficial geothermal phenomena at convergent plate boundaries is 5×10^{10} cal/s (7), less than 1% of the estimated total rate of heat loss from the earth. Considerable potential exists for utilization of geothermal energy at subducting convergent plate boundaries. The geothermal energy also plays an important role in hydrothermal ore forming processes.

PLATE TECTONICS AND METAL DEPOSITS

The mining industry has been slower than the petroleum industry to utilize plate tectonics in their exploration programs due to less emphasis on research and an innate conservatism. Plate tectonics has considerable, as yet largely undeveloped, potential to guide metals exploration to regions of undiscovered deposits. Economically important types of metal deposits are concentrated by geological processes acting at lithospheric plate boundaries and the distribution of these deposits may be related to present as well as to former plate boundaries.

Metals and Divergent Plate Boundaries

Until recently the consensus among earth scientists was that no concentrated metal deposits would be found associated with divergent plate boundaries. They based their opinion on the fact that the rock type produced at divergent plate boundaries (ocean ridges) is basalt, which is a homogeneous, economically uninteresting rock that floors all the ocean basins of the world (8). Subsequently, two discoveries have demonstrated that concentrated metal deposits are associated with divergent plate boundaries and may be present in oceanic crust (basalt) that underlies the ocean basins.

The first of these two discoveries was the metalliferous sediments of the Red Sea discovered by earth scientists participating in the International Indian Ocean Exploration (1963-1965). The Red Sea represents the earliest stage of opening of an ocean basin about a divergent plate boundary that has rifted Africa and Arabia apart (Figure 2). The metalliferous sediments occur in basins along the axis of the Red Sea at a depth of about 2,000 m (6,600 ft.) below sea level (9,10). Sampling of the upper 10 m (33 ft.) of metalliferous sediment in the largest of the basins reveals a total dry weight of about 80 million tons with average metal content of 29% iron, 3.4% zinc, 1.3% copper, 0.1% lead, 0.000 05% silver and 0.000 000 5% gold. It has been estimated that the market value of the metals in sediments of just this one basin is about 2.5 thousand million dollars exclusive of recovery and refining costs which exceed present technology (11). Metalliferous sediments with lower metal concentration than those of the Red Sea have also been sampled on oceanic ridges in all the major ocean basins by the Deep Sea Drilling Project ("Glomar Challenger") (12) indicating that metalliferous sediments are formed by processes at divergent plate boundaries.

The second of the two discoveries regarding metal deposits at divergent plate boundaries is the TAG Hydrothermal Field discovered in 1973 by the Trans-Atlantic Geotraverse (TAG) project of the National Oceanic and Atmospheric Administration (NOAA) (13). The TAG Hydrothermal Field is an area at least 10 km square on the Mid-Atlantic Ridge (a divergent plate boundary) at latitude 26°N (Figure 2), where hot springs enriched in various metals are apparently discharging from the sea floor and depositing a solid layer of nearly pure manganese oxide up to 5 cm (2 inches) thick. It is not technically feasible at present to drill through the manganese oxide layer into the underlying hard rock (basalt). However, observations of oceanic crust exposed on land, to be considered in the discussion of metal deposits at convergent plate boundaries, suggest that the manganese oxide layer may be underlain by massive metallic sulphide bodies, an economically important type of metal deposit on land. As exploration of the ocean bottom progresses, it is expected that hydrothermal fields similar to the TAG Hydrothermal Field will be found at other locations along oceanic ridges (divergent plate boundaries). The metalliferous deposits of the Red Sea and the TAG Hydrothermal Field indicate that hydrothermal processes of metal concentration in oceanic crust can act continuously from the sea stage through the ocean stage in the opening of an ocean basin about a divergent plate boundary.

The two discoveries cited represent three types of metal deposits that occur in oceanic crust formed by sea floor spreading about oceanic ridges (divergent plate boundaries), as follows: (1) metalliferous sediments, (2) metallic oxide layers, and (3) massive metallic sulphide bodies. The three types of deposits have a common origin as hydrothermal mineral deposits, that is, mineral deposits formed by precipitation of metals from hot aqueous solutions. According to the prevalent hypothesis, cold dense seawater penetrates fractures in the rocks of oceanic ridges and is heated by contact with hot volcanic rocks at depth. The heated, less dense seawater rises and dissolves metals from the fractured rocks of the oceanic crust (basalt) through which it flows. As the hot metal-enriched seawater rises it precipitates metals depositing massive metallic sulphide bodies within the fractured rocks of the oceanic crust, and depositing metallic oxide layers and metalliferous sediments on top of the rocks of the oceanic crust. The three types of metal deposits do not occur continuously along oceanic ridges, but only where conditions are favorable; the distribution of localities is presently unknown. Once formed at an oceanic ridge the three types of deposits are carried away in the conveyor belts of oceanic crust that continuously spread to either side of the oceanic ridge from early (Red Sea) to advanced (Atlantic Ocean) stages in the opening of an ocean basin about a divergent plate boundary (oceanic ridge). Therefore, these three types of deposits may be present at localities in oceanic crust on and away from oceanic ridges.

The three types of metal deposits described in oceanic crust have both a long term and a short term significance for mineral exploration. The long term significance is actual recovery of these metal deposits from the ocean basins. This involves new technology and huge costs that will only become feasible when more accessible metal deposits are depleted. The volume of these three types of metal deposits cannot be estimated because their distribution is unknown. However, they may constitute an important resource for the future because the oceanic crust in which they occur underlies all ocean basins covering nearly two-thirds of the earth. The short term significance of these three types of metal deposits in oceanic crust is based on the finding that large slices of oceanic crust termed "ophiolites" are exposed on land accessible to present exploration (Figure 4). The new knowledge of metallic mineral occurrence in oceanic crust gained from investigations of the ocean basins should both stimulate exploration of oceanic crust exposed on land and provide practical guidelines for the execution of this exploration.

Two distinct situations relevant to mineral exploration exist when a continent rifts apart and an intervening ocean basin grows as a result of sea floor spreading about a divergent plate boundary (oceanic ridge). In the first situation already considered, metal deposits are concentrated in the oceanic crust by geological processes at the divergent plate boundary. In the second situation, pre-existing mineral provinces of the continent are rifted apart and separated as the ocean basin grows between the continental fragments. Knowledge of the location of a mineral province that trends transverse to the margin of one continental fragment can lead to the continuation of that mineral province in the other continental fragment when the continental fragments are reconstructed like a jig-saw puzzle to their pre-rifting configuration. Examples of such separated mineral provinces include tin belts (14), gold (15) and diamond (16) deposits of eastern South America and western Africa, as well as tin belts of North America and Europe and of Australia and southeast Africa. The potential for new discoveries exists where mineral provinces formed prior to rifting trend transverse to the rifted margin of a continent or island (2).

Metals and Convergent Plate Boundaries

Unlike metal deposits at divergent plate boundaries (oceanic ridges) in ocean basins that are difficult to explore and presently inaccessible to exploit, metal deposits at convergent plate boundaries are exposed on land where they are accessible to exploration and exploitation. Although a major portion of the world's current supply of metals already comes from deposits at convergent plate boundaries, plate tectonics provides insights that can guide systematic exploration programs to regions of as yet undiscovered deposits. According to plate tectonics, metal deposits are concentrated at convergent plate boundaries by two fundamentally different processes related to the cases of obduction and of subduction.

Recall that when two plates come together at a convergent plate boundary, in the special case of obduction the edge of one plate is thrust up and overrides the edge of the other plate (Figure 1). Earth scientists had long suspected that slices of oceanic crust are exposed on certain islands and in regions on all the continents. Plate tectonics now offers the mechanism of obduction by which slices of oceanic crust, perhaps ten kilometers thick by hundreds of kilometers long, may be uprooted from ocean basins and emplaced upon land. As a consequence of obduction, the three types of metal deposits (metalliferous sediments, metallic oxide layers, massive metallic sulphide bodies) formed in oceanic crust by processes at divergent plate boundaries (ocean ridges) are exposed on land where these deposits become targets for exploration.

The Troodos Massif of Cyprus in the eastern Mediterranean provides a representative example of oceanic crust emplaced on land by obduction that contains economically important metal deposits. One of several massive metallic sulphide ore bodies of the Troodos Massif (Mavrovouni) contains an estimated mass greater than 15 million tons with average composition of 4.2% copper, 48% sulphur, 43% iron, 0.4% zinc, 0.25 ounce per ton gold, and 0.25 ounce per ton silver. A representative ore body, the Skouriotissa, is roughly elliptical in plan view, measures approximately 600 m long by 200 m wide and is lens-shaped in cross section. Having been mined since classical times, the estimated value of the mineral products exported from Cyprus in 1970 amounted to $30 million. Other slices of oceanic crust exposed on land (ophiolites) exist along present and former convergent plate boundaries including regions within major mountain ranges such as the Alps, Himalayas, mountainous regions of the Middle East, Urals, and coastal ranges of western North America and South America (Figure 4). Slices of oceanic crust are also exposed in the volcanic island chains along the western margin of the Pacific Ocean. These and other exposed slices of oceanic crust have new significance for metal exploration as a result of insights gained through plate tectonics.

Recall the general case of subduction at convergent plate boundaries, when one plate descends under an adjacent plate and is resorbed into the earth (Figure 1). A major portion of known base, precious, iron and ferro-alloy metal deposits occur on continents and island chains along convergent plate boundaries. The "geostill concept" attempts to explain how these metal deposits are formed by distillation from one plate and transferred to another plate during subduction. When the conveyor belt of oceanic lithosphere generated at a divergent plate boundary (oceanic ridge) encounters the margin of a continent at a convergent plate boundary, the oceanic lithosphere is generally subducted under the continental lithosphere because the former is heavier than the latter. During its descent, the rocks of the oceanic lithosphere, including the metals in oceanic crust, selectively melt at progressively higher temperatures and pressures. Molten rocks, other fluids, and gases containing the metals melted from oceanic lithosphere ascend through the overlying continental lithosphere, pick up additional metals and erupt at the surface of the earth. The eruptions form volcanic island chains, as along the western margin of the Pacific, or create a volcanic mountain range at the margin of a continent, such as the Andes along the western margin of South America (Figures 3 and 5; 17). The metals are concentrated as deposits in the volcanic island chains and mountain ranges by primary processes at the time of solidification of the rocks, and by secondary processes following solidification.

The observation that a major portion of known base, precious, iron and ferro-alloy metal deposits are situated along either present or former convergent plate boundaries establishes trends of mineralization that can be used to steer systematic mineral exploration programs. The developing understanding of how the metal deposits are concentrated at convergent plate boundaries, including emplacement of oceanic crust on land by obduction, and the geostill concept associated with subduction, can be used to identify those places where geological conditions favor the occurrence of metals.

INTRAPLATE MINERAL DEPOSITS

The petroleum and metal deposits directly concentrated by geological processes at present or former plate boundaries have been considered. Certain other mineral deposits occur within the vast interior or intraplate areas of individual plates away from present or former plate boundaries. As a global theory that views the earth as an interacting system, plate tectonics permeates all earth processes. Even though intraplate mineral deposits are not directly concentrated by geological processes at plate boundaries, the concentration of these deposits may be indirectly influenced by plate movements that control such other relevant factors as climate and sea level. For this reason, plate tectonic considerations may provide useful clues to exploration for intraplate mineral deposits.

Light metal deposits including aluminum, beryllium, lithium, and titanium are primarily concentrated from granitic rocks of continents in intraplate areas by tropical weathering processes. The climate that determines the weathering process is related to the geographic position of the continents which, in turn, is controlled by continental drift. With regard to petroleum, many of the world's most productive petroleum accumulations occur in sedimentary basins in intraplate areas of continents. The nature of the sediments and organic matter that accumulated in these basins was influenced by climate and sea level, which are related to plate tectonics (2,18). The basins themselves were created by differential vertical crustal movements involving subsidence and uplift of the continental crust; such movements are not yet understood in terms of plate tectonics. Manganese nodules, the golf to tennis ball-sized spherules that cover vast areas of the ocean bottom, are also intraplate deposits (Figure 5). Volcanic emanations at divergent plate boundaries (oceanic ridges) may be a source of manganese and associated metals that are precipitated from seawater to form the nodules. Our understanding of economically important surficial minerals of continental shelves including sand and gravel, shells, phosphorite, and placer deposits remains essentially unchanged by plate tectonics.

IMPLICATIONS FOR MARINE ENGINEERING

Resources at Divergent Plate Boundaries

Petroleum. Petroleum potential exists beneath the continental shelf, continental slope, and continental rise of those rifted seas and ocean basins that have opened by sea floor spreading about a divergent plate boundary such as the Red Sea and the Atlantic Ocean (Figures 2 and 3). Exploration involves emphasis on continued development of seismic techniques in conjunction with gravity and magnetic methods to penetrate and resolve structure and stratigraphy beneath sediment thicknesses up to about 15 km (50,000 ft.). Environment of exploitation consists of progressively deeper water up to about 6 km (20,000 ft.) below sea level under a wide range of sea surface and sea bottom conditions. A major hazard is submarine landslides.

Geothermal Energy. Sites of potential geothermal energy development include islands along oceanic ridges, such as Iceland, along the Mid-Atlantic Ridge, and places where divergent plate boundaries intersect continents, such as the Gulf of California and Imperial Valley of southwestern United States. Terrestrial methods of geothermal exploration and exploitation are applied in an environment subject to earthquakes and volcanism.

Metallic Mineral Deposits. Metallic mineral deposits comprising metalliferous sediments, encrustations, and massive sulphide bodies (exclusive of manganese nodules) are concentrated by hydrothermal processes in oceanic crust generated at divergent plate boundaries from initial rift (Red Sea stage) to ocean basin (Atlantic Ocean stage) in the opening of an ocean basin (Figures 2 and 3). Evaluation of the metallic mineral potential of oceanic crust requires improvement of marine geological, geophysical and geochemical exploration techniques to detect and delineate the metallic mineral deposits. The outlook for exploitation is long term, with the possible exception of certain deposits, such as the metalliferous sediments of the Red Sea which are undergoing initial feasibility studies.

Resources at Convergent Plate Boundaries

Petroleum. Petroleum potential exists in marginal seas enclosed by volcanic island chains, as well as in portions of oceanic trenches and adjacent continental margins around the perimeter of ocean basins that are closing about convergent plate boundaries. Examples are the marginal seas of the western Pacific and the oceanic trenches and continental margins of the eastern Pacific (Figures 2 and 3). Exploration requirements and conditions of exploitation are generally similar to those specified in relation to petroleum in opening ocean basins, with the additional environmental hazards of earthquakes and volcanism (19,20).

Geothermal Energy. The geothermal energy sites occur in volcanic mountain ranges and island chains on the landward side of convergent plate boundaries around closing ocean basins, such as the Pacific (Figures 2 and 3). Terrestrial methods of exploration and exploitation are employed in an environment subject to earthquakes and volcanism (19,20).

Metallic Mineral Deposits. Metal deposits in volcanic mountain ranges and island chains formed above subduction zones at convergent plate boundaries will be the subject of more effective exploration as a consequence of increased understanding of their genesis and distribution (Figures 2, 3 and 5). Oceanic crust obducted along portions of convergent plate boundaries (Figure 4) is now prospective largely as a consequence of new insights gained from studies of metallogenesis at divergent plate boundaries (21).

Intraplate Marine Mineral Deposits

Manganese nodules which occur in varying composition, size and volume over wide areas of ocean basins (Figure 5) are presently at the stage of prototype mining operations. Exploration methods need to be improved in order to more efficiently survey nodule composition and volume. Exploitation of nodules involving recovery, transportation, processing, and waste disposal is providing a significant challenge to marine engineering.

REFERENCES

1. P. A. Rona, "Plate Tectonics and Mineral Resources," Scientific American, July, 1973.

2. P. A. Rona, "Plate Tectonics, Energy and Mineral Resources: Basic Research Leading to Payoff," *EOS, Transactions American Geophysical Union*, August, 1977.

3. X. Le Pichon, J. Francheteau, and J. Bonnin, *Plate Tectonics*, Amsterdam, Elsevier, 1973.

4. P. A. Rona, "Comparison of Continental Margins of Eastern North America at Cape Hatteras and Northwestern Africa at Cap Blanc," *American Association of Petroleum Geologists Bulletin*, January, 1970.

5. World Petroleum Congress, "Petroleum Prospects in the Deep Ocean Regions (Beyond Continental Shelves)," Proceedings 9th World Petroleum Congress, Panel Discussion 5, 1975.

6. D. L. Williams, and R. P. Von Herzen, "Heat Loss From the Earth: New Estimate," *Geology*, July, 1974.

7. J. W. Elder, "Physical Processes in Geothermal Areas" in *Terrestrial Heat Flow*, edited by W. H. K. Lee, Washington, Geophysical Monograph Series, v. 8, American Geophysical Union, 1965.

8. R. S. Dietz, "Ocean Floor in the Decade Ahead," *Marine Technology Society Journal*, September - October, 1969.

9. E. T. Degens, and D. A. Ross, editors, *Hot Brines and Recent Heavy Metal Deposits in the Red Sea*, New York, Springer, 1969.

10. H. Bäcker, and M. Schoell, "New Deeps with Brines and Metalliferous Sediments in the Red Sea," *Nature Physical Science*, December, 1972.

11. J. L. Bischoff, and F. T. Manheim, "Economic Potential of the Red Sea Heavy Metal Deposits" in *Hot Brines and Recent Heavy Metal Deposits in the Red Sea*, edited by E. T. Degens and D. A. Ross, New York, Springer, 1969.

12. A. L. Hammond, "Deep Sea Drilling: Research Lags Exploration," *Science*, August, 1973.

13. P. A. Rona, R. N. Harbison, B. G. Bassinger, R. B. Scott, and A. J. Nalwalk, "Tectonic Fabric and Hydrothermal Activity of Mid-Atlantic Ridge Crest (lat 26°N)," *Geological Society of America Bulletin*, May, 1976.

14. R. D. Schuiling, "Tin Belts on the Continents Around the Atlantic Ocean," *Economic Geology*, v. 62, 1967.

15. W. E. Petrascheck, "Some Aspects of the Relations Between Continental Drift and Metallogenic Provinces" in *Implications of Continental Drift to the Earth Sciences*, edited by D. H. Tarling and S. K. Runcorn, v. 1, 1973.

16. A. R. Reid, "Proposed Origin for Guianian Diamonds," *Geology*, February, 1974.

17. P. A. Rona, and L. D. Neuman, "Energy and Mineral Resources of the Pacific Region in Light of Plate Tectonics," *Ocean Management*, April, 1976.

18. E. Irving, F. K. North, and R. Couillard, "Oil, Climate and Tectonics," *Canadian Journal of Earth Sciences*, January, 1974.

19. B. A. Bolt, W. L. Horn, G. A. Macdonald, and R. F. Scott, *Geological Hazards*, revised second edition, New York, Springer-Verlag, 1977.

20. C. Lomnitz and E. Rosenblueth, editors, *Seismic Risk and Engineering Decisions*, Developments in Geotechnical Engineering 15, New York, Elsevier Scientific Publishing Company, 1976.

21. P. A. Rona, "Criteria for Recognition of Hydrothermal Mineral Deposits in Oceanic Crust," *Economic Geology*, March - April, 1978.

22. P. A. Rona, "New Evidence for Seabed Resources from Global Tectonics," *Ocean Management*, v. 1, 1973.

23. P. A. Rona, and L. D. Neuman, "Plate Tectonics and Mineral Resources of Circum-Pacific Region" in *Circum-Pacific Energy and Mineral Resources*, Memoir 25, Tulsa, Oklahoma, American Association of Petroleum Geologists, 1976.

IRON AND FERRO-ALLOY METAL DEPOSITS

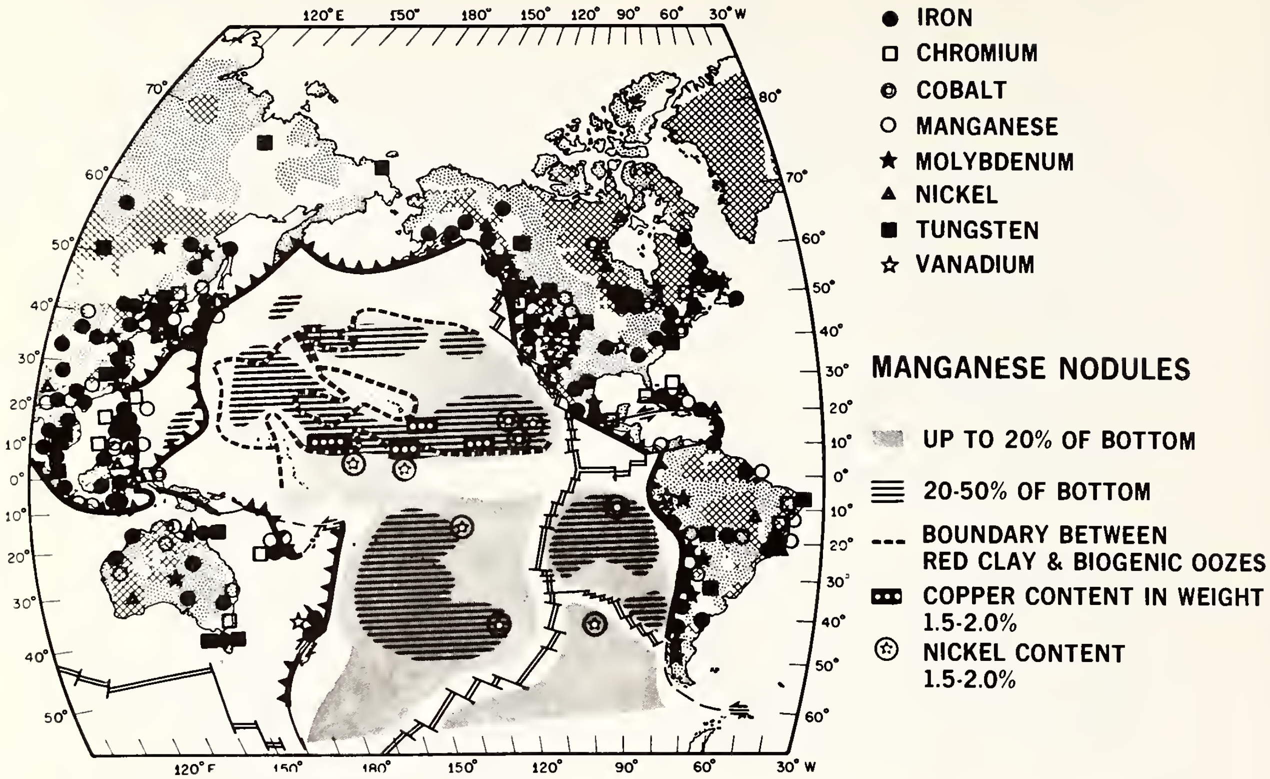
120° E
150°
180°
150°
120°
90°
60°
30° W
70°
60°
50°
40°
30°
20°
10°
0°
10°
20°
30°
40°
50°
80°
70°
60°
50°
40°
30°
20°
10°
0°
10°
20°
30°
40°
50°
60°
120° E
150°
180°
150°
120°
90°
60°
30° W
● IRON
□ CHROMIUM
◎ COBALT
○ MANGANESE
★ MOLYBDENUM
▲ NICKEL
■ TUNGSTEN
☆ VANADIUM
MANGANESE NODULES
UP TO 20% OF BOTTOM
20-50% OF BOTTOM
BOUNDARY BETWEEN RED CLAY & BIOGENIC OOZES
COPPER CONTENT IN WEIGHT 1.5-2.0%
NICKEL CONTENT 1.5-2.0%

Figure 5. Map showing distribution of iron and ferro-alloy metal deposits along the convergent plate boundaries around the Pacific Ocean and manganese nodules in the intraplate region (23). Plate boundaries are drawn as in Figure 4.

SYMPOSIUM REPORT

Geology 6, 299-300.

Hydrothermal Systems at Oceanic Spreading Centers

Peter A. Rona and Robert P. Lowell, Presiding

A half-day symposium, "Hydrothermal Systems at Oceanic Spreading Centers," sponsored by the Geophysics Division of the Geological Society of America, was convened at the 1977 Annual Meeting of the Society. Only recently has the existence—much less the significance—of hydrothermal systems at oceanic spreading centers (active oceanic ridges and rift zones) been realized. It has been estimated that a volume of sea water equal to the world ocean convects through oceanic spreading centers on a time scale of 5 to 10 m.y., based on evidence from oceanic heat flow, hydrous metamorphosed oceanic crust, and isotopic composition of hydrated rocks. The voluminous hydrothermal circulation of sea water driven by intrusive heat sources at oceanic spreading centers facilitates the transport of material from the oceanic mantle to the oceanic crust and hydrosphere with major implications for global heat budget, geochemical mass balances, and metallic ore deposits. The symposium was planned to be representative rather than comprehensive, with presentations of selected theoretical, experimental, and field studies of hydrothermal systems at oceanic spreading centers.

A major unknown in theoretical models of hydrothermal systems at oceanic spreading centers is the permeability of oceanic crust. Clive R. B. Lister, of the University of Washington, originally expounded the theory of sea-water penetration into hot rock by means of thermal contraction cracking (Lister, 1974). His revised analysis limiting crack cooling to vertical advection (at water penetration rates of 8 m/yr) produces an upper bound to crack spacing of about 1.4 m, which encompasses values found in nature (Lister, 1977).

Robert P. Lowell, Patricia L. Patterson, and James K. Fulford of Georgia Institute of Technology developed numerical models of hydrothermal convection under conditions considered prevalent at slow-spreading oceanic ridges. Given episodic igneous intrusions at intervals of 15×10^3 yr and permeability of the order of 1.0 darcy, they calculated that high-temperature hydrothermal convection may be a transient phenomenon, decaying to low-temperature convection at sea-floor ages greater than several million years (Lowell and others, 1977).

An observed discrepancy between high-predicted and low-observed average values of conductive heat flow at oceanic spreading centers has generally been attributed to heat transport by deep hydrothermal convection. Modeling the occurrence of hydrothermal convection systems at oceanic spreading centers using two-temperature thermal convection, Donald L. Turcotte of Cornell University showed that shallow convection cells circulating through highly permeable cracks can not only account for, but are the likely cause of the observed low values of conductive heat flow (Turcotte, 1977).

Bridging the gap between theroetical and experimental studies, Thomas J. Wolery and Norman H. Sleep of Northwestern University considered geochemical mass balances, heat-flow data, and basalt/sea water alteration experiments to analyze the process of discharge of hydrothermal fluids at active oceanic ridges. They deduced the average spacing and flow rates for hydrothermal vents with crack and tube-like geometries and demonstrated that clogging of the vents by mineral precipitation depends on flow rates of the hydrothermal discharge (Wolery and Sleep, 1976, 1977).

Andrew Hajash of Texas A&M University stressed the role of effective water/rock mass ratio and fluid temperature gradient in controlling the products of sea water/basalt alteration experiments (Hajash, 1975). At comparable temperatures, significant differences in solution chemistry occur between 50:1 and 5:1 water/rock-mass ratios. The solution tends toward the composition of the constant temperature runs for the temperature gradient runs (Hajash, 1977).

The water/rock-mass ratio was stressed by Michael J. Mottl and William E. Seyfried of Stanford University as the primary parameter that determines the course of reaction and solution chemistry in sea water/basalt alteration experiments (Seyfried and Bischoff, 1977). The general case of rock-dominated systems favors the formation of typical greenschist assemblages, whereas the special case of sea-water–dominated systems favors the production of metalliferous sediments, as at the East Pacific Rise; the transition between the two types of systems takes place at a water/rock ratio of about 50, at a temperature of 300 °C (Mottl and Seyfried, 1977).

Kurt Boström of the University of Lulea, Sweden, demonstrated graphically that the variable distribution of metals in marine sediments (Boström, 1973) can be explained as products of mechanical mixing between three end members. The end members comprise average geologic and terrigenous matter (Si, Al, Ti, Zr, Ca) and volcanic exhalatative precipitates from oceanic spreading centers (Fe, Mn, Ba, B, Cu, Ni, V) of such constant composition that a deep source is indicated (Boström, 1977).

Field investigations to date have revealed only three active submarine hydrothermal fields at oceanic spreading centers: The Atlantis II Deep of the Red Sea (Degens and Ross, 1969), the TAG Hydrothermal Field on the Mid-Atlantic Ridge crest at latitude 26°N (Rona and others, 1976), and the Mounds Hydrothermal Field of the Galapagos spreading center (Lonsdale, 1977).

Peter A. Rona of the National Oceanic and Atmospheric Administration (NOAA) described the discovery and investigation of the TAG Hydrothermal Field by the NOAA Trans-Atlantic Geotraverse (TAG) project. Interdisciplinary studies by

NOAA and university scientists are in progress on the complete hydrothermal system present at the TAB Hydrothermal Field comprising fresh basalts, altered basalts, hydrothermal effluents, and hydrothermal precipitates (Rona, 1977). Recent results include repeated measurements of near-bottom water temperature anomalies attributed to discharge from faults in the wall of the rift valley that act as conduits for hydrothermal circulation and delineation of the pattern of hydrothermal deposition in space and time (Rona, 1976).

Thermal measurements by surface ship and submersible at the Galapagos spreading center by Richard Von Herzen and Kenneth E. Green of Woods Hole Oceanographic Institution and David L. Williams of the U.S. Geological Survey and the Energy Research and Development Administration reveal both regional and local patterns of heat flux influenced by hydrothermal convection (Williams and others, 1974). The regional pattern comprises wave-like variation on a scale of kilometres normal to the spreading axis attributed to two-dimensional, roll-type convection within the upper 3 to 6 km of the oceanic crust; the local pattern at mounds of hydrothermal material comprises high values of conductive heat flow and water termperatures up to 5 °C above ambient temperature (Von Herzen and others, 1977).

Submersible observations of the Mounds Hydrothermal Field at the Galapagos spreading center were described by members of the diving team including John B. Corliss, Jack Dymond, Mitchell Lyle, and Richard Cobler of Oregon State University; David L. Williams of the U.S. Geological Survey; Richard Von Herzen of Woods Hole Oceanographic Institution; and Tjeerd van Andel of Stanford University. The mounds reach heights of 10 m, are plated with crusts of hydrothermal manganese and iron oxides, and are saturated with water as warm as 10 °C above ambient temperature (Corliss and others, 1977).

The symposium concluded with a film made by the Galagos diving team from the Deep Submergence Research Vehicle ALVIN. The film showed the giant, abyssal, benthic invertebrate fauna that thrives on a food chain sustained by geothermal heat. Refraction of light from the submersible produced a spectacular shimmering effect as hydrothermal fluids discharging from vents on the sea floor mixed with overlying normal sea water. It is interesting to recall that until recently the existence of hydrothermal systems at oceanic spreading centers had been in doubt.

REFERENCES CITED

Boström, K., 1973, The origin and fate of ferromagnanoan active ridge sediments: Stockholm Contr. Geology, v. 24, p. 149-243.

———1977, The origin and quatitative significance of submarine volcanic exhalations as a source of deep sea sediments: Geol. Soc. America, Abs. with Programs, v. 9, no. 7, p. 906.

Corliss, J. B., Dymond, J., Lyle, M., Cobler, R., Williams, D. L., Von Herzen, R. P., and van Andel, T. 1977, Observations of the sediment mounds of the Galapagos rift during the ALVIN diving programs: Geol. Soc. America, Abs. with Programs, v. 9, no. 7, p. 937.

Degens, E. T., and Ross, D. A., 1969, eds., Hot brines and recent heavy metal deposits in the Red Sea: New York, Springer-Verlag, 600 p.

Hajash, A., 1975, Hydrothermal processes along mid-ocean ridges: An experimental investigation: Contrib. Mineralogy and Petrology, v. 53, p. 205-226.

———1977, Experimental seawater/basalt interactions: Effects of water/rock ratio and temperature gradient: Geol. Soc. America, Abs. with Programs, v. 9, no. 7, p. 1002.

Lister, C.R.B., 1974, On the penetration of water into hot rocks: Royal Astron. Soc. Geophys. Jour., v. 39, p. 465-509.

———1977, Stability of estimates of water-penetration rate to theoretical assumptions: Geol. Soc. America Abs. with Programs, v. 9, no. 7, p. 1072.

Lonsdale, P., 1977, Deep-tow observations at the Mounds Abyssal Hydrothermal Field, Galapagos Rift: Earth and Planetary Sci. Letters, v. 36, p. 92-110.

Lowell, R. P., Patterson, P. L., and Fulford, J. K., 1977, Numerical modeling of hydrothermal circulation at slow-spreading ridges: Geol. Soc. America, Abs. with Programs, v. 9, no. 7, p. 1075-1076.

Mottl, M. J., and Seyfried, W. E., 1977, Experimental basalt-seawater interaction: Rock- versus seawater-dominated systems and the origin of submarine hydrothermal deposits: Geol. Soc. America, Abs. with Programs, v. 9, no. 7, p. 1104-1105.

Rona, P. A., 1976, Pattern of hydrothermal mineral deposition: Mid-Atlantic Ridge crest at latitude 26°N: Marine Geology, v. 21, p. M59-M66.

———1977, TAG Hydrothermal Field: Mid-Atlantic Ridge crest (lat. 26°N): Geol. Soc. America, Abs. with Programs, v. 9, no. 7, p. 1146-1147.

Rona, P. A., Harbison, R. N., Bassinger, B. G., Scott, R. B., and Nalwalk, A. J., 1976, Tectonic fabric and hydrothermal activity of Mid-Atlantic Ridge crest (lat. 26°N): Geol. Soc. America Bull., v. 87, p. 661-674.

Seyfried, W. and Bischoff, J. L., 1977, Hydrothermal transport of heavy metals by seawater: The role of seawater/basalt ratio: Earth and Planetary Sci. Letters, v. 34, p. 71-77.

Turcotte, D. L., 1977, Models of hydrothermal circulation systems at oceanic spreading centers: Geol. Soc. America, Abs. with Programs, v. 9, no. 7, p. 1207.

Von Herzen, R. P., Green, K. E., and Williams, D. L., 1977, Hydrothermal circulation at the Galapagos spreading center: Geol. Soc. America, Abs. with Programs, v. 9, no. 7, p. 1212-1213.

Williams, D. L., Von Herzen, R. P., Sclater, J. G., and Anderson, R. N., 1974, The Galapagos spreading center: Lithospheric cooling and hydrothermal circulation: Royal Astron Soc. Geophys. Jour., v. 38, p. 587-608.

Wolery, T. J., and Sleep, N. H., 1976, Hydrothermal circulation and geochemical flux at mid-ocean ridges: Jour. Geology, v. 84, p. 249-275.

———1977, The egress of hydrothermal fluid at mid-oceanic ridges: Geol. Soc. America, Abs. with Programs, v. 9, no. 7, p. 1233-1234.

Bulletin of Marine Science 28, No. 2, 371-375.

A BENTHIC INVERTEBRATE FROM THE MID-ATLANTIC RIDGE

Peter A. Rona and George F. Merrill

Abstract—About 100 deep-sea photographs revealed discoidal shaped objects several centimeters in diameter with marked hexagonal symmetry lying on sediment-covered step-like levels of the wall of the rift valley of the Mid-Atlantic Ridge at latitude 26°N between depths of 3200 and 3700 m below sea level. The characteristics of the discoidal shaped objects, including the symmetry and inferred individual growth stages, are closest to compressed forms of a hexactinelid sponge adapted to an unconsolidated sediment substrate.

The National Oceanic and Atmospheric Administration Trans-Atlantic Geotraverse (TAG) Project has been carrying out geological, geophysical, and geochemical investigations of a hydrothermally active portion of the Mid-Atlantic Ridge crest at latitude 26°N between depths of 2000 and 4000 m below sea level (Rona et al., 1976). As part of this investigation, three photographic transects of the east wall of the rift valley were made in August 1976 using a sequentially fired deep-sea camera and acoustic pinger towed about 5 m above the sea floor (Fig. 1). About 100 photographs along a 3-km long segment of one of the three photographic transects revealed numerous discoidal objects several centimeters in diameter with strikingly symmetric hexagonal patterns on sediment covered portions of the east wall of the rift valley (Fig. 2). The discoidal objects are inferred to be invertebrates of uncertain identity.

Description

Sequential photographs of the east wall of

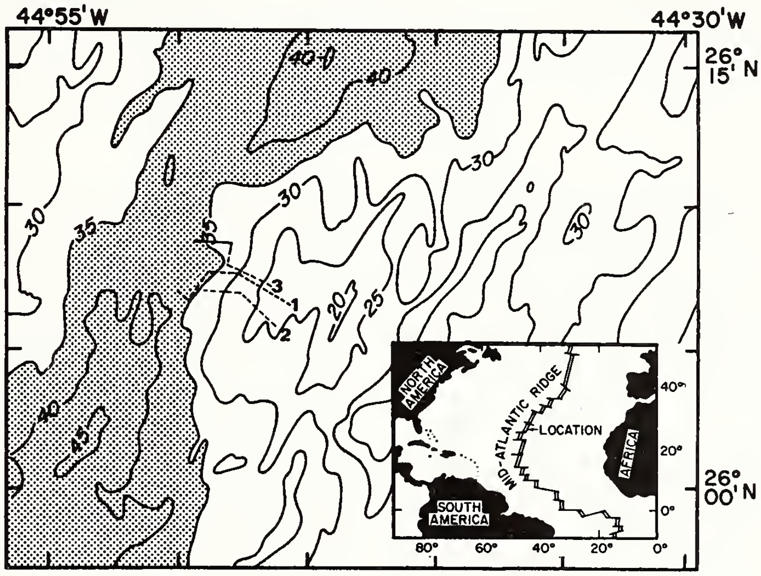

Figure 1. Bathymetric map contoured in hundreds of meters showing positions of photographic transects one, two, and three on the east wall of the rift valley (shaded) of the Mid-Atlantic Ridge crest at latitude 26°N. The discoidal objects are present along the solid portion of transect three and absent along the dashed portions of transect one, two, and three. An index map (inset) shows the location of the camera transects on the Mid-Atlantic Ridge crest in the central North Atlantic.

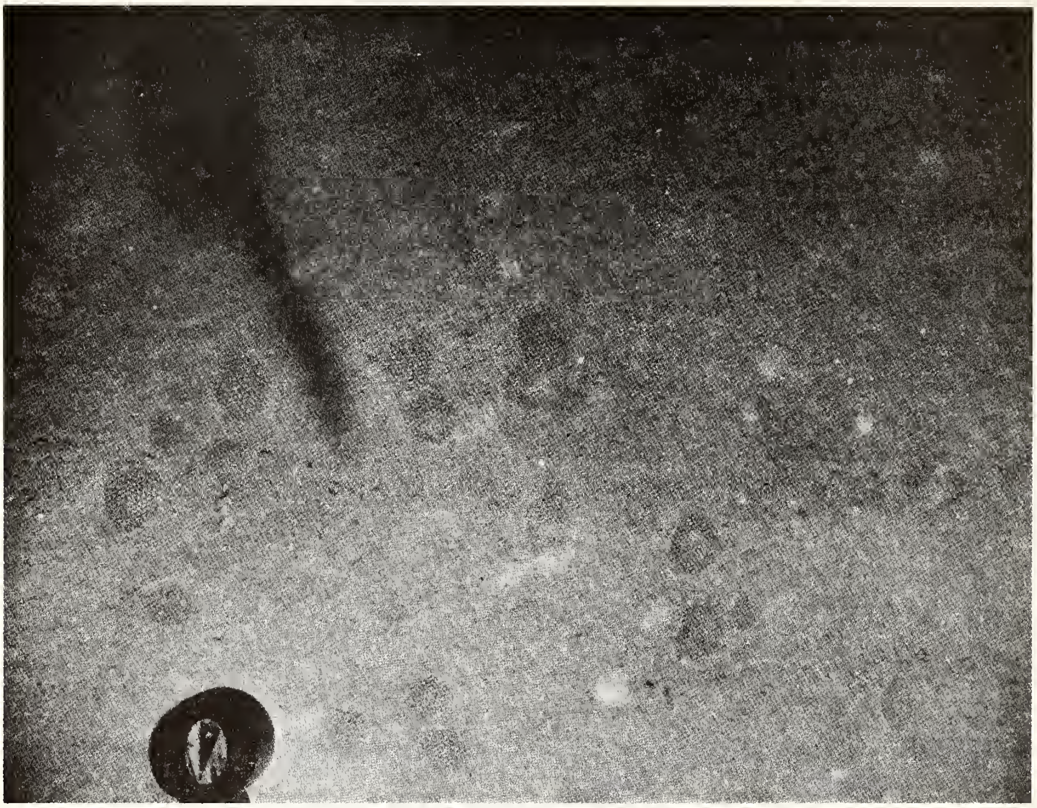

Figure 2. Deep-sea photograph showing discoidal objects on sediments of the east wall of the rift valley along photographic transect three (Fig. 1). A compass hanging beneath the camera projects a shadow onto the sea floor.

the rift valley were made at 8-second intervals equivalent to a horizontal spacing of about 8 m at a ship's speed of about 2 knots covering an area of about 3 by 4 m at a camera distance of 5 m above the sea floor. The wall of the rift valley is composed of basalt arranged in step-like blocks. The vertical offset of separate steps ranges between tens and hundreds of meters, and the horizontal spacing between steps is hundreds of meters (Rona et al., 1976). Where present along a portion of photographic transect three (Fig. 2), the discoidal objects lie on unconsolidated silt and clay sized sediment up to several meters thick that accumulated in pockets on the irregular basalt surface of each step-like level between 3200 and 3700 m below sea level. The observed density of these objects ranges between 1 and 45 per square meter. Where the sediment surface is uneven, the discoidal objects tend to lie along the highest areas. The objects are absent in sediment covered areas of the remaining portion of photographic transect three between 3200 and 2400 m below sea level, and of adjacent photographic transects one and two (Fig. 1) made during the same week. Two photographic transects made along the same portion of the rift valley wall with the same camera in October 1973 did not reveal any such objects (McGregor and Rona, 1975).

The discoidal objects are distinctly hexagonal in outline and range up to about 5 cm

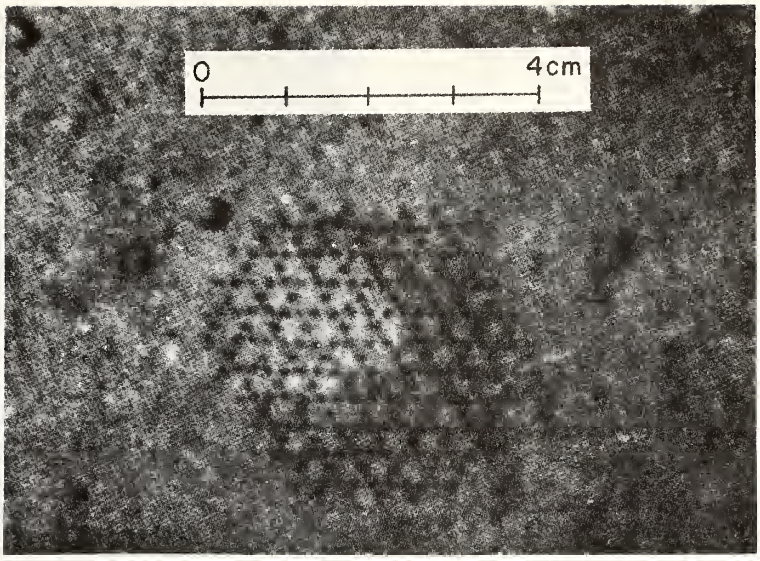

Figure 3. An enlargement of a portion of a deep-sea photograph from transect three (Fig. 1) showing an individual discoidal object.

in diameter (Fig. 3). The objects do not cast a shadow in any of the photographs, indicating that they are nearly flush with the sediment surface. The objects consist of dark dots arranged in three distinct rows that intersect at angles of 120° within a single plane to form the external hexagonal shape, as well as internal hexagonal units (Fig. 4). Counts of 10 individual objects reveal a range in number of rows per object between 10 × 10 × 10 and 13 × 13 × 12; the number of dots per object ranged between 232 and 361. One of the objects observed exhibits twinning (Fig. 5). The dark dots may be holes or spherules; they are not sufficiently clear on the photographs to unambiguously distinguish between the two possibilities.

Identifiable organisms observed in photographs of the discoidal objects include shrimp and small fish. Free-standing sessile sponges are present in areas of basalt outcrop between the sediment pockets where the objects occur. Traces of worm trails are present in the surrounding sediment. Light-colored, roughly circular patches of sediment several centimeters in diameter interspersed between and underlying certain of the discoidal objects may be worm or shrimp burrows, or may be related to the presence of the objects themselves.

Discussion

The nature of the dark dots is critical in interpretation of the discoidal objects. If the dark dots are spherules, then the objects could be egg clusters in a nearly transparent matrix. However, known egg clusters do not possess the regular symmetry exhibited by the dark dots (G. L. Voss, University of Miami, personal communication). Alternatively, the dark dots may be holes that are pores in an organism, or vents or worm burrows in sediment.

The wide distribution, distinct hexagonal symmetry, and evidence of proportional size increase indicative of growth stages favor interpretation of the discoidal objects as some type of invertebrate, rather than a pattern of vents or worm burrows in sediment. The narrow range in number of rows

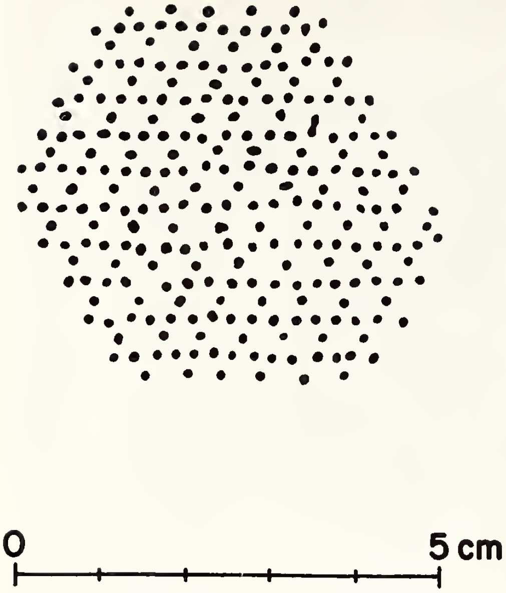

Figure 4. An ink drawing of an individual discoidal object copied from a deep-sea photograph from transect three (Fig. 1).

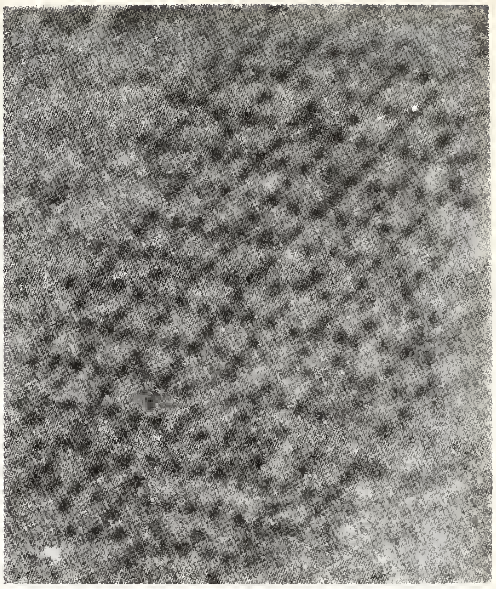

Figure 5. An enlargement of a portion of a deep sea photograph from transect three (Fig. 1) showing a twinned discoidal object. The continuity of rows of dots evidences twinning, as distinguished from two overlapping individuals.

of dots in individual objects, the apparent growth stages, and the occurrence of twinned specimens, evidences an individual rather than colonial form.

Attribution of the discoidal objects to several invertebrate phyla was considered, based on interpretation of the dark dots as pores. An encrusting form of bryozoa was ruled out because of the inferred individual form, the coarse pattern of pores, and the occurrence on a sediment rather than rock substrate (F. M. Bayer, Smithsonian Institution, personal communication). Echinoderms are ruled out because none are known with hexagonal symmetry (D. Pawson, Smithsonian Institution, personal communication). Coelenterates are ruled out as septa and polyps are absent on the discoidal objects, although forms with hexagonal symmetry exist (F. M. Bayer, personal communication). The characteristics of the discoidal objects are considered to be closest to a compressed form of a hexactinelid sponge adapted to an unconsolidated sediment substrate (G. L. Voss, University of Miami; F. M. Bayer and K. Ruetzler, Smithsonian Institution, personal communication). The discoidal object corresponds either to the sieve (water inflow) or body wall (water outflow) of the sponge, raising questions as to the mode of water circulation.

Definitive study of the discoidal objects will require recovery of specimens. Considering their location at a depth of several kilometers below sea level on the Mid-Atlantic Ridge, a submersible would provide the most effective means to recover the specimens.

ACKNOWLEDGMENTS

We thank Dr. G. L. Voss of the Rosenstiel School of Marine and Atmospheric Sciences of the University of Miami, and Dr. F. M. Bayer of the Smithsonian Institution, for their guidance. A. M. Meyer of NOAA operated the deep-sea camera.

LITERATURE CITED

McGregor, B. A., and P. A. Rona. 1975. Crest of the Mid-Atlantic Ridge at 26°N. J. Geophysical Res. 80: 3307–3314.

Rona, P. A., R. N. Harbison, B. G. Bassinger, R. B. Scott, and A. J. Nalwalk. 1976. Tectonic fabric and hydrothermal activity of Mid-Atlantic Ridge crest (lat. 26°N). Geol. Soc. America Bull. 87: 661–674.

DATE ACCEPTED: October 12, 1977.

ADDRESS: *National Oceanic and Atmospheric Administration, Atlantic Oceanographic and Meteorological Laboratories, Marine Geology and Geophysics Laboratory, 15 Rickenbacker Causeway, Miami, Florida 33149.*

Earth and Planetary Science 40, 1-11.

EARLY CENOZOIC GLOBAL PLATE REORGANIZATION

PETER A. RONA and EVAN S. RICHARDSON *
National Oceanic and Atmospheric Administration, Atlantic Oceanographic and Meteorological Laboratories, Miami, FL 33149 (U.S.A.)

Received November 9, 1977
Revised version received February 28, 1978

Synthesis of regional plate movements reveals a major reorganization of global plate motion from Mesozoic to Cenozoic patterns that occurred primarily during the Eocene epoch (53.5 to 37.5 m.y. B.P.). The reorganization involved reorientation of relative plate motions with large N-S components into large E-W components, continuation of pre-existing E-W sea floor spreading, initiation of new E-W spreading, deceleration of spreading rates, and obduction of ophiolites. The reorganization is attributed to increase in resistance imposed on the global plate system by increase in length of E-W-trending collisional plate boundaries from 2500 to 28,500 km during the interval 55 to 40 m.y. B.P., forcing the system to reorient along lines of less resistance. The pattern of global plate motion resulting from the reorganization is constrained by the resistance imposed by 19,000 km of collisional plate boundaries.

1. Introduction

The extensive literature treating regional plate motions of Mesozoic and Cenozoic age provides a basis for determining global patterns of plate motions and evaluating the degree of interaction between plates. The Early Mesozoic beginning of the breakup and dispersion of Pangaea is a recognized time of global plate reorganization [1]. Synthesis of regional information on sea floor spreading (Table 1), orogenic activity (Table 1), and obduction of ophiolites (Table 2), evidences a global plate reorganization from Mesozoic to Cenozoic patterns of plate motion during the interval between 55 and 40 m.y. B.P. The interval includes portions of the Paleocene (65 to 53.5 m.y. B.P.) and Eocene (53.5 to 37.5 m.y. B.P.), employing revised time scales for the Cretaceous [2], the Cenozoic [3], and for magnetic polarity reversals [4].

2. Regional plate reorganization

Consideration of regional plate motions follows a global circuit of plate boundaries from the Indian Ocean, to the Pacific, Arctic, Atlantic, Caribbean, Mediterranean, and Red Sea. Pertinent information and references are summarized in Tables 1 and 2, so the text will simply outline major events with reference to the tables and to Figs. 1 and 2.

Plate reorganization in the Indian Ocean region involved reorientation of the oceanic ridge system from a predominantly E-W trend that had prevailed since about 100 m.y. B.P., to a NW-SE trend beginning between 53 and 50 m.y. B.P. (Table 1, Fig. 1). The ridge orientation was nearly synchronous with the inferred time of initial collision and decrease in rate of relative motion between India and Eurasia (55 to 40 m.y. B.P.), termination of ophiolite obduction at the Indus suture zone (49 m.y. B.P.; Table 2), and marked decrease in rate of sea floor spreading (approximately 50%; 53 to 40 m.y. B.P.; Table 1). A change in pattern of plate motion occurred south of Australia. Sea floor spreading about a nearly N-S-trending ridge system ended in the Tasman Sea (59 to 56 m.y. B.P.),

---

* Also University of Miami, Rosenstiel School of Marine and Atmospheric Sciences, Miami, Florida 33149, U.S.A. Present address: Deep Sea Exploration, Phillips Petroleum Company, Bartlesville, Oklahoma 74004, U.S.A.

TABLE 1

Regional plate motions (see Figs. 1, 2)

Region	Event	Time (evidence)	Reference
Indian Ocean	Beginning of continental collision between India and Eurasia	55 to 40 m.y. B.P. (structural and stratigraphic relations)	[5–9]
Indian Ocean	Decrease in sea floor spreading rates between India and Antarctica-Australia by a factor of approximately 2 from >8 to <4 cm/yr (half rate)	53 to 40 m.y. B.P. (magnetic anomalies 21 and 22)	[10–12]
Indian Ocean	Subduction of nearly E-W-trending oceanic ridge between Australia and Eurasia at convergent plate boundary along the southern margin of Eurasia	53 to 32 m.y. B.P. (magnetic anomalies 11 and 22)	[10]
Indian Ocean	Reorientation of oceanic ridge system from nearly E-W to NW-SE with concommitant change in sea floor spreading direction from nearly N-S to NE-SW.	53 to 50 m.y. B.P. (magnetic anomalies 21 and 22)	[10,13]
Indian Ocean	Ending of sea floor spreading with large E-W component in Tasman Sea	59 to 56 m.y. B.P. (after magnetic anomaly 25)	[14]
Indian Ocean	Beginning of sea floor spreading with large N-S component between Australia–Broken Ridge and Antarctica–Kerguelen Plateau	53 to 50 m.y. B.P. (magnetic anomalies 21 and 22)	[15]
Indian Ocean	Decrease in rate of relative motion between India and Eurasia plates by a factor of approximately 2 from about 10 to 5 cm/yr	50 to 38 m.y. B.P. (magnetic anomalies)	[11,9]
South Pacific	Decrease in rate of sea floor spreading by a factor of approximately 2 from about 5 to 2.3 cm/yr	56 m.y. B.P. (magnetic anomaly 24)	[18,19]
South Pacific	Collision between Australian shield and New Guinea island arc	49 to 43 m.y. B.P. (Middle Eocene; structural and stratigraphic relations)	[16]
South Pacific	Beginning of sea floor spreading west of Scotia Sea	54 to 30 m.y. B.P. (magnetic anomalies)	[20]
South Pacific	Rifting of South America from Antarctic peninsula	54 to 30 m.y. B.P. (magnetic anomalies)	[20]
North Pacific	Laramide orogeny predominantly E-W compressive deformation and plutonism in western North America and northwestern South America	80 to 40 m.y. B.P.	[21]
North Pacific	Change in direction of sea floor spreading from ENE-WSW to E-W evidenced by Zed pattern of magnetic anomalies and trends of fracture zones	55 to 50 m.y. B.P. (magnetic anomalies 21 to 23)	[22,13]
North Pacific	Beginning of subduction along Philippine, Bonin, Marianas, Yap, Palau, and Tonga trench-arc systems	Shortly after 45 m.y. B.P. (maximum ages and trends of associated island arcs)	[23–25]
North Pacific	Change in direction of plate motion from NNW to WNW with respect to Hawaiian hot spot evidenced by Emperor Seamount–Hawaiian Ridge bend	43 to 41 m.y. B.P. (radiometric dating)	[26]
Arctic	Beginning of sea floor spreading in an E-W direction about the Gakkel Ridge resulting in opening of the Eurasian Basin	63 m.y. B.P. (magnetic anomalies)	[27,28]

TABLE 1 (continued)

Region	Event	Time (evidence)	Reference
North Atlantic	Duration of sea floor spreading in the Norwegian Basin	56 to 42 m.y. B.P. (magnetic anomalies)	[29]
North Atlantic	Beginning of spreading at Iceland–Jan Mayen Ridge	42 m.y. B.P. (magnetic anomalies)	[29]
North Atlantic	Duration of second episode of sea floor spreading in the Labrador Sea	56 to 44 m.y. B.P. (magnetic anomalies 19 to 24)	[30,31]
North Atlantic	Beginning of spreading on Reykjanes Ridge	56 m.y. B.P. (magnetic anomaly 24)	[32,33]
North Atlantic	Change in spreading direction on Reykjanes Ridge from indeterminate to E-W	40 m.y. B.P. (magnetic anomalies)	[32,33]
North Atlantic	Decrease in rate of sea floor spreading north of the Azores-Gibraltar lineament by a factor of approximately 2 from about 2.5 to 1.0 cm/yr	59 to 50 m.y. B.P. (magnetic anomalies 21 to 25)	[27]
North Atlantic	Decrease in rate of sea floor spreading south of the Azores-Gibraltar lineament by a factor of approximately 1.5 from about 1.7 to 1.2 cm/yr	59 to 50 m.y. B.P. (magnetic anomalies 21 to 25)	[27,34]
North Atlantic	Change in relative direction of spreading from nearly E-W to WNW-ESE evidenced by bend in Kane fracture zone	59 to 50 m.y. B.P. (magnetic anomalies 21 to 25)	[35]
South Atlantic	No apparent changes in sea floor spreading rate and direction based on limited data	72 to 0 m.y. B.P. (axial magnetic anomaly to anomaly 31)	[36–38]
Caribbean	Separation of Caribbean plate from Pacific plate as a consequence of southward extension of the Middle Americas Trench	54 to 38 m.y. B.P. (Eocene age of earliest volcanics in Central America)	[39]
Caribbean	Jump of subduction zone from Aves Ridge to Lesser Antilles island arc	54 m.y. B.P. (60 m.y. B.P. radiogenic date of granodiorite from Aves Ridge; 54 m.y. B.P. initiation of volcanism in Lesser Antilles)	[40,39]
Caribbean	Collision of Bahama Banks with Greater Antilles (Cuba)	Post-70 to 43 m.y. B.P. (Late Cretaceous to Middle Eocene based on structural relations)	[41,42]
Caribbean	End of N-S subduction at Puerto Rico	49 to 43 m.y. B.P. (Middle Eocene radiogenic age of youngest volcanic rocks present)	[42]
Caribbean	Beginning of present Puerto Rico Trench	Post-43 m.y. B.P. (post-Middle Eocene based on structural and stratigraphic relations)	[43–45]
Caribbean	End of N-S subduction at Cuba	49 to 43 m.y. B.P. (Middle to Late Eocene based on structural relations)	[41,44]
Caribbean	End of N-S subduction at Hispaniola	Prior to 43 m.y. B.P. (pre-Late Eocene based on stratigraphic relations)	[46]
Caribbean	General change of plate motion from N-S compression to E-W strike slip	54 to 38 m.y. B.P. (Eocene based on structural relations at northern and southern boundaries of Caribbean plate)	[39]
Caribbean	Beginning of sea floor spreading in present Cayman Trough	49 to 43 m.y. B.P. (Middle Eocene based on estimated spreading and sedimentation rates)	[47,48]
Mediterranean	Right lateral E-W strike slip motion along Tethys	80 to 53 m.y. B.P. (deduced from relative plate motions in the North Atlantic)	[49]
Mediterranean	Change to N-S collision, compression and subduction along Tethys	53 m.y. B.P. (deduced from relative plate motions in the North Atlantic)	[49]

TABLE 1 (continued)

Region	Event	Time (evidence)	Reference
Mediterranean	Collision of Iberian peninsula with Eurasia	54 to 38 m.y. B.P. (Eocene based on structural relations)	[50]
Mediterranean	Beginning of deformation of Betic mountains in southern Spain	49 to 43 m.y. B.P. (Middle Eocene based on structural relations)	[49]
Mediterranean	Possible reversal of subduction polarity in Swiss Alps	49 to 43 m.y. B.P. (Middle Eocene based on structural relations)	[51]
Mediterranean	Meso-Alpine orogeny involving main movements of Penninic and Austroalpine nappes in Swiss Alps	43 to 38 m.y. B.P. (Late Eocene to Early Oligocene based on structural relations)	[52]
Mediterranean	Subduction in Tellian Atlas and Sicilides	54 to 38 m.y. B.P. (Eocene based on active flysch sedimentation)	[49]
Mediterranean	End of subduction in eastern Alps as a consequence of continental collision	45 to 42 m.y. B.P. (structural and stratigraphic relations)	[53]
Mediterranean	Orogeny in High Atlas and Saharan Atlas	43 to 30 m.y. B.P. (post-Middle Eocene and pre-Middle Oligocene based on structural and stratigraphic relations)	[54,55]
Red Sea	Beginning of sea floor spreading with large E-W component	38 m.y. B.P. (magnetic anomalies)	[56]

TABLE 2

Early Cenozoic ophiolites (see Figs. 1, 2)

Region	Location	Age of obduction (evidence)	Reference
Indian Ocean	Indus suture zone of the Himalayas	100 to 49 m.y. B.P. (Late Cretaceous through Early Eocene based on Eocene age of youngest ophiolites and of granites that intrude ophiolites)	[6]
Indian Ocean	Andaman Islands	53 to 43 m.y. B.P. (Early and Middle Eocene based on overlying Miocene shale and other stratigraphic evidence)	[16]
South Pacific	East Papua and West Irian, New Guinea	52 m.y. B.P. (Early Eocene based on radiometric dating of metamorphic and intrusive rocks in the ophiolites	[57]
South Pacific	New Caledonia	43 to 37 m.y. B.P. (Late Eocene based on Lower and Middle Eocene sediments underlying ophiolite and ophiolite debris in Upper Eocene flysch)	[58,59]
North Pacific	Philippine Islands	54 to 37 m.y. B.P. (Eocene based on structural relations)	[60]
North Pacific	Knight Island, southern Alaska	65 to 52 m.y. B.P. (Paleocene through Early Eocene age of intrusion of ophiolitic type rocks and trench-type flysch sediments)	[61]
North Pacific	Coastal Cordillera of Venezuela and Western Cordillera of Colombia	54 to 30 m.y. B.P. (Eocene and Early Oligocene based on structural relations)	[62]
Arctic	No Eocene ophiolites known		
North Atlantic	No Eocene ophiolites known		
South Atlantic	No Eocene ophiolites known		
Mediterranean	Eastern Alps	100 to 45 m.y. B.P. (Late Cretaceous to Late Eocene based on structural relations and radiogenic dates)	[53,63]
Mediterranean	Corsica	54 to 37 m.y. B.P. (Eocene)	[49]

and spreading about a nearly E-W-trending ridge system began between Australia–Broken Ridge and Antarctica–Kerguelen Plateau (53 to 50 m.y.; Table 1; Fig. 1).

In the South Pacific region the largest known change in rate of sea floor spreading during the past 72 m.y. is inferred to have occurred about 56 m.y. B.P. (Table 1); no major changes of direction are known to have accompanied the spreading rate change at that time. Ophiolites were obducted in New Guinea (52 m.y. B.P.; Table 2; Fig. 2) and New Caledonia (43 to 37 m.y. B.P.), possibly related to collision of those islands with the Australian shield (49 to 43 m.y. B.P.; Table 1). Events in the southeastern Pacific (Table 1) require further documentation.

Structures inferred to have been transform faults during the late Mesozoic along the western margin of the South Pacific and North Pacific became subduction zones shortly after 45 m.y. B.P. (Table 1; Fig. 2). This conversion from transform motion to subduction may be related to the changes in direction of sea floor spreading from large N-S to large E-W components in the Indian Ocean as already noted (53 to 50 m.y. B.P.), and in the North Pacific evidenced by trends of magnetic anomalies and fracture zones (55 to 50 m.y. B.P.; Table 1), and the Emperor Seamount–Hawaiian Ridge bend (43 to 41 m.y. B.P.; Table 1; Fig. 2). The large E-W component of relative motion was manifested at the eastern margin of the North Pacific by continued E-W compressive deformation of the Laramide orogeny (80 to 40 m.y. B.P.; Table 1), and in the South Pacific by continued subduction along the western margin of South America (Fig. 2).

In the Arctic region E-W sea floor spreading about the Gakkel Ridge, a northward continuation of the Mid-Atlantic Ridge, began about 63 m.y. B.P. (Table 1; Fig. 1). Several prominent changes in sea floor spreading occurred in the northern North Atlantic during the interval between 56 and 42 m.y. B.P. involving shifts in spreading about essentially N-S ridges (Table 1; Fig. 1). In the North Atlantic marked decreases in rate of sea floor spreading (approximately 50%) about the Mid-Atlantic Ridge occurred both north and south of the Azores–Gibraltar lineament within the interval 59 to 50 m.y. B.P. (Table 1; Fig. 1). A change in relative direction of spreading from nearly E-W to WNW-ESE documented at the Kane fracture zone occurred synchronously with the change in spreading rate (Table 1; Fig. 1). Limited data from the South Atlantic region do not reveal any apparent major changes in spreading rate or direction in the Early Cenozoic.

The Caribbean region underwent plate reorganization during the Eocene. A pattern of N-S compression and subduction that had prevailed since about 110 m.y. B.P. at the northern and southern boundaries of the Caribbean plate changed to predominant E-W strike slip motion from 54 to 38 m.y. B.P. (Table 1; Fig. 2). The termination of N-S subduction at the northern margin of the Greater Antilles between 49 and 43 m.y. B.P., and the initiation of the present Puerto Rico (43 m.y. B.P.) and Cayman trenches (49 to 43 m.y. B.P.) manifest this change. The change may not have been synchronous or complete along the southern boundary of the Caribbean as evidenced, for example, by the obduction of ophiolites at the northern margin of South America as recently as 30 m.y. B.P. (Table 2; Fig. 1).

A change in pattern of plate motion in the Mediterranean region was nearly antithetic to that described in the Caribbean region. Right lateral E-W strike slip motion, inferred to have prevailed along the Tethys between 80 and 53 m.y. B.P., changed to N-S compression and subduction at about 53 m.y. B.P. with associated orogenic episodes and ophiolite obduction at the bounding plate margins (Table 1; Fig. 1). In the Red Sea, the final segment in the global circuit of plate boundaries, sea floor spreading with a large E-W component, began about 38 m.y. B.P. (Table 1; Fig. 1).

3. Global plate reorganization

Consideration of the regional changes in plate motion (Table 1; Figs. 1, 2) reveals patterns of Early Cenozoic plate reorganization which occurred primarily during the Eocene (53.5 to 37.5 m.y. B.P.), as follows:

(1) Major reorientation of those relative plate motions with large N-S components to large E-W components. This pattern is exhibited by changes in the direction of spreading in the Indian Ocean (53 to 50 m.y. B.P.) and the North Pacific Ocean (55 to 50 m.y. B.P.), as well as by change in the direction of motion of the North Pacific sea floor with respect

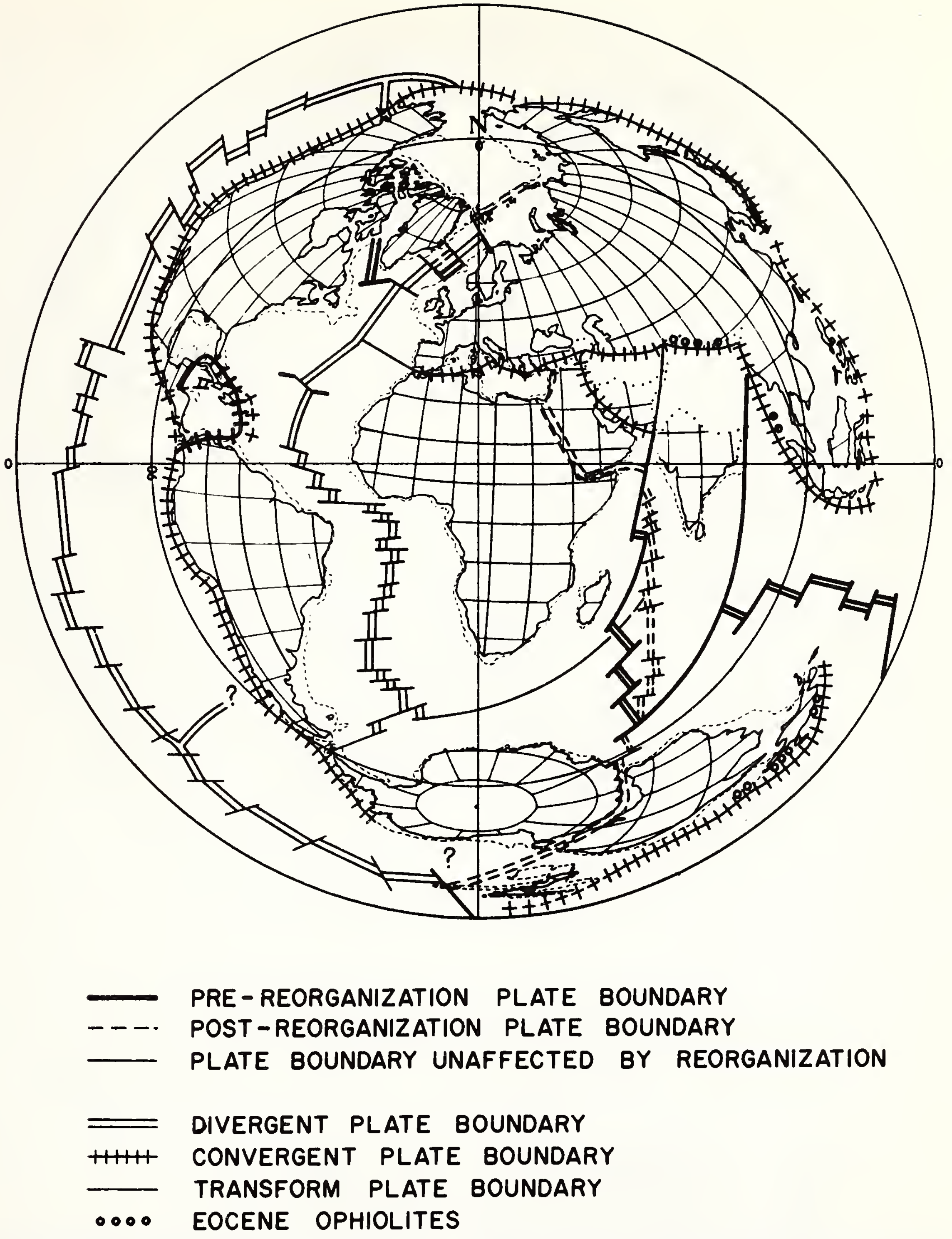
N
0
0
?
?
PRE-REORGANIZATION PLATE BOUNDARY
POST-REORGANIZATION PLATE BOUNDARY
PLATE BOUNDARY UNAFFECTED BY REORGANIZATION
DIVERGENT PLATE BOUNDARY
CONVERGENT PLATE BOUNDARY
TRANSFORM PLATE BOUNDARY
EOCENE OPHIOLITES

Fig. 1. Plate boundaries before and after Early Cenozoic plate reorganization plotted on Lambert equal area projection showing Eocene (50 ± 5 m.y. B.P.) distribution of continents [65]. Front view.

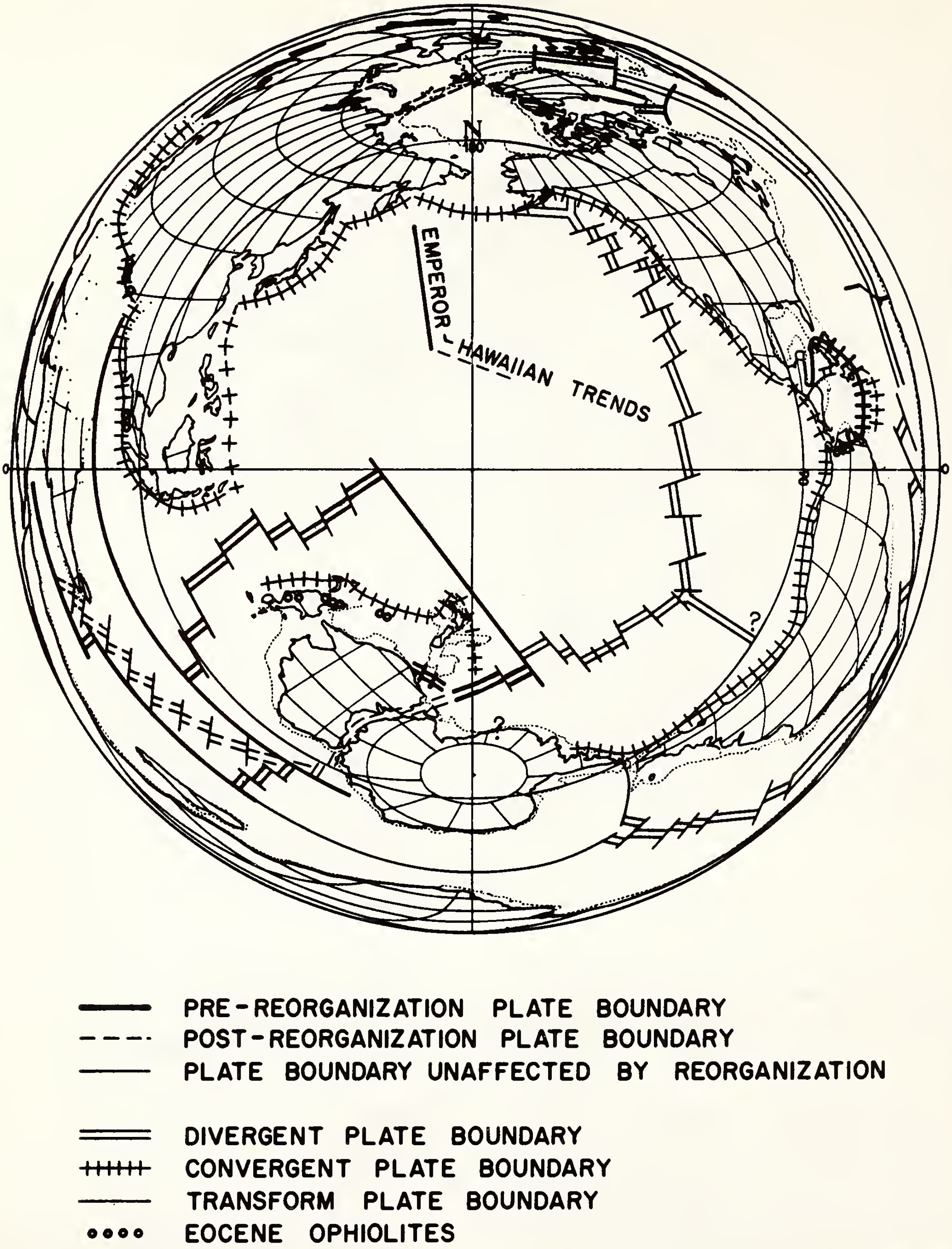
N
180
EMPEROR-HAWAIIAN TRENDS
?
?
?
0
0
PRE-REORGANIZATION PLATE BOUNDARY
POST-REORGANIZATION PLATE BOUNDARY
PLATE BOUNDARY UNAFFECTED BY REORGANIZATION
DIVERGENT PLATE BOUNDARY
CONVERGENT PLATE BOUNDARY
TRANSFORM PLATE BOUNDARY
EOCENE OPHIOLITES

Fig. 2. Plate boundaries before and after Early Cenozoic plate reorganization plotted on Lambert equal area projection showing Eocene (50 ± 5 m.y. B.P.) distribution of continents [65]. Back view.

to the Hawaiian hot spot (43 to 41 m.y. B.P.).

(2) Continuation with only minor reorientation of these plate motions with large E-W components and initiation of new E-W relative plate motions. This pattern is exhibited by continued E-W sea floor spreading about the Mid-Atlantic Ridge in the North Atlantic and South Atlantic, and by the initiation of predominantly E-W spreading about centers in the Arctic Ocean (63 m.y. B.P.), the northern North Atlantic Ocean (56 to 42 m.y. B.P.), and the Red Sea (38 m.y. B.P.).

(3) Decrease in rate of sea floor spreading affecting both regions of major and minor reorientation of sea floor spreading (patterns 1 and 2). Such decreases in spreading rate occurred in the Indian Ocean (53 to 40 m.y. B.P.), the South Pacific (56 m.y. B.P.), and the North Atlantic (59 to 50 m.y. B.P.), concurrently with reorientation of spreading direction.

(4) Change in nature of motion at certain plate boundaries between convergence with compression and strike slip. Such change occurred antithetically in two different regions within similar latitudes. In the Caribbean region N-S compression and subduction at E-W-trending convergent plate boundaries changed to predominant E-W strike slip motion (54 to 38 m.y. B.P.). In the Mediterranean region E-W-trending strike slip motion changed to N-S compression at a convergent plate boundary (53 m.y. B.P.).

(5) Conversion of certain transform plate boundaries to convergent plate boundaries as a consequence of major reorientation of plate motions. During the change in direction of sea floor spreading from large N-S to large E-W components in the Indian Ocean and North Pacific regions (55 to 41 m.y. B.P.), inferred pre-existing N-S-trending transform faults along the western margin of the Pacific became subduction zones.

(6) Sequential extinction of one spreading center and initiation of another spreading center with major reorientation of spreading. Such a change occurred within the same region within similar latitudes. The end of E-W spreading in the Tasman Sea (59 to 56 m.y. B.P.) was followed by the beginning of N-S spreading south of Australia (53 to 50 m.y. B.P.).

(7) Obduction of ophiolites at certain convergent plate boundaries involved in reorganization of plate motion in the Indian Ocean (100 to 43 m.y. B.P.), the South Pacific (52 to 37 m.y. B.P), the North Pacific (65 to 30 m.y. B.P.), and the Mediterranean (100 to 37 m.y. B.P.) regions (Table 3). Obduction of ophiolites may be a prime indicator of plate reorganization.

4. Global plate interaction

The nature of the plate interactions which produced the observed patterns of Early Cenozoic global plate reorganization may be deduced from assessment of global plate boundaries. The lengths of convergent and divergent plate boundaries were measured and totaled before and after the plate reorganization (Table 3). Regarding convergent plate boundaries, the process of subduction of oceanic crust which offers relatively low resistance to plate convergence, is distinguished from the process of collision involving continental or transitional (island arc) crust which offers relatively high resistance to plate convergence as a consequence of crustal buoyancy.

Immediately preceding the Early Cenozoic plate reorganization the total lengths of convergent and divergent plate boundaries were nearly equal at 52,000 and 50,000 km, respectively (Table 3). Of the 52,000 km of convergent plate boundaries, only about 2500 km in the Zagros area is known to have been a collisional boundary; subduction is inferred to have prevailed at the balance of the convergent plate boundaries (Figs. 1, 2). In the transition interval during the plate reorganization the length of collisional plate boundaries increased to 28,500 km (Table 3) due to the beginning of the collision of India and Eurasia along an E-W-trending boundary (5000 km; 55 to 40 m.y. B.P.), collision of the Australian shield with the New Guinea island arc along an E-W-trending boundary (8000 km; 49 to 43 m.y. B.P.), collision of the Bahama Banks with the Greater Antilles along an E-W-trending boundary region (1500 km; post-70 to 43 m.y. B.P.), and the change from E-W strike slip to N-S collision and compression along an E-W-trending boundary in the Mediterranean region (11,500 km; 53 m.y. B.P). Shortly following plate reorganization the collisions in the Australian shield–New Guinea island arc (8000 km) and the Bahamas Banks–Greater Antilles (1500 km) stopped, leaving a balance of 19,000 km of collisions in effect (Table 3). The total length of convergent plate bound-

TABLE 3

Early Cenozoic plate organization (see Figs. 1, 2)

All convergent plate boundaries (subduction and collision)

	Length * (km)		
	before	after	net change
South America and North America	17,000	18,000	+1,000
Aleutian-Kurile-Japan	8,000	8,000	0
Philippine-Ryuku-Marianas-Yap	0	9,000	+9,000
Zagros-Indus-Indonesia	14,000	14,000	0
New Guinea-Tonga	8,000	11,500	+3,500
Caribbean	5,000	2,500	−2,500
Mediterranean	0	11,500	+11,500
Worldwide total	52,000	74,500	22,500

Convergent plate boundaries: collision

	Length * (km)		
	before	transition	after
Zagros-Indus-Indonesia	2,500	7,500	7,500
New Guinea-Tonga	0	8,000	0
Caribbean	0	1,500	0
Mediterranean	0	11,500	11,500
Worldwide total	2,500	28,500	19,000

All divergent plate boundaries

	Length * (km)		
	before	after	net change
East Pacific	16,000	16,000	0
Australia-Antarctic-Indian	3,000	12,000	+9,000
Indonesian	10,000	0	−10,000
Red Sea	0	2,000	+2,000
Atlantic-Arctic	19,000	20,000	+1,000
Tasman	2,000	0	−2,000
Worldwide total	50,000	50,000	0

* Measured with estimated 5% accuracy on 40 cm diameter globe.

aries including both subduction and collision had increased to 74,500 km, an addition of 22,500 km over the pre-organizational total, while that of divergent plate boundaries remained at 50,000 km, no change from the pre-reorganizational total.

5. Conclusions

A statement by McKenzie and Sclater [64] with reference to the Indian Ocean region helps to elucidate the global observations presented: "Since the momentum of plates can always be neglected, any change in their motion must involve a change in either the driving forces or the resistive forces." The evidence presented clearly supports the interpretation that the plate reorganization from Mesozoic to Cenozoic patterns of plate motion was primarily a response to the global distribution of resistive forces.

The increase in E-W-trending collisional plate boundaries from about 2500 to 28,500 (5–38% of total length of convergent plate boundaries) during the interval between 55 and 40 m.y. B.P. (Tables 1, 3) produced a corresponding increase in resistance that apparently forced the global plate system to reorganize along lines of less resistance. The reorganization involved reorientation of relative plate motions with large N-S components into large E-W components, continuation of pre-existing E-W sea floor spreading, initiation of new E-W spreading, deceleration of spreading rates, complex antithetic and sequential events limited to certain regions, and obduction of ophiolites. The persistence of about 19,000 km of collisional plate boundaries subsequent to 40 m.y. B.P. has acted to constrain the global pattern of plate motion established by the Early Cenozoic plate reorganization. The occurrence of global plate reorganizations in Early Mesozoic and Early Cenozoic suggests a plate tectonic basis for the division of the Phanerozoic time scale into eras.

Acknowledgements

We thank Steven Schamel for guidance in the structural history of the Mediterranean region. We thank C.G.A. Harrison and Walter C. Pitman III for helpful reviews. This research was supported by NOAA. Contribution from NOAA and the University of Miami, Rosenstiel School of Marine and Atmospheric Sciences.

References

[1] R.S. Dietz and J.C. Holden, Reconstruction of Pangaea: breakup and dispersion of continents, Permian to

present, J. Geophys. Res. 75 (1970) 4939.
[2] J.E. Van Hinte, A Cretaceous time scale, Am. Assoc. Pet. Geol. Bull. 60 (1976) 498.
[3] W.A. Berggren, Cenozoic chronostratigraphy, planktonic foraminiferal zonation and the radiometric time-scale, Nature 224 (1969) 1072.
[4] J.L. La Brecque, D.V. Kent and S.C. Cande, Revised magnetic polarity time scale for Late Cretaceous and Cenozoic times, Geology 5 (1977) 330.
[5] A. Gansser, Geology of the Himalayas (Interscience, London, 1964) 289.
[6] A. Gansser, The Indian Ocean and the Himalayas—geological interpretation, Eclogae Geol. Helv. (59) 831.
[7] A. Sahni and V. Kumar, Paleogene palaeobiogeography of the Indian subcontinent, Palaeogeogr., Palaeoclimatol., Palaeoecol. 15 (1974) 209.
[8] P. Le Fort, Himalayas: the collided range. Present knowledge of continental arc, Am. J. Sci. 275-A (1975) 1.
[9] P. Molnar and P. Tapponier, The collision between India and Eurasia, Sci. Am. 236 (1977) 30.
[10] J.G. Sclater and R.L. Fisher, Evolution of the East Central Indian Ocean with emphasis on the tectonic setting of the Ninetyeast Ridge, Geol. Soc. Am. Bull. 85 (1974) 683.
[11] B.D. Johnson, C. McA. Powell and J.J. Veevers, Spreading history of the eastern Indian Ocean and Greater India's northward flight from Antarctica and Australia, Geol. Soc. Am. Bull. 87 (1976) 1560.
[12] J.W. Pierce, The origin of the Ninetyeast Ridge and the northward motion of India, based on DSDP paleolatitudes, Doctoral Dissertation, Woods Hole Oceanographic Institution (1977) 283.
[13] W.C. Pitman III, R.L. Larson and E.M. Herron, The Age of the Ocean Basins (Geological Society of America, 1974) 2 maps.
[14] D.E. Hayes and J. Ringis, The early opening of the central Tasman Sea, EOS, Trans. Am. Geophys. Union 53 (1972) 413 (abstract).
[15] J.K. Weissel and D.E. Hayes, Magnetic anomalies in the southeast Indian Ocean; in: Antarctic Oceanology II: The Australian–New Zealand sector, D.E. Hayes, ed., Am. Geophys. Union, Antarctic Res. Ser. 19 (1972) 165.
[16] M.E. Brookfield, The emplacement of giant ophiolite nappes, I. Mesozoic-Cenozoic examples, Tectonophysics 37 (1977) 247.
[17] P. Molnar and P. Tapponnier, Cenozoic tectonics of Asia: effects of a continental collision, Science 189 (1975) 419.
[18] W.C. Pitman III, E.M. Herron and J.R. Heirtzler, Magnetic anomalies in the Pacific and sea floor spreading, J. Geophys. Res. 73 (1968) 2069.
[19] J.R. Heirtzler, G.O. Dickson, E.M. Herron, W.C. Pitman III and X. Le Pichon, Marine magnetic anomalies, geomagnetic field reversals, and motions of the ocean floor and continents, J. Geophys. Res. 73 (1968) 2119.
[20] E.M. Herron, Magnetic lineations in the extreme southeast Pacific and their bearing on the evolution of the Scotia Arc and Pategonia, Geol. Soc. Am., Abstr. Progr, 6 (1974) 791.
[21] P.J. Coney, Cordilleran tectonic transitions and motion of the North American plate, Nature 233 (1971) 462.
[22] H.W. Menard and T. Atwater, Changes in direction of sea floor spreading, Nature 219 (1968) 463.
[23] S. Uyeda and Z. Ben-Arraham, Origin and development of the Philippine Sea, Nature Phys. Sci. 240 (1972) 176.
[24] T.W.C. Hilde, S. Uyeda and L. Kroenke, Evolution of the western Pacific and its margins, in: Present State of Plate Tectonics, J. Bonnin and R.S. Dietz, eds. Tectonophysics 38 (1977) 145.
[25] S. Uyeda, Some basic problems in the trench-arc-back arc system, in: Island Arcs, Deep Sea Trenches and Back-Arc Basins, M. Talwani and W.C. Pitman III, eds., Am. Geophys. Union, Maurice Ewing Ser. 1 (1977) 1.
[26] D.A. Clague, G.B. Dalrymple and R. Moberly, Petrography and K-Ar ages of dredged volcanic rocks from the western Hawaiian Ridge and the southern Emperor Seamount, Geol. Soc. Am. Bull. 86 (1975) 991.
[27] W.C. Pitman III and M. Talwani, Sea-floor spreading in the North Atlantic, Geol. Soc. Am. Bull. 83 (1972) 619.
[28] E.M. Herron, J.F. Dewey and W.C. Pitman III, Plate tectonics model for the evolution of the Arctic, Geology 2 (1974) 377.
[29] P.R. Vogt, N.A. Ostenso and G.L. Johnson, Magnetic and bathymetric data bearing in sea-floor spreading north of Iceland, J. Geophys. Res. 75 (1970) 903.
[30] M. Mayhew, C.L. Drake and J.F. Nafe, Marine geophysical measurements on the continental margins of Labrador Sea, Can. J. Earth Sci. 7 (1970) 199.
[31] X. Le Pichon, R.D. Hyndman and G. Pautot, Geophysical study of the opening of the Labrador Sea, J. Geophys. Res. 76 (1971) 4724.
[32] P.R. Vogt, O.E. Avery, W.J. Morgan, G.L. Johnson, E.D. Schneider and R.H. Higgs, Morphology, magnetic anomalies and evolution of the northeast Atlantic and Labrador Sea, 3. Evolution, EOS, Trans. Am. Geophys. Union 50 (1969) 184 (abstract).
[33] E.M. Herron and M. Talwani, Magnetic anomalies on the Reykjanes Ridge, Nature 238 (1972) 390.
[34] R.K. Lattimore, P.A. Rona and O.E. DeWald, Magnetic anomaly sequence in the Central North Atlantic, J. Geophys. Res. 79 (1974) 1207.
[35] P.D. Rabinowitz and G.M. Purdy, The Kane fracture zone in the western Central North Atlantic Ocean, Earth Planet. Sci. Lett. 33 (1976) 21.
[36] G.O. Dickson, W.C. Pitman III and J.R. Heirtzler, Magnetic anomalies in the South Atlantic and ocean floor spreading, J. Geophys. Res. 73 (1968) 2087.
[37] A.E. Maxwell, Initial Reports of the Deep Sea Drilling Project III, U.S. Government Printing Office, Washington, D.C. (1970) 806.
[38] J.W. Ladd, G.P. Dickson and W.C. Pitman III, The age of the South Atlantic, in: The Ocean Basins and Margins, 1. The South Atlantic, A.E.M. Nairn and F.G. Stehli,

eds. (Plenum Press, New York, N.Y., 1973) 555.

[39] B.T. Malfait and M.G. Dinkelman, Circum-Caribbean tectonic and igneous activity and the evolution of the Caribbean plate, Geol. Soc. Am. Bull. 83 (1972) 251.

[40] R. Weyl, Die Geologie der Antillen (Gebr. Borntraeger, Berlin, 1966) 410.

[41] A.A. Meyerhoff and C.W. Hatten, Diapiric structures in central Cuba, Am. Assoc. Pet. Geol. Mem. 8 (1968) 315.

[42] P.H. Mattson, Middle Cretaceous nappe structures in Puerto Rican ophiolites and their relation to the tectonic history of the Greater Antilles, Geol. Soc. Am. Bull. 84 (1973) 21.

[43] W.H. Monroe, The age of the Puerto Rico Trench, Geol. Soc. Am. Bull. 79 (1978) 487.

[44] K.M. Khudoley and A.A. Meyerhoff, Paleogeography and geological history of the Greater Antilles, Geol. Soc. Am. Mem. 129 (1971) 199.

[45] B.E. Tucholke and J.I. Ewing, Bathymetry and sedimentary structure of the Greater Antilles outer ridge and vicinity, Geol. Soc. Am. Bull. 85 (1974) 1789.

[46] F. Nagle, Geology of the Puerto Plata area, Dominican Republic, relative to the Puerto Rico Trench, in: Transactions, 5th Caribbean Geological Conference, St. Thomas, V.I., P.H. Mattson, ed., Queens College Geol. Bull. 5 (1971) 79.

[47] T.L. Holcombe, P.R. Vogt, J.E. Matthews and R.R. Murchison, Evidence for sea floor spreading in the Cayman Trough, Earth Planet. Sci. Lett. 20 (1973) 357.

[48] B.C. Heezen, M.R. Perfit and M. Dreyfus, The Cayman Ridge, Geol. Soc. Am., Abstr. Progr. 5 (1973) 663.

[49] J.F. Dewey, W.C. Pitman III, W.B.F. Ryan and J. Bonnin, Plate tectonics and the evolution of the Alpine system, Geol. Soc. Am. Bull. 84 (1973) 3137.

[50] G. Boillot and R. Capdevila, The Pyrenees: subduction and collision?, Earth Planet. Sci. Lett. 35 (1977) 151.

[51] K.J. Hsü and S.O. Schlanger, Ultrahelvetic flysch sedimentation and deformation related to plate tectonics, Geol. Soc. Am. Bull. 82 (1971) 1207.

[52] R. Trümpy, Penninic-Austroalpine boundary in the Swiss Alps: a presumed former continental margin and its problems, Am. J. Sci. 275-A (1975) 209.

[53] V.J. Dietrich, Evolution of the Eastern Alps: a plate tectonics working hypothesis, Geology 4 (1976) 147.

[54] R. Lafitte, Les plissements post-nummalitiques dans l'Atlas Saharien, Bull. Soc. Geol. Fr. 5 (1939) 135.

[55] Société Chérifienne des Pétroles, Le Bassin du Sud-Ouest Marocain, in: Sedimentary Basins of the African Coasts, 1. Atlantic Coast, D. Reyre, ed. (Assoc. African Geol. Surveys, Paris, 1966) 5.

[56] R.W. Girdler and P. Styles, Two stage Red Sea floor spreading, Nature 247 (1974) 7.

[57] H.L. Davies and I.E. Smith, Geology of Eastern Papua, Geol. Soc. Am. Bull. 82 (1971) 3299.

[58] J. Avias, Overthrust structure of the main ultrabasic New Caledonian Massives, Tectonophysics 4 (1967) 531.

[59] J.J. Guillon and P. Rothier, Les stades d'evolution et de mise en place des Massifs ultramafiques de Nouvelle Calédonie, Bull. B.R.G.M. 2 (1971) 5.

[60] R.G. Coleman and W.P. Irwin, Ophiolites and ancient continental margins in: The Geology of Continental Margins, C.A. Burk and C.L. Drake, eds. (Springer-Verlag, New York, N.Y., 1974) 921.

[61] R.G. Tysdale, J.E. Case, G.R. Winkler and S.H.B. Clark, Sheeted dikes, gabbro, and pillow basalt in flysch of coastal southern Alaska, Geology 5 (1977) 377.

[62] A. Gansser, Asseralpine ophiolithprobleme, Eclogae Geol. Helv. 52 (1959) 659.

[63] W.G. Ernst, Interpretative synthesis of metamorphism in the Alps, Geol. Soc. Am. Bull. 84 (1973) 2053.

[64] D.P. McKenzie and J.G. Sclater, The evolution of the Indian Ocean since the Late Cretaceous, Geophys. R. Astron. Soc. J. 25 (1971) 437.

[65] J.C. Briden, G.E. Drewry and A.G. Smith, Phanerozoic equal-area world maps, J. Geol. 82 (1974) 555.

Nature 276, No. 21/28, 811-813.

Metal-enriched sediments from the TAG Hydrothermal Field

A SERIES of sediment samples from the TAG Hydrothermal Field[1] have been collected and analysed for transition metals, and for uranium and thorium isotopes. We show here that metal enrichment of sediment samples is ubiquitous, but geographically variable. Non-detrital metal accumulation rates in one core are Fe and Mn 15.0 and 0.7 mg cm^{-2} 10^{-3} yr; and Ni, 180; Co, 93; Cu, 134; and Cr, 148 μg cm^{-2} 10^{-3}yr. The hydrothermal field is located on the eastern wall of the Mid-Atlantic Ridge Rift Valley at 26°N and covers ~100 km^2. It is characterised by extensive deposits of thick, rapidly growing MnO_2 (ref. 2) and by a magnetic low in the axial anomaly[1].

Figure 1 shows that the sediment thickness is quite variable even over a small area of the valley floor. Core 4A (132 cm of sediment) and core 4G (15 cm of sediment) both terminated with basaltic glass, and a core from site 4C recovered glass only, with no overlying sediment. A study of bottom photographs of this section of the median valley[3] shows ripple marked sand and other evidence of the strong bottom currents responsible for sweeping sediment off some portions of the valley floor into sediment ponds of uneven distribution.

Three types of sediment were collected during the 1973 cruise of the Discoverer: (1) samples 4A, 4B and 4H are cores of ponded carbonate ooze sediment in the median valley; (2) $CaCO_3$-rich clay was dredged from the top of a small terrace (dredge site 2A); and (3) sediment interstitial to and covering boulders in the talus was recovered from dredge sites 2A and 3A. This material was less than 5% carbonate and consisted largely of altered basalt debris.

Chemical analyses were made on the sediment samples by atomic absorption spectrophotometry. The results are given in Table 1 along with metal-to-aluminium ratios for average North Atlantic pelagic clay[4-11] for comparison. The metal-to-aluminium ratios for the average North Atlantic clay is considered to be characteristic of the detrital component of the sediment on which hydrothermal additions are superimposed. Note that none of the samples analysed are very highly enriched in metals compared to the average North Atlantic pelagic clay values. The highest Mn/Al ratios were observed in one of the samples from Dredge Site 2A and the $CaCO_3$-rich terrace sediment, but the maximum enrichment of Mn relative to the average North Atlantic clay Mn/Al value was only about 7, in contrast to enrichments of 100 or higher found on the East Pacific Rise[12]. The presence of a large deposit of Mn oxide found in the nearby hydrothermal field[2] clearly suggests a significant flux of Mn into seawater in this general vicinity. Scott *et al.*[2] have measured the accumulation rate of the Mn oxide deposit and found it to be 100–200 mm Myr^{-1} or 2 orders of magnitude faster than typical deep sea ferromanganese deposits. It is surprising that so little of the Mn is deposited in the adjacent sediments.

Iron-to-aluminium ratios in the TAG sediments showed even less pronounced enrichment than the Mn/Al ratios. The average Fe/Al ratio for all samples analysed is 0.89 in comparison with the average North Atlantic pelagic clay ratio of 0.56 (Table 1). Most of the Fe in these sediments is detrital in origin. Betzer *et al.*[13] have found much higher Fe/Al and Mn/Al ratios on a total sample basis for the suspended matter sampled from near bottom water over the ridge crest than for similar particles sampled to either side of the ridge crest. Some of the Fe and Mn in the hydrothermal fluids are probably precipitating in the water column after they enter the ocean. They are diluted in the underlying sediment by biogenic and detrital material being deposited at the same site, and are undoubtedly also being wafted away from the area by currents. The nearly total absence of Fe in the massive hydrothermal MnO_2 deposit[2] (Fig. 1) suggests that the Fe may be removed as pyrite[14] or other minerals before the hydrothermal fluids debouch onto the sea floor from that vent. The variability in metal enrichments between the massive MnO_2 deposits and the metal enriched sediments indicates variability in the chemistry of the hydrothermal fluids in both space and time.

The metal-to-aluminium ratios of samples from core 4A show that the core is somewhat enriched throughout its length in Fe, Mn, Ni, Cu, Co and Cr with respect to average North Atlantic pelagic clay (Table 1). The Mn content of the 30–32 cm interval falls below the average pelagic clay value, but this is probably the result of dilution by basaltic glass fragments at that depth that were not removed from the sediment before analysis. The Co and Cu values are very strongly correlated with Mn content, showing correlation coefficients of +0.95 and +0.97 respectively. These metals may be concentrated from seawater by precipitating hydrothermal Mn, or they may also be contributed by the hydrothermal solutions themselves. Nickel and Cr in the core are not correlated with Fe, nor with Mn, nor with each other. The factors controlling their distribution cannot be determined without further investigation.

Metal enrichment studies of ridge crest sediments based only on metal-to-aluminium ratios omit a very important parameter—time. The ratios observed in the sediment reflect not only the intensity of the metal source, but also all of the other processes operating to dilute the metals being added by ridge crest processes. An estimate of the rate at which the metals are added compared to analogous rates for non-metalliferous sediments avoids this problem.

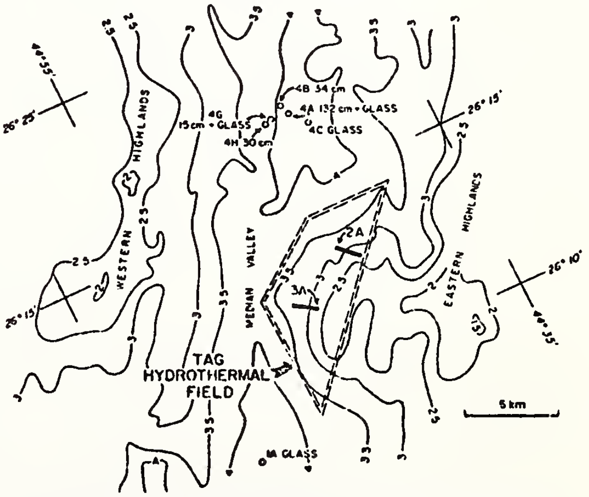

Fig. 1 Sample location map of cores and dredge hauls from the TAG area on the Mid-Atlantic Ridge. Contours are in hundreds of metres.

Table 1 Sediment analyses ($CaCO_3$-free basis)

	Fe (%)	Mn (%)	Al (%)	Ni (p.p.m.)	Co (p.p.m.)	Cu (p.p.m.)	Cr (p.p.m.)	Fe/Al	Mn/Al	Ni/Al ∓g3	Co/Al $\times 10^3$	Cu/Al $\times 10^3$	Cr/Al $\times 10^3$	$\%CaCO_3$	Porosity (ml cm^{-3})
2A8-2	6.34	0.145	7.40	128	54.0	47.7	254	0.86	0.0196	1.73	0.730	0.645	3.43	nd*	—
2A8-3	4.26	0.226	2.97	123	59.6	269	242	1.43	0.0761	4.14	2.01	9.06	8.15	nd	—
2A8-4	6.97	1.19	6.63	164	58.2	88.5	342	1.05	0.179	2.47	0.878	1.33	5.16	nd	—
Dredge Site 3A†															
3A2-1	7.47	0.146	8.04	135	61.3	91.3	370	0.93	0.0181	1.68	0.762	1.14	4.60	nd	—
3A2-2	3.15	0.096	3.45	76	42.6	61.2	94	0.91	0.0278	2.20	1.23	1.77	2.72	nd	—
3A2-3	3.73	0.105	3.79	92	35.7	74.0	236	0.98	0.0277	2.43	0.942	1.95	6.23	nd	—
Terrace Sediment‡															
2A8-5	2.90	0.932	3.15	341	140	150	126	0.92	0.296	10.8	4.44	4.76	4.00	77.0	—
Core Tops															
4B02	5.98	0.349	6.74	147	105	166	230	0.89	0.0539	2.18	1.62	2.46	3.41	60.3	—
4G04	5.50	0.528	6.10	204	150	197	208	0.90	0.0866	3.34	2.46	3.23	3.41	72.8	—
4H08	4.89	0.343	5.58	178	108	179	212	0.88	0.0615	3.19	1.94	3.21	3.80	61.2	—
Core 4A															
0–4 cm	5.32	0.407	6.19	218	138	212	244	0.86	0.0658	3.52	2.22	3.41	3.94	67.3	0.73
4–8	5.15	0.421	4.98	198	140	221	204	1.03	0.0845	3.98	2.81	4.44	4.10	69.6	0.74
8–14	3.90	0.478	4.99	229	161	247	180	0.78	0.0958	4.59	3.23	4.95	3.61	73.9	0.75
14–18	3.49	0.419	5.64	212	154	225	169	0.62	0.0743	3.76	2.73	3.99	3.00	72.8	0.71
18–22	4.08	0.472	5.98	235	164	240	184	0.68	0.0784	4.23	2.74	4.01	3.08	75.0	0.73
22–26	4.93	0.441	6.49	206	156	230	190	0.76	0.0680	3.17	2.40	3.54	2.92	73.1	0.75
26–30	5.33	0.254	6.94	261	87.6	146	232	0.77	0.0366	3.76	1.26	2.10	3.34	46.5	0.75
30–31§	4.68	0.205	7.04	276	88.9	442	220	0.65	0.0291	3.92	1.26	6.28	3.12	44.6	—
31–32§	5.53	0.184	8.39	254	81.6	119	256	0.66	0.0219	3.03	0.973	1.42	3.05	31.8	—
32–33§	5.35	0.257	5.01	286	87.8	148	228	1.07	0.0513	5.71	1.75	2.95	4.55	48.6	—
33–37	5.84	0.333	6.12	312	99.9	190	125	0.95	0.0544	5.10	1.63	3.10	2.04	55.9	0.79
120–127	5.86	0.296	6.53	134	79.9	146	212	0.90	0.0453	2.05	1.22	2.24	3.25	51.6	0.77
Avg. N Atlantic pelagic clay[t–tt]	5.0	0.4	9.0	79	39	115	80	0.56	0.04	0.9	0.4	1.3	0.9	—	—
Mid-Atlantic Ridge 45°N[7]	9.6	0.5	5.3	214	—	399	128	1.8	0.1	4.0	—	7.5	2.4	—	—
East Pacific Rise[12]	18.0	6.0	0.5	430	105	730	55	36	12	86	21	146	11	—	—
Avg. Pacific pelagic clay[4]	5.1	0.9	8.3	300	110	400	78	0.61	0.11	3.6	1.3	4.8	0.9	—	—

* Negligible, not determined. † Material interstitial to talus blocks. ‡ $CaCO_3$-rich sediment from step-fault terrace. § Most glass shards removed as >0.088 mm fraction. Porosity measurements were made by John Morse.

Table 2 Radiometric data from TAG sediment core 4A

Sample depth (m)	U (p.p.m.)	$^{234}U/^{238}U$	Th (p.p.m.)	^{230}Th $d(pm\ g^{-1})$	$^{230}Th/^{232}Th$	$^{230}Th_{xs}$ $d(pm\ g^{-1})$
0–4	0.58 ± 0.03	1.12 ± 0.07	1.38 ± 0.06	14.06 ± 0.40	10.22 ± 0.38	13.58 ± 0.40
18–22	0.75 ± 0.03	1.40 ± 0.07	4.07 ± 0.11	11.60 ± 0.18	11.58 ± 0.27	10.82 ± 0.18
22–26	0.83 ± 0.03	1.37 ± 0.05	6.47 ± 0.44	11.83 ± 0.50	7.43 ± 0.45	10.99 ± 0.50
26–30	0.59 ± 0.03	1.20 ± 0.07	4.55 ± 0.16	10.88 ± 0.24	9.72 ± 0.30	10.37 ± 0.24
33–37	0.73 ± 0.01	1.00 ± 0.02	3.55 ± 0.23	11.32 ± 0.37	12.93 ± 0.77	10.79 ± 0.37
41–50	0.64 ± 0.03	1.26 ± 0.08	6.82 ± 0.19	11.72 ± 0.22	6.98 ± 0.16	11.11 ± 0.22
57–70	0.36 ± 0.04	0.75 ± 0.11	2.51 ± 0.08	8.09 ± 0.11	13.12 ± 0.41	7.89 ± 0.11
120–127	0.65 ± 0.01	1.17 ± 0.03	4.04 ± 0.24	8.27 ± 0.27	8.31 ± 0.46	7.71 ± 0.27

1 s.d. errors from counting statistics are listed.

Table 3 Metal accumulation rates for core 4A

		Fe	Mn	Al	Ni	Co	Cu	Cr	$CaCO_3$-free sedimentation rate (mm kyr^{-1})
			(mg cm^{-2} kyr^{-1})			(μg cm^{-2} kyr^{-1})			
Core 4A, whole sediment		49.5	3.47	61.9	235.0	120.0	214.0	204.0	6.8
Core 4A, detrital fraction		34.5	2.78	61.9	54.8	27.0	80.1	55.6	—
Core 4A, nondetrital* fraction		15.0	0.69	0	180	93	134	148	—
Average N. Atlantic pelagic clay		8.7	0.7	15.6	13.8	6.8	20.2	14.0	2.5
East Pacific Rise	a	82.0	28.0	0.61	160.0	—	—	—	0.5
East Pacific Rise	b	58	18	3	153	47	254	21	5.3

* The accumulation rate for the non-detrital fraction of Core 4A was calculated by subtracting a detrital metal component based on the detrital metal-to-aluminium ratio (average North Atlantic pelagic clay) and the accumulation rate of aluminium in Core 4A.

The sedimentation rate of core 4A was measured by means of the ^{230}Th excess method (Table 2). The rate at which this sediment is accumulating is ~1.8 cm kyr^{-1}. This rate is consistent with Mid-Atlantic Ridge sedimentation rates measured by other workers[15–17]. Note in Table 2 that ^{234}U/^{238}U activity ratios >1 exist over the whole length of the core, in some cases beyond corrections for 3 s.d. of counting statistics. Post depositional hydrothermal additions of uranium to ridge crest sediments have been previously noted[18–21]. The same interpretation seems reasonable for these data. Addition of ^{234}U-rich uranium would distort the accumulation rate towards a lower value.

Metal accumulation rates have been calculated for core 4A on the basis of average metal concentrations and porosity (Table 1) and the measured sediment accumulation rate of 1.8 cm kyr^{-1} and are listed in Table 3. The Al content of marine sediments is commonly used as an index of the detrital component. We calculated the metal accumulation rates for the detrital component of core 4A using the average Al content of 4A (Table 1), the sediment accumulation rate of 4A, and the metal-to-aluminum ratios for average North Atlantic pelagic clay (Table 1). These values were subtracted from the whole sediment values, yielding the non-detrital accumulation rates listed in Table 3. These rates include only material from non-detrital sources.

The non-detrital metal accumulation rates (Table 3) show that Fe, Mn and the trace metals are being added to sediment in the TAG area at rates that are well above the background values for the North Atlantic Ocean. Iron and manganese accumulation rates on the East Pacific Rise[22–24] are much greater than at this site on the Mid-Atlantic Ridge. However, the Ni, Co, Cu, and Cr accumulation rates are conspicuously high in comparison with East Pacific Rise data. The differences observed in sediments from the two active ridge areas may be related to water circulation differences in the hydrothermal systems of fast and slow spreading ridges[25]. Note also that metal enrichment in TAG area sediments may be higher than average for hydrothermal areas on the Mid-Atlantic Ridge. Sediments from the FAMOUS area at 37° N were found to be accumulating metals at much slower rates than those reported here[18].

This research was supported by the NSF, International Decade of Ocean Exploration, Office of Naval Research and National Oceanic and Atmospheric Administration.

MARTHA R. SCOTT

Department of Oceanography,
Texas A & M University

ROBERT B. SCOTT

Department of Geology,
Texas A & M University,
College Station, Texas 77843

JOHN W. MORSE

Rosensteil School of Marine and Atmospheric Sciences,
University of Miami, 4600 Rickenbacker Causeway,
Miami, Florida 33124

PETER R. BETZER

Department of Marine Sciences,
University of South Florida,
St Petersburg, Florida 33701

LOUIS W. BUTLER
PETER A. RONA

National Oceanic and Atmospheric Administration,
15 Rickenbacker Couseway,
Miami, Florida 33149

Received 3 August; accepted 27 October 1978.

1. Scott, R. B., Rona, P. A., McGregor, B. A. & Scott, M. R. *Nature* **251**, 301–302 (1974).
2. Scott, M. R., Scott, R. B., Rona, P. A., Butler, L. W. & Nalwalk, A. J. *Geophys. Res. Lett.* **1**, 355–358 (1974).
3. Temple, D. G., Scott, R. B. & Rona, P. A. (in the press).
4. Turekian, K. K. & Imbrie, J. *Earth planet. Sci. Lett.* **1**, 166–168 (1966).
5. Cronan, D. S. *Can. J. Earth Sci.* **9**, 319–323 (1972).
6. Bostrom, K. & Valdes, S. *Lithos* **2**, 351–360 (1969).
7. Horowitz, A. & Cronan, D. S. *Mar. Geol.* **20**, 205–228 (1976).
8. Landergren, S. *Rep. Swed. Deep-Sea Expdn.* **10**, 61–156 (1964).
9. Van der Weijden, C. H., Schuiling, R. D. & Das, H. A. *Mar. Geol.* **9**, 81–99 (1970).
10. El Wakeel, S. K. & Riley, J. P. *Geochim. cosmochim. Acta* **25**, 110–146 (1961).
11. Bruty, D., Chester, R., Royle, L. G. & Elderfield, H. *Nature phys. Sci.* **237**, 86–87 (1972).
12. Bostrom, K. & Peterson, M. N. A. *Mar. Geol.* **7**, 427–47(1969).
13. Betzer, P. R., Bolger, G. W., McGregor, B. A. & Rona, P. A. *Trans. Am. Geophys. Un.* **55**, 293 (1974).
14. Spooner, E. T. C. & Fyfe, W. S. *Contr. Miner. Petrol.* **42**, 287–304 (1973).
15. Ku, T. L., Bischoff, J. L. & Boersma, A. *Deep-Sea Res.* **19**, 223–247 (1972).
16. Scott, M. R., Salter, P. F. & Barnard, L. A. *Second Maurice Ewing Symp. Vol.* (in the press).
17. Nozaki, Y., Cochran, J. K. & Turekian, K. K. *Earth planet. Sci. Lett.* **34**, 167–174 (1977).
18. Rydell, H. S., Kraemer, T., Bostrom, K. & Joensuu, O. *Mar. Geol.* **17**, 151–164 (1974).
19. Fisher, D. E. & Bostrom, K. *Nature* **224**, 64–65 (19).
20. Veeh, H. H. & Bostrom, K. *Earth planet. Sci. Lett.* **10**, 372–374 (1971).
21. Scott, M. R. & Salter, P. F. *Trans. Am. Geophys. Un.* **58**, 420 (1977).
22. Dymond, J. & Veeh, H. H. *Earth planet. Sci. Lett.* **28**, 13–22 (1975).
23. Bender, M. *et al. Earth planet. Sci. Lett.* **12**, 425–433 (1971).
24. Bertine, K. K. *Geochim. cosmochim. Acta* **38**, 629–635 (1974).
25. Scott, R. B., Temple, D. G. & Peron, P. R. (in the press).

0028-0836/78/0276–0813$01.00

Marine Geology 26, M37-M46.

Letter Section

THE EROSION—DEPOSITION BOUNDARY IN THE HEAD OF HUDSON SUBMARINE CANYON DEFINED ON THE BASIS OF SUBMARINE OBSERVATIONS

DANIEL JEAN STANLEY and GEORGE L. FREELAND

Division of Sedimentology, Smithsonian Institution, Washington, D.C. 20560 (U.S.A.)
National Oceanic and Atmospheric Administration, Atlantic Oceanographic and Meteorological Laboratories, Miami, Fla. 33149 (U.S.A.)

(Revised version accepted December 30, 1977)

ABSTRACT

Stanley, D.J. and Freeland, G.L., 1978. The erosion—deposition boundary in the head of Hudson Submarine Canyon defined on the basis of submarine observations. Mar. Geol., 26: M37—M46.

Submersible observations in the head of Hudson Canyon, to depths of 305 m, indicate that coarse relict sediment at and below the shelf edge (at about 105 m) has been reworked by currents and benthic organisms during the Holocene and at present. The sharp boundary between an upper gravel—shell—sand facies and a deeper mud facies is herein termed "mud line". This "mud line", present at depths ranging from 130 m to 175 m, appears to record a long-term separation of energy levels, i.e., below these depths, current speeds necessary to erode fine sediments decrease significantly in frequency and intensity. We observed that the shelf break and uppermost slope in the canyon is a zone of continuing resuspension where there is no permanent accumulation of fines above the "mud line". Defining the "mud line" position relative to regional lithofacies patterns may provide an additional, albeit indirect, measure of depth of impingement of current speed sufficient to exceed the threshold of sediment transport on the outer continental margin.

INTRODUCTION

A series of eleven submersible dives was made in the head of the Hudson Submarine Canyon from 22 to 27 July 1976 as part of the National Oceanic and Atmospheric Administration's (NOAA) environmental studies of the sea floor in the New York Bight. The study area lies 160 km southeast of the New York Harbor entrance where the canyon is incised 31 km into the shelf (Fig. 1).

Previous studies of the area have centered on topography and shallow stratigraphy which show the shelf-edge effects of major Quaternary eustatic sea-level oscillations. These include terraces (Veatch and Smith, 1939; Ewing et al., 1963) and subbottom erosional disconformities (Knott and Hoskins, 1968). Further evidence that the coastline was periodically at or near the

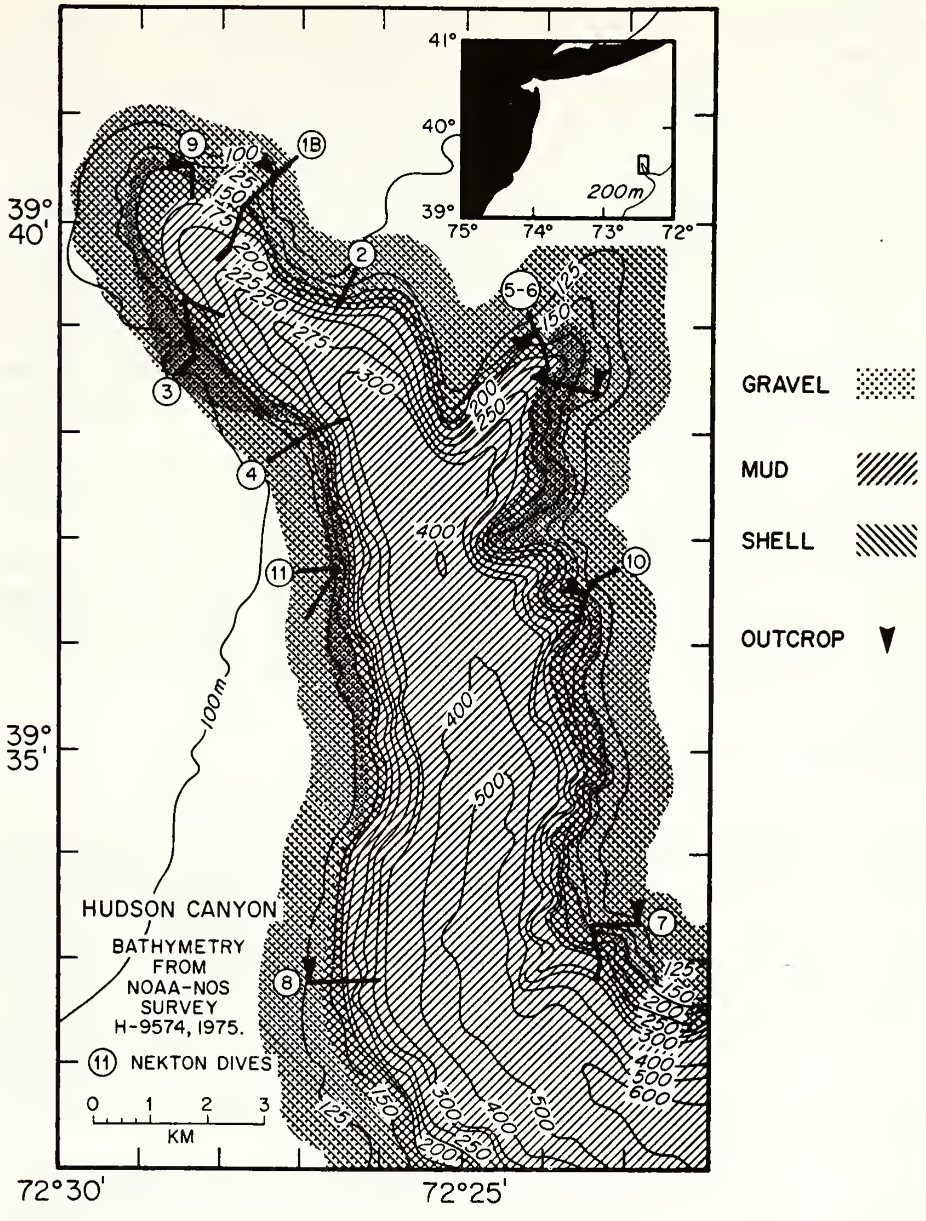
41°
40°
39°
75°
74°
73°
72°
200m
39° 40'
39° 35'
72°30'
72°25'
100m
GRAVEL
MUD
SHELL
OUTCROP
HUDSON CANYON
BATHYMETRY FROM NOAA-NOS SURVEY H-9574, 1975.
⑪ NEKTON DIVES
0 1 2 3
KM
⑨
①B
②
③
④
⑤-⑥
⑦
⑧
⑩
⑪
100
125
150
175
200
225
250
275
300
400
500
600

Fig. 1. Location of submersible dives and outcrops and distribution of **major** sediment types in the head of the Hudson Submarine Canyon. Depth in meters.

present shelf break is indicated by the nature of the sediments. Concentrations of gravel and coarse sand (Schlee and Pratt, 1970; Trumbull, 1972) and heavy-mineral composition (Kelling et al., 1975) show that the ancestral Hudson River, which incised a deep valley across the subaerially exposed shelf, was largely responsible for the transport of coarse materials directly to the study area. The alignment of the canyon with the shelf valley, the canyon configuration, and the stratigraphic and surficial-sediment evidence cited above point to the pre-Holocene imprint on the area. Although the study area now lies deeper than 100 m, water-mass data indicate that active sediment transport should be occurring at present. Particularly significant in this respect are bottom-current measurements showing occasional current speeds exceeding transport threshold velocities (Keller et al., 1973; Keller and Shepard, 1977). Furthermore, high concentrations of suspended material have been measured (Meade et al., 1975; Drake et al., 1977).

Clearly, there appears to be a modification of the relict sediment pattern by modern processes. What we see today is the result of both. This study summarizes the observations pertaining to major sediment changes along transects across the shelf break into the head of the canyon. The in-situ observations from the submersible enable us to detail the surficial sedimentary facies. Facies distribution, in turn, can be used to define areas of erosion versus deposition. We can then speculate on the causative mechanisms of the patterns observed.

METHODS AND TOPOGRAPHY

Dives were made in the two-man submersible "Nekton Gamma" during low seastate conditions. Traverses were planned to cross the shelf break perpendicular to isobaths from depths of about 125 m to the submersible limit of 305 m. Locations were selected on the basis of canyon morphology (steepest slopes, tributaries) on opposite canyon walls using Coast and Geodetic Survey Bathymetric Map 0801N-52 (based on 1936 data). Downslope traverses averaged about 1.5 km in length and took two to three hours. Ship-to-submersible communication was maintained by radio. The ship tracked a float towed by the submersible, recording its position by Loran A. Submersible observations were recorded on audiotape and by hand-held cameras; approximately 700 useable color photographs were obtained.

The canyon area examined includes the north—south trending head; the northern end divides into a main northwest-trending tributary and a smaller northeast-trending tributary (Fig. 1). The canyon width between the 125-m isobaths at dives 7 and 8 is about 5 km; maximum depth is about 510 m. Seaward of stations 7 and 8 the canyon turns and continues to traverse the shelf another 16 km to the southeast.

The shelf break depth generally ranges from about 90 m at the head of the canyon to about 105 m at stations 7 and 8; the break at the northeast tributary is about 110 m deep. The break in the slope on the open shelf northeast of the canyon is about 150 m deep versus about 160 m southwest of the canyon. Canyon wall slopes generally range from 3 to 10°; a slope of 25° was recorded in dive 10.

OBSERVATIONS

The two most obvious surficial sediment facies in the study are (1) an upper gravel—shell—sand facies (Fig. 2A) and (2) a lower mud facies (Fig. 2B) containing sand percentages decreasing with depth (cf. Schlee, 1975).

The gravel—shell—sand facies consists of a mixture of cobbles, boulders, sand and shell. Cobbles vary in size from 5 to 25 cm in diameter on the east side of the canyon (Fig. 2C), and from 5 to 15 cm on the west side. They were seen in all dives from the shallowest depths (93—125 m) down to the lower depth limit of the gravel facies. The average lower limit of gravel in west canyon wall dives is about 130 m; the average lower limit on the east wall is 147 m. Locally, gravel accounts for up to 80% of the surficial sediment. Many cobbles are iron-stained; their shapes record both beach (rounded, flattened; arrows on Fig. 2C) and fluvial (rounded, subspherical) origins.

Large boulders, on the other hand, were seen only in and near the head of the canyon in dives 3, 9, 1 and 5. Boulders (to 100 cm) were most common in dive 5 between 116 and 140 m depth (Fig. 2D); the largest (300 cm) was observed in dive 3 at 98 m.

Sand, coarse-grained and generally iron-stained, is always present in varying amounts in this gravel—shell facies (Fig. 2A). Shell, an integral part of this facies, is locally equal to the percentage of gravel. Shell material consists mostly of whole or large fragments of pelecypod shells (mostly surf clams, *Spisula solidissima;* ocean quahog, *Arctica islandica;* and pecten), and a few gastropods.

The mud facies is herein defined as a soft gray-green to green, fine-grained sediment locally containing a visually estimated minimum of 10—15% finer-than-sand fraction. The sediment—water interface in this facies appears organic, consisting of larger-than-silt-sized organic agglomerated particles which are easily stirred into the water column by fish (Fig. 2B), crabs, squid and the submarine touching the bottom.

The upper depth limit of the mud facies, herein termed the "mud line" (cf. Gardiner, 1915), ranges from greater than 127 m to 174 m and always lies below the shelf break. On the west wall, the "mud line" occurs at an average depth of 145 m, while on the east wall it is at an average depth of 162 m.

A zone of overlap exists in which shell and gravel extend downslope into the mud facies (Fig. 2F), shell further than gravel. On the west canyon wall, shell extends from 175 to 190 m, while on the east wall it extends to 205 m. The deepest occurrence is at 245 m in station 7. With depth, shell material is broken into progressively finer pieces (shell hash, Fig. 3D). Overlap of gravel—shell and mud facies is minimal, except along dive traverses 3 and 6.

Reworking of the sea floor by benthic organisms is most apparent in the

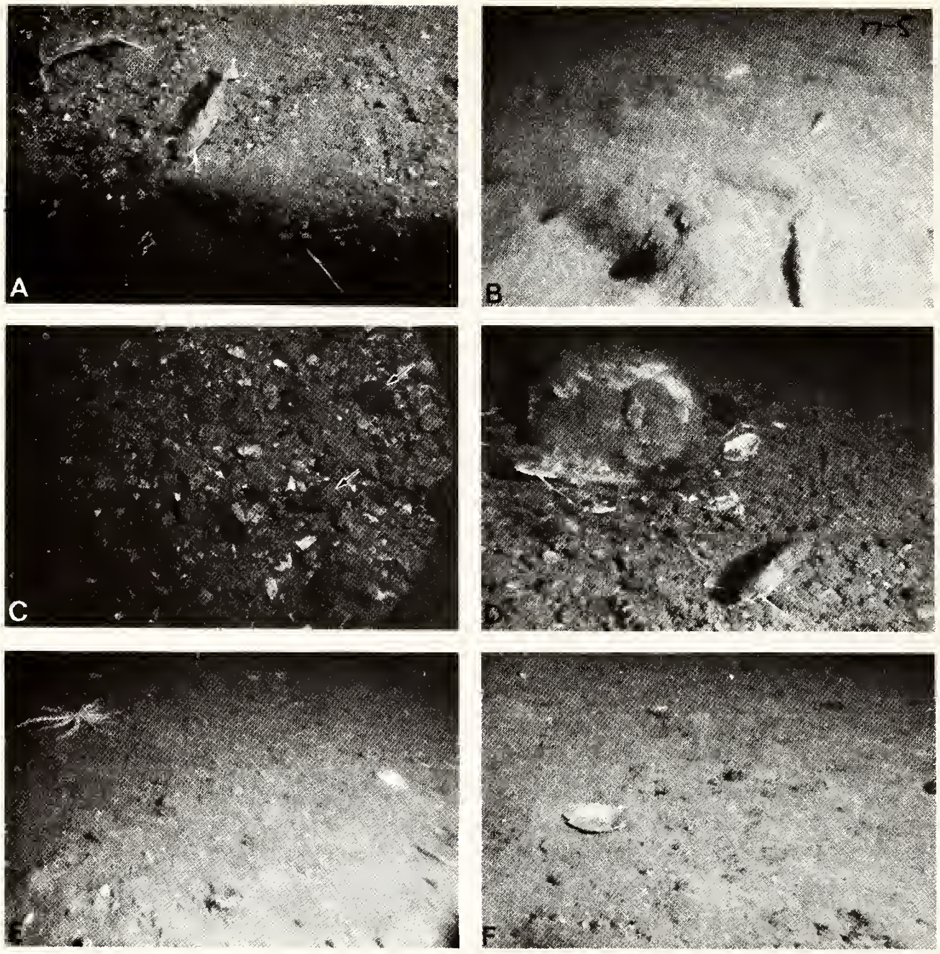

Fig. 2. Selected bottom photographs in the head of the Hudson Submarine Canyon (explanation in text).

mud-rich facies, although highest bioturbation does not always coincide with the highest observed faunal concentrations. Obvious bioturbation features include small conical mounds, fish-resting depressions and crab tracks. Fields of conical mounds (5—7 cm high and 15 cm in diameter) were observed in both gravel—shell—sand and mud facies (Fig. 3A); highest concentrations were found below the "mud line" between 122 and 213 m. These mounds have apical holes and are formed by infauna expelling sediments from below the sediment—water interface.

Oval depressions, some larger than 20 × 50 cm^2 across and 10—15 cm deep, are also common. Many were occupied by fish (Fig. 3B), typically hake, indicating scour by these and other benthic fish. They also occur below the

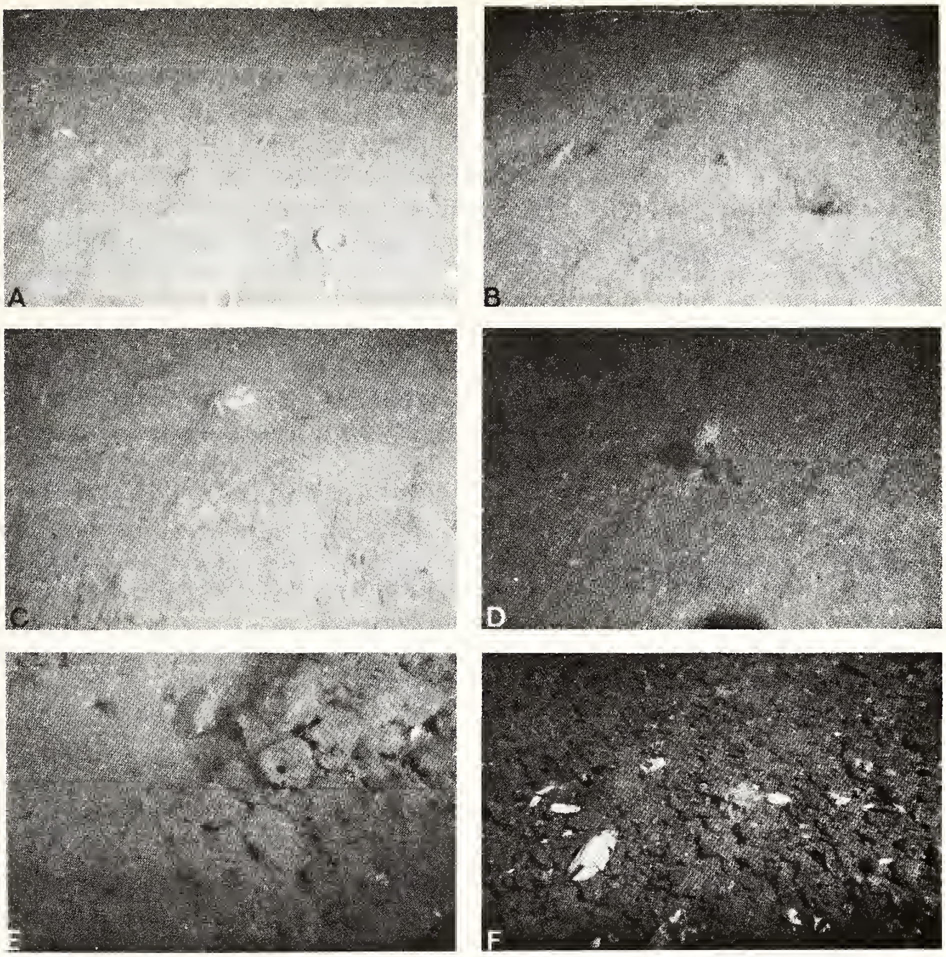

Fig. 3. Selected bottom photographs in the head of the Hudson Submarine Canyon (explanation in text).

"mud line", primarily between 140 and 240 m. Frequency of depressions in not always coincident with observed fish abundance, but more closely reflects the soft nature of the sea floor. Also noted was stirring of the soft bottom by fish as they fed, moved, and burrowed into the bottom (Fig. 2B).

Other obvious fauna include crabs (particularly *Cancer* sp.), lobsters (*Homarus americanus*), and starfish which track and rework the bottom (Figs. 2B, 2E, 3C), and anemones (Fig. 3D) which require a hard substrate. Deep holes in the mud, quite common, were apparently dug by crabs (Figs. 2A, 3B). Although these fauna appear at all depths in the eleven dives, they are most apparent on the soft mud-rich bottom between 140 and 210 m.

Outcrops were observed in six of seven east wall dives at depths from 98 to

172 m, and in dive 8 at 125 m (Fig. 1). These generally consist of blue-gray to gray stiff clay, burrowed (Fig. 3E) and broken into angular fist-sized fragments. These are probably lagoonal clays of late Pleistocene age (cf. Gibson et al., 1968). A different outcrop lithology, brownish silty sandstone (Fig. 3F), overlies the stiff blue clay at a depth of 151 m in dive 6.

Particulate matter in the water column consists mostly of living organic matter. As concentration of total suspended matter increased downslope, so did abundance of nonliving organic and inorganic matter. Total concentration, estimated by visual observation through submersible portholes, was low to moderate at shallower depths coincident with the shelly gravel facies, and moderate to high overlying the mud facies. High concentrations which appear at shallower depths (below 150 m) at the head of the canyon are found progressively deeper (180—240 m) in the southern part of the area.

Instantaneous current speeds were obtained from a Savonius rotor mounted near the submersible bow; directions were estimated from compass readings. Currents were generally 5—15 cm/sec at depths down to about 130 m; speeds of up to 30 cm/sec were measured at 130 m during dive 1. Generally, measurements showed no currents deeper than 130 m except at dive 3 (5—10 cm/sec at 208 m) and dive 6 (10—20 cm/sec at 200 m). Current directions varied, generally being stronger to the west. Indirect current evidence is the scoured base of large boulders (Fig. 2D) and anemones (Fig. 3D).

DISCUSSION

This study shows that the Pleistocene overprint on the study area has been modified by modern processes. Among relict features are shelf break and terrace depths that are coincident with known sea-level stillstands (Knott and Hoskins, 1968). Cobbles and coarse sand record fluvial and beach deposition at times of lower sea level, while large boulders are of probable ice-rafted origin (Schlee and Pratt, 1970). The extension of these coarse fractions to depths below the shelf break records off-shelf spillover onto the upper slope during these earlier times of accelerated sedimentation at the mouth of the ancestral Hudson River. The present supply of additional sediment to the shelf edge and slope is restricted to fine particulate matter transported across the shelf (Meade et al., 1975; Biscaye and Olsen, 1976).

Relict, coarse surficial-sediment characteristics of the shelf edge have been modified during the Holocene by the addition of shell and a probable change in the original texture and structure. These changes appear to be caused by the long-term effects of both currents and organisms acting upon the sea floor. These reworked coarse-grained sediments are thus identified as palimpsest facies (cf. Swift et al., 1971). The coarse sediment below the shelf break may also result from continuing slow downslope creep and other mass processes including slumping. Such mass failure migh explain the local exposures of older, hard layers on the upper slope.

There is strong evidence for on-going processes: (1) moderate to high suspended matter (even during the fair-weather regime we experienced during the dives); (2) movement of water mass (to speeds of 30 cm/sec); (3) absence of fines at the shelf edge proper, and (4) an obviously modern surficial mud cover overlying coarse material on the upper slope. The role of benthic organisms observed is also important in reworking of the mud-rich facies. Bioturbation, coupled with currents, contributes significantly to concentrations of suspended matter. Processes which may induce bottom currents include surface waves, tidal currents, pressure-induced currents, internal waves, and the effect of shear between major water masses (oceanic fronts) as outlined by Southard and Stanley (1976). At any given time, one or another process may be dominant, but typically there is a superposition of various mechanisms.

The "mud line" we observed appears to be the most significant evidence reflecting a separation of energy zones. It is concluded that the depth zone below which mud occurs (usually below 130 m), always lying below the shelf break, records a depth below which the threshold current velocities needed to erode fine sediment decrease significantly in frequency and intensity. Thus, there may exist a close relationship between lithofacies and the effects of physical oceanographic phenomena acting at the shelf edge and upper slope. The "mud line" appears to reflect the sum of these phenomena over the long term. It may be significant that the "mud line" depth observed is almost coincident with the intersection of the density front separating shelf and slope waters with the slope at about 150 m during the winter (Gordon et al., 1976; Bowman, 1977; Ruzecki and Welch, 1977). It is noteworthy that these events occur at the time of greatest storm activity, suggesting intensified erosion and scour during the winter.

Other factors likely to affect the "mud line" include the up and down canyon currents, probably tidal, recorded by Keller et al. (1973) and Keller and Shepard (1977) in the canyon axis near the head of the canyon. Internal waves formed at the shelf edge (Cacchione and Southard, 1974; Apel et al., 1975) along the summer pycnocline may also contribute to high suspended sediment concentration (Newman et al., in press). High current speeds (to 35 cm/sec, 3 m off the bottom) in the head of the Hudson Canyon have been observed to coincide with high suspended sediment concentration (> 3mg/l) consisting of coarse silt particles and very fine sand (Drake et al., 1977). Our study also supports the conclusion of Rowe et al. (1974) that biological activity and bottom currents act synergistically in the canyon head to cause enhanced sediment erosion.

The above phenomena point to bottom energy concentrating at the shelf edge and uppermost slope. The appearance of mud on the bottom signals a rapid energy decrease, separating the zones of long-term erosion and deposition. This "mud line" probably shifts somewhat in time and space due to variations of suspended sediment concentrations and current velocities. In this respect, cross-canyon currents, similar to those recorded by Keller and Shepard (1977) at 1700 m, may be active in the head of the canyon to produce this variation.

In summary, this study lends additional proof that the shelf break and uppermost slope is a zone of active resuspension. The "mud line" is an effective indicator of the boundary between erosion and deposition. As an energy-level indicator, this phenomenon has direct applicability to water-mass studies at the shelf edge.

ACKNOWLEDGEMENTS

We thank the NOAA Manned Undersea Science and Technology Office for submersible time; G. Shiller, M. Fisher, and W. Forman of General Oceanographics as submersible pilots; A. Maldonado of the University of Barcelona, Spain, for assistance in data collection; and W. Van Horn, captain, and the crew of the support vessel, "Atlantic Twin". Funds were supplied by Smithsonian Research Foundation grant 71702120 and NOAA's Rational Use of the Sea Floor (RUSEF) Program.

REFERENCES

Apel, J.R., Byrne, H.M., Proni, J.R. and Charnell, R.L., 1975. Observations of oceanic internal and surface waves from the Earth Resources Technology Satellite. J. Geophys. Res., 80: 865—881.

Biscaye, P.E. and Olsen, C.R., 1976. Suspended particulate concentrations and compositions in the New York Bight. In: M.G. Gross (Editor), Middle Atlantic Continental Shelf and the New York Bight. American Society of Limnology and Oceanography, Inc., Lawrence, Kans., pp. 124—137.

Bowman, M.J., 1977. Hydrographic Properties. MESA New York Bight Atlas Monograph, 1. New York Sea Grant Institute, Albany, N.Y., 78 pp.

Cacchione, D.A. and Southard, J.B., 1974. Incipient sediment movement by shoaling internal gravity waves. J. Geophys. Res., 79: 2237—2241.

Drake, D.E., Hatcher, P.G. and Keller, G.H., 1977. Suspended particulate matter and mud deposition in upper Hudson Canyon. In: D.J. Stanley and G. Kelling (Editors), Sedimentation in Submarine Canyons, Fans, and Trenches. Dowden, Hutchinson and Ross, Stroudsburg, Pa., pp 33—41.

Ewing, E., Le Pichon, X. and Ewing, M., 1963. Upper stratification of Hudson apron region. J. Geophys. Res., 68: 6303—6316.

Gardiner, J.S., 1915. Submarine slopes. Geogr. J., 45: 202—216.

Gibson, T.G., Hazel, J.E. and Mello, J.F., 1968. Fossiliferous rocks from submarine canyons off the Northeastern United States. U.S. Geol. Surv. Prof. Pap., 600-D: D222—D230.

Gordon, A.L., Amos, A.F. and Gerard, R.D., 1976. New York Bight water stratification — October 1974. In: M.G. Gross (Editor), Middle Atlantic Continental Shelf and the New York Bight. American Society of Limnology and Oceanography, Inc., Lawrence, Kans., pp. 58—68.

Keller, G.H. and Shepard, F.P., 1977. Currents and sedimentary processes in submarine canyons off the northeast United States. In: D.J. Stanley and G. Kelling (Editors), Sedimentation in Submarine Canyons, Fans, and Trenches. Dowden, Hutchinson and Ross, Stroudsburg, Pa., pp. 15—32.

Keller, G.H., Lambert, D., Rowe, G. and Staresinic, N., 1973. Bottom currents in the Hudson Canyon. Science, 180: 181—183.

Kelling, G., Sheng, H. and Stanley, D.J., 1975. Mineralogic composition of sand-sized sediment on the outer margin off the mid-Atlantic states: assessment of the influence of the ancestral Hudson and other fluvial systems. Geol. Soc. Am. Bull., 86: 853—862.

Knott, S.T. and Hoskins, H., 1968. Evidence of Pleistocene events in the structure of the continental shelf off the northeastern United States. Mar. Geol., 6: 5—43.

Meade, R.H., Sachs, P.L., Manheim, F.T., Hathaway, J.C. and Spencer, D.W., 1975. Sources of suspended matter in waters of the Middle Atlantic Bight. J. Sediment. Petrol., 45: 171—188.

Newman, F.C., Proni, J.R. and Nelsen, T., in press. Observations of suspended sediment in a bottom mixed layer during the passage of internal waves. J. Geophys. Res.

Rowe, G.T., Keller, G.H., Edgerton, H., Staresinic, N. and MacIlvaine, J., 1974. Time-lapse photography of the biological reworking of sediments in Hudson Submarine Canyon. J. Sediment. Petrol., 44: 549—552.

Ruzecki, E.P. and Welch, C.S., 1977. Description of shelf water—slope water fronts in the Middle Atlantic Bight. Trans. Am. Geophys. Union, 58: p. 888 (abstract).

Schlee, J., 1975. Sand and Gravel. MESA New York Bight Atlas Monograph, 21. New York Sea Grant Institute, Albany, N.Y., 26 pp.

Schlee, J. and Pratt, R.M., 1970. Atlantic continental shelf and slope of the United States — Gravels of the northeastern part. U.S. Geol. Surv. Prof. Pap., 529-H: 39 pp.

Southard, J.B. and Stanley, D.J., 1976. Shelf-break processes and sedimentation. In: D.J. Stanley and D.J.P. Swift (Editors), Marine Sediment Transport and Environmental Management. J. Wiley, New York, N.Y., pp. 351—377.

Swift, D.J.P., Stanley, D.J. and Curray, J.R., 1971. Relict sediments, a reconsideration. J. Geol., 79: 322—346.

Trumbull, J.V.A., 1972. Atlantic continental shelf and slope of the United States — Sand-sized fraction of bottom sediments, New Jersey to Nova Scotia. U.S. Geol. Surv. Prof. Pap., 529-K: 45 pp.

Veatch, A.C. and Smith, P.A., 1939. Atlantic submarine valleys of the United States and the Congo Submarine Valley. Geol. Soc. Am. Spec. Pap., 7: 101 pp.

Sedimentary Geology 21, 311-312.

Book Reviews

Holocene Tidal Sedimentation (Benchmark Papers in Geology, 30). George deVries Klein (Editor). Wiley, London, 1976, 423 pp., U.S. $ 36.90 or £22.00.

This Benchmark volume brings together a diverse series of papers with the common theme of deposition of sediment in response to rhythmically varying tidal currents. The volume begins with the classic papers of the "North Sea School" of coastal studies, culminating in the burst of creativity at mid-century as Van Straaten, Kuenen, Reineck, Postma, and colleagues resolved the mechanisms responsible for mud deposition on the tide flats of the German Bight and the Dutch Wadden Sea. Their papers demonstrate that tide flats have served as natural sedimentation laboratories in which, with a minimum of equipment and expense, a sedimentologist can determine the principles of loose boundary hydraulics. These are laboratories in which the experiment is conveniently shut off and the working surface exposed for examination punctually every 12.5 hours; furthermore, laboratories generally adjacent to resort accommodations and with a pleasant sea view!

The paper in the initial sections, and in subsequent sections dealing with tidal sand bodies and carbonate tidal sediments, demonstrate a growing awareness of the dynamical aspects of sedimentation, and a growing sophistication of approach. It is possible to argue, however, that these students of tidal sedimentation have found their niche a little too comfortable; a number of biases occur in this collection, which surely are a faithful reflection of the field, rather than just the biases of the editor. The papers deal primarily with intertidal sedimentation; only a minority of the authors have been willing to, or interested in, pursuing the financial, organizational, and logistical support needed to mount shipborne operations and explore the far more extensive world of subtidal sedimentation.

The papers tend to be uniformitarian in outlook. Study of the present to illuminate the past is a vital function, but only part of a sedimentologist's job. The "why's" of sedimentation are being primarily answered by people with a more nearly analytical than comparative approach, who examine modern processes for their own sake.

Some further comments reflect perhaps my own biases. Hydrodynamical studies of tidal sedimentation did not end in the sixties, and I would have liked to have seen reprinted, or at least mentioned, more of the recent studies of fluid motions and sediment flux in tidal seas, such as the studies of Sternberg and students, Heathershaw, McCave's 1973 study, the work of Channon and Hamilton, and Ludwick's 1975 and 1976 papers. Sternberg, Heathershaw, McCave, and Channon and Hamilton have pioneered in what will surely be an increasingly productive approach — the deployment of sea-floor sensing systems in tidal boundary layers. Ludwick and McCave have presented simple numerical models of tidal sedimentation.

A collection such as this might also have placed in perspective the chaotic literature on forcing mechanisms in tidal sand bodies — how do "mutually evasive ebb channel—flood channel systems" differ from "ebb and flood shields," "spillover lobes," and "ramps to the sea"? It could also have traced the growing awareness of the role of the turbidity maximum in estuarine and coastal sedimentation. It must be realized, however, that the editor was working within space constraints and could not review all aspects of tidal sedimentation. The papers for the fields that he has chosen are carefully selected and provide a fascinating perspective of the evolution of coastal sedimentation studies during the twentieth century.

DONALD J. P. SWIFT (Miami, Fla.)

43
The Encyclopedia of Sedimentology, The Encyclopedia of Earth Sciences Series, VI, 190-199.

CONTINENTAL-SHELF SEDIMENTATION

Continental shelves comprise a major subsystem in the world's dominant sediment transport system, i.e., that system whereby continents are weathered, the soil transported to the shore by rivers, across shelves and over the shelf break by shallow marine currents, and down slopes on to the abyssal plains by turbidity currents and other processes.

Shelf Hydraulics

The Shelf Velocity Field. An analysis of shelf-sediment transport requires an understanding of the shelf velocity field. The pattern of shelf flow is complex in time and space (Fig. 1). Shelves such as the North and Celtic seas of Europe experience tidal ranges generally in excess of 3 m as a consequence of shelf geometry, which amplifies the tidal wave by a shoaling process or causes the shelf tide to co-oscillate with the oceanic tide. On such *tide-dominated shelves* mid-tide surface velocities may exceed 200 cm/sec over broad areas; and rates of sediment transport, both as bed and suspended load, are high. On *weather-dominated shelves*, where tides are weaker, storm currents drive sedimentation. During fair weather, a weak thermohaline and wind-driven circulation distributes suspended fine sediment; but significant transport of sand seaward of the surf is accomplished mainly by high-velocity pulses of water movement associated with storms.

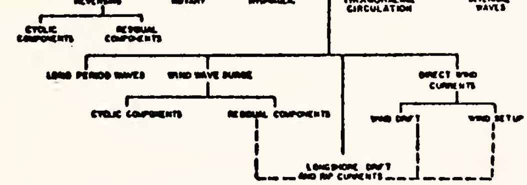

FIGURE 1. Components of the shelf velocity field.

Transport is most efficient during the winter months, when thermohaline stratification has broken down, and the downward transfer of momentum from surface wind-drift currents is unimpeded. Such wind-drift currents dominate the inner shelf; in deeper water, where the effects of friction are proportionately less, a coast-parallel geostrophic flow results in response to the pile-up of water against the coast by winds. Oscillatory wave surge plays an important but poorly understood secondary role in shelf-sediment transport; its peak velocities affect bottom roughness by generating ripples and aid entrainment of sediment into the flow field.

Numerical Modeling of Shelf-Sediment Transport. Numerical modeling of shelf-sediment transport may eventually be feasible, but both data and techniques are inadequate at present. Models of the tidal flow field may be applied directly to sediment-transport calculations (McCave, 1971). Models of the storm velocity field (Jelesnianski, 1967) may be modified to describe resulting shear stress on the bottom. Regional wave-propagation models are available, although these also must be modified, to determine the effect of wave energy input into the sea floor (Cherry, 1966).

Tidal models are directly applicable to assessment of mean annual sediment transport because plots of surface tidal velocities against time at a given point on the shelf are (relatively) simple polyharmonic curves. In order to determine mean annual transport on wave-dominated inner shelves, or storm-dominated shelves, however, the problem of climatic weighting of the aperiodic velocity field must be faced. Wave climatology has been explored by a number of workers (e.g., see Harris, in Swift et al., 1972) as a consequence of the importance of such studies to coastal erosion and structural stability, but no attempts have been made to apply these studies to sediment transport. The hydraulic climate of the shelf water column as a function of wind-driven currents has not been considered.

Numerical modeling of shelf-sediment transport requires estimates of the instantaneous or time-integrated coupling of the velocity field to the sea floor. Bottom shear stresses may be estimated from a point velocity determination by the quadratic stress law, or if a vertical array of three meters are used, by means of the

Von Karman-Prandtl velocity profile equation (Sternberg, in Swift et al., 1972). With greater vertical resolution of the velocity field, the Landweber method may be used (Ludwick, 1973).

A variety of threshold criteria for sediment transport are available in the literature. All are empirical relationships determined by experimentation in shallow flumes, and their utility in the marine environment is uncertain (Sternberg, in Swift et al., 1972). Volume and mass transport rates are calculated from such threshold criteria by application of transport functions such as those of Bagnold (1963), which relate the transport rate to the power expended by the fluid moving over the boundary. Such calculations are probably simplistic in that they do not take into account the possible synergistic effects of oscillatory wave surge on sediment transport or other complexities of the shelf flow field.

Smith and Hopkins (in Swift et al., 1972) have performed such calculations on current meter data from the Washington shelf. They estimate that a typical winter storm with current speeds of 60 cm/sec 3 m off the bottom transports on the order of 6 m^3/hr per meter transverse to the transport direction. A single one-month current-meter record from the Virginia shelf indicates that during this particular November, the threshold velocity of the finest sediment present was exceeded 17% of the time, and that 5.2 m^3 was transported per meter transverse to transport direction during that time (Fig. 2). Equivalent estimates are not available from tide-dominated shelves, although a semiquantitative approach has been considered by McCave (1971).

Models of the shelf velocity field modified by means of such equations to permit estimates of bottom shear stress and volume transport rates, should lead to finite difference models of shelf-sediment transport. Bottom-sediment grain-size data, and a time history of shear stress at a grid of bottom stations should permit assessment of sediment transport by means of a continuity equation of the form

$$\nabla \cdot \left(\overrightarrow{v\bar{c}}\right) = -\frac{\rho}{d}\,\frac{dh}{dt}$$

where v is velocity, $\bar{c}$ is sediment concentration averaged over depth, t is time, h is height above a reference level, ρ is density, d is water depth, and ∇ is an operator indicating net difference. The equation states that the difference between sediment input and sediment output at a grid point is a function of the change in bottom elevation with time.

Such a finite-difference model must be verified by means of direct observation. Radioisotope tracers appear to be a promising technique for verification (Duane, 1970; see *Tracer Techniques*).

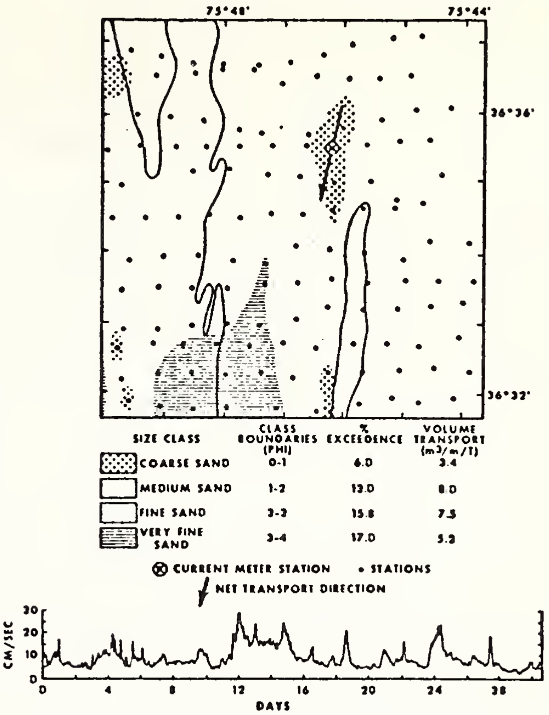

FIGURE 2. Calculations of volume sediment transport through the sand ridges of the Virginia Inner Shelf, based on record of bottom-mounted geodyne current meter, recorded during November 1972.

Patterns of Shelf Sedimentation

The Secular Controls. Numerical process modeling is a potentially powerful tool for assessing and predicting shelf-sediment transport. Such assessment becomes meaningful, however, only in the context of a broader conceptual model that considers the secular or long-term variables of shelf-sediment transport. Students of shelf sedimentation (e.g., Curray, 1964) tend to isolate the following as major variables: rate of sediment input to the shelf, S; sea-level rise relative to land, R; rate of input of energy available to transport sediment, E; and character of sediment (grain size and mineral composition), G (see Fig. 3). These variables may be related to each other in quasi-quantitative fashion, $(S/E)_G - R = K$, to indicate that for a given sediment character (for instance, grain size) the ratio between the rate of sediment input, S, and the energy, E, available to disperse it must be balanced by the relative rate of sea level rise, R; otherwise the shoreline will advance or retreat.

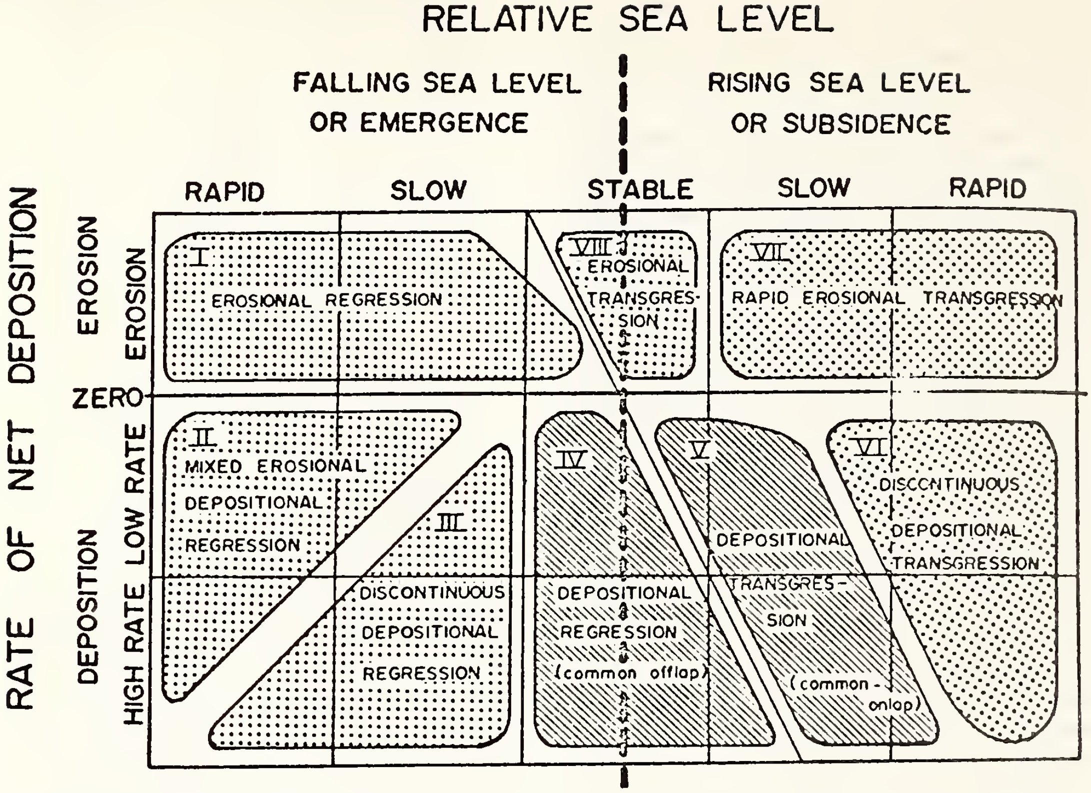
RELATIVE SEA LEVEL
FALLING SEA LEVEL OR EMERGENCE
RISING SEA LEVEL OR SUBSIDENCE
RAPID
SLOW
STABLE
SLOW
RAPID
RATE OF NET DEPOSITION
EROSION
DEPOSITION
EROSION
ZERO
LOW RATE
HIGH RATE
I EROSIONAL REGRESSION
VIII EROSIONAL TRANSGRESSION
VII RAPID EROSIONAL TRANSGRESSION
II MIXED EROSIONAL DEPOSITIONAL REGRESSION
III DISCONTINUOUS DEPOSITIONAL REGRESSION
IV DEPOSITIONAL REGRESSION (common offlap)
V DEPOSITIONAL TRANSGRESSION (common onlap)
VI DISCONTINUOUS DEPOSITIONAL TRANSGRESSION

FIGURE 3. Varieties of shelf sedimentary regimes, as determined by rate of sediment input and sense of relative sea-level change (from Curray, 1964; Copyright © 1964, Macmillan Publishing Co., Inc.).

Shoreface Translation. The shoreline is the permeable boundary across which sediment is introduced into the shelf transport system, and its movements (as governed by the variables described above) and dynamic geometry thus determine the nature of the sedimentary regime.

One of the oldest concepts of shelf sedimentation, often presented but rarely evaluated, is the concept of the equilibrium profile (Swift, 1970). This hypothesis states that the profile of the shelf surface approximates an exponential curve, concave up, with the steepest part being the shoreface. This profile is seen as a substrate response to the hydraulic climate such that the slope at each point is just adequate to bypass sediment of the available grain size and concentration; the curve as a whole is seen as the best adjusted profile to absorb the energy of shoaling waves of the prevailing height and length.

The simplistic model is most nearly valid on the inner shelf of low, unconsolidated coasts, where the break in slope between the inner shelf and the wave-agitated shoreface generally occurs at 15 m or less. In fact, a true wave-graded profile is rarely attained even here, and the actual profile is instead a resultant response to the constructional, wave-dominated processes of fair weather on one hand, and strong, wind-driven contour currents which sweep the shoreface during storms on the other. On tide-dominated shelves, tidal currents are also important in shaping the lower shoreface.

The model is useful, however, in that the translation of the shoreface profile with the relative rise and fall of sea level determines the character of sediment supplied to the shelf (Fig. 4). In a relatively rapid transgression, as experienced by most shelves during the post-Pleistocene rise of sea level, river mouths are drowned and become traps for shelf-derived as well as river-derived sediment. As a consequence, the shoreface profile translates landward by means of shoreface erosion (Swift et al., in Swift et al., 1972). During storms, onshore winds generate coast-parallel shoreface currents with an onshore surface component and a seaward bottom component. These currents strip off the fair-weather veneer of fine sand deposited from rip currents and erode the underlying

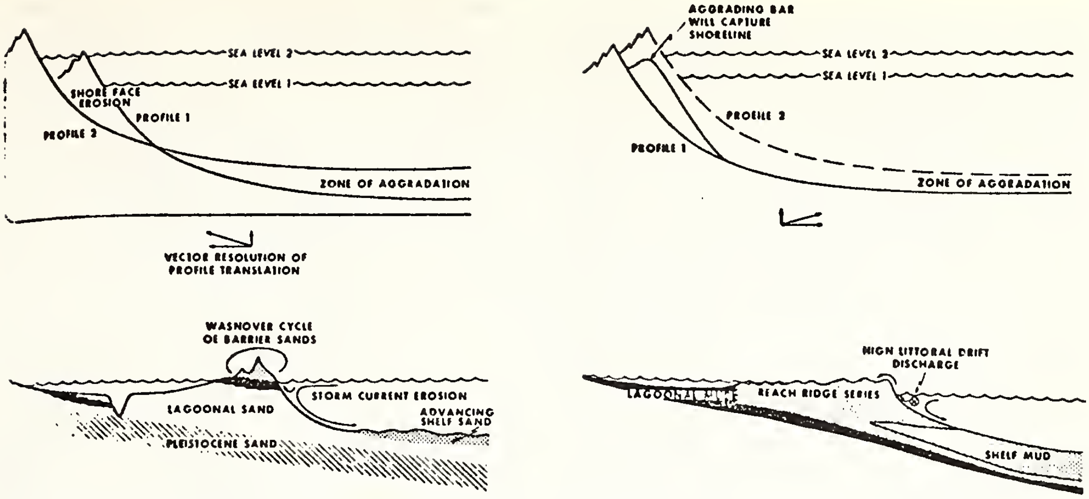
AGGRADING BAR WILL CAPTURE SHORELINE
SEA LEVEL 2
SEA LEVEL 1
SHORE FACE EROSION
PROFILE 1
PROFILE 2
ZONE OF AGGRADATION
VECTOR RESOLUTION OF PROFILE TRANSLATION
WASHOVER CYCLE OF BARRIER SANDS
STORM CURRENT EROSION
LAGOONAL SAND
ADVANCING SHELF SAND
PLEISTOCENE SAND
HIGH LITTORAL DRIFT DISCHARGE
BEACH RIDGE SERIES
SHELF MUD

FIGURE 4. *Left*: Landward translation of the shoreface profile during a sea-level rise, and resulting stratigraphy. *Right*: Seaward translation of shoreface profile during a sea-level rise, and resulting stratigraphy.

barrier base and the pre-Holocene substrate on which it rests (Fig. 4). The debris of shoreface erosion is left behind on the beveled shelf surface as an intermittent sheet of relatively clean and well-sorted sand. Most grains in this sheet have probably rested on a beach at least once, but they now comprise an entirely new deposit which is properly termed a marine sand. Beach deposits are replaced in the stratigraphic section by a disconformity.

Autochthonous Shelf Sedimentation. Shelf deposits thus derived from shoreface erosion during a transgression are the product of *autochthonous shelf sedimentation.* The stratigraphy of autochthonous shelves is threefold in nature, consisting of a pre-Holocene substrate, the Holocene back-barrier sequence, and the Holocene nearshore deposits.

The nearshore sand sheet, where well developed, tends to have a complex structure (Fig. 5). First-order morphologic and stratigraphic elements consist of shelf-transverse

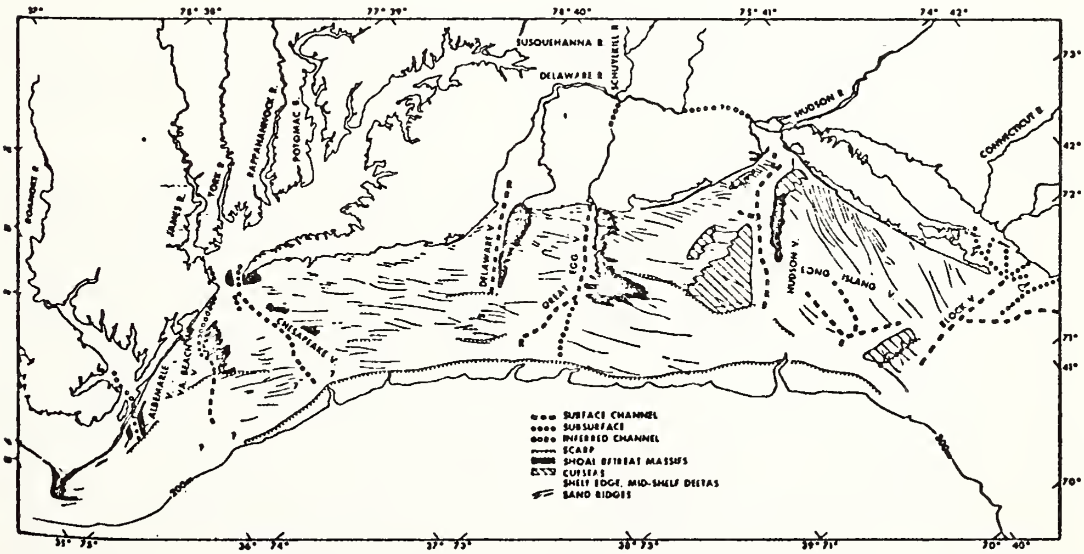
SUSQUEHANNA R.
DELAWARE R.
SCHUYLKILL R.
HUDSON R.
CONNECTICUT R.
ROANOKE R.
JAMES R.
YORK R.
RAPPAHANNOCK R.
POTOMAC R.
DELAWARE V.
GREAT EGG V.
HUDSON V.
LONG ISLAND V.
BLOCK V.
CHESAPEAKE V.
VA. BEACH
ALBEMARLE
SURFACE CHANNEL
SUBSURFACE
INFERRED CHANNEL
SCARP
SHOAL RETREAT MASSIFS
CUESTAS
SHELF EDGE, MID-SHELF DELTAS
SAND RIDGES

FIGURE 5. First-order morphologic elements (shelf valleys, shoal retreat massifs, deltas, scarps, cuestas) and second-order morphologic elements (sand ridges) of the Middle Atlantic Bight, and autochthonous, storm-dominated shelf.

thickenings of the sand sheet, which may have surface expression as shelf-transverse ridges and valleys. These are the retreat paths of zones of deposition and erosion associated with the transgressing shoreline (Swift et al., in Swift et al., 1972). Zones of littoral drift convergence at estuary mouths and at cuspate forelands result in shelf-transverse sand ridges or *shoal-retreat massifs.* Estuarine shoal-retreat massifs may be paired with troughs that are the retreat paths of flood channels built by the reversing tides of estuary mouths. Such paired morphologic elements comprise *shelf valley complexes.* On high, indurated coasts, however, such relict components of the topographic pattern of constructional nearshore marine origin are less conspicuous than relict components of subaerial erosional origin such as cuestas and drowned fluvial or glacial valleys.

Few shelves are sufficiently quiescent to preserve first-order, shelf-transverse, morphologic and stratigraphic elements without modification. In the Middle Atlantic Bight, a well-studied, storm-dominated shelf, dominantly southerly storm currents have molded the surficial sand sheet into a subdued, pervasive *ridge and swale topography* (see Swift et al., 1972). Ridges are up to 10 m high, tens of kms long, and converge southward with the coastline. Side slopes are usually $<1^\circ$. Shoreface-connected ridges are initiated at the leading edge of the sand sheet by storm currents and storm-wave trains, and are detached and isolated during shoreface retreat. Shoal-retreat massifs constrict and accelerate the storm flow field; they are remolded into massif-transverse ridges and swales. Zones of flow expansion and deceleration in the lee of shoal-retreat massifs and other highs become sinks for fine sand, which may be carried for long distances during periods of peak velocity. The precise relationship of the ridge topography of the Middle Atlantic Bight to the structure of the storm flow field is not clearly understood, but the apparent mobility of the sediment suggests that such a relationship does exist, and that the ridges are large-scale substrate responses to hydraulic process, analogous in some respects to longitudinal desert dunes.

Remobilization of the surficial sand sheet of high-energy, tide-dominated shelves is yet more striking (Fig. 6). European studies of the tide-swept shelf of Western Europe (e.g., Kenyon and Stride, 1970) reveal that over large areas, a thin surficial sand sheet is in transit over its basal gravel. *Sand streams,* or paths of net sand transport, may be traced for great distances. Such paths tend to start at "bed-load partings," or zones of divergence of the residual component of tidal currents and of divergence of the sense of bed-load transport.

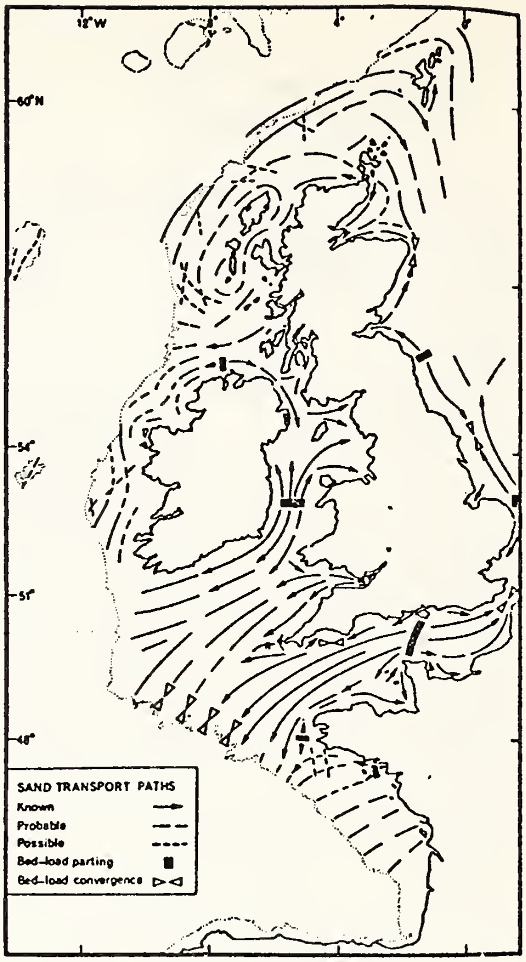

FIGURE 6. Pattern of sediment transport on the western European shelf, an autochthonous tide-dominated shelf (from Kenyon and Stride, 1970).

A sequence of sediment facies tends to occur along such transport paths, down the velocity gradient of mid-tide surface currents, from the erosional source area, to the depositional zone. Zones of scour and bedrock outcrop tend to occur where mid-tide surface velocities exceed 3 knots. Ribbons of sand in transit over the basal Holocene gravel occur where mid-tide surface velocities exceed 2 knots. Extensive beds of sand, and, locally, fields of sand waves occur at the depositional ends of sand streams (sand transport paths), where mid-tide surface velocities range from 1-2 knots. Sand-wave field development is locally enhanced by elongation of the tidal ellipse, so that the destructive effects of mid-tide cross flow is minimized. Farther down the velocity gradient, beyond the main depositional center, there may be patchy growth of the sand sheet. Patches may be current transverse ("starved sand waves") or current parallel, but without the elongation ratio (40:1) that Kenyon and Stride (1970) have set for true sand ribbons.

Allochthonous Shelf Sedimentation. A very different sedimentary regime prevails on continental shelves when the rate of sediment input is sufficiently high relative to the rise of sea level and to the ability of the hydraulic climate to disperse it, such that the sense of shoreface translation is that of very slow transgression, or depositional regression (Fig. 4). A broad zone of subaerial (fluvial or eolian) and transitional (lagoonal, estuarine, or deltaic) environments develops, and the regional gradient is reduced. If the sense of shoreline movement is still negative (transgressional), estuaries are no longer drowned river valleys with dendritic patterns (e.g., Chesapeake Bay), but are instead simple, trumpet-shaped, constructional forms, whose dimensions are in equilibrium with tidal discharge (i.e., any cross-sectional area therein is a logarithmic function of the tidal prism landward of that point).

Such estuaries are no longer efficient sediment traps and tend to bypass some size fraction of the sediment load delivered to them by rivers. "Stratigraphic" bypassing of sediment also occurs as sediment delivered to and deposited in estuaries and lagoons is released to the shelf by shoreface erosion and by tidal scour at estuary mouths. The inner and outer estuary environments serve as a seaward series of filters, retaining decreasingly coarser fractions and bypassing increasingly finer fractions of the original sediment load, so that material ultimately released to the continental shelf by either mode of bypassing consists primarily of fine sand, silt, and clay. This material travels in suspension at relatively low threshold velocities and is readily transported to all portions of the shelf. This regime of shelf aggradation by fine, far-traveled sediment bypassed through the shoreface is termed *allochthonous shelf sedimentation,* as distinct from the autochthonous sedimentation characteristic of rapid or sediment-starved transgressions in which the shelf cannibalizes its own substrate. Should the rate of sediment input increase to the point that the sense of shoreface translation is reversed and the shoreline progrades, then deltaic deposits build out over inner marine deposits. Deltas, however, are equally efficient filters and fractionators of sediment; fine sediment continues to be bypassed to the shelf, and the allochthonous regime is maintained (Fig. 7).

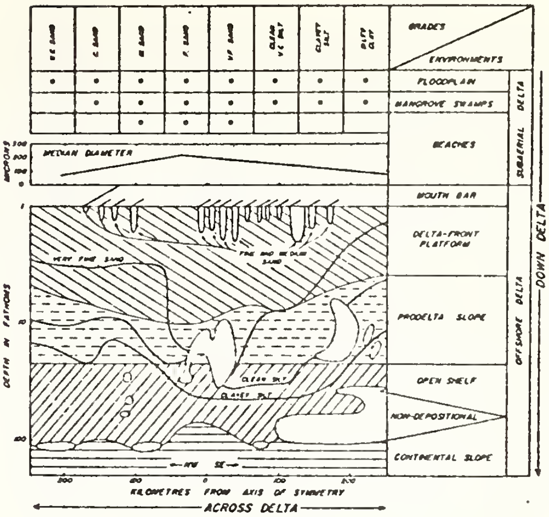
V.C. SAND
C. SAND
M. SAND
F. SAND
V.F. SAND
CLEAN V.C. SILT
CLAYEY SILT
SILTY CLAY
GRADES
ENVIRONMENTS
FLOODPLAIN
MANGROVE SWAMPS
BEACHES
MOUTH BAR
DELTA-FRONT PLATFORM
PRODELTA SLOPE
OPEN SHELF
NON-DEPOSITIONAL
CONTINENTAL SLOPE
SUBAERIAL DELTA
OFFSHORE DELTA
DOWN DELTA
MICRONS
300
200
100
0
MEDIAN DIAMETER
VERY FINE SAND
FINE AND MEDIUM SAND
CLEAN SILT
CLAYEY SILT
DEPTH IN FATHOMS
1
10
100
NW
SE
200
100
0
100
200
KILOMETRES FROM AXIS OF SYMMETRY
ACROSS DELTA

FIGURE 7. Textural gradients of the Niger shelf, an allochthonous shelf (from Allen, 1965).

The input of sediment to allochthonous shelves may be highly episodic as a consequence of river flooding. Exceptionally heavy flooding may deposit enormous tonnages of sediment beneath the turbidity plumes of river mouths in a matter of weeks, to be redistributed over the shelf during ensuing years (Drake et al., in Swift et al., 1972). Reentrainment may occur with the aid of the oscillatory surge of storm waves, as in the case of the coarser sediment of autochthonous shelves; unlike the latter material, fine allochthonous sediment is retained in suspension and is transported for long distances by thermohaline shelf circulation, and wind-drift currents and tidal residuals too weak to affect coarser material (Fig. 8). Advective

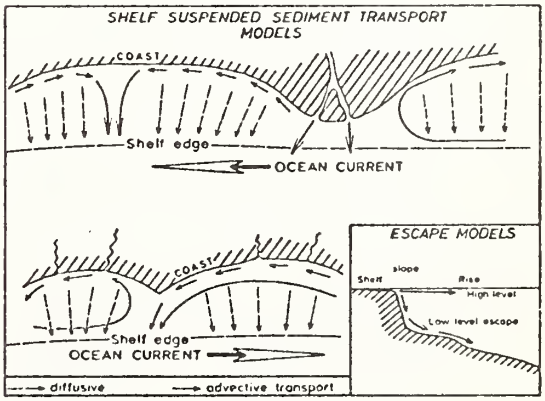
SHELF SUSPENDED SEDIMENT TRANSPORT MODELS
COAST
Shelf edge
OCEAN CURRENT
COAST
Shelf edge
OCEAN CURRENT
ESCAPE MODELS
slope
Shelf
Rise
High level
Low level escape
diffusive
advective transport

FIGURE 8. Modes of suspended sediment transport on shelves (from McCave, in Swift et al., 1972).

transport of suspended fine sediment is dominantly coast-parallel, but the more nearly continuous nature of transport enhances cross-shelf diffusion. Advective cross-shelf transport occurs at coastal current convergences. As indicated by McCave in Swift et al., 1972), the localization of fine sediment deposition depends not on the absolute hydraulic activity of the shelf floor, but rather on the relationship of sediment concentration in the water column and hydraulic activity.

The fine sediments of allochthonous shelf surfaces have lower effective angles of repose and do not as a rule sustain the large-scale bedforms of autochthonous shelves. The greater effective mobility of fine allochthonous sediment results in gentle textural gradients that are maintained over many kilometers. Such gradients reflect decreasing values of maximum orbital velocity attendant on water deepening. They are also the consequence of progressive sorting, whereby sediment at rest during intermittent transport over an aggrading surface will tend to leave behind its coarsest fraction if reentrained by the currents of a storm weaker than the previous one.

DONALD J. P. SWIFT

References

Allen, J. R. L., 1965. Late Quaternary Niger Delta, and adjacent areas: Sedimentary environments and lithofacies, *Bull. Am. Assoc. Petrol. Geologists*, 49, 547-600.

Bagnold, R. A., 1963. Mechanics of marine sedimentation, in M. N. Hill, ed., *The Sea*, vol. 3. New York: Wiley Interscience, 507-525.

Cherry, J. A., 1966. Sand movement along equilibrium beaches north of San Francisco. *J. Sed. Petrology*, 36, 341-357.

Curray, J. R., 1964. Transgressions and regressions, in R. L. Miller, ed., *Papers in Marine Geology*. New York: MacMillan, 175-203.

Curray, J. R.; Emmel, F. J.; and Crampton, P. J. S., 1969. Holocene history of a strand plain, lagoonal coast, Nayarit, Mexico, in Lagunas costeras, un simposio, *Mem. Simp. Intern. Lagunos Costeras, UNAM-UNESCO*, 1967, Mexico, 63-100.

Duane, D. B., 1970. Tracing sand movement in the littoral zone: progress in the radioisotope sand tracer (RIST) study July 1968–February 1969, *Coastal Eng. Research Cen., Misc. Pap., April 1970*, 52p.

Jelesnianski, C. P., 1967. Numerical computations of storm surges with bottom stress, *Monthly Weather Rev.*, 95, 740-750.

Kenyon, N. H., and Stride, A. H., 1970. The tide swept continental shelf sediments between the Shetland Isles and France, *Sedimentology*, 15, 154-173.

Ludwick, J. C., 1973. Tidal currents and zig-zag sand shoals in a wide estuary entrance, *Old Dominion Univ. Inst. Oceanog., Tech. Rept., Sept. 7*, 23p.

McCave, I. N., 1971. Sand waves in the North Sea off the coast of Holland, *Marine Geol.*, 10, 199-2

Smith, D. B., 1974. Sedimentation of upper Artesia (Guadalupian) cyclic shelf deposits of northern Guadalupe Mountains, New Mexico, *Bull. Am. Assoc. Petrol. Geologists*, 58, 1699-1730.

Stanley, D. J., and Swift, D. J. P., 1976. *Marine Sediment Transport and Environmental Management*. New York: Wiley, 602p.

Swift, D. J. P., 1970. Quaternary shelves and the return to grade, *Marine Geol.*, 8, 5-30.

Swift, D. J. P.; Duane, D. B.; and Pilkey, O. H., 1972. *Shelf Sediment Transport: Process and Pattern*. Stroudsburg, Pa.: Dowden, Hutchinson & Ross, 656p.

Werner, F., and Newton, R. S., 1975. The pattern of large-scale bed forms in the Langeland Belt (Baltic Sea), *Marine Geology*, 19, 29-59.

Cross-references: *Continental-Rise Sediments; Continental-Shelf Sediments; Deltaic Sediments; Estuarine Sedimentation; Flow Regimes; Lagoonal Sedimentation; Littoral Sedimentation; Neritic Sedimentary Facies; Outer Continental-Shelf Sediments; Paralic Sedimentary Facies; Relict Sediments; Storm Deposits; Tidal-Current Deposits*; Vol. 1: *Continental Shelf, Classification; Grand Banks.*

CONTINENTAL-SHELF SEDIMENTS

Stratigraphy

On shelves undergoing autochthonous sedimentation (see *Continental-Shelf Sedimentation*) the stratigraphy is threefold in nature (see Fig. 1). A pre-Holocene substrate (C to P_1) may be overlain by Holocene back-barrier deposits (H_6 to H_4) and Holocene nearshore sands (H_2 to H_3). The pre-Holocene substrate is variable. On low coasts (Fig. 1A, B), it may consist of fine-grained regressive shelf and lagoonal deposits which date from the retreat of the mid-Wisconsin highstand of the sea. On high coasts (Fig. 1E), the indurated substrate may have considerable relief and may be the dominant sea-floor element, with other facies occurring mainly as lenses in low areas. A Holocene sequence is variable in thickness and complexity. It may start with lagoonal or estuarine deposits and may pass upward into fine-grained, barrier-base sands (Fig. 1B) which have escaped destruction by the process of erosional shoreface retreat. These deposits rest disconformably on the old subaerial erosional surface. This back-barrier sequence, if present, has been beveled by shoreface retreat, resulting in a major disconformity within the Holocene sequence. It is overlain by the shelf surficial sand sheet, starting with a sporadic basal gravel of terrigenous clasts (if available) or shell hash, and grading upward

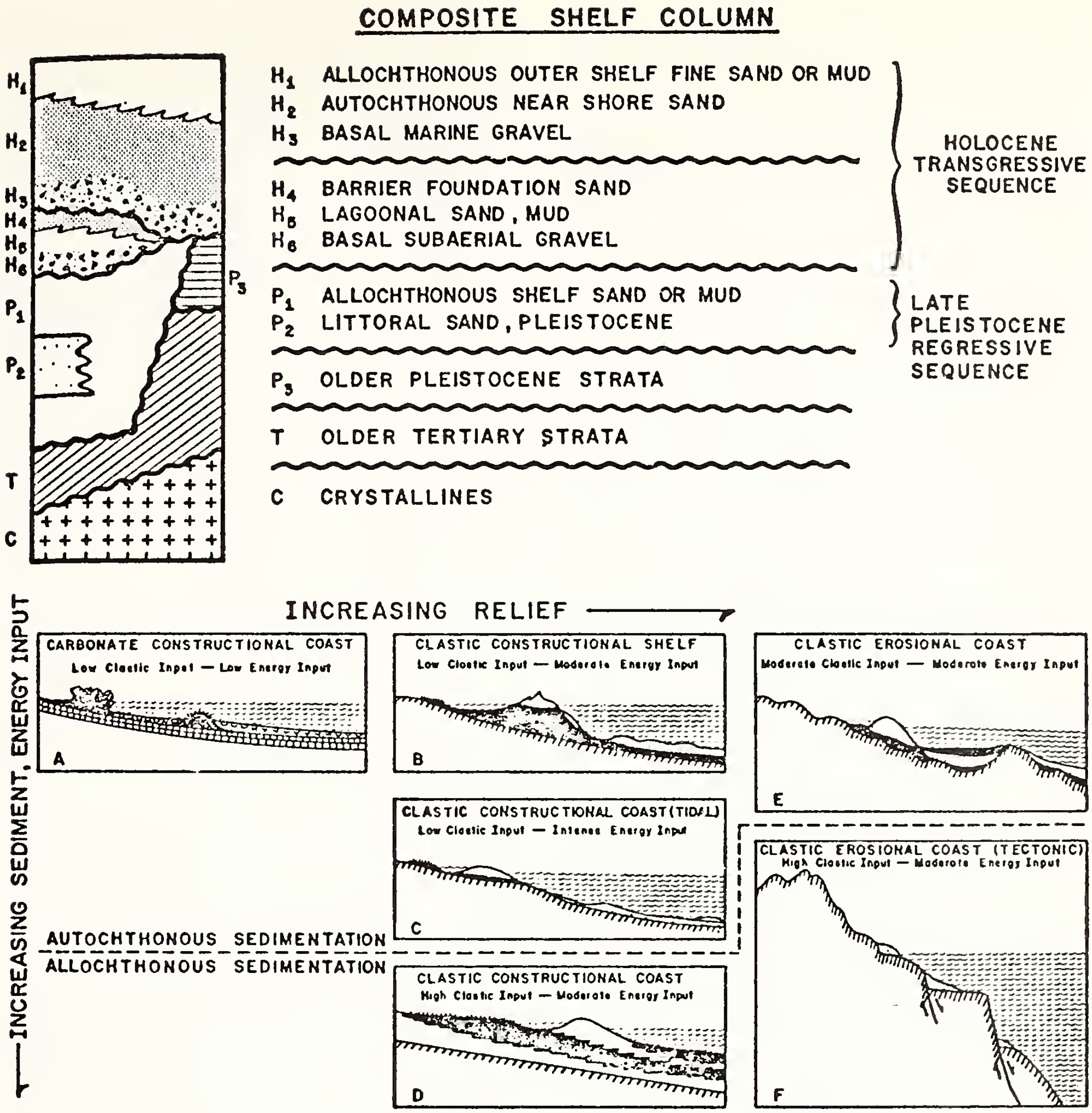
COMPOSITE SHELF COLUMN
H1 ALLOCHTHONOUS OUTER SHELF FINE SAND OR MUD
H2 AUTOCHTHONOUS NEAR SHORE SAND
H3 BASAL MARINE GRAVEL
H4 BARRIER FOUNDATION SAND
H5 LAGOONAL SAND, MUD
H6 BASAL SUBAERIAL GRAVEL
HOLOCENE TRANSGRESSIVE SEQUENCE
P1 ALLOCHTHONOUS SHELF SAND OR MUD
P2 LITTORAL SAND, PLEISTOCENE
LATE PLEISTOCENE REGRESSIVE SEQUENCE
P3 OLDER PLEISTOCENE STRATA
T OLDER TERTIARY STRATA
C CRYSTALLINES
H1
H2
H3
H4
H5
H6
P1
P2
P3
T
C
INCREASING RELIEF
INCREASING SEDIMENT, ENERGY INPUT
CARBONATE CONSTRUCTIONAL COAST
Low Clastic Input — Low Energy Input
A
CLASTIC CONSTRUCTIONAL SHELF
Low Clastic Input — Moderate Energy Input
B
CLASTIC EROSIONAL COAST
Moderate Clastic Input — Moderate Energy Input
E
CLASTIC CONSTRUCTIONAL COAST (TIDAL)
Low Clastic Input — Intense Energy Input
C
CLASTIC EROSIONAL COAST (TECTONIC)
High Clastic Input — Moderate Energy Input
F
AUTOCHTHONOUS SEDIMENTATION
ALLOCHTHONOUS SEDIMENTATION
CLASTIC CONSTRUCTIONAL COAST
High Clastic Input — Moderate Energy Input
D

FIGURE 1. *Above*: Generalized stratigraphic column on the continental shelf. *Below*: Continuum of shelf depositional schemes in terms of variables of shelf sedimentation and relief.

into a well-sorted sand. On tide-dominated shelves (Fig. 1C), the nearshore sand may be swept into large-scale bed forms, leaving the basal gravel exposed over broad areas. On low, carbonate coasts (Fig. 1A), a basal coquina may be overlain by calcite mud. In many cases, shoreface erosion cuts through barrier-base, lagoonal, or estuarine deposits. the intra-Holocene and basal Holocene disconformities merge, and the surficial sand sheet rests directly and disconformably on the pre-Holocene substrate (Fig. 1C).

The Holocene nearshore sequence is transitional upward with Holocene outer-shelf deposits, which are, by definition, poorly developed on autochthonous shelves, (see *Outer Continental-Shelf Sediments*). The stratigraphy of allochthonous shelves is similar to that of autochthonous shelves, except that in many cases, facies H_4 to H_6 (back-barrier deposits) and in all cases facies H_1 (outer-shelf deposits) are better developed than facies H_2 to H_3 (nearshore deposits). In fact, many modern shelves (e.g., northern Gulf of Mexico) are in a state of transition between these two sedimentary regimes or have recently shifted to the allochthonous regime—a consequence of the stabilization of the shoreline after the late Holocene reduction in the rate of sea-level rise about 4000 years ago.

Petrography and Classification

There is nothing unique about shelf sediments observed out of context, and operational or descriptive classification must be by means of the textural and compositional parameters employed for other sediments. As in the case of other sediments, the size-frequency distribution is composed of log-normal subpopulations that reflect the building of the bed (see *Grain-Size Frequency Studies*). "Clogs" of coarse, traction sediment occur in a framework population of medium size. A third population is interstitial to the other two. The relative percentages of the three populations are a function of the intensity of the depositional regime (Moss, 1972). Mean diameter of a sample reflects that of the source area as modified by transport and site history. It varies with the local hydraulic climate, and also with the location of the sample in the regional dispersal pattern. Such patterns may be broad and simple on outer allochthonous shelves, but many are localized and complex near shore, or on autochthonous shelves. Shelf highs tend to be mantled by coarser lags, surrounded by aprons of out-winnowed finer sediment. Constructional forms such as current-parallel sand ridges usually comprise sand circulation cells, whose textural patterns tend to reflect the radial dispersive component of sediment transport, rather than the concentric advective component. Grain size tends to vary rhythmically over fields of transverse sand waves or current-parallel sand ribbons, in sympathy with the hydraulic microclimate.

As noted by Emery (1968), the composition and genesis of shelf sediments vary with latitude (Fig. 2). Polar sediments are compositionally immature, being enriched in such labile (easily weathered) constituents as feldspar and rock fragments. Such sediments become increasingly quartzose toward the equator. On the eastern margins of ocean basins, shelf-edge sediments may be enriched with such authigenic chemical precipitates as phosphorite and silica. Toward low latitudes, eastern margin shelves may be deserts during low stands and may then accumulate eolian sediments. Biogenic precipitation of calcium carbonate dominates equatorial shelves.

Such source considerations, and process and environmental considerations, led Emery (1968) to propose a genetic classification of shelf sediments: *authigenic* (glauconite or phosphorite), *organic* (foraminifera, shells), *residual* (weathered from underlying rocks), *relict* (remnant from a different earlier environment such as a now-submerged beach or dune), and *detrital*, which includes material supplied by rivers, coastal erosion, and glacial or eolian activity.

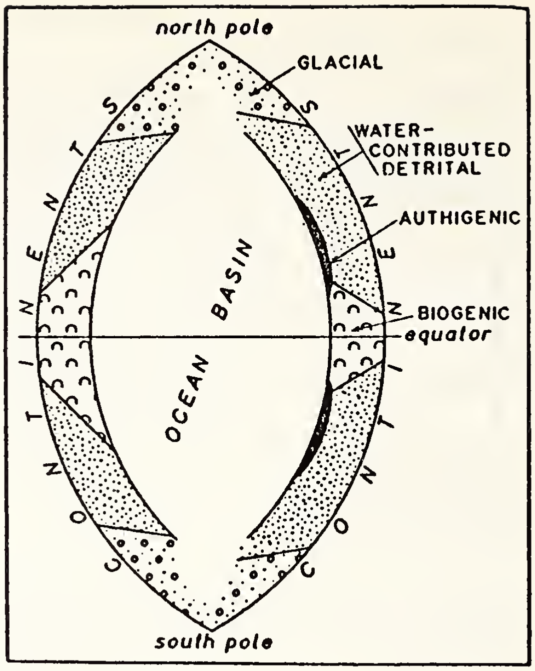

FIGURE 2. Idealized distribution of the chief classes of sediment on continental shelves (from Emery, 1968). Assumes asymmetric, clockwise water circulation, with upwelling on E coast.

The implications of this classification should be carefully considered. First, it is a genetic, rather than a descriptive, or operational, classification; it can thus be applied only after inferences are drawn from sediment attributes. As such, it is a paradigm, or conceptual model, for shelf-sediment genesis. It modifies an earlier view which held that shelf sediments are size graded as a result of a seaward (depth) decreasing gradient of energy input into the sea floor; or in other words, that all shelf sediments other than organic ones are detrital.

Recent advances in shelf studies suggest that a further modification is in order. The problem lies in the definition of relict and residual sediments on one hand, versus detrital on the other. These are in part environment-determined categories. The concept of environment is itself a high-order abstraction; the geographic locus over which a given dynamic system (another abstraction) or subsystem of sediment distribution prevails.

Relict shelf sediments have exchanged, in situ, one environment and its dynamic system for another during the Holocene transgression. The term *relict* however, tends to distort our thinking by overemphasizing the effects of the first environment. Relict sediments are acknowledged to have been "reworked"; the reworking, however, is as systematic and complex as the original "working." Such reworking may be referred to as autochthonous sedimentation (deposition of sediments whose origin within the present sedimentary cycle is local). The reworking deserves equal or greater emphasis than the earlier cycle; the attributes of shelf sediments may reflect both environments, but those of the later tend to obliterate those of the earlier. If sediment attributes reflecting both cycles are present, then the sediments are *palimpsest* (similar to a medieval scroll, partly erased, then rewritten; Swift et al., 1971). The term *relict* is perhaps better applied to a given sediment attribute such as the surface textures of a shelf sand sample dominated by high-velocity impact scars acquired in the surf. The sample's size-frequency distribution, however, will almost certainly reflect reconstitution of the granular fabric in a deeper environment, after the erosional retreat of the shoreface. Thus the sample is a palimpsest sand because attributes of both a former and the present environment are detected; because the sediment is of local origin, it is the product of autochthonous sedimentation.

DONALD J. P. SWIFT

References

Alexander, A. E., 1934. A petrographic and petrologic study of some continental shelf sediments, *J. Sed. Petrology*, 4, 12–22.

Curray, J. R., 1965. Late Quaternary history, continental shelves of the United States, in H. E. Wright, Jr. and D. G. Frey, eds., *The Quaternary of the United States.* Princeton: Princeton Univ. Press, 723–736.

Dott, R. H., Jr. and Dalziel, I. W. D., 1972. Age and correlations of the Precambrian Baraboo Quartzite, *J. Geol.*, 80, 552–568.

Emery, K. O., 1968. Relict sediments on continental shelves of world, *Bull. Am. Assoc. Petrol. Geologists*, 52, 445–464.

Field, M. E., and Duane, D. B., 1974. Geomorphology and sediments of the inner continental shelf, Cape Canaveral, Florida, *U.S. Army Coastal Eng. Research Center, Tech. Memo 42,* 87p.

Frank, W. M., and Friedman, G. M., 1973. Continental-shelf sediments off New Jersey, *J. Sed. Petrology*, 43, 224–237.

Goldring, R., and Bridges, P., 1973. Sublittoral sheet sandstones, *J. Sed. Petrology*, 43, 736–747.

Hite, R. J., 1972. Shelf carbonate sedimentation controlled by salinity in the Paradox basin, south east Utah, *Mtn. Geol.*, 9, 329–344.

Hommeril, P.; Larsonneur, C.; and Pinot, J-P., 1972. Les sédiments du précontinent armoricain, *Soc. Géol. Fr. Bull.*, 7, 237–247.

McKinney, T. F., and Friedman, G. M., 1970. Continental shelf sediments of Long Island, New York, *J. Sed. Petrology*, 40, 213–248.

McManus, D. A., 1975. Modern versus relicit sediment on the continental shelf, *Geol. Soc. Am. Bull.*, 86, 1154–1160.

Moss, A. J., 1972. Bed-load sediments, *Sedimentology*, 18, 159–220.

Owens, J. P., and Sohl, N. F., 1969. Shelf and deltaic paleoenvironments in Cretaceous-Tertiary formations of the New Jersey coastal plain, in S. Subitsky, ed., *Geology of Selected Areas in New Jersey and Eastern Pennsylvania.* New Brunswick: Rutgers University Press, 235–278.

Schlee, J., 1973. Atlantic continental shelf and slope of the United States sediment texture of the northeastern part, *U.S. Geol. Surv. Prof. Pap. 529-L*, 64p.

Schopf, T. J. M., 1968. Atlantic continental shelf and slope of the United States: nineteenth century exploration, *U.S. Geol. Surv. Prof. Pap. 529-F*, 19p.

Shepard, F. P., 1932. Sediments of the continental shelves, *Geol. Soc. Amer. Bull.*, 43, 1017–1040.

Slatt, R. M., 1974. Formation of palimpsest sediments, Conception Bay, southeastern Newfoundland, *Geol. Soc. Amer. Bull.*, 85, 821–826.

Spearing, D. R., 1975. Shallow marine sands, *Soc. Econ. Paleont. Minerol. Short Course*, 2 (April 5, 1975), 103–132.

Stanley, D. J., ed., 1969. *The NEW Concepts of Continental Margin Sedimentation.* Washington, D.C.: Amer. Geol. Inst.

Stetson, H. C., 1938. The sediments of the continental shelf off the eastern coast of the United States, *Mass. Inst. Tech. Woods Hole Oceanog. Inst. Pap. Phys. Oceanog. Meteorol.*, 5(4), 49p.

Swift, D. J. P.; Stanley, D. J.; and Curray, J. R., 1971. Relict sediments on continental shelves: a reconsideration, *J. Geol.*, 79, 322–346.

Trumbull, J. V. A., 1972. Atlantic continental shelf and slope of the United States sand-size fraction of bottom sediments, New Jersey to Nova Scotia, *U.S. Geol. Surv. Prof. Pap. 529-K*, 45p.

Wantland, K. F., and Pusey, W. K., III, eds., 1975. Belize (British Honduras) Shelf–carbonate sediments, clastic sediments, and ecology, *Am. Assoc. Petrol. Geologists, Stud. Geol.*, 2, 599p.

Wilson, J. L., 1974. Characteristics of carbonate-platform margins, *Bull. Am. Assoc. Petrol. Geologists*, 58, 810–824.

Cross-references: *Authigenesis; Barrier Island Facies; Blanket Sands; Continental-Shelf Sedimentation; Continental-Shelf Sediments in High Latitudes; Glauconite; Littoral Sedimentation; Neritic Sedimentary Facies; Outer Continental-Shelf Sediments; Relict Sediments.*

Journal of Sedimentary Petrology 48, No. 4, 1257-1266.

CURRENT LINEATIONS AND SAND WAVES ON THE INNER SHELF, MIDDLE ATLANTIC BIGHT OF NORTH AMERICA[1]

DONALD J. P. SWIFT
GEORGE L. FREELAND
Atlantic Oceanographic and Meteorological Laboratories, NOAA,
Miami, Florida 33149

ABSTRACT: Elongate bedforms of less than one meter relief are abundant on the North Atlantic shelf floor. Spacing between features, and width of solitary forms, ranges from 15 to 50 m. Length-to-width ratios observed by side-scan sonar are in excess of 10:1. The most common form consists of a band of coarse sand or shelly gravel that is depressed slightly below the level of the finer sand on either side. In some cases these bedforms appear to be erosional windows exposing the basal coarse sand or gravel of the Holocene Transgression; elsewhere they are merely localized lag concentrates.

Bedforms on the shore face and adjacent inner shelf tend to be nearly shore-normal with slightly acute angles opening to the northeast. Further seaward most bedforms are parallel to the coast, and to the generalized trend of the isobaths. These relationships lead to the inference that the nearshore features are the troughs of low amplitude, flow-transverse sand waves, and that they are probably responses to the intense, downwelling, along-coast flows that occur during northeaster storms. The offshore bedforms may also be responses to storm flow, but their orientation suggests that they are flow-parallel current lineations, perhaps responses to longitudinal vortices in the flow. The bedforms indicate that the shelf floor is responding to the modern hydraulic regime. Time-averaged bed load transport is directed downshelf, to the south and west. On the inner shelf there is also an offshore transport component.

INTRODUCTION

Side-scan sonar surveys of the central Atlantic shelf of North America between Cape Hatteras and Long Island (Fig. 1) have revealed that the most widespread mesoscale bedform is a streak of coarser sand or shelly or pebbly sand (McKinney et al., 1974; Swift et al., 1978a, b). Such streaks range from 15 to 50 m wide, are generally at least ten times as long, and are of negligible (less than one meter) relief. Such relief as is usually apparent is negative; the streaks are troughs, not crests. This class of bedform appears to constitute a "signature" of the short-lived, high intensity storm events that accomplish most of the bed load transport in the Middle Atlantic Bight and similar shelf surfaces, and any advance in our understanding of their formation will also constitute a step toward a solution of the more general problems of the nature of bed load transport on the continental shelf.

The data presented in this paper indicate that these bedforms occur in two contrasting inner shelf patterns, a nearshore pattern on the shoreface and adjacent inner shelf, and an onshore pattern. The differences between the patterns are only apparent when orientations of bedforms on sonographs are corrected for angular distortion due to the relationship of ship's speed to recording speed. Analysis of these bedform patterns must begin with an attempt to relate them to bedforms that have been previously described and analyzed. However, in this case it has proved difficult to make the most basic analysis of bedform category, namely the relation of the long axis of the features to the direction of the generating flow, whether flow-transverse or flow-parallel, and this paper is concerned in part with making such an assessment.

Data in this paper are expressed whenever possible in metric units. However, completed maps in English units that were obtained from outside sources have not been reconstructed with metric values due to limitations of funds and manpower, and in some cases due to inaccessibility of the original data.

---

[1] Manuscript received December 6, 1977; revised June 15, 1978.

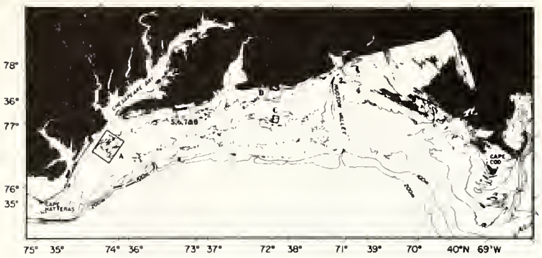

FIG. 1.—Map of the Middle Atlantic Bight of North America, showing locations of some of figures in this paper and the locations of other studies referred to in this report: Swift et al. (1978b)(A); Stubblefield et al. (1974)(B); and McKinney et al. (1974)(C).

NEARSHORE BEDFORMS

On the smoothly curved shoreface, from the surf zone down to perhaps 20 m depth, mesoscale bedforms occur singly or in well-defined sets with spacings of 10 to 100 m (Fig. 2). They tend to form at high angles to the coast, but the north- or east-opening angle on this northeast-trending coast is generally acute, whereas the south- or west-opening angle is generally obtuse (Figs. 2-5). In many cases the bedforms are asymmetrical, with the northeast sides of the dark bands more sharply defined than the southwest sides (Fig. 2).

Seaward of the shoreface, the inner-shelf floor is more gently inclined (1:2000 slope versus 1:200 for the upper shoreface) and in profile is gently undulating. In plan view, these undulations appear as an indistinct to well-defined ridge and swale topography consisting of sand ridges up to 10 m high and 2 to 5 km apart, with side slopes of less than a degree (Swift et al., 1978c). These large-scale bedforms converge with the shoreline, forming northeast- or east-opening angles of 20 to 35 degrees. Sand ridges start on the lower shoreface, where mesoscale bedforms make a larger angle to the shoreline than the ridges do (Figs. 2-5) but extend to the offshore shelf floor where an offshore pattern of mesoscale bedforms occurs.

Sonographs from the Maryland coast over a period of two years suggest that shoreface bedforms may persist for such a length of time and undergo relatively little movement (Fig. 6; see also Stubblefield et al., 1977, plate VIII).

OFFSHORE BEDFORMS

At least two types of bedform pattern occur in the ridge topography of the shelf floor seaward of the nearshore zone of wide-angle features. In the troughs between the ridges the surficial sand sheet locally thins to a veneer of coarse, pebbly, shelly sand or shell hash a few centimeters thick; the "basal gravel" of the Holocene Transgression (Figs. 7, 8). These "deflation zones" (Swift et al., 1978, Fig. 16) are tens to hundreds of meters wide, and several kilometers long. They tend to be displaced to the seaward side of the trough, and frequently extend up the landward flank of the adjacent ridge (Fig. 7; Swift et al., 1978a, b, c). The deflation zones appear to be partly "stratigraphic" in genesis, to the extent that they are more or less random exposures of the basal Holocene gravel, and partly hydrodynamic in origin in that they tend to occur on or adjacent to the landward (upstream) flanks of the ridges, the side which is inferred to experience erosion during episodes of southward storm flow (Swift et al., 1978a, b).

A second type of shelf floor bedform is very similar in scale to that described from the nearshore; dark bands on sonographs are several meters to tens of meters wide (Fig. 8; see also Swift et al., 1977, Fig. 16) and tend to occur in sets. Both the large-scale deflation zones and the smaller-scale bedforms of the inner-shelf floor differ from the shoreface bedforms in their orientations; instead of being nearly coast-normal, they are nearly coast-parallel. They tend to parallel the trend of the ridge topography, or in the case of the smaller lineations, may cross it at a small angle (see McKinney et al., 1974, Fig. 7).

SIGINIFICANCE OF THE PATTERNS

Flow Regimes and Bedform Class

Circulation over the Middle Atlantic Bight of North America consists of a weak south-

FIG. 2.—Shoreface bedforms, Long Island inner shelf. See Figures 1 and 3 for location. From Freeland and Swift.

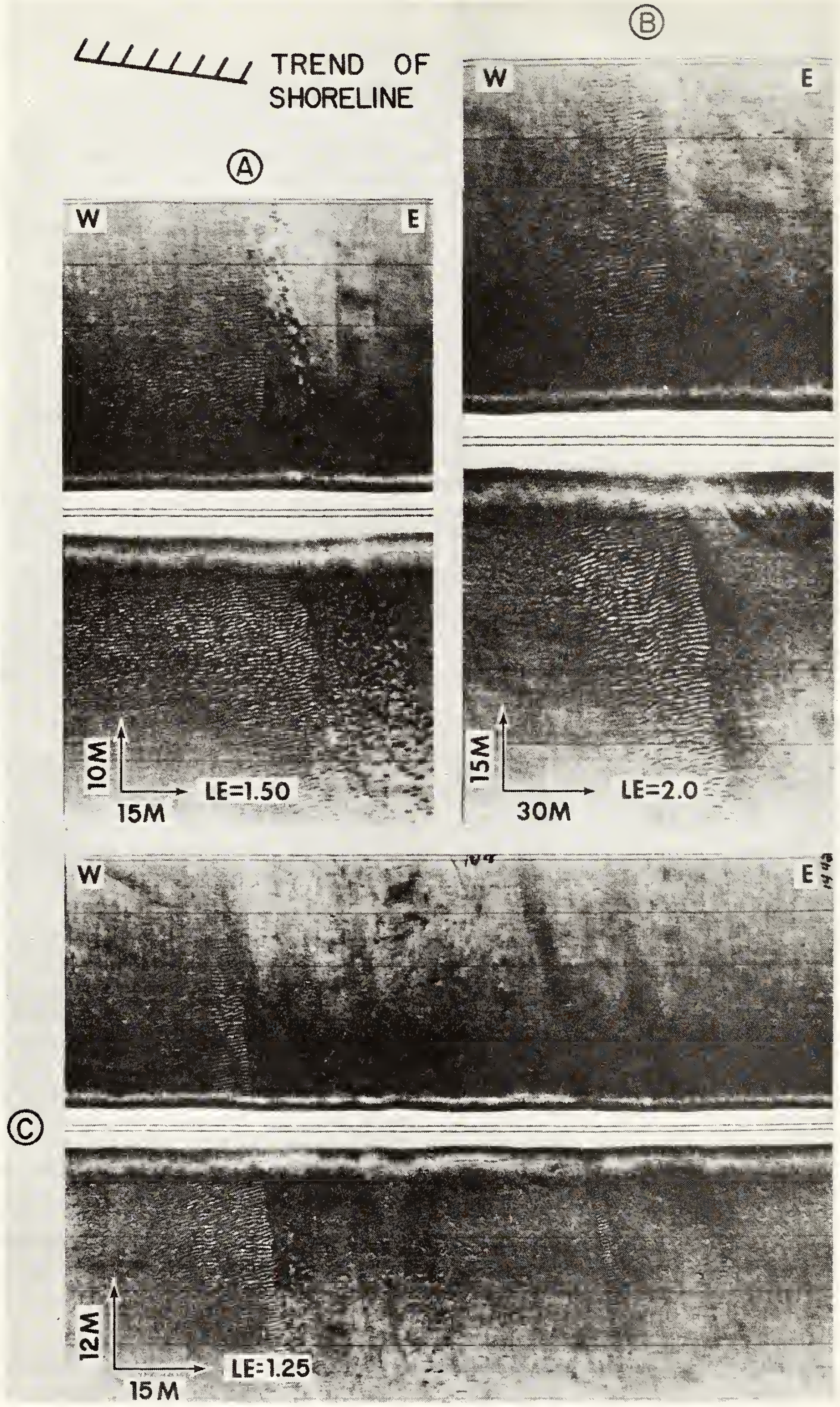
TREND OF SHORELINE
Ⓐ
W
E
10M
15M
LE=1.50
Ⓑ
W
E
15M
30M
LE=2.0
Ⓒ
W
E
12M
15 M
LE=1.25

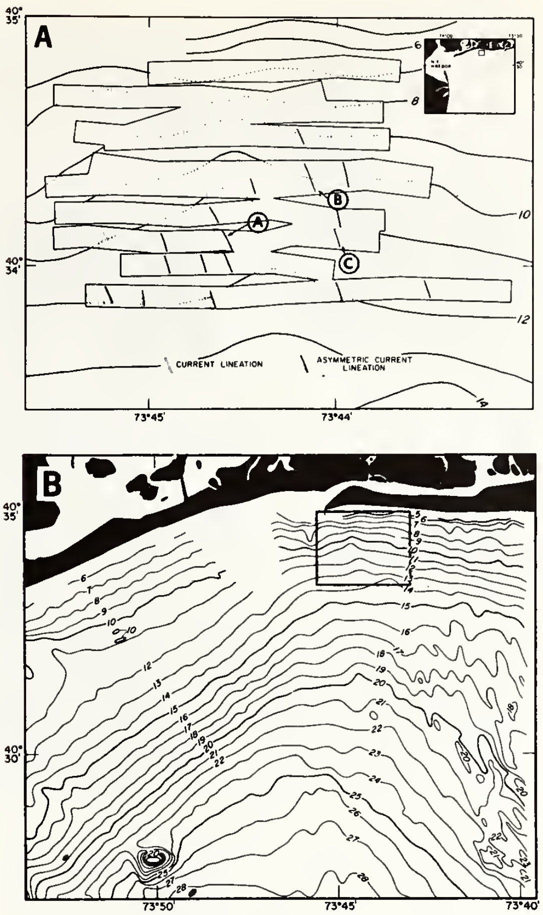
A
40° 35'
40° 34'
6
8
10
12
14
Ⓐ
Ⓑ
Ⓒ
CURRENT LINEATION
ASYMMETRIC CURRENT LINEATION
73°45'
73°44'
B
40° 35'
40° 30'
73°50'
73°45'
73°40'

FIG. 3.—(A) Bedform pattern at Atlantic Beach, inner Long Island shelf as revealed by side scan sonar. Letters refer to photographs of Figure 2. (B) Bathymetric setting of panel A. Note large-scale sand wavelike features outlined by contours, seaward of panel A. See Figure 1 for location. Depths in meters. From Freeland and Swift.

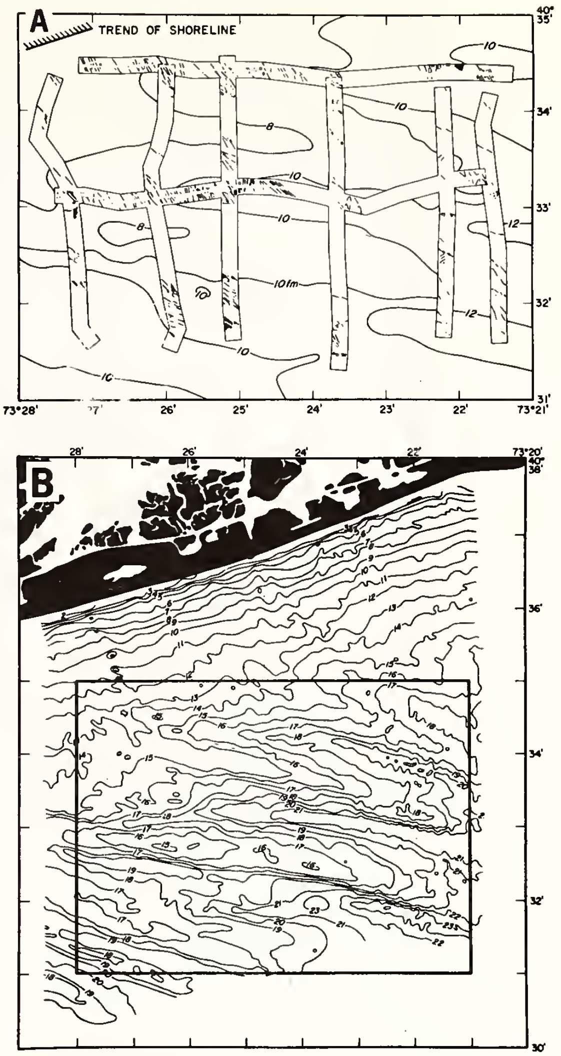
A
TREND OF SHORELINE
40° 35'
34'
33'
32'
31'
10
8
12
10fm
73°28'
27'
26'
25'
24'
23'
22'
73°21'
B
28'
26'
24'
22'
73°20'
40° 38'
36'
34'
32'
30'

FIG. 4.—(A) Bedform pattern at Tobay Beach, Long Island inner shelf, as revealed by side scan sonar. Width of trackline exaggerated 4 times for clarity. (B) Topographic setting of panel A, in ridge and swale topography of inner Long Island shelf. See Figure 1 for location. From Freeland and Swift.

erly flow which, especially in the winter, may be mildly reversed or strongly reinforced by intense winds associated with mid-latitude low pressure systems (Beardsley and Butman, 1974; Boicourt and Hacker, 1976). Some of the strongest flows are southward flows that occur when "scale-matching" storms transit the Middle Atlantic Bight. These storms follow a path such that for a period of time, the curve of the isobars of atmospheric pressure coincides with the curve of the regional isobaths of the shelf surface. Winds then blow down the arc of the Middle Atlantic Bight and induce a sustained southward geostrophic flow. Such flows typically exceed threshold speed for the fine to medium sand of the Atlantic inner-shelf floor (see for instance, Lavelle et al., 1976). We believe such storm-generated southward flows generate the bedform patterns described above.

We do not have flow observations of our bedforms at times when they are active. We can, however, assume that the alongshore component of the storm flow field is very much stronger than the onshore-offshore component and that, except within a short

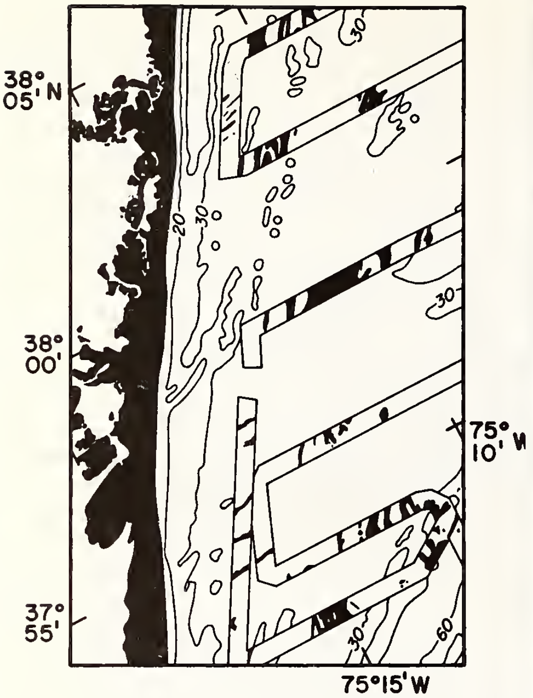

FIG. 5.—Shoreface bedforms off Assateague Island, Maryland inner shelf, as revealed by side scan sonar. Tracklines exaggerated 4 times for clarity. Note shore-oblique orientation of inner ridges, and shore-parallel orientation of outer ridges. See Figure 1 for location.

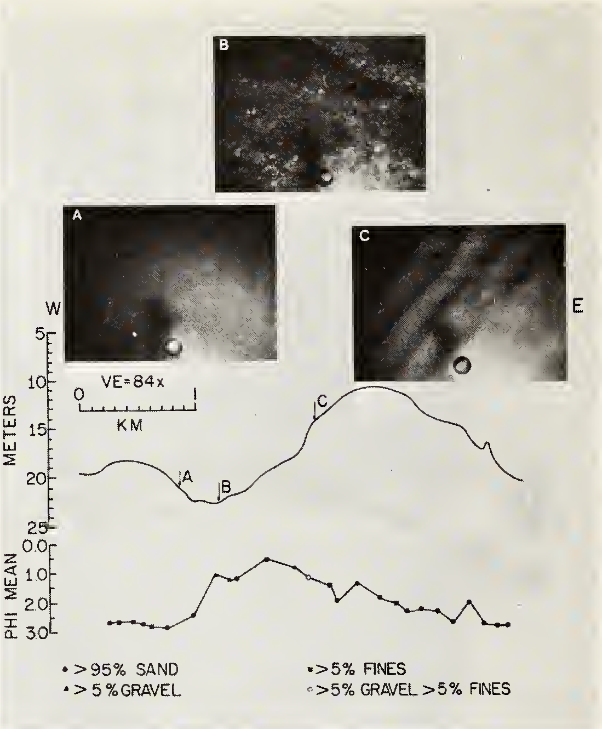

FIG. 7.—Offshore bedform in a trough between two sand ridges, seaward of Assateague Island, Maryland inner coast. Above: bottom photographs. (A) Fine sand, landward flank of trough. (B) Coarse, gravelly, shelly sand (offshore bedform). (C) Medium sand, seaward side of trough. Spacing of ripples varied with grain size. Upper center panel: bathymetric profile. Lower center panel: grain size profile. Bottom panel: schematic of sonograph. Dark tone: Shelly, gravelly, coarse sand (offshore bedform). Stipple: medium sand. See Figure 1 for location.

distance (several radii) of tidal inlets and estuary mouths, shelf storm flows are very nearly coast-parallel (see data in Boicourt and Hacker, 1976; discussion in Beardsley et al., 1975). This reasoning concludes that the nearshore bedforms, which make a large angle with the shoreline, are flow-transverse, whereas the coast-parallel lineations of the ridge and swale topography are flow-parallel.

The nature of the transition zone between the two bedform provinces is in most areas rather obscure. In the lower shoreface ridge topography at Tobay Beach, Long Island (Fig. 4), numerous bedforms lie at angles of 40° to 60° in the most shoreward trough, whereas in the troughs to the south, bedforms are parallel to the axis. On the Maryland coast (Fig. 5), the transition between the two current lineation types is quite abrupt. The east-west tracklines are characterized by ridge-parallel, generally symmetrical lineations, but the north-south tie lines near the coast reveal asymmetrical lineations that make a large angle with the trend of the sand ridge topography.

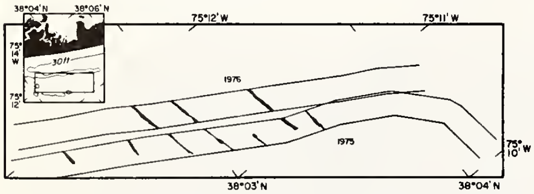

FIG. 6.—Shoreface bedforms off Assateague Island, over two consecutive years, as revealed by side scan sonar. Trackline width exaggerated 4 times for clarity. See Figure 1 for location.

Significance of Nearshore Bedforms

The orientation of the flow-transverse bedforms, with steeper slopes facing south-

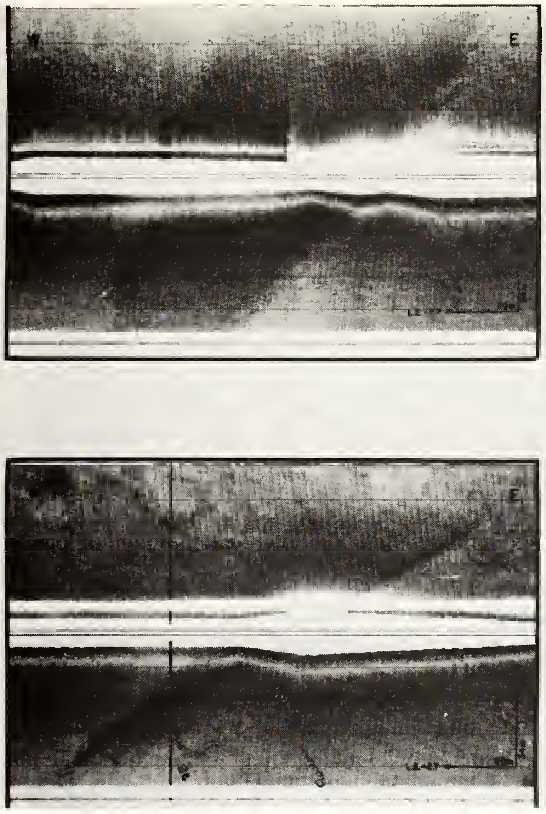

Fig. 8.—Two types of "offshore bedforms" seaward of Assateague Island, Maryland inner shelf, as revealed by side scan sonar. Above: "deflation zone" on seaward flank of trough (landward flank of ridge). Below: Small-scale, well-defined bedform.

west and slightly offshore, is compatible with what little is known about the behavior of the coastal boundary layer during northeaster storms; the most intense flows are downcoast to the southwest, and are two-layered, with an offshore component of bottom flow (Boicourt and Hacker, 1976; Fig. 6 above; Scott and Csanady, 1976, Fig. 7d; Magnell, 1976, p. 6–114 to 6–119, Figs. 6.5-1e, 6.5-5c; Swift et al., 1976, Fig. 13). There is some evidence to indicate that during storms, coastal flow becomes jet-like in nature, with more intense flow over the shoreface and innermost shelf than further offshore (Csanady, 1976; Boicourt and Hacker, 1976; Ludwick, 1977, in press), and it may be this jet-like characteristic of the "coastal boundary layer" during storms that determines the character of inner-shelf bedforms.

The flow-transverse bedforms are therefore best understood as low amplitude sand waves. The term "sand wave" is not used here as a general term for flow-transverse bedforms, but in the more rigorous sense of a transverse bedform larger in scale than either ripples or megaripples (dunes); see Jackson, 1975, and Middleton and Southard, 1977, for a discussion of the relationship between classes of transverse bedforms. Ripples and megaripples may be present together with sand waves in the nearshore bedform province (Swift et al., in press).

Figure 2 presents sonographs of typical inner-shelf sand waves. Resolution is unusually good because of the tranquil sea state that prevailed when the records were taken. However, the sonographs must be interpreted carefully. The wave-rippled, coarse, pebbly sand of the trough is readily apparent, because such coarse material strongly reflects acoustic energy. But the long, gentle upcurrent slopes, low poorly-defined crests, and gentle downcurrent slopes are composed of finer and therefore more weakly reflective sand, and are not readily apparent. Flow direction may be inferred from trough asymmetry; the sharply-defined side of the trough borders the downcurrent slope of the adjacent sand wave. The wave-generated ripples of the sand wave trough of Figure 2 are well-developed because trough sands are so coarse; ripples on the finer sand of the adjacent sand wave crest are too closely-spaced to be resolved in the sonograph, or too low to survive the bulldozing activities of invertebrates, or both. The wave ripples are shore-parallel at nearly right angles to the orientation of the sand wave, and are parallel to the surface wave train observed at the time that the sonograph was taken.

The sand waves of Figure 2 are described by Harris (1976) as tending to contain mud patches in the troughs during the quiescent summer period. On the Atlantic inner-shelf there tends to be a positive correlation between gravel and mud in grab samples. This relationship is interpreted to mean that the gravel-floored lows (troughs) that are created by winter storms become hydraulically quiet microenvironments that trap mud during the summer.

Perhaps the most satisfactory analysis of the genesis of transverse bedforms is that provided by J. D. Smith (1970) in which a sand bed is shown to be innately unstable in response to fluid shear in excess of the critical shear-stress value. Any slightly irregular sand bottom causes a corresponding perturbation of flow, and components of the velocity and bottom stress will be out of phase with the bottom profile; the distribution of these parameters is such that the crests and downcurrent faces of bottom highs will tend to undergo deposition, whereas the upcurrent faces will erode, so that the bedform grows and migrates. Slip faces may appear on mature bedforms but are not essential to bedform growth and migration; hence the features observed on the Atlantic inner-shelf, though lacking slip faces, are compatible with Smith's model.

The sand waves are of low relief, probably because they are responses to brief flow events separated by long periods of quiescence, during which grovelling organisms and wave surge tend to reduce slopes. At several localities, inner-shelf sand waves do grow to maturity, with heights in excess of 2 m and downcurrent slopes at the angle of repose (Platt Shoals, North Carolina, Virginia Beach, Virginia; Swift et al., 1978a, b). Exceptional sand wave development in these areas may be due to acceleration of the regional flow field as it passes over an inner-shelf shoal, with the result that sand waves on the shoal experience threshold velocity exceedence more frequently.

It should be noted that the nearly shore-normal bedforms of the shore-face are susceptible to interpretations other than the sand wave model. Reimnitz et al. (1976) have interpreted lineations that are symmetrical, but otherwise of similar appearance, as induced by rip currents. Karl (in press) has attributed symmetrical, shore-normal lineations on the California inner shelf to wind-driven Langmuir circulation.

Significance of Offshore Bedforms

Mesoscale, flow-parallel bedforms were first described in detail from the continental shelf around the British Isles (see summary study by Kenyon, 1970). Here they were described as sand ribbons since they generally consist of thin, narrow strips of sand over a coarser substrate, separated by wide exposures of the substrate. Less commonly the zones of slight positive relief are wider than the zones of slight negative relief. These features have been referred to as longitudinal furrows (Dyer, 1970; Stride et al., 1972). Their relationship to sand ribbons is not clear, since there seems to be little textural contrast between furrow and adjacent high.

In the case of the Sahara Shelf, however (Newton et al., 1973), and the Middle Atlantic Bight (McKinney et al., 1973; Swift et al., 1978a, b) the bedforms are more clearly the converse of sand ribbons; narrow elongate depressions of shallow depth within a sand sheet, floored by coarser material. In some cases the depressions are clearly "windows" through a thin sand sheet exposing a basal gravel.

We adopt the term "current lineation" (McKinney et al., 1974) as a general class, encompassing both the sand ribbons of the British seas and the gravel strips and windows of the central Atlantic shelf. The term is used in a purely descriptive sense, but there may be a genetic relationship between the two sub-categories; sand ribbons may form in response to marine flows on sand-deficient bottoms, where the basal Holocene gravel is exposed on the sea floor (Belderson et al., 1966), whereas gravel windows and gravel ribbons may form in response to similar flows, where the surficial sand sheet is thicker and is more nearly continuous. If this hypothesis is correct, then "sand ribbon" sets and sets of "linear erosional windows" are classes of bedforms differing primarily in degree; erosional troughs are developed at the expense of depositional crests, or vice versa.

Allen (1970, p. 69) has attributed sand ribbons to longitudinal roll vortices, and Wilson (1972) suggests that all longitudinal bedforms are responses to this flow structure. Longitudinal roll vortices, or helical flow cells, appear to be a basic pattern of shear flow that may arise in response to a variety of forcing mechanisms. "Microscale" longitudinal roll vortices occur in the viscous sublayer (summary discussion in Jackson, 1975), and longitudinal roll vortices of somewhat larger scale occur in flumes as a consequence of the interaction of the flow with the flume floor (Müller, 1976). Laboratory experiments and numerical models suggest that longitudinal vortices may occur at yet larger scales on the outer shelf where a Coriolis term is significant (Faller, 1971) and on the inner shelf where flow vortices are forced instead by vertical wind-driven shear (Gammelsrod, 1976). Atlantic shelf current lineations are compatible with a longitudinal vortex origin in that they are nearly contour-parallel. Their slight negative relief and coarser grain size suggest that they would form in the high velocity downwelling zones of such flow. Once formed, the alternating rough and smooth surfaces would presumably tend to reinforce the secondary structure in the flow over them. Flow-parallel current lineations, like flow-transverse current lineations, can be asymmetrical, since the flow vortices themselves may be skewed with respect to the mean flow, and may thus be asymmetrical (Gammelsrod, 1976).

While a relationship between contour-parallel lineations and longitudinal roll vortices seems probable, there have been to date no direct observations of concurrent fluid structure and substrate response on the sea floor.

The phenomenon of nearly shore-normal current lineations on the shore-face, and more nearly shore-parallel current lineations on the adjacent shelf do not appear limited to the Middle Atlantic Bight. A comparison of a recently published side-scan sonar map of the southern Brazilian continental shelf (Figueiredo and Kowsmann, 1976) with the original sonographs (Kowsmann, personal communication) reveals a pattern similar to that shown in Figure 5.

Bedforms as Transport Indicators

The sand waves and current lineations of the Middle Atlantic Bight serve as clues to the nature of bedload sediment transport. They are important because they survive from year to year, undergoing brief, intensive reactivation in response to storm flows that are widely spaced in time; they therefore contribute time-averaged information of a sort not obtainable from direct observation until we have more large-scale deployments of bottom-mounted current meters.

The bedform patterns tell us that the shelf floor in the areas studied is responding to the modern hydraulic regime and that the term "relict" is therefore inappropriate for these sediments. The current lineations tell us that the flows significant for sediment transport, like the observed flows cited on previous pages, are contour-parallel. The sand waves indicate that the mean sediment flux, like the most intense observed flows, is directed towards the southwest. The sand waves further indicate that on the inner shelf, the mean sediment flux has an offshore component—an aspect of sediment transport not clearly apparent from the limited flow measurements presently available.

ACKNOWLEDGEMENTS

This study was supported in part by the New York Bight Project Office of the Marine Ecosystems Analysis Program, National Oceanic and Atmospheric Administration, and by the Division of Biomedical and Environmental Research, Department of Energy. We thank the captains and crews of the NOAA vessels *George B. Kelez, Mt. Mitchell,* and *Pierce.*

REFERENCES

Allen, J. R. L., 1970, Physical processes of sedimentation, American Elsevier, New York, 433 p.

Anonymous, 1976, Evaluation of proposed sewage sludge dumpsite areas in the New York Bight: NOAA Tech. Memo. ERL Mesa-11, Marine Ecosystems Analysis Program Off., Environmental Res. Labs., NOAA, Boulder, CO, 212 p.

Beardsley, R. C., W. C. Boicourt, and D. V. Hansen, 1976, Physical oceanography of the Middle Atlantic Bight: *in:* Gross, M. G. (*ed.*), Middle Atlantic Continental Shelf and the New York Bight: Special Symposia, v. 2, Am. Soc. of Limnology and Oceanography, p. 20–34.

Beardsley, R. C., and B. Butman, 1974, Circulation on the New England continental shelf: response to strong winter storms: Geophys. Res. Ltrs., p. 181–184.

Belderson, R. H., N. H. Kenyon, and A. H. Stride, 1970, Holocene sediments on the continental shelf west of the British Isles: Inst. Geol. Sci. Rept. No. 70, p. 157–170.

———, and A. H. Stride, 1966, Tidal current fashioning of a basal bed: Marine Geology, 4, p. 237–257.

Boicourt, W. C., and P. W. Hacker, 1976, Circulation of the Atlantic continental shelf of the United States, Cape May to Cape Hatteras: Mem. Soc. Royale des Sciences de Liege, 16th Series, 10, p. 181–200.

Bouma, A. H., and M. A. Hampton, 1977, Large dunes and other bedforms in lower Cook Inlet, Alaska: Ninth Annual Offshore Tech. Conf., Houston, TX, preprint, p. 74–85.

Csanady, G. T., 1976, Wind-driven and thermohaline circulation over the continental shelves, p. 31–47: *in* Manowitz, B. (*ed.*), Effects of Energy-Related Activities on the Atlantic Continental Shelf, Conf. at

Brookhaven Nat'l lab., Nov. 10–12, 1975. 260 p.

Dyer, K. R., 1970, Liner erosional furrows in Southampton water: Nature, 225, p. 56–58.

Faller, A. J., 1971, Oceanic turbulence and the Langmuir circulations: Ann. Rev. Ecology and Systematics, 2, p. 201–236.

Figueiredo, A. G., Jr., and R. O. Kowsmann, 1976, Interpretacao dos registros de sonar de varredura lateral obtidos na plataformal sul Riograndense durante a operacao Geomar VII: Projeto REMAC, Companhia de Resquisa de Recursos Minerais, Av. Pasteur 404, Rio de Janeiro, Brasil, 9 p.

Freeland, G. L., and D. J. P. Swift, in press, Surficial sediments and bedforms of the Long Island inner shelf: NOAA-MESA Tech. Memo., Boulder, CO.

Gammelsrod, T.,1975, Instability of Couette flow in a rotating fluid and origin of Langmuir circulations: Jour. Geophys. Res., 80, p. 5069–5075.

Harris, W. H., 1976, Spatial and temporal variation in sedimentary grain size facies and sediment heavy metal ratios in the New York Bight apex, p. 102–123: *in* Gross, M. G., (*ed.*), Middle Atlantic Continental Shelf and the New York Bight: Special Symposia v. 2., Am. Soc. Limnology and Oceanography, 440 p.

Hunt, R. E., D. J. P. Swift, and H. Palmer, 1977, Constructional shelf topography, Diamond Shoals, North Carolina: Geol. Soc. Amer. Bull., v. 88, p. 299–311.

Jackson, R. G., 1975, Hierarchical attributes and a unifying model of bedforms composed of cohesionless material and produced by shearing flow: Geol. Soc. Amer. Bull., v. 86, p. 1523–1533.

Karl, H. A., in press, Speculations on processes responsible for mesoscale current lineations on the continental shelf, southern California: Submitted to Marine Geology.

Kenyon, N. H., 1970, The origin of some transverse sand patches in the Celtic Sea: Geol. Mag., p. 389–394.

———, 1970, Sand ribbons of European tidal seas: Marine Geology, v. 9, p. 25–39.

Lavelle, J. W., H. R. Brashear, F. N. Case, R. L. Charnell, P. E. Gadd, K. W. Haff, G. A. Han, C. A. Kunselman, D. A. Mayer, W. L. Stubblefield, and D. J. P. Swift, 1976, Preliminary results of coincident current meter and sediment transport observations for wintertime conditions, Long Island inner shelf: Geophys. Res. Ltrs., 3, p. 97–100.

Ludwick, J. C., 1977, Jet-like coastal currents and bottom sediment transport off Virginia Beach, Virginia (abstract): EOS, 58, p. 408.

———, in press, Coastal currents and bottom sediment transport off Virginia Beach, Virginia: J. Geophys. Res.

McKinney, T. F., W. L. Stubblefield, and D. J. P. Swift, 1974, Large-scale current lineations on the Great Egg shoal retreat massif: investigations by side scan sonar: Marine Geology, v. 17, p. 79–102.

Magnell, B., 1976, Summary of oceanographic observations in New Jersey coastal waters near 39°28′ N latitude and 74°15′ W longitude during the period May 1974 through May 1975: Waltham, Mass., EG&G Inc.

Middleton, G. V., and J. B. Southard, 1977, Mechanics of sediment transport: SEPM Short Course #3, Tulsa, OK, Soc. Econ. Paleontologists and Mineralogists.

Müller, A., 1977, Effect of secondary flow on turbulence in an open channel flow: *in* Hydraulic Problems Solved by Stochastic Methods, 2nd Internat'l Symposium on Stochastic Hydraulics, Lund, Sweden, 1976.

Newton, R. S., E. Seebold, and F. Werner, 1973, Facies distribution patterns on the Spanish Sahara continental shelf mapped with side scan sonar: Meteor. Forsch., Ergebnisse, 15, p. 55–77.

Reimnitz, E., L. J. Toemil, F. Shepard, and M. Gutierrez-Estrada, 1976, Possible rip current origin for bottom ripple zones to 30-m depth: Geology, v. 4, p. 395–400.

Scott, J. T., and G. T. Scanady, 1976, Nearshore currents off Long Island: J. Geophys. Res., v. 81, p. 5403–5407.

Sheridan, R. E., C. E. Dill, Jr., and J. C. Kraft, 1974, Holocene sedimentary environment of the Atlantic inner shelf off Delaware: Geol. Soc. Amer. Bull., v. 85, p. 1319–1329.

Smith, J. D., 1970, Stability of a sand bed subjected to a shear flow of low Froude number: J. Geophys. Res., v. 75, p. 5928–5940.

Stahl, L., J. Koczan, and D. J. P. Swift, 1974, Anatomy of a shoreface-connected sand ridge on the New Jersey shelf: implications for the genesis of the shelf surficial sand sheet: Geology, v. 2, p. 117–120.

Stride, A. H., R. H. Delelerson, and N. H. Kenyon, 1972, Longitudinal furrows and depositional sand bodies of the English Channel: *in* Memoir du Bureau Recherches Geologique et Minieres, No. 79, p. 233–244.

Stubblefield, W. L., M. Dicken, and D. J. P. Swift, 1974, Reconnaissance of bottom sediments on the inner and central New Jersey Shelf: Marine Ecosystems Analysis Program Report No. 1, Superintendent of Documents, U.S. Gov't Printing Office, Wash. D.C. 20402, 34 p.

Stubblefield, W. L., R. W. Permenter, and D. J. P. Swift, 1977, Time and space variation in the surficial sediments of the New York Bight apex: Estuarine and Coastal Mar. Sci., v. 5, p. 597–607.

Swift, D. J. P., G. L. Freeland, P. E. Gadd, G. A. Han, J. W. Lavelle, and W. L. Stubblefield, 1976, Morphologic evolution and coastal sand transport, New York, New Jersey shelf: *in* Gross, M. G. (*ed.*), Middle Atlantic Continental Shelf and the New York Bight: Am. Soc. Limnology and Oceanography Spec. Symposia, v. 2, p. 69–89.

———, and R. A. Young, in press, Time and space distributions of megaripples and associated bedforms, Middle Atlantic Bight, North American Atlantic shelf: Sedimentology.

———, B. Holliday, N. Avignone, and G. Shideler, 1972, Anatomy of a shoreface ridge system, False Cape, Virginia: Marine Geology, v. 12, p. 59–84.

———, and J. C. Ludwick, 1976, Substrate response to hydraulic process: grain-size frequency distributions and bedforms, Chap. 10, p. 159–196: *in* Stanley, D. J., and D. J. P. Swift, (*eds.*), Marine Sediment Transport and Environmental Management, John Wiley & Sons, NY, 602 p.

———, T. Nelsen, J. McHone, B. Holliday, H. Palmer, G. Shideler, 1978a, Holocene evolution of the inner shelf of southern Virginia: Jour. Sed. Petrology, v. 47, p. 1454–1474.

———, P. C. Sears, B. Bohlke, and R. Hunt, 1978b, in press, Evolution of a shoal retreat massif, North Carolina shelf: inferences from areal geology: Jour. Sed. Petrology.

———, G. Parker, N. W. lanfredi, G. Perillo, and K. Figge, 1978c, in press, Shoreface-connected sand ridges on American and European shelves: a comparison: Estuarine and Coastal marine Res.

Werner, F., and R. S. Newton, 1975, The pattern of large-scale bedforms in the Langeland Belt (Baltic Sea): Marine Geology, v. 19, p. 29–59.

———, ———, 1975, High-energy bedforms in the nontidal great belt linking North Sea and Baltic Sea: *in* Cronin, L. E. (*ed.*), Estuarine Res. Academic Press, N.Y., p. 381–389.

Wilson, I. G., 1972, Aeolian bedforms—their development and origins: Sedimentology, v. 19, p. 173–210.

Journal of Sedimentary Petrology 48, No. 3, 897-900.

INTERMITTENT STRUCTURE IN THE ATMOSPHERIC BOUNDARY LAYER MADE VISIBLE BY ENTRAINED SEDIMENT—EXAMPLE FROM THE COPPER RIVER DELTA, ALASKA

DONALD J. P. SWIFT
Atlantic Oceanographic and Meteorological Laboratories, National Oceanic
and Atmospheric Administration, Miami, Florida 33149
BRUCE F. MOLNIA
U.S. Geological Survey, Menlo Park, California 94025
ROSCOE G. JACKSON II
Department of Geological Sciences
Northwestern University, Evanston, Illinois 60201

ABSTRACT: On September 30, 1974, a katabatic wind (williwaw) swept seaward across the Copper River delta for 72 hours at velocities up to 39 m/sec. Sediment entrained in the basal 200 meters of the atmosphere seaward of the beach revealed a structured flow, consisting of large streaks 30 to 50 m in diameter, separated by clear lanes of approximately equal width. The driving mechanism may be the large-scale helical flow patterns that have been described in the atmospheric and oceanic boundary layers. The large streaks are of the same scale as desert sand strips, or continental shelf sand ribbons.

INTRODUCTION

The structure of the basal boundary layer in the atmospheric and marine flows has become a topic of special concern to geophysical scientists in general (McCave, 1976) and in particular to sedimentologists who wish to apply the insights of fluid dynamics to problems of sediment transport. The elucidation of boundary flow structure has been a particular problem in such studies. While dye has sometimes been used to determine the structure of small scale flows in laboratory experiments (Kline *et al.*, 1967), observations of boundary layers at geophysical scales have been generally confined to time series of velocity measurements at a point, or at best, vertical profiles (Gordon, 1974; Heathershaw, 1974; Panofsky, 1974; for a recent exception see Nakata *et al.*, 1976).

One of us (Molnia) has recently had an opportunity to directly observe boundary layer flow at a geophysical scale, in which sediment transport served to make flow structure visible (Fig. 1). While the observations are primarily qualitative in nature, we present them as an unusual opportunity to visualize phenomena that can usually be detected only with instruments.

THE OBSERVATION

The observation took place at the mouth of the Copper River, in the Gulf of Alaska, on September 30, 1974. The area is subject to williwaws, a local name for intense north winds of orographic origin (katabatic winds) from the Chugach and Alaska ranges of the hinterland; similar to the Santa Ana and Chinook winds of California and the Great Plains. Such winds accelerate on the downwind slopes of mountain ranges because the decrease in altitude increases density, and in the case of the williwaws, because of cooling over glacial ice. The September 30, 1974 episode lasted for 72 hours, and affected an area from just east of Cordova, Alaska, to the west side of Kayak Island. Winds up to 39 m/sec were reported on September 30, and intermittently for the next 72 hours.

An overflight from 1100 to 1300 hours on September 30 showed that the Copper River Delta was obscured by a haze estimated to be 150 to 200 m high. The haze was particularly apparent from the delta front barrier islands to a distance of several kilometers seaward, where it probably consisted in large part of sand and dust from the aeolian flats,

---

Manuscript received June 16, 1977; revised February 14, 1978.

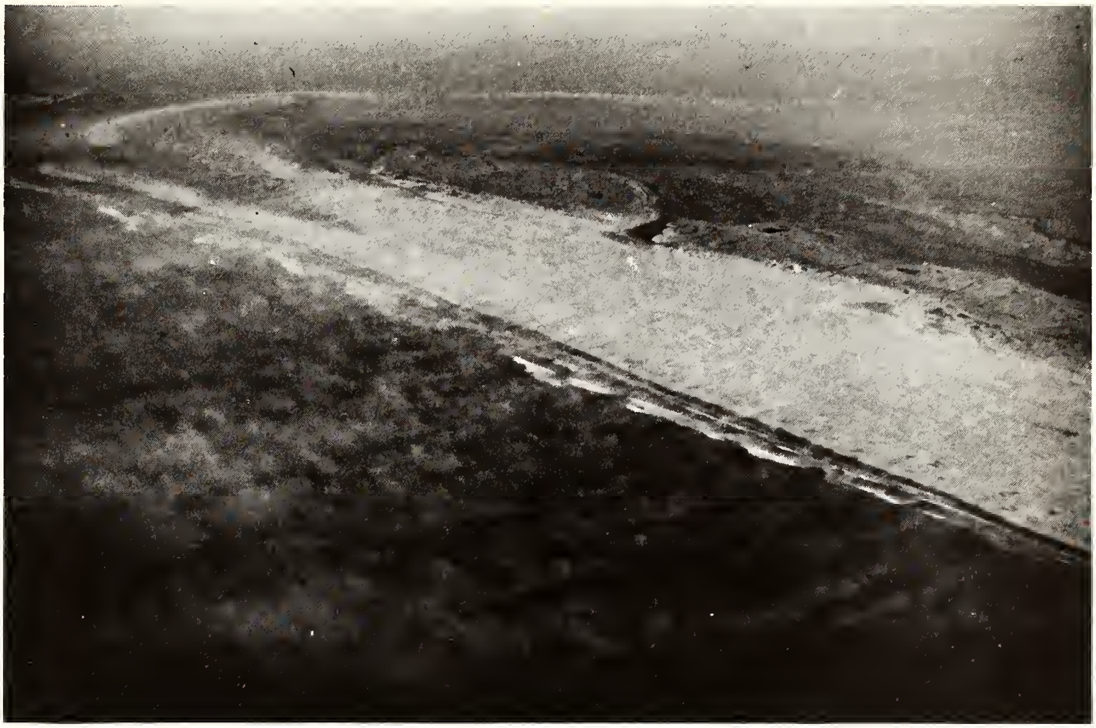

FIG. 1.—Entrained sediment revealing a boundary layer structure, Copper River Delta, Alaska. Altitude 800 m. Wind speed about 39 m/sec. Note landward-moving surf with crests blown seaward by wind.

dunes and beaches of the islands. The basal portion of the over-ocean haze was structured as streaks 25 to 30 m wide, separated by clear lanes of approximately equal width. In the accompanying photograph, individual streaks and lanes can be traced for at least 300 m. They are not uniform in appearance along their length, in that haze plumes tend to rise from their backs every 10–50 m. The streaks expand, merge, and become more diffuse from right to left, across the picture, as the wind moves offshore.

DISCUSSION

The phenomenon of "streamwise streakiness" (Kline, 1967; Kim and others, 1971) in aqueous boundary layer flow has been known for some time. Small scale streakiness (transverse spacing on the order of centimeters) has come to be considered as part of a general process of intermittent momentum exchange known as boundary layer bursting, in which streaks of slowly moving fluid in the upper part of the viscous sublayer are carried as sudden bursts or ejections from the floor into the faster, turbulent, outer boundary layer; between these bursts there tend to form inrushes or sweeps of higher momentum fluid toward the floor (Rao *et al.*, 1971; Grass, 1971, especially p. 251; see also review by Miller, 1976, especially p. 178–180). The bursting process has been reported in the atmospheric boundary layer as well (Jackson, 1976, p. 536). Boundary layer bursting has been implicated as a mechanism of sediment entrainment and transport, and the small scale streakiness appears to produce the small longitudinal bedforms generally referred to as current lineation (Jackson, 1976, p. 551).

The boundary layer structure revealed by suspended sediment in Figure 1 resembles that described from laboratory models of boundary layer bursting (Kline *et al.*, 1967). Laboratory studies suggest that boundary layer bursting scales with variables of the outer boundary layer such as U_∞, the free stream velocity, and δ, the boundary layer thickness, with

$$U_\infty \bar{T}/\delta \simeq 5$$

where $\bar{T}$ is the mean periodicity of bursts at a point in the flow (Jackson, 1976, p. 535, after Rao *et al.*, 1971). The relationship is, however, difficult to apply to Figure 1. Boundary layer thickness cannot be reliably estimated in the abnormal flow condition of the williwaw, and, furthermore, a secondary, internal boundary appears to be developing where the roughness changes at the landward (upcurrent) edge of the beach. In any case, the difference in scale between boundary layer bursting described in the laboratory and the structure observed in Figure 1 is sufficiently great that different mechanisms are probably operative, such as those believed to occur in volcanic eruptions (*nuées ardentes*) and in desert dust storms (Idso, 1974), or those driving the large scale helical flow patterns in the atmospheric boundary layer (Brown, 1970; LeMone, 1973) or in marine flows (Faller, 1962, 1971; Faller and Kaylor, 1966; Gammelsrod, 1975).

The spacing, λ, of helical flow cells in the atmosphere is 2–4 δ, where δ is boundary layer thickness. With cells 50 to 60 m wide, δ must be on the order of 15 to 30 m. The values seem small for a katabatic wind, but not unreasonably so, and can perhaps be supported by the following simplistic argument. A boundary layer growth relationship may be expressed as:

$$\delta = 0.37l \left(\frac{U\infty l}{\nu}\right) - 1/5$$

(Schlicting, 1968, p. 40), where l is the downstream distance and ν is the kinematic viscosity. With U_∞ estimated at 40 m/sec and ν as 0.12 cm^2/sec, the equation yields:

$$\delta = 0.046 l^{4/5} \text{ } (\delta, l \text{ in meters}).$$

The value for l is perhaps 500 m, judging from Figure 1, so δ (500 m) is 6.6 m, while δ (100 m) is 11.6 m. Considering the gross estimates in the procedure, and the crude "flat plate" analogy, the order of magnitude agreement between these estimates and the 15–30 m values seems encouraging.

The physical scale of the structure outlined in the photograph is approximately that of the low amplitude flow-parallel bedforms known in deserts as sand strips (Bagnold, 1941, p. 178; Wilson, 1972, p. 185) and on the continental shelf floor as sand ribbons (Kenyon, 1970) or current lineations (McKinney *et al.*, 1974), and a cause and effect relationship between fluid process and these response features should be investigated.

ACKNOWLEDGMENTS

We wish to thank Robert Young, J. W. Lavelle, and H. B. Stewart, Jr., for helpful suggestions made during the preparation of this note.

REFERENCES

Bagnold, R. A., 1941, The Physics of Blown Sand and Desert Dunes, Methuen, London, 265 p.

Brown, R. A., 1970, A secondary flow model for the planetary boundary layer: Jour. Atmos. Sci., v. 27, p. 742–757.

Faller, A. J., 1962, An experimental study of the instability of the laminar Ekman boundary layer: Jour. Fluid Mech., v. 15, p. 560–576.

Faller, A. J., 1971, Oceanic turbulence and the Langmuir circulations: Ann. Rev. Ecology and Systematics, v. 2, p. 201–236.

Faller, A. J., and R. E. Kaylor, 1966, A numerical study of the instability of the laminar Ekman boundary layer: Jour. Atmos. Sci., v. 23, p. 466–480.

Gammelsrod, T., 1975, Instability of Couette flow in a rotating fluid and origin of Langmuir circulations: Jour. Geophys. Res., v. 80, p. 5069–5075.

Gordon, C. M., 1974, Intermittent momentum transport in a geophysical boundary layer: Nature, v. 248, p. 392–394.

Grass, A. J., 1971, Structural features of turbulent flow over smooth and rough boundaries: Jour. Fluid Mech., v. 50, p. 233–255.

Heathershaw, A. D., 1974, "Bursting" phenomena in the sea: Nature, v. 248, p. 394–395.

Idso, S. B., 1974, Tornado or dust devil: The enigma of desert whirlwinds: Amer. Scientist, v. 62, p. 530–541.

Jackson, R. G., Sedimentological and fluid-dynamic implications of the turbulent bursting phenomenon in geophysical flows: Jour. Fluid Mech., v. 77, p. 531–560.

Kenyon, N. H., 1970, Sand ribbons of European tidal seas: Mar. Geol., v. 9, p. 25–39.

Kim, H. T., S. J. Kline, and W. C. Reynolds, 1971, The production of turbulence near a smooth wall in a turbulent boundary layer: Jour. Fluid Mech., v. 50, p. 133–160.

Kline, S. J., W. C. Reynolds, F. A. Schraub, and P. W. Runstadler, 1967, The structure of turbulent boundary layers: Jour. Fluid Mech., v. 30, p. 741–773.

LeMone, A. M., 1973, The structure and dynamics of horizontal roll vortices in the planetary boundary layer: Jour. Atmos. Sci., v. 30, p. 1077–1091.

McCave, I. N., 1976, The Benthic Boundary Layer. Plenum Press, New York, 322 p.

McKinney, T. F., W. L. Stubblefield, and D. J. P. Swift, Large scale current lineations on the Great Egg Shoal retreat massif: Investigations by side scan sonar: Mar. Geol., v. 17, p. 79–102.

Muller, R. L., 1976, Some aspects of bottom sediment transport mechanics on the continental shelf. p. 167–184, *In* Manowitz, B. (*ed.*), Effects of Energy Related Activities on the Atlantic Continental Shelf. Brookhaven National Laboratory and U.S. Energy Research and Development Administration (available from U.S. Govt. Printing Office), 260 p.

Nakata, J. K., H. G. Wilshire, and G. G. Barnes, 1976, Origin of desert dust plumes photographed from space: Geology, v. 4, p. 644–648.

Panofsky, H. A., 1974, The atmospheric boundary layer below 150 meters: Ann. Rev. Fluid Mech., v. 6, p. 147–177.

Rao, K. N., R. Narasimha, and M. A. B. Narayanan, 1971, The "bursting" phenomenon in a turbulent boundary layer: Jour. Fluid Mech., v. 48, p. 339-352.

Schlicting, H., 1968, Boundary Layer Theory. McGraw Hill, New York, 647 p.

Townsend, A. A., 1965, Excitation of internal waves on turbulent boundary layers: Jour. Fluid Mech., v. 22, p. 241–252.

Wilson, I. G., 1972, Aeolian bedforms: Their development and origins: Sedimentology, v. 19, p. 173-210.

Marine Geology 27, 19-42.

EVOLUTION OF A SHOAL RETREAT MASSIF, NORTH CAROLINA SHELF: INFERENCES FROM AREAL GEOLOGY

DONALD J.P. SWIFT, PHILLIP C. SEARS*, BRENDA BOHLKE, and ROBERT HUNT**

Atlantic Oceanographic and Meteorological Laboratories, Miami, Fla. 33149 (U.S.A.)

(Received December 2, 1976; revised and accepted April 11, 1977)

ABSTRACT

Swift, D.J.P., Sears, P.C., Bohlke, B. and Hunt, R., 1978. Evolution of a shoal retreat massif, North Carolina Shelf: inferences from areal geology. Mar. Geol., 27: 19—42.

The Albemarle Shelf Valley Complex on the northern North Carolina Shelf is a leveed shelf-floor channel trending seaward from the modern Albemarle estuary. Vibracores and seismic profiles indicate that the levees have a twofold internal structure. Levee cores consist of fine sand interbedded with mud lenses. The cores are mantled with a generally coarser, cleaner sand. The levees are interpreted as shoal retreat massifs; deposits formed as the littoral-drift depositional centers on either side of the ancestral Albemarle estuary retreated landward during the Holocene transgression.

The shelf-valley complex underwent systematic changes in bottom morphology and sediment character as the reversing tidal jet of the estuary mouth was replaced by the intermittent south-trending storm flows of the open shelf. A pattern of ridges and troughs with 10 m of relief was incised into north sides of the massifs flanking the shelf valley.

The coarser surficial sand into which the bedform pattern has been impressed appears to be a lag deposit formed by the winnowing of the massifs during storm flow. On ridge crests this surficial sand sheet has been molded into sand waves up to 3 m high. The relative orientations of sand waves, ridges, and the shoreline indicate that the structure of the velocity field during peak flows must be quite complex. Ridges converge southward with the shoreline at angles of 15—20°, while the sand waves atop them make angles of about 75° with the shoreline; the sand waves are thus neither orthogonal with respect to the shoreline nor with respect to the ridges. Sand-wave orientation indicates southward bottom flow with an offshore component.

Existing hydrodynamical theory does not adequately explain this pattern. Extensive hydraulic measurements of careful design will be required so we can interpret the bedform pattern and its role in the coastal sand budget.

---

*Present address: Van Houten Associates, 420 Lexington Place, New York, N.Y. 10017 (U.S.A.)

**Present address: NOAA Ship "Oceanographer", Pacific Marine Center, Seattle, Wash. (U.S.A.)

INTRODUCTION

The Middle Atlantic Shelf of North America is divided into a series of compartments by transverse shelf-valley complexes (Swift, 1973; Swift and Sears, 1974; Fig.1, this paper). Shelf-valley complexes are suites of topographic elements generated by the landward displacement of estuary mouths during the Holocene transgression. A shelf-valley complex may include (1) a mid-shelf or shelf-edge delta, (2) a shelf valley, and (3) shoal retreat massifs. The latter features are broad, poorly defined sand ridges on the north flanks or on both flanks of shelf valleys that mark the retreat

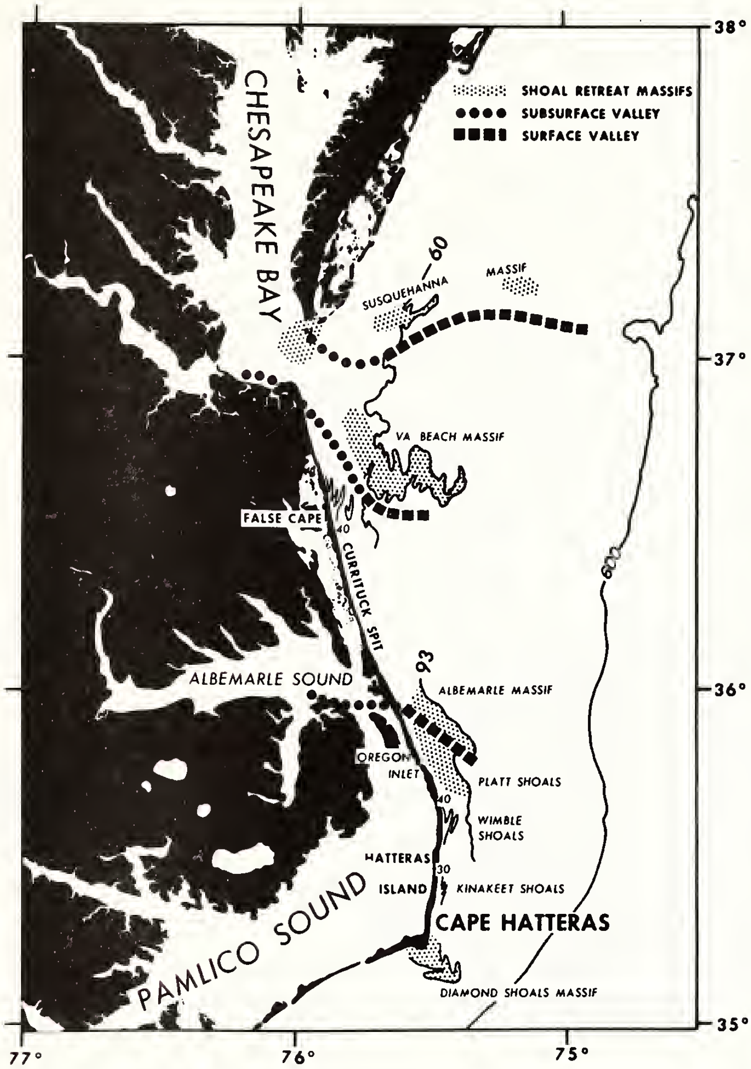
38°
37°
36°
35°
77°
76°
75°
▨ SHOAL RETREAT MASSIFS
●●●● SUBSURFACE VALLEY
■■■■ SURFACE VALLEY
CHESAPEAKE BAY
60
SUSQUEHANNA
MASSIF
VA BEACH MASSIF
FALSE CAPE
40
CURRITUCK SPIT
600
93
ALBEMARLE SOUND
ALBEMARLE MASSIF
OREGON INLET
PLATT SHOALS
40
WIMBLE SHOALS
HATTERAS ISLAND
30
KINAKEET SHOALS
CAPE HATTERAS
PAMLICO SOUND
DIAMOND SHOALS MASSIF

Fig.1. Morphologic framework of the Virginia and northern North Carolina Shelf. Contours in feet.

paths of the littoral-drift depositional centers on the sides of estuary mouths. The term "massif" is used in the sense of a topographic high that is itself composed of smaller-scale topographic highs, for the massifs characteristically consist of arrays of sand ridges, whose axes are parallel to the shoreline, and perpendicular to the trend of the massif. The purpose of this paper is to describe the topography, stratigraphy, and surficial sediments of a classic example, the Albemarle Shelf Valley Complex of the northern North Carolina coast, and to assess on the basis of this information the extent to which the inherited estuarine topography has been remodeled in response to the modern hydraulic climate.

The metric system will be used in this paper except for maps prepared from National Ocean Survey data. These maps will be presented in English units, and will be described in both English and metric units in the text.

TOPOGRAPHY

The northern North Carolina Shelf consists of a broad sand plain. Its surface is molded into sand ridges, up to 10 m in relief, but with side slopes of less than a degree (Figs. 2 and 3). The ridges trend north—south, making

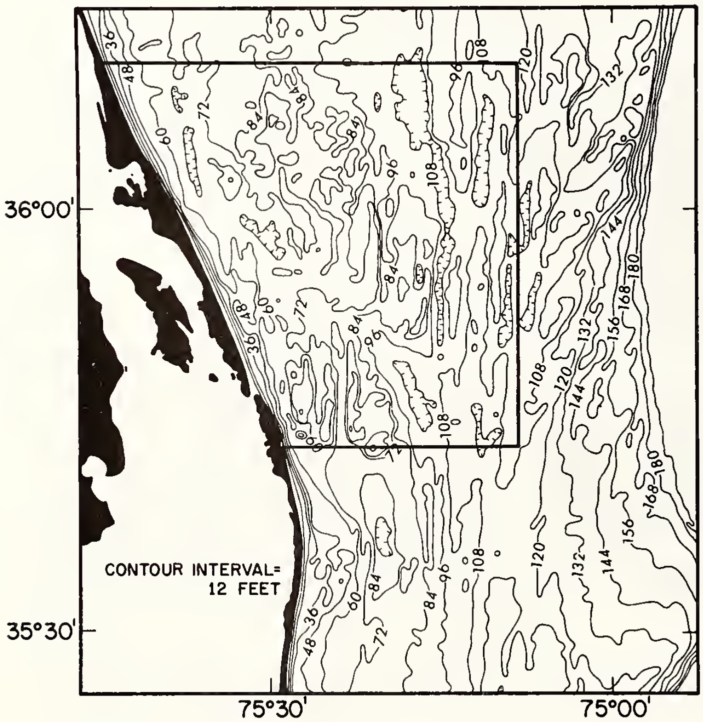

Fig.2. Bathymetry of the northern North Carolina Shelf. Box indicates study area. Note that the pervasive north—south "grain" of the study area conforms to regional topographic trend. From Goldsmith et al. (1974).

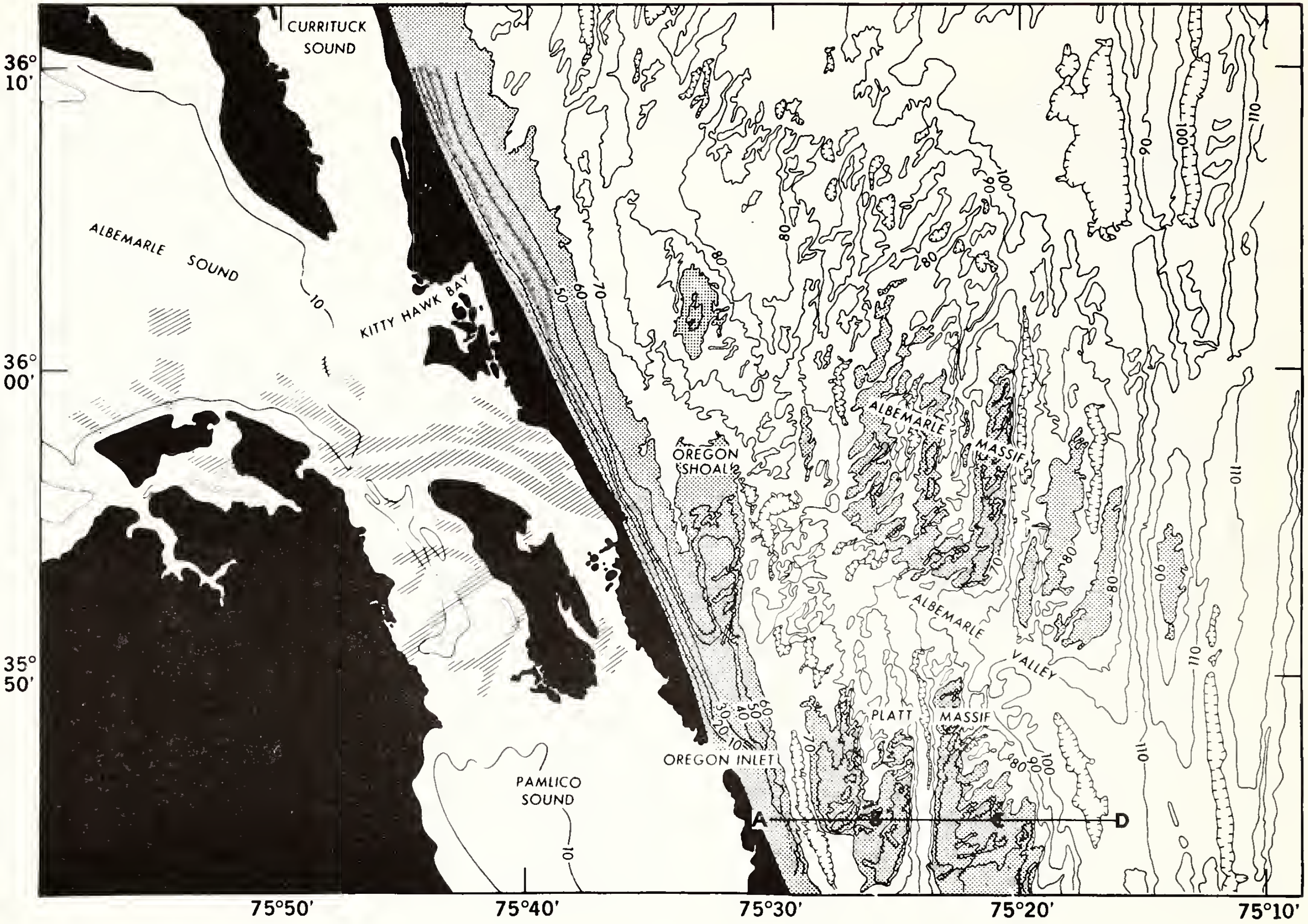
CURRITUCK SOUND
ALBEMARLE SOUND
KITTY HAWK BAY
PAMLICO SOUND
OREGON SHOAL
OREGON INLET
ALBEMARLE MASSIF
ALBEMARLE VALLEY
PLATT MASSIF
A
B
C
D
10
30
40
50
60
70
80
90
100
110
36° 10'
36° 00'
35° 50'
75°50'
75°40'
75°30'
75°20'
75°10'

Fig.3. Bathymetry of the study area. Contour interval 10 ft. Significant shoal areas are stippled. Diagonal ruling indicates subsurface channels in Albemarle Sound as indicated by seismic profiling (O'Connor et al., 1972). Cross-section *A—D* is presented as Fig.4.

an angle of up to 20° with the more easterly trending shoreline. Relief becomes marked immediately north of Oregon Inlet (Fig.3). Here three scales of topographic elements are superimposed. At the coarsest scale, the Albemarle Shelf Valley is an apparent extension of the subsurface channel system of Albemarle Sound (Fig.3; O'Connor et al., 1972). It lies between two areas of considerable relief, the Albemarle Massif and the Platt Massif.

These massifs consist of smaller-scale sand ridges trending north and south. Each massif comprises a comb-like array of ridges. Crests rise and broaden toward the south; troughs likewise tend to become shoaler toward the south. The arrays are not symmetrical about the shelf valley; the comb-like "teeth" tend to point north both north and south of the valley. The ridges of the two massifs tend to share other characteristics, although not without exception. The steepest dips occur on the upper portions of the seaward flanks (Fig.4), and the crest lines either merge with the shoreface, or tend to curve shoreward, forming a J-pattern in plan view (Fig.5). The sand ridges of the Platt Shoals massif are unique in that double and triple ridges occur. Inner Platt Shoals consists of two ridges flanked by deep troughs and separated by a raised shallow trough; the inner of the two ridges is itself double, with a shallow interior trough. Outer Platt Shoals likewise is a double ridge.

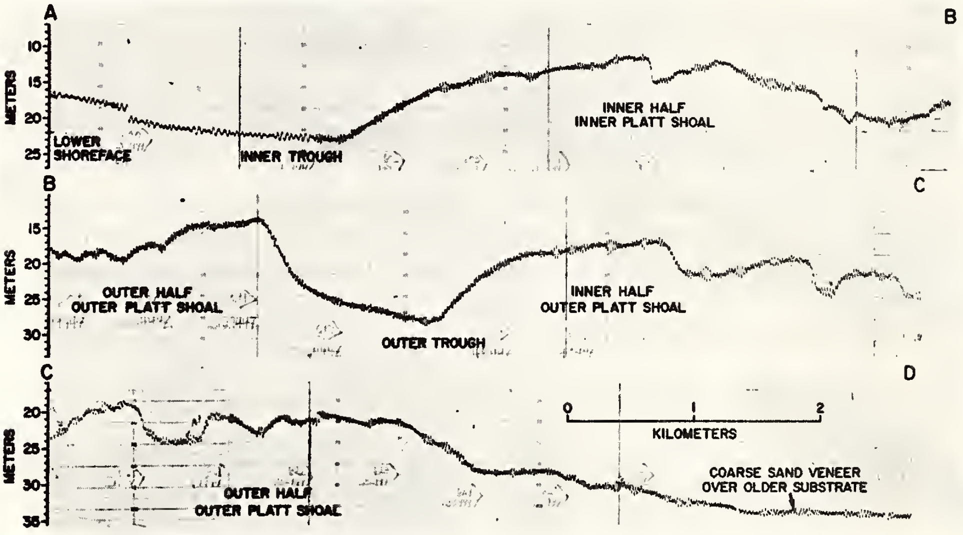

Fig.4. Bathymetric profile through the study area. See Fig.3. for locations.

At the third, finest, scale of topographic relief, a sand-wave pattern is imprinted on the sand-ridge topography. Sand-wave crests trend northeast—southwest. The sand waves are imperfectly resolved by the 10-ft contour interval of Figs. 3 and 5, but it is evident that they are between 2 and 5 m (6 and 15 ft) high, with crest lines that tend to be convex to the

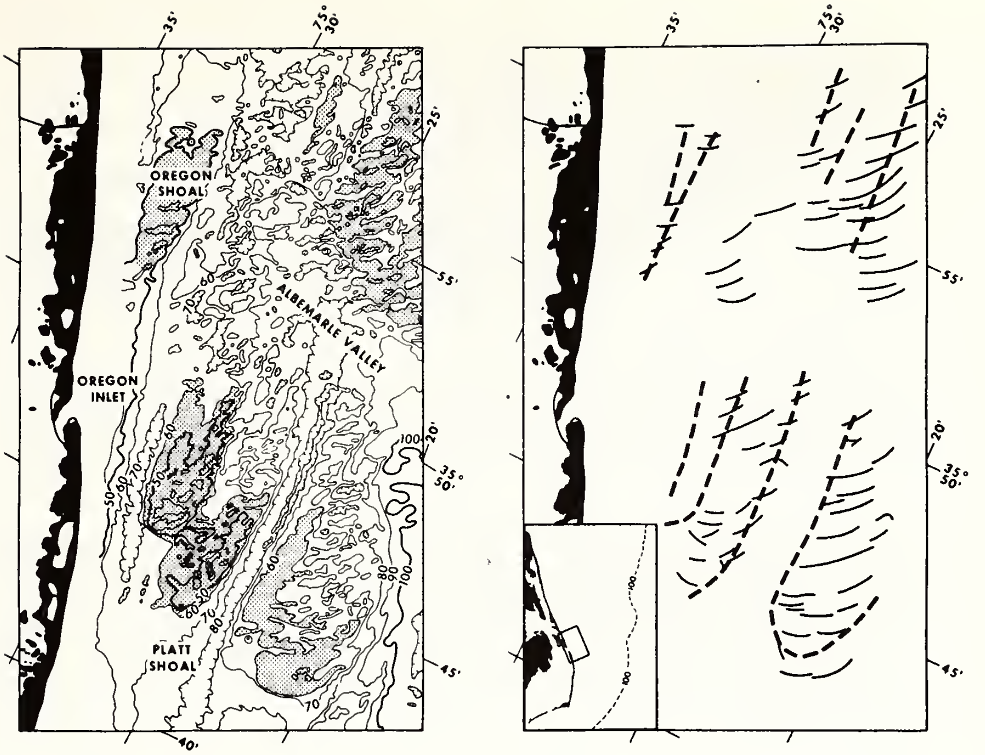

Fig.5. Bathymetric map of the inner Albemarle Shelf. Contour interval 10 ft. Pattern of ridges (dashed) and sand waves (solid) is indicated in the right-hand panel.

south, and tend to make a northward-opening angle of slightly less than 90° with the shoreline. They are primarily confined to ridge crests, being largely absent from the shoreface, the Albemarle Shelf Valley, and troughs between the ridges. The relationship of sand waves to sand ridges is presented schematically in Fig.6.

The topographic plan of the Albemarle Shelf Valley Complex with its asymmetrical massifs is very similar to that of the Virginia Beach Shelf Valley Complex (Swift et al., 1977).

Fig.7 presents a topographic net-change map for Platt Shoals. It is based on the Coast and Geodetic Survey smooth sheets for 1870 and 1970, respectively. The 1870 map was compiled by Robert Platt, by means of lead-line soundings and horizontal sextant angles. Survey lines were 300—2700 m apart. The 1970 chart was compiled by the NOAA Ship "Explorer" by means of acoustic profiling and Shoran navigation. Survey lines were approximately 208 m apart. Both sets of data were adjusted to mean sea level and the 1927 North American Datum.

Fig.7 indicates that the troughs became shoaler during the 100-year period, while the ridges have extended to the southeast. Comparison of the complete sets of contours and volumetric estimates based on these sets suggests that

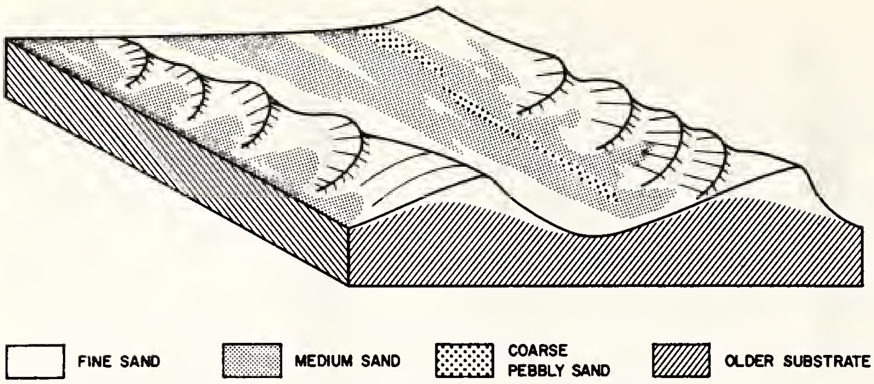
FINE SAND
MEDIUM SAND
COARSE PEBBLY SAND
OLDER SUBSTRATE

Fig.6. Schematic of ridge architecture showing relation of sand ridges to sand waves.

the upper levels of the troughs have become longer and wider and that the crests of the ridges have aggraded (Sears, 1973). Zones of bathymetric change on the order of 3—9 ft (1—3 m) extend over many square miles of sea floor, a degree of change greater than can be readily accounted for by navigational and sounding inaccuracies (see Goldsmith et al., 1975; Sallenger et al., 1975).

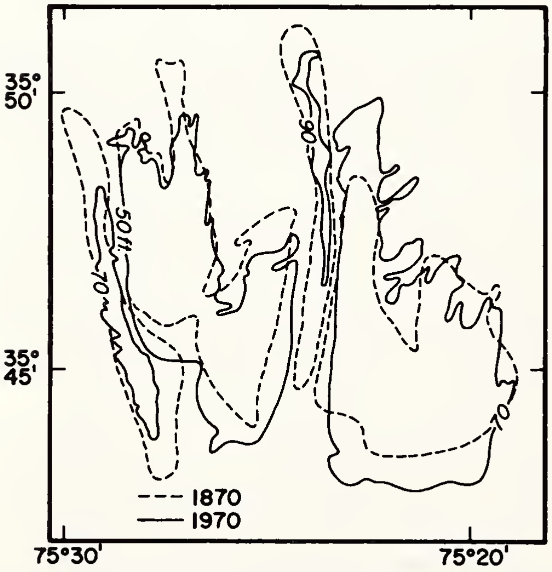
35° 50'
35° 45'
50ft
70
90
70
--- 1870
—— 1970
75°30'
75°20'

Fig.7. Map showing change in position of significant contours of the Platt Massiff between the 1870 and 1970 surveys.

STRATIGRAPHY AND GEOLOGICAL HISTORY

Vibracores and seismic profiles collected across the Platt Massif reveal a threefold stratigraphy (Fig.8). A basal sequence (Layer C) consists of massive, greenish gray, muddy sand. It is generally devoid of mollusc shells except for a *Mulinia* stratum found 43 m below sea level. The *Mulinia* bed dates at 22,750 ± 2000 years B.P. which places the age of the bed at the beginning of the late Wisconsin regression (Milliman and Emery, 1968). The core penetrating the *Mulinia* bed is not figured (see Sears, 1973). Seismic profiles suggest that the surface of the basal layer extends as a near plane seaward beneath the ridges. An intermediate sequence (Layer B) consists of greenish-gray fine sand with intercalations of mud, medium sand, and shell hash. It appears to form a nucleus within the ridges, being found at shallower depth within them than in the troughs (Fig.8). Molluscan shells are abundant; *Crassostrea virginica* and *Donax* sp. are the most common. A single large *Crassostrea* shell yielded a radiocarbon date of 10,720 ± 800 years B.P., and a sample of unbroken *Donax* shells from the outer trough yielded a date of 10,900 ± 900 years B.P. A similar sample from the seaward flank of the outer ridge yielded a radiocarbon date of 5618 + 100 years B.P. All dates fall within the earlier part of the Holocene transgression (Milliman and Emery, 1968).

The uppermost layer (Layer A) is a mantle of medium to coarse, well-sorted sand. It is thicker over the ridges than in the trough, and thickest on the seaward sides of the troughs (Fig.8). It is characterized by an open-water fauna including *Mercenaria mercenaria*, *Spisula solidisima*, and *Donax* sp.

Our stratigraphic analysis indicates that the Albemarle Shelf Valley Complex existed as an estuary mouth between 10,000 and 5000 years B.P. Its inherited morphology and internal characteristics (*Crassostrea* and clay beds) suggest a lunate estuary-mouth shoal similar to those described from the Georgia coast by Howard and Reineck (1972) and Oertel and Howard (1972); see Fig.9A. The existing shelf-valley complex may not necessarily have been formed during a single brief interval, but may instead have formed as a series of successively active shoal segments during a general period of sea-level rise and coastal retreat. Its demise may have been coincident with the reduction in the rate of sea-level rise of about 5000 years ago. The shelf-valley complex is presently separated from the Albemarle estuary by Currituck spit, part of the Virginia—North Carolina barrier chain. We have suggested elsewhere (Swift and Sears, 1974; Swift, 1975) that the reduction in the rate of sea-level rise during a period of constant sand supply may have caused the retreating barrier system to shift to a regime of near stillstand, in which the barriers grew primarily upward, while the lagoons behind them grew wider. The expansion of the intracoastal lagoonal system may have diverted the tidal discharge of Albemarle Sound into Pamlico Sound, allowing Currituck spit to seal off the former estuary mouth. Kitty Hawk Bay (Fig.3) is flanked by beach-ridge sets, and has been interpreted by Fisher (1967) as a former inlet.

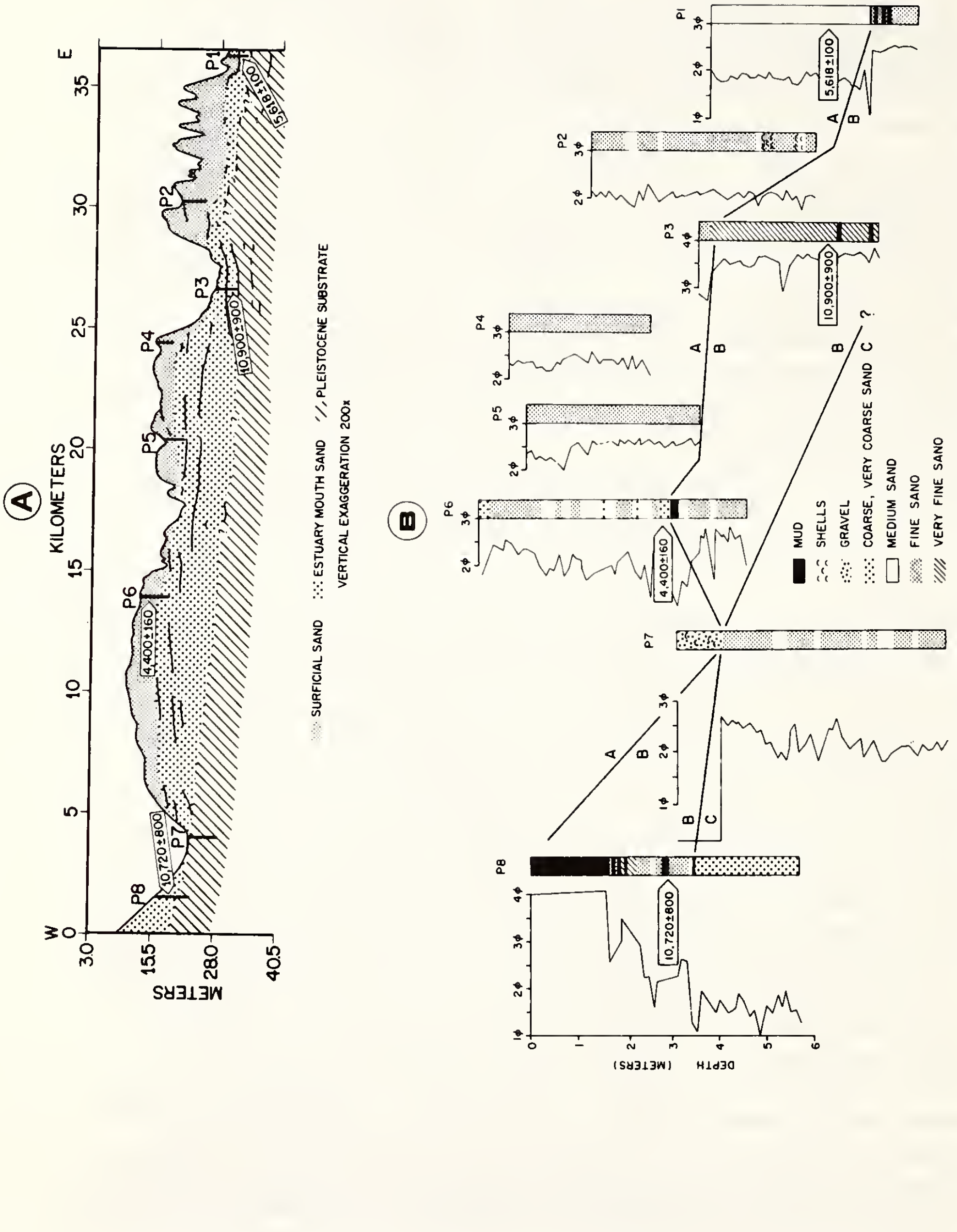
A
KILOMETERS
W
E
0
5
10
15
20
25
30
35
METERS
3.0
15.5
28.0
40.5
P1
P2
P3
P4
P5
P6
P7
P8
10,720±800
4,400±160
10,900±900
5,618±100
SURFICIAL SAND
ESTUARY MOUTH SAND
PLEISTOCENE SUBSTRATE
VERTICAL EXAGGERATION 200x
B
DEPTH (METERS)
0
1
2
3
4
5
6
1φ
2φ
3φ
4φ
A
B
C
?
MUD
SHELLS
GRAVEL
COARSE, VERY COARSE SAND
MEDIUM SAND
FINE SAND
VERY FINE SAND

Fig.8. A. 3.5 kHz profile through Platt Massif showing reflecting horizons, positions of vibracores, gross lithology as indicated by vibracores, and radiocarbon dates (location: section *A–D*, Fig. 3). B. Correlation of vibracores shown in A. Unit A is surficial sand. Unit B is estuarine sand. Unit C is older substrate. See text for explanation.

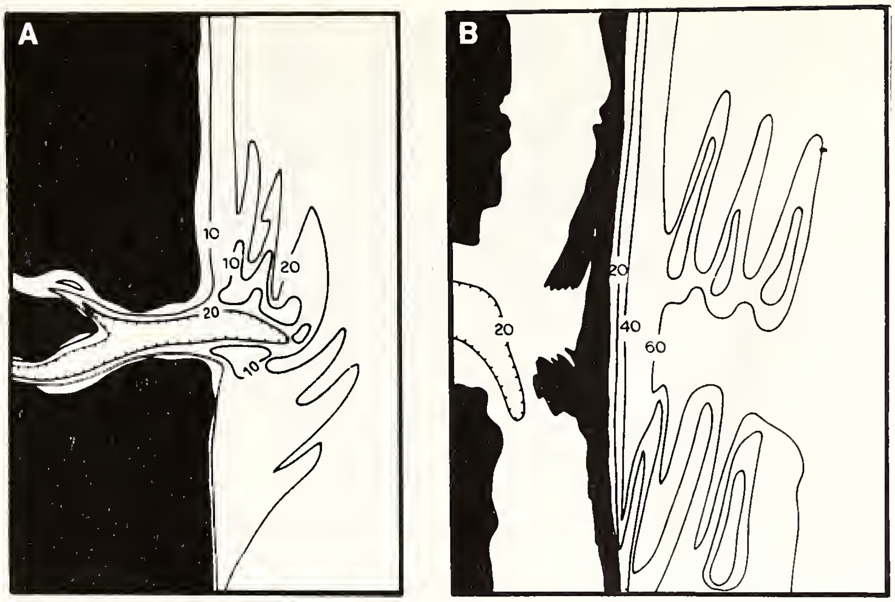

Fig.9. Schematic diagram illustrating the inferred evolution of ancestral Albemarle estuary mouth into a shelf-valley complex. Depth in feet.

SURFICIAL SEDIMENTS AND SMALL-SCALE RELIEF ELEMENTS

Surficial sediments were grab-sampled in a portion of the study area (Fig.10), and the entire surface of the study area was examined by means of an EG&G sidescan sonar unit (Fig.11). Navigation for the grab-sample net was provided by Loran A, and for the sidescan-sonar net by means of Raydist.

The mean-diameter map (Fig.10) is based on the phi moment mean of the sand fraction as determined by a rapid sediment analyser (Sanford and Swift, 1972). The 1 × 4 km^2 sample grid is barely able to resolve the pattern of grain-size distribution, which consists of a north—south banding of contrasting grain sizes that appears to vary in sympathy with the ridge topography. The pattern is partly obscured by noise in the form of single anomalous samples, which may be due to a smaller-scale grain-size variation controlled by a sand-wave topography (see sand waves in profile, Fig.4). The most obvious aspect of the pattern is the tendency for troughs to be floored by coarse sands (frequently pebbly sand or sandy gravel). Ridges are mantled by fine sand (2.0—2.5 ϕ). Ridge-flank deposits are not symmetrical; seaward-flank sands tend to be finer than crest sands, while landward flanks are similar to crest sands or coarser.

Fig.12 presents a scatter plot of phi moment standard deviation against phi moment mean for the sand fraction of the samples. Points are distinguished by depositional environment. Separation of environmental types is poor. The noisy nature of the data may be due to small-scale grain-size variations induced by the sand-wave topography, to the

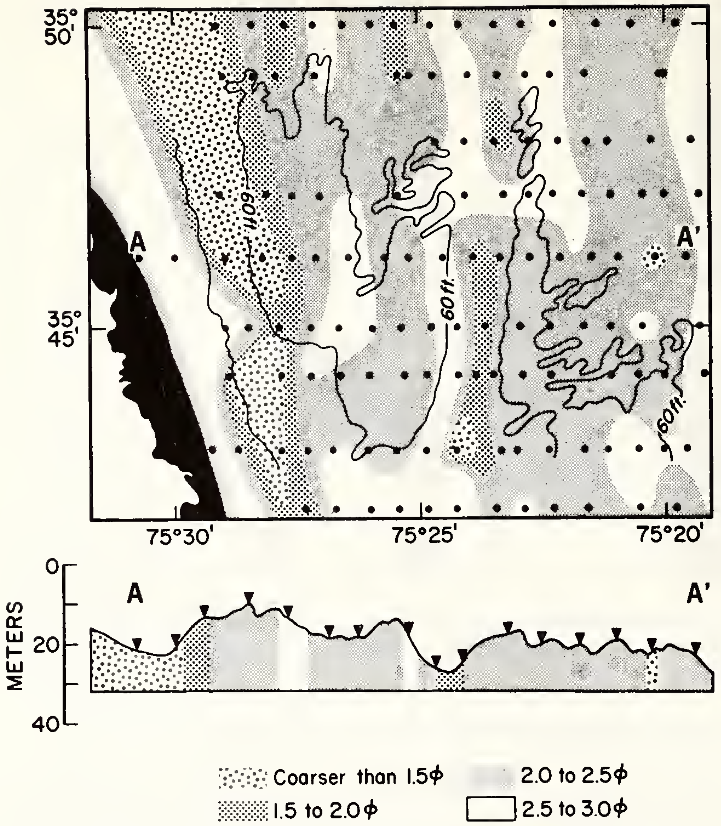

Fig.10. Distribution of mean grain diameter over Platt Massif.

subjective nature of designation of trough, flank, and ridge, or it may be an innate characteristic. Nevertheless, differences in sand type appear, similar to those seen in the grain-size map. Crest and seaward-flank sands comprise relatively compact, overlapping scatters. Crestal sands tend to be coarser than seaward-flank sands. Landward-flank sands are similarly coarser than seaward-flank sands but are more poorly sorted. Trough sands overlap all other domains and include the coarsest and most poorly sorted sands.

The sidescan sonar records reveal that the sands of the study area are molded into a hierarchical association of bedforms (Allen, 1968; Jackson, 1975). An association of bedforms exists in that the pattern consists of two orthogonal components. Bedforms trend either east—west, normal to the prevailing current direction, or north—south, parallel to the prevailing direction. The bedform pattern is hierarchical in that within each class bedforms occur at several spatial scales. Bedform arrays appear on sidescan sonar records as alternating bands of light and dark tones, because of the systematic variation in bottom elevation and because of the equally systematic variation in bottom grain size.

The largest scale of flow-parallel elements is the sand ridges and intervening troughs. The morphology and grain-size patterns of these ridges have already been discussed. A smaller-scale, flow-parallel pattern is caused by current lineations (McKinny et al., 1974); bands of contrasting grain size of negligible relief that vary from several tens of meters to hundreds of meters in width. They appear on sidescan sonar records as light or dark streaks against a contrasting background (Fig.13). Some appear to be sand ribbons (Kenyon, 1970) in the sense of strips of sand of negligible relief resting on a surface of coarser material. However, most appear on sidescan sonar as streaks darker than the adjacent zones. They are therefore

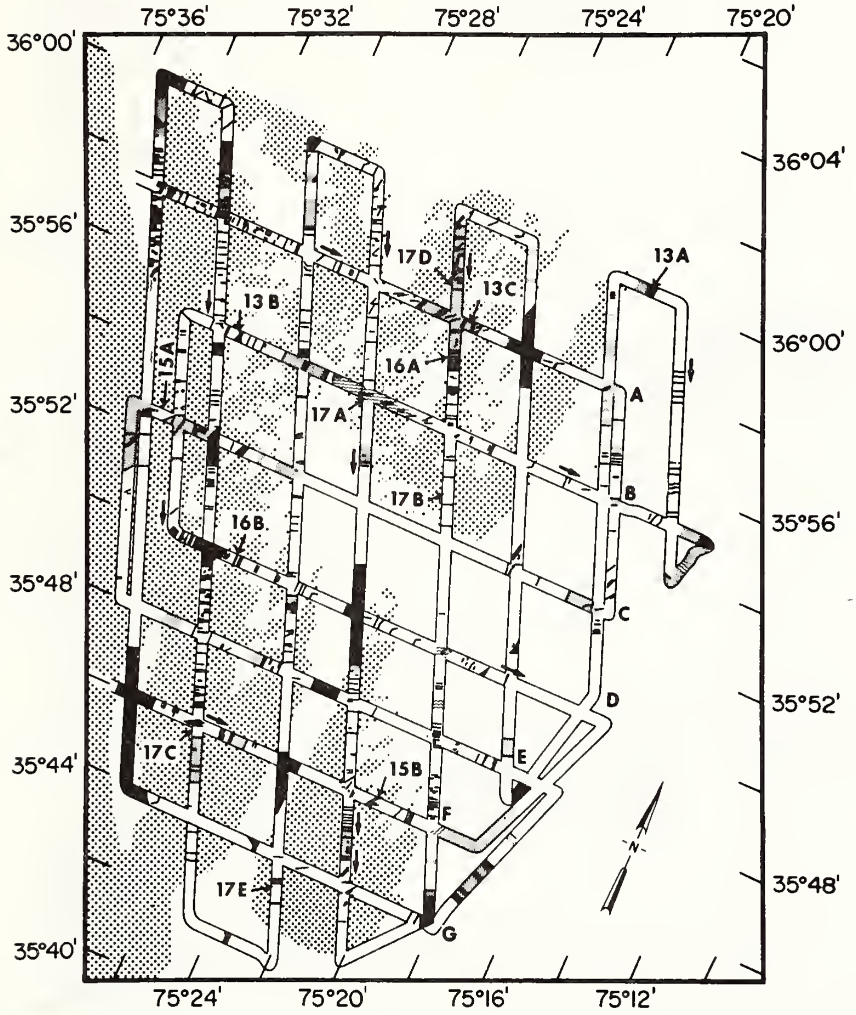
75°36'
75°32'
75°28'
75°24'
75°20'
36°00'
35°56'
35°52'
35°48'
35°44'
35°40'
36°04'
36°00'
35°56'
35°52'
35°48'
75°24'
75°20'
75°16'
75°12'
13A
13B
13C
15A
15B
16A
16B
17A
17B
17C
17D
17E
A
B
C
D
E
F
G
N

Fig.11. Schematic composite of sidescan-sonar records. Trackline and schematic sonar image are presented four times actual width for clarity. Letters and numbers indicate locations of other figures. Topographic highs are stippled.

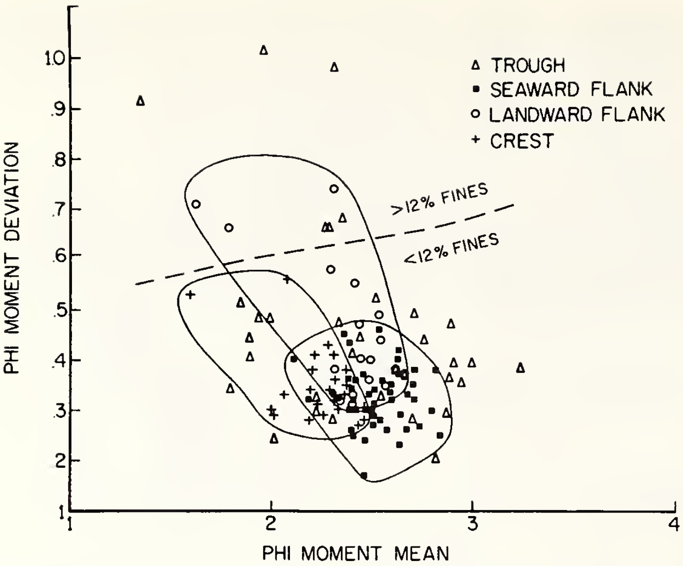

Fig.12. Scatter plot of phi moment mean diameter against phi moment standard deviation, keyed against depositional environment.

believed to be similar to the linear erosional furrows of Stride et al. (1972): elongate windows in a thin sand sheet exposing a coarser underlying stratum. The negative relief of the erosional windows tends to be a little more sharply pronounced than the positive relief of the sand ribbons and they appear in the vertical exaggeration of the bathymeter records as notches separated by plateaux (Fig.13b).

Current lineations occur primarily in the troughs between the large-scale sand ridges, where vibracores and grab samples indicate that the surficial sediment has thinned to a coarse-sand or sandy-gravel veneer overlying an older substrate. At least three categories of current lineations appear to exist (Fig.14). Regular bands of contrasting grain size with spacings on the order of 100 m appear to be strips of sand overlying the basal gravel that veneers the older substrate. These alternations of erosional furrows and sand ribbons appear to be bedforms in the strict sense of regular perturbations of bottom morphology and grain size that reflect regular flow perturbations. Elsewhere, irregular broad zones of sandy gravel appear to be deflation zones, where all easily transportable material has been removed during repeated flow events. Broad, well-defined deflation zones occur in the larger troughs of the ridge topography (Fig.11). They tend to be displaced toward the seaward sides of the troughs. Locally, erosional furrow patterns occur on ridge flanks where the dark bands presumably do not represent the basal gravel; they may be "perched" lag deposits due to localized current action.

East—west trending bedforms have been designated "sand waves" in the discussion of topography, on the grounds that they are flow-transverse

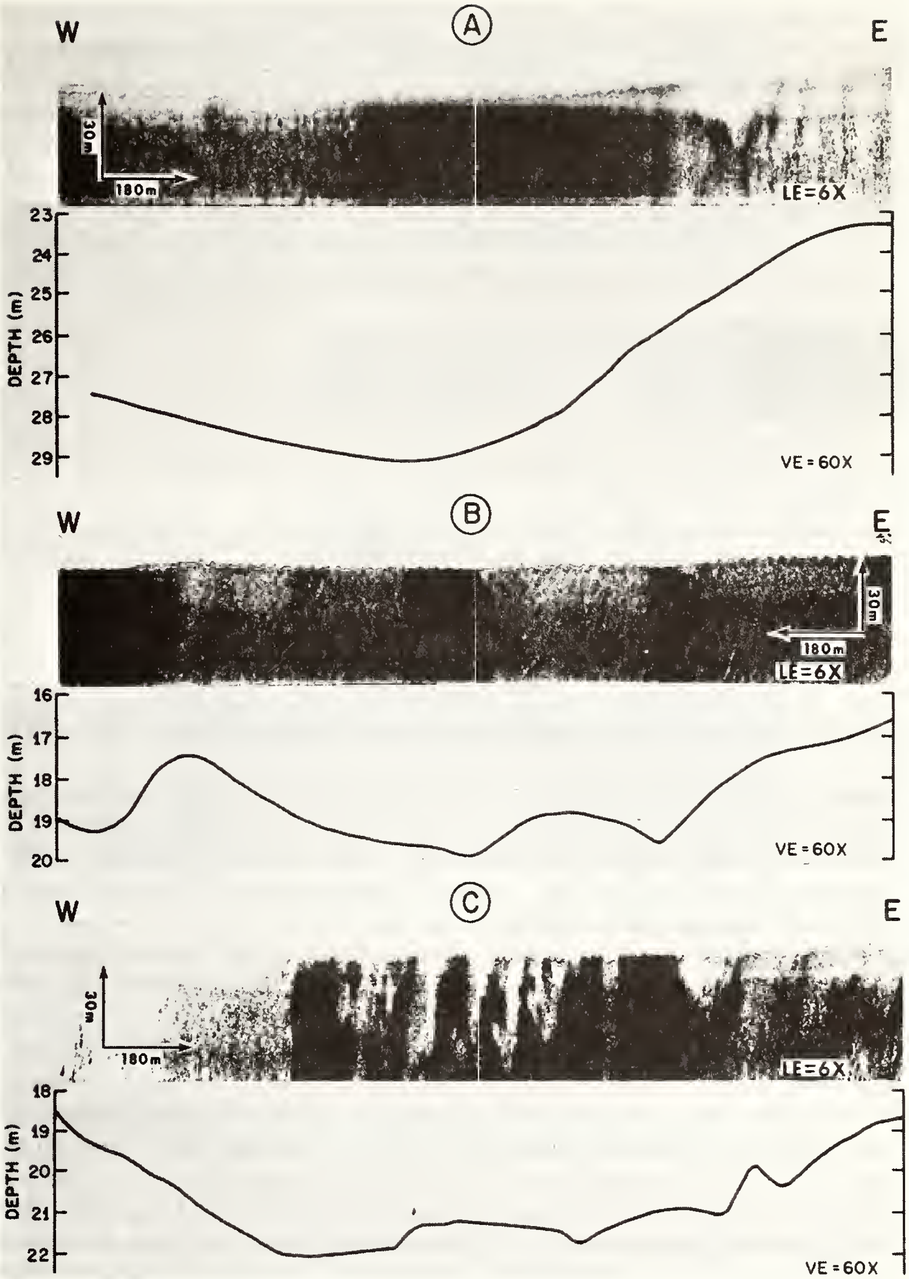

Fig.13. A. Deflation zone in trough. Dark tone indicates coarser sediment. Note displacement from axis of trough toward seaward side. B. Well-defined erosional furrows. C. Anastomosing deflation pattern. See Fig. 11 for locations.

bedforms; that is, sand ridges with steeper slopes on the side that is down-current with respect to the presumed direction of prevailing flow (Figs. 15 and 16).

Sidescan sonar and fathometer records reveal that the sand waves occur at two scales (Fig.15B). Features with spacings of 20—120 m and heights up to 2 m will be referred to as megaripples. Large-scale sand waves have spacings of 0.2—1.2 km and heights of 2—6 m. Their downcurrent slopes are generally below the angle of repose, although well-defined avalanche slopes are locally present (Fig.15A). Saw-tooth profiles occur, but a more typical profile is trapezoidal, with a relatively steep downcurrent slope, an upper surface inclined gently toward the upcurrent direction, and an upcurrent slope of intermediate steepness (Fig.17). "Cat-backed" sand waves (Van Veen, 1935) locally occur. The profiles of these features exhibit a bump or "ear" at the angulation between the downcurrent slope and the upper surface. Both the cat-backed and trapezoidal profiles may be the consequence of periodic flow reversal. Mud lenses may occur in the troughs between large-scale sand waves (Fig.16B).

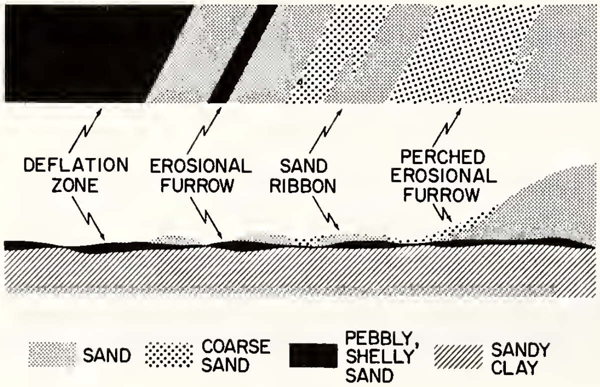

Fig.14. Schematic diagram indicating catagories of current lineations.

Sidescan-sonar profiles clearly indicate that grain size varies systematically across the sand-wave profile. The tone of the sidescan record tends to be darkest (coarsest grain size) in the trough at the foot of the downcurrent slope (Fig.15B). The record tends to lighten (become finer) across the upcurrent slope, and down the downcurrent slope.

Relatively extensive fields of megaripples occur at several areas, as indicated by the wavy-line symbol in Fig.11. Spacings range from 20 to 120 m; heights do not exceed 2 m. Elsewhere, megaripples are locally apparent on the upper surfaces of large-scale sand waves (Fig.15B). The better-defined sand ridges tend to have a band of megaripples along the upper edge of the seaward flank (not figured). The band is parallel to the ridge trend, but the megaripples themselves tend to form a northward-opening angle of up to 20° with the ridge crest. Megaripple asymmetry in these areas indicates flow to the southeast.

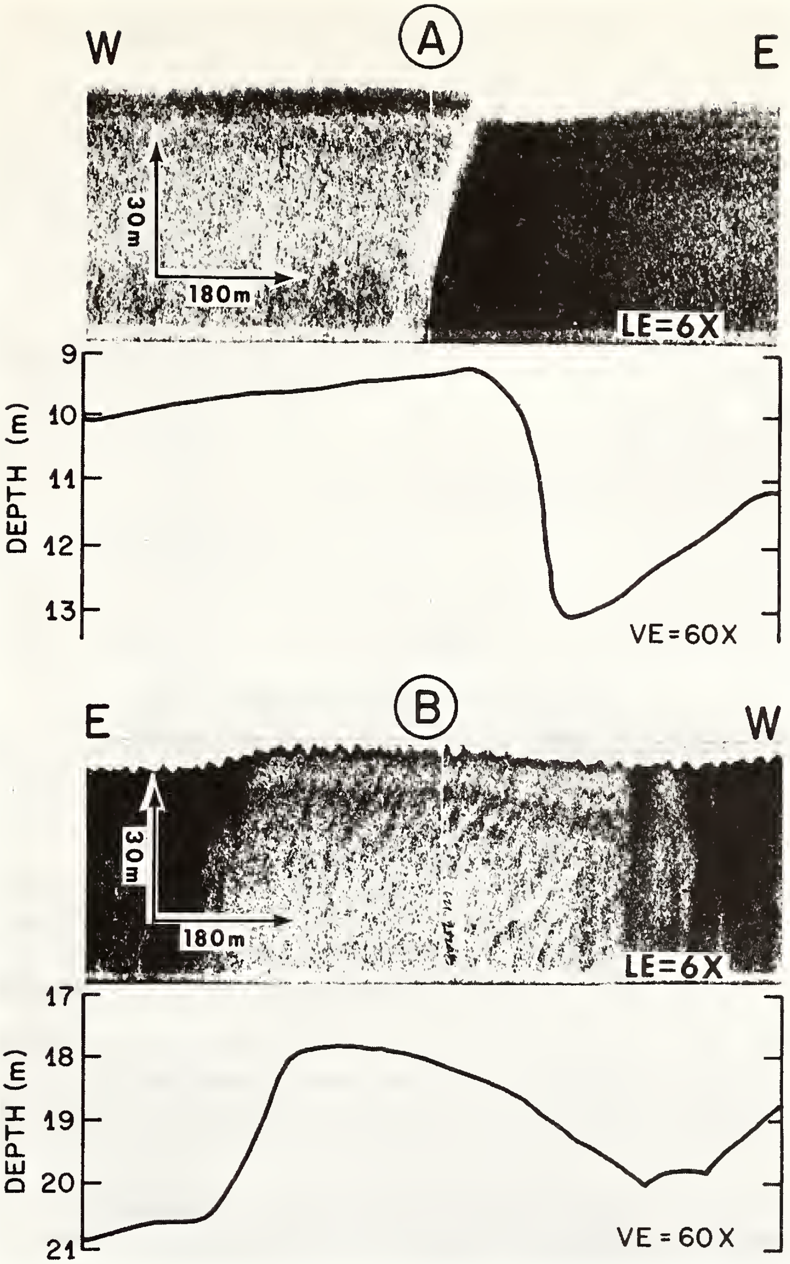

Fig.15. A. Sand wave with well developed slip face. B. Sand wave with megaripples on back (note sidescan-sonar record). See Fig. 11 for locations.

A third order of flow-parallel bedforms revealed by sidescan sonar consists of bands of contrasting grain size up to 2 m long, with spacings measured in decimeters (Fig.16B). Although they trend north—south, they are inferred

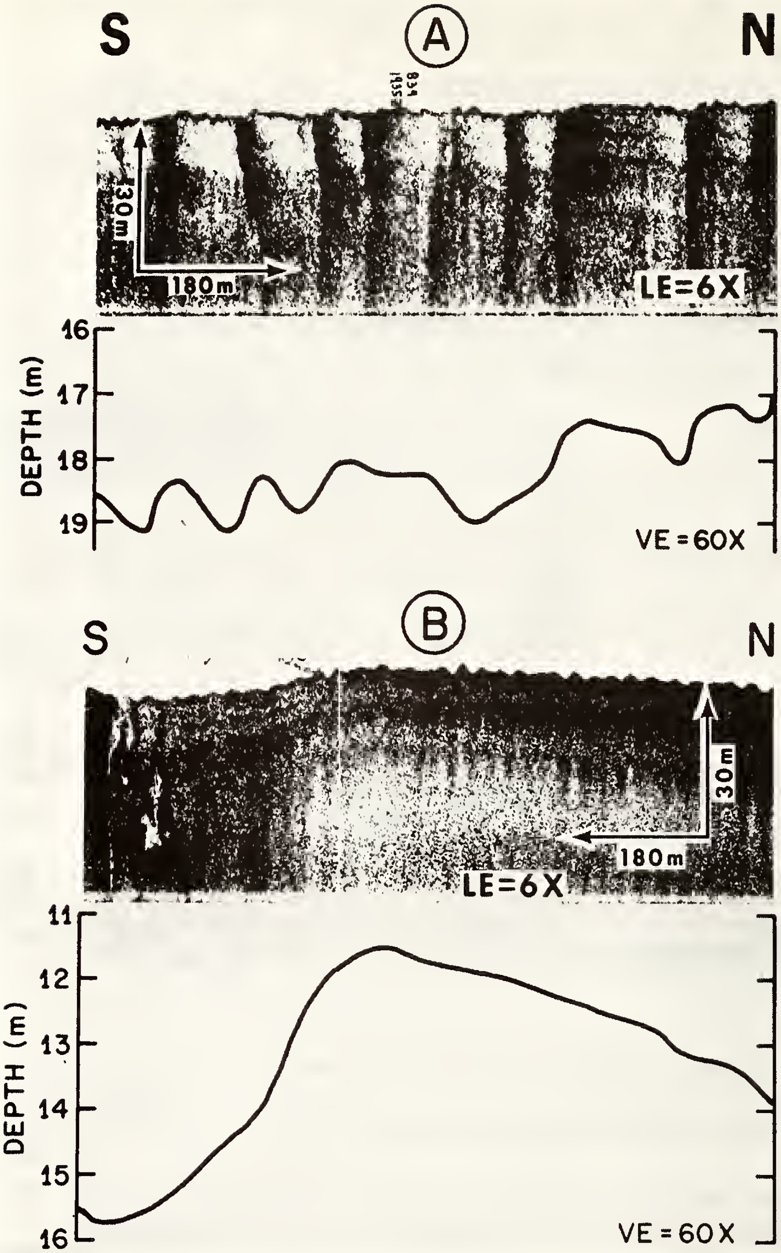

Fig.16. A. Small-scale sand-wave pattern. B. Sand wave with wave-generated ripples on back (barely resolved on sidescan-sonar record) and mud patches in trough (white areas on sidescan-sonar record). See Fig. 11 for locations.

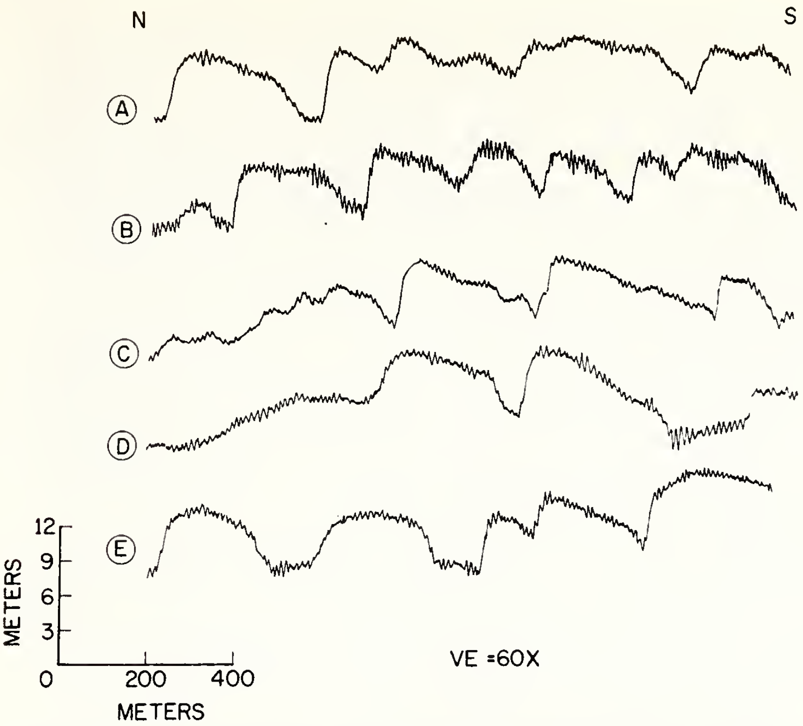

Fig.17. Characteristic sand-wave profiles. Note abundance of three-faceted patterns (steep lee slope, gentle sloping top, steep upcurrent slope) as well as classic saw-tooth profiles. See Fig. 11 for locations. Wiggles in profiles are due to motion of recording vessel in response to surface waves.

to be flow-transverse ripples, generated by wave surge on coarse sand bottoms, with spacings sufficient to be resolved by sidescan sonar. They may have been responses to the shoreward-trending train of surface swells observed during the sidescan-sonar cruise.

HYDRAULIC PROCESS AND SUBSTRATE RESPONSE

Evolution of the Albemarle Shelf Valley Complex

While the gross morphology of the Albemarle Shelf Valley Complex appears to be inherited from an earlier estuary-mouth environment, its surficial grain-size patterns and bedform arrays cannot be readily explained in this manner. Unit B, which forms the cores of the Platt and Albemarle Massifs, appears to be the dissected remnants of the original estuary mouth shoal. However Unit A appears to have been deposited subsequent to closure of the Albemarle estuary. Its grain size and morphological patterns must be considered in terms of the modern hydraulic climate.

A first task in harmonizing the hydraulic climate with the pattern of substrate response must be an explanation of the ridge topography. There seems to be little profit in seeking a relict origin. Estuary-mouth shoals, such as the Albemarle Shelf Valley Complex is presumed to have been, do have ridge topographies impressed upon them. These are interdigitating ebb—flood channel systems, caused by the phase lag in the tidal wave during its reflection from the estuary interior (Swift and Ludwick, 1976), but the resemblance between such ebb—flood channel systems and the present Albemarle ridge topography is superficial.

The postulated models for the ancestral Albemarle estuary are the estuaries of the Georgia Bight (Oertel and Howard, 1972). Their channel systems are similar to the pattern seen on the Albemarle Massif in that channels occur on the north side of the estuary mouth, but the troughs of the Albemarle Massif are larger, longer, and more deeply incised than those of the modern Georgia estuaries and, unlike them, do not radiate from the estuary mouth. Furthermore, the same pattern is seen, even more prominently developed, on the Platt Massif. There is no symmetry of the two ridge patterns about the central valley; trough talwegs and crest lines climb to the south on *both* massifs; compare Figs. 8A and 8B. The ridge topography of the Albemarle and Platt Massifs appears to be oriented with respect to the southward storm flows that are characteristic of the Middle Atlantic Bight (Beardsley and Butman, 1974), rather than with respect to a reversing estuary-mouth jet.

The regional topographic pattern places a further constraint on the origin of the ridge systems of the Albemarle and Platt Massifs. Fig.2 clearly indicates that the ridges of the Platt and Albemarle Massifs are an integral part of a regional north—south trending topographic "grain". This grain is distinctly more regular than the south-southeast trending shoreline. The portion of the ridge system superimposed on the shelf-valley complex, however, is unique for three reasons: (1) the ridge topography has greater relief, (2) the ridges and troughs are incised primarily in the northern sides of the massifs, hence the "comb-like" pattern, and (3) only in the vicinity of the shelf-valley complex are the ridges accompanied by flow-transverse sand waves.

If the ridge topography is in fact produced by south-trending storm flows, then the points listed above are most simply explained as a result of constriction of the flow cross-section over the shelf-valley complex, and its consequent acceleration. Constriction of flow cross-section would be a vertical constriction from bottom shoaling, and perhaps also a lateral constriction due to the more pronounced easterly trend of the shoreline immediately north of Oregon Inlet. Acceleration of flow would incise the ridge topography more deeply into the northern flanks of the massifs than elsewhere. Acceleration of flow over the massifs would mean that velocity would more frequently exceed the threshold velocity of sand transport in this area, and that sand waves would have a greater probability of surviving the intervening periods of degradation by fair-weather wave surge. It is noteworthy that sand waves occur elsewhere on the Middle Atlantic Shelf of North America only where flows are locally accelerated for continuity reasons; beneath the reversing tidal jets of major estuaries (Ludwick, 1972) or on such shoal areas as Diamond Shoals off Cape Hatteras (Swift et al., 1972, p.526; Hunt et al., 1977), or on Georges Bank (Uchupi, 1968) and Nantucket Shoals (Swift, 1975).

Relation of ridges to flow. We suggest above that the ridges are responses to modern flows, and that specifically they are due to the southward acceleration of storm flows over the massifs. But why does such acceleration produce flow-parallel ridges and troughs? Why doesn't it uniformly erode the upcurrent flanks of the massif? What determines the angular relationships of shoreline, ridge axes, and sand-wave crests? We cannot answer these questions without a better theoretical understanding of geophysical boundary layers, and we also need extensive velocity observations to which hydrodynamical theory can be applied. However, the geomorphic and textural data reported in this paper will allow us to set constraints that any model of fluid process and substrate response must meet. These constraints may be listed as follows:

(1) The sand ridges and sand waves of the study area are responses to peak southward flows. Ridges indicate a southward flow in that their crest and trough lines climb to the south (Figs. 3 and 5). Sand waves at two scales have steeper south-facing slopes (Fig.17).

(2) The sand ridges are not truly flow parallel, for they converge southward with the shoreline (Figs. 2, 3 and 5). Vectors of depth-averaged flow must trend parallel to the coast, and obliquely over ridge crests for continuity reasons.

(3) Southward, cross-ridge flow is further indicated by the grain-size asymmetry (Figs. 10, 12 and 13A) and morphologic asymmetry (Fig.4) of the sand ridges. Northwest flanks are flatter and coarser grained, suggesting that they are upcurrent-facing slopes, subject to erosion and selective removal of finer sand grains. Southeast flanks are steeper and finer grained, suggesting that they are downcurrent slopes, subject to deposition of finer sand grains. This interpretation is supported by the greater thickness of modern sand on the fine, seaward flanks (Fig.8A) and the aggradation of these flanks over time (Fig.7).

(4) The responsible flows are two-layered, with an offshore component of surface flow coastal downwelling, and an offshore component of bottom flow. This flow structure is indicated by the orientation of sandwaves on ridge crests; their steeper slopes face slightly offshore as well as downcoast to the south (Fig.5).

(5) The strongest flows may be experienced at the foot of the shoreface, where it adjoins the more gently dipping inner-shelf floor, rather than further seaward where the water is deeper. This seemingly reversed velocity—depth relationship is indicated by the broad band of gravel at the foot of the shoreface (Fig.10). Further seaward, the basal Holocene gravel is generally veneered with sand and gravel, and is only exposed in narrow windows. The gravel band corresponds with the floor of an intermittent trough that separates the Platt and Albemarle Massifs from the shoreface (Fig.3).

There are a number of points of similarity between this model of the time-averaged peak flow field inferred from substrate response characteristics, and the model of the storm flow field that stems from the observations of physical oceanographers. Peak flows in the Middle Atlantic Bight are in fact associated with winter storms and the most energetic storm flows trend southward (Beardsley and Butman, 1974; Boicourt and Hacker, 1976; Scott and Csanady, 1976; Lavelle et al., 1976). Southward storm flows are frequently associated with coastal downwelling and an offshore component of bottom flow (Boicourt and Hacker, 1976; Scott and Csanady, 1976). There are theoretical grounds for assuming that the landward margin of the shelf flow field may become a coastal jet during storms (Csanady, 1973, 1976), and Boicourt and Hacker have in fact observed a coastal jet during a February, 1974, storm in 10 m of water off the southern Virginia coast, north of our study area. Longshore, mid-depth velocity averaged 52.5 cm/sec over a 58-hr period in contrast to a value of 26.3 cm/sec for longshore, mid-depth velocity averaged over the same period several kilometers further offshore. Boicourt and Hacker (1976, p.194) attributed the high longshore velocity to the "wind driven outflow surge of low salinity water from Chesapeake Bay which forms a southward flowing, high velocity jet along the Virginia and North Carolina coast". Within the study area, such a storm-generated jet would occupy the water column over the gravel band noted above.

Neither the reconnaissance data of physical oceanographers nor the generalized and inferential flow model based on substrate response to peak flow are fully adequate to explain the formation of the sand ridges. Their grain size and morphologic asymmetry are features that they share with flow-transverse sand waves and the analytical model for sand-wave formation of Smith (1910) may therefore be applicable. The sand ridges are oriented obliquely across the prevailing direction of peak flow, rather than transverse to it, but Furness (1976) has recently shown that sand waves may be oriented obliquely with respect to flow if there is a cross-flow velocity gradient. The possibility that such a velocity gradient might be supplied by the jet-like coastal margin of the storm flow field should be investigated.

A second hydrodynamical model may be applicable to the problem of sand ridge formation. Shelf storm flows are potentially capable of developing helical flow structure, in which zones of upwelling alternate with zones of downwelling (Faller, 1971; Gammelsrod, 1975), and flow structure of this sort has been cited as the probable mechanism for sand-ridge formation (Houbolt, 1969; Wilson, 1972). The applicability of sand-wave theory and helical-flow theory to problems of sand-ridge formation have been discussed elsewhere (Swift and Ludwick, 1976; Swift et al, 1977).

It does not seem possible to extract further insights concerning the origin of the Albemarle topography until extensive hydraulic measurements are obtained. Our substrate data do, however, indicate the main outlines of topographic evolution. The surface of the Albemarle estuary shoal was no longer in equilibrium with the hydraulic climate of the inner shelf after the reversing tidal jet that maintained it ceased to function, at perhaps 5000 B.P. However, the adjustment of the shoal to the altered regime has not resulted in the total destruction. Instead, a systematically corrugated surface has resulted, whose superimposed sand wave and ridge patterns indicate a recurrent velocity field of complex structure. Grain-size analyses of cores indicate that the surficial sand of Layer A is distinctly coarser than the underlying estuarine stratum. The hydraulically adjusted surface of the Albemarle Shelf Valley Complex has been molded into a relatively coarse lag; finer sand has been winnowed out and transported in the direction of the prevailing southerly flow.

REFERENCES

Allen, J.R.L., 1968. The nature and origin of bedform hierarchies. Sedimentology, 10: 161—182.

Beardsley, R.C. and Butman, B., 1974. Circulation on the New England continental shelf: response to strong winter storms. Geophys. Res. Lett., 1: 181—184.

Boicourt, W.C. and Hacker, P.W., 1976. Circulation on the Atlantic continental shelf of the United States, Cape May to Cape Hatteras. Mem. Soc. R. Sci. Liege, 16th Ser., 10: 187—200.

Brown, R.A., 1970. A secondary flow model for the planetary boundary layer. J. Atmos. Sci., 27: 742—757.

Bumpus, D.F., 1973. A description of circulation on the continental shelf of the east coast of the United States. Prog. Oceanogr., 6: 117—157.

Csanady, G.T., 1973. Barotropic currents over the continental shelf. J. Phys. Oceanogr., 4: 357—371.

Csanady, G.T., 1976. Wind driven and thermohaline circulation over the continental shelves. In: B. Manowitz (Editor), Effects of Energy Related Activities on the Atlantic Continental Shelf. Conference at Brookhaven National Laboratory, November 10—12, 1975, pp.31—47.

Faller, A.J., 1971. Oceanic turbulence and the Langmuir circulations. Annu. Rev. Ecol. Syst., 2: 201—236.

Fisher, J.J., 1967. Development Pattern of Relict Beach Ridges, Outer Banks Barrier Chain, North Carolina. Thesis, University of North Carolina, 250 pp.

Furness, G.K., 1976. Formation of Oblique Dunes. Danish Center for Applied Mathematics and Mechanics, Technical University of Denmark, Report 105, 34 pp.

Gammelsrod, T., 1975. Instability of Couette flow in a rotating fluid and origin of Langmuir circulations. J. Geophys. Res., 80: 5069—5075.

Goldsmith, V., Sutton, C.H. and Davis, J.S., 1974. Bathymetry of the Virginia Sea, Part I. Chesapeake Bight. Transverse Mercator Projection Map. Virginia Institute of Marine Sciences, Gloucester Point, Va.

Goldsmith, V., Byrne, R.J., Sallenger, A.H. and Drucker, D.M., 1975. The influence of waves on the origin and development of the offset coastal inlets of the southern Delmarva peninsula, Virginia. In: L.E. Cronin (Editor), Estuarine Research, VII. Geology and Engineering. Academic Press, New York, N.Y., pp.183—200.

Houbolt, J.H.C., 1968. Recent sediment in the Southern Bight of the North Sea. Geol. Mijnbouw, 47: 245—273.

Howard, J.D. and Reinbeck, H.E., 1972. Georgia coastal region, Sapelo Island, U.S.A.: Sedimentology and biology, IV. Physical and biogenic sedimentary structures of the nearshore shelf. Senckenbergiana Marit., 4: 81—123.

Hunt, R.E., Swift, D.J.P. and Palmer, H.P., 1977. Constructional shelf topography — Diamond Shoals, North Carolina. Geol. Soc. Am. Bull., 88: 299—311.

Jackson, R.A., 1975. Hierarchical attributes and a unifying model of bedforms composed of cohesionless material and produced by shearing flow. Geol. Soc. Am. Bull., 86: 1523—1533.

Kenyon, N.H., 1970. Sand ribbons of European tidal seas. Mar. Geol., 9: 25—39.

Lavelle, J.W., Brashear, H.R., Case, F.N., Charnell, R.L., Gadd, P.E., Haff, K.W., Han, G.A., Kunselman, C.A., Mayer, D.A., Stubblefield, W.L. and Swift, D.J.P., 1976. Preliminary results of coincident current meter and sediment transport observations for wintertime conditions on the Long Island inner shelf. Geophys. Res. Lett., 3: 97—100.

Ludwick, J.C., 1972. Migration of tidal sandwaves in Chesapeake Bay entrance. In: D.J.P. Swift, D.B. Duane and O.H. Pilkey (Editors), Shelf Sediment Transport: Process and Pattern. Dowden, Hutchinson and Ross, Stroudsburg, Pa., pp.377—410.

McKinney, T.F., Stubblefield, W.L. and Swift, D.J.P., 1974. Large-scale current lineations on the Great Egg Shoal retreat massif: investigations by sidescan sonar. Mar. Geol., 17: 79—102.

Milliman, J.D. and Emery, K.O., 1968. Sealevels during the past 35,000 years. Science, 162: 1121—1123.

O'Connor, M.P., Riggs, S.R. and Winston, D., 1972. Recent estuarine sediment history in the Roanoke Island area, North Carolina. In: B.W. Nelson (Editor), Environmental Framework of Coastal Plain Estuaries. Geol. Soc. Am. Mem., 133: pp.435—464.

Oertel, G.F. and Howard, J.P., 1972. Water circulation and sedimentation at estuary entrances on the Georgia coast. In: D.J.P. Swift, D.B. Duane and O.H. Pilkey (Editors), Shelf Sediment Transport: Process and Pattern. Dowden, Hutchinson and Ross, Stroudsburg, Pa., pp.411—427.

Sallenger, A.H., Goldsmith, V. and Sutton, C.H., 1975. Bathymetric comparisons: A manual of methodology, error criteria and techniques. Virginia Institute of Marine Science, Gloucester Point, Va., Special Report 66, 34 pp.

Sanford, R.B. and Swift, D.J.P., 1971. Comparison of sieving and settling techniques for size analysis, using a Benthos Rapid Sediment Analyzer. Sedimentology, 17: 257—264.

Scott, J.T. and Csanady, G.T., 1976. Nearshore currents off Long Island. J. Geophys. Res., 81: 5403—5409.

Sears, P.C., 1973. Evolution of Platt Shoals, Northern North Carolina Shelf: Inferences from Areal Geology. Thesis, Inst. Oceanogr., Old Dominion University, Norfolk, Va., 74 pp.

Smith, J.D., 1970. Stability of a sand bed subjected to a shear flow of low Froude number. J. Geophys. Res., 75: 5928—5940.

Stride, A.H., Belderson, R.H. and Kenyon, N.H., 1972. Longitudinal furrows and depositional sand bodies of the English Channel. Mem. Bur. Rech. Geol. Min., 79: 233—244.

Swift, D.J.P., 1973. Delaware Shelf Valley: estuary retreat path, not drowned river valley. Geol. Soc. Am. Bull., 84: 2743—2748.

Swift, D.J.P., 1975. Tidal sand ridges and shoal-retreat massifs. Mar. Geol., 18: 105—134.

Swift, D.J.P. and Ludwick, J.C., 1976. Substrate response to hydraulic process: grain-size frequency distributions and bedforms. In: D.J. Stanley and D.J.P. Swift (Editors), Marine Sediment Transport and Environmental Management. Wiley, New York, N.Y., pp.159—196.

Swift, D.J.P. and Sears, P., 1974. Estuarine and littoral depositional patterns in the surficial sand sheet, central and southern Atlantic shelf of North America. Inst. Geol. Bassin Aquitaine, Mem. 7: 171—189.

Swift, D.J.P., Kofoed, J.W., Saulsbury, F.P. and Sears, P., 1972. Holocene evolution of the shelf surface, central and southern shelf of North America. In: D.J.P. Swift, D.B. Duane and O.H. Pilkey (Editors), Shelf Sediment Transport: Process and Pattern. Dowden, Hutchinson and Ross, Stroudsburg, Pa., pp.499—574.

Swift, D.J.P., Nelsen, T., McHone, J., Holliday, B., Palmer, H. and Shideler, G., 1977. Holocene evolution of the inner shelf of southern Virginia. J. Sediment. Petrol., in press.

Uchupi, E., 1968. Atlantic continental shelf and slope of the United States — physiography. U.S. Geol. Surv. Prof. Pap., 529—C: 1—30.
Van Veen, J., 1935. Sand waves in the North Sea. Hydrogr. Rev., 12: 21—29.
Wilson, I.G., 1972. Aeolian bedforms — their development and origins. Sedimentology, 19: 173—210.

Estuarine and Coastal Marine Science 7, 257-273.

Shoreface-connected Sand Ridges on American and European Shelves: A Comparison

Donald J. P. Swift
NOAA, Atlantic Oceanographic and Meteorological Laboratories,
Miami, Florida 33149, U.S.A.

Gerardo Parker, Nestor W. Lanfredi, Gerardo Perillo
Servicio de Hidrografia Naval, Avenida Montes de Oca,
Buenos Aires, Argentina

and Klaus Figge
Deutches Hydrographisches Institut, Hamburg, West Germany

Received 25 April 1977

Keywords: sand ridges; shoreface; bedforms; Delaware coast; Maryland coast; Argentina coast; Guiana; German Bight

Large scale sand ridges, 10 m or more in height and 2–4 km apart have long been accepted as characteristic of shelves experiencing strong tidal flow. However, they also occur on inner continental shelves whose strongest flows are wind-induced. The Middle Atlantic Bight of North America is the best known example, but inner shelf ridge topographies occur extensively on other Atlantic shelves. We wish to call attention to similarities and differences among the inner shelf ridges of North America, South America, and Europe, as a necessary step prior to the framing and testing of hypotheses concerning the hydrodynamics of ridge formation.

Inner shelf ridge fields occur primarily on low, unconsolidated coasts whose substrates provide an ample supply of sediment for ridge formation. The constituent materials are commonly coarse to fine sand, but on the Guiana coast of South America, similar ridges appear to be forming in a mud substrate. Here ridges have much greater spacing (tens of km versus km), less relief, and much flatter slopes (1:3000 versus 1:500).

Inner shelf ridges are characteristically aligned obliquely to the shoreline, with acute angles opening into the prevailing flow direction. Downcurrent slopes tend to be steeper and finer grained. The ridges tend to migrate downcoast and offshore, extending their crestlines so as to maintain contact with the shoreface. Where ridges are nearly shore-parallel (current parallel), the movement is expressed as downcurrent growth of ridges and downcurrent extension of swales between ridges.

The textural and morphologic asymmetry of inner shelf sand ridges can be explained in terms of existing models for sand wave formation. The oblique orientation with respect to the shoreline is also possibly compatible with these models. An alternative, or perhaps complementary explanation for sand ridge genesis requires helical flow structure in the shelf flow field during peak events, but both theory and observation are less well developed for this model.

Inner shelf sand ridges appear to be responses to periods of intense flow induced by the passage of storms. The extent to which a given shelf sector develops ridge topography may depend on the efficiency with which the local water mass responds to storm passage.

Ridge behavior, and especially ridge migration rates, are necessary information for marine environmental management, since ridges are most active in the nearshore zone where the shelf floor is used for sewage outfalls, deepwater ports, nuclear reactor sites, and other structures requiring a measure of sea floor stability.

Introduction

The sand ridge topography of the Middle Atlantic Bight of the U.S. Atlantic shelf has been under scrutiny since the pioneer work of Veatch & Smith (1939). Here sand ridges extend for tens of kilometers, are spaced 2–5 km apart, and converge to the southwest with the coastline at an angle of 20–40°. Side slopes are a degree or less.

These large scale bedforms rest on a surface of marine transgression, and clues to their origin are therefore best sought in the nearshore zone, where formation presumably begins (Duane *et al.*, 1972; Swift *et al.*, 1972). In fact, in the Middle Atlantic Bight, sand ridges

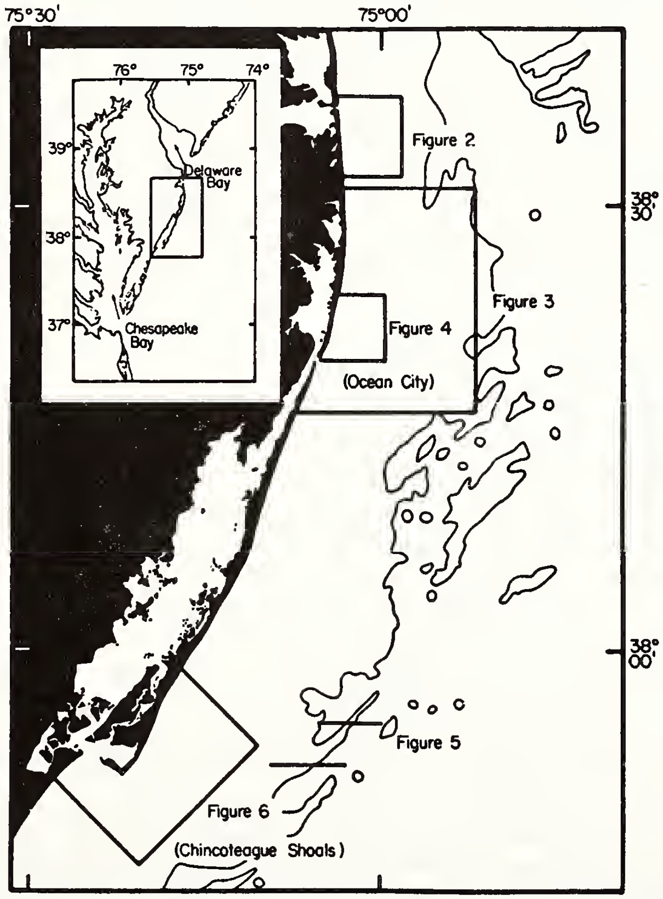

Figure 1. Delaware–Maryland coast showing locations of figures presented in this paper.

extend from the inner shelf onto the shoreface, at depths as shoal as 4 m (Figures 1, 2; see Swift *et al.*, 1972*a*, *b*; Duane *et al.*, 1972; Stahl *et al.*, 1974). The ridges are clearly responses to strong southwesterly coastal flows associated with the passage of extra-tropical cyclones (Lavelle *et al.*, 1976; Swift *et al.*, in press), but the mechanics of formation are poorly understood.

The nearshore zone is also the zone of most intense utilization of the sea floor, and sand ridge behavior is becoming a matter of increasing interest to coastal engineers. A utility company of the state of New Jersey, U.S.A., proposes to build an offshore nuclear power station on the New Jersey coast, between a shoreface-connected sand ridge and the beach. Elsewhere on the New Jersey and Long Island coasts of the United States, sewage outfalls traverse inner shelf ridge topographies (Swift *et al.*, 1976). The data from the Argentine shelf presented in this paper were collected during the course of a feasibility study for a deep-water port. The data from the German Bight of the North Sea were collected in part as a study of potential pipeline corridors for the Ekofisk oil field. Sand ridge migration rates are of critical concern in these areas.

We have determined that inner shelf ridge topographies are not confined to the U.S. Atlantic shelf, but occur extensively on other Atlantic shelves. We wish to call attention to the similarities and differences among the inner shelf ridges of North America, South America, and the North Sea, as a necessary step prior to framing and testing hypotheses concerning the hydrodynamics of ridge formation. We are not duplicating Off's classic survey paper of 1963, but rather are supplementing it; Off was concerned with the world-wide distribution of tide-induced, free-standing sand ridges, in estuary mouths or on the shelf floor. We are concerned with shoreface-connected sand ridges, in areas where tidal currents do not seem to be indicated as the formative agent.

Wherever possible, data in this paper have been reported in the metric system. However, no attempt has been made to recontour the maps that we have obtained which were drawn in English format, since to do so accurately would require reprocessing all of the original bathymetric data.

North American Atlantic Shelf

Inner shelf ridge systems occur sporadically from Long Island south to Florida on the North American Atlantic Shelf but reach their maximum expression on the Delmarva (Delaware–Maryland–Virginia) peninsula between Delaware and Chesapeake Bays (Figure 1). In this classic area, the sand ridges rest on a substrate of lagoonal clay which extends under the retreating barrier and adjoins the modern lagoon floor (Sheridan *et al.*, 1974).

From Delaware Bay to Chincoteague Shoals, the orientation of the ridges remains relatively constant at about 40°E, while the angle with respect to the coastline decreases from 50° to less than 20° (Duane *et al.*, 1972). The orientation of the ridges is approximately that of the direction of approach of storm waves generated by 'northeasters'. Near Cape Henlopen, Moody (1964) has shown that the wide-angle (>45°) ridges are texturally and morphologically asymmetrical, with steeper, finer-grained southern flanks (Figure 2). These flanks are down-current with respect to the dominant direction of storm flow on the Middle Atlantic shelf (Beardsley & Butman, 1973; Lavelle *et al.*, 1976; Boicourt & Hacker, 1976). Textural asymmetry is consistent along the length of the ridge, but the morphological asymmetry may reverse at the base of the ridge where it joins the shoreface. Here the upcurrent flank may be coarser and steeper than the downcurrent flank, apparently as a consequence of the

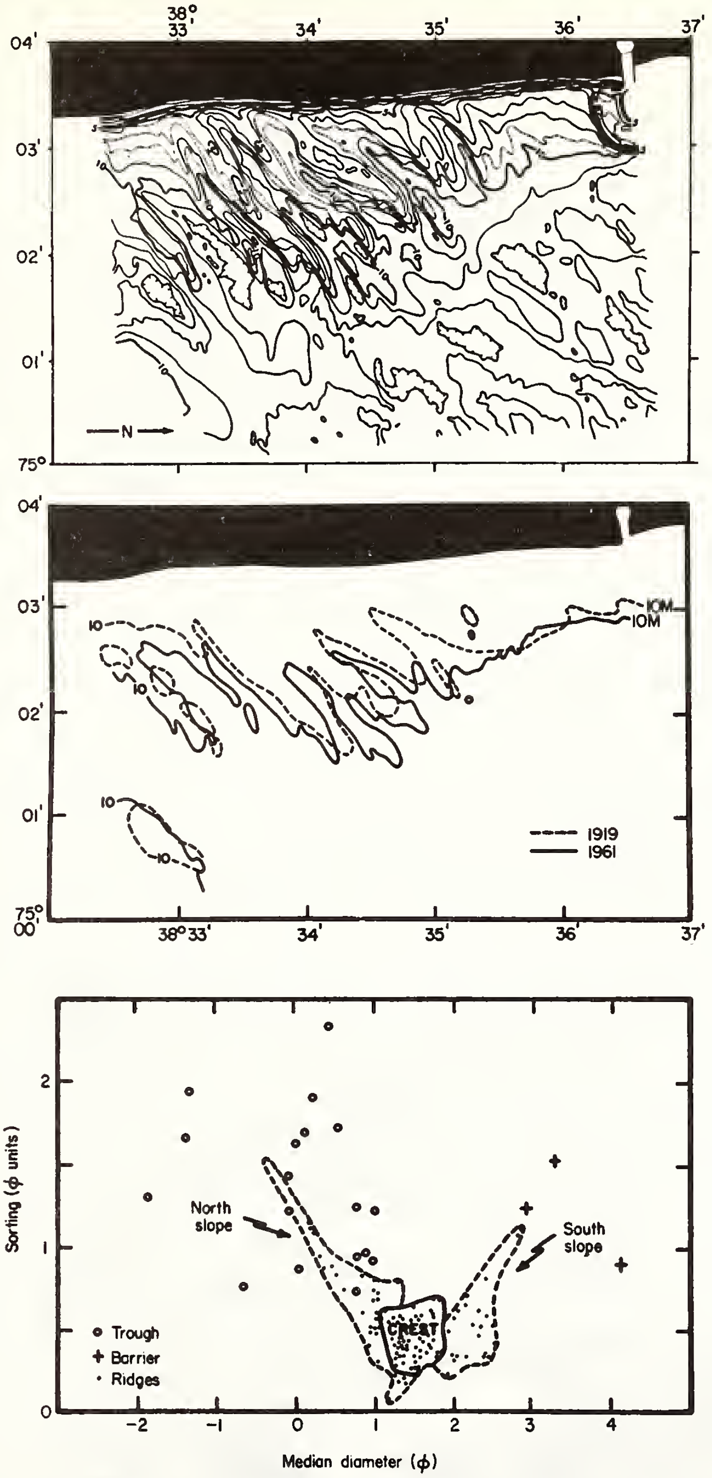
38°
33'
34'
35'
36'
37'
04'
03'
02'
01'
75°
N
04'
03'
02'
01'
75°
00'
38°33'
34'
35'
36'
37'
10
10M
10M
1919
1961
2
1
0
Sorting (φ units)
-2
-1
0
1
2
3
4
Median diameter (φ)
North slope
South slope
CREST
o Trough
+ Barrier
• Ridges

Figure 2. The Bethany Beach ridges, Delaware inner shelf. (a) Bathymetry, depth in fathoms. (b) Changes in bottom elevation between 1919 and 1961, shoreline is 1961 shoreline. (c) Plot of median diameter against graphic inclusive standard deviation for 3 morphologic provinces (troughs, ridges, and barrier face between ridges and beach). From Moody (1964). See Figure 1 for location.

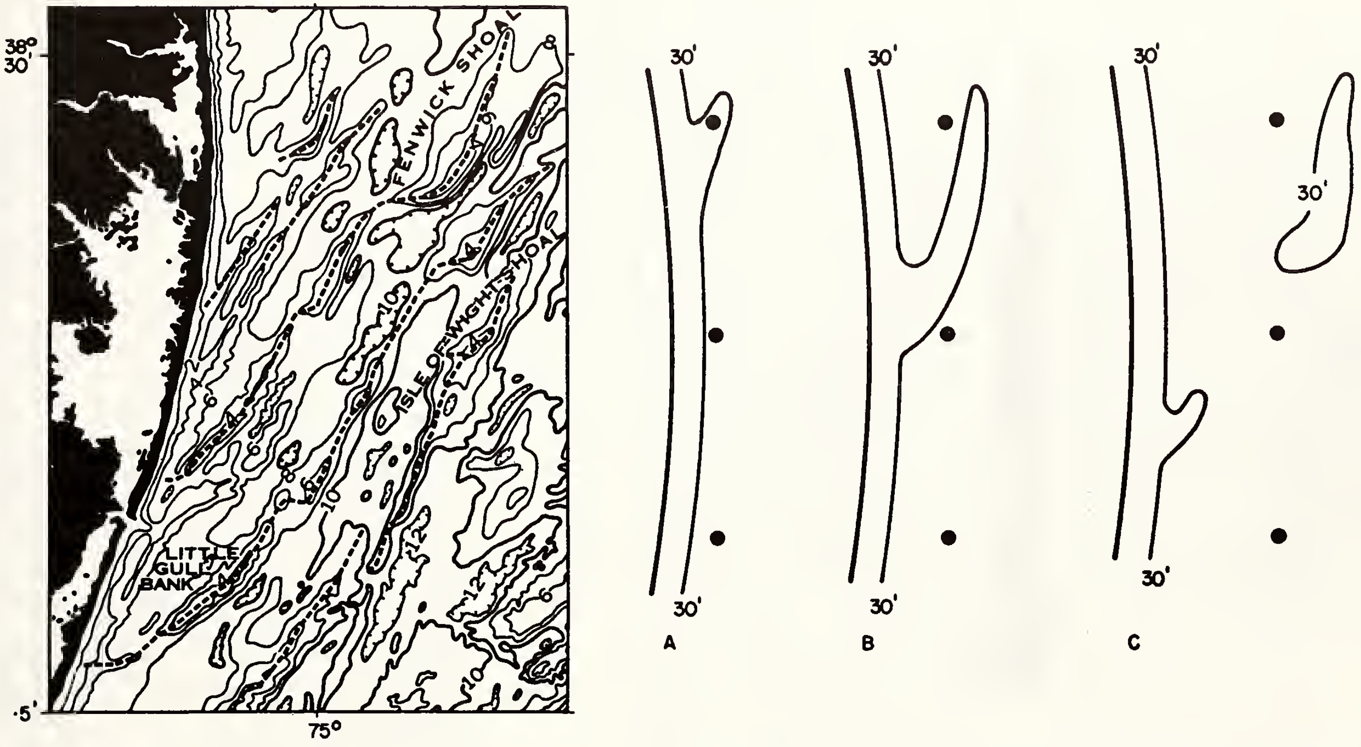
38°
30'
·5'
75°
FENWICK SHOAL
ISLE OF WIGHT SHOAL
LITTLE GULL BANK
8
10
12
30'
A
B
C

Figure 3. Fenwick Shoals sector, Maryland inner shelf. (a) Bathymetric map, based on USC&GS map 0807N–57. Contoured at 2 fathom interval. Dashed lines are crestlines of ridges. (b) Model for ridge growth and detachment during a period of rising sealevel and shoreface retreat. Dots represent fixed reference points. From Swift (1976). See Figure 1 for location.

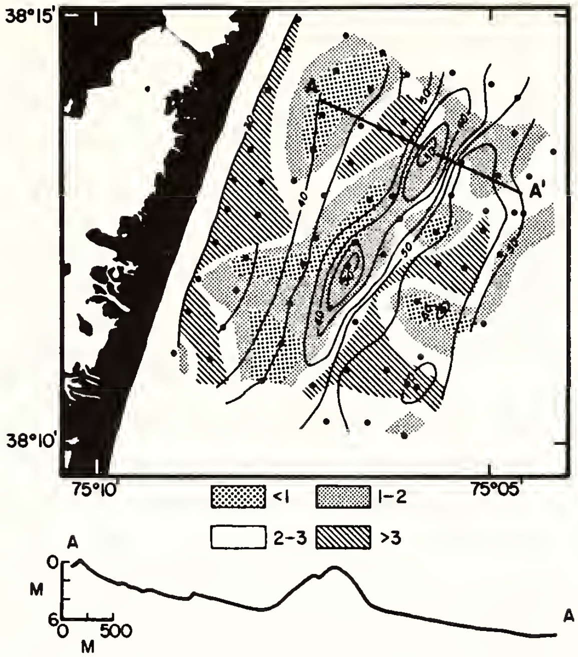

Figure 4. Distribution of graphic mean diameter in phi units over San Antonio Shoal. From Palmer *et al.* (1975). Landward crest is coarse, seaward crest is fine-grained. In the troughs, patches of fine muddy sand largely obscure the coarse pebbly basal sand. Contours in feet, profile in metres. See Figure 1 for location.

intense scour to which it is subjected, and as a consequence of the preferential deposition of fine sand on the downcurrent side. The ridges are moving downcoast (southward) and offshore, extending their crestlines to maintain contact with the shoreface as they do so. Migration rates were reported by Moody (1964) as 3 m per year, but movement appears to be variable, with up to 70 m of translation occurring during 1962, the year of the great Ash Wednesday storm.

South of Ocean City, the ridges make angles of 35° or less with the beach (Field, 1976) and generally have steeper southern (downcurrent) flanks (Figure 3). One of these, San Antonio Shoal, has been instrumented and studied by Palmer & Wilson (1975; see also Palmer *et al.*, 1975). It exhibits the characteristic grain size asymmetry, with a finer-grained, steeper southward (downcurrent) flank (Figure 4).

Telemetering current meters have recorded strong offshore- and downcoast-trending bottom flows over the ridge crest (Palmer *et al.*, 1975). Continuity suggests that such offshore-trending bottom flows occur as part of a downwelling regime. Although the measurements of Palmer *et al.* were not sufficiently sustained to qualify as records of marine climate, there is evidence in other areas to indicate that offshore bottom flows are part of the regime that maintains ridges. The inner shelf sand ridges at Platt Shoals, North Carolina, bear on their crests sand waves up to 3 m high that may constitute time averaged responses to such flows (Swift *et al.*, 1978). Their crests are oriented obliquely to the coast, with the offshore, southeast sides the steepest.

The larger ridges between Ocean City, Maryland, and Chincoteague Shoals are not straight, but are joined to the shoreface by a curved neck. Offshore ridges tend to be similarly

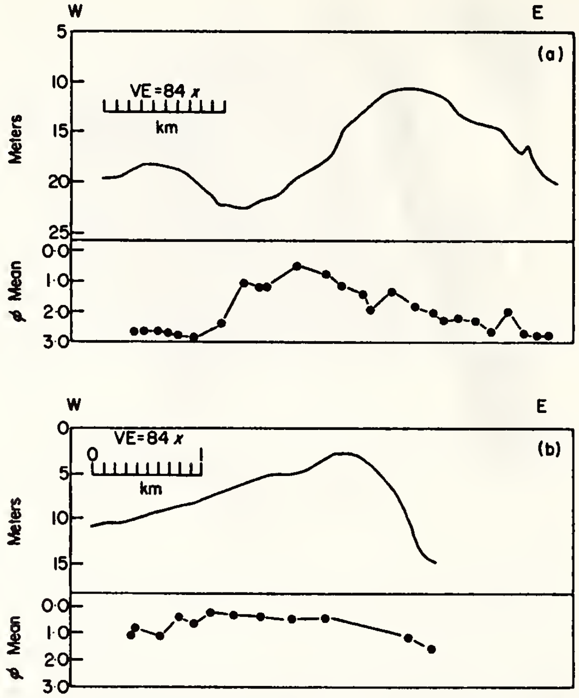

Figure 5. Bathymetric profile, and grain size profile of sand ridges 10 km west of Chincoteague Shoals, Maryland. Phi mean diameter of sand fraction is based on settling tube analysis. Note morphologic asymmetry of (b); textural asymmetry of (a) and (b). See Figure 1 for location.

comma-shaped in plan view (Figure 3). It is possible to trace crestlines of offshore ridges through a series of offset, comma-shaped, ridge segments (Figure 3). The topographic pattern suggests that ridge segments are presently being molded out of a shoreface undergoing slow erosional retreat in response to post-glacial sealevel rise (Swift *et al.*, 1972, Figure 197) and are being successively stranded on the deepening sea floor. Ridge orientation is remarkably uniform across the inner shelf, suggesting that the process has transpired continuously under uniform conditions through much of the period of post-glacial sealevel rise (Duane *et al.*, 1972). Steeper, finer southward-facing (downcurrent) slopes are characteristic of the offshore ridges also (Figure 5).

The cuspate foreland of Chincoteague Shoals constitutes a discontinuity in the wave-driven littoral current and the shoal area on the inner shelf is aggrading, probably as a consequence of the loss in competency of the littoral current at this abrupt change in coastal orientation (see discussion of this mechanism in Tanner, 1961). Ridge topography is being impressed on the shoal area (Figure 6). Maps separated by 53 years indicate that the swales between ridges have extended southward into the shoal area during this period. Blackfish Bank rises to within 3 m of the surface. Sand ridges build upward into the wave-agitated zone until crestal aggradation by storm flows is balanced by crestal erosion due to wave surge, hence the shallow nature of Blackfish Bank suggests a rapid rate of sedimentation and shallow equilibrium depth for this area.

On such ridges as these, that are very nearly parallel to the beach, a second kind of morphological asymmetry becomes apparent. The 'peak' (highest point) of the ridge is not

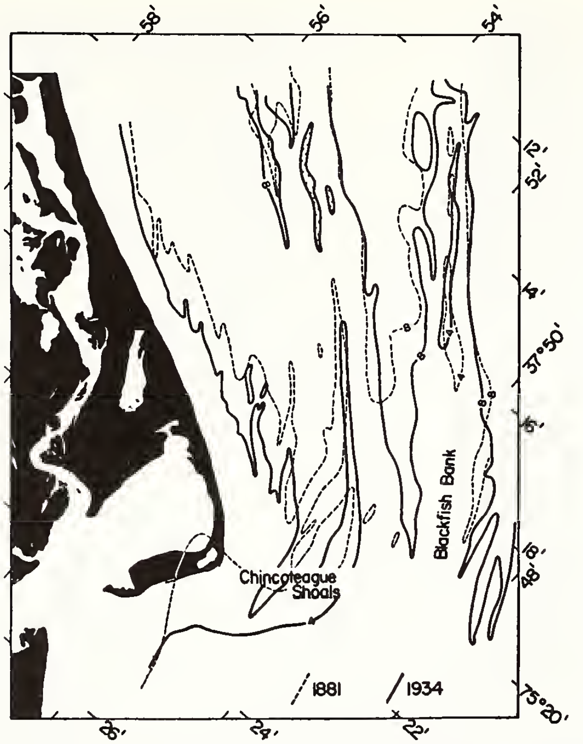

Figure 6. Topographic changes in the Chincoteague Shoals sector between 1881 (dashed line) and 1934 (solid line). Smooth sheets showing bathymetry between these two dates are available from the U.S. Ocean Survey. Swales between ridges have extended toward the south. Isobaths are in fathoms. Shoreline is 1934 shoreline. From Swift *et al.* (1972).

on the center of the crestline but is displaced toward the downcurrent end, so that as the crestline is traced in a downcurrent direction, it rises gradually toward the peak, then falls abruptly to the sea floor.

The inner shelf immediately south of Chincoteague Shoals is markedly finer-grained (Nichols, 1972). Ridge topography is absent. South-directed storm flows would tend to expand and decelerate in the Bight protected by Chincoteague Shoals, and the reduced capacity of such flows to transport sediment may have resulted in deposition of fine material excavated from the swales between ridges to the north.

Middle Atlantic Shelf of South America

The coast of Argentina, Uruguay, and Southern Brazil has undergone an intensive period of Holocene progradation, as indicated by beach ridge plains north and south of the La Plata Estuary (Urien & Ewing, 1974). However, successive modern surveys of the Argentine Hydrographic Service suggest that the present coastline is stationary or retreating. The adjacent continental shelf exhibits an inner shelf ridge topography that is very similar to that of the Middle Atlantic Shelf of North America (Urien, 1974; Figueiredo, 1975) with one striking discrepancy; ridges make a consistently southward-opening angle with the

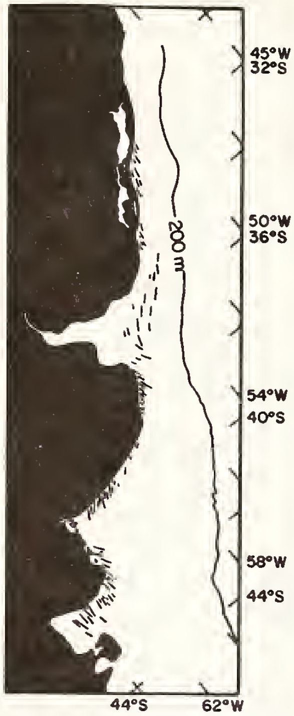

Figure 7. Shelf of northern Argentina, Uruguay, and Brazil, showing distribution of inner shelf ridges. From Urien & Ewing (1974).

shoreline, rather than northward, as in the case of the northern hemisphere (Figure 7). Studies by the Argentine Hydrographic Service (Parker & Perillo, 1976) of the inner shelf south of the La Plata estuary reveal a closely spaced series of sand ridges forming angles of about 35° with the coast between Punta Medanos and Pinamar (Figure 8). The ridges are steeper on their northern flanks, or are symmetrical.

Current information for this coast is too fragmentary to establish prevailing directions of storm flow. It is possible to surmise, however, that southern hemisphere storms would be 'southeasters' analogous to the northeasters of the North American Atlantic shelf, and would drive northward currents, analogous to the southward storm currents described for the Middle Atlantic Bight by Beardsley & Butman (1973), Boicourt & Hacker (1976), and Lavelle *et al.* (1976).

The morphologic pattern of the Punta Medanos sector of the northern Argentine shelf appears to be a north–south inversion of the pattern of the Chincoteague Shoals sector of the Maryland–Delaware shelf. As in the case of Blackfish Bank off Chincoteague Shoals, ridge crests are the most shallow off Punta Medanos, suggesting a high rate of sedimentation in the vicinity of a coastal discontinuity. A comparison of bathymetric surveys of 1964 and 1974 indicates that swales between ridges in the Punta Medanos have deepened and have extended to the north (Figure 9) as the swales at Chincoteague Shaols have extended to the south. The shallow, flat sea floor seaward of Mar de Ajo may be a zone of aggradation for fine sand swept out of the ridge topography to the south, as the Bight south of Chincoteague Shoals appears to be a catchment basin for fine sand swept out of the ridge topography to the north. Detailed grain size data are not presently available.

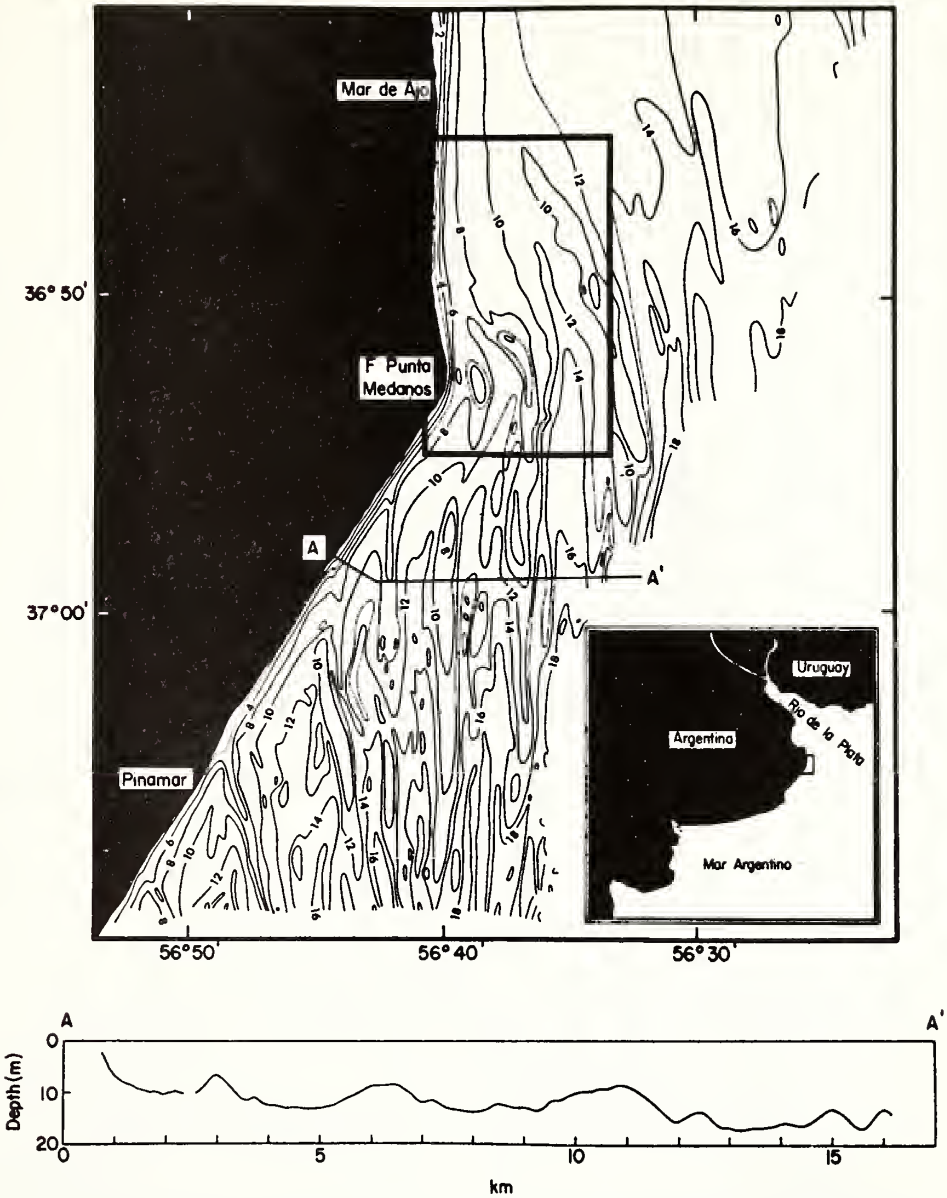
Mar de Ajo
F Punta Medanos
A
A'
Pinamar
Uruguay
Argentina
Rio de la Plata
Mar Argentino
36° 50'
37°00'
56°50'
56°40'
56°30'
A
A'
Depth (m)
0
10
20
0
5
10
15
km

Figure 8. Bathymetry of a portion of the inner Argentine shelf. Depth in meters. Rectangle indicates area of Figure 9. From an Argentine Naval Hydrographic Survey map.

East Frisian Shelf

The Frisian Shelf experiences strong tidal currents. The spring tidal range is 4 m (Houbolt, 1968). Barrier islands are short, tidal inlets are wide and closely spaced, and the lagoon behind the barrier is largely intertidal (Figure 10). The Frisian Coast, like the Argentine Coast, has a history of Holocene progradation followed by modern coastal retreat (Van

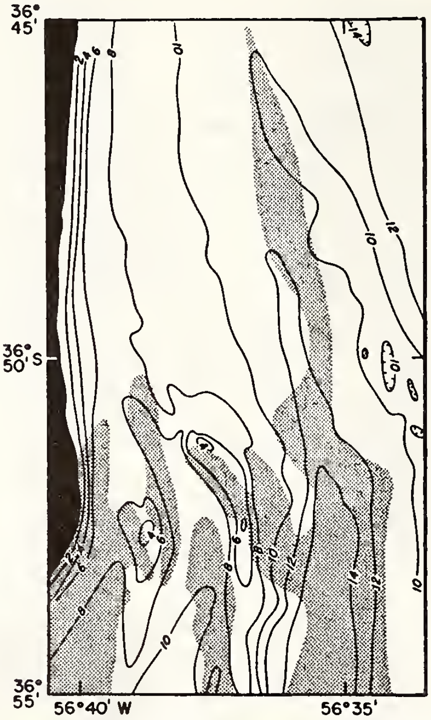
36°
45'
36°
50' S
36°
55'
56°40' W
56°35'
2
4
6
8
10
12
14

Figure 9. Pattern of net bottom change on the inner Argentine shelf off Punta Medanos between 1964 and 1974. Depth in meters. Stippled areas have undergone 1–3 m of erosion. Clear area has undergone 0–3 m of aggradation. From Parker & Perillo (1976).

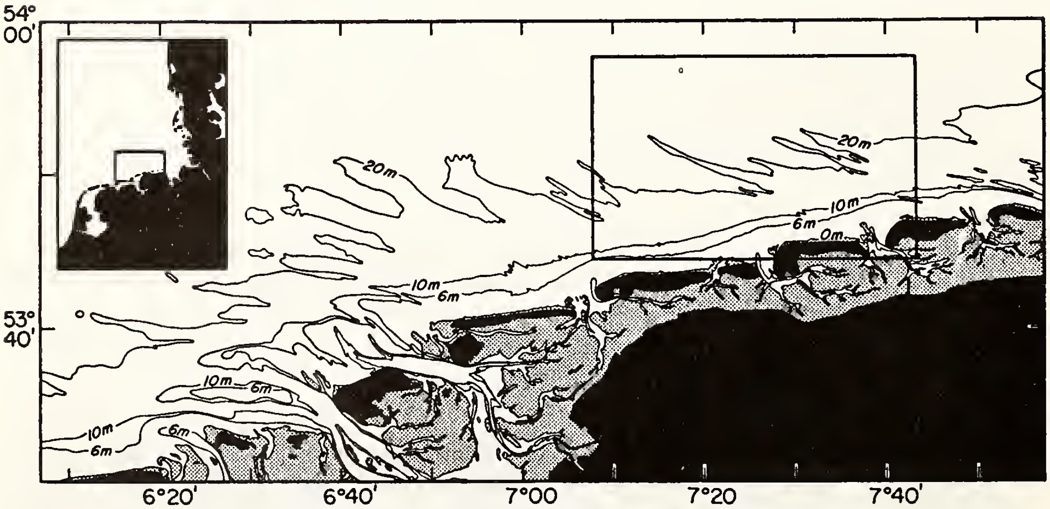
54°
00'
53°
40'
6°20'
6°40'
7°00
7°20
7°40'
20m
20m
10m
6m
0m
10m
6m
10m
6m
10m
6m

Figure 10. East Frisian coast of the North Sea. From Defense Mapping Agency Hydrographic Center chart 37221. Rectangle indicates location of Figures 11 and 12.

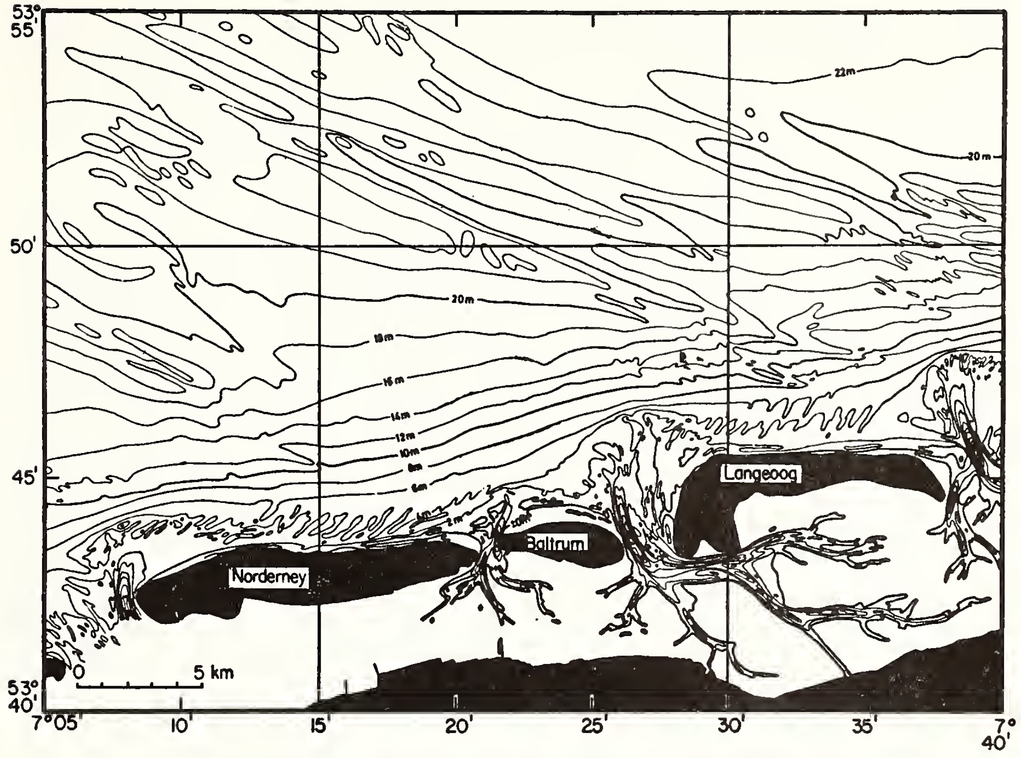
53° 55'
50'
45'
53° 40'
7°05'
10'
15'
20'
25'
30'
35'
7° 40'
22m
20m
20m
18m
16m
14m
12m
10m
8m
6m
4m
2m
Langeoog
Baltrum
Norderney
0
5 km

Figure 11. Bathymetry of a portion of the East Frisian coast.

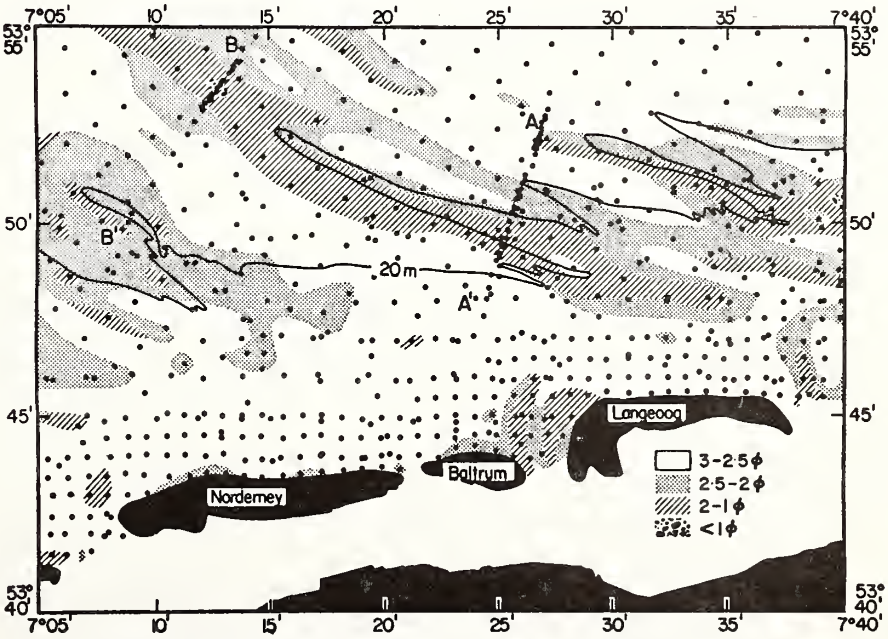
7°05'
10'
15'
20'
25'
30'
35'
7°40'
53° 55'
50'
45'
53° 40'
B
B'
A
A'
20m
Langeoog
Baltrum
Norderney
3-2·5ϕ
2·5-2ϕ
2-1ϕ
<1ϕ

Figure 12. Distribution of size classes of sand on a portion of the East Frisian coast. Dots are sample stations.

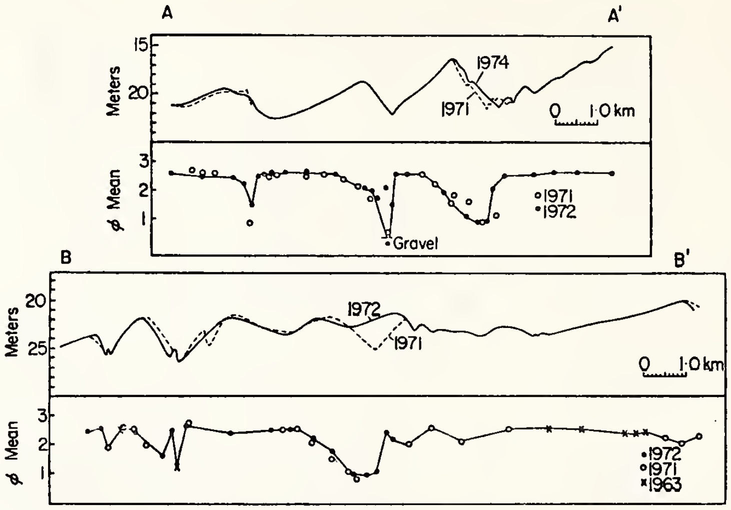

Figure 13. Cross-section of ridges shown in Figure 12.

Straaten, 1965). On the East Frisian Shelf, a smooth shoreface extends down to about 12 m, where it gives way to a ridged inner shelf floor. Sub-bottom profiles (unpublished data, K. Figge) show the Pleistocene surface slopes smoothly beneath the shoreface toward the inner shelf floor, and is not part of the ridge structure.

Ridges form westward-opening angles of about 35° with the beach. The prevailing current on the inner shelf trends from west to east [Houbolt, 1968, Figure 3(d)]. Between the ridges and the beach the 4 m contour is perturbed by a series of oblique, wave-built bars that are orthogonal with respect to the ridges (Figure 11).

The landward (upcurrent) flanks of the ridges are coarser than the seaward flanks (Figure 12). The transition from fine to coarse sand is abrupt in the trough, while the coarse sand passes gradually into fine sand over the crest (Figure 13), a phenomenon also noticed by Moody on the Delmarva coast (1964; Figure 2, this paper). Samples taken in different years but at morphologically identical positions have the same grain size characteristics, suggesting that morphology and grain size are equilibrium responses to flow.

Near their junctions with the shoreface (profile A–A′, Figure 13), the ridges tend to be steeper on the landward (upcurrent) side. Further seaward, ridges tend to be nearly symmetrical, or steeper on their seaward (downcurrent) sides (Figures 11 and 13).

One of us (Figge) has instituted a program of repetitive survey of onshore-offshore transects. Early results show that significant changes occur on a yearly basis (Figure 13), but the time series is too short to reveal what systematic trends, if any, exist.

Similar sand ridges occur on the Danish coast of the German Bight, off the Island of Sylt. Here they are oriented nearly perpendicular to the coast, and exhibit an asymmetrical distribution of grain size with respect to ridge morphology. Shoreface-connected sand ridges also occur elsewhere in the North Sea, notably on the East Anglian coast of Great Britain. There, however, the morphologic pattern is rather different. The ridges occur as partitions separating ebb-dominated and flood-dominated channels (Robinson, 1967). Ridges making northward-opening angles with the shoreface dominate, but 'Z'-shaped patterns are also common, separating *en echelon* ebb and flood channel sets. On the East Anglian coast, the semidiurnal tidal cycle appears to be the dominant ridge-building agent. Only the German Bight of the North Sea has the simple pattern of straight ridges trending obliquely or nearly normal to the shoreface, into depths as shoal as 10 m, that is closely analogous to the patterns of the Argentine and Maryland shelves. The lack of ebb–flood channel patterns in the German Bight may mean that wind-driven flows are more important than tidal currents in building ridges in this region.

Guiana Shelf

A final example of shoreface-connected ridges is the ridge system of the Guiana inner shelf as described by Allersma (1972). The Guiana coast has prograded through the Holocene. Progradation has locally been cyclic, leading to the formation of chenier plains (Allersma, 1972). Unlike the preceeding three examples, the ridges of the adjoining shelf are composed of mud, not sand. The mud blanket is continuous; and the ridges constitute gentle undulations in its upper surface. They extend seaward to a depth of 20 m. As befits ridges composed of so markedly different material, their scale is also very different; mud ridge spacing ranges from 30 to 60 km and the maximum relief is 2 m versus 10 m for sand ridges. It is by no means clear that they bear any genetic relation to the inner shelf sand ridges described elsewhere in this paper. There are a number of points of similarity, however. The ridges form angles of 20–30 degrees with the shoreline, opening to the east, into the Guiana Current. Western (downcurrent) slopes are steeper, with gradients of 1:500 versus 1:3000 for upcurrent slopes. The ridges are migrating westward (downcurrent) at a rate of 1·5 km per annum (Allersma, 1972).

Conclusions

Comparisons of ridge fields

Inner shelf ridge fields occur primarily on low, unconsolidated coasts whose noncohesive substrates provide an ample supply of the medium-grained or coarser sand necessary for ridge formation. An anomalous situation occurs on the Guiana shelf where shoreface-connected mud ridges exist. If these ridges are of similar origin, their formation in anomalously fine sediment may be due to the very heavy mud load or 'coastwise advective mud stream' (McCave, 1972) carried along the Guiana shelf. The mud ridges have much greater spacings (tens of km versus km), less relief, and much flatter slopes (1:500 versus 1:3000) than do sand ridges.

On the best-studied example, the North American Atlantic shelf, sand ridges rest on a substrate of lagoonal deposits exposed by erosional retreat of the shoreface during the post-glacial rise of sea level. The Argentine and Frisian coasts described in this paper have a more complex Holocene history but appear to be retreating or stationary at the present time. The Guiana coast is prograding.

Inner shelf sand ridges have highly correlated orientations within a given area. In examples described from the North American Atlantic shelf, Guiana shelf, and West Frisian shelf, ridges form angles with the coast that open into the direction of prevailing flow. For the South American shelf, the direction of prevailing flow is not adequately known.

The seaward (downcurrent) flanks of sand ridges are consistently finer grained than the landward (upcurrent) flanks. Ridges tend to be steeper on the downcurrent (seaward) side, although this pattern may be reversed very close to the landward end of the ridge where scour between the ridge and beach becomes intense, but morphologic asymmetry is not as consistent as textural asymmetry.

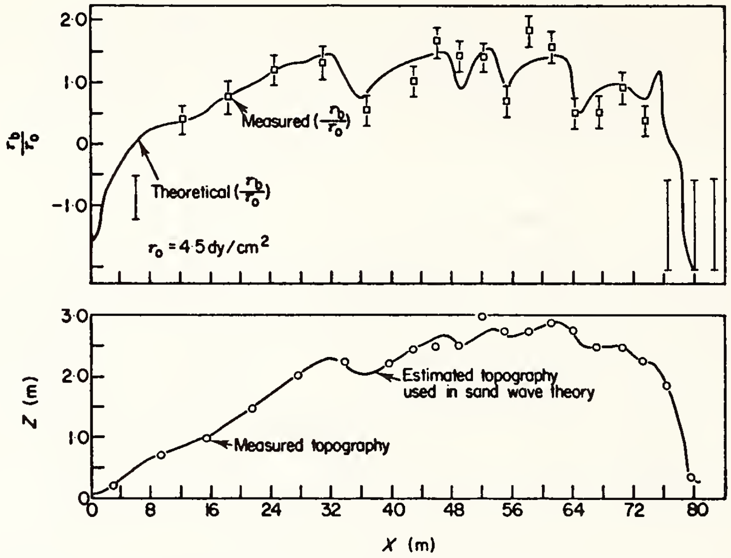

Figure 14. Comparison of boundary shear stress measured over a sand wave with that calculated from the constant eddy viscosity theory. τ_0 is bottom shear stress required to initiate sediment motion, z is height above the bottom, and x is downstream distance. From Smith (1970).

In examples described from the North American, South American, and Guiana shelves, ridges migrate. Where they form appreciable angles with the shoreline, the movement is downcurrent and offshore, with the ridges extending their crestlines so as to maintain contact with the shoreface. Where the ridges are nearly shore-parallel, the movement is expressed as downcurrent growth of ridges and downcurrent extension of swales between ridges.

Ridge genesis

The mobility of sand ridges, and the systematic relationship of their morphologic and textural patterns to the prevailing flow field indicate that the systems of inner shelf sand ridges described in this paper are bedforms, in the sense of hills or hollows in a cohesionless (usually) substrate, that constitute an equilibrium response to peak flow conditions. Bedforms can be classified into two broad categories on the basis of orientation of the long axis of the bedform with respect to flow, as flow-transverse and flow-parallel forms, and this descriptive distinction is inferred to be ultimately genetic in nature (Wilson, 1972).

Perhaps the most effective attempt to devise an analytic model for flow-transverse bedforms is that of Smith (1970) in which ripples or sand waves grow from an initially irregular bed as a consequence of a phase lag between bottom shear stress and bottom topography. Flow-parallel bedforms have been attributed, with considerably less certainty, to a secondary flow structure theoretically occurring in broad shallow flows of large scale. In this structure, zones of flow-parallel downwelling that form swales alternate with zones of flow-parallel upwelling that localize ridges (see Faller, 1971; Gammelsrod, 1976, for theoretical studies; Houbolt, 1968, for field application).

Two aspects of the ridges described in this report may be explained by theories of sand wave formation and probably only by such theories. These are the morphologic and textural asymmetries of ridge cross-sections. Smith's analysis predicts that bottom shear stress will increase up the upcurrent slope, reach a maximum, then decrease across the crest and down the downcurrent slope (Figure 14). We argue that the observed grain size patterns (Figures 2(c), 4, 5, 12, 13) are time averaged responses to such bottom shear-stress gradients, $d\tau/dx$, as required by the sediment continuity equation:

$$\frac{\partial q}{\partial x} = -k\frac{\partial h}{\partial t}$$

where q is discharge (weight rate of sediment discharge per unit width of bed), x is downstream distance, h is bed elevation relative to a datum plane, t is time, and k is a dimensional constant related to sediment porosity.

Since the concentration of entrained sediment increases with bottom shear stress, the positive shear stress gradient up the upcurrent flank of the ridge must result in erosion and selective removal of the finer grains of sand, while the negative gradient of the crest and downcurrent slope should result in deposition of the finer sand. Since the position of maximum positive rate of bottom elevation change, $\partial h/\partial t$, is displaced towards the seaward edge of the ridge, the seaward side will tend to be steeper.

Sand wave theory cannot by itself explain sand ridge formation, since the sand ridges are oriented obliquely with respect to the prevailing flow, whereas the theory calls for flow-transverse bedforms. Helical flow theory is compatible with an oblique orientation, since the flow cells may be skewed with respect to the mean flow direction, but the detailed measurements of storm flow over ridges that would test the helical flow hypothesis have not yet been made. We do not yet have an adequate general model for the formation of shoreface-connected sand ridges, but we can, by comparing the examples presented in this paper, arrive at constraints which such a model must meet.

References

Allersma, E. 1972 Mud on the oceanic shelf off Guiana. In *Symposium on Investigations and Resources of the Caribbean Sea and Adjacent Regions.* UNESCO (Unipub, N.Y.), Paris. pp. 193–203.

Beardsley, R. C. & Butman, B. 1974 Circulation on the New England continental shelf: response to strong winter storms. *Geophysical Research Letters* **1,** 181–184.

Boicourt, W. C. & Hacker, P. W. 1976 Circulation of the Atlantic continental shelf of the United States, Cape May to Cape Hatteras. *Memoirs Société Royale des Sciences de Liege, 16th Series* **10,** 187–200.

Duane, D. B., Field, M. E., Meisberger, E. P., Swift, D. J. P. & Williams, S. J. 1972 Linear shoals on the Atlantic continental shelf, Florida to Long Island. In *Shelf Sediment Transport: Process and Pattern* (Swift, D. J. P., Duane, D. B. & Pilkey, O. H., eds). Dowden, Hutchinson and Ross, Inc., Stroudsburg, Pa. pp. 447–498.

Faller, A. J. 1971 Oceanic turbulence and the Langmuir circulations. *Annual Review of Ecology and Systematics* **2,** 201–236.

Field, M. E. 1976 Quaternary evolution and sedimentary record of a coastal plain shelf: central Delmarva peninsula, Mid-Atlantic Bight, U.S.A. Dissertation, George Washington University, Washington, D.C.

Figueiredo, A. G., Jr. 1975 Geologia dos depositos calcarios biodetriticos de plataforma continental do Rio Grande do Sul. Tese de Mestrado en Geosciencias, Universidade Federal do Rio Grande do Sul, Puerto Alegre, Brazil.

Figueiredo, A. G., Jr. 1978 Some notes about Quaternary geology of Rio Grande do Sul inner continental shelf—Brazil. In *Proceedings of the International Symposium on the Quaternary, Southern Brazil, July 15–31, 1975* (in press).

Gammelsrod, T. 1975 Instability of Couette flow in a rotating fluid and origin of Langmuir circulations. *Journal of Geophysical Research* **80,** 5069–5075.

Houbolt, J. H. C. 1968 Recent sediment in the Southern Bight of the North Sea. *Geologie en Mijnbouw* **47,** 245–273.

Köster, R. 1974 Geologie des Seegrundes vor den Nordfriesischen Inseln Sylt und Amrun. *Mayniana* **24,** 27–41.

Lavelle, J. W., Brashear, H. R., Case, F. N., Charnell, R. L., Gadd, P. E., Haff, K. W., Han, G. A., Kunselman, C. A., Mayer, D. A., Stubblefield, W. L. & Swift, D. J. P. 1976 Preliminary results of coincident current meter and sediment transport observations for wintertime conditions, Long Island inner shelf. *Geophysical Research Letters* 3, 97–100.

McCave, I. N. 1972 Transport and escape of fine grained sediment from shelf areas. In *Shelf Sediment Transport: Process and Pattern* (Swift, D. J. P., Duane, D. B. & Pilkey, O. H., eds). Dowden, Hutchinson and Ross, Inc., Stroudsburg, Pa. pp. 246–262.

Moody, D. W. 1964 Coastal morphology and processes in relation to the development of submarine sand ridges off Bethany Beach, Delaware. Ph.D. Thesis, Johns Hopkins University.

Off, T. 1963 Rhythmic linear sand bodies caused by tidal currents. *American Association of Petroleum Geologists Bulletin* 47, 324–341.

Palmer, H. D. & Wilson, D. G. 1975 Nearshore current regimes in a linear shoal field, Middle Atlantic Bight. IX. *International Congress of Sedimentology, Nice, France.*

Palmer, H. D., Wilson, D. G. & Guala, J. R. 1975 Sediment response to inner shelf hydraulic regimes: progress report February 1975–November 1975. Unpublished report, Westinghouse Ocean Research Laboratory, Anapolis, Maryland.

Parker, G. & Perillo, G. 1976 Movemento del Fondo Marino. *Informe Tecnico* No. 1, *Contrato COPUAP-SIHN, Servicio de Hidrografia Naval, Armada Argentina, Republica Argentina.*

Robinson, A. H. W. 1966 Residual currents in relation to shoreline evolution of the East Anglian coast. *Marine Geology* 4, 57–84.

Sheridan, R. E., Dill, C. E., Jr. & Kraft, J. C. 1974 Holocene sedimentary environment of the Atlantic inner shelf off Delaware. *Geological Society of America Bulletin* 85, 1319–1328.

Smith, J. D. 1970 Stability of a sand bed subjected to a shear flow of low Froude number. *Journal of Geophysical Research* 30, 5928–5940.

Stahl, L., Koczan, J. & Swift, D. J. P. 1974 Anatomy of a shoreface-connected sand ridge on the New Jersey shelf: implications for the genesis of the shelf surficial sand sheet. *Geology* 2, 117–120.

Swift, D. J. P. 1975 Barrier island genesis: evidence from the central Atlantic shelf, eastern U.S.A. *Sedimentary Geology* 14, 1–43.

Swift, D. J. P., Duane, D. B. & McKinney, T. F. 1974 Ridge and swale topography of the Middle Atlantic Bight: secular response to Holocene hydraulic regime. *Marine Geology* 15, 227–247.

Swift, D. J. P., Freeland, G. L., Gadd, P. E., Han, G., Lavelle, J. W. & Stubblefield, W. L. 1976 Morphologic evolution and coastal sand transport, New York–New Jersey shelf. In *Middle Atlantic Continental Shelf and the New York Bight* (Gross, M. G., ed.). American Society of Limnology and Oceanography Special Symposia Vol. 2. pp. 69–90.

Swift, D. J. P., Holliday, B., Avignone, N. & Shideler, G. 1972*a* Anatomy of a shore face ridge system, False Cape, Virginia. *Marine Geology* 12, 59–84.

Swift, D. J. P., Kofoed, J. W., Saulsbury, F. P. & Sears, P. 1972*b* Holocene evolution of the shelf surface, south and central Atlantic shelf of North America. In *Shelf Sediment Transport: Process and Pattern* (Swift, D. J. P., Duane, D. B. & Pilkey, O. H., eds). Dowden, Hutchinson and Ross, Inc., Stroudsburg, Pa. pp. 499–574.

Swift, D. J. P., Sears, P. C., Bohlke, B. & Hunt, R. 1978 Evolution of a shoal retreat massif, North Carolina shelf: inferences from areal geology. *Journal of Sedimentary Petrology* 27, 19–42.

Tanner, W. F. 1961 Offshore shoals in areas of energy deficit. *Journal of Sedimentary Petrology* 31, 87–95.

Uchupi, E. 1970 Atlantic continental shelf and slope of the United States—shallow structure. *U.S. Geological Survey Professional Paper* 529-I.

Urien, C. M. & Ewing, M. 1974 Recent sediments and environment of southern Brazil, Uruguay, Buenos Aires, and Rio Negro continental shelf. In *The Geology of Continental Margins* (Burke, C. A. & Drake, C. L., eds). Springer Verlag, New York. pp. 157–177.

Veatch, A. C. & Smith, P. A. 1939 Atlantic submarine valleys of the United States and the Congo submarine valley. *Geological Society of America Special Paper* No. 7.

Wilson, I. G. 1972 Aeolian bedforms—their development and origins. *Sedimentology* 19, 173–210.

Printed in Great Britain by Henry Ling Ltd., at the Dorset Press, Dorchester, Dorset

Oceanology 17, No. 5, 544-551 (Academy of Sciences of the USSR).

MARINE GEOLOGY

New Data on the Morphostructure of the Central Part of the Mid-Atlantic Ridge

G.B. UDINTSEV, V.M. LITVIN, N.A. MAROVA, M.V. RUDENKO, L.YA. BUDANOVA AND P.A. RONA

The results of geomorphologic investigations in three polygons in the central part of the Mid-Atlantic Ridge between latitudes 8 and 27°N, carried out on the 20th cruise of the R/V Akademik Kurchatov in 1975, are presented. Work was carried out in regions of future drilling operations: in the rift zone (Polygon I), on the flank of the ridge, 100 nautical miles to the east of the rift zone (Polygon VI), and in the region of the trench on the Vema Trench transform fault (Polygon II). The construction of the ridge in these regions has been significantly refined. Detailed bathymetric maps of the regions examined and of the seafloor, have been presented. Records of numerous transverse faults along the eastern flank of the ridge have been obtained. It has been established that only some of them are transform faults and divide the ridge into individual blocks. The remaining faults, having a transverse section of similar form, are not of significant extent, and being the result of differential vertical movements, serve only as the boundaries between separate mosaically arranged blocks. The results of the work have confirmed the structural heterogeneity of the Mid-Atlantic Ridge.

The main structural features of the Ridge are quite well-known [1, 4, 5, 8, etc.], yet the polygon investigations provide new facts each time, and to a certain degree, force a reconsideration of our ideas on the construction and evolution of this most important morphostructure on the ocean floor. Particularly intensely detailed investigations have been carried out in the polygons in recent years in connection with the fulfilment of the International Phase of Ocean Drilling (IPOD).

In the central part of the Mid-Atlantic Ridge, between 10 and 30°N, a number of polygon studies have been conducted, using a broad complex of geological and geophysical investigations. American scientists have studied the Vema fault zone at 11°N, and later on, the D/S Glomar Challenger drilled two holes here [9, 12]. Another polygon was completed in the rift zone between 22 and 23°N [11]. Along the section between North America and Africa, polygon investigations were also carried out in the rift zone at 26°N [10]. In the Atlantis fault zone (30°N), detailed work was carried out during the 6th cruise of the R/V Akademik Kurchatov [3, 4]. Finally, geophysical surveys of the entire region were carried out for several vessels during different years by Dutch expeditions [6, 7]. In the last work, in particular, the conclusion was reached, on the basis of a study of many bottom profiles, that no longitudinal but transverse structures of the ridge predominated here, which are, according to Collette et al. [7], associated with the presence of a large number of transform faults.

During the 20th cruise of the R/V Akademik Kurchatov in 1975, geological and geophysical investigations were carried out in three polygons in the central part of the Mid-Atlantic Ridge (Fig. 1). Polygon I is located in the rift zone at 26°N, where American scientists have previously worked. The bathymetric map compiled by them [10] was used by us and refined. Polygon II is located in the eastern part of the transverse Vema Trench fault, where it was proposed to drill a new hole. Here, the survey was conducted in company with American scientists from the R/V Vema. Polygon VI is located on the eastern flank of the ridge, 30 nautical miles east of the American polygon [11] at 22-23°N. We made a very detailed survey here in order to establish a basis for deep-sea drilling in this region (on the 45th cruise of the D/S Glomar Challenger, drill-hole No. 396). The information obtained provided new data on the morphostructure of the rift zone and the upper part of the flank of the Mid-Atlantic Ridge. In addition, on passage between the polygons, we made two runs of ancillary measurements along the eastern flank of the ridge, which enabled us to judge the nature of the transverse dissection of the surface of the slope.

In the first polygon, a rift valley, in the form of en échelon, narrow hollows with depths of more than 4000 m, is readily traced. The maximum depth, established by us in the middle part of the polygon, reached 4600 m. The overall strike of the rift valley, like that of the blocks on the slopes, is northeasterly (Fig. 2). These blocks have been formed, as in other sectors of the Mid-Atlantic Ridge [4], by a series of elongate

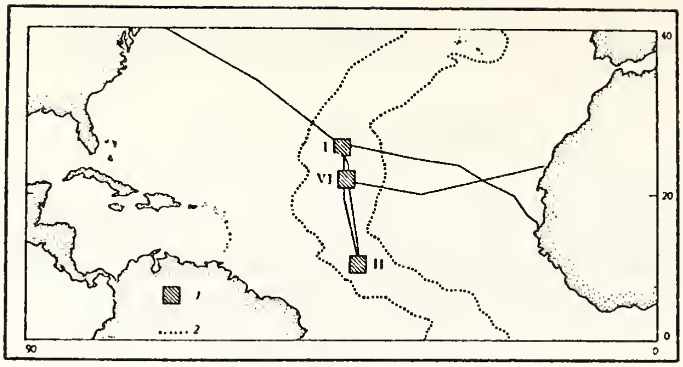

Fig. 1. Location of polygons in the central part of the Mid-Atlantic Ridge.

1) Polygons; 2) outline of Mid-Atlantic Ridge.

ridges and crests, 5-8 nautical miles wide and up to 15 nautical miles long, which are separated by longitudinal hollows. The depths in the hollows are 3200-3900 m, and over the crests of the ridges, less than 3000 m. The ridges in the blocks either replace one another along strike, or are combined en échelon. Sometimes, where they join, quite large massifs of complex configuration are formed, as, for example, to the east of the rift valley in the middle part of the polygon. The minimum depths above this massif is 1500-2000 m. The slopes of the blocks and ridges, as in the rift valley, are steep, sloping 15-20°, and are almost undissected. The floors of the hollows are concave, and flat sectors have not been observed, which suggests an extremely feeble development of processes of accumulative levelling. This has been emphasized by seismic-profiling information, indicating the absence here of any marked sedimentary cover. The depth of dissection within the polygon varies from 500 up to 1000 m, but along the rift valley, it increases to 1500 m. It should be stressed that in the polygon, which is quite distant from the nearest transform fault, almost no transversely oriented structures have been seen. All the structures here strike along the ridge axis.

In the vicinity of Polygon VI, located to the south of Polygon I, the overall strike of the ridge approximates to meridional. Accordingly, almost all the structures here are also elongated from north to south (Fig. 3). Transversely oriented structures, with the exception of two broad but short depressions, have not been observed. The relief has been formed by several blocks, consisting of ridges replacing one another along strike, separated by longitudinal hollows and saddles. The depths in the hollows reach 4200-4700 m, and above the crests of the ridges, they are less than 3500 m. The depth of dissection varies from 300 to 800 m (Fig. 4). As in the first polygon, the slopes are steep and almost undissected. However, the floors of the deepest sectors of the hollows and several steps on the slopes have been levelled. According to the seismic-profiling data, the presence of "pockets" has been recorded here, filled with sediments. It must be noted that this polygon occurs in the upper part of the eastern flank of the Mid-Atlantic Ridge at a distance of about 100 nautical miles from the rift valley. According to the ocean-floor spreading hypothesis, it is older than the rift zone, and the processes of accumulative levelling have begun to be expressed here in significant measure.

Polygon II lies in the zone of the great Vema Trench transform fault. According to Van Andel et al. [2], the fault is expressed in a deep trough-like trench, along which the rift structures have been shifted for a distance of about 170 nautical miles. The overall length of the trench exceeds 200 nautical miles. Its floor has been levelled as a result of the deposition of a sequence of sediments, more than 1 km thick. Drill-hole No. 26, bored in the western part of the trench during the 4th cruise of the D/S Glomar Challenger, went through 483 m of Pleistocene deposits with a large amount of turbidite layers, which indicates periodic slides and turbidity currents, which carried the sedimentary material here [9]. Polygon II embraces the eastern part of the trench and the adjacent rift structures (Fig. 5). The floor of the trench, up to 10 nautical miles wide, is located here at depths of 5180-5200 m. Along its axis in the eastern part, there is a weakly defined crest, which is, according to the seismic-profiling data, the top of a longitudinal range buried below the sediments, and complicating the floor of the trench. Both slopes of the trench are steep (up to 30-35°) and are practically undissected (Fig. 6). Along the northern lip of the trench, there is a weakly upraised crest with depths above it of 3000-3500 m. To the north of it, there are meridionally oriented rift structures, consisting of elongated blocks and hollows separating them. The depth of dissection here is 300-500 m. Along the southern lip of the trench, there is a high, well-defined, narrow, monolithic crest, the top of which is located at depths of less than 2500 m. To the south, there are two quite broad depressions, which strike parallel to the trench, and are separated by a weakly dissected, uplifted massif. The depths in these depressions reach more than 4000 m, and their floors have been levelled as a result of sedimentation, indicated by seismic-profiling data. It should be noted that such depressions parallel to the main trench have also been recorded

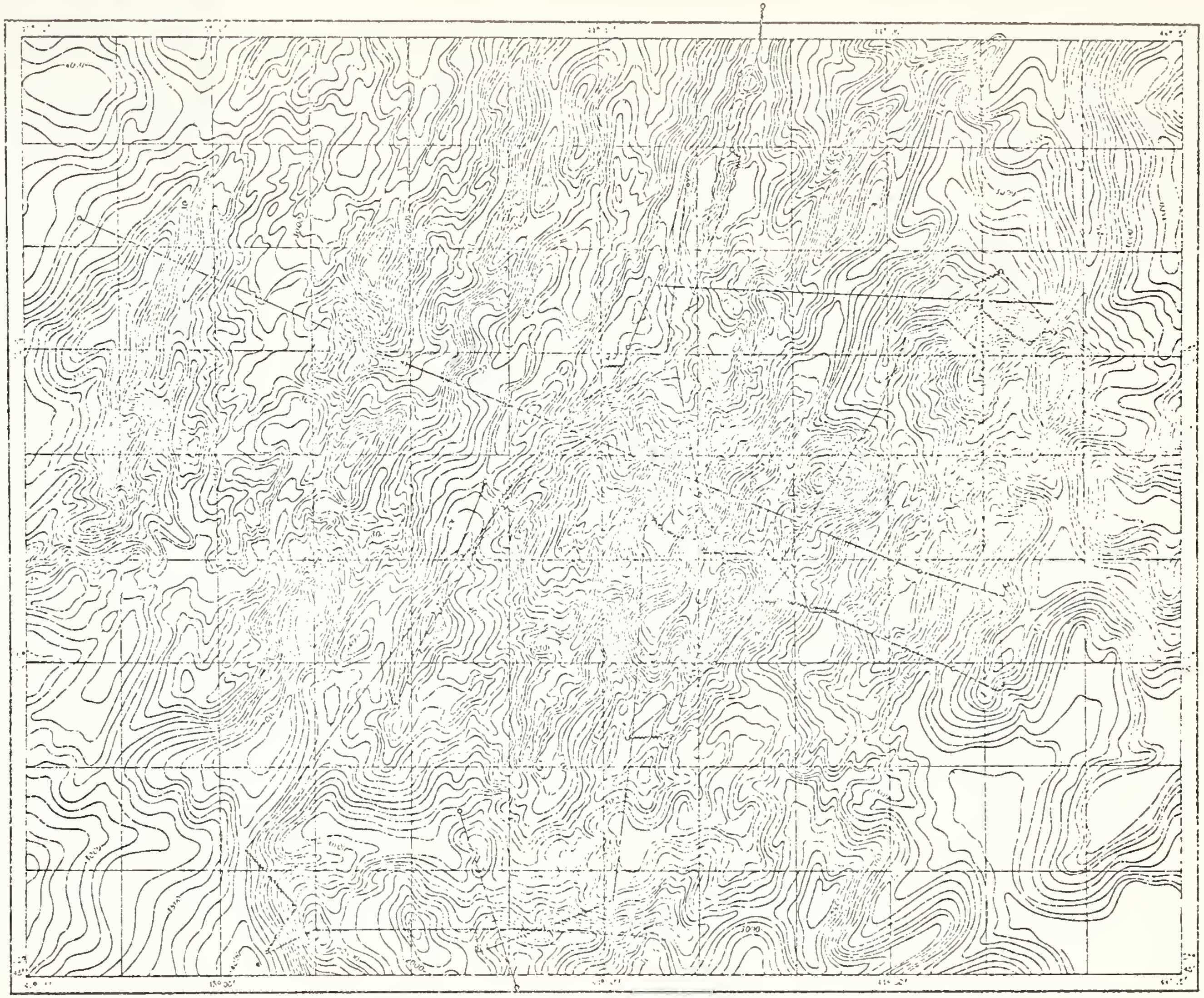

Fig. 2. Bathymetry of Polygon I:

isobaths are plotted at 100-m intervals; echo-sounding tracks are shown. Illustration of bottom relief after Rona's map [10] with addenda from data obtained on 20th cruise of the R/V Akademik Kurchatov.

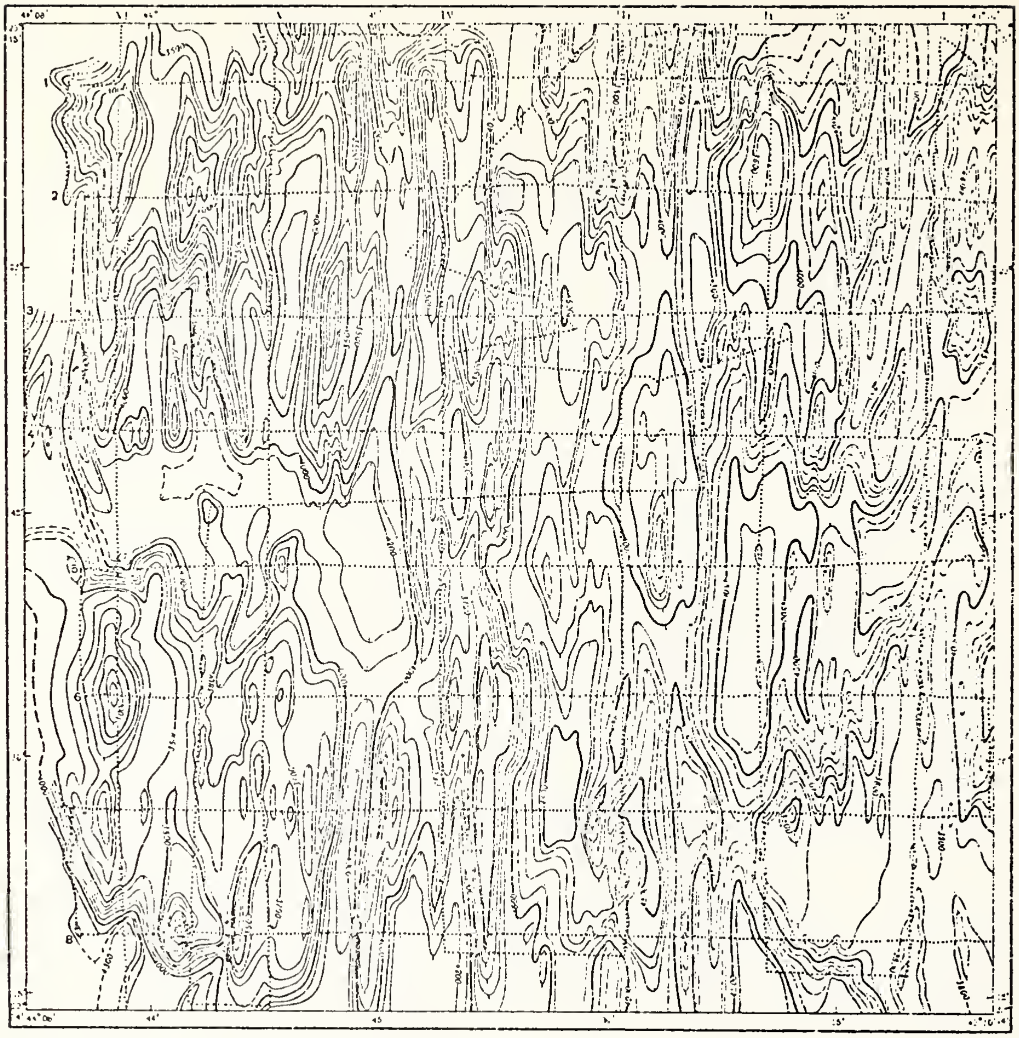

Fig. 3. Bathymetric map of Polygon VI

isobaths are plotted at 100-m intervals; dotted lines show echo-sounding tracks; I-VI) profiles (see Fig. 4).

along other major faults, for example, on the Gibbs and Chain faults. To the south of the second depression, the structures are meridionally oriented, which has been observed as far as the southern boundary of the polygon. This suggests that transversely-oriented (along the trench) structures are located only near the transform fault and do not occur in the remaining sectors of the Ridge. This may also be seen in two longitudinal profiles, located between the first and second polygons at a distance of about 30 nautical miles from each other (Fig. 7). Here, only the depressions, confined to the Chain, Cape Verde, Vema, and other faults, may be quite well correlated, whereas the remaining depressions in the floor, separated by blocks, in the neighboring sectors of the profiles, are not correlated.

Thus, the morphostructure of the Mid-Atlantic Ridge is characterized by dissection of two types. The large-scale dissection has been caused by the presence of transform faults, cutting the ridge into large blocks (or segments), which are oriented transversely to the ridge and strike along the entire breadth of the ridge. Neighboring blocks have been displaced along the transform faults relatively to one another, which is clearly seen in the displacement of the rift structures in the vicinity of the transverse trenches. Small-scale dissection within these blocks has been controlled by the presence of blocks and ridges elongated along the strike of the ridge, arranged sequentially or en échelon and separated by longitudinal hollows and saddles. These ridges and hollows, in contrast to the transform faults, are local structures and do not extend for significant distances.

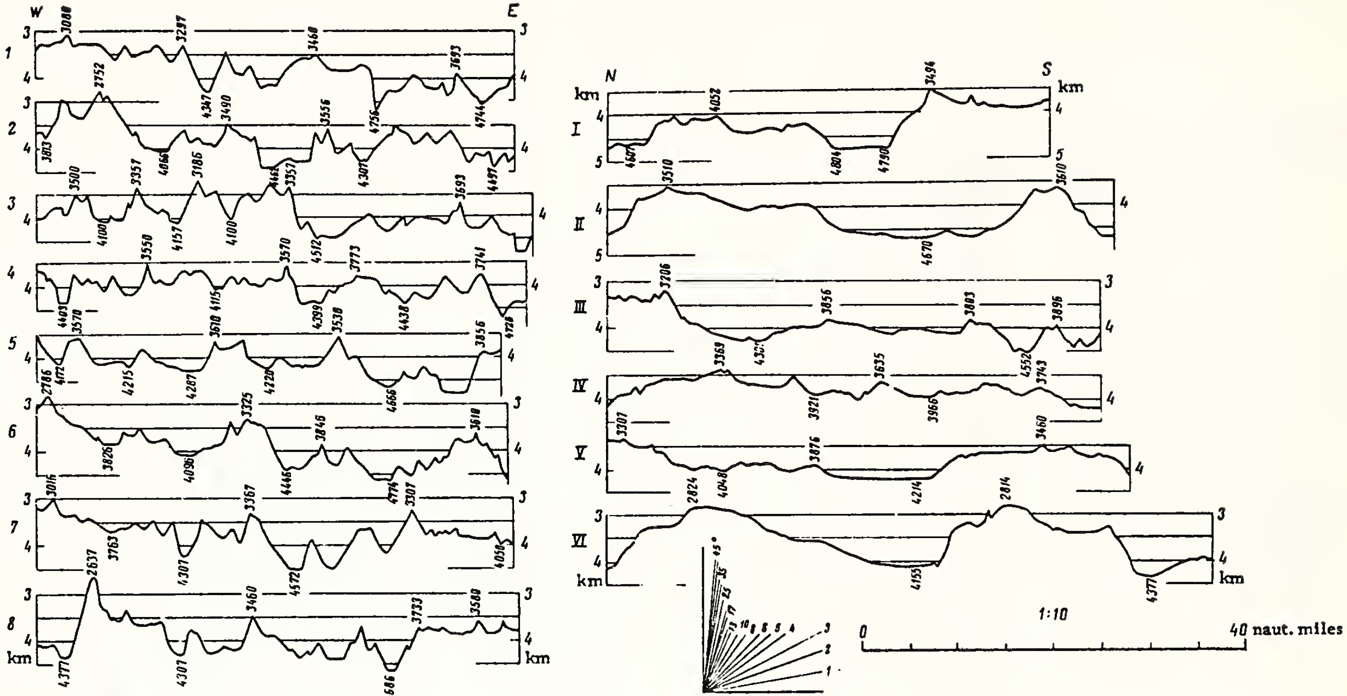

Fig. 4. Bottom profiles for Polygon VI

1–8) sublatitudinal profiles; I–VI) submeridional profiles. Position of profiles shown on Fig. 3.

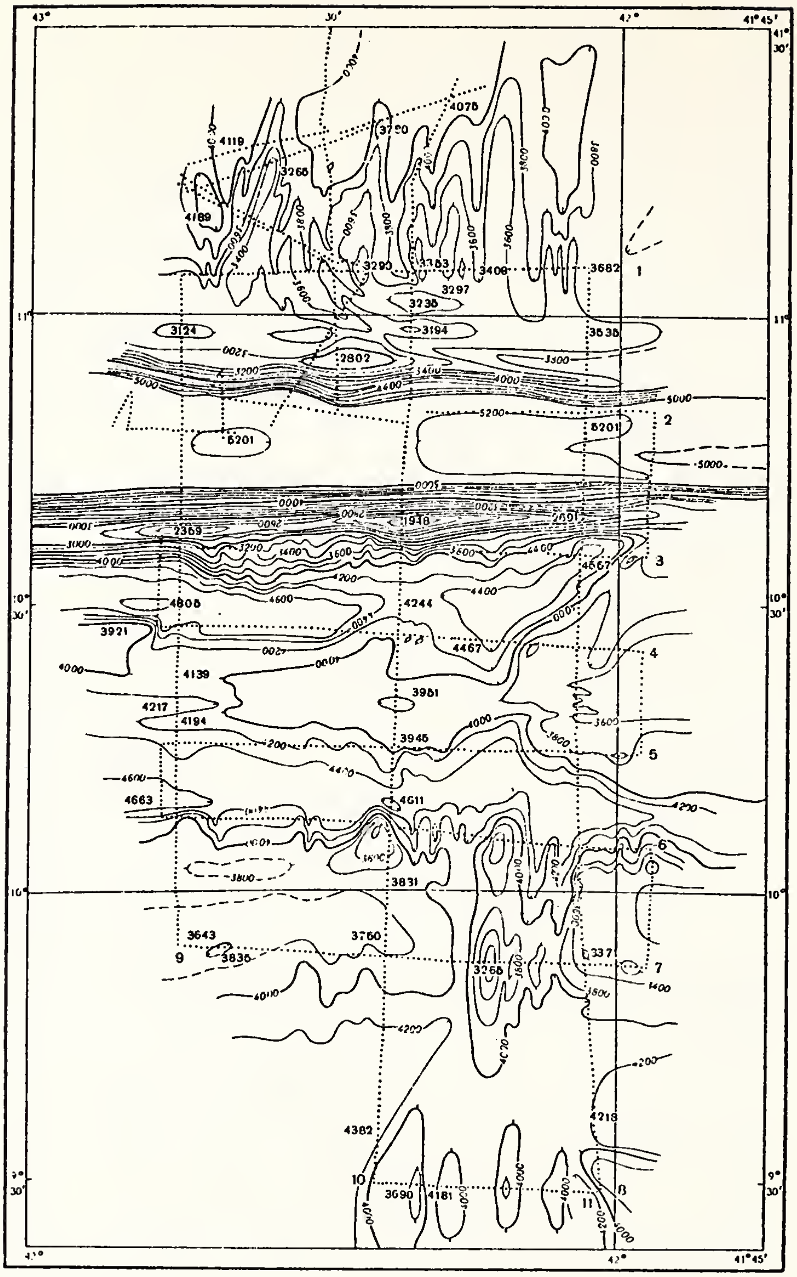
43°
30'
42°
41°45'
41° 30'
11°
10° 30'
10°
9° 30'
4076
4119
3720
3266
4189
3290
3353
3408
3682
3297
3238
3124
3194
3538
2802
5201
5201
2369
1948
4667
4806
4244
3921
4467
4139
3981
4217
4194
3945
4663
4611
3831
3643
3836
3760
3371
3268
4218
4382
3690
4181
1
2
3
4
5
6
7
8
9
10
11

Fig. 5. Bathymetry of Polygon II

Isobaths are plotted at 200-m intervals; dotted lines show echo-sounding tracks; 1-11) profiles (see Fig. 6).

These features of the dissection of the Mid-Atlantic Ridge have evidently been caused by tectonic effects and have been controlled by the presence of systems of planetary and regional faults, arising during the process of evolution of the ridge. The transform faults, which cut the entire ridge and are continued, as is well-known, within the oceanic depressions as far as the continental margins, are of ancient origin, possibly even prior to the beginning of ocean-floor spreading [2]. Subsequently, they became the controlling factor in the formation of the Mid-Atlantic Ridge. The sectors of faults, lying in the rift zone,

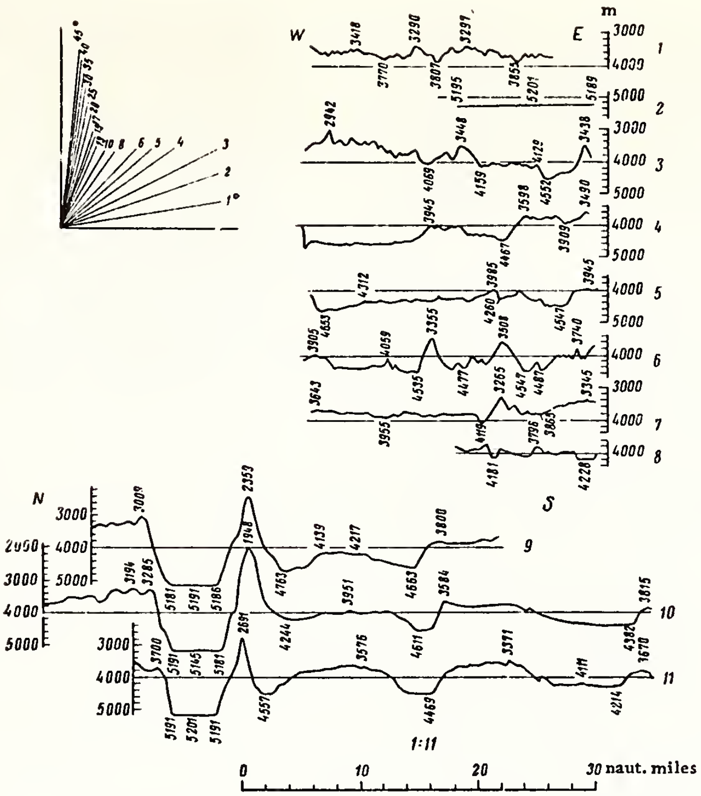

Fig. 6. Bottom profiles for Polygon II

1-8) latitudinal profiles; 9-11) meridional profiles. Position of profiles shown on Fig. 5.

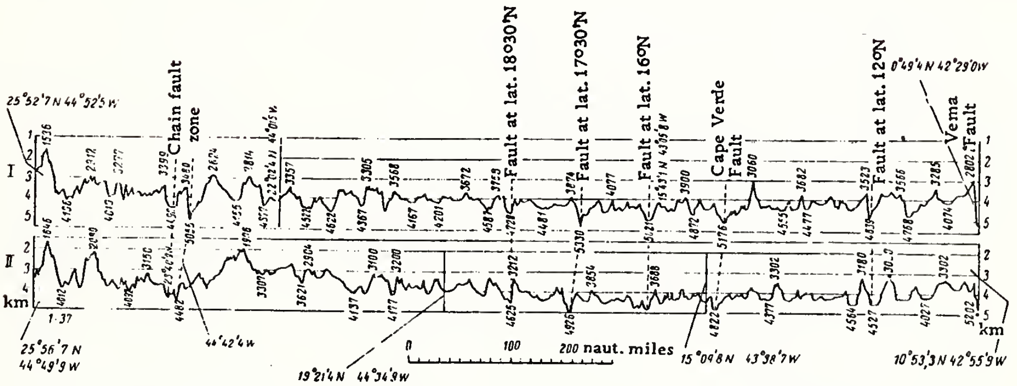

Fig. 7. Longitudinal profiles along the eastern flank of the Mid-Atlantic Ridge between Polygons I and II.

were involved in the process of rifting, and are therefore tectonically active. During ocean-floor spreading, the movement of the neighboring blocks on both sides of the fault on the flanks of the ridge proceeded in one direction, whereas in the rift zone, they moved in opposite directions, leading to the formation of the deep transverse trench. During the rifting process, along with ocean-floor spreading, there were active vertical movements of the crust, injection of protrusions, and eruptions of basalt lavas, accompanied by regional faults and shifts. As a result, the displaced blocks appear to have been broken up by a network of mutually perpendicular faults, among which the longitudinal faults are predominant. This has undoubtedly been determined by the nature of the rifting, where a successive accretion of blocks of new oceanic crust takes place during the process of ocean-floor spreading. The presence of such a network of faults also controls the small-scale dissection of the Mid-Atlantic ridge.

REFERENCES

1. Il'in, A. V. Geomorfologiya dna Atlanticheskogo okeana (Geomorphology of the floor of the Atlantic Ocean). Moscow, Nauka, 1976.
2. Litvin, V. M. Fault tectonics of the floor of the Atlantic Ocean. Geotektonika, No. 6, 1975.
3. Litvin, V. M. et al. Morphostructure of Atlantic Rift Zone in the area of the Kurchatov Fault and Atlantis Canyon. Okeanologiya, 12, No. 4, 1972.
4. Litvin, V. M., N. A. Marova and M. V. Rudenko. The geomorphology of the rift zone of the Mid-Atlantic Ridge. In: Issledovaniye po probleme riftovykh zon Mirovogo okeana (A study of the problem of the rift zones of the World Ocean). Vol. 3. Moscow, Nauka, 1974.
5. Litvin, V. M., et al. On the heterogeneity of the rift zone in the Atlantic Ocean. Okeanologiya, 15, No. 1, 1975.
6. Collette, B. J., J. Ewing, R. A. Lagaay and M. Truchan. Sediment distribution in the oceans: the Atlantic between 10° and 19°N. Marine Geol., 7, No. 4, 1969.
7. Collette, B. J., H. Schouten, K. Rutten and A. P. Slootweg. Structure of the Mid-Atlantic Ridge province between 12° and 18°N. Marine Geophys. Res., 2, No. 12, 1974.
8. Heezen, B. C. and M. Tharp. Physiographic diagram of the North Atlantic Ocean. Geol. Soc. Amer., N. Y., 1968.
9. Initial Reports of the Deep-Sea Drilling Project. 1969. Nat. Sci. Found. Vol. 4.
10. McGregor, B. A. and P. A. Rona. Crest of the Mid-Atlantic Ridge at 26°N. J. Geophys. Res., 80, No. 23, 1975.
11. Van Andel, T. H. and C. O. Bowin. Mid-Atlantic Ridge between 22 degrees and 23 degrees N and the Tectonics of Mid-Ocean. J. Geophys. Res., 73, No. 4, 1968.
12. Van Andel, T. H., R. P. Von Herzen and J. D. Phillips. The Vema fracture zone and the Tectonics of transverse shear zones in oceanic crustal plates. Marine Geophys. Res., 1, No. 3, 1971.

P. P. Shirshov Institute of Oceanology
USSR Academy of Sciences

Received April 7, 1976

Geology 6, 301-304.

Suspended-matter distribution in the New York Bight apex related to Hurricane Belle

Robert A. Young
National Oceanic and Atmospheric Administration, Atlantic Oceanographic
and Meteorological Laboratories, Marine Geology and Geophysics Laboratory
15 Rickenbacker Causeway, Miami, Florida 33149

ABSTRACT

Suspended matter and hydrographic properties of the New York Bight apex were studied three days after passage of Hurricane Belle (August 1976). Distributions of suspended matter were found to be similar to those present during previous periods of calm summer weather. By comparing the present poststorm observations with previous poststorm sampling, it is hypothesized that during summer a stratified water column can restrict vertical mixing of resuspended bottom material to the relatively thin near-bottom layer, whereas mixing throughout the water column takes place during unstratified winter conditions. Clearing times for resuspended material, therefore, are shorter in summer than in winter. Both extent of vertical mixing and clearing times are important considerations for those concerned with problems of marine ecology.

INTRODUCTION

Most workers have assumed that severe storms are responsible for the majority of sediment resuspension and transport on the continental shelf and that relatively lower energy tidal and wind-driven flows have little effect on sediment transport. A previous study of suspended-matter distributions before and after a hurricane on the inner shelf off North Carolina indicated that suspended loads increased by approximately an order of magnitude during and just following the storm, but they decreased to prestorm levels six days after the storm (Rodolfo and others, 1971). There is little fine sediment (<62 μm) available on the shelf off North Carolina, and resuspended sandy bottom sediments from this area should rapidly settle once wave stirring of the bottom has ceased. In other areas, where fine sediments are more abundant, the resuspension effects of severe storms should be more noticeable and longer lived, because of the lower settling velocities of fine sediments.

During the morning of August 10, 1976, Hurricane Belle, a moderate-sized hurricane, traversed from south to north through the New York Bight and then over western Long Island. Wind speeds at sea were estimated to be as much as 44.4 m/s (100 mph), moderating to 22.2 m/s (50 mph) or less on land. The main part of the storm traversed the bight in 6 to 8 hr.

The possible effects of this storm on the distribution and concentration of suspended matter in the apex of the New York Bight is also of interest to environmental managers, because contaminated anthropogenic wastes dumped or otherwise deposited into the apex are typically associated with the fine sediment fraction and with suspended matter in general (Charnell and others, 1972).

SAMPLING

Sampling was carried out on board the R/V *Onrust* jointly with the Marine Sciences Research Center of the State University of New York at Stony Brook. Aliquots from water samples collected in 10-l PVC bottles were filtered through preweighed 0.4-μm Nuclepore filters, rinsed thoroughly and weighed after critical-point freeze drying. Temperature profiles were obtained at each station using Sippican T-10 expendable bathythermographs, and salinities were determined from water samples on a Beckman salinometer in the laboratory.

Ten stations were occupied in the New York Bight apex (Fig. 1); these encom-

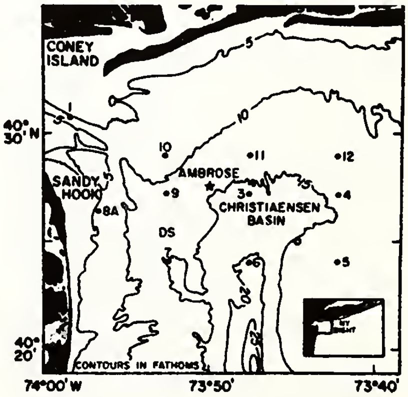

Figure 1. Contour map of New York Bight apex, showing station locations. Star marks sewage sludge dumpsite; dredge spoil dumping takes place just south of station 9.

passed the dredge spoil dumping grounds, a cellar dirt dumpsite, a sewage sludge disposal site, and Christiaensen Basin at the head of the Hudson shelf valley. Bottom sediments in these areas have greater concentrations of fine (<62 μm) sediments (in the range of 5% to 50% by weight) than do most of the surrounding shelf sediments, which are mainly fine to medium quartz-feldspar sands (Freeland and others, 1976). It was thought that resuspension effects due to the storm would be most noticeable in these areas.

SUSPENDED-MATTER AND HYDROGRAPHIC MEASUREMENTS

Strong, thermally controlled stratification was present, separating well-mixed surface and near-bottom layers. Surface temperatures were about 22 °C, while bottom temperatures were about 7 to 10 °C. Although temperatures in the apex were somewhat cooler than during previous years (Fig. 2), the thickness, position, and form of the thermocline three days after Hurricane Belle did not differ greatly from measurements made during August of past years (Hazelworth and others, 1974, 1977).

Suspended-matter distributions (Table 1; Fig. 3) exhibited both vertical and lateral gradients. Concentration maxima generally occurred within the relatively thin, thermally well-mixed surface and bottom layers. Highest concentrations occurred in the Hudson River plume along the New Jersey coast and near the Hudson estuary mouth.

DISCUSSION

Suspended-matter distribution and concentration three days after Hurrican Belle were strikingly similar to distributions observed during relatively calm periods in August of previous years (Drake, 1977; Nelsen, 1977). By comparison, previous observations of suspended-matter concentrations in the apex some ten days after a severe winter storm of three days duration (Dec. 1 to 3, 1974) were higher by a factor of two to three than during other times of the year (Nelsen, 1977, Fig. 39). The primary difference in oceanographic conditions between the present and previous observations of suspended-matter distributions following storms appears to be the presence of stratification in the water column.

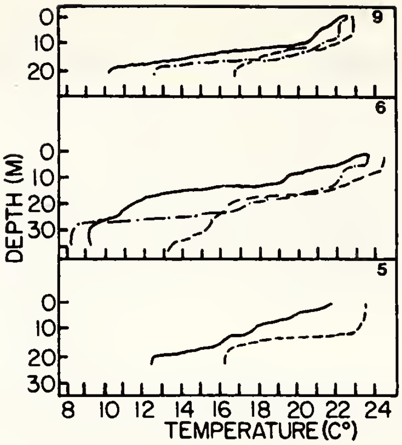

Figure 2. Temperature profiles at stations 5, 6, and 9 made during this study and at same locations during 1973 and 1974. Solid line = posthurricane (1976) profiles; dotted line = 1973 profiles, from Hazelworth and others (1974); dashed line = 1974 profiles, from Hazelworth and others (1977).

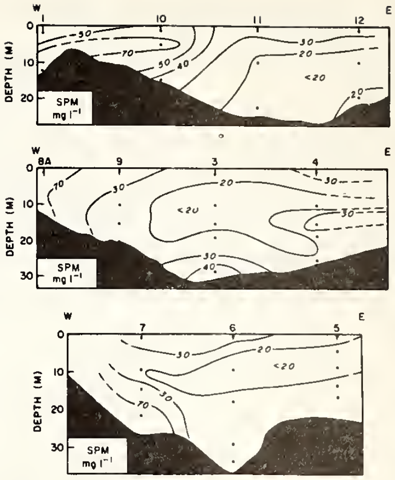

Figure 3. Vertical sections of suspended-matter concentration. Sample data are given in Table 1; station locations given along upper margin are also shown in Figure 1.

Water stratification before Hurricane Belle probably was similar to that illustrated by the 1973 and 1974 temperature profiles shown in Figure 2. Downward mixing momentum during Belle was no doubt initially inhibited by the thermocline, resulting in a partial decoupling of surface and bottom-water movements. For storms of longer duration, greater mixing could be expected.

An indication of how bottom flow responded to the storm can be seen in a current-meter record from a mooring in about 30 m of water some 50 km east of the apex (Fig. 4). Wind records from Kennedy airport in New York City are also shown for the same period. Mean current speeds at 1 m above the bottom exceeded 10 cm/s for a period of 12 hr at this mooring, reaching a peak of 50 cm/s, but mean speeds of 30 cm/s or more lasted only about 4 to 5 hr during that period. By contrast, surface flow speeds of 40 cm/s or more persisted for more than 16 hr. Previous studies of circulation in the New York Bight (Charnell and Mayer, 1975; Beardsley and others, 1976) have demonstrated excellent cross-shelf spatial coherence for flows at subtidal frequencies and a fairly strong relationship between meteorological forcing and current motions. Thus, it can be assumed that bottom currents in the apex showed a similar response and that mean current speeds competent to erode the fine to medium silty sands in the apex probably persisted for only a few hours.

During winter, when the water column is unstratified, or at times when stratification is broken down by long-lasting storms, flow at all depths is driven directly by wind stress (Charnell and Mayer, 1975). In this situation, surface wind stress would be balanced by shear stress at the bottom, and such a wind-forced mean flow could be a direct cause of resuspension.

Resuspension of bottom sediments on the continental shelf is not accomplished by the mean flow alone. Bottom wave surge, especially from high-amplitude storm waves, plays a significant if not dominant role in many instances (see, for example, Lavelle and others, 1975, 1977). However, during stratified summer conditions, vertical mixing of resuspended bottom sediments by wave surge would be limited to the bottom of the thermocline (Fig. 2), typically some 5 to 10 m above the sea floor in the New York Bight apex. Thus, the first-order effect of wave surge

TABLE 1. SUSPENDED MATTER AND HYDROGRAPHIC DATA OBTAINED ON AUGUST 13, 1976, IN NEW YORK BIGHT APEX

Station	Depth (m)	Salinity (°/₀₀)	Temperature (°C)	Suspended-matter concentration (mg/l)
1	2	23.63	23.0	2.74
	12	29.39	20.8	7.7
3	2	28.96	22.1	2.3
	10	31.31	18.5	1.4
	15	31.84	14.5	1.7
	20	32.03	12.0	2.4
	28	32.44	8.6	4.2
4	1	28.60	21.4	3.1
	10	31.54	18.6	1.5
	15	31.76	16.7	3.4
	20	32.06	15.0	2.1
	25	32.30	11.1	2.2
5	1	..	21.7	2.6
	5	31.28	20.0	1.1
	10	31.57	17.8	1.2
	15	31.76	16.1	2.8
	20	31.97	12.7	2.6
6	1	29.35	22.1	3.4
	10	31.27	18.4	0.86
	20	..	10.3	2.5
	30	32.52	7.9	2.1
	35	32.53	7.9	2.6
7	1	28.71	23.0	3.4
	10	30.41	19.6	2.1
	15	29.68	15.4	3.4
	22	32.31	10.5	7.2
8A	1	27.56	..	7.7
9	1	29.12	22.2	3.4
	10	30.00	20.8	2.8
	15	31.61	14.5	2.4
	22	32.24	10.2	2.5
10	1	26.40	23.2	5.7
	5	27.31	21.6	7.2
	15	31.79	14.5	3.5
11	1	29.43	22.1	3.3
	10	30.60	17.7	1.8
	22	32.32	10.0	1.5
12	1	..	22.3	3.7
	10	..	18.4	0.72
	21	..	11.0	2.3

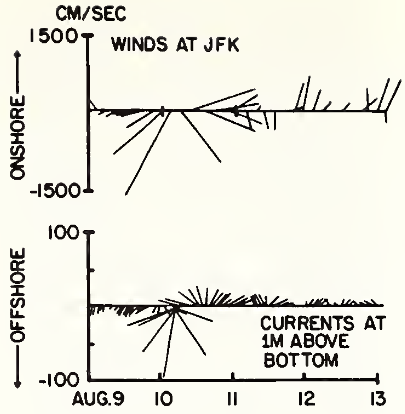

Figure 4. Current velocity at 1 m above bottom from NOAA-AOML mooring LT-4C about 50 km east of apex (G. Han, 1977, personal commun.) compared with wind velocity records taken at Kennedy airport for period August 8–13, 1976 (D. Mayer, 1977, personal commun.).

would be to increase the near-bottom concentration maximum until continued wave turbulence breaks down the thermocline, which would then allow surface-to-bottom mixing of resuspended particles. This near-bottom maximum is often referred to as the "shelf nepheloid layer" by analogy with its deep-water counterpart (Eittreim and others, 1969) and is seen over many parts of the continental shelf (Drake, 1976). Since particles within this layer are held in suspension by the balance between particle-fall velocity and vertical turbulence, a decrease in concentration generally follows a decrease in wave surge turbulence. The fall velocity of particles in a turbulent fluid and the turbulence levels created by wave surge are not well known, but a crude estimate can be made for the clearing time of a nepheloid layer created by intense wave surge and which consists mainly of resuspended bottom sediments. Using as parameters a presumed 10-m thickness for the subthermocline nepheloid layer and the still-water Stoke's fall velocities of 0.1 to 1.0 cm/s for quartz spheres with diameters typical of sediments in the New York Bight apex (20 to 120 μm; Freeland and others, 1976), we arrive at an estimate of about 2 hr for redeposition of the >20-μm particles in the nepheloid layer. Thus, relatively rapid deposition of most resuspended bottom sediments would occur within hours after dissipation of storm-induced wave turbulence within the bottom layer, and only very small particles or those with densities lower than quartz would remain in suspension. Microscopic examination of the particles in the filtered sea-water samples, and rough estimates of their grain sizes, tend to confirm that near-bottom suspended matter is fine-grained (<50 μm) and consists primarily of low-density biogenic material, as has been previously reported in this area (Drake, 1977; Nelsen, 1977).

There are factors other than storm resuspension that may be responsible for greater or less than normal suspended loads in the apex waters. Some of these factors include changes in primary productivity, estuarine suspended-matter discharge, offshore dumping, and regional-scale advection of water masses. Because precipitation in the Hudson watershed was low, changes in estuarine discharge were small after Hurricane Belle (Bowman, 1976; see Drake, 1972, and Schubel, 1974, for examples of the effects of higher than normal estuarine-riverine discharge on shelf suspended loads). Productivity changes were presumed negligible; therefore, advective transport is considered significant in the case of Hurricane Belle's occurrence in the bight apex. In this case, set-up of the continental-shelf water offshore in response to the westerly winds may have forced a compensatory shoreward bottom flow of relatively clear water to displace the turbid near-bottom waters caused by Belle. Shoreward bottom flows have been previously observed or inferred in response to westerly winds within the inner bight and apex (Charnell and Mayer, 1975). Suspended-matter concentrations associated with these flows were low, typically <1.0 mg/l, compared to inner-shelf concentrations of ≥1.0 mg/l (Drake, 1977; Terry Nelsen, 1977, personal commun.). Such flows typically lag the meteorological forcing by as much as 18 hr. Thus, advective replacement of inner-shelf bottom waters high in particle concentration by offshore waters typically lower in particle concentration may in part account for the relative "normality" of the suspended load three days after Hurricane Belle.

SUMMARY

Comparison of observations reported here with previous observations indicates seasonally dependent differences in the effects of severe storms on the resuspension of bottom materials on the inner shelf. During summer and early fall, the extent of vertical mixing due to storms of short duration is limited to the lower part of the water column by the thermocline, provided that the thermocline is not destroyed, and the horizontal advection of resuspended materials is controlled mainly by adjustments in the regional circulation rather than direct forcing by the wind. During winter and early spring, or at other times when stratification is weak or absent, vertical mixing of resuspended bottom sediments throughout the water column is possible, and the effects of wind forcing can directly drive the flow at all depths. Finally, the strong association of toxic materials and contaminants with suspended matter and the effects of the biogenic fraction of suspended matter on such ecological factors as oxygen demand and primary productivity stress the practical need for a better understanding of the effects of storms on the suspended matter of inner-shelf waters.

REFERENCES CITED

Beardsley, R. C., Boicourt, W. C., and Hansen, D. V., 1976, Physical oceanography of the Middle Atlantic Bight, *in* Gross, M. G., ed., Middle Atlantic continental shelf and the New York Bight, special symposia, Vol. 2: Lawrence, Kansas, Am. Soc. Limnology and Oceanography, p. 20-34.

Bowman, M. J., 1976, Response of the Hudson River plume to Hurricane Belle [abs.]: EOS (Am. Geophys. Union Trans.), v. 57, p. 934.

Charnell, R. L., and Mayer, D. A., 1975, Water movement within the apex of the New York Bight during summer and fall of 1973: Boulder, Colo., NOAA Marine Ecosystems Analysis Program Office, NOAA TM-ERL-MESA-3, 29 p.

Charnell, R. L., Hansen, D. V., and Wicklund, R. I., 1972, The effects of waste disposal in the New York Bight: Final Rept. to U.S. Army Corps Engineers, Nat. Marine Fisheries Service, Sandy Hook Lab., Highlands, N.J., chap. 8.

Drake, D. E., 1972, Sediment transport on the Santa Barbara-Oxnard shelf, Santa Barbara Channel, California, *in* Swift, D.J.P., and others, eds., Shelf sediment transport: Process and pattern: Stroudsburg, Pa., Dowden, Hutchinson, & Ross, p. 307-331.

——1976, Suspended sediment transport and mud deposition on continental shelves, *in* Stanley, D. J., and Swift, D.J.P., eds., Marine sediment transport and environmental management: New York, Wiley-interscience, p. 127-158.

——1977, Suspended particulate matter in the New York Bight apex, fall 1973: Jour. Sed. Petrology, v. 47, p. 209-228.

Eittreim, S., Ewing, M., and Thorndike, E. M., 1969, Suspended matter along the continental margin of the North American Basin: Deep-Sea Research, v. 16, p. 613-624.

Freeland, G. L., Swift, D.J.P., and Stubblefield, W. L., 1976, Surficial sediments of the NOAA-MESA study areas in the New York Bight, *in* Gross, M. G., ed., Middle Atlantic continental shelf and the New York Bight, special symposia, Vol. 2: Lawrence, Kansas, Am. Soc. Limnology and Oceanography, p. 90-101.

Hazelworth, J. B., and others, 1974, New York Bight project, water column sampling cruises #1-5 of the NOAA ship *Ferrel*, August-November, 1973: NOAA MESA Rept. 74-2.

Hazelworth, J. B., and others, 1977, New York Bight project, water column sampling cruises #9-12 of the NOAA ship *Ferrel*, July-November, 1974: NOAA ERL-MESA Data Rept.

Lavelle, J. W., Keller, G. H., and Clarke, T. L., 1975, Possible bottom current response to surface winds in the Hudson shelf channel: Jour. Geophys. Research, v. 80, p. 1953-1956.

Lavelle, J. W., Young, R. A., Swift, D.J.P., and Clarke, T. L., 1977, Temporal variability of inner shelf near-bottom fluid velocity and particulate concentration measurements [abs.]: EOS (Am. Geophys. Union Trans.), v. 58, p. 408.

Nelsen, T. A., 1977, Suspended matter in the New York Bight apex: Observations from April, 1974, through January, 1975: NOAA Tech. Rept., ERL-MESA, NOAA.

Rodolfo, K. S., Buss, B. A., and Pilkey, O. H., 1971, Suspended sediment increase due to Hurricane Gerda in continental shelf waters off Cape Lookout, North Carolina: Jour. Sed. Petrology, v. 41, p. 1121-1125.

Schubel, J. R., 1974, Effects of Agnes on the suspended sediment of the Chesapeake Bay and contiguous shelf waters, *in* Davis, J., ed., Report on the effects of tropical storm Agnes on the Chesapeake Bay estuarine system: Chesapeake Research Consortium Pub. 34, p. B1-B26.

ACKNOWLEDGMENTS

Reviewed by M. Dinkelman. Supported at the Atlantic Oceanographic and Meteorological Laboratories by the Marine Ecosystems Analysis Project (MESA) of the National Oceanic and Atmospheric Administration. The R/V *Onrust* was made available by the Marine Sciences Research Center (MSRC) at the State University of New York, and work at sea was done jointly with M. Bowman and others in the scientific party from MSRC. I thank C. Belgodere for assistance at sea, J. Proni for making the XBT system available, and G. Han and D. Mayer for the use of unpublished wind and current data. J. W. Lavelle, D.J.P. Swift, and G. Han critically read an earlier version of the manuscript.

MANUSCRIPT RECEIVED NOV. 7, 1977
MANUSCRIPT ACCEPTED FEB. 27, 1978

Geological Society of America Bulletin 89, 663-672.

Erosion of fine-grained marine sediments: Sea-floor and laboratory experiments

ROBERT A. YOUNG[*] *Massachusetts Institute of Technology–Woods Hole Oceanographic Institution Joint Program in Oceanography, Woods Hole, Massachusetts 02543*
JOHN B. SOUTHARD *Department of Earth and Planetary Sciences, Massachusetts Institute of Technology, Cambridge, Massachusetts 02139*

ABSTRACT

Estimates of threshold erosion velocities have been obtained in the field and in the laboratory for marine mud relatively rich in organic matter and having an active infauna. A sea-floor flume was used to erode undisturbed sediments on the sea floor, and a laboratory flume was used to study the effects of sampling, redeposition, bioturbation, organic-matter content, and compaction time on erosion resistance.

Critical shear velocity, u_{*c}, for erosion of muds in situ ranged from 0.32 to 0.84 cm/s, and u_{*c} was apparently independent of season or bulk physical properties. Erosion was often but not always initiated in biogenically disturbed parts of the bed. Lee drifts around small bed-roughness elements were the most common constructional bedforms observed during the sea-floor experiments, and narrow and shallow longitudinal furrows were the most commonly observed erosional features. Tidal u_{*c} values measured at the field site were of the same magnitude as the u_{*c} values measured with the sea-floor flume.

Mean u_{*c} for muds redeposited and bioturbated for 1 to 60 days in the laboratory flume (0.92 cm/s) was greater by a factor of two than mean u_{*c} for muds eroded in situ (0.45 cm/s). As bioturbation time in the laboratory increased, u_{*c} decreased. Increases in sediment organic content were found to increase u_{*c} systematically in flat, nonbioturbated laboratory beds.

INTRODUCTION

Muddy marine sediments exhibit a resistance to erosion in excess of that which would be expected from considerations of the size and weight of the constituent sediment particles alone. This additional erosion resistance is mainly the result of both interparticle surface attractions induced by flocculation in sea water and organic binding. The additional binding force in excess of the weight force that must be overcome to initiate erosion is called cohesion. Thus, simple relationships between grain size and threshold erosion velocity, similar to the one put forth by Shields (1936) for coarser, noncohesive sediments, are not directly applicable to muddy sediments.

Many studies on erosion of muds have been made in the laboratory on fresh-water mud deposits (Graf, 1971, chap. 12; Migniot, 1968; Einsele and others, 1974). Since salt-water flocculation strongly affects the behavior of muds during deposition and erosion, experiments made with fresh water are of uncertain applicability to studies of the marine environment.

Cohesion and erosion resistance in muds are complex functions of a number of interrelated physical properties such as water content, mineral and organic composition, grain size, depositional history, and fabric, as well as other factors which are largely obscure (van Olphen, 1963, chap. 12). For example, fabric, the spatial arrangement of particles within the bed, is a bed property that, like water content, depends on grain size, mineral and organic composition, and depositional history. The different types of cohesive bonds formed by the particles result in a characteristic resistance to erosion or cohesion. Fabrics characteristic of naturally deposited marine muds are typically not reproducible upon redeposition or remolding in the laboratory (Collins and McGown, 1974). Thus, unnoticed and subtle disturbances during sampling in the field or during preparation in the laboratory of the complexly interrelated physical properties affecting sediment fabric may have a significant but unknown effect on the outcome of laboratory erosion experiments.

Other workers (Partheniades, 1965; Postma, 1962, 1967; Southard and others, 1971; MacIlvaine, 1973; Lonsdale and Southard, 1974) have investigated the effects of water content changes on threshold erosion velocity of fine sediments. Their results show a generally inverse relationship between water content and threshold erosion velocity which is internally consistent, although absolute values of threshold velocity corresponding to a particular water content vary between workers. Explanations for these variations are probably related to variations in the physical properties that have to do with cohesion.

Using the results mentioned above and other laboratory work (partially summarized in Graf, 1971, chap. 8, 12), semiquantitative models have been constructed describing the transportation (Dobbins, 1943), deposition (Einstein and Krone, 1962; McCave, 1970; McCave and Swift, 1976), and erosion (Migniot, 1968; Odd and Owen, 1972) of muds. One assumption that must be made in using the models of these workers is that behavior of muds in the laboratory is representative of their behavior in situ.

In order to test this assumption, we have investigated the erosional resistance and behavior of undisturbed muddy sediments on the sea floor for comparison with the erosional resistance and behavior of similar sediments after redeposition in the laboratory. To accomplish this, a sea-floor flume (Seaflume) has been used to obtain estimates of the critical shear stress, τ_0, for erosion of undis-

---

[*] Present address: NOAA, Atlantic Oceanographic and Meteorological Laboratories, Maine Geology and Geophysics Laboratory, 15 Rickenbacker Causeway, Miami, Florida 33149.

Geological Society of American Bulletin, v. 89, p. 663–672, 8 figs., 3 tables, May 1978, Doc. no. 80503.

turbed marine muds. Redeposited sediments were eroded in a laboratory flume to determine the effects of sampling on resistance to erosion and to conduct controlled laboratory experiments on the influence of biological reworking, concentration of organic material, and compaction time on resistance to erosion.

FIELD EXPERIMENTS

Methods

Sea-floor flumes have been used previously to obtain rough estimates of erosion velocities or erosion rates for shallow-water calcereous sands, estuarine muds, and coastal muds (Neumann and others, 1970; Peirce and others, 1970; Southern California Coastal Water Research Project, 1975). Unlike other sea-going flumes, Seaflume has been designed to be self-contained, to function automatically at any depth, and to produce a controllable and well-developed uniform flow over the undisturbed sea floor. Values of erosional velocities obtained with Seaflume are therefore likely to yield the best available estimates of bottom current velocities required to erode the undisturbed sediments.

Description of Seaflume

A detailed description of Seaflume is given in Young (1977). Seaflume is a rectangular open-bottomed duct, 4.1 m long, with a gently contracting entrance section and an observation section 0.6 m wide by 0.15 m high (Fig. 1). The entrance section smooths out entrance effects and accelerates the flow while keeping it below the threshold for erosion. At the end of the straight observation section, the flow is drawn through a slowly opening by-pass (panel) valve (driven by a small DC motor). The flow in the duct is produced by a battery-powered propeller pump running at constant speed. Pump, panel valve, and other systems are turned on when a bottom-contact switch activates a series of relays.

Flow velocity inside the duct increases continuously with time from zero to a maximum value along the centerline of about 50 cm/s. The opening rate of the panel valve is such that maximum flow is reached after about 30 min. Because of the slow rate of increase of flow in the duct, flow is considered steady, an important assumption in choosing the methods of calculating τ_0, as discussed below.

Erosion of a 15-cm^2 area of the sea floor in the straight observation section, and midchannel flow velocity below the point of observation (see below), are recorded photographically about every 15 s with a 35-mm Edgerton, Germerhausen and Grier (EGG) camera mounted above the top of the duct. The sea floor is lighted from the side at a low angle by a 100 W-s EGG strobe. Objects as small as about 500 μm can be resolved on the resulting photographic prints.

The size of the individual aggregates first removed is probably less than the resolution of the photographs. Thus, the true initiation of motion could not be observed. However, if the average aggregate size is on the order of ten times the average particle size ($\sim$ 10 μm) or $\sim$ 100 μm, then photographic resolution of modifications of the bed surface can be discerned after five or more aggregates are eroded (or deposited). Criteria used for selecting a threshold velocity involved examining the photographs for first signs of bed modification of the scale noted above.

Flow Measurements and Calculation of Bed Shear Stress

Flow velocity is measured at a single point in the upper half of the channel by the horizontal deflection of a ballasted nylon sphere (1.6 cm diameter) suspended on a thin nylon line about 7.5 cm long fastened to the top of the duct under the camera. Velocity profiles observed in a scale-model study of flow in the flume duct (Young, 1975) indicate that the turbulent boundary layer is essentially fully developed at the point of observation, as should be expected because the ratio of flow half-depth to distance between flume entrance and observation point is $\sim$ 1/30. Horizontal deflections of the sphere measured by photography are compared to a calibration curve obtained in laboratory flume runs with similar flow dimensions (Young, 1977, Fig. 2). Taking into account measurement and calibration errors, velocity can be estimated to within ±10% by this method.

No correction was made for possible curvature in the tethering line of the sphere in the calculation of z. However, this correction has a secondary effect, because z enters into the calculation of τ_0 to the one-fourth power.

Estimates of bed shear stress, τ_0, were calculated from Prandtl's seventh-power law (Prandtl and Tietjens, 1934, p. 70) for flow in a duct by the relation

$$\tau_0 = 0.0228 \rho \left(\frac{u^7 \nu}{z} \right)^{1/4} , \qquad (1)$$

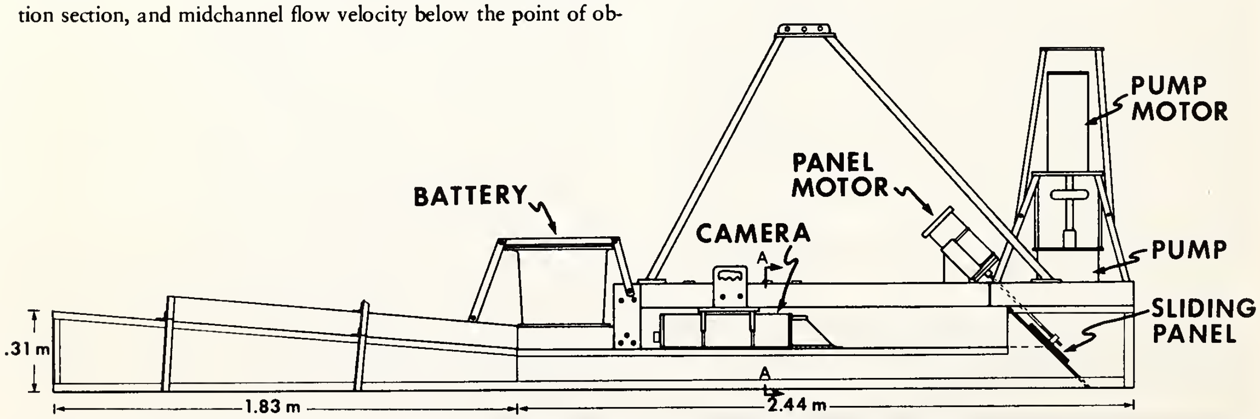

Figure 1. Side view of Seaflume. Small flanges along bottom edges of side walls and solid bottom under pump chamber create sufficient bearing surface to prevent flume from sinking into most marine muds. Strobe light source (not shown) is mounted on opposite side of flume.

where ρ is fluid density, ν is kinematic viscosity, and u is velocity at a distance z from the wall. The distance, z, is calculated from the simple relationship z^2 = (sphere string length)^2 − (horizontal deflection distance)^2. Errors in estimating u can lead to a maximum error of ±17% in estimating τ_0 in the range of velocities encountered during the experiments. However, it is difficult to evaluate precisely the accuracy of τ_0 obtained in this way for several reasons. First, the boundary layers developed in the duct flow are generated along surfaces composed of differing roughness, the duct top being smooth plastic while the duct bottom is muddy sediment. Young (1977) has noted that the shear velocity, $u_* = (\tau_0/\rho)^{\frac{1}{2}}$, may be underestimated by no more than 12% due to this effect, which is comparable to the limits of accuracy for measuring the flow velocity.

More fundamentally, the boundary layer developed over the sediment surface may be transitional to hydrodynamically rough rather than hydrodynamically smooth, as assumed in use of equation 1, thereby causing underestimation of τ_0. This effect should not be substantial, however, both because the bottom photographs show a largely smooth bed, with only scattered roughness elements, and because resistance in rough flow is not greatly different from that in smooth flow at the mean-flow Reynolds numbers of $\sim 5 \times 10^3$ prevailing at erosional velocities in the Seaflume experiments. Thus, use of the smooth-flow equation 1 should provide reasonable estimates of τ_0 in the duct.

Threshold flume velocities, u_c, obtained during the Seaflume experiments were used to calculate τ_0 by equation 1, which was used in turn to calculate threshold shear velocity, u_{*c}. Assuming a uniform flow over a smooth bottom, and using u_{*c} obtained from the Seaflume experiments, estimates of u_{100}, the threshold erosion velocity at 100 cm above the bed that would be expected in a benthic boundary layer, were made from the well-known law of the wall for velocity distribution over a smooth boundary in uniform turbulent boundary-layer flow (Daily and Harleman, 1966, p. 234),

$$u/u_{*c} = 5.6 \log_{10} \left(\frac{u_{*c} z}{\nu} \right) + 4.9, \qquad (2)$$

where $u = u_{100}$ and z = 100 cm. Considering the magnitude of the errors in measuring u_c as previously discussed, the actual value of u_{100} is estimated to be within ±10% of its calculated value.

Field Procedures

Initially, it was necessary to operate the panel-valve motor on 120-v AC power, so a direct connection with ship power was required. This necessitated hand-tending the winch wire and electrical cable attached to the flume after first anchoring the ship and lowering the flume to the sea floor. Observations made by SCUBA divers during these experiments indicate that movements of the ship were effectively decoupled from the flume. In later experiments, the AC motor was replaced by a small DC motor powered by the battery on the flume (see Fig. 1). For these later experiments, the flume was lowered to the sea floor with a nylon rope, and the free end of the rope was tied to a small float and cast free, ensuring complete decoupling from surface motions. Duration of a typical experiment was 40 to 50 min.

Study Area

The sea-floor erosion experiments were carried out in Buzzards Bay, a marine embayment on the west coast of Cape Cod, Massachusetts, which is floored by muddy sediments in its central regions. The muddy sediments are relatively rich in organic detritus, and an active deposit-feeding infauna (mainly polychaetes and small burrowing bivalves) is present during much of the year (Sanders, 1958, 1960). The burrowing, crawling, and mound-building activities of the infauna keep the sediment-water interface loose and uncompacted (Rhoads and Young, 1970). During some parts of the summer and fall, as much as 20% by volume of the surface sediments may consist of sand-sized fecal pellets of relatively low density which in some instances can be easily resuspended by low-velocity bottom currents (Young, 1971; Rhoads, 1973). A near-bottom turbid layer is often present over the muddy sediments, especially during the summer, when benthic activity peaks and apparently enhances resuspension by tidal bottom currents (Rhoads, 1973). Organic secretions by infaunal and epifaunal organisms also serve to bind the muddy sediments in some instances, but the relative effects of pelletization versus binding on sediment strength and erosion resistance are poorly understood (Rowe, 1974).

All experiments described here were performed at station K in Buzzards Bay (lat 41°32′10″N, long 70°44′55″W, water depth 16 m; see Fig. 2) because (1) the sediment and fauna at this station have been studied previously (see references cited above), (2) replicate experiments at the same site would allow comparison of both seasonal and small spatial differences in erosion, and (3) station K sediments and fauna are typical of the muddy areas in Buzzards Bay and may be typical of other shallow-marine environments.

Average values of some physical properties from three groups of cores taken by SCUBA divers at station K are given in Table 1. Two groups were taken randomly within squares 1 m and 10 m on a side, while a third group was sampled at 5-m intervals along a 100-m transect. Most of the particles are < 16 μm in size, and the sediment can be described as a clayey-sandy silt. The fine silt and clay fraction was dominated by the clay minerals kaolinite and il-

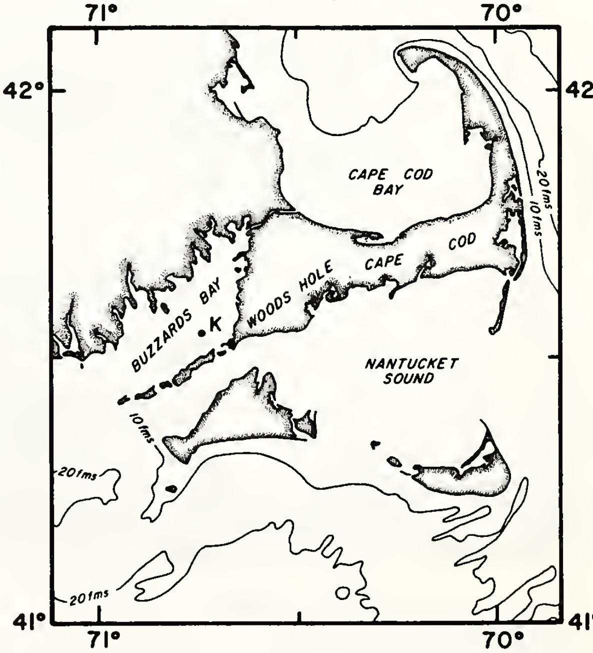

Figure 2. Location of field experiments in Buzzards Bay, Massachusetts.

TABLE 1. PHYSICAL PROPERTIES OF SEDIMENTS AT STATION K

Cruise, date	Sampling scheme	Depth interval (cm)	Water content (wt %)	Grain size (wt %)				Organic content (% carbon)
				>62 μm	62–16 μm	16–2 μm	<2 μm	
BBPS 1, 11/6/72	7 cores from 1-m square	0.5–2.0 5.5–7.5	56 ± 3 55 ± 1	14 ± 3 11 ± 9	77 ± 5* 76 ± 10*		9 ± 4 13 ± 8	2.3 ± 0.2 2.4 ± 0.2
BBPS 2, 1/12/73	5 cores from 10-m square	0.5–1.5 5.0–6.0	55 ± 1 55 ± 2	13 ± 3 6 ± 2	71 ± 2* 74 ± 0*		16 ± 2 19 ± 2	2.3 ± 0.1 2.3 ± 0.2
AST 74-4, 3/1/74	20 cores from 100-m transect	0.0–1.0	62 ± 2	7 ± 2	27 ± 6	20 ± 2	46 ± 5	3.2 ± 1.3
Sanders (1958)	Anchor dredge	Surface	..	7	28	48	17	..

* In 2–62 μm fraction.

lite, with substantial quartz and some feldspar. Little variation was observed in the water content, organic carbon content, grain size, and mineralogy within the first 5 to 7 cm below the water-sediment interface (see Table 1).

Results of Seaflume Runs

Values of u_c, u_{*c}, and u_{100} for the seven erosion experiments performed at station K are given in Table 2. Biogenic tracks, burrows, and fecal mounds were present at the beginning of some experiments, and on several occasions epibenthic invertebrates (probably snails or hermit crabs) created fresh trails in the field of view of the camera during the first few minutes of the experiment before the flow began to erode the bottom sediments. Such occurrences are fortunate from our point of view, because they allow comparisons of the erosion resistance of a freshly bioturbated part of the bed with the surrounding undisturbed sediments. Biogenic features were less common during the fall experiments than during the summer and winter experiments.

TABLE 2. RESULTS OF SEAFLUME EROSION EXPERIMENTS AT STATION K

Cruise, date	Experiment	u_c (cm/s)	τ_0 dyne/cm^2	u_{*c} (cm/s)	u_{100} (cm/s)
AST 74-17, 8/15/74	2*† 2‡	6.5 8.5	0.12 0.20	0.35 0.45	8.6 11.3
AST 74-18, 8/20/74	3*† 3‡	6.5 9.5	0.12 0.24	0.35 0.49	8.6 12.4
AST 74-19, 8/30/74	4‡	7.5	0.16	0.40	9.9
AST 74-21, 9/19/74	6‡	11.0	0.31	0.56	14.3
AST 74-23, 10/30/74	7‡	6.0	0.10	0.32	7.7
AST 74-24, 10/30/74	8‡	17.0	0.71	0.84	22.3
AST 75-1, 2/4/75	9‡	6.0	0.10	0.32	7.5
Mean values			0.23	0.45	11.3

Note: u_c = threshold flume erosion velocity; τ_0 = threshold shear stress; u_{*c} = threshold shear velocity; u_{100} = threshold velocity at 100 cm above bed.

* Erosion around biogenic tracks and trails.

† Used in calculation of mean values.

‡ Erosion of flat parts of bed.

Examples of the pre-erosional and post-erosional appearance of the sea floor during summer and winter experiments are shown in Figures 3 and 4. Observations made by SCUBA divers during several experiments and from the close-up photography indicates that the principal mode of erosion was by removal of small sediment aggregates, even at high velocities. The effects of erosion first appeared around biogenic mounds or shell fragments, where more intense turbulence was generated. Small sediment drifts formed first in the lee of the mounds and shell fragments, but as the velocity continued to increase, the material in the mounds was gradually eroded, as were the lee-drift deposits. Concurrent with the formation of lee drifts at low velocities was the erosion of small longitudinal furrows, which continued to erode as velocities increased. In several experiments, particularly those made later in the year, erosion at high velocities created a lag deposit, apparently consisting of shell fragments.

Estimates of u_* produced by tidal bottom currents (known from work of investigators cited in Study Area, above, to resuspend Buzzards Bay muds) were made from a series of current-velocity profiles obtained during a complete tidal cycle at station K (for details, see Young, 1975, chap. II). Velocities were measured at four or more points within 2 m of the bed using a Bendix direct-reading Savonius rotor current meter. Tidal u_* values calculated from four of these profiles averaged about 0.25 cm/s, ranging from 0.16 to 0.45 cm/s. The overlap between tidal u_* values and values of u_{*c} obtained during Seaflume experiments (see Table 2 and following discussion) tends to support our confidence in the representativeness of the u_{*c} measurements obtainable with Seaflume.

LABORATORY EXPERIMENTS

Methods

A tilting recirculating sea-water flume, ~25 m long by 0.61 m wide, was used for the laboratory experiments. Surface flow velocity, u_s, was measured with small floats after adjusting the slope of the flume to ensure uniform flow depth.

The effects of duration and mode of biologic reworking on erosion resistance were investigated by placing trays filled with sediment collected during early summer at the field site into a well 0.5 m^2 and 0.1 m deep in the flume bottom. After the sediment surface was smoothed by hand to make it roughly coplanar with the flume bottom, the benthic organisms in the sediment were allowed to rework the sediment for periods of several days to two months, at which time flow was gradually increased until erosion was observed.

The relationship between concentration of organic matter and resistance to erosion was investigated by using a special sediment preparation technique designed to vary systematically the concentration of organic matter. A sediment sample from the field site was first treated with 30% hydrogen peroxide (H_2O_2) to remove organic matter, and then mixed in various proportions with untreated sediments from the same site to create a series of six sediment mixtures, the organic fraction of which was composed of a naturally occurring assemblage of organic detritus. It was thought that this technique would create sediment mixtures most representative of sediments with similar organic compositions and concentrations on the sea floor.

A section of the flume channel 2 m long was walled off with bulkheads, and the sediment mixtures were deposited (during a standard period of 15 to 17 hr) from flowing suspensions onto a false bottom built into the well in the channel bottom. After siphoning away sediment deposited on the surrounding fixed false bottom, a movable 15-cm^2 false bottom was lowered gently to make the surface of the flat sediment bed remaining on it coplanar with the fixed false bottom. After the bulkheads were removed, flow was gradually increased until erosion was observed, then stopped after recording critical velocity and flow depth at the initiation of erosion. A sediment sample of 1 to 2 g was siphoned off the bed, and the concentration of organic carbon was determined on a LECO carbon analyzer.

Flow Observations and Calculation of Bed Shear Stress

Threshold erosion conditions during the laboratory experiments were determined by visual observation supported by high-resolution photography. Although it would have been desirable to calculate u_{*c} for the laboratory experiments by the same method used in the field experiments, equation 1 applies only to closed conduits. Therefore, a relationship was required that would give τ_0 in terms of u_s. Such a relationship has been previously given by

TABLE 3. RESULTS OF LABORATORY EROSION EXPERIMENTS ON BUZZARDS BAY MUDS

Run	h (cm)	u_s (cm/s)	u_* (cm/s)	u_{100} (cm/s)	Days of reworking	Total organic carbon (wt %)
Bioturbation						
1	6.51	11.0	0.51	13.1	61	~2.0
11	5.52	25.0	1.08	21.7	5	~2.0
10	4.45	27.5	1.18	32.8	1	~2.0
Flat beds						
2	7.47	31.4	1.29	36.1	..	2.0
7	7.0	30.5	1.26	35.2	..	1.84
6	7.0	23.5	1.00	27.4	..	1.62
8	6.20	24.9	1.06	29.1	..	1.28
5	5.89	20.2	0.89	24.1	..	1.02
4	6.25	19.0	0.83	22.3	..	0.82

Note: h = flow depth; u_s = threshold surface velocity; u_* = estimated threshold shear velocity; u_{100} = estimated velocity 100 cm above bed.

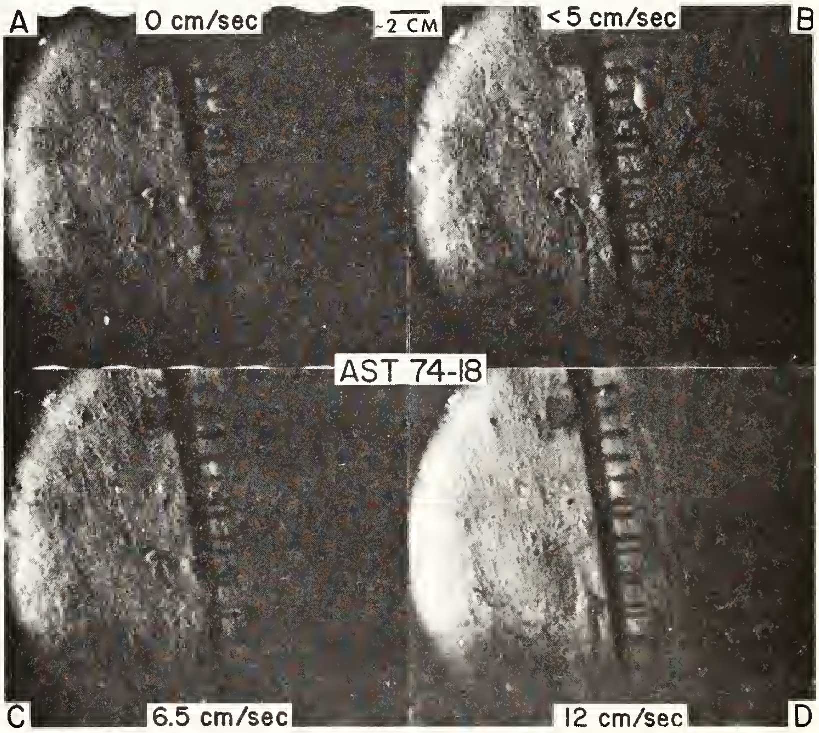

Figure 3. Seaflume experiment 3, a summer experiment. Velocities shown are those determined by sphere flow meter. Flow is from top to bottom in all photographs. A, Bed is initially covered with biogenic mounds, tracks, and burrows; B, snail(?) crawling upstream creates new trail while flow velocity is < 5 cm/s; C, at u_c = 6.5 cm/s, smoothing of new trail is noticed while other parts of bed begin to erode at slightly higher velocities (u_c = 9.5 cm/s); D, small lee drifts then occur behind more resistant parts of bed surface.

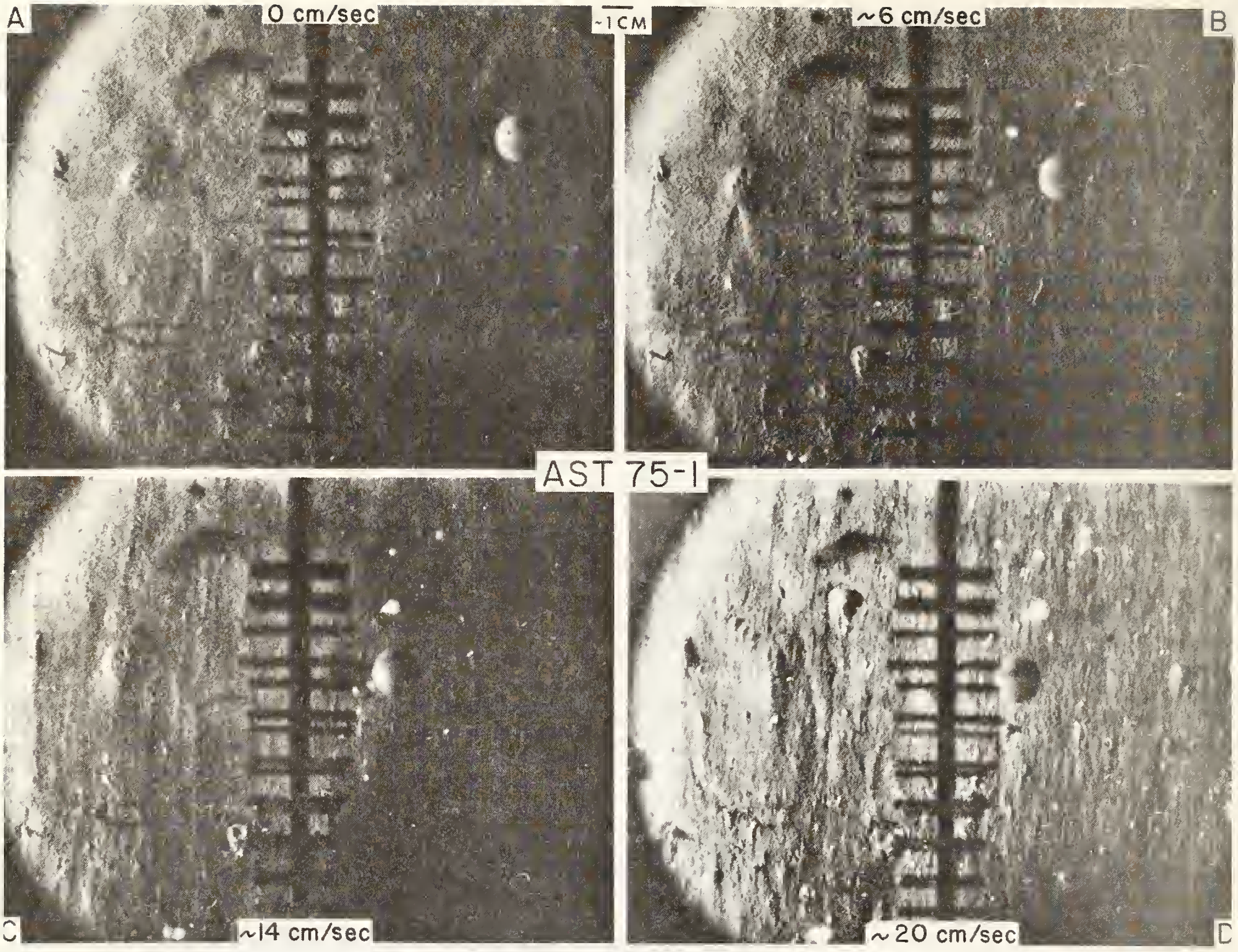

Figure 4. Seaflume experiment 9, a winter experiment. Ballast in sphere flow meter fell out during this experiment; velocities shown in A through D were estimated from a least-squares fit between velocity and time after initiation of flow measured during previous experiments. Fewer biogenic features were present initially on bed (A) than during summer and fall experiments. General erosion of all photographically resolvable portions of bed occurred (B) at relatively low velocity ($u_c = 6.0$ cm/s). Continued erosion at higher velocities first built additional lee drifts on old bed surface (C), then began to deeply dissect bed, exposing shell fragments (D).

Southard and others (1971, p. 5908), although the constant in their equation 3 was inadvertently given the incorrect sign. The correct relationship between u_s and u_* is given here in Table 3 and its development shown in Appendix 1.

Results

Values of u_{*c} for the reworked beds are given in Table 3. The surface of the 61-day bed (Fig. 5, A) was covered with tracks, burrows, and fecal pellets and strongly resembled the bioturbated sea floor of Buzzards Bay (compare Fig. 5, A with Fig. 3). Erosion was initiated at many places on the bed surface. As the flow increased, incised biogenic trails were first filled with aggregates of loose sediment being transported as bed load and then were smoothed as the surrounding sediment was eroded (Fig. 5, B). Bedload transport was observed at all stages of transport and occurred as elongated streamers of individual sediment aggregates moving intermittently and parallel to the flow. Longitudinal erosional furrows were created, and lee drifts were formed behind resistant elements on the bed (Fig. 5, B).

The surface of the five-day bed is shown in Figure 6, A. Except for a few tracks and fecal mounds, there was little over evidence of biogenic reworking on the pre-erosional surfaces of the 1-day and 5-day beds. Erosion was initiated at localized areas, sometimes at biogenic trails, as the removal of an almost uniformly thick surface layer (Fig. 6, B). Paradoxically, the subsurface sediment appeared less compact than the surface layer. Formation of erosional furrows (except those caused by leading-edge disturbances; see Fig. 5, B) or less-drift deposits was not observed.

Results of the runs on flat beds with varying concentrations of organic matter are summarized in Table 3 and in Figure 7, and the appearance of a typical flat bed before and after erosion is shown in Figure 8. In several runs, the small gap at the leading edge of the flat bed caused erosion to begin there before general erosion began at other parts of the bed. Attention was therefore focused on parts of the bed well downstream of the leading edge in choosing the incipient bed condition for erosion.

Before general erosion began, the flat beds often became roughened with small pits or tool marks from bed-load particles being recirculated in the flume. These disturbances of the bed sur-

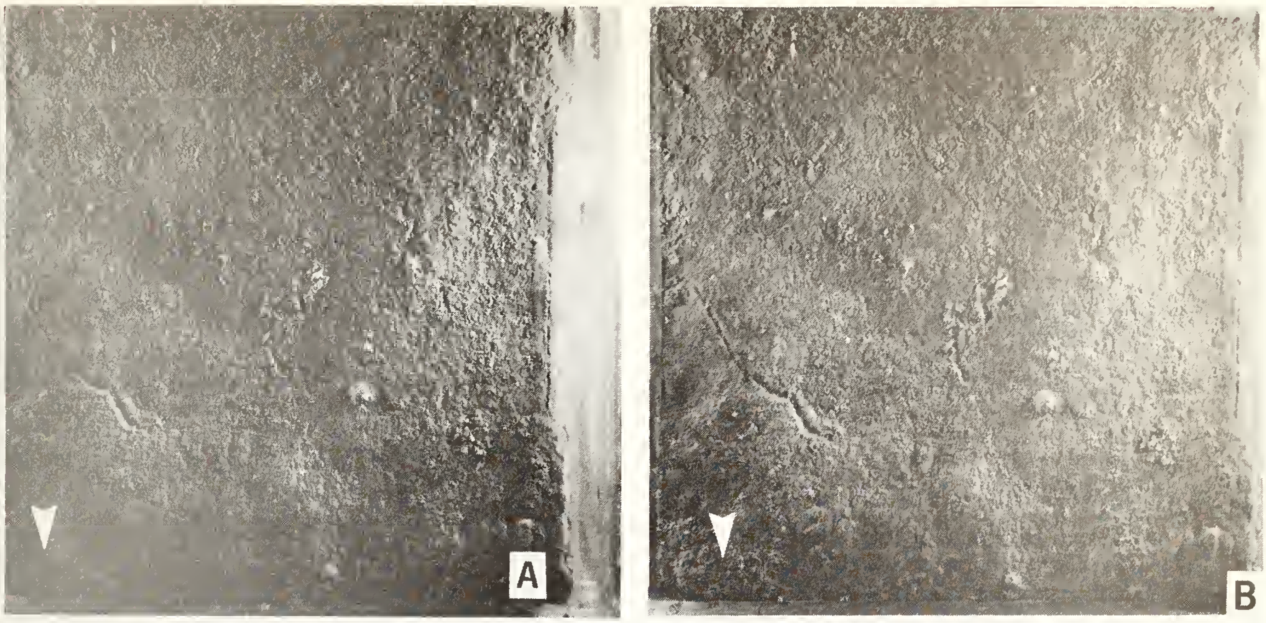

Figure 5. Buzzards Bay muds biogenically reworked for 61 days in laboratory flume. Flow is from top to bottom (see arrow), and bed is 60 cm wide from left to right. A. Before erosion; note fresh trail being created by snail in center of bed and fecal mounds in right center of bed. B. After erosion (u_{*c} = 0.51 cm/s); longitudinal furrows are present, and lee drifts have formed behind erosion-resistant fecal mounds.

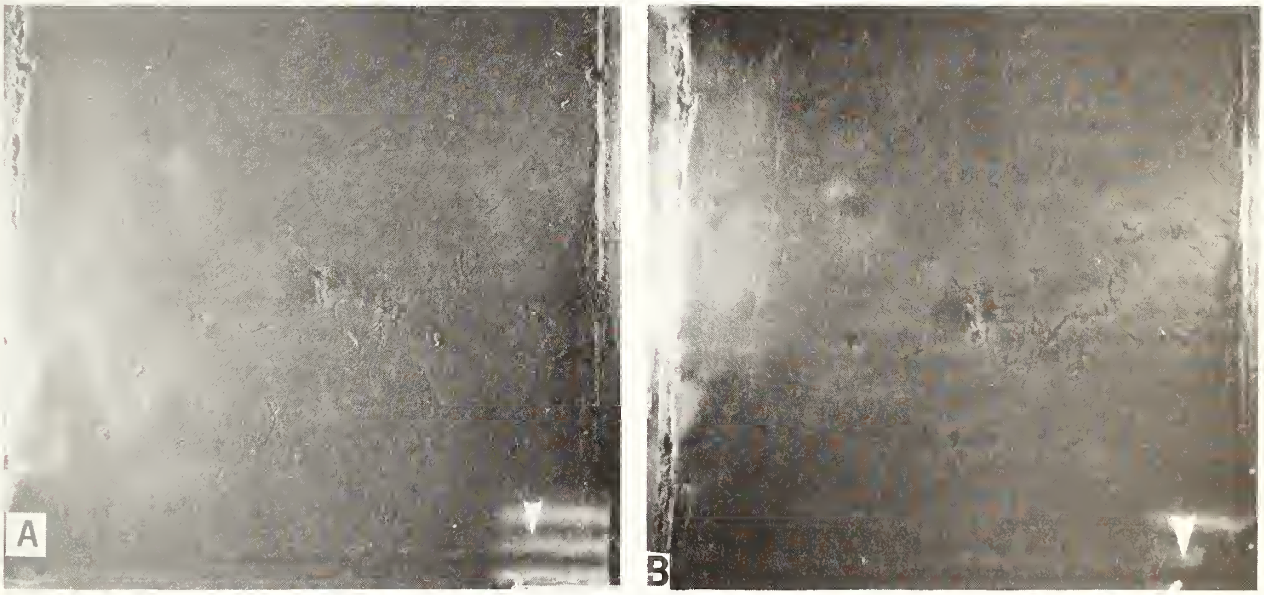

Figure 6. Buzzards Bay muds deposited in laboratory flume and reworked for five days. Flow is from top to bottom (see arrow), and bed is 60 cm across. A. Bed surface at beginning of the experiment. Some biogenic (worm?) trails and several bivalves are present. B. At initiation of erosion, u_{*c} = 1.08 cm/s; eroded jagged areas at leading edge began to erode at $u_* < u_{*c}$. Longitudinal furrows are apparently related to flow disturbances at leading edge, whereas small irregular patches eroded from right center of bed are probably representative of general erosion of bed. Layer being eroded gives appearance of being uniformly thick over its entire extent, whether associated with erosion from leading edge or with erosion of small patches on rest of bed.

face would sometimes become the loci for erosion, but erosion was initiated just as often at sites on the bed that appeared smooth.

DISCUSSION

It seems reasonable to assume that the laboratory biogenic reworking experiments, to a first approximation, are representative of the extremes in biogenic reworking encountered during the field experiments. Other sedimentary properties (such as grain size, mineralogy, organic content, and water content) being similar, we may then determine if there is a significant difference between the means of u_{*c} measured in the laboratory and in the field.

Applying Student's t test (Guttman and Wilks, 1965, p. 168) to the means of the u_{*c} measurements given in Tables 2 and 3 indi-

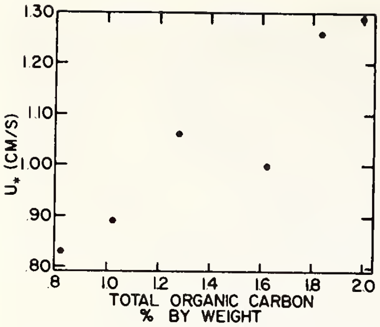

Figure 7. Values of u_{*c} for erosion of flat laboratory beds of Buzzards Bay muds having varying concentrations of organic matter. Here, total organic carbon (percent by weight) is used as measure of concentration of organic matter.

cates that at the 95% level of significance, $\bar{u}_{*c}$ (laboratory) > $\bar{u}_{*c}$ (field). To ensure that the t test applies to this set of measurements requires that the variance, s^2, of the two sets of measurements be equal. The Snedecor F ratio (Guttman and Wilks, 1965, p. 151) was used to verify that at the 95% level of significance, s^2 (laboratory) = s^2 (field).

Since the field experiments were all carried out within 100 m of station K, it is interesting to note that critical u_* values vary by a factor of more than two, apparently independently of seasons. In fact, differences in the value of u_{*c} between Seaflume experiments 7 and 8 (see Tables 2 and 3) were the greatest of any two experiments, yet these two experiments took place on the same day 3 hr apart while the ship remained at anchor. These observations suggest that although seasonal differences may exist in u_{*c}, they may be no greater than differences in u_{*c} expectable between closely spaced parts of the sea floor in Buzzards Bay. The spatial heterogeneity of benthic populations and resulting differences in biologically related physical properties of the sediments are probably responsible for spatial variability of u_{*c}, although these aspects were not investigated during the Seaflume experiments.

Reasons for the differences in the results of the laboratory and field experiments are probably related to laboratory preparation techniques. In the natural environment, current-meter and bottom-camera deployments on the bottom and observations by divers during this and the previous studies discussed above show that benthic and biological activity, wave surge, and tidal currents constantly work together to resuspend sediment and maintain surface layers in a loose, watery, and uncompacted state. During the laboratory reworking experiments, the effects of wave surge and tidal currents were absent, thus allowing the sediment to compact and become more cohesive in those parts of the bed not undergoing biogenic reworking than would ordinarily be the case. For the flat-bed laboratory experiments it was necessary to deposit the beds from flowing dense (> 1,000 mg/l) suspensions, a depositional condition probably not often experienced on the muddy floor of Buzzards Bay. At such high concentrations, important differences must exist in flocculation, aggregation, settling, and bed fabric between the laboratory and sea-floor environments.

The observations made during the reworking experiments would seem to substantiate what has been proposed in previous studies: intensity or extent of bioturbation can be the primary factor in destabilizing muddy sediments on the shallow sea floor and decreasing their resistance to erosion. One could infer from our laboratory data (see Table 3) that as activity of benthic organisms in Buzzards Bay increases from spring to fall, erosion resistance of the sediments should decrease. Conversely, our field experiments suggest that erosion resistance is more strongly influenced by local inhomogeneities in sediment properties than by season or benthic activity. Resolution of this question must await more complete studies of both animal-sediment relationships and threshold velocities.

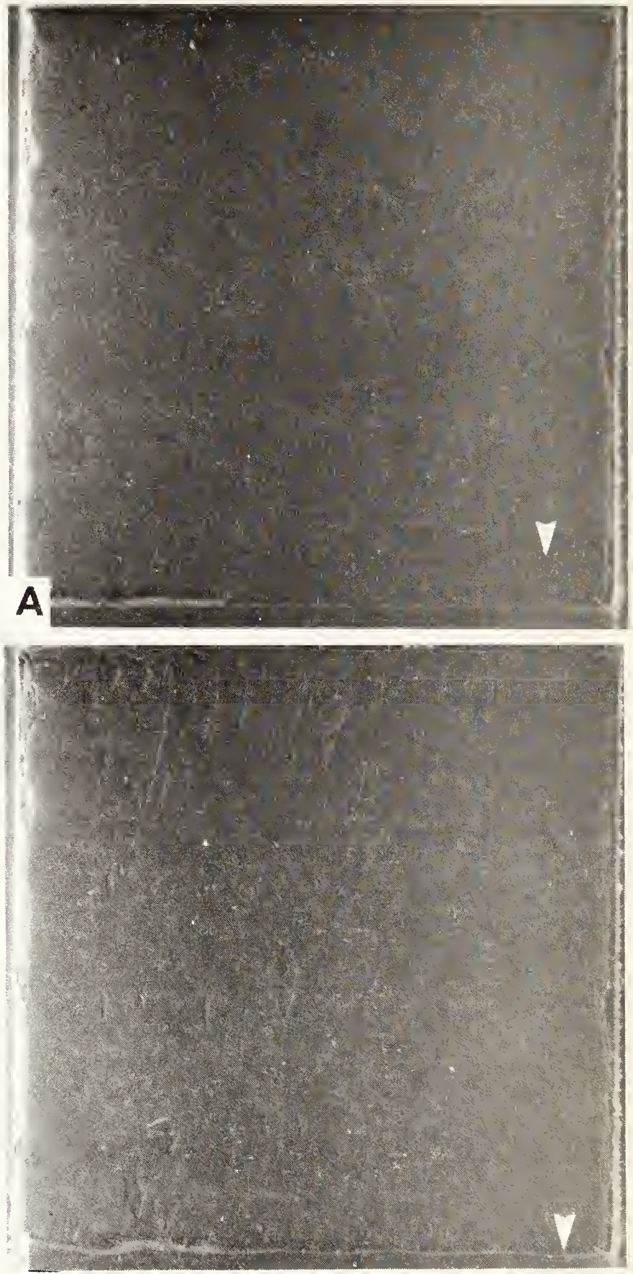

Figure 8. Flat-bed run number 7; Buzzards Bay muds containing 1.84% organic carbon. Bed is featureless before erosion (A). Small gap at leading edge of bed causes erosion to begin there at $u_* < u_{*c} = 1.26$ cm/s. At $u_* > u_{*c}$ thin layers of seemingly uniform texture are removed (B).

From the experiments on the influence of concentration of organic matter it was shown that u_{*c} systematically decreases with decreasing organic matter. In deep-sea muds, organic content is typically much lower than in our sediments, implying that u_{*c}

should also be low. We speculate that this need not be the case, because the effects of compaction and incipient cementation in the deep sea simultaneously increase the cohesiveness and hence erosion resistance of the sediments. However, where biological processes are involved, our experience during this study suggests that extrapolations from specific to general cases must be considered tentative at best.

The range of laboratory threshold u_* values for unreworked beds reported here (0.8 to 1.3 cm/s) is generally greater than values determined for similar estuarine and shelf muds as reported by others (Partheniades, 1965; Migniot, 1968). Real differences in erosion resistance may exist among these muds, but these differences are probably secondary compared to the differences created by the differing and highly specialized preparation techniques used by each worker and also by the inconsistencies between workers in establishing a uniform definition for the threshold condition for erosion. For example, in this study, modifications of the bed surface exceeding 500 μm in length have been used to establish the incipient condition for erosion, whereas in other studies, increases in suspended-matter concentration as a function of u_* have been extrapolated backward to zero concentration to establish threshold u_*. It would seem that an attempt should be made to define "threshold erosion velocity" in a more uniform and perhaps more rigorous manner.

One surprising result of our experiments is that u_{*c} for the bioturbated Buzzards Bay muds is less, rather than more, than u_{*c} for noncohesive fine sands. This result is contrary to the inferences and speculations of previous workers, such as Hjulström (1955) and Sundborg (1956), who predicted that u_{*c} (mud) $>$ u_{*c} (fine sand) for partially consolidated muds. This result may be a consequence of the lower bulk density of biologically aggregated sediments.

Perhaps the most important of our conclusions is that there can be significant differences between threshold erosion velocities measured in the laboratory and in the field. These differences are probably related to changes in sediment cohesion caused by biological activity and also by mechanical reworking. In addition, we have observed that erosion velocities of areas on the sea floor only meters apart can vary by as much as a factor of two. Since bulk physical properties of the sediments apparently vary only slightly on a scale of meters (see Table 1), differences in erosion resistance must be related to more subtle and as yet unmeasured physical or biochemical parameters.

ACKNOWLEDGMENTS

We thank D. A. Ross for advice and assistance given during the study. Discussions with C. D. Hollister were also helpful, as was critical review of an earlier version of the manuscript by J. W. Lavelle. Technical assistance was rendered by W. Gardner, S. Briggs, R. Flood, M. McCamus, R. Nowak, and S. Shor. G. Rowe, C. H. Clifford, and T. Stetson assisted in diving operations. The expert seamanship of R. Coburn, mate on the R/V *Asterias*, contributed to the success of the field work. This work was supported by Office of Naval Research Contracts NONR 4029 (00) NR 260-101 to the Woods Hole Oceanographic Institution and N00014-75-C-0291 to the Massachusetts Institute of Technology, and under National Oceanic and Atmospheric Administration contract 04-5-022-7 to MIT. Early development of the Seaflume was funded through the Ocean Industries Program at Woods Hole and through a fellowship from the Education Office there.

APPENDIX 1. Method of Determining u_* from u_s

The resistance formula for smooth-walled duct flow (Rouse, 1946, p. 214) is

$$\frac{1}{\sqrt{f}} = 2.03 \log_{10} \left(R_D \sqrt{f} \right) - 0.47, \tag{1}$$

where f is the Darcy-Wiesbach friction factor, $R_D = 2\,B\bar{u}/\nu$ is the duct Reynolds number, B is duct height, $\bar{u}$ is mean flow velocity, and ν is kinematic viscosity. Equation 1 can be rewritten in terms of $\bar{u}$ for open-channel flow by letting $B/2 = h$, the flow depth, and by making use of the definition of f, $\sqrt{f} = 2\sqrt{2\,(u_*/\bar{u})}$, where u_* is the shear velocity, $(\tau_0/\rho)^{\frac{1}{2}}$, which allows equation 1 to be rewritten in its equivalent form

$$\frac{\bar{u}}{u_*} = 5.74 \log_{10} \frac{u_* h}{\nu} + 4.72. \tag{2}$$

Note that the sign of the constant in equation 2 above, which is positive, was inadvertently given as negative in equation 3 of Southard and others (1971).

The remainder of the development of a relationship between u_* and u_s follows that of Southard and others (1971) and is given here for completeness as follows. The velocity defect law (Daily and Harleman, 1966, p. 299) that applies to the outer part of the boundary layer in open-channel flow is

$$\frac{u_s - u}{u_*} = 5.75 \log_{10} \frac{h}{z}, \tag{3}$$

where u_s is surface velocity, u is local velocity, and z is distance from the boundary, can be integrated over the flow depth to give

$$\frac{\bar{u} - u}{u_*} = 5.75 \log \frac{h}{z} - 2.5. \tag{4}$$

Allowing $u = u_s$ and $z = h$ in equation 4 gives

$$u_s - \bar{u} = 2.5\, u_*. \tag{5}$$

By combining equations 2 and 5, we obtain u_* in terms of u_s, or

$$\frac{u_s}{u_*} = 5.74 \log \frac{u_* h}{\nu} + 7.22. \tag{6}$$

REFERENCES CITED

Collins, K., and McGown, A., 1974, The form and function of microfabric features in a variety of natural soils: Geotechnique, v. 24, p. 233–254.

Daily, J. W., and Harleman, D.R.F., 1966, Fluid dynamics: Reading, Mass., Addison-Wesley, 454 p.

Dobbins, W. E., 1943, Effect of turbulence on sedimentation: Am. Soc. Civil Engineers Trans., v. 108, p. 629–678.

Einsele, G., Overbeck, R., Schwarz, H. U., and Unsöld, G., 1974, Mass physical properties, sliding and erodability of experimentally deposited and differently consolidated clayey muds: Sedimentology, v. 21, p. 339–372.

Einstein, H. A., and Krone, R. B., 1962, Experiments to determine modes of cohesive sediment transport in salt water: Jour. Geophys. Research, v. 67, p. 1451–1464.

Graf, W. H., 1971, Hydraulics of sediment transport: New York, McGraw-Hill Book Co., 513 p.

Guttman, I., and Wilks, S. S., 1965, Introductory engineering statistics: New York, John Wiley & Sons, 340 p.

Hjulström, F., 1955, Transportation of debris by moving water, *in* Trask, P. D., ed., Recent marine sediments: Soc. Econ. Paleontologists and Mineralogists Spec. Pub. 4, p. 5–31.

Lonsdale, P., and Southard, J. B., 1974, Experimental erosion of North Pacific red clay: Marine Geology, v. 17, p. M51–M60.

MacIlvaine, J. C., 1973, Sedimentary processes on the continental slope off New England: Woods Hole Oceanog. Inst. Tech. Rept. 73-58, 211 p.

McCave, I. N., 1970, Deposition of fine-grained sediment from tidal currents: Jour. Geophys. Research, v. 75, p. 4151–4159.

McCave, I. N., and Swift, S., 1976, A physical model for the rate of deposition of fine-grained sediment in the deep sea: Geol. Soc. America Bull., v. 87, p. 541–546.

Migniot, C., 1968, Etude des propriétés physiques de differents sédiments très fins et de leur comportement sous des actions hydrodynamiques: La Houille Blanche, v. 7, p. 591–620.

Neumann, A. C., Gebelein, C. D., and Scoffin, T. P., 1970, The composition, structure and erodibility of subtidal mats, Abaco, Bahama: Jour. Sed. Petrology, v. 40, p. 274–297.

Odd, N.V.M., and Owen, M. W., 1972, A two-layer model of mud transport in the Thames estuary: Inst. Civil Engineers (England), Proc., suppl. ix, p. 175–205.

Partheniades, E., 1965, Erosion and deposition of cohesive soils: Am. Soc. Civil Engineers Proc., Jour. Hydraulics Div., HY1, v. 91, p. 105–139.

Peirce, T. J., Jarman, R. T., and de Turville, C. M., 1970, An experimental study of silt scouring: Inst. Civil Engineers (England), Proc., v. 38, p. 231–243.

Postma, H., 1962, Sediment, *in* Demerara coastal investigation: Delft, Netherlands, Hydrodynamics Laboratory, p. 105–164.

——1967, Sediment transport and sedimentation in the estuarine environment, *in* Lauff, G. H., ed., Estuaries: Am. Assoc. Adv. Sci. Pub. 83, p. 158–179.

Prandtl. L., and Tietjens, O. G., 1934, Applied hydro- and aero-mechanics: New York, Dover, 311 p.

Rhoads, D. C., 1973, The influence of deposit-feeding benthos on water turbidity and nutrient recycling: Am. Jour. Sci., v. 273, p. 1–22.

Rhoads, D. C., and Young, D. K., 1970, The influence of deposit-feeding organisms on sediment stability and community trophic structure: Jour. Marine Research, v. 28, p. 150–178.

Rouse, H., 1946, Elementary mechanics of fluids: New York, John Wiley & Sons, 376 p.

Rowe, G. T., 1974, The effects of the benthic fauna on the physical properties of deep-sea sediments, *in* Inderbitzen, A. L., ed., Deep sea sediments: New York, Plenum Press., p. 381–399.

Sanders, H. L., 1958, Benthic studies in Buzzards Bay, I. Animal-sediment relationships: Limnology and Oceanography, v. 3, p. 245–258.

——1960, Benthic studies in Buzzards Bay, III. The structure of the soft-bottom community: Limnology and Oceanography, v. 5, p. 138–153.

Shields, I. A., 1936, Anwendung der Aehnlichkeitsmechanik und der turbulenzforschung auf die Geschiebebewegung: Berlin, Mitterlungen der Preussischen Versuchsanstalt fuer Wasserbau und Schiffbau, 37 p.

Southard, J. B., Young, R. A., and Hollister, C. D., 1971, Experimental erosion of calcareous ooze: Jour. Geophys. Research, v. 76, p. 5903–5909.

Southern California Coastal Water Research Project, 1975, Progress report 15: El Segundo, Calif., 7 p.

Sundborg, A. F., 1956, The river Klarelven, a study of fluvial processes: Geog. Annaler, v. 37, p. 125–316.

van Olphen, H., 1963, An introduction to clay colloid chemistry: New York, John Wiley & Sons, 301 p.

Young, D. K., 1971, Effects of infauna on the sediment and seston of a subtidal environment: Vie et Milieu, suppl. 22, p. 557–571.

Young, R. A., 1975, Flow and sediment properties influencing erosion of fine-grained marine sediments: Sea floor and laboratory experiments [Ph.D. thesis]: Woods Hole, Massachusetts Inst. Technology–Woods Hole Oceanographic Inst. Joint Program in Oceanography, 202 p.

——1977, Seaflume: A device for in situ studies of threshold erosion velocity and erosional behavior of undisturbed marine muds: Marine Geology, v. 23, p. M11–M18.

MANUSCRIPT RECEIVED BY THE SOCIETY OCTOBER 21, 1976
REVISED MANUSCRIPT RECEIVED APRIL 25, 1977
MANUSCRIPT ACCEPTED JUNE 10, 1977
CONTRIBUTION NO. 3957, WOODS HOLE OCEANOGRAPHIC INSTITUTION

Volume of Conference Papers: 11th Technical Conference on Hurricanes and Tropical Meteorology, 688-695.

AN EXPERIMENT IN FORECASTING HURRICANE GENERATED SEA STATES

Vincent J. Cardone

Oceanweather, Inc.
White Plains, New York, 10601

Duncan B. Ross and Merlin R. Ahrens

National Oceanic and Atmospheric Administration
Atlantic Oceanographic and Meteorological Laboratories
Miami, Florida, 33149

1. INTRODUCTION

The need for better design surface wind and wave data in oceanic regions affected by tropical cyclones has stimulated measurement and modelling programs directed specifically towards describing surface environmental conditions. For example, a cooperative oil industry sponsored program known as the Ocean Data Gathering Program (Ward, 1974) resulted in the acquisition of a unique set of surface wave measurements in severe Gulf of Mexico hurricane Camille, 1969. The data were then used to calibrate numerical wind and surface wave specification models developed in a study described by Cardone, Pierson, and Ward (1976). They found the models to be capable of accurately specifying the anemometer level wind and directional wave spectrum for a variety of storm types if given an accurate description of certain meteorological characteristics of the storm and its track.

Recently new measurement capabilities have made possible the study of the hurricane surface environment from aircraft. Ross (1975) describes a NOAA research aircraft mission into severe Pacific hurricane Ava, which obtained boundary layer wind measurements and surface wave height and frequency spectral information.

In addition, NOAA data buoys positioned off the U. S. East and Gulf coasts have acquired interesting meteorological and oceanographic data sets, including wave spectra, in hurricanes Eloise, 1975 (Withee and Johnson, 1975), Belle, 1976, and Anita, 1977. Ross (1976) combined forty measured hurricane wave spectra from these rig, aircraft, and buoy (Eloise, 1975) sources and developed an empirically based parametric model of the wave characteristics in tropical cyclones.

Hurricane wave specification models are most often applied in a hindcast mode to simulate severe historical storms for climatological or design studies, or to validate model physics in well documented storms (cf. Cardone and Ross, 1977). The models, however, may be applied in real time to forecast winds and waves associated with hurricanes and typhoons (cf. Brand *et al*., 1977). The model outputs can therefore provide objective guidance for the marine forecaster.

In the study reported here, the numerical spectral model of Cardone *et al*. (1976) and the parametric model of Ross (1976) were used experimentally to make wave forecasts in real time. The models were installed on the NOAA/AOML 1108 computer facility along with the numerical wind model described by Cardone et al., which was used to calculate hurricane surface winds from available National Hurricane Center hurricane advisory products.

Since the program began, real time forecasts have been made experimentally in hurricane Belle, 1976, in the pre-landfall period and in hurricane Anita, 1977, in the central and western Gulf of Mexico. This paper describes briefly the models used and presents verification of the forecasts against wind and wave measurements obtained as the storms passed near and over NOAA data buoys.

2. WAVE PREDICTION MODELS

This section summarizes the spectral and parametric wave prediction models. Only a brief review is attempted here - readers interested in the spectral model should refer to Cardone et al. (1976) while those interested in the basic approach followed by Ross (1976) should refer to Hasselmann *et al*. (1976).

2.1 Spectral Model

The approach taken in this model is based upon the numerical integration of the wave energy-balance equation:

$$\frac{\partial S(f,\theta)}{\partial t} = -v_g(f,\theta)\cdot\nabla S(f,\theta) - F \qquad (1)$$

where S is the directional wave spectrum, f is wave frequency, θ wave propagation direction, v_g is group velocity, and F, the so-called source function, represents all processes that can transfer energy to or from the spectrum. In the model, equation (1) is solved by the successive simulation at each time step and on a regular grid array of points covering the spatial domain of interest of the processes of wave propagation (the first term on the r.h.s. of (1)) and wave growth and dissipation (in the source function, F).

In the model the grid system is hexagonal and consists of 1521 points nominally spaced 20 n. mi. apart, laid out on a gnomonic map projection. At each grid point, the directional spectrum is resolved into fourteen frequency bands and twenty-four directional bands. Thus at each grid point there are 336 numbers, each of which represents the contribution to the variance spectrum of wave components in a finite frequency and directional band. At each model time step, which simulates one hour, equation (1) is solved, effectively, for each of the 336 spectral elements. The growth calculation uses a form for F which is applied only to spectral components propagating within ± 90° of the local wind direction and is consistent with models of the physical mechanisms that are believed to be responsible for the transfer of energy from the wind to surface waves.

Spectral components travelling against the wind are attenuated at a rate that depends on wave frequency and the energy of the local wind sea. The weak non-linear wave interactions of the type discussed by Hasselmann et al. (1976) are not modelled explicitly in the source function, but non-linear effects are certainly modelled implicitly by the form of F used.

Propagation of spectral components in deep water is accomplished by a Lagrangian scheme whereby spectral components simply translate (jump) to adjacent grid points in the appropriate direction after a sufficient number of time steps have elapsed to account for the displacement according to that component's deep water group velocity.

A version of the model includes a shallow water algorithm that accounts for wave refraction, shoaling and bottom friction, but this effect was not modelled in the experimental forecast in order to reduce costs.

The execution of the model starts with the calculation of the hurricane wind fiel and the mapping of hourly wind fields onto the model grid system. The ocean surface is taken initially as calm. Then, for each subsequent time step, the program updates the wind field, computes the changes in the spectrum at each grid point caused by growth and dissipative processes, and then propagates spectral components across the grid. The spectral field is at first unrealistic because of the initial conditions, but after a short spin-up period, usually 6-12 hours or so, it becomes indicative of the storm environment and responds thereafter to changes in storm size, intensity, and track.

It takes about eight minutes of central processor time on a Univac 1108 computer to execute one time step of the model for the full grid. For typical hurricanes, parts of the full grid can be made inactive, and a 24-hour storm period can thus be simulated in about two hours of computer time (including the calculation of the wind field).

2.2 The Parametric Model

The model proposed by Ross (1976) is a simplification of the parametric approach to wave prediction proposed by Hasselmann et al. (1976). The method follows from the data collected in the JONSWAP study, the analysis of which suggested that fetch-limited wave spectra can be normalized in a way such that there is an approximate invariance of normalized spectral shape with fetch. The spectra can therefore be parameterized in terms of a small (2-5) number of parameters, for which forecast equations can be derived.

The original analysis of JONSWAP data followed the procedure proposed by Kitaigorodskii (1961) that for ideal fetch-limited wind seas, all wave variables, when non-dimensionalized in terms of g, gravity, and the wind speed U, should be functions only of the single non-dimensional fetch, $\xi=gX/U^2$, where X is the fetch. In JONSWAP, the non-dimensional peak frequency $\nu=Uf_m/g$, where f_m is the peak frequency, was found to be described well by the relation

$$\nu = 2.84\ \xi^{-0.3} \tag{2}$$

Similarly, the non-dimensional total energy $\varepsilon=E^2g/U^4$ where $E=\int S(f,\Theta)d\Theta df$ showed a linear fetch dependence

$$\varepsilon = 1.6 \times 10^{-7}\xi \tag{3}$$

In the Ross (1976) model, the fetch, X, is replaced by R, the radial distance to the eye of the hurricane, which represents a parameterization of fetch or duration. The data set from hurricanes Ava, Camille, and Eloise were then combined to produce the following power law fits:

$$\left.\begin{aligned} \nu &= .97\ \xi'^{-.21} \\ \varepsilon &= 2.25 \times 10^{-5}\ \xi'^{.45} \end{aligned}\right\} \xi' = 3.0 \times 10^{+4} \tag{4}$$

where $\xi'=gX/U^2$. It is noted, however, that the above mentioned hurricanes were relatively slow moving ($v_f<15$ knots), and therefore the power law fits could be appreciably different for fast moving storms or significantly smaller storms.

The application of the parametric model is, of course, much simpler and computationally more efficient than the spectral model. Given a specification of the average surface (10 m) wind field on an arbitrary set of grid points and the location of the storm center, ξ', ε, and ν can quickly be computed, and E, or significant wave height ($4\sqrt{E}$), and f_m can then be easily displayed.

3. THE WIND SPECIFICATION

The hurricane wind-field model used in this study is an application of the theoretical model of the horizontal air flow in the boundary layer of a moving vortex, as originally derived by Chow (1971). This model is based on the numerical integration of the vertically averaged (over the depth of the boundary layer) equations of motion that govern a boundary layer subject to horizontal and vertical shear stresses on the rotating earth. In vector form, the equation of motion is written in coordinates fixed to the earth:

$$\frac{dv}{dt}+\psi\vec{k}\ x\ \vec{v} = \frac{-1}{\rho}\ \nabla P+\nabla(K_H\nabla\cdot\vec{v})-\ \frac{K_d}{h}|\vec{v}|\vec{v}\ \ldots \tag{5}$$

where $\vec{v}$ is the vertically averaged horizontal velocity, ψ is the Coriolis parameter, ρ is air pressure, h is the depth of the boundary layer, K_H is the horizontal eddy viscosity coefficient, and K_d is the drag coefficient. The equation is resolved in a Cartesian coordinate system the origin of which is allowed to translate at constant velocity (v_f) with the center of the pressure field associated with the vortex (in this case, the hurricane pressure eye). The variations in storm intensity and motion are represented by a series of quasi-steady states. With this representation, the pressure gradient becomes independent of time and may be simply prescribed. This nonlinear system of equations is solved numerically on a fine-mesh nested grid system as an initial value problem for the steady-state solution of the horizontal component of the vertically averaged velocity; that is, until the wind field on the moving grid becomes approximately steady. A simple transformation then yields the wind field with respect to the fixed-earth coordinate system. The calibration of the model involved the development of a scaling relationship between the anemometer level wind speed and the integrated boundary layer wind speed. This scaling law was developed mainly on the basis of wind data from a rig in the path of Camille, 1969, but it appears to be valid rather generally.

The adoption of the pressure specification technique orignally suggested by Chow satisfied the constraint that the model be capable of initialization with the type of data available for historical storms. That is, the hurricane pressure field could be prescribed as the sum of an axially symmetric part ($\tilde{p}$) and a large-scale pressure field ($\overline{p}$) of a constant gradient. The latter could be interpreted as a mean surface geostrophic flow ($\vec{v}_g$) in which the storm is embedded, as determined from

$$\psi\vec{k}\ x\ \vec{v}_g = -\ \frac{1}{\rho}\ \nabla\overline{p} \tag{6}$$

The symmetric variation of pressure with radius away from the storm's central pressure (p_0) is described as

$$\tilde{p} = p_0 + \Delta p\ e^{-r_a/r} \tag{7}$$

where r is the radial distance from the center of the hurricane, r_a is the scale radius (at approximately the radius of maximum wind) of the radial pressure profile. and Δp is the storm pressure anomaly. In this form, the theoretical model can be initialized from the parameters that are available or that can be determined from historical meteorological records; i.e., Δp (which also determines p_0), r_a, $\vec{v}_g$, v_f, and the location (latitude and longitude) of the hurricane center. The wind-field history for a storm then can be computed from knowledge of the variation of these parameters along the storm track.

A forecast wind field can be specified similarly from forecast track information and forecasts of storm central pressure, scale, and forward velocity.

Figure 1, is an example of the solution of the model for a typical storm; that is, one which is moving in the direction of the surface steering gradient. The parameters applicable to that representation are those of hurricane Belle actually observed when it was off the mid-Atlantic coast.

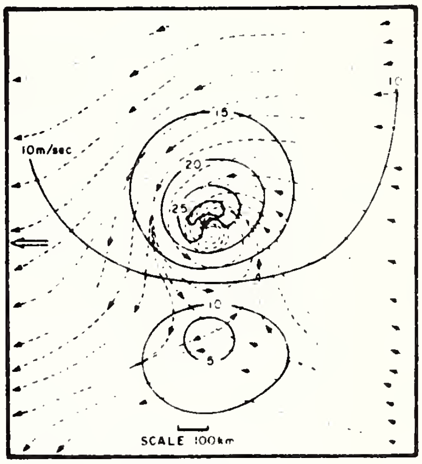

Figure 1. Typical solution of vortex boundary layer model for "steering flow" pressure specification. Streamlines and isotachs of 20 meter level wind shown.

4. HURRICANE BELLE FORECAST

The first opportunity to run the forecast program in real time was provided by Hurricane Belle, which formed east of Florida on August 6, 1976. By the morning of August 9, it was apparent that Belle would likely move up the east coast of the U. S. passing near Buoys EB 15 and EB 41 and enter New England within 24 hours. A forecast run was initiated from 10 GMT August 9 inputs. The forecast track and wind model input parameters were extracted wherever possible from official NHC advisories and products, but were supplemented with information obtained in personal communication with the NHC forecaster on duty.

The forecast track used for the Belle forecast is compared to the actual track in Figure 2 which also depicts the relative location of the NOAA data buoy EB 41. The forecast parameters of storm intensity and scale are compared to observed data in Figure 3. Clearly, errors in the forecast track, at least up to the approximate locations of EB 41, are small, but

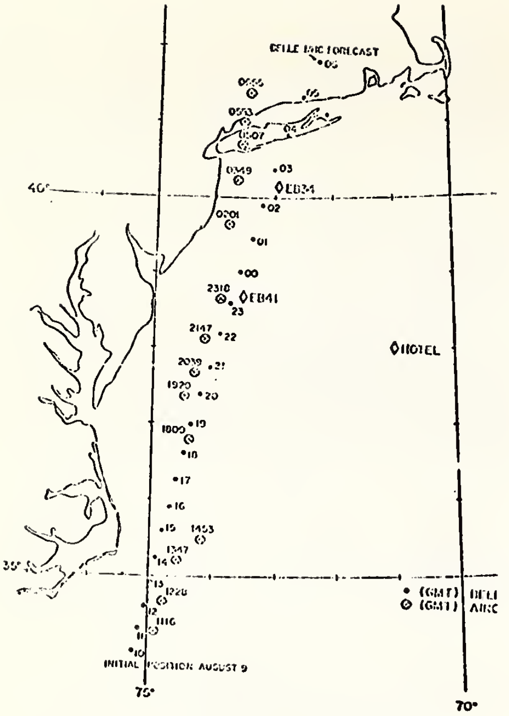

Figure 2. Forecast and observed track in Hurricane Belle 8/9-8/10.

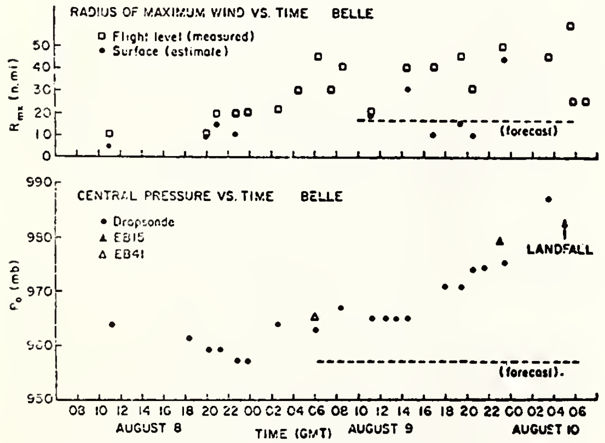

Figure 3. Observed and forecast storm parameters in Hurricane Belle.

but errors in forecast storm characteristics are large.

Since the forecast track moved Belle almost directly over EB 41, the maximum storm sea states were forecast by both models to pass just to the right of the buoy. EB 41 recorded a 15-minute sample of wave height every three hours. The data are processed on board, and spectra and derived quantities are transmitted to a shore facility for dissemination on the standard synoptic communications network. The buoy also measured wind speed and direction over an 8.5-minute interval once per hour. The vortex shedder anemometer is mounted at a height of five meters. Data from EB 34 are considered unreliable as the buoy broke loose from its mooring during the storm.

Figure 4 compares the model forecasts of average wind speed at an anemometer height of 20 meters, wind direction, and Figure 5 the significant wave height, at EB 41 to the buoy measurements. For this comparison, wind speeds measured by the buoy were adjusted to a height of 20 meters using the method of Cardone (1969).

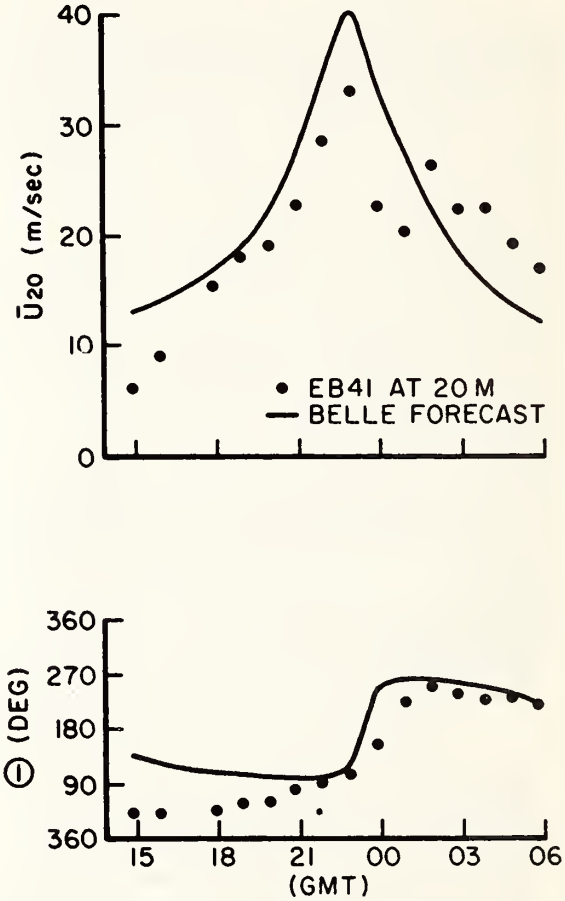

Figure 4. Comparison of measured (adjusted to 20 meter height) and forecast wind speed and direction in Belle at EB 41.

The "errors" in the forecast time-histories shown in Figures 4 and 5 require very cautious interpretation, as they represent a complicated mix of errors from the forecast of storm track, intensity, and size and errors due to model deficiencies. In addition there is some indication that the buoy vortex shedder winds may be degraded by rain, which surely was present for most of the period of interest. Finally, the wave measurements are available only once per three hours, which in a hurricane environment is insufficient to sample and resolve the true evolution of the wave history at the site. It is quite possible that maximum sea states at the buoy site were higher than the highest measured value.

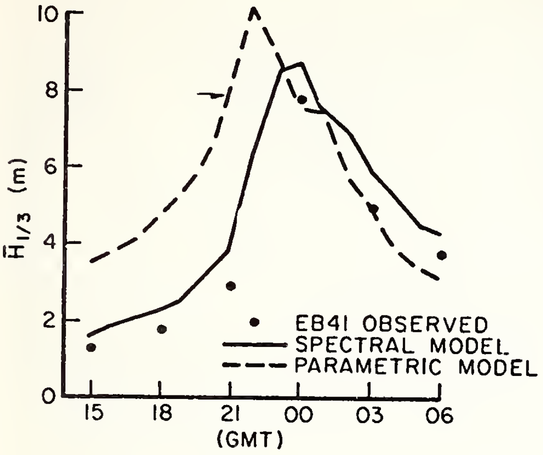

Figure 5. Verification of significant wave height time history forecast from spectral and parametric wave models at EB 41 in Belle.

Nevertheless, it may be said that both wave forecast models do a creditable job of specifying the maximum sea states likely experienced at the buoy, while the spectral model appears to better forecast the overall time history. At least part of the overall positive bias in the forecasts of both models is due to the unforecast rapid weakening of Belle in the pre-landfall period.

The forecast wind errors in the Belle wave forecast has been investigated by performing a detailed post analysis and hindcast of the winds and waves in this storm. Using post analysis values for storm input parameters, the wind model calculated winds at EB 41 that compared very well with those measured (Figure 6).

The wave height predictions from hindcast winds are compared to the EB 41 measurements in Figure 7. As expected, the hindcast time histories are closer to the observations than those forecast, but infra-model differences remain. For example, the parametric model hindcast positive bias early in the EB 41 time history implies that the model is overpredicting wave heights in Belle's forward quadrants. This is believed to be a consequence of the calibration of the model against data from slow moving storms and the more wind duration limited characteristics of waves in the forward quadrants of fast moving storms.

As an example of the more detailed forecast products potentially available from wave models, Figure 8 compares maximum hindcast one-dimensional frequency spectra specified directly by the spectral model, computed from the forecast parameters of the parametric model, and observed at EB 41.

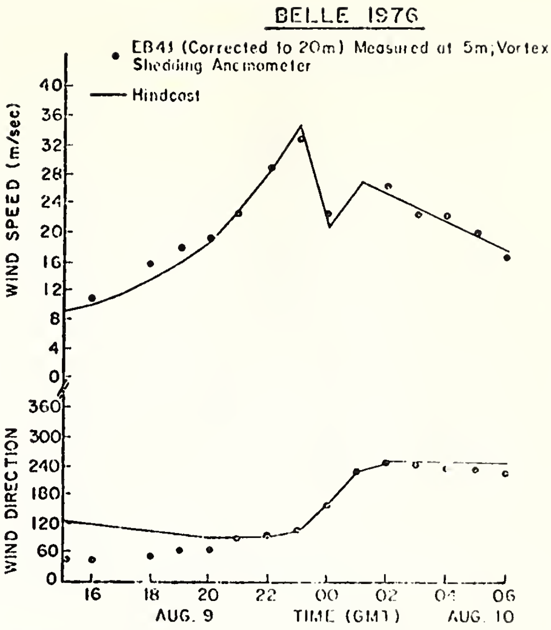

Figure 6. Hindcast wind speed and direction at EB 41 in Belle (Cardone and Ross, 1977).

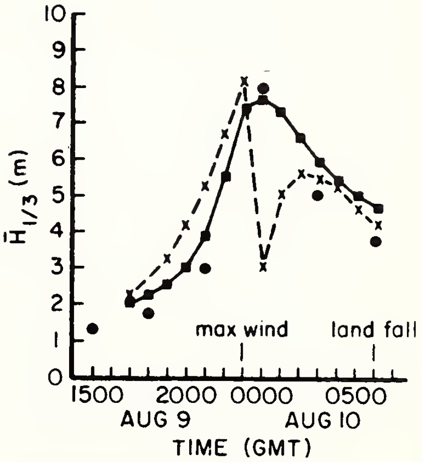

Figure 7. Hindcast significant wave height time history at EB 41 in Belle (Ross and Cardone, 1977): ● - measured; x - parametric model; ■ - spectral model.

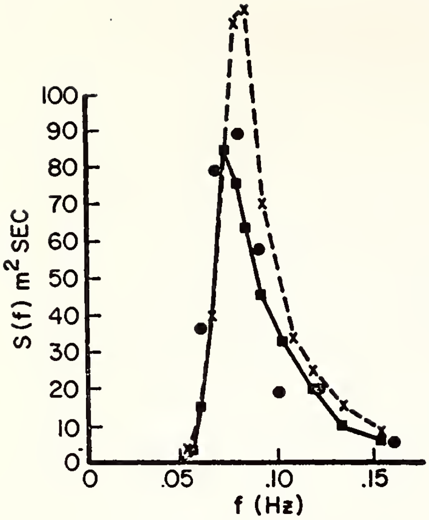

Figure 8. Maximum hindcast spectra for Hurricane Belle at EB 41 (Ross and Cardone, 1977): x - parameteric model, $\overline{H}_{1/3}$=8.2 m; ■ - spectral model, $\overline{H}_{1/3}$=7.8 m. Also shown is maximum observed spectrum (●) $\overline{H}_{1/3}$=7.8 m.

5. HURRICANE ANITA FORECAST

A series of forecasts were prepared in real time during Hurricane Anita and made available as guidance for the National Hurricane Center forecasters. Only a brief preliminary evaluation of one of the series is presented here as the forecast data sets are presently under study. The forecast described here was prepared from 2200 GMT 8/31/77 inputs and covered the 21 hour period ending 1800 GMT 9/1/77.

During the forecast period, Hurricane Anita passed very near buoy EB 71, at which hourly wind and 3-hourly wave measurements were made. Similar measurements were made at EB 04, which was on the periphery of the storm during the period of the forecast. Figure 9 shows the forecast wave height distribution around Anita produced by the parametric model, the forecast track used, the actual track, and the locations of the data buoys. Figures 10 and 11 compare the forecast parameters of intensity, p_0, and scale, r_p, used as input to the wind model, and the characteristics actually observed. As in Belle, the scatter in r_p is large. The most significant error in Anita's forecast, however, is the forecast position error.

In view of the large error in forecast track, especially with respect to the location of EB 71, the track error, which would have overwhelmed the comparisons at the buoy, was removed completely before "forecast" wind and wave time histories at EB 71 and EB 04 were compared to measurements. Figures 10 through 15 pre-

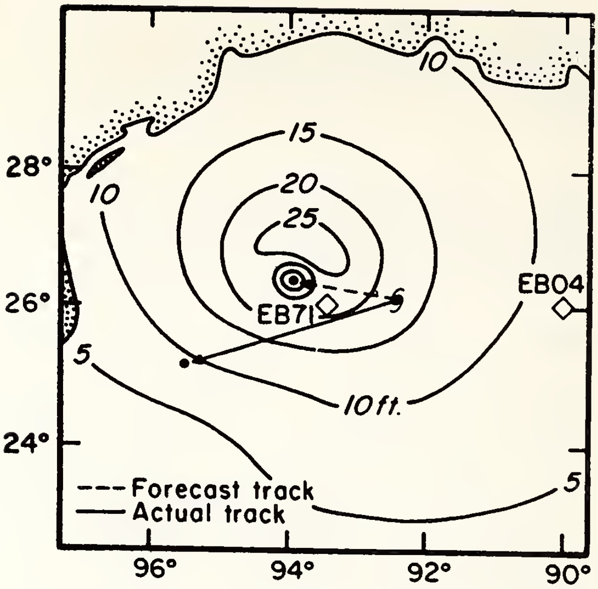

Figure 9. Parametric model derived forecast of significant wave height around Anita. Forecast made at 22 GMT 8/31/77, valid at 18 GMT 9/1/77. Buoy positions, forecast track, and actual track also are shown.

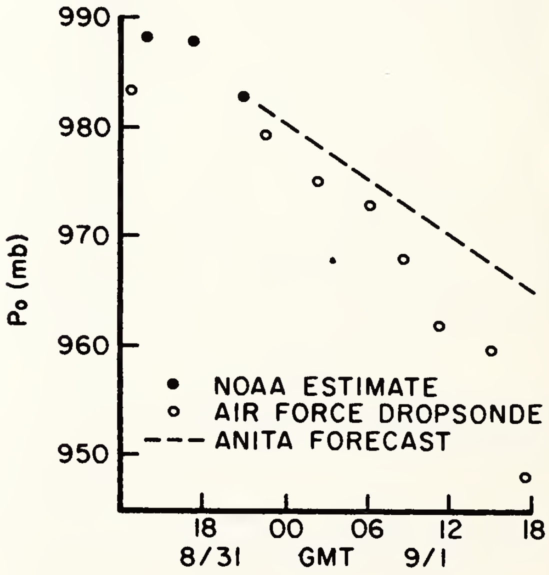

Figure 10. Observed and forecast central pressure in Hurricane Anita.

sent those "best track" forecast wind and wave time histories. The forecast wind time histories compare favorably with those observed. The mean and rms differences between forecasts and measured significant wave heights are -.75 ± .54 m (spectral) and .21 ± .83 m (parametric) at EB 71, and -.64 ± .23 m (spectral), and -.48 ± .64 m (parametric) at EB 04.

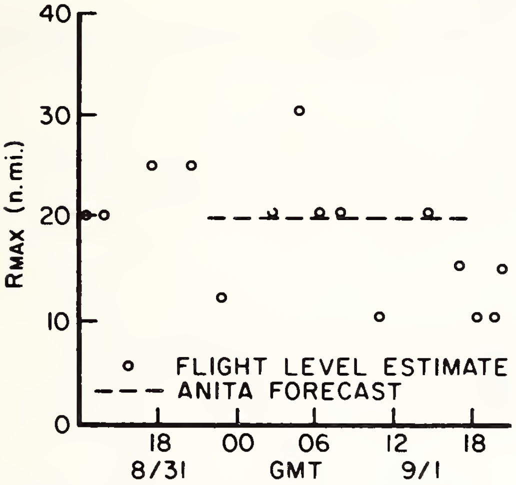

Figure 11. Observed and forecast radius of maximum wind in Anita.

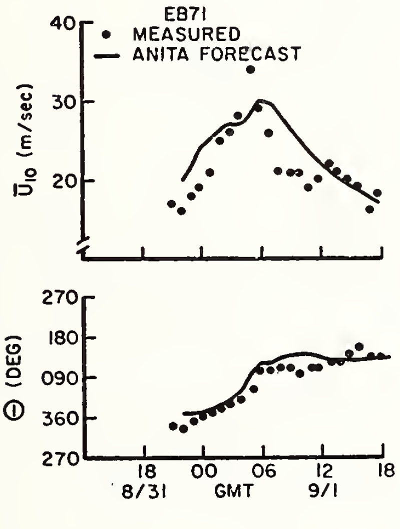

Figure 12. Measured and forecast wind speed and direction in Hurricane Anita at EB 71.

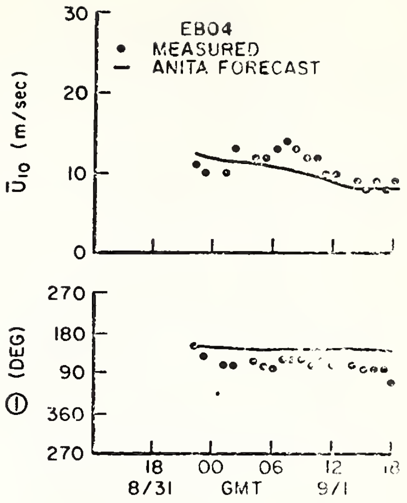

Figure 13. Measured and forecast wind speed and direction in Hurricane Anita at EB 04.

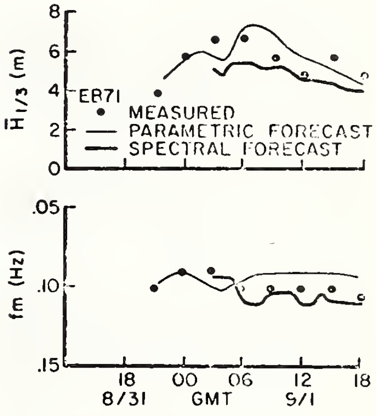

Figure 14. Measured and forecast significant wave height and peak frequency in Hurricane Anita at EB 71.

6. CONCLUSIONS

This study demonstrates feasibility of obtaining useful forecasts of sea state in hurricanes with existing model capabilities. However, it must be remembered that the models are critically dependent upon a proper specification of the wind field which in turn depends upon accurate forecasts of storm track, intensity, and size. The errors seen in the forecast wave conditions of Belle and Anita are typical of the current state of the art.

In view of those errors, it is appropriate that the computationally efficient parametric model be employed in operational

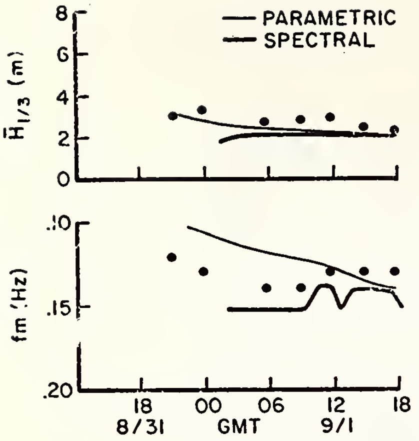

Figure 15. Measured and forecast significant wave height and peak frequency in Hurricane Anita at EB04.

forecasting, as it can be quickly updated as changes in storm intensity and track occur.

A particularly important parameter in the wind specification model is the radius of maximum wind. This parameter is not routinely forecast nor is it reliably measured to the desired accuracy. The scatter in the estimates of this parameter, strongly suggests the need for improvements in the monitoring of this storm characteristic, possibly through consistent low altitude eye penetration by reconnaissance aircraft and use of enhanced satellite imagery.

Finally, this study begins to reveal the tremendous potential of the NOAA data buoy system. The data buoys not only are important elements of the operational marine observing system but can provide unique measurements in extreme conditions for use in research programs concerned with the development of improved environmental prediction models. The outstanding performance of the prototype buoys in hurricanes Eloise, Belle, and Anita has resulted in unique data that will be particularly valuable in the further development of hurricane wind and wave models.

7. ACKNOWLEDGEMENTS

We thank Shell Development Company, for supporting jointly with NOAA, the adaptation of the Ocean Data Gathering Program hurricane wind and spectral models to the NOAA, AOML computer facility.

Dr. Cardone's participation in this study was supported by NOAA under Grant 04-7-022-44014.

8. REFERENCES

Brand, S., K. Rabe, and T. Laevastu, 1977: Parameterization characteristics of a wind-wave tropical cyclone model for the Western North Pacific Ocean. J. of Phys. Oceanog., Vol. 7, 5, 739-746.

Cardone, V. J., 1969: Specification of the wind distribution in the marine boundary layer for wave forecasting. TR69-1 Geophysical Sciences Laboratory, New York University. (NTIS No. AD702490).

Cardone, V. J., W. J. Pierson, and E. G. Ward, 1976: Hindcasting the directional spectra of hurricane generated waves. J. Pet. Tech., April, pp. 385-394.

Cardone, V. J. and D. B. Ross, 1977: State of art wave prediction methods and data requirements. Prepared for the NOAA Ocean Wave Climate Symposium, July 12-14, 1977, Washington, D. C. Proceedings to be published by Plenum Company, 1978.

Chow, S., 1971: A study of the wind field in the planetary boundary layer of a moving tropical cyclone. MS thesis, Dept. of Meteorology and Oceanography, New York University.

Hasselmann, K., D. B. Ross, P. Muller, and W. Sell 1976: A parametric wave prediction model. J. Phys. Oceanogr., 6, pp. 200-228.

Kitaigorodskii, S. A., 1961: Applications of the theory of similarity to the analysis of wind-generated wave motion as a stochastic process. 1 zu. Akad. Nank. SSSR, Ser. Geophiz., No. 1, 73-80.

Ross, D. B., 1975: A comparison of SKYLAB S-193 and aircraft views of surface roughness and a look toward Seasat. Proceedings of the NASA Earth Resources Survey Symposium, L. B. Johnson Space Center, Houston, Texas, June,1975, 1911-1920.

Ross, D. B., 1976: A simplified model for forecasting hurricane generated waves (Abstract). B. Amer. Met. Soc., January, p. 113. Presented at Conference on Atmospheric and Oceanic Waves, Seattle, Washington, March 29-April 2.

Ross, D. B., and V. J. Cardone, 1977: A comparison of parametric and spectral hurricane wave prediction products. To be published in the Proceedings of "NATO Symposium on Turbulent Fluxes through the Sea Surface, Wave Dynamics and Prediction", Marseille, France, 12-16 September 1977 (Plenum Publishing Corporation, New York, New York).

Ward, E. C.: Ocean Data Gathering Program - An overview. Paper OTC 2108-B presented at Sixth Annual Offshore Technology Conference, Houston, May 6-8, 1974.

Withee, G. W., and A. Johnson, Jr., 1975: Buoy observations during hurricane Eloise. Data Buoy Office National Oceanic and Atmospheric Administration, Bay St. Louis, Mississippi.

Interciencia 3, No. 1, ENE, 24-27.

ACOUSTIC TECNHNIQUES FOR OCEAN POLLUTION STUDIES AND THEIR EASY TRANSFERABILITY TO DEVELOPING NATIONS

J. R. PRONI and H. B. STEWART Jr.

SUMMARY *A new technique, namely an environmental acoustic technique, has been developed which appears to be a genuine break-through in the fundamental area of chemical sampling in the ocean and coastal zone. Using this technique, water samples may be taken directly in areas of highest particulate and biological concentrations. By using acoustic techniques in conjunction with traditional oceanic measurements of quantities such as temperature, current, salinity, dissolved oxygen, and others and by making measurements covering sufficiently long periods of time, scientists may be able to evolve a scientific and perhaps management model of the coastal zone of a given area in a given country.*

Furthermore, acoustic techniques may be developed relatively easily in any Central or South American nation particularly if surplus acoustic echo-sounders may be obtained either from the particular country's fishing fleet or Navy.

In closing, it is pointed out that navigational accuracy is important in using acoustic techniques as it is in most fields of oceanographic research. It is also pointed out that one need not think in terms of expensive navigational aids for positioning; for example, a simple sextant and protractor may be used in many circumstances to provide the desired navigational accuracy.

One of the major challenges facing ocean scientists today is to determine what effects man is having on the ocean in the coastal zone. In general, it is very difficult to gather reliable scientific data on the effects of man-generated pollution, waste dumping, harbor construction, etc. A fundamental question facing ocean chemists is what is the fate of foreign matter introduced by man into the ocean and particularly into the coastal zone. A new approach to this problem has been developed at the Atlantic Oceanographic and Meteorological Laboratories (in Miami, Florida, U.S.A. —a part of the National Oceanic and Atmospheric Administration) which has proven to be a genuine breakthrough. This approach is centered about one of man's oldest yet newest sciences— the science of acoustics. Furthermore, the acoustical approach can be easily and relatively cheaply developed by South and Central American nations. The purpose of this paper is to provide an introduction to the subject with ample references (Jeffers, 1960; Proni and Apel, 1975; Proni *et al.*, 1976a, and Proni *et al.*, 1976b), for those who are interested in further information on the subject.

The basic concept involved in the acoustical approach is simple. A sound projector is mounted on a suitable platform which may, for example, be a ship or the sea floor itself. Sound pulses are emitted by a sound transducer and then received, after having been reflected by any material within the water column and/or the bottom. The acoustic approach, when used in conjunction with ships as platforms (see Fig. 1), normally involves towing the acoustic transducer (i.e., the sound emitting and receiving element) alongside the ship in a hydrodynamically designed towbody. The ship then proceeds along tracklines designed to map out the water area of interest.

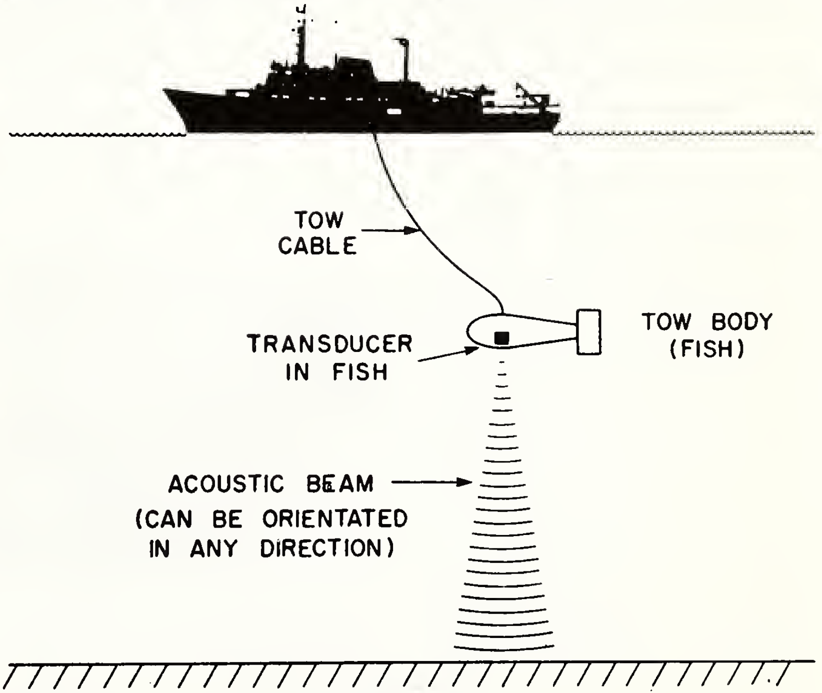

Figure 1

Typical Acoustic Equipment Configuration when used aboard a ship.

Dr. John R. Proni and Dr. Harris B. Stewart, Jr., **are both with the Atlantic Oceanographic and Meteorological Laboratories of NOAA (National Oceanic and Atmospheric Administration) on Virginia Key, Miami, Florida, U.S.A. Dr. Proni is a Senior Researcher in the fields of underwater acoustics, and Dr. Stewart, an oceanographer, is Director of AOML. Both scientists have been active in Caribbean marine science projects for a number of years. Address: AOML/SAIL, 15 Rickenbacker Causeway, Miami, Florida 33149 U.S.A.**

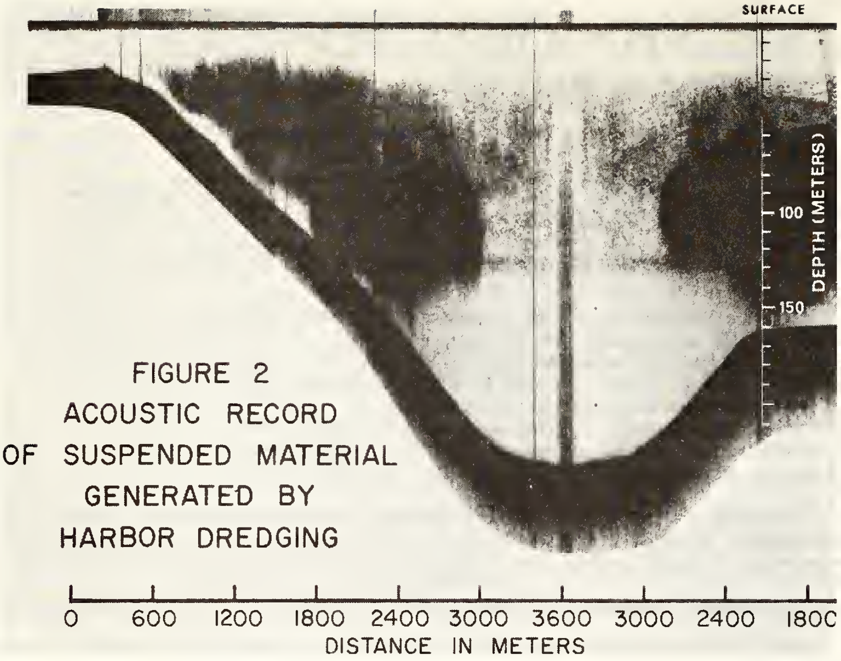

FIGURE 2
ACOUSTIC RECORD
OF SUSPENDED MATERIAL
GENERATED BY
HARBOR DREDGING

Applications

Example One: It has been determined by the Port Authorities of a certain coastal city that the city's harbor must be deepened in order to receive larger ships. Such deepening is to be accomplished by dredging. The questions of interest are: 1) Is silt or other fine material moving out of the harbor with the currents? 2) If it is, how are the turbidity levels in the water going to be affected by the presence of the silt or other fine material? 3) Where is the material going once it is below the surface of the water? Using an acoustic device mounted on board a ship, these questions may be addressed. Figure 2 shows an acoustic record gathered while a dredge was operating in Miami, U.S.A. shipping channel.

In order to obtain the data shown in Figure 2, a research ship sailed out of Miami harbor and passed over the resulting subsurface "cloud" of silt and suspended sediment produced by the dredging operation (the dredging stirred up material and placed it in the water column; the material was then advected out of the shipping channel by tidal currents). The axes of the figure are depth, in meters, versus distance, in meters. A large cloud of suspended material is clearly visible in the 30 m to 150 m depth range and 0 to 3,000 m distance range. At about the 3,600 m range, the ship reversed course and took station at 160 m depth to carry out chemical sampling.

An example of the sensitivity of the acoustic technique when used in chemical sampling may be seen in Figure 3. Once again a cloud of suspended sediment is visible in the acoustic record. The sampling vessel was "on-station" from 1540 to 1600 hours. Two water bottles were lowered to gather water samples; these are labeled A and B in Figure 3. The shallow water bottle is at 55 m depth, and the deep water bottle is at 110 m depth. Both bottles were on a single wire. Not only are the bottles detectable, but the messenger on its way down to trigger them is detectable as well.

It is deemed desirable to have knowledge of factors involved in the upwelling process, including thermocline structure and possibly internal waves. Figure 4 shows acoustic data gathered in the Caribbean, a few hundred miles north of the Colombian/Venezuelan border. In this figure a concentration of biological particles in layers is shown, with the concentration onsetting at the beginning of the thermocline. As can be seen from this figure, only a low level of internal wave activity is indicated at the time the data were gathered (i.e., the reflecting layers remain at constant depth, thus indicating little internal wave activity). A small amount of oscillatory activity may be seen at the time Tl in Figure 4 (peak-to-peak amplitude internal waves of roughly 2 m are present). These data (i.e., the data in Figure 4) may be compared to a period of high internal wave activity such as described in the first three references at the end of this paper. A series of temperature profiles gathered at the same time as the acoustic data shown in Figure 4 is presented as Figure 5 and indicates that the reflecting layers are concentrated in the thermocline.

Implementation

The preceding examples present just two of many possible applications of the acoustic technique to coastal zone marine problems. Now, how difficult is it for a South or Central American nation to begin using acoustic techniques? The two basic concerns when entering the acoustics field are the availability of a) trained personnel and b)

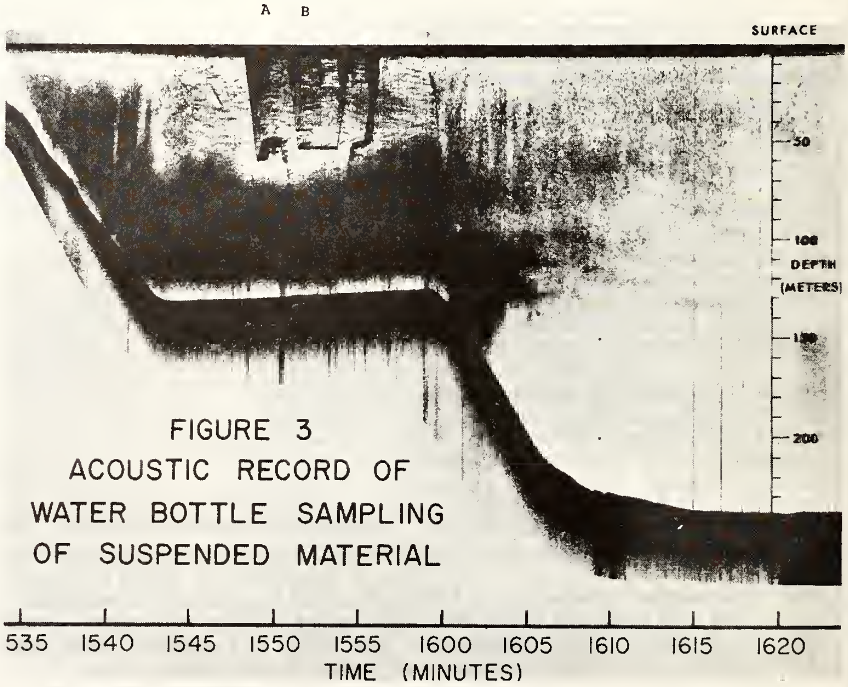

FIGURE 3
ACOUSTIC RECORD OF
WATER BOTTLE SAMPLING
OF SUSPENDED MATERIAL

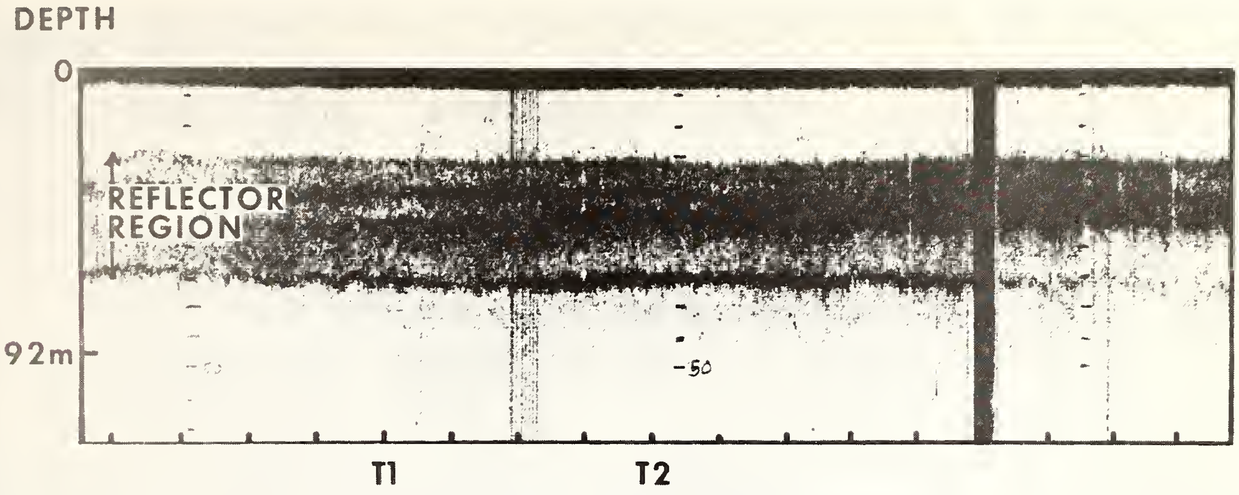

TIME MARKS EVERY FIVE MINUTES

Figure 4

ACOUSTIC OBSERVATIONS OF INTERNAL OCEANIC REFLECTORS DURING A RELATIVELY QUIESCENT PERIOD

equipment. The training required to acquire a reasonable ability to interpret acoustic records is not great and presents no real obstacle. The question of equipment may be addressed in one of two manners, that is, new acoustic equipment or used acoustic equipment. If the nation in question has a fishing industry or a navy, then it may be possible to acquire a used "fish-finder" or used "sonar" system and adapt it for use in acoustic pollutional or coastal zone research programs. The adaptation process is not very difficult. If a used system is not available, then a new acoustic system must be purchased.

Navigation

Navigation of the ship carrying the acoustic equipment must be of an accuracy determined by the particular mission on which it is engaged. If, for example, a subsurface plume of suspended material is being tracked acoustically, it is necessary to know the position of the ship during each successive pass over the plume. In this case, position accuracy on the order of several tens of meters would probably be required.

Too often one tends to think in terms of highly sophisticated and expensive electronic navigation systems for control of offshore surveys, when much simpler and less expensive techniques can provide the desired accuracy, such as celestial navigation methods. For example, using horizontal sextant angles to obtain three-point fixes, one can use a threearm protractor to plot the ship's position on a chart on which are plotted the three shore features being used as signals. This inexpensive technique is accurate and allows on-board plotting of the ship's position as far from shore as the signals on land can be seen. On shallow shelves, the system can be extended farther seaward by emplacing buoys which have been located using the shore signals at the seaward limit of visibility.

The three-point fix technique is easily mastered, and a complete description is found in Jeffers (1960).

Conclusion

The coastal zone is a very complex region of the world's oceans. Most of the processes which take place there are poorly understood. The task of the coastal zone manager is made immensely difficult by the lack of proper scientific understanding of processes occurring in the zone. Unfortunately, many times major decisions on coastal zone use such as harbor construction, deep water port siting, oilwell drilling, beach remodeling, etc., must be made fairly quickly, thus not permitting adequate scientific studies of the impact of the proposed use. Usually an adequate coastal zone study resulting in a meaningful model of the coastal zone requires many years of data. The acoustic techniques described in this paper will surely become a mainstay of future multi-year coastal zone studies. South and Central American nations will find good use for acoustics in their coastal zone programs.

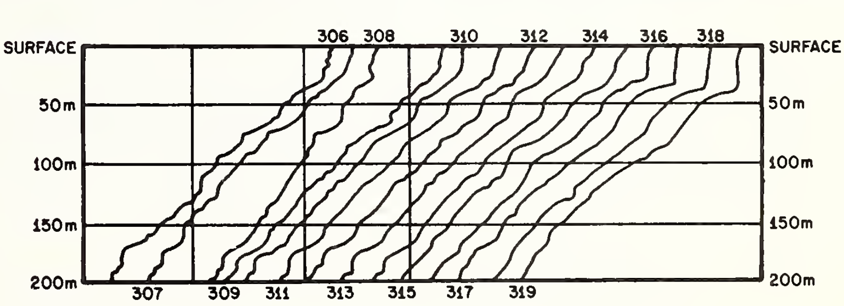

Figure 5

EXPENDABLE BATHYTHERMOGRAPHS CORRESPONDING TO FIGURE 4

REFERENCES

Jeffers, Karl B., (1960): *Hydrographic Manual,* U. S. Coast and Geodetic Survey, Special Pub. 20-2, (3rd, Edition).

Proni, John R., and John R. Apel (1975): On the Use of High Frequency Acoustics for the Study of Internal Waves and Microstructure. *J Geophys Res, 80:* 1147-1151.

Proni, John R., Fred C. Newman, Ronald L. Sellers, and Charles Parker (1976a): Acoustic Tracking of Ocean-Dumped Sewage Sludge. *Science, 193:* 1005-1007.

Proni, John R., Fred C. Newman. Donna C. Rona, David E. Drake, George A. Berberian, Charles A. Lauter, Jr., and Ronald L. Sellers (1976b): On the Use of Acoustics for Studying Suspended Oceanic Sediment and for Determining the Onset of the Shallow Thermocline. *Deep-Sea Res, 23:* 831-837.

TECNICAS ACUSTICAS PARA LOS ESTUDIOS DE LA CONTAMINACION OCEANICA: FACILIDAD DE SU TRANSFERENCIA A LOS PAISES EN DESARROLLO

J. R. PRONI y H. B. STEWART Jr.

SUMMARY *Se ha desarrollado una nueva técnica de acústica ambiental que puede representar un verdadero avance en el área básica de la obtención de muestras químicas en el océano y en costas. Con la ayuda de esta técnica, las muestras de agua pueden obtenerse directamente en áreas con elevadísimas concentraciones de partículas y materiales biológicos. El empleo de técnicas acústicas conjuntamente con la medición oceánica tradicional de parámetros tales como temperatura, corrientes, salinidad, tensión del oxígeno disuelto y otros, así como hacer mediciones que cubran períodos de tiempo suficientemente largos, permitirá que los investigadores puedan desarrollar un modelo científico, quizás de orden práctico también, de la costa de una zona cualquiera y en cualquier país.*

Las técnicas acústicas pueden desarrollarse con relativa facilidad en cualquier país de Centro o Suramérica, especialmente si se puede obtener el excedente de receptores acústicos, ya sea de alguna flota pesquera o de la Marina del país.

Para concluir, se comenta sobre la importancia de la precisión de navegación al emplearse técnicas acústicas, igual que ocurre en la mayoría de los campos de la investigación oceanográfica. Igualmente, se hace notar que no es necesario pensar en términos de instrumentos de navegación costosos para establecer la posición; por ejemplo, en muchas circunstancias un simple sextante y un transportador son suficientes para dar la precisión navegacional

---

TÉCNICAS ACÚSTICAS PARA ESTUDOS DA POLUIÇÃO OCEÂNICA: FACILIDADE DE SUA TRANSFERÊNCIA AOS PAISES EM DESENVOLVIMENTO

J. R. PRONI e H. B. STEWART Jr.

RESUMO *Desenvolveu-se uma nova técnica de acústica ambiental que pode representar um verdadeiro avanço na importante área da obtenção de amostras químicas no oceano e nas zonas litorâneas. Com a ajuda desta técnica, as amostras da água podem ser obtidas diretamente em áreas com as mais elevadas concentrações de partículas e de materiais biológicos. Usando técnicas acústicas, associadas às medidas tradicionais de grandezas tais como: temperatura, correntes, salinidade, tensão do oxigênio dissolvido e outros dados oceânicos durante períodos de tempo suficientemente longos, os pesquisadores poderão desenvolver um modelo científico, talvez de ordem prática, da zona costeira de uma dada área de um dado país.*

As técnicas acústicas podem desenvolver-se com relativa facilidade em qualquer país da América Central ou do Sul, particularmente se o excedente de receptores acústicos puder ser obtido de alguma frota pesqueira ou da Marinha do país.

Considera-se ainda, a importância da precisão da navegação ao empregar técnicas acústicas, tal qual ocorre na maioria dos campos da investigação oceanográfica. Pondera-se também, que não é necessário pensar em termos de instrumentos de navegação custosos para estabelecer a posição; em muitas circunstâncias um simples sextante e um transferidor são suficientes para dar a precisão desejada na navegação.

Deep-Sea Research 25, 299-307.

Acoustic observations of high-frequency, near-surface internal wave groups in the deep ocean during GATE*

J. R. PRONI†, F. OSTAPOFF† and R. L. SELLERS†

(*Received* 14 *February* 1977; *in revised form* 18 *August* 1977; *accepted* 31 *August* 1977)

Abstract—High-frequency, near-surface internal wave groups in the deep ocean were observed during GATE.‡ The wave groups have several structural features in common with internal wave groups observed on continental shelves. It is suggested that the wave groups are (a) distinguishable because of their structural features from the generally present high-frequency internal wave background and (b) that these same features are to be expected on a theoretical basis from the work of T. B. BENJAMIN (*Journal of Fluid Mechanics*, **29**, 559–592, 1967). Some evidence supporting the acoustic data is derived from simultaneously observed temperature and salinity data and from some imaging radar gathered in the same overall area.

INTRODUCTION

PART OF the oceanographic subprogram of the GARP (Global Atmospheric Research Program) Atlantic Tropical Experimant (GATE) addresses the problem of coupling between the motions in the mixed layer and in the interior ocean. Internal gravity waves in the main thermocline may locally enhance the shear flow, thus providing a mechanism for turbulence and mixing.

During the third phase of GATE (August 30 to September 21, 1974) a high resolution experiment that included an internal wave program was carried out. The main components of this program were a two-legged mooring instrumented with current meters and temperature sensors with a horizontal spatial separation resolution of 500 m (University of Kiel) and the acoustic probing that will be discussed in this paper. Acoustic data on the detailed spatial structure of some internal wave groups near the ocean's surface but in deep ocean water will be presented. The observed wave groups have certain structures that distinguish them from the generally present high-frequency internal waves.

Observations of high-frequency internal wave groups along the United States and on other continental shelves have been made in the last several years (LAFOND, 1961; GARGETT and HUGHES, 1972; ZIEGENBEIN, 1969; HALPERN, 1971), and internal surges in lakes (a closely related phenomenon) have been reported (THORPE, 1968; HUNKINS and FLIEGEL, 1973; THORPE, 1974). Recent measurements of continental shelf wave packets have been made by satellite (APEL, BYRNE, PRONI and CHARNELL, 1975) and acoustically (PRONI and APEL, 1975). The theory governing the propagation of these wave groups or wave packets for the continental shelf was developed by LEE and BEARDSLEY (1974) and for lakes (Loch Ness in particular) by THORPE (1974). A feature shared by shelf and lake theories is that they apply to shallow water (more precisely, the ratio of depth to wavelength of the internal waves is small).

---

* A GATE Contribution.

† Atlantic Oceanographic and Meteorological Laboratories, Sea–Air Interaction Laboratory, 15 Rickenbacker Causeway, Miami, FL 33149, U.S.A.

‡ GATE is the acronym for the GARP (Global Atmospheric Research Program) Atlantic Tropical Experiment.

The existence of wave packets or groups having limited spatial extent has been described particularly in recent Soviet literature (SABININ, 1971; MIROPOL'SKIY, 1973; BREKHOVSKIKH, KONJAEV, SABININ and SERIKOV, 1975). The inferences on the existence of internal wave groups are based on the assumption that: (i) certain characteristics of internal waves have non-Gaussian probability distributions, (ii) certain time series of internal waves are non-stationary, and (iii) the high-frequency internal wave field is directionally anisotropic. Relatively little attention was paid to the detailed structure of the internal wave packets.

METHOD

Deep-ocean internal waves were observed acoustically. The acoustic device, which was towed behind the R.V. *Columbus Iselin* during the third phase of GATE, utilized 1-ms-long pulses with a carrier frequency of 20 kHz. The beamwidth was 12 by 18°. Normally the acoustic transducer (i.e. the actual sound emitting element) is towed in a hydrodynamically streamlined towbody. The tow depth is normally a few meters below the surface.

For the acoustic device to be able to detect subsurface water movements, some acoustic scatterers must be present. It is presently known on theoretical and experimental grounds that at least three classes of acoustic scatterers exist. These include (i) biological scatterers and suspended material both organic and inorganic, (ii) turbulence, and (iii) small-scale temperature and density microstructure.

Acoustic scatterers often have a clear vertical stratification. The scatterers align themselves in layers separated vertically by regions of much lower acoustic reflectivity. Examples of such layering have been published by PRONI and APEL (1975) (see the Appendix of this paper for an example of layering). Upon passage of internal waves, these layers are caused to oscillate and thus outline the internal wave structure. Internal wave amplitude can then be obtained directly from the acoustic records. Acoustically derived layer depth variations and simultaneous temperature variations from the scattering layer have shown good agreement (OSTAPOFF, PRONI and SELLERS, 1975).

OBSERVATIONS

The R.V. *Columbus Iselin* track for September 16, 1974, is shown in Fig. 1, as are the areas (hatched) in which synthetic aperture radar data were gathered by the National Aeronautics and Space Administration device CV990 on September 16, 1974. Fig. 2(a) shows a portion of the acoustic record from 1130 to 1215 U.T. on September 16, 1974. Time runs from left to right with a total record length of about 4.4 km (ship's speed = 1.6 m s^{-1}). There is evidence that an internal wave packet is portrayed between the points marked 'front' and 'end' of a wave packet in Fig. 2(a). The packet seems to be proceeding toward the right in Fig. 2(a); (see the discussion on page 303). Figure 2(b) delineates graphically the acoustic scattering layer to facilitate the discussion.

The wave group begins with a sharp downgoing oscillation. A range of wavelengths is visible in the wave packets ranging from a few hundred meters to about 600 m. Because the direction of the propagation of the wave packet is not known exactly (see, however, the discussion in the analysis section), the distances of a few hundred meters to 600 m must be regarded as *upper limits* on the distance between downgoing oscillations. The packet

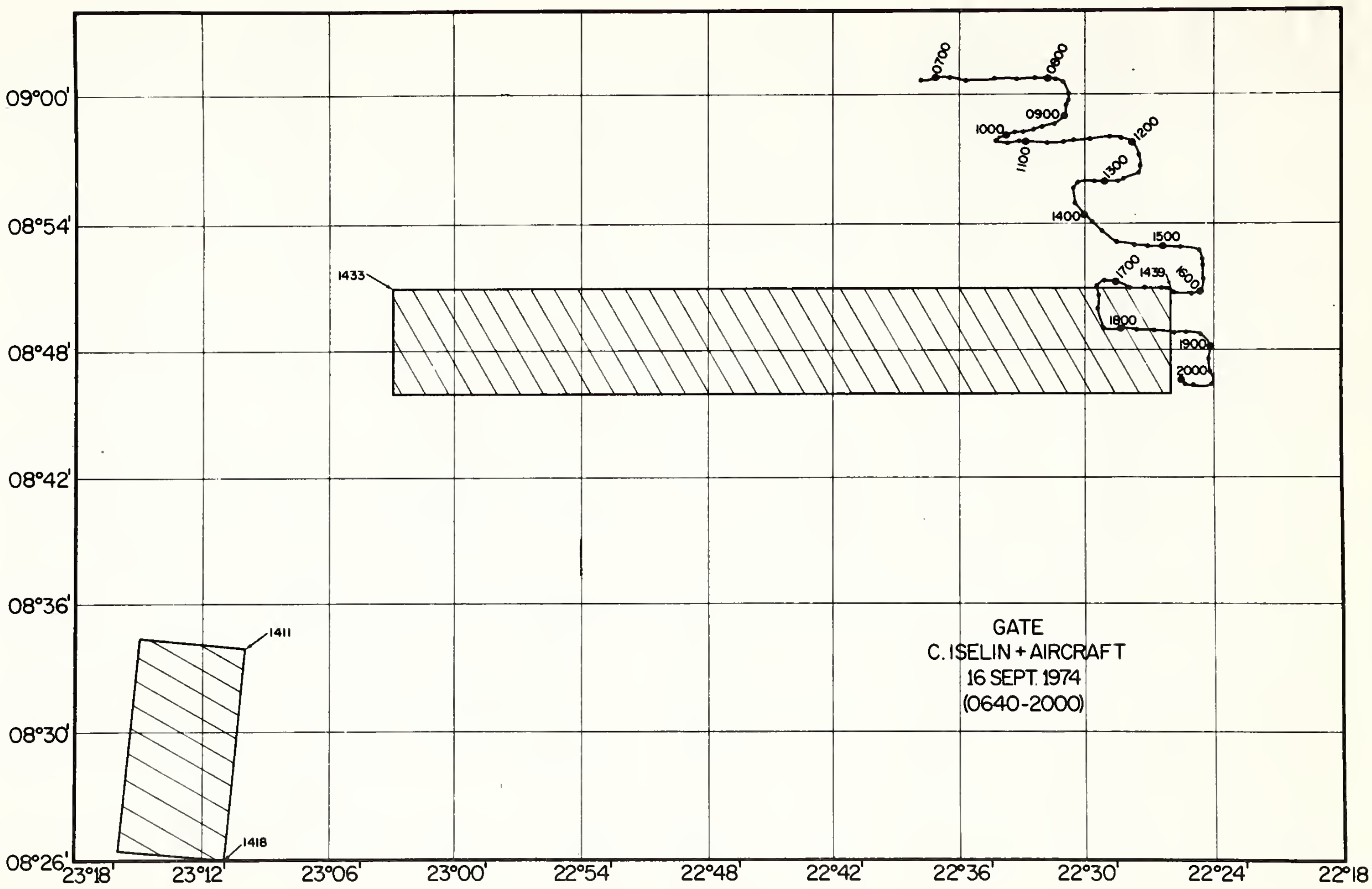
GATE
C. ISELIN + AIRCRAFT
16 SEPT. 1974
(0640-2000)
0700
0800
0900
1000
1100
1200
1300
1400
1500
1600
1439
1700
1800
1900
2000
1433
1411
1418
09°00'
08°54'
08°48'
08°42'
08°36'
08°30'
08°26'
23°18'
23°12'
23°06'
23°00'
22°54'
22°48'
22°42'
22°36'
22°30'
22°24'
22°18

Fig. 1. Track of the R.V. *Columbus Iselin* on September 16, 1974.

length (again an upper limit) is estimated to be roughly 3.2 km. At a depth of 30 m, the horizontal resolution of the acoustic system is roughly 7 m. Any oscillation of this order or larger should be detected (assuming of course, that an acoustic scatterer is present). The maximum amplitude in the packet is approximately 10 m. The acoustic scatterer before the onset of the wave packet is at a fixed depth (i.e. no oscillations at or near the 350-m-wavelength range*); the scattering layer after the passage of the packet is slightly lower ($\sim$4 m) than before the passage of the packet.

A second observation of a possible internal wave packet was made between 0240 and 0320 U.T. on September 16, 1974 (Fig. 3). There was an area of high acoustic return ranging from a depth of about 25 m to a depth of about 70 m. This area of high acoustic return is a manifestation of the deep scattering layer, which is known to be biological in origin. A second area of acoustic return ranges from a depth of about 220 to 230 m. Time runs from left to right in the figure. The ship was underway at a speed of approximately $2.0\,\mathrm{m\,s^{-1}}$. A sequence of four expendable bathythermograph (XBT) observations was made during and after the ship's passage through the internal wave group. The launching times of the four XBTs are indicated in Fig. 3, and the XBT records are shown in Fig. 4.

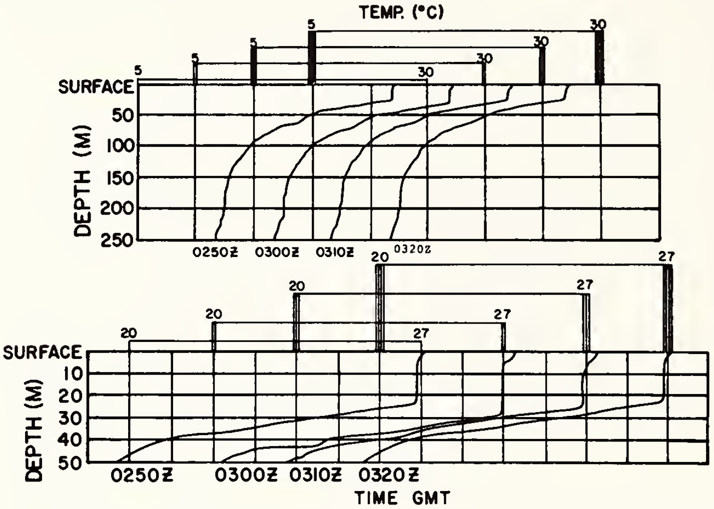

Fig. 4. XBT records obtained during the traversal of the wave group shown in Fig. 3.

The wave packet begins with a downgoing oscillation (the packet is thought to be propagating from left to right in Fig. 3; see page 303 for a discussion of this choice of propagation direction) as did the packet shown in Fig. 2. Note also the depression of 2 to 3 m in the mean depth of the uppermost portion of the deep scattering layer, which results upon passage of the internal wave packet.

Consider now the XBT taken at 0320 U.T. (Fig. 4). This observation was before the wave group had arrived at its location (Lat. 08°55.4′N, Long. 22°46.3′W). The mixed layer extended to a depth of about 32 m. A second layer of uniform temperature is visible in the depth range 162 to 200 m. Consider now the XBT observation at 0310 U.T.; the upper mixed layer had increased its depth to about 25 m. This XBT appears to have

---

*There may be present, of course, oscillations of the scattering layer in other lower frequency bands, such as the semi-diurnal tide, for example.

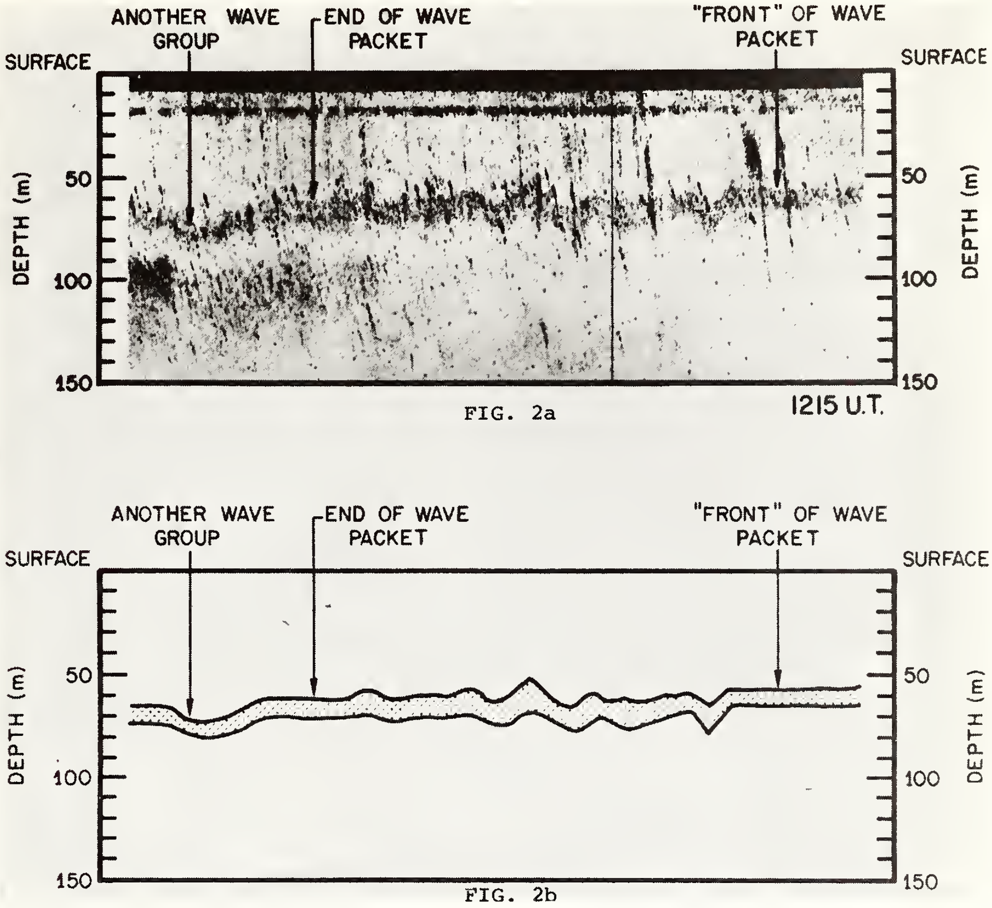

Fig. 2. (a) Acoustic record of an internal wave group observed from 1130 to 1230 U.T. on September 16, 1974. The record length is roughly 4.4 km. (b) Schematic portrayal of the wave packet record in (a).

[*facing p.* 302]

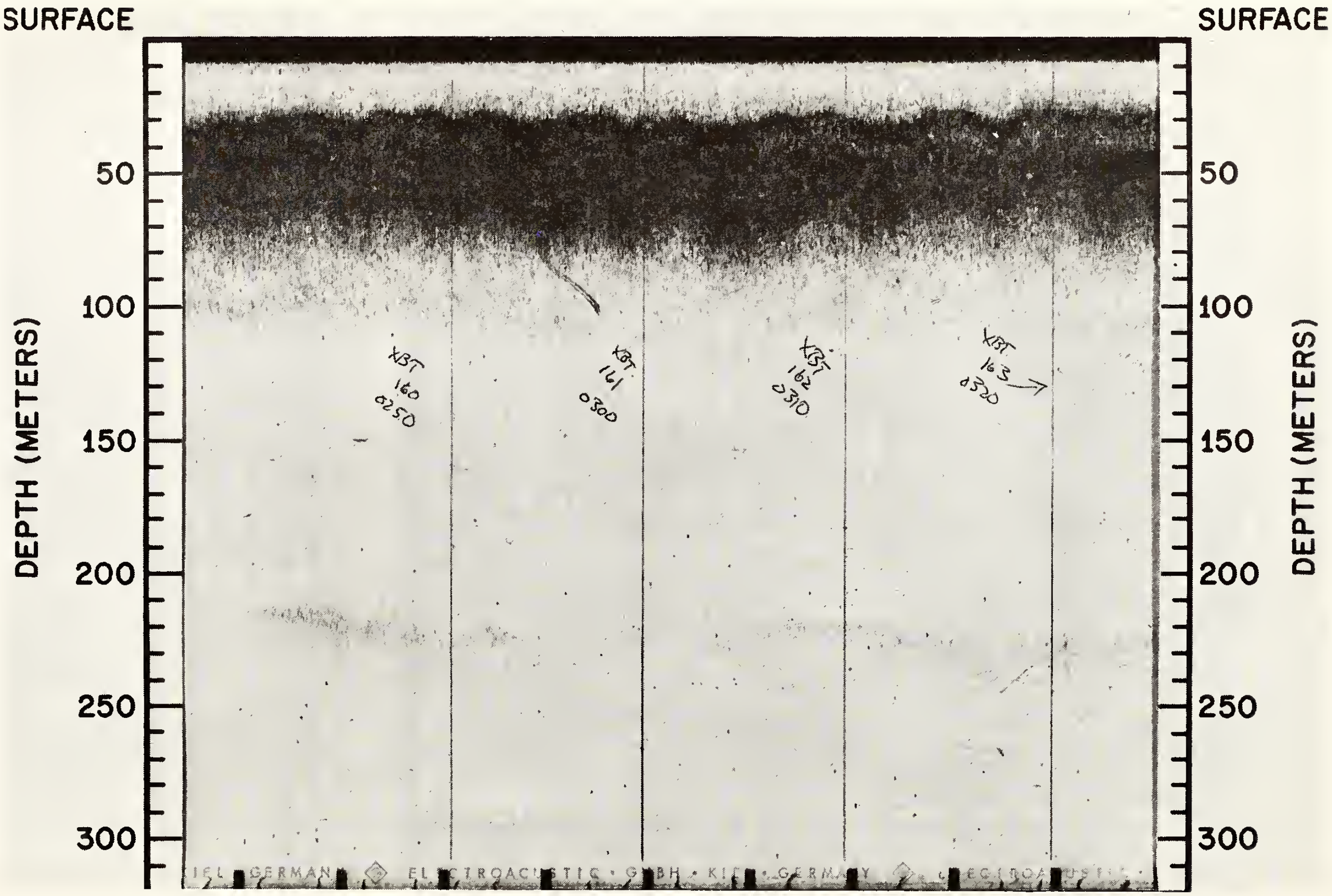

Fig. 3. Acoustic record of an internal wave group observed at night on September 16, 1974. The deep scattering layer is clearly seen in the 25- to 80-m depth range. Four XBT records were taken as the R.V. *Columbus Iselin* traversed the wave group; their respective launch times are indicated in the figure.

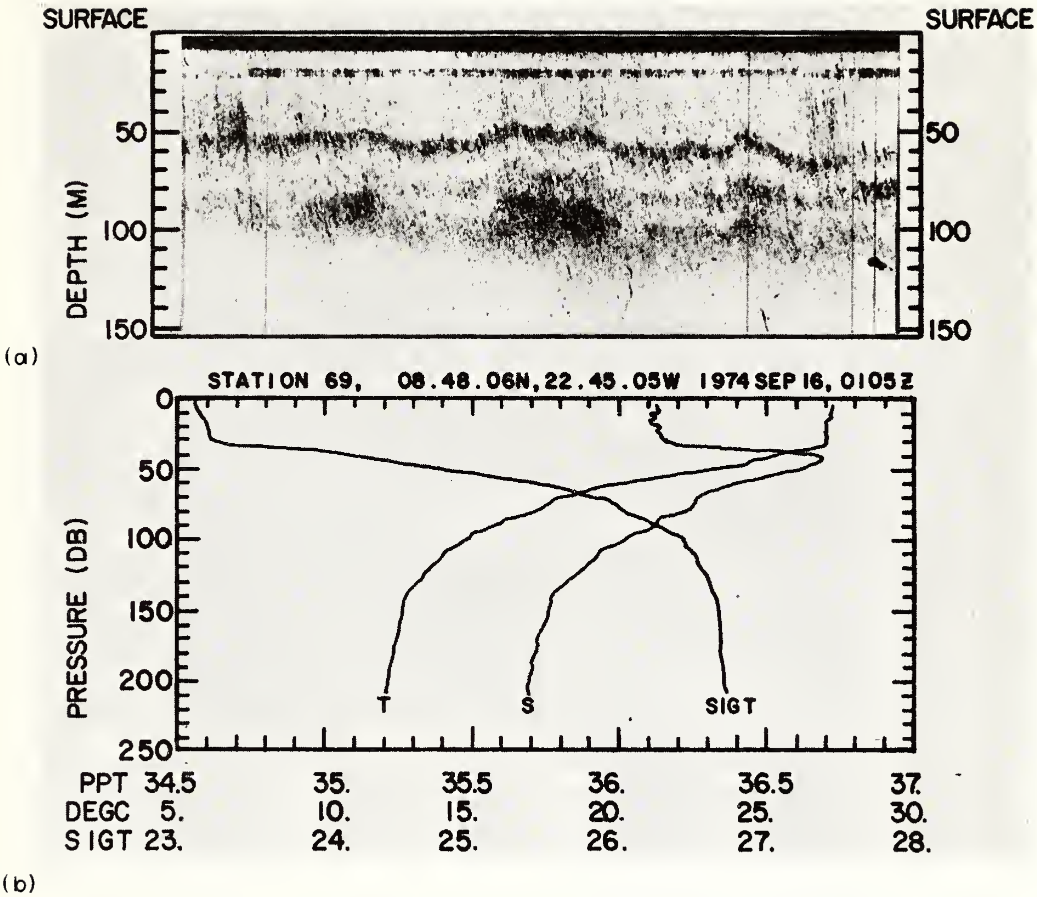

Fig. 5. (a) Example of typical internal wave activity observed in the GATE area (no clearly defined wave packets are visible). (b) Temperature, salinity, and (computed) density profiles for September 16, 1974.

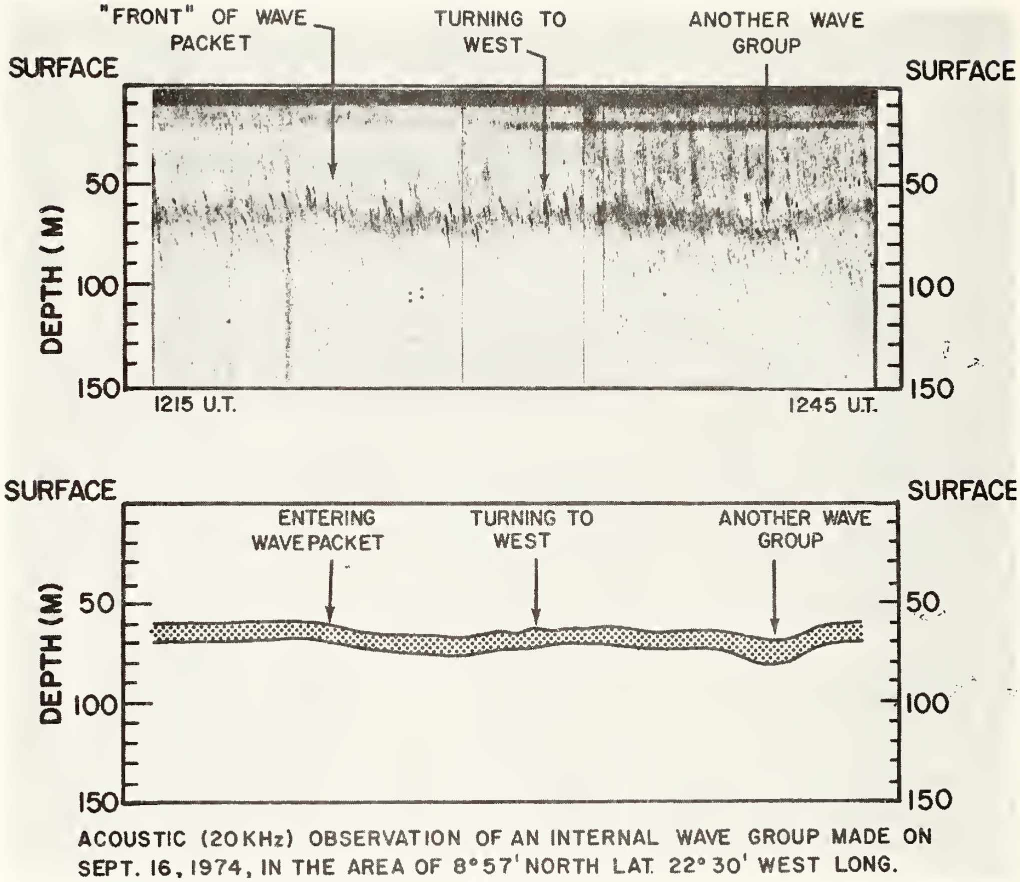

Fig. 6. Acoustic record obtained from about 1210 to 1245 U.T. These data were obtained immediately after the data shown in Fig. 2.

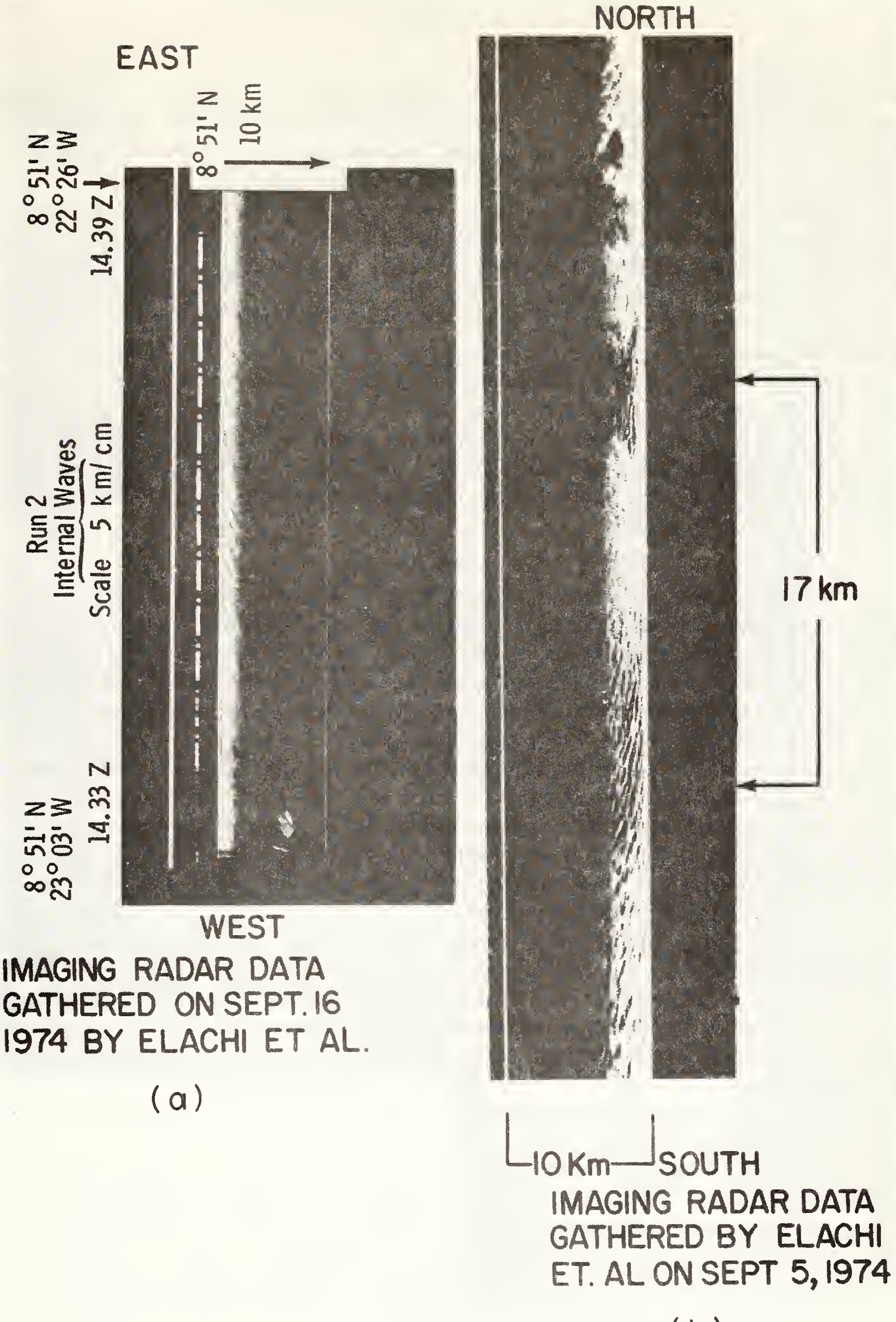
EAST
8°51' N
22°26' W
14.39 Z
8°51' N
10 km
Run 2
Internal Waves
Scale 5 km/cm
14.33 Z
8°51' N
23°03' W
WEST
IMAGING RADAR DATA GATHERED ON SEPT. 16 1974 BY ELACHI ET AL.
(a)
NORTH
17 km
10 Km
SOUTH
IMAGING RADAR DATA GATHERED BY ELACHI ET. AL ON SEPT 5, 1974
(b)

Fig. 7. (a) Imaging radar data from September 16, 1974 by ELACHI *et al.* (1977), while flying west to east. (b) Imaging radar data gathered by ELACHI *et al.*, on September 5, 1974 while flying on a north–south course.

been taken between a trough and a crest of the internal wave packet. The remaining two XBT records (0300 and 0250 U.T.) were made during the passage of the vessel over a trough. The latter three XBTs clearly show the depression (the depth extension of the mixed layer) generated by the passage of the internal wave group.

Another interesting comparison can be made between acoustic and XBT information by examining the acoustic scattering layer in the 220- to 230-m range. In the data from the XBT taken at 0320 U.T. (Fig. 4) a deep mixed layer (i.e. a layer of uniform temperature) is evident between 158 and 200 m. In the XBT at 0310 U.T., this deep mixed layer occupies the range 156 to 190 m. At 0300 U.T., the deep mixed layer was in the depth range 180 to 212 m. The general trend of the vertical movement of the mixed layer depth is in agreement with the trend observable in the acoustic data in Fig. 4. For example, at 0320 U.T., the acoustic scattering layer was several meters deeper than at 0310 U.T. Also the shorter internal waves visible within the packet at a depth of about 25 m are absent from the deeper oscillations. Such short wavelength oscillations would have been detected if they were present, because the horizontal resolution of the acoustic system at 200 m is approximately 50 m.

ANALYSIS

An attempt is made to interpret the acoustic data using an open ocean internal wave surge as a model. The original interpretation of the GATE data as an internal surge was inspired by the similarity of the structural form of the GATE wave packet to the form of continental shelf wave packets.* A typical continental shelf internal wave packet is shown in Fig. 2 of the paper by **Proni** and **Apel** (1975).† This wave packet shows several features in common with wave packets observed in the GATE area. These features are as follows: (i) the wave packets begin with a downgoing oscillation; (ii) the largest oscillations are at the leading edge of the packet; (iii) the mean scatterer depth before the onset of the wave packet is less than the mean scatterer depth after the onset of the wave packet. (This effect is more marked in the continental shelf wave packet than in the GATE data.)

Similarity in form alone is not enough to have confidence in a surge interpretation. The next step in establishing a surge interpretation is to determine what are the expected governing equations and then to determine whether these governing equations admit surges as solutions.

The propagation of the continental shelf wave packet (**Lee** and **Beardsley**, 1974) is known to be described by the non-linear Korteweg–deVries–Burger equation. The downward initial oscillation of the continental surge follows as a natural consequence of energy dissipation. The initial oscillations are thought to be so-called solitons. The causative mechanism for shelf packets is thought to be the interaction of tides with bottom topographic features.

Benjamin (1967) appears to have pioneered the study of non-linear internal waves in fluids of great depth. He has shown that: (i) the non-linear governing equations of a two-fluid system, one of finite thickness, *h*, and the other of infinite depth, admit solitary waves as solutions; (ii) these same non-linear equations admit the existence of internal bores or surges.

The above conclusions are derived using (and are valid only to the limit of) a first approximation to the effects of finite wave amplitude. The necessary condition for non-linear effects to manifest themselves and for the applicability of Benjamin's theory is:

---

*This does not mean to imply that the mechanism of generating the deep ocean internal wave group under consideration need be the same as that of continental shelf internal wave groups.

†This figure is reproduced in the Appendix of this paper.

$$\frac{a\cdot\lambda}{h_1^2}\approx 0(1), \tag{1}$$

where a is the internal wave amplitude, λ is the internal wave length, and h_1 is the depth of the mixed layer.

A typical density profile from the GATE area is shown in Fig. 5. From that figure, we have $h_1 \sim 35$ m. From Fig. 2, we have a $\sim$ 10 m, $\lambda \sim 400$ m, hence:

$$\frac{a.\lambda}{h_1^2}\approx 4. \tag{2}$$

Therefore, we assume the applicability of Benjamin's theory and its consequences (i) and (ii) listed earlier.

According to BENJAMIN (1967), the speed of propagation, C_{NL}, for a deep ocean solitary wave is:

$$C_{NL}^2 = C_L^2\left(1+\frac{3\rho_2 a}{4\rho_1 h_1}\right), \tag{3}$$

where ρ_1 is the mixed layer density, ρ_2 is the density of the lower layer (Benjamin has a two-layer model), and C_L is the speed of propagation of a linear internal wave and is given by

$$C_L^2 = \left(\frac{\rho_2-\rho_1}{\rho_2}\right)gh_1, \tag{4}$$

where g is gravitational acceleration.

It is of interest to try to estimate the place of origin of the internal wave packet. This can be done if it is assumed that the leading edge of the packet travels C_{NL} and the tail of the packet travels at C_L. It is also necessary to know the true length of the packet, Lp. From Fig. 2 the observed length, L, of the packet is roughly 3.5 km. From Fig. 5 one obtains $\rho_2 = 1.0265$ and $\rho_1 = 1.0234$. Then, using equation (4), it is estimated that $C_L = 87\,\mathrm{cm\,s^{-1}}$. Now,

$$L_p = (C_{NL}-C_L)(t_{\mathrm{obs}}-t_{\mathrm{origin}}), \tag{5}$$

where t_{obs} is the time of observation of the wave packet and t_{origin} is the time of origin of the wave packet. If r is the distance from the point of observation of the wave packet and L the observed packet length, then

$$r = C_{NL}(t_{\mathrm{obs}}-t_{\mathrm{origin}}) = C_{NL}\cdot\frac{Lp}{(C_{NL}-C_L)} \leqq C_{NL}\frac{L}{(C_{NL}-C_L)}. \tag{6}$$

Thus the maximum value for r is roughly 30 km.

Benjamin also gives an estimate for the width of a soliton Λ:

$$\Lambda = \frac{4}{3}\left(\frac{\rho_1}{\rho_2}\right)^2\left(\frac{h^2}{a}\right)\cong 83\,\mathrm{m}. \tag{7}$$

Note that the condition [equation (2)] for the appearance of non-linearity is relatively weakly dependent on λ, so that even if Λ replaced λ in equation (2), the non-linearity condition is satisfied.

A question of importance is whether there is any observational evidence to support the conjecture that the internal wavegroup shown in Fig. 2 is moving in an easterly or southeasterly direction. There are four data sets that can possibly shed light on this question: (i) additional 20-kHz observations by the authors; (ii) coherent imaging radar observations by ELACHI, CAILLAT and ROSS (1977); (iii) hydroglider (a towed variable depth device) data gathered by MOLLO-CHRISTENSEN, MOREY and STRIMAITIS (1975); and (iv) Batfish (a towed variable depth device) data gathered by WOODS (1974).

Examination of the ship's track (Fig. 1) suggests that the R.V. *Columbus Iselin* may have traversed the internal wave packet more than once. The acoustic data between 1200 and 1400 U.T. suggest the idea of an east-southeasterly traveling wave packet. Suppose (as a working hypothesis), that one has an easterly traveling wave packet and that the ship overtook the wave packet while traveling in an easterly direction. At about 1210 U.T., the vessel has passed over the leading oscillation of the wave packet. At about 1218 U.T., the ship turned toward the south and thus should have crossed the wave packet along a trough or crest; this should have resulted in diminished internal wave oscillations (as seen in the acoustic data) but an overall depression of the acoustic reflector level (compared to the reflector level before the onset of the wave group—e.g. at 1210 U.T.) should have been present. That this is the case may be seen by an examination of Fig. 6. As the vessel turned west (about 1237 U.T. Fig. 6) it encountered the latter part of the wave group and apparently once again encountered the depression (identified in Fig. 2 as 'another wave group') following the wave packet of interest. The length of the southerly leg (1210 to 1230 U.T.) was about 3 km, suggesting at least this lateral (i.e. along a crest) horizontal extent for the wave group. Imaging radar observations by ELACHI *et al.* (1977), show the presence of surface bands of low radar reflectivity. [For a discussion of imaging radar techniques in oceanography see the paper by BROWN, ELACHI and THOMPSON (1976)]. If these bands are interpreted as surface manifestations of an internal wave field, then an east-southeasterly (or west-northwesterly) direction of propagation is indicated.

Imaging data gathered by Elachi and his colleagues on September 16, 1974 in the large rectangle shown in Fig. 1, are presented in Fig. 7(a). These data are not precisely coincident with the acoustic data shown in Fig. 1. Also shown in Fig. 7(b) are imaging radar observations in the same general GATE area on September 5, 1974. Several long surface bands, marked 'internal waves' in Fig. 7, appear in the data from September 16. From the alignment of the bands, it can be inferred that internal waves, assumed to be associated with the bands, travel in a southeasterly (or northwesterly) direction. More dramatic records were obtained on September 5, 1974. In these data, two areas that may be internal wave packets are evident. Once again an east-southeasterly direction of propagation is indicated. The imaging radar data, while not confirming the acoustic data in detail, generally support the existence of discrete internal wave groups in the GATE area at the time the acoustic data were gathered.

Mollo-Christensen has published a preliminary analysis of his hydroglider observations, which were simultaneous with the acoustic observations aboard the R.V. *Colombus Iselin* (MOLLO-CHRISTENSEN *et al.*, 1975). Temperature and salinity data (obtained by towing the hydroglider) also indicate the presence of an internal wave field propagating either in the southeasterly or northwesterly direction.

To facilitate comparison with other data obtained from the hydroglider (MOLLO-CHRISTENSEN *et al.*, 1975) and the Batfish (WOODS, 1974, 1976), the acoustic data were analyzed to determine the mean depth of the acoustic reflecting layer for each of the R.V. *Columbus Iselin* track segments (Fig. 1) and for the standard deviation of the reflector depth, (Table 1). A deepening of the average reflector depth during the passage of the ship over the packet is indicated.

Table 1. *Mean depths and standard deviations of the acoustic reflecting layers for certain R.V.* Columbus Iselin *track segments shown in Fig. 1.*

TIME INTERVAL	MEAN (m)	STANDARD DEVIATION (m)
0820 - 0905	50.4	3.8
0905 - 1015	56.0	3.3
1015 - 1210	58.3	5.2
1210 - 1230	56.7	2.1
1230 - 1330	57.3	2.9
1330 - 1420	56.2	

A substantial amount of additional acoustic data were gathered during GATE. However, although much internal wave activity was detected, few wave packets were detected. A typical example of the internal wave activity frequently seen is shown in Fig. 5(b).

CONCLUSIONS

The main conclusions of this study are: (i) acoustic data indicate the presence in the deep ocean of spatially discrete, high-frequency internal wave packets; (ii) the form of the internal wave packet is similar to that of internal wave packets along continental shelves. The main features of the wave packet include (a) a weak non-linearity, (b) a downgoing first oscillation, and (c) a slight deepening of the reflecting acoustic layer; (iii) the place of origin is estimated to be on the order of 30 km from the place of observation.

A referee of this paper has asked about the possibility that the wave groups reported in this paper might arise from periods of 'intermittency' in a general background of quasi-random, high-frequency internal waves. To define an internal wave packet, two calm periods (i.e. periods of no high-frequency internal wave activity) are required to define the beginning and the end of the packet. Two such calm periods can arise either by being genuinely calm (i.e. truly devoid of high-frequency internal wave activity) or as a consequence of a momentary nulling of a superposition of quasi-random internal waves.

The authors believe that, while it is not impossible, it is highly unlikely that the structural form required of the internal wave group (as stated on page 303) would be produced by a chance (double) nulling of the quasi-random internal wave field. The calm periods on either side of the wave group shown in Fig. 2(a) are several kilometers long, the calm area being terminated by the abrupt onset of the internal wave group. Had the calm period been produced by an extensive null, it is unlikely that such an abrupt large amplitude internal wave onset should occur, rather, one should expect a gentle period of

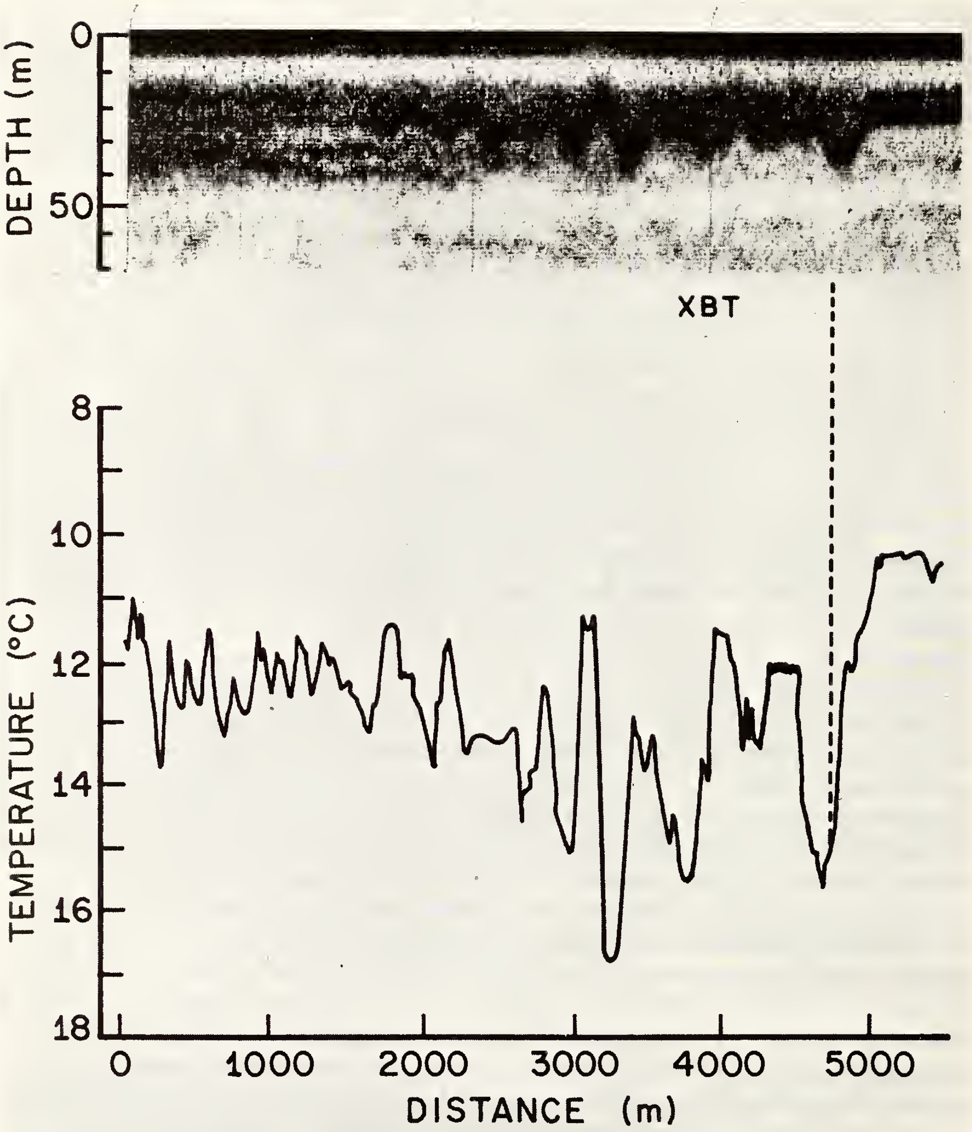

APPENDIX

Fig. A1. The figure is a reproduction of Fig. 2 in PRONI and APEL (1975). The leading edge of the wave packet is on the right. The water depth is about 110 m (New York Continental Shelf).

[*facing p.* 306]

wave amplitude growth as the null departed. At the present time, the authors can offer no information on the processes of generation of the internal wave groups.

Acknowledgements—Useful suggestions and comments were made to the authors at the Southampton (England) GATE data review in the summer of 1975. Thanks are extended to our colleagues at this meeting, particularly STEVEN THORPE, JOHN WOODS, ERIC MOLLO-CHRISTENSEN, and KLAUS HASSELMANN. CHARLES ELACHI has been most generous in allowing us to use a portion of the imaging radar data he gathered in 1974, we sincerely thank him for his kindness. DUNCAN ROSS made the original suggestion that the imaging radar data lend support to the acoustic wave packet interpretations. T. BROOK BENJAMIN was also kind enough to review this manuscript. CHARLES LAUTER carried out, in expert fashion, the electronics work required in the acoustic observations.

REFERENCES

APEL J. R., H. M. BYRNE, J. R. PRONI and R. L. CHARNELL (1975) Observations of oceanic and internal surface waves from the Earth Resources Technology Satellite. *Journal of Geophysical Research*, **80**, 865–881.

BENJAMIN, B. (1967) Internal waves of permanent form in fluids of great depth. *Journal of Fluid Mechanics*, **29**, 559–592.

BREKHOVSKIKH L. M., K. V. KONJAEV, K. O. SABININ and A. N. SERIKOV (1975) Short period internal waves in the sea. *Journal of Geophysical Research*, **80**, 856.

BROWN W. E., JR., C. ELACHI and T. W. THOMPSON (1976) Radar imaging of ocean surface patterns. *Journal of Geophysical Research*, **81**, 2657–2667.

ELACHI C., J. CAILLAT and D. ROSS (1977) Imaging radar observations in GATE. To be submitted to *Journal of Geophysical Research.*

GARGETT A. E. and B. A. HUGHES (1972) On the interaction of surface and internal waves. *Journal of Fluid Mechanics*, **52**, 179–191.

HALPERN D. (1971) Semidiurnal internal tides in Massachusetts Bay. *Journal of Geophysical Research*, **76**, 6573–6584.

HUNKINS K. and M. FLIEGEL (1973) Internal undular surges in Seneca Lake: a natural occurrence of solitons. *Journal of Geophysical Research*, **78**, 539–548.

LAFOND E. C. (1961) Boundary effects on the shape of internal temperature waves. *Indian Journal of Meteorology*, **12**, 335.

LEE C. and R. C. BEARDSLEY (1974) The generation of non-linear internal waves in a weakly stratified shear flow. *Journal of Geophisical Research*, **79**, 453–462.

MIROPOL'SKIY YU. Z. (1973) Probability distribution of certain characteristics of internal waves in the ocean. *Izvestiya, Atmospheric and Ocean Physics*, **9**, 411.

MOLLO-CHRISTENSEN E., K. A. MOREY and D. STRIMAITIS (1975) Towed probe observations of upper ocean; made from R.V. *Columbus Iselin* during GATE III, September 1974, Vols. 1 and 2, Massachusetts Institute of Technology, Department of Meteorology Report, October 1975. pp. 32–34.

OSTAPOFF F., J. R. PRONI and R. L. SELLERS (1975) Preliminary analysis of ocean internal wave observations by acoustic soundings. GATE Report, **14**, World Meteorological Organization, Geneva, 392–397.

PRONI J. R. and J. R. APEL (1975) On the use of high-frequency acoustics for the study of internal waves and microstructure. *Journal of Geophysical Research*, **80**, 1147–1151.

SABININ K. D. (1971) Measurement of the parameters of internal waves by means of a moving, spatially separated system of sensors. *Izvestiya, Atmospheric and Oceanic Physics*, **7**, 379.

THORPE S. (1968) On the shape of progressive internal waves. *Philosophical Transactions of the Royal Society London*, Series A, **263**, 563.

THORPE S. (1974) Near-resonant forcing in shallow two-layer fluid: a model for the internal surge in Loch Ness? *Journal of Fluid Mechanics*, **63**, 509.

WOODS J. (1974) Batfish experiments on RRS *Discovery*. Part 1: Measurements and analysis at sea. Oceanography Department, Southampton University, pp. 1–3.

WOODS J. (1976) Batfish experiments on RRS *Discovery* during Phase III of GATE, 2–16 September, 1974. Part 2: Data processing at Southampton. Oceanography Department, Southampton University, 2nd revised edition, January 1976, 413–414.

ZIEGENBEIN J. (1969) Short internal waves in the Strait of Gibraltar. *Deep-Sea Research*, **16**, 479.

Nature 276, No. 5686, 360-362.

Vertical particulate spires or walls within the Florida Current and near the Antilles Current

John R. Proni, Fred C. Newman, Feodor Ostapoff & Donald J. Walter

National Oceanic and Atmospheric Administration, Atlantic Oceanographic and Meteorological Laboratories,
Ocean Acoustics, Miami, Florida 33149

Spires or humps of particulate material extending from the bottom of the oceanic mixed layer to near the ocean's surface have been observed in the Florida Current and in the regions of other current systems, using an ultrasensitive, 20-kHz acoustical echo sounding system. These spires may be the result of oceanic circulation rather than a purely biological phenomenon.

ACOUSTIC observations of spires of particulate matter extending from the bottom of the mixed layer to near the surface of the ocean have been made in the Florida Current (November 1977), in the region of the Antilles Current (January 1973) and in the Caribbean (April 1978). The Florida Current observations were made in the vicinity of 80° W long, and in latitudes between 25 and 28° N; Antilles Current region observations were made in around 70° W long, 25° N lat, and the Caribbean observations were made in a region ~200 nm north of Caracas, Venezuela. The observations were made using an ultrasensitive, short pulse length (<1 ms), towed, narrow beam (18°), 20 kHz acoustic echo sounding system. The use of this system to detect layers of particulate matter and internal waves in the ocean has previously been documented[1,2]. The acoustical frequency (20 kHz) and receiver sensitivity are such that scattering from oceanic turbulence or density gradients is not detectable, so that particulates and/or biota are the most likely sound scatterers detected.

Acoustic and XBT data

Figure 1 shows real-time acoustic data obtained from the RV Researcher while crossing the Gulf Stream off Palm Beach, Florida. The ship proceeded due east from Palm Beach, at a speed of 2 m s^{-1} beginning in water of depth 220 m. A layer of particulate matter corresponding to the depth of the bottom of the mixed layer may be seen gradually descending spatially from left to right (labelled A in Fig. 1). Lines of constant density (isopycnals) are known to slope down proceeding from west to east across the Gulf Stream[3]. The slope of the reflecting layer has a value ~4×10^{-3} which compares favourably with the 3×10^{-3} isopycnal slope, a value deducible from the isopycnal data of Schmitz and Richardson[3]. Interference lines generated by the Researcher's echo sounder are indicated and should be disregarded.

The most interesting features are the spires of particulate material which are seen to extend vertically from the particulate layer corresponding to the bottom of the mixed layer. Figure 1 shows that the spires eventually disappear in a shorewards direction; the mean horizontal spacing of the spires is ~200 m. Spire widths at the base of a spire seem to be 100 m or more. An important characteristic of the acoustical system used in gathering the data presented in Fig. 1, is that it was not designed for obtaining data near the ocean's surface, say, within 10 m. Accordingly, information or acoustical signals coming from this region is suppressed by the electronics. Thus it is uncertain whether the particulate spires observed in Fig. 1 reach the ocean surface.

Expendable bathythermograph (XBT) records were gathered at the same time as for the acoustic data. Three XBT records taken at 21.30, 21.45, and 22.00 LT, are shown in Fig. 2. Note that the temperature profiles are essentially featureless down to the depth of the acoustic reflecting layer, at which depth small temperature gradients are visible. Previous experience[4-6] has shown that a particulate layer is often observed in coincidence with a temperature gradient. In addition to the shallowest temperature gradient (clearly visible at 45 m), the temperature profile gathered at 21.45 LT has two small temperature gradients (I and II in Fig. 2; with the corresponding reflecting layers marked I and II in Fig. 1).

From the data of Schmitz and Richardson[3], it is reasonable to expect that the northwards surface current varies from ~100 cm s^{-1} at the left of Fig. 1, to ~180 cm s^{-1} at the right of Fig. 1. The mean eastwards current is very small, being maximum at the right of Fig. 1, with a magnitude no larger than ~5 cm s^{-1}.

The acoustical data shown in Fig. 1 are greatly exaggerated in the vertical; Fig. 3 is a geometrically corrected interpretation of the data between the 7.7 and 8.8 km range limits of Fig. 1. Figure 3 shows that what we are calling spires, because of their appearance of the acoustic records, are in fact more like humps or mounds. 'Hump' may not be an adequate description, however, because the along-stream extent of a particular hump may greatly exceed its cross-stream extent; in which case perhaps the term 'wall' would be more appropriate. There is acoustical evidence that the along-stream length of a hump or spire could be >1 km.

Vertical structures

We can be certain that the vertical structures were observed in each cross-stream traverse made by the ship between longitude 28 and 25° N, but whether given spires in a crossing along-stream are continuations of given spires in another traverse is not.

Fig. 1 Acoustic reflecting layers and particulate columns observed while crossing the Gulf Stream: interference lines are labelled (i).

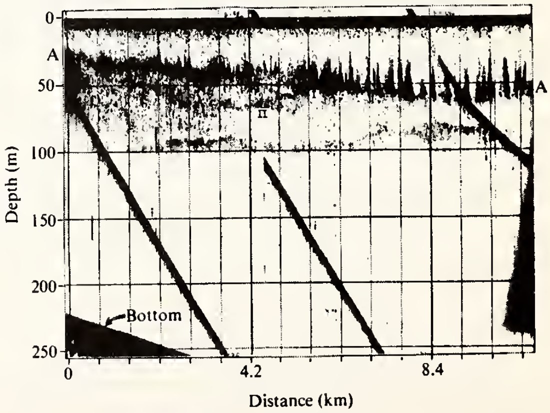

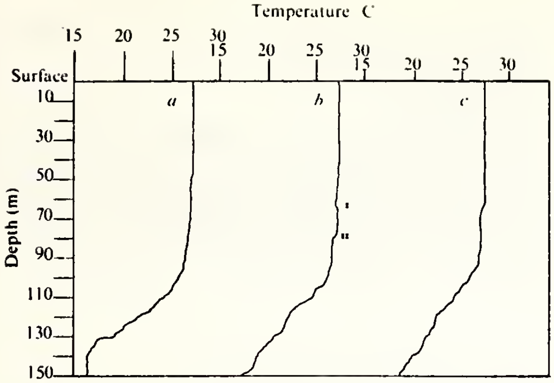

Fig. 2 Temperature profiles corresponding to the acoustic data in Fig. 1. *a*, T-11-38, 21.25LT; *b*, T-11-39, 21.43LT; *c*, T-11-40, 22.05LT.

The columns shown in Fig. 1 have a vertical extent, L, which is of the order of the depth of the bottom of the mixed layer, that is, if d is the depth of the bottom of the mixed layer, then

$$L \sim d \tag{1}$$

The spires have a horizontal spacing, h, which on average seems to be ~2–4 times the depth of the mixed layer:

$$2d \leq h \leq 4d \tag{2}$$

This conclusion is reached by examining substantial additional data to that shown in Fig. 1. Not all the spires are of equal size and dimensions; equation (2) is an average statement and implies that as the depth of the thermocline changes, as occurs in traversing the Gulf Stream, so too should N (the number of spires per unit horizontal distance) vary:

$$\frac{1}{4d} \geq N \geq \frac{1}{2d} \tag{3}$$

The spire width, w, at the spire base in the cross-stream direction is of the order of 2–5 times the mixed layer depth:

$$2d \leq w \leq 5d \tag{4}$$

A typical dimension for d is 50 m, so that $L = 50$ m, $100\ \text{m} \leq h \leq 200\ \text{m}$, $0.005\ \text{m}^{-1} \leq N \leq 0.01\ \text{m}^{-1}$, and $100\ \text{m} \leq w \leq 250$ m. The spire structures persist over a 24-h period and are not changed due to the rise of the deep scattering layer (DSL). In fact, the DSL rises to the thermocline depth and then contributes (for example, biota) to the particulate spires.

As we have stated, we are uncertain about the phenomena generating and sustaining the particulate spires. However, the hypothesis for the origin of the spires (or, perhaps walls) has two parts. First, the spires are not primarily the result of biological behaviour. The particulates comprising the reflecting layer, out of which the spires extend, are thought to be plankton, and in the case of the Florida Current, at least, are also thought to be sediment, perhaps in combination with biota. It is unlikely that such particulates are highly mobile, and, in any case, there is no report of innate particulate spire-forming behaviour for oceanic marine biota. Second, the spires arise from oceanic water circulation and congregate in spires (or walls) as a result of that circulation.

Fig. 3 Interpretation of the acoustic data in Fig. 1 from 7.7 to 8 km with the vertical exaggeration removed.

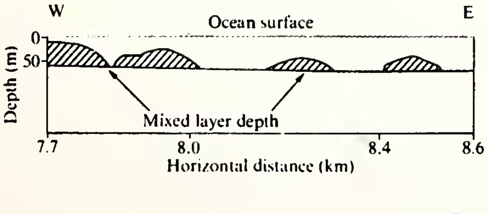

Water circulation

If the particulate structures arise from water circulation, what would be the form of that circulation? The structures might be formed by an upwards directed flow so that the particulates are carried upwards from the reflecting layer. If there is such a vertically directed flow, then only the uppermost reflecting layer contributes particulates to the flow. This can be seen by examining some of the deeper reflecting layers in Figs 1 and 4. No particulate spires extend from any other than the shallowest reflecting layer which suggests that the vertical flow is confined between the thermocline and the surface.

We feel that the proposed circulation is not due to the presence of internal waves. As may be seen from Figs 1 or 3, little or no vertical spatial variation of the shallowest reflecting layer appears on the 50–500 m length scale. Internal waves of this horizontal scale, of amplitude as small as a couple of metres, are detectable with this acoustic system[2]. However, small scale perturbations are visible on some of the deeper reflecting layers in Fig. 4. The kind of wind conditions at the time the spire observations were made may be relevant to whether circulation cells of some type are present. For example, Faller[7] has shown that certain wind and wave conditions must be present for Langmuir type circulations to occur. Table 1 shows wind and other data for various spire observations: such as measured winds exceed 5 m s^{-1} in all observations. This contradicts the results reported in ref. 8: in which it is stated that the "columnar scattering" is observed in the wind mixed layer during very calm weather conditions. Table 1 also indicates that observations of spires were made during daylight and night-time conditions. We do not wish to speculate any further, questions as to whether the flows are some sort of circulation cells (so-called Langmuir cells) must be put off for the moment.

Table 1 Data from observations of vertical particulate spires

Date	Location	Time interval of observation	Wind speed (m s^{-1})	Wind direction
19 Mar. 1978	14°12′ N 66°39.0′ W	20.56–22.06 LT	10	090°
11 Nov. 1977	28°59.5′ N 79°07.1′ W	08.30–13.00 LT	7–9	350–000°
11 Nov. 1977	29°03.9′ N 80°04.3′ W	19.00 LT–01.00 12 Nov.	8–10	330–350°
12 Nov. 1977	29°14.1′ N 79°42.7′ W	18.00 LT–06.30 13 Nov.	10–12	330–360°
14 Nov. 1977	26°49.3′ N 79°54.1′ W	21.00–23.30 LT	7	065–085°
31 Jan. 1973	25°21.8′ N 71°12.2′ W	11.35 LT	10	080°

Implications of particulate spires in the Gulf Stream

One of the most important implications of the existence of particulate spires in the Gulf Stream is the small scale variability in the horizontal of particulate densities. Figure 1 shows the small scale variability of particulate densities, both in the vertical and the horizontal. While on-station, the particulate columns have the appearance of patches as the ship slowly drifts. Depending on the along-stream length of the cells, there may be a distinct difference in a biological net tow, depending on whether the tow is along-stream or cross-stream. The behaviour in the deep scattering layer, mentioned above, is interesting in

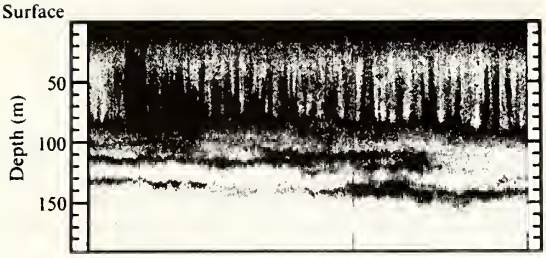

Fig. 4 Acoustic reflecting layers and spires in the area of the Antilles Current.

that the DSL is generally thought to be mobile, but, nevertheless, preferentially aligned above the thermocline into the spires.

There are also some interesting potential implications for ocean-mixed layer studies; particularly if spire formation indicates an underlying circulation. As Pollard[9] pointed out, circulations such as those of Langmuir are potentially efficient in mixed layer momentum redistribution. A major question remains: how widespread or typical are the phenomena described here? We do not know, for example, if such spires are in some way related to the presence of ocean currents. The data gathered in Fig. 1 were clearly in a current system—the Gulf Stream. The observations shown in Fig. 4 may have been of a less well known current system[10].

Conclusion

Spires of particulate matter have been observed extending from the bottom of the mixed layer to near the surface of the ocean and in the region of different ocean current systems. The detection of the spires was made possible through the use of an ultrasensitive 20 kHz acoustical system. Further research is required into the nature of the particulates present and of the phenomena generating the spires.

Received 2 May; accepted 2 October 1978.

1. Proni, J. R. *et al. Deep Sea Res.* **23**, 8, 831–837 (1976).
2. Proni, J. R. & Apel, J. R. *J. geophys. Res.* **80**, 9, 1147–1151 (1975).
3. Schmitz, W. J. & Richardson, W. S. *Inst. Mar. Sci. Lab.* 222 (University of Miami, ML 66202 (Mimeographed) 1966).
4. Newman, F. C., Proni, J. R., Walter, D. J. & Byrne, H. M. *Nature* **269**, 790–791 (1977).
5. Drake, D. E. *Deep Sea Res.* **18**, 763–769 (1971).
6. Heathershaw, D. C. & Simpson, J. H. *Estuar. Coastal Mar. Sci.* **2**, 91–103 (1974).
7. Faller, A. J. *Science* **201**, 618–629 (1978).
8. Angel, M. V. in *Oceanic Sound Scattering Prediction* (eds Andersen N. R. & Zahuranec, B. J.) 217–248 (Plenum, New York 1977).
9. Pollard, R. T. in *Modelling and Prediction of the Upper Layers of the Ocean* (ed. Kraus, F. B.) 102–117 (Pergamon, Oxford, 1977).
10. Hansen, D. V. *A.I.A.A. Conf. Free Drifting Buoys* NASA CP-2003, Hampton, Virginia, 175–192 (1974).

Turbulent Fluxes Through the Sea Surface, Wave Dynamics, and Prediction, Series V: Air-Sea Interactions 1, 647-665.

A COMPARISON OF PARAMETRIC AND SPECTRAL HURRICANE WAVE PREDICTION PRODUCTS

Duncan Ross* and Vincent Cardone**

*National Oceanic and Atmospheric Administration,
Atlantic Oceanographic and Meteorological Laboratories, Miami, Florida, 33149
**City University of New York, New York, 10031

INTRODUCTION

Statistics of extreme wave heights created by tropical cyclones are urgently needed for the design of harbor breakwaters, ships, and offshore structures to prevent accidents from underdesign and to avoid the untenable costs of overdesign. Wave data alone cannot provide the needed statistics due to the long periods required to collect statistically reliable data sets and the inability to deploy enough systems to obtain measurements of maximum conditions. Needed statistics, therefore, are usually extracted from models which attempt to specify the wave environment associated with particular storm systems. These models are either largely untested against measurements, or are validated over a limited range of storm conditions. One such model is that of Cardone et al. (1976a) which was developed and calibrated using a data set obtained in hurricane Camille, a severe Gulf of Mexico storm which struck the coast of the U. S. in August 1969. Another is an empirically-based parametric model proposed by Ross (1976), based upon forty measurements of one-dimensional frequency spectra obtained in Camille, Pacific hurricane Ava (Ross, 1975), and Gulf of Mexico hurricane Eloise (Withee and Johnson, 1975).

A brief comparison of the Cardone et al. (1976a) model and the Ross (1976) parametric model, including data obtained in Atlantic hurricane Belle, has been conducted by Cardone et al. (1976b) and Cardone and Ross (1977). That study shows that both models produced comparable results for maximum wave conditions for storms moving at a forward velocity within the range of the calibration data sets (20-40 km/hr) but that the Cardone et al. model produces higher waves at lower frequencies than the parametric model for storms moving at higher forward velocities.

In this paper, the parametric and spectral models are intercompared systematically through a sensitivity study involving several hindcasts of a hypothetical hurricane, with the forward velocity varying from 0 to 80 km/hr. The differences between the spectral and parametric hindcasts are interpreted in terms of the alternate parameterizations of the physics of wave generation in the two methods.

The divergent results documented in the sensitivity study emphasize the limitations of state-of-art spectral and parametric models which are quasi-empirical and which depend upon observations of net wave growth for calibration.

Tropical cyclones provide a powerful test of wave prediction models since they exercise model parameterizations of growth and dissipative processes over a broad range. Fast moving tropical cyclones are associated with "moving fetches" which emphasize the differences between wave growth algorithms which are coupled and decoupled in frequency space. Wave measurements under such conditions would enable further testing of existing models and possibly provide insight into the nature of the spectral energy balance at large fetch.

PARAMETRIC AND SPECTRAL WAVE PREDICTION MODELS

The spectral model (Cardone et al., 1976a) is based upon the numerical integration of the wave energy balance equation

$$\frac{\partial S(f,\theta)}{\partial t} = -V_g(f,\theta) \cdot \nabla S(f,\theta) - F \qquad (1)$$

where S is the directional wave energy spectrum, f is wave frequency, θ propagation direction, V_g is the group velocity, and F represents a source function which accounts for all processes that transfer energy to, from, and within the wave spectrum. Equation (1) is solved by the successive simulation of the processes of wave growth, dissipation, and propagation at each time step, on a hexagonal grid of 1694 points nominally spaced 35 km apart on a gnomonic map projection. At each grid point, the spectrum is resolved into fourteen frequency and twenty-four direction bands. During each one-hour time step, equation (1) is solved for each of the 336 spectral elements. The source function F is applied only to spectral components propagating within $\pm 90^\circ$ of the local wind direction according to

$$F=\left[A(f,\theta,\vec{V})+B(f,\theta,\vec{V})\cdot S(f,\theta)\right] \times\left\{1-\left[\frac{S(f,\theta)}{S_{\infty}(f,\theta,\vec{V})}\right]^{2}\right\} \quad (2)$$

where A represents the linear growth rate (Phillips, 1957), B is the exponential growth term of the form suggested by Miles (1957), and $S_{\infty}(f,\theta,V)$ is the Pierson-Moskowitz (1964) fully-developed form of the spectrum with a windspeed-dependent high-frequency equilibrium range (Phillips, 1958) as suggested by Stacy (1973). Spectral components travelling against the wind are attenuated at a rate proportional to the fourth power of the wave frequency and the local energy of the wind sea. A frequency-dependent functional form for the directional spread of wave energy is prescribed, and in regions of rapidly shifting wind direction, an angular redistribution of spectral energy is imposed to preserve the known tendency for a growing spectrum to redistribute directionally, probably through non-linear interactions about the local wind direction. Propagation is accomplished by a Lagrangian scheme whereby spectral components jump to adjacent grid points in the appropriate direction after a sufficient number of time steps have elapsed to account for the displacement according to that component's deep water group velocity.

The parametric model is a simplification of the parametric approach to wave prediction proposed by Hasselmann et al. (1976). The method is considered to be applicable only to growing wind seas. The method follows from the data collected in the JONSWAP study, the analysis of which (Hasselmann et al., 1973) suggested that fetch-limited wave spectra can be normalized in a way such that there is an approximate invariance of normalized spectral shape with fetch. It was proposed that non-linear resonant wave-wave interactions were responsible for the shape invariance and that it characterized not only idealized fetch-limited siutations but growing wind seas in general.

The parametric approach exploits the shape invariance by representing the spectrum in terms of a small number of shape and scale parameters (e.g., five in the JONSWAP spectrum) and projecting equation (1) onto a set of prognostic equations for the parameters. The wave prediction problem then becomes computationally much simpler than the explicit application of equation (1) to a discrete two-dimensional spectrum.

Evidence of the shape-invariance of hurricane-generated wave spectra has been provided from spectra measured in hurricane Ava from an aircraft equipped with a laser altimeter, from wave measurements made in hurricane Camille as part of an oil industry measurement program (cf. Hasselmann et al., 1976), and from a meteorological data buoy during hurricane Eloise (Withee and Johnson, 1976). Those spectra matched well the JONSWAP spectral form, and Ross (1976) proposed that the advecting wave field in a hurricane might be determined by the local wind and a fetch determined by the local radius of curvature of the wind field, which is proportional to the radial distance to the eye, and derived a special parametric solution applicable only to hurricane generated seas.

The original analysis of JONSWAP data followed the procedure proposed by Kitaigorodskii (1961) such that for ideal fetch-limited wind seas, all wave variables, when non-dimensionalized in terms of g, gravity, and the windspeed, U, should be functions only of the single non-dimensional fetch, $\xi=gX/U^2$, where X is the fetch. In Hasselmann et al. (1976), the non-dimensional peak frequency $\nu=Uf_m/g$, where f_m is the peak frequency, was found to be described well by the relation

$$\nu=2.84\ \xi^{-0.3} \tag{3}$$

The non-dimensional total energy $\varepsilon=Eg^2/U^4$ where $E=\int S(f,\theta)d\theta df$ showed a linear fetch dependence

$$\varepsilon=1.6\times 10^{-7}\xi \tag{4}$$

Similar power-law fits were obtained for γ, σ_a, σ_b, and α (see Hasselmann et al., 1976, for a further discussion of these parameters).

In the Ross (1975) model, the fetch, X, is replaced by r, the radial distance to the eye of the hurricane, which should parameterize fetch or duration. The data set from hurricane Ava, Camille, and Eloise were then combined to produce the following power-law fits:

$$\left.\begin{array}{l} \nu=.97\ \xi'^{-.21} \\ \varepsilon=2.25\times 10^{-5}\xi'^{.45} \\ \gamma=4.7\ \xi'^{-.13} \\ \alpha=.035\ \nu^{.82} \end{array}\right\}\ \xi'\leq 3.0\times 10^{+4} \qquad \begin{array}{r} (5)\\ (6)\\ (7)\\ (8) \end{array}$$

where $\xi'=gr/U^2$. σ_a and σ_b were found to scatter somewhat about an average of approximately .1 but showed no consistent dependence on ξ'.

The wind field used to initialize both models is an adaptation of the theoretical model of horizontal air flow in the boundary layer of a moving vortex developed by Chow (1971). The model is based upon the numerical integration of the vertically averaged equations of motion that govern a boundary layer subject to horizontal and vertical shear stresses on the rotating earth. The model was calibrated against wind data collected in hurricane Camille, after the windspeed measurements were adjusted from measurement altitude to 20 meters using the boundary layer theory of Cardone (1969). For a more detailed description of the model, including comparison of predicted to observed winds, the reader is referred to Cardone et al. (1976a) and Forristall, Hamilton, and Cardone (1977).

MODEL VALIDATION

The spectral model, though calibrated largely on the basis of hurricane Camille wave data, has been rather extensively applied both in hindcast studies of historical hurricanes and in detailed hindcast studies of more recent storms for which wave data in one form or another exist. Cardone et al. (1976a) compared hindcast and measured or estimated maximum wave height in five separate Gulf of Mexico hurricanes. In eighteen cases, with measured maximum heights ranging from 6 to 24 meters, the RMS difference was 1.5 meters. The hindcast spectra of maximum conditions agreed well with a more limited number of available measured frequency spectra.

More recently, the deployment of automatic recording buoys equipped with wave recorders, by the National Oceanic and Atmospheric Administration National Data Buoy Office (NDBO), has resulted in the acquisition of unique wave data sets in hurricane Eloise (1975), in the Gulf of Mexico, and hurricane Belle (1976) on the U. S. East Coast. Cardone and Ross (1977) compared the spectral and parametric hindcasts of NOAA NDBO buoy EB10, which experienced eye passage and maximum wind and wave conditions in Eloise. Figures 1 and 2 from that study compare observed to hindcast time histories of wind and wave conditions during hurricane Eloise. It should be noted that wave data in Eloise from this buoy were used in the calibration of the parametric method.

Since it has only recently been proposed, the parametric method has not been extensively tested on storms independent of those which provided a basis for model tuning. Using both models, Cardone et al. (1976b) made a real-time wave forecast of hurricane Belle (1976), a moderately intense U. S. East Coast storm which passed directly over buoys EB15 and EB41, as shown in Figure 8. Errors in the wave forecasts were found to be caused mainly by errors in the official forecasts of storm intensity and the track

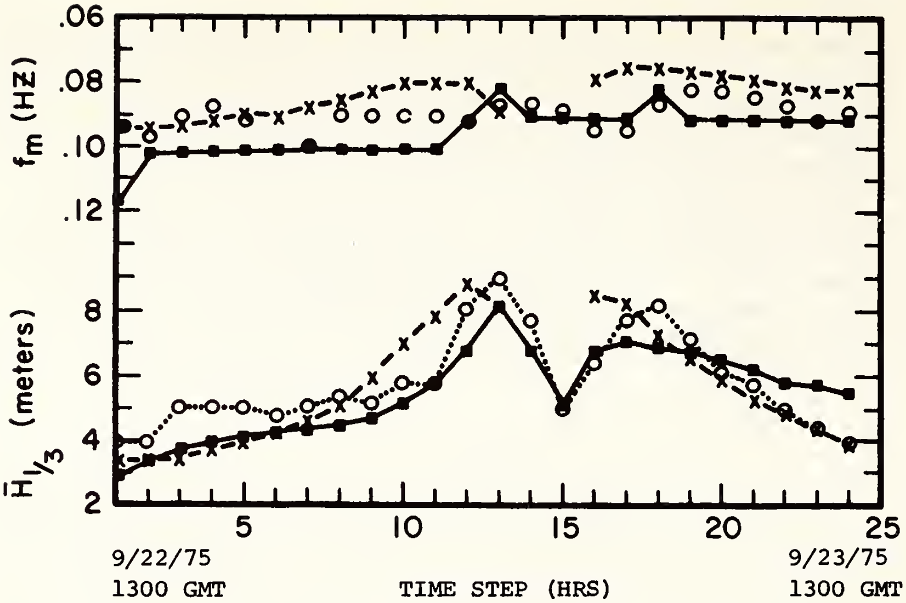

Figure 1. Comparison of measured (O), and hindcast significant wave height and spectral peak frequency from the parametric (X), and spectral (■) models at EB10 in hurricane Eloise.

used to calculate the forecast wind field. In the same study, the parametric and spectral models were used to hindcast two severe historical East Coast storms, Donna (1960) and a September, 1944, storm. Significant differences in maximum hindcast wave height and peak frequency were found, with the spectral model producing much higher sea states and much lower peak frequencies. This was a surprising result and was related at the time to the major difference between East Coast and Gulf hurricanes - the fast forward motion (65-85 km/hr) of the former.

It was hoped that the relatively fast forward motion (40 km/hr) of Belle along the upper coast and the availability of frequency spectra from EB41 would provide a basis for resolving the discrepancy noted in the historical hindcasts. Thus a detailed hindcast study of Belle was performed. It was found possible to specify the wind field quite accurately throughout its history, as verified by observed wind time histories at the buoys. The hindcast time histories of significant wave height are compared to the measurements in Figures 3 and 4. Hindcast frequency spectra associated with maximum sea states when the eye was near EB15 and 41 are compared in Figures 5 and 6. The sampling interval of three hours at the buoy apparently was not sufficient to resolve maximum conditions at EB15, as the measured hourly winds and both

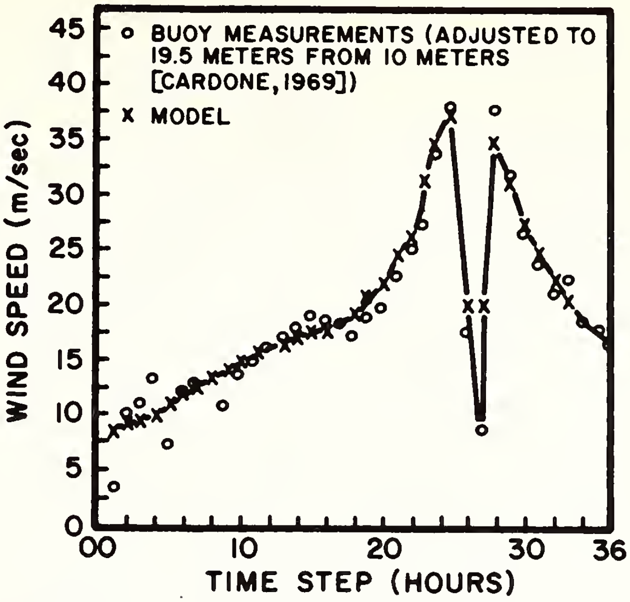

Figure 2. Comparison of measured and modeled average windspeed time history at EB10.

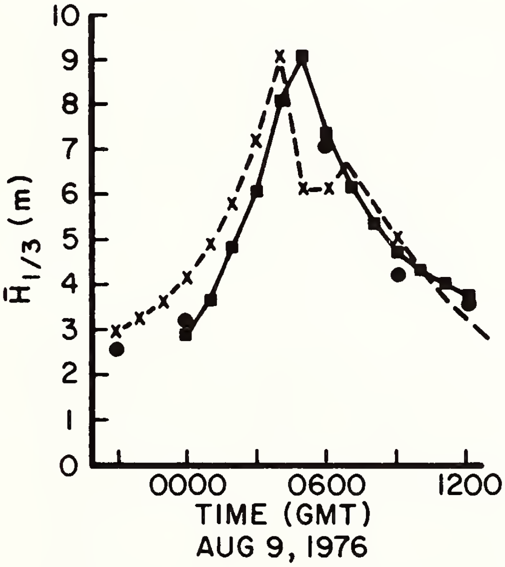

Figure 3. Comparison of measured and hindcast significant wave height at EB15 during hurricane Belle: ● - measured; X - parametric model; ■ - spectral model.

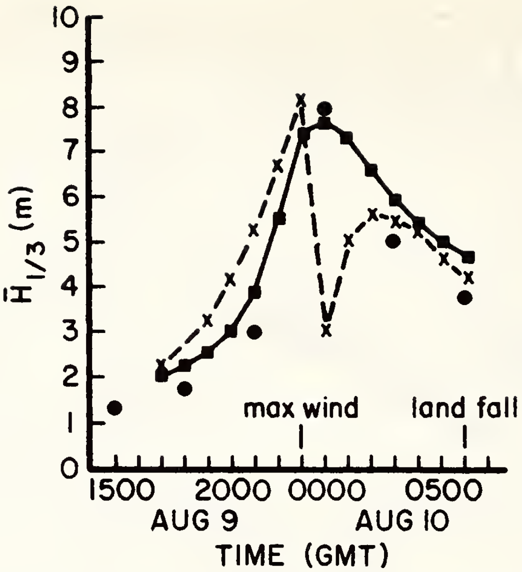

Figure 4. Comparison of measured and hindcast significant wave height at EB41 during hurricane Belle: ● - measured; X - parametric; ■ - spectral.

hindcast time histories suggest that peak sea states occurred just prior to the 0600 GMT buoy wave measurement. At EB41, however, peak conditions were more likely measured, and it is possible to compare the hindcasts and the measurement. Differences in the hindcasts for this storm are small, though the spectral model appears to simulate better the observed time history of wave height at the buoy locations. Belle, therefore, provided further validation of both models but failed to provide information on the divergence of the solutions for faster moving storms.

SENSITIVITY STUDY

To study the effect of storm motion on the relative differences between the parametric and spectral hindcast models in a more controlled fashion, a sensitivity study was conducted that involved four hindcasts. In that study, the wind field was specified for a hypothetical hurricane with attributes of central pressure (975 mb), peripheral pressure (1013 mb), pressure radius (75 km), ambient geostrophic flow (9 m/s), and forward velocity (10 m/s) that are close to the median values observed in the population of important hurricanes that have affected the U. S. East Coast this century. A similar sensitivity study has been reported recently by Uji (1975), but

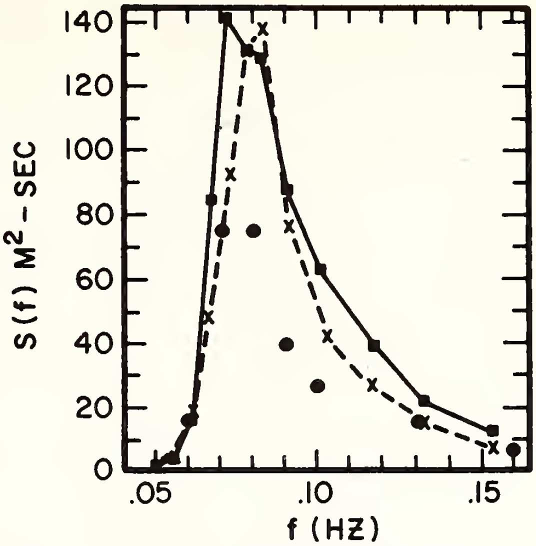

Figure 5. Maximum predicted spectra for hurricane Belle: X - parametric model, $\overline{H}_{1/3}$=9.0 m; ■ - spectral model, $\overline{H}_{1/3}$=10.1 m. Also shown is the maximum observed spectrum (●), $\overline{H}_{1/3}$=7.1 m, at EB15.

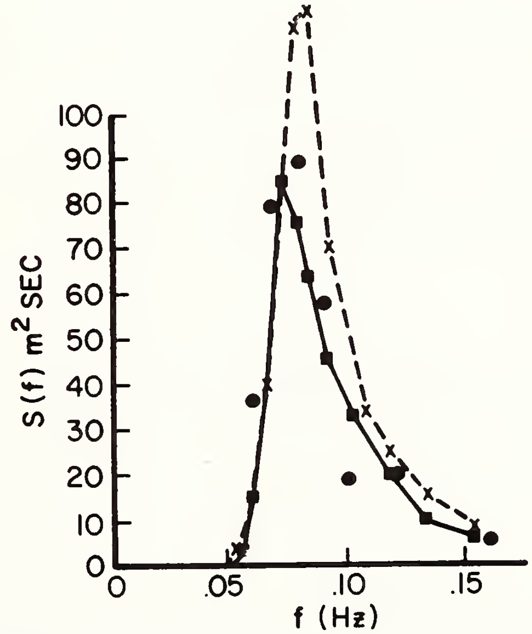

Figure 6. Maximum predicted spectra for hurricane Belle at EB41: X - parametric model, $\overline{H}_{1/3}$=8.2 m; ■ - spectral model, $\overline{H}_{1/3}$=7.8 m. Also shown is the maximum observed spectrum (●), $\overline{H}_{1/3}$=7.8 m.

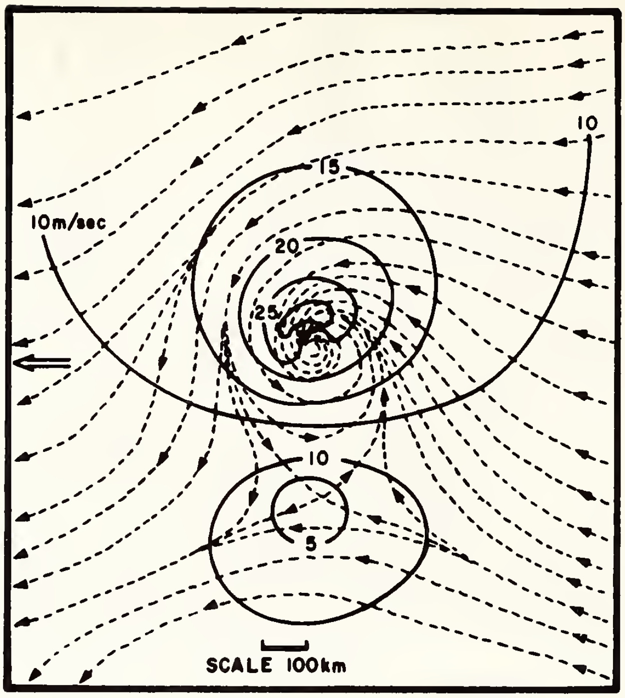

Figure 7. Hindcast wind field analysis for hurricane Belle.

no evidence is presented on the accuracy of the hindcast model when applied to actual tropical cyclones.

The computed wind field is shown in Figure 7. The maximum average 19.5 meter windspeed is 37 m/s at a distance of 50 km from the pressure eye. The wind field shown is very similar to that specified for hurricane Belle near EB41, though at that time in its history, the Belle wind field was undergoing rapid changes. In this sensitivity study, the wind field was assumed steady state and was translated across the hindcast grid to reflect storm forward velocities of 0, 27 km/hr, 55 km/hr and 80 km/hr. The location of the grid system used is shown in Figure 8. For the stationary storm simulation, the hurricane eye was placed at 35°N, 74°W. The moving storms arrived at 40°N, 70°W at the end of the 21 time step hindcasts. The origin of the track simulated for all three of the moving storm cases is also shown in Figure 8.

Since all spectral hindcast runs are started from initially calm conditions, there is a spinup period required before the distribution of simulated directional spectra reflects an equilibrium relationship with the driving input steady state wind field. The parametric model provides its equilibrium solution directly from the wind field and is independent of storm motion variations. Also,

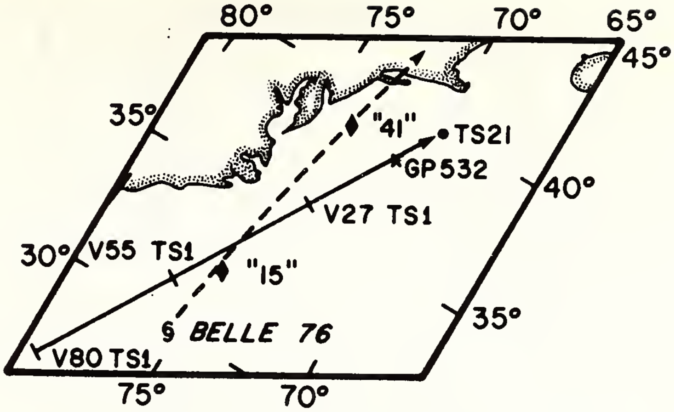

Figure 8. Domain of grid system for "Belle" hindcast and sensitivity study: ◆ - location of buoys EB15 and 41. Solid line shows track of hypothetical storms; ticks indicate initial position for indicated storm velocity in km/hr.

because of the time required for swell generated in the areas of highest winds around the eye to propagate away from the storm, the spinup period for the spectral hindcasts increases with increasing distance from the storm center.

The behavior of the solution near the eye for the spectral hindcasts is shown in Figure 9. The solution shown is for the grid point which exhibits maximum energy each time step. This grid point is near, but not always coincident with, the grid point in a given time step with the highest wind. It is evident that steady state maximum wave conditions are very nearly reached within the 21 time step run, and that there is a significant dependence of the maximum sea state hindcast on storm forward speed. The significant wave height and peak frequency hindcast by the parametric model for maximum conditions are 9.2 m and .078 Hz, respectively, values which match closely the spectral predictions for the 27 km/hr run.

In Figure 10 the one-dimensional spectra predicted for equilibrium maximum sea states by the spectral model are compared to the frequency spectrum constructed from the scale and shape parameters predicted by the parametric model. Again, the solutions are most similar for the 27 km/hr run but are quite different for slower or faster moving storms. The difference is especially pronounced for the 50 km/hr run.

Figure 11 (a-e), displays the distribution of significant wave height about the storm. The parametric solution and the spectral

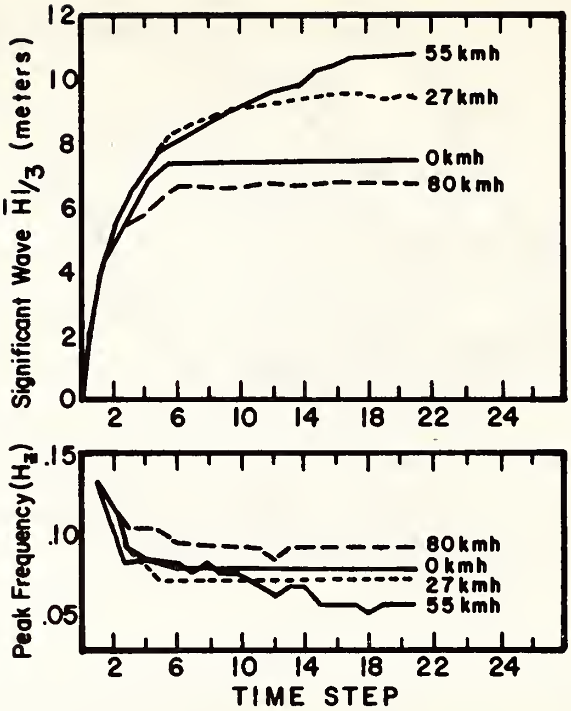

Figure 9. Time history of significant wave height and peak frequency for grid point 532.

solutions for the stationary and 27 km/hr cases show patterns of wave height resembling the isotach pattern. For faster moving storms, however, the wave height distribution predicted by the spectral model is affected by the storm motion, as wave heights decrease in the forward quadrants and increase in the rear quadrants, relative to the slow-moving case. The 50 km/hr case exhibits not only the highest waves, but the greatest areal coverage of high sea states. The solution is apparently very sensitive to storm speeds near and above 50 km/hr.

DISCUSSION

In a stationary cyclone, the stage of wave development, as gauged by the non-dimensional peak frequency, is limited in the area of strong winds by the physical fetch limitation imposed by the highly curved flow. In a moving cyclone, however, the effective fetch is determined by both the vector wind pattern and the propagation vector of storm motion.

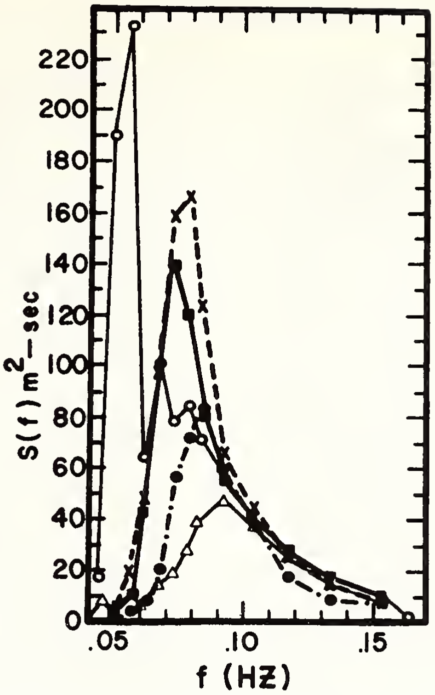

Figure 10. Maximum conditions for storms of sensitivity study. Spectral model: ● - 0 km/hr; O - 27 km/hr; ■ - 55 km/hr; Δ - 80 km/hr; X - parametric solution.

In the spectral growth model used here, wave growth, in the absence of swell, is essentially uncoupled in frequency, and each spectral component travelling within ±90° of the local wind direction responds independently to the linear and exponential growth mechanisms for the local windspeed. For simply defined linear fetches, such a spectral growth model is in reasonably good agreement with observed fetch-limited spectra (e.g., Pierson, 1977). However, in more complicated wind systems the method can produce spectral growth patterns which do not obey, even approximately, the shape invariance theorem upon which the parametric method is based.

Moving tropical cyclones appear to be especially capable of differentiating between the two approaches. If growth can be considered a process decoupled in frequency, then moving hurricanes provide, over limited regions of wave number space, infinite fetch conditions over small regions of the storm circulation. Thus, if in those regions of the circulation, the local windspeed is suffi-

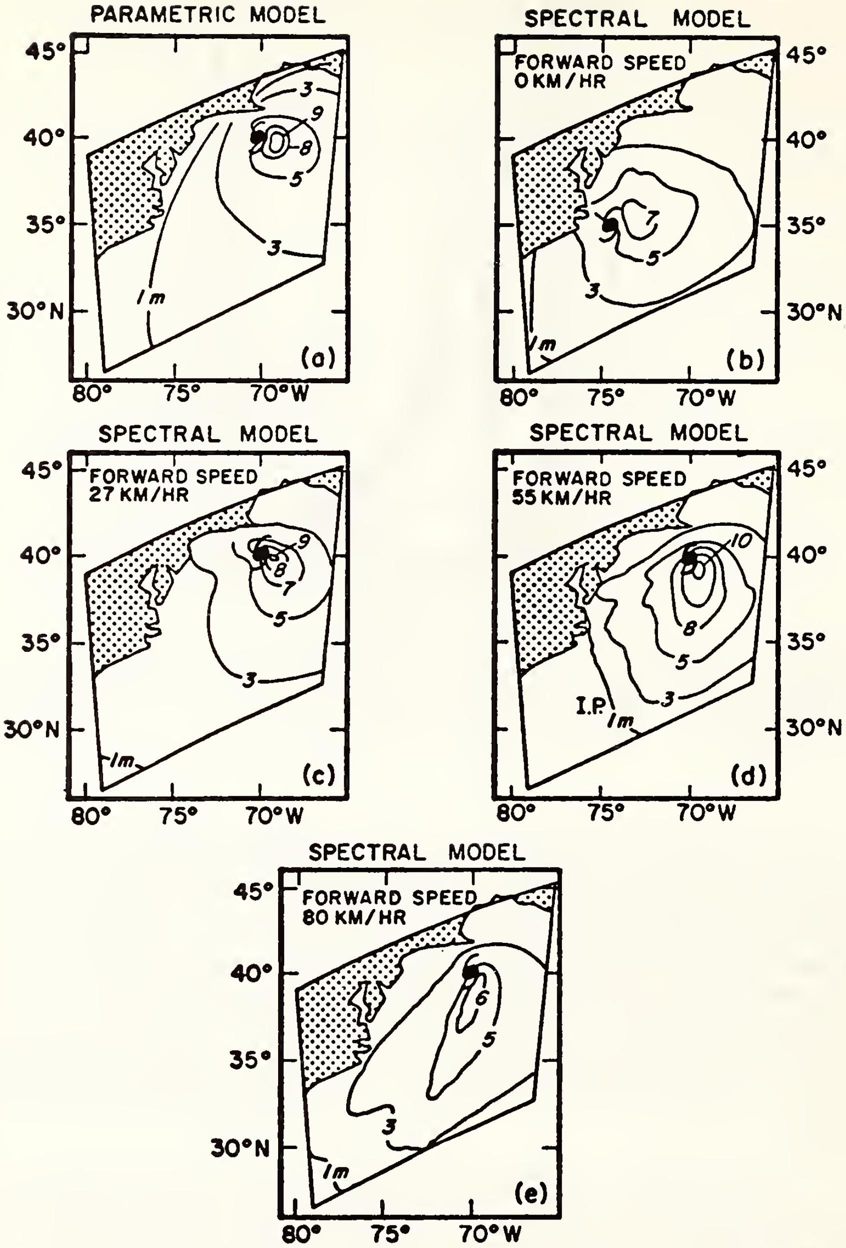
PARAMETRIC MODEL
SPECTRAL MODEL
FORWARD SPEED 0 KM/HR
SPECTRAL MODEL
FORWARD SPEED 27 KM/HR
SPECTRAL MODEL
FORWARD SPEED 55 KM/HR
SPECTRAL MODEL
FORWARD SPEED 80 KM/HR
45°
40°
35°
30°N
80°
75°
70°W
1m
3
5
6
7
8
9
10
I.P.
(a)
(b)
(c)
(d)
(e)

Figure 11 (a-e). Contour diagrams of significant wave height for storms of the sensitivity study.

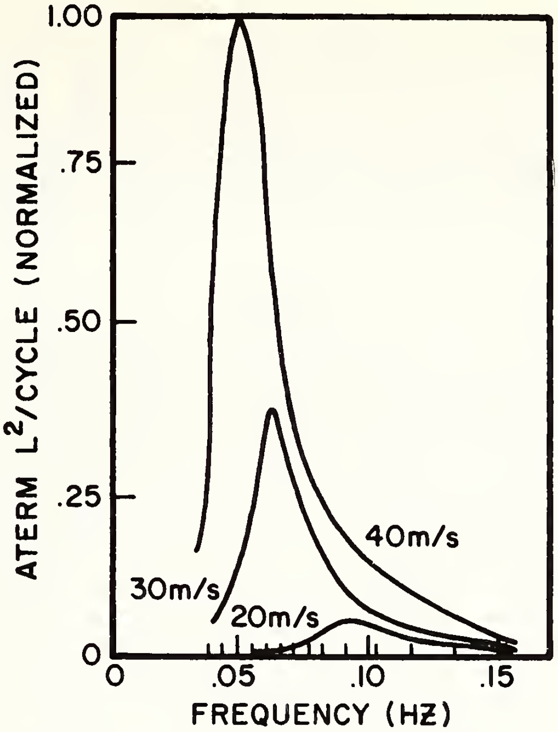

Figure 12. Characteristic growth due to resonance mechanism.

cient to provide excitation by means of the linear growth mechanism, or A term in equation (2), then spectral components are able to grow exponentially to saturation levels determined by the Pierson-Moskowitz fully-developed spectrum, which at hurricane windspeeds can support enormous energies. The dependence of the resonance mechanism growth rate (A term) on frequency and windspeed is shown in Figure 12. It can be inferred that, for the spectral growth method, wave generation in tropical cyclones will be maximized if the windspeed in that portion of the circulation where the wind direction matches the storm direction (the right rear quadrant) is such that the peak frequency in the resonance mechanism parameterization is at a frequency associated with gravity wave group velocities that match the propagation speed of the storm. In the sensitivity study described above, this condition was met for the 55 km/hr storm.

On the other hand, the parametric method derives from a picture of the spectral energy balance involving wave-wave interactions as well as processes uncoupled in frequency. The non-linear component of the source function is in fact a function of the position of a spectral component with respect to the peak in the spectrum, which itself migrates from high to low frequency more slowly as the stage of wave development increases. Growth of low-frequency energy in fast-moving cyclones therefore may not be expected to be significantly different from that in slow-moving storms of the same meteorological nature, although detailed integrations with full multi-parameter models would be required to quantify the differences.

SUMMARY

Given a proper specification of the wind field within tropical cyclones, it has been shown that accurate predictions of the generated wave field can be produced by both the spectral and parametric methods. Nevertheless, significant differences do occur for the unusual case of very slow and very fast moving storms. While these storms are rare, they may be the most significant from the standpoint of engineering designs. The measurements required to verify the differences probably can only be obtained in the near future by means of aircraft (equipped with air-droppable buoys or laser altimeters for the determination of energy spectra and real aperture imaging radar for directional spectral information) which are capable of seeking out the proper quadrant of a fast-moving storm. The aircraft techniques are well within the state-of-the-art and are not costly. It is imperative, therefore, that a measurement program be undertaken to validate the model predictions.

ACKNOWLEDGMENTS

The development of the spectral model employed in this study was supported by a consortium of U. S. oil companies as part of the Ocean Data Gathering Program (ODGP). We thank the administrator of the ODGP program, Shell Development Company, for supporting, jointly with NOAA, the adaptation of the model to the NOAA AOML computer facility. Dr. Cardone's participation in the study reported herein and in the NATO Symposium was supported by NOAA under Grant 04-7-022-44014.

The authors thank Merlin Ahrens of the National Oceanic and Atmospheric Administration's Atlantic Oceanographic and Meteorological Laboratories for his diligent computer programming assistance.

REFERENCES

Cardone, V. J., 1969: Specification of the wind distribution in the marine boundary layer for wave forecasting. Rept. TR 69-1, Geophys. Sci. Lab., New York University NTIS No. AD702490 .

———, W. J. Pierson, and E. G. Ward, 1976a: Hindcasting the directional spectra of hurricane generated waves. *J. Petrol. Technol.*, *28*, 385-394.

———, D. Ross, M. Ahrens, J. A. Greenwood, C. Greenwood, and R. E. Salfi, 1976b: Forecasting hurricane winds and waves - A pilot study. Final report to NOAA Sea-Air Interaction Laboratory and Shell Development Company. CUNY Institute of Marine and Atmospheric Sciences at the City College, New York.

———, and D. B. Ross, 1977: State of art wave predictions and data requirements. Paper presented at the NOAA Climate Symposium, Washington, D. C., July 12-14, 1977. Proceedings to be published by Plenum Company in 1978.

Chow, S., 1971: A study of the wind field in the planetary boundary layer of a moving cyclone. M.S. Thesis, Department of Meteorology and Oceanography, New York University.

Forristall, G. Z., R. C. Hamilton, and V. J. Cardone, 1977: Continental shelf currents in tropical storm Delia: observations and theory. *J. Phys. Oceanogr.*, *7*, 532-546.

Hasselmann, K., T. T. Barnett, E. Bouws, H. Carlson, D. E. Cartwright, K. Enke, J. A. Ewing, H. Gienapp, D. E. Hasselmann, P. Kruseman, A. Meerburg, P. Müller, D. J. Olbers, K. Richter, W. Sell, and H. Walden, 1973: Measurements of wind-wave growth and swell decay during the Joint North Sea Wave Project (JONSWAP). *Deut. Hydrogr. Z.*, *Suppl. A 8*: #12.

———, D. B. Ross, P. Müller, and W. Sell, 1976: A parametric wave prediction model. *J. Phys. Oceanogr.*, *6*, 200-228.

Kitaigorodskii, S. A., 1961: Applications of the theory of similarity to the analysis of wind-generated wave motion as a stochastic process. *Izv. Akad. Nauk SSSR*, *Ser. Geofiz.*, No. 1, 73-80.

Miles, J. W., 1957: On the generation of surface waves by shear flows, *J. Fluid Mech.*, *3*, 185-204 233 .

Phillips, O. M., 1957: On the generation of waves by turbulent wind. *J. Fluid Mech.*, *2*, 417-445.

———, 1958: The equilibrium range in the spectrum of wind generated waves. *J. Fluid Mech.*, *4*, 426-434.

Pierson, W. J., Jr., and L. Moskowitz, 1964: A proposed spectral form for fully developed wind seas based on the similarity theory of S. A. Kitaigorodskii. *J. Geophys. Res.*, *69*, 5181-5190.

———, 1977: Comments on "A parametric wave prediction model". *J. Phys. Oceanogr.*, *7*, 127-134.

Ross, D. B., 1975: A comparison of SKYLAB S-193 and aircraft views of surface roughness and a look toward Seasat. Proceedings of the NASA Earth Resources Survey Symposium, Lyndon B. Johnson Space Center, Houston, Texas, June 1975, 1911-1920.

Ross, D. B., 1976: A simplified model for forecasting hurricane generated waves (Abstract). Bull. A.M.S. January, 113. Presented at conferences on Atmospheric and Oceanic Waves, Seattle, Washington, March 29-April 2. American Meteorological Society.

Stacey, R. A., 1973: High frequency gravity waves in hurricanes. M.S. Thesis, Department of Meteorology and Oceanography, New York University.

Uji, T., 1975: Numerical estimation of the sea wave in a typhoon area. Papers in Meteorology and Geophysics, 26, 199-217.

Withee, G. W., and A. Johnson, 1975: Buoy observations during hurricane Eloise. Data Buoy Office, National Oceanic and Atmospheric Administration, Bay St. Louis, Mississippi.

DISCUSSION

W. Rosenthal:

Can you give the functional dependence and the parameters for the directional coupling of different frequencies that you mentioned.

V. Cardone:

As in other parts of the model, the effects of non-linear interactions are simulated in a highly implicit way with regard to directional coupling. In the present model, the algorithm operates only in developing or fully developed sea situations, and has the effect, in rapidly shifting wind direction zones, of "turning" the directional spectrum gradually so that the maximum energy is located in the wind direction. However the adjustment time is long, as spectral components that become overdeveloped with respect to the local wind direction and the SWOP spreading function, are attenuated at a rate proportional to the degree of overdevelopment. In hurricanes, this algorithm is responsible in part for the simulation of the rather flat directional spread of energy observed in recent measurements.

K. Hasselmann:

I agree it would be very valuable to use hurricane data to test the different physics of models with and without significant non-linear coupling between different rays. This would be a very valuable exercise. In this context I should perhaps mention as a point of clarification that the parametric hurricane model discussed here - which is based on dimensional argument without use of the transport equation - should be distinguished from the dynamical parametrical models discussed in the previous papers, which are based on the projection of the full transport equation on the parametric space. These latter models are not different in principle from the usual spectral models, they use only different numerical techniques.

Boundary-Layer Meteorology 13, 151-163.

ON THE RELATIONSHIP OF RADAR BACKSCATTER TO WIND SPEED AND FETCH

DUNCAN ROSS

National Oceanic and Atmospheric Administration, Atlantic Oceanographic and Meteorological Laboratories, Sea-Air Interaction Laboratory, Miami, Florida.

and

W. LINWOOD JONES

National Aeronautics and Space Administration, Langley Research Center, Hampton, Virginia

(Received 12 September, 1977)

Abstract. The physics of the interaction of electromagnetic waves with the ocean surface has been an active area of research for a number of years. We present here the results of satellite and aircraft experiments to investigate the ability of active microwave radars to infer surface wind speeds remotely. Data obtained from the recent National Aeronautics and Space Administration (NASA) Skylab experiment are compared with surface wind speeds measured by low-flying aircraft and ships-of-opportunity and found to give useful estimates of the oceanic wind field. We also investigate the influence of varying wave height on radar measurements of wind speed by measuring the backscattering cross-section for constant wind speed but variable wave conditions. We conclude that this effect is of little importance.

1. Introduction

Worldwide observations of ocean-surface wind fields from satellites is a goal actively being pursued by the National Aeronautics and Space Adminstration (NASA). Presented herein are results from satellite and aircraft experiments which show that the characteristics of radar backscatter over the ocean are related to the local wind, with little influence by the longer gravity-wave structure, and that they may be used to infer oceanic wind fields from space.

The behavior of radar backscatter from water at off-nadir incidence angles is satisfactorily explained by two-scale composite theories. These attribute the backscatter to the amplitude of those ocean waves, with wavelength approximately half the wavelength of the incident electromagnetic energy, which satisfy the Bragg scatter equation (cf. Wright, 1968; Bass *et al.*, 1968) and to their average tilt due to the large-scale structure (see also Wright and Keller, 1971; Rouse and Moore, 1972; Guinard and Daley, 1970; Valenzuela, 1971; Valenzuela *et al.*, 1971; and Krishen, 1971).

The experiments cited above used radars operating at wavelengths which included L-Band (≈25 cm), X-Band (≈3 cm), and KU-Band (≈1 cm). Surface waves responsible for the backscatter, therefore, have ranged between waves controlled mainly by gravity to those controlled mainly by surface tension, so-called capillary waves. Phillips (1958) proposed that the high-frequency end of the wave spectrum was controlled by dissipation and, neglecting long-wave short-wave interaction, proposed a power-law form for the spectrum with a constant coefficient and an exponent determined by the appropriate dissipation mechanism [i.e., $E(K) \sim \alpha K^{-4}$ for the gravity region of the spectrum where $E(K)$ is the energy density of the spectrum for the wave number $K = 2\pi/\lambda$; λ is the wavelength of the wave, and $\alpha = \text{const.} = 0.006$ as suggested by Phillips (1966)]. Exploitation of radar backscatter to infer surface winds, however, requires α to be a function of the local wind speed. Such a dependence has been suggested by Pierson and Stacy, according to Cardone *et al.* (1976) in the gravity and capillary region of the spectrum, and by Toba (1974) in the gravity region. In contrast, Hasselmann *et al.* (1973), (1976) and Ramamonjiarisoa (1974) find α in the gravity region to decrease with increasing fetch suggesting long-wave short-wave interaction is an important factor in the behavior of the high-frequency end of the wave spectrum. An attempt by Ross (1975) to observe a dependence of radar backscatter on wave development suggested a possible strong dependence, but due to a lack of good wave data and interference by rain, the data were not conclusive. An understanding of α as a function of the local wind speed and long-wave short-wave interaction is therefore central to the problem of inferring local winds from radar backscatter results.

In this paper we attempt to study the wind speed dependence of α in the capillary region by empirically establishing a dependence of radar backscatter on the local surface wind speed. The relative importance of long-wave short-wave interaction is then studied in a fetch-limited experiment where long-wave energy changes considerably while the surface winds remain approximately constant.

2. Wind Speed Dependence

The NASA Skylab experiment, launched in May of 1973, was manned during three separate periods termed SL2, 3, and 4. One of the complement of instruments aboard the satellite was a microwave device, termed S193, capable of measuring both radar backscatter, σ_0, and the naturally emitted microwave energy of the earth and atmosphere at a frequency of 13.9 GHz. Its antenna was movable and normally obtained data at incidence angles which varied between nadir (0°) and about 50° in the along-track or across-track directions.

During the Skylab experiments, the authors conducted an extensive aircraft underflight program designed to obtain environmental and active and passive microwave data to assess the accuracy and precision of the satellite sensor and its ability to infer surface winds during variable atmospheric conditions. For a more complete description of the satellite and aircraft program, the reader is referred to Cardone *et al.* (1976), Jones *et al.* (1977), Ross *et al.* (1974), Ross (1975), and Moore *et al.* (1974).

An extensive set of radar backscatter data was obtained by the Skylab during both the SL2 and SL4 periods. Surface conditions varied from essentially calm to $30\ \text{m s}^{-1}$ in a tropical hurricane during SL2, and from 7.5 to $30\ \text{m s}^{-1}$ in several severe winter storms in both the Atlantic and Pacific Oceans during SL4. Figure 1,

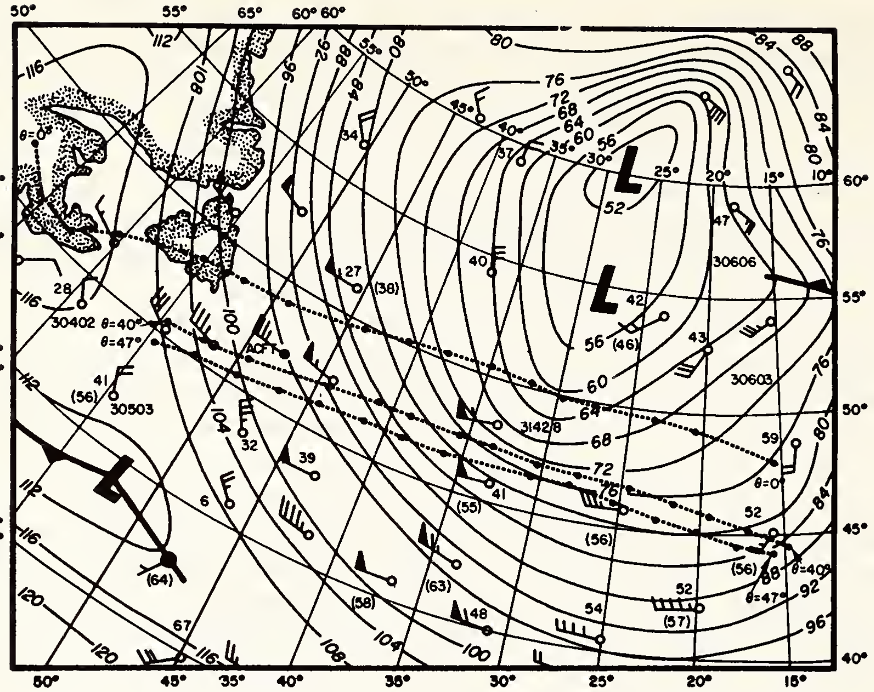
50°
55°
65°
60° 60°
45°
65°
40°
60°
35°
55°
60°
55°
50°
45°
40°
50°
45°
35°
40°
35°
30°
25°
20°
15°
L
L
L
θ=0°
30402 θ=40°
θ=47°
30503
30606
30603
31428
ACFT
θ=0
θ=40°
θ=47°
112
116
108
100
96
92
88
84
80
76
72
68
64
60
56
52
104
120
112
116
120
116
108
104
100
76
80
84
88
84
80
76
76
80
84
88
92
96
64
68
72
76
56
60

Fig. 1. Surface-pressure analysis for 4 January, 1974, showing ship and aircraft reports and the surface positions viewed by Skylab along the sub-satellite ground track ($\theta = 0°$) and at incidence angles of 40° and 47°.

for example, shows a surface-weather analysis and the area observed by Skylab at incidence angles of 0°, 40°, and 47° on 4 January, 1974. Similar storms were overflown on 9 and 24 January, 1974 (Figures 2 and 3). During the 9 January pass, however, a malfunction occurred in the scanning mechanism limiting the scanning range to angles of 40° and 50° to the right of the ground track during most of the pass. This winter storm was unusual in that surface winds varied from 7.5 to 30 m s^{-1} in the area viewed by the satellite. The σ_0 and coincident surface winds of 9 January are shown in Figure 4 along with passive microwave measurements obtained by Skylab at both 1.4 GHz (nadir only) and 13.9 GHz. Because the light rain reported by ships in the area was confirmed by the passive measurements (which show only an expected wind speed dependence), this track and the SL2 data were suitable to establish wind speed relationships which could be tested using data obtained from other storms.

Surface wind speeds and directions were extracted from a meteorological analysis based upon ship and low-flying aircraft reports for all areas viewed by the Skylab from selected passes during SL2 and the 4, 9, and 24 January storms of SL4. As previously cited experiments showed that σ_0 over the ocean is strongly dependent upon the direction of the wind, all data were adjusted to the upwind aspect angle according to the technique of Pierson *et al.* (1974).

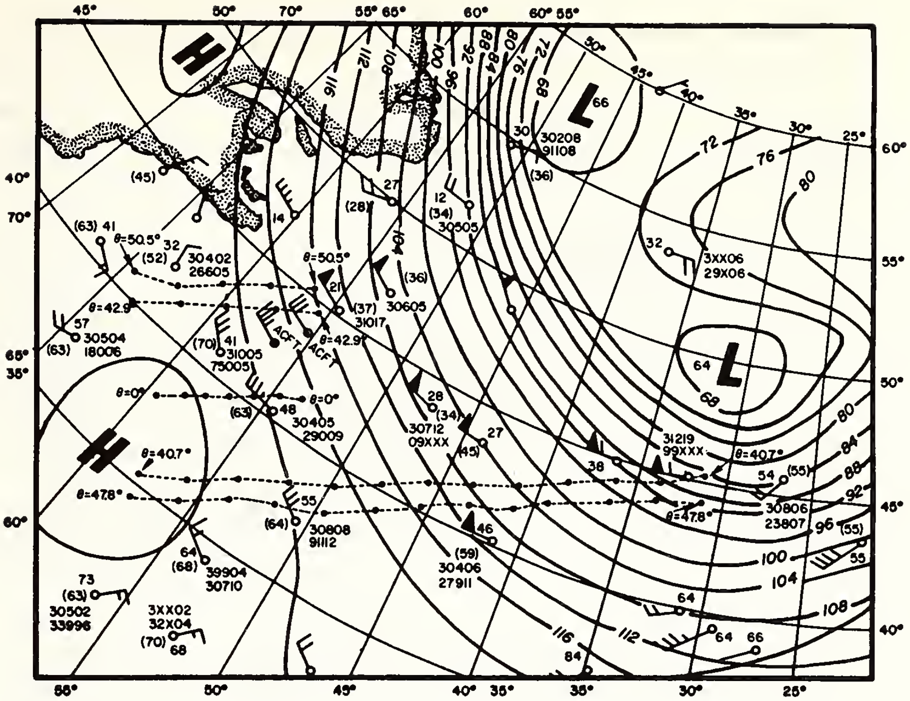

Fig. 2. Surface-pressure analysis for 9 January, 1974, showing ship reports and surface positions viewed by Skylab along the sub-satellite track ($\theta = 0°$) at incidence angles of 40.7° and 47.6° to the right of the track, and at 42.9° and 50.5° to the left of the ground track.

A power law of the form

$$U_{10} = a\sigma^{b}, \tag{1}$$

where $\sigma_0 = 10 \log \sigma =$ the normalized radar backscattering cross-section (cf. Long, 1975), was then fitted to the data of SL2 and the 9 January pass during SL4. The resulting regression coefficients and the correlation coefficient, r^2, a measure of the goodness of fit (cf. CRC Standard Tables, 1968), for selected incidence angles are contained in Table I. A value of $r^2 = 1$ indicates a perfect fit. It can be seen from Table I that the regression coefficient, a, associates higher wind speeds with horizontal polarization for a given σ_0, consistent with composite theory. Moreover, the exponent, b, is quite similar for each incidence angle except for the data from SL2 at $\theta = 44°$. The latter set, however, has a low correlation coefficient and includes tropical hurricane data which may have been contaminated by rain.

The most notable difference between the SL2 and SL4 data is in the absolute values of a. During SL4, the feed to the S193 antenna was damaged, greatly altering the antenna pattern and its calibration. This is believed to be the major cause of the change in level of the SL4 results, although the preponderance of data at higher wind speeds for the SL4 data set may also explain the difference. Thus, if a

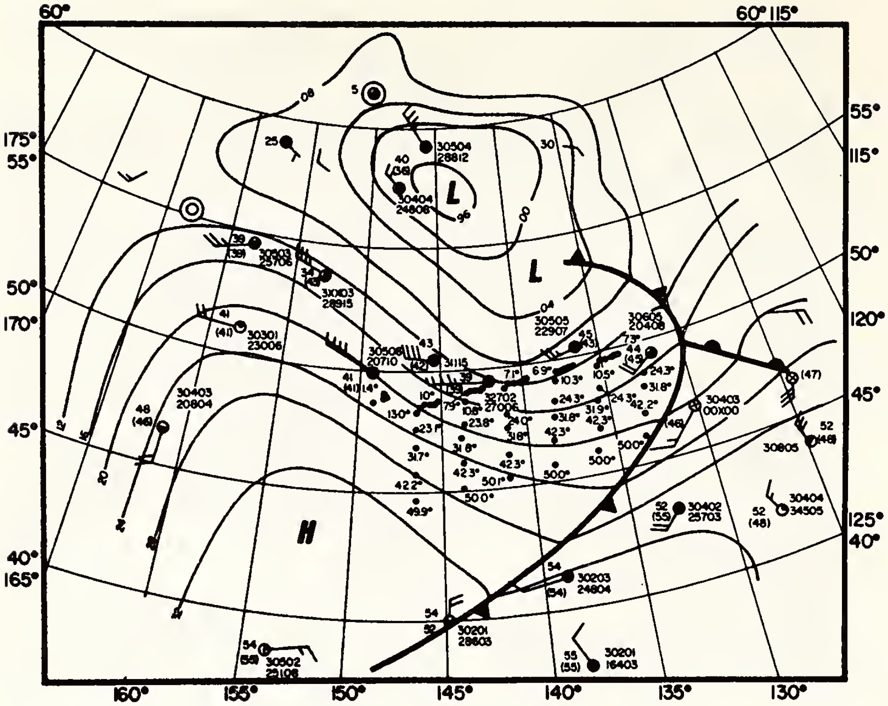

Fig. 3. Surface-pressure analysis for 24 January, 1974, showing ship reports and surface areas viewed by Skylab at the indicated incidence angles.

power-law fit were not appropriate for the entire range of winds, the SL4 results would introduce a positive bias in low-wind speed situations. In any case, it is inappropriate to include SL4 data with that from other experiments because of the physical damage to the antenna.

Because a complete range of winds was not observed during SL3 and because the aforementioned damage to the antenna occurred at the beginning of SL4, it was not possible to test the SL2-derived power-law relationships. However, the data obtained during SL4 on 4 January (Figure 1) and from a Pacific storm observed on 24 January (Figure 3) are suitable for testing the relationships resulting from the 9 January data set. Accordingly, surface winds for the areas viewed during the 4 and 24 January storms were calculated from the adjusted (to upwind) σ_0 measurements, and mean and standard deviations of differences between the analyzed and calculated winds were obtained and are presented in Table II.

To assess these results, we compare our analysis for the reference surface wind field with the analysis by Cardone *et al.* (1976) for the same Skylab data of 4, 9, and 24 January. Their winds were determined by means of an analysis based mainly upon the synoptic-scale pressure field and then weighted by the ship and aircraft winds. It should be noted, however, that their procedure was designed to obtain

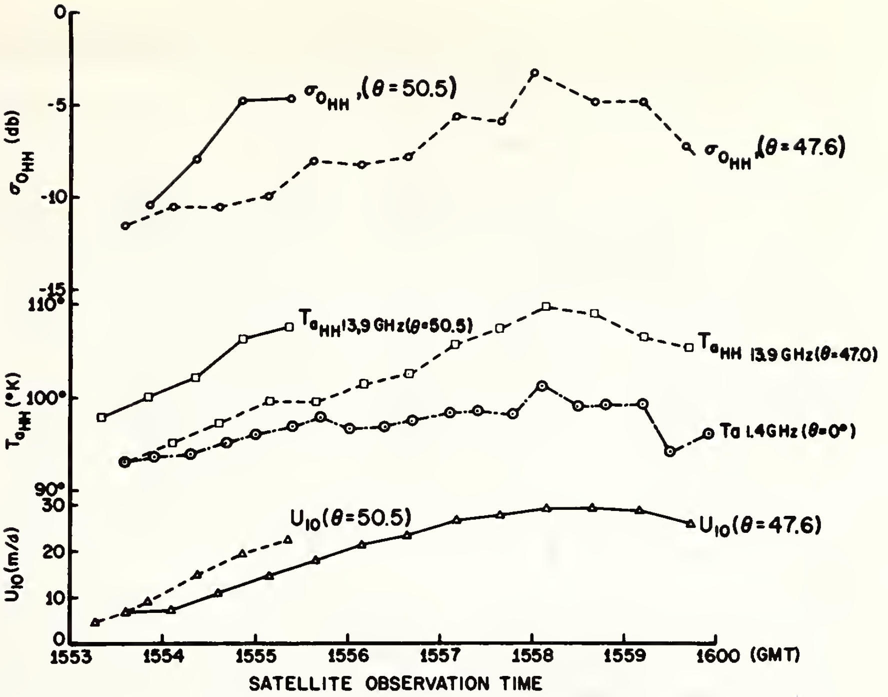

Fig. 4. Skylab measurements of radar backscatter σ_0 and microwave brightness temperature T_a for the 9 January, 1974 data pass. See Figure 2 for locations of the surface positions. The surface winds, U_{10}, shown correspond to the indicated incidence angles and were derived from a contour analysis using the ship and aircraft reports shown in Figure 2.

TABLE I

Skylab regression analysis results $U_{10} = a\sigma^b$, r^2 = correlation coefficient

Launch	Polarization	Incidence angle	a	b	r^2
SL2	σ_{0VV}	44°	29.3	0.33	0.22
SL2	σ_{0HH}	44°	58.9	0.43	0.37
SL2	σ_{0VV}	51°	63.2	0.53	0.75
SL2	σ_{0HH}	51°	122.0	0.54	0.74
SL4	σ_{0VV}	30°	16.7	0.55	0.87
SL4	σ_{0HH}	30°	24.16	0.59	0.78
SL4	σ_{0VV}	40.8°	22.26	0.57	0.94
SL4	σ_{0HH}	40.8°	34.09	0.59	0.83
SL4	σ_{0VV}	47.6°	26.61	0.61	0.91
SL4	σ_{0HH}	47.6°	40.07	0.53	0.65

reference winds for a large number of Skylab data points, whereas our analysis was tediously carried out for only a relatively few data points and was very heavily weighted by ship and aircraft reports. The means and standard deviations of the

TABLE II

Comparison between analyzed and calculated winds during the Skylab experiment using the SL4 power-law fits of Table 1

		4 January		24 January		
θ	Polarization	Mean difference ($m\,s^{-1}$)	Standard deviation ($m\,s^{-1}$)	Mean difference ($m\,s^{-1}$)	Standard deviation ($m\,s^{-1}$)	Incidence angle
30°	VV	2.66	2.63	2.67	2.5	32°
30°	HH	3.53	4.10	−0.85	2.54	32°
40.8°	VV	0.68	2.57	0.00	1.59	41°
40.8°	HH	2.57	3.63	1.47	1.86	41°
47°	VV	1.91	3.70	−1.01	2.49	48°
47°	HH	−0.9	3.73	−3.11	2.67	48°
Average		1.74	3.79	−0.14	2.28	

differences between our data and those of Cardone *et al.* (1976) are presented in Table III. Their winds are lower than ours, possibly due to the heavy weighting, in our case, by ship reports. It is interesting to note, however, that the standard deviations of the differences are greater than those resulting from the use of the SL4 relationships.

The results of our analysis show that σ_0 is a function of the local wind speed and that it can be used to estimate surface winds with an accuracy comparable to established analysis procedures ***given an a priori knowledge of the wind direction.***

TABLE III

Comparison of analyzed winds from this experiment with those of Cardone *et al.* (1976)

Day	Mean difference ($m\,s^{-1}$)	Standard deviation ($m\,s^{-1}$)	Incidence angle
9 Jan.	−4.65	3.63	30°
	−4.10	3.21	40.7°
	−2.99	3.02	47.6°
4 Jan.	−3.33	3.0	30°
	−1.78	3.87	40°
	−2.74	2.21	47°
24 Jan.	−0.02	0.16	30°
	−3.05	1.56	40°
	−2.85	0.93	50°
Average	−2.83	2.40	

3. Dependence of σ_0 on Wave Development

A dependence of horizontally polarized σ_0 on fetch due to the variance of the large-scale slope is predictable from composite theory but is not observed in practice due to the very large contribution to the slope from short gravity and capillary waves which are essentially fully developed at relatively short fetches. Thus, if there is an important fetch- or duration-dependency, it must be associated with modifications of the average amplitude of the Bragg waves through higher-order non-linear interactions. To determine whether this latter dependence exists, special tracks were flown by the NASA Johnson Space Center (JSC) C130 aircraft on 11 April, 1973 and by a National Oceanic and Atmospheric Administration (NOAA) C130 aircraft on 15 March, 1975 during the joint NOAA/NASA *Wi*nter *S*torm *Ex*periment (WISEX-75). In both cases, a NASA radar, operating at 13.9 GHz (Jones *et al.*, 1977), measured the scattering cross-section, σ_0, as a function of polarization at a fixed incidence angle while the aircraft flew between shore and a point approximately 45 km offshore in the downwind direction. At the end of each track, the incidence angle was changed and the track reflown in the opposite direction. Thus, data were obtained as the radar looked 'upwind' and 'downwind' at incidence angles which varied between 0° (nadir) and 53°. Plots of data obtained on two such tracks are shown in Figure 5 and 6. Offshore winds averaged 13 m s^{-1} for the 11 April flight and 10 m s^{-1} for the 15 March flight.

To study the dependence of σ_0 (and hence α) on the state of wave development a comparison of σ_0 with some measure of the surface wave field is required. Hasselmann *et al.* (1973, 1976) following Kitaigorodskii (1961) show that the peak

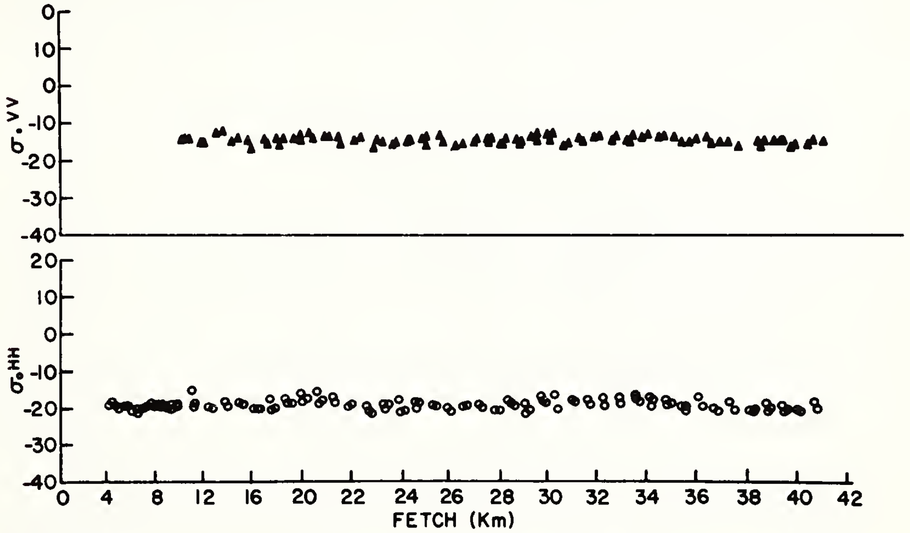

Fig. 5. Radar scattering cross section σ_0 as a function of fetch at an incidence angle of 53°. Surface wind speeds were 13.0 m s^{-1}.

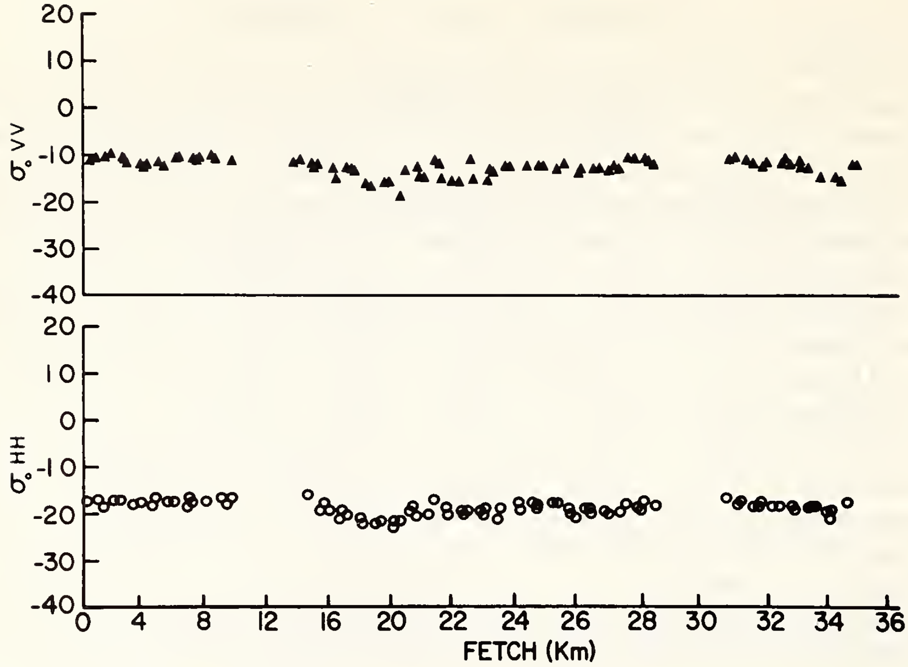

Fig. 6. Radar scattering cross section σ_0 as a function of fetch at an incidence angle of 40°. Surface wind speeds were 9.0 m s^{-1}

frequency f_m of the wave energy spectrum when normalized by the gravity constant g and the surface wind speed U is a convenient measure of the stage of development of the spectrum (see also Liu, 1971) and is a function of the similarly non-dimensionalized fetch x according to the equation

$$\nu = 2.84\xi^{-0.3} \tag{2}$$

where $\nu = f_m U_{10}/g$, non-dimensional frequency and

$\xi = xg/U_{10}^2$, non-dimensional fetch.

Using equation (2) to calculate ν as the independent variable, we obtained power-law fits to the aircraft data; the results and standard deviations are presented in Table IV. Examination of the off-nadir results suggests that σ_0 varies considerably but has no systematic dependence on ν.

Observations of σ_0 as a function of wind speed and fetch (hence ν) in wave tanks (cf. Duncan *et al.*, 1974; and Keller and Wright, 1976) and a theoretical study conducted by Banner and Phillips (1974) suggest σ_0 should depend on wave development. In the case of the wave-tank experiments for wind-generated waves, however, the close proximity of the peak frequency f_m to the Bragg wave frequency makes comparisons with oceanic results less than perspicuous (Wright, 1976 – personal communication).

TABLE IV

Fetch-limited regression analysis results ($\sigma = c\nu^d$)

Flight	Incidence angle	Polarization	c	d	Standard deviation
NASA-JSC	0°	HH	17.5	0.512	0.62
	0°	VV	15.9	0.56	0.61
WISEX	23°	HH	0.47	0.16	1.01
	23°	VV	0.26	−0.68	1.17
NASA-JSC	30°	HH	0.057	−0.12	1.15
	30°	VV	0.087	0.079	0.97
WISEX	40°	HH	0.015	0.19	2.06
	40°	VV	0.033	−0.75	2.02
NASA-JSC	53°	HH	0.0124	−0.03	1.20
	53°	VV	0.082	0.77	0.73

The failure to observe any dependence of σ_0 on wave development in our results may be due to a lack of homogeneity in other variables important to the scattering process such as surface wind conditions. For example, it is generally accepted that, for a given pressure gradient, winds blowing offshore will increase with distance offshore (cf. Richards *et al.*, 1966). This results from modifications in the thickness of the surface boundary layer due to changing surface roughness. The effect of increasing ***wind speed***, therefore, might offset any decrease in σ_0 due to nonlinear interactions.

To investigate the possibility of a fetch-dependent wind speed, we note that the boundary-layer winds for the 15 March, 1975 flight were measured at low flight altitudes (150 m) by the aircraft's Omega-updated inertial-navigation system. The design accuracy of the system for the determination of wind speed is ±0.5 m/s and the output is filtered with a 10-s time constant. The winds were measured every second along the low-level tracks, averaged over 90 s (a distance of approximately 7 km), and adjusted to the equivalent value of a wind as measured at 10 m, using the boundary-layer theory of Cardone (1969). The calculated 10-m surface winds and their standard deviations for two of the tracks, along with calculations of ν using Equation (2), the air-sea temperature differences, and the boundary-layer parameters, friction velocity, U_*, and roughness length, z_0, and their standard deviations, calculated using the theory and notation of Cardone (1969) are contained in Table V. It can be seen that both tracks show surface winds to be approximately $1\ \mathrm{m\,s^{-1}}$ higher at the seaward end of the fetch. The actual flight tracks responsible for the data of Figures 4 and 5 were obtained at higher altitudes and approximately two hours later. While it is possible that surface conditions had changed significantly during this time, the experimental conditions did not exhibit such changes.

To determine if the observed $1\ \mathrm{m\,s^{-1}}$ change in wind speed is significant, we estimated the accuracy of aircraft wind measurements by making wind observations

TABLE V

Experimental variables and their standard deviations (SD) for the WISEX Flight of 15 March 1975

Date	Time GMT	Fetch (km)	U_{10} (m s^{-1})	SD$_{U_{10}}$	ν	U_* (m s^{-1})	SD$_{U_*}$ (±)	z_0 (×10^4)	SD$_{z_0}$ (×10^4)	$T_a - T_s$ (°C)
3/15/75	1634:30	52.5	10.44	0.6	0.23	0.48	0.03	7	1	−5
	1637:00	46.05	10.90	0.48	0.24	0.46	0.07	6	1	−5
	1638:30	40.46	10.70	0.78	0.25	0.48	0.05	7	2	−5
	1640:01	33.49	10.80	0.69	0.26	0.47	0.04	7	2	−6
	1641:32	27.34	10.64	0.60	0.28	0.48	0.03	7	1	−6
	1643:02	21.20	10.38	0.65	0.29	0.45	0.04	6	1	−6
	1644:33	15.48	9.3	0.69	0.30	0.39	0.04	4	1	−6
	1646:04	9.51	9.38	0.83	0.35	0.38	0.04	4	1	−6
	1649:25	5.42	9.21	±0.9	0.4	0.39	±0.05	4	1	−9
	1650:55	11.27	8.9	0.77	0.32	0.38	0.04	4	1	−8
	1652:26	18.76	8.9	0.67	0.27	0.37	0.04	3	2	−8
	1653:57	25.12	8.7	0.70	0.27	0.37	0.04	5	1	−8
	1655:27	34.63	9.8	0.67	0.24	0.43	0.04	5	1	−9
	1656:58	44.14	9.68	0.71	0.23	0.42	0.04	5	1	−8
	1658:28	53.63	9.64	0.93	0.21	0.42	0.04	5	2	−8
Average			9.82	0.62	0.28					

on this flight while the aircraft was near weather station ‘Hotel’, occupied by a U.S. Coast Guard vessel, approximately 288 km offshore. Surface winds observed by the ship at 1800 GMT and 1900 GMT at an anemometer height of 19.5 m adjusted to 10 m were 13.0 and 12.2 m s^{-1}, respectively. A number of 90-s averages of surface wind speed (a spatial average of ≈7 km) were obtained by the aircraft while flying at low altitude (150 m) within a 32-km radius of the station. These had a mean value of 12.9 ± 0.89 m s^{-1}, and are in good agreement with the ship reports. They show that the natural variability of the wind field is about equal to the standard deviation of an individual measurement (≈1 m s^{-1}); and suggest that the characteristic surface wind can be specified only to an accuracy of about 1 m s^{-1} for this type of experiment. Therefore, the observed change in U with fetch may not be significant.

The standard deviation of the radar data in Table 4 scatters somewhat but averages 1.29 db and suggests considerable variability may have been present in the local winds. From equation (1) and values of a and b from Table I for $\sigma_{0_{VV}}$ at an incidence angle of 51°, and using $\bar{U}_{10} = 9.82 \pm 0.62$ m s^{-1}, the average and standard deviation for the two low-level WISEX flights, we obtain a scattering cross-section $\sigma_0 = -12.79 \pm 0.4$ db. However, as noted previously, the aircraft wind computer produces a low pass output with a 10-s time constant, whereas the radar data are averaged for about one second. The authors’ personal experiences suggest a standard deviation of about 1.0 to 1.5 m s^{-1} in $\bar{U}$ is to be expected using one-second averages for wind speeds of about 10 m s^{-1}. This produces a variation in σ_0 of about ±1.0 db, consistent with our observations.

Finally, using the α-ν relationship of Hasselmann *et al.* (1976), one expects α in the gravity region to decrease over the fetch range observed by about 30%, which, if the Bragg wave behaved similarly, is equivalent to a decrease in σ_0 of 1.58 db. In contrast, the apparent increase of $\bar{U}$ by about 1 m s^{-1} over the same range of fetch will produce an increase in σ_0 of about 1 db using equation (1). Thus, the fetch dependence of $\bar{U}$ may have cancelled the fetch dependence of α rendering σ_0 independent of fetch, as was observed. It is apparent, therefore, that while the effects of long-wave structure on Bragg wave amplitude may be important locally, they are weak in the mean and not observable over the range of fetch and wind variations involved in this experiment.

4. Conclusions

That the characteristics of radar backscatter over the ocean are determined mainly by the small-scale wave structure cannot be doubted. The attempt herein to relate an amplitude dependence of small-scale structure to readily predictable parameters of the large-scale roughness suggests that the interactions between large- and small-scale structure produce relatively small changes in *mean* cross-section for the higher wind speeds (>7 m s^{-1}). Thus, σ_0 relationships parameterizing the amplitude of the small-scale wave structure as a function of the local wind speed appear useful at 13.9 GHz, and comparisons of calculated to observed winds by means of wind speed-dependent relationships during the Skylab experiment show good agreement.

Acknowledgments

The authors are grateful to Mr Zack Byrns of the NASA Johnson Space Center for his support and encouragement during the Skylab experiment, to the Skylab Astronauts, and to the flight crews of the NOAA, NASA, and USAF C130 aircraft for their role in obtaining the data sets used in this paper.

References

Banner, M. L. and Phillips, O. M.: 1974, 'On Small Scale Breaking Waves', *J. Fluid Mech.* **65**, 647–657.

Bass, F. G., Fuks, I. M., Kalmykov, A. I., Ostrovsky, I. E., and Rosenberg, A. D.: 1968, 'Very High Frequency Radiowave Scattering by a Disturbed Sea Surface', *IEEE Trans. on Antennas and Propagation* **AP-16**, No. 5, 554–568.

Cardone, V. J.: 1969, 'Specification of the Wind Distribution in the Marine Boundary Layer for Wave Forecasting', New York Univ. Technical Report TR-69-1, Bronx, New York.

Cardone, V. J., Young, J. D., Pierson, W. J., Moore, R. K., Greenwood, J. A., Greenwood, C., Fung, A., Salfi, R., Chan, H., Afarani, M., and Komen, M.: 1976, 'The Measurement of Winds Near the Ocean Surface with a Radiometer-Scatterometer on Skylab', Final Report on EPN550, Cont. No. NAS-9-13642, City Univ. of New York, 324 pp.

CRC Standard Mathematical Tables, 16th Edition, 1968, 533.

Duncan, J. W., Keller, W. C., and Wright, J. W.: 1974, 'Fetch and Windspeed Dependence of Doppler Spectra', *Radio Sci.* 9, 809–819.

Guinard, N. W. and Daley, J. C.: 1970, 'An Experimental Study of a Sea Clutter Model', *Proc. IEEE* **58**, 543–550.

Hasselmann, K., Barnett, T. P., Bouws, E., Carlson, H., Cartwright, D. E., Enke, K., Ewing, J. A., Gienappe, H., Hasselmann, D. E., Kruseman, P., Meerburg, A., Mueller, P., Olbers, Richter, K., Sell, W., and Walden, H.: 1973, 'Measurements of Wind-Wave Growth and Swell Decay During the Joint North Sea Wave Project (JONSWAP)', *Deut. Hydrogr. Z., Suppl. A*, **8**, 95 pp.

Hasselmann, K., Ross, D. B., Muller, P., and Sell, W.: 1976 'A Parametrical Wave Prediction Model', *J. Phys. Oceanogr.* **6**, 200–228.

Jones, W. L., Schroeder, L. C., and Mitchell, J. L.: 1977, 'Aircraft Measurements of the Microwave Scattering of the Ocean', *IEEE Trans. on Antennas and Propagation*, Special Issue on Radio Oceanography **AP-25**, No. 1, 22 pp.

Keller, W. C. and Wright, J. W.: 1976, 'Modulation of Microwave Backscatter by Gravity Waves in a Wave Tank', Naval Research Laboratory, Report 7968, Washington, D.C., 21 pp.

Kitaigorodskii, S. A.: 1961, 'Applications of the Theory of Similarity to the Analysis of Wind-Generated Wave Motion as a Stochastic Process', *Izv. Akad. Nauk. Oceanogr.* **1**, 249–257.

Krishen, K.: 1971, 'Correlation of Radar Backscattering Cross Section with Ocean Wave Height and Wind Velocity', *J. Geophys. Res.* **76**, 6528–6539.

Liu, P. C.: 1971, 'Normalized and Equilibrium Spectra of Wind Waves in Lake Michigan', *J. Phys. Oceanogr.* **1**, 249–257.

Long, M. W.: 1975, *Radar Reflectivity of Land and Sea*, Lexington Books, 366 pp.

Moore, R. K., Classen, J. P., Cook, A. C., Fayman, D. L., Holtzman, J. C., Sobti, A., Spencer, W. E., Ulaby, F. T., Young, J. D., Pierson, W. J., Cardone, V. J., Hayes, J., Spring, W., Kern, R. J., and Hatcher, N. M.: 1974, 'Simultaneous Active and Passive Microwave Response to the Earth – The Skylab RADSCAT Experiment', *Ninth International Symposium on Remote Sensing of Environment*, Anne Arbor, Michigan.

Phillips, O. M.: 1958, 'The Equilibrium Range in the Spectrum of Wind-generated Waves', *J. Fluid Mech.* **4**, 426–434.

Phillips, O. M.: 1966, *The dynamics of the Upper Ocean*, The University Press, Cambridge, England.

Pierson, W. J., Cardone, V. J., and Greenwood, J. A.: 1974, 'The Applications of SEASAT-A to Meteorology', prepared for SPOC Group of NOAA under Grant No. 04-4-158-11, Univ. Inst. of Oceanography, City Univ. of New York.

Ramamonjiarisoa, A.: 1974, 'Contribution à l'étude de la structure statistique et des mécanismes de génération des vagues de vent', Ph.D. Thesis, à l'Université de Provence, Institut de Mécanique Statistique de la Turbulence, Luminy, France, 160 pp.

Richards, T. L., Dragert, H., and McIntyre, D. R.: 1966, 'Influence of Atmospheric Stability and Overwater Fetch on Winds over the Lower Great Lakes', *Mon. Weather Rev.* **94**, 454–458.

Ross, D., Au, B., Brown, W., and McFadden, J.: 1974, 'A Remote Sensing Study of Pacific Hurricane AVA', *Proc. of the Remote Sensing Symposium*, Willow Run Laboratories, Ann Arbor, Mich., 15–20 April.

Ross, D.: 1975, 'A Comparison of SKYLAB S-193 and Aircraft Views of Surface Roughness and Look Toward SEASAT', *Proc. of the NASA Earth Resources Symposium*, Houston, Texas, 9–13 June.

Rouse, J. W. and Moore, R. K.: 1972, 'Measured Surface Spectrum Dependence of Backscattering from Rough Surface', *IEEE Trans. on Antennas and Propagation* **AP-20**, 211–214.

Toba, Y.: 1974, 'Macroscopic Principles on the Growth of Wind Waves', *Sci. Rep. Tohoku Univ.*, Ser. 5, *Geophysics* **22**, 61–73.

Valenzuela, G. R.: 1968, 'Scattering of Electromagnetic Waves from a Tilted Slightly Rough Surface', *Radio Sci.* **3**, 1057–1066.

Valenzuela, G. R., Laing, M. B., and Daley, J. C.: 1971, 'Ocean Spectra for the High Frequency Waves as Determined from Airborne Radar Measurements', *J. Mar. Res.* **29**, 69–84.

Wright, J. W.: 1968, 'A New Model for Sea Clutter', *IEEE Trans. on Antennas and Propagation* **AP-16**, 217–223.

Wright, J. W., and Keller, W. C.: 1971, 'Doppler Spectra in Microwave Scattering from Wind Waves', *Phys. Fluids* **14**, 466.

Boundary-Layer Meteorology 13, 193-202.

COMPARISON OF *IN SITU* AND REMOTELY SENSED OCEAN WAVES OFF MARINELAND, FLORIDA

O. H. SHEMDIN, W. E. BROWN, JR., and F. G. STAUDHAMMER
Jet Propulsion Laboratory, California Institute of Technology, Pasadena, California, U.S.A.
R. SHUCHMAN, R. RAWSON, and J. ZELENKA*
Environmental Research Institute of Michigan, Ann Arbor, Michigan, U.S.A.
and
D. B. ROSS, W. McLEISH, and R. A. BERLES
Sea-Air Interaction Laboratory – NOAA, Miami, Florida, U.S.A.

(Received 23 August, 1977)

Abstract. Some early results from an oceanographic experiment staged off Marineland, Florida, in December 1975 are presented, viz., intercomparisons between the X-band and L-band imagery obtained by the Environmental Research Institute of Michigan's (ERIM) dual-wavelength, dual-polarization multiplexed radar. This radar allows direct comparison since the images are produced simultaneously. The wave data obtained from the radar imagery are compared with surface measurements of waves obtained with a pitch-and-roll buoy. The conclusions are only applicable to medium and low wind and wave conditions encountered during the Marineland test. The results indicate that X-band images provide superior quality wave imagery and more useful Fourier Transforms compared to L-band under equivalent signal-to-noise ratios and resolution. Optimum wave imagery is seen when waves propagate in the range direction. Comparisons between *in situ* measurements and X-band imagery of the same area indicate that the dominant wave direction can be obtained from imagery to within a few degrees. A one-dimensional spectrum obtained from X-band imagery compares favorably with an equivalent wave frequency spectrum obtained from the pitch-and-roll buoy after suitable transformation using linear wave theory.

1. Introduction

A major collaborative oceanographic experiment was staged offshore of Marineland, Florida, in December 1975. The objectives and details of measurement systems were described by Shemdin *et al.* (1975). Briefly, the important objectives of the experiment are:

1. Determine the nature of synthetic-aperture-radar (SAR) image formation mechanisms by measuring the slope spectrum of short gravity and capillary waves and simultaneously imaging the same surface area with the ERIM X- and L-band SAR system.
2. Measure the modulation of short gravity and capillary waves by long ocean waves.
3. Determine the wave spectral transformation in shallow water.
4. Obtain SAR imagery in the vicinity and across the Gulf Stream to test SAR imaging capability of current boundaries.
5. Measure waves and currents in the surf zone.

---

* Now at Science Applications, Inc., Tucson, Arizona.

Three surface stations were instrumented in 10, 20, and 60 m depths along a line normal to shore. An attending ship was provided for each station. Three aircraft equipped with X and L, and K_a band radars were flown in patterns over the surface sites and across the Gulf Stream. The site was selected because there was a reasonable probability of encountering waves with lengths longer than 80 m and heights of the order of 2 m, and because of the availability of surface support facilities operated by the University of Florida. The locations of the instrumented surface-truth sites and the basic flight patterns are shown in Figure 1.

Much of the data analysis remains in progress and will be forthcoming in various technical papers. The results reported here are confined to inter-comparisons between the ERIM X- and L-band high resolution imagery and respective comparisons with *in situ* measurements obtained with the pitch-and-roll buoy.

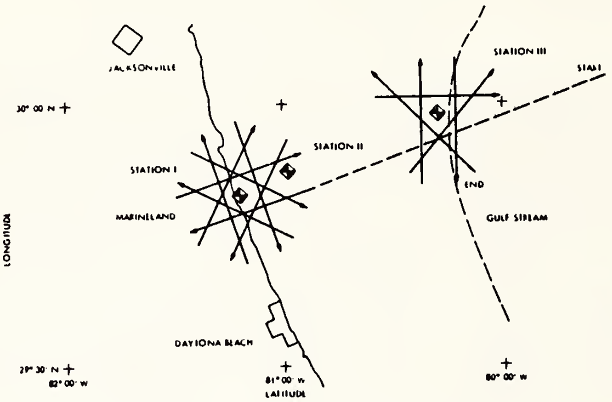

Fig. 1. Location of instrumented sites and flight paths for the Marineland Test. An eight-sided pattern is shown at station 1, and a five-sided pattern is shown at station 3.

2. The ERIM X-L band radar system

The ERIM X-L system described by Rawson *et al.* (1975) consists of a dual-wavelength and dual-polarization Synthetic-Aperture Radar that simultaneously images at X-band (3.2 cm) and L-band (23.5 cm). Alternate X- and L-band pulses (chosen to be either horizontally or vertically polarized) are transmitted, and reflections of both polarizations received; thus four channels of radar imagery are simultaneously obtained. Both polarizations of X-band are recorded on one film, both polarizations of L-band on the other. The Marineland data presented in this paper were obtained from the horizontal-transmit horizontal-receive channel (HH) of both the X and L-band receivers. Polarization effects have not been analyzed. The polarization of the electromagnetic radiation is defined by the direction of the electric field intensity, **E**, vector. For example, a horizontally polarized wave will have its **E** vector parallel to the local horizon.

The along-track or azimuth resolution on the ERIM system is obtained from the Synthetic-Aperture techniques given by Brown and Porcello (1969) and the cross-track or range resolution from the frequency-modulated pulse compression. During flight, the radar signals are recorded in their frequency-dispersed form and are later optically compressed in a ground-based processor. The latter has been extensively described by Kozma *et al.* (1972).

The SAR data were processed on the ERIM optical processor. The raw images were further processed at the Image Processing Laboratory of Jet Propulsion Laboratory to remove geometrical distortions and to enhance contrast. The Fourier transforms were obtained for segments of the enhanced images.

3. Surface Measurements—Pitch-and-Roll Buoy

A pitch-and-roll buoy developed by the National Institute of Oceanography (now called the Institute for Oceanographic Services), England, was operated by the Sea-Air Interaction Laboratory of NOAA during the Marineland Test. The characteristics of the system were described by Ewing (1969) and Tyler *et al.* (1974). The directional wave spectra are presented as one-dimensional frequency

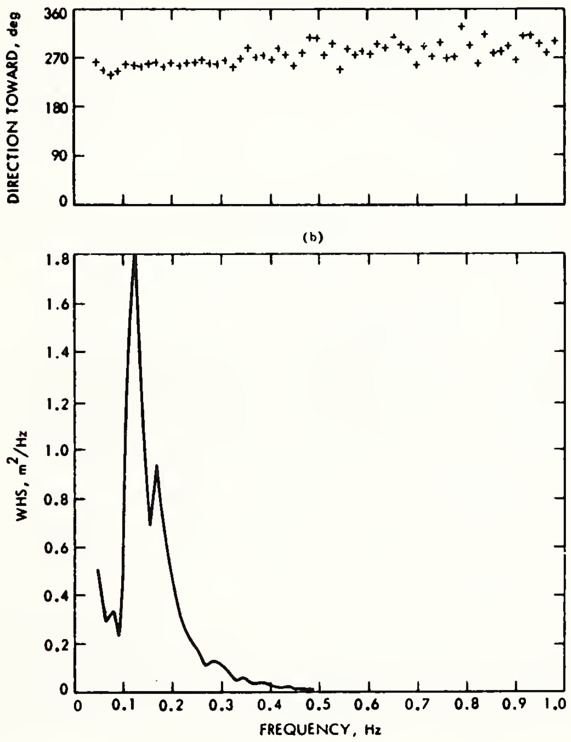

Fig. 2. A wave directional spectrum for December 14 1975, obtained with pitch-and-roll buoy: (a) centroid of wave directions as function of frequency, (b) frequency spectrum of wave energy.

spectra with directional characteristics at each frequency expressed in terms of the exponent of a cosine distribution centered on the mean wave direction. A typical spectrum measured on 14 December, 1975, is shown in the lower graph of Figure 2. The significant wave height was 1.56 m. The top graph in the same figure gives mean wave directions (centroid of the cosine distribution) as a function of frequency. On this day, the waves appear to be propagating uniformly towards 270° with respect to true north. The pitch-and-roll buoy was located at Station 1 (see Figure 1). The wind speed at the site was 3.0 m s^{-1} from the east, a direction of 90° with respect to true north. The wave system shown in Figure 2 is considered to be *swell.* The spectrum will be compared to a one-dimensional spectrum derived from radar imagery in section 4C2.

4. Results

A. X-BAND VS. L-BAND SAR WAVE IMAGERY

The Marineland test indicates that better wave images can be generated from the X-band radar with parallel polarization than from the L-band radar. Simultaneously-obtained, identical-resolution X-band (HH) ocean-wave images are compared with L-band (HH) images of the same area in Figure 3. Both X- and L-bands have approximately the same signal-to-noise ratio (SNR). Scans of image density in the direction perpendicular to the dominant crest direction indicate a higher crest-to-trough modulation for X-band than for L-band. Consequently, better definition is seen in wave-spectral peaks derived from X-band images than from L-band.

A possible explanation for the higher quality of X-band imagery was given by Shuchman and Zelenka (1978). They suggested that X-band data have a larger

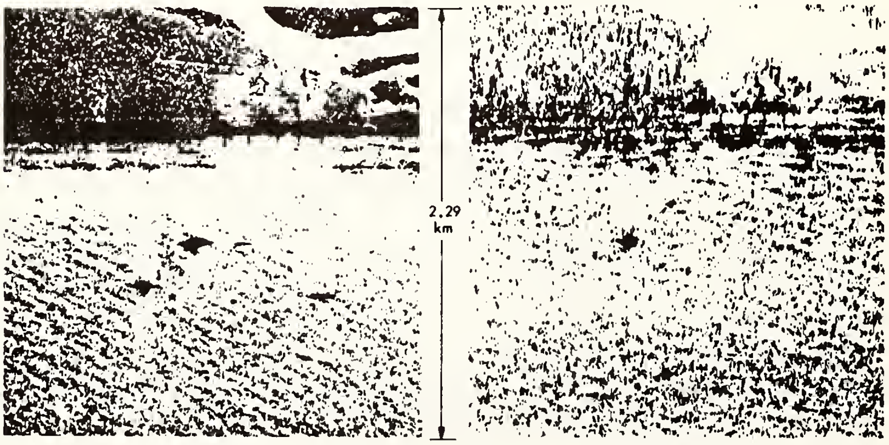

(a) X-BAND

(b) L-BAND

Fig. 3. Comparison of X-band and L-band images, 3 × 5 m resolution, at station 1 for 15 December 1975, with radar looking away from shore.

depth of focus than L-band, and therefore the azimuthally moving waves are not appreciably defocused as commonly occurs on L-band images of comparable resolution. The X-band also incorporates a shorter synthetic-aperture length or integration time than L-band. By using a shorter integration time, there are fewer motion errors which directly affect the azimuth or Doppler resolution.

The theoretical Rayleigh resolution of SAR is

$$\rho = \frac{\lambda}{2L}\frac{H}{\cos\theta}, \qquad (1)$$

where λ = radar wavelength,
$L = VT$ = synthetic-aperture length,
V = velocity of aircraft,
T = flight time required to collect synthetic-aperture data,
H = altitude of radar, and
θ = angle from nadir.

For an estimated aircraft altitude of $H = 4.1$ km, a velocity of $V = 75\ \mathrm{m\,s^{-1}}$ and off-nadir angle $\theta = 20°$ (depression angle = 70°), Equation (1) yields

$$\rho = 29.1\frac{\lambda}{T}. \qquad (2)$$

For $\rho = 5$ m, the required time for the wave to be within the aperture for X-band is

$$T_X = \frac{29.1 \times 0.032}{5} = 0.19\ \mathrm{s}, \qquad (3)$$

and for the L-band, the wave must be in the aperture for

$$T_L = \frac{29.1 \times 0.235}{5} = 1.37\ \mathrm{s}. \qquad (4)$$

Thus for the same resolution, the angular beamwidth must be 7-8 times larger for L-band than for X-band.

Acceleration inherent in wave motion during these times causes degradation of resolution. In contrast, a constant horizontal velocity merely displaces the apparent position rather than degrading the resolution. The maximum allowable acceleration, A, as a function of H, V, and T can be found as follows. The apparent range, R, while generating a synthetic aperture is

$$R = R_0 + v_0 t + \tfrac{1}{2}a_0 t^2, \qquad (5)$$

where R_0 is range to a typical cell at time zero, v_0 and a_0 are components of target velocity and acceleration in the range direction; v_0 is a constant which only displaces the wave in the image.

The error, ε_R, in the range which degrades resolution is

$$\varepsilon_R = \tfrac{1}{2}a_0 t^2. \qquad (6)$$

The corresponding phase error is given by

$$\phi_\epsilon = \varepsilon_R \frac{4\pi}{\lambda} = \frac{2\pi a_0 t^2}{\lambda} \leq \frac{2\pi}{\lambda} a_0 \left(\frac{T}{2}\right)^2 , \tag{7}$$

where the upperbound is realized at both ends of the synthetic aperture. The phase error should be kept within $\pi/2$ in order to achieve a properly focused image and to prevent resolution degradation, so that

$$\phi_\epsilon \leq \pi/2 . \tag{8}$$

The time, T, within the aperture is therefore restricted to

$$T \leq \left(\frac{\lambda}{A}\right)^{\frac{1}{2}} . \tag{9}$$

Using Equations (1) and (9), it follows that

$$A \leq [4V^2 \cos^2 \theta \rho^2 / H^2 \lambda] . \tag{10}$$

Using known values of H, V, and θ, it can be shown that

$$A = 1.18 \times 10^{-3} \rho^2 / \lambda . \tag{11}$$

Figure 4 graphs the maximum tolerable acceleration, A, in m s^{-2} vs. radar wavelength, λ, in cm; and is plotted for various resolutions, ρ, in meters. Thus one reason the X-band yields superior wave spectra is because it is less subject to wave velocity and acceleration effects than L-band.

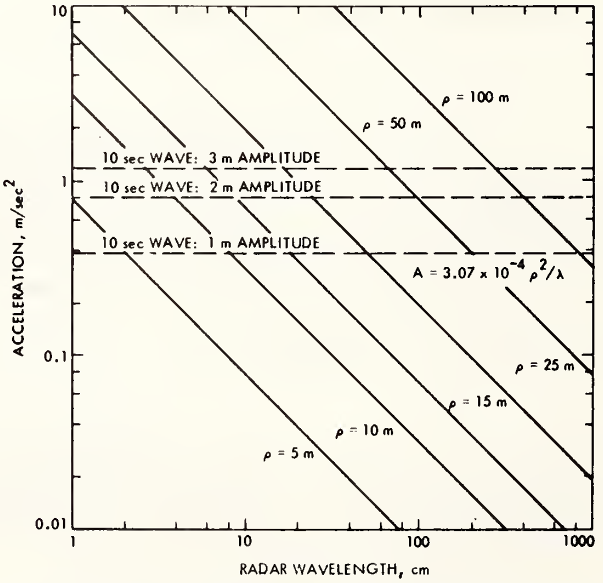

Fig. 4. Maximum wave acceleration tolerated by SAR as a function of radar wavelength and resolution ρ.

B. WAVE IMAGES AS A FUNCTION OF RADAR LOOK DIRECTION

Analysis of Marineland data also indicates that optimum wave images result when the radar is looking essentially up-wave or when waves propagate towards the aircraft in the range direction as shown in Figure 5. Shuchman and Zelenka (1978) indicate that waves traveling in the range direction yield images that are insensitive to defocusing effects. The lack of defocusing sensitivity in range becomes apparent when one considers that SAR employs in the range dimension a pulse train of very

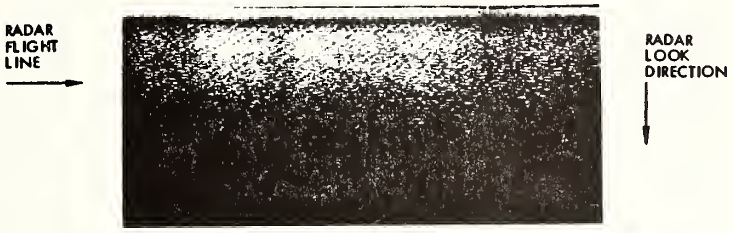
RADAR FLIGHT LINE
RADAR LOOK DIRECTION

RADAR LOOKING UP-WAVE. WAVES ESSENTIALLY TRAVELING IN RANGE DIRECTION

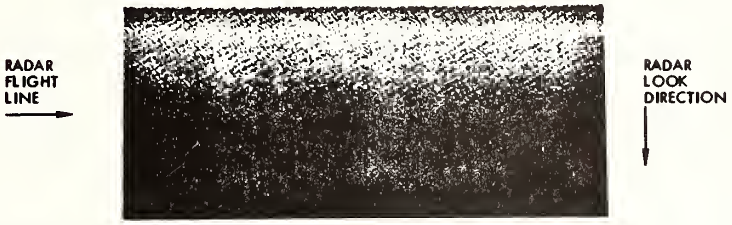
RADAR FLIGHT LINE
RADAR LOOK DIRECTION

RADAR LOOKING CROSS-WAVE. WAVES ESSENTIALLY TRAVELING IN AZIMUTH DIRECTION

Fig. 5. Identical ocean area viewed with a different look direction, X-band 3×5 m resolution, on 14 December 1975, station 1.

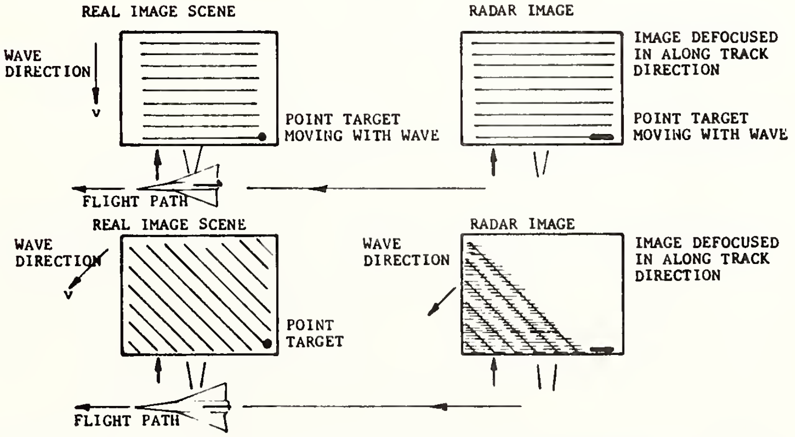
REAL IMAGE SCENE
WAVE DIRECTION
V
POINT TARGET MOVING WITH WAVE
RADAR IMAGE
IMAGE DEFOCUSED IN ALONG TRACK DIRECTION
POINT TARGET MOVING WITH WAVE
FLIGHT PATH
REAL IMAGE SCENE
WAVE DIRECTION
V
POINT TARGET
RADAR IMAGE
WAVE DIRECTION
IMAGE DEFOCUSED IN ALONG TRACK DIRECTION
FLIGHT PATH

Fig. 6. Schematic representation of defocusing of waves as a function of propagation angle with respect to radar look direction.

short pulses or a coded pulse. Thus to the SAR the waves traveling in the range appear stationary over the short sampling time. Furthermore, when waves cause a displacement or defocusing, the displacement is in the along-track dimension (along wave crests) and therefore is not visible in the imagery. Figure 6 graphically demonstrates the displacement or defocusing of waves as a function of motion in the resulting image. From the figure it becomes apparent that range resolution controls only the quality of the wave imagery when waves travel in the range direction.

C. COMPARISON WITH SURFACE MEASUREMENTS

1. *Wave Direction*

The directional properties of waves from the pitch-and-roll buoy are given in the top graph in Figure 2. The results suggest that the waves are predominantly unidirectional propagating towards 270°. The pitch-and-roll buoy location with respect to shore is shown in Figure 7, the X-band radar image of the area. The shoreline alignment with respect to true north is 340° at this location. The pitch-and-roll spectra then suggest that the waves are approaching the shore at a 20° angle.

An examination of the radar image in Figure 7 for wave-crest direction in the vicinity of the pitch-and-roll buoy yields 20° alignment of wave crest with respect to the shoreline. Alternatively, the direction of the peak energy in the Fourier transform of the image at Column 1, frame 4, also yields 20°. This comparison suggests

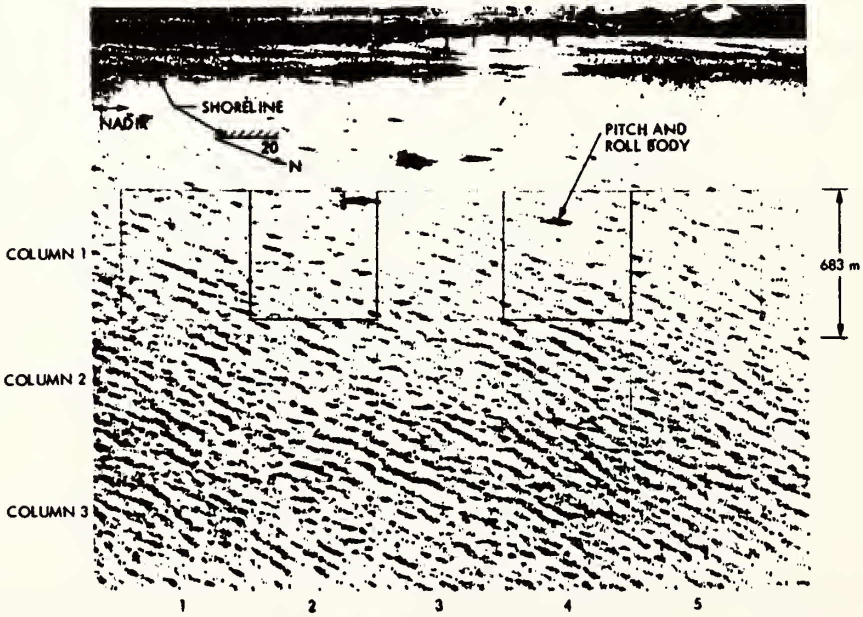

Fig. 7. Nearshore X-band image, 3×5 m resolution, on 14 December 1975.

that radar images, at least X-band images, provide information on wave direction to within a few degrees.

2. *Wave Spectral Shape*

A comparison between a surface wave spectrum obtained by a buoy with one derived from a radar image requires transformation of the spectrum from frequency to wave-number space. The one-dimensional wave-number spectrum derived from the two-dimensional Fourier transform of the image in the vicinity of the pitch-and-roll buoy was normalized in both coordinates using its peak energy value and the dominant wave number from the pitch-and-roll buoy spectrum. A comparison with the similarly normalized pitch-and-roll buoy spectrum is shown in Figure 8. The comparison is surprisingly good considering that little is known about wave imaging mechanisms for the SAR. The comparison provides encouragement for using imaging radars for wave studies. Certainly, more research is deserved and is in progress.

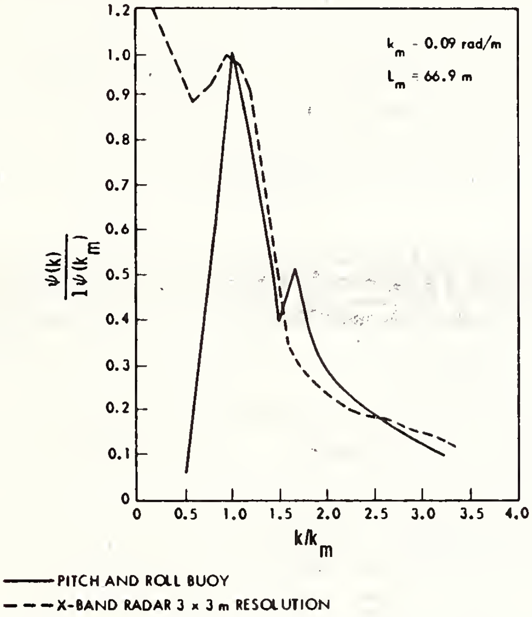

Fig. 8. Comparison of one-dimensional spectra derived from X-band radar image with that measured by the pitch-and-roll buoy at the same location on 14 December 1975. Both spectra are normalized by wave number k_m at peak of buoy spectrum, and by value of spectral energy density at peak of each spectrum. $L_m = 2\pi/k_m$.

5. Conclusion

The conclusions derived from early results of the Marineland Test are summarized below:

1. Under equivalent signal-to-noise ratio and synthetic-aperture resolution, superior wave imagery and more useful Fourier transforms are obtained with the X-band SAR compared to L-band.
2. Optimum wave imagery is obtained when waves propagate in the range direction under otherwise identical conditions.
3. A comparison between X-band wave images and *in situ* measurements with a pitch-and-roll buoy shows agreement in the dominant wave direction to within a few degrees. The normalized spectra show a surprising resemblance in the spectral shape. A better understanding of radar image-formation mechanisms is required to develop a sound basis for comparing radar-derived spectra with surface-truth spectra.

Acknowledgement

The organizations that participated in the experiment were: Coastal Engineering Research Center, Environmental Research Institute of Michigan, Fleet Numerical Weather Central, City University of New York, Jet Propulsion Laboratory, Sea-Air Interaction Laboratory of NOAA, and the University of Florida. The experiment was formulated by members of the Synthetic Aperture Radar Team and sponsored by the Surface Truth Program of SEASAT-A.

References

Brown, W. M. and Porcello, L. J.: 1969, 'An Introduction to Synthetic Aperture Radar', *IEEE Spectrum* **6**, 57–62.

Ewing, J. A.: 1969, 'Some Measurements of the Directional Wave Spectrum', *J. Mar. Res.* **27**, 163–171.

Kozma, A., Leith, E. N., and Massey, N. G.: 1972, 'Tilted Plane Optical Processor', *Appl. Optics* **11**, 1766.

Rawson, R., Smith, F., and Larson, R.: 1975, 'The ERIM Simultaneous X- and L-Band Dual Polarized Radar', IEEE 1975 International Radar Conference, New York, p. 505.

Shemdin, O. H., Blue, J. E., and Dunne, J. A.: 1975, 'Seasat-A Surface Truth Program—Marineland Test Plan', Jet Propulsion Laboratory Document No. 622-5, 86, Pasadena, California.

Shuchman, R. A. and Zelenka, J. S.: 1978, 'Processing of Ocean Wave Data from a Synthetic Aperture Radar', this volume, pp. 181–191.

Tyler, G. L., Teague. C. C., Stewart, R. H., Peterson, A. M., Munk, W. H., and Joy, J. W.: 1974, 'Wave Directional Spectra from Synthetic Aperture Observations of Radio Scatter', *Deep-Sea Research* **21**, 989–1016.

Turbulent Fluxes Through the Sea Surface, Wave Dynamics, and Predictions,
Series V: Air-Sea Interactions 1, 433-443.

THE BIGHT OF ABACO PRESSURE EXPERIMENT

R.L. SNYDER,[1] R.B. LONG,[2] F.W. DOBSON,[3] AND J.A. ELLIOTT[3]

1. NOVA UNIVERSITY, DANIA, FLORIDA, USA
2. NOAA/AOML/SAIL, MIAMI, FLORIDA, USA
3. BEDFORD INSTITUTE OF OCEANOGRAPHY, DARTMOUTH, N.S., CANADA

In November-December of 1974, we conducted a joint experiment to investigate microscale air pressure fluctuations above surface gravity waves. The primary objective of this experiment was to study the vertical structure of the wave-induced component of these fluctuations and to estimate the corresponding differential and integral momentum transfer to the wave field. Secondary objectives included the resolution of differences between previous independent field measurements of wave-induced pressure by Dobson (1971), Elliott (1972), and Snyder (1974), and the construction of a multidimensional model of the turbulent component of the air pressure field. We have, to one extent or another, succeeded in achieving all of these objectives and in due course will publish details in the literature. In this brief report, we wish to convey only the flavour of the investigation along with several somewhat preliminary findings.

The evolution of the wave field is controlled by the radiative transfer equation (Hasselman, 1960)

$$\frac{\partial}{\partial t} E_{\zeta^2} + \vec{V} \cdot \vec{\nabla} E_{\zeta^2} = \alpha + \beta E_{\zeta^2} + S_{NL} + S_D$$

Here $E_{\zeta^2}(\vec{x}, t, \omega, \theta)$ is the spectral density of the wave component with radial frequency ω and direction of travel θ, evaluated at horizontal position $\vec{x}$ and time t, $\vec{V}(\omega,\theta)$ is the group velocity,

$\alpha(\vec{x},t,\omega,\theta)$ and $\beta(\vec{x},t,\omega,\theta)$ are coefficients representing two sources of atmospheric input of spectral density corresponding to the theories of Phillips (1957) and Miles (1957), S_{NL} is the nonlinear source term (Hasselmann, 1962), and S_D represents dissipation. Both α and β are directly related to the microscale air pressure field at the mean surface, α to the three-dimensional spectral density of turbulent pressure F_{Q^2}

$$\alpha = \frac{2\pi}{\rho^2 g^4} \omega^5 F_{Q^2}(\vec{k},-\omega),$$

and β to the imaginary part γ_i of the dimensionless ratio between wave-induced air pressure and surface elevation defined by

$$\hat{P} = s \rho g \gamma \hat{\zeta}$$

In the above equations, Q is the turbulent component of the air pressure, $\hat{P}$ and $\hat{\zeta}$ are complex wave-coherent amplitudes, g is the acceleration of gravity, ρ is the density of water, s is the air/water density ratio, and $\vec{k}$ is defined by

$$\vec{k} = \frac{\omega^2}{g} (\cos\theta, \sin\theta)$$

The earlier measurements of wave-induced pressure by Dobson, Elliott, and Snyder had emphasized single aspects of the experimental task, while ignoring or dealing only partially with other aspects. Dobson's measurements from a floating buoy provided a direct estimate of momentum transfer, integrated over wave azimuth. Elliott's fixed vertical array measurements allowed a coarse extrapolation to the mean surface, also resulting in an estimate of integral momentum transfer. Neither experimental design provided the directional information necessary to properly estimate the differential transfer for a single wave component. Snyder's fixed horizontal array measurements allowed a resolution of the directional dependence of the wave-induced fields, but did not permit a proper extrapolation to the mean surface. The present effort was conceived as an attempt to combine in a single array experiment the separate features of these three earlier experiments in order to deal properly both with the extrapolation of fixed observations to the mean surface and with the resolution of the directional dependence of the wave-induced fields.

The experiment began with a two-week-long instrument intercalibration at Nova University's Ocean Sciences Center, during which instruments and calibration techniques were compared.

This intercalibration revealed that the response of the pressure standard used by Snyder *et al.* (1974) in previous calibrations of the response of the Nova air pressure instruments was slower than assumed, resulting in a systematic bias in Snyder's (1974) results at higher frequencies. Correction for this bias helps to resolve the discrepancy between his results and those of Elliott.

The month-long field experiment was conducted at the same Bight of Abaco site previously used by Snyder. Principal vehicle for the experiment was the University of Miami's 20 m laboratory vessel *Calanus*, which provided power for the instruments and a site for the acquisition of data. The field instruments were deployed in two areas northwest of the *Calanus* mooring. An existing tower 100 m to the northwest supported a three-component vertical array of cup anemometers, a wind vane, tide gauge, and, to monitor the mean surface current, an electromagnetic current meter (which unfortunately did not work). The main instrument array 200 m to the northwest contained seven air pressure sensors and six wave sensors surrounding an instrument mast in a three-legged star pattern. In the centre of the array was Dobson's wave follower-mounted pressure sensor (Dobson and Elliott, 1977). Stacked vertically on the instrument mast were two Elliott sensors. Four Nova instruments, mounted on remotely adjustable stands, formed the legs of the array. Each of the Nova instruments measured both air pressure and water pressure. A fifth wave sensor, a resistance wire wave staff, was attached to the instrument mast. The wave follower itself constituted the sixth wave sensor. Finally, a sonic anemometer was mounted at the top of the instrument mast.

Signals from the instruments were conducted to the *Calanus* by a series of cables lying on the bottom. These signals were acquired simultaneously on two data acquisition systems, a 12-channel FM system used by the Canadians, and a 40-channel digital system used by the Americans. The latter system acquired all signals except those of the sonic anemometer.

The field experiment lasted approximately one month, yielding 37 runs of 40 to 45 minutes duration. Seven of these runs contain wave follower information. Most of our preliminary conclusions are derived from an analysis of runs 14 to 20, during which the wind blew from northeast to east at 6 to 7 m/s (dimensionless fetch $\sim 2\times10^3$), and during which the wave follower was not operating. During run 14, a second vessel, the 11 m ketch *Catspaw*, was placed immediately downwind of the main instrument array in order to backscatter waves.

It is not possible in the limited space available to adequately describe the conceptually straightforward yet operationally very complex analysis by which we have attempted to understand the data. Suffice to say we have proceeded along two parallel fronts: one (Bedford), a simplified analysis of a subset of the data very similar in spirit to the previous analyses of Dobson and Elliott; and the second (Nova), a very much more sophisticated and considerably less transparent analysis of the full data set which attempts to account for a number of effects in a fundamental way. It is the latter analysis which we will discuss briefly in this report.

The Nova analysis can be understood qualitatively in the following terms: we assume that the relevant experimental data for each run are the mean wind parameters, the instrument positions, and the matrix of cross spectra for all instrument pairs in the main array $G_{ij}(\omega)$. Analytical tasks are (1) to identify the set of physical unknowns which is responsible for the values which the matrix elements assume, (2) to work out the relationships between these unknowns and the matrix elements, and (3) to use these relationships to estimate the physical unknowns. The physical unknowns in turn form the basis for the physical interpretation of the results of the experiment.

As unknowns, we identify three run-dependent variables, the spectral density E_{ζ^2}, the effective mean current $\vec{D}(\omega,\theta)$ seen by a given wave component, and the spectral density of turbulent pressure F_{Q^2}. We also identify one global variable, the previously-defined dimensionless wave-induced air pressure ratio γ. γ is taken to be a function of two parameters, a dimensionless wind speed μ

$$\mu \equiv \frac{\vec{k} \cdot \vec{U}_5}{\omega}$$

where U_5 is the mean wind velocity at 5 m elevation, and a dimensionless height γ

$$\gamma \equiv kz$$

where z is the height above the mean surface. We note that this parameterization is certainly not complete. At least two parameters are required to fix the mean wind profile. Therefore γ should be a function of at least three parameters. Such a parameterization is compatible with our analytical scheme, but we doubt that the data are sufficient to resolve a dependence on a third parameter. Rather we shall interpret our results as being characteristic of some mean value of all implicit parameters.

To implement the Nova analysis, we expand the physical unknowns in series containing unknown coefficients and then fix these coefficients by a series of linear, bilinear, and more highly linear least squares analyses. In this manner we estimate the variables $E_{\zeta}2$ and $\vec{D}$ from an iterative computation involving wave sensor/wave sensor elements. γ is in turn estimated from wave sensor/air pressure sensor elements. Two computational schemes are employed, one linear and the other bilinear. In the bilinear case, the phase of the resulting estimate for γ is independent of λ. These schemes are based on the representations

$$\gamma(\mu,\lambda) = \sum_{r,s}^{R,S} \Gamma_{rs}\, \mu^{r} L_{s}(\lambda)$$

and

$$\gamma(\mu,\lambda) = \sum_{q}^{Q} \Gamma_{q}\, \mu^{q} \sum_{r,s}^{R,S} \Lambda_{rs} \mu^{r} L_{s}(\lambda)$$

respectively. Here the coefficients Γ_{rs} and Γ_{q} are complex and the coefficients Λ_{rs} real. These coefficients are typically constrained to match potential theory for $\mu = 0$. Two sets of basis functions to represent the λ dependence are employed. The first of these is the set

$$L_{s}(\lambda) \equiv \lambda^{s}\, e^{-\lambda}$$

The second is a set of empirical orthogonal eigenfunctions recently computed for the Miles theory by R.B. Long, who finds that over the customary range of wind profile parameters, a linear combination of the first three eigenfunctions does an extremely good job of representing the Miles solutions.

A third iterative analysis is used to estimate both the upwind travelling component of $E_{\zeta}2$ and γ for negative μ by fitting wave sensor/air pressure sensor and air pressure sensor/air pressure sensor elements (backscatter runs). Finally, $F_{Q}2$ is estimated from air pressure sensor/air pressure sensor elements. This analysis assumes that the turbulence is 'frozen' in the air flow.

Application of the above analyses to runs 14 to 20 results in the following preliminary conclusions:

(1) In the range $1 < \mu < 3$ and $1 < \lambda < 3$, the vertical dependence of the wave-induced air pressure is approximately exponential and slightly less steep than the potential theory result

$$|\gamma| \sim e^{-\lambda}$$

The phase of γ is independent of λ. These conslusions are consistent with the previous findings of Elliott (1972) and Snyder (1974). The Nova analysis yields a somewhat larger effective vertical decay (closer to potential theory) than does Elliott's analysis or the Bedford analysis of the present data (Dobson and Elliott, 1977).

(2) For $1 < \mu < 3$, this analysis yields an estimate for the imaginary part of γ, extrapolated to the mean surface, which is in good agreement with both Elliott and Snyder (corrected for the response of his pressure standard) and with the Bedford analysis of the present data. These estimates are approximated by the simple relation

$$\gamma_i = 0.2 \begin{pmatrix} +0.1 \\ -0.05 \end{pmatrix} (\mu - 1) \tag{1}$$

(3) Over the same range, this analysis yields an estimate for the real part of γ which is in reasonable agreement with Snyder (corrected) but is somewhat larger than both Elliott's estimate and the Bedford estimate for the present data. In all cases excepting Elliott, Arg γ has its maximum departure from 180° near $\mu = 1$.

(4) For $3 < \mu < 5$, it appears that γ_i continues to increase more or less linearly with μ, although there is some indication that the increase may be faster than linear.

(5) The Nova analysis of limited backscatter observations does not support earlier conclusions by Dobson (1971) and Snyder (1974) that for $\mu < 0$ the wave field is strongly damped. This analysis suggests that the phase of the wave-induced pressure is essentially 180°. Further experimental investigation of waves travelling against the wind is warranted.

(6) The observed wave-induced air pressure field is comparable with, but not identical to, the predictions of Miles' 1957 theory.

(7) Based on an extrapolation of (1) to higher μ, with $\gamma_i \equiv 0$ for $\mu < 1$, we estimate that, for a JONSWAP spectrum (Hasselmann *et al.*, 1973), the total momentum transfer is an inverse function of frequency roughly equal to 100% of the wind stress at dimensionless fetch of 10^2 and 10% of this stress at dimensionless fetch of 10^5.

(8) For small to moderate dimensionless fetch, momentum transfer to the spectral peak is a significant but not dominant fraction of the total momentum transfer to the wave field. This fraction is an inverse function of dimensionless fetch. For the present experiment, transfer at frequencies less than twice the peak frequency is estimated to be roughly one-third of the total transfer to the wave field.

(9) An accurate determination of the total momentum transfer to the wave field will be possible only after reliable field observations of wave-induced pressure have been made for large $\mu (3 < \mu < 10)$. Such observations could be obtained from a Bight-like experiment designed for small dimensionless fetch.

(10) An understanding of the momentum and energy balance for fully developed seas will be possible only after reliable field observations of wave-induced pressure have been made for small $\mu (0 < \mu < 1)$. Such observations will probably require the development of open ocean instrumentation for use at large dimensionless fetch.

(11) The turbulent component of the air pressure field close to the mean surface is reasonably consistent with the 'frozen turbulence' hypothesis.

(12) A two-dimensional turbulent pressure spectrum can be estimated from the cross spectral data.

REFERENCES

Dobson, F.W. (1971) Measurements of atmospheric pressure on wind-generated sea waves. *Journal of Fluid Mechanics, 48:* 91-127.

Dobson, F.W. and J.A. Elliott (1977) Wave-pressure correlation measurements over growing sea waves with a wave follower and fixed-height pressure sensors. Proceedings, NATO Symposium on Fluxes through the Air/Sea Interface and Wave Prediction, at Ile de Bendor, France, September 1977.

Elliott, J.A. (1972) Microscale pressure fluctuations near waves being generated by wind. *Journal of Fluid Mechanics, 54:* 427-448.

Hasselmann, K. (1960) Grundgleichungen der Seegangsvoraussage. *Schiffstechnik, 7:* 191-195.

Hasselmann, K. (1962) On the non-linear energy transfer in a gravity-wave spectrum. I. General theory. *Journal of Fluid Mechanics, 12:* 481-500.

Hasselmann, K., T.P. Barnett, E. Bouws, H. Carlson, D.E. Cartwright, K. Enke, J.A. Ewing, H. Gienapp, D.E. Hasselmann, P. Krusemann, A. Meerburg, P. Müller, D.J. Olbers, K. Richter, W. Sell, and H. Walden (1973) Measurement of wind-wave growth and swell decay during the Joint North Sea Wave Project (JONSWAP). Erganzungsheft zur Deutschen Hydrographischen Zeitschrift, Reihe A (8^o), Nr. 12.

Miles, J.W. (1957) On the generation of surface waves by shear flows. *Journal of Fluid Mechanics, 2:* 417-445.

Snyder, R.L. (1974) A field study of wave-induced pressure fluctuations above surface gravity waves. *Journal of Marine Research, 32:* 497-531.

Snyder, R.L., R.B. Long, J. Irish, D.G. Hunley and N.C. Pflaum (1974) An instrument to measure atmospheric pressure fluctuations above surface gravity waves. *Journal of Marine Research, 32:* 485-496.

DISCUSSION

joint discussion of papers 3.1.3

F.W. DOBSON AND J.A. ELLIOTT
BEDFORD INSTITUTE OF OCEANOGRAPHY
DARTMOUTH, N.S., CANADA

WAVE-PRESSURE CORRELATION MEASUREMENTS OVER GROWING SEA WAVES WITH A WAVE FOLLOWER AND FIXED-HEIGHT PRESSURE SENSORS

and 3.1.4

R.L. SNYDER, R.B. LONG, F.W. DOBSON, and J.A. ELLIOTT

THE BIGHT OF ABACO PRESSURE EXPERIMENT

O. M. Phillips:

These two papers, by Dobson, Elliott, Long and Snyder and by Dobson describe very difficult measurements and their successful outcome is a considerable tribute to the skill of the authors.

When they started out on this, I thought it was an impossible task, but I am happy to have been wrong.

E. J. Plate:

We have learned to expect that in the ocean momentum is transferred through the high frequency waves. Your data seem to show that momentum is transferred more or less uniformly from frequencies near f_m to at least $2f_m$. Could you estimate the value of f_m (smaller than the one observed by you?) for which we may expect our old notion to be true?

F. W. Dobson:

The relevant information is in Snyder's figure showing the momentum-transfer integrand plotted against f/f_m for various values of dimensionless fetch. You see there that at large dimensionless fetch, the integrand, though small, has its peak at the highest values of f/f_m. Your "notion" is most true when the momentum transfer is most widely separated from f_m and so the answer is that this occurs at large dimensionless fetch.

K. Hasselmann:

(1) It is encouraging to see that you obtain similar ratios for the wave induced to total momentum flux across the air-sea interface by direct measurement as was inferred indirectly from the JONSWAP measurements: up to 100 % for small fetches, decreasing to 10 - 20 % for large fetches.

(2) Is it possible that some of the scatter in the atmospheric wave input data may be due to the fact that the data cannot be pacified in terms of the single parameter $k \cdot U/\omega$. This would be the case, for example, if the generating mechanisms are nonlinear, as suggested by recent investigations on the role of whitecaps in flow separation over the wave crests. It should be possible to estimate the degree of nonlinearity from the pressure-wave height coherence. It is possible that the relatively low coherences typically observed in the wind-wave peak as compared with the swell peaks (even when there is a pronounced wind-wave induced peak observed in the pressure spectrum) may be an expression of this nonlinearity?

F. W. Dobson:

Elliott, in his 1972 J. F. M. paper, attempts to quantify this by removing from his pressure power spectra the wave induced part; he finds a substantial residual, not found over land, but incoherent with the waves. The waves therefore are contributing a significant component to the field of turbulent pressure fluctuations in the general frequency range of the wave spectrum. The mechanism for this contribution is not understood.

R. L. Snyder:

As Fred Dobson has indicated, there is some evidence for a wave-turbulence whose effect would be to reduce the coherence between the surface elevation and air pressure. There is, however, another mechanism which in many experimental situations will dominate. For non-dimensional fetches of order 10^3 to 10^4, the peak of the spectrum corresponds to $\mu \sim 1$ to 2, where γ is a minimum. Thus the pressure signal for downwind travelling waves can easily be dominated by the pressure signal for waves of the same frequency travelling in other directions, in particular, waves travelling against the wind. This latter signal is incoherent with the dominant part of the wave signal, resulting from waves travelling downwind.

Thus the overall coherence between surface elevation and air pressure is low. In my experience, a well defined wave-induced peak in a generation situation is indicative of waves travelling in directions other than the wind direction. In a situation where these waves are absent, the wave induced peak is not that well defined.

V. Cardone:

The Phillips linear growth rate parameter, α, remains a part of all contemporary discrete and hybrid-parametric wave prediction models. It is usually simply prescribed on the basis of net wave growth and incorporates Priestley's (1964) form for the shape of the atmospheric pressure spectrum and a wind speed power law relation for the intensity of the fluctuations (e.g. u^4 or u^6). How does your measured spectrum of the incoherent atmospheric turbulent pressure fluctuations over the sea surface compare to Priestley's? Also, do your experimental conditions extend over a broad enough range of wind speeds to reveal the variation of the root mean square pressure intensity with wind speed?

R. L. Snyder:

Priestley's (1964) measurements yielded downwind and crosswind coherences, both of which fell off as exp $(-\mu_i|\xi_i|)$, where μ_1 and μ_2 are comparable coefficients and ξ_1 and ξ_2 are the downwind and crosswind components of instrument displacement. Priestley assumed that where the displacement was neither downwind nor crosswind, the coherence would go as the product of these two exponentials. The Bight of Abaco data do not support this picture. We find that the coherence is largely independent of downwind displacement, consistent with the frozen turbulence assumption. We explain Priestley's downwind coherences in terms of statistical variations in mean wind direction. Unfortunately, this kind of model confines $F_Q^2(k,\omega)$ to the dispersion curve $\omega=k\cdot U$ (where it is infinite).

Elsewhere, F_Q^2 is zero. Thus we can not presently estimate the α term in the radiative transfer equation. As indicated in our paper, it may be possible to make such an estimate by relaxing the delta function dependence of F_Q^2 in some appropriate way. My expectation would be that such a computation would produce smaller α's than does Priestley's model.

We can probably learn something about the wind speed dependence of the r.m.s. turbulent pressure, but as yet have not looked at this particular aspect of the data.

Library of Congress Cataloging in Publication Data

NATO Conference on Turbulent Fluxes through the Sea Surface, Wave Dynamics, and Prediction, France, 1977.
Turbulent fluxes through the sea surface, wave dynamics, and prediction.

(NATO conference series: V, Air—sea interactions; v. 1)
Includes index.
1. Eddy flux—Congresses. 2. Ocean-atmosphere interaction—Congresses. 3. Ocean waves — Congresses. I. Favre, Alexandre. II. Hasselmann, Klaus, 1931- III. Title. IV. Series.
GC190.2.N17 1977 551.4'7022 78-7339
ISBN 0-306-40005-7

SCIENTIFIC COMMITTEE

A. FAVRE, Institut de Mécanique Statistique de la Turbulence, Marseille, France
K. HASSELMANN, Max-Planck-Institut für Meteorologie, Hamburg, Germany
H. LACOMBE, Muséum National d'Histoire Naturelle, Paris, France
M. S. LONGUET-HIGGINS, University of Cambridge, Cambridge, England
E. MOLLO-CHRISTENSEN, Massachusetts Institute of Technology, Cambridge, U.S.A.

ADMINISTRATIVE DIRECTOR

F. RESCH, Institut de Mécanique Statisque de la Turbulence, Marseille, France

DIRECTORS OF THE SYMPOSIUM

A. FAVRE, Institut de Mécanique Statistique de la Turbulence, Marseille
K. HASSELMANN, Max-Planck-Institut für Meteorologie, Hamburg

LOCAL ORGANIZING COMMITTEE

A. FAVRE, M. COANTIC, and F. J. RESCH,
Institut de Mécanique Statistique de la Turbulence, Marseille

Proceedings of the NATO Conference on Turbulent Fluxes through the Sea Surface, Wave Dynamics, and Prediction held in Marseille, France, September 12–16, 1977 sponsored by the NATO Special Program Panel on Air–Sea Interactions

MTS/IEEE - Oceans '78 Conference, 639-648.

OCEAN WAVE DETECTION AND DIRECTION MEASUREMENTS WITH MICROWAVE RADARS

Paul G. Teleki
U. S. Geological Survey
915 National Center
Reston, Virginia 22092

Robert A. Shuchman
Environmental Research Institute
P. O. Box 618
Ann Arbor, Michigan 48107

Walter E. Brown, Jr.
Jet Propulsion Laboratory
California Institute of Technology
Pasadena, California 91103

William McLeish
Sea Air Interaction Laboratory
National Oceanic and Atmospheric Administration
Miami, Florida 33149

Duncan Ross
Sea Air Interaction Laboratory
National Oceanic and Atmospheric Adminstration
Miami, Florida 33149

Michael Mattie
U.S. Army
Coastal Engineering Research Center
Fort Belvoir, Virginia 22060

Abstract

Electromagnetic energy at microwave frequencies is backscattered by the short-wave component of the ocean wave spectrum. Complex scattering models, which include both Bragg resonance and Rayleigh scattering, have been postulated to describe the amplitude of radar return. The actual return is complicated by the intensity and distribution of the facets of infra-gravity waves. Furthermore, long gravity waves modulate short waves, their tilt and displacement depending on their instantaneous position relative to the long wave profile and extraneous vector quantities such as surface current gradients.

As the maximum modulation is in the direction of wave motion, the discernibility of ocean waves is dependent on the radar look direction. Waves traveling or containing components in the azimuth direction (along track direction of the flight) are sensitive to defocusing due to Doppler shifts in the case of the synthetic aperture radar (SAR), introduced primarily by velocity components such as perturbations due to long wave orbital velocities, Bragg wave velocities, and surface current velocities. For a given velocity component, defocusing is greater at L-band frequencies than at X-band, resulting from the longer residence time of a moving target in the L-band aperture, given equivalent resolution.

The principal uses of radar imagery for wave studies are to derive direction and length information. While length and direction are determinable from the radar signal, the accuracy with which this information can be established had to be tested against more conventional ocean instrumentation. Data obtained with a pitch-and-roll buoy and current meters were compared to X-band SAR wave imagery obtained simultaneously over a test site offshore of Florida. Analysis shows that the wave direction at the peak frequency of the wave spectrum from buoy and current meter measurements agrees with the frequency-averaged radar directions within 2 degrees. Agreement in the data is considered exceptional, given that the measurements were made in 8-12 m water depth, where wave refraction is strong.

Shore-based radars have also been used to derive wave direction and length information. Comparison between the measured wave directions for the principal wave trains, as seen on aerial photographs and shore-based radar images, simultaneously obtained show agreements within 3 degrees.

In the case of airborne real-aperture radars, wave length information derived from the radar is in good agreement with that determined from simultaneous laser profilometer spectra, and the direction observed is essentially the same as the local wind.

With case-by-case determination of the modulation depth and focusing parameters, the SEASAT-A L-band SAR will produce much needed information for wave refraction studies on continental shelves.

1. Introduction

Imaging radars are active devices that sense the environment with short wavelength electromagnetic waves. With the advent of the SEASAT-A data on dynamic ocean properties, interest in understanding the uses and limitations of radars has been increasing. As active sensors, radars provide their own illumination in the microwave region of the electromagnetic spectrum and thus are not affected by diurnal changes in emitted or reflected from the earth's surface. Most radars operate in the frequency region of 300 MHz (1 m) to 30 GHz (1 cm), and bandwidths within this region are commonly designated by letters. Radars discussed in this paper are designated as L-band (23.5 cm), X-band (3.2 cm) and Ka-band (0.86 cm), all having been operated as airborne side-looking radars, and one X-band (3 cm) PPI (plan position indicator) radar operated in a fixed position.

Side-looking radars use pulse ranging, whereby the radar antenna attached to a moving aircraft illuminates a section of the ground and the amplitude, phase and polarization of the returned echoes are processed to determine the distance to the scene and to obtain the measure of relative strength of the return (σ_o). In real-aperture systems, the resolution in azimuth is limited by the beamwidth (i.e. the physical length) of the antenna. Synthetic aperture radars utilize the Doppler history (change of phase) associated with the motion of the aircraft, recording both the phase and the amplitude of the backscattered energy, thus improving the azimuthal resolution. The longer the radar length, the greater improvement in the along-track resolution of the system.

Conventional radars of the PPI presentation commonly use a fixed pulse repetition frequency and CRT (cathode ray tube) displays of the brightness pattern (energy scattered by surfaces and objects) that represents topographic features in view of the azimuth scanning radar antenna. The CRT displays the returned echoes by representing azimuth as an angle and range as radial distance. The X-band shore-based radar described is of the PPI type used in measuring the sea-echo in nearshore waters.

Among the recognized advantages of radars are their ability to image the earth's surface independently of weather conditions or solar illumination and to provide synoptic views at high resolution. These attributes make space-borne radars attractive to studies of surface dynamics of the oceans. The synthetic aperture radar (SAR) on SEASAT-A, operating a L-band (1.275 MHz) in horizonal polarization was designed to image principally ocean wave patterns. Potentially, the SAR can also provide information on the dominant wavelength and direction of surface waves, on wave height, surface currents, and internal waves. Insofar that the principal aim of the SAR Experiment, relative to oceans, is the derivation of two-dimensional wave spectra, it should be noted that until now few meaningful SAR ocean spectra have been generated (Brown, et al. 1976). Wave height information is theoretically obtainable from SAR, but an algorithm has yet to be developed. Elachi and Apel (1976) and Moskowitz (1973) published radar imagery with features that resemble, respectively, internal waves and surface currents, but these observations were not supported with in-situ measurements.

In the course of designing the SEASAT-A SAR, it was realized that in the absence of experience with spaceborne SARs and in view of the limited amount of ocean data existing at L-band, aircraft based experiments had to be conducted prior to launch of the satellite. The aim of these experiments was to study the physical coupling between electromagnetic waves and water waves (Shemdin, et al. 1975). Thus, in December 1975, an experiment took place near Marineland, Florida, wherein X- and L-band synthetic aperture radars were flown on aircraft to image waves in varying meteorological conditions and sea states on the adjacent continental shelf. Wave height and direction and the amplitude and direction and the amplitude and direction of currents (due to orbital motion in waves and due to wind) were measured by an array of in-situ instruments, of which data obtained by a pitch-and-roll buoy and paired orthogonal current meters are relevant to this study. With regard to wave direction measurements, this report quantifies results, reported by Shemdin et al. (1977), for tests conducted on December 14.

2. Radar concepts

Imaging mechanisms: The principle in imaging any surface with a radar is that in the backscatter of microwave energy (echo) received by the radar antenna contains information on the roughness characteristics (shapes, dimensions and orientation) of the reflecting area. These parameters that influence the echo received from ocean waves include the motion of the scattering surfaces, the so-called speckle effect, system resolution, digital sampling, non-coherent integration and thermal noise level and contributions attributable to wind, surface currents and surface tension. Factors described herein are those pertaining to wave orbital velocity, Bragg scatterer velocity, and long (or resolvable) wave phase velocity. To illustrate the various effects, relatively simple models have been chosen.

Several models exist that attempt to explain wave image formation with synthetic aperture radars. In general, static models show dependence on instantaneous surface features and dynamic models draw on surface velocities. Considerable debate exists on the acceptability of either model. We attempt to draw together both analytical and experimental results and use arguments from both types of models.

The three principal static models for the backscatter (σ_o) from the ocean are the facet, Bragg-Rice, and the Rayleigh scattering models. The tangent plane or facet model is based on reflections from areas whose slopes are oriented normal to the line of sight. It is assumed that the surface radius of curvature exceeds the radar's wavelength and that one can neglect random scattering and shadowing effects (Brown, et al. 1976). The radar cross section of the facet model, according to Beckman and Spizzichino (1963) is

$$\sigma_o\ (\theta) = \cot^2\beta_o\ \exp\ (-\tan\theta/\tan\beta_o)^2 \qquad (1)$$

where θ in the radar incidence angle, and $\tan\beta_o = 2\ \sigma/T$, T being the autocorrelation distance for a rough surface whose heights are distributed with standard deviations σ.

The Bragg-Rice model uses the concept that the ocean surface can be represented by a combination of periodic surfaces, so that the dominant backscatter will match some portion of the ocean wave spectrum. The model assumes that the number of favorable additions satisfy the criterion of adequate sample size, the height and slopes of the backscattering elements are small relative to the incident wavelength and that their distribution is isotropic. The maximum return, as measured by Wright (1966), is obtained when

$$k_w = 2\ k\ \sin\ \theta \qquad (2)$$

where $k_w = 2\ \pi/L$ and $K = 2\ \pi/\lambda$ are the wave numbers and L and λ the wavelengths, respectively, of the capillary waves and the radar. For this model, the cross section

$$\sigma_o\ (\theta) = 4\pi\ k^4\ \cos^4\theta\ R(\theta,\psi)\ W(k) \qquad (3)$$

where R (θ,ψ) is the reflectivity as function of the surface electromagnetic properties and the incidence and polarization angles and where W(k) is the energy density spectrum of surface height variation evaluated at the Bragg resonant condition in Eq. 2. According to Trunk (1976), Phillips (1966) gives a bound for W(k) as Bk^{-4}, where B is approximately 6×10^{-3} for gravity waves and 1.5×10^{-2} for capillary waves. Trunk shows, that this model, which can be related to breaking or steep-crested waves, is dependent on short-pulse radars.

Backscatter from the sea is composed of contributions from many fluctuating individual scatterers, which in the Rayleigh scattering model are represented by segments of spheres or complex shapes that are small relative to the radar wavelength. The resultant echo varies in time, reflecting relative phase differences among the echoes received from each scattering element (Skolnik, 1970). The resultant cross section, which is relatively insensitive to look-direction because the scattering elements are moving randomly and are distributed nearly isotropically, is described by a probability density function. According to Trunk (1976), the Rayleigh scattering is more sensitive to vertical polarization and more applicable to wide pulse widths, wherein the received echo contains returns from several breaking waves, added non-coherently.

Two of the static models, the facet and Bragg-Rice scattering models were evaluated with data from the Marineland experiment. Analysis indicates the facet model agrees only marginally with the data obtained with the synthetic aperture radars operated by the Environmental Research Institute of Michigan (ERIM). Results shown in Fig. 1 include the range of data reported by Bechman and Spizzichino (1963), and X-band (λ=3.2 cm) and L-band (λ=23.5 cm) measurements normalized to the 12 knot wind speed measured at Marineland (equivalent to β_o = 10°).

In comparison, the Bragg-Rice model offers more promise, at least for the L-band data. Data summarized by Guinard and Daley (1970), together with data obtained by ERIM on December 15, are shown on Fig. 2 for X-band and in Fig. 3 for L-band. The Bragg-Rice-Phillips upper bound is shown as a solid line. For the limited range of incidence angles agreement between theory and data is good.

Static models are particularly applicable to imaging with real-aperture radars. Synthetic aperture radars, however, are very sensitive to Doppler velocity components present in the imaged scene. Effects of aircraft motion on wave elements present in SAR imagery, include in order of importance, displacement, image smearing and loss of focus in the azimuth direction, reduction of wave contrast and loss of focus in the range direction. Because the origin of these effects is in the velocity components present on the ocean surface, dynamic models applied to SAR imaging concentrate on either the phase velocity or on the orbital velocity of ocean waves. Early attempts to explain these effects observed in SAR wave imagery based arguments on phase velocity; more recent work tends to develop models dependent on orbital motion. The topic is an exciting and controversial one in that experimental evidence exists to support aspects of both approaches. However, the degrees of freedom associated with coherent SAR processing are not sufficient to uniquely explore cause/effect relationships for the image perturbations cited. In addition, influence of spatially distributed currents, including those generated by wind stress are just beginning to be investigated (Weissman and Thompson, 1977).

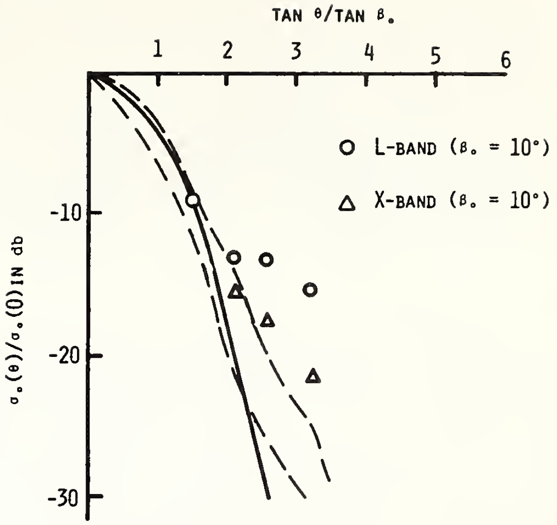

Fig. 1 Comparison of X-band and L-band data obtained at Marineland on December 15, 1975, with the facet model (solid line) and with the range of data reported by Beckman and Spizzichino (dashed lines).

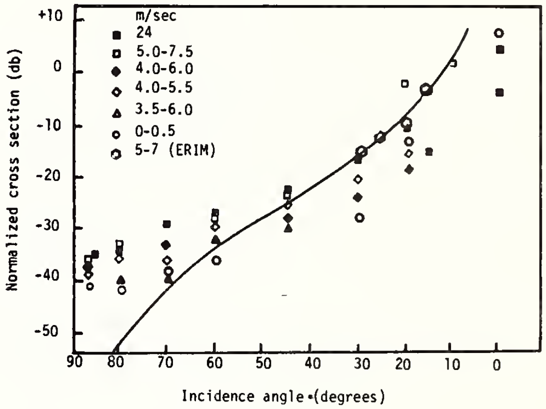

Fig. 2 Variation of the normalized σ_o (HH) at X-band with incidence angle and wind speed. The line represents the Bragg scattering relationship. Data from Guinard and Daley (1970) and the ERIM radar.

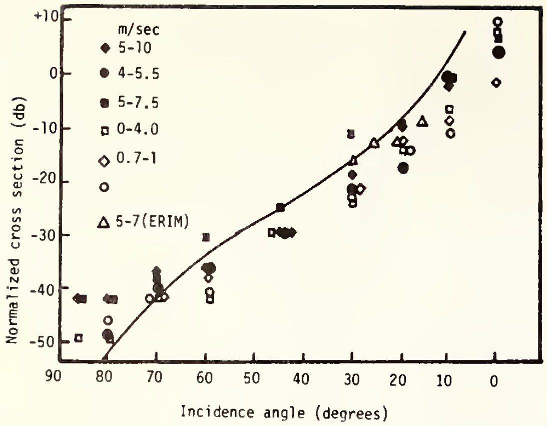

Fig. 3. Variation of the normalized σ_o (HH) at L-band with incidence angle and wind speed. The line represents the Bragg scattering relationship. Data from Guinard and Daley (1970) and the ERIM radar.

Geometry and motion effects. There are two inherent problems in the collection of ocean wave data with synthetic aperture radars that must be accounted for before dominant wavelength and directional information can be obtained. The two problems are geometry and wave motion effects.

Figure 4 shows the typical configuration of the SAR and the resulting distortion near nadir. Two aspects of the slant range geometry must be considered. First, wave imagery will be compressed, introducing a high range-frequency component with increasing slant range, so that a Fourier transform of a large area containing waves will include a wide range of frequency-modulated wave components. This smears the spectrum and reduces the signal-to-noise ration. Optical or digital slant-to-ground range conversions alleviate this problem.

Another aspect of geometry is the distortion of imagery near nadir resulting from the time delay in range shown in Fig. 5. This, however, is routinely correctable by digital techniques.

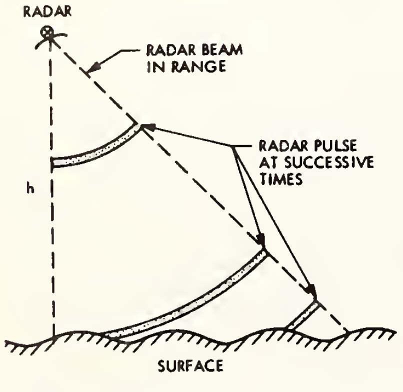

Fig. 4 Range geometry of side-looking radars.

Ocean waves imaged by a SAR system may be blurred if the wave move a substantial distance during the time they are in the radar antenna beamwidth. These blurring effects may, in some cases, be removed by compensatory adjustments of the optical correlator. Azimuthal velocity compensation is achieved by adjusting the correlator azimuth focus according to an algorithm utilizing radar, processor and moving target parameters. Similarly, the blurring effects of range traveling waves may be removed by suitable rotation of cylindrical optical elements in the correlator. For azimuth traveling waves, the focus correction needed to produce the best azimuth focus can be explained assuming the radar scatterer moves at the phase velocity of the ocean wave. This is not the case, however, for range traveling waves where a point scatterer moving at the phase velocity of the wave would displace, but not defocus the wave image. The observed defocusing can be accounted for by assuming the radar signals are reflected from a stationary scattering surface with variable reflectivity modulated by the passage of a moving ocean wave.

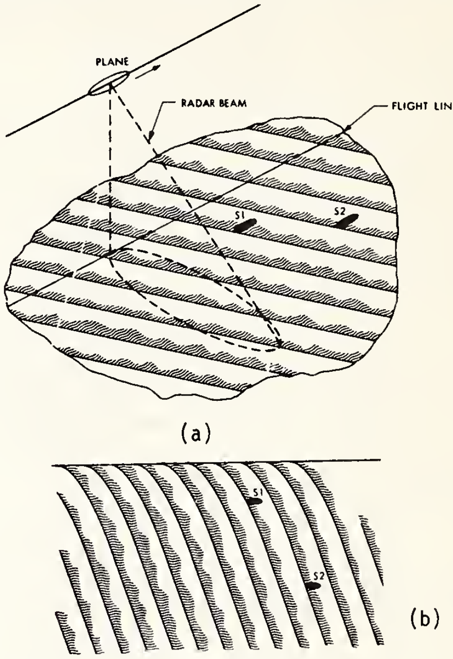

Fig. 5 Relationship between the radar look direction (a) and the corresponding image (b).

The appropriate model assumes that the energy returned to the radar receiver is reflected or scattered from an ocean surface that is stationary relative to its geographic location. The reflecting surface may, in fact, be moving slowly relative to the phase velocity of the wave, such as the orbital velocity of the wave that usually is an order of magnitude lower than its phase velocity. In this case, the stationary surface model would still apply, since the scattering surface is more nearly stationary compared to the phase velocity of the wave. This is consistent with the fact that the predominant echo in Bragg scattering is from waves either traveling toward or away from the radar.

This model is based on the following observations made on the ERIM-SAR optical correlator: 1. Measurement of the azimuth Doppler spectrum shift for a series of range traveling waves indicate a scattering surface velocity, at most an order of magnitude lower in value than the phase velocity of the waves; 2. Radar image contrast for range traveling waves is maximized when the cylindrical optics used to focus the azimuth signal histories are rotated an amount proportional to the waves phase velocity; 3. Wave images made from separated Doppler spectral bonds show range displacements equal to the wave phase velocity times the equivalent time between the two Doppler spectra for a stationary traget at the same radar range; 4. Azimuth traveling waves are defocused an amount equal in magnitude to that produced by radar reflectors moving at the phase velocity of the wave and defocusing is more pronounced at L-band than at X-band.

Figure 6 demonstrates dependence of azimuth traveling ocean waves on focus setting in the SAR processor. Modulation depth, defined as the variation in image intensity associated with individual wave returns (wave crest to trough contrast), is plotted against focus shift for an area of waves simultaneously imaged by X- and L-band SAR. Results show the relative insensitivity of X-band to focusing while an optimum detectability (high modulation depth) occurs at L-band at a setting shifted 1.0 mm from a stationary (land) object. Similar results were reported by Jain (1978). Analysis of Marineland data indicates that optimum wave images result when the radar is looking essentially up-wave or downwave, that is when waves propagate towards or away from the aircraft in the range direction as is shown in Fig. 7. This principally indicates Bragg-type scattering. Because in the range direction the SAR uses a train of very short pulses, waves traveling in range appear quasi-stationary relative to the sampling time. Differences in modulation depth of range traveling waves (Fig. 8) also indicate that better quality wave images can be generated with X-band at parallel polarization than with L-band radar. Simultaneously obtained, identical resolution and signal-to-noise ratio X-band (HH) ocean wave images are compared to L-band (HH) images of the same area in Fig. 9. Scans of image density in the direction perpendicular to the dominant crest direction show higher crest-to-trough modulation for X-band. Consequently, wave spectral peaks derived from X-band images can be more accurately defined than those from L-band.

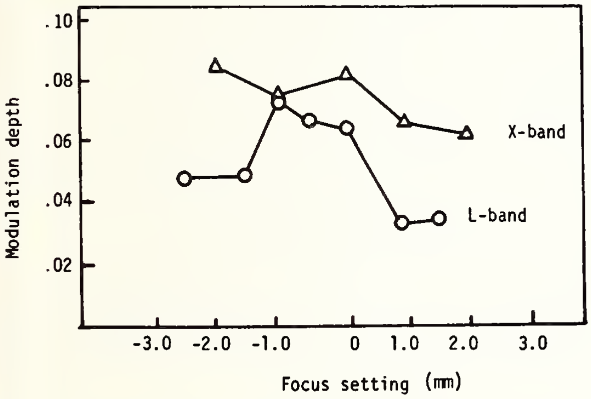

Fig. 6 Modulation depth as function of focus shift for X- and L-band data from Pass 9, Location E, Marineland, Florida, December 14, 1975. Zero represents the stationary focus.

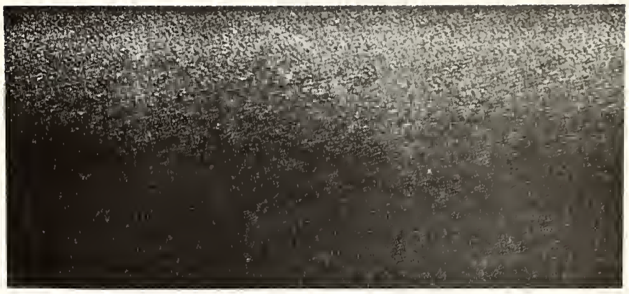

Radar look direction up-wave. Waves are essentially traveling in the range direction

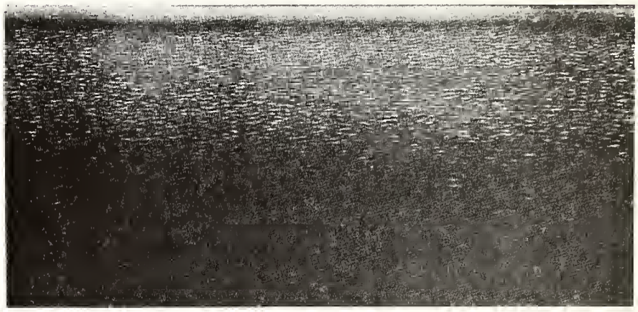

Radar look direction cross-wave. Waves are essentially traveling in the azimuth direction

Fig. 7 Identical ocean area imaged on December 14, 1975, with X-band radar and processed to 3 x 5 meter resolution. Radar flight line from left to right. Radar look direction toward bottom of page with a scale of 5 km in range.

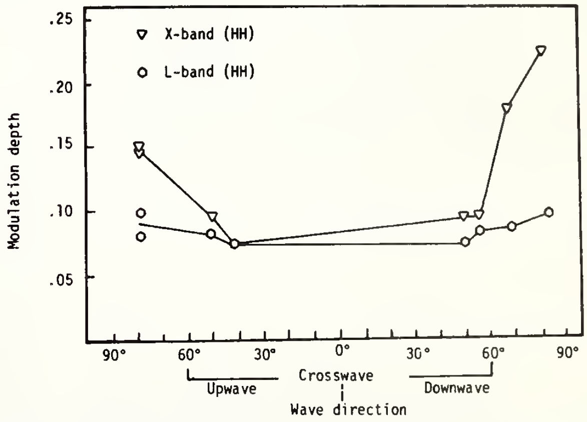

Fig. 8 Modulation depth at X-band and L-band as function of the direction of wave propagation.

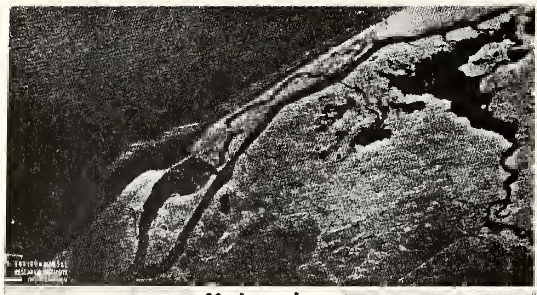

X-band$_{HH}$

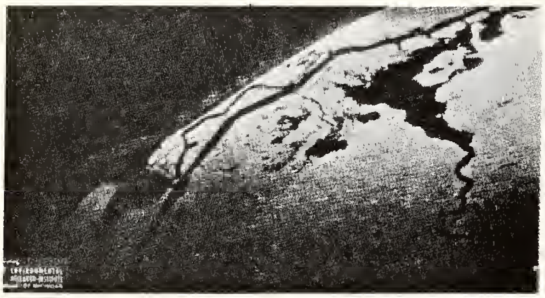

X-band$_{HV}$

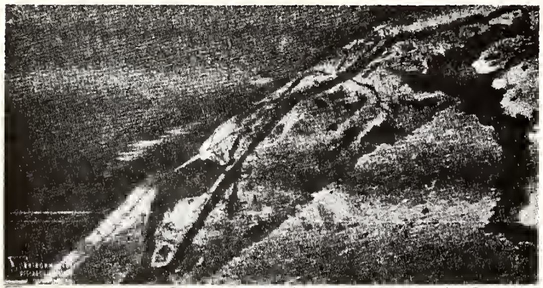

L-band$_{HH}$

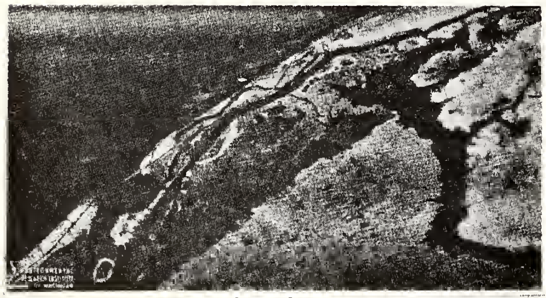

L-band$_{HV}$

ig. 9 Radar imagery of the nearshore area at arineland, Florida, on December 15, 1975, at X- and -band frequencies and parallel and cross-polarizations.

A possible explanation for the higher quality of -band imagery was given by Shuchman and Zelenka 1977), who suggested that X-band data have a larger epth of focus than L-band, and therefore the waves oving in the azimuth direction are not appreciably efocused as commonly occurs on L-band images of omparable resolution. The X-band also incorporates a shorter synthetic-aperture length or integration time than L-band, hence reducing motion errors. Also, Trunk (1976) noted that data at horizontal polarization have larger echo spreads than at vertical polarization, and that L-band data have larger clutter spreads than X-band data.

Aspect angle. Besides such factors as sea state and radar frequency and polarization, the intensity of the backscatter return (σ_0) from a SAR also depends on the radar look direction (aspect angle) relative to wind speed and direction. Variation of σ_0 at X-band with incidence angle and wind speed was given in Fig. 2. The data indicate that the reduction in the incidence angle toward nadir corresponds to an increase in σ_0. In a comparison of four frequencies, K-band (0.89 cm), X-band (3.2 cm), S-band (15 cm), and L-band (23.5 cm), Long (1956) has shown that the general trend also indicates σ_0 increases toward nadir, but correlation of these data to wind speed or direction is not demonstrable. It is known, however, that the backscatter is usually higher in the upwind direction, and in a recent report Fontanel (1978) mentions a 6 db difference at X-band.

3. Data acquisition

The Marineland experiment, whose objectives have described by Shemdin et al. (1975), took place ecember 1975. Data we have analyzed were collecon December 14, with airborne X- and L-band dual-ized synthetic aperture radars flown on ERIM's aircraft. In-situ data on wave properties were ected by a pitch-and-roll buoy (wave height and tion) operated by NOAA's Atlantic Oceanographic leteorological Laboratory (AOML) and an instrution package consisting of a pressure gauge and gonally mounted current meters on a sea-sled height, orbital velocities and mean current velocities) operated by the U.S. Army's Coastal Engineering Research Center (CERC). Additional data presented herein were obtained with two real-aperture systems, one an X-band (3 cm) stationary scanning (Raytheon 1020/9XR) radar operated by CERC and a Ka-band (APD-7) radar operated on NP3C aircraft by AOML. Data obtained by these radars were in geographic areas and at times different from those of the Marineland experiment. We included this information to exemplify techniques by which wave spectra and direction can be obtained.

Characteristics of the ERIM SAR system have been described by Shuchman and Zelenka (1977). The CERC radar uses a nine foot slotted array antenna with a beamwidth of 0.9° at 3 db rotating at the rate of 33 rpm. Pulse width is 0.05 µsec which results in a range resolution of 10-20 m. This will generally permit imaging waves of 30 m length. The PPI has a 10-inch CRT with a fast decay phosphor photographed with a Bolex 16 mm reflex camera. The radius of the region displayed may be varied by discrete steps from 3/8 of a nautical mile (0.695 km) to 24 nautical miles (44.4 km). Signal-to-noise limitations restrict wave imaging to a range of 3 nmi or less. The optimum range for obtaining information on wave direction depends on the length and height of the incident waves.

The real-aperture Ka-band radar, operated by NOAA is a military version of the APQ-97 system developed by Westinghouse, that uses a narrow transmitted pulse width to achieve a range resolution of 8 m.

Physical charteristics and operational modes of the sea-sled instrumentation have been reported by Teleki, et al. (1975). The pitch-and-roll buoy operated by NOAA is the type described by Ewing (1969).

4. Wave spectra

In converting raw SAR data to wave spectra, two basic steps are used: 1) to generate an image by correlating the SAR signal amplitude and phase histories and 2) to derive the wave frequency and wave number spectra. In this procedure SAR signal data were digitized and corrected for geometry. The slant-to-ground range conversion, $R_g=(R_s^2 - h^2)^{\frac{1}{2}}$, where R_g and R_s are the ground and slant range distances and h is the altitude of the aircraft, also requires knowledge of the sampling interval and geoidal surface elevation. Using the antenna gain as a function of angle, each image element in range was weighted to account for the two-way propagation loss that is proportional to range (Lowry, et al., 1977). A form of radiometric correction, it involves calculating the average intensity in each range cell.

Figure 10 is a geometrically corrected image of wave conditions at Marineland on December 14, 1975, obtained with the ERIM X-band (HH) radar and processed at the Jet Propulsion Laboratory. Location of the pitch-and-roll buoy (PRB) is marked. The local water depth, adjusted for the tide was 12 m. The sea-sled gauges were operating in 7.7 m water depth directly shoreward of the buoy. For the square subarea in which the buoy was operating, an FFT transform of the radar image was generated in digital form. After averaging, the two-dimensional energy density spectrum E (k, θ), was mapped (Fig. 11) that shows presence of two wave trains. The dominant energy is at k=0.076 rad/m (L=82m) with wave direction α=270°. The contour interval is 2.718.

Pitch-and-roll buoy data were digitized at two samples/second and cross correlated to obtain the directional distribution of wave energy, E (f,θ). After applying the shallow water correction to the radar data using the dispersion relationship $\omega^2 = gk \tanh kd$, where $\omega = 2\pi f$ and d is the local water depth, the frequency-dependent energy density spectra of the buoy and radar measurements were calculated. This is shown in the lower half of Fig. 12 wherein the peak of the spectra match at the frequency of 0.124 Hz. In order to compare the spectral shapes, especially in the high frequency region of the spectrum, ln(f) was plotted again ln (E(f)) in Fig. 13. Comparison of the slopes of the radar and buoy spectra indicate both sensors having measured the same wave components.

5. Wave direction

Wave direction was computed from the radar, pitch-and-roll buoy and the current meter data (Table 1) for the total frequency range observed.

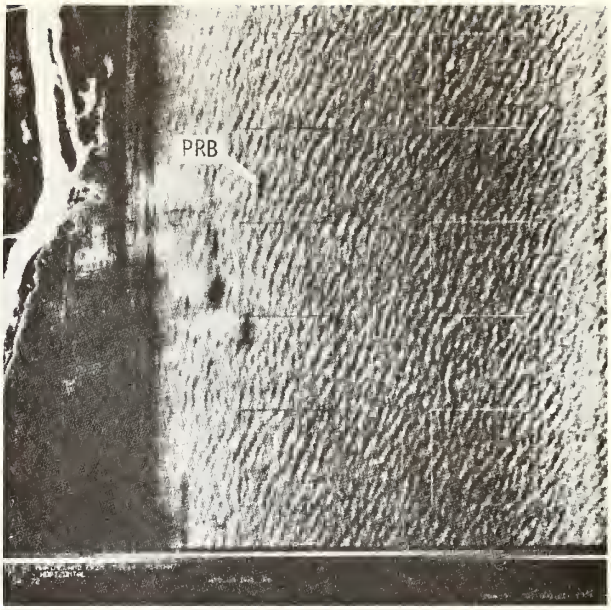

Fig. 10 Geometrically corrected radar imagery of ocean wave conditions on December 14, 1975, at Marineland.

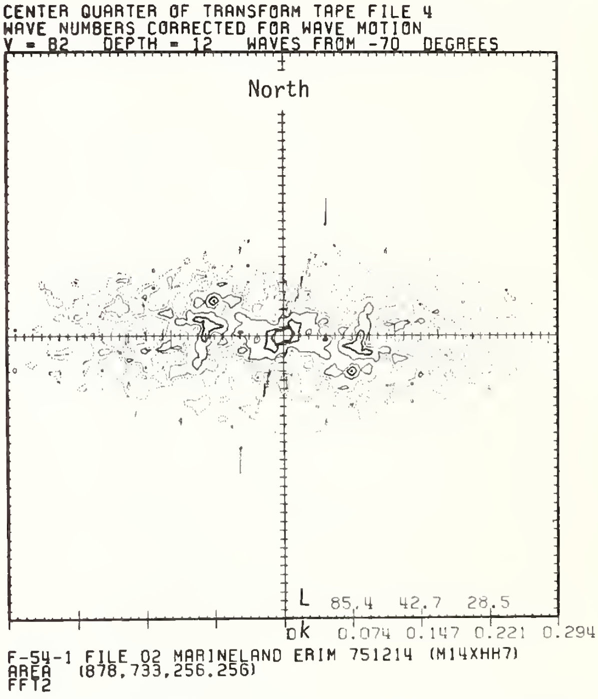

Fig. 11 Contour plot of E(k,θ) derived from X-band radar data at the location of the buoy in Fig. 10. Scales of L and k are in m and rad/m.

Because different algorithms were used to compute directions from the current meter data, the frequency bands do not match those of the other sensors. Results shown in the upper half of Fig. 12 indicate very good agreement for wave directions for all three measurements in the region 0.12<f<0.22 Hz. At the peak of the spectra the difference between radar and

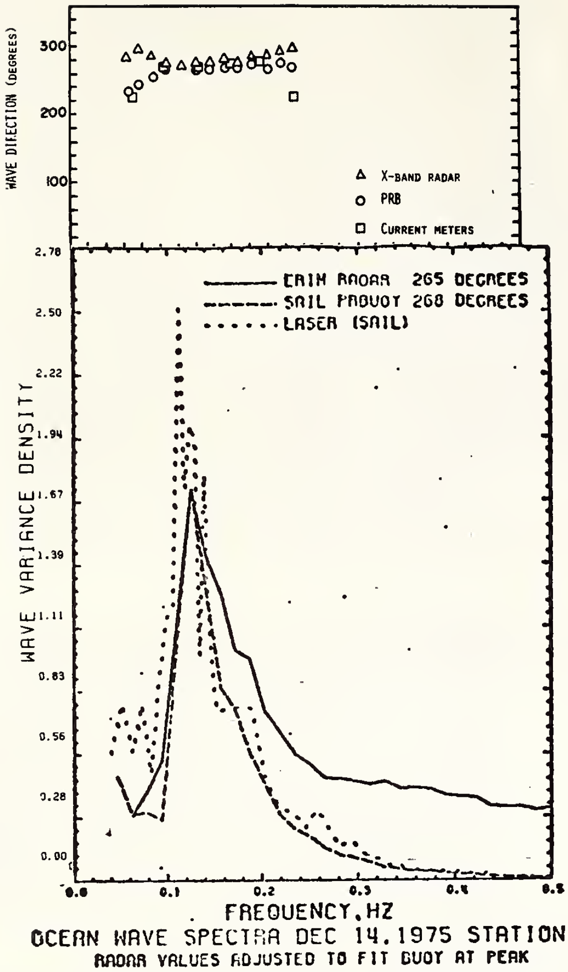

Fig. 12 Ocean wave spectra and wave direction computed for the area identified in Fig. 10 and 11. Energy density is in units of m²/Hz.

buoy measurements is 2°. In the current meter data, the peak frequency lies between $.107<f<.143$ with $270°<\alpha<271°$. This agrees to within 2° of the buoy data and within 1° of the wave directions measured with the SAR. Calculation of the weighted averages of wave directions over 3 frequency bands centered on the peak frequency (0.124 Hz) gave results of 273° for the radar. The equivalent averaged direction for the buoy was 266°.

Data are also shown from real aperture radars. For the CERC radar experiments, U2 aerial photographic missions were flown off the California coast in the area of San Diego, during the West Coast Experiment in March of 1977. Simultaneously, radar images of the waves were obtained with the CERC radar system (Fig. 14), located at Mission Beach. From data obtained on March 14 and 29, 1977, directions of long crested wave trains detectable on the radar image and the U2 photographs were measured manually (Table 2) referenced to the bearing of 275° from the NUC tower to the radar site. On both dates, two wave trains were detected with the radar, whose

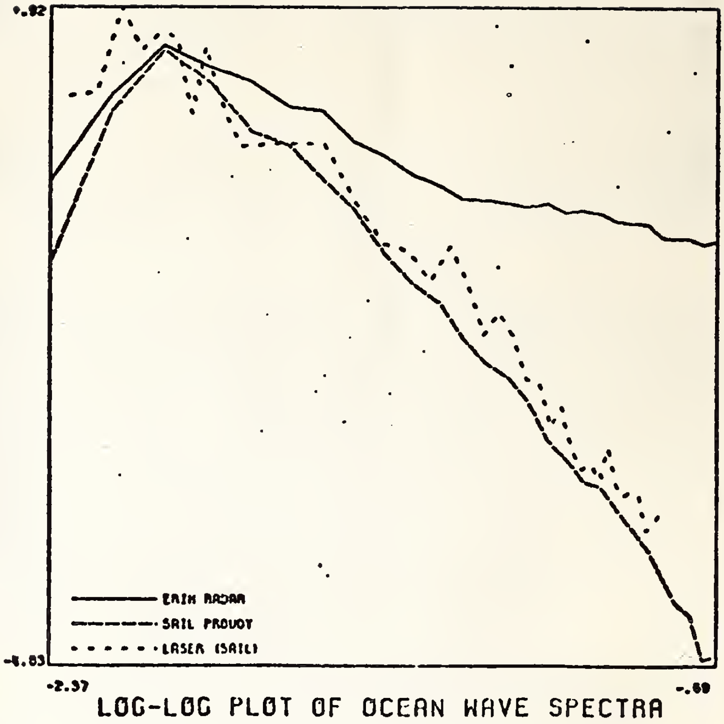

directions agree well with those obtained from U2 images. A third wave train, with short wavelength was seen in the aerial but not in the radar images. Its absence in the radar may have resulted from a misadjustment of the pulse width, so that the radar's resolution became too degraded to image the short waves. With proper adjustment, it is expected that the radar could image waves with lengths on the order of 30 m, as lengths of 35 m have already been measured with radar similar in resolution to the CERC system.

Table 1 Summary of wave direction computations (in degrees) at Marineland, Florida, December 14, 1975.

f	(1)	(2)	(3)	(4)
.063	235	288	283	-
.071	-	-	-	225
.078	242	296	296	-
.094	254	287	287	-
.107	-	-	-	270
.109	266	277	275	-
.125	268	270	270	-
.141	263	275	275	-
.143	-	-	-	271
.156	265	282	277	-
.172	267	285	280	-
.179	-	-	-	275
.188	267	281	275	-
.203	272	290	285	-
.219	266	289	287	-
.234	275	288	292	-
.250	269	295	296	224

(1) NOAA pitch-and-roll buoy
(2) ERIM X-band data shown in Fig. 10
(3) ERIM X-band data, with image elements of the ship having been removed
(4) CERC sea-sled based current measurements

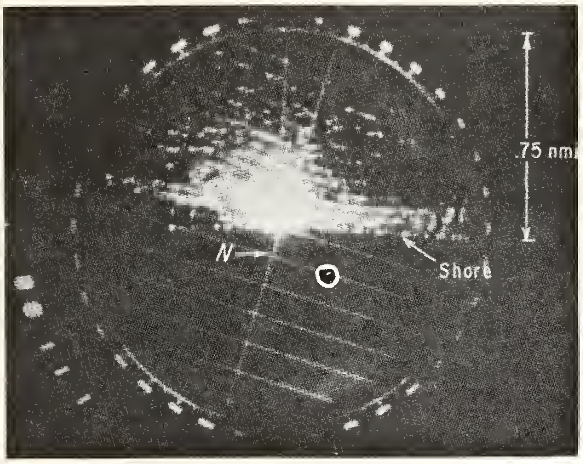

Fig. 14 Radar image of waves in the Mission Beach area, San Diego, California, obtained on March 29, 1977, with the CERC X-band radar. Radar range is 0.75 nautical mile.

Table 2 Comparison of wave directions measured with the shore radar to those observed on photos.

Date (1977)	Time	CERC RADAR (α)	CERC RADAR (L)	U2 AERIAL PHOTO (α)	U2 AERIAL PHOTO (L)
3/14	11:30	281°±4°	84±11m	284°±2°	long
		263°±4°	168±22m	264°±3°	longest
				316°±2°	short
3/29	11:00	284°±4°	132±21m	288°±2°	long
		257°±4°	168±22m	257°±2°	longest
				320°±2°	short

The NOAA Ka-band radar was flown in May 1978, near the coast of Puerto Rico. Fig. 15a and Fig. 15b are examples, respectively of deep ocean and coastal waves imaged with this system. The waves apparent in Fig. 15a have a wavelength of 110-130 m compared to the value of 130 m derived from a wave spectrum (Fig. 16), for which data were obtained with a laser profilometer operated simultaneously onboard the aircraft. The waves are propagating in the downwind direction.

6. Conclusions

As demonstrated in comparison of radar and in-situ data, radar imagery of the ocean surface can be used to measure wave direction. Hence, SEASAT-A SAR data should prove useful to studies of wave refraction, provided shortcomings in present knowledge about radar backscatter of ocean waves are recognized. This study shows that, the Bragg-Rice model appears to give good results for the incidence angles investigated. Dynamic models are still in the development stage, therefore, one can only conclude that investigations on the causes of Doppler effects will have to continue on a case-by-case basis and with assistance from adequate and properly calibrated in-situ sensors. The principal task in the geophysical evaluation of SEASAT-A SAR data,therefore,will have to include testing of both the scattering principles and the limits of imagibility in a wide range of wave and wind conditions.

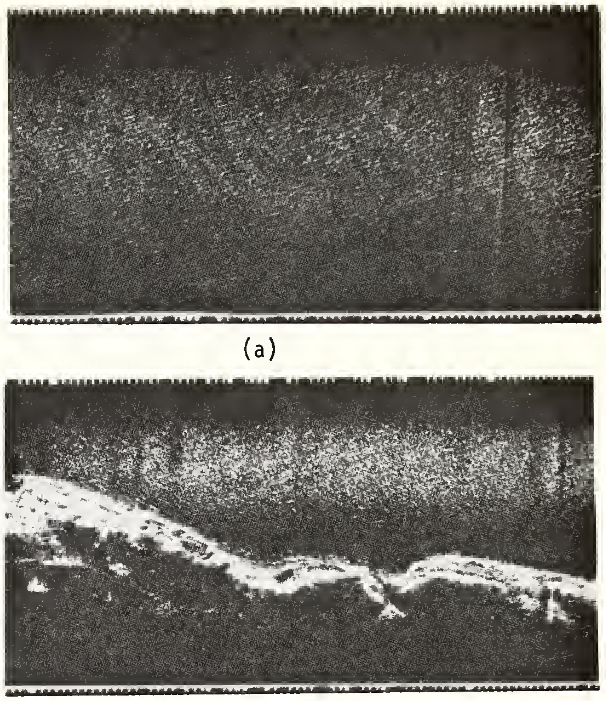
(a)

(b)

Fig. 15 Waves imaged (a) in deep water, (b) in coastal area near Puerto Rico with the NOAA Ka-band radar in May 1978.

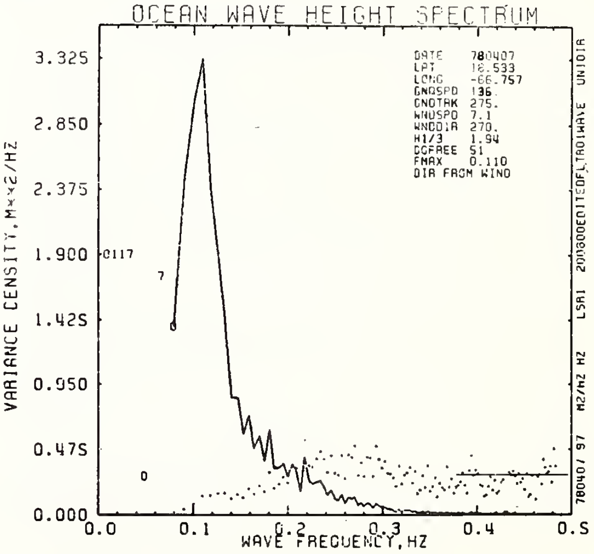

Fig. 16 One-dimensional wave spectra associated with the image of Fig. 15a. Dots represent the equilibrium range constant α, assuming an f^{-5} form of the spectrum

Acknowledgements

The ERIM contribution was the result of work performed under ONR contract Nooo14-76-C-1048 and NOAA/NESS grant No. 04-6-158-44078. The authors benefited from discussions with members of the SEASAT-A SAR Experiment Team.

References

Beckman, P. and A. Spizzichino, "The scattering of electromagnetic waves from rough surfaces," McMillan Co., New York, 1963.

Brown, W. E., Jr., C. Elachi, and T. W. Thompson, "Radar imaging of ocean surface patterns," Jour. of Geophys. Res., v. 81, 1976, pp 2657-2667.

Elachi, C., and J. R. Apel, "Internal wave observations made with an airborne synthetic aperture imaging radar," Geophys. Res. Letters, v. 3, 1976, pp. 647-650.

Ewing, J. A., "Some measurements of the directional wave spectrum," Jour. Mar. Res., v. 27, 1969, pp. 163-171.

Fontanel, A., "Experiences d'étude de l'état de la mer par radar latéral," Actes. Colloq., no. 5, CNEXO, 1978, (in press).

Guinard, N. W. and J. C. Daley, "An experimental study of a sea clutter model," Proc. IEEE, v. 58, 1978, pp. 543-550.

Jain, A., "Focusing effects in the synthetic aperture radar imaging of ocean waves," Jour. Appl. Phys., v. 15, 1978, pp. 323-333.

Long, M. W., "On the polarization and wavelength dependence of sea echo," IEEE Trans. on Ant. & Propag., v. AP-13, 1965, pp. 749-754.

Lowry, R. T., D. G. Goodenough, J. S. Zelenka, and R. A. Shuchman, "On the analysis of airborne synthetic aperture radar imagery of the ocean," Proc. 4th Canadian Symp. on Rem. Sensing, Quebec City, 1977, pp. 480-505.

Moskowitz, L. I., "The feasibility of ocean current mapping via synthetic aperture radar methods," Proc. Fall Conv., Amer. Soc. Photogrammetry, 1973, pp. 760-771.

Phillips, O. M., "The dynamics of the upper ocean," Cambridge Univ. Press, London, 1966.

Shemdin, O. H., J. E. Blue, and J. A. Dunne, "SEASAT-A surface truth program: Marineland test plan," Jet Propulsion Laboratory Rept. 622-6, 1975.

Shemdin, O. H., W. E. Brown, Jr., F. G. Staudhammer, R. Shuchman, R. Rawson, J. Zelenka, D. B. Ross, W. McLeish, and R. A. Berles, "Comparison of in-situ and remotely sensed ocean waves off Marineland, Florida," Boundary Layer Meteorology, v. 13, 1977, pp. 225-234.

Shuchman, R. A., and J. S. Zelenka, "Processing of ocean wave data from a synthetic aperture radar," Boundary Layer Meteorology, v. 13, 1977, pp. 181-192.

Skolnik, M. I., "Sea echo," Ch. 26 in M. I. Skolnik (ed.): Radar handbook, McGraw-Hill, New York, 1970.

Teleki, P. G., F. R. Musialowski and D. A. Prins, "Data acquisition methods for coastal currents," Proc. ASCE Conf. on Civil Eng. in the Oceans/III, 1975, pp. 1190-1210.

Trunk, G. V., "Non-Rayleigh sea clutter: properties and detection of targets," NRL Rept. 7986, 1976.

Weissman, D. E. and T. W. Thompson, "Detection and interpretation of ocean roughness variations across the Gulf Stream inferred from radar cross section observations," Proc. Oceans '77, 1977, pp. 14B/1-10.

Wright, J. W., "Backscattering from capillary waves with application to sea clutter," IEEE Trans. Ant. and Propag., v. AP-14, 1966, pp. 749-754.

Journal of Physical Oceanography 8, No. 4, 676-679.

Comparison of Finite-Element and Finite-Difference Schemes. Part I: One-Dimensional Gravity Wave Motion

W. C. THACKER

Sea-Air Interaction Laboratory, Atlantic Oceanographic and Meteorological Laboratories, NOAA, Miami, FL 33149

(Manuscript received 1 August 1977, in final form 27 March 1978)

ABSTRACT

The finite-element scheme requires more computational expense because it is time-implicit and because it requires a smaller time step than the finite-difference scheme. Simulations of normal mode oscillations reveal that for cases where the basin depth and the numerical grid are uniform, the finite-difference scheme is more accurate, but for cases where the depth or the grid varies, the finite-element scheme is more accurate.

1. Introduction

In recent years finite-element methods have begun to be used in calculations of fluid dynamics (see, e.g., Shen, 1977). These methods have the advantage over the conventional finite-difference methods when the calculations are complicated by the presence of irregular boundaries. Irregular-grid, finite-difference techniques (Thacker, 1977) are also well suited for calculations involving irregular boundaries and have the additional advantage of an explicit time step which avoids the computationally lengthy inversions of the finite-element equations. Natural questions to ask are what relationships might exist between the two methods and what advantages belong to each.

The example of one-dimensional oscillations such as seiche motions in canals provides the simplest possible framework for discussing these questions. It allows the point to be made quite clearly that there is a fundamental distinction between the two methods. The complications of two-dimensional calculations can obscure this fact. Because of the simplicity of the equations, it also allows the similarities of the two methods to be made apparent. In a companion paper (Part II) the methods are compared in the context of oscillations in circular basins where all of the complicating features of a two-dimensional calculation are present. When the results of the two parts of the comparison study are taken together, it becomes clearer which features of the two methods are intrinsic to their finite-element or finite-difference nature and which are dependent on the dimensionality of the problem.

A variety of numerical schemes can be used for both the finite-difference and finite-element calculations. The finite-difference scheme considered here involves simple differences for spatial derivatives and a leapfrog structure for time derivatives. In order that the finite-element scheme be as analogous to the finite-difference scheme as possible, it is based upon linear interpolation over the same spatial grid, and the same leapfrog structure is used to step forward in time.

Both numerical schemes produced excellent simulations of the lowest normal modes of oscillation. However, the finite-element scheme required significantly more computational expense because matrix inversions are required for each step forward in time and because the Courant stability condition restricts the size of the time step for the finite-element scheme to be smaller by a factor of $1/3^{1/2}$ than the time step for the finite-difference scheme. Dispersion analysis indicates that phase and group velocities are generally overestimated by the finite-element scheme and underestimated by the finite-difference scheme. Similar results were found for the two-dimensional comparison of Part II. The finite-difference scheme more accurately simulated normal mode oscillations for cases where both the depth and the grid were uniform, whereas the finite-element scheme yielded better results if the depth or the grid were not uniform. However (see Part II), the two-dimensional finite-element scheme was unstable for variable depth, and both two-dimensional schemes were unstable for a highly irregular grid.

2. The finite-difference and finite-element equations

One-dimensional waves in shallow canals are governed by the equations

$$\left.\begin{aligned} \frac{\partial U}{\partial t} &= -gD\frac{\partial H}{\partial x} \\ \frac{\partial H}{\partial t} &= -\frac{\partial U}{\partial x} \end{aligned}\right\}, \quad -L/2 \leqslant x \leqslant L/2, \tag{1}$$

so long as viscous, inertial and Coriolis forces can be ignored and so long as there are no variations across the canal. The dynamic variables U and H are the volume transport and the surface elevation, respectively; D is the stillwater depth and g the gravitational acceleration. If the ends of the canal are closed, these equations are supplemented by the boundary conditions, $U = 0$ at $x = -L/2$ and at $x = L/2$, where L is the length of the canal.

The corresponding finite-difference equations are

$$\left.\begin{aligned} &\left.\begin{aligned} U_i^{n+1/2} &= U_i^{n-1/2} - (\tau g D_i/\Delta_i) \\ &\qquad \times (H_{i+1}^n - H_{i-1}^n) \\ H_i^{n+1} &= H_i^n - (\tau/\Delta_i) \\ &\qquad \times (U_{i+1}^{n+1/2} - U_{i-1}^{n+1/2}) \end{aligned}\right\} \begin{gathered} i=2,\ldots, \\ N-1 \end{gathered} \\ &U_1^{n+1/2} = U_N^{n+1/2} = 0 \\ &H_1^{n+1} = H_1^n - (\tau/\Delta_1^+)(U_2^{n+1/2} - U_1^{n+1/2}) \\ &H_N^{n+1} = H_N^n - (\tau/\Delta_N^-)(U_N^{n+1/2} - U_{N-1}^{n+1/2}) \end{aligned}\right\}, \tag{2}$$

where τ is the time step, $t = n\tau$, and the grid spacings are $\Delta_i = x_{i+1} - x_{i-1}$, $\Delta_i^+ = x_{i+1} - x_i$ and $\Delta_i^- = x_i - x_{i-1}$, and N is the number of grid points. Note that the grid is not necessarily uniform. This is a one-dimensional version of an irregular grid finite-difference scheme (Thacker, 1977).

The corresponding finite-element equations are obtained by requiring that piecewise linear interpolating functions which approximate the solution be optimal. The approximating functions

$$\left.\begin{aligned} \tilde{U}(x,t) &= \sum_{i=1}^{N} U_i(t)\phi_i(x) \\ \tilde{H}(x,t) &= \sum_{i=1}^{N} H_i(t)\phi_i(x) \\ \tilde{D}(x) &= \sum_{i=1}^{N} D_i\phi_i(x) \end{aligned}\right\} \tag{3}$$

are expressed in terms of products of values at grid points and "hill" or "roof" functions, which decrease from unity at the grid point to zero at adjacent grid points and remain zero outside of that interval. The criterion for the approximation to be optimal is that the integrals of products of the residuals

$$R_1 = \partial\tilde{U}/\partial t + g\tilde{D}(\partial\tilde{H}/\partial x) \quad ,$$

and

$$R_2 = \partial\tilde{H}/\partial t + \partial\tilde{U}/\partial x \quad ,$$

with the hill functions must vanish. This is a Galerkin-type criterion. Other criteria could be used (see, e.g., Norrie and de Vries, 1973), but this is both simple and popular. For time-independent problems variational formulations can be used to obtain the same finite-element equations that are obtained from the Galerkin formulations, but the variational formulation is not well suited for time-dependent problems.

The finite-element equations which result from the integral constraints are similar in form to the finite-difference equations

$$\left.\begin{aligned} &\bar{U}_i^{n+1/2} \\ &\left.\begin{aligned} &= \bar{U}_i^{n-1/2} - (\tau g/3\Delta_i) \\ &\times [D_{i-1}(H_i^n - H_{i-1}^n) \\ &+ 2D_i(H_{i+1}^n - H_{i-1}^n) \\ &+ D_{i+1}(H_{i+1}^n - H_i^n)] \end{aligned}\right\} i=2,\ldots,N-1 \\ &\bar{H}_i^{n+1} = \bar{H}_i^n - (\tau/\Delta_i)(U_{i+1}^{n+1/2} - U_{i-1}^{n+1/2}) \\ &U_1^{n+1/2} = U_N^{n+1/2} = 0 \\ &\bar{H}_1^{n+1} = \bar{H}_1^n - (\tau/\Delta_1^+)(U_2^{n+1/2} - U_1^{n+1/2}) \\ &\bar{H}_N^{n+1} = \bar{H}_N^n - (\tau/\Delta_i^-)(U_N^{n+1/2} - U_{N-1}^{n+1/2}) \end{aligned}\right\}. \tag{4}$$

The overbar indicates a spatial average; if f represents U or H, then

$$\left.\begin{aligned} \bar{f}_i &= \tfrac{1}{3}[(\Delta_i^-/\Delta_i)f_{i-1} + 2f_i \\ &\qquad + (\Delta_i^+/\Delta_i)f_{i+1}],\ i = 2, \ldots, N-1 \\ \bar{f}_1 &= \tfrac{1}{3}(2f_1 + f_2) \\ \bar{f}_N &= \tfrac{1}{3}(f_{N-1} + 2f_N) \end{aligned}\right\}. \tag{5}$$

The principal difference between the two sets of equations is in the terms corresponding to time derivatives. For the finite-element equations, these terms involve averages of values at neighboring points. These averages are a result of the fact that the hill functions do not provide an orthogonal basis for the piecewise polynomial functions used in finite-element methods. The practical consequence of this is that the system of equations for the new values of the dynamic variables at each time step is coupled and must be solved. This is equivalent to inverting two $N \times N$ matrices each time step. On the other hand, the finite-difference equations are uncoupled (time-explicit), and the values of the dynamic variables can be determined entirely from the values for the previous time step.

3. Numerical stability and numerical dispersion

By assuming that the grid is uniform with $\Delta = x_{i+1} - x_{i-1}$ and that there are no boundaries nor depth variation, these two schemes can be analyzed for stability. The results of this analysis are that the schemes are unstable unless the time steps are sufficiently small and that the maximum

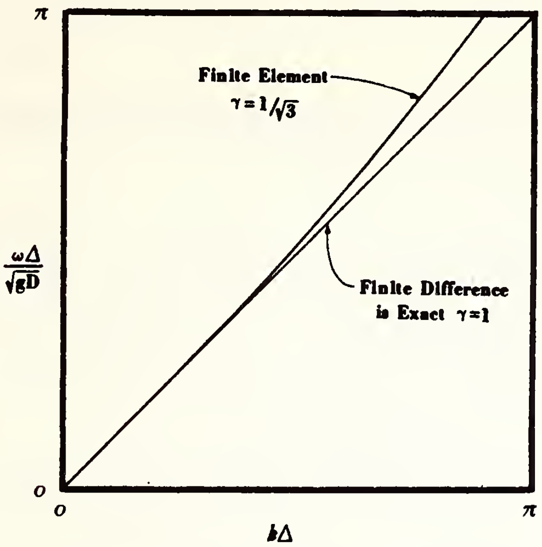

FIG. 1. Frequency as a function of wavenumber for the maximum allowable time steps for the finite-difference and finite-element schemes. The finite-element frequency coincides with the exact frequency for this case, but the finite-element frequency is overestimated. For low wavenumbers, the finite-element scheme is sufficiently accurate. Smaller time steps (see Fig. 2) cause the accuracy of the finite-difference scheme to decrease.

allowable time step for the finite-element scheme is smaller than that for the finite-difference scheme. The Courant number $\gamma = (gD)^{1/2}\,\tau/\Delta$, which is a dimensionless measure of the size of the time step, must be less than 1 for the finite-difference scheme and less than $1/3^{1/2}$ for the finite-element scheme. Numerical computations verified these stability criteria. The practical result is that, not only must the finite-element equations be inverted at each time step, but also more time steps by a factor $3^{1/2}$ are required for the finite-element scheme than for the finite-difference scheme.

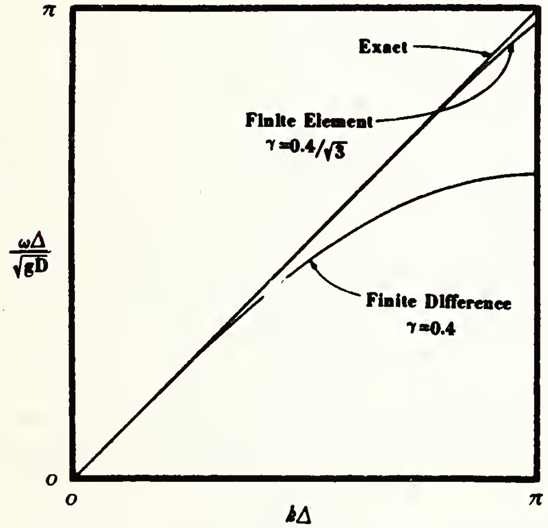

FIG. 2. Frequency as a function of wavenumber for time steps which are 40% less than their maximum allowable values. The finite-difference curve lies below the straight line corresponding to exact frequency dependence, while the finite-element curve lies imperceptibly above the straight line for low wavenumbers and below for high wavenumbers. The finite-element frequency is more accurate for this choice of time step than for the maximum allowable time step of Fig. 1.

Under similar assumptions, it is possible to obtain dispersion equations relating the frequencies and wavenumbers of the numerical solutions

$$\left.\begin{aligned}
&\text{Finite-difference:}\\
&\frac{\omega\Delta}{(gD)^{1/2}} = \frac{2}{\gamma}\sin^{-1}\left[\gamma \sin\frac{k\Delta}{2}\right]\\
&\text{Finite-element:}\\
&\frac{\omega\Delta}{(gD)^{1/2}} = \frac{2}{\gamma}\sin^{-1}\left[\frac{\gamma\sin(k\Delta/2)}{\frac{2}{3}+\frac{1}{3}\cos(k\Delta/2)}\right]\\
&\text{Exact:}\\
&\frac{\omega\Delta}{(gD)^{1/2}} = k\Delta
\end{aligned}\right\} \qquad (6)$$

These dispersion equations are illustrated in Figs. 1 and 2.

For the maximum value, $\gamma = 1$, the finite-difference scheme is exact. However, for the maximum value $\gamma = 1/3^{1/2}$, the finite-element scheme overestimates the phase and group velocities of the waves. This is illustrated in Fig. 1. Values of γ equal to 0.4 times the maximum values were used for the curves in Fig. 2. For this case the finite-element dispersion equation is more nearly exact, but overestimates the frequency of long waves and underestimates the frequency of short waves. The finite-difference dispersion equation underestimates the frequency of all waves. Thus the analysis indicates that for the finite-element scheme to begin to compare in accuracy with the finite-difference scheme, it must use a time step that is about 25% smaller. A similar result is found for the two-dimensional case in Part II.

4. Results of computations

Computations were made simulating the two lowest modes of oscillation for both uniform depth,

TABLE 1. Nondimensional frequencies $\omega L(gD_0)^{-1/2}$ for case of uniform depth using 11 grid points.

	Mode 1	Mode 2
Exact	1.5708	3.1416
Finite-difference	1.57	3.14
Finite-element	1.59	3.20

$D = D_0$, and parabolic depth, $D = D_0[1 - (2x/L)^2]$, profiles. Three grids were used; a uniform grid with 101 grid points and two with 11 grid points, one uniform and one irregular. The dynamic variables were initialized to agree with the analytic solutions at $t = 0$:

$$\left.\begin{array}{ll} \left.\begin{array}{ll} H(x) = \sin(\pi x/2); & \text{mode } 1 \\ H(x) = \cos(\pi x/2); & \text{mode } 2 \end{array}\right\} \text{uniform depth} \\ \left.\begin{array}{ll} H(x) = x; & \text{mode } 1 \\ H(x) = x^2 - \tfrac{1}{3}; & \text{mode } 2 \end{array}\right\} \text{parabolic depth} \end{array}\right\} \quad (7)$$

with $U(x) = 0$ for all cases. The first nonzero values for the transport were obtained by a forward half-step in time. The ensuing values of H and U were simulated using the discrete equations (2) and (3).

For both the finite-difference equations and the finite-element equations, the simulations using the finer uniform grid were excellent. Neither seemed to offer an advantage in accuracy.

Results obtained using the coarser uniform grid were more interesting. At each grid point the frequencies of the oscillations were estimated from the number of times the sign of the surface elevation changed in 100 cycles. For the case of uniform depth, the finite-difference solution was more accurate. These results are given in Table 1. The finite-element scheme overestimated the frequencies. On the other hand, for the case of parabolic depth variation, the finite-difference scheme produced some variation in the estimates of frequency from grid point to grid point, indicated by the tildes in Table 2. There was no variation in the estimates obtained from the finite-element simulations except for that which should be expected in the vicinity of the nodes of the normal modes, but the frequency of mode 2 was overestimated.

In order to determine if the better results of the finite-element scheme for the variable depth cases were due to the depth-averaged form for approximating $gD\partial H/\partial x$, the finite-difference scheme was modified to incorporate this form. The variation in the frequency estimates was eliminated for mode 1, but not for mode 2. These results suggest that only part of the advantage of the finite-element scheme for variable depth cases can be attributed to this depth-averaged form.

TABLE 2. As in Table 1 except for case of parabolic depth variation

	Mode 1	Mode 2
Exact	1.4142	2.4495
Finite-difference	~1.4	~2.4
Finite-element	1.41	2.48

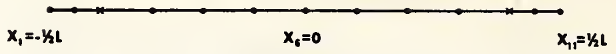

FIG. 3. The irregular grid, where dots indicate the positions of the grid points and crosses indicate positions from which the points next to the ends have been moved.

Grid irregularities have resulted in instabilities for two-dimensional calculations (Thacker, 1977). In order to test if similar instabilities occur in one-dimensional calculations, the uniform grid was modified by moving the two grid points next to the boundaries closer to the boundaries by half the previous distance. This is illustrated in Fig. 3 for the case of 11 grid points.

The finite-difference equations yielded a variation in frequency estimates after 100 cycles of simulation for the second uniform depth mode. This variation was similar to that encountered in simulations involving variable depth. After 10 000 cycles, the surface elevation no longer resembled the sinusoid, but the amplitudes did not grow. However, the finite-element simulations yielded good, though slightly high, frequency estimates and preserved the sinusoidal shape even after 10 000 cycles.

5. Summary

The finite-element and finite-difference equations are quite similar, the principal difference being that those terms of the finite-element equations corresponding to time derivatives involve spatial averages which do not appear in the corresponding terms of the finite-difference equations. These averages cause the finite-element scheme to be computationally more expensive for two reasons. The first is that they cause the equations to be coupled, and computation must be devoted to inverting the equations at each time step. The second is that they necessitate a smaller time step than that allowable for the finite-difference equations. Both features of increased computational expense are also present in the two-dimensional calculations of Part II.

Simulations were made of normal mode oscillations for uniform and parabolic depth profiles using both uniform and non-uniform numerical grids. The results were that the finite-difference scheme was more accurate for uniform depth and uniform grid cases, while the finite-element scheme was more accurate for cases of varying depth or varying grid.

REFERENCES

Norrie, Douglas H., and Gerard de Vries, 1973: *The Finite Element Method*. Academic Press, 322 pp.

Shen, Shan-fu, 1977: Finite-element method in fluid mechanics. *Annual Reviews of Fluid Mechanics*, Vol. 9, Annual Reviews, Inc., 421–445.

Thacker, W. C., 1977: Irregular grid finite-difference techniques: Simulations of oscillations in shallow circular basins. *J. Phys. Oceanogr.*, **7**, 284–292.

Journal of Physical Oceanography 8, No. 4, 680-689.

Comparison of Finite-Element and Finite-Difference Schemes. Part II: Two-Dimensional Gravity Wave Motion

W. C. Thacker

Sea-Air Interaction Laboratory, Atlantic Oceanographic and Meteorological Laboratories, NOAA, Miami, FL 33149

(Manuscript received 1 August 1977, in final form 27 March 1978)

ABSTRACT

Irregular grid finite-difference techniques lead to equations similar to those obtained using finite-element techniques. The simpler finite-difference equations offer the advantage of greater computational economy. The time-implicit finite-element equations must be inverted at each time step, and the maximum size of the time step is only half that which can be used with the finite-difference equations. Both techniques result in instabilities when used with highly irregular grids, and the finite-element equations are also unstable if the basin depth is variable. Although the finite-element results are better when compared with finite-difference results from the same grid, comparable finite-difference results can be obtained using a finer grid at less computational expense.

1. Introduction

Calculation of nearshore circulation and water surface elevation as required for forecasting storm surges in bays and estuaries is made difficult by the curvature of the shoreline. Finite-element techniques (Taylor and Davis, 1975; King *et al.*, 1975; Wang and Connor, 1975; Shen, 1977) are attractive for such calculations because they can be used in conjunction with an irregular computational grid that allows for better resolution of the shoreline than does a conventional rectangular grid. Irregular grid finite-difference techniques (Thacker, 1977a) offer the same possibility of resolving the coastline and an additional advantage of computational economy due to the possibility of an explicit time step. This paper compares the two types of techniques.

This comparison focuses on two numerical schemes, one finite-element and one finite-difference, for simulating oscillations in shallow circular basins. The well-known behavior of these oscillations (Lamb, 1945; Thacker, 1977a) provides a standard for judging the accuracy of the simulations. Both schemes incorporate the same computational grids with the volume transport and surface elevation calculated at each grid point and the same leapfrog time structure with the transport and elevation calculated at alternate time levels. The two schemes are similar in that the terms in each, which correspond to spatial derivatives, are the same, provided the basin depth does not vary. The principal difference is in the terms corresponding to temporal derivatives, which for the finite-element scheme involve spatial averages that necessitate an implicit time step.

2. Computational schemes

Oscillations in shallow circular basins are governed by the equations

$$\left.\begin{aligned} \frac{\partial U}{\partial t} &= -gD\frac{\partial H}{\partial x} + fV \\ \frac{\partial V}{\partial t} &= -gD\frac{\partial H}{\partial y} - fU \\ \frac{\partial H}{\partial t} &= -\left(\frac{\partial U}{\partial x} + \frac{\partial V}{\partial y}\right) \end{aligned}\right\}, \quad x^2 + y^2 \leq R^2, \qquad (1)$$

together with the boundary condition

$$U\cos\theta + V\sin\theta = 0, \quad x^2 + y^2 = R^2, \qquad (2)$$

where U and V are the x and y components of the volume transport per unit width, H is the surface elevation, D and R are the depth and radius of the basin, g the gravitational acceleration, f the Coriolis parameter, $\cos\theta = x/R$ and $\sin\theta = y/R$.

The object of both the finite-difference and finite-element methods is to approximate the solutions of these equations at a manageable number of points, in this case points on the grids shown in Figs. 1–3. In the finite-element method the approximate solutions are assumed to vary linearly over each of the triangular grid elements, and the equations are obtained by requiring that the approximations be optimal throughout the basin. In the finite-difference method the nature of the approximation within the triangular elements is left unspecified and the equations are obtained from (1) by replacing the spatial derivatives by approximations based on the values of the variables at adjacent grid points.

Piecewise linear functions can be written in terms of their values at grid points with the aid of "hill" or "roof" functions $h_i(x,y)$ which have a value of unity at the ith grid point and decrease linearly to zero over each of the triangular elements that surround that point and remain zero outside of those elements. The piecewise linear approximating functions for the variables U, V, H and D are

$$\left.\begin{aligned} \tilde{U} &= \sum_{i=1}^{I} U_i h_i \\ \tilde{V} &= \sum_{i=1}^{I} V_i h_i \\ \tilde{H} &= \sum_{i=1}^{I} H_i h_i \\ \tilde{D} &= \sum_{i=1}^{I} D_i h_i \end{aligned}\right\} \quad (3)$$

Since these functions should approximate the solutions to (1), the residuals

$$\left.\begin{aligned} R_1 &= \frac{\partial \tilde{U}}{\partial t} + g\tilde{D}\frac{\partial \tilde{H}}{\partial x} - f\tilde{V} \\ R_2 &= \frac{\partial \tilde{V}}{\partial t} + g\tilde{D}\frac{\partial \tilde{H}}{\partial y} + f\tilde{U} \\ R_3 &= \frac{\partial \tilde{H}}{\partial t} + \frac{\partial \tilde{U}}{\partial x} + \frac{\partial \tilde{V}}{\partial y} \end{aligned}\right\} \quad (4)$$

should be small. The criterion used here for judging the residuals to be small and the approximating functions to be optimal throughout the basin is that the integrals of the products of each of the residuals with each of the hill functions should vanish, i.e.,

$$\int R_j h_i dxdy = 0, \quad j = 1, 2, 3, \quad i = 1, \ldots, I. \quad (5)$$

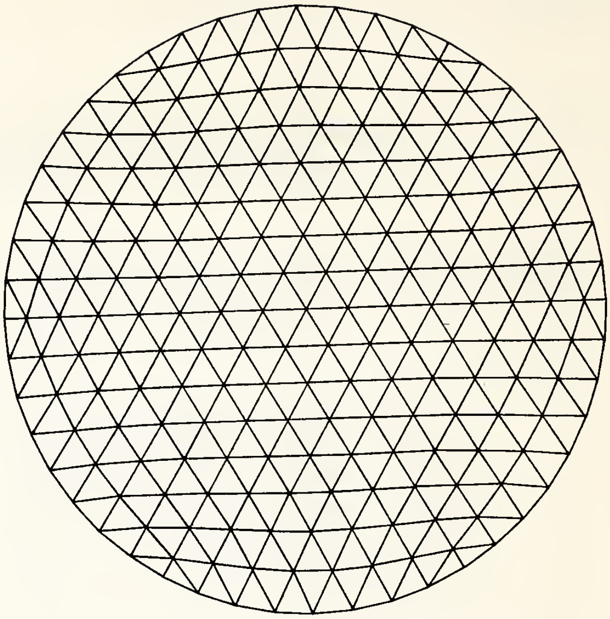

FIG. 2. Grid 2. Computations on this grid were more accurate but two orders of magnitude more expensive for the finite-element scheme than for the finite-difference scheme.

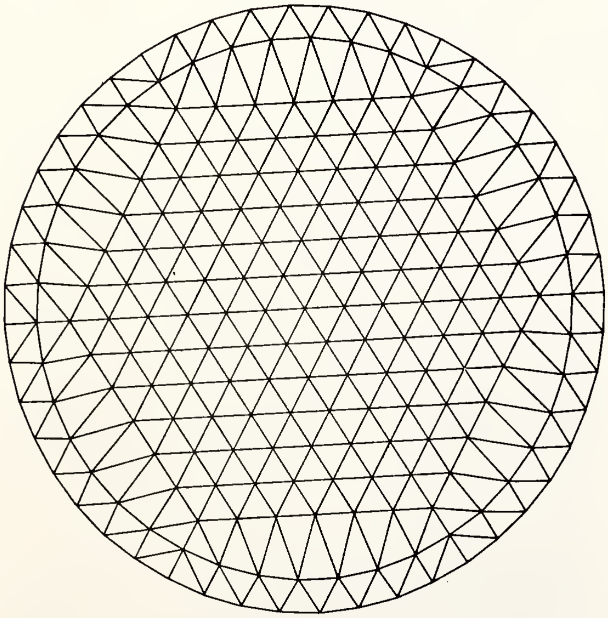

FIG. 1. Grid 1. This grid is much more irregular than the grids shown in Figs. 2 and 3. Computations on this grid were unstable for both schemes.

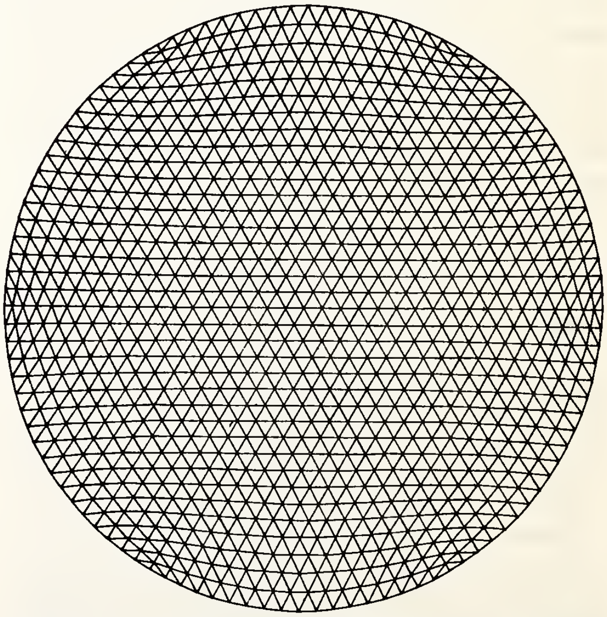

FIG. 3. Grid 3. Computations on this grid with the finite-difference scheme were comparable in accuracy to and less expensive than corresponding computations with the finite-element scheme on grid 2.

These integral conditions lead to the finite-element equations.

The evaluation of the integrals involved in (5) is straightforward. Since each of the residual functions can be expressed as sums of terms involving hill functions by using Eqs. (3) and (4), these integrals can be expressed in terms of integrals of products of hill functions, which in turn can be expressed in terms of integrals over the triangular elements of the form

$$\int \phi_i^l \phi_j^m \phi_k^n dxdy = 2A \frac{l!m!n!}{(l+m+n+2)!}, \qquad (6)$$

where l, m and n are exponents that are determined by the number of hill functions in the product associated with vertices of the triangular elements, i, j and k, respectively, where A is the area of the triangle, and where ϕ_i is the facet of the hill function decreasing from unity at point i to zero at points j and k (i, j, k cyclic).

After the integrals are evaluated, Eqs. (5) can be written in the form

$$\left.\begin{aligned}
\frac{d\bar{U}_i}{dt} &= -g\overline{\left(D\frac{\partial H}{\partial x}\right)}_i + f\bar{V}_i \\
\frac{d\bar{V}_i}{dt} &= -g\overline{\left(D\frac{\partial H}{\partial y}\right)}_i - f\bar{U}_i \\
\frac{d\bar{H}_i}{dt} &= -\left[\left(\frac{\overline{\partial U}}{\partial x}\right)_i + \left(\frac{\overline{\partial V}}{\partial y}\right)_i\right]
\end{aligned}\right\}, \quad i = 1, \ldots, I, \qquad (7)$$

where the overbar indicates that the quantities are averages calculated from values at grid points surrounding the point i. Formulas for these average quantities are given in Appendix A.

At this stage it is useful to compare Eq. (7) with those obtained from (1) by replacing the spatial derivatives with approximations based on values at adjacent grid points (Thacker, 1977a):

$$\left.\begin{aligned}
\frac{dU_i}{dt} &= -gD_i\left(\frac{\overline{\partial H}}{\partial x}\right)_i + fV_i \\
\frac{dV_i}{dt} &= -gD_i\left(\frac{\overline{\partial H}}{\partial y}\right)_i - fU_i \\
\frac{dH_i}{dt} &= -\left[\left(\frac{\overline{\partial U}}{\partial x}\right)_i + \left(\frac{\overline{\partial V}}{\partial y}\right)_i\right]
\end{aligned}\right\}, \quad i = 1, \ldots, I. \qquad (8)$$

The principal difference in these two sets of equations is that the terms in (8) which do not correspond to spatial derivatives involve only values at the ith grid point and do not involve averages of values at neighboring points. The terms corresponding to the divergence of the transport are the same in both (7) and (8), and so long as the depth is uniform, the terms corresponding to gradients of the surface elevation are also the same (see Appendix A).

Eqs. (7) and (8) are two steps removed from the final forms of the finite-element and finite-difference equations. The first step is to incorporate the boundary conditions

$$U_i \cos\theta_i + V_i \sin\theta_i = 0, \quad i = 1, \ldots, B, \qquad (9)$$

into those equations of (7) and (8) corresponding to the boundary points. This is done by altering the boundary momentum equations so that (9) is satisfied and flow parallel to the boundary is unaltered:

$$\left.\begin{aligned}
&\frac{d}{dt}(U_i + \sin^2\theta_i\bar{\bar{U}}_i - \sin\theta_i\cos\theta_i\bar{\bar{V}}_i) \\
&\quad = \sin^2\theta_i\left[-2g\overline{\left(D\frac{\partial H}{\partial x}\right)}_i + f\bar{\bar{V}}_i\right] \\
&\qquad - \sin\theta_i\cos\theta_i\left[-2g\right. \\
&\qquad\qquad \left.\times\overline{\left(D\frac{\partial H}{\partial y}\right)}_i - f\bar{\bar{U}}_i\right] \\
&\frac{d}{dt}(V_i + \cos^2\theta_i\bar{\bar{V}}_i - \sin\theta_i\cos\theta_i\bar{\bar{U}}_i) \\
&\quad = \cos^2\theta_i\left[-2g\overline{\left(D\frac{\partial H}{\partial y}\right)}_i - f\bar{\bar{U}}_i\right] \\
&\qquad - \sin\theta_i\cos\theta_i\left[-2g\right. \\
&\qquad\qquad \left.\times\overline{\left(D\frac{\partial H}{\partial x}\right)}_i + f\bar{\bar{V}}_i\right]
\end{aligned}\right\} \quad \begin{aligned} i &= 1, \\ &\ldots, B \end{aligned} \qquad (7')$$

$$\left.\begin{aligned}
\frac{dU_i}{dt} &= -gD_i\left[\sin^2\theta_i\left(\frac{\overline{\partial H}}{\partial x}\right)_i\right. \\
&\qquad \left.- \sin\theta_i\cos\theta_i\left(\frac{\overline{\partial H}}{\partial y}\right)_i\right] \\
\frac{dV_i}{dt} &= -gD_i\left[\cos^2\theta_i\left(\frac{\overline{\partial H}}{\partial y}\right)_i\right. \\
&\qquad \left.- \sin\theta_i\cos\theta_i\left(\frac{\overline{\partial H}}{\partial x}\right)_i\right]
\end{aligned}\right\}, \quad \begin{aligned} i &= 1, \\ &\ldots, B. \end{aligned} \qquad (8')$$

The double overbars in (7′) indicate the contribution to the average quantities from values at neighboring points (see Appendix A). The Coriolis parameter does not appear in (8′), but it does appear in (7′) in conjunction with average quantities involving interior points.

The final step in obtaining the finite-element and finite-difference equations is to approximate the continuous evolution in time with a sequence of discrete time steps. It is possible to use the finite-element method for temporal variation, but this is generally avoided because it leads to temporal averages, analogous to the spatial averages of Appendix A, which complicate the resulting equations. Instead, finite-differences are used to approximate the time derivatives. Here a leapfrog scheme is used, with the surface elevation calculated at time levels $t = n\tau$, and the transports at intermediate time levels $t = (n + ½)\tau$, where $n = 1, 2, \ldots$, and τ is the time step parameter. For stability, terms involving the Coriolis parameter are calculated at the advanced time level, even though this introduces a small amount of numerical dissipation. The neutrally stable average of Coriolis terms corresponding to advanced and previous time steps gives equally good results.

Finite-element equations

$$\left.\begin{aligned}
&\left.\begin{aligned}
\frac{1}{\tau}(\bar{U}_i^{n+1/2} - \bar{U}_i^{n-1/2}) &= -g\left(\overline{D\frac{\partial H}{\partial x}}\right)_i^n + f\bar{V}_i^{n+1/2}\\
\frac{1}{\tau}(\bar{V}_i^{n+1/2} - \bar{V}_i^{n-1/2}) &= -g\left(\overline{D\frac{\partial H}{\partial y}}\right)_i^n - f\bar{U}_i^{n+1/2}
\end{aligned}\right\},\quad i = B+1, \ldots, I\\
&\left.\begin{aligned}
&\frac{1}{\tau}[(U_i + \sin^2\theta_i\bar{U}_i - \sin\theta_i\cos\theta_i\bar{V}_i)^{n+1/2} - (U_i + \sin^2\theta_i\bar{U}_i - \sin\theta_i\cos\theta_i\bar{V}_i)^{n-1/2}]\\
&\quad = \sin^2\theta_i\left[-2g\left(\overline{D\frac{\partial H}{\partial x}}\right)_i^n + f\bar{V}_i^{n+1/2}\right] - \sin\theta_i\cos\theta_i\left[-2g\left(\overline{D\frac{\partial H}{\partial y}}\right)_i^n - f\bar{U}_i^{n+1/2}\right]\\
&\frac{1}{\tau}[(V_i + \cos^2\theta_i\bar{V}_i - \sin\theta_i\cos\theta_i\bar{U}_i)^{n+1/2} - (V_i + \cos^2\theta_i\bar{V}_i - \sin\theta_i\cos\theta_i\bar{U}_i)^{n-1/2}]\\
&\quad = \cos^2\theta_i\left[-2g\left(\overline{D\frac{\partial H}{\partial y}}\right)_i^n - f\bar{U}_i^{n+1/2}\right] - \sin\theta_i\cos\theta_i\left[-2g\left(\overline{D\frac{\partial H}{\partial x}}\right)_i^n + f\bar{V}_i^{n+1/2}\right]
\end{aligned}\right\}\quad i = 1, \ldots, B\\
&\frac{1}{\tau}(\bar{H}_i^{n+1} - \bar{H}_i^n) = -\left[\left(\frac{\overline{\partial U}}{\partial x}\right)_i + \left(\frac{\overline{\partial V}}{\partial y}\right)_i\right]^{n+1/2},\quad i = 1, \ldots, I
\end{aligned}\right\}\cdot \qquad (10)$$

Finite-difference equations

$$\left.\begin{aligned}
&\left.\begin{aligned}
\frac{1}{\tau}(U_i^{n+1/2} - U_i^{n-1/2}) &= -gD_i\left(\frac{\overline{\partial H}}{\partial x}\right)_i^n + fV_i^{n+1/2}\\
\frac{1}{\tau}(V_i^{n+1/2} - V_i^{n-1/2}) &= -gD_i\left(\frac{\overline{\partial H}}{\partial y}\right)_i^n - fU_i^{n+1/2}
\end{aligned}\right\},\quad i = B+1, \ldots, I\\
&\left.\begin{aligned}
\frac{1}{\tau}(U_i^{n+1/2} - U_i^{n-1/2}) &= -gD_i\left[\sin^2\theta_i\left(\frac{\overline{\partial H}}{\partial x}\right)_i^n - \sin\theta_i\cos\theta_i\left(\frac{\overline{\partial H}}{\partial y}\right)_i^n\right]\\
\frac{1}{\tau}(V_i^{n+1/2} - V_i^{n-1/2}) &= -gD_i\left[\cos^2\theta_i\left(\frac{\overline{\partial H}}{\partial y}\right)_i^n - \sin\theta_i\cos\theta_i\left(\frac{\overline{\partial H}}{\partial x}\right)_i^n\right]
\end{aligned}\right\},\quad i = 1, \ldots, B\\
&\frac{1}{\tau}(H_i^{n+1} - H_i^n) = -\left[\left(\frac{\overline{\partial U}}{\partial x}\right)_i + \left(\frac{\overline{\partial V}}{\partial y}\right)_i\right]^{n+1/2},\quad i = 1, \ldots, I
\end{aligned}\right\}\cdot \qquad (11)$$

The finite-difference equations might appear to be implicit since the Coriolis terms, which are evaluated at the advanced time level, cause the interior momentum equations to be coupled. However, they are only coupled in pairs and through variables evaluated at the same grid point, so they can be rewritten in explicit form

$$\left.\begin{aligned}
U_i^{n+1/2} &= f_1\left[U_i^{n-1/2} - gD_i\left(\frac{\overline{\partial H}}{\partial x}\right)_i^n\tau\right] + f_2\left[V_i^{n-1/2} - gD_i\left(\frac{\overline{\partial H}}{\partial y}\right)_i^n\tau\right]\\
V_i^{n+1/2} &= -f_2\left[U_i^{n-1/2} - gD_i\left(\frac{\overline{\partial H}}{\partial x}\right)_i^n\tau\right] + f_1\left[V_i^{n-1/2} - gD_i\left(\frac{\overline{\partial H}}{\partial y}\right)_i^n\tau\right]
\end{aligned}\right\} i = B+1, \ldots, I, \qquad (11')$$

where $f_1 = (1 + f^2\tau^2)^{-1}$ and $f_2 = f_1 f\tau$.

On the other hand, the finite-element equations are irrevocably implicit. Not just the interior momentum equations but all of Eqs. (10) are coupled through the spatial averages. Since each equation involves variables corresponding to several neighboring grid points, the system of equations must be solved simultaneously in order to advance one time step. A Gauss-Seidel type iterative technique (Appendix B) was used to solve these equations. Perhaps more efficient techniques could be found, but the one used converged in approximately 10 iterations, which should be comparable in computational expense with direct schemes when the number of grid points is large. Because this technique is independent of the manner in which the grid points are indexed, it is easily adaptable to other situations. In any case, approximately an order of magnitude more computational expense is required to advance a single time step for the finite-element equations than for the finite-difference equations. As will be shown in Section 3, more time steps are required for finite-element simulations than for the corresponding finite-difference simulations, increasing the computational expense by at least another factor of 2.

It should also be noted that the presence of the spatial averages in the finite-element calculations requires either additional computer storage for saving the coefficients involved in calculating these averages (see Appendix A) or additional computer time for reevaluating these coefficients each time they are used. Both alternatives cause additional computational expense over that of the finite-difference scheme.

3. Numerical dispersion and stability

If the computational grid is uniform and if the depth does not vary, then it is possible to analyze the distortion of wave motion for the computational schemes. This distortion, which is due to the finite sizes of the grid spacing and the time step, can be seen by comparing the dispersion equations for the finite-element and finite-difference schemes with the exact dispersion equation. For the case $f = 0$, these equations are

$$\left.\begin{aligned}
&\text{Finite-element:}\\
&\frac{\omega\Delta}{(gD)^{1/2}} = \pm\frac{2}{\gamma}\sin^{-1}\left[\frac{\gamma}{C}(A^2+B^2)^{1/2}\right]\\
&\text{Finite-difference:}\\
&\frac{\omega\Delta}{(gD)^{1/2}} = \pm\frac{2}{\gamma}\sin^{-1}[\gamma(A^2+B^2)^{1/2}]\\
&\text{Exact:}\\
&\frac{\omega\Delta}{(gD)^{1/2}} = \pm[(k\Delta)^2+(l\Delta)^2]^{1/2}
\end{aligned}\right\}, \quad (12)$$

where ω is the frequency of the wave and k and l are components of the wave vector in directions parallel and perpendicular, respectively, to a row of grid points. The quantities A and B result from terms corresponding to spatial derivatives, C results from the spatial averages that cause the finite-element scheme to be implicit, and γ is the Courant number. They depend on k, l, Δ and τ as follows:

$$\left.\begin{aligned}
A &= \sin(k\Delta/2)[\tfrac{2}{3}\cos(k\Delta/2)\\
&\qquad + \tfrac{1}{3}\cos(3^{1/2}l\Delta/2)]\\
B &= 3^{-1/2}\sin(3^{1/2}l\Delta/2)\cos(k\Delta/2)\\
C &= \tfrac{1}{3}[1+\cos^2(k\Delta/2)\\
&\qquad + \cos(k\Delta/2)\cos(3^{1/2}l\Delta/2)]\\
\gamma &= (gD)^{1/2}\tau/\Delta
\end{aligned}\right\}. \quad (13)$$

The factors of Δ are introduced into the exact dispersion equation so that the wave vector components and the frequency appear in the same nondimensional combinations as in the other dispersion equations; the exact frequency does not depend on the sizes of Δ or τ.

If γ is not sufficiently small, then the magnitudes of the arguments of the inverse sine functions can be greater than unity. This would require that ω be complex and corresponds to numerical instability. For stability, $\gamma < 0.90288$ for the finite-element scheme and $\gamma < 1.70437$ for the finite-difference scheme. Thus, the maximum allowable time step for the finite-difference scheme is almost twice that for the finite-element scheme.

In the limit $k\Delta \ll 1$, $l\Delta \ll 1$ and $\omega\Delta/(gD)^{1/2} \ll 1$, and for γ less than the stability limit, the dispersion equations for both numerical schemes are good approximations to the exact dispersion equation. However, for wavelengths $<4\Delta$, the numerical schemes no longer provide sufficient resolution and the waves are distorted. This can be seen by comparing the contour plots of frequency in Figs. 4–7. For the waves which are adequately resolved, the finite-element scheme overestimates the frequency and the finite-difference scheme underestimates the frequency. If the maximum time step is used for each scheme (Figs. 5 and 6), the finite-difference scheme gives the better approximation to the frequencies of the well-resolved waves. However, reducing the time step improves the finite-element frequency approximations and worsens the finite-difference frequency approximations. Fig. 7 shows the finite-element frequency contours for $\tau = \tau_{\max}/5$. For this case, the accuracy is somewhat better than for the finite-difference scheme with maximum time step, but the time step for the finite-difference scheme is a factor 10 larger. Fig. 8 is included to indicate the frequency contours of a simple centered difference scheme on a square grid

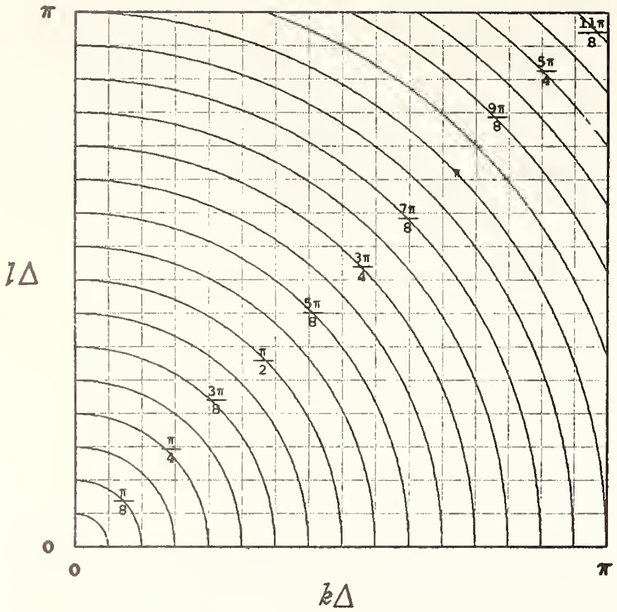

FIG. 4. Exact frequency contours. The curves are contours of $\omega\Delta/(gD)^{1/2}$ for levels equally spaced at intervals of $\pi/16$. The background grid is also equally spaced at intervals of $\pi/16$. The same contour levels and background grid are used in Figs. 5–8.

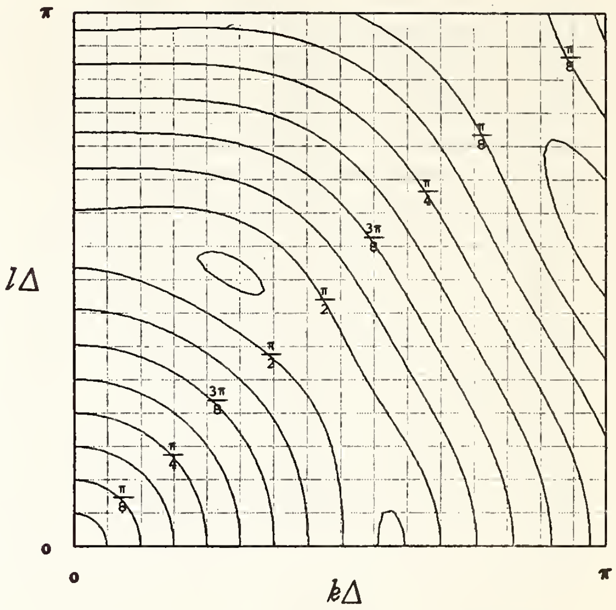

FIG. 6. Finite-difference frequency contours for maximum time step. Frequencies are well approximated for waves larger than four grid spaces. The frequencies are low, but closer to the exact frequencies than those shown in Fig. 5.

with the same grid spacing as for the triangular grids.

4. Computational instability

Instability associated with grid irregularity was observed when computations were performed with the finite-difference scheme using the grid shown in Fig. 1 but not when the grids shown in Figs. 2 and 3 were used. Instability was also observed when these computations were repeated with the finite-element scheme using the irregular grid. However, contrary to a preliminary report (Thacker, 1977b), the finite-element instability only manifests itself when the Coriolis terms were present; when $f = 0$ computations were stable for several hundred

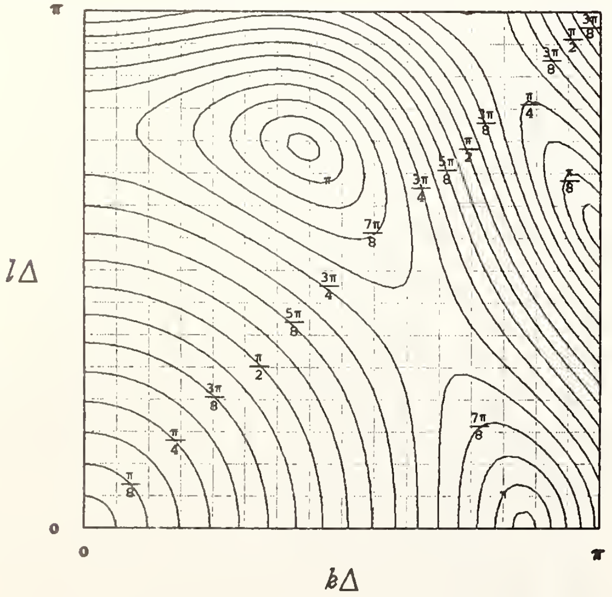

FIG. 5. Finite-element frequency contours for maximum time step. For $k\Delta$ and $l\Delta$ less than $\pi/2$, corresponding to waves longer than four grid spaces, the exact frequency contours are well approximated, although the frequency values are high.

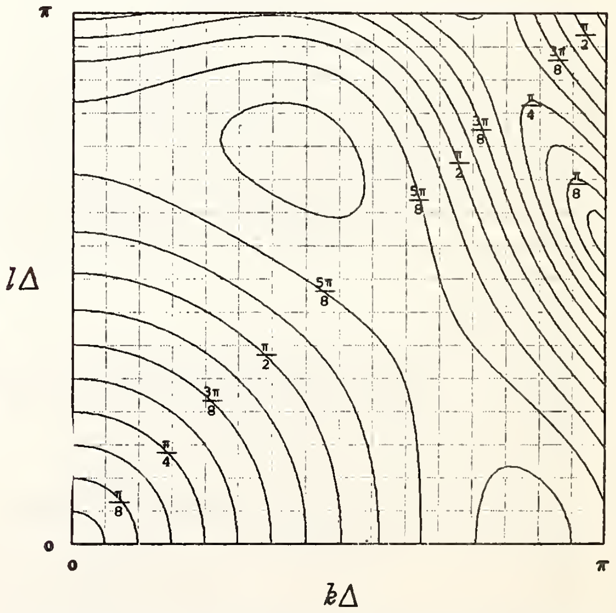

FIG. 7. Finite-element frequencies for time step that is one-fifth of maximum. The frequencies are somewhat closer to the exact frequencies than for Fig. 6.

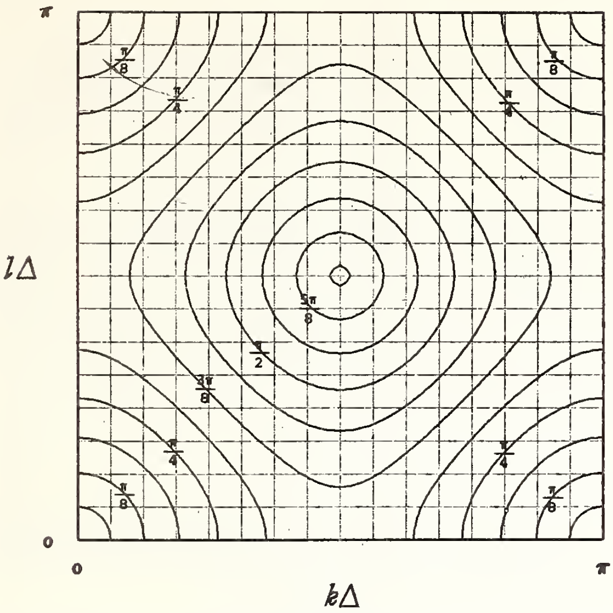

FIG. 8. Rectangular finite-difference contours. The grid spacing is the same for the centered-difference rectangular scheme as for the triangular schemes of Figs. 5–7.

cycles of the lowest frequency normal mode oscillations of the flat circular basin. Although the growth rate of the instability increased with increasing f for both schemes, the instability was still observable for the finite-difference computations for $f = 0$.

Another instability, associated with variable depth, was observed for the finite-element scheme but was not observed for the finite-difference scheme. The finite-element variable depth instability was apparent after 25 cycles of the lowest frequency normal mode oscillation, whereas the finite-difference scheme was capable of simulations of 50 cycles with no indication of instability. This result is contrary to that found for the one-dimensional case, where the finite-element results for variable depth were better than those of the one-dimensional finite-difference scheme. Because the simulations of normal mode oscillations were quite accurate before the instability dominated, there is no reason to believe that the instability can be attributed to an error in the computer code.

TABLE 1. Nondimensional frequencies $\omega R(gD_0)^{-1/2}$ for case of $D = D_0$, uniform depth circular basin.

n	m	$fR(gD_0)^{-1/2}$	Exact	Finite-difference	Finite-element
0	1	0.0	3.8317	3.79	3.87
0	3	0.0	10.1735	9.77	10.6
1	1	0.3	5.3507	5.30	5.40
0	4	0.3	13.3271	12.4	14.0

TABLE 2. Nondimensional frequencies $\omega R(gD_0)^{-1/2}$ for case $D = D_0(1 - r^2/R^2)$, parabolic depth circular basin. Although the finite-element simulations were unstable, the results of 10 cycles were quite good.

n	m	$fR(gD_0)^{-1/2}$	Exact	Finite-difference	Finite-element
1	0	0.0	1.4142	1.41	1.4
2	0	0.0	2.0000	1.99	2.0
2	0	0.3	2.1556	2.14	2.2
0	1	0.3	2.8443	2.83	3.0

5. Results of simulations

Comparisons of frequency estimates of the finite-element and finite-difference schemes for normal mode oscillations are given in Tables 1 and 2. The integers n and m correspond to the number of radial and concentric circular nodes of the normal modes and appear as parameters in the exact solutions (Thacker, 1977a). The third column is the value of the nondimensional Coriolis parameter. The exact nondimensional frequency is the highest of the three possible frequencies corresponding to the mode indices n and m. The simulations were initialized to agree with the exact solutions and were continued for 50 cycles of each mode, except for the variable depth finite-element simulations that were continued for only 10 cycles due to instability. Frequencies were estimated from the number of times the surface elevation crossed the still-water level. Because of computational expense, the finite-element simulations were restricted to grid 2. These simulations were still more expensive than the simulations of the finite-difference scheme with grid 3.

The variation in frequency estimates from the different grid points was less for the finite-element simulations than for the finite-difference simulations when calculations are compared which correspond to the same grid. Based upon the dispersion analysis, a possible explanation of this might be that, because of varying grid size, the time step used must be less than the maximum suitable for most of the grid, which results in a decrease in accuracy for the finite-difference scheme and an increase in accuracy for the finite-element scheme. The finite-element frequency estimates were high and the finite-difference estimates were low, in agreement with the results of the dispersion analysis. When comparing the results of the finer grid for the finite-difference scheme with those of the coarser grid for the finite-element scheme in Tables 1 and 2, the accuracy of the two schemes is comparable. However, the finite-difference scheme has the advantage of being computationally more economical, even with the finer grid.

6. Summary

Although the principles involved in deriving the finite-element and finite-difference schemes are quite different, the governing equations are similar in form. For the case of a uniform depth basin, the terms corresponding to spatial derivatives are identical for the two schemes. The most important difference in the schemes is the presence of spatial averages in the terms corresponding to temporal derivatives in the finite-element scheme, which are absent in the finite-difference scheme.

These spatial averages cause the finite-element scheme to be computationally much more expensive in several ways. First, they cause the equations to be implicit, so that they must be solved simultaneously to advance each time step. Also, they limit the size of the time step, so that more time steps are required for a finite-element calculation than for the corresponding finite-difference calculation. Furthermore, the coefficients involved in computing these averages must either be stored and retrieved or be reevaluated each time they are needed. Finally, additional multiplications and additions are required to evaluate these averages.

These spatial averages are also responsible for the differences in the dispersion characteristics of the two schemes. The finite-element scheme overestimates wave frequencies for the maximum allowable time step and increases in accuracy as the time step is decreased until it is about one-fifth maximum. The finite-difference scheme underestimates wave frequencies for all allowable time step sizes, but it is most accurate for the largest and most economical time step.

Both schemes are subject to computational instabilities. Instability associated with a highly irregular grid was observed for both schemes; however, for the finite-element scheme it was observed only for cases with the Coriolis force included. The finite-element scheme was also unstable when the depth of the basin was not uniform, but this instability was not observed for the finite-difference scheme.

In simulating normal mode oscillations, the finite-element scheme performed better than the finite-difference scheme when results obtained using the same computational grid were compared. However, the level of performance provided by the finite-element scheme can be obtained more economically by using a finer computational grid with the finite-difference scheme.

APPENDIX A

Formulas for Spatial Averages and for Approximations to Spatial Derivatives

If F represents U, V or H, then the average quantity $\bar{F}_i$ associated with the point i can be written

$$\bar{F}_i = \tfrac{1}{2}(F_i + \bar{\bar{F}}_i), \tag{A1}$$

where the contribution from adjacent points j is given by

$$\bar{\bar{F}}_i = \tfrac{1}{2} \sum_j a_j F_j. \tag{A2}$$

The factors a_j are given by the ratio of the total area of those triangular elements with vertices i and j (only one element if both i and j lie on the boundary, otherwise two) to the area A of the polygon formed by all the triangular elements with vertices at i (pentagon or quadralateral if i lies on the boundary, otherwise hexagon). The areas can be calculated from

$$A = \tfrac{1}{2} \sum_j x_j(y_{j+1} - y_{j-1}), \tag{A3}$$

where the summation index is cyclic in the clockwise direction over the vertex points of the polygons.

The approximations to the partial derivatives are calculated using the formulas

$$\left.\begin{aligned} \left(\overline{\frac{\partial F}{\partial x}}\right)_i &= (2A_i)^{-1} \sum_j F_j(y_{j+1} - y_{j-1}) \\ \left(\overline{\frac{\partial F}{\partial y}}\right)_i &= (2A_i)^{-1} \sum_j F_j(x_{j+1} - x_{j-1}) \end{aligned}\right\}, \tag{A4}$$

where the summation index is cyclic over neighboring points and where A_i is the area of the polygon formed by the triangular elements with vertices at point i.

The terms corresponding to gradients of surface elevation can be written

$$\left.\begin{aligned} \left(D\overline{\frac{\partial H}{\partial x}}\right)_i &= \tfrac{1}{2}\left[D_i\left(\overline{\frac{\partial H}{\partial x}}\right)_i + \left(D\overline{\overline{\frac{\partial H}{\partial x}}}\right)_i\right] \\ \left(D\overline{\frac{\partial H}{\partial y}}\right)_i &= \tfrac{1}{2}\left[D_i\left(\overline{\frac{\partial H}{\partial y}}\right)_i + \left(D\overline{\overline{\frac{\partial H}{\partial y}}}\right)_i\right] \end{aligned}\right\}, \tag{A5}$$

where the terms with double overbars are given by

$$\left.\begin{aligned} &\left(D\overline{\overline{\frac{\partial H}{\partial x}}}\right)_i \\ &\quad = (4A_i)^{-1} \sum_j [(D_j + D_{j+1}) \\ &\quad \times (H_j y_{j+1} - H_{j+1} y_j) - D_j H_i(y_{j+1} - y_{j-1}), \\ &\qquad\qquad + D_j(H_{j+1} - H_{j-1}) y_i] \\ &\left(D\overline{\overline{\frac{\partial H}{\partial y}}}\right)_i \\ &\quad = -(4A_i)^{-1} \sum_j [(D_j + D_{j+1}) \\ &\quad \times (H_j x_{j+1} - H_{j+1} x_j) - D_j H_i(x_{j+1} - x_{j-1}) \\ &\qquad\qquad + D_j(H_{j+1} - H_{j-1}) x_i] \end{aligned}\right\}, \tag{A6}$$

where the summation index is again cyclic over neighboring points.

If the depth is uniform, so that all D_j are equal, then the second and third terms within the brackets sum to zero with the result that

$$[\overline{D(\partial H/\partial x)}]_i = D_i(\overline{\partial H/\partial x})_i$$

and

$$[\overline{D(\partial H/\partial y)}]_i = D_i(\overline{\partial H/\partial y})_i.$$

APPENDIX B

Iterative Solution of Finite-Element Equations

Eqs. (10) can be written with the variables to be solved isolated on the left-hand side and with terms associated with neighboring grid points and previous time steps on the right-hand side, i.e.,

$$\left.\begin{array}{l}
\left.\begin{array}{l}
U_i^{n+1/2} = -\bar{\bar{U}}_i^{n+1/2} + X_i \\
V_i^{n+1/2} = -\bar{\bar{V}}_i^{n+1/2} + Y_i
\end{array}\right\}, \quad i = B+1, \ldots, I \\
\left.\begin{array}{l}
U_i^{n+1/2} = -\sin^2\theta_i[\bar{\bar{U}}_i - f\tau\bar{\bar{V}}_i]^{n+1/2} \\
\qquad + \sin\theta_i \cos\theta_i[\bar{\bar{V}}_i + f\tau\bar{\bar{U}}_i]^{n+1/2} + X_i \\
V_i^{n+1/2} = -\cos^2\theta_i[\bar{\bar{V}}_i + f\tau\bar{\bar{U}}_i]^{n+1/2} \\
\qquad + \sin\theta_i \cos\theta_i[\bar{\bar{U}}_i - f\tau\bar{\bar{V}}_i]^{n+1/2} + Y_i
\end{array}\right\}, \quad i = 1, \ldots, B \\
H_i^{n+1} = -\bar{\bar{H}}_i^{n+1} + Z_i, \quad i = 1, \ldots, I
\end{array}\right\} \tag{B1}$$

where

$$\left.\begin{array}{l}
\left.\begin{array}{l}
X_i = 2f_1\left[\bar{U}_i^{n-1/2} - g\tau\left(\overline{D\dfrac{\partial H}{\partial x}}\right)_i^n\right] + 2f_2\left[\bar{V}_i^{n-1/2} - g\tau\left(\overline{D\dfrac{\partial H}{\partial y}}\right)_i^n\right] \\
Y_i = -2f_2\left[\bar{U}_i^{n-1/2} - g\tau\left(\overline{D\dfrac{\partial H}{\partial x}}\right)_i^n\right] + 2f_1\left[\bar{V}_i^{n-1/2} - g\tau\left(\overline{D\dfrac{\partial H}{\partial y}}\right)_i^n\right]
\end{array}\right\}, \quad i = B+1, \ldots, I \\
\left.\begin{array}{l}
X_i = (U_i + \sin^2\theta_i\bar{\bar{U}}_i - \sin\theta_i \cos\theta_i\bar{\bar{V}}_i)^{n-1/2} \\
\qquad - 2g\tau\left[\sin^2\theta_i\left(\overline{D\dfrac{\partial H}{\partial x}}\right)_i^n - \sin\theta_i \cos\theta_i\left(\overline{D\dfrac{\partial H}{\partial y}}\right)_i^n\right] \\
Y_i = (V_i + \cos^2\theta_i\bar{\bar{V}}_i - \sin\theta_i \cos\theta_i\bar{\bar{U}}_i)^{n-1/2} \\
\qquad - 2g\tau\left[\cos^2\theta_i\left(\overline{D\dfrac{\partial H}{\partial y}}\right)_i^n - \sin\theta_i \cos\theta_i\left(\overline{D\dfrac{\partial H}{\partial x}}\right)_i^n\right]
\end{array}\right\}, \quad i = 1, \ldots, B \\
Z_i = (H_i + \bar{\bar{H}}_i)^n - 2\tau\left[\left(\dfrac{\overline{\partial U}}{\partial x}\right)_i + \left(\dfrac{\overline{\partial V}}{\partial y}\right)_i\right]^{n+1/2} \quad i = 1, \ldots, I
\end{array}\right\} \tag{B2}$$

The constants X_i, Y_i and Z_i can be evaluated from values at the previous time step. The average quantities $\bar{\bar{U}}_i^{n+1/2}$, $\bar{\bar{V}}_i^{n+1/2}$ and $\bar{\bar{H}}_i^{n+1}$ involve the unknown values of the variables at the next time step.

The strategy of the iterative solution technique is to obtain successive approximations that converge to the unknown values. Each approximation is obtained by substituting the previous values in the right-hand side of Eqs. (B1) and evaluating the left-hand side. Because of the leapfrog time structure, the momentum equations and continuity equations are iterated separately. For the first approximations, the values of the variables at the previous time step can be used. The next approximations to the variables are calculated in sequence, $i = 1, \ldots, I$. The $(k+1)$th approximation to the variables at grid point i involves the $(k+1)$th approximation to variables at points less than i, which are available because they have already been evaluated, and the kth approximations at points greater than i. Thus the equations are of the Gauss-Seidel type, and they require a minimal amount of computer storage locations.

Approximately 10 iterations are needed for convergence. No more iterations are needed if the number of grid points is increased. With increased number of grid points, the value of variables at neighboring points is more nearly the same and the time step is smaller, so the initial approximation based on previous values is better.

Overrelaxation did not improve convergence. No attempt was made to improve convergence by using block iterative or alternating direction techniques. Also, no comparisons were made to direct techniques.

REFERENCES

King, I. P., W. R. Norton and K. R. Iceman, 1975: A finite-element solution for two-dimensional stratified flow problems. *Finite Elements in Fluids*, Vol. 1, R. H. Gallagher, *et al.*, Eds., Wiley, 133–156.

Lamb, Horace, 1945: *Hydrodynamics*. Dover, Sections 191, 193, 210, 212.

Shen, Shan-fu, 1977: Finite-element method in fluid mechanics. *Annual Reviews of Fluid Mechanics*, Vol. 9, Annual Reviews, Inc., 421–445.

Taylor, C., and J. M. Davis, 1975: Tidal propagation in estuaries. *Finite Elements in Fluids*, Vol. 1, R. H. Gallagher, *et al.*, Eds., Wiley, 95–118.

Thacker, W. C., 1977a: Irregular grid finite-difference techniques: simulations of oscillations in shallow circular basins. *J. Phys. Oceanogr.*, 7, 284–292.

——, 1977b: Reply (to Comments of J. D. Wang), *J. Phys. Oceanogr.*, **7**, 933–934.

Wang, John D., and Jerome J. Conner, 1975: Mathematical modeling of near coastal circulation. MIT Sea Grant Program Rep. No. MITSG 75-13.

Physics of Fluids 21, No. 2, 291-292.

Stability of settling of suspended sediments

W. C. Thacker and J. W. Lavelle

Atlantic Oceanographic and Meteorological Laboratories, National Oceanic and Atmospheric Administration, Miami, Florida 33149

(Received 16 May 1977; final manuscript received 7 October 1977)

The solution to the equations of two-phase flow which describes hindered settling is unstable to small perturbations.

It is well recognized that the settling velocity of sediment in suspension decreases with increasing sediment concentrations when the suspension is horizontally homogeneous. On the other hand, if the suspended particles are clustered together, they can fall at a relatively high velocity. The former effect is called hindered settling and the latter, convective settling.[1] The existence of convective settling suggests that hindered settling might be unstable in some cases if the homogeneous distribution is slightly perturbed.

Recently, Thacker and Lavelle[2] showed that hindered settling is due to the increase in the apparent density of the suspension, to the upward counterflow of the suspending fluid, and to an increase in the drag force, all of which result from an increase in sediment concentration. The equations which were used in that previous work can also provide a framework for investigating the stability of hindered settling.

The equations

$$\rho_1 C\left(\frac{\partial \mathrm{u}_1}{\partial t} + \mathrm{u}_1 \cdot \nabla \mathrm{u}_1 + g\hat{k}\right) = -C\nabla p - DC(\mathrm{u}_1 - \mathrm{u}_2),$$

$$\rho_2(1-C)\left(\frac{\partial \mathrm{u}_2}{\partial t} + \mathrm{u}_2 \cdot \nabla \mathrm{u}_2 + g\hat{k}\right) = -(1-C)\nabla p + DC(\mathrm{u}_1 - \mathrm{u}_2),$$

$$\frac{\partial C}{\partial t} + \nabla \cdot (\mathrm{u}_1 C) = 0,$$

$$\nabla \cdot [\mathrm{u}_1 C + \mathrm{u}_2(1-C)] = 0, \tag{1}$$

were used by Thacker and Lavelle[2] as the starting point for their discussion of hindered settling. The first two are momentum equations for the sediment and for the suspending fluid, respectively. The third equation guarantees conservation of sediment, and the fourth is the incompressibility condition for the suspension. The density, velocity, and volume fraction concentration for the sediment and for the suspending fluid are ρ_1, u_1, C, and ρ_2, u_2, $1-C$, respectively; g is the gravitational acceleration, $\hat{k}$ is a unit vector in the vertical direction, p is the pressure, and D sets the strength of the drag force. The drag force is assumed to be linear in the relative velocity, but D is assumed to depend upon the sediment concentration.

The solution to these equations for hindered settling is

$$w_1 = -[(\rho_1 - \rho_2)g/D](1-C)^2,$$

$$w_2 = -w_1[C/(1-C)], \tag{2}$$

$$\partial p/\partial z = -[\rho_1 C + \rho_2(1-C)]g,$$

where $\mathrm{u}_1 = (0, 0, w_1)$ and $\mathrm{u}_2 = (0, 0, w_2)$. If D is assumed to have the form

$$D = D_0(1-C)^{2-\alpha}, \tag{3}$$

where D_0 is constant, w_1 will contain the hindering factor, $(1-C)^\alpha$, determined by Maude and Whitmore.[3]

Small perturbations from the homogeneous state described by Eq. (2) will grow if hindered settling is unstable. It is sufficient to assume that the perturbations are waves with variation $\exp[i(kx + lz - \omega t)]$, where k and l are horizontal and vertical wavenumbers, respectively, and ω is the frequency. For simplicity, variation is assumed to occur in only one horizontal direction.

The equations governing the perturbation amplitudes $\mathrm{u}_1^* = (u_1^*, 0, w_1^*)$, $\mathrm{u}_2^* = (u_2^*, 0, w_2^*)$, C^*, and p^* are

$$(\rho_1\Omega_1 - iD)u_1^* + iDu_2^* + kp^* = 0,$$

$$(\rho_1\Omega_1 - iD)w_1^* + iDw_2^* + lp^* - iD(1+r)Fw_1(C^*/C) = 0,$$

$$(\rho_2\Omega_2 - irD)u_2^* + irDu_1^* + kp^* = 0,$$

$$(\rho_2\Omega_2 - irD)w_2^* + irDw_1^* + lp^* + iD(1+r)(F+1+r)rw_1(C^*/C) = 0$$

$$\Omega_1(C^*/C) + ku_1^* + lw_1^* = 0,$$

$$ku_1^* + lw_1^* + \frac{k}{r}u_2^* + \frac{l}{r}w_2^* + lw_1(1+r)(C^*/C) = 0, \tag{4}$$

where $\Omega_1 = -\omega + lw_1$, $\Omega_2 = -\omega - rlw_1$, $r = C(1-C)^{-1}$, and where D and $F = CD^{-1}\,dD/dC$ are evaluated at the value of C which determines the base state. These equations are obtainable from Eq. (1) by assuming that the variables are the sum of the base state solutions given in Eq. (2) and the perturbation amplitudes and by neglecting terms which are nonlinear in perturbation amplitudes.

Solutions to Eq. (4) exist only if the determinant of the coefficient matrix vanishes. This determinant can be written as the product of two second-degree polynomials in the variable, ω/lw_1, so the condition that the determinant vanishes is that either

$$\omega^2 + [r - 1 + id(\rho r + 1)]\omega_0\omega - r[1 - id(\rho - 1)]\omega_0^2 = 0 \tag{5}$$

or

$$(r+\rho)\omega^2 + [2(r^2 - \rho) + id\rho(r+1)^2]\omega_0\omega$$
$$+ [r^3 + \rho + id\rho(r+1)^2(2r - 1 + F)]\omega_0^2 = 0, \tag{6}$$

where $d = D(\rho_1\omega_0)^{-1}$, $\omega_0 = -l(\rho_1 - \rho_2)gD^{-1}(1+r)^{-2}$, and $\rho = \rho_1/\rho_2$. It is interesting to note that these equations do not involve the horizontal wavenumber.

Equations (5) and (6) can be solved by the quadratic formula, and the solutions can be examined to see if the imaginary part of ω is positive. For the solutions to Eq. (5), $\mathrm{Im}(\omega)$ is never positive. However, for Eq. (6), $\mathrm{Im}(\omega)$ is always positive, so Eqs. (1) are unstable.

In order to test whether this result of unconditional instability, which contradicts the fact that hindered settling is observable, stems from neglect of viscous, virtual mass, or inertial[4] forces, Eqs. (1) were modified by adding terms, $\mathbf{F}_1$ and $\mathbf{F}_2$, to the right-hand sides of the momentum equations for sediment and for suspending fluid, respectively, and the stability analysis was repeated. For the case of viscous forces these terms were of the form,

$$\begin{aligned} \mathbf{F}_1 &= \mu_1 \nabla^2 \mathbf{u}_1 , \\ \mathbf{F}_2 &= \mu_2 \nabla^2 \mathbf{u}_2 . \end{aligned} \tag{7}$$

For the case of virtual mass forces, three forms[4–6] were used,

$$\begin{aligned} \mathbf{F}_1 &= -M\left[\frac{\partial \mathbf{u}_1}{\partial t} + \mathbf{u}_1 \cdot \nabla \mathbf{u}_1 - \left(\frac{\partial \mathbf{u}_2}{\partial t} + \mathbf{u}_2 \cdot \nabla \mathbf{u}_2\right)\right], \\ \mathbf{F}_1 &= -M\left[\frac{\partial}{\partial t}(\mathbf{u}_1 - \mathbf{u}_2) + \mathbf{u}_1 \cdot \nabla(\mathbf{u}_1 - \mathbf{u}_2)\right], \\ \mathbf{F}_1 &= -M\left[\frac{\partial \mathbf{u}_1}{\partial t} + (\mathbf{u}_1 - \mathbf{u}_2) \cdot \nabla \mathbf{u}_1 - \frac{\partial \mathbf{u}_2}{\partial t} + (\mathbf{u}_1 - \mathbf{u}_2) \cdot \nabla \mathbf{u}_2\right], \end{aligned} \tag{8}$$

with $\mathbf{F}_2 = -\mathbf{F}_1$ in every case. For the case of inertial forces,

$$\begin{aligned} \mathbf{F}_1 &= \nabla \cdot \left[\left(\frac{\rho_1 C \rho_2 (1-C)}{\rho_1 C + \rho_2 (1-C)}\right)(\mathbf{u}_1 - \mathbf{u}_2)(\mathbf{u}_1 - \mathbf{u}_2)\right], \\ \mathbf{F}_2 &= 0 . \end{aligned} \tag{9}$$

None of these terms was sufficient to prevent the instability.

Similar negative results of stability analyses of apparently stable two-phase flows have also been reported by Murray[7] and by Drew and Segel.[6]

[1] C. Kranenburg and H. J. Geldof, J. Hydraulic Res. 12, 337 (1974).

[2] W. C. Thacker and J. W. Lavelle, Phys. Fluids 20, 1577 (1977).

[3] A. D. Maude and R. L. Whitmore, Brit. J. Appl. Phys. 9, 477 (1958).

[4] S. L. Soo, Phys. Fluids 20, 568 (1977).

[5] T. B. Anderson and R. Jackson, Ind. Eng. Chem. Fundam. 6, 527 (1967).

[6] D. A. Drew and L. A. Segel, Stud. Appl. Math. 50, 233 (1971).

[7] J. D. Murray, J. Fluid Mech. 21, 465 (1965).

U. S. GOVERNMENT PRINTING OFFICE 1980 677-096/1236 Reg. 8

PENN STATE UNIVERSITY LIBRARIES
A000072832776